PROCEEDINGS

21st Canadian Rock Mechanics Symposium

RockEng12 - Rock Engineering for Natural Resources

Editor

Chris Hawkes

Associate Editors

Derek Kinakin, Sam Proskin, Denis Thibodeau

Symposium Jointly Organized by the Canadian Rock Mechanics Association and the Canadian Institute of Mining, Metallurgy and Petroleum

A Publication of:

The Canadian Rock Mechanics Association
http://www.carma-rocks.ca/

and

The Canadian Institute of Mining, Metallurgy and Petroleum
1250 - 3500 de Maisonneuve Blvd. West
Westmount, Québec, Canada H3Z 3C1
http://www.cim.org

Printed in Canada

Foreword

The 21st Canadian Rock Mechanics Symposium represents the continuation of a series that began in 1962; a series which has undergone many transformations over the course of its fifty year history. The 20th symposium in this series, held in Toronto in May, 2009, was the first to carry the RockEng (Rock Engineering) subtitle, and the first to be jointly organized by the Canadian Rock Mechanics Association (CARMA) and the Canadian Institute of Mining, Metallurgy and Petroleum (CIM). CARMA itself is a partnership between the CIM's Rock Engineering Society and the Canadian Geotechnical Society's Rock Mechanics Division. As such, this symposium may be viewed as a symbol of the cooperative spirit that exists amongst Rock Mechanics and Rock Engineering specialists across different disciplines in Canada.

Following on the success of RockEng09, which ran under the theme of "Rock Engineering in Difficult Conditions", CARMA and CIM decided to proceed with the 21st Canadian Rock Mechanics Symposium, RockEng12, in Edmonton. An organizing committee was appointed, and the theme "Rock Engineering for Natural Resources" was selected. In the context of natural resource development, Rock Engineering plays an essential role in the design and operation of oil and gas wells, mine shafts, underground excavations and surface mines. Further, Rock Engineering plays an important role in the measures taken to mitigate the impacts of natural resource development, and in the development of renewable energy sources. As the pursuit of these resources pushes to more extreme environments and the methods used to develop them become more complex, it has become imperative to account for a broad spectrum of processes on rock behaviour, and to seek means of characterizing rocks - and their responses to resource development operations - more thoroughly and more accurately.

This symposium proceedings volume is the result of over a year of effort, which included the formulation of the technical program by the Organizing Committee and the preparation of manuscripts by the authors. As we write this Foreword, RockEng12 itself lies ahead. We expect that it will bring together nationally and internationally recognized experts from industry, government and academia to discuss the advances made in Rock Mechanics and Rock Engineering for natural resource development. The symposium will include two days of short courses and a technical program that will run over three days. The symposium will expose graduate students, junior and senior industry engineers, academics and government representatives to the latest Rock Engineering challenges and solutions. When the symposium itself is over, it is the editors' belief that this proceedings volume will remain a valuable record of the materials presented, and will become a valuable reference for those working in Rock Mechanics and Rock Engineering. It is hoped that it will also be a constant reminder of the knowledge gained and the friendships made or renewed.

The production of this proceedings volume was a major undertaking, which involved a number of individuals. In this regard, we - the editors - would like to express our gratitude to all authors for their significant contributions, members of the RockEng12 Scientific Advisory Committee for guidance and – along with a number of other professionals - review of abstracts and papers, and to CIM National Office Staff for their hard work in organizing and administering the symposium. Chantal Murphy and Ronona Saunders of the CIM National Office deserve special mention for their efforts, as well as Cynthia Hanke (University of Saskatchewan) who administered the paper review process. Thanks is also due to RockEng12's sponsoring organizations for their support of this important event.

Chris Hawkes
Editor

Derek Kinakin
Sam Proskin
Denis Thibodeau
Associate Editors

About the Editors

Chris Hawkes attended the University of New Brunswick, where he received his B.Sc. in Geology-Physics in 1990 and his Ph.D. in Geology 1996. Upon graduation, he worked for Calgary-based consulting firm Advanced Geotechnology until 2002, at which time he became a faculty member in the Department of Civil and Geological Engineering at the University of Saskatchewan. His research interests include petroleum geomechanics (caprock integrity, wellbore stability), geological storage of greenhouse gases, and hydrogeological characterization of underground mine sites. He is the author of numerous papers and reports on these subjects. Dr. Hawkes is registered as a Professional Geoscientist in Saskatchewan and Alberta, and is Past-Chair of both the Canadian Rock Mechanics Association and the Rock Mechanics Division of the Canadian Geotechnical Society.

Derek Kinakin is a consulting engineering geologist and rock mechanics specialist based in Vancouver, B.C. with BGC Engineering Inc. Since completing his M.Sc. in the Department of Earth Sciences at Simon Fraser University in 2004, he has worked on mining projects in British Columbia, Alberta, Ontario, Alaska, Nevada, Mexico, the Dominican Republic, Eritrea, and Madagascar. Derek is interested in rock mass characterization, open pit design, rock foundations, and numerical modeling of large rock slope failures. His publications range from work on large slope failures to tunnels. He has completed multiple projects at the preliminary economic assessment, pre-feasibility, and feasibility levels of study and provides ongoing support to operating open pit mines. Derek Kinakin is a member of the Canadian Institute of Mining, Metallurgy and Petroleum and CARMA; he is a registered Professional Geoscientist in B.C.

Sam Proskin is Vice President Technical Services of Terracon Geotechnique Ltd. where he's responsible for providing business management and technical leadership to the civil engineering and geoscience teams. Prior to joining Terracon, Dr. Proskin was a Principal Specialist in the Geotechnical Group at EBA, A Tetra Tech Company where he worked over 15 years as a consulting engineer with projects encompassing geotechnical engineering, permafrost engineering, and ice engineering for clients in the prairies, NWT, Nunavut and Yukon. Dr. Proskin holds a B.Sc. in Geological Engineering from the University of Manitoba, and a M.Sc. and Ph.D. in geotechnical engineering from the University of Alberta. He has published and presented papers on topics in petroleum geomechanics, geotechnical engineering and ice engineering. Dr. Proskin is a member of the Canadian Geotechnical Society, APEGA, NAPEG and APEGM.

Denis Thibodeau is a Professional Engineer in Ontario and Quebec and holds a Doctorate in Civil and Mining Engineering from INPL (Institut national polytechnique de Lorraine, Nancy, France), a B.Eng. in Mining from McGill and B.Sc. in Geology from Montréal University. Denis has 17 years of experience in the mining industry working for Vale Inco and Barrick. He is currently the Manager of Strategic Rock Mechanics at Vale Inco.

Table of Contents

21st Canadian Rock Mechanic Symposium

RockEng12 - Rock Engineering for Natural Resources

PETROLEUM GEOMECHANICS

CONSTITUTIVE BEHAVIOUR

CARBON DIOXIDE SEQUESTRATION

KEYNOTES

MINING-RELATED ROCK MECHANICS

The Effect of Weak Layers on Pillar Performance in South African Chrome and Platinum Mines

Gregory C. More O'Ferrall
Rock Mechanics Manager, Tetra Tech
Daniel F. Malan
Group Rock Engineer, Gold Fields SA

ABSTRACT: Generally pillars in the Southern African hard rock tabular underground mining environment are designed using either empirical pillar design formulae or numerical modelling (analytical) methods utilizing the Hoek-Brown failure criterion. However, none of the pillar design methodologies employed takes cognizance of weak layers either within the pillar material or in the immediate foundation of the pillar.

Over the past few years, the presence of a weak layer either within the pillar material or within the immediate foundation of the pillar has resulted in the closure of one platinum mine (Everest Mine), closure of one chrome mine (Wonderkop Chrome) and large-scale instability in a couple of chrome and platinum mines in South Africa and Zimbabwe. A study has been initiated to better understand the failure mode and strengths of the pillars where pillar failure associated with weak layers occurred.

Owing to the infancy of the study into the failed pillar strength and failure mechanism, the purpose of this paper is to highlight the circumstances that led to the collapse of mining sections and a shaft, and the difficulty associated with designing pillars in the Southern African chrome and platinum mining operations.

1. INTRODUCTION

Southern African chrome and platinum mines generally operate at shallow to intermediate depths (surface to an approximate average depth of 700 metres below surface). Except for Northam Platinum, which is the deepest operating platinum mine in Southern Africa utilizing backfill for regional stability, all the operations make use of pillars to ensure local and regional stability for the on-reef excavations. Pillar performance requirements vary with some operations making use of crush pillars, one operation making use of yielding pillars and others making use of stable pillars.

Not all operations use the same methodology for pillar design, despite the operations typically being in close proximity to one another. Most operations make use of a typical Hedley-Grant type power formula, or some variation thereof, whilst another operation has made use of numerical modeling utilizing the Hoek-Brown failure criterion. However, both these methods make use of a number of assumptions regarding the rock mass strength and pillar loading mechanisms.

A number of operations have been adversely affected, from a stability point of view, owing to inappropriate assumptions being made whilst determining the pillar strengths. These operations are typically the shallower operations (average depth approximately 240 metres below surface). The case presented in this paper is one where there is a layer of weak material within the pillar material.

2. PILLAR DESIGN PRACTICES

As mentioned, pillar design in the Southern African chrome and platinum mines makes use of either some variation of the Hedley-Grant pillar design formula, or by making use of the Hoek-Brown failure criterion

to assess pillar stability in elastic numerical models (e.g. BESOL MSCalc). These methodologies are discussed below.

2.1 Empirical Method

Empirical design formulae are commonly used in pillar design, due to the simplicity in use. However, most "designers" do not take cognizance of the fact that the derivation of these formulae were in very different mining environments. The most commonly used formula is that of Hedley and Grant (1972), and takes the form:

$$P_s = k\frac{w^{\alpha}}{h^{\beta}} \quad [MPa] \tag{1}$$

where: P_s = pillar strength
k = strength of 1 m^3 of pillar material [MPa]
w = pillar width (sometimes the effective pillar width is used) [m]
h = pillar height [m]
α, β = numerical constants

Typical values for k vary from ⅓ Uniaxial Compressive Strength (UCS) to some form of down-rated rock mass strength (DRMS) where a rock mass rating system is used to estimate the rock mass strength. The UCS values are obtained from laboratory UCS tests conducted on core samples or from figures published in literature on similar commodities. Some mines make use of square pillars, and others make use of rectangular pillars, and hence use the effective pillar width in the calculations, where

$$w_{eff} = \frac{4\ x\ pillar\ area}{pillar\ perimeter} \quad [m] \tag{2}$$

The average pillar stress (APS) is determined by making use of the Tributary Area Theory (TAT). Acceptable factors of safety (P_s/APS) of greater than 1.5 are deemed acceptable for a stable pillar environment, and this is used to determine the pillar size.

Numerous studies have been conducted as part of research programmes in order to obtain design formulae specific to the platinum-bearing reefs, but these have yet to be verified in the operations. These formulae were derived for typical ground conditions, where no weak layers are present in the pillar material. To date none of these design formulae have been implemented, with the Rock Engineers preferring to use what is currently in use. This could be due to the fact that no large-scale pillar failures have occurred in normal ground conditions, on which these studies have been conducted.

2.2 Analytical Method

A single operation in South Africa makes use of the analytical design methodology. The pillar design method (Day and Godden, 2000) relies on Hoek-Brown's failure criterion to define non-linear relationships between pillar strength and pillar volume. The choice of using the Hoek-Brown criterion is based on the geotechnical characteristics of the UG2 and Merensky platinum-bearing reefs. These characteristics include:

- The effects of joints are limited and localized for reasons of their orientation and generally wide spacing; therefore

- The insitu performance of both reefs depends on their bulk strength and insitu stiffness, hence the strength of pillars depends on their volume that may be represented as width/height ratios for any fixed mining width.

A basis for the use of the Hoek-Brown criterion is the assumption that if the failure criterion depicts the laboratory-determined strength of the reef material to an acceptable degree of accuracy, then it is reasonable to suppose that it predicts the insitu strength of the reef material to a similar degree of accuracy.

The starting point of the pillar strength estimation process (Godden, 2011) is the determination of the average intact and bulk insitu Hoek-Brown constants for the pillar-forming material. This process is summarized as follows:

- The potential for variable seam/reef strengths should first be tested using the point load index method applied to drillcore intersections of the target mining horizon;
- The pillar section and resource block of interest should then be characterized, and in terms of the distribution of any identified groups or ranges of material strengths, from which a targeted laboratory testing programme should be scoped;
- Validated laboratory test results should be used to establish statistically acceptable average intact material properties for each material type within the pillar section and resource block of interest (specifically m_i and σ_c of the Hoek-Brown criterion);
- Additional tests and/or refinement of the initially defined material type groupings may be required;
- The distribution and persistence of material types within a single pillar volume located in each defined material type domain, should then be considered in detail, thereby realizing average design properties for cut pillars within each material type domain; and
- Average, best and worst-case RMRs for each area for each encompassing material type domain should then be estimated and applied to define bulk insitu material properties for each material type domain, using relevant bridging solutions to derive the constants m_b, s_b and $\sigma_{c\ (mass)}$ of the Hoek-Brown criterion.

A 2-dimensional boundary- or finite-element numerical model, to which bulk insitu modelling constants should be applied, is then used to determine the Average Pillar Stress on various size pillars at various depth ranges. It is important to reduce the bulk insitu pillar stiffness by the extraction ratio across the modelled pillar width in the out-of-plane direction. The pillar size is determined by altering the pillar width until such time that the ratio of Average Pillar Stress to Average Compressive Strength is a minimum of 1.5.

3. CHROME MINE CASE STUDY

This case history indicates what happens in an operation where a weak layer within the pillar material may initially appear not to have any effect on the strength of the pillar. However a change in the loading orientation on the pillar resulted in large-scale pillar failure associated with the weak layer.

A chrome mine in the North-West Province of South Africa is mining the MG2 chrome seams at an average depth of 270 metres below surface (mbs) and dip of 12°. Typical stratigraphy in the immediate vicinity of the chrome seams is indicated in Figure 1.

The initial mining method was strike-orientated conventional hand-held drilling with mechanical scraper cleaning. Layouts indicated 8-metre wide x 15-metre long pillars separated by a 2-metre wide ventilation holing (Treloar, 2012). Panel spans were 16-metres wide and the mining height was on average 2.4 metres. A 2-metre square pillar was required, in the centre of the panel, every 25 metres. The purpose of

the 2-metre square pillar was to prevent the occurrence of a back-break of the immediate 5-metre thick Anorthosite hangingwall layer. This layout was suitable for a mining depth up to 200 m (Figure 2).

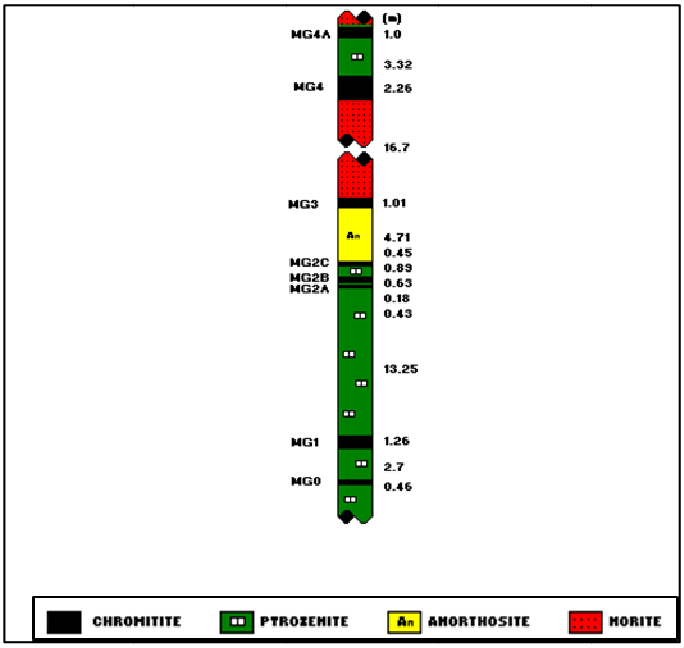

Figure 1 - Typical stratigraphic column on mining property

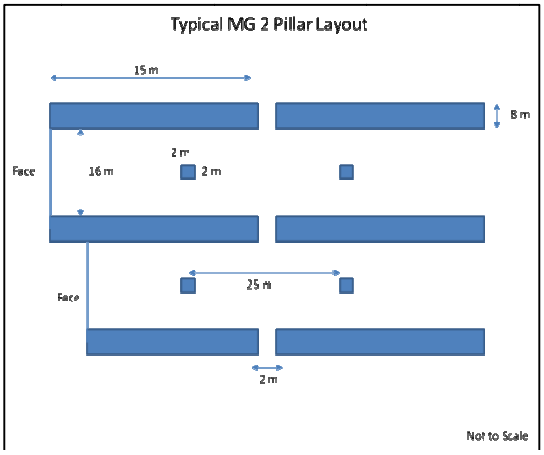

Figure 2 - Typical layout for the MG2 seam horizon up to a depth of 200 m

With a change in Rock Engineering management, changes were made to this layout. Pillar widths were reduced to 6-metres in working places deeper than 200 m and the 2-metre square pillars were removed. A mechanized bord and pillar mining method, at a mining height of 2.1 metres, was introduced in order to increase the rate of production and address safety-related issues due to an increase in falls of ground in the panels. Pillar dimensions remained 6-metres wide x 15-metres long, but strike and dip bords were developed at a width of 8-metres.

Pillar design was done using the Power Formula (1) with k = 35 MPa, α = 0.5 and β = 0.75 (after Stacey and Page recommendations for w:h ratios < 4.5). The k-value used was based on data that was obtained decades earlier when the Feasibility Study was conducted on the mining property (UCS = 110 MPa). Owing to the low commodity price of chrome, no further testing was done to determine a representative strength of the chrome seams on the property. A value of ⅓ the UCS of the values for chrome was used. Pillar design was carried out making use of the following formula:

$$P_s = 35\frac{w^{0.5}}{h^{0.75}} \quad [MPa] \tag{3}$$

Bord and pillar mining was carried out on a chrome seam for many years without any indication of a detrimental influence of the weathered pyroxenite layer within the MG2 chrome seams.

Mining commenced on a second chrome seam, MG1, approximately 13 metres below the MG2 seams. Initially the pillars were superimposed below the top seam, but a decision was made by mine management to change the direction of advance of the lower seam. This resulted in the rectangular pillars of the lower seam punching into the bords of the top seam (Figure 3).

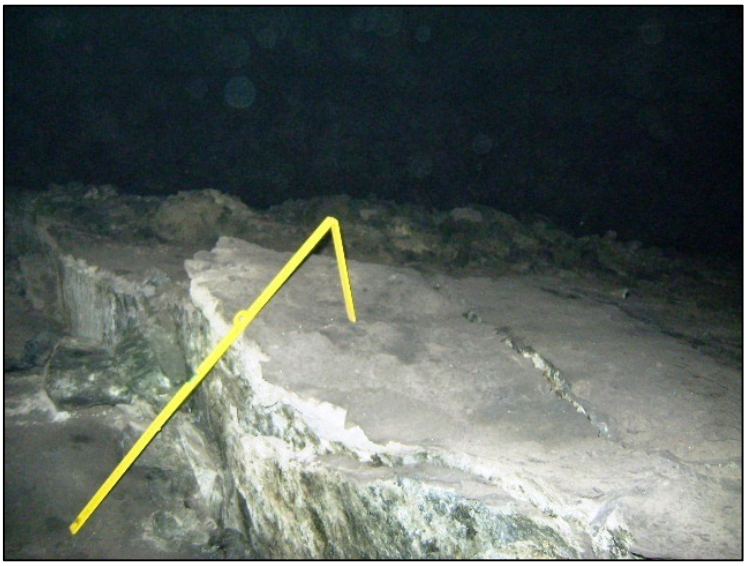

Figure 3 - Footwall heave in the bords on the MG2 chrome seam horizon

The change in pillar load resulted in the activation of shear failure along a weathered pyroxenite layer that was present within the pillar material (Figure 4). Large-scale pillar failure resulted in the abandonment of entire mining sections on both reef horizons and instability in the on-reef decline shaft on the MG1 seam.

Figure 4 - Deformation of 75 cm along weathered pyroxenite layer

4. CONCLUSION

Although there is no evidence that the pillar design formula implemented on the MG2 and MG1 chrome seams may have been inappropriate, the purpose of discussing this case history is to indicate that the pillar systems should not be designed in isolation from future mining operations. The major assumption made in any pillar design exercise, is that the direction of maximum pillar load is normal to the reef/seam horizon. A change in this direction will affect the performance of the pillar, as has been indicated in the above example. Pillar design is not a once-off exercise, and continuous analysis and potential improvements into the design methodology must be conducted. Mining layouts should consider the effect that they may have on previously mined areas which may, in turn, impact on current mining activities.

5. PILLAR DESIGN WITH THE PRESENCE OF WEAK LAYERS WITHIN THE PILLAR MATERIAL

Although a significant amount of research has been conducted into the effect of jointing in pillar-forming material (e.g. Iannacchione, 1999, Esterhuizen, 2000, Esterhuizen et al, 2006), research into pillar design where layers of weak material are present within the pillar material is minimal in comparison.

Malan (2009) conducted a study into the effects of weak discontinuity interfaces on pillar strength for a platinum mine in South Africa. The study made use of a continuum finite difference model, and results indicated that there is small or negligible influence of slippery multi-layer jointing within the pillar material, but major influence of slippery foundation contact jointing. The presence of a weak parting 1 metre into the foundation of the pillar also has a marked weakening effect on the pillar. Investigation into the cause of the weakening effect revealed that a pillar, especially while its elements are failing, tends to strongly dilate laterally. With normal frictional contacts, both in the laboratory and insitu, this dilation is restrained; thus generating lateral confining stresses which strengthen the pillar.

Iannacchione (1990) conducted a study on the influence of slippery interfaces within coal pillars. The results of his study concluded that:

- Interface slip tends to control the rate at which the inelastic yield zone develops in response to increasing increments of applied pressure;
- As the material properties of the interface approach that of the yielded coal pillar, its effect on pillar strength diminishes almost uniformly;

- The interface slip mechanism allows the coal pillar to move into the mine opening;
- The addition of the interface slip mechanism with a linear failure criterion/strain softening model still does not correctly reproduce the behaviour of the coal pillars; and
- The effects of interface slip should be considered in designing large coal pillars. Failure to do so may result in overestimating pillar strength.

Esterhuizen and Ellenberger (2007) conducted studies into the effect of weak bands on pillars in U.S. stone mines. Numerical modelling and field observation assessments were made and it was concluded that:

- The extrusion-tensile failure mode typically initiates at the perimeter of a pillar and progresses inwards, reducing the effective width of the pillar;
- Weak bands can cause rib failure to initiate when the average pillar strength is only about 10% of the limestone strength;
- Slender pillars are more severely affected by the presence of weak bands than wider pillars;
- Pillar strength is adversely affected as the thickness of the weak bands increase; and
- Model results show that single weak bands can have a significant effect on pillar strength if their thickness exceeds about 2% of the pillar height.

Godden (2011) has identified the shortcoming with the analytic approach where weak layers are present within the pillar-forming material stating: “Established rock engineering theory shows that where a band of weak material exists, it can squeeze out of its confined state once the applied normal stress exceed some critical magnitude that depends on the condition, hence material properties of the shear-forming material.”. A methodology that he has recommended to solving the issue associated with weak material is to perform applicable numerical modelling (in his example using FLAC^{3D}) to determine a maximum Average Pillar Stress that may be applied to the pillar before shear failure commences along the weak layer. This design approach must be followed for each instance where weak layers are present within the pillar-forming material, and caution must be taken not to use the results from one study area to design pillars in a different geotechnical environment.

6. CONCLUSIONS

Pillar design in the South African Bushveld Complex is being conducted using either empirical design formulae or analytic methods. Both methods have historically appeared to be applicable, as no large-scale pillar system failure has been recorded. However, the applicability of the implemented designs is questionable.

Empirical designs have typically employed a power formula, locally termed the Hedley-Grant pillar design formula, with very little understanding as to the derivation thereof and the geotechnical environment for which it was derived.

Analytic pillar designs have historically only been used for one platinum producer, but a second platinum producer has adopted this methodology within the past year. This design approach at first appears to be more applicable than the empirical design approach in that more of the pillar-forming and loading material properties are considered compared to that of the empirical method. However, many assumptions are made in this methodology, a major one being that the test samples are representative of the rock mass in which the pillar system will be employed.

None of the systems takes cognizance of the presence of weak layers within the pillar-forming material or within the immediate foundation of the pillars. Failure to recognize the influence of the weak layers has

resulted in the closure of a chrome and a platinum mine, and collapse of large sections of operating mines. To date there is no defined methodology to design pillars where these layers exist, although caution is given not to overestimate the strength of pillars where these layers do exist.

According to Malan (2010), it appears that neither of the two design approaches currently provide a solid basis on which to conduct pillar design, but recommends that both techniques be utilized in order to obtain the best possible insight into the effect these layers will have on the pillar strength.

7. ACKNOWLEDGEMENT

This review into pillar design in the chromitite-bearing rocks within the Bushveld Complex forms part of the PhD studies of Gregory More O'Ferrall. This study is being conducted through the University of Pretoria.

8. REFERENCES

DAY, A.P. and GODDEN, S.J., 2000. The design of panel pillars on Lonmin Platinum's mines. South African National Institute of Rock Engineering Symposium.

ESTERHUIZEN, G.S., 2000. Jointing effects on pillar strength, 19th conference on Ground Control in Mining, p.286-290.

ESTERHUIZEN, G.S. and ELLENBERGER, J.L., 2007. Effects of Weak Bands on Pillar Stability in Stone Mines: Field Observations and Numerical Model Assessment. 26th International Conference on Ground Control in Mining

GODDEN, S.J., 2011. Pillar Design for Bushveld Mining, p.58.

HEDLEY, D.G.F. and GRANT, F., 1972. Stope-and-Pillar Design for the Elliot Lake Uranium Mines. CIM Bulletin for July 1972, p. 37 – 44.

IANNACCHIONE, A.T., 1999, Analysis of pillar design practices and techniques for U.S. limestone mines, Institution of Mining and Metallurgy.

IANNACCHIONE, A.T., 1990. The effects of roof and floor interface slip on coal pillar behaviour.

MALAN, D.F., 2009. The effects of weak discontinuity interfaces on pillar strength. Technical note.

MALAN, D.F., 2010. Pillar design in hard rock mines – can we do this with confidence? Second Australian Ground Control in Mining Conference.

TRELOAR, M.L., 2012. Personal communication on the historical design of pillars on Samancor's Mooinooi Chrome Mine, South Africa.

Implications of Shear Loading for Mine Planning and Design

Fidelis T. Suorineni
MIRARCO – Mining Innovation / Geomechanics Research Centre
Peter K. Kaiser
Centre for Excellence in Mining Innovation (CEMI
Joseph J. Mgumbwa
MIRARCO – Mining Innovation / Geomechanics Research Centre
Denis Thibodeau
Vale, Mines and Mill Technical Services

ABSTRACT: The conditions for rockburst occurrence are traditionally identified as: high stress, high extraction ratio, strong brittle rocks, folding, faulting, and unfavourable excavation geometry. Based on a critical review of case histories, this paper identifies oblique loading of orebodies by the major far field principal stress as a cause of rockbursts. Orebodies subjected to this loading condition are termed orebodies in shear. Orebodies in shear are subjected to compressive and shear loads. The case histories presented unambiguously show that the magnitudes of the far field principal stress alone, and a knowledge of the conventional rockburst causing factors are not sufficient for mine planning and design. The orientation of the major far field principal stress, or for that matter the driving stress relative to the orebody axis, should be recognised as one of the causes of rockbursts. It is suggested that since stress orientation is an important factor, and orientations from stress measurements are so variable, orientations from stress measurement data be complemented with underground observations from borehole and excavation breakouts to determine the actual in situ stress orientation, whenever possible. Also stress modelling for the design of critical elements (pillars) should include a sensitivity analysis on the relative critical field stress direction. The paper emphasises that special attention should be paid to orebodies loaded in shear in mine planning and design to minimize risk in the mining of such orebodies.

1. INTRODUCTION

The factors previously identified as favourable conditions for the occurrence of rockbursts include high extraction ratio, strong brittle rocks, depth (high stress) with the major principal stress perpendicular to orebody strike, discrete geological structures such as faults and shear zones, dip and shape of orebody, stoping sequence and mining rate.

Not all the causes of rockbursts are known. Salamon (1983) states as follows: ‘A disconcerting feature of rockbursts is that they defy conventional explanation.’ Blake and Hedley (2003) state that rockbursts occurred at a depth of 150 m at the Director Fluorspar Mine in Newfoundland and on the surface in granite quarries in Vermont. Homestake Gold Mine in South Dakota did not experience rockbursts until at a depth of 2100 m after operating for a century. Blake and Hedley (2003) report that the worst rockburst in North America occurred in the Solvay Trona Mine in Wyoming in 1995 with a magnitude of 5.2 local magnitude (ML). They noted that these observations contradict current understanding of causes of rockbursts.

The geometry of an orebody as it relates to the principal stress orientation has been paid little attention as another cause of rockbursts because of the assumption that most orebodies have the maximum principal stress perpendicular to the strike.

Orebody geometry is controlled by its genesis and can be complex or consist of multiple lenses at different orientations. For these reasons the major in situ principal stress may not be aligned perpendicular to an orebody but oblique to it.

Over the past 10 years, experience at the Geomechanics Research Centre (GRC) (Kaiser and Suorineni, 2005) has included reviewing from three orebodies with major far field stress oblique to the strike or dip. This work shows several characteristics that differentiate them from those having major far field stresses perpendicular to the strike or dip. It was observed that these orebodies were characterised by high dilution and unusually frequent seismic activities at locations where they were least expected during mining.

When the major far field in situ or driving stress is oblique to the dip (Figure 1a) or strike (Figure 1b) of an orebody, it subjects the orebody to both compressive and shear stresses. In this paper, these orebodies are termed orebodies in shear.

a. Major principal stress being oblique to orebody dip

b. Major principal stress being oblique to orebody strike (plan view)

Figure 1 - Schematic of shear loading mechanisms

This paper presents the characteristics and consequences of shear loading from case histories, to create awareness, identify characteristics of this loading mechanism, and point out the risks of not accounting for it in the planning and design for the extraction of such orebodies. The next section discusses hints that an orebody, or some orebody lenses in a mine, may be subjected to shear loading.

2. CAUSES AND EVIDENCE OF SHEAR LOADING IN OREBODIES

2.1 Orebody Complexity

Francis et al. (1997) states that orebody complexity relates to such parameters as the morphological, grade, geotechnical and geological characteristics. These parameters are related to the orebody genesis. Thus, understanding the genesis of mineralisation is vital for planning the orebody extraction method and sequence. Brown and Rosengren (2000) states that poor detailed knowledge of the orebody geometry in underground metalliferous mines can result in dilution or incomplete recovery or both. Generalisation of the orebody, such as assumptions about the in situ stress relationship for a complex orebody, can result in unforeseen stability issues.

Vein type deposits often present the most complex orebody geometries, and are more prone to some parts being loaded in shear and others not, in the same stress regime.

2.2 Misinterpretation of Stress Measurement Data

Regional and local stress measurement results often show great variability in both stress magnitudes and orientations (Arjang and Herget, 1997). Grabinsky et al. (1997) state that even in the most homogeneous geomechanical domains, the stress magnitudes and orientations can vary by ±15 to ±30% about the component's mean values and direction.

In order to minimise the risk of mischaracterising orebody–stress relationships, it is suggested that in situ stress measurements be complemented with borehole and excavation breakout surveys when possible.

3. CASE HISTORIES

This section presents case studies on some of the consequences and implications when mining orebodies under shear loading without recognising the shear loading phenomenon and planning to mitigate the consequences. The mines discussed were identified based on published information and the observations of abnormal behaviour after the fact. The orebodies in these mines were found to fulfil one or a combination of the following conditions:

- Major far-field stress is oblique to the strike or dip, and orebodies continuous or discontinuous.
- Pillars are loaded in shear, causing them to be burst prone.
- Orebodies are 'narrow veins' with a width less than or equal to 5 m.

The descriptions of these case studies focus on the impact of shear loading on the failure mechanisms of pillars, stopes and offsets. Efforts were made to describe the failure mechanisms as they relate to the orebody geometry, in situ stress regime, geology, rock mass properties and mining practice. Four underground hard rock mines, three in Canada and one in Chile, and one soft rock German potash mine are presented to show the impact of shear loading on mining orebodies in shear.

3.1 Quirke Mine

3.1.1 Background

This case history is well documented in Coates et al. (1973), Hedley et al. (1985), Hedley (1992) and Blake and Hedley (2003). It shows how change in pillar alignment resulted in shear loading and affected pillar stability. The pre-mining state of stress is described by Coates et al. (1973). Room and pillar mining was the selected mining method. Rib pillars were used. The extraction ratio ranged from 70 to 80% depending on the depth and reef thickness.

In the central part of the mine plan (Figure 2) a local roll in the orebody with a dip of 15° produced a distance of 180 m between the 7 and 8 sill drifts. This would have resulted in stope lengths too long to be effectively recovered with slushers as was the practice at the mine. Hence, the top 60 m was converted to a trial trackless area with the pillars aligned 45° to strike with width to height ratios retained as before.

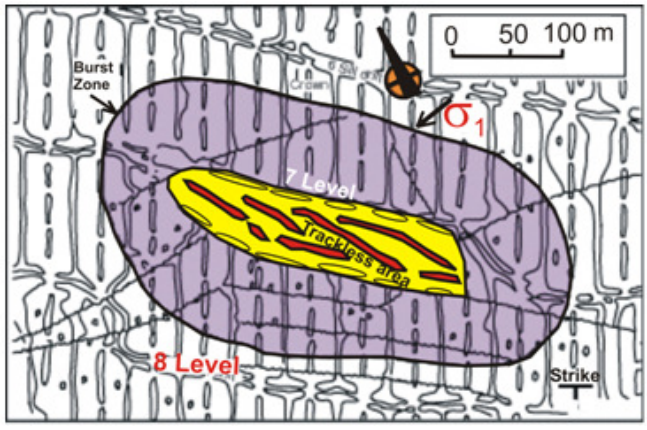

Figure 2 - Mine plan between 7 and 8 level drifts showing trackless area (yellow) with re-aligned pillars and rockbursts zone: (violet) (modified after Martin 2006)(From Suorineni et al., 2007)

3.1.2 Ensuing Ground Control Problems

A summary of the ensuing ground control problems at Quirke Mine 4 years after mining the trackless area is given by Hedley et al. (1984) as follows:

- Rockbursts initiated in the sill and crown pillars on the 7 level near the trackless area.
- Relatively non-violent failure appeared to have occurred in the slender rib pillars, especially those in the trackless area (about 6 m high by 3 m wide).
- Roof falls that occurred appeared to have been controlled by geological structure and triggered by vibrations from nearby seismic events.
- The area of pillar deterioration expanded gradually over a period of about two years.
- Accelerating convergence rates coincided, and in some cases preceded increasing seismicity.

3.1.3 Impact of Shear Loading

It is considered likely that the re-aligned rib pillars at 45° to the strike of the orebody and to the major far field principal stress resulted in their being loaded in shear along the short axis, causing them to be weaker. They then yielded gradually, shedding their load to the neighbouring pillars aligned on dip. The neighbouring rib pillars, with high width (W) to height (H) ratios (squat pillars), then failed violently.

Hedley et al. (1984) conducted stress analysis on the Quirke Mine pillars. Two identical pillars at the same extraction ratio with one pillar being aligned on dip and the other on strike were analysed. The results are shown in Figure 3. The on-dip rib pillar is stable while the pillar on strike failed.

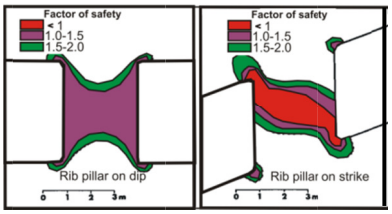

Figure 3 - Stability of rib pillars aligned on dip and strike (modified after Hedley et al., 1984) (From Suorineni, Kaiser, Mgumbwa, & Thibodeau, 2011)

3.2 Lac Shortt Mine

3.2.1 Background

A detailed description of Lac Shortt case history can be found in Ecobichon et al. (1992) and Falmagne (2001). This case history shows how not taking shear loading into account in mine planning and sequencing resulted in elevated risks of seismicity and high dilution.

The maximum principal stress was inclined at 45° with respect to the strike of the orebody in the NW–SE direction. The k-ratio is about 4 in the NW-SE and 2 in the NE–SW directions. The high k ratio of 4 is unusual in the Canadian Shield where it is on average 2.

The upper zone was mined using open stoping. The mining in the upper zone resulted in secondary pillars that were rockburst prone. The lessons learnt in this zone, resulted in change in the mining method to a modified AVOCA with delayed backfill (Ecobichon et al., 1992).

3.2.2 Ground Control Issues Experienced

Falmagne (2001) summarised the ground control problems encountered at Lac Shortt Mine as: deterioration of footwall and orebody developments, stope dilution, major falls of ground and caving of stopes, and sill pillar rockburst at shallow depth of ~250 m, and common shakedown failures were wide spread.

A review of seismic activity from microseismic monitoring indicated the rockbursts were either in the hanging wall or footwall depending on the mining direction (Falmagne, 2001) (Figure 4).

3.2.3 Impact of Shear Loading

The conclusion from microseismic monitoring was related to the major far field stress orientation relative to the strike of the orebody (Figures 4a and b). The two figures show that depending on the mining direction the hangingwall or footwall is continuously degraded as the mining front advances.

3.3 F zone at Campbell Red Lake Mine

3.3.1 Background

Campbell Mine is an underground gold mine in Balmertown on Highway 125, 4 km east of the town of Red Lake. The detailed geology of Campbell Mine is in Zhang et al. (1997).

Various consultants' reports (Hedley et al., 1985; Golder Associates, 1999) on the F zone, following the first rockburst in this area of the Campbell Mine, contain detailed descriptions of the mine, mining practices, and the problems encountered during mining.

The mining method in the F zone of Campbell Mine changed over the years to suit the ground conditions. Initially, the main mining method was shrinkage stoping with box hole pillars and 6.1 m wide sill pillars. By 1992 mining below 600 m was by overhand cut and fill with de-slimed tailings as backfill. Current production is from cut and fill and longhole stoping.

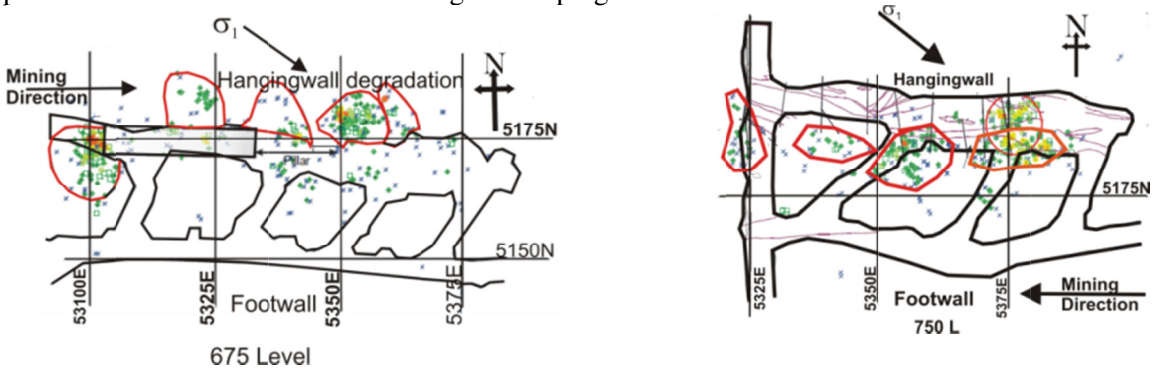

(a) Mining from west to east (b) Mining from east to east

Figure 4 - Effect of mining direction on host rock stability (Falmagne, 2001)

3.3.2 F Zone Ground Control Problems

Figure 5 shows the overall pattern of ground control problems in the F zone. Problems started with the deterioration of the boxhole pillars, leading to the first rockburst on the 11 level in 1981. A major

rockburst occurred on the 8 level on 31 December 1983. The extent of damage caused by the event was widespread resulting in production shut down.

The historical burst records and in situ stress measurement data were reviewed by Kaiser and Suorineni, (2005) including an underground tour to observe the mine infrastructure performance. As stated in Suorineni (2007) the reviewed data suggested that contrary to Arjang (1991) and previous consultants' conclusions, the major far field principal stress is not normal to the orebody strike, but is instead 25° to it (Figure 6). Figure 6 shows details of the F zone orebody geometry and how it relates to the major far field principal stress. A unique feature of the F zone orebody is that it consists of four en-echelon primary ore lenses with offsets of various geometries. Numerical modelling of the F zone with the major far field stress oblique to it showed that the offsets were highly stressed and burst prone.

3.4 El Teniente Mine

3.4.1 Background

This case study is drawn heavily from Kvapil et al. (1989). Between 1976 and 1980, a series of rockbursts occurred in one of the mine production zones resulting in short and long term disruption of mining activities. Following the assumption that a rockburst will not reoccur at the same place, a new mining level was developed 12 m below the former production level destroyed by a rockburst in 1980. On 17 December 1987, the new level was again destroyed by a more massive rockburst than those that occurred between 1976 and 1980.

3.4.2 Cause of unusual rockbursts at El Teniente

To explain the cause of the unusual rockbursts, Kvapil et al. (1989) hypothesised that in triaxial compression rock accumulates a much higher strain energy than the same rock in uniaxial compression, and that in shear the same rock will accumulate still less energy before failure. A change in the loading mechanism from pure compression to compression and shear makes a rock behave as a more brittle material and allowing it to fracture by rockbursting.

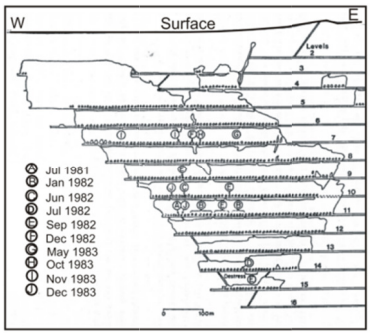

Figure 5 - Vertical section showing F zone sequence of boxhole pillars deterioration between 1981 and 1983 (Hedley, 1992)

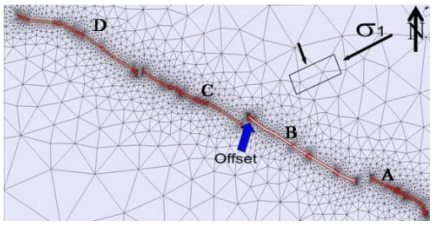

Figure 6 - Oblique loading by major far field principal stress and offsets (Kaiser and Suorineni, 2005)

3.5 Thalmann Potash Mine Disaster

The Thalmann Potash Mine disaster on 8 July 1958 resulted in the collapse of Merkers (Whyatt and Varley, 2008). A 4.8 M_L rockburst destroyed Merkers and generated microseismic activity 2000 km away from the source. Shear loading was for the first time used to explain the cause of this rockburst.

4. IMPLICATIONS OF SHEAR LOADING FOR MINE PLANNING AND DESIGN

The case histories presented, unambiguously show that the magnitudes of the far field principal stress alone are not sufficient for mine planning and design. They also show that the present generalisation that most orebodies, particularly tabular orebodies, are oriented perpendicular to the major far field principal stress is can be misleading in some cases.

The orientation of the major field stress relative to the orebody axis is critical for the safe and economic extraction of orebodies and should always be taken into account in mine planning and design. The case histories show that improper establishment of the orebody geometry-major far field stress relationship can result in ground control problems where they are least expected.

More favourable ground conditions could be created, and many of the disasters avoided or at least minimised, if in the mine planning and design stages the engineers in the various case histories had established that the orebodies at hand were subjected to both compression and shear loading, and more importantly had the awareness that orebodies under shear loading require a different mine planning and design approach to avert ground control problems.

5. CONCLUSIONS

The complex geometries of orebodies, the occurrence of orebodies in multiple lenses within a mine, and inaccuracies in the determination of actual in situ stress orientations imply that there are more orebodies under shear loading than generally assumed. The generalisation that most orebodies have their axis perpendicular to the major far field stress is misleading.

6. REFERENCES

ARJANG, B. 1991. Pre-mining stresses at some hard rock mines in the Canadian Shield, Bull. Can. Min. Metall., 84, (945), p. 80–86.

ARJANG, B. and HERGET, G. 1997. In situ ground stresses in the Canadian hard rock mines: an update. Int. J. Rock Mech. Min. Sci., 34, (3/4), p. 1–16.

BLAKE, W. and HEDLEY, D. G. F. 2003. Rockbursts: case studies from North American hard-rock mines, Littleton, SME, 121 p.

COATES, D. F., BIELENSTEIN, H. U. and HEDLEY, D. F. G. 1973. A rock mechanics case history of Elliot Lake. Can. J. Earth Sci., 10, (7), p. 1023–1058.

ECOBICHON, D., HUDYMA, M. R. and LAPLANTE, B. 1992. Underground geomechanics problems through microseismics monitoring at Lac Short, Proc. 94th Ann. General Meet. CIM, Montreal, Que., Canada, 2003 May, CIM, 13 p.

FALMAGNE, V. 2001. Quantification of rock mass degradation using micro-seismic monitoring and application for mine design, PhD thesis, Queen's University, Kingston, Ont., Canada.

GOLDER ASSOCIATES. 1999. Numerical modelling analysis of proposed F-Zone mining, unpublished report, Placer Dome North America Campbell Mine, Balmertown, Ont., Canada, 23.Golden, CO, ARMA.

GRABINSKY, M. W., CURRAN, J. H. and BAWDEN, W. F. 1997. Interaction between stress, mine geometry and rock mass behavior at a Canadian Shield mine. Bull. Can. Min. Metall., 90, p. 45–51.

HEDLEY, D. G. F., NEUMANN, M., MAKUCH, T. and BLAKE, W. 1985. Rockbursts at Campbell Red Lake Mine. Mineral Research Program, Division report MRP/MRL85, Mining Research Laboratories, Ottawa, Ont., Canada, 27 p.

HEDLEY, D. G. F. 1992. Rockburst handbook for Ontario hardrock mines; Ottawa, Ont, CANMET.
KAISER, P. K. and SUORINENI, F. T. 2005. Hazard assessment for mining in F-zone (4L to 15L) Campbell Mine, unpublished report, Campbell Red Lake Mine, Balmertown, Ont., Canada, 47 p.

KVAPIL, R. L., BEAZA, J. R. and FLORES, G. 1989. Block caving at EI Teniente Mine, Chile, Inst. Min. Metall., 98, (6), p. A43–A56.

SALAMON, M. D. G. 1983. Rockburst hazard and the fight for its alleviation in South African gold mines, Proc. Conf. On 'Rockbursts, prediction and control', p. 11–52.

SUORINENI, F.T. KAISER, P.K. and DELGADO, J. 2007. Hazard assessment when mining orebodies under shear loading. Proc.1st Can. US Rock Mech. Symp., (ed. E. Eberhardt et al.), 1377–1384; Rotterdam, Balkema.

SUORINENI, F.T., KAISER, P.K., MGUMBWA, J.J. AND THIBODEAU, D. 2011. Mining of orebodies under shear loading Part 1 – case histories. Mining Technology, 120(3) 137-147.

WHYATT, J. and VARLEY, F. 2008. Catastrophic failures of underground evaporite mines, Proc. 27th Int. Conf. on 'Ground control in mining', p. 113–122; Morgantown, WV, ICGCM.

ZHANG, G., HATORI, K. and CRUDEN, A. R. 1997. Structural evolution of auriferous deformation zones at the Campbell mine, Red Lake greenstone belt, Superior Province of Canada. Precambr. Res., 84, p. 83–103.

Numerical Simulation of Accumulated Damage in Critical Mine Infrastructure and Prediction of Further Damage Over Mine Life

Kathy S. Kalenchuk
Mine Design Engineering
Will F. Bawden
Mine Design Engineering
Bill Curry
Newmont
Changshou Sun
Newmont

ABSTRACT: Damages have been observed in shafts, backfill infrastructure and the slick line at the Leeville Mine. Shaft damage (shearing and spalling of the concrete liner) is attributed to mine-induced rock mass deformations concentrated where regional faults intersect the shafts. Aggregate bin, mixer station and conveyor drive damage (shotcrete shearing, heave of concrete floor slabs and bending of a vertical steel beams) is attributed to rock mass squeezing induced by elevated magnitudes of the vertically orientated major principal stresses. Separation of the slick line has occurred do to extension of the stress-shadowed rock mass immediately above the mined out areas. Three-dimensional numerical models have been developed and calibrated to simulated rock mass deformations with magnitudes similar to those believed to have produced the observed damages. By stepping through the mine sequence, models reproduce deformations at the same mining stage as when damage has occurred. Calibrated models have been used to forward project further damage over the remaining mine life.

1. INTRODUCTION

Recent damages to critical infrastructure at Leeville Mine (see Figure 1 for location of infrastructure relative to mining zones) have triggered major concerns for the potential risk of further damage over the remaining mine life. Mine Design Engineering has developed three-dimensional numerical models to assess the mine-induced change to the in situ stress state, the subsequent deformations through the host rock and on regional faults (Blue Fault, Robert's Mountain Thrust (RMT) and West Bounding Fault (WBF)) and the relationship between these changes and observed infrastructure damage. Models have been calibrated using predicted deformations at points in the mine life which correspond with actual observations of damage accumulation. The calibrated models have been used to predict the potential for continued infrastructure damage over the planned mine life up to 2018.

2. BACKGROUND

Ventilation shaft damage (Figure 2a, b and c), concentrated where major regional faults are projected to intersect the shaft, was first noticed in the fall of 2010 and accelerated over the following quarter, increasing in size and severity. The severity of damage, including cracking and spalling of the concrete liner, is in part attributed to poor quality concrete which was not strong enough to resist compaction based loading. Only minor damage, correlating with the projected locations of fault-shaft intersections, has been reported in the production shaft. The slick line has separated about 150 mm vertically, requiring a new section of pipe to be welded on (Figure 2d and e). Damage to back fill infrastructure (aggregate bins, mixer stations and conveyor drives) was first noticed in late 2009 and includes bending of steel beams in aggregate silo feeders and shearing and cracking of shotcrete (particularly in conveyor drive ribs) (Figure 2f, g and h). Thirty foot (9.1 m) Multi-Point Borehole eXtensometers (MPBX) are installed in the back of each aggregate bin and mixer station. Only one MPBX, in the back of the west aggregate bin, shows significant deformation. This shows about 25 m of movement at the collar and 12 mm roughly 4.6 m into the back; with continued deformation beyond the instrument depth.

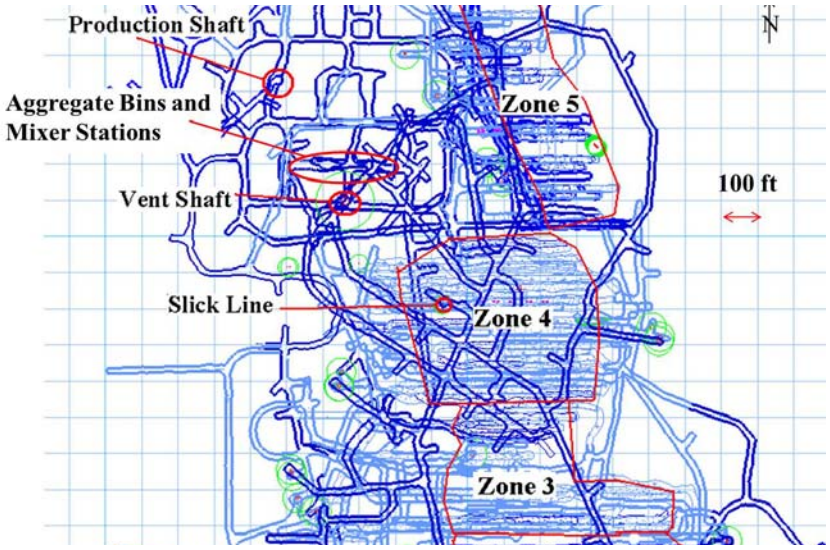

Figure 1 - Plan view of Leeville mining area showing location of shafts, backfill infrastructure and slick line

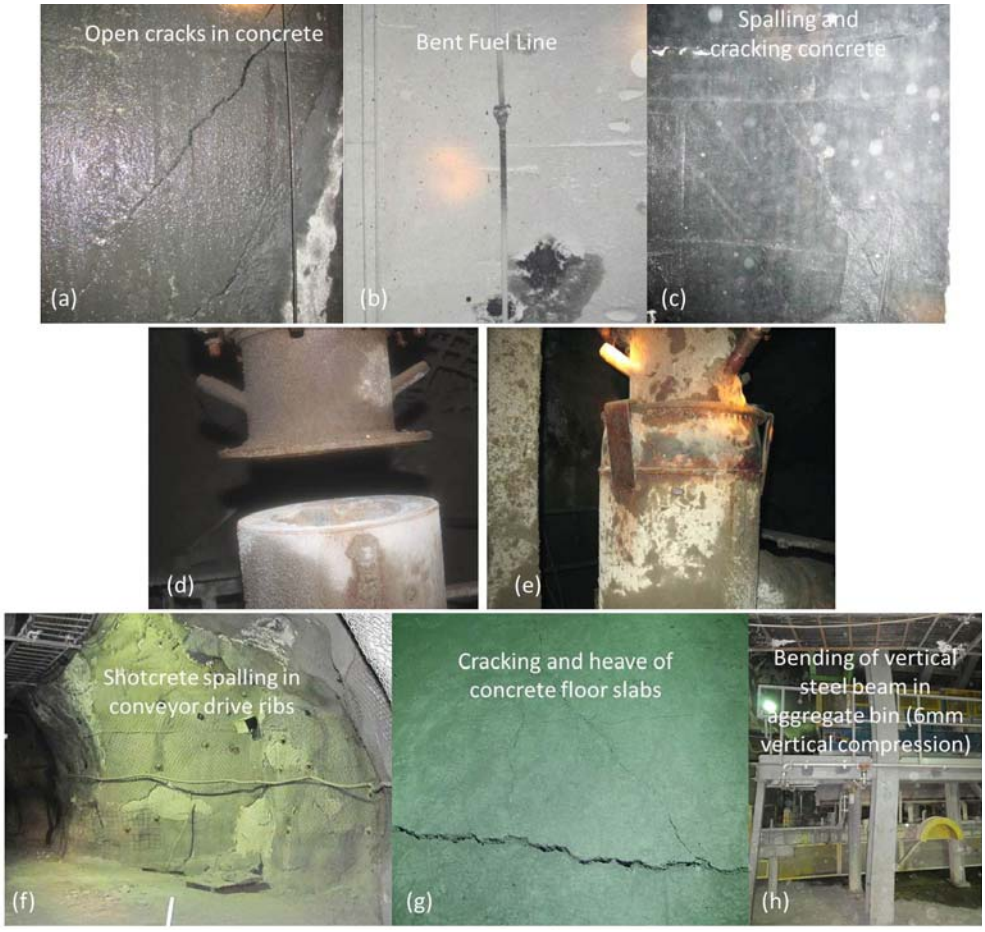

Figure 2 - Damage to the (top) ventilation shaft, (middle) slick line and (bottom) backfill infrastructure

3. NUMERICAL MODELING

FLAC3D (Fast Lagrangian Analysis of Continua in 3 Dimensions), by Itasca (Itasca Consulting Group), has been selected for numerical simulation of the Leeville Mine based on its ability to simulate continuous, deformable medium with the inclusion of discrete interfaces to numerically represent faults or shears. The Leeville Mine model geometry (Figure 3) includes all mine stopes up to the end of 2018 mine plans, as well as the ventilation shaft, production shaft, and backfill infrastructure. The rock mass is defined as a continuum with discrete interfaces representing the RMT and the WBF. The Blue Fault is represented as a continuum zone of elements defined by fault zone strength parameters.

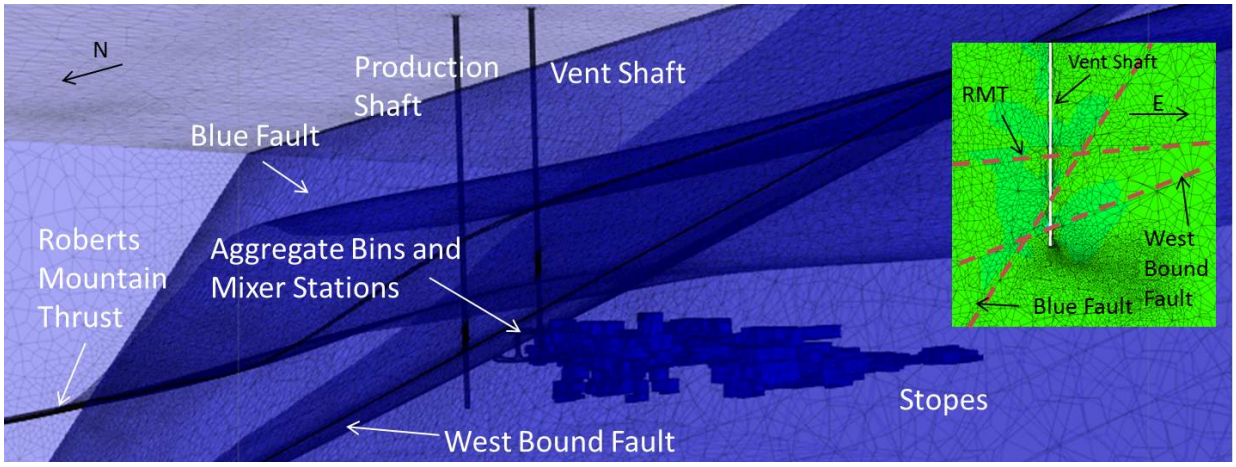

Figure 3 - Leeville Mine model geometry

Hoek-Brown rock mass parameters have been defined as: UCS=30 MPa, m_b=2.0355 and s=0.0093 with density equal to 2650 kg/m^3. These strength parameters are based on GSI=55-60, D=0 and m_i=9 which are representative of the Leeville rockmass. The rock mass modulus (E_{RM}) has been estimated at 20 GPa to 15 GPa with Poisson's Ratio (ν)=0.3. E_{RM} is based on the empirical Hoek-Diederichs equation relating GSI, D and E_{RM} (Hoek and Diederichs, 2006). Cemented rockfill (CRF) strength parameters have been assigned based on findings from various literature sources (Brechtel et al. 1999, Hustrulid and Bullock 2001, and Tersarick et al. 2003, Farsangi 1996, Kockler 2007 as summarized in Shrestha 2008) and CRF testing results from Leeville Mine. CRF parameters are: E=1 GPa, tensile strength=0.75 MPa, cohesion=800 kPa, friction=38˚, density=2100 kg/m3 and ν=0.25. Three regional faults have been simulated in the Leeville models. The Blue Fault is a steep dipping structure estimated to be roughly 50 ft thick. The RMT is a low angle feature dipping shallowly to the west-northwest and the WBF is inclined dipping to the northwest. Base case fault parameters have been estimated as: friction=20˚, cohesion=0 MPa, dilation=0˚, ks=50 MPa and kn=100 MPa.

Four constitutive models have been utilized for the numerical simulation of the Leeville Mine. Elastic isotropic (homogeneous, isotropic continuous material with linear stress-strain behaviour) is used to bring models to initial equilibrium. Hoek-Brown (nonlinear failure surface defined by Hoek-Brown failure criterion) is applied to the (assumed isotropic) intact rock mass. Mohr-Coulomb (Linear Mohr-Coulomb failure criterion) is applied to fault zones and interface elements as well as CRF. Null (all affected zones are set to zero stress) is used to simulate excavations.

The in situ stress state is approximated with the vertical stress defined by gravitational loading. Horizontal stresses (σ_h) are assumed to be equal to 50% of the vertical load (σ_v). Zero velocity normal boundaries are applied to the vertical model edges and base (upper surface is free), then gradational

horizontal and vertical stresses are applied and the model is time-stepped to achieve initial equilibrium in an elastic state (to avoid material yield during model set-up). This approach is taken rather than simply forcing an initial stress state to ensure that the local influence of faults and shears on the regional stress-regime is captured. Groundwater is not included in the model as the problem is assumed to be primarily driven by redistribution of in situ stresses rather than pore pressure.

4. MODEL CALIBRATION

Numerical models have been calibrated based on qualitative and quantitative observations of damage at the end of the fourth quarter (Q4) of 2010. Quantitative calibration includes matching deformation magnitudes simulated at the base of the east aggregate bin to measured steel beam deformations (roughly 6 mm of vertical compression). MPBX data from the west aggregate bin has also been quantitatively compared to numerical simulations. Exact deformation magnitudes in the ventilation shaft are impossible to quantify as there is no instrumentation data or physical measurements available. Model behavior in the shafts is therefore qualitatively compared to reported damage. Qualitative comparisons are also made between the model results and damage observations in the backfill infrastructure and in the pillar separating the shafts and the backfill infrastructure from the mined out areas.

Rock mass strength calibration has been achieved by varying Hoek-Brown strength parameters (mb=2.0355 and s=0.0093 vs. mb=1.5 and s=0.004, an effective drop in GSI from 60 to 50). Figure 4 uses a cross section through the aggregate bins and mixer stations to demonstrate the drop in strength factor (SF) through the pillar separating the backfill infrastructure from the mining zone over 2010. The lower SF in the weaker rock mass model suggests the pillar is in a quasi-stable state which correlates well with observations of damage in this area of the mine. Simulated deformations in the vicinity of the deformed vertical steel beam (Figure 2) were 2 and 4 mm for the strong and weak rock masses, respectively. The weaker rock mass model has been selected as a better calibrated model.

MPBX data from above the west aggregate bin has been compared with deformations simulated by the weak rock mass model. The WBF is projected to be approximately 7 m above the bin. Instrument data suggests extension across the fault zone, and models capture this differential movement. The simulated magnitude (4mm) is less than measured field deformations (20 mm) and the discrepancy is related to the continuum nature of the numerical models. In reality the low strength rock mass beam is a fractured discontinuum while the FLAC3D simulations define this beam as a continuum. The continuum is not subject to inter-block slip and dilation and therefore, dilations are understandably smaller in simulations than they are in reality.

Numerical simulations have been completed using the weak rock mass strength parameters with E_{RM}=15 and 20 GPa. Model deformations suggest that the stiffer rock mass model is better calibrated to ground behavior at the Leeville Mine. The softer rock mass model predicts excessive magnitudes of deformation.

The friction parameter of simulated fault zones and interfaces has been tested at 12˚, 16˚ and 20˚, cohesive strength has been tested as 0.05 MPa and 0 MPa, and interface stiffness has been tested as both ks=0.5 GPa/kn=1 GPa and ks=0.05 GPa/kn=0.1 GPa. Fault friction and cohesion are not significant controlling factors on damage accumulated at the Leeville Mine, as there is negligible difference in SF through the surrounding rock mass and only minor change in shear slip on the low angle faults (RMT and WBF). The Blue fault is influenced by cohesion; at zero cohesion yield occurs within the fault zone and vertical compaction is significantly greater. The higher deformations for the weaker fault model are deemed excessive when qualitatively compared to reported shaft liner damage. Stiff interface elements ([RMT and WBF) have been found to localize stress concentrations and therefore, accumulate more yield. The amount of yield predicted in the stiff interface model is deemed excessive. Based on these findings,

calibrated fault parameters have been defined as friction=20˚, cohesion=0.05 MPa, ks=0.05 GPa and kn=0.1 GPa.

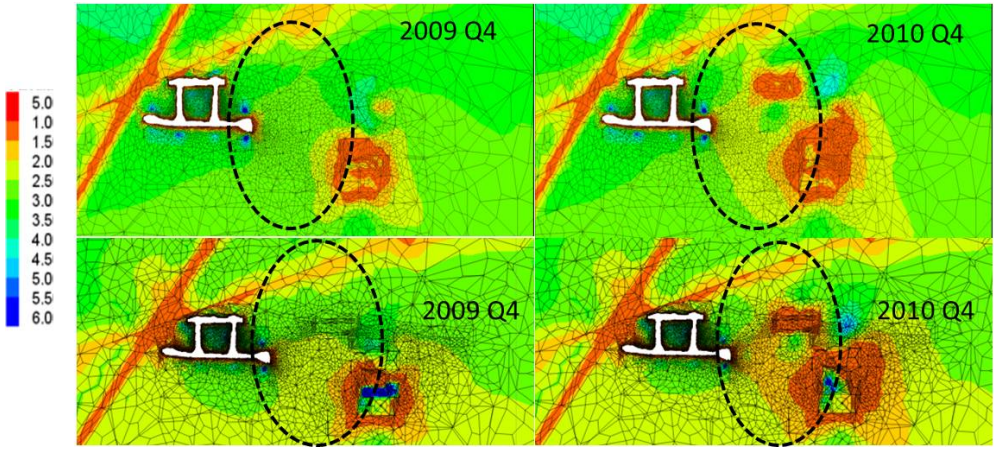

Figure 4 - Pillar damage east of the backfill infrastructure; (top) stronger rock mass and (bottom) weaker rock mass

5. RESULTS

Figure 5 illustrates the accumulated vertical deformations through the rock mass on a vertical section through the backfill infrastructure (looking north) at key points over the life of mine, up to 2010 Q4. It is important to note that deformation values predicted by numerical models are not meant to be exact predictions of displacements; simulated deformations provide an order of magnitude prediction and an estimation of the deformations that can be expected. Surficial deformations accumulate in the backfill infrastructure early in mine life. This immediate closure is in response to initial excavation. In the rock mass surrounding the backfill infrastructure vertical deformations accumulate gradually over the life of mine up to the end of 2009 Q2, at which point there is acceleration. This corresponds well with observed damage to excavations in the area. The loss in SF through the pillar which separates this infrastructure and the active mining area is gradual, and subtle, up to the end of 2010 Q2 (Figure 4). After that point in time, there is a marked drop in SF over the second half of 2010.

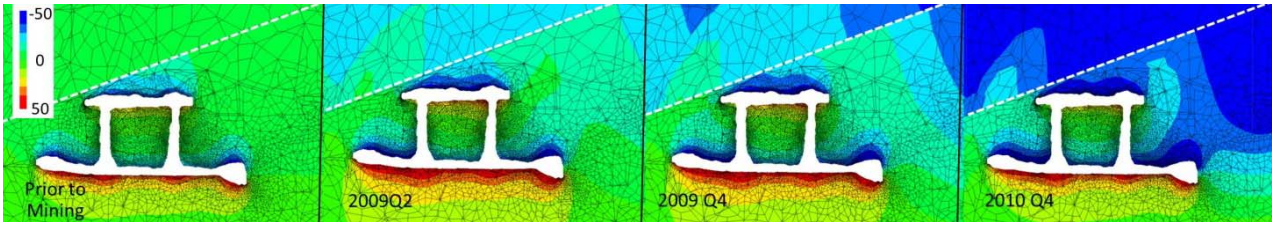

Figure 5 - Accumulated deformation (in m) at the backfill infrastructure (vertical section looking North)

Cumulative simulated vertical deformations in the rock mass immediately adjacent to the ventilation shaft correspond well with observed shaft liner damage (Figure 6). There are initial deformations accumulated during shaft excavation in close proximity to faults. This is the simulated response of the rock mass to shaft excavation; weaker regions of the shaft profile display greater deformations. Early deformations are exaggerated in numerical simulations as there is no confinement that would, in reality, be provided by ground support and the shaft liner. More extensive (vertical) deformations are predicted to initiate late in 2009 (near 5 mm across the Blue Fault zone) and accelerate through to the end of 2010 (exceeding 10 mm

across the Blue fault zone). Most deformation is localized below the RMT. An accelerated drop in SF near the active mining area adjacent to the ventilation shaft is predicted to occur early in 2010 (Figure 7), while the SF in the rock mass immediately surrounding the ventilation shaft shows negligible change up to the end of 2010 Q4.

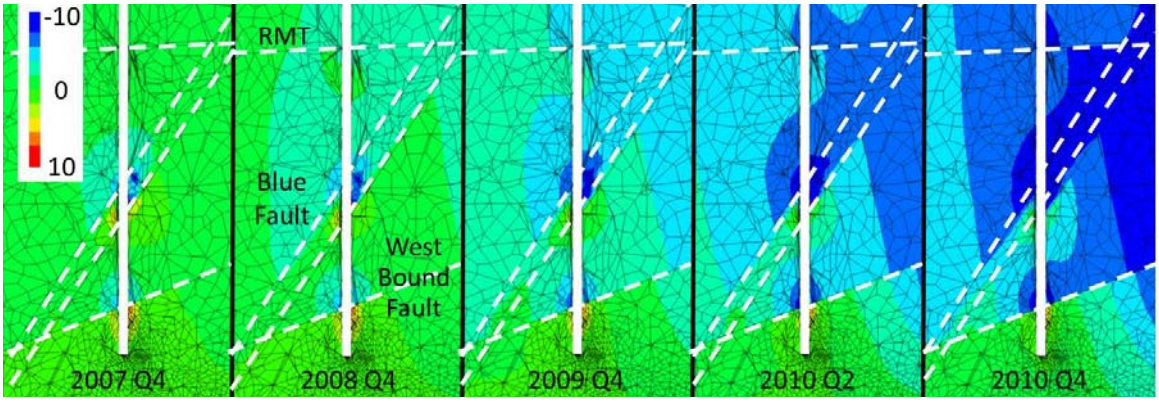

Figure 6 - Vertical deformations (in meters) in the ventilation shaft vicinity over life of mine up to 2010 Q4 (vertical section looking North)

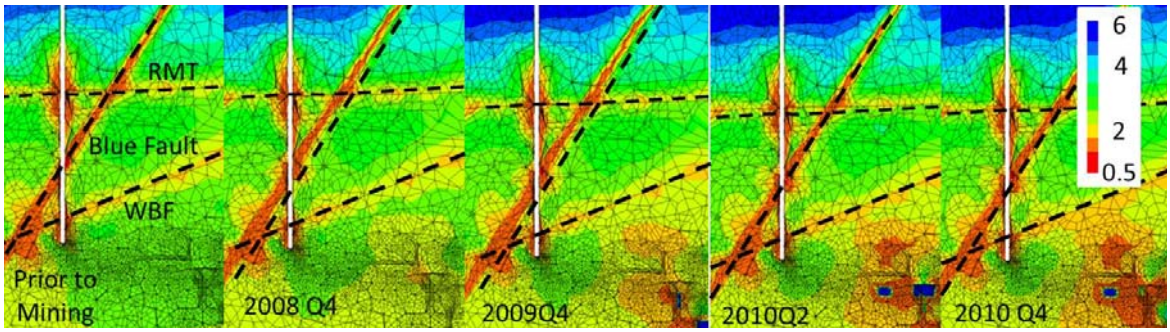

Figure 7 - Change in SF over the mine life up to 2010 Q4 contoured on a vertical section through the ventilation shaft (looking North)

Cumulative vertical deformations (exceeds 5 mm near the Blue Fault) in the rock mass immediately adjacent to the production shaft are significantly lower than those predicted near the ventilation shaft. The significantly higher deformation magnitudes predicted in the ventilation shaft compared to the production shaft correlate well with the more severe damage observations in the ventilation shaft. Additionally the production shaft liner is believed to be of significantly higher strength than the ventilation shaft liner and should therefore withstand higher loads. Change in SF through the rock mass near the production shaft is similar to the ground response near the backfill infrastructure and the ventilation shaft. Subtle reduction in SF occurs near the active mining area, and this accelerates over 2010. The SF in the rock mass immediately surrounding the production shaft shows negligible change up to the end of 2010 Q4.

Figure 8 illustrates simulated vertical deformations on a vertical cross section (looking north) through the rock mass in proximity to the slick line over the mine life up to 2010 Q4. A gradual accumulation of extensional vertical deformation is apparent over the mine life and this accelerates from roughly 20 mm at 2009 Q4 to nearly 50 mm by 2010 Q4. These magnitudes of deformation are less than those implied by

slick line damage which required a 6 inch (150 mm) extension to the slick line pipe, likely due to the continuum nature of the FLAC3D model.

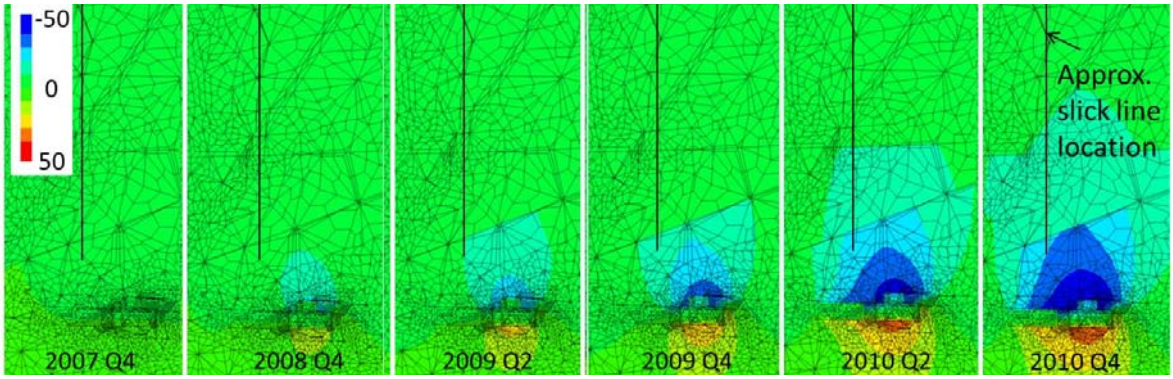

Figure 8 - Accumulation of deformation in approximate slick line area (vertical section looking North)

6. ANALYSIS

The mechanisms for deformations which have contributed to significant damage in critical mine infrastructure are explained by mine induced changes to the in situ stress state. When stope excavations are created, stresses are redistributed around the mine voids to re-establish equilibrium. This stress redistribution reduces the major principal stress (σ_1), which is vertically oriented, above the mined stopes and increases the major principal stress in the abutments adjacent to the mine excavations (Figure 9). As mining progresses stress magnitudes and the area of influence increase.

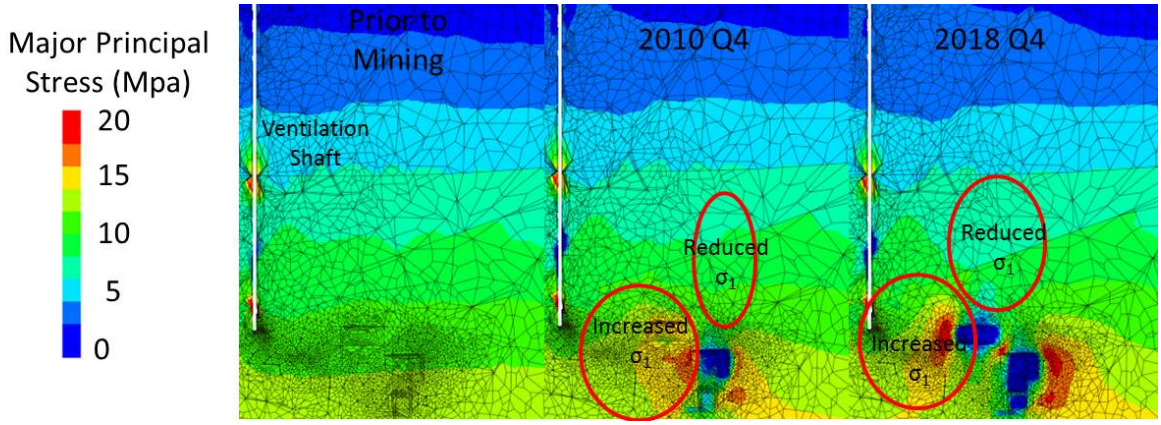

Figure 9 - Redistribution of major principal stress over Leeville Mine life (vertical section through the ventilation shaft looking North)

Relaxation of in situ stresses above the mined out areas has contributed to normal extension across regional faults and through the relaxed rock mass. This is the cause of slick line damage. There is no shear offset predicted on any of the faults, and the WBF has the largest magnitude vertical extension as it is the closest fault to the mined out stopes, and therefore, experiences the most significant reduction in normal stress. Numerical models, compared to observed slick line damage, underestimate the total vertical extension over the mined out stopes. This may be due to a hypothesis that a reduction in vertical stress may have allowed more water to locally enter the fault zones and enhance swelling of clay

minerals. Numerical models do not include any groundwater modelling and therefore, this hydro-mechanical response to change in stress state is not accounted for.

Vertical deformation in the ventilation shaft is thought to be largely due to compaction of the fault zones which are less stiff than the surrounding rock mass. Differential vertical deformations are due to the stiffness contrasts between the faults and the surrounding rock mass. This mechanism compares well with observed shaft damage, including spalling, slack in pipes and electrical lines. Numerical models also demonstrate that significant shaft deformation incurred where the Blue Fault is intercepted. This fault is steeply inclined and vertical deformations are a combination of both normal compression and shear deformation. Deformations are believed to be predominantly elastic because the predicted yield in the Blue Fault is very shallow at the shaft boundary.

7. FORWARD PREDICTION

Forward projection has been completed to assess the potential of further damage as mining progresses past 2010 Q4. Over the remaining mine life, the ventilation shaft can be expected to incur 100% more deformation than has already occurred. A new steel liner, presently being installed, has been designed with slots to accommodate vertical deformations. However shaft guides, piping, etc., will require ongoing adjustment to accommodate future deformations. An instrumentation system has been designed to monitor future deformations within and around the ventilation shaft. This system will be installed as part of the present shaft rehabilitation program.

The production shaft up to 2010 Q4 is predicted to have incurred only 50% of magnitude of the ventilation shaft deformations in that same time frame. Numerical models suggest that the cumulative production shaft deformations will double by 2018. Accumulated damage in the production shaft will ultimately depend on the shaft liner response to vertical compression. It is therefore difficult to predict the magnitude of damage that will occur over the remaining mine life. Routine inspections are recommended to visually monitor shaft liner performance. If the onset of significant damage does occur, accelerated deterioration can be expected due to classic strain-softening post-yield behavior. An instrumentation system has been designed and is being implemented to monitor future deformations within the production shaft.

Predictions for further deformations to backfill infrastructure indicate that the east end is at significantly more risk to further damage than the west end. The west end of this infrastructure is not predicted to accumulate any significant deformation over the remaining mine life. The east mixer station is predicted to see major deformations continuing over the remaining mine life. Models indicate that only 37% of the total anticipated vertical closure had occurred by the end of 2010. This mixer station has been abandoned and backfilled.

The rock mass region immediately to the west of the mined out stopes will see a continued drop in SF over the remaining mine life, with SF dropping below 1.5 in proximity to the stopes. Any mine infrastructure in this region will likely incur significant damage and continuing rehabilitation will be required.

Extensional deformations in the rock mass regions near the slick line are expected to have already incurred 75% of the total deformation expected over the entire mine life. It is quite possible that the slick line will rupture again in future. If this occurs, another section can simply be added to the line. This area should be monitored routinely to check for damage to the pipe. Alternately, a flexible section could be added to the pipe to accommodate future deformations.

8. CONCLUSIONS

Numerical models of the Leeville Mine have performed well in simulating observed ground deformations that have contributed to significant damage to critical mine infrastructure. Rigorous model calibration enables numerical simulations to reasonably reproduce the magnitudes and timing of ground movements which qualitatively and quantitatively correspond to underground observations. These calibrated models have been used to forward predict continued deformations up the end of 2018 mine plans. Forward prediction has enabled mine operations to take the appropriate steps, including shaft liner rehabilitation, installation of instrumentation, and adjustments to long term mine plans, to mitigate the risks associated with continued infrastructure damage.

9. REFERENCES

BRECHTEL, C. E., STRUBLE, G.R., GUENTHER, B., 1999. The evaluation of cemented rockfill spans at the Murray Mine. In: Proceedings, 37th U.S. Rock Mechanics Symposium, Vail, CO. Balkema.

FARSANGI, P.N., 1996. Improved Cemented Rockfill Design in Open Stoping, Ph.D. Thesis, Department of Mining and Metallurgical Engineering, McGill University.

HOEK, E. and DIEDERICHS, M.S., 2006. Empirical estimation of rock mass modulus. International Journal of Rock Mechanics and Mining Sciences, 43; p 203-215.

HUSTRULID, W.A., BULLOCK, R.L., (eds) 2001. Underground mining methods: engineering fundamentals and international case studies.

KOCKLER, M., 2007. Design of Cemented Rockfill Spans for Longhole Stoping at the Rain Mine, Carlin,Nevada, Ph.D. Thesis, Mining Engineering-Metallurgy, University of Idaho.

SHRESTHA, B.K., 2008. Properties of Cemented Rockfill at Diavik Mine. M. Sc. Thesis, University of Alberta.

TESARICK, D. R., SEYMOUR, J.B., and JONES, F.M., 2003. Determination of in situ deformation modulus for cemented rockfill, ISRM 2003 – Technology Roadmap for Rock Mechanics, South Africa Institute of Mining and Metallurgy, p 1209-1220.

Analysis of the Influence of the Mining Sequence on a Remnant Pillar with FLAC^{3D}

Shahé Shnorhokian
McGill University
Hani S. Mitri
McGill University
Denis Thibodeau
Vale
Lindsay Moreau-Verlaan
Vale

ABSTRACT: Remnant pillars evolve towards the latter stages of mining in an orebody and act as repositories of mining-induced stress. It is therefore crucial to plan ahead as to their dimensions and location with respect to the local geology. A case study of a Canadian base metal mine was examined for the planned mining sequence scenario to identify the stress regimes acting on a future remnant pillar occurring between levels 4800 and 5100, near a brittle dyke. A mine-wide model was constructed in FLAC^{3D} and input parameters included results from field measurements of the direction and magnitude of the principal stresses, and the geomechanical properties of the different formations. Prior to the study, the model was calibrated based on a 6-year record of mining-induced seismicity and rockburst events, focusing on large event clusters. The mining sequence followed at the mine was then used in the model to study the planned future extraction program around the remnant pillar. It is shown that the distance of the remnant pillar from the dyke and another orebody plays an influential role on the stress levels developed in the pillar.

1. INTRODUCTION

Towards the latter stages of a mining operation, remnant ore pillars remain after the mining and backfilling stages are completed. Due to the potential for accumulation of mining-induced stress within these pillars, their timing, location, and dimensions must be well-planned in order to ensure successful recovery. Recovery can be difficult due to complicated geology and structural features present, in addition to mining-induced seismicity caused by the readjustment of stresses in the rockmass due to the excavations. This latter phenomenon has been studied all over the world during the past decades, especially in relation to rockburst events at greater depths, and has relied heavily on methods and techniques transferred from earthquake seismology. For example, Spottiswoode (1989) conducted a comprehensive review of rockburst research in South Africa, while a summary of seismicity induced by mining in Canada was prepared by Hasegawa et al. (1989). This paper covers a study of a planned remnant pillar at the Vale Garson Mine in Sudbury, Canada.

2. GARSON MINE

The Garson Mine is located in the southeast section of the Sudbury Basin (Eckstrand and Hulbert, 2007) as shown in Figure 1, and has been in operation for more than 100 years. Deposits at the mine are comprised of Sudbury Igneous Complex (SIC) copper-nickel sulphides (Trifu and Suorineni, 2009).

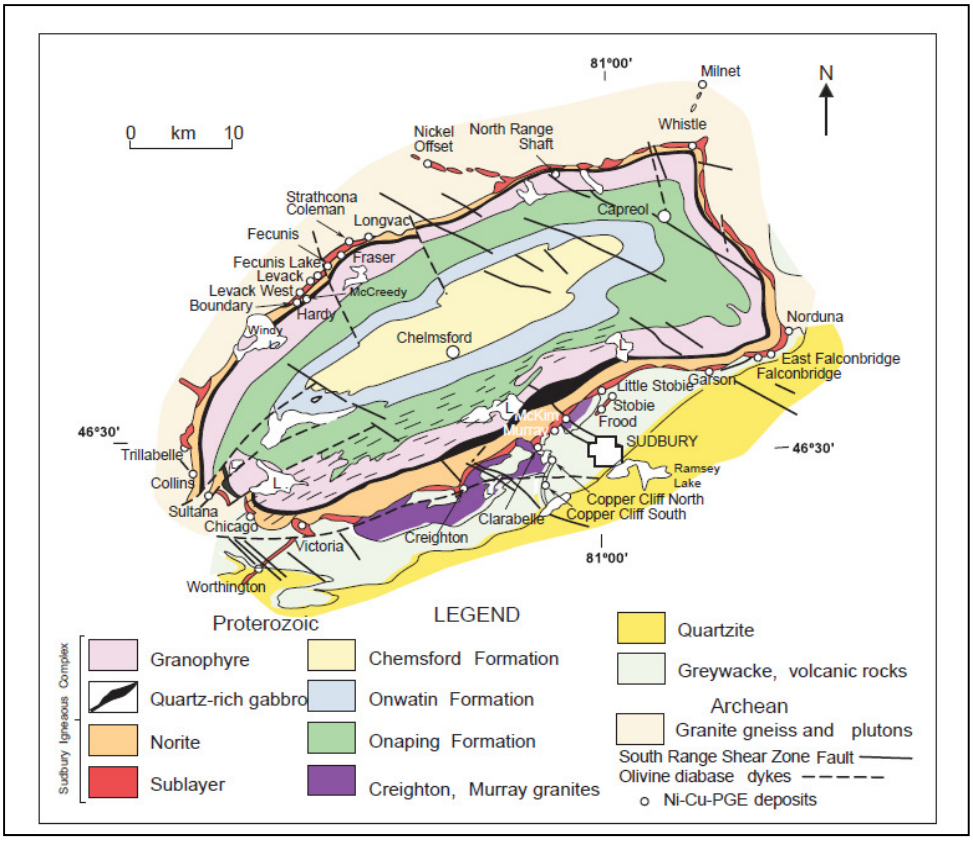

Figure 1 - Location of the Garson Mine within the Sudbury Basin (Eckstrand and Hulbert, 2007)

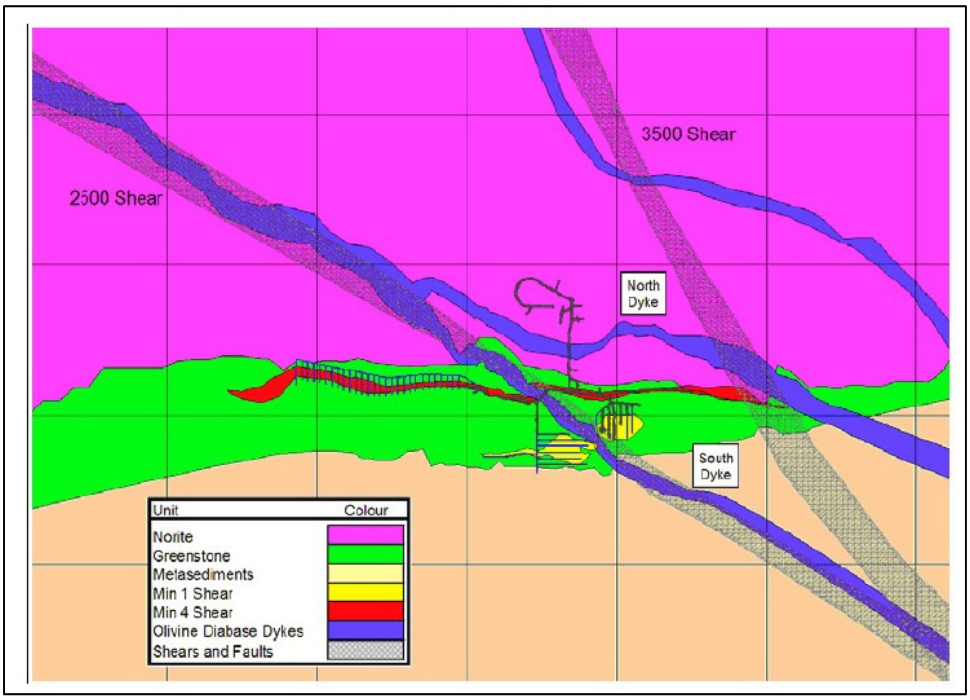

Figure 2 - Aerial view of the geology at the Garson Mine (Yao and Moreau-Verlaan, 2010)

There are two primary orebodies, designated as #1 and #4, located between 1200 – 1700 m (4000 – 5600 ft) below surface, and dipping 60-75º to the south. The sheared host rocks include a norite formation to the north and metasediments to the south. These formations are offset by a swarm of olivine diabase dykes (Yao and Moreau-Verlaan, 2010), one of which runs through the mine in a NW-SE direction and has an average thickness of 30 m (100 ft). It branches into a northern section (north dyke) running parallel to and above #4 orebody in a W-E trend, and a southern section (south dyke) that runs NW-SE. The south dyke cuts the two orebodies into western and eastern segments – #1 Shear West, #1 Shear East, #4 Shear West, and #4 Shear East (Figure 2). Other structural features include a fault zone trending E-W and two other fault/shear zones – trending NW-SE – designated as the 2500 and 3500 structural zones.

3. METHODOLOGY

The initial phase of the study comprised an analysis of the microseismic database and field reports from the mine during the period between 2002 and 2008. These microseismic events were grouped based on magnitude and location so as to identify areas vulnerable to induced seismicity. In the next phase, a FLAC^{3D} (Fast Lagrangian Analysis of Continua) numerical model was constructed using the stopes and different geologic units of eight mine levels. A detailed analysis of the stress regimes in the mine, with respect to the extraction sequence, was conducted between January 2006 and July 2011, and this was implemented in 3-month units. The final phase of the study comprised a study of the stresses on an ore pillar in orebody #1 Shear West between levels 5100 and 4800. As extraction commences in this orebody, the planned sequence is to mine it out from both sides, which will eventually produce a remnant ore pillar at one point before it is completely mined out.

3.1 Microseismic Database

Microseismic monitoring is conducted at the Garson Mine with a Paladin microseismic monitoring system using uniaxial geophones. The system assigns northing, easting, and elevation, local and moment magnitudes, energy, and a date/time stamp for each event. After an initial analysis of the data, it was observed that the readings after 2006 were more reliable following a system upgrade, and these events were used for further analysis. Specific attention was given to events with a very large energy signature, i.e., larger than 10^{+5} Joules. In order to reduce the large database to a meaningful set, the events were filtered by a location error with those of 65 m (200 ft) or more being discarded from further analysis.

3.2 Rockbursts

The mine reported several minor rockbursts and fall-of-ground events during the period between 2002 and 2008, and eight major rockbursts. The first one took place in December 2006 on the 5000 level and the second one in January 2007 on levels 4600 and 4700. The other rockbursts took place during 2008 on levels 4800 to 5000. The locations of the rockbursts were plotted and compared to those of the larger microseismic events to check for any overlaps or trends.

3.3 FLAC^{3D} Modeling

In addition to the analysis of microseismic database and rockburst events, a detailed mine-wide numerical model was constructed for this study using the finite difference code FLAC^{3D} by Itasca. The main purpose of the model was to verify the stress redistribution patterns in the mine that took place subsequent to mine and backfill operations. The model was constructed for levels 4370 to 5100, with replicated extensions down to 5500 and up to 4000 to provide boundaries sufficiently far from the openings in the vertical direction. The four orebodies at the mine – #1 Shear East, #1 Shear West, #4 Shear East, and #4 Shear West – were represented by a grouping of their individual stopes. In terms of geology, the two sections of

the dyke, norite, greenstone, and metasediments formations were all incorporated into the model. Due to the use of imperial units in the map plans, all data was converted to that system for use in the model.

3.4 Geotechnical Properties

The material properties used in the model were based on results from unconfined compressive strength tests done by MIRARCO (2005) on samples obtained from the mine. Due to the large variation reported for the various geologic units, the average values were used as input parameters for the numerical model. Rockmass values were obtained from the results based on additional borehole log data from the mine, and the final numbers used in the FLAC^{3D} model are given in Table 1.

Table 1 - Rock properties used in FLAC^{3D}

Geology	E in GPa [lb/ft^2]	ν
Greenstone	65 [1.36E+09]	0.23
Dyke	86 [1.80E+09]	0.26
Metasediments	46 [9.50E+08]	0.24
Norite	56 [1.18E+09]	0.25
Ore	44 [9.15E+08]	0.3
Backfill	0.3 [6.27E+06]	0.2

In most cases, rockbursts occur in brittle lithologies where differences exist in material stiffness amongst the various geologic units (Blake and Hedley, 2003). For this reason, the elastic material model in FLAC^{3D} was chosen to conduct the numerical analysis, and the required mechanical properties were restricted to the bulk (K) and shear (G) moduli, which were calculated based on Young's Modulus (E) and Poisson's Ratio (ν) values (Itasca, 2009).

3.5 In-situ Stresses

In-situ stresses within the Canadian Shield have been the topic of numerous studies and a stress database is continually maintained at CANMET for this purpose (Arjang and Herget, 1997; Martin et al., 2003). Specifically for the Garson Mine, in-situ stress values were monitored by Cochrane (1991) and MIRARCO (2005), and their results are presented in Tables 2 and 3, respectively. For the purpose of this study, the MIRARCO numbers were relied upon since they were measured on level 4900, which was part of the constructed model. The boundaries were fixed far at least 350 ft (100 m) away from any excavation in three directions, and the model was allowed to equilibrate before mine and backfill stages commenced.

Table 2 - In-situ stress measurements according to Cochrane (1991) – level 3800

Principal Stress	3800 L (MPa)	Trend	Plunge
σ1	66	270º	0º
σ2	33	180º	0º
σ3	33	0º	90º

Table 3 - In-situ stress measurements according to MIRARCO (2005) – level 4900

Principal Stress	**4900 L (MPa)**	**Trend**	**Plunge**
σ1	72	70º	2º
σ2	45	162º	44º
σ3	40	157º	-46º

3.6 Stope Sequence

The same extraction sequence that was followed at the Garson Mine was replicated in the model based on a 3-month-per-stage rate. For example, all stopes mined during January to March 2006 were extracted in one step and the model was allowed to reach equilibrium, and then they were all backfilled in the next step. The mine and backfill step described above was implemented for the period 2006 to 2011 before analysis was conducted on the remnant ore pillar itself.

After this initial stage, the planned sequence in #1 Shear West was implemented in the model, which would leave a remnant ore pillar close to the south dyke at one point in time before it is completely mined out. Mining commenced from level 5100 and moved diagonally upwards from both sides of the orebody up to level 4800. Extraction and backfill stages were implemented in the sequence alternating between the east and west sides of the orebody at a rate of 7 stopes per stage, and the planned remnant pillar appeared after 14 stages.

4. RESULTS AND DISCUSSION

4.1 Microseismic Database

The microseismic database consisted of 130,446 events between 2006 and 2008 after date filtering due to the system upgrade. Based on further analysis, it was observed that most of the major rockburst events consistently registered energy levels greater than 10^{+5} J. Therefore, the data was further filtered to show readings with energy levels higher than this value. The outcome provided 4 events in 2006, 12 ones in 2007, and 12 ones in 2008, for a total of 28 large events during the 3-year period. With the inclusion of the 8 rockbursts, the sum of events with high energy outputs and rockbursts would be 36 during this period. The locations of these events between levels 4000 and 5500 are presented graphically in plan and vertical sections in Figures 3 and 4, respectively. It can be observed that the vast majority of large events form clusters at different locations of the mine, which denotes that those areas are more prone to high energy microseismicity than others.

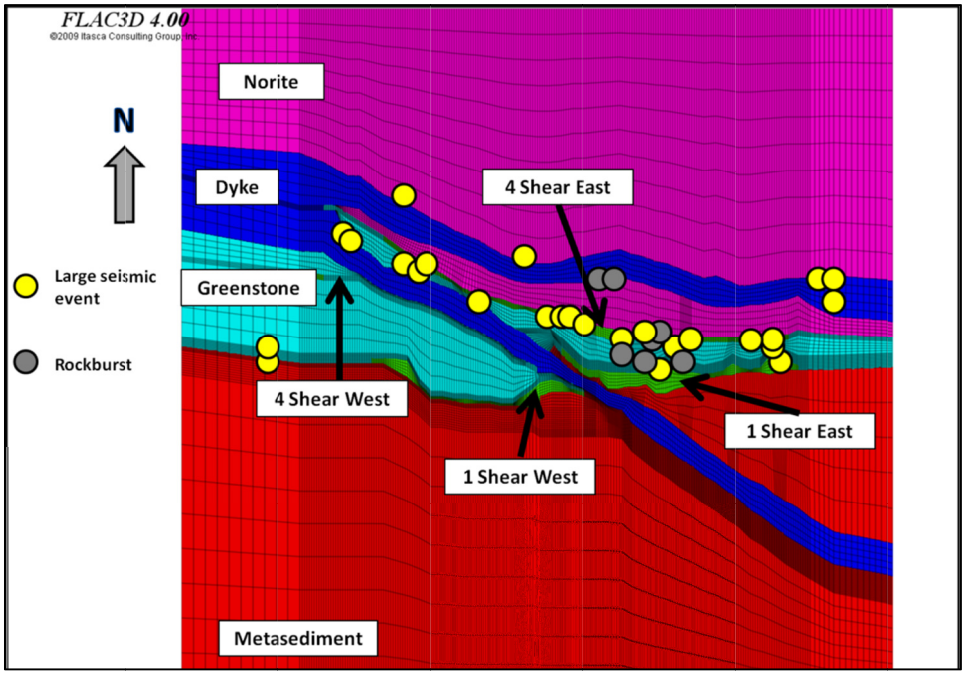

Figure 3 - Location of large microseismic events and rockbursts (shown on level 4700)

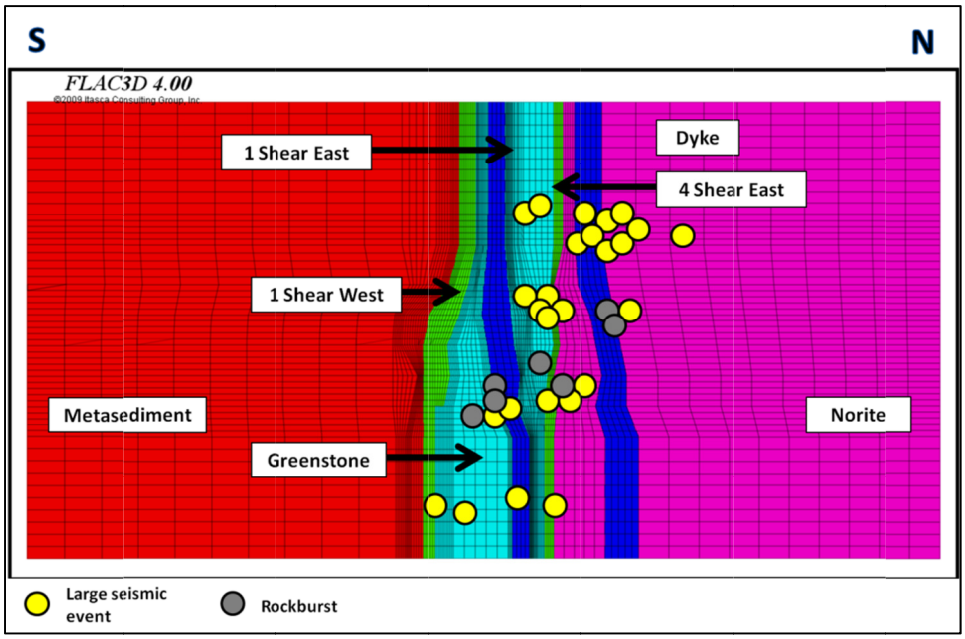

Figure 4 - Location of large microseismic events and rockbursts (shown on vertical section E 2500)

Moreover, the figures indicate that these clusters populate a narrow band about 165 m (500 ft) in width located between the north and south dykes, and which trends WNW-ESE and dips about 30º east. In terms of depth, levels 4500, 4700, and 5000 are the ones around which most activity of this magnitude has taken place, with 24 events occurring between levels 4400 and 5100. The largest cluster can be observed between #4 Shear East and #1 Shear East in the central part of Figure 3 and comprises 5 events. Two clusters come in second in terms of numbers, and these occur just west and east of the main one

along the #4 Shear East/ greenstone contacts, and comprise 4 events each. Other clusters can be observed further west on the border with the south dyke whereas the north dyke comprises 5 events by itself along its length. This is an indication that the brittle nature of the dyke plays a significant role in the induced microseismic events of larger magnitudes at the Garson Mine. In terms of depth, the highest number of large events have taken place between levels 4300 and 4500 (11 events), followed by the 4600 to 4700 interval (6 events), and level 5000 (5 events).

4.2 Rockbursts

Eight rockbursts took place within the study period at the mine (2002 to 2008), 7 of which were located between levels 4000 and 5500, and 6 of them occurred during 2008. The locations of these rockbursts have been plotted in Figures 3 and 4 along with the large microseismic events and it can be observed that they fall squarely within the narrow band defined by the clusters. Hence, it can be concluded that the microseismic events with larger energy outputs form a consistent trend within the geologic system at the mine, and that the rockbursts that have taken place during the study period have not deviated from this trend. Rather, they confirm that when the conditions are right, some of the larger microseismic events will translate into rockbursts. The locations indicate that the rockbursts have been restricted to the eastern part of the mine, specifically in the middle of the main event cluster, as well as the border between the north dyke and norite formation. As far as depth is concerned, the main locus occurs between levels 4800 and 5100, while the ones in the north dyke are at level 4700.

4.3 FLAC^{3D} Modeling – Calibration using the Microseismic Database

FLAC^{3D} modeling was conducted for levels 4000 to 5500 for two main purposes. The first was to verify the stress regimes in the mine and their readjustment patterns due to the ongoing mine and backfill stages, and to evaluate their relationship to the location of the large microseismic event clusters discussed earlier. This would constitute a calibration of the numerical model. The second purpose was to use the model to study the planned remnant ore pillar that would be left in the latter stages in terms of stress accumulation. Figures 5 to 8 present the maximum shear stress regimes in different vertical sections observed at the end of 2006, 2007, and 2008.

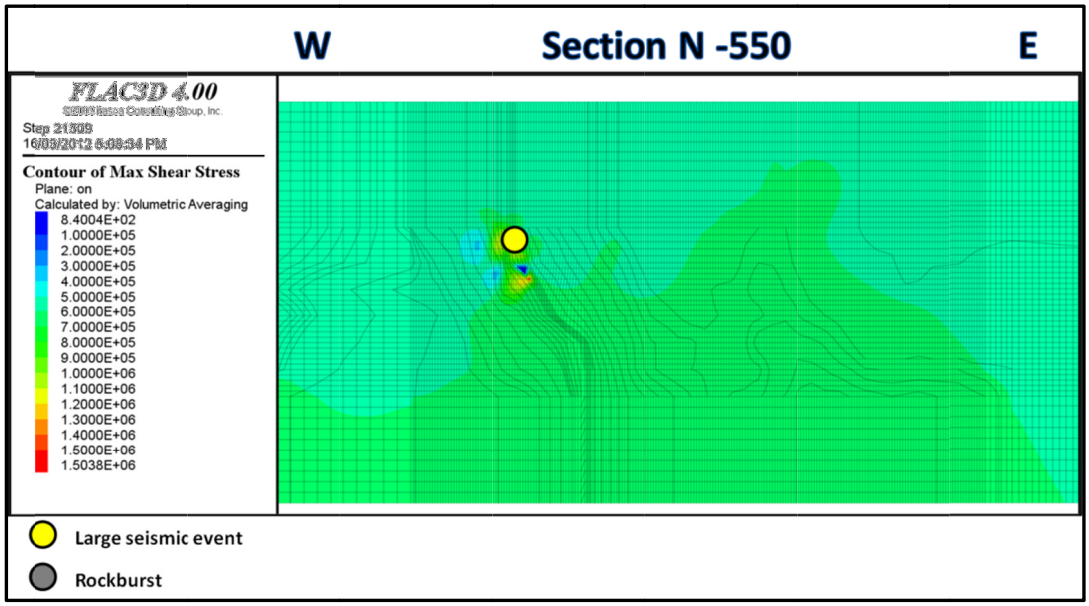

Figure 5 - Vertical cross section at N -550 – December 2006

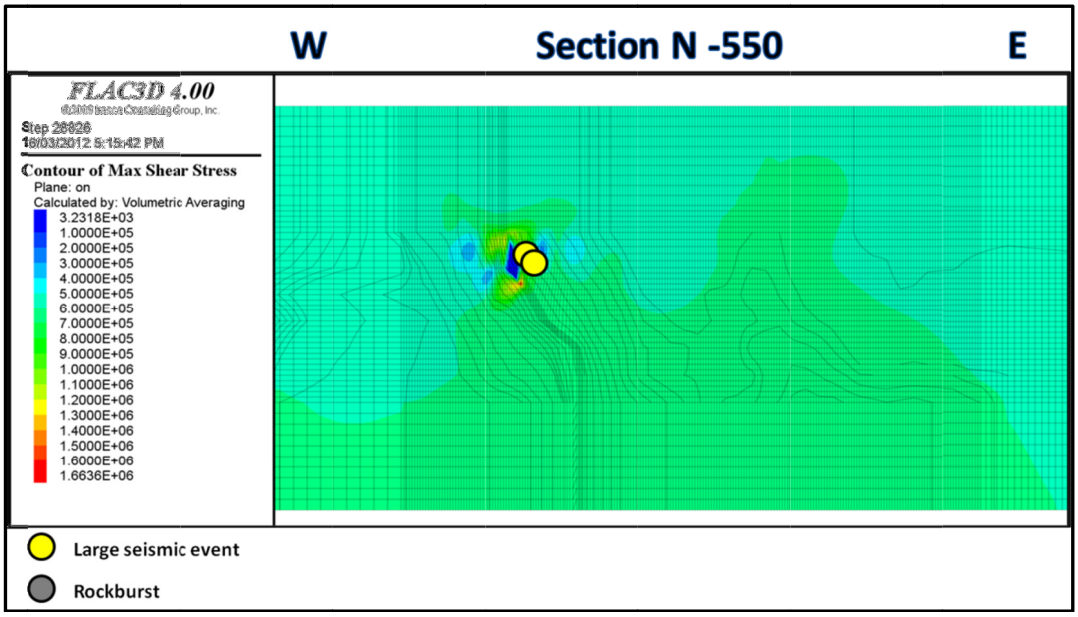

Figure 6 - Vertical cross section at N -550 – December 2007

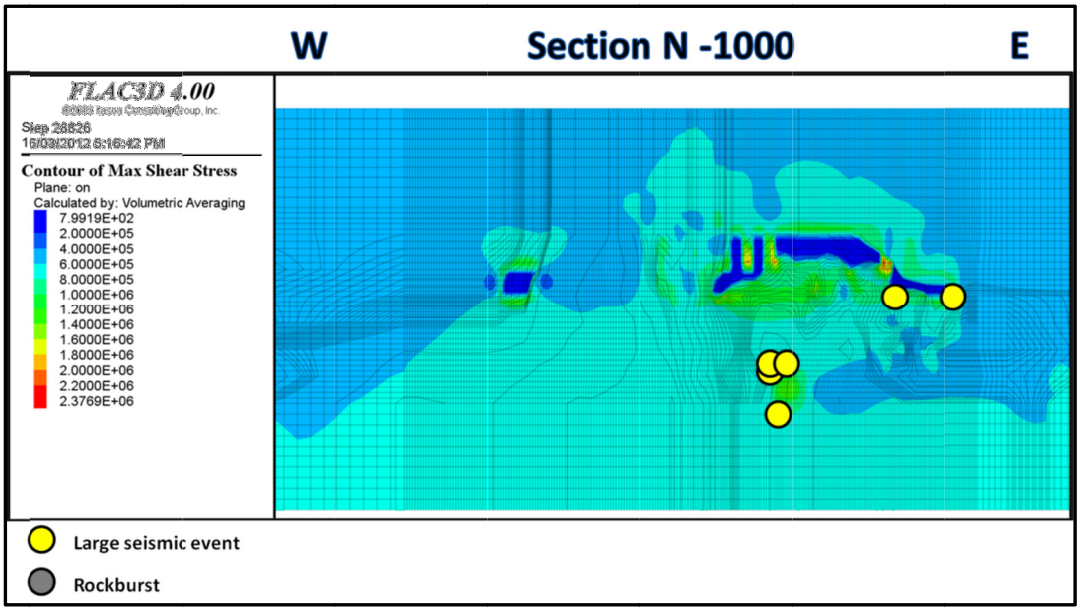

Figure 7 - Vertical cross section at N -1000 – December 2007

When an analysis is conducted on the locations of microseismic events during the 2006 to 2008 period, it can be observed that all of these coincide with zones of anomalies in terms of maximum shear stress levels. Figures 5 and 6 present an E-W vertical section between levels 4000 and 5500 where shear stresses are very high in the same area at the end of 2006 and 2007, respectively. A total of three large events coincide exactly with this location, which is the narrow band of greenstone between the south dyke and #4 Shear East. Figures 7 and 8 are vertical cross sections at the end of 2007 and 2008, respectively, and show 4 events and 2 rockbursts at a depth near level 5000, which coincide with zones of higher shear stress. Based on these observations, it can be deduced that the numerical model is well calibrated and is

able to replicate the stress conditions at the mine. It can therefore be used for further analysis such as the stress regimes dominating the planned temporary remnant pillar in #1 Shear West.

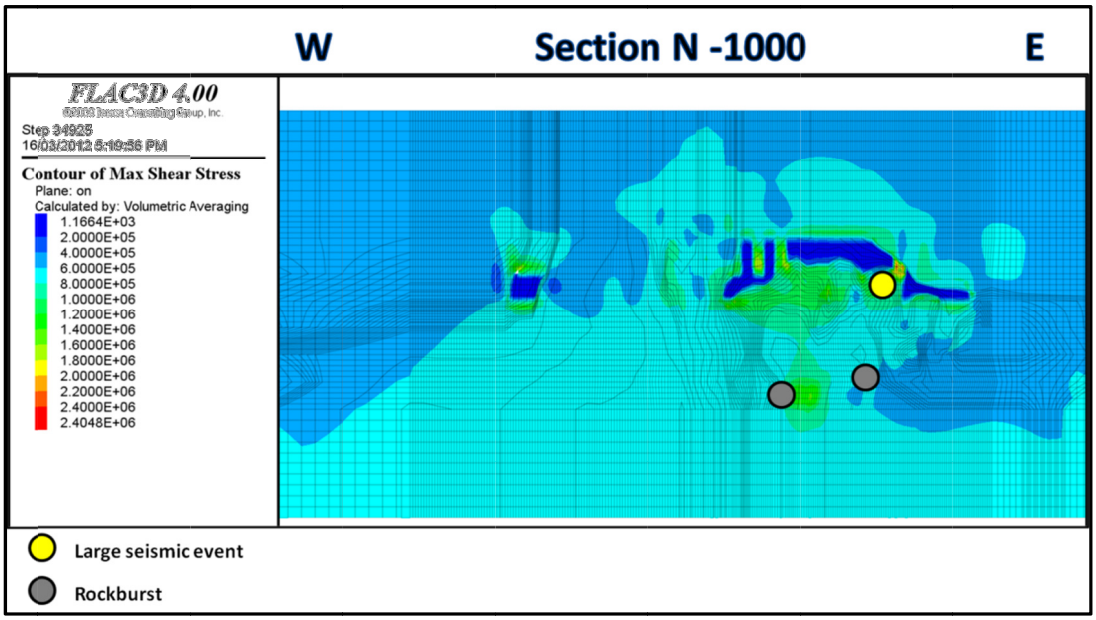

Figure 8 - Vertical cross section at N -1000 – December 2008

4.4 FLAC^{3D} Modeling – Remnant Pillar in #1 Shear West

The stope sequence followed at the mine was continued until 2011 in order to prepare the model for the simulation of the remnant ore pillar in #1 Shear West. Based on the sequence to be followed, the orebody is planned to be mined out diagonally from level 5100 up until level 4800 from both the east and the west as shown in Figure 9. A production rate of 7 stopes per 3 months was considered, based on previous average rates, which alternated between east and west. This resulted in 14 mine-and-backfill stages (with 7 stopes each) at the end of which the remnant pillar would appear in the middle of the orebody before it is completely mined out. Results were taken after stages 7, 10, 12, and 14 in order to follow the evolution of the stress regime in the orebody.

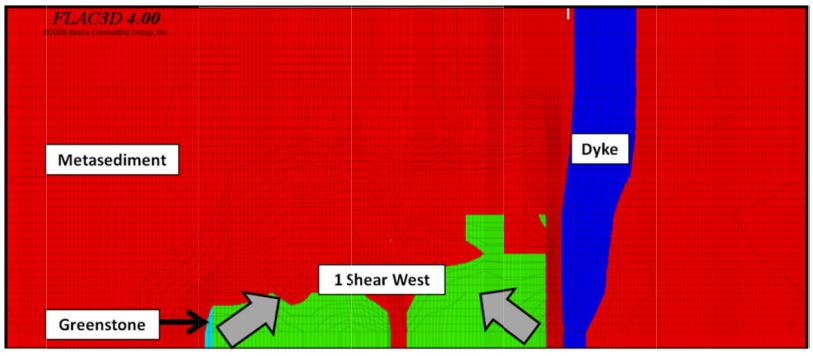

Figure 9 - Vertical Cross Section of #1 Shear West At N -1250 Showing Direction of Mining

A vertical cross section at N -1250 captures most of #1 Shear West and Figures 10 and 11 present the stress evolution at the end of stages 7, 10, 12, and 14. As expected, zones of higher shear stress values are

seen to increase in size as the orebody is mined and backfilled with values in the range of 72 MPa ($1.50*10^6$ lb/ft^2) and a zone of very high shear stress near level 4800 at 132 MPa ($2.75*10^6$ lb/ft^2).

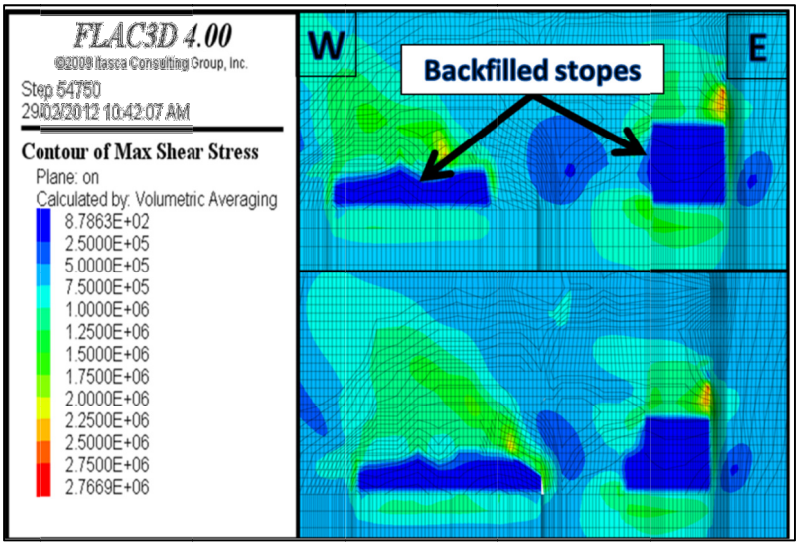

Figure 10 - Vertical cross section of remnant pillar at N -1250 – after stages 7 (top) and 10 (bottom)

If the various levels are studied, it is observed that the lower ones (5000 and 5100) would carry the highest shear stress values at the end of the stage 14 as shown in Figures 12 and 13. Ranges of about 84 MPa ($1.75*10^6$ lb/ft^2) surround the extracted stopes and connect together in the center of the remnant pillar. Due to the sequence followed in both orebodies, a second pillar appears between the eastern stopes of #1 Shear West and the western part of #1 Shear East, which would be composed mainly of the south dyke, and thus form a waste pillar (Figure 13).

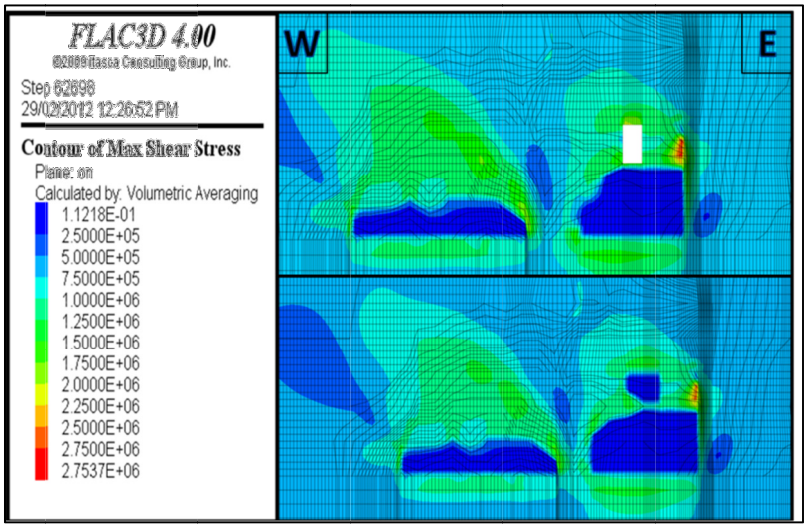

Figure 11 - Vertical cross section of remnant pillar at N -1250 – after stages 12 (top) and 14 (bottom)

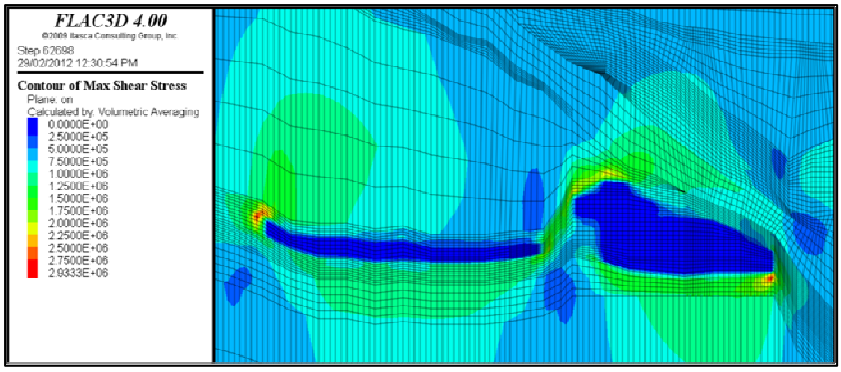

Figure 12 - Level 5000 plan showing #1 Shear West and remnant pillar (centre) after stage 14

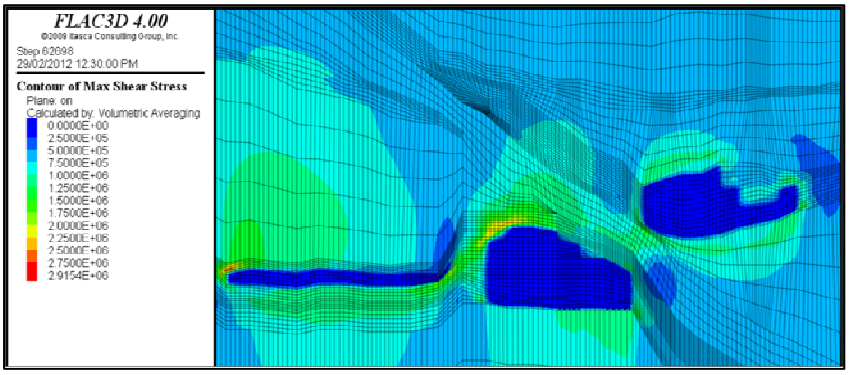

Figure 13 - Level 5100 plan showing #1 Shear West and remnant (left) and waste (right) pillars after stage 14

5. CONCLUSIONS

A combined study of microseismic analysis, rockburst events, and numerical modeling with FLAC^{3D} was conducted for the Garson Mine in order to evaluate the stress levels in a temporary remnant ore pillar in #1 Shear West. The model was calibrated using clusters of microseismic events with large energy levels as well as rockburst events between 2006 and 2008. The locations of these events were observed to correlate well with the maximum shear stress values obtained. After following the stope sequence at the mine until 2011, the model was run with the planned extraction of #1 Shear West between levels 5100 and 4800. The remnant ore pillar that would appear temporarily before being mined out was seen to carry stress levels of 84 MPa ($1.75*10^6$ lb/ft^2). In addition, a second pillar was seen to appear between #1 Shear West and #1 Shear East that was composed mainly of the brittle south dyke (waste pillar), which should also be taken into consideration.

6. ACKNOWLEDGEMENTS

This work is financially supported by a research grant from the Natural Sciences and Engineering Research Council of Canada in partnership with Vale Ltd (CRD Program). The authors are grateful for their financial support.

7. REFERENCES

ARJANG, B. and HERGET, G., 1997. In situ ground stresses in the Canadian hardrock mines: an update. International Journal of Rock Mechanics and Mining Sciences, 34(3-4), Paper 015, 16 p.

BLAKE, W. and HEDLEY, D.G.F., 2003. Rockbursts: case studies from North American hard-rock mines. Littleton: Society for Mining, Metallurgy, and Exploration.

COCHRANE, L.B., 1991. Analysis of the structural and tectonic environments associated with rock-mass failures in the mines of the Sudbury district. Ph.D. Thesis. Queen‘s University, Kingston, Canada.

ECKSTRAND, O.R. and HULBERT, L.J., 2007. Magmatic nickel-copper-platinum group element deposits. In Mineral Deposits of Canada: A Synthesis of Major Deposit Types, District Metallogeny, the Evolution of Geological Provinces, and Exploration Methods, ed. W.D. Goodfellow, Geological Association of Canada, Mineral Deposits Division, Special Publication 5, pp. 205-222.

HASEGAWA, H.S., WETMILLER, R.J., and GENDZWILL, D.J., 1989. Induced seismicity in mines in Canada – an overview. In Seismicity in Mines, ed. S.J. Gibowicz; reprinted from Special Issue, Pure and Applied Geophysics, 129, pp. 423-453, Basel: Birkhauser Verlag.

ITASCA, 2009. FLAC^{3D} Version 4.0: User’s guide. 4th edition.

MARTIN, C.D., KAISER, P.K., and CHRISTIANSSON, R., 2003. Stress, instability and design of underground excavations. International Journal of Rock Mechanics and Mining Sciences. 40, pp. 1027-1047.

MIRARCO, 2005. UCS testing results for Garson Mine, 58 p.

SPOTTISWOODE, S.M., 1989. Perspectives on seismic and rockburst research in the South African gold mining industry: 1983-1987. In Seismicity in Mines, ed. S.J. Gibowicz; reprinted from Special Issue, Pure and Applied Geophysics, 129, pp. 673-680, Basel: Birkhauser Verlag.

TRIFU, C.I. and SUORINENI, F.T., 2009. Use of microseismic monitoring for rockburst management at Vale Inco mines. In Controlling Seismic Hazard and Sustainable Development of Deep Mines, ed. C. Tang, pp. 1105-1114.

YAO, M. and MOREAU-VERLAAN, L., 2010. Strategies for mining in highly burst-prone ground conditions at Vale Garson mine. In Proceedings of the 5th International Seminar in Deep and High Stress Mining, 5-8 October, Santiago (Chile), eds. M. Van Sint Jan and Y. Potvin, pp. 549-560.

Comparison of Two Failure Criteria for the Assessment of Haulage Drift Stability Using Stochastic Analysis and Numerical Modelling

Wael Abdellah
McGill University
Hani S. Mitri
McGill University
Denis Thibodeau
Vale Ltd.
Lindsay Moreau-Verlaan
Vale Ltd.

ABSTRACT: Mine haulage drifts are the primary access to the mining blocks of an orebody in a multilevel mining system of a tabular ore deposit. The stability and functionality of haulage drifts are thus crucial to the success of a mining operation. Drift instability could lead to serious consequences such as injuries, production delays and higher operational cost. In this paper, the performance of the haulage drift stability is evaluated on the basis of the primary rock support system comprising 1.8 m resin grouted rebars in the drift walls and 2.1 m long bolt in the back. Two failure criteria namely the extent of Mohr-Coulomb yield zones around the drift, and linear elastic brittle shear failure are adopted and compared, with respect to lower level and same-level mining and filling sequence in the vicinity of the haulage drift. The case study is one of the #1 Shear East zone of the Garson Mine in Sudbury, Ontario. Random Monte Carlo (RMC) technique, which has been previously established to assess the haulage drift stability, is employed in this investigation. The RMC technique is used in conjunction with finite difference modelling software FLAC for random assignment of model input parameters in the FLAC grid. Deterministic model results reveal the drift behaviour in terms of deformation (convergence) and mining-induced stress distribution. Comparison between the two different criteria is carried out to determine which method is most suitable in evaluating unsatisfactory drift performance. The results are presented in terms of probability of instability and categorized with respect to failure condition and mining step. It is shown that the brittle shear failure condition based on linear elastic response calls for enhanced support system at a later mining step than what Mohr-Coulomb yielding condition does. The paper presents a detailed discussion of the stochastic analysis results.

1. INTRODUCTION

Sublevel stoping method with delayed backfill has been widely adopted by many Canadian metal mines. In this method, ore is mined out in stopes (blocks), which are drilled and blasted. The blasted ore from each stope is mucked out with loaders and transported from a draw point to a nearby ore pass or dumping point. As the haulage drifts are the only access where loaders and/or trucks travel through, thus their stability and functionality are crucial to the success of a mining operation. Hence, they must remain stable during their service life. The stability of haulage drifts may be influenced by many factors such as the strength and quality of the rock mass, mining depth, the distance between haulage drifts and the stopes, mining steps, the dip and thickness of orebody, the geometry of haulage drift (e.g. shape and size), and more importantly nearby mining activity. As mines continue to reach deeper deposits, haulage drifts are expected to experience higher pre-mining stress conditions, thus suffering from more stability problems.

1.1 Study Problem

To examine the stability of haulage drift, a typical section is taken in the #1 Shear East-Orebody, as shown in Figure 1, of Garson Mine, Vale, Sudbury, Ontario. The study zone is divided into three

zones; hanging wall, orebody and footwall. The orebody consists of massive sulphide rock. Six stopes each one 10 m wide by 30 m high are modelled to simulate the ore extraction. The hanging wall contains meta sediments and the footwall is primarily norite rock. The haulage drift is driven in the footwall and its dimensions are 5 m by 5 m with a slightly arched roof. The drift primary support system uses Grade 60, 19 mm (3/4 inch) resin grouted rebars 1.8 m (6 ft) long in the walls and 2.1 m (7 ft) in the back.

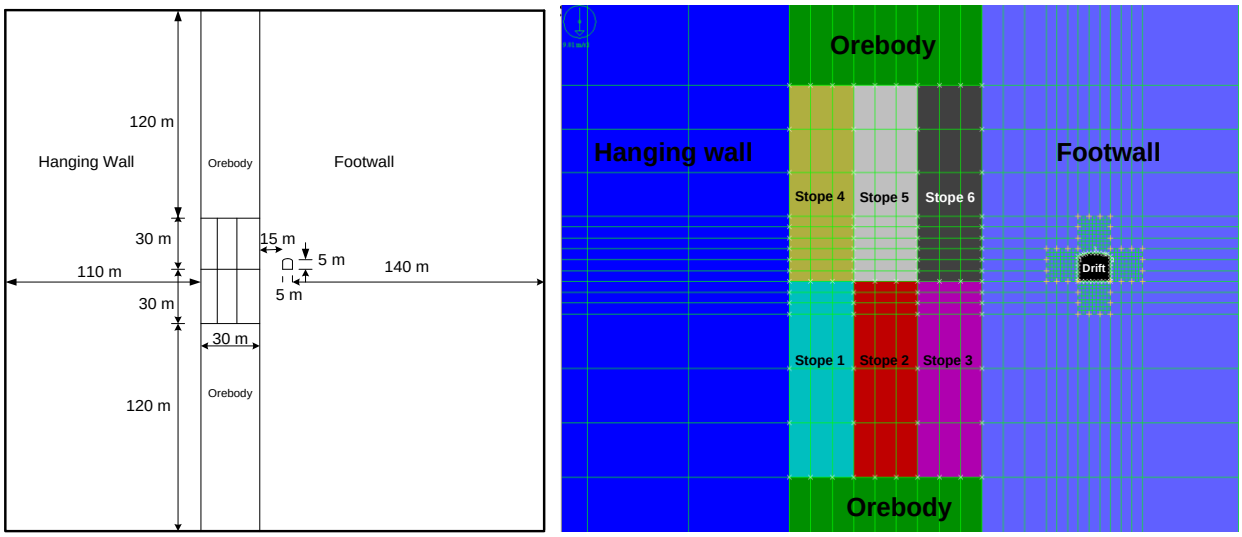

Figure 1 - Model geometry and FLAC model setup

Rock mass properties, backfill mechanical properties and in-situ stress values are obtained from a study conducted by Golder Associate and MIRARCO (2008) and are listed in Tables 1, 2 and 3 respectively.

Table 1 - Model geomechanical properties

Rock mass property	Domain		
	Hanging Wall	Orebody	Footwall
Density (kg/m^3)	2782	4531	2916
UCS (MPa)	90	90	172
E_i (intact) (GPa)	68	72	115
Q'	0.4-2.1	30-37.5	5.8-16.7
E (GPa)	25	20	40
Poisson's ratio, υ	0.25	0.26	0.18
Cohesion, C (MPa)	4.8	10.2	14.13
Tensile strength, σ_t (MPa)	0.11	0.31	1.52
Friction angle, φ (deg)	38	43	42.5
Dilation angle, Ψ (deg)	9.5	10.8	10.6

Table 2- Pastefill mechanical properties

Rock mass property	Paste Backfill
Density (kg/m^3)	2000
UCS (MPa)	3
E (MPa)	100
Poisson's ratio, υ	0.3
Cohesion, C (MPa)	1
Tensile strength, σ_t (MPa)	0.01
Friction angle, φ (deg)	30
Dilation angle, Ψ (deg)	0

Table 3 - In-situ stress values at a depth of 5100 ft (1555 m)

Principal stress	Magnitude, MPa	Orientation	*K*
σ_1	66	EW	1.8
σ_2	56	NS	1.16
σ_3	39	Vertical	

2. PROBABILISTIC METHODS

Due to the heterogeneity of the rock mass, the collected data from underground excavations are limited. Therefore, a great deal of uncertainty is inherent in the design of underground excavations. In order to develop a reliable design approach, one must use methods that incorporate the statistical variation of the numerical model input parameters representing the rock mass properties, i.e. mean, variance and standard deviation, as well as the design of rock failure criteria (Kwangho, Yeonjun and Jun, 2005).

To quantify the uncertainty related to the model input parameters, three possible ways can be used: deterministic analysis, sensitivity analysis, and stochastic simulation approach. In deterministic analysis, the average values of the variables are used as inputs for the simulation model. However, the single values do not give any information about the variability of the input variables. In a sensitivity analysis, a single parameter is systematically varied while all the other parameters are kept constant. The sensitivity analysis provides an understanding of the effect of each parameter on the overall behavior of the model; however, it produces an output with limited practical use. The simulation approach is known as stochastic or probabilistic methods. These methods are used to quantify the uncertainty of drift stability which results from the inaccuracy of underground properties such as Young's modulus, cohesion, friction angle and in-situ stresses. One of the most popular stochastic methods, which is used here in this study, is Random Monte-Carlo (RMC) technique. In this method, material properties vary spatially within the same region; for example, varying the cohesion and friction angle properties spatially within the footwall by randomly assigning values from a defined distribution to zones within the region (Kalamaras, 1996).

2.1 Random Monte Carlo Technique (RMC)

The RMC technique is used to define the unsatisfactory performance of haulage drift. Means and Standard deviations are used to define the input parameters, and then pick random values from a normal distribution. It includes varying the material properties spatially within the same region. One of the primary goals of RMCS is to estimate means, variances, and the probabilities associated with the response of the system to the input random seed. To implement the above mentioned technique, one needs to define a priori, an unsatisfactory performance condition, of the haulage drift. These are discussed below.

3. DRIFT PERFORMANCE EVALUATION CRITERIA

In the following, two evaluation criteria are described, which are used as a basis for the interpretation of numerical model results for the assessment of geotechnical stability of the modeled haulage drift.

3.1 Extent of Yield Zones

Yielding is the most common criterion used in elasto-plastic numerical modelling. The condition of yielding is reached when the stress state reaches the surface of the yield function, which is when the

rock is loaded beyond its elastic limit. Thus, this criterion is used to estimate drift instability or unsatisfactory performance. In this investigation, the Mohr-Coulomb yield function is adopted and elastoplastic behavior of the rock mass is used (Zhang and Mitri, 2008). Further, yielding will be considered a cause for drift unsatisfactory performance if it extends beyond a certain depth into the roof. A rule of thumb is being used herein, whereby the resin grouted rebar can sustain 1 ton of axial load per inch (3.86 KN/cm)anchorage length of the bolt. For the purpose of this study, it is assumed that the resin grouted rebar installed in the sidewall 6ft (1.8 m long) requires at least 12 inches or 30 cm of resin anchorage, and the rebar installed in the drift back 7ft (2.1m long) requires 24 inches or 60 cm of anchorage, in order to achieve full design strength. Based on the support system practice at Garson Mine, the lengths of primary support on the roof and sidewalls (for openings of width ≤ 18 ft or 5.5 m) are 2.1m rebars (7ft) and 1.8m rebars (6ft) respectively. Based on that, the drift unsatisfactory performance occurs when the extent of yield zones exceeds 1.5 m (4.92ft) since insufficient anchorage length is available beyond the yield zone.

3.2. Linear Elastic Brittle Shear

The brittle shear factor (BSF) is similar to factor of safety (FS). In this method, the difference between maximum and minimum principal stresses is calculated according to the following equation (derived from: MARTIN, C. D., KAISER, P. K., and McCreath, 1999):

$$FSS = \frac{\sigma_{1-}\sigma_3}{0.6} \geq UCS \quad (1)$$

Where, FSS is the factored shear stress. Then BSF is calculated from:

$$BSF = \frac{UCS}{FSS} \quad (2)$$

If BSF ≥ 1 safe otherwise, unsafe.

4. RESULTS AND DISCUSSION

Numerical simulation has been performed, using Itasca's FLAC software (Itasca, 2008), to investigate the effect of mining steps on the drift stability. In the numerical modelling process, "modelling steps" are used to simulate the mining and backfilling sequence. All mean values of rock mass are used in the deterministic model, whilst means and standard deviations are used to perform random simulation. This section is divided into two parts, the deterministic and the random simulations.

4.1 Deterministic Analysis

4.1.1 Extent of Yielding Zone (Mohr-Coulomb)

Deterministic model results are shown in Figure 2. These represent the development of yield zones around the haulage drift due to the effect of mining extraction. It can be seen that the yielding zone extends around the haulage drift as mining progresses. The maximum length of the yielding zone exceeds 15 m in the left sidewall (LW) of the haulage drift (after excavating stope 6).

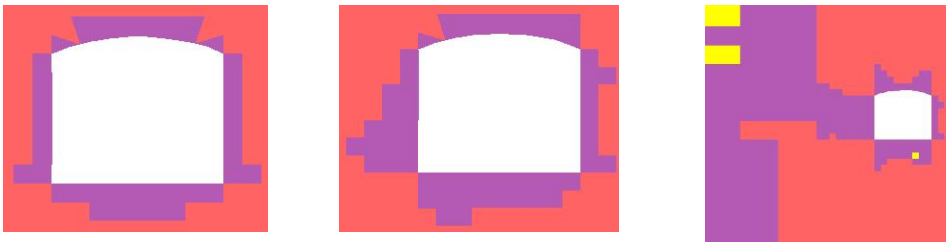

a) after excavating drift b) after excavating stope 3 c) after excavating stope 6

Figure 2 - Progression of yield zones with modelling Mining steps

For this drift size (5 m x 5 m), this progression of yielding depth greatly exceeds the support lengths of 1.8 m and 2.1 m. The extent of yielding in the roof, left wall (LW) and right wall (RW) after each mining step is reported in Table 4. Figure 3 shows the mining steps with respect to the extent of yield zones (Deterministic Model).

Table 4 - Extent of yield zones at different mining steps (Deterministic Model)

Mining step	*Extent of yield zones, m*		
	Roof	LW	RW
0 (Drift excavation)	0.67	1.09	1.14
1(Stope 1 excavation)	0.80	1.65	1.09
2(Stope 2 excavation)	1.14	1.67	1.12
3(Stope 3 excavation)	1.15	2.25	1.11
4(Stope 4 excavation)	1.63	5.04	1.12
5 (Stope 5 excavation)	1.68	5.02	1.09
6 (Stope 6 excavation)	2.80	15.07	1.11

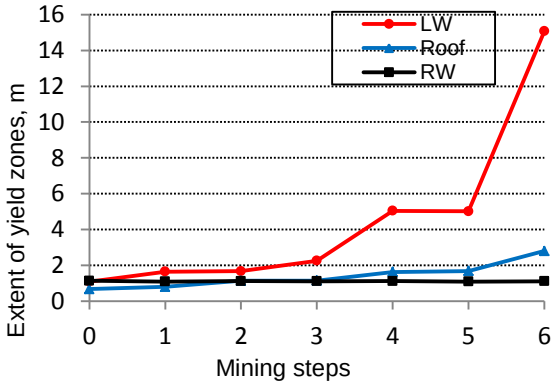

Figure 3 - Mining steps vs. extent of yield zones

4.1.2 Linear Elastic Brittle Shear Failure

A new brittle shear factor (BSF) is used to evaluate drift instability with elastic analysis, as presented in Equations 1 and 2. The difference between Major and Minimum principal stresses, expressed as factored shear stress (FSS) around the haulage drift, is shown in Figure 4. This Figure indicates that the increase in stress concentration around the drift back is directly related to the increase in mining steps. The maximum stress value reaches (FSS =225 MPa) after excavating stope 3. Stress relaxation occurs after excavating stopes 4 to 6 (FSS=112.5 MPa).

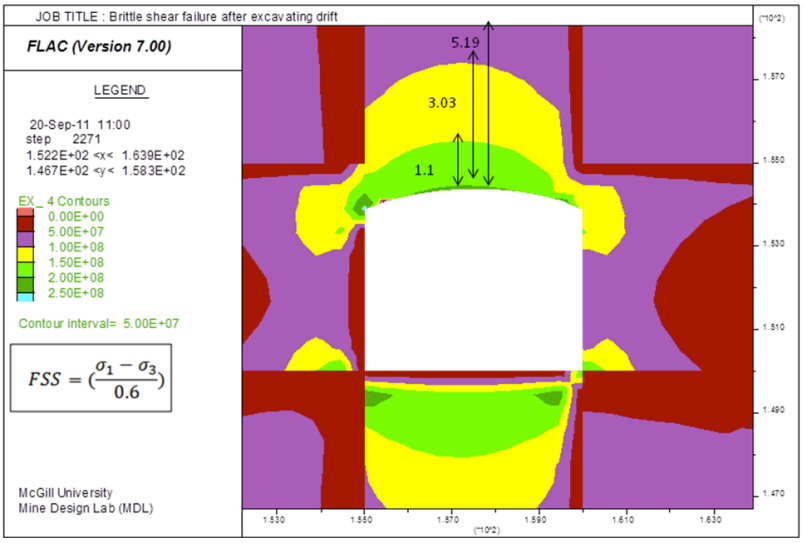

a) after excavating drift

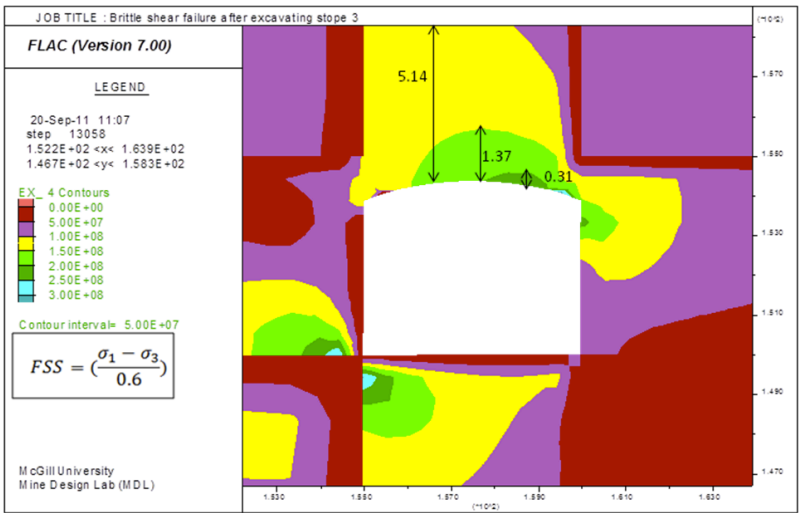

b) after excavating stope 3

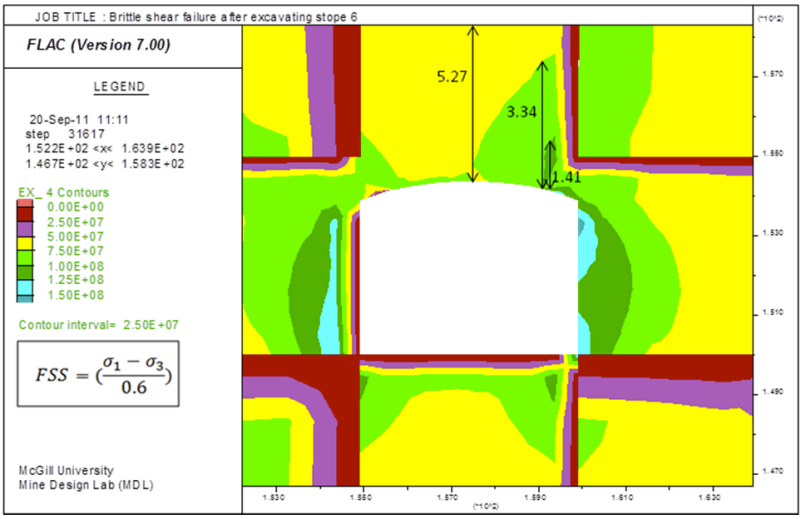

c) after excavating stope 6

Figure 4 - Factored shear stress contours (elastic deterministic model)

Brittle shear factor (BSF) is calculated according to Equation 2 and the results are shown in Table 5 and Figure 5.

Table 5 - Mining induced stresses around drift and brittle shear factor calculations

Mining step	UCS, MPa	FSS, MPa	BSF	Location around drift
0 (Drift excavation)	172	175	0.98	Back
1(Stope 1 excavation)	172	175	0.98	Back
2(Stope 2 excavation)	172	175	0.98	Back
3(Stope 3 excavation)	172	225	0.76	Back
4(Stope 4 excavation)	172	112.5	1.53	Shoulder
5(Stope 5 excavation)	172	112.5	1.53	Shoulder
6(Stope 6 excavation)	172	112.5	1.53	Shoulder

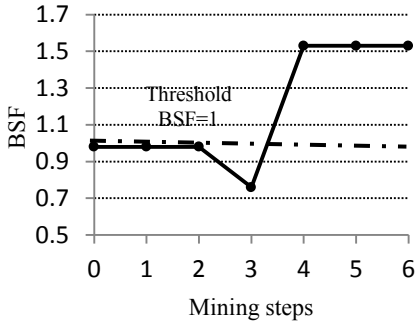

Figure 5 - BSF versus mining steps

4.2 Stochastic Analysis

Random Monte-Carlo (RMC) technique is adopted to carry out this simulation. It includes varying the material properties spatially within the same region. Random material properties of footwall (due to its close proximity to the shear zone orebody and the dyke) were assigned using an inbuilt function in FLAC. The means and standard deviations of these values are picked from a normal distribution. One hundred runs are completed to analyze the performance criteria of the model output; extent of yield zones, brittle shear failure, and BSF. Based on the parametric study that has been conducted, the most influencing model input parameters are Young's modulus (E), cohesion (C), angle of internal friction (Φ), and horizontal-to-vertical stress ratio (K). In this study, only three footwall parameters are considered, cohesion (C), friction angle (Φ) and Young's modulus (E), as shown in Table 6.

Table 6 - Random properties for footwall rock

Rock mass property	Mean (μ)	Standard deviation (SD)	Coefficient of variation (COV)	Remarks
Cohesion (C), MPa	14.13	2.83	0.20	Used with Mohr-Coulomb yield zones
Friction angle (Φ), (deg.)	42.5	8.5	0.20	
Young's modulus (E), GPa	40	8	0.2	Used with Linear elastic brittle shear

4.2.1 Stochastic Results of Yielding

As introduced before from deterministic model results, it is obvious that the maximum extension of yielding occurs in the drift left wall (LW) and in the back, so only stochastic analyses using RMC for the left wall and back will be introduced here as shown in Figures 6 and 7 respectively. The yielding cut-off (threshold) for performance function is 1.5 m, as the anchorage length of primary support is considered to be 12 inches (30 cm).

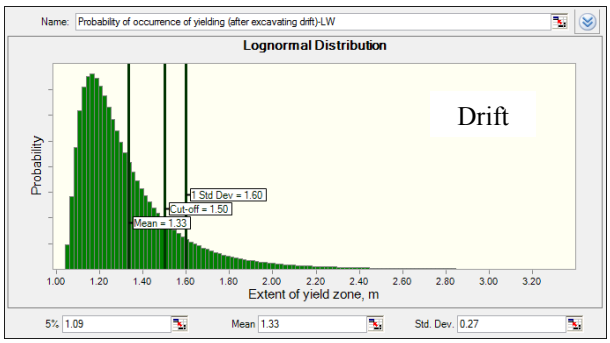

a) PDF of yielding (drift)- LW

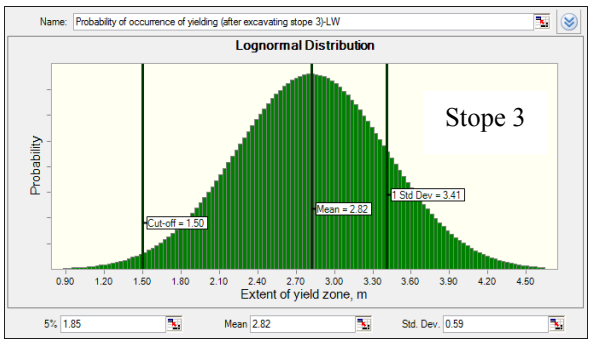

b) PDF of yielding (stope 3)- LW

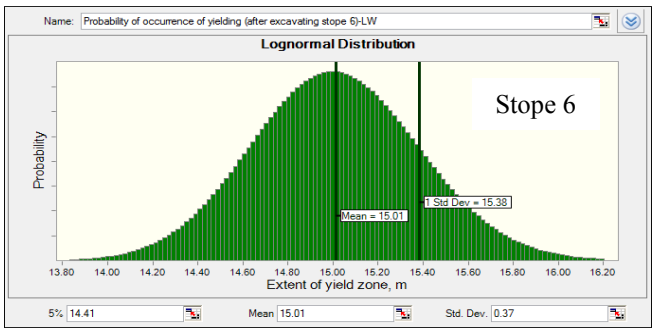

c) PDF of yielding (stope 6)- LW

Figure 6 - Probability Density Function (PDF) of yielding after 100 simulations-LW

It is clear from all these lognormal distributions that, with mining advance the progression of yielding depth increases (e.g. lateral shift of cut-off "red marked circle" towards the vertical axis of probability of occurrence). This is evident through an increase in the area under the distribution curves.

The probability of instability (P(i)) of the haulage drift based on yielding criterion is estimated as shown in Figure 8.

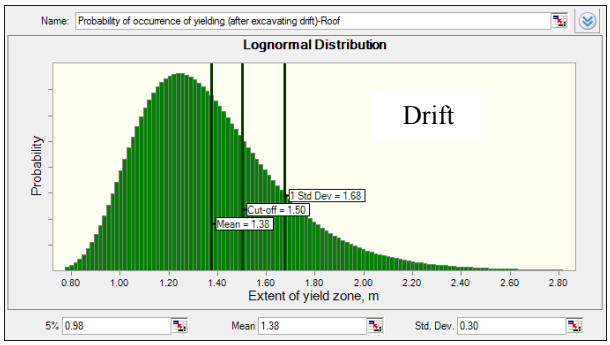

a) PDF of yielding (drift)- roof

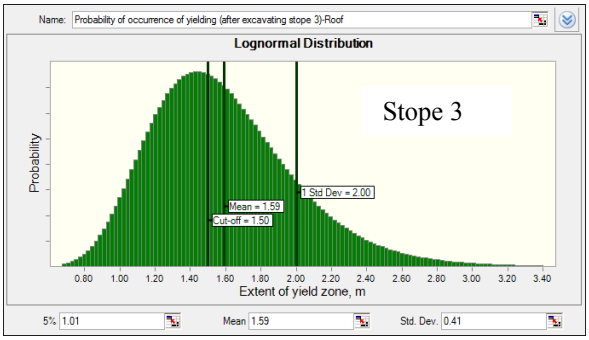

b) PDF of yielding (stope 3)- roof

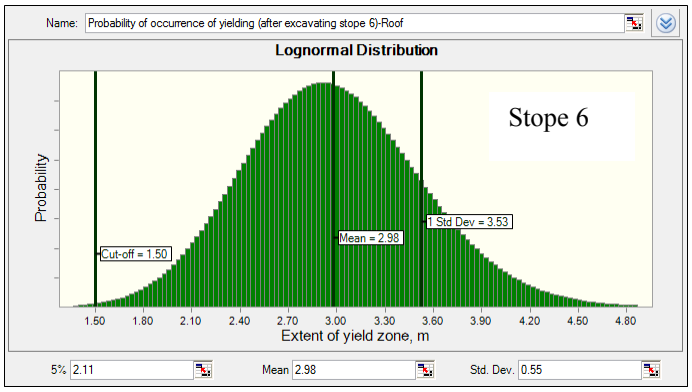

c) PDF of yielding (stope 6)- roof

Figure 7 - Probability Density Function (PDF) of yielding after 100 simulations-Roof

4.2.2 Stochastic Results of Linear Elastic Brittle Shear

The stochastic analysis for the BSF is shown in Figure 9. It is obvious that the ratio of brittle shear factor (BSF) with respect to mining lower stopes (stopes 1 to 3) of the same level is less than unity and this is due to high stress concentrations around the drift back. However, this ratio of BSF exceeds unity when mining upper stopes (stopes 4 to 6) of the same level and this is due to stress relaxation occurrence.

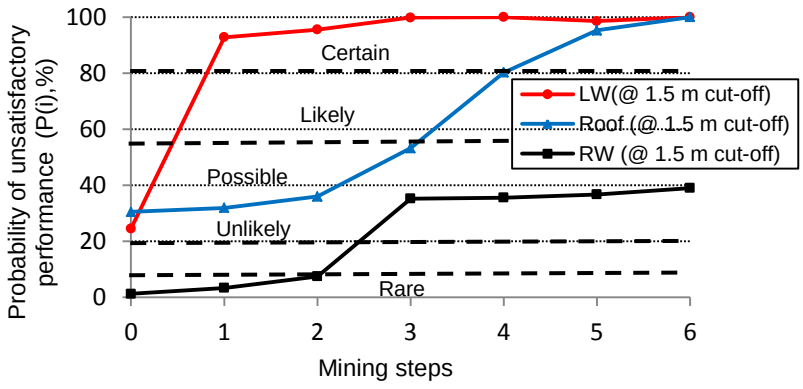

Figure 8 - Probability of instability (P(i)) for haulage drift due to yielding condition

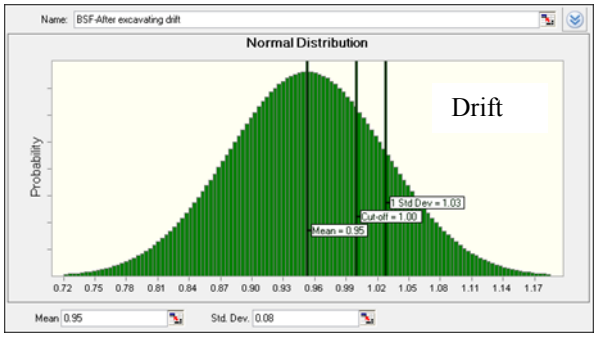

a) PDF of brittle shear (drift)

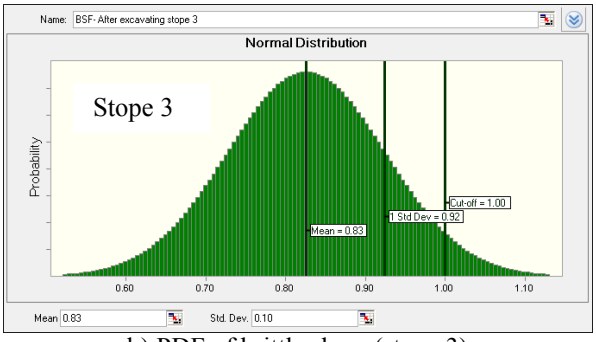

b) PDF of brittle shear (stope 3)

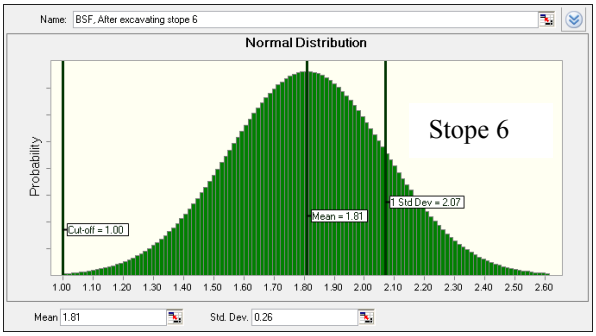

c) PDF of brittle shear (stope 6)

Figure 9 - Probability Density Function (PDF) of brittle shear factor (BSF) after 100 simulations-Roof

The probability of instability (P(i)) or unsatisfactory performance of haulage drift based on linear elastic brittle shear factor is estimated as shown in Figure 10.

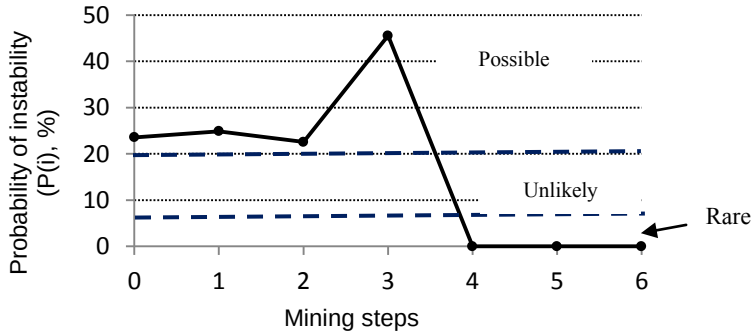

Figure 10 - Probability of instability (P(i)) for haulage drift back due to linear elastic brittle shear condition

5. CONCLUSION

This paper presents the results of a stepwise methodology to evaluate the drift performance due to interaction between haulage drift and nearby mining activity related to sublevel stoping method with delayed backfill, one of the most popular mining methods in Canadian underground metal mines. The methodology used to implement probability of unsatisfactory performance in drift stability modelling is presented using Random Monte-Carlo (RMC) in conjunction with Finite difference modelling software FLAC. Two evaluation criteria are adopted namely; Mohr-Coulomb yield zones, and linear elastic brittle shear. Minimum resin embedment lengths of 12 inches (30 cm) and 24 inches (60 cm) are taken for Grade 60, ¾-inch (19 mm) resin grouted rebar to reach the 134 kN full capacity. Thus,

the haulage drift performance is considered unsatisfactory when the extent of yield zones exceed 1.5 m. Based on these two evaluation criteria, it was concluded that the yielding criterion is more conservative. The highest probability of unsatisfactory performance is found in the left wall of the drift (facing the orebody) as mining progresses. Brittle Shear Factor (BSF) is a good indicator to evaluate drift instability with elastic analysis; however, it is still less conservative than yielding criterion. It is noteworthy that failure criteria must be calibrated based on underground measurements and this work is currently underway at Garson Mine.

6. ACKNOWLEDGEMENT

This work is financially supported by a research grant from the Natural Sciences and Engineering Research Council of Canada in partnership with Vale ltd. The authors are grateful for their support.

7. REFERENCES

Golder Associate and MIRARCO (2008), Geotechnical study -Garson Mine, Project Report: October 31, 2008, 07-1117-0060.

ITASCA Consulting Group, Inc., (2008). FLAC, Fast Lagrangian Analysis of Continua, Version 6., Itasca Consulting Group, Minneapolis, Minnesota, USA.

KALAMARAS, G. S., (1996), "A case method approach for interactive risk analysis of tunnel design-for-constructability concept", Ph.D. Thesis, The Pennsylvania State University, 217 p

KWANGHO Y., YEONJUN P., and JUN L. S.(2005), "Risk analysis for determination of a tunnel support pattern", Tunnelling and Underground Space Technology 20 (2005) 479-486.

MARTIN, C. D., KAISER, P. K., and McCreath, (1999), "Hoek-Brown parameters for predicting the depth of brittle failure around tunnels", Can. Geotech. J. 36: 136-151 (1999).

ZHANG, Y., and MITRI, H. S., (2008), "Elastoplastic stability analysis of mine haulage drift in the vicinity of mined stopes", International Journal of Rock Mechanics and Mining Sciences, 45 (2008) 574-593.

Quantifying the Loss of Support Capacity Due to Corrosion

Jean-François Dorion
Niobec Inc.
John Hadjigeorgiou
Lassonde Institute of Mining, University of Toronto
Edward Ghali
Université Laval

ABSTRACT: In an underground mine rock reinforcement elements and surface support units are often exposed to conditions that make them susceptible to corrosion. These unfavourable conditions include high relative humidity, the presence of dust and various other particles in the atmosphere, splashing of water and gases from blasting and diesel equipment. The corrosion of support systems is often associated with a loss in capacity that can be a major safety and economic concern in underground mines. A support system is composed of several components such as bolts, mesh, plate, retaining nut, cable ties. Every individual component can deteriorate due to atmospheric or aqueous corrosion and consequently can damage the integrity of the support system. This paper reports the results of a 5-yr study on the loss in capacity of individual support and reinforcement components at selected underground hard rock mines. As part of this investigation corrosion coupons were installed at selected locations at participating mines. A number of these coupons were recovered at regular time intervals and analysed for any signs of corrosion and subsequently tested to quantify any loss in capacity. The testing of the corrosion coupons was complemented by similar tests on recovered mesh and friction bolt specimens from the site. The collected data have provided useful insights on the factors that contribute to the corrosion of support systems. This knowledge can aid in the selection of appropriate support strategies and a reliable assessment of the predicted useful life of a support system and the need for rehabilitation.

1. INTRODUCTION

The design and installation of reinforcement and support systems in underground mines is well advanced. Nevertheless, despite great strides in design and quality control practice, it has been difficult to eliminate ground falls. An important problem is the reduction in the capacity of support systems over time. In certain cases reduction in capacity can be attributed to the corrosion of support systems. The impact of corrosion on the integrity of support is illustrated in Figure 1 where a ground fall occurred in a drift immediately following a production blast. The corroded rock bolts and mesh no longer provided the support for which they were designed and installed resulting in the fall of ground.

The loss in capacity of support systems over time is not explicitly considered in the design of support systems. The conventional wisdom is that certain rock bolts corrode more than others and are not suitable for certain mines but this is not part of the design process. Instead, corrosion issues come into the forefront following important ground falls. In these cases, depending on the consequences of failure, the emphasis is on fracture analysis aiming to identify whether corrosion was a contributing factor to the system failure (Hadjigeorgiou, J. et al., 2002). Nevertheless, recognising the importance of corrosion on ground support performance, there have been some serious efforts towards developing classification systems to determine the susceptibility of an environment towards corrosion (Robinson and Tyler, 1999, Hassel et al., 2004). However, for a variety of reasons these classification systems have not gained widespread acceptance.

Figure 1 - Ground fall after a seismic event where rock support was corroded

This paper summarizes efforts in gaining an improved insight on the factors that contribute to the loss of capacity due to corrosion of support systems. This investigation program combined on site analysis with comprehensive laboratory experiments and testing. The long term objective is to develop sufficient data and understanding that can be used in the selection of appropriate support strategies, and eventually to a reliable assessment of the predicted useful life of a support system. This knowledge can have important safety and economic repercussions for underground mines.

2. UNDERGROUND SUPPORT SYSTEMS

The type of rock support types used in underground mines does not differ much from site to site, although there are some variations in the choice and density of support to account for specific ground conditions such as mine seismicity, squeezing rock, etc.

Mechanical point anchored rock bolts are typically used in average to good ground conditions. A mechanical point anchor bolt uses an expansion shell to secure an anchor point at the end of a drilled hole in competent ground. Resin and cement grouted bolts rely on the bonding strength of the cement/resin to transfer rock loads. Resin grouted bolts employ a number of sealed polyester resin and catalyst cartridges that are mixed within the hole by spinning of the bolt. Different types of rods can be used. In general they provide a high degree of resistance to corrosion. Friction anchored rock bolts consist of a variable-length steel tube slotted along its length. The bolts are pushed, using a drill adapter or a bolter, into slightly smaller boreholes. Expanded rock bolts (e.g. Swellex) employ friction as the reinforcement mechanism. Their pullout resistance is due to the friction and pressure of the bolt on the wall of the borehole. The bolt consists of a steel tube, folded in, and expanded in a smaller hole through high water pressure.

Cable bolts consist of a flexible tendon of steel wires wound in a strand. The tendons are grouted into a borehole and can be used for long reinforcement in a number of excavations such as stope support, draw points, intersections, etc.

The role of bolt plates is to transfer loads to the mesh as well as maintain tension in the bolts and to keep the mesh and straps in place. They are also used to maintain the confinement of rock blocks beneath the collar. Two types of wire mesh are commonly used in mining: weld mesh and chain link. The main purpose of mesh is to retain small blocks of broken ground between rock bolts. The use of surface support such as mesh in conjunction with bolts constitutes the support system.

2.1 The Use of Corrosion Inhibitors

Given the susceptibility of steel to corrosion it is not surprising that certain mines resort to the use of more resistant support systems. This includes the use of galvanised support systems, e.g. galvanised mesh, the use of special coatings such for example applied to Mn Swellex bolts. These approaches result

in higher costs and can only be justified if it can be demonstrated that they prolong the useful life of a support system.

3. QUANTIFYING CORROSION

3.1 Visual Qualification

In the early stages of this study we developed a chart, presented in Figure 2, to describe the level of corrosion of installed rock support. The chart was developed based on experience gained from several site visits over the years. This chart identified six corrosion levels for both atmospheric and aqueous corrosion. The chart provided a reference point to compare observations at different sites. The usefulness of the chart increases when there is also information on how long the support has been installed at a particular site. This is necessary if the objective becomes the determination of the corrosivity of an environment. A corrosion level #4 for support installed 15 years ago, does not raise the same level of concern as a support of only 3 months of exposure. For this reason, any prediction on the performance of support and loss of capacity, based on visual observations, requires that the time in service is also known.

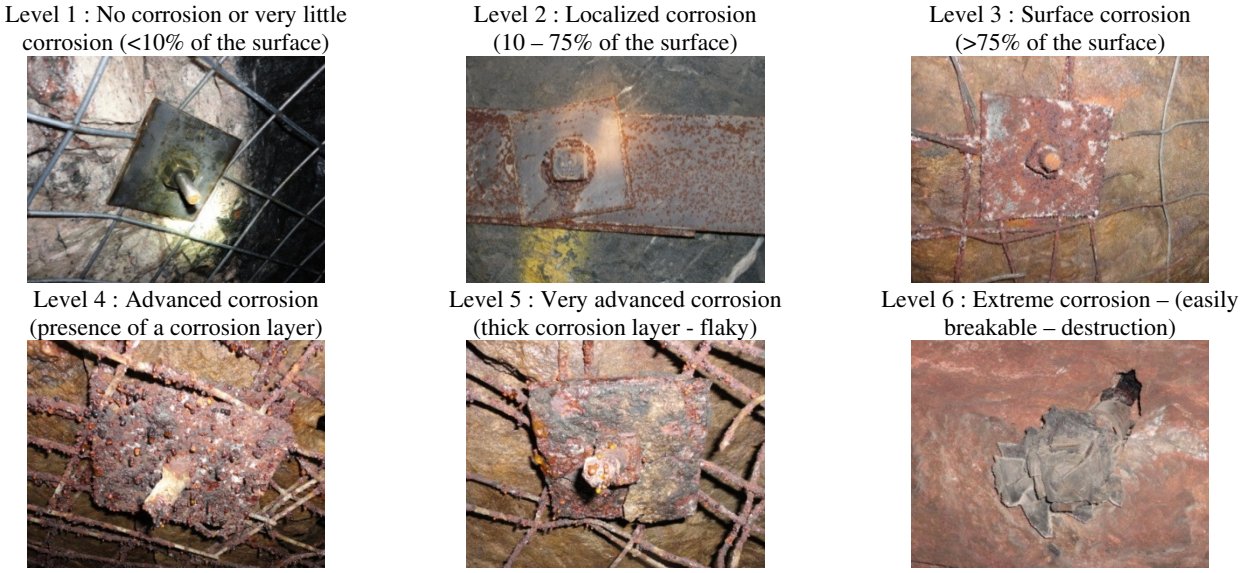

Figure 2 - Visual corrosion level chart (Dorion and Hadjigeorgiou, 2008)

3.2 Measurements of Corrosion Rate

At the participating mines a simple method of corrosion monitoring, coupon testing, was used to monitor the corrosivity of different environments over time. In this study we employed standard coupons (100 x 15 x 1.5 mm) prepared and cleaned following the ASTM Standard G4 (ASTM Standard, Designation: G 4 – 01, 2003). Figure 3 provides a visual and qualitative assessment of the evolution of corrosion after several months of exposure. At this particular site the non-galvanized plates were subject to corrosion attack but there were no signs of penetration. Instead, what was observed was that thin superficial corrosion layer was deposited on the plates. The same site was revisited after six and 12 months.

Figure 3 - Corrosion coupons attached to the mine screen on the drift wall, after a three-month exposure

These visual observations are both illustrative and provide an understanding of the process. In parallel, this investigation aimed to quantify the impact of corrosion on support capacity. For these purposes selected coupons were recovered, after three, six, twelve and sixteen months since installation. These collected coupons were brought into the laboratory in order to determine the corrosion rate and eventually estimate their reduction in strength. Once the coupons were brought into the laboratory they were treated in order to remove corrosion products following the ASTM Standard G1 (ASTM Standard, Designation: G 1–03, 2001). The initial total surface area and the mass lost during the time that the coupons were exposed underground were used to estimate the average corrosion rate (mm/year):

$$\text{Corrosion Rate} = \left(\frac{K \times W}{A \times t \times d} \right) \tag{1}$$

where: $K = 8.76 \times 10^4$ (for units in mm/y); t = time of exposure in hours; A = area in cm^2; W = mass loss of coupon in grams, and d = density of coupon in g/cm^3.

An interesting question is the link between corrosion rate and observed corrosion. There has been minimal information in a ground support context. A useful indicator has been proposed by Li and Lindblad (1999) and is reproduced in Table 1.

Table 1 - Corrosion rate and level of corrosion

Corrosion rate (mm/yr)	Description
<0.05	Very little corrosion
0.05 – 0.10	Little corrosion
0.10 – 0.15	Moderate corrosion
0.15 – 0.30	Severe corrosion

Another question that is often raised in the selection of reinforcement and support units is the gains from using galvanization as a corrosion inhibitor. In this study the galvanized coupons were consistently more resistant to corrosion after 12 months of underground exposure at the monitored mine sites (Hadjigeorgiou, Dorion and Ghali, 2008).

4. QUANTIFYING THE LOSS OF CAPACITY

4.1 Tensile Strength of Corrosion Coupons

The tensile strength of recovered coupons was determined following the ASTM E8 standard (ASTM Standard, Designation: E 8– 99). This has allowed the determination of loss in the capacity as a function of the coupon corrosion rate. The reference samples were coupons not installed underground. It was then possible to correlate the corrosion rate (loss of mass) and reduction of steel strength. The observed trends

are illustrated in Figure 4 based on data are from all underground sites where the coupons were exposed for 12 months. The results demonstrate a strong correlation between a reduction in coupon strength and a uniform corrosion rate (Dorion, Hadjigeorgiou and Ghali 2010).

A major challenge in ground control management is the ability to predict the reduction in the capacity of a support system when exposed to a corrosive environment. Access to such information can allow the mine to identify areas of risk, to monitor these areas and consider mitigating risk by installing secondary support, planning rehabilitation strategies, etc. The results of this investigation, based on data collected over 12 months indicate that there is a direct correlation between loss in strength and corrosion rate, Figure 4.

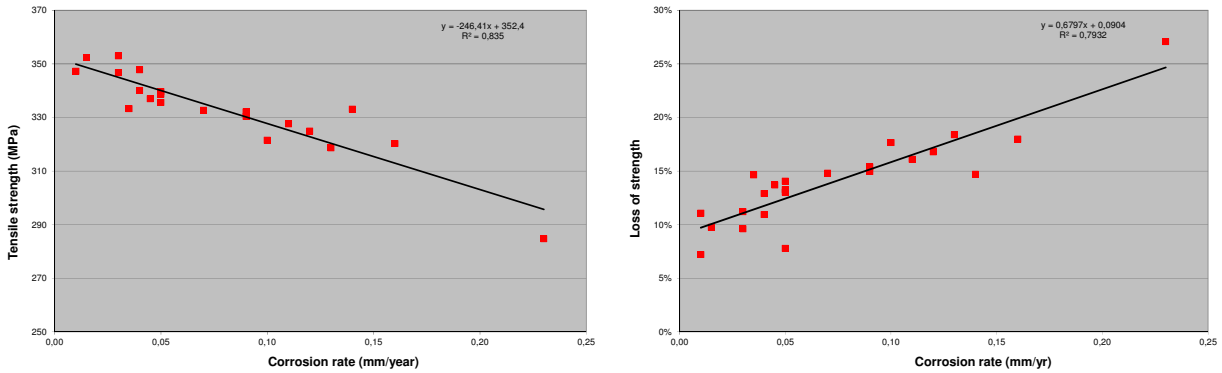

Figure 4 - A) Relation between tensile strength and corrosion rate, and B) Percentage loss of strength as a function of corrosion rates after 12 months of exposure

Preliminary analysis, of the recovered coupons from the mine sites, focused on the influence of uniform corrosion in the reduction of capacity of the coupons. For these purposes, the thickness of the coupons was determined along its full surface using a caliper. This approach is useful but does not take into consideration the impact of localised corrosion. In a second part of this investigation, individual coupons were reviewed under a microscope where it was possible to observe the influence of crevice corrosion and pitting on the thickness of the coupons. This approach, illustrated in Figure 5, can eventually be employed to identify the frequency of corrosion types and their impact on support capacity.

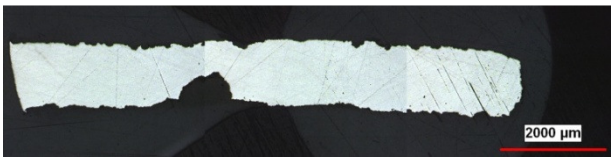

Figure 5 - Photomicrography of a section of a corrosion coupon representative of crevice corrosion

The results clearly demonstrated that the influence of corrosion on the strength of the steel coupons can be quantified. Furthermore, there is an important correlation between the corrosion rate and the strength of the steel coupons. It is recognised, however that further work will have to address the importance of non-uniform corrosion, pitting, crevice types of corrosion as compared to uniform corrosion on the performance of support systems.

4.2 Results for Weld Mesh

In an underground mine corroded mesh is quite often the "weakest link", i.e. the first component of a support system to fail. During this investigation portions and elements of screen where recovered from different mines sites. Figure 6 illustrates some elements of screen at different levels of corrosion including non-corroded strands. Each sampled was photographed, described, and its level of corrosion recorded. The objective is to establish a procedure where readings underground are used as a quality control procedure and as the primary input to the developed charts. Consequently the following simplified procedure was used. The corrosion crust at every strand was removed using a brush and steel wool. The samples were not cleaned from all corrosion products. This allowed the same cleaning procedure, if required, to be reproduced underground. A digital caliper was used to measure the diameter. Since mesh is expected to break at its minimal cross section during tensile strength testing, we recorded the minimal strand diameter for each sample.

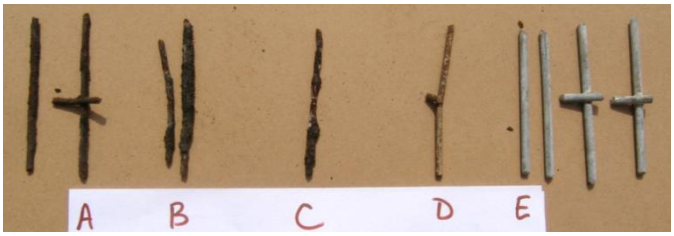

Figure 6 - Weld mesh samples for tensile strength test

A total of 94 mesh strand samples were submitted to tensile strength testing. Among those 94 samples, 32 had a weld joint in the middle and of those 31% failed at or in the immediate vicinity of the weld joint. This is interesting and is in general agreement with the work of Villaescusa (2004) on identifying the areas of weakness of mesh tested under ideal conditions. It was observed that welded wire mesh, failed at three locations: 1) break at the weld; 2) failure in the area affected by the heat from the welding, i.e. the Heat Affected Zone (HAZ); and 3) failure of a strand. The shear strength tests indicated that 90% of the tested mesh failed at the area affected by the heat of welding (HAZ). The potential of corrosion was not part of the investigation by Villaescusa.

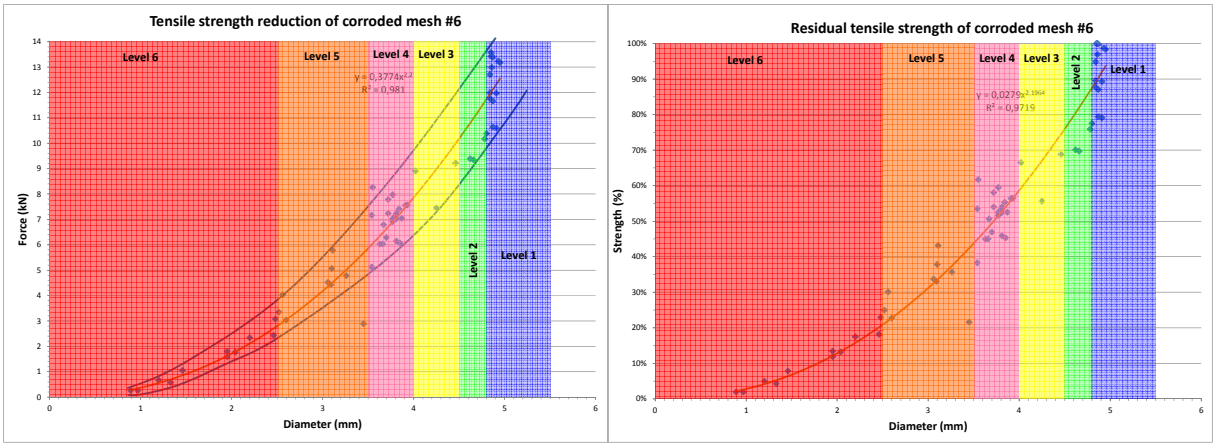

Figure 7 - Weld mesh tensile strength test results a) peak load as a function of diameter and b) residual strength (%) as a function of diameter

The results of the present study are illustrated in Figure 7. A strong correlation was observed between the tensile strength and the diameter of the mesh strand. However, as the tests were on corroded samples, they were affected by pitting and crevice corrosion types of localized corrosion form. Consequently the tested mesh was not of a uniform strand diameter.

The mathematical relation between the force of a corroded mesh and its diameter is:

$$Force\ (kN) = 0.38 \times d^{2,2} \tag{2}$$

The mathematical relation between the residual tensile strength of a corroded mesh and its diameter is:

$$Strength\ (\%) = 2.8 \times d^{2.2} = 100 \frac{\left(0.38 \times d^{2.2}\right)}{13.4} \tag{3}$$

$$Loss\ of\ strength\ (\%) = 100 - 2.8 \times d^{2.2} \tag{4}$$

It is possible to use the graphs to estimate the residual resistance or loss of strength of a corroded rock support mesh only by measuring the diameter after removing the corrosion crust. Qualifying the corrosion level can also provide a good estimate of its residual strength. An on-going analysis of further tests should improve our understanding of the link between corrosion rate and the loss of strength. Variation in results can be attributed to pitting and crevice corrosion (Figure 8). It was also observed that when a corrosion crust is formed around the strand, the thickness of the mesh is greater than its initial diameter. Even with a good brushing, some adherent corrosion products remain and the thickness of the strand can be over-estimated.

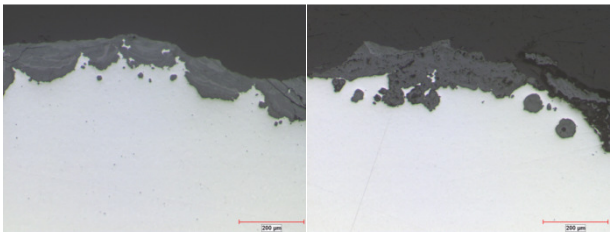

Figure 8 - Photomicrography of sections of weld mesh with crevice corrosion and pitting

4.3 Further Tensile Strength Tests

In order to complement this investigation, samples from plates and friction bolts were also tested. The plates and bolts displayed the complete range of corrosion levels, including plates that were not exposed. The same sample preparation procedure was used as before, to remove the corrosion crust and each sample was measured to determine its thickness. The results are in general agreement with those obtained for the weld mesh. This work is on-going.

5. CONCLUSIONS

It has been demonstrated that corrosion coupons provide an excellent method to quantify the corrosion rate of support in an underground mining environment. Coupons installed at different sites provided a consistent narrative on the evolution of corrosion of support in a range of environments. The implementation of a tensile test program has provided further information. There is a direct relationship between the tensile strength of corroded samples and the recorded corrosion rate, or thickness, of the component. This has allowed the construction of a design chart to quantify the impact of corrosion on the

loss of capacity of rock support. A review of on-site observations over a five year period and from the experimental program has allowed the authors to prepare a series of guidelines on the susceptibility of different support elements.

6. ACKNOWLEDGEMENTS

The authors would like to acknowledge the continued support of the management and on-site personnel of the following mine sites: LaRonde, Mouska, Doyon-Weswood, Niobec, Persévérance and Géant-Dormant. The authors would further like to acknowledge the technical support provided by Vicky Dodier, Daniel Marcotte, Geneviève Bruneau, Maude Larouche, Jean Frenette and Marie-Josée Bouchard.

7. REFERENCES

HADJIGEORGIOU, J., E. GHALI, F. CHARETTE and M.R. KRISHNADEV, 2002. Fracture Analysis of friction rock bolts, Proceedings of the 5th North American Rock Mechanics Symposium and the 17th Tunneling Association of Canada, Conference: NARMS-TAC, pp. 881-887.

ROBINSON, J. and D.B. TYLER, 1999. A study of corrosion in underground reinforcement at Mount Isa Mines, Corrosion classification of the underground environment, Rock Support and Reinforcement Practice in mining, Villaescusa, Windsor, & Thompson (eds), Balkema, Rotterdam, pp. 77-82.

HASSELL, R., E. VILLAESCUSA, A.G. THOMPSON, and B., KINSELLA, 2004. Corrosion assessment of ground support systems, Ground Support in Mining and Underground Construction, Villaescusa & Potvin (eds.), Taylor and Francis Group, London, pp. 529-542.

DORION, J.F. and J. HADJIGEORGIOU, 2008. Caractérisation des environnements miniers menant à la corrosion des systèmes de soutènement. Maintenance Engineering Underground Mine Operators Conference, CIM, Val D'Or, Cd-rom.

ASTM Standard, Designation: G 4 – 01, 2003, Standard Guide for Conducting Corrosion Tests in Field Applications, ASTM International, 100 Barr Harbor Drive, PO Box C700, West Conshohocken, PA 19428-2959, United States.

ASTM Standard, Designation: G 1–03, 2001, Standard Practice for Preparing, Cleaning, and Evaluating Corrosion Test Specimens, ASTM International, 100 Barr Harbor Drive, PO Box C700, West Conshohocken, PA 19428-2959, United States.

LI, C. and K. LINDBLAD, 1999, Corrosion classification of the underground environment, Rock Support and Reinforcement Practice in Mining, Villaescusa, Windsor & Thompson (eds), Balkema, Rotterdam, pp. 69-75.

HADJIGEORGIOU J., J.F. DORION AND E. GHALI, 2008. Support System Performance Under Different Corrosion Conditions. The Journal of the Southern African Institute of Mining and Metallurgy, Vol. 108 June 2008 pp. 359-365.

ASTM Standard, Designation: E 8– 99, Standard Test Methods to Tension Testing of Metallic Materials, ASTM International, 100 Barr Harbor Drive, PO Box C700, West Conshohocken, PA 19428-2959, United States, 1999.

DORION, J.F., J. HADJIGEORGIOU and E. GHALI 2010. Influence of corrosion rate on the capacity of rock support, ARMA 10-259, American Rock Mechanics Association, the 44th US Rock Mechanics Symposium and 5th U.S.-Canada Rock Mechanics Symposium, held in Salt Lake City, UT June 27–30, 2010.

VILLAESCUSA, E., 2004. Weld Mesh for static rock support in Australia, Chapter 14, Surface Support in Mining Potvin, Stacey and Hadjigeorgiou (eds) pp. 385-389.

Evaluating Immediate Mining Induced Ground Movement by Monitoring the Performance of the Primary Support System

Wei Wei
Area Mines Engineering, Vale Manitoba Operation
Hani S. Mitri
McGill University
Cecile Kelly
Vale Manitoba Operation

ABSTRACT: Mining induced ground movement and/or stress redistribution could cause ground instability issues. This is particularly true when the extraction of large stopes is done with one or two large production blasts. Often enough, it is the nearby mine development like haulage drifts and cross cuts that are influenced the most by production blasts. Proper and timely mitigation of ground control issues due to stress redistribution is required. This is usually done by drift rehabilitation involving the installation of secondary support system in the affected areas of the mine development which include; slashing, wire mesh, and in some cases the use of shotcrete liners. It is imperative that such rehabilitation be implemented to the mine infrastructure in a timely manner in order to avoid aggravated ground control problems and production delays. If the real time performance of the support system is captured, it would be possible to determine the timing for rehabilitation job. Birchtree Mine in Thompson, at the Vale Manitoba Operation, has begun mining the 84 Deep Orebody. One of the identified risks is the stability of the crusher room under mining induced stress redistribution. It is proposed to use the U-Cell technology to monitor the primary support system performance (rebar bolts and extension bolts) and monitor the real time performances of the bolt axial loads. The U-Cell technology is a 7-inch long, coupler load cell that is screwed onto the threaded portion of a rock bolt prior to installation. Rehabilitation in the vicinity of the crusher area where U-Cells are installed is recommended when the bolts have reached 70% of their yielding capacity. Catastrophic ground failure can be avoided by adding secondary support in a timely fashion. This paper presents a case study at Birchtree Mine in Thompson Manitoba, where the performance of primary ground support system is monitored and recorded during production.

1. INTRODUCTION

Ground control challenges at Birchtree Mine, Vale Manitoba Operation are mainly due to the complex geological conditions, which typically could be identified as a combination of Ultramafic hosted orebody, localized shear zone, and faults. This paper will introduce and discuss ground control practices in the 84 Deep Orebody, Figure 1, where 1) Peridotite is usually encountered in crosscuts, which makes it difficult to support this rock type that is soft and has very low adhesion; 2) infrastructure is located in moderately foliated schist zone and slightly above the intersection of fault 1080 and 609; 3) the crusher room is merely 82m (270ft) away from the nearest future block 20m L x 12m W x 30m H (60ft L x 40ft W x 100ft H). Because of the complexity of the orebody, concerns were raised about the stability of the haulage drifts on 4000L and 4100L, crosscuts, and imperatively the crusher room. Numerical analysis using Map3D linear code was conducted on the 84 Deep Orebody in order to gain a better understanding of local stress state. Calibration of the model was done by comparing to the real existing conditions underground. Rockbolt load cells, commercially known as U-Cells, have been installed into primary support system and will be used to provide warning when the bolts have approached their yielding capacity. This is a proactive approach rather than the traditional method “rehab after failure”. It was

decided that when the monitored loads reach 70% of the bolt yield capacity, proper rehabilitation would then be applied to the infrastructure to avoid aggravated ground control problems and production delays.

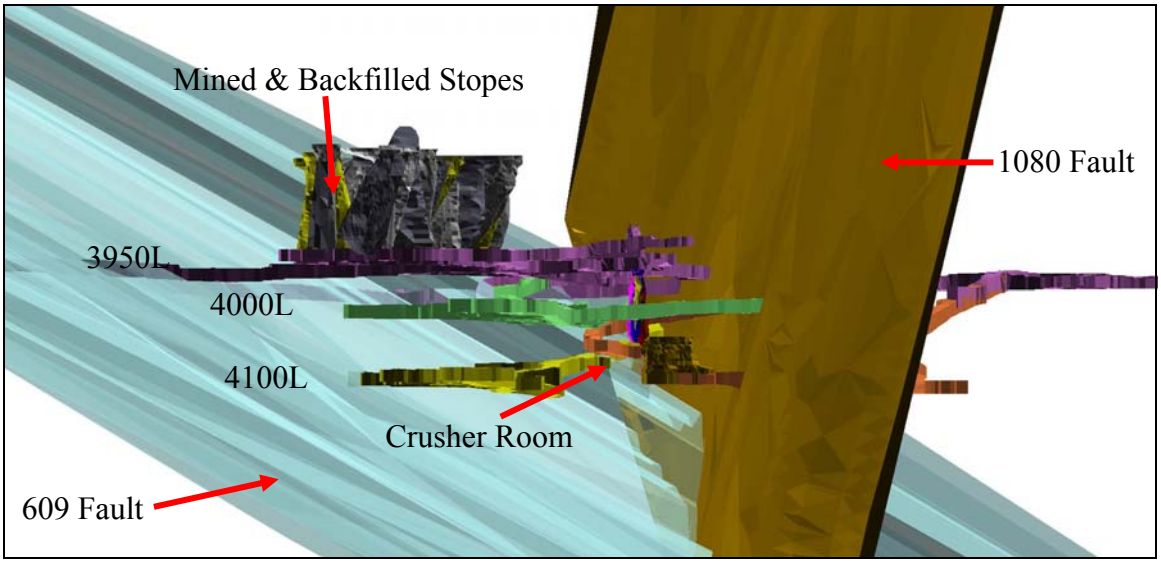

Figure 1 - 84 deep orebody, Birchtree Mine - looking North

2. MINING METHOD AND MONITORING SYSTEM DESIGN

2.1 Mining Method

Signs of deterioration in the crusher room were observed during the development of 4000L haulage drift. Therefore a centre-out and bottom-up mining sequence was selected to push the peak stress contour away and minimize the influence of stress concentration in crusher area, Figure 2. The Numerical analysis results of redistributed stresses indicate the crown blocks have mostly yielded due to previous mining activities above 3950L. However rock mass under such condition could still be successfully recovered (Coulson, 2009, Bawden and Jones, 2005, Mercier-Langevin, 2008). Attempts will be made to take them with the third blast (final blast) of each VBM block underneath, given that Vale Manitoba Operation has been successfully mining 30m (100ft) lift blocks with merely 3 blasts.

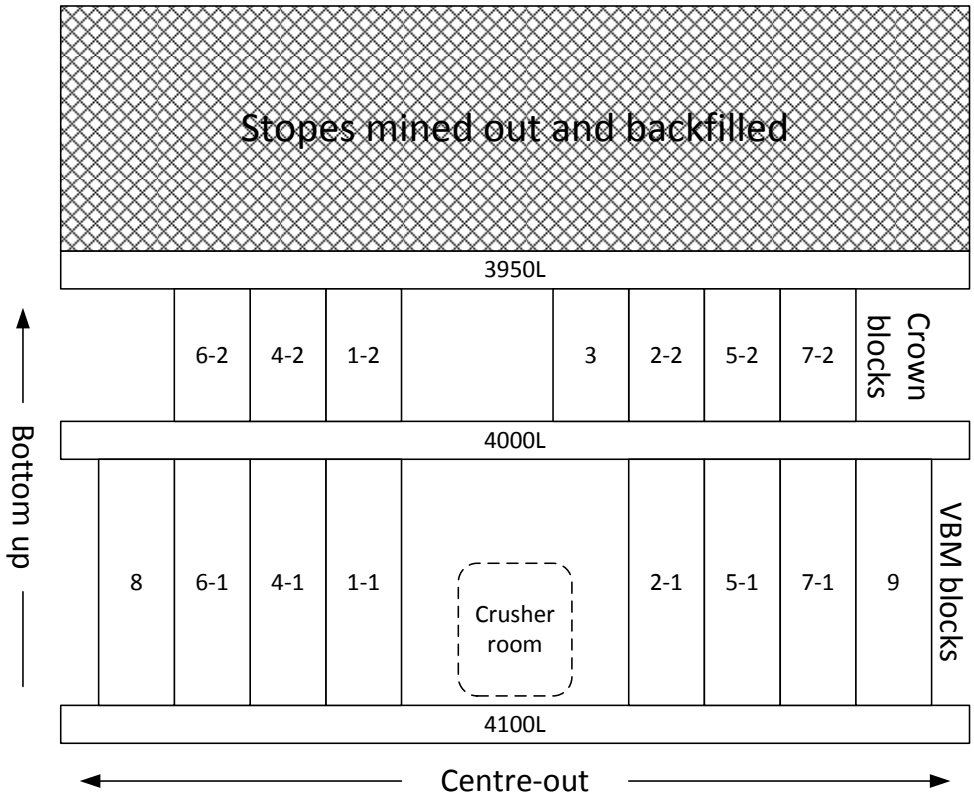

Figure 2 - Concept of the mining sequence of 84 deep, looking West

2.2 Monitoring System Design

It has raised enough interest to monitor and maintain/enhance the performance of the ground support system in the overcuts (stope drill rooms).

Three locations, headings 904 and 948 on 4000L and the crusher ramp on 4050L, are selected for U-Cell installation, Figure 3. As presented, the 4000L haulage drift is located in moderately foliated Schist zone (dotted grey lines) and is accompanied with local shears parallel to the drift axis (blue lines inside the drift). Green lines inside the drift stand for the Amphibolite zone which in this case is extremely wet and corrosive. 10 cm (4 inch)-thick layer of shotcrete has been applied to this area to enhance the primary support system.

The 904 heading is the first scheduled block to be mined on this level. In addition, the intersection of 948 access drift and the truck turnaround area has been suffering from previous mining, local structure and ground water. Therefore these two headings on 4000L are selected for U-Cell installation in order to capture real time performance of 2.4 m (8ft) rebars with respect to mining induced stress concentrations and ground movement.

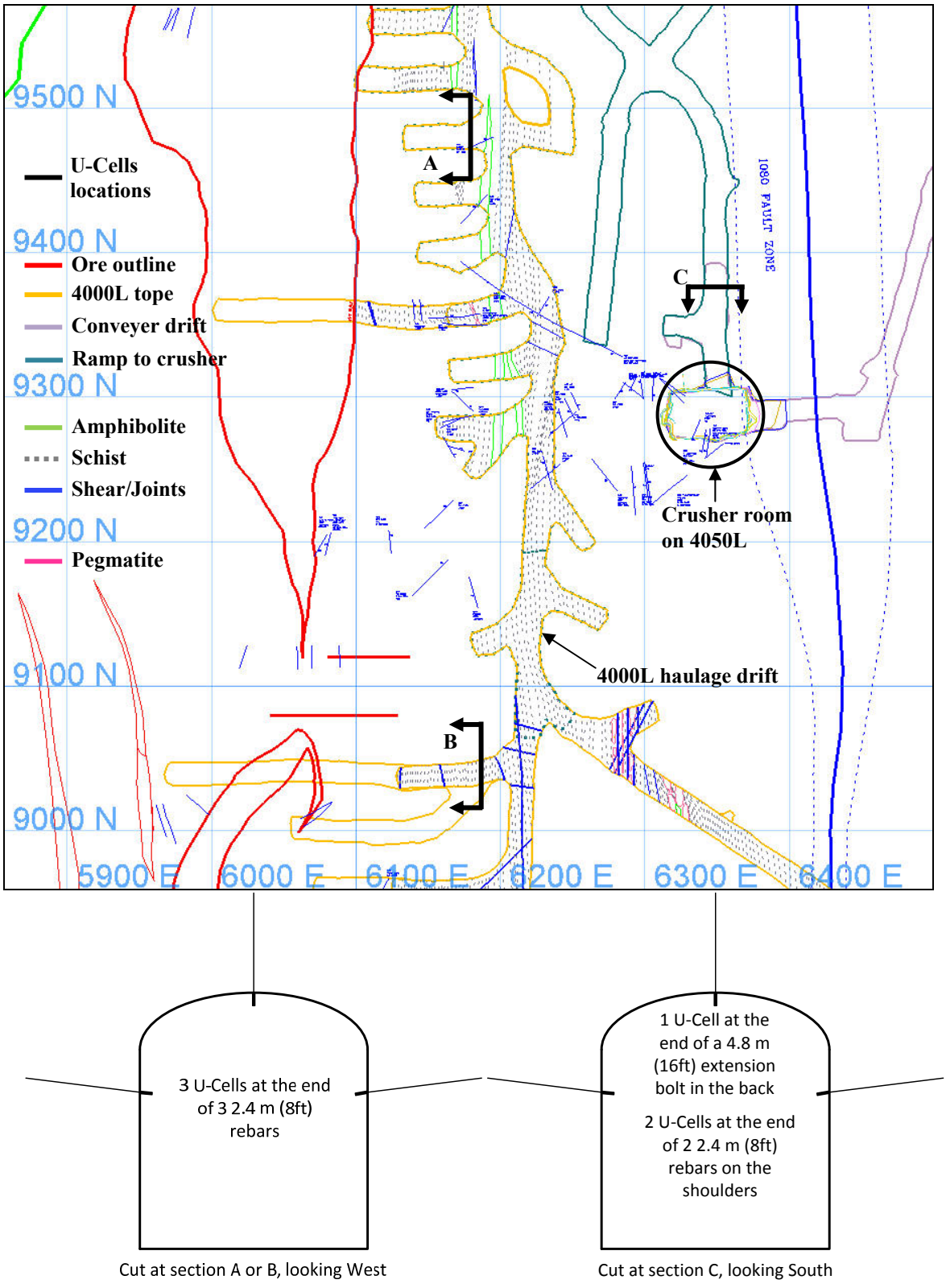

Figure 3 - Geological features of 4000L, crusher room on 4050L and selected U-cell locations

3. U-CELL INTRODUCTION AND INSTALLATION

Mechanical and rebar bolts are widely used in underground hard rock mines as primary support bolts. U-Cell can be customized to accommodate a mechanical bolt, rebar bolt or extension bolt as a monitoring device. It will be advantageous to monitor the real time performance of these bolts to enable proper and timely mitigation methods to 4000L, 4100L haulage drifts and the crusher room with respect to current mining sequence.

3.1 U-Cell Introduction

In 2001, Mitri and Marwan (2001) introduced a bolt load measuring concept that is based on placing a strain gauge directly in the bolt head by drilling a central blind hole that extends beyond the threaded portion. This technique measures the load induced axial strains of embedded strain gauge which could be further converted to axial load. While this design concept offers unique advantages over the traditional

The coupler load cell is fitted onto the rock anchor, which, once installed in the rock, permits the monitoring of the anchor head axial load. The advantages of this new design concept are numerous. The coupler is designed so that its yield load is greater than the tensile (breaking) strength of the rock anchor. This design ensures a complete load path monitoring of rock support performance until failure. The coupler design offers the advantages of light weight in shipping and handling as well as ease of installation in the field. As shown in Figure 4, the upper end of the coupler load cell is a threaded hole that is tapped to fit the desired thread diameter of the rock anchor. This technology is commercially known as U-Cell.

3.2 Underground Installation of U-Cells

A 1 7/8 inch dolly that fits on both Maclean bolter and Jackleg was ordered from DSI to facilitate the installation, Figure 5 as well as several 1 ¼ spherical seats.

The end square cap on the U-Cell could also serve the role of a shear pin nut at the end of a rebar to spin the bar into the resin grout. Therefore 2.4 m (8ft) rebars were used without shear pin nuts for the U-Cell installations. One tip is to place a spherical seat washer between the hex nut and the bearing plate. Then it becomes straight forward to assemble rebar, plate and U-Cell together, Figure 6.

Although the U-Cell is not fragile, it needs to be protected from mobile equipment, blasting damage or other potential damage hazards in a mine. There is a technique to hide the main body of the device into the hole: drill an extra foot at the beginning of the hole (a collar) with a 51 or 54mm bit and then switch back to a regular 31mm bit to finish the total length of a rebar hole, see Figure 7.

At the end drop the U-Cell - rebar assembly into the customized dolly and finish the bolt installation as per standard practice. To make it more visible, a frame is spray-painted around it, Figure 8. Last but not least, connect a lead wire to the U-Cell and take initial readings.

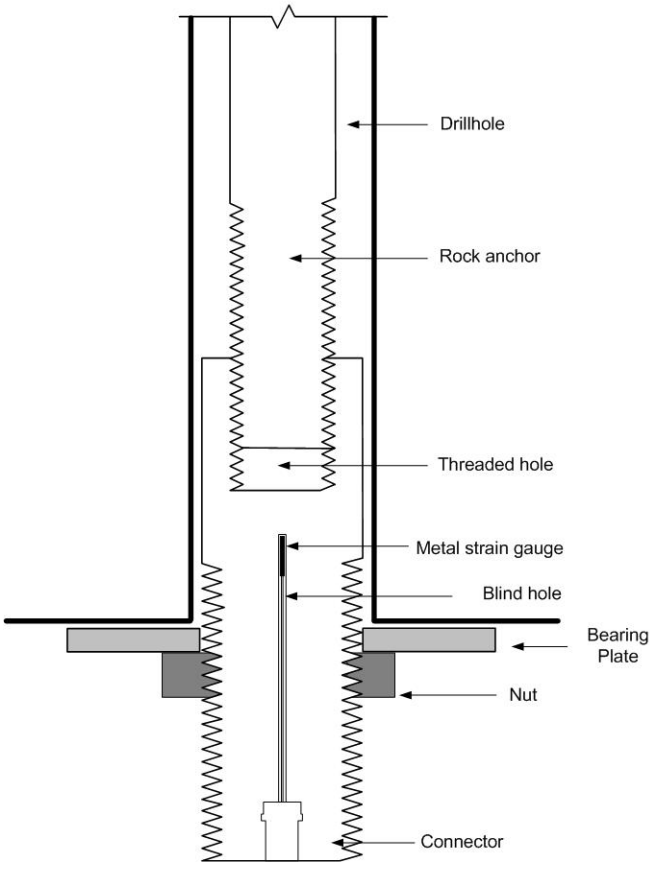

Figure 4 - Design concept of the U-Cell, Mitri (2011)

Figure 5 - 1 7/8 inch dolly for U-cell installation

Figure 6 - Demonstration of a U-cell attached to a rebar

Figure 7 - Drill the rebar hole with different size bits to create a shelter for the U-cell

Figure 8 - U-cells are succesfully installed

A d4LOGGER, Figure 9, is connected to all the U-Cells at each location to record the axial loads along the bolts on an hourly basis. All the data will be extracted to a computer after each production blast on 4000L.

Figure 9 - d4LOGGER provided by YieldPoint Inc.

4. INITIAL READINGS

Initial readings were collected immediately after installation as a baseline for future reference, Table 1. As can be seen, the initial loads vary from 1.35 to 4.65 tons. Such variation may be attributed to the use of different bolt installation equipment (stoper and rockbolter machine), as well as the amount of torque applied when tightening the bolt. The monitoring system also records the mine temperature at the time of taking each reading. As the U-cells are calibrated at room temperature (22°C), a temperature compensation correction is made by the data acquisition system. Further data collection and analysis will take place after each production blast on 4000L. It was decided that enhanced support will be applied to the drift wherever the bolts have reached 70% of their yielding capacity.

Table 1 - Initial reading of U-cells

U-Cell ID	Bolt Type	Location[1]	Axial Load (tons)	Temp
110525022	8ft rebar	4000L_904 right wall	3.35	19°
110525023	8ft rebar	4000L_904 back	4.65	21°
110525024	8ft rebar	4000L_904 left wall	3.12	20°
110525021	8ft rebar	4000L_948 right wall	3.57	21°
110525025	8ft rebar	4000L_948 back	3.23	21°
110525015	8ft rebar	4000L_948 left wall	3.42	20°
110525012	8ft rebar	4050 Crusher Ramp right wall	2.17	20°
110525013	16ft ext bolt	4050 Crusher Ramp back	1.01	19°
110525014	8ft rebar	4050 Crusher Ramp left wall	1.53	20°

Note:Facing West on 4000L and facing South on 4050L

5. CONCLUSIONS AND DISCUSSIONS

The paper presents a ground control case study in which the planned mining sequence, together with the poor quality of the rock mass are likely to cause deterioration of the haulage drift stability conditions and possibly the nearby crusher room. Preliminary estimate of these conditions has been done with 3D linear elastic modeling. A ground control monitoring program, based on rockbolt load monitoring with U-Cell technology, has been successfully launched. The initial readings indicate bolt loads in the range of 1 to 4.65 tones. Bolt loads will be monitored during the planned mining sequence and compared to the yielding capacities. It was decided that where the bolt loads are found to reach 70% of their yield capacity, a ground rehabilitation program with enhanced support will be carried out in those areas.

6. REFERENCE

BAWDEN, W.F. and JONES, S., (2005). The use of mine sequencing controlled through numerical modelling and instrumentation to destress a highly burst prone sill pillar. In Proc. 107th Can. Inst. Min. & Met., CIM-AGM, Toronto, Ont. March. (CD-ROM)

COULSON, A.L., (2009). Investigation of the Pre to Post Peak Strength State and Behaviour of Confined Rock Masses Using Mine Induced Microseismicity. Ph.D. Thesis, Dept. of Civil Engineering, University of Toronto, p 457.

MERCIER-LANGEVIN, F., (2008). Stope Performance Under Post Peak Conditions. In Proc. 3rd Int. Sem. On Strategic vs Tactical Approaches to Mining, Sept 28th to Oct. 1st, Quebec City, Canada, pp 240-250.

MITRI, H. AND MARWAN, J., (2001). “A New Rockbolt Axial Load Measuring Device,” Proc 20th Intl. Conf. on Ground Control in Mining, Morgantown, WV, pp. 367- 373.

MITRI, H., (2011). Evaluation of Rock Support Performance through Instrumentation and Monitoring of Bolt Axial Load, 11th Underground Coal Operators' Conference, University of Wollongong & the Australasian Institute of Mining and Metallurgy, pp. 136-140.

Monitoring of Dynamic Bolts for High Stress Mining

F. Charette
Dynamic Rock Support NA

ABSTRACT: The paper reviews the requirements of the instrumentation required to monitor mining excavations in a high stress environment, and the development plan to instrument the D-Bolt in such a fashion as to be able to follow the behaviour of the bolts in relationship to the ground movements and support performance. Recent field observations of D-Bolts under static and dynamic conditions are also presented. Also discussed is the assumed mechanical behaviour of the D-Bolt. D-Bolts are used in two (2) Canadian underground mines operating in high stress environments and tested in three (3) other operations.

1. INTRODUCTION

High stress environments can occur in hard rock masses as well as in soft or broken rock masses. Deep or large excavations can experience stress levels leading to an unstable state of deformation. Appropriate reinforcement and support is necessary to control the stability of these excavations. Monitoring of highly stressed rock masses can be performed through the use of conventional instruments like extensometers, but also through the use of instrumented ground support. The particular adaptation of a rock bolt into an instrument allows a glimpse of the state of deformation of the rock mass at the instrument location, as experienced by rock bolts. Not only this kind of instrument can provide information on the deformation pattern around the excavation, it can also offer an insight into the mechanical behaviour of the bolt when submitted to in situ loading conditions.

First, the physical configuration of the instrument must be compatible with the information it needs to measure, as well as with the deformation of the rock mass it is aiming to monitor. Also, the capacity of an instrument to survive many changes of stress conditions as experienced by the rock bolt is a key parameter for a successful monitoring program. Finally, visual monitoring and documentation is a necessary part of a monitoring program; visual and anecdotal information can be used to evaluate the performance of a ground support in allowing a step by step comparison of the stability of an excavation during its loading history.

Understanding the mode of deformation and state of stress of the rock mass surrounding an excavation is the first step of a monitoring program. The engineer must be able to predict, at least qualitatively, the deformation of the walls and roof to be monitored.

2. MODES OF DEFORMATION AROUND AN INSTRUMENTED ROCK BOLT

The simplest mode of deformation that can be measured is linear convergence, where the rock mass or the excavation surface is moving toward the inside of the excavation without generating much shear displacement along the axis of the instrumented bolt; the bolt will work in elongation mode, and this assessment is valid either for a fully grouted rebar or a point load anchor bolt. This situation can occur in squeezing ground conditions (Figure 1) or in rockbursting conditions (Figure 2, from Potvin et al, 2010). By contrast, in heavily foliated hard rock, the axis of the rock bolt can be submitted to shear displacements that can easily lock-in a rebar (Figure 3), but a smooth bar, fully grouted or not, is more likely to be able to stretch or deform axially without failing prematurely. Bending and tensile stresses can

provide a good indication of the state of deformation of the rock mass if the instrument is able to detect bending; most instrument systems are designed solely to measure axial strain on a steel bar.

Figure 1 - Squeezing ground conditions

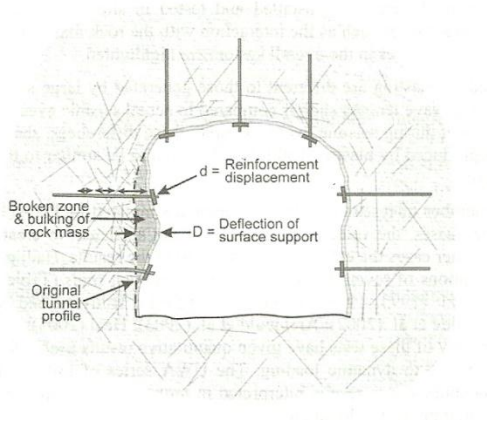

Figure 2 - Rock deformation pattern in rockburst event (Potvin et al, 2010)

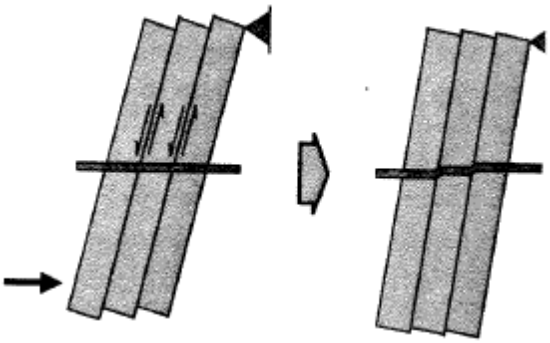

Figure 3 - Shear displacement during compression of foliated rock mass

In very weak or soft rock, shearing can induce some localised bending of the rock bolt, but if the bond between the grout and the bolt is weak enough to allow it, the bolt will still elongate with minimal shear as the grout will fail, liberating the bar. Smooth bars or point anchor rock bolts (Hyett et al, 2012) will be able to elongate better than fully grouted ribbed rebars in shearing and bending conditions.

3. ROCK MONITORING USING D-BOLTS

Considering the D-Bolt claims on large displacement capability, it was natural that an instrumented D-Bolt should provide the user with useful insights on the ground deformation and bolt deformation pattern. The first attempt to instrumentation was with conventional strain gauges (Li, 2010). Figure 4 shows a monitoring sequence comparing the loading results on D-Bolts and rebars in an underground stope in a deep Scandinavian mine. Similar results on the loading range as well as the location of the broken zone suggest that both reinforcements behave in a similar fashion in the elastic range. Since most resistive strain gauges are generally not able to consistently follow deformations above 10000 microstrains, they cannot be used to monitor a rock bolt in its yielding phase.

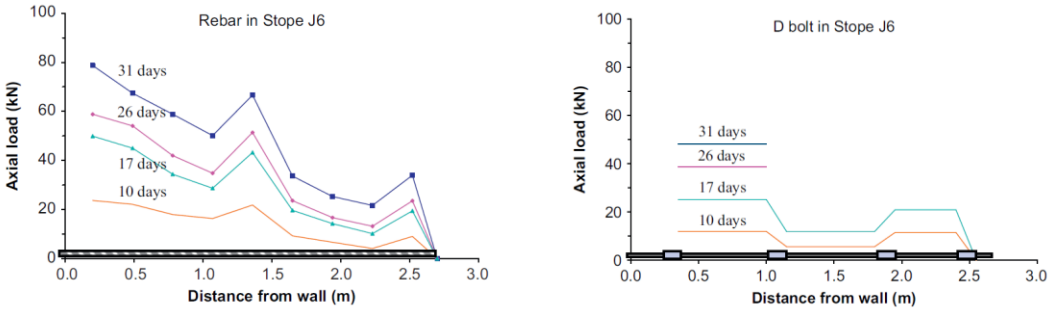

a) Deformation readings on a rebar b) Deformation readings on a D-Bolt

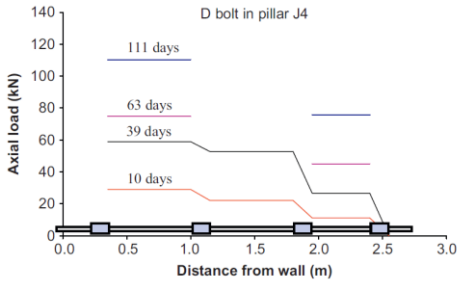

b) Deformation readings on a D-Bolt

Figure 4 - Monitoring of ground deformation using a) strain gauges instrumented rebar, b) and c) strain gauges instrumented D-Bolts (from Li, 2010)

4. ALTERNATIVES TO RESISTIVE STRAIN GAUGES

An alternative to strain gauges for cables and rock bolts, developed by Bawden and Hyett (2000), consists in a system similar to a large scale potentiometer. More recently, a clever system consisting in populating rock bolts with multiple small-diameter long-baselength displacement sensors (Hyett et al, 2012) is showing promising results in providing significant and consistent readings of deformations along a rebar. An example of measurements using this technique in a deep Canadian mine, is found on Figure 5. Figure 6 shows the measurements made on an adjacent D-Bolt instrumented with resistive strain gauges, results that are in essence very similar to the rebars with displacement sensors. Table 1 compares the displacements calculated for similar intervals along the D-Bolt and the rebar, and readings for both rock bolts are very similar. Due to failure of the last strain gauge during installation, the D-Bolt could not be monitored over its full length.

A major impediment in using resistive strain gauges for monitoring excavations in high stress conditions is the small range of deformation that strain gauges can handle. Strain gauges cannot effectively monitor more than 1 to 1.5 % elongation and therefore cannot fulfill the need when trying to measure a deformation up to 10%. They provide reliable information in the elastic loading phase of a rock bolt only. Following this field test, it was decided that D-Bolts would be instrumented with a different system that would allow larger deformations to be measured, and the method described by Hyett et al (2012) was chosen. Its capability to detect bending forces was also considered a favorable advantage. Unfortunately the project was delayed by several months due to several issues and the field tests will begin only during Spring 2012.

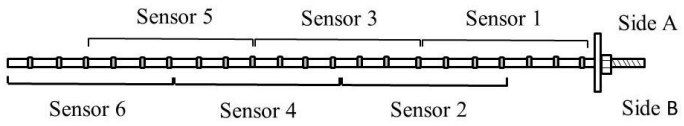

a)

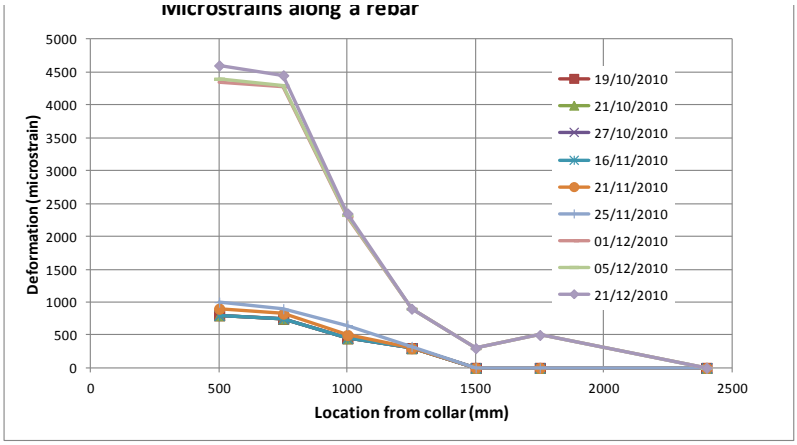

b)

Figure 5 - Monitoring rebar a) with displacement sensors and b) field results (Punkinnen, 2011), (Charette et al, 2011)

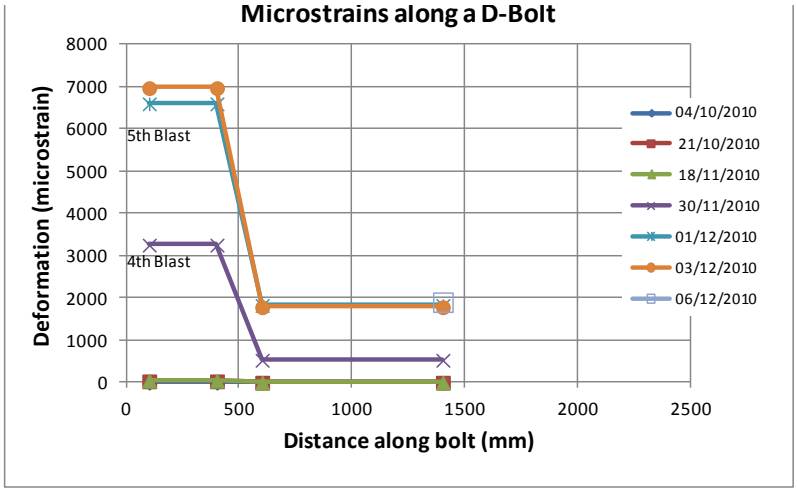

Figure 6 - Monitoring D-Bolt with standard resistive strain gauges (Punkinnen, 2011), (Charette et al, 2011)

Table 1 - Comparison of displacement readings calculated for D-Bolt and rebar (Figures 5 and 6)

Date	Readings D-Bolt (mm)		Readings Rebar (mm)	
	250-625 mm	625-1450 mm	250-625 mm	625-1450 mm
06/12/2010	1.5	1.6	1.8	1.9

5. OTHER MEASUREMENT DEVICES

Others means of quantitative monitoring of rock bolts have been widely used, such as load cells installed at the collar. While these methods can provide rapid data on the loading conditions of the plates, they cannot give information on the deformation and displacements occurring along the bolts and deep into the rock mass. Visual observation of the state of a dome plate will provide similar but qualitative information.

Table 2 suggest a non-exhaustive list of parameters that can be used while choosing a rock bolt monitoring system.

Table 2 - Evaluation of instrumented system to handle field conditions

Parameter	Resistive strain gauges	Potentiometer	Displacement sensors	Load cells at collar
Detect shear and bending	No	Unknown	Possible	No
High survival rate in shear	Unknown	Depending of the bolt used	Yes	N/A
Survives large deformation	No	Yes	Yes	Yes
Handle bending	Unknown	Depending of the bolt used	Yes	N/A
Easy to use with datalogging system	Sometimes	Yes	Yes	Yes
Easy installation with resin grout cartridges	No	Yes	Yes	Yes
Easy installation with cement grout	Yes	Yes	Yes	Yes

6. VISUAL MONITORING

As mentioned previously, visual documentation is a strong tool for the long term monitoring of a support system. High quality digital photographs, taken at strategic locations, can enhance our understanding of the field performance of rock bolts. Figure 7 shows the condition of the ground support following a seismic event of magnitude 1.9 Mn; the rock is fractured but still in place, showing some moderate bulking. Figure 8 shows the condition of ground support following a seismic event, then how it survives the bulking that follows the rising stress level in the area. The D-Bolts did adapt well to the deformation of the rock face. The fibre-reinforced shotcrete showed some cracking but provided a stable shell for the control and retention of the bulked up rock mass. Performance of the plates can also be determined: the plates did show some loading but did not cut or sheared the mesh during the event and thus provided a strong link between the bolts and the surface support.

Figure 7 - State of ground support (D-Bolt and mesh) after a 1.9 Mn seismic event

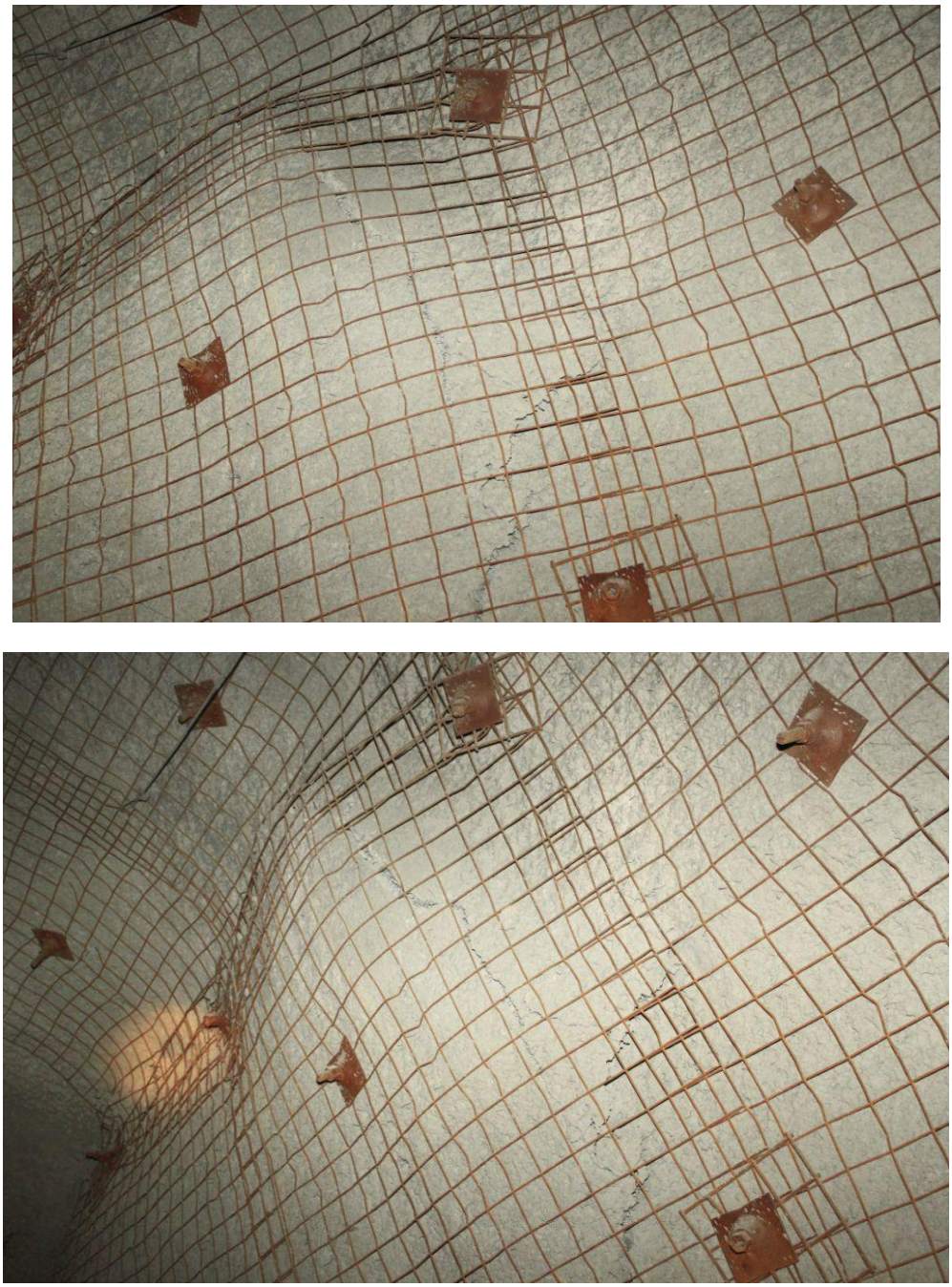

Figure 8 - State of ground support after a) seismic event located close to the wall and b) subsequent bulking from additional loading due to rising in situ stresses

7. CONCLUSION

A review of the monitoring of rebars and D-Bolts in high stress conditions has been presented. Measurements data with strain gauges and displacements sensors have been analysed and the results found to be very similar in the elastic range of the rock bolts.

8. REFERENCES

BAWDEN, W. and HYETT, A.J., Canadian Patent 220083, 2000.

CHARETTE, F. and LI, C.L., Innovative Engineering Approach to the Stabilisation of Rock Masses in High Stress Conditions, CIM Conference and Exhibition, Montreal 2011.

HYETT, A.J. and SPEARING, A.J.S., Accepted for publication at the 46th U.S. Rock Mechanics Symposium, Chicago, 2012.

LI, C.L., A new energy-absorbing bolt for rock support in high stress rock masses, International Journal of Rock Mechanics and Mining Sciences, Vol 47 pp396-404, 2010.

POTVIN, Y., WESSELOO, J. and HEAL, D., An interpretation of ground support capacity submitted to dynamic loading, Fifth International Seminar on Deep and High Stress Mining, 6 – 8 October 2010, Santiago, Chile.

PUNKKINEN, A.R., 2011, Rock stope ground control risk mitigation – 4408 rock stope, Personal communication.

Changes in Hydro-Mechanical Monitoring Parameters During Construction of a Deep Geological Repository

A.K. Verma
Center for Research on Energy Security, The Energy and Resources Institute India
T.N. Singh
Department of Earth Sciences, Indian Institute of Technology-Bombay
Avi Dutt
Institute of Technology, Banaras Hindu University

ABSTRACT: This paper provides a brief overview of evolution of deformations, stresses, and pore pressures due to different excavation stages during construction of an URL. Excavation of a rockmass develops a damage zone of finite width around the excavated zone which is associated with changes in permeability and which affects the fluid flow mechanism. In this study, a coupled hydromechanical (HM) analysis has been conducted for a water saturated porous rock mass which has been created by sequential excavation and backfill of vertical disposal pit of an URL. For this purpose, an Atomic Energy of Canada Limited's in-floor concept for a deep geologic repository suitable for Indian conditions has been used. Changes in rock deformations, stresses, strains and mechanically induced pore pressure in an undrained condition, during excavation, as well as those caused by mechanically induced rock deformations after backfill of the disposal pit, have been modeled. A three-dimensional finite difference tool FLAC^{3D} has been used for the analysis.

1. INTRODUCTION

Development of nuclear power in the 1950s was hailed as a major technological advancement providing an unlimited source of cheap power, without the shortcomings of finite hydrocarbon and hydroelectric resources (Witherspoon and Bodvarsson 2001). The disadvantages associated with high-level waste (HLW) in the short-term are due to exposure of radiation and significant heat generation. Hence, there is a need to isolate it from the wider environment and to keep the wastes cool until ready to dispose. In the long-term, the release of heat and radiation from the wastes into the environment tends to induce chronic impacts and hence it needs to be permanently isolated for longer periods (Fairhurst, 2004).

The space between the canisters containing the spent HLW wastes and the excavation is to be backfilled with a material selected in such a way that the backfill constitutes an engineered barrier with especially designed characteristics. In most envisaged designs, expansive clays have been chosen as the most adequate material, on its own or in combination with other materials, as it regains the original stresses after saturation (Booker and Savvidou 1985; Stephansson et al. 1999). In repositories built in rock salt, crushed salt is deemed to be preferable to a clay-based barrier. The clay constituting the barrier is to be compacted to a high density to ensure sufficient swelling upon wetting. Selection of a clay with a high smectite content assists in giving the buffer material the required expansive properties. Therefore, the clay-rich barrier surrounding the waste will be a low permeability, high-density material that, at least initially, will be in an unsaturated state (Radhakrishna et al. 1992; Thomas et al. 1996).

The design of a nuclear waste repository involves modeling a complex system that operates over a long period of time. The perturbations caused by both the engineering excavation and the backfilling of the disposal pit have to be modeled, taking into account the short- and long-term hydromechanical (HM) processes. Hence, a hydromechanical coupling analysis was carried out using a three-dimensional Finite

difference code, FLAC^{3D} (Itasca Consulting Group Inc. FLAC-3D, 1997) to investigate the effect of the excavation of tunnel and vertical disposal pit before and after the emplacement of a canister. On a large scale, continuum models are useful for investigating the general hydraulic processes and for assessing different scenarios from a sensitivity analysis point of view.

The design of a typical, conceptual Atomic Energy of Canada Limited URL has been studied to find its suitability for Indian conditions as shown in Fig. 1. The disposal tunnel would be located in a granitic rock mass at about 150 m below the surface (Verma et al. 2010). Spent fuel canisters having a height of 2.05 m would be placed in vertical disposal pit from the base of the tunnel followed by backfill which would consist of compacted clay (Table 1; Fig. 2).

Table 1 - Type of geomaterials used in the model

• Host rock	Granite
• Buffer rock	Compacted clay
• Backfill	Compacted clay+sand

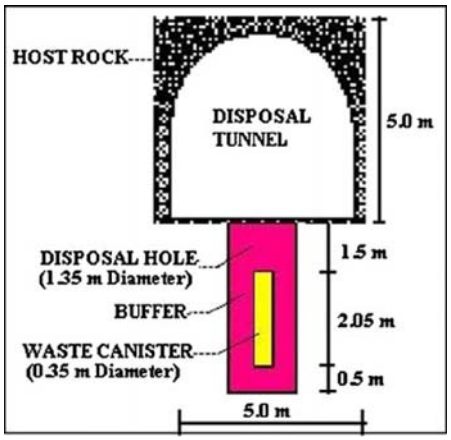

Figure 1 - Schematic diagram of conceptual geological repositories

2. EXCAVATION SEQUENCE

The hydromechanical analysis has been carried out both before and after the emplacement of canisters. The excavation is carried out in the form of a horseshoe-shaped tunnel with a size of 5 m×5 m. A horseshoe-shaped tunnel was chosen because of its mechanical stability and accessibility during construction. In the model, the tunnel was excavated with a 10-m advance in the first stage, and hydromechanical analyses were done after each advance in order to consider the influence of a sequential excavation. After a 10-m excavation of the tunnel, a cylindrical-shaped disposal pit of 1.35 m diameter was excavated at the floor of the tunnel and filled with canister and backfilled with compacted clay. Hydromechanical equilibrium conditions were studied both before and after the excavation of the disposal pit.

Tables 2 and 3 list the measured rock, buffer, and backfill properties from laboratory experiments and collected literature. The hydraulic properties used for the study are given in Table 3.

Table 2 - Rock, buffer and backfill properties

Property	Units	Rock	Buffer	Backfill
Modulus	GPa	Granite Bulk = 33.05 Shear = 20.10	Compacted clay Bulk = 0.321 Shear = 0.243	Compacted clay 70% + sand 30% Bulk = 0.029 Shear = 0.025
Density	kg/m³	2600	2050	2100
UCS	MPa	100	7.66	0.85
Cohesion	MPa	60	1.5	0.98
Friction angle	Degree	58	48	13

Table 3 - Hydraulic properties of the rock and compacted clay

Property	Units	Rock	Compacted clay
Porosity	–	0.05	0.3
Permeability	m^2	4.26e-16	2.0e-19
Fluid modulus	Pa		2e8
Fluid tensile strength	Pa		−1e20
Fluid density	kg/m^3		1e3

3. NUMERICAL MODELING

3.1 Geometry and Mesh Generation

Fig. 2 exhibits the geometry and mesh generated. Due to symmetry, one-fourth of the tunnel has been modeled which reduces the computational time and more hydraulic phenomena can be investigated appropriately. The dimensions (width, length, and height) of the model mesh are 40 m×25 m×11.3 m, respectively having a 5 m×5 m tunnel. The total number of zones in the model mesh is 27,250.

3.2 Initial Conditions

The values of the initial material and hydraulic properties of properties are assigned from Tables 2 and 3 for the three types of material. Fluid flow inside the canister has been neglected and hence no fluid model has been assigned to the canister. The tunnel was saturated up to a height of 9 m above the tunnel crown. Initial pore pressure of 0.05 MPa with gradient of −6.25e3 Pa up to tunnel center and a gradient of −0.05 MPa to the bottom of the center has been applied to simulate the water table effect.

3.3 Boundary Conditions

A vertical stress of 3.99 MPa has been applied at the top face to simulate the stress due to the 150 m of overburden. Roller boundary conditions are applied on the four sides

3.4 Excavation Stages

Stage 1: Hydromechanically coupled analysis is carried out for the model without excavation.

Stage 2: Hydromechanically coupled analysis is carried out after a 10 m tunnel is excavated in a single stage. The excavation of the 10 m long tunnel causes disturbance of the surrounding rock mass. The extent of disturbance mainly depends on the nature of the excavation method, the geometry, and rock mass properties. The excavation redistributes the stresses around outer boundary and in turn affects permeability, local fracture aperture, and deformation of the rock mass. As such, the excess unbalanced forces needs to be brought into equilibrium before any further excavation. Various other parameters like pore pressureand stresses have been monitored during the simulations. The excavation also represents a relatively sudden event and hence the normal and shear stress across nearby fractures change in a short time, producing sudden aperture changes. This may cause the pore pressure to rise quickly before the water has a chance to move and equilibrate. The tunnel at this early stage should be well ventilated. This means that dewatering of the tunnel should be done and the hence pore pressure near the repository will be reduced from the original condition, which may induce fracture closure or self-sealing.

Stage 3: Hydromechanically coupled analysis after excavation of a single disposal pit

During this stage, a single disposal pit has been constructed after excavation for emplacement of the canister, clay barrier, and backfilling. Excavation will induce disturbances and points nearby need to be monitored for various mechanical and fluid parameters of the rock. Parameters like deformations, pore pressures, and stresses have been monitored and assessed during simulation of the HM processes.

Stage 4: Hydromechanically coupled analysis after emplacement of canister in the disposal pit.

Water ingress from the surrounding rock will increase the saturation of the backfilling material and cause it to swell, which will increase the stress inside it and help to regain the original stress.

4. RESULTS AND DISCUSSIONS

Seven monitoring points were identified where parameters like deformations, pore pressures and stresses have been measured. Two points have been considered at the crown and side walls of the tunnel while rest five points were taken along the vertical disposal pit (Fig. 3).

4.1 Evolution of Vertical Displacement

Vertical displacements due to hydromechanical effects for stages 3 and 4 are small and therefore the HM effects are only examined carefully at points as shown in Fig. 4.

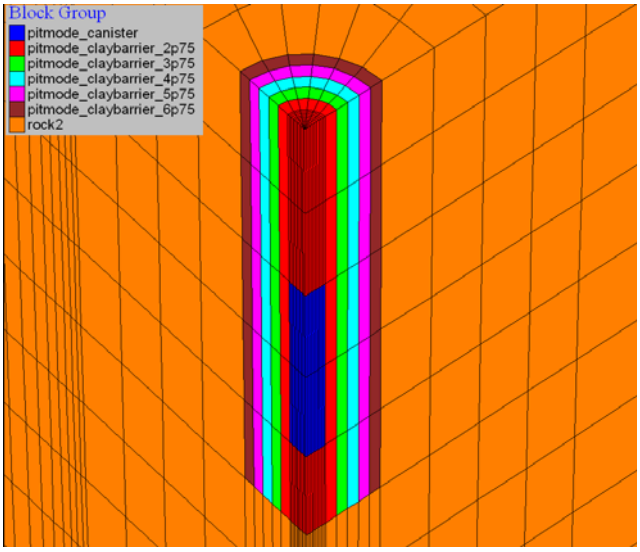

Figure 2 - Mesh for vertical disposal pit with one overpack (OP)

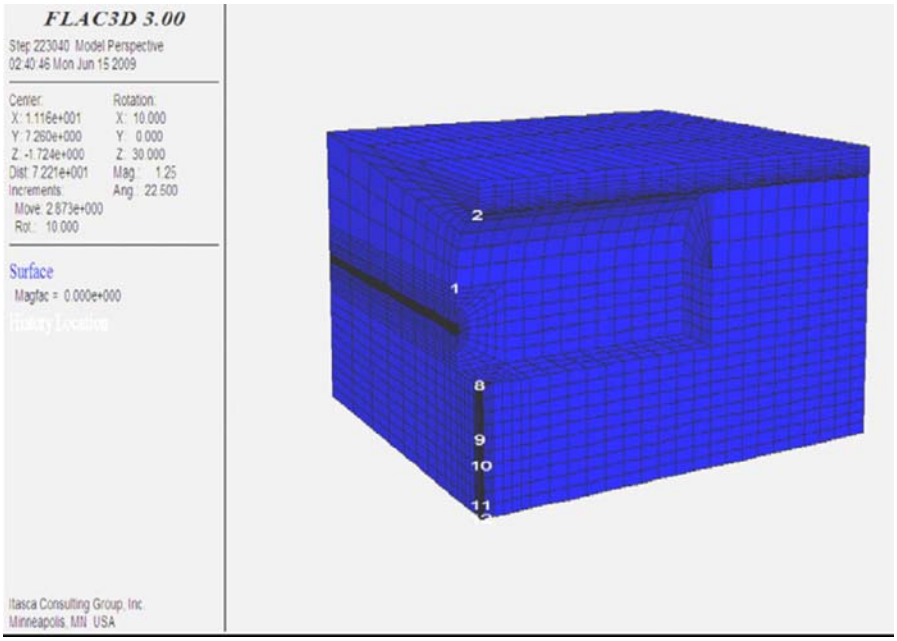

Figure 3 - Geometry, mesh and monitoring points

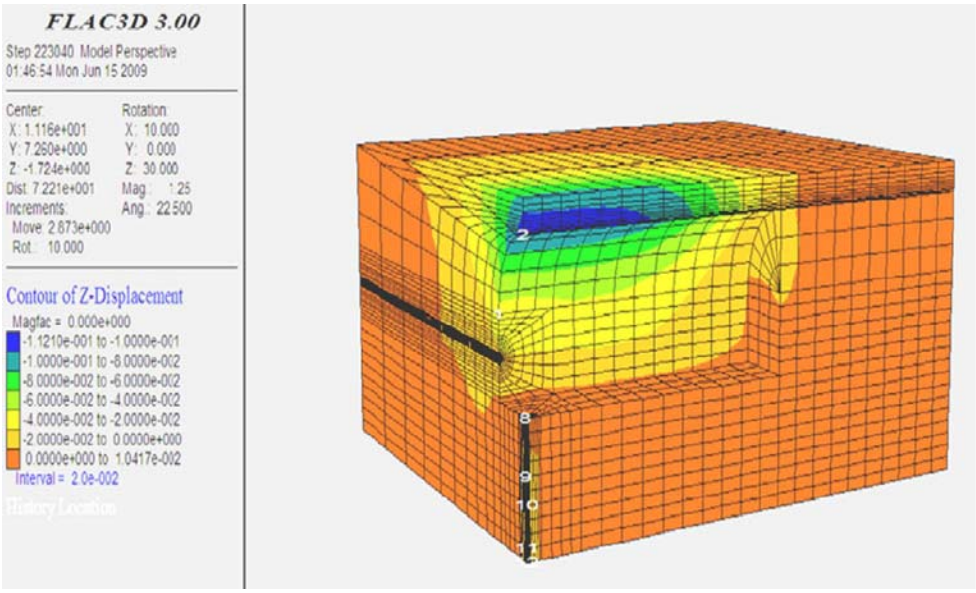

Figure 4 - Contour plot of vertical displacement at stage 4

Figures 5 and 6 show the variation of vertical displacements for all the monitoring points. It is seen that initially the point 8 at the floor of the tunnel is heaved upward by 0.2 mm. The other points 9, 10, 11, 12 near the proposed canister show an upward vertical displacement of less than 40% of the vertical displacement of point 8 (Fig. 5). Points 1 and 2 near the crown of the tunnel are initially displaced by a very small amount of the order of 0.01 mm for stage 1 due to mechanical equilibrium (Fig. 6).

After a 10-m excavation of the tunnel, it is seen that the point 8 gets heaved upward and reaches a value of 0.9 mm. The other points 9, 10, 11 near the proposed canister also get displaced upward by 3.9, 1.9, and 0.37 mm, respectively.

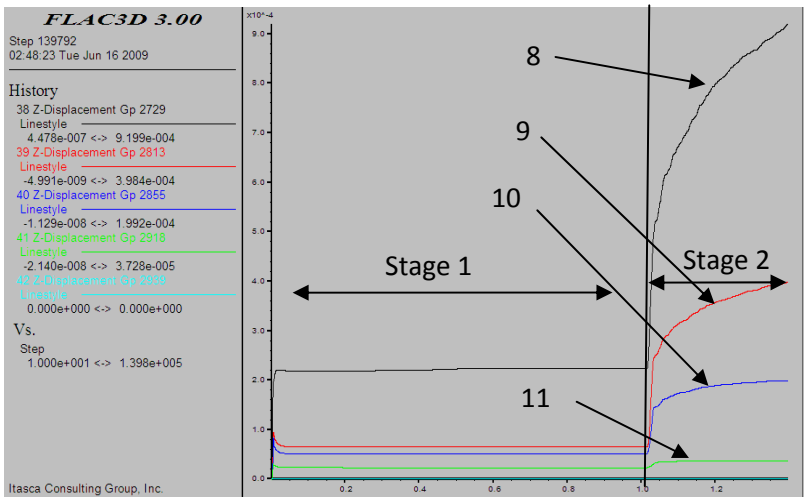

Figure 5 - Variation of vertical displacements at different stages for monitoring points 8,9,10 and 11

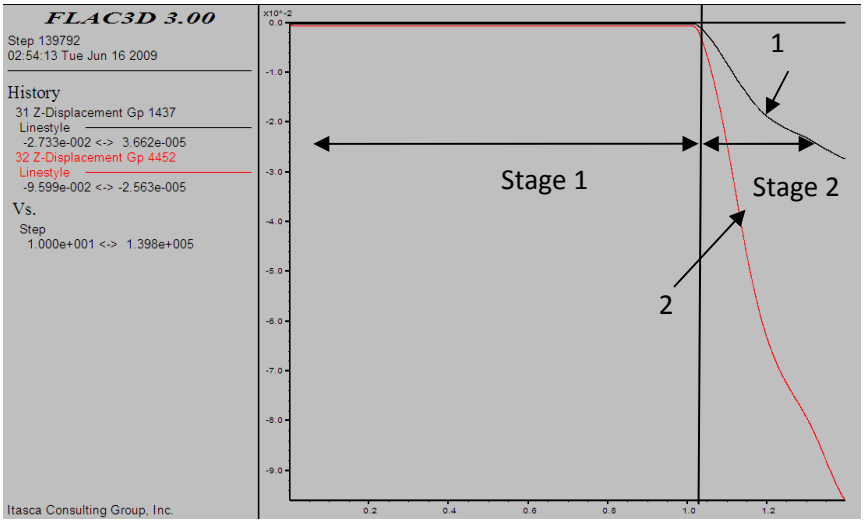

Figure 6 - Variation of vertical displacements at different stages for monitoring points 1 and 2

4.2 Evolution of Vertical Stress

Figure 7 shows the variation of vertical stresses at different stages of the excavation. It is found that before the excavation of tunnel (stage 1), vertical stresses attain an equilibrium value as per the general theory of variation of vertical stresses with depth. After the 10 m single-stage excavation (stage 2) of the tunnel, the value of vertical stresses for all the points shows change as seen in Fig. 7. At points 1 and 2, the compressive stresses show an increase of value between 0.04 to 0.4 MPa while for points 8, 9,10,11,12 the compressive stress decreases. At stage 3, when the vertical disposal pit is excavated, the vertical stress for the above points becomes zero due to removal of rockmass. Again, when the canister is emplaced in the pit (stage 4), vertical stresses for the points in the clay barrier increases with time due to increase in water saturation which helps to regain the stresses (Figs. 7 and 8).

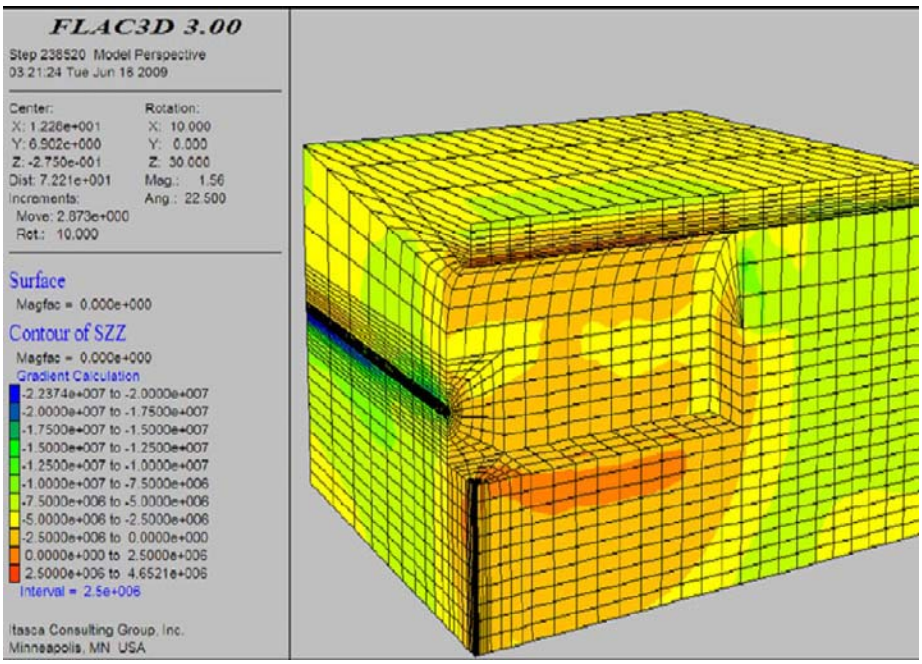

Figure 7 - Contour plot of vertical stresses at stage 4

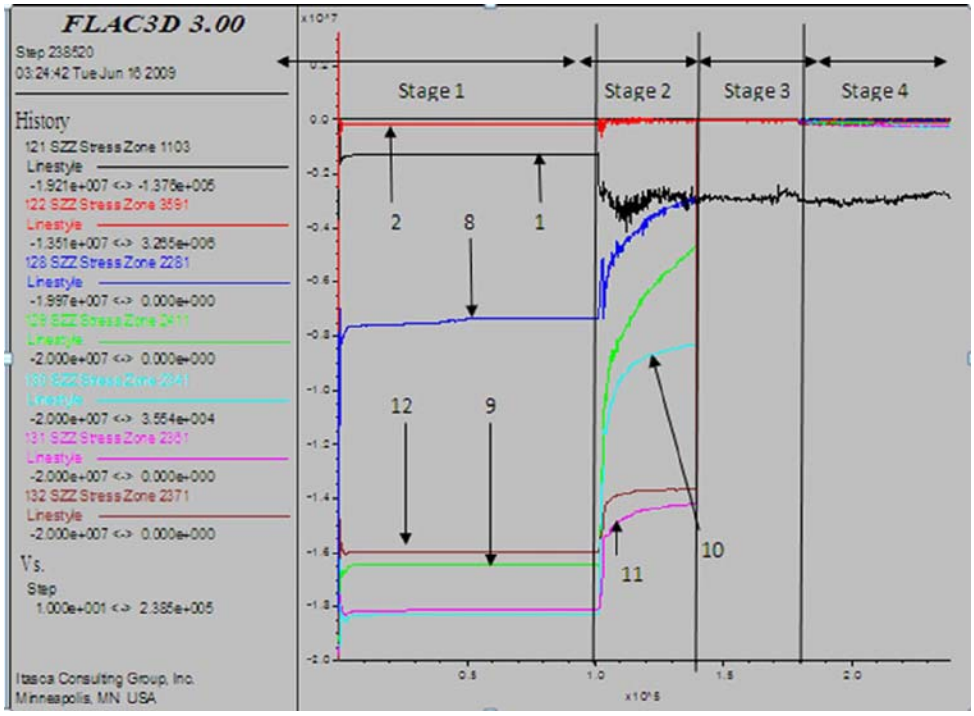

Figure 8 - Variation of vertical stresses at monitoring points

4.3 Evolution of Pore Pressure

Figure 9 shows the variations in pore pressure at seven monitoring points. Points with increasing depth along the tunnel axis have a higher value of pore pressures. Point 8 at the top of clay barrier has a pore pressure of 0.25 MPa while lowest point 12 at the bottom of model has a pore pressure of 0.15 MPa. After 10 m excavation of the tunnel (stage 2) there has been a sudden change in pore pressure at all the points due to disturbance by excavation. After disposal pit excavation (stage 3), pore pressure at points 8, 9, 10, 11, 12 suddenly reduces to zero as the rockmass is removed from the model, while pore pressure remains constant for pits 1 and 2. After emplacement of canister (stage 4) it is observed that pore pressure starts increasing due to increase in water saturation of the clay barrier.

5. CONCLUSION

Hydromechanical processes during construction of an URL have been studied to develop an understanding of the behavior of rock mass and fluid flow during and after excavation using three-dimensional finite difference method. The study has provided useful insights for safe disposal of canisters with spent nuclear fuel as well as estimation of deformations, stresses, and pore pressures to due to HM effects. Points near the proposed canister show an upward vertical displacement of less than 40% of the vertical displacement of the point at the top of clay barrier. In most of the cases, points near the crown and wall of the tunnel remain stationary except stage 2, during which the crown and side walls experienced maximum displacement of 90 to 25 mm, respectively. Pore pressure remains constant for points near the crown and side walls of the tunnel throughout the excavation stages, while there will be a variation of pore pressure at points near the canister, mostly dominated by variation with depth. The effect of volumetric strain is more prominent at the floor of the tunnel as compared to sidewall and crown.

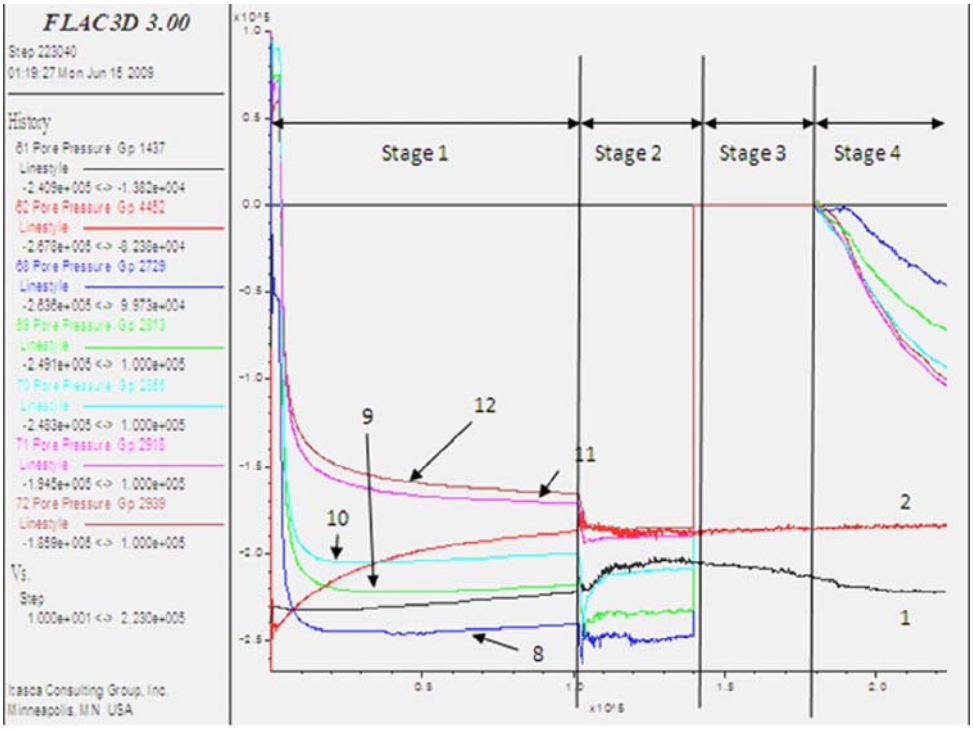

Figure 9 - Variation of pore pressure at different monitoring points

6. REFERENCES

BOOKER J.R. and SAVVIDOU, C., 1985. Consolidation around a heat source, Int. J Numer Anal Methods Geomech, p 173–184.

FAIRHURST, C. ,2004. Nuclear Waste Disposal and Rock Mechanics: Contributions of the Underground Research Laboratory (URL), Pinawa, Manitoba, Canada, Int. J. Rock Mech. Min. Sci., 41, p 1221-1227.

ITASCA CONSULTING GROUP INC. FLAC-3D, 1997. Manual: fast Lagrangian analysis of continua in 3 dimensions–Version 2.0., Itasca Consulting Group, Minnesota, USA.

RADHAKRISHNA, H.S., CRAWFORD, A.M., KJARTANSON, B.H. and LAU, K.C., 1992. Numerical modeling of heat moisture transfer through bentonite-sand buffer, Can. Geotech J., 29, p1044–1059.

STEPHANSSON, O., HUDSON, J.A., TSANG, C-F, JING, L. and ANDERSON, J., 1999. DECOVALEX II project: coupled THM issues related to repository design and performance—task 4. SKI Report 99:7.

THOMAS, H.R., SANSOM, M.R. and CRW, L.I., 1996. On the development of a model of the thermo-mechanical-hydraulic behaviours of unsat-urated soils, Eng Geol, 41, p197–218.

VERMA, A.K., BAJPAI, R.K., SINGH, T.N., NARAYAN, P.K. and DUTT, A., 2010. 3D instability analysis of an underground geological repository—an Indian case study, Arabian Jol. of Geosciences, doi: 10.1007/ s12517-010-0131-4.

WITHERSPOON P.A. and BODVARSSON G.S., 2001. Geological challenges in radioactive waste isolation, Third worldwide review, Report LBNL-49767, Berkeley, CA 94720. Lawrence Berkeley National Laboratory, CA.

Design of an Overburden Storage Structure in Northern Alberta

Nabeel Khan
Geological Engineering Program, University of Waterloo
Maurice B. Dusseault
Department of Earth and Environmental Sciences, University of Waterloo

ABSTRACT: Annual oil production from the Canadian Oil Sands in Northern Alberta has been rising for several decades, and more ore and overburden are excavated each year from an increasing number of open pit mines. Overburden meeting certain specifications will be used to dam tailings and fill open pits, but the remaining material must be stored in overburden storage structures (OBSS). Well-designed overburden storage structures are more stable and cost less in the short- and long-term. The purpose of this paper is to explore OBSS designs that will be stable yet economical in the short- and long-term. The geological background of the site is briefly discussed, including the effect of each of the main geologic layers (recently deposited till and muskeg, Clearwater Formation clay shales, McMurray Formation oil sands, and the Devonian limestone) on the slope stability of the OBSS. Cost is considered in the analysis when balancing between minimizing costs (steeper slopes) and acceptable factors of safety (flatter slopes), all the while considering the financial consequences of failure. Potential failure planes are identified and probabilistic analysis is conducted on the critical failure surface. The variations in the factor of safety caused by varying pore water pressure, friction angle, and cohesion, are plotted and discussed.

1. INTRODUCTION

From 2008 to 2035, the global demand for energy is expected to increase by 47%. Oil will consistently be needed to meet that energy demand. With nearly 175 billion barrels of economically recoverable oil, Canada has the third largest oil reserves in the world after Saudi Arabia and Venezuela. Nearly 97% of Canada's oil reserves are found in the viscous oil sands of Alberta and Saskatchewan (CAPP, 2011). The Canadian oil sands are largely located in Alberta and have been geographically classified into the Athabasca, Peace River, Wabasca, and Cold Lake deposits (Mossop, 1980). The burial depth of the reserves varies substantially within the oil sands from 0 to over 500 m, and different methods are required to economically extract the oil. In areas where the overburden is thin, like north of Fort McMurray, surface mining using shovel and truck methods is feasible. In areas with thicker overburden, where stripping the overburden is not economical, *in situ* extraction methods such as steam injection into horizontal wells must be used.

Surface mining techniques involve stripping the overburden and mining the underlying ore and are currently being employed in the shallow oil sands region of the Athabasca deposit. The ratio of overburden to recovered oil sands is expected to increase as deeper, harder-to-reach deposits are pursued (Hartman, 1992). Overburden that meets specific criteria is used on-site to build tailings dikes (Mossop, 1980). The remaining overburden will be used to fill open pits or will be stored in overburden storage structures (OBSSs).The purpose of this paper is to explore OBSS designs that will be stable in the long-term, maximizing the amount of overburden that can be stored while minimizing short- and long-term costs.

2. SITE GEOLOGY

The archetypal design site is located in the Athabasca deposit and consists of overburden and ore lying unconformably on Devonian limestone from the Waterways Formation. The overburden consists of Holocene organic soils (muskeg), Pleistocene till, Cretaceous Clearwater Formation clay shales, and some Cretaceous lean upper McMurray Formation oil sands (Stephens *et al*., 2006; Mossop, 1980). The Clearwater Formation consists of shallow marine origin smectitic-illitic-kaolinitic clay-shales, clayey siltstones, and a few thin beds of clayey fine-grained sandstones (McRoberts *et al*., 2008). These strata are best described as transitional strata (Dusseault *et al.*, 1983), and their properties may have been affected by exposure and glacial drag (pre-shearing).The overburden is generally thin, from 0 to 60 m, and can be removed economically by stripping to access the underlying oil-rich sand.

Ore mining activities take place within the oil-bearing Cretaceous McMurray Formation (Stephens *et al.*, 2006). Unlike the Clearwater Formation, the McMurray Formation is composed of coarse-grained channel-lag deposits that can be classified as gravels to fine-grained and very fine-grained high porosity sandstones (Mossop, 1980). A varying clay mineralogy in the formation includes illite, kaolinite, and mixed layer clays in the upper part of the formation to vermiculite basal clays at the base, and the clays in the ore body are of great engineering significance because they affect the extraction efficiency and lead to large accumulations of mature fine-grained tailings with a high oil content and poor consolidation performance (Dusseault and Scott, 1984).

2.1 Weak Layers

The horizontally bedded clay-shales located at the design site are highly overconsolidated and fairly strong because of previous deep burial (~800m deeper) during their geological history. However, the presence of smectitic layers that are probably slickensided control the design of the OBSS. In this paper, pre-existing shear planes, slickensided surfaces, and other surfaces where the strength of the soil has been reduced to a residual shear strength condition are referred to as weak layers. Past soil engineering projects in geologically similar locations revealed that the pre-sheared surfaces are associated with glacial action through the process of adhesion to the glacier base and basal drag (Alencar *et al.*, 1993; Cameron *et al.*, 2008). Close to river valleys, excavation and rebound can also lead to pre-sheared, slickensided surfaces.

The basal clay-rich member of the McMurray Formation directly overlies the Devonian Limestone and has been documented to contain slickensides. Past studies show that these slickensides were found in the basal clays kilometres away from valley walls, in flat lying areas, suggesting that they are not exclusively the result of displacements associated with stress relief (Dusseault and Scafe, 1979), although their specific origin remains obscure. Marine clay layers of the upper McMurray Formation that were affected by glacial drag are also expected to be at residual strength (Cameron *et al.*, 2008).

During the design it is assumed that both the McMurray and Clearwater Formations contain weak layers. For the McMurray Formation, the weak layers are assumed to be the vermiculitic basal clay, which has a low residual friction angle, ϕ'_r (Dusseault and Scafe, 1979), similar to the smectitic clay-shales of the lower part of the Clearwater Formation (Alencar *et al.*, 1993; Cameron *et al.*, 2008).

3. ANALYSIS

3.1 Software

The stability analysis is conducted using the Morgenstern and Price Method on GeoStudio's Slope/W 2007, a 2D slope stability program. Even though Slope/W is capable of other limiting equilibrium

methods, including Bishop Simplified and Janbu Simplified, the Morgenstern and Price Method is given preference because it takes into account both horizontal and vertical interslice forces and satisfies both force and moment equilibrium (Krahn, 2003).

In the analysis all geologic layers are assumed to be horizontal. For the expected and worst case scenarios, tension cracks half and fully filled with water are assumed, respectively. Since the hypothetical design site is in a seismically inactive area, seismic analysis is not conducted.

3.2 Factor of Safety Cut-Offs

It is assumed that failures in the OBSS could affect the company's secondary access roads which have low traffic density. As such the OBSS is classified as a low economic risk and low risk-to-life structure (US Army Corps of Engineers, 2003). Good engineering supervision is assumed during construction and a factor of safety (FS) cut-off of 1.3 is used for the expected case in the analysis.

Slickensided or weak layers have been known to control engineering design in overconsolidated clays (US Army Corps of Engineers, 2003). Repeated stability analysis confirmed that the FS is significantly more sensitive to variations in the input parameters of the weak layers than the actual soil layer. As such, probabilistic and sensitivity analyses are only conducted on the weak layers. For example, the worst case scenario assumes weak layers with little to no cohesion, low ϕ'_r (based on smectite-dominant clay mineralogy), and high pore pressures. Since each of the three conditions, even individually, are unlikely to occur throughout the weak layer at the same time, the FS cut-off for the worst case scenario is 0.8.

3.3 Probabilistic and Sensitivity Analysis

Probabilistic analysis is conducted to better understand the risks associated with the development of overburden storage sites because risk is a function of both probability and consequence ($R = P \times C$). The consequences of failure, and hence the risk, can be reduced through careful mine sequencing. Also, because the risk to land and life is exceptionally low, it is reasonable to design to a greater probability of a failure. To reduce risk by the reducing the probability of unsatisfactory performance (P_u), it is important to identify and quantify uncertainties associated with the project. These uncertainties can arise from model, parameter, and human uncertainty (Morgenstern, 1995).

Monte Carlo simulation is used in the probabilistic analysis to predict the behaviour of the OBSS. The optimum number of iterations is found through trial simulations to be 27,000. Since "…the simulation process uses random sampling of the input variables, the calculated probability of unsatisfactory performance is also a variable" (El-Ramly *et al.*, 2003). As such, the Monte Carlo simulation is repeated 20 times using different random numbers. P_u is determined by finding the probability of the $FS \leq 1.00$ using the cumulative probability graph produced by Slope/W.

The geological properties of the weak layers are expected to vary horizontally and vertically within the subsurface. Spatial variability is considered in the probabilistic analysis by using a sampling distance of 66 m in the analysis for the Clearwater Formation (a marine deposit with low heterogeneity) (El-Ramly *et al.*, 2003). Since all weak layers introduced in the analysis are only 0.1m thick, vertical spatial variation within the weak layer is ignored in the analysis. It is commonly observed that in the layered smectitic clay-shales along river valleys in the Prairies, the dominant failure plane is very thin, and largely flat-lying, following an exceptionally weak, usually pre-sheared slip surface.

Unlike the probabilistic analysis, sensitivity analysis conducted on the strength parameters illustrates how the OBSS will perform under extreme cases. Also, sensitivity analysis conducted on geometric design

parameters helps identify minor adjustments in slopes, heights, and offsets that have a large impact on the FS.

3.4 Residual Shear Strength Parameters (ϕ'_r and c')

At the design site, the ϕ'_r of the pre-sheared strata is dependent on the mineralogy of the clays present in the layer (Dusseault *et al.*, 1978). Since each geological layer is expected to contain several minerals with different friction angles, weak layers found in the field are expected to have higher friction angles than that of a pure clay mineral such as smectite or vermiculite. For the analysis, the ϕ'_r values were taken directly or modified from various published sources.

Soil structures have been successfully designed within the Clearwater Formation using both 7.5° and 8° for ϕ'_r (Alencar *et al.*, 1993; Cameron *et al.*, 2008; El-Ramly *et al.*, 2003; McRoberts *et al.*, 2008). In this paper ϕ'_r is assumed to be 7.5° but sensitivity analysis is conducted using 8°. For the worst case, ϕ'_r is dropped to 6°, assuming a smectite-dominant mineralogy, to account for deterioration within the clay shales (Picarelly and Di Maio, 2010). In the probabilistic analysis a lognormal distribution is used and ϕ'_r is assumed to be between 6° and 14° with a mean of 7.5° and a standard deviation of 2.1 (El-Ramly *et al.*, 2003).

The McMurray Formation is divided into the marine (top) and estuarine (bottom) layers. For the worst case scenario in the marine layer, a ϕ'_r of 9° is used based on past instability back-calculations in the Athabasca oil sands (Cameron *et al.*, 2008). For the expected case, a fully-softened peak strength of 19.5° is used with a 9° minimum for ϕ'_r. Whether the marine layer is at the residual or the fully-softened state is expected to be related to the depth of the layer during glacial drag and the amount of displacement experienced (Cameron *et al.*, 2008).

For basal sliding layer at the base of the McMurray Formation, ϕ'_r of 9° is used for the worst case scenario, and is roughly based on the ϕ'_r of pure kaolinite (Chattopadhyay, 1972). However, for the expected case (probabilistic and sensitivity analysis) a more probable ϕ'_r of 18° is used – based on published multireversal shear-box tests on intraformational McMurray Formation clayey silts with illite, kaolinite, and minor amounts of smectite (Dusseault and Scafe, 1979).

In the analysis, it is assumed that weak layers have not fully approached residual conditions and that failure planes are uneven, which results in a minimum cohesion of 10 kPa for subsurface weak layers. Since the failure planes are so large and presence of weak layers is not certain, cohesion is increased from 10 kPa to 50 kPa in the probabilistic and sensitivity analysis. For weak layers occurring within the OBSS fill, cohesion is held at 0 kPa and ϕ'_r values of 20° and 10° are used for the expected and worst case, respectively.

3.5 Pore Pressures

Pore pressures for the Clearwater clay-shales are based on personal communication with engineering consultants working in the area and on published data (Morgenstern *et al.*, 1993; El-Ramly *et al.*, 2003; Cameron *et al.*, 2008). At the design site, the pore pressures within the Clearwater Formation will be a function of the stress distribution of the OBSS loading. That is, the highest pore pressure will roughly exist underneath the crest of the OBSS, and is expected to decrease with each bench. The analysis simplifies the pore pressure distribution by assuming any Clearwater clay shale under the OBSS as loaded. When subjected to loading, these Clearwater units have been documented to show significant increases in pore pressures with low dissipation rates. As such, excess pore pressures caused by

construction are expected to have a long-term impact on stability (List, 2001) because the permeability is so low.

For the worst case, the Clearwater clay shales are assumed to have an r_u value of 0.5 for the unloaded layers and 0.7 for the loaded layers. For the expected case, the r_u for the unloaded layer drops to 0.45 (Cameron *et al.*, 2008) but remains at 0.7 for the loaded layers. In the probabilistic analysis, a lognormal distribution is used for the loaded Clearwater layers and r_u is assumed to be between 0.4 and 0.7 with a mean of 0.7 and a standard deviation of 0.1. On the other hand, a normal distribution is used for the unloaded layers and r_u is assumed to be between 0.2 and 0.5 with a mean of 0.45 and a standard deviation of 0.1. These pore water pressure distributions can be seen in Figure 1.

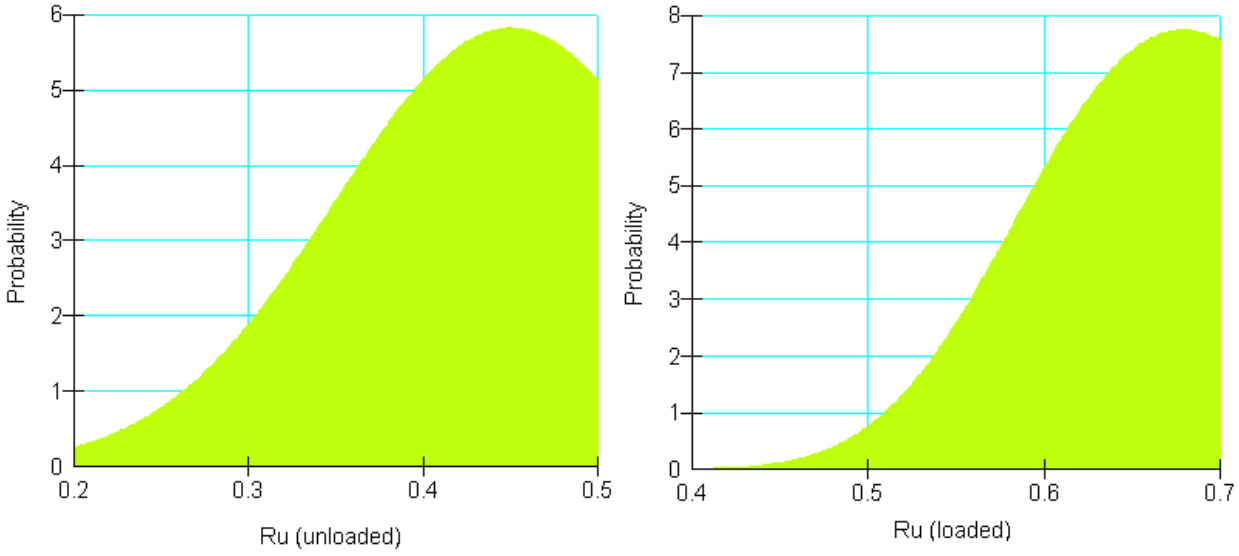

Figure 1 - Assumed r_u distribution for the Clearwater Clay shales

R_u values higher than 0.8 have been measured in previous OBSS constructions in the area (McRoberts, 2008). In the analysis, it is assumed that this will occur underneath the highest bench of the OBSS and, hence, far behind potential failure surfaces.

Pore pressures within the McMurray Formation are also based on personal communication and confirmed through published data (Stephens *et al.*, 2006; Chapman, 2008). R_u of 0.2 is used for the estuarine layer and underlying limestone for the worst and expected cases; whereas the pore pressures within the marine layer is based on a piezometric head varying from 290 m to 315 m.

4. RESULTS

4.1 Overburden Storage Structure Design

The OBSS is designed using deterministic slope stability analysis (Fig. 2). The purpose of this design is to create a stable OBSS that is economical in the short- and long-term. In the analysis, a minimum FS of 1.3 is used for the expected case and 0.8 for the worst case. The critical slip surface associated with the design is shown in Figure 3(a).

4.2 Bench Heights

Bench heights are increased in 0.5 m increments while maintaining the minimum FS by increasing offsets and flattening bench slopes. It is noted that benches higher than 4.5 m require drastically wider OBSS offsets to maintain the required stability. This is due to the increased probability of a secondary critical failure surface (Fig. 3b). With the current design, the FS along this secondary slip surface is about 1.34. When compared to the 4.5 m configuration, the 5 m bench configuration requires more than a 75 m width increase within the OBSS to maintain the minimum FS. As such, it is recommended that benches be built 4.5 m high. Additional benches can be added with a 75 m offset from the top bench.

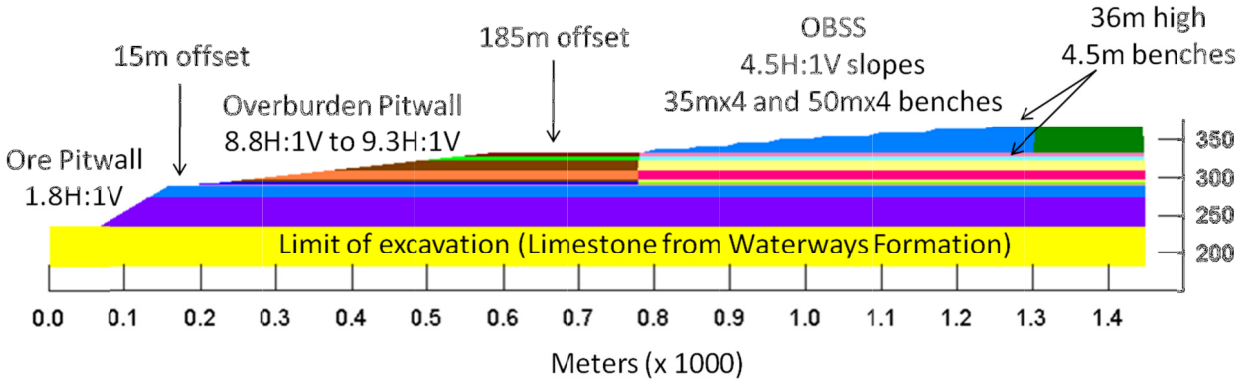

Figure 2 - OBSS design based on the deterministic analysis

4.3 Offsets

Using different OBSS configurations and offsets, 185 m is found to be the optimal offset between the OBSS and the overburden pitwall. The purpose of the offset is to increase the FS associated with the critical failure surface by increasing the sliding mass. With a smaller offset, like 150 m, it is noted that OBSS bench offsets need to be drastically increased to maintain the minimum FS of 1.3.

A 15 m offset is used between the overburden and ore pitwall. The purpose of this offset is to increase the stability associated with failures in which the sliding mass slides along the marine layer. In this study, ϕ'_r of the marine layer is assumed to be 9° due to glacial drag (Cameron *et al.*, 2008). In areas where there is no evidence of glacial drag and the McMurray Formation is well drained, lower offsets may be used.

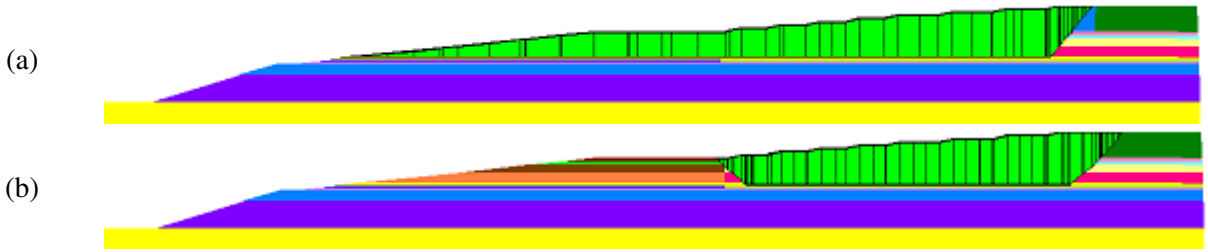

Figure 3 - (a) The critical failure surface. (b) Potential critical failure surface when bench heights are greater than 4.5m

4.4 Overburden and Ore Pitwall Stability

The 9.3H:1V overburden pitwall slope is designed using a ϕ'_r value of 7.5° for the Clearwater clay shales. Assuming the worst case where ϕ'_r drops to 6° and r_u is higher, the pitwall slope still maintain a FS > 1. If slopes in designed with ϕ'_r of 7.5° for the Clearwater strata have been found to be stable, the overburden pitwall may be steepened to 8.8H:1V.

The 1.8H:1V ore pitwall is designed using the expected ϕ'_r of 18° for the basal sliding layer. In the worst case scenario, where ϕ'_r drops to 9°, FS drops below 1 but is still higher than the 0.8 cut-off used in this analysis. To maintain a FS of 1 even in the worst case scenario, the ore pitwall needs to be flattened to 2.3H:1V.

It is noted that high piezometric heads can cause sliding to occur within the marine layer. These failures are not significant with the current configuration and input parameters. However, in mine sites where the location, friction angle, or pore pressure of the marine clay layer is not known, appropriate adjustments may need to be made to the OBSS design.

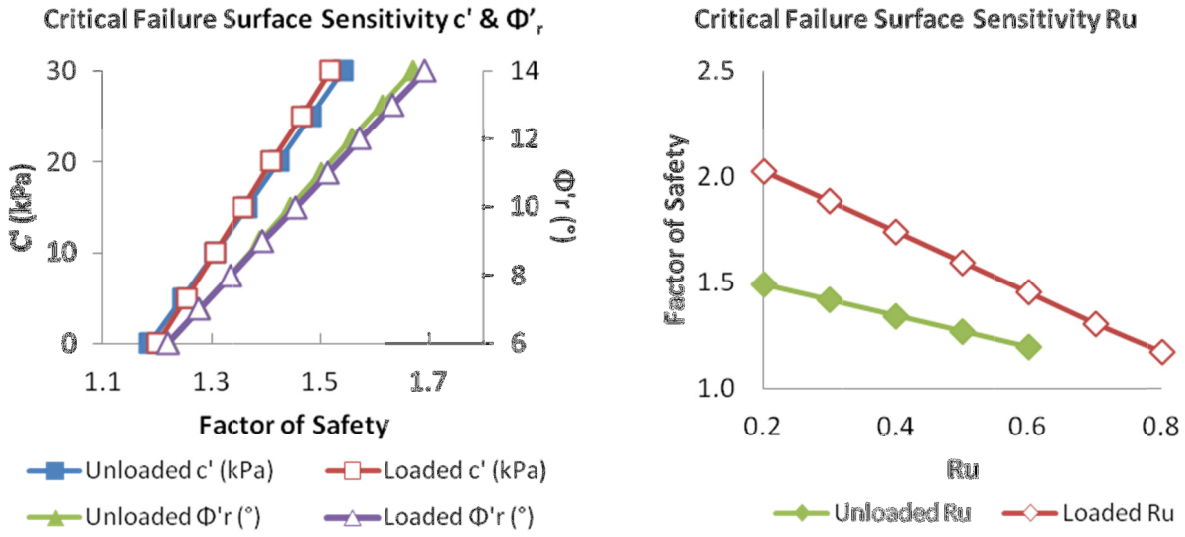

Figure 4 - Results of the sensitivity analysis conducted on the weak layers associated with the critical failure plane

4.5 Critical Slip Surface

The critical slip surface specified by the deterministic method is also found to have the highest probability of failure of all the high-consequence failures. Further probabilistic and sensitivity analyses are conducted on the critical failure plane to better understand the failure and the material parameters that have the largest effect on stability. The critical failure plane passes through both loaded and unloaded layers and the volume of the sliding mass associated with the critical failure surface is estimated to be 38,779 m^2. Sensitivity analysis conducted on the input parameters of the weak layers reveals that c′, ϕ'_r, and r_u all have significant impacts on the FS (Figure 4).

To determine the mean P_u, probabilistic analysis is conducted 20 times on the unloaded and loaded weak layers associated with the critical failure plane. The results of one of these runs, using FS intervals of 0.2

can be seen in Figure 5a. When using a simplified probabilistic approach (where no spatial variability is considered), mean P_u is estimated to be 1.37 $x10^{-3}$ (when c′ of the failure surface > 10 kPa) and 3.87 $x10^{-2}$ (when c′ = 0 kPa). On the other hand, when spatial variability is considered, with a sampling distance of 66 m and constant c′ of 0 kPa, P_u is estimated to be 2.11 $x10^{-3}$ with a standard deviation of $8.11x10^{-5}$ (Fig. 5b).

In all cases, the estimated P_u for the critical failure surface is higher than the recommendations stated in general literature. The US Army Corps of Engineers (1995), for example, recommends a P_u of $3x10^{-5}$. However, it is important to note that in published papers on probabilistic dike designs, other comparatively high P_u values of $1.6x10^{-3}$ and of $4.7x10^{-3}$ were found to be reasonable (El-Ramly *et al.*, 2003; Ladd *et al.*, 1983).

5. CONCLUSIONS

In this study slope stability analysis is used to design an overburden storage structure in the Athabasca oil sands. Naturally occurring weak layers are assumed to exist throughout the subsurface, in both the Clearwater and McMurray Formations. The critical failure surface is identified using deterministic slope stability and is also found to have the highest probability of failure out of all 'high consequence' failures. Further probabilistic and sensitivity analysis is conducted to better understand the critical failure surface. Spatial variability is considered with a sampling distance of 66 m (and c′ = 0 kPa), the mean probability of unsatisfactory performance is estimated at 2.11 $x10^{-3}$ with a standard deviation of $8.11x10^{-5}$. These values are comparable to the probability of unsatisfactory performance of 1.6 x 10^{-3}, which was found to be reasonable for dike construction in the Athabasca oil sands (El-Ramly *et al.*, 2003). This study is based on published data on various sites in the Athabasca oil sands deposit rather than a single site. As such, at design sites where more subsurface information is known, more economical overburden storage structures may be designed.

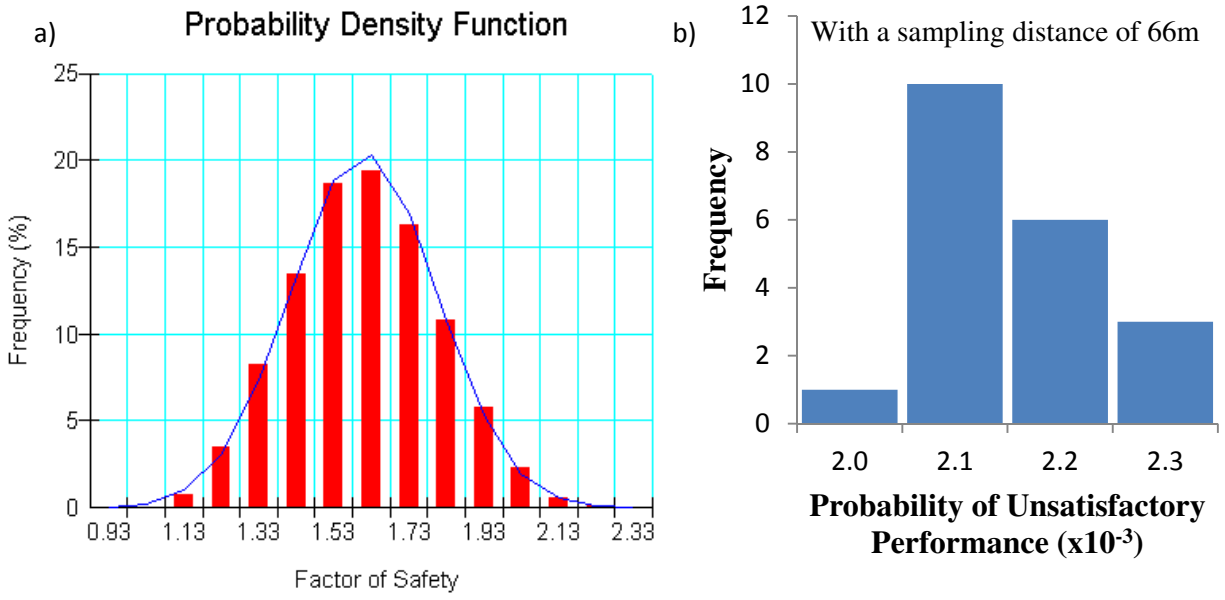

Figure 5 - a) Results of one probabilistic analysis run on the critical failure plane; b) probability of unsatisfactory performance based on 20 runs

Designs with higher probabilities of unsatisfactory performances than those recommended in the general literature have been found to be stable in the Athabasca oil sands (El-Ramly *et al.*, 2003). As a result,

further studies at specific sites must be conducted using the probabilistic slope stability approach for both past failures and successes. This will allow for better guidelines for OBSS's in the mining region.

6. REFERENCES

ALENCAR, J., MORGENSTERN, N.R., and CHAN, D.H., 1993. Analysis of foundation deformations beneath the Syncrude tailings dyke. Canadian Geotechnical Journal, 31, p. 868–884.

CANADIAN ASSOCIATION OF PETROLEUM PRODUCERS (CAPP), 2011. The Facts on Oil Sands.

CAMERON, R., MURRAY, D., and GURPREET, P., 2008. Oil Sands Mine Pitwall Design and Performance at Syncrude. GeoEdmonton Conference 2008, Edmonton, Alberta.

CHAPMAN, D.E., 2008. Hydrogeologic Characterization of a Newly Constructed Saline-Sodic Clay Overburden Hill. Masters thesis, Department of Civil and Geological Engineering, University of Saskatchewan, Saskatoon, Saskatchewan.

CHATTOPADHYAY, P.K., 1972. Residual shear strength of some pure clay minerals. Ph.D. thesis, Department of Civil Engineering, University of Alberta, Edmonton, Alberta. p. 459

DUSSEAULT, M. B., 2001. Comparing Venezuelan and Canadian Heavy Oil and Tar Sands. Canadian International Petroleum Conference 2001, Calgary, Alberta.

DUSSEAULT, M. B. and SCAFE, D.W., 1979. Mineralogical and Engineering Index Properties of the Basal McMurray Formation Clayshales. Canadian Geotechnical Journal, 16, p. 285–294.

DUSSEAULT, M.B., and SCOTT, J.D., 1984. Tailings pond behaviour and characterization of oil sand tailings sludge, J. of Particulate Science and Technology, 1, p. 295-309.

DUSSEAULT, M.B., CIMOLINI, P., SODERBERG, H. and SCAFE, D.W., 1983. Rapid index tests for transitional material, ASTM Geotechnical Testing Journal, 6, 2, p. 64-72.

EL-RAMLY, H., MORGENSTERN, N.R., and CRUDEN, D.M., 2003. Probabilistic stability analysis of a tailings dyke on presheared clay-shale. Canadian Geotechnical Journal 40, p. 192-208.

HARTMAN, H., 1992. SME Mining Engineering Handbook Volume 2. SME Inc., Littleton, Colorado.

KRAHN, J., 2003. The 2001 R.M. Hardy Lecture: The Limits of Limit Equilibrium Analyses. Canadian Geotechnical Journal 40.3 p. 643-60.

LIST, B.R., 2001. Surveillance and Monitoring of Syncrude's Mildred Lake Settling Basin. Canadian Dam Association 2001 Annual Conference, 341-349.

MCROBERTS, E.C., CAMERON R., and MIMURA, W., 2008. Residual Shear Strength Direct Shear Testing in Clearwater Formation Clays to Model Actual Field Conditions. GeoEdmonton Conference 2008, Edmonton, Alberta.

MORGENSTERN, N.R., 1995. Managing risk in geotechnical engineering. The 3rd Casagrande Lecture. 10th Pan-American Conference on Soil Mechanics and Foundation Engineering, Guadalajara, Mexico. Mexican Society of Soil Mechanics, Mexico City. Vol. 4, p. 102–126

MOSSOP, G.D., 1980. Geology of the Athabasca Oil Sands. Science 207.4427, p. 145-52.

PICARELLI, L., and DI MAIO, C., 2010. Deterioration Processes of Hard Clays and Clay Shales. Geological Society, London, Engineering Geology Special Publications 23.1, p. 15-32.

RADLER, M., 2005. Global reserves, oil production show small increases for 2005. Oil & Gas Journal, 103, 47, p. 20–21.

SAUER, E.K., 1978. The engineering significance of glacier ice-thrusting. Canadian Geotechnical Journal, 15, p. 457–472.

STEPHENS, B., LANGTON, C., and BOWRON, M., 2006. Design of Tailings Dams on Large Pleistocene Channel Deposits a Case Study – Suncor's South Tailings Pond.

US ARMY CORPS OF ENGINEERS, 1995. Introduction to probability and reliability methods for use in geotechnical engineering. Eng. Technical Letter No. 1110–2–547, Washington D.C.

US ARMY CORPS OF ENGINEERS, 2003. Engineering and design slope stability. Manual No. 1110-2-1902, Washington D.C.

Combined Finite-Discrete Element Modelling of the Influence of Bedding Planes on the Mechanical Behaviour of Opalinus Clay

Andrea Lisjak
Department of Civil Engineering, University of Toronto
Bryan S. A. Tatone
Department of Civil Engineering, University of Toronto
Giovanni Grasselli
Department of Civil Engineering, University of Toronto
Tim Vietor
NAGRA

ABSTRACT: The mechanical behaviour of Opalinus Clay, an indurated over-consolidated argillaceous rock, is heavily influenced by the presence of preferably oriented bedding planes. The objective of this study is to illustrate a new modeling approach aimed at capturing the bedding-induced anisotropy of Opalinus Clay as observed in the laboratory and *in situ*. The combined finite-discrete element method (FEM/DEM) is employed as the main simulation tool. FEM/DEM is a numerical method that models material damage processes by explicitly considering fracture nucleation and propagation. A transversely isotropic elastic constitutive law is used to account for different elastic property values in the direction parallel and perpendicular to the layering, while strength anisotropy is captured using a directional cohesive fracture model. Quantitative calibration and validation of the model is based on laboratory results of indirect tensile tests and uniaxial compression tests. Emergent strength and deformation properties, together with the simulated damage mechanisms, are shown to be in good agreement with experimental observations. Preliminary results relative to the analysis of a circular tunnel show that the approach is able to reproduce the main Excavation Damaged Zone (EDZ) formation mechanisms as observed in the field.

1. INTRODUCTION

Due to the favorable transport and geochemical properties, the Opalinus Clay, an indurated over-consolidated claystone, has been chosen in Switzerland as host rock formation for a high-level nuclear waste underground repository. The microstructure of Opalinus Clay is characterized by preferably oriented bedding planes which induce a strong anisotropy in the deformation and strength response of the rock under loading. The presence of bedding planes has been shown to heavily influence the hydro-mechanical behaviour of laboratory samples (Popp et al., 2008) and the development of the Excavation Damaged Zone (EDZ) at the Mont Terri Underground Research Laboratory (Bossart et al., 2002; Blümling et al., 2007).

Objective of this study is to illustrate a new modeling approach aimed at capturing the influence of material bedding on the undrained response of the Opalinus Clay as observed during laboratory tests and around circular tunnels at the Mont Terri URL. Following the work done by Stefanizzi et al. (2008), the combined finite-discrete element method (FEM/DEM) (Munjiza, 2004) was chosen as the main simulation tool. Distinctive characteristic of the method is the capability to simulate material damage and failure process by explicitly modeling fracture initiation and growth inside the model. For this study, an extension of the original Y2D FEM/DEM code (Munjiza, 2004), specifically developed for geomechanical applications and known as Y-Geo (Mahabadi et al., 2012), was used.

2. BASIC PRINCIPLES OF THE COMBINED FINITE-DISCRETE ELEMENT METHOD

Widely used continuum-based numerical models are limited in their ability to realistically address rock engineering problems involving failure along existing joint sets together with fracturing of intact rock material. In order to overcome these limitations, Munjiza et al. (1995) proposed a new hybrid finite-discrete element (FEM/DEM) method. Within the framework of FEM/DEM, discrete element method (DEM) principles are used to model interaction between different solids, whose deformation is analyzed using finite elements (FEM). Since an explicit time-marching scheme is used to integrate Newton's equations of motion, fully dynamic simulations can be performed. A unique characteristic of such a numerical tool is the ability to model the transition from continuum to discontinuum by explicitly simulating fracture and fragmentation processes.

The key processes of this hybrid approach include: contact detection and interaction between discrete bodies; elastic deformation of discrete bodies; and fracture of discrete bodies. The contact detection and interaction and fracture are discussed further in the following sub-sections. Deformability, however, follows an approach similar to that in any standard explicit finite element analysis and is not discussed any further here.

2.1 Contact Detection and Interaction

A FEM/DEM simulation can comprise a very large number of potentially interacting distinct elements. To correctly capture this behaviour, contacting couples (i.e., pairs of contacting discrete elements) must first be detected. Subsequently, the interaction forces resulting from such contacts can be defined. Contact interaction forces are calculated between all pairs of elements that overlap in space. Two types of force are applied to the elements of each contacting pair: repulsive forces and frictional forces. The repulsive forces between the elements of each contacting pair are calculated using a penalty function method (Munjiza and Andrews, 2000). Contacting couples tend to penetrate into each other, generating distributed contact forces, which depend on the shape and size of the overlap between the two bodies. Body impenetrability condition is reached as a limit condition for penalty values that tend to infinity. The frictional forces are calculated using a Coulomb-type friction law and used to simulate the shear strength of intact material and the frictional behaviour of pre-existing and newly created fractures.

2.2 Fracture Model

The transition from continua to discontinua is accomplished by driving fractures at the interface between adjacent triangular finite elements. A modified version of the discrete crack model developed by Munjiza et al. (1999) is implemented in the Y-Geo code used for this study. Rock material behaves elastically until the strength limit, defined by a Mohr-Coulomb criterion with tension cut-off, is locally reached. Upon overcoming the elastic limit, a new fracture is propagated at the interface between adjacent triangular elements. Material separation mechanisms and crack process zone are modeled by means of dedicated crack elements as a gradual strength reduction governed by a softening law. Material strength mobilization is represented by normal and shear bonding stresses, σ and τ, which are generated by the separation of the crack edges. As depicted in Figure 1, these stresses are assumed to be a function of crack opening, o, and crack slip, s. Fracture behaviour is ultimately controlled by the following input parameters: tensile strength, f_t, internal cohesion, c, and internal friction angle, ϕ, and mode I and II fracture energy release rates, G_{Ic} and G_{IIc}. Although re-meshing is not performed ahead of the crack tips, the direction of fracture propagation can be correctly captured as long as a sufficiently fine mesh is adopted.

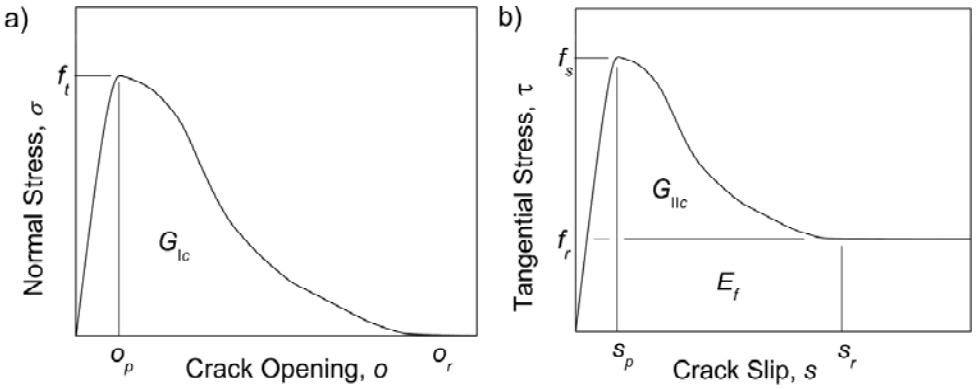

Figure 1 - Fracture model implemented in FEM/DEM: a) fracture process zone model for mode I (tension) and b) and slip-weakening model for mode II (shear)

3. MODELLING THE PRESENCE OF BEDDING PLANES IN FEM/DEM

3.1 Anisotropy of Deformability

The Opalinus Clay is a distinctively bedded material with elastic behaviour that is best described as transversely isotropic (Popp and Salzer, 2007). In other words, the deformability of the rock can be considered isotropic within any plane normal to an axis of rotational symmetry coincident with the normal to the bedding plane orientation. The naming convention of Figure 2a) is used in the present work to identify the test specimens according to the direction of anisotropy.

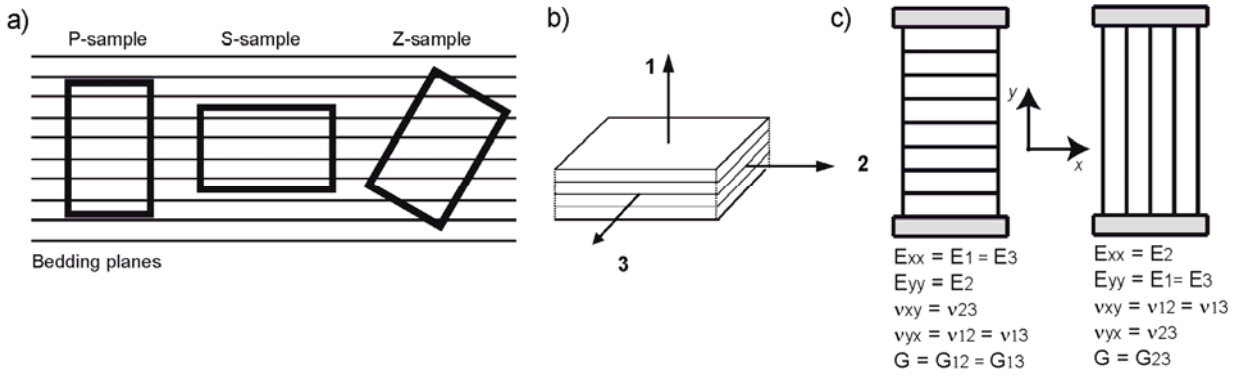

Figure 2 - a) Naming convention of test samples of Opalinus Clay, b) conventional reference axis for a transversely isotropic rock, and c) reduction to bi-dimensional models in the *x*-*y* plane

In order to correctly capture the deformation response of the Opalinus Clay, a two-dimensional stress-strain constitutive law for transversely isotropic elastic solids was adopted for the FEM/DEM numerical analyses. Five elastic constants are needed to describe the elastic behaviour: two orthogonal elastic moduli, E_x and E_y, two Poisson's ratios, ν_{xy} and ν_{yx}, and the shear modulus, G (Jaeger et al., 2007). As illustrated in Figure 2b) and c), the values of these constants are chosen so that the elastic behaviour parallel and perpendicular to the layering can be captured.

3.2 Anisotropy of Strength

To capture the effect of the bedding planes on the strength of the Opalinus Clay, a new constitutive law for the fracture model illustrated in Section 2.2 was introduced. In the new implementation, the material

strength parameters are functions of the angle γ between the edges of the crack elements and the orientation of the bedding planes (Figure 3).

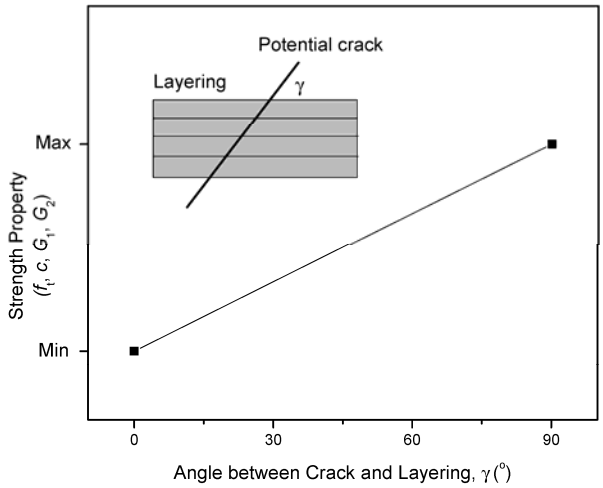

Figure 3 - Anisotropic cohesive fracture model with linear variation of strength with the angle between cracks and layering

The tensile strength, f_t, and the mode I fracture energy, G_{Ic}, assume minimum value for $\gamma = 0^o$ and maximum value for $\gamma = 90^o$, corresponding to axial loading conditions parallel and perpendicular to the bedding, respectively. The internal cohesion, *c,* and the mode II fracture energy, G_{IIc}, are minimum for $\gamma = 0^o$ and maximum for $\gamma = 90^o$, corresponding to shear loading conditions parallel and perpendicular to the bedding respectively. A linear variation with γ between the minimum and maximum value is assumed for each parameter. The friction angle ϕ is kept constant.

4. LAB-SCALE SIMULATIONS

The FEM/DEM model of Opalinus Clay was calibrated using the laboratory experimental results of uniaxial compressive strength and indirect tensile strength (Brazilian test) reported by Bock (2009). Successively, the calibrated model was used to investigate the influence of the specimen anisotropy direction on the mechanical response of the rock in compression. Model boundary conditions and modeling results are illustrated in the following subsections.

4.1 Geometry and Boundary Conditions

Figure 4 shows the geometry and boundary conditions of the laboratory test models. Rock specimens were discretized with triangular elements having an average size of 0.30 mm. Load was applied to the models by means of two rigid triangular platens moving at a constant velocity $v = 0.1$ m/s. Input files for the FEM/DEM simulations were created using the Y-GUI (Mahabadi et al., 2010).

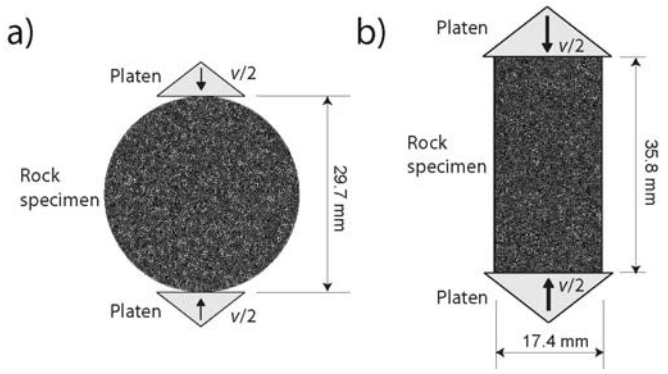

Figure 4 - Schematic of the rock specimens: a) indirect tension test and b) uniaxial compression test

4.2 Results

A comparison between numerical emergent properties and experimental values is reported in Table 1. As can be noticed from the table, a strong agreement between modelling and experimental results was achieved. In particular, the model is able to capture the strength and deformability anisotropy ratios induced by the presence of the bedding planes.

Table 1 - Comparison between experimental values from Bock (2009) and FEM/DEM numerical results

Sample	Indirect Tensile Strength (MPa)		UCS (MPa)		E @ 50% UCS (GPa)	
	Lab value	FEM/DEM model	Lab value	FEM/DEM model	Lab value	FEM/DEM model
P	1.3	1.2	11.6 ± 3.9	11.7	3.8 ± 1.5	3.6
S	0.7	0.6	14.9±5.1	15.6	1.3 ± 0.7	1.3

Figure 5 shows the plot of tensile stress versus vertical displacement and axial stress, σ_1, versus axial strain, ε_1, for the Brazilian test and UCS simulations, respectively. The response of the rock is linear until the failure stress is reached and brittle failure, characterized by a sudden and complete loss of strength, is simulated.

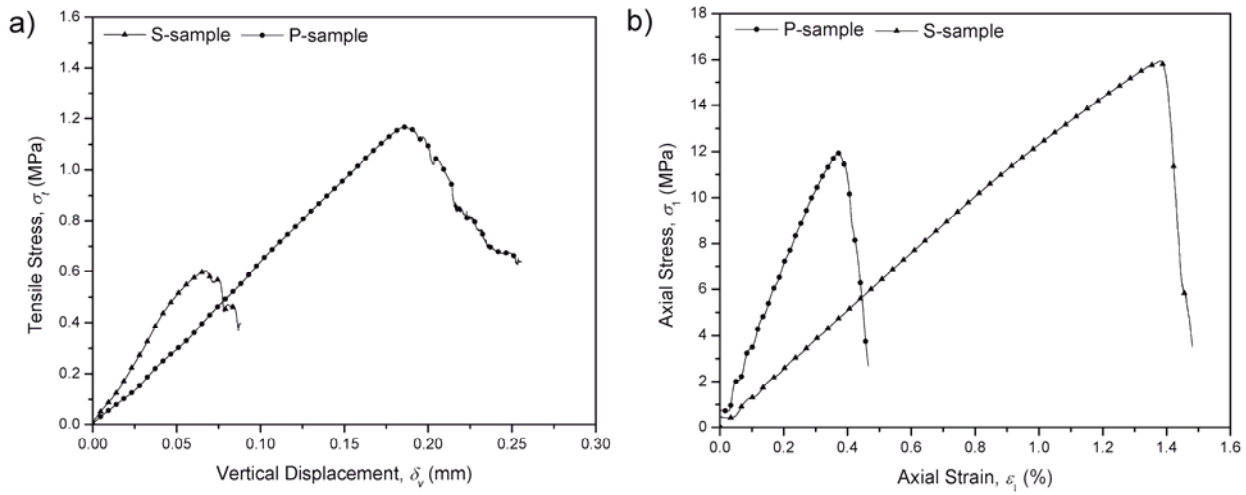

Figure 5 - a) Tensile stress vs. vertical displacement in the Brazilian numerical test and b) axial stress vs. axial strain in the UCS numerical test

The influence of loading direction with respect to the bedding plane orientation was analyzed by rotating the layering angle and the transversely isotropic stiffness matrix of the material at the prescribed angle, θ, to the axial direction. Material properties and numerical parameters obtained as a result of the calibration process were left unchanged. Values of uniaxial compressive strength (UCS) and elastic modulus, E, for different loading angles, are plotted in Figure 6. As the loading angle increases, the UCS value first decreases from the P-sample value (UCS_P) to a minimum value for θ = 30 - 45°, approximately equal to 50% of the UCS_P, and then increases again to reach the UCS_S for θ = 90°. This behaviour is in good agreement with published experimental results (Jahns, 2010) where a reduction of UCS between 50% and 80% was measured for Z-samples inclined at 30°.

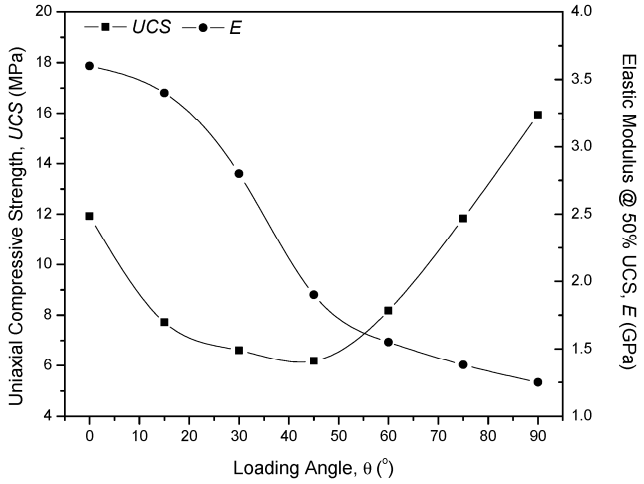

Figure 6 - Uniaxial compressive strength and elastic modulus plotted as a function of the loading angle θ. Continuous line represents numerical fitting

As shown in Figure 7, the influence of the bedding planes on the mechanical response of the sample varies substantially as a function of the loading angle. For θ = 0° (P-sample) the failure mode is given by unstable tensile crack propagation from the tips of the pre-existing cracks in the direction parallel to the maximum principal stress. For loading angle comprised between 15° and 60° failure occurs due to pure shear failure along the bedding planes. For loading angles equal to 75° and 90° (S-sample) inclined shear fractures propagating through intact material in combination with some axial splitting are simulated.

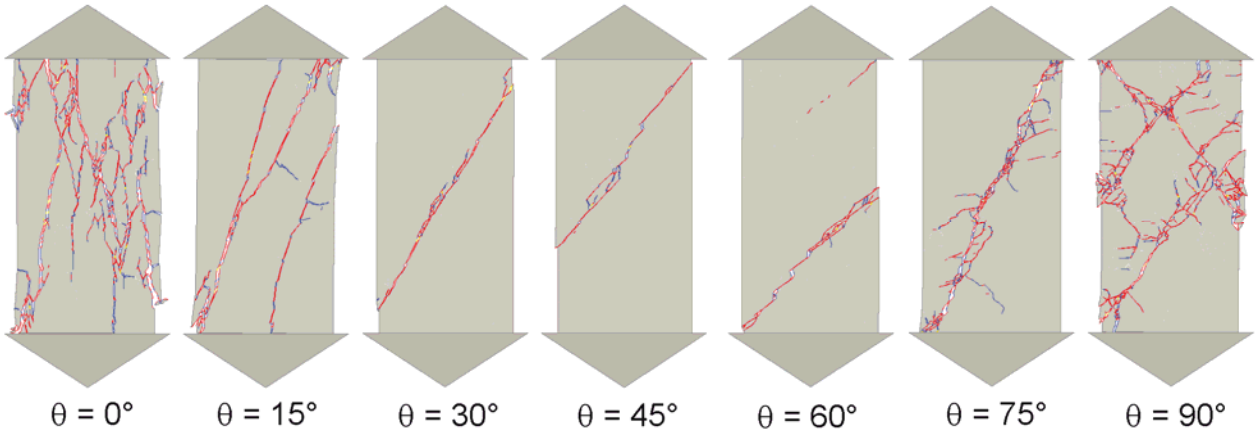

Figure 7 - Fracture patterns of UCS samples for different loading angles θ. Blue lines represent tensile fractures, red lines represent shear fractures

5. EXCAVATION DAMAGED ZONE MODELLING

5.1 Model Geometry and Boundary Conditions

The formation of the Excavation Damaged Zone (EDZ) around a 2.8 m circular opening excavated in Opalinus Clay was simulated. The tunnel was assumed to be driven parallel to the strike of flat-lying bedding planes and a 2D plane strain cross section was analyzed. Prior to excavation, the model was initialized with a maximum vertical *in situ* stress equal to 6.5 MPa and a minimum horizontal *in situ* stress equal to 2.2 MPa. Tunnel excavation was simulated by removing elements from the domain.

5.2 Preliminary Results

Figure 8 shows the EDZ for the simulated tunnel excavation. As can be observed, these preliminary results demonstrate that the numerical approach is able to reproduce the main damage mechanisms that have been observed around underground openings in Opalinus Clay. These include extensional fractures in the sidewalls (Bossart et al., 2002), bedding plane shear slip in the back and invert (Blümling et al., 2007) and conjugated shear fractures (Thury and Bossart, 1999).

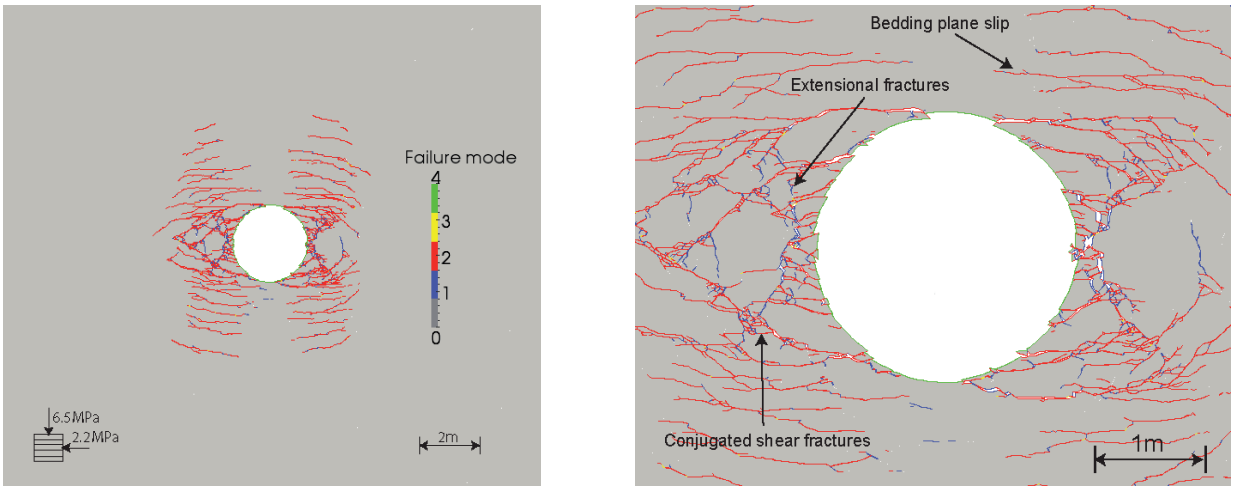

Figure 8 - Preliminary modelling results of damage mechanisms in Opalinus Clay around a circular tunnel parallel to flat-lying bedding. Blue lines represent tensile fractures, red lines represent shear fractures

6. SUMMARY AND CONCLUSIONS

A new modeling approach, based on the combined finite-discrete element method, was introduced aimed at capturing the role played by bedding planes on the mechanical behaviour of layered materials. Bedding-induced material anisotropy was numerically captured using a transversely isotropic elastic constitutive law and a directional cohesive fracture model. Calibration and validation of the approach was carried out using experimental values from standard rock mechanics tests performed on Opalinus Clay. Following the calibration procedure, a strong agreement between experimentally derived and modeled UCS and Brazilian test results was obtained. A variation of specimen compressive strength, crack pattern and damage mechanism, was captured as a function of the orientation of the bedding planes to the maximum compressive stress. This emergent property of the model was shown to be in agreement with published experimental findings. Finally, preliminary results relative to the modelling of the Excavation Damaged Zone around circular tunnels were shown.

7. REFERENCES

BLÜMLING, P., BERNIER, F., LEBON, P., and MARTIN, C.D., 2007. The excavation damaged zone in clay formations: time-dependent behaviour and influence on performance assessment. Physics and Chemistry of the Earth, 32, p. 588-599.

BOCK, H., 2009. RA Experiment: updated review of rock mechanics properties of the Opalinus Clay of the Mont Terri URL based on Laboratory and Field Testing. Technical Report 2008-04, Mont Terri Project, NAGRA.

BOSSART, P., MEIER, P.M., MOERI, A., TRICK, T., and MAYOR, J.C., 2002. Geological and hydraulic characterization of the excavation disturbed zone in the Opalinus Clay of the Mont Terri Rock Laboratory. Engineering Geology, 66, p. 19-38.

JAEGER, J.C., COOK, N.G.W., and ZIMMERMANN, R.W., 2007. Fundamentals of Rock Mechanics. Blackwell Publishing.

JAHNS, E., 2010. RA Experiment: Opalinus Clay rock characterization. Technical Note 2008-55rev, Mont Terri Project, NAGRA.

MAHABADI, O.K., GRASSELLI, G., and MUNJIZA, A., 2010. Y-GUI: A graphical user interface and pre-processor for the combined finite-discrete element code, Y2D, incorporating material inhomogeneity. Computer and Geosciences, 36, p. 241-252.

MAHABADI, O.K., LISJAK, A., MUNJIZA, A., and GRASSELLI, G., 2012. Y-Geo: a new combined finite - discrete element numerical code for geomechanical applications. Accepted for publication in the International Journal of Geomechanics.

MUNJIZA, A., 2004. The combined finite-discrete element method. Hoboken, NJ: John Wiley & Sons Ltd.

MUNJIZA, A., ANDREWS, K.R.F., and WHITE, J.K., 1999. Combined single and smeared crack model in combined finite-discrete element analysis. International Journal for Numerical Methods in Engineering, 44, p. 41-57.

MUNJIZA, A., OWEN, D.R.J., and BICANIC, N., 1995. A combined finite-discrete element method in transient dynamics of fracturing solids. Engineering Computations, 12, p. 145-174.

POPP, T., SALZER, K., 2007. Anisotropy of seismic and mechanical properties of Opalinus Clay during triaxial deformation in a multi-anvil apparatus, Physics and Chemistry of the Earth, 32, p. 879-888.

POPP, T., SALZER, K., and MINKLEY, W., 2008. Influence of bedding planes to EDZ-evolution and the coupled HM properties of Opalinus Clay. Physics and Chemistry of the Earth, 33, p. 374-387.

STEFANIZZI, S., BARLA, G., KAISER, P.K., and G. GRASSELLI, G., 2008. Numerical modeling of rock mechanics tests in layered media using a finite/discrete element approach. In Proceedings of the Twelfth International Conference on Computer Methods and Advances in Geomechanics (IACMAG). Rotterdam: Balkema.

Assessment of In Situ Stresses at Depth Using Borehole Breakouts

Richard Simon
École Polytechnique de Montréal
Denis Labrie
CANMET-MMSL, Natural Resources Canada

ABSTRACT: This paper presents an ongoing study on the use of borehole breakouts to estimate in situ stresses at depth in a Canadian underground mine. Breakouts were identified using an acoustic televiewer (ATV) probe. Rock samples were tested in a laboratory to determine their failure curve. Breakout analyses were performed using a 2D failure criterion and a multiaxial failure criterion. Analyses were carried out using both short-term (peak) and long-term strengths (the latter considered here as being represented by the damage initiation threshold DIT). The analyses have shown that the use of the long-term strength and a multiaxial failure criterion leads to results that are more consistent with stress measurements performed in the field, in the vicinity of the mine.

1. INTRODUCTION

Knowledge of in situ stresses is important for an adequate and safe design of underground openings. There are many techniques available to accurately determine in situ stress regimes (Amadei and Stephansson, 1997). Most of these techniques are based on strain recovery when the rock is relieved from its original stress conditions. However, their use poses problems at depth when high stress regimes cause disking, borehole breakouts, hole closure, etc. When using these techniques, the accuracy is often less than acceptable or the measurement is not possible at all. Nonetheless, it is imperative for the engineer to assess in situ stress conditions to make a proper design. The development of alternative or indirect methods is then needed to assess stress levels and stability of underground excavations under deep mine conditions.

A borehole breakout is a failure of the rock inside a drilled hole resulting from the stress redistribution around the hole after its creation. Occurrence of borehole breakouts was identified by earlier research (Leeman, 1964). Bell and Gough (1979) have suggested that these breakouts are indicators of the principal stress perpendicular to the borehole axis. Several authors have investigated the use of breakouts to assess in situ stresses for both direction and amplitude (Anderson et al., 1985; Hickman et al., 1985; Zoback et al. 1985; Plumb and Hickman, 1985; Zheng and Cook, 1985; Maury, 1987; Mastin, 1988; Barton et al. 1988; Guenot, 1989; Plumb, 1989; Zheng et al., 1989; Vernik and Zoback, 1992; Cheatham, 1993; Haimson and Song, 1993; Martin, 1993; Peska and Zoback, 1995; Elata, 1997; Aglawe, 1999). In this paper, the authors present an approach to assess in situ stresses based upon borehole breakouts observed in a Canadian deep underground mine (Li and Aubertin, 1999; Li et al., 2000; Aubertin et al., 2002). The authors also compare the use of a multiaxial failure criterion named $MSDP_u$ (Aubertin and Simon, 1996; Aubertin et al., 2000) and a simpler 2D criterion; i.e., the well-known Hoek-Brown criterion (Hoek and Brown, 1997).

The case presented here is the result of an ongoing project in a Canadian deep underground mine. The objective of the project is to assess in situ stresses for future mine developments. For analyses presented in this paper, the case of a single borehole breakout is considered (more breakouts are being analyzed and will be presented in future publications). The hole started at a depth of 2380 m, was 500 meters long, with a dip of 44°, and targeted a zone some 2700 m deep. An acoustic televiewer (ATV) probe was passed

through the hole for geological characterization purposes. This operation also allowed the identification of borehole breakouts along the hole. These breakouts were numerous, pointing to a very high in situ stress regime. Further indication of the high stress level in the area is the closure/failure of boreholes in a relatively short time (a few weeks) after drilling.

2. ROCK STRENGTH CRITERIA

Two rock failure criteria were used for the analysis of the borehole breakout, i.e. the well known Hoek-Brown criterion and the multiaxial $MSDP_u$ criterion.

2.1 Hoek-Brown Criterion

The Hoek-Brown criterion (Hoek and Brown 1980, 1988, 1997; Hoek et al., 2002) can be expressed for the intact rock as:

$$\sigma_1' = \sigma_3' + \sigma_c (m \sigma_3'/\sigma_c + s)^a \tag{1}$$

where σ_1' and σ_3' are the major and minor principal stresses at failure, σ_c is the uniaxial compressive strength, *m, s* and *a* are material constants, with s = 1 and $a \cong 0.5$ is for intact rock.

2.2 $MSDP_u$ Criterion

The $MSDP_u$ failure criterion is based on the integration of Mises-Schleicher and Drucker-Prager criteria (Aubertin and Simon, 1996; Aubertin et al., 2000). The multiaxial expression for general applications with rock media is written as follows, using common stress tensor invariants:

$$\sqrt{J_2} - F_0 F_\pi = 0 \tag{2}$$

Here, F_0 pertains to the shape and position of the failure surface in the $\sqrt{J_2}$ - I_1 plane (I_1 is the first invariant of the stress tensor σ_{ij} ; J_2 is the second invariant of the deviatoric stress tensor S_{ij}), while F_π defines the same surface in the octahedral (π) plane. The two functions, for intact low porosity rocks, can be defined in their simplified expression as (Aubertin et al. 2000):

$$F_0 = \left[\alpha^2\left(I_1^2 - 2a_1 I_1\right) + a_2^2\right]^{1/2} \tag{3}$$

$$F_\pi = \frac{b}{\left[b^2 + (1-b^2)\sin^2(45^\circ - 1.5\theta)\right]^{1/2}} \tag{4}$$

The main parameters of these two functions are obtained from the following equations:

$$\alpha = \frac{2\sin\phi}{\sqrt{3}(3-\sin\phi)} \tag{5}$$

$$a_1 = \left(\frac{\sigma_c - \sigma_t}{2}\right) - \left(\frac{\sigma_c^2 - (\sigma_t/b)^2}{6\alpha^2(\sigma_c + \sigma_t)}\right) \tag{6}$$

$$a_2 = \left\{ \left(\frac{\sigma_c + (\sigma_t / b^2)}{3(\sigma_c + \sigma_t)} - \alpha^2 \right) \sigma_c \sigma_t \right\}^{1/2} \quad (7)$$

In these equations, α represents the slope of the linear portion of the criterion in the $\sqrt{J_2}$ - I_1 plane when the Lode angle θ is 30° (conventional triaxial compression CTC), σ_c is the uniaxial compressive strength, σ_t is the tensile strength, ϕ is the residual friction angle, and *b* is the ratio of strength in reduced triaxial extension RTE (θ = -30°) over the CTC strength (θ = -30°). For most rocks, the value of *b* is close to 0.75.

Figure 1 shows the shape of the criterion in the $\sqrt{J_2}$ - I_1 and π planes. The criterion can also be used to define the limits of the damage initiation threshold (DIT) (Aubertin and Simon, 1997). It is considered here that, for intact isotropic rock, the DIT (sometimes called crack damage stress level CD) given by the onset of microcracking (seen through volumetric strain reversal or onset of acoustic emission events) represents the long-term rock strength. In this application, parameters σ_c and σ_t, corresponding to short-term failure, are replaced in $MSDP_u$ by properties corresponding to the DIT measured on the stress-strain curves (i.e. σ_{cd} and σ_{td}).

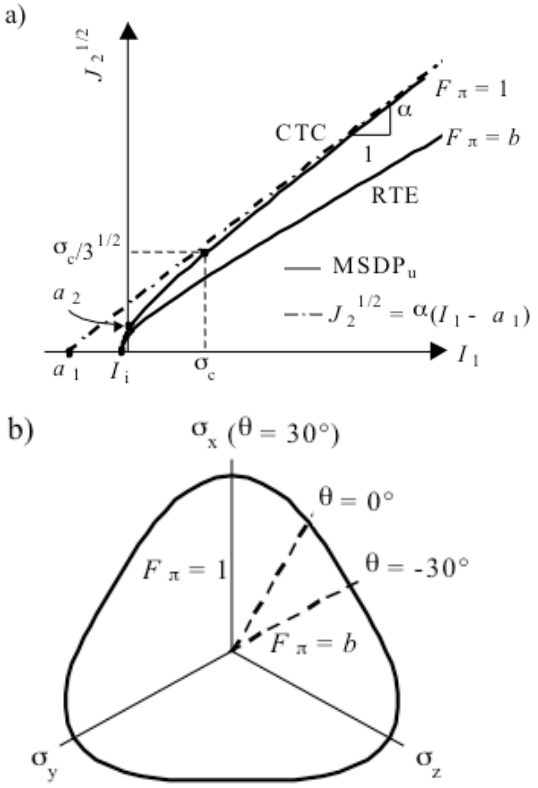

Figure 1 - Schematic representation of the $MSDP_u$ criterion: a) in the $\sqrt{J_2}$ - I_1 plane, CTC is the conventional triaxial compression (θ = 30°), RTE is the reduced triaxial extension (θ = -30°); b) in the π plane (after Aubertin et al., 2000)

3. ANALYSIS OF BOREHOLE BREAKOUTS

Borehole breakout analyses are based on the analytical stress distribution around a circular opening. The in situ principal stress tensor is defined by σ_v, the vertical stress, σ_H, the maximum horizontal stress, and σ_h, the minimum horizontal stress. In the area of the Canadian Shield where the study was performed (i.e., the Sudbury Basin), one usually considers $\sigma_1 = \sigma_H$, $\sigma_2 = \sigma_h$ and $\sigma_3 = \sigma_v$. For a vertical hole, the stress distribution around the borehole is given by the analytical solution proposed by Hiramatsu and Oka (1962):

$$\begin{aligned} \sigma_1 &= \sigma_H + \sigma_h - 2(\sigma_H - \sigma_h)\cos 2\Theta \\ \sigma_2 &= \sigma_v - 2\nu(\sigma_H - \sigma_h)\cos 2\Theta \\ \sigma_3 &= 0 \end{aligned} \quad (8)$$

where υ is the Poisson's ratio, and Θ, the angle between σ_H and the limit of the breakout, as represented by point B in Figure 2. When performing the analysis in 2D (and neglecting the influence of σ_2) with the Hoek-Brown criterion, the safety factor SF_{2D} around the borehole is then given by:

$$SF_{2D} = \frac{\sigma_c}{\sigma_1} \tag{9}$$

where σ_c is the uniaxial compressive strength, and σ_1 is given by equation 8. When performing the analysis with the $MSDP_u$ criterion, the safety factor SF_{3D} is given by

$$SF_{3D} = \frac{F_o F_\pi}{\sqrt{J_2}} \tag{10}$$

where

$$\sqrt{J_2} = \frac{1}{\sqrt{3}}(\sigma_1^2 - \sigma_1\sigma_2 + \sigma_2^2)^{1/2} \tag{11}$$

The Lode angle is given by:

$$\theta = \tan^{-1}\frac{\sigma_1 - 2\sigma_2}{\sqrt{3}\sigma_1} \tag{12}$$

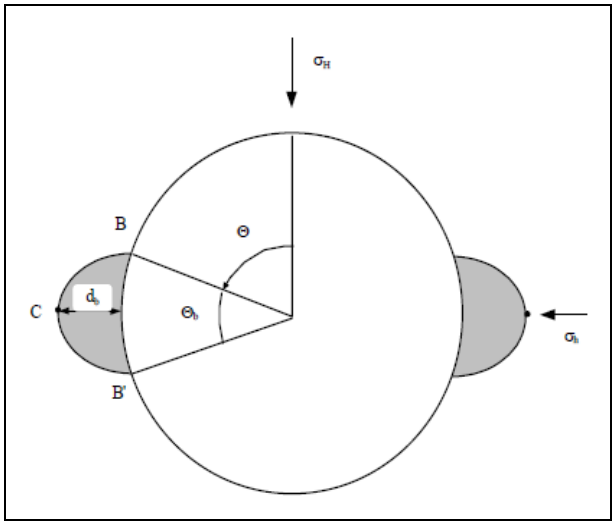

Figure 2 - Definition of a borehole breakout (after Li and Aubertin, 1999)

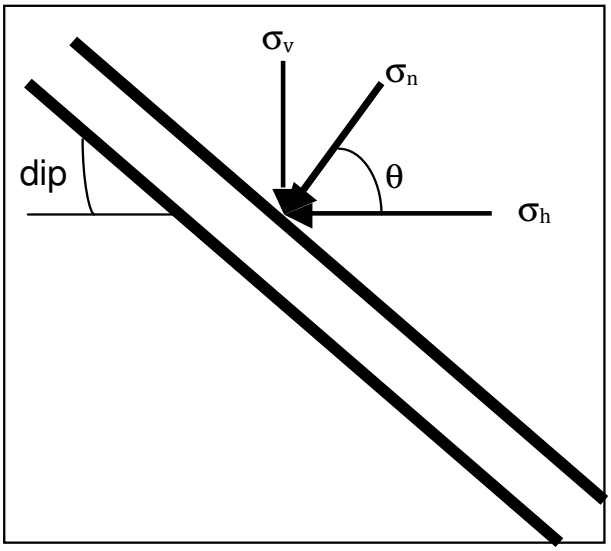

Figure 3 - Stresses acting on a borehole

For a horizontal hole, σ_H or σ_h is swapped with σ_v in Equation 8, depending on the orientation of the hole. For a dipping hole (as those analyzed in this study), one must then use the normal stress σ_n acting on the hole as shown in Figure 3, to take into account the in situ shear stress component. This normal stress can be obtained using usual transformation equations of the Mohr circle. Borehole stress equations used also assume isotropic mechanical properties. Pore pressure is neglected in the analysis because of hard-rock low-porosity materials.

4. LABORATORY TESTING

Rock samples were collected from the hole at the location of the breakout analyzed here, and tested at the CANMET-MMSL Rock Mechanics Laboratory in Ottawa, Canada. Rock samples were tested in uniaxial, triaxial and diametral compression. Table 1 gives the results of these tests. Figure 4 shows the stress-strain curves of the uniaxial compression test and one of the triaxial tests (also showing the damage initiation threshold DIT). These results have been used to determine the parameters of the Hoek-Brown

and $MSDP_u$ criteria (Table 2). Figure 5 shows the strength curves for both peak strength and damage initiation threshold.

Table 1 - Results of laboratory compression tests performed on rock samples

Rock type	Test	Confinement (MPa)	Peak strength (MPa)	Long-term strength (DIT) (MPa)
Gabbro	Diametral	---	-15.3	---
Gabbro	Uniaxial	0	211.8	139.6
Gabbro	Triaxial	10	287.3	211.0
Gabbro	Triaxial	20	360.7	262.4

Table 2 - Failure criteria parameters used for the analysis

	Hoek-Brown				$MSDP_u$			
	σ_c (MPa)	m	s	a	σ_c (MPa)	σ_t (MPa)	ϕ	b
Peak Strength	212	15.0	1.0	0.5	212	15.3	50	0.75
Long-term strength (DIT)	140	15.0	1.0	0.5	140	10.1	42	0.75

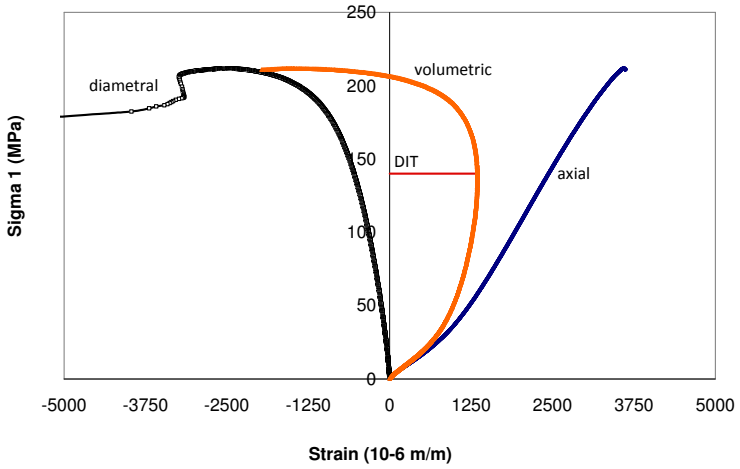

a)

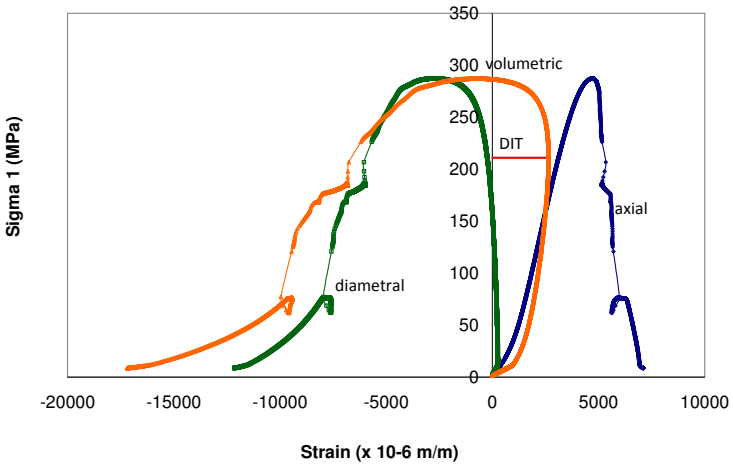

b)

Figure 4 - Stress-strain curves of the tested rock samples showing the damage initiation threshold DIT: a) Uniaxial Compression Test, b) Triaxial Test with a confinement stress level of 10 MPa

5. CASE STUDY: BOREHOLE BREAKOUT ANALYSES

A breakout was observed at depth of 2575 m in the borehole using the acoustic televiewer probe (ATV) (Figure 6). The angle of the breakout Θ_b was measured as being 20°. To assess the in situ stresses, assumptions must be made on σ_v and σ_h orientation and magnitude, in order to calculate the value of σ_H. The borehole analyzed was assumed north-south and perpendicular to the inferred maximum horizontal stress. All breakouts observed were almost at angles of 0° and 180°, confirming that this hypothesis is adequate, hence can be used in the following calculations. The vertical stress is considered to be a function of the overburden weight, with a gradient of 0.027 MPa/m. The minimum horizontal stress is assumed to be between 1.1 and 1.5 times the vertical stress. These assumptions are based on numerous stress measurements performed in the study area (Arjang and Herget, 1997). This leads to values of σ_v = 69.5 MPa and σ_h = 77 – 104 MPa. For a borehole dipping at 44° and using Mohr's circle equations (see Fig. 3), the stress σ_n perpendicular to the borehole varies between 73 and 87 MPa, and the stress parallel to its axis, between 73 and 86 MPa.

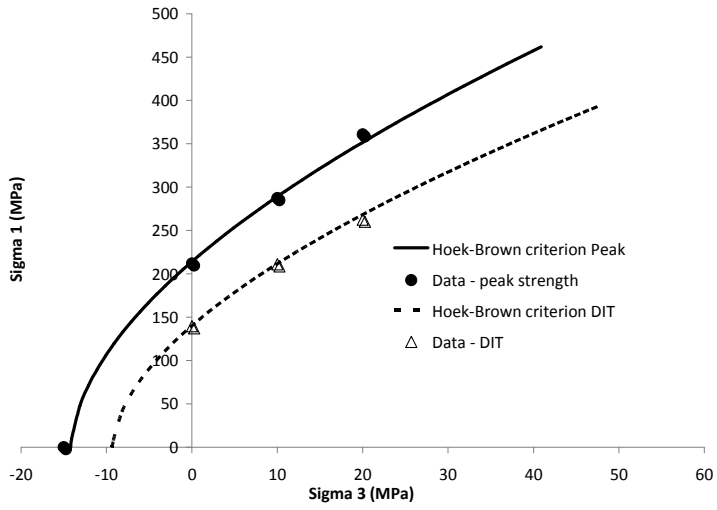

a)

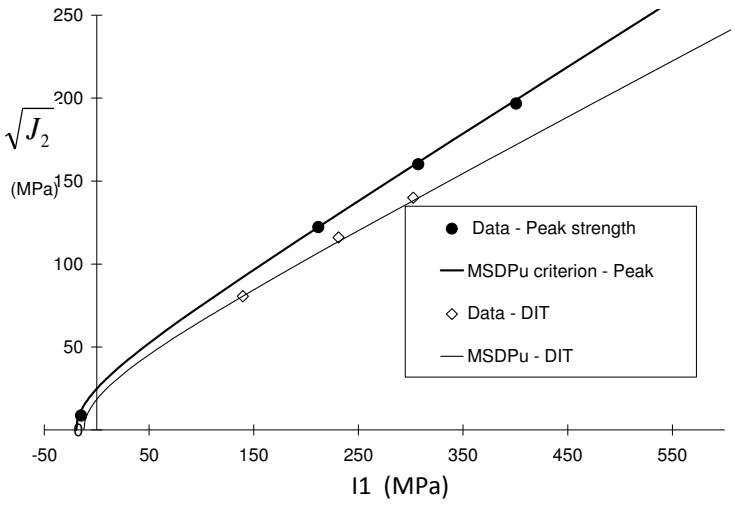

b)

Figure 5 - Failure and damage initiation threshold (DIT) curves based on the failure criteria: a) Hoek-Brown criterion, b) $MSDP_u$ criterion. Criteria parameters are given in Table 2

5.1 2D Analysis using the Hoek-Brown Criterion

Using Equations 8 and 9, it is possible to assess the maximum horizontal stress. The maximum horizontal stress σ_H then ranges between 96 and 100 MPa. This leads to a σ_H/σ_v ratio around 1.4. This is not in agreement at all with stress measurements performed in this area of the Canadian Shield, as the σ_H/σ_v ratio is expected to be between 2 and 2.5 (Arjang and Herget, 1997).

5.2 3D Analysis using the $MSDP_u$ Criterion

Using Equations 8 and 10 to 12, the maximum horizontal stress σ_H is then between 342 and 357 MPa. This leads to a σ_H/σ_v ratio around 5. This is a very high ratio that is not corroborated by stress measurements made in the area either. However, it could be argued that, with the presence of high stress regimes at depth, the rock strength around the borehole can be better assessed by the long-term strength of the rock as represented by the damage initiation threshold DIT curve shown in Figures 4 and 5. For the rock tested, the long-term strength varies between 0.6 and 0.8 time the short-term strength. When using the long-term strength, the analysis leads to a value for the maximum horizontal stress σ_H of 150 to 158 MPa, thus a σ_H/σ_v ratio around 2.2. This is in very good agreement with stress measurements performed in this area.

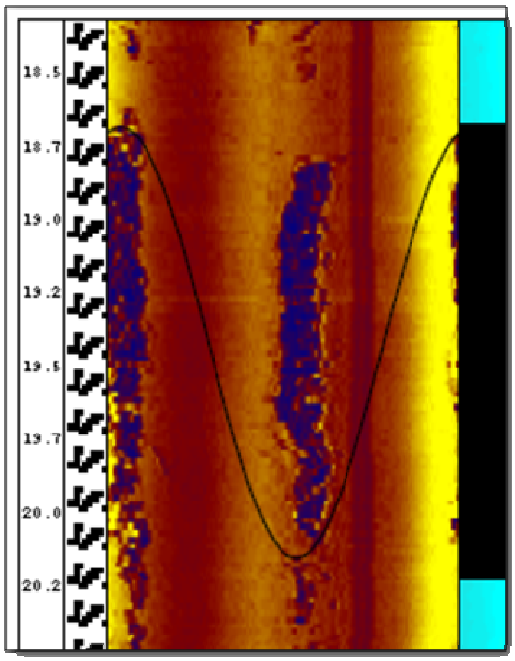

Figure 6 - Borehole breakout in hole 790 at a depth of 2575 m (Azimuth 340°, Dip: 44°). Rock type is gabbro

6. DISCUSSION AND CONCLUSION

Borehole breakout analyses indicate that using the long-term strength of the rock, as defined by the damage initiation threshold DIT, yields results in better accordance with stress measurements performed in this sector of the Canadian Shield. This is supported by the fact that there was a delay of several days between the drilling and observations being made with the acoustic televiewer. Moreover, the mining zone studied is obviously under a high stress regime. Most holes drilled in the zone investigated are lost after a few weeks due to creep or major breakouts. Under stress levels higher than the DIT, rock failure can occur relatively rapidly. The analysis also shows that using a 2D strength criterion is not adequate for borehole breakout investigations. Although the Hoek-Brown criterion can represent the short and long-term strength of the rock as adequately as the $MSDP_u$ criterion (as indicated in Fig. 5), a 2D analysis leads to stress results that are not realistic for the area investigated. In fact, when using a σ_h/σ_v ratio of 1.5, the results lead to a σ_H/σ_v ratio of 1.4, which means that $\sigma_H < \sigma_h$ in this case. This is not corroborated by the orientation of the breakout, either. More boreholes will be analyzed in the coming months, this should help to further explain and validate the approach used.

7. REFERENCES

AGLAWE, J.P., 1999. Unstable and violent failure around underground openings in highly stresses ground. Ph.D. thesis, Queen's University, Kingston (Ontario).

AMADEI, B. and STEPHANSSON, O., 1997. Rock stress and its measurement. Chapman & Hall, London (England).

ANDERSON, R., MOOS, D., GOLDBERG, D. and ZOBACK, M.D., 1985. Hydraulically induced breakouts: A new method for determining stress orientation in the crust? EOS, 66-18: 363.

ARJANG, B. and HERGET, G., 1997. In situ ground stresses in the Canadian hardrock mines: An update. International Journal of Rock Mechanics and Mineral Sciences, 34-3/4, Paper 015, CD-ROM, Elsevier.

AUBERTIN, M., LI, L. and SIMON, R., 2002. Effet de l'endommagement sur la stabilité des excavations souterraines en roche dure. Rapport R-312, soumis à l'Institut de recherche Robert-Sauvé en santé et en sécurité du travail (IRSST), Montréal (Québec).

AUBERTIN, M., LI, L. and SIMON, R., 2000. A multiaxial stress criterion for short term and long term strength of isotropic rock media. International Journal of Rock Mechanics and Mineral Sciences, 37-8: 1169-1193.

AUBERTIN, M., LI, L., SIMON, R. and KHALFI, S., 1999. Formulation and application of a short term strength criterion for isotropic rocks. Canadian Geotechnical Journal, 36-5: 947-960.

AUBERTIN, M. and SIMON, R., 1996. A multiaxial failure criterion that combines two quadric surfaces. In Rock Mechanics: Tools and Techniques in Rock Mechanics, eds. M. Aubertin, F. Hassani, H. Mitri, Balkema: 1729-1736.

AUBERTIN, M. and SIMON, R., 1997. A damage initiation criterion for low porosity rocks. International Journal of Rock Mechanics and Mineral Sciences, 34-3/4, Paper 017, CD-ROM, Elsevier.

BARTON, C.A., ZOBACK, M.D. and BURNS, K.L., 1988. In situ stress orientation and magnitude at the Fenton geothermal site, New Mexico, determined from wellbore breakouts. Geophysical Research Letter, 15-5: 467-470.

BELL, J.S. and GOUGH, D.I., 1979. Northeast-southwest compressive stress in Alberta: Evidence from oil wells. Earth and Planetary Sciences Letter, 45-2: 475-482.

CHANG, C. and HAIMSON, B., 2001. Two distinct modes of compressive failure on rocks. In Rock Mechanics in the National Interest, Proc. 38th U.S. Rock Mechanics Symposium, eds. D. Elsworth, J.P. Tinucci, K.A. Heasley, Balkema, 2: 1259-1265.

CHEATHAM JR., J.B., 1993. A new hypothesis to explain stability of borehole breakouts. International Journal of Rock Mechanics and Mineral Sciences & Geomechanical Abstracts, 30-7: 1095-1101.

ELATA, D., 1997. Modeling wellbore breakouts. International Journal of Rock Mechanics and Mineral Sciences, 34-3/4: Paper 072, CD-ROM, Elsevier.

GUENOT, A., 1989. Borehole breakouts and stress fields. International Journal of Rock Mechanics and Mineral Sciences, 26-3/4: 185-195.

HAIMSON, B.C. and SONG, I., 1993. Laboratory study of borehole breakouts in Cordova Cream: A case of shear failure mechanism. International Journal of Rock Mechanics and Mineral Sciences, 30-7: 1047-1056.

HICKMAN, S.H., HEALY, J.H. and ZOBACK, M.D., 1985. In situ stress, natural fracture distribution, and borehole elongation in the Auburn Geothermal well, Auburn, New York. Journal of Geophysical Research, 90-B7: 5497-5512.

HIRAMATSU, Y. and OKA, Y., 1962. Stress around a shaft or level excavated in ground with a three dimensional stress state. Memoirs of Faculty of Engineering, Kyoto University, 24: 56-76.

HOEK, E. and BROWN, E.T., 1980. Underground Excavations in Rock. Institution of Mining and Metallurgy, London (England).

HOEK, E. and BROWN, E.T., 1988. The Hoek-Brown failure criterion - a 1988 update. In Rock Engineering for Underground Excavations, Proc. 15th Canadian Rock Mechanics Symposium, ed. J.C. Curran, Dept. Civil Engineering, University of Toronto, Toronto (Ontario): 31-38.

HOEK, E. and BROWN, E.T., 1997. Practical estimates of rock mass strength. International Journal of Rock Mechanics and Mineral Sciences, 34-8: 1165-1186.

HOEK, E., CARRANZA-TORRES, C. and CORKUM, B., 2002. The Hoek-Brown failure criterion – 2002 Edition. Proc. 5th North American Rock Mechanics Symposium and 17th Tunneling Association of Canada Conference (NARMS-TAC), Toronto (Ontario): 267-271.

LADE, P.V., 1993. Rock strength criteria - the theories and evidence. In Comprehensive Rock Engineering – Principles, Practice and Projects, ed. J.A. Hudson, Pergamon Press, 1: 255-284.

LEE, M. and HAIMSON, B., 1993. Laboratory study of breakouts in Lac du Bonnet granite: A case of extensile failure mechanism. International Journal of Rock Mechanics and Mineral Sciences & Geomechanical Abstracts, 30-7: 1039-1945.

LEEMAN, E.R., 1964. The measurement of stress in rock. Journal of the South African Institute of Mining and Metallurgy: 45- 114.

LI, L. and AUBERTIN, M., 1999. Estimation des contraintes dans les roches à partir de l'écaillage autour de trous de forage. Revue Française de Géotechnique, 89: 3-11.

LI, L., AUBERTIN, M. and SIMON, R., 2000. Maximum and minimum horizontal stress evaluation based on the geometry of a single borehole breakout. In Pacific Rocks 2000, Rock around the Rim, Proc. 4th North American Rock Mechanics Symposium, eds. J. Girard, M. Liebman, C. Breeds, T. Doe, Balkema: 865-871.

LI, L, GAMACHE, M and AUBERTIN, M., 2000. Parameter determination for nonlinear stress criteria using a simple regression tool. Canadian Geotechnical Journal, 37-6: 1332-1347.

MAURY, V., 1987. Observations, researches and recent results about failure mechanisms around single galleries. In Proc. 6th International Congress Rock Mechanics, eds G. Herget, S. Vongpaisal, Balkema, 2: 1119-1128.

MARTIN, C.D., 1993. The strength of massive Lac du Bonnet granite around underground openings. Ph.D. thesis, University of Manitoba, Winnipeg (Manitoba).

MASTIN, L.G., 1988. Effect of borehole deviation on breakout orientations. Journal of Geophysical Research, 93-B8: 9187-9195.

MOGI, K., 1971. Effect of the triaxial stress system on the failure of dolomite and limestone. Tectonophysics, 11: 111-127.

PAN, X.D. and HUDSON, J.A., 1988. A simplified three dimensional Hoek-Brown yield criterion. In Rock Mechanics and Power Plants, ed. M. Romana, Balkema: 95-103.

PESKA, P. and ZOBACK, M.D., 1995. Compressive and tensile failure of inclined well bore and determination of in situ stress and rock strength. Journal of Geophysical Research, 100- B7: 12781-12811.

PLUMB, R.A. and HICKMAN, S.H., 1985. Stress-induced borehole elongation: A comparison between the four-arm dipmeter and the borehole televiewer in the Auburn geothermal well. Journal of Geophysical Research, 90-B7: 5513-5521.

PLUMB, R.A., 1989. Fracture patterns associated with incipient wellbore breakouts. In Rock at Great Depth, eds V. Maury, D. Fourmaintraux, Balkema, 2: 761-768.

VERNIK, L. and ZOBACK, M.D., 1992. Estimation of maximum horizontal principal stress magnitude from stress-induced well bore breakouts in the Cajon Pass scientific research borehole. Journal of Geophysical Research, 97-B4: 5109-5112.

ZHENG, Z. and COOK, N.G.W., 1985. Generation and analysis of stable wellbore cross section. EOS, 66-46: 1056.

ZHENG, Z., KEMENY, J. and COOK, N.G.W., 1989. Analysis of borehole breakouts. Journal of Geophysical Research, 94-B6: 7171-7182.

ZOBACK, M.D., MOOS, D., MASTIN, L. and ANDERSON, R.N., 1985. Well bore breakouts and in situ stress. Journal of Geophysical Research, 90-B7: 5523-5530.

Effect of Anisotropy of Permeability in Slope Stability of Large Open Pit Mines

Azadeh Riahi
Itasca Consulting Group, Inc
Jim Hazzard
Itasca Consulting Group, Inc
Loren Lorig
Itasca Consulting Group, Inc

ABSTRACT: The main goal of this paper is to investigate the effects of permeability anisotropy in Large Open Pit (LOP) mines for problems that exhibit homogeneous anisotropic characteristics. The most important effect of the groundwater flow in open pit mines is on the stability of the pit slopes. This study will investigate the effects of having increased permeability in both horizontal and vertical directions on three aspects of LOP behavior, location of phreatic surface, pore pressure distribution and stability of slopes. The hydromechanical coupling is simulated using a one-way coupling approach. The Shear Strength Reduction method (SSR) is applied to assess the stability of slopes. The studies performed in this paper suggest that anisotropy in permeability leads to a significantly different regime of pore pressure dissipation depending on two aspects, ratio of anisotropy and the relative magnitude of permeability to simulated time. As a result, variation in safety factors and the location and depth of the failure surface must be expected.

1. INTRODUCTION

1.1 Anisotropic Permeability Tensor

Fluid flow through porous media is governed by Darcy's law for fluid transport. By taking into account the effects of degree of saturation on the permeability, the Darcy equation can be expressed as (Itasca, 2008):

$$q_i = -k_{ij}\hat{k}(s)\frac{\partial}{\partial x_j}(P - \rho_w g_k x_k), \tag{1}$$

where q_i is the specific discharge vector, $k(s)$ is the relative permeability, which is a function of the saturation, s ,and k_{ij}, the permeability tensor (hydraulic conductivity), P is the fluid pressure, ρ is the mass density of the fluid and g is the gravity vector.

In general, k_{ij} is a second-rank symmetric tensor (Liakopoulos, 1965) with six components in a three-dimensional medium and three components in a two-dimensional medium. When permeability is the same in all directions, (i.e., it is isotropic), the second-rank tensor can be represented by a scalar value. When permeability varies in different directions, the permeability tensor is anisotropic.

1.2 Anisotropic of Permeability in Rock Masses

Many rock masses and soils show a directional preference in their permeability, with orders of magnitude difference between the horizontal and vertical components. The observed anisotropy can be the result of directional quality to the rock mass structure, such as the schistosity in metamorphic rocks and horizontal stratification in sedimentary rocks (Domenico and Schwartz, 1998), or it can result from significant anisotropy of in-situ stresses. The latter situation is encountered often in hard rocks, such as granitic rock

with a natural fracture network and significantly larger horizontal component of in-situ stress (Brawner, 1982). For bedded sediments, it is most common that permeability is greatest in the direction of stratification and smallest perpendicular to stratification. Similarly, it can be argued that in metamorphic rocks, maximum permeability can be associated with the direction of structures such as schistosity (Domenico and Schwartz, 1998). Field measurements suggest that for a specific rock deposition, it is common to have the horizontal and vertical component of permeability tensor vary by up to three orders of magnitude. In the horizontal plane, however, permeability in different directions is often the same. Thus, the 2D isotropic permeability tensor for the horizontal plane can be represented by a scalar value.

Figure 1 shows the permeability data gathered for 23 mines. This figure suggests that in a typical mine, it is more probable to have higher horizontal permeability than vertical permeability. However, there are many cases where permeability is greater in the vertical direction (Schlumberger, 2010).

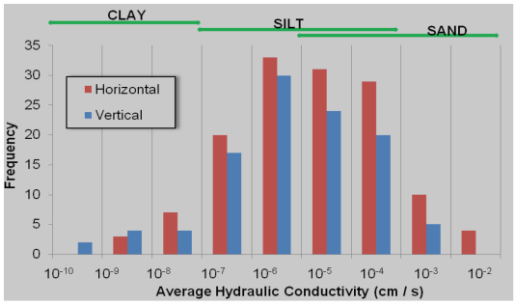

Figure 1 - Histogram of horizontal and vertical permeability for 23 mines (Lorig, 2009)

2. MODELING APPROACH

The main goal of this work is to investigate the effects of anisotropy of the permeability in Large Open Pit (LOP) mines. This study focuses on the problems that exhibit homogeneous anisotropic characteristics. Anisotropy of flow due to presence of faults or heterogeneities in the hydrogeological features is not considered. The effects of anisotropy of permeability will be investigated evaluating three aspects of LOP behaviour: (i) location of phreatic surface, (ii) pore pressure distribution and (iii) stability of slopes. The hydromechanical coupling is simulated using a one-way coupling approach (pore pressures are used to calculated effective stresses in the mechanical model). The Shear Strength Reduction method (SSR) is applied to assess the stability of slopes.

A model of a typical mining scenario was created with the two-dimensional finite difference program *FLAC* (Itasca Consulting Group, 2008), assuming a plane-strain (2D) condition. Values of permeability tensor were chosen based on common ranges for rock masses.

2.1 Model Geometry

The model geometry and mesh discretization used in this study are shown in Figure 2. Assuming that the LOP is symmetric, only half of the problem is modeled. The total height of the problem is 1600 m and the width is 2550 m. The total height of the slope at the end of the excavation is 1000 m. The bottom of the pit (in the half model) is 50-m wide. Each excavation increment is 200-m wide. The excavations of interest are the seven stages or increments numbered 5 to 11. Each of the increments 5 to 10 is 133.33-m high (for a total height of 800 m) and they each excavated over 9 months. Increment 11 is excavated 33 months after increment 10.After the excavation of increment 11, the model is run for 33 months. The initial water table is located at 50-m below the surface. The boundary conditions for the flow problem correspond to fixed hydrostatic pressure on the right side of the model, no flow boundary at the base (impermeability condition) and left-hand side (symmetry condition). A zero (atmospheric) pore pressure

is assigned to the slope face. To simulate mining, each block is removed instantaneously, and the model is run for a certain amount of time corresponding to the assumed mining rate (one 15-m bench per month)so that transient changes in pore pressure could be observed.

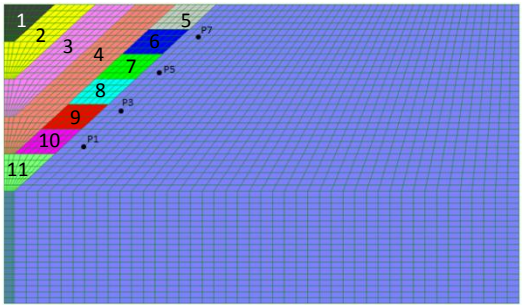

Figure 2 - LOP geometry and meshing used in FLAC models

2.2 Material Properties and Permeability Values

All material properties, except for the coefficient of permeability, are assumed to be homogeneous and constant. It is assumed that the host rock has a Young's modulus of 5 GPa, a Poisson's ratio of 0.25 and a density of 2500 kg/m^3.The rock strength properties (cohesion and friction) are used solely in the FOS calculations, the cohesion is assumed to be 0.5 MPa and the friction angle is 45^o. All other simulations are performed using elastic material properties. Fluid density, ρ_w, is 1000 kg/m^3,fluid bulk modulus, K_w, is 2.2 GPa, and porosity, n, is 1%.

In this study, it is assumed that the principal directions of permeability tensor coincide with the horizontal and vertical directions. Effects of anisotropy in permeability are investigated by considering the following:

(i) Increasing horizontal permeability: $k = k_0 \begin{bmatrix} \alpha & 0 \\ 0 & 1 \end{bmatrix}$, $\alpha = k_h / k_v = 1$, 10, 50, 100; and

(ii) Increasing vertical permeability: $k = k_0 \begin{bmatrix} 1 & 0 \\ 0 & \beta \end{bmatrix}$, $\beta = k_v / k_h = 1$, 10, 50, 100,

where α and β represents the anisotropy ratio. α is defined as the ratio between horizontal to vertical components, while β is the inverse of that. k_0 represents the overall magnitude of permeability, and is chosen to $k_0 = 10^{-8}$ m/s or 10^{-7} m/s.

3. RESULTS AND DISCUSSIONS

3.1 Pore Pressures and Phreatic Surface

Figure 3 shows the phreatic surface and the pore pressure distribution for increasing horizontal and vertical anisotropy. As the ratio of horizontal permeability $\alpha = k_h / k_v$ increases, the following three effects can be observed.

(i) The effect of zero pressure boundary condition at the slope face is pushed further into the slope in the horizontal direction. As a result of increased contrast between the horizontal and vertical permeability, flow lines tend to become more horizontal, and pore pressures dissipation due to horizontal drainage can occur at longer distances from the slope face.

(ii) Compared to the model with isotropic permeability ($\alpha = 1$), the phreatic surface aligns more horizontally, and the draw-down of the phreatic surface becomes slower particularly for high ratios

of α. In such cases, a region of low pressure is formed below the phreatic surface, where little desaturation occurs. Also, the phreatic surface's profile becomes different from the pore pressure contours profile.

(iii) Pressure gradient at the pit bottom and below the slope toe significantly increase. Therefore, it can be expected that artesian conditions be observed if open (Cassagrande-type) wells are installed in these locations.

Increasing ratio of vertical anisotropy $\beta = k_v / k_h$ results in accelerated draw-down of the phreatic surface. The profile of pore pressure contours closely resembles the phreatic surface profile, i.e., the pore pressure profile in these cases is compatible with the convex shape of the phreatic surface, and forms a significant curvature at the region adjacent to the slope face. How pore pressures are distributed behind the slope face (relative to isotropic model) is a function of this curvature. With respect to pressure gradients at the pit bottom, increasing vertical permeability has a favorable effect in reducing the pressure gradients at the pit bottom and below the slope toe.

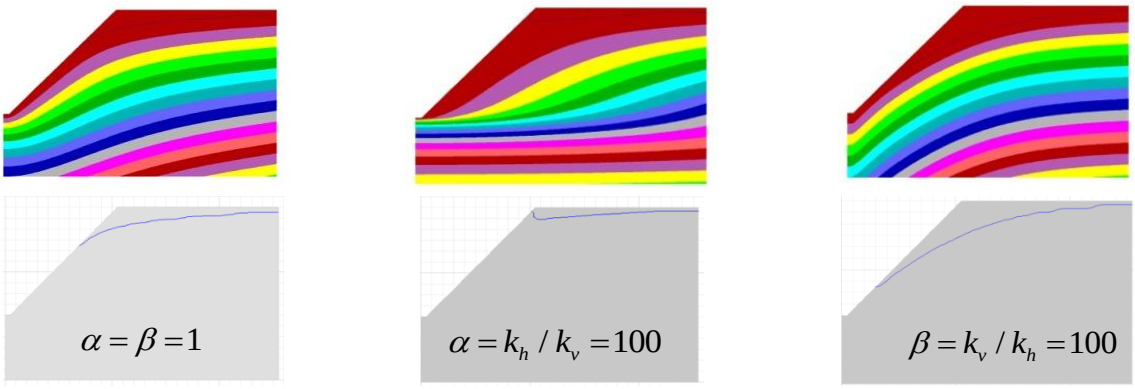

Figure 3 - Pore pressure distribution and the phreatic surface

In this paper, effects of permeability anisotropy are investigated for low and high permeable host rocks. Figures 4and 5 show pore pressure histories for flow points (P1 and P5, shown in Figure 2) adjacent to the slope face. Figures 6 and 7 show the distribution of pore pressures for LOP models with different k_0.

For increasing horizontal permeability, the results show that in low permeability rocks ($k_0 = 10^{-8}$ m/s), the pore pressures in the vicinity of the slope for the anisotropic model with $\alpha = 100$ are significantly smaller than those of the isotropic model. However, at the top of the slope, pressures are lower (close to zero) in the model with isotropic permeability. The difference between the pore pressures at the top of the slopes (between anisotropic models and their isotropic counter parts) becomes more significant at the later stages of excavation. Similar behavior is controlling the pore water distribution in models with increasing horizontal permeability and $k_0 = 10^{-7}$ m/s. However, in these models, the host rock is more permeable. As a result, the draw-down of the phreatic surface in the isotropic model can be more favorable in reducing pressures than the accelerated horizontal drainage through the slope face in the anisotropic models.

For increasing vertical anisotropy, results suggest that in general, the sensitivity of the LOP model to permeability anisotropy is not as significant as its response to increasing horizontal permeability. Close comparison of the pore pressure results for anisotropic models with those of isotropic models suggest that the increase in the vertical permeability can result in further draw-down of the phreatic surface and in some cases a decrease in pore pressures. However, the curvature of pore pressure contours behind the slope face can become high enough to result in significant increases in the pore pressures at Region (B) behind the slope face (Figure 5, point P5). This effect is more pronounced in model with $k_0 = 10^{-7}$ m/s.

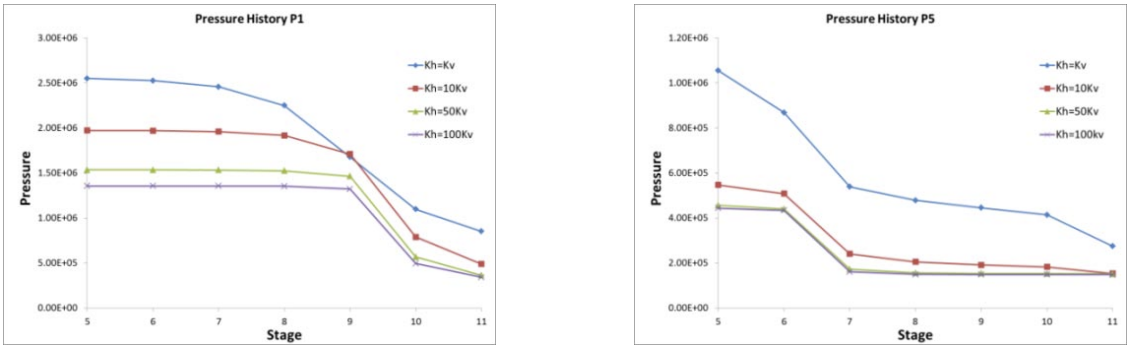

(a) $k_0 = 10^{-8}$ m/s

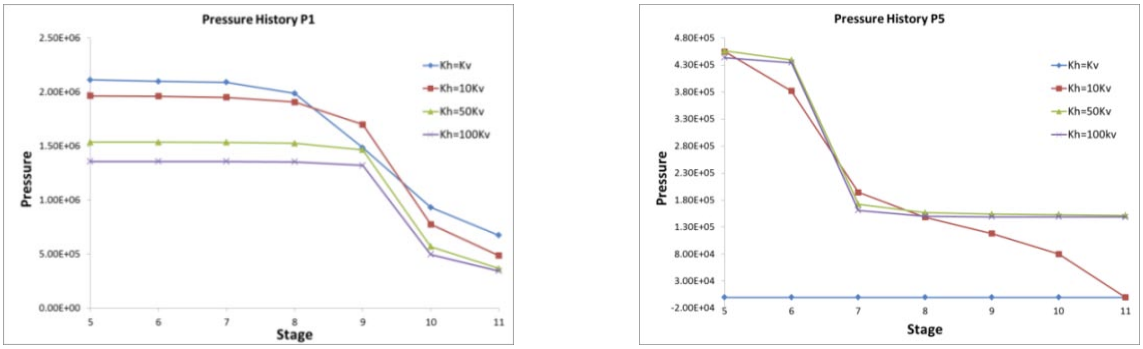

(b) $k_0 = 10^{-7}$ m/s

Figure 4 - Pore pressure history for models with $k_h > k_v$

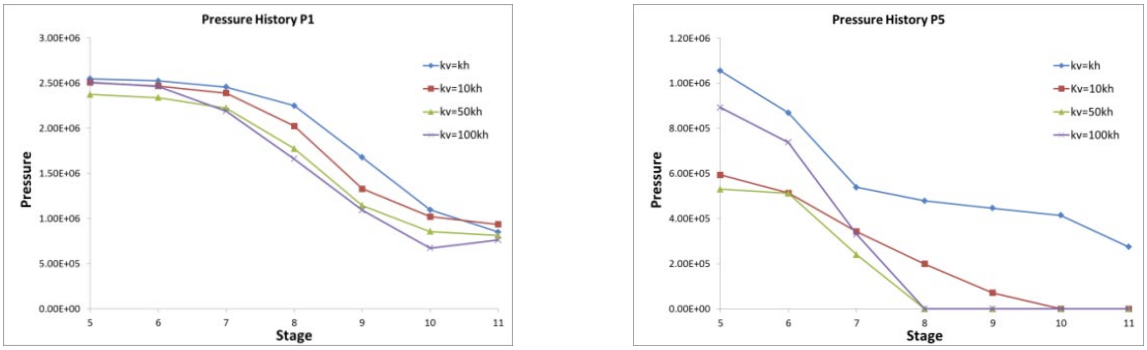

(a) $k_0 = 10^{-8}$ m/s

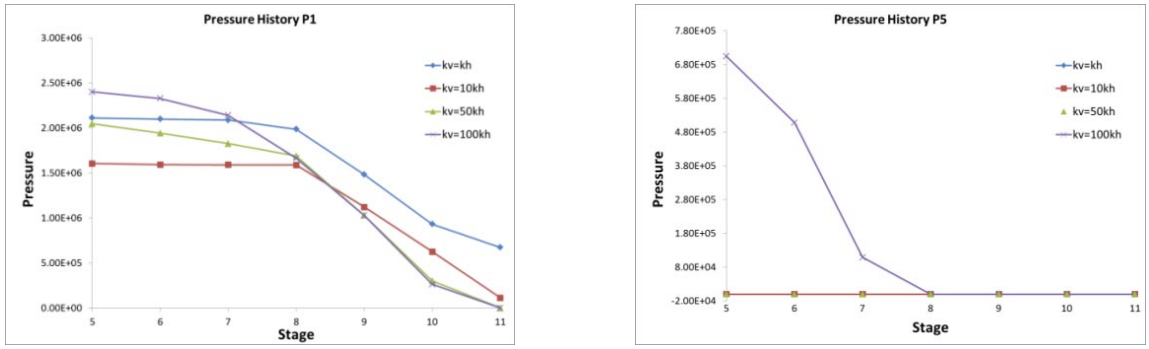

(b) $k_0 = 10^{-7}$ m/s

Figure 5 - Pore pressure history for models with $k_v > k_h$

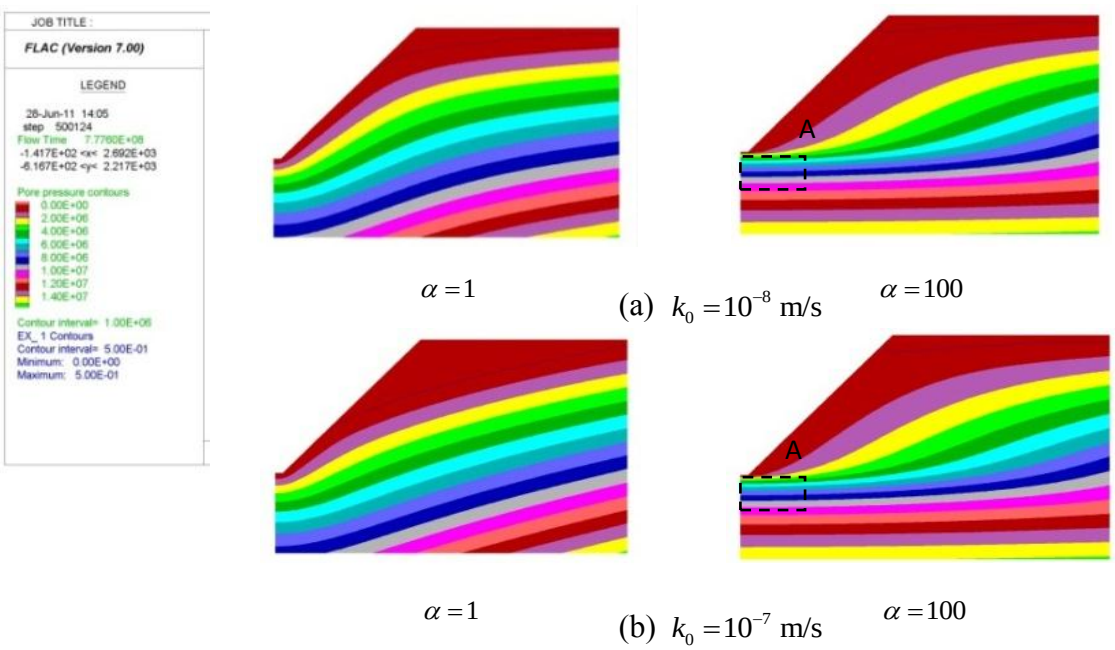

Figure 6 - Pore pressure contours for models with $k_h > k_v$ at stage 11

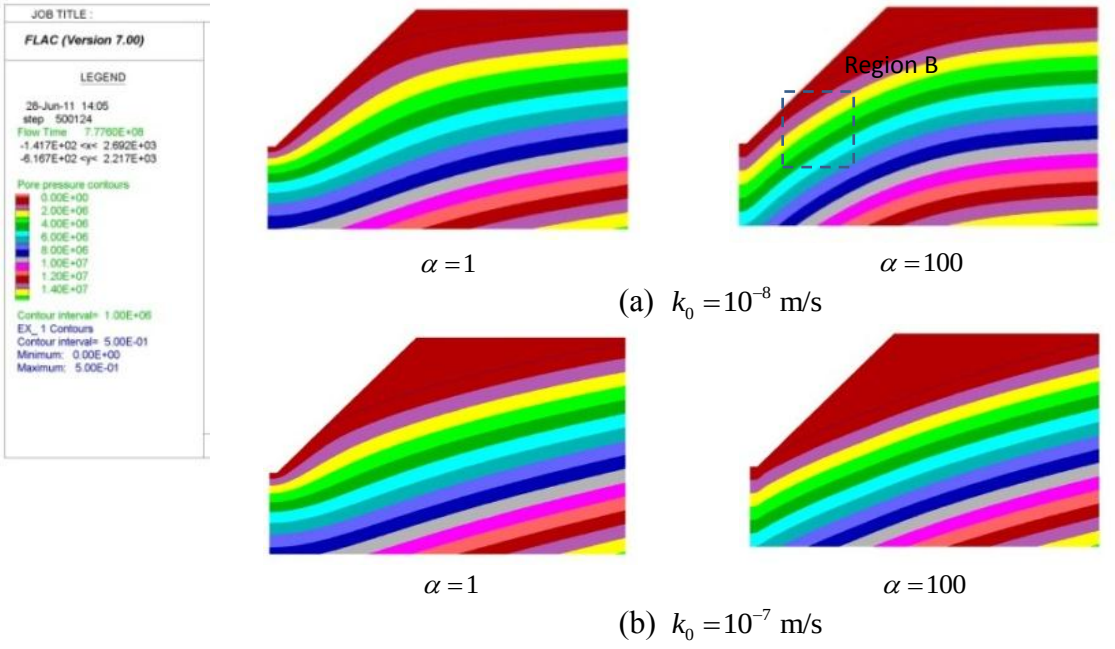

Figure 7 - Distribution of pore pressure for models with $k_v > k_h$ at stage 11

3.2 Factor of Safety Results

The average FOS values for stages 5 to 10 of models with increasing horizontal and vertical permeability are shown in Figure 8. It is noted that the numerical simulation of LOP models predicts significant pressure gradients at the pit bottom. However, this mechanism is not realistic due to the drainage that likely takes place in the fractured zone adjacent to the pit bottom. In order to eliminate the unrealistic blow-up failure modes associated with high pressures at the pit bottom, a manual FOS analysis is performed. Reduction factor is increased in intervals of 0.05, and contours of shear straining are inspected visually, until a continuous surface with relatively large values of shear strain is formed.

Figure 8a shows that when host rock permeability is low, increasing ratio of horizontal anisotropy, $\alpha = k_h / k_v$, results in an increase in FOS values. This observation is consistent with the effect of horizontal anisotropy in reducing pore pressures at locations adjacent to the slope face. For the slope geometry used in these analyses, the simulated time, and host considered rock permeability values, the increasing trend in FOS is observed in the range of $\alpha < 50$. After this threshold, the increase in FOS values relative to model with $\alpha = 50$, is insignificant.

When host rock permeability is high, increasing ratio of horizontal anisotropy is not helpful in significantly reducing FOS. It is observed that the model with $\alpha = 10$ shows a general decrease in the FOS values, and for $\alpha > 50$, changes in FOS values are insignificant. The decrease in FOS for model with $\alpha = 10$ is consistent with the observed increase in the pore pressures at the lower part of the slope in this model. It is important to note that the location of the critical failure surface may be different for different anisotropy ratios, because high pressures at different locations (e.g., below the toe versus behind the slope face) may mobilize different critical surfaces. Therefore, it is difficult to map out consistent trends in FOS with changing ratios.

Figure 8b shows that similar to the pore pressure trends, establishing a general trend for changes in FOS with respect to vertical anisotropy ratio is not feasible. However, it seems that vertical permeability is often favorable in increasing the FOS values. It helps in the drawdown of the phreatic surface and reduces the pressures close to the slope face, and thus, increases the FOS. For very high anisotropy ratios, the contrast between vertical and horizontal permeability can have an adverse effect by disfavoring the horizontal drainage. In such cases, a high curvature forms in the pore pressure contours that leads to elevated pore pressures in the middle and lower part of the slope. As a result, a decrease in FOS and a change in location and depth of critical failure surface may be expected.

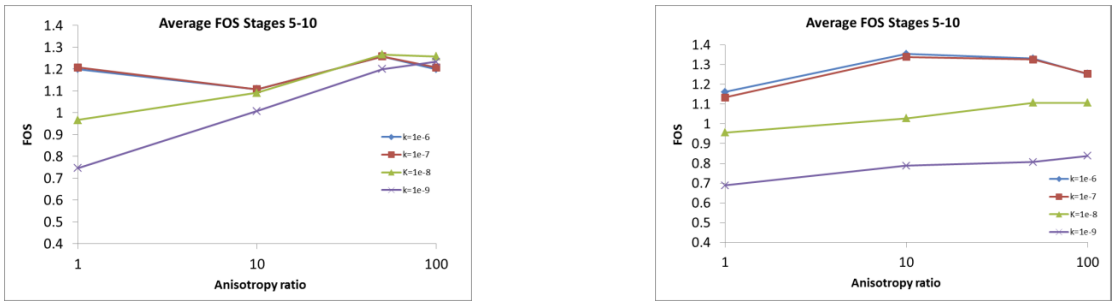

$\alpha = k_h / k_v$ $\beta = k_v / k_h$

Figure 8 - Average FOS for (a) increasing horizontal (b) increasing vertical anisotropy

4. CONCLUSIONS

This study is focused on the significance of anisotropy in rock mass permeability, and the practical consequences of it in the behavior of large open mines. In large open pit mines, increasing ratio of horizontal permeability accelerates the pore pressure dissipation due to horizontal drainage through the slope face. In most cases, this condition leads to a decrease in pore pressures at the lower part of slopes above the toe. At elevations below the toe, however, both pressures and pressure gradients significantly increase. At the same time, increasing ratio of horizontal permeability enforces a more horizontal flow path, and slows the desaturation process. Therefore, as the anisotropy ratio increases, presence of water with low pressures at the upper part of slopes (compared to isotropic models) must be expected. However, the elevated pressures at the top of the slope do not affect the stability significantly, as failure often initiates at the lower part of the model. When horizontal permeability of rock masses is greater than the vertical component, the following must be taken into consideration.

- Location and profile of the phreatic surface is not indicative of pore pressures profile and distribution. In particular, assuming a hydrostatic pore pressure distribution below the phreatic surface is incorrect.
- The artesian condition that may be observed for wells in a depth below the toe cannot indicate the pore pressure distribution within the slope. In fact, while increasing anisotropy ratio increases the pressure below the toe, it accelerates pressure dissipation within the slope.
- When the host rock has a low permeability (k_0 is small), horizontal anisotropy is advantageous in increasing FOS values. It accelerates the depressurization by providing horizontal drainage path to the slope face.
- When the host rock has a high permeability (k_0 is large), horizontal anisotropy may not have a significant effect on FOS values for the simulation time scales considered in this paper. In this case, the combined effect of horizontal and vertical flow that occurs in isotropic models can outweigh the accelerated one-directional flow that occurs in the highly anisotropic models.

Increasing vertical permeability helps the desaturation process and accelerates draw-down of phreatic surface. However, if the contrast between the vertical and horizontal permeability is high, it can lead to an increase in pore pressure distribution behind the slope. In most cases, increasing vertical permeability leads to a slight increase in FOS values. In general, it can be postulated that response of LOP models is less sensitive to the ratio of increasing vertical anisotropy compared to increasing horizontal anisotropy.

The results of this study emphasize the importance of permeability anisotropy on the depressurization in LOP models. Compared to problems with isotropic permeability, anisotropy in permeability leads to a significantly different regime of pore pressure dissipation depending on ratio of anisotropy and simulation time relative to the magnitude of permeability. As a result, variation in the values of FOS and the location and depth of failure surface must be expected.

5. ACKNOWLEDGEMENTS

The work described here was performed as part of the LOP (Large Open Pit project, administered by Dr. John Read of CSIRO Brisbane).Sponsors of this project are thanked for their support.

6. REFERENCES

BRAWNER, C.O. (1982) “Control of Groundwater Flow in Surface Mining,” Int. J. Mine Water, 1-16.

Schlumberger Water Services. (2010) “Depressurization of Pit Slopes in Fractured Rock,” Report to LOP Group, CSIRO, (UK) Ltd., United Kingdom.

DOMENICO, P.A., and SCHWARTZ, F.W., (1998) Physical and Chemical Hydrology, Second Edition. New York: Wiley.

Itasca Consulting Group, Inc. (2008) FLAC (Fast Lagrangian Analysis of Continua), Version 6.0. Minneapolis: Itasca.

LIAKOPOULOS, A.C., (1965) “Darcy’s Coefficient of Permeability as Symmetric Tensor of Second Rank,” Int. Assoc. Scientific Hydrology, 10(3), 41- 48.

LORIG, L.J., (2009) “Challenges in Current Slope Stability Analysis Methods,” in Slope Stability 2009 (Universidad de Los Andes, Santiago, Chile, November 2009).

Modeling Depth of Failure using Brittle Mohr-Coulomb Failure Model

Nader Golchinfar
Geomechanics Research Centre, MIRARCO – Mining Innovation
Ming Cai
Bharti School of Engineering, Laurentian University

ABSTRACT**:** The V-shaped breakout zones around excavation boundary have been captured by a variety of numerical methods such as FEM and DEM methods and failure criteria such as linear Mohr-Coulomb and non-linear Hoek-Brown failure criteria. Diederichs (2007) used Hoek-Brown parameters in his spalling parameter approach; however, it is convenient to use the Mohr-Coulomb failure criterion in numerical modeling because the material parameters can easily be determined from triaxial tests. It is shown in this study that when peak and residual strength parameters as well as dilation angle are properly defined, the brittle Mohr-Coulomb failure criterion can be used to model depth of failure near underground excavations satisfactorily.

1. INTRODUCTION

From a ground control perspective, it is of great importance to precisely predict the depth of failure around the underground openings in order to design a safe and cost-effective rock support system. Several numerical approaches have been used to simulate the behavior of brittle rocks around underground openings. These numerical approaches can be divided into two broad classes: (1) continuum and (2) discontinuum methods. The continuum approach, which is utilized in this paper, relies on specific constitutive models to determine the distribution of failure zone. In recent years, the cohesion-weakening and friction-strengthening (CWFS) model was applied to simulate brittle rock behavior satisfactorily (Hajiabdolmajid et al., 2002). As an alternative, elastic-brittle constitute model using Hoek-Brown parameters has been used to simulate brittle rock failure more recently (Diederichs, 2007). Although the equivalent Mohr-Coulomb strength parameters can also be obtained using linear regression based on the Hoek-Brown failure envelopes, we found that the derived Mohr-Coulomb strength parameters, when used in an elastic-brittle-plastic analysis, could not capture the URL (Underground Research Laboratory) Mine-by tunnel notch breakout satisfactorily.

This issue is investigated in this study. Firstly, a summary of previous numerical models for the study of rock failure related to excavations is presented. A brief review of peak and residual strength envelops of brittle rocks is presented. Following a parametric study and verification using the Mine-by tunnel case history, we suggest that elastic-brittle Mohr-Coulomb failure criterion can be used to simulate depth of failure around excavation boundaries adequately.

2. SIMULATION OF BRITTLE FAILURE USING CONTINUUM MODELS

To model the failure of brittle hard rocks, Martin (1997), Hajiabdolmajid et al. (2002), Diederichs (2007) and others proposed several methods primarily based on field observation at the Mine-by tunnel. The approaches were developed by calibrating the yielded elements against the depth, extent and shape of the brittle failures observed in-situ. In this section the most commonly adopted approaches that were successful in predicting the failure zones are reviewed.

2.1 Plastic Strain Dependent Cohesion-Weakening Frictional-Strengthening Model

Martin (1997) demonstrated that brittle rock failure is a gradual process from cohesive strength weakening by tensile cracking at the early stages of loading, and mobilization of frictional strength component when the cohesional strength component is significantly reduced. Therefore, a constitutive law that captures the cohesion loss and frictional strength mobilization should be able to simulate the brittle rock failure process realistically. Hajiabdolmajid et al. (2002) adopted a plastic strain dependent CWFS model in FLAC where the residual cohesion and friction angle were assigned to the model as a function of plastic shear strain as shown in the insert in Figure 1. Using the CWFS model, Hajiabdolmajid et al. (2002) were able to simulate the V-shaped notches observed at the Mine-by tunnel (Figure 1).

The CWFS model shows a strain-softening behavior post peak. However, under low confinement conditions, the transition from peak strength to residual strength for hard rocks occurs in a sudden and brittle manner, as shown by Curve-A in Figure 2. Only when the confinement (σ_3) increases sufficiently can the brittle rocks exhibit strain-softening behavior post peak (e.g., Curves-C&D in Figure 2).

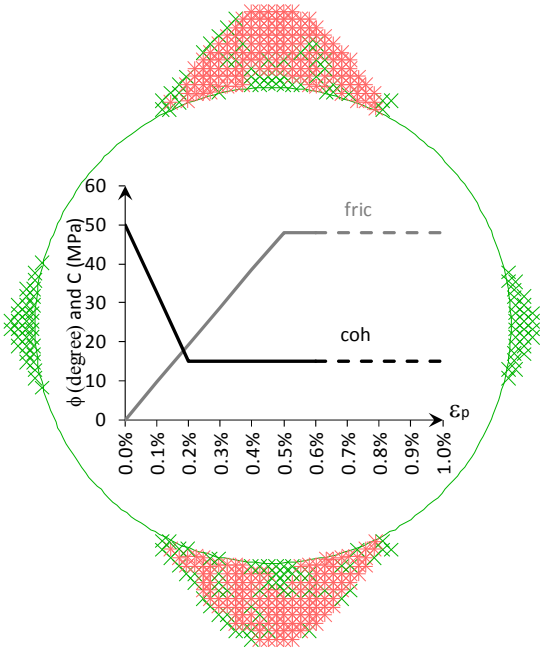

Figure 1 - Prediction of the V-shaped notch by the CWFS model in FLAC (modified from Hajiabdolmajid et al., 2002)

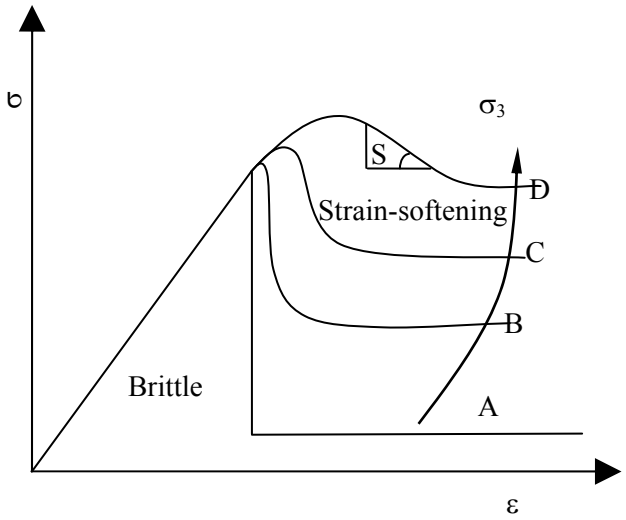

Figure 2 - Influence of confinement on post-peak behavior of brittle rocks. S-softening parameter

2.2 Spalling Failure Criterion

Diederichs (2007) proposed a set of spalling failure parameters to simulate brittle rock failure that eventually leads to the formation of V-shaped notches observed at the Mine-by tunnel. The simulation was conducted using Phase2 with the Hoek-Brown failure criterion defined by two different envelopes for the peak and residual strengths as shown in Figure 3a. As shown in Figure 3b, the spall extent is accurately modeled using the spalling failure parameters.

In this approach, which is an alternative for the plastic strain dependent CWFS model, the initial yield strength (peak strength) is defined by UCS (unconfined compressive strength) = 235 MPa, m = 1, s = 0.033, a = 0.25 (m, s, and a are Hoek-Brown failure criterion parameters), and the strength envelope is equivalent to the crack initiation threshold in-situ. The subsequent residual strength envelope is defined

by a low *s* value and a high *m* value (as well as a high *a* value). When realized in Phase2, this model shows the elastic-brittle plastic behavior (e.g., Curve-A in Figure 2 at low confinement). It is interesting to observe that the elastic-brittle plastic model is considered by Hajiabdolmajid et al. (2002) as unsuitable for modeling brittle rock breakout failure observed at the Mine-by tunnel.

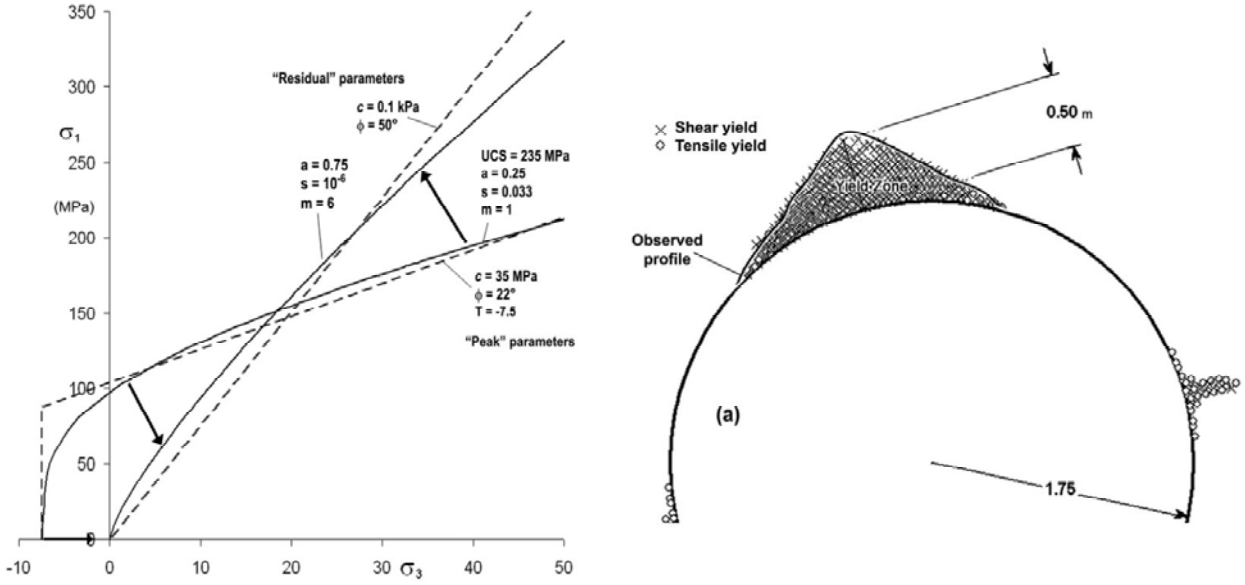

Figure 3 - (a) Strength envelopes defined by spalling failure parameters; (b) V-shaped notch simulated using the spalling failure parameters (Diederichs, 2007)

2.3 Plastic Strain Independent (Instantaneous) Cohesion-Weakening Frictional-Strengthening Model

Edelbro (2010) utilized an approach in Phase2 which was similar to the spalling failure parameter approach proposed by Diederichs (2007) to simulate brittle rock failure. Instead of Hoek-Brown strength parameters, Mohr-Coulomb strength parameters were used in the simulation. Edelbro (2010) claimed that the maximum shear strain obtained from this modeling approach provided a reliable indicator for predicting compression failure-induced fallouts. Most people use yielding zone to represent the rock failure (fallout) around excavations. However, it was found that the region of yielded elements (either in tension or shear) over predicted the depth of failure in this approach.

3. NUMERICAL MODELING OF DEPTH OF FAILURE USING BRITTLE MOHR-COULOMB MODEL

In this study, the brittle Mohr-Coulomb strength parameters are used to simulate depth of failure in underground excavations. The approach is demonstrated using the well-documented Mine-by tunnel cause history.

FLAC and Phase2 are based on explicit finite difference formulation and implicit finite element formulation, respectively, but FLAC can follow the physical process of stress redistribution automatically. It is shown that for elastic problems both codes provide the same results but for stress-path dependent problems they may provide different yielding zone distributions depending on the excavation

method employed (Cai, 2008). Near the tunnel boundary where dynamic unloading induced tensile stress is high, more rocks will fail in tension than in compression, and this will require a tool like FLAC which is capable of handling dynamic loading by default. Hence, FLAC is chosen in this study. Another reason for selecting FLAC is that it has a built-in programming language FISH, which allows the user to manipulate the model easily.

As mentioned above, an elastic-brittle plastic material model requires simultaneous reduction in cohesion and increase in friction angle once the rock fails. To realize brittle failure in FLAC, a very small value for critical plastic strain (at the point of reaching residual strength) equaling to 10^{-4} is chosen. To study the influence of different strength parameters and to indicate which combination of strength parameters will best capture the observed breakouts at the Mine-by tunnel, a parametric study is conducted. It is well-known that micro-cracks can affect the deformation properties of rocks (Martin and Stimpson, 1994). For simplicity, Young's modulus and Poisson's ratio are kept constant at 60 GPa and 0.25, respectively. The horizontal, vertical, and tunnel axis parallel in-situ stress components are σ_x = 60 MPa, σ_y = 11 MPa, σ_z = 45 MPa, respectively (Martin, 1997). Because tensile strength has no influence on the initiation of compression failure, variation of this parameter has no significant effect on depth of failure in the compression zones. However, to minimize the tensile yielding zone around opening, a tensile strength of 18 MPa is used in the simulation. When the rock fails in tension, its residual tensile strength is reduced to zero.

3.1 Peak Cohesion and Friction Angle

The peak strength is the maximum stress that a rock can sustain at a given stress state. Peak strength is normally obtained from cylindrical test samples at different confinements. When the test data are represented by a linear line, the parameters (c and ϕ) for the Mohr-Coulomb failure criterion defined in Eq.(1) can be determined.

$$\tau = c + \sigma_n tan\phi \quad (1)$$

c : cohesion (MPa)
σ_n : normal stress (MPa)
ϕ :friction angle (degree)

The peak friction angle influences the results (especially on the zone of yielded elements) significantly (Edelbro, 2010). The peak friction angle for the plastic strain dependent CWFS model varies between 0° and 22° (e.g. Hajiabdolmajid et al. 2002; Corthesy and Leite 2008). The choice of this value is based on distribution of yielded element. For an elastic-brittle plastic material, a close to zero peak friction angle, as suggested by Hajiabdolmajid et al. (2002), will result in a wider and deeper failure zone. As can be seen from Eq.(1), an increase in peak friction angle while keeping cohesion constant results in higher rock strength. By keeping the residual failure envelope with parameters indicated in Table 1 and peak cohesion constant with a value of 60 MPa, we found that a peak friction angle of 10° simulate the depth of notch breakout well (Figure 5a). Increasing the friction angle beyond 20° with a peak cohesion of 60 MPa will result in an UCS value higher than the maximum stress given by $3\sigma_1 - \sigma_3 = 169\ MPa$.

To study the influence of peak cohesion on depth of failure, the peak friction angle is fixed at 10° and the residual strength parameters indicated in Table 1 are used. It is seen from Figure 5b that the peak cohesion has a large influence on the depth of failure. For the elastic-brittle plastic model, a peak cohesion of 60 MPa simulates the failure zone that best represents the notch shape in-situ. As can be seen from Figure 4, the peak UCS for the elastic-brittle model is 143 MPa. On the other hand, the peak UCSs for both the CWFS and the spalling parameter models were 100 MPa (Figure 3a and Figure 4).

Table 1 - Strength parameters for the strain-dependent CWFS model and the brittle Mohr-Coulomb model

		Peak	residual	ε_p^s	*tans*
fricition angle (ϕ)	~Brittle	10	50	0.01%	280,000
	Strain-softenin	0	48	0.50%	9,600
cohesion (MPa)	~Brittle	60	0.5	0.01%	450,000
	Strain-softenin	50	15	0.20%	17,500

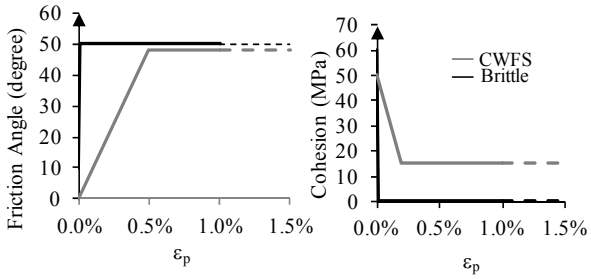

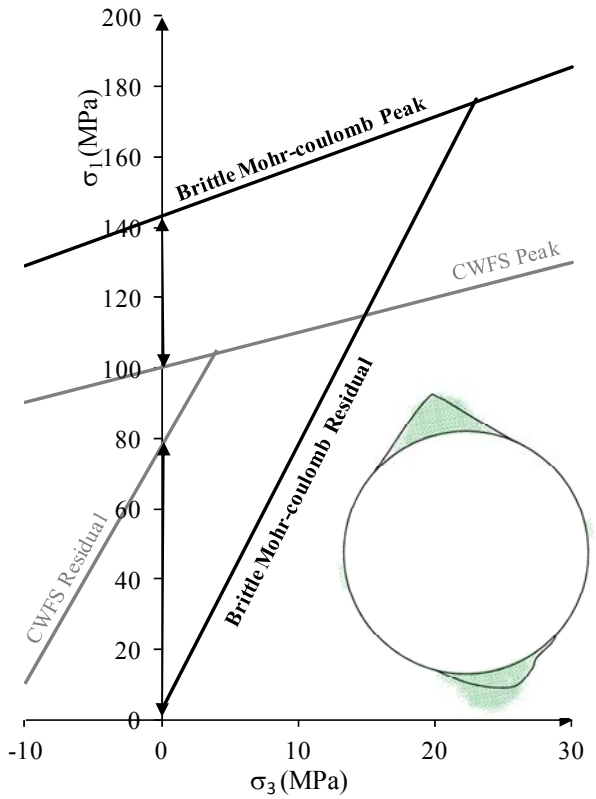

Figure 4 - Comparison of failure envelopes defined by the CWFS model and the elastic-brittle plastic model (failure zone obtained from elastic-brittle plastic model)

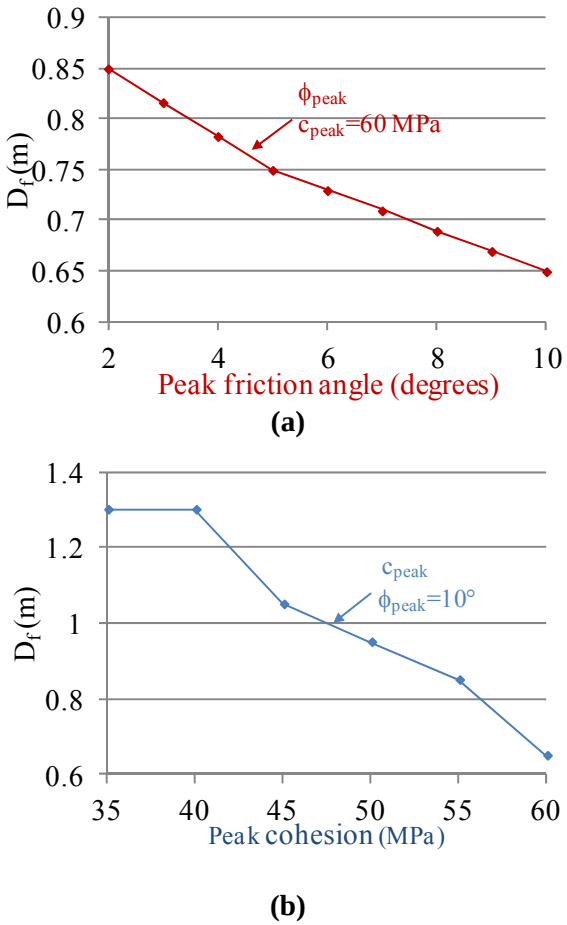

Figure 5 - Influence of peak friction angle (a) and peak cohesion (b) on depth of failure (D_f)

3.2 Residual Cohesion and Friction Angle

As the stress is increased, a rock will eventually reach the peak strength and then enter the post peak region. Figure 6 summarizes triaxial test data of Tailuko marble and Karelia granite, showing the peak

and residual strength envelopes. It is seen that both the peak and residual strength envelopes can be represented by linear Mohr-Coulomb failure criterion. A common feature of the residual strength envelopes for brittle rocks is that the residual cohesion is very small (0.5 MPa) and the residual friction angle is higher than the peak friction angle. For example, the peak and residual friction angles for the Tailuko marble are 26° and 41°, respectively. Other test data we analyzed show that the residual friction angles of hard rocks vary primarily between 40° and 55°.

Because no triaxial test data with well-defined residual strength on Lac du Bonnet granite are available, results from rocks with similar brittleness are used to determine the residual cohesion and friction angle in the numerical simulation. As shown in Table 1, the residual cohesion and friction angle that best simulate the Mine-by tunnel notch breakout are 0.5 MPa and 50°, respectively, for the elastic-brittle plastic model.

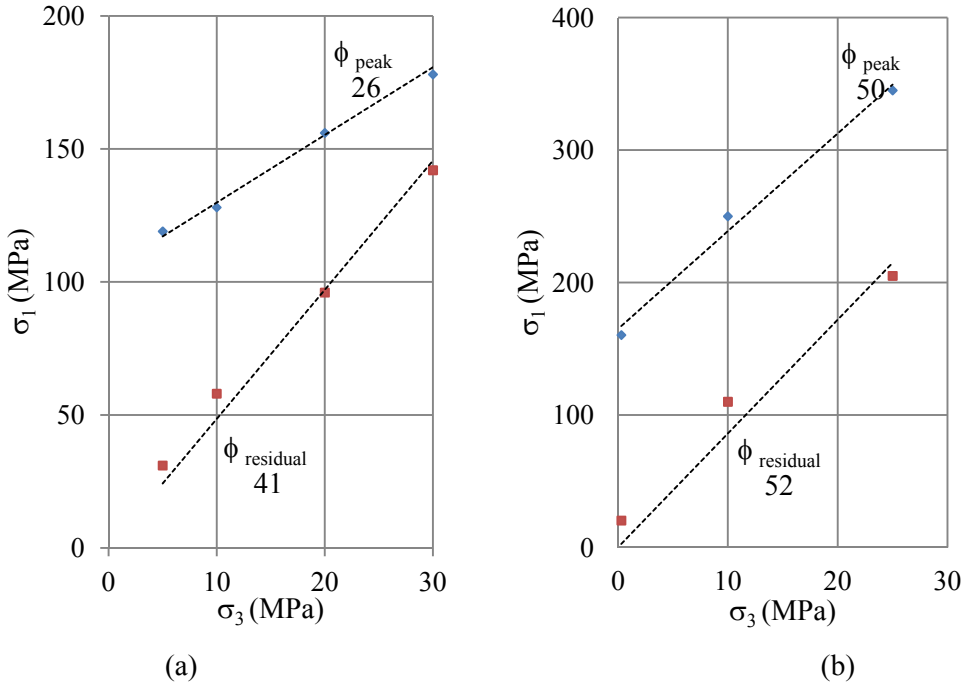

Figure 6 - Peak and residual Mohr-Coulomb failure envelopes for (a) Tailuko marble (Hsiao et al., 2011) and (b) Karelia granite (Stavrogin et al., 1982)

As mentioned above, cohesion strength needs to be reduced significantly before friction strength is mobilized. The residual cohesion of 15 MPa and friction angle of 48°, used by Hajiabdolmajid et al. (2002) in their CWFS model, leads to a residual uniaxial compression strength of 78 MPa. This residual uniaxial compression strength and the strength envelope, also illustrated in Figure 4, clearly are not in agreement with test data (Figure 6), all shows a close to zero residual UCS. In comparison, the residual uniaxial compression strength of the brittle Mohr-Coulomb model is 2.75 MPa. Figure 7 presents the results of influence of residual cohesion and friction angle on the depth of failure. Residual friction or cohesion is varied while keeping peak failure envelope constant with the parameters defined in Table 1. As the residual cohesion or friction angle increases, the depth of failure decreases significantly. This is contradictory to the conclusion by Edlebro (2010), who stated that residual cohesion has less impact on the depth of failure than the peak cohesion.

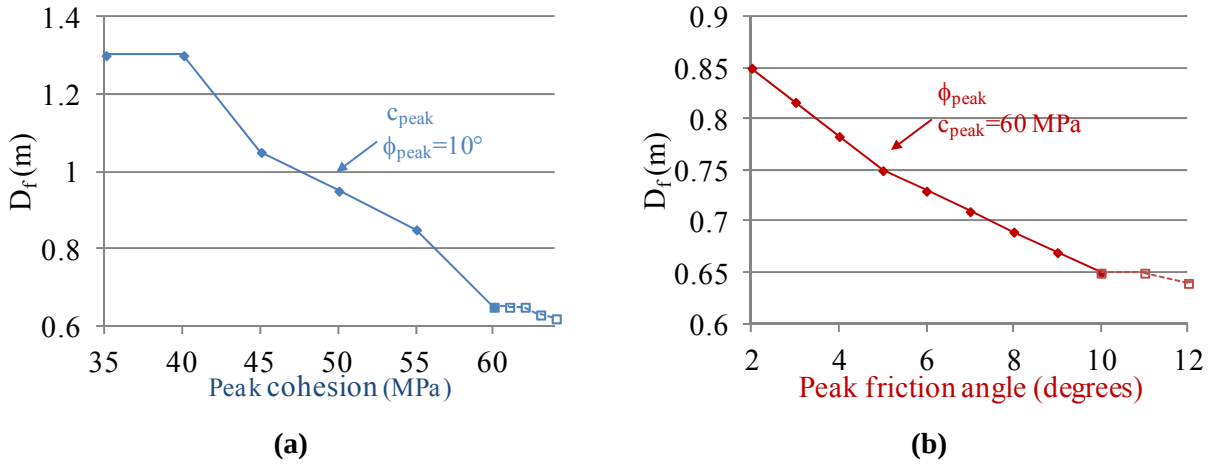

Figure 7 - Influence of residual cohesion (a) and friction angle (b) on depth of failure

3.3 Dilation Angle

Dilation angle is often used as a measure of the volume increase in a material during shearing. In continuum mechanics modeling, dilation angle for rocks is small and it should be less than the friction angle according plasticity theory (Vermeer and De Borst, 1984; Zhao and Cai, 2010). A higher dilation angle leads to higher wall deformation and hence rock load. Using the brittle Mohr-Coulomb parameters with zero dilation will result in non-V-shaped failure around opening (Figure 8). To simulate the notch breakout correctly, the effect of rock dilation is considered. Results presented in Figure 8 are obtained using the brittle Mohr-Coulomb parameters from Table 1 with different dilation angles and a tensile strength of 18 MPa. It is seen that when the dilation angles are small, failure zones tend to propagate horizontally. When the dilation angle is greater than 20° (lower than $\phi_{residual}$ = 50°), the V-shaped breakouts can be captured reasonably.

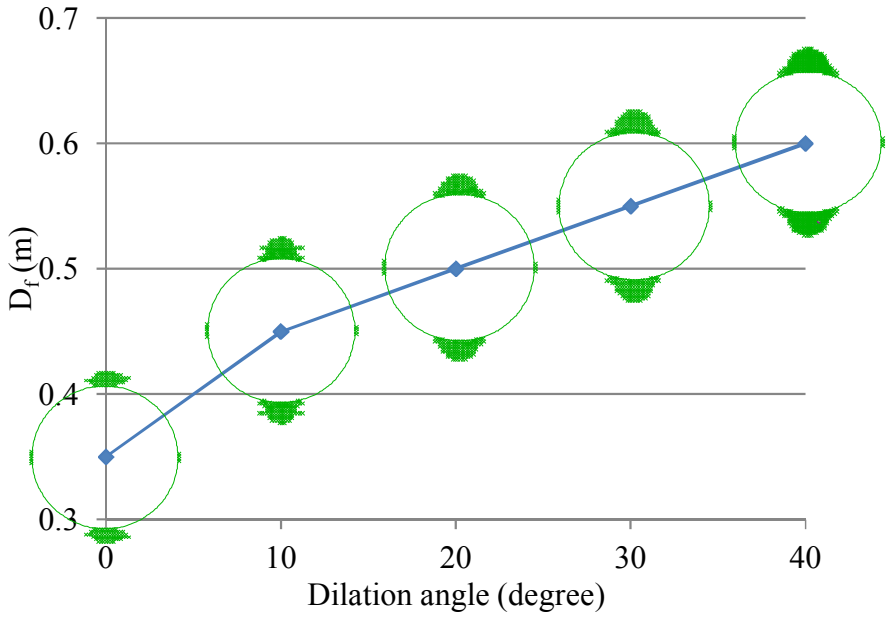

Figure 8 - Influence of dilation angle on brittle rock failure

4. CONCLUSIONS

In the present study, the brittle Mohr-Coulomb model is used to simulate the depth of failure around excavation boundaries. It is found that when the peak and residual strength parameters as well as the dilation angle are properly determined, this model can capture brittle rock failure satisfactorily.

The advantage of using the brittle Mohr-Coulomb model is that the strength parameters (peak and residual cohesions and friction angles) can be obtained easily from lab test. For plastic strain dependent CWFS models, it is very challenging to determine the characteristic plastic strains. In addition, rock failure is always initiated near excavation boundary where the confinement is small or zero and the brittle Mohr-Coulomb model captures the physics of rock failure under low confinement underground.

5. ACKNOWLEDGEMENT

Financial supports from NSERC, Laurentian University, CEMI, MIRARCO, LKAB, VALE, Xstrata Nickel, and the William Shaver Masters Scholarship in Mining Health and Safety are greatly appreciated.

6. REFERENCES

CAI, M., 2008. Influence of stress path on tunnel excavation response – Numerical tool selection and modeling strategy. *Tunnelling and Underground Space Technology*, 23(6), p.618–628.

CORTHESY, R. and LEITE, M., 2008. A strain-softening numerical model of core discing and damage. *International Journal of Rock Mechanics and Mining Sciences*, 45(3), p.329–350.

DIEDERICHS, M.S., 2007. Mechanistic interpretation and practical application of damage and spalling prediction criteria for deep tunnelling. *Canadian Geotechnical Journal*, 44(9), p.1082-116.

EDELBRO, C., 2010. Different Approaches for Simulating Brittle Failure in Two Hard Rock Mass Cases: A Parametric Study. *Rock Mechanics and Rock Engineering*, 43(2), p.151-65.

HAJIABDOLMAJID, V., KAISER, P. and MARTIN, C., 2002. Modelling brittle failure of rock. *International Journal of Rock Mechanics & Mining Sciences*, 39(6), p.731-41.

HSIAO, F.-Y., WANG, C.-L. and SHAO, H.-J., 2011. Mechanical parameters estimation and tunnel deformation study for brittle rock under high overburden condition. *Rock and soil mechanics*, 32(S2), p.109-14.

MARTIN, C.D., 1993. The strength of massive Lac du Bonnet granite around underground openings. PHD thesis: Univeristy of Alberta.

MARTIN, C.D., 1997. Seventeenth Canadian Geotechnical Colloquium: The effect of cohesion loss and stress path on brittle rock strength. *Canadian Geotechnical Journal*, 34(5), p.698-725.

MARTIN, C.D. and STIMPSON, B., 1994. The effect of sample disturbance on labratory properties of lac du bonnet granite. *Canadian Geotechnical Journal*, 5(31), p.692-702.

STAVROGIN, A.N., TARASOV, B.G., SHIRKES, O.A. and PEVZNER, E.D., 1982. Strength and deformation of rocks before and after the breakdown point. *Journal of Mining Science*, 17(6), p.487-93.

VERMEER, P. and DE BORST, R., 1984. Non-associated plasticity for soils, concrete and rock. *Delft University of Technology*, 3(29), p.1–64.

WANG, S., ZHENG, H., LI, C. and GE, X., 2011. A finite element implementation of strain-softening rock mass. *International Journal of Rock Mechanics & Mining Sciences*, (48), p.67–76.

ZHAO, X. and CAI, M., 2010. A mobilized dilation angle model for rocks. *International Journal of Rock Mechanics and Mining sciences*, 47(3), p.368-84.

Influence of Rock Mass Foliation on Impact-Induced Damage of an Ore Pass Wall

Kamran Esmaieli
Lassonde Institute of Mining, University of Toronto
John Hadjigeorgiou
Lassonde Institute of Mining, University of Toronto

ABSTRACT: This paper investigates the behavior of ore pass walls under impact loads caused by material transiting through an ore pass. In particular it considers the influence of foliation in the rock mass surrounding an ore pass as both a triggering and accentuating cause of degradation. Based on empirical observations in several underground mines a numerical experiment was designed to understand the influence of rock mass foliation on impact-induced damage on ore pass walls. The distinct element method, and in particular the Particle Flow Code (PFC2D) was used to simulate three different rock masses surrounding an ore pass. Each simulated rock mass has similar properties but was defined by distinct dominant foliation (70^o, 80^o, 90^o) along the foot wall. The numerical experiments investigated different scenarios whereby the walls were loaded by a projected rock fragment striking the foliated walls at a constant impact angle and velocity. The damage inflicted by the projectile rock fragment, on the foliated rock mass, was quantified using the number of impact-induced micro-cracks initiated on the ore pass wall. The results of the numerical analysis indicated that the presence of foliation resulted in greater damage zones in the surrounding rock mass. In addition, the extent of impact-induced damage to the ore pass wall increased as the angle of interception between the ore pass wall and the rock mass foliations decreases. This is in agreement with qualitative field observations.

1. INTRODUCTION

The design of ore pass systems requires important trade-offs between several options. It is necessary to consider the impact of ore pass dimensions, ensuring free flow and minimizing wall damage. An important consideration is the degradation of ore pass walls as a result of material dumped into an ore pass through a finger.

The importance of driving the ore passes against the foliation or strata dip has been recognized by (Stacey and Swart, 1997). They recommended that ore passes are constructed to intersect foliation planes as close to perpendicular as possible. Based on experience from South African mines, (Joughin and Stacey, 2005) demonstrated the relationship between the extent of ore pass degradation and the angle between the ore pass and strata for various qualities of rock mass. According to Joughin and Stacey 2005, when the angle between the ore pass and rock mass strata approaches 90°, in moderate to good quality rock mass, the ore passes become more stable. This was also reported by (Hadjigeorgiou et al., 2005) in a study of several ore pass systems in Canadian underground mines. Figure 1 illustrates this principle by referring to two actual case studies of ore passes constructed in a rock mass characterized by steep bedding. It can be seen that in case (a), in which the ore pass was inclined against the bedding, the ore pass was stable with no sign of degradation. In case (b), the ore pass was driven sub-parallel to the bedding planes and the ore pass was subject to wall instability and its cross cut area expanded considerably along its length. The severity of the expansion was confirmed by cavity monitoring surveys and the mine experienced significant production loss.

A further example of the importance of driving ore passes against the foliation was presented by (Hadjigeorgiou et al., 2008). The 1000SRF ore pass system at Brunswick mine comprised of two long sections. The upper section of the ore pass, which was constructed sub-parallel to the host rock foliation

(Quartz Augen Schist), has been significantly expanded along the upper section. The lower part of the ore pass, which was developed in a more favorable orientation, maintained its integrity.

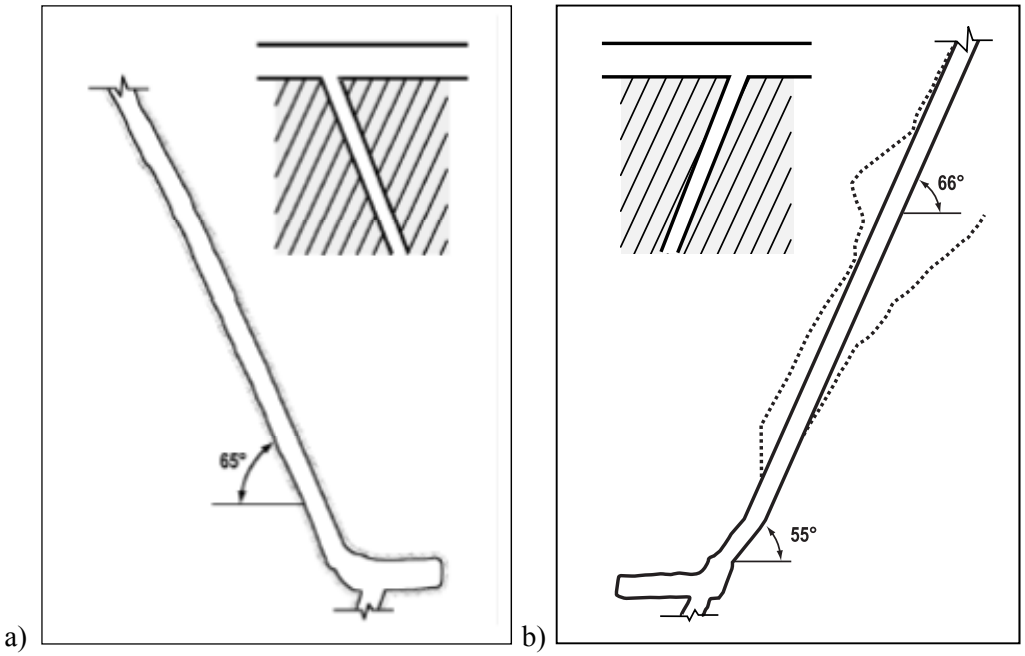

Figure 1 - Case studies of ore pass development with respect to rock bedding: a) favorable orientation; b) poor orientation (Hadjigeorgiou et al., 2005)

There are several numerical tools that can investigate the influence of structural defects on the stability of ore pass systems, including boundary element models that employ ubiquitous joints. These models however cannot simulate the impact of material transfer in an ore pass. The flow of material within an ore pass can be a source of scouring or damage on the walls. This is more pronounced in ore passes constructed in foliated rocks. The phenomenon can be best addressed by linking stress analysis models with models that are capable to simulate material flow.

In establishing the longevity of ore pass systems, it is often necessary to quantify the results of the interaction of material flow impact and rock mass foliation on ore pass wall degradation. The present paper shows the results of a series of numerical experiments that investigate the damage due to the impact of material acting on ore pass walls in a foliated rock mass. To these purposes we employed the distinct element method (DEM), and in particular the Particle Flow Code (PFC2D-V4.0) developed by Itasca (2008). In the constructed models a projectile particle was thrown against a foliated rock mass, and the extent of damage zone inflicted by the projectile particle on the rock mass block was quantified.

2. CONSTRUCTION OF THE NUMERICAL MODELS

In order to investigate the response of a foliated ore pass wall to rock fragment impact, a series of numerical experiments were designed using PFC2D. In these numerical experiments, the rock mass along an ore pass wall was simulated by a bonded particle model. This included the construction of a block of rock mass of 5 m x 5 m along an ore pass wall, represented by an assembly of circular particles bonded together at their contact points, Figure 2. The model was composed of 55960 circular particles with a minimum diameter of 0.86 cm. The ratio of maximum versus minimum particle size was fixed at 1.66 in order to generate a uniform particle size distribution in the model. The micro-mechanical properties listed in Table 1 were assigned to the particles and bonds in the model. These micro-mechanical properties

resulted in the macro-mechanical properties of the intact rock summarized in Table 2. In order to depict the damage caused by impact on the ore pass wall, micro mechanical properties were selected which would result in intact rock with a moderate compressive strength, (UCS = 103 MPa), for the rock block along the ore pass wall.

Table 1 - Micro-mechanical properties employed for generation of the 2D bonded particle model

Particle micro-mechanical parameter	Value	Bond micro-mechanical parameter	Value
Particle density (kg/m^3)	2800	Parallel bond modulus (GPa)	53
Particle contact modulus (GPa)	53	Bond normal/shear stiffness	2
Particle normal/shear stiffness	2	Bond normal and shear strength (MPa)	75
Particle friction coefficient	0.4	Bond strength standard deviation (MPa)	20

Table 2 - Macro-mechanical properties of the 2D bonded particle model

Property	Value
UCS (MPa)	103
Elastic Modulus (GPa)	65
Poisson Ratio	0.26

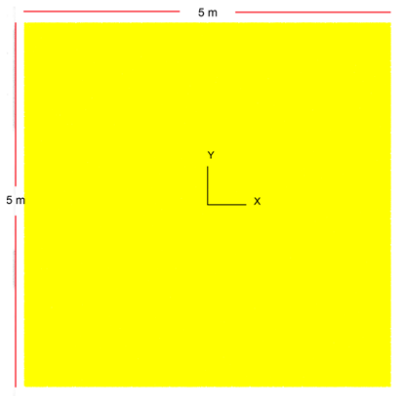

Figure 2 - A 5m x 5 m bonded particle model represents a block of rock along an ore pass wall

In order to examine the influence of foliation, three models with foliation angles of 60^o, 90^o and 120^o were generated using the bonded particle model. The normal spacing between the foliation planes was fixed at 0.2 m. The models are presented in Figure 3. To simulate the mechanical properties of foliation planes, the smooth joint function was employed. Parallel bonds along the foliation planes were deleted and both the normal and shear stiffness of particles located along the foliation planes were modified to

1.3 x 10^{13} N/m^3. A coefficient of friction of 0.3 was assigned to the particles adjacent to the foliation planes. The applied micro-mechanical properties have resulted in macro-properties of zero cohesion and an angle of friction of 30° for the foliation planes.

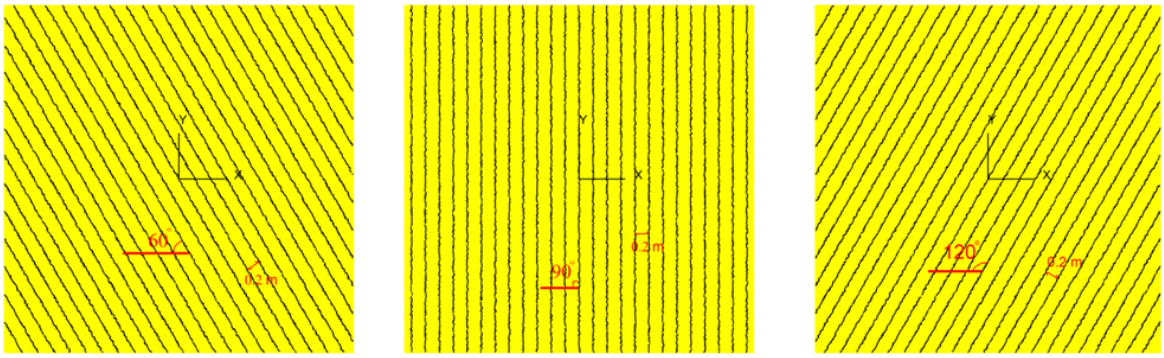

Figure 3 - Foliated rock mass models with foliation angles of a) 60°, b) 90° and c) 120°

3. IMPACT INDUCED DAMAGE ON ORE PASS WALLS

Once the foliated rock mass models were generated, the desired ore pass inclinations were simulated by deleting the particles along the ore pass wall. In order to investigate the influence of foliation planes, on the impact induced damage of a projectile particle, an ore pass inclination of 80° was simulated in the three foliated rock mass models. A projectile rock fragment of 0.8 m in diameter was generated to the right of the ore pass walls (see Figure 4) . The mechanical properties listed in Table 1 were assigned to the projectile particle. The projectile particle was thrown against the foliated ore pass walls at an impact angle of 60° and an impact velocity of 22.5 m/s. These values were selected based on previous simulation of material flow in ore pass systems, (Esmaieli and Hadjigeorgiou, 2011).

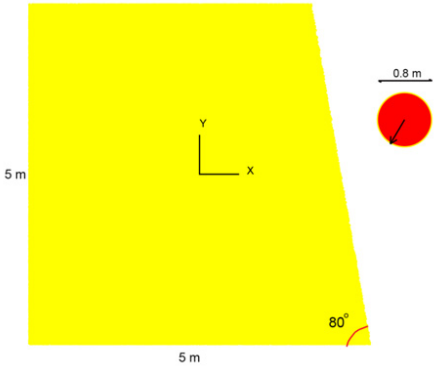

Figure 4 - A projectile particle impacting the 80° inclined ore pass

The collision of the projectile particle with the ore pass walls results in the creation of micro cracks. In this work, damage was defined as the appearance and growth of cracks induced by particle impact loading. This is one of the definitions proposed by Kachanov (1986). The shear and tension cracks were generated on the ore pass walls and inside of the rock mass.

The inflicted damage by the rock fragment on the three foliated rock masses is presented in Figure 5, where it is also compared to damage inflicted on an ore pass wall in the absence of defects. A close-up of

the zone of interest is presented to the right of the models. It was observed that the majority of the inter-particle bonds fail in tension. In all illustrations in this paper, tension cracks are indicated in blue, while shear cracks are identified in red.

The results of the numerical experiments demonstrated that the presence of foliation planes in the rock mass, along the ore pass wall increased the extent of impact induced damage. Furthermore, the number of micro-cracks developed in the foliated rock models, due to the rock fragment impact was raised significantly. This confirms that foliation accelerates the formation of impact-induced cracks. Moreover, the interaction of impact induced micro-cracks within the foliation planes in the rock mass resulted in the creation of small rock slabs. These slabs detached from the rock mass and fell or slid into the ore pass and result in an enlargement of the ore pass.

The numerical experiments demonstrated that the presence of foliation planes results in greater damage zones. The damage pattern generally forms as a layer of heavily crushed area around the impact point from which several radial (wing) cracks extend. Radial cracks develop perpendicular to the foliation.

The resulting damage zones on the ore pass wall, which contained 60^{o} foliation planes and inclined at angles of 90^{o}, 80^{o} and 70^{o} are presented in Figure 6 with a close up shown to the right of each model. It can be seen that, regardless of the ore pass inclination angle, radial cracks inflicted by the rock fragment impact are almost perpendicular to the foliation planes. The inclination angle of the ore pass wall has a small influence on the number of micro-cracks formed on the ore pass wall.

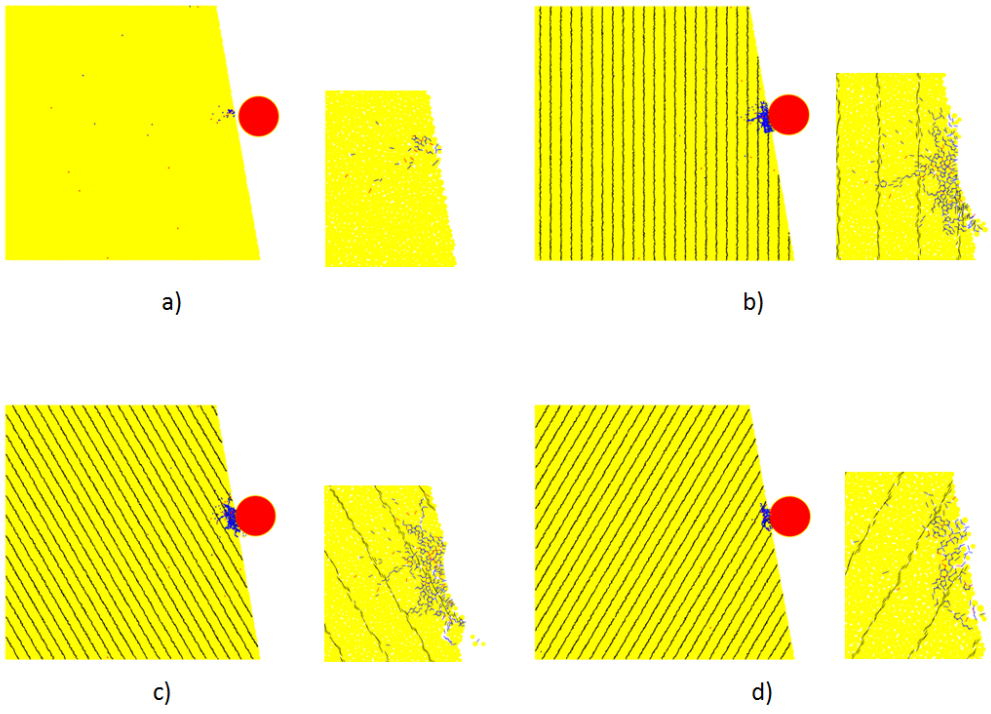

Figure 5 - Impact induced damage on the ore pass walls inclined at 80° and comprising, a) a solid rock mass, b) a 60° foliated rock mass, c) a 90° foliated rock mass and d) a 120° foliated rock mass

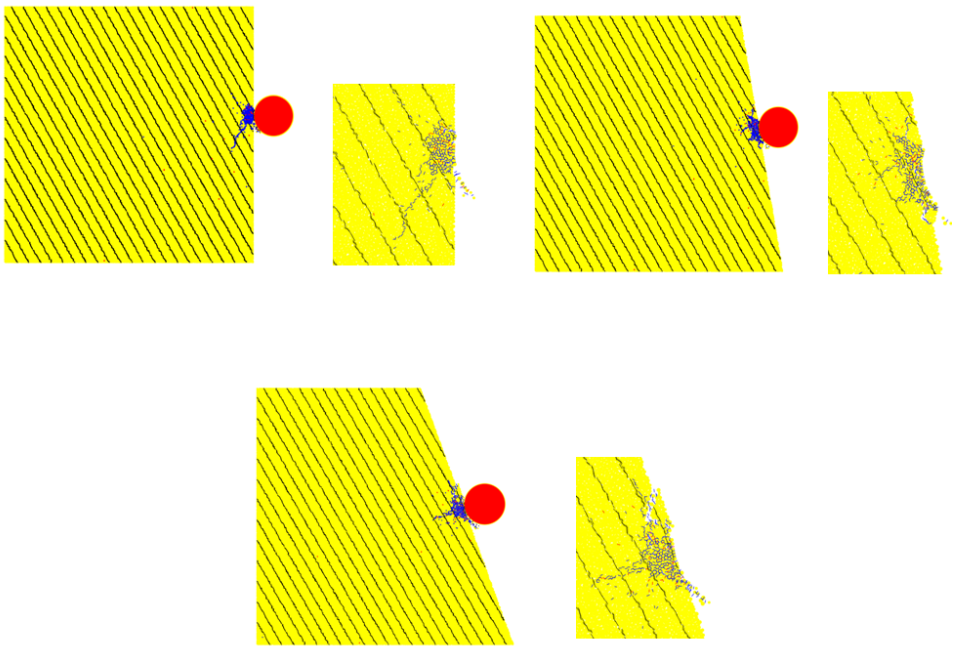

Figure 6 - The patterns of impact induced damage on the ore pass wall inclined at a) 90° b) 80° and c) 70° which contains foliation planes of 60°

The effect of repeated loads acting on ore pass walls investigated further. A projectile particle was thrown three times against each foliated ore pass wall. After each impact, the particles along the ore pass wall, which were fully detached from the foliated rock mass, were deleted. Figure 7 displays the evolution of impact induced damage on ore pass walls of varying foliation inclination. A close up view of models described in Figure 7, are shown in Figure 8. Both figures clearly show that the extent of damage to the ore pass wall with a foliation of 60^{o} is greater than of the ore pass wall with foliation planes of 120^{o}. In the first configuration, the ore pass wall is semi-parallel to the foliation planes, while in the last configuration, the ore pass intersected the foliation planes at an oblique angle.

At the mine scale, ore pass degradation is often expressed as the volume of rock that falls or is scoured from the ore pass walls. This is often reported as a function of the material volume transferred in the ore pass. For the purposes of this study the impact induced damage on the ore pass walls was quantified by assuming a unit thickness for the ore pass walls. The damage zone associated to each rock mass foliation was estimated from the models presented for each foliation configuration in Figure 8. This allowed the estimation of the volume of the damage zone for each foliated ore pass wall after three consecutive impact loads. The volume of the projectile particle was also estimated, assuming a unit thickness for the particle. Finally, the degradation rate for each ore pass wall foliation was estimated as the ratio of the volume of the rock detached from the foliated rock masses in damage zones and the total volume of the projectile particles contributing to the wall damage. Table 3 summarizes the degradation rate for the three foliated ore pass walls.

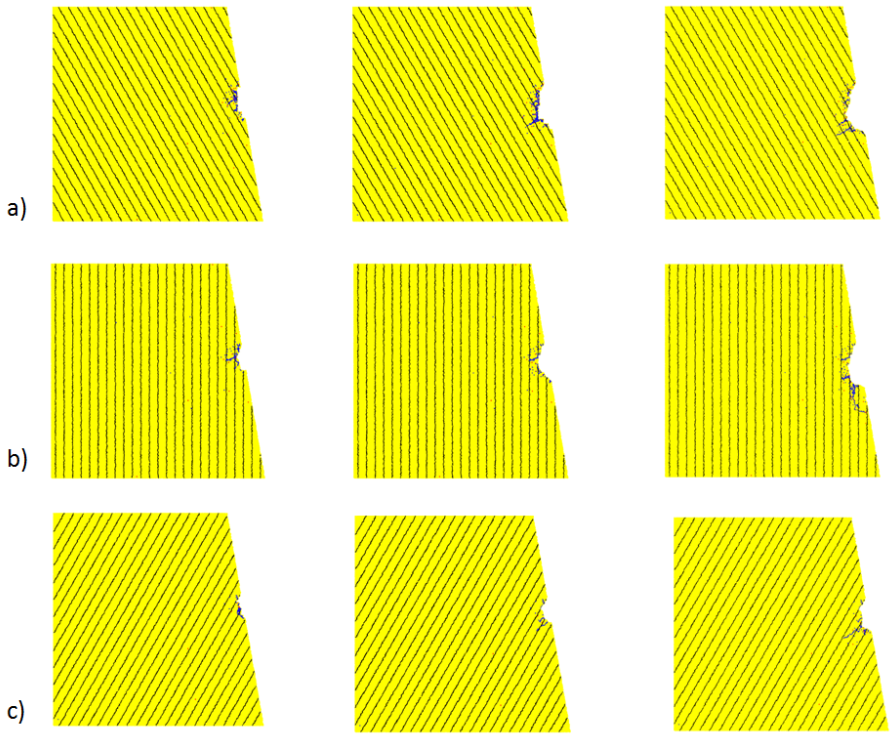

Figure 7 - Evolution of an impact induced damage zone in an ore pass wall with an inclination of 80° and containing foliation planes of a) 60°, b) 90° and c) 120°

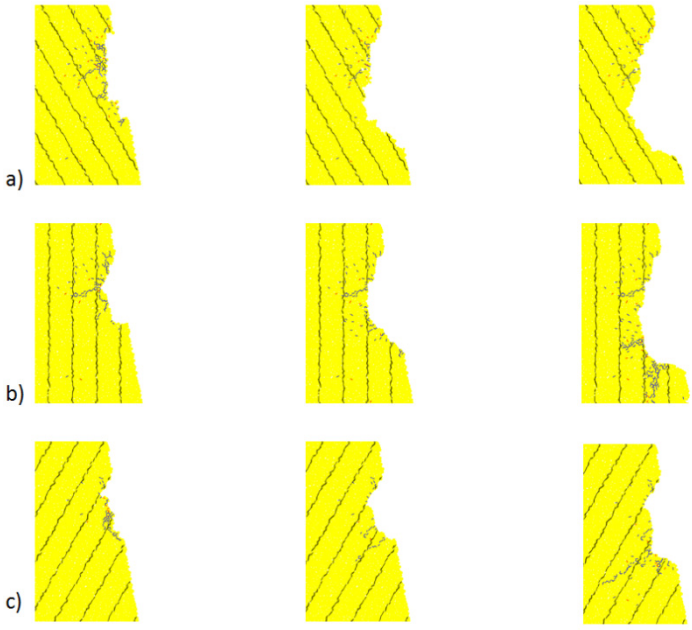

Figure 8 - A zoom view of the evolution of a damage zone along the ore pass wall with an inclination of 80° and containing foliation planes of a) 60°, b) 90° and c) 120°

The numerical experiments suggest that the degradation rate for an ore pass wall constructed sub-parallel to the foliation is almost three times greater than the ore pass inclined against the foliation. Although the estimated values for degradation rate may over or under estimate the real condition due to the 2D

simplification of modeling, nevertheless, this approach can provide useful information in comparing different design options.

Table 3 - Estimation of the ore pass wall degradation rate for different foliated rock mass

Rock mass foliation angle	Area of damage zone after three times of impact (m^2)	Volume of damage zone after three times of impact (m^3)	Total volume of the projectile particles (m^3)	Degradation rate (m^3/m^3)
60	0.25	0.25	1.5	0.16
90	0.15	0.15	1.5	0.10
120	0.09	0.09	1.5	0.06

The impact of rock fragments striking the foliated rock can also result in the delineation of rock wedges along the ore pass walls. These wedges can slide or fall into the ore pass if the foliation angle is favorable with respect to the ore pass wall. This type of collapse was simulated in a model with foliation planes of 60^o, in which a large rock wedge that was created on the ore pass wall slide into the ore pass and caused an expansion of the degradation zone, Figure 9.

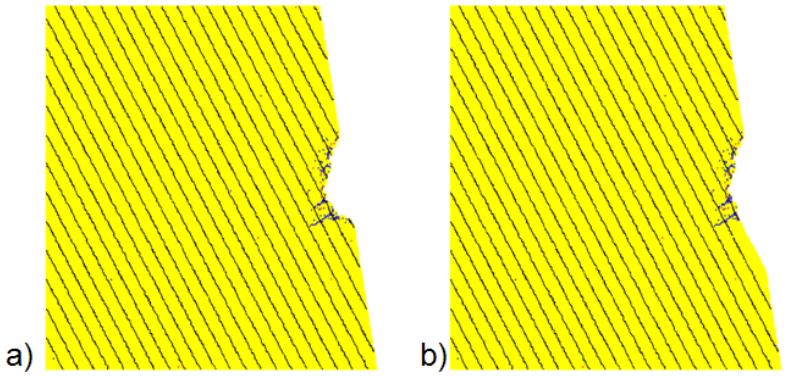

Figure 9 - a) Impact induced damage on the ore pass wall with foliation angle of 60°, b) the same model after sliding of a rock wedge into the ore pass

4. CONCLUSIONS

The distinct element method was used to investigate the influence of rock mass foliation on the degradation of ore pass walls by material impact. In the numerical experiments the material properties were kept constant during all simulations while the foliation angle, of the rock mass along the ore pass wall, and the ore pass inclination angle were allowed to vary. A single projectile particle was then thrown against the ore pass walls at a constant velocity and impact angle. The impact of the projectile particle with the ore pass wall resulted in wall damage in the form of tensile or shear micro-cracks. It is recognized that the actual loading mechanisms in ore passes are more complex. These experiments aimed to isolate specific elements of the mechanisms.

The results demonstrated that the presence of foliation planes on the ore pass wall can significantly increase the extent and depth of damage zone on the ore pass wall. In addition, the rate of ore pass wall degradation by material flow impact on an ore pass wall constructed sub-parallel to the rock mass foliation planes is considerably greater than the rate for an ore pass wall that intersects the foliation planes at an oblique angle. This conclusion validates the observation first suggested by (Stacey and Swart 1997) and subsequently corroborated by (Hadjigeorgiou et al., 2005) in Quebec underground mines and (Hadjigeorgiou et al., 2008) in Brunswick mine.

Although it has already been suggested by (Stacey and Swart, 1997) and by (Hadjigeorgiou et al., 2005) to that an ore pass section should be driven so as to intersect the foliation planes of a rock mass perpendicularly, the current work corroborated those qualitative recommendations. Furthermore the undertaken simulations demonstrated the pertinence of accounting for ore pass foliation.

5. ACKNOWLEDGEMENTS

The authors would like to acknowledge the support of the Natural Science and Engineering Research Council of Canada and Xstrata Zinc.

6. REFERENCES

ESMAIELI, K. and HADJIGEORGIOU J., 2011. Selecting ore pass-finger raise configurations in underground mines. Rock Mechanics and Rock Engineering, vol. 44, No. 3, p. 291-303.

HADJIGEORGIOU, J., ESMAIELI, K., and HARRISSON, R., 2008. Observations of Ore Pass System Performance at Brunswick Mine. CIM Bulletin, Vol. 3, No.5.

HADJIGEORGIOU, J., LESSARD, J.F. and MERCIER-LANGEVIN, F., 2005. Ore pass practice in Canadian mines. The Journal of South African Institute of Mining and Metallurgy. 105, p. 809-816.

Itasca, 2008. Particle Flow Code, PFC2D/3D-V.4.0, Itasca Consulting Group, Inc.

JOUGHIN, W.C. and STACEY, T.R., 2005. Risk Associated with Rockpasses in Deep-level Tabular Mines Based on Historical Pass Performance. The Journal of South African Institute of Mining and Metallurgy. 105, p. 795-802.

KACHANOV, L.M., 1986. Introduction to continuum damage mechanics. M. Nijhoff, Dordrecht, The Netherlands.

STACEY, T.R. and SWART, A.H., 1997. Investigation into Drawpoints, Tips Orepasses and Chutes. Vol. 1. Report to the Safety in Mines Research Advisory Committee, 112 pp.

Laboratory Investigation of Flow Through Fractured Sandstone

Jarret Thomson
Golder Associates,University of Saskatchewan
Chris Hawkes
University of Saskatchewan
Doug Milne
University of Saskatchewan
Stephen Klemmer
Cameco Corporation
Rashid Brashir
Golder Associates

ABSTRACT: An understanding of groundwater flow is essential for many aspects of mining. This is especially true for the process of shaft sinking through the sandstones of the Manitou Falls Group in the Athabasca Basin of northern Saskatchewan. Experience has shown that the hydraulic conductivities of these sandstones can be relatively high, especially in zones containing natural fractures. To develop a better understanding of the inflow potential into a shaft, a laboratory testing program was undertaken to investigate the hydraulic conductivity of fracture core samples from the Manitou Falls Group. This program involved the measurement of hydraulic conductivities under steady-state flow conditions, while cycling the effective confining pressure across a span that is representative of in-situ conditions. The change in fracture aperture was simultaneously recorded at each confining stress level. It was found that existing relationships relating aperture and flow did not accurately capture the behavior of the samples tested. The effects of fracture staining and infilling were also investigated, and were found to have a notable impact on the hydraulic conductivity.

1. INTRODUCTION

The Athabasca Basin is located in northern Saskatchewan, Canada (Figure 1), and is a major source of the world's uranium. The Manitou Falls Group (MFG) of the Athabasca Basin is a hydrogeologically complex set of clastic (predominantly sandstone) units that is unconformably underlain by crystalline basement rocks; the basin's uranium deposits are primarily found at this unconformity. The work presented in this paper focuses on the hydrogeological characterization of the MFG at Cameco Corporation's McArthur River operation.

Predicting and mitigating groundwater inflow is a priority during the process of shaft sinking. This presents a need to improve our understanding of the inflow potential that may be encountered when sinking a shaft in the MFG. The work presented in this paper is a component of a broader research project that was undertaken to study the hydrogeological properties of the sandstones of the MFG, so as to develop a stronger understanding of the conditions that may be encountered during shaft sinking. More specifically, the primary objective of research was to develop an understanding of the features that affect the inflow potential of the MFG sandstones. The broader research project included an analysis of borehole data (packer testing, geophysical logging), core logging and laboratory testing of fractured core samples. This paper provides a brief summary of the packer testing and core logging results, and focuses on the results of the laboratory testing program. A secondary objective of the research, which is specific to the laboratory testing, was to evaluate existing theoretical relationships between fracture aperture and hydraulic conductivity.

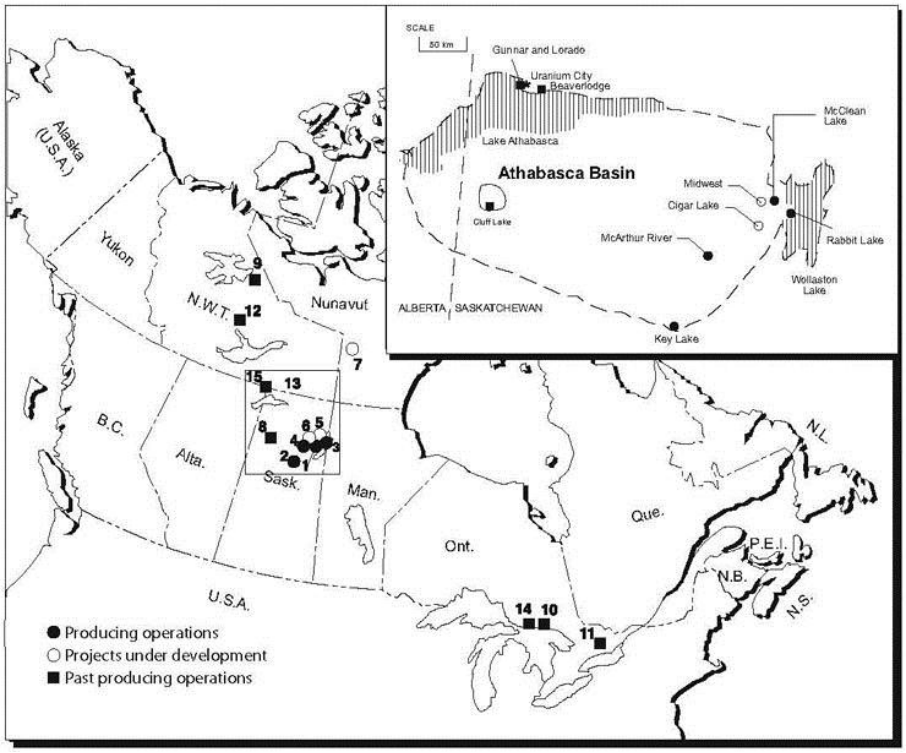

Figure 1 – Location of McArthur River operation (site #4 on the based map) relative to other uranium mines in Canada (Calvert, 2009)

2. SUMMARY OF FIELD TESTING

Two boreholes (pilot holes for a planned shaft, referred to as Hole A and Hole B in this work) were selected for detailed study, based on the abundance and quality of available data. Core logging and geophysical logging had previously been conducted by contract consultants, as well as packer testing to assess hydraulic conductivities of several depth intervals throughout the MFG. The results suggested that vertical and high-angle (collectively referred to as "sub-vertical") fractures and fractures with iron (limonite) staining were both found to be prevalent in zones of higher hydraulic conductivity. Several site visits were subsequently made by the authors, during which selected intervals of core were re-logged in more detail (including the measurement of joint roughness coefficients using a hand-held laser profilometer). This work confirmed that sub-vertical fractures appear to be the dominant conduits of flow in the intervals of high conductivity (as determined from packer tests), particularly so in cases where these fractures show iron staining (darker, thicker stained zones being indicators of highest hydraulic conductivity) and partial infilling with quartz crystals.

3. SAMPLE SELECTION FOR LABORATORY TESTING OF HYDRAULIC CONDUCTIVITY

Several core samples were taken to the Rock Mechanics Laboratory at the University of Saskatchewan for further analysis, from which six were ultimately selected for hydraulic conductivity testing. Of these six, the results of five are presented here; the first sample was in relatively poor condition, and was used as a "dummy" sample during a testing sequence that was conducted to refine testing procedures.

Table 1 presents a summary of the five samples for which results are reported in this paper; photographs of these samples are shown in Figures 2 through 6. The samples all contained fractures that were oriented sub-parallel to the core axis. Fractures with a variety of attributes (notably staining and quartz infilling) were selected, so as to assess the variability of hydraulic conductivity as a function of these attributes. Three of the five samples were fully parted along the fracture plane when they were found in the core box. Though the fracture surfaces did not contain any obvious signs of coring and handling-related damage, it is possible that the mating of their surfaces during the lab testing was not identical to in-situ conditions. Two of the samples, though containing a through-going fracture, were mated (i.e., intact) when found in their core boxes, and remained mated throughout sample preparation and testing. As such, it is felt that the mating of these fractures during the lab testing should match in-situ conditions.

Further to the fractured samples, four intact samples were selected from various depths for analysis of matrix properties.

Table 1 – List of fractured samples that were tested in this work

Sample No.	Hole	Depth (m)	Description	Separated on fracture surface?
1	A	335.44 – 335.76	Medium stain	no
2	B	132.8 – 133.1	Heavy stain	yes
3	B	150.0 – 150.3	Partially quartz-filled	yes
4	A	306.60 – 306.87	Medium stain, loose sand grains	no
5	B	288.7 – 289.0	Very heavy stain	no

Figure 2 – Photograph of sample 1 (medium stain)

Figure 3 – Photograph of sample 2 (which was observed to have heavy iron-staining after testing, when the sample was pulled apart)

Figure 4 – Photograph of sample 3 (partially quartz-filled)

Figure 5 – Photograph of sample 4 (medium stain, lose sand grains)

Figure 6 – Photograph of sample 5, prior to cutting the ends square for testing (heavy stain)

4. LABORATORY TESTING PROCEDURES

The porosities of intact samples were measured by gravimetric methods (i.e., based on a comparison of dry mass and water-saturated mass). Matrix hydraulic conductivities were measured on 25 mm core plugs that were drilled from the MFG cores, at nominal confining pressure (< 100 kPa) using a Ruska liquid permeameter.

The hydraulic conductivity testing of fractured samples was conducted in a triaxial cell; however, hydrostatic confinement was used (axial load = confining pressure) for all the tests presented in this paper. The diameters of the samples tested were 63 mm (± 1 mm), and the lengths (after cutting) varied from 97 to 146 mm. Each sample was sandwiched between a pair of porous stainless steel disks (1 cm thick, each), which distributed pore fluid over the surface of each sample end, and loading platens which each contained a single pore fluid port near the platen centre (to supply or collect fluid). [Note: The sample and porous plates were saturated with water prior to jacketing.] A heat shrinkable Teflon jacket was used to enclose each sample, the porous disks at its ends, and roughly half of each platen. During initial trial testing, the jacket ruptured at high confining pressure at a point adjacent to an open fracture segment with relatively sharp edges. In all of the tests presented in this paper, two layers of heat shrink were used. To mitigate the potential for leakage of hydraulic oil from the triaxial cell into the sample, a layer of elastomer (Skinflex) was set around each end of the Teflon jacket using a purpose-built mould. Figure 7 displays a jacketed sample, prior to insertion into the triaxial cell. Not shown in this figure, but used in most of the tests for added assurance against leakage, are hose clamps that were tightened around the Skinflex at the Skinflex-Teflon interface, and a bead of silicone sealant that was applied at this interface.

A strain chain was placed around the middle of the sample (also shown in Figure 7). The chain was used to measure circumferential displacement, which was ultimately used to estimate fracture closure (aperture change) during testing. This was accomplished by measuring circumferential displacements as a function of confining pressure on an intact sample; this provided a baseline measurement of displacement due to matrix compression, which was subtracted from the displacements measured on fractured samples.

A syringe pump was used to supply a constant flow rate of water to one end of the sample. The other end of the sample was vented to atmosphere. The flow rate at the outlet pipe was measured and compared against the input flow rate, to confirm that steady-state flow conditions were reached. The pressure at the inlet end of the sample was measured with a transducer. To correct for pressure drop within the apparatus,

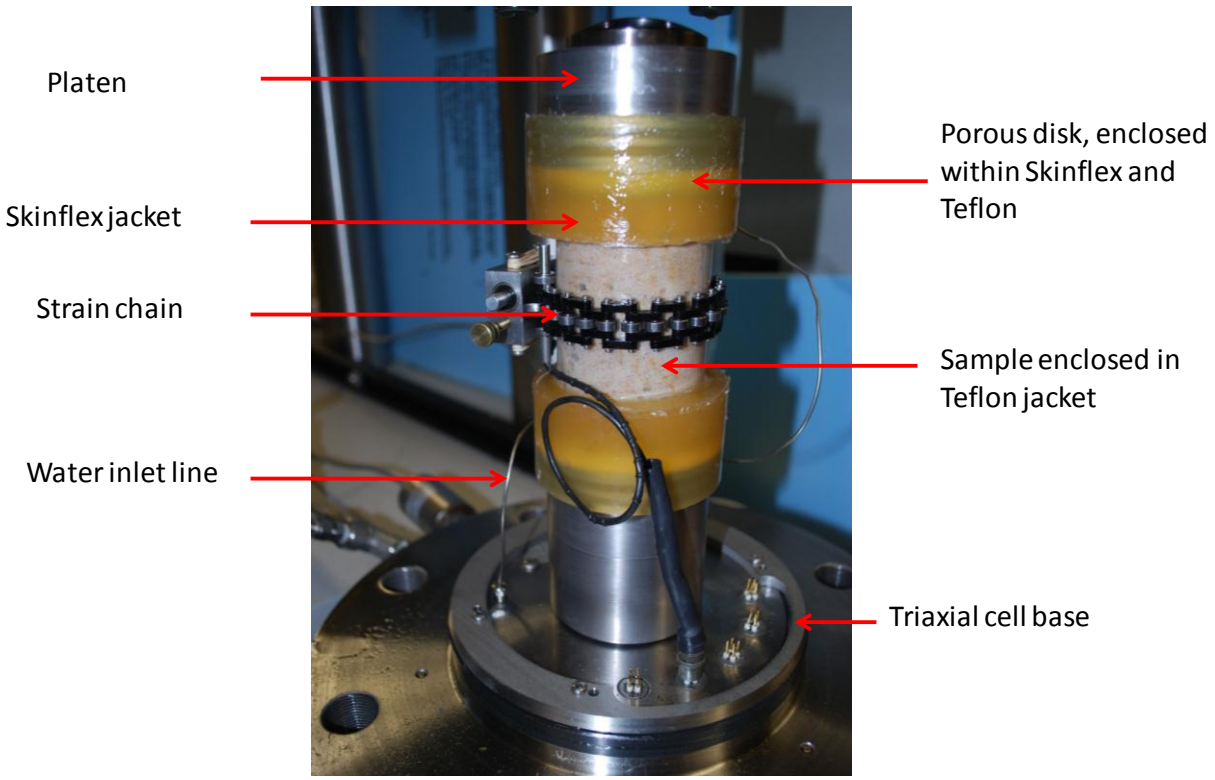

Figure 7 – A fully jacketed and instrumented fractured core sample prior to testing

a test was conducted with no sample (i.e., two porous disks sandwiched between platens), and pressure drop as a function of injection rate was measured.

Thus, the equivalent hydraulic conductivity (K_{eq}) for a given fractured core sample was calculated using the corrected pressure drop across the sample, the specified flow rate, and the cross sectional-area and length of the sample, assuming that the relationship between flow rate and pressure was controlled by Darcy's law.

The term equivalent hydraulic conductivity is used here to denote the hydraulic conductivity that an intact sample would possess in order to flow at the prescribed rate at the pressure drop that was measured during the test (i.e., the matrix permeability of an equivalent continuum). Proper scaling of the transport properties measured in this work to field conditions could be done, if the total trace-length of fracture for a given cross-sectional area of rock mass is known. The equivalent hydraulic conductivities presented in the following section may be regarded as the hydraulic conductivity per metre squared of cross-sectional area, for an impermeable matrix containing a fracture trace length (in the cross-sectional plane) of approximately 20 m (based on a fracture trace length of roughly 60 mm for each of the samples tested, with a cross-sectional area of roughly 3000 mm^2 each). Assuming parallel, equally-spaced fractures oriented normal to a cross-sectional plane of rock mass that is 1 m by 1m, this would correspond to a fracture spacing of 50 mm.

The goal was to measure hydraulic conductivities as a function of effective confining pressure, over a range extending up to the maximum value of mean effective in-situ stress at the study site (estimated to be between 6000 and 7000 kPa). Further, it was desired to measure hydraulic conductivities as effective confining pressures were cyclically increased then decreased, to assess if hysteresis is observed. In some cases, it was not possible to achieve the targeted number of load cycles due to test failure (e.g., jacket

leakage) or time constraints (e.g., long testing times required for low hydraulic conductivity samples). For the final test (sample 5), the final cycle was conducted to a significantly higher effective confining pressure (18000 kPa) in order to assess the limits of the testing system.

5. TEST RESULTS

Matrix porosities measured on intact samples ranged from 3.0 to 8.5%, with an average value of 6.4%. Hydraulic conductivities measured on these intact samples ranged from 1.9 x 10^{-11} to 3.2 x 10^{-10} m/s, with an average of 1.2 x 10^{-10} m/s.

Figures 8 through 12 show the equivalent hydraulic conductivities (K_{eq}) measured as a function of effective confining pressure (P_c') for samples 1 through 5. With the exception of sample 3, the K_{eq} values measured are orders of magnitude greater than the values measured on intact samples; this suggest that fracture flow is the dominant transport mechanism in samples 1, 2, 4 and 5. As expected, K_{eq} for the fractured samples decreased with increasing confinement; in all cases, K_{eq} measured at maximum P_c' was more than an order of magnitude smaller than the initial value, which was measured at low P_c'. For the samples that were subjected to two or more loading cycles (i.e., samples 1, 2, 4 and 5), hysteresis was observed; i.e., K_{eq} was less sensitive to P_c' upon initial unloading from the maximum P_c' value reached at a given stage in a testing sequence. Upon re-loading, the form of the $K_{eq} - P_c$' curve was generally similar to the unloading curve. The authors suggest that the behavior observed during unloading is likely more representative of in-situ behavior, given that the behavior observed during initial loading is affected by the reversal of aperture increase that occurred during coring and sample handling.

For samples 1 through 4, which were loaded to a maximum P_c' less than 9000 kPa, the general form of the $K_{eq} - P_c$' curves is concave upwards. For sample 5, which was loaded to a maximum P_c' of 18000 kPa, a more complex behavior was observed, with more of a concave-downwards form during loading to progressively higher P_c' values. This behavior is suggestive of the type of response expected for a porous medium that is being loaded above its pre-consolidation stress level.

To provide a consistent basis for comparing K_{eq} values amongst all of the samples, the value measured upon reaching a *Pc'* value between 6000 and 7000 kPa, for the first time during a testing sequence, was recorded and plotted in Figure 13. It is clear from this graph that the two samples that were fractured but intact (samples 2 and 3) are considerable less conductive than the other samples. Though a component of the relatively high conductivities of the latter samples may be due to damage that occurred when (or after) the fracture surfaces were separated, it is suggested that these fractures likely had greater apertures in-situ. Of these samples, K_{eq} of the one with the heaviest staining (sample 5; 2.3 x 10^{-6} m/s) was significantly greater than the samples with medium staining (samples 1 and 4; 9.9 x 10^{-8} and 1.3 x 10^{-7} m/s, respectively).

As a final comment, it is worth noting that – though the only sample tested with partial infilling of quartz (sample 3) had the lowest K_{eq} value - this is not viewed as a representative result on the whole. Based on core logging and packer testing of these boreholes, partial infilling with quartz crystals is believed to be an indicator of potentially high conductivity. This was qualitatively confirmed by the core inspection conducted during this project, given that partially quartz-filled fractures were observed with apertures locally in the vicinity of 10 mm. These fractures were noted to correspond to high-conductivity zones identified in the packer tests. These samples were deemed unsuitable for laboratory testing, however, partly due to the assessment that these fracture surfaces had been mechanically damaged during coring and handling, and partly because the hydraulic conductivities measured at the core scale would likely have been too high to measure.

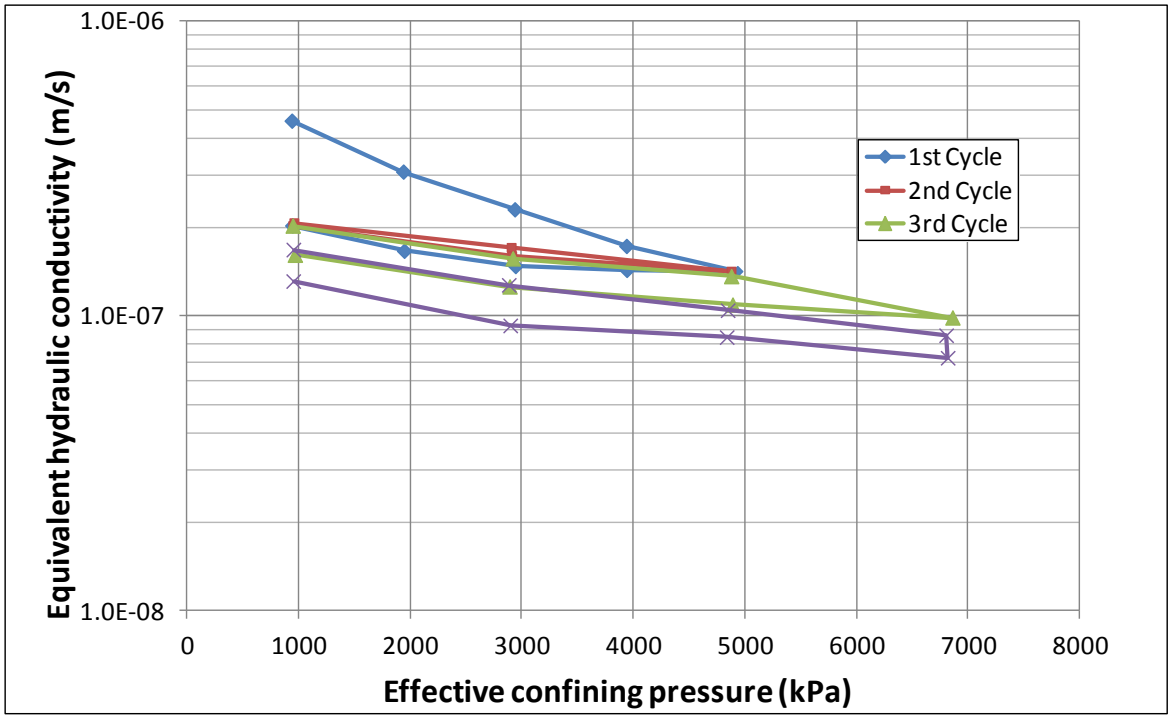

Figure 8 – Equivalent hydraulic conductivity as a function of effective confining pressure, sample 1

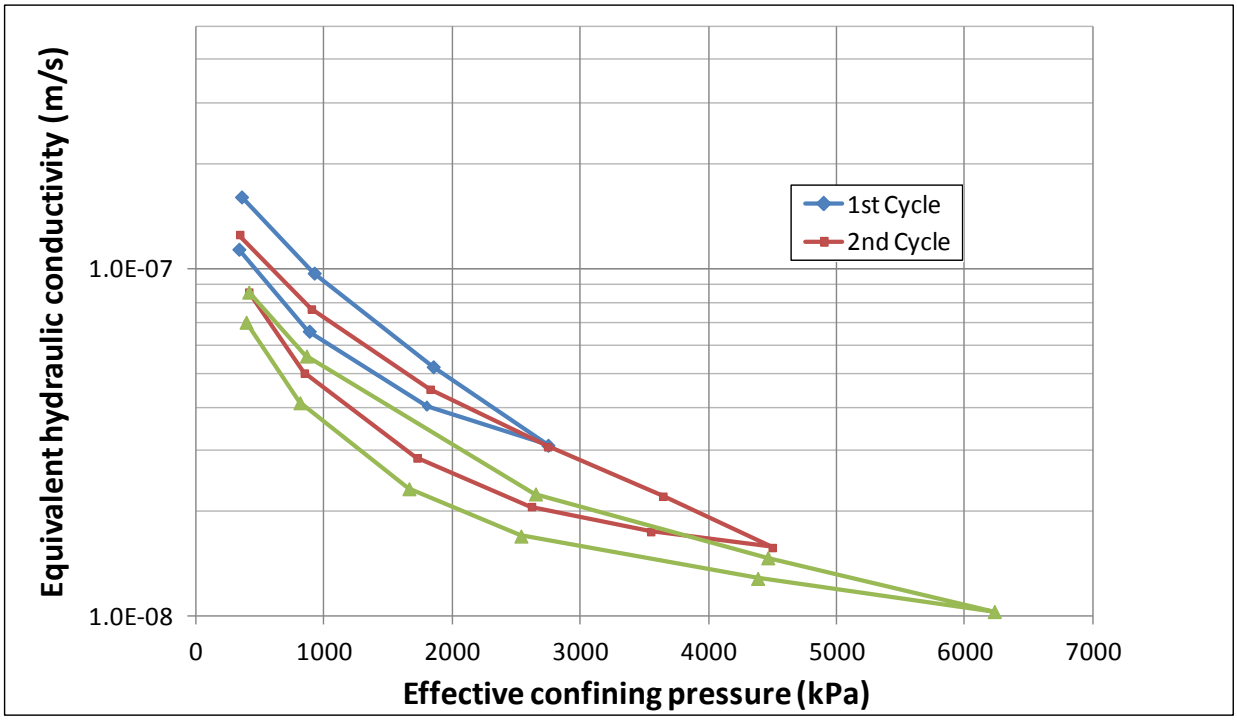

Figure 9 – Equivalent hydraulic conductivity as a function of effective confining pressure, sample 2

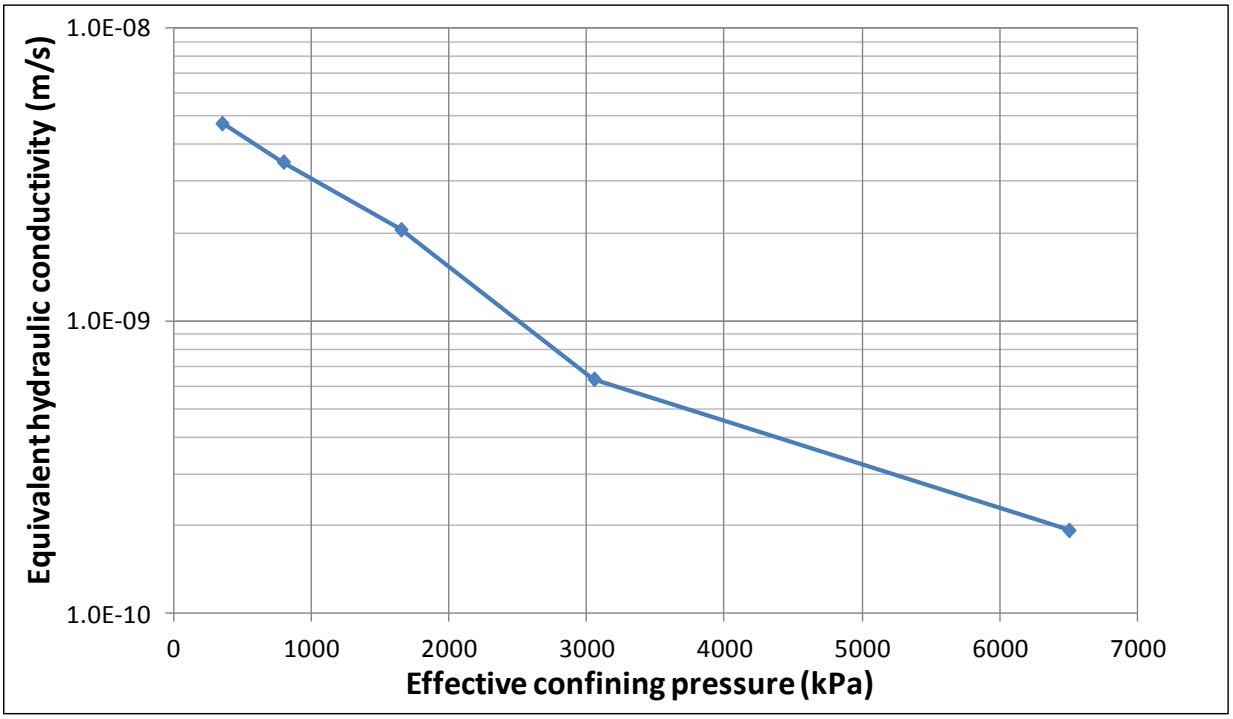

Figure 10 – Equivalent hydraulic conductivity as a function of effective confining pressure, sample 3

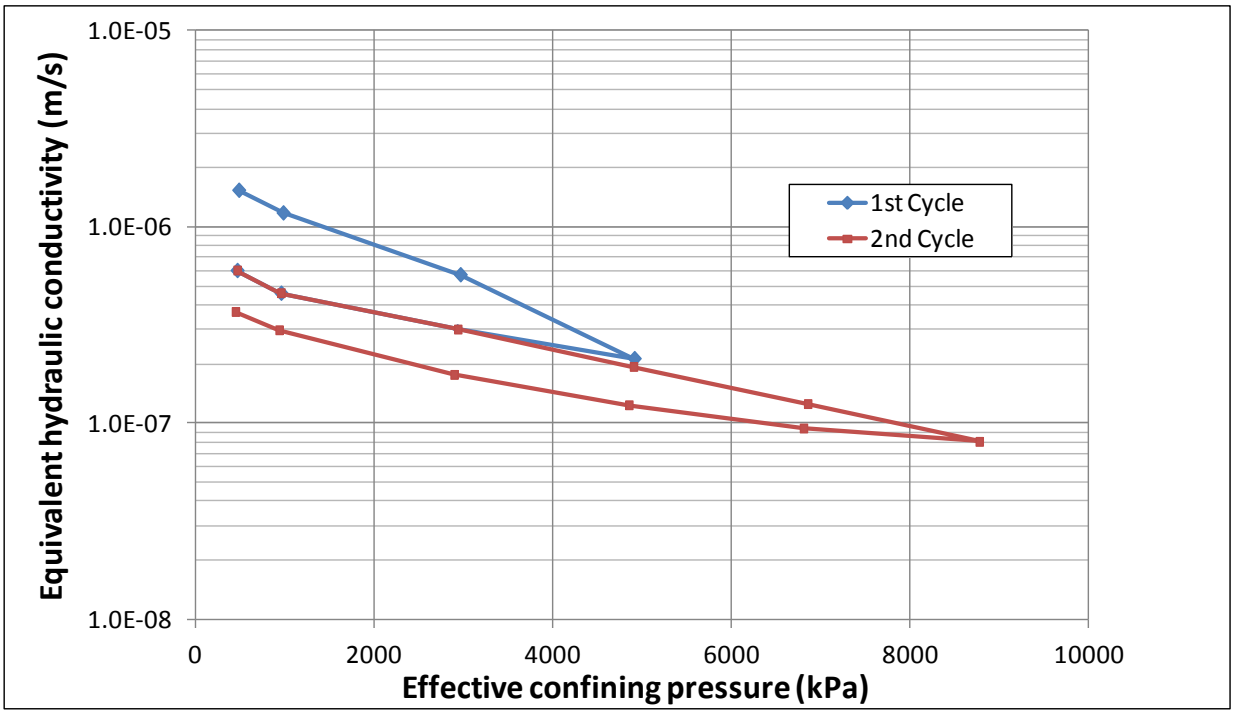

Figure 11 – Equivalent hydraulic conductivity as a function of effective confining pressure, sample 4

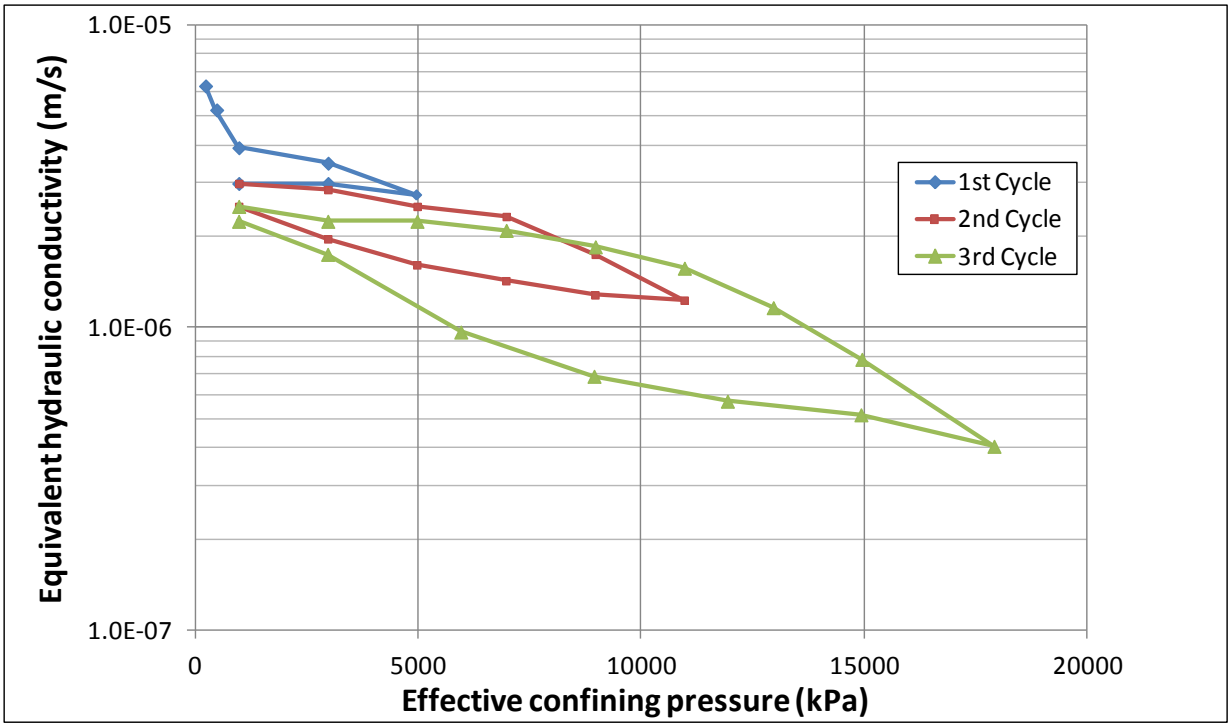

Figure 12 – Equivalent hydraulic conductivity as a function of effective confining pressure, sample 5

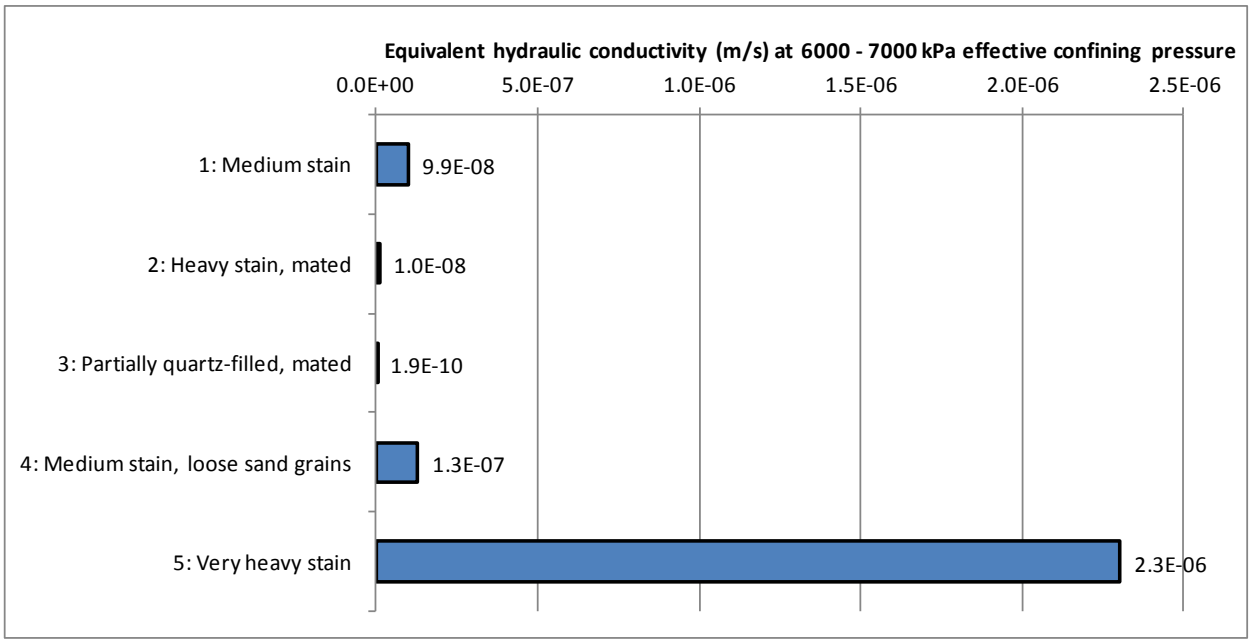

Figure 13 – Hydraulic conductivity for each fractured sample, measured upon reaching an effective confining pressure between 6000 and 7000 kPa for the first time

6. PRELIMINARY ASSESSMENT OF THEORETICAL APERTURE – CONDUCTIVITY RELATIONSHIPS

To test the applicability of theoretical equations used to calculate hydraulic conductivity from fracture aperture, three equations were compared to data obtained in this project. The following three equations were used:

$$K_{frac} = \frac{g}{12\nu} e^2 \qquad \text{Smooth parallel plate model} \qquad (1)$$

$$K_{frac} = \frac{g}{12\nu\left[1+8.8\left(1+\frac{r_a}{e}\right)^{1.5}\right]} e^2 \qquad \text{Louis (1969)} \qquad (2)$$

$$K_{frac} = \frac{g}{12\nu\left[1+8.8\left(0.5-\frac{10^6 \cdot e}{2JRC^{2.5}}\right)^{1.5}\right]} e^2 \qquad \text{Scesi and Gattinoni (2007)} \qquad (3)$$

Where:

K_{frac} is hydraulic conductivity of the fracture (m/s)
g is gravitational acceleration (m/s^2)
ν is kinematic viscosity (10^{-6} m^2/s for water at ambient conditions)
e is mechanical aperture of the fracture (m)
r_a is average asperity height of rough-walled fracture (m)
JRC is joint roughness coefficient

To convert K_{frac} to a form that can be compared directly to the equivalent hydraulic conductivity (K_{eq}) values measured in this work, the following correction was made:

$$K_{eq} = K_{frac} \cdot Area_{frac} / Area_{sample} \approx K_{frac} \cdot e \cdot D_{sample} \Big/ \left\{\pi\left(\frac{D_{sample}}{2}\right)\right\}^2 \qquad (4)$$

Where D_{sample} is sample diameter (m).

Given that initial fracture aperture was unknown, a value was selected for each equation that provided a match to the initial measured value of K_{eq}.

Figure 14 shows a comparison of measured and theoretical equivalent hydraulic conductivities for sample 2. Equation 2 was assessed using r_a = 0.001 m, and equation 3 was assessed using JRC = 10; fracture parameters that were interpreted for this sample from core inspection. It is clear that the theoretical predictions provide a poor comparison to the actual data; all three overestimate the sensitivity of K_{eq} to aperture change. As expected, the equations that account for fracture roughness (especially equation 2) compare slightly more favourably to the data, especially when comparing the trend of the data measured during unloading with the trend of equation 2. It is suggested that a better approach to obtain a match between theoretical equations and actual data might be to back-calculate the "initial" fracture based on the K_{eq} measured at the maximum effective confining pressure for a given testing sequence. This

approach, as well as an assessment of other theoretical equations against data for all five samples, is a topic of ongoing investigation.

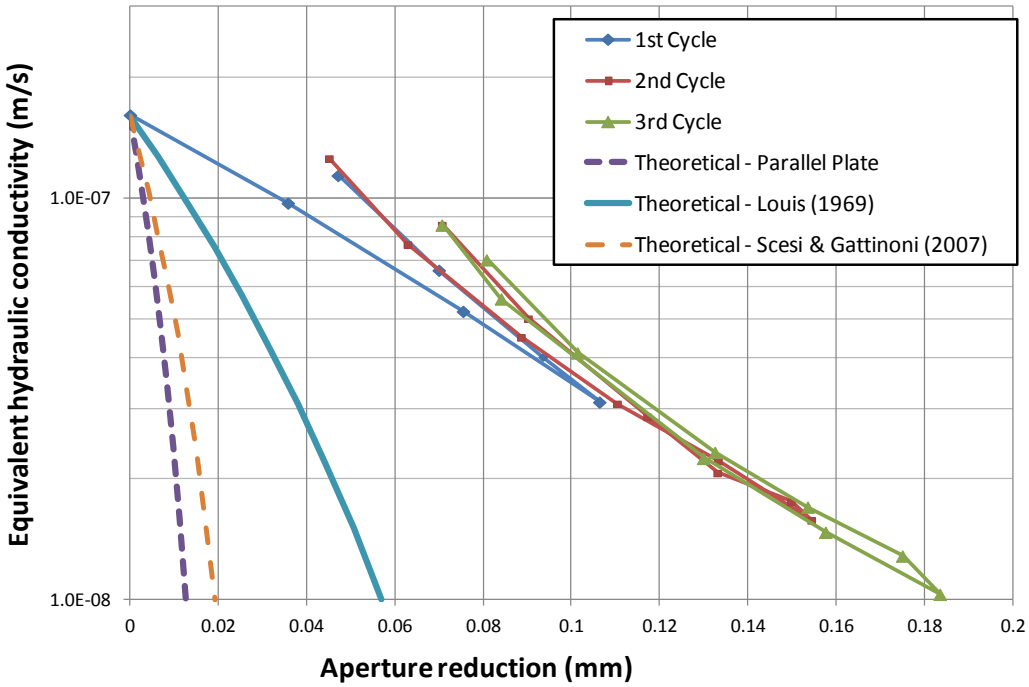

Figure 14 – Equivalent hydraulic conductivity as a function of aperture change (reduction); comparison of data for sample 2 against theoretical relationships

7. SUMMARY AND CONCLUSIONS

A testing methodology has been developed for measuring the equivalent hydraulic conductivity and fracture aperture change of fractured core samples. Data obtained using this methodology confirm the previous observation (based on packer testing) that heavily-stained, sub-vertical fractures in sandstones of the Manitou Falls Group tend to have relatively high hydraulic conductivities. The lone sample that was tested with partial infilling of quartz had a relatively low hydraulic conductivity, though previous work (packer testing and core logging) suggests that partially quartz-filled sub-vertical fractures exist that possess significantly larger apertures that the sample used in this work, and that these fractures have relatively high hydraulic conductivities. Analyses conducted to date show a poor comparison between theoretical relationships for hydraulic conductivity as a function of fracture aperture.

8. ACKNOWLEDGEMENTS

The authors gratefully acknowledge the support received from Cameco Corporation for this research.

9. REFERENCES

CALVERT, H.T., 2009. Canadian Minerals Yearbook - 2009: Uranium. Natural Resources Canada (Energy Sector), http://www.nrcan.gc.ca/minerals-metals/business-market/canadian-minerals-yearbook/2009-review/3587, accessed March, 2012.

LOUIS, C., 1969. A Study of Groundwater in Jointed Rock and its Influence on the Stability of Rock Masses, Ph.D. Thesis, Imperial College, London.

SCESI, L. and GATTINONI, P., 2007. Roughness control on hydraulic conductivity in fractured rocks. Hydrogeology Journal, 15 p. 201-211.

Numerical Investigation of Flow Regimes in Fractured Rock Slopes

Jim Hazzard
Itasca Consulting Group Inc.
Branko Damjanac
Itasca Consulting Group Inc.
Christine Detournay
Itasca Consulting Group Inc.
Loren Lorig
Itasca Consulting Group Inc.

ABSTRACT: A numerical investigation is presented to examine fluid flow in fractured rock slopes. In mining geomechanics, different numerical modelling approaches are used to estimate fluid pressures in open pit mines. The most common technique is the Equivalent Porous Medium (EPM) approach in which the fractured rock is assumed to behave as a porous continuum. Depending on the geometry and properties of the problem, this may not always be the best approach. The paper presents a parametric study to examine the effect of fracture spacing, fracture and matrix diffusivity and excavation rate on the fluid behaviour in rock slopes. Based on the model results, guidelines are provided as to when EPM models can be used and when different modelling approaches (e.g., discrete fracture flow) may be necessary.

1. INTRODUCTION

Accurate determination of groundwater conditions in large open-pit mines is critical in the assessment of slope stability. Water pressure decreases the normal stress on fractures, and therefore, increases the likelihood of slip. The overall effect of an increase in water pressure is to decrease slope stability as the shear strength of many fractures is approached or exceeded. Estimates of fluid pressure in open pit slopes generally are obtained from numerical models.

The most common way to model fluid flow in fractured rock masses is to use an equivalent porous medium (EPM) model. This assumes that the most conductive fractures are spaced closely, relative to the dimensions of interest (e.g., slope height). With this approach, it is assumed that a porous continuum will yield a flow response essentially the same as that of a fractured rock mass. Various researchers have investigated the conditions under which flow in a fractured rock mass can be modelled as flow in an equivalent continuum (e.g., Long, 1983).

Less commonly, fracture flow models are used in which it is assumed that the fractures dominate the fluid flow behaviour and flow in the 'matrix' blocks between the fractures is not considered. Discrete fractures are modelled and flow usually is assumed to obey a 'cubic law' in which the hydraulic conductivity of the fractures is proportional to the aperture cubed. Such models may be very computationally expensive due to (1) a very large number of fractures that generally are required to adequately represent the system, and (2) each model simulates only one possible representation of a fracture network, so it is often necessary to perform multiple analyses with different configurations (e.g., Monte-Carlo analysis).

In the oil and gas industry, dual-porosity or dual-permeability type models often are used in which flow occurs in both the fractures and the matrix blocks, and there is fluid transfer between the different components. Equations for flow through a fractured porous medium were first proposed by Barenblatt et al (1960) and were expanded upon by Warren and Root (1963). A dual porosity model essentially

consists of two overlapping continua. One continuum represents the flow in the fractures, while the other continuum represents the flow in the matrix. Much research has been done on determining appropriate fluid transfer functions, refining the dual-porosity calculation scheme and numerically solving problems common in the oil and gas industry. Dual-porosity models are used rarely in mining, however, knowing the pressure differences in the different components (fracture and matrix) is important in open-pit mine design, because slow draining 'compartments' can maintain elevated pore pressures and may affect the stability of the slope adversely (Beale, 2009).

This paper presents an investigation of when the different types of modelling approaches should be used in analyses of open-pit slope stability based on fracture spacing, contrast in diffusivities between the fractures and the rock matrix and the rate of excavation. A parametric study is performed in which slope-scale 'dual-porosity' models are executed with different fracture spacings, permeabilities and diffusivity contrasts between the fractures and matrix material. Boundaries between different flow regimes are mapped out based on ranges of the relevant parameters. These boundaries delineate when EPM modelling is acceptable, when fracture flow models should be used and when dual-porosity modelling should be considered.

2. TERMINOLOGY

Different practitioners of hydrogeology often use different terms for the same concepts or physical parameters. This section briefly describes the terminology used in the remainder of the paper.

Hydraulic conductivity: Hydraulic conductivity, or simply conductivity, often is referred to as permeability in geomechanics. In this paper, conductivity is the discharge rate per unit area under a unit hydraulic gradient. The metric units are m/s.

Specific storage: Specific storage, or storage, can have different meanings for unconfined and confined aquifers. In this paper, the storage refers to the confined storage and refers to the volume of water released from storage, per unit volume of aquifer per unit change in hydraulic head, while remaining fully saturated. This can be calculated by (Strack, 1989):

$$S = \gamma_w \left(\frac{n}{K_w} + \frac{(1+\nu)(1-\nu)}{E(1-\nu)} \right) \tag{1}$$

Where γ_w is the unit weight of water, n is the porosity, K_w is the bulk modulus of water, ν is the Poisson's ratio of the rock mass and E is the Young's modulus of the rock mass. The metric units are m^{-1}.

Hydraulic Diffusivity: Hydraulic diffusivity, or diffusivity, is the hydraulic conductivity divided by the specific storage:

$$c = \frac{k}{S} \tag{2}$$

Metric units are m^2/s.

Dimensionless excavation rate: The dimensionless excavation rate is not a common hydrogeological term. This parameter was conceived by the authors to account for effect of the mining rate on the rate of fluid flow in rock. The volumetric mining rate (per unit model thickness), M_r, is defined, with reference to Figure 1, as

$$M_r = L\frac{dH}{dt} \tag{3}$$

We therefore can propose a *dimensionless excavation rate* metric based on the mining rate and the diffusivity,

$$R = \frac{M_r}{c} \tag{4}$$

as a number to be used to quantify the effect of different model parameters on pore pressures.

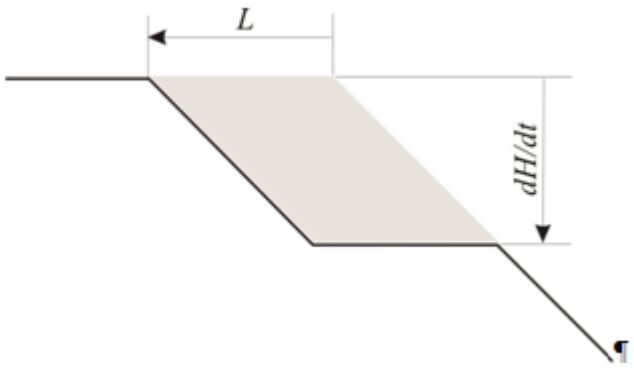

Figure 1 - Sketch of mining excavation showing quantities used to define excavation rate

3. FRACTURED ROCK MODELS

This section presents models of rock that consider fractures and matrix material of different properties (for convenience, these will be referred to as dual porosity models, even though this is not the standard dual-porosity approach used in the petroleum industry). With this analysis, we hope to be able to determine the transitions between different flow regimes (i.e., fracture flow with impermeable matrix, dual porosity and EPM with equilibrium pressure between the matrix and the fractures).

3.1 Numerical Model

A 'typical' large open pit was modelled with the two-dimensional finite difference program *FLAC* (Itasca, 2008). The model geometry is shown in Figure 2. The initial pit is excavated gradually over a period of 18 years to set up the initial state for the study (shown). Blocks 1 through 6 then are excavated at 9-month intervals. Excavation 7 in Figure 4 is not considered in this study. Each of these excavation blocks are removed instantaneously, after which the model is run for 9 months to obtain the pore pressures in the slope. Therefore, the rate of mining is M_r = 200 m × 133 m / 9 months ≈ 0.001 m^2/s. In this analysis, the instantaneous pressure change due to undrained deformation was not considered. Only the pressure change due to dissipation to the slope face was analyzed.

The initial water table is 50 m below the surface. The head is fixed on the right boundary at a distance of 2500 m from the middle of the pit. The model base is an impermeable boundary, as is the left boundary (symmetry condition). After each excavation stage, the pore pressure is fixed to 0 on the exposed face.

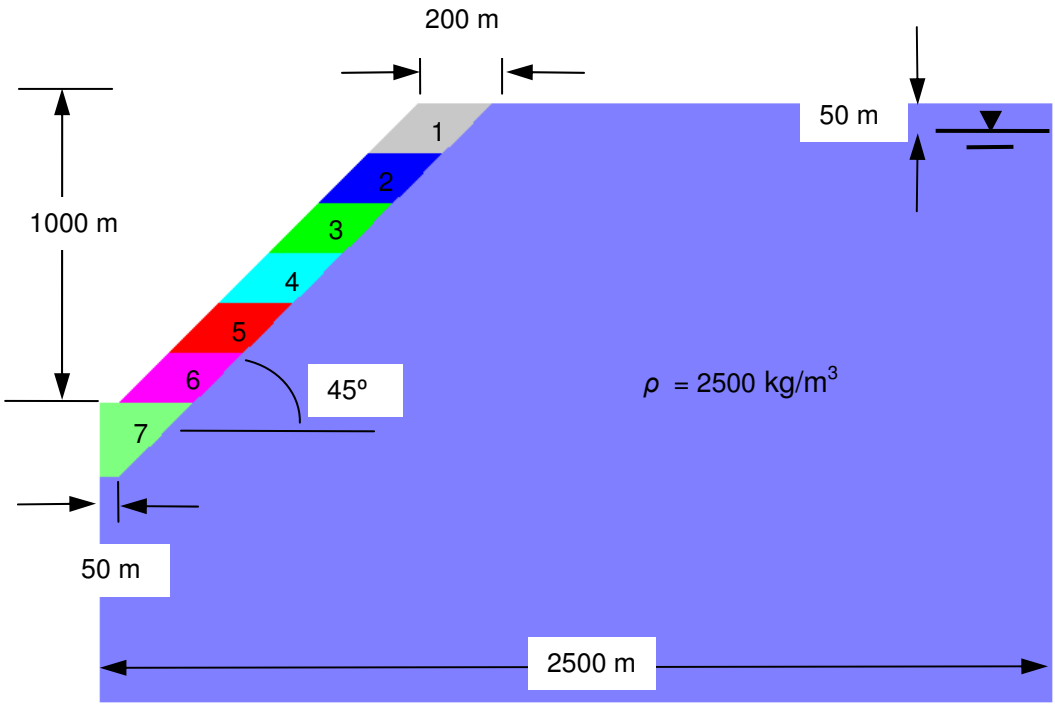

Figure 2 - Geometry of the idealized open pit model

Fractures were modelled as thin zones of material with different hydraulic properties. An example is shown in Figure 3. Note that the specific storage of the matrix blocks is ~ 50 times the specific storage of the fractures. The slope height H = 800 m. The fracture spacing and the conductivities of the fractures and matrix blocks were varied as follows:

- 10^{-8} m/s $< k_{fracture} < 10^{-6}$ m/s;
- 2 m^2/s $< c_{fracture} / c_{matrix} < 2\times10^{6}$ m^2/s (10^{-15} m/s $< k_{matrix} < 10^{-9}$ m/s); and
- 50 m $< s <$ 300 m.

If we assume that the rate of flow is dominated by the fractures, then we obtain dimensionless excavation rates of $1 < R < 0.1$.

The measurement point is 200 m behind the slope face and was chosen to lie on the most likely failure surface. Obviously, the location of the measurement point influences the results, but for stability studies, the pore pressures along potential failure planes are often the most relevant. The measurement point lies in the centre of a matrix block in each model. To compare fracture pressures to matrix pressures, the pressures in the fractures on the four sides of the block are averaged.

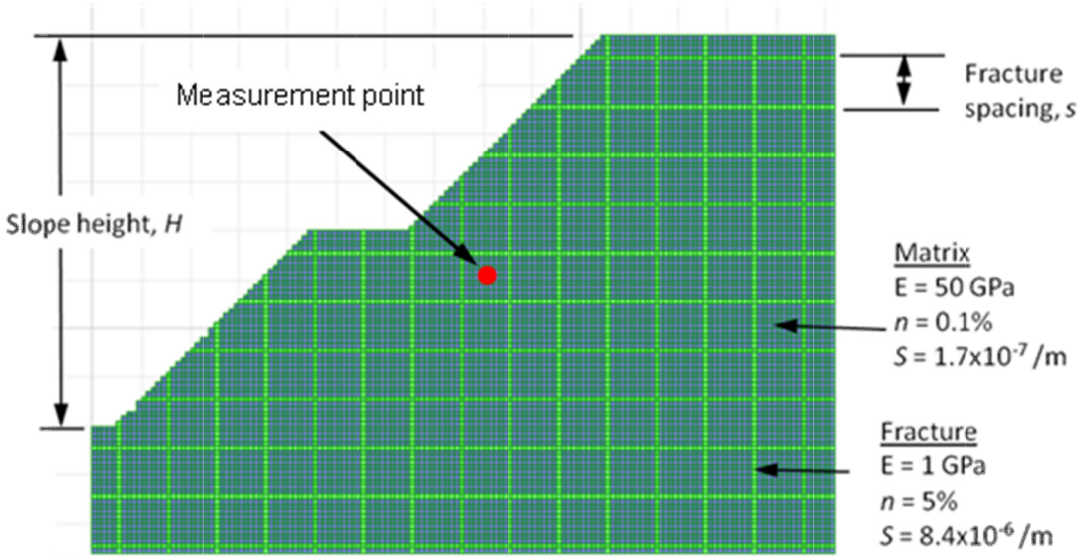

Figure 3 - "Dual porosity" model used to test flow regimes

3.2 Results

As the pit is excavated, fluid drains first from the permeable fractures and then from the less permeable matrix blocks. In general, the pressure in the blocks is higher than in the fractures. The model behaviour was analyzed by observing the *change* in pressure in the matrix relative to the blocks for different fracture spacings, diffusivity contrasts and dimensionless excavation rates. Plots summarizing the model behaviour are shown in Figure 4. From these plots, we can make the following comments.

- When c_f / c_m is very low (< 10), $\Delta P_m / \Delta P_f$ is close to 1, indicating the model is behaving approximately as a homogeneous continuum.
- When c_f / c_m is very high (> 10^6), $\Delta P_m / \Delta P_f$ is close to zero, indicating the matrix blocks are behaving essentially as impermeable material.
- As fracture spacing increases, the curves shift left, meaning that larger blocks drain more slowly (the pressure change in the matrix relative to the fractures is lower for the same diffusivity ratio).
- As dimensionless excavation rate decreases (permeabilities increase), the curves shift right. This indicates that the matrix blocks drain more quickly (relative to the fractures) for the same diffusivity ratio. This can be explained by considering that a decrease in R corresponds to an increase in the permeability of the fractures *and* the matrix blocks (for a constant c_f / c_m). The rate of drainage in the matrix blocks is more sensitive to permeability changes than the rate of drainage of the fractures. Therefore, the ratio $\Delta P_m / \Delta P_f$ increases as R decreases.

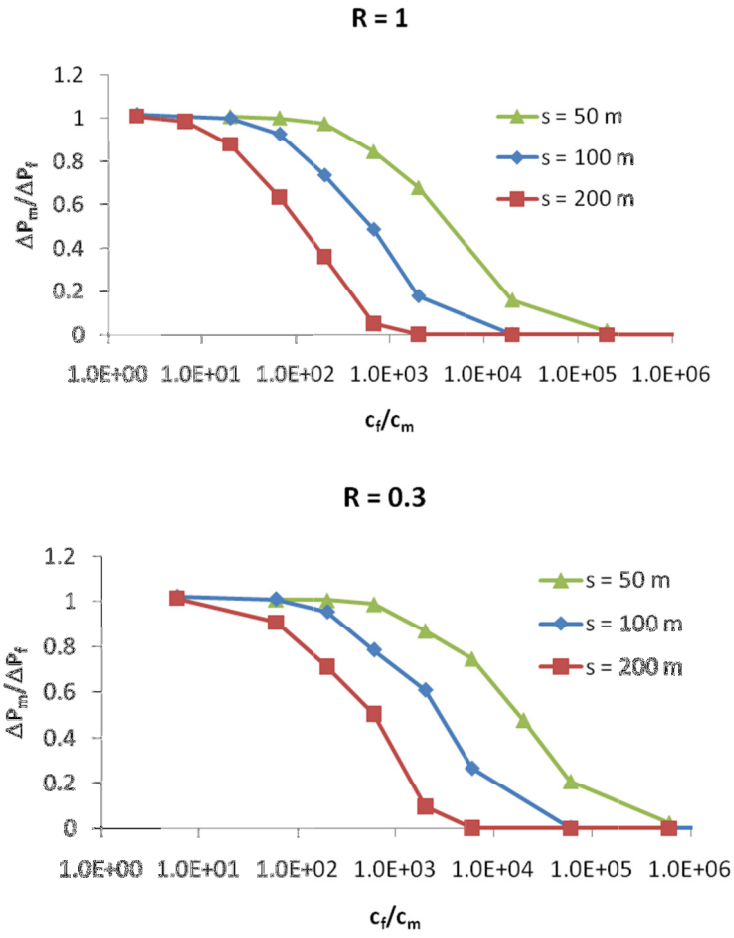

Figure 4 - Behaviour of dual-porosity model for different dimensionless excavation rates, fracture spacings and diffusivity ratios

The goal of this work is to delineate conditions under which the matrix can be considered approximately equivalent to the fractures (in which case the slope can be modelled as an EPM), and when the matrix appears essentially impermeable (i.e., fracture flow only). It is assumed that the model is behaving approximately like an EPM if $\Delta P_m / \Delta P_f > 0.9$. Similarly, the matrix blocks are assumed to be acting as impermeable units if $\Delta P_m / \Delta P_f < 0.1$. By picking off these points from Figure 4 (and other similar figures not shown), we can construct limits delineating the different regions. These are shown in Figure 5.

Now, for a given fracture spacing (normalized by slope height) and dimensionless excavation rate, the ratio of $c_{fracture}/c_{matrix}$ can be obtained that will yield an equivalent continuum or apparently impermeable matrix block. For example, for a fracture spacing of 100 m, a slope height of 800 m, and a dimensionless excavation rate of 0.1 ($c_{fracture}$ = 10^{-7} m/s in this model), then if $c_{fracture}/c_{matrix} < 1000$, the slope acts as a homogenous material. If $c_{fracture}/c_{matrix} > 1.2\times10^{5}$, then the matrix acts as impermeable material. This means that in this model, a matrix conductivity > 5×10^{-9} m/s suggests that EPM modelling is suitable, but for a matrix conductivity < 4×10^{-11} m/s, fracture flow models should be used.

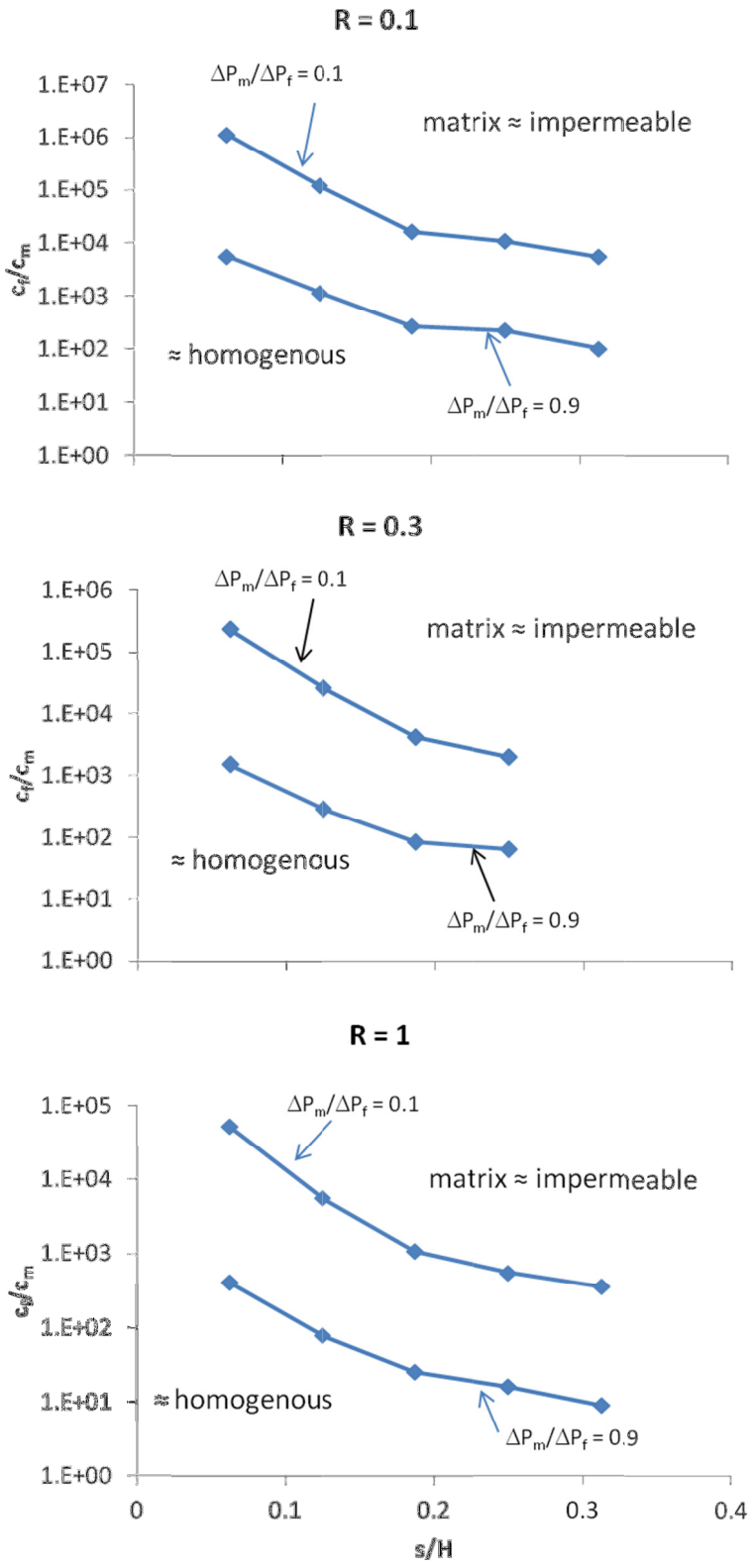

Figure 5 - Values of $c_{fracture}/c_{matrix}$ that delineate zones for which the slope appears approximately homogeneous and zones for which the matrix blocks appear impermeable

4. SUMMARY AND CONCLUSIONS

Fluid flow in fractured rock is simulated with 2D continuum models in which fractures are represented by thin linear regions with high conductivities. Flow occurs preferentially through the 'fractures,' and therefore after an excavation step, the pressure drops first in the fracture zones. Fluid then flows from the less permeable matrix blocks to the fractures. By observing the pressure changes in the matrix blocks relative to those in the fractures, guidelines are proposed as to when the rock mass can be considered a single continuum and when fractures should be modelled discretely.

The observed behaviour is fairly intuitive – rocks with closely spaced fractures and/or low conductivity contrasts behave like an equivalent porous medium, whereas rocks with large fracture spacings and/or large differences in conductivities probably should be modelled with some sort of discontinuum or fracture flow approach. The main contribution of this paper is to estimate quantitatively where these boundaries lie. By using Figure 5, a practitioner with knowledge of fracture spacing, slope height, excavation rate and rock and fracture diffusivities can locate themselves on the charts and determine what type of fluid flow analysis is required to simulate pore pressures in the slope.

Obviously, this analysis encompasses many simplifications: the flow is 2D, the fractures are evenly spaced, the area of interest is half way down the slope, etc. However, it is hoped that these graphs will provide a good starting point for hydrogeological analyses of large open pits.

5. ACKNOWLEDGEMENTS

The work described here was performed as part of the LOP (Large Open Pit project, administered by Dr. John Read of CSIRO Brisbane). Sponsors of this project are thanked for their support.

6. REFERENCES

BARENBLATT, G.I., ZHELTOV, Iu.P. and KOCHINA, I.N., 1960. Basic concepts in the theory of seepage of homogeneous liquids in fissured rock, Journal of Applied Mathematics and Mechanics, 24, 1286-1303.

BEALE, G. 2009. Hydrogeological model, in Read & Stacey (eds.), Guidelines for Open-pit Slope Design. CSIRO Publishing, Collingwood, pp. 141-200.

ITASCA CONSULTING GROUP INC., 2008. FLAC (Fast Lagrangian Analysis of Continua), Version 6.0. Minneapolis, MN, USA.

LONG, J. C. S., 1983. Investigation of Equivalent Porous Medium Permeability in Networks of Discontinuous Fractures. Ph. D. Thesis, University of California, Berkeley.

STRACK, O.D.L., 1989. Groundwater Mechanics, Prentice Hall, Englewood Cliffs, New Jersey, 732 p.

WARREN, J.E., and ROOT, P.J., 1963. The Behavior of Naturally Fractured Reservoirs. Society of Petroleum Engineering Journal, 3, 245-255.

Development of an Innovative Hydrostatic Shaft Liner Design for a New Shaft in Saskatchewan's Athabasca Basin

J. Ouellet
Tetra Tech Inc.
J. Hatley
Cameco Corporation
B. Stanley
Thyssen Mining
M. Harper
Stirling Lloyd

ABSTRACT: The authors participated in a study for a new mine shaft in Saskatchewan's Athabasca Basin where ground freezing is desired to reduce water inflows. Constraints were imposed on the design in terms of permissible water leakage (less than 10 m^3 / hour) inside the shaft. Since the shaft goes through highly permeable formations, water control measures had to be incorporated into the design. Ground freezing was selected as the most reliable and proven method for the sinking and a hydrostatic liner design was implemented. While exploring various technological options available for providing a fully hydrostatic liner, the authors came up with a new design concept that offers a more cost effective solution while meeting all the design constraints. The new liner concept is a composite design using concrete and a sprayed-on membrane system. A proof of concept program comprising laboratory testing and field testing was successfully implemented. This paper presents the innovative liner design, as well as the adapted sinking methodology, developed for this type of project. The new concept offers a new cost effective high performance hydrostatic mine shaft liner comparing favorably with traditional methods.

RESUME: Les auteurs ont réalisé une étude pour un nouveau puits de mine dans le Bassin de l'Athabasca en Saskatchewan. Des limites sévères sont imposées sur le design en terme de volume d'infiltration d'eau acceptable (moins de 10 m^3 / heure). Comme ce puits de mine traverse des formations très perméables la congélation des terrains a été sélectionnée, une méthode éprouvée et fiable. Un design hydrostatique a été choisi pour le revêtement du puits. Dans le processus de design, les différentes technologies disponibles ont été étudiées. Les auteurs ont développé un nouveau concept de revêtement composite offrant un rapport performance/prix plus avantageux que les technologies conventionnelles. Le nouveau design proposé est composé de béton et d'une membrane projetée. Un programme expérimental a été réalisé pour démontrer la faisabilité du concept. Cet article présente le nouveau concept ainsi que la méthodologie de fonçage de puits adaptée. Ce concept innovateur offre un revêtement hydrostatique performant à un cout avantageux par rapport aux techniques de construction utilisées jusqu'à maintenant.

1. INTRODUCTION

The recent years saw a big push of new expansion projects both in potash mining as well as uranium mining in the province of Saskatchewan, Canada. The authors had the opportunity to be involved with most of these projects. These mine shaft projects involved sinking through difficult ground conditions with the potential of high water inflows at depth. For instance, the Saskatchewan potash mines must sink through very challenging ground conditions. The most difficult one being the Blairmore Formation where the shaft sinking must deal with unconsolidated ground and high water pressures. The only successful methods for sinking through such conditions use ground freezing technology and these applications demand waterproof liner designs. The shaft liner designs must be able to handle the high hydrostatic pressures encountered as well as being fully waterproof. Interest for waterproof liners was also very high

for uranium mining projects in the Athabasca Basin. Consequently, time and effort were invested in reviewing existing hydrostatic liners designs.

The existing potash shafts in Canada were constructed more than 30 years ago. The hydrostatic liner designs used at that time were mostly based on the cast iron tubbing system; an example is illustrated in Figure 1. Except for the Lannigan mine shafts which were based on the composite steel/concrete technology. The former was very innovative for its time using welded steel sheets as the waterproof membrane component. These technologies are actually still used today in shaft liner design where waterproof hydrostatic liners are required. They have been and are still very effective. The downsides are the slow sinking rates imposed on construction because of the time consuming installation and the high costs involved. The typical cost of only the tubbing segments in a shaft project done in Canada in 2011 was in excess of $50,000 per meter. This cost excludes all concrete, grouting operations as well as installation. The knowledge to design, produce technical specifications, manufacture and install a tubbing liner is very limited in Canada. The composite liner employs welded steel sheets as the water membrane component and has slightly cheaper per metre material cost. However the precise and high quality welding required in this liner construction is very challenging to execute in the conditions of a frozen mine shaft. In terms of sinking rate with this methodology, the method is very slow as well.

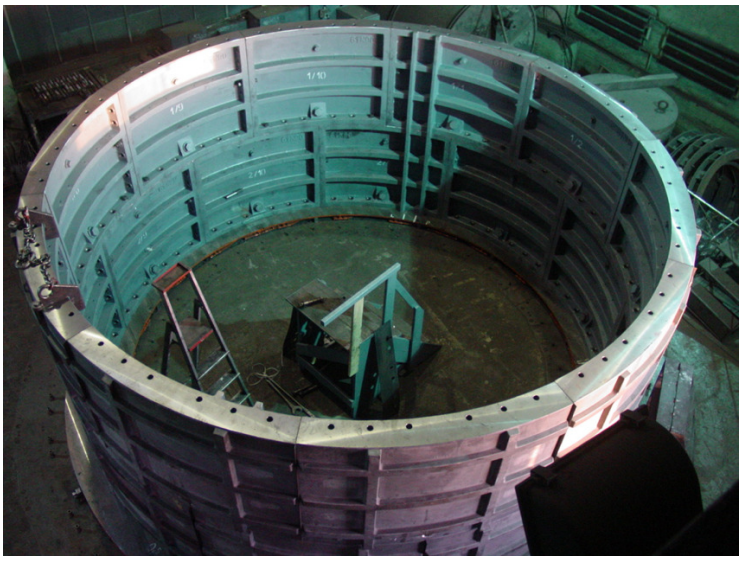

Figure 1 - Tubbing design produced by TMCC engineering team in 2010

The authors were interested in exploring new materials and technologies to come up with a more cost effective and easier to install liner design. Through value engineering exercises it was determined that a composite concrete design with an internal waterproofing membrane offered significant advantages in terms of preventing water migration. The sprayed-on membrane or sheet membrane was considered as a replacement for the conventional welded steel membrane. By putting in place a continuous barrier to the water from ever reaching the concrete liner, potential construction weaknesses in the liner, such as cold joints and or cracks, are no longer an issue. So the new concept would add to a conventional concrete design a water membrane component.

2. SELECTION OF THE MEMBRANE MATERIAL FOR THE NEW COMPOSITE LINER DESIGN

For this application, the desirable attributes of such a membrane are:

- Rapid installation minimizing the impact on the shaft sinking cycle,
- Material, equipment and installation procedures that are easily manageable in the shaft sinking environment,
- Allows for a thorough quality control and testing of membrane integrity during construction,
- Can accommodate complex geometries,
- Offers excellent crack bridging capabilities,
- Forms a consistent bond with the concrete liner material,
- Can bridge cold joints without risk of failure,
- Robust and durable (mine lifespan of 50 years or more),
- Withstands hydrostatic water pressures of up to 70 bars.

In the civil engineering domain, waterproofing membranes are used extensively in shallow shafts (depths in the order of 60 metres) and tunnels. A survey of the various products showed that the technologies available could be regrouped in two categories: sheet membranes and sprayed-on membranes. Sheet membranes are delivered as rolls of a given width and length that must be tacked or pinned to the shaft wall and then glued or fused to form a continuous membrane preventing any water from reaching the inside liner. Aside from being very difficult to handle, insuring the integrity of the membrane with these products is dubious for a long and relatively deep shaft of 500 metres or more. Thousands of meters of seams need to be welded without any defects. Potential to puncture or tear the membrane during the construction is high. Moreover, handling complex geometries with these sheets is very difficult if not impossible. Actual performance in tunnels demonstrated a low rate of successfully meeting design requirements. Consequently all the conventional membrane materials were eliminated in the value engineering process for shaft liner design.

The following characteristics were key driving attributes in selecting the product:

- Seamless membrane,
- Effective and fast application,
- Rapid curing,
- High resistance to site operations (no special protection required),
- An integrated quality assurance program,
- Electronic testing after application providing proof of integrity,
- Application in a wide range of conditions such as high humidity and cold temperatures,
- A design life in excess of that of the structure it protects.

The sprayed-on membranes products, from an implementation point of view in a mine shaft, seem to offer the best solution. Various products have been considered and two were initially retained: a competitor membrane product and the Integritank® HF from Stirling Lloyd.

The competitor membrane product is a hydrating cement polymer product that is sprayed on a shotcrete base. This is a one coat product that bonds to the cement. The product was tested for high water pressure (80 bars) successfully. The design life, as well as the crack bridging tests results, met the initial requirements. However, weak points were identified with this product for shaft sinking in frozen ground conditions:

- Requires at least +5 °C to be installed,
- Requires 12 to 24 hours to cure enough before working against it and warm temperature must be maintained during all this period, otherwise it is very soft and can be damaged easily,

- A single coat application making it more prone to missing spots thus creating pin holes that would be detrimental to the performance,
- No established quality control procedure to verify membrane integrity,
- Some instances of tunnelling applications were found to be less than ideal.

The sensitivity of the competitor membrane product to impact damage during curing was not favorable and the long curing time would seriously impact on the sinking cycle time. Moreover, in frozen ground conditions, the application surface (shotcrete preliminary liner) must be maintained at a warm temperature for the minimum 24 hours. The problem with a hydrating material is that the hydration rate is very sensitive to ambient temperature. This can lead to a potentially very long curing time in a frozen shaft.

There was not a well-established procedure to insure or verify the actual membrane integrity for this product during construction, which renders the quality control aspect in this option lacking. A significant advantage of the product was the fact that little if no surface preparation was required when applied onto a shotcrete base layer.

The Integritank® HF product from Stirling Lloyd is applied in three coats during installation. The first coat is a primer which aims at limiting the detrimental effect of out-gazing from the curing shotcrete which tend to produce pinholes in sprayed-on membranes. The actual membrane is formed by two layers of a polymer material. Both coats are the same although with different color pigments. The first coat is a bright yellow and the second one is white. The principle behind the two coat system is to minimize the risk of missing spots or layers. Whatever could have been missed with the first application will be covered with the second coat. The color coding allows for an effective visual check of the quality of the coverage. The system requires only one hour per coat to reach full curing, which is a significant advantage for the sinking cycle time.

The membrane is non-toxic and provides a low flash point, which is highly desirable for work in confined areas. This product, being based on methyl methacrylate chemistry, allows for a chemical cure rather than a hydrating cure. This resulted in cure times reduced to one hour for each layer application instead of six to eight hours in other products. In addition, tests on the membrane material demonstrated hydrostatic pressure strengths in excess of 90 bars. Application time for the material is well within time limits encountered in the sinking and lining cycle. Contrary to hydrating cure material such as the competitor membrane product, the Integritank® HF product exothermic chemical curing makes for a material much less sensitive to ambient temperature variations.

The most attractive feature of the Integritank® HF product is the quality control program. The producer has a technology to verify the membrane integrity after application, thus allowing detection of any defect before completion of the construction. It then becomes possible to detect and repair any such defects during the work. The membrane offers all the desirable characteristics of a waterproofing system, seamless, crack bridging, composite effect and rapid installation (Harper, 2011). It is very robust against shock and friction, a significant advantage when construction of the permanent concrete liner is done in front of this membrane. Crack bridging testing had been performed successfully at below freezing temperature which was an interesting attribute where frozen ground technology would be used.

The weak points identified on this product are:

- Requires +10 °C degrees on the application surface,
- Application surface must be relatively smooth, floating of the shotcrete or use of a rendering product is recommended by the supplier.

The low temperature condition is an issue since most instances where high strength hydrostatic shaft liners are required; these often also involve shaft sinking conditions where ground freezing is used. For instance, the potash mines in Saskatchewan are a good example. The low temperature issue was studied by the author through a pilot scale proof of concept test program completed in 2011 (Ouellet, 2011). Results of these tests were presented in the SME Conference of February 2012 in Seattle (Stanley et al, 2012). The test results demonstrate that the membrane system, combined with the appropriate shotcrete mix, can be used in frozen shaft conditions. Using shotcrete as a substrate on frozen ground conditions was done successfully, demonstrating the effectiveness of the approach. The following Figure 2 illustrates a data sample of temperature profile over time that was obtained during this proof of concept testing in 2010. Laboratory testing was conducted on core samples of the shotcrete to determine its compressive strength. The compressive strength of the samples ranged from 40 to 75 MPa. These tests showed that the quality of the cured shotcrete, even after being applied and curing on a frozen surface was excellent.

In studying typical shaft sinking cycles for a concrete jump formed operation, it was estimated that the preparation, application and testing of the complete membrane system had to be achievable within a six hour window. In order to resolve this issue, the lead author proposed using shotcrete to create a warm layer over the frozen excavation surface. The objective was to provide a surface with a temperature above +10 ºC for duration of at least 6 hours. Experimental results, such as the sample illustrated in Figure 2, demonstrate that a suitable surface temperature can be achieved for duration of up to 20 hours in frozen shaft conditions. The test program included two different shotcrete mixes, three different thicknesses and various dosages of accelerators. Without membrane, tests results showed that the target surface temperature (+10 ºC) could be maintained for:

- 75 mm produced 3 hours
- 100 mm produced 5 hours
- 150 mm produced 6 1/2 hours

When the first membrane coat was applied (yellow layer) a sharp temperature increase was observed in the shotcrete. Monitoring the temperature over time it was observed that a suitable surface temperature could be maintained for more than 20 hours. Considering this result, the 6 hours requirements could be reduced down to 3 hours. A time within which primer and first coat needs to be applied. This suggests that the shotcrete thickness required could be reduced to 75 mm.

Providing the shotcrete surface is relatively smooth, the testing showed it could be successfully sprayed on at the cost of an added layer to the normally sprayed on two coats (yellow and white) system. The supplier of the membrane product is considering development a filler/sealer product that could avoid the floating requirement. They also are looking into using alternate products as primer that could be used at lower temperatures than the +10 ºC. The main issue identified was with the primer component which is a water based system. By developing a product better able to withstand cold temperature, the flexibility of the membrane system for frozen ground conditions could be further improved.

Considering the technical advantages and disadvantages of the two products considered we came to the conclusion that the Integritank® HF product offers the best potential for this application. The integrated quality assurance program including integrity membrane testing at application time was paramount in our final selection. The high durability of the material made it an interesting product able to better withstand the harsh conditions of shaft sinking.

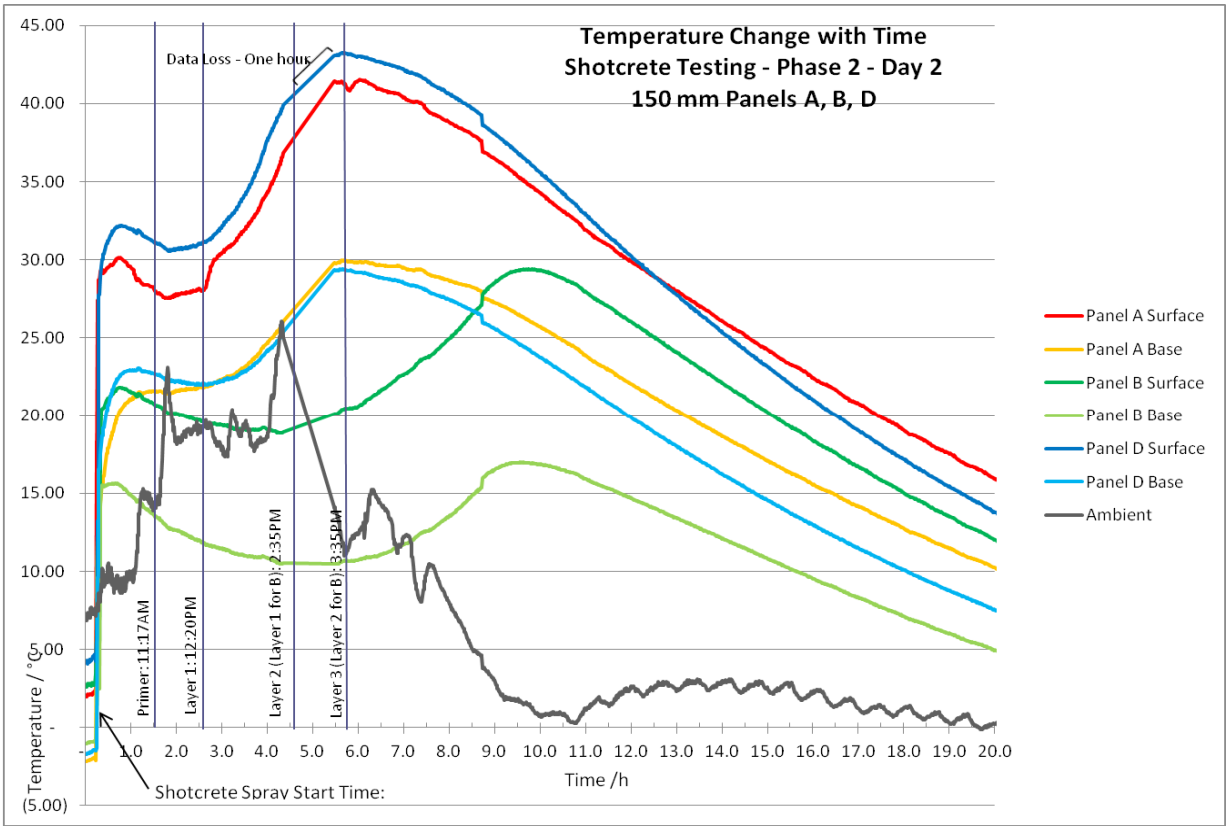

Figure 2 - Temperature profiles of shotcrete on frozen rock, (Ouellet, 2011)

3. NEW COMPOSITE MEMBRANE DESIGN

The membrane material requires a subgrade of shotcrete in order to smooth the irregular rock excavation surface. In the case of a frozen ground situation the shotcrete must serve two functions. The first function is to produce an application surface suitable for the membrane. The second one is to generate a sufficient amount of heat to counterbalance the freezing conditions of the rock wall and maintain a suitable surface temperature for the duration required to construct the membrane.

The sprayed-on membrane creates the water barrier in the same way as the welded steel membrane in the classic composite liner design. For design, the load acting on the liner must be considered. The shotcrete primary liner was not considered to be a contributing structural component for resisting the hydrostatic pressure. The designer must assume that water can reach through the shotcrete layer and act directly on the membrane. Consequently the inner concrete liner must be designed to sustain the full hydrostatic loading. The total load acting on the liner includes a ground load component. For this component of the load, the primary shotcrete liner could be considered in the calculation. But, depending on ground conditions, the major load component is usually the hydrostatic head.

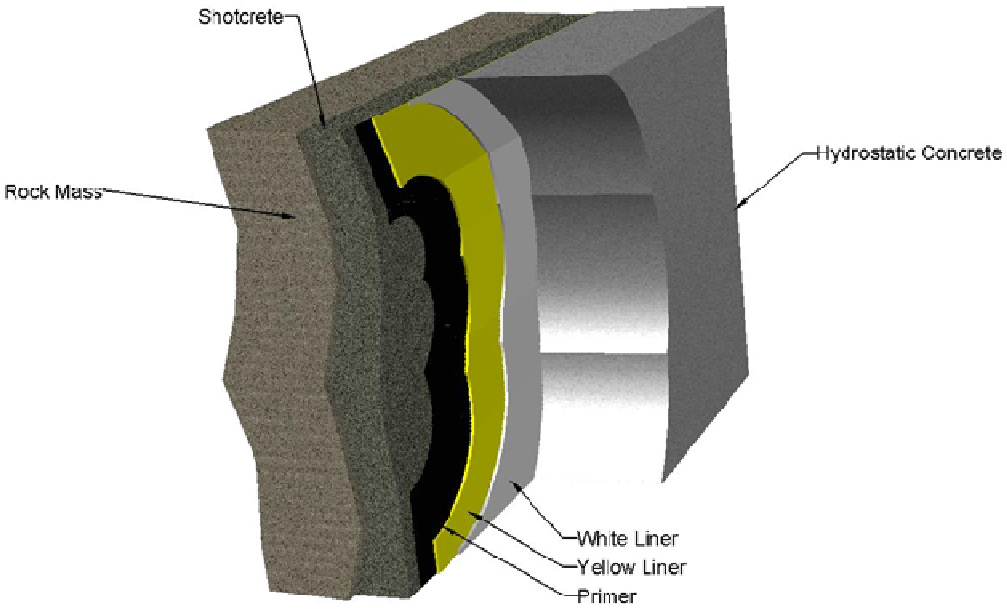

Figure 3 - Composite liner concept with sprayed on membrane

Figure 3 illustrates a schematic view of the proposed composite liner design. In this example, a simple hydrostatic concrete liner design is considered. Actually the final hydrostatic liner does not need to be simply concrete. Various combinations could be considered where high stresses are expected. An inner bolted steel component could be added to keep the overall thickness of the liner smaller. The new membrane could be combined with any style of composite design. The extreme flexibility a sprayed-on membrane provides to the construction process allows accommodating diameter and liner thickness changes very easily.

A value engineering exercise was conducted comparing, for a given mine shaft project, the cost for constructing a hydrostatic liner with tubbing liner, a conventional composite steel/concrete liner and the new design proposed here. This exercise showed that, for the same shaft, the new liner concept was saving $50M. For instance, the cost of tubbing segments alone in this case would have been $50M where the membrane (installed) was estimated at $5,5M.

4. CONCLUSIONS

The authors developed a new composite liner concept incorporating the most recent technologies developed in the civil engineering tunnelling industry. Supplementary testing demonstrated that the sprayed-on membrane developed in tunnelling can meet deep shaft lining requirements in terms of hydrostatic pressure, design life and crack bridging capabilities. The proposed new concept provides a much more advantageous alternative to the previous technologies relying on cast iron or welded steel components. In the majority of cases where fully hydrostatic shaft liners are required, ground freezing is used for sinking. Although water proofing sprayed-on membranes suitable for below freezing temperatures exists, their formulation renders them unsuitable for underground applications.

The authors, through the experimental work described in this paper, developed a system that makes possible the use of the existing membrane products in frozen ground conditions. It was shown that suitable temperature conditions could be provided through the application of a shotcrete layer over the

frozen excavation walls. The hydration phase of the specially formulated shotcrete produced enough heat to sustain the required application temperature for a time window well in excess of the minimum time requirements. It was observed that the application of the first Integritank® HF layer exothermic reaction actually boosted the shotcrete temperature maintaining the required surface temperature for more than 20 hours.

The most important conclusion is the cost effectiveness of the proposed liner design (Eddie et al., 2010). When comparing to a conventional welded steel composite design or a cast iron tubbing design we could expect a sinking ratio more than twice as fast with the sprayed-on membrane. When costing a shaft using the design proposed in this paper we see a huge difference. The sprayed-on membrane system is one order of magnitude less expensive than the tubbing liner system or the conventional steel composite liner.

Stirling Lloyd has now developed a new primer that can be used down to 0 ºC and are working in lowering Integritank® HF application temperature range. Further work that should be undertaken is combining a filler material to the primer formulation that would reduce the amount of material required as well as the application time of the membrane. Presently, recommended practice in tunnelling applications is to float the surface of the shotcrete or apply a rendering layer on top of it. This insures a smooth surface ideal for sprayed-on membranes. Combining the primer with rendering filler would improve cycle time in the sinking process.

5. REFERENCES

STANLEY, T. B.; OUELLET, J.; HATLEY, J. 2012., New Waterproof Shaft Lining Concept for Frozen ground Applications. SME Conference, February, Seattle, USA, 8 p.

OUELLET, J., 2011. Proof of concept testing program for a sprayed on membrane shaft lining system in frozen ground. Technical report TMCC for Cameco Corporation, 250 p.

EDDIE, C., HARPER, M. & PSOMAS, S., 2010. Sustainable tunnel linings – Asset protection that will not cost the Earth. Proceedings of the North American Tunnelling Congress 2010.

HARPER, M., 2011. Sprayed Waterproofing Membranes – The Future. 6th International Symposium on Use of Wet-Mix Sprayed Concrete for Underground Support. September 2011, Tromso, Norway, p 176-189.

Comparing the Behaviour of Modeled Paste in 2D and 3D, Using Both Simplified and Complex Stope Geometries

Ryan L. Veenstra
University of Toronto
Will F. Bawden
University of Toronto
Murray W. Grabinsky
University of Toronto

ABSTRACT: This paper presents a modelling study of a cemented paste backfill in an underground stope. The model was developed to help provide a better understanding of what is happening in the stope during the filling stage of the stope. In order to do this, the model incorporates the paste rise rate, stope geometry, and time-dependent input parameters. This paper looks at the effect of geometry in two parts. The first part compares a series of simple rectangular stope models. These models differ in size both in two and three dimensions. The second part compares the results of four 2D models together and then to the field instrumentation data. Part of this section introduces the geometry and instrumentation within the test stope.

1. INTRODUCTION

Cemented paste backfill (CPB) is a popular backfilling method for underground mining operations due to its delivery speed, its versatility, and its engineered strength. It also decreases the area needed for and the degree of risk associated with surface disposal. However, understanding of how CPB behaves in an underground opening, particularly during the early curing ages is limited. This lack of understanding poses several problems for mining engineers including how to optimize the design of backfill barricades and backfilling procedures. For instance, most mines use a two staged pour which is divided into a plug pour and a final pour. There is a delay in-between the two pours, usually 3 to 7 days, to allow the paste in the plug to harden and gain strength. This delay and subsequent paste strengthening is used to protect the backfill barricade when the rest of the stope is filled. There is a significant potential for cost savings if stope cycle times can be reduced or continuous pour procedures can be adopted. Increased understanding of CPB behaviour would also decrease the uncertainty associated with the barricade fences themselves, allowing for better and cheaper fence designs. However, these cost savings cannot be realized unless there is a reasonable and reliable method for determining what stresses the backfill barricade will experience. These stresses are dictated by a range of parameters including: binder content, binder type, tailings type, additional aggregates, filling rate, stope geometry, etc.

This paper will examine and discuss modelling results obtained from a paste-fill model developed by the authors using Itasca's Flac3D code (Itasca, 2009). This model attempts to incorporate the time-dependent strength behaviour of the paste by incorporating both stope filling time and paste curing time into the model. However, numerical modelling only provides a starting point for investigating in-situ pressures within the stope and at the backfill barricade. What is then needed are in-situ pressure measurements, obtained from within a test stope, which can be compared with the modelling results. Fortunately the authors, due to a larger University of Toronto (UofT) field project, have access to in-situ monitoring data from several test stopes obtained from several mining operations (Thompson et al., 2010).

The question this paper will examine is how the stope geometry affects the modeling results. The first section of the paper will compare simple geometrical changes in hypothetical stope geometries. These

comparisons will examine the effect of increasing stope size in both 2 and 3 dimensions and what this does to the baseline results.

The second section will use the geometry and instrumentation data from one of the actual test stopes involved in the larger UofT field study. The actual geometry of the stope was obtained from a cavity monitoring survey (CMS) taken after the stope was mucked but prior to backfilling. Two dimensional models were run using both the complex and simplified (based on the complex) geometries. The results from these models were compared to each other and with the actual instrumentation results to determine: 1) how close the modelled results are to the instrumentation results and, 2) what is the difference between using the complex and simple geometry. Note that the same paste parameters were used for both the first and second part. For more information on the model refer to Veenstra et al., 2011.

2. SHAPE MODELLING STUDY

In this section of the paper all inputs besides geometry will remain the same. This means that the rise-rate and input parameters for the paste will be the same for all models. The initial 2D stope geometry will be 6m wide by 17m high. Figure 1 presents the first set of modelling results, where the width of the stope is increased to twice and then 4 times the original width (12 and 24 metres). Part a) of Figure 1 is a graph showing the results for a common measurement location while part b) contains stress contours taken from the model. Note that the contour plots are for the right half side of the models, mirrored at the centerline of the stope.

Note that for all stopes the measurement location was along the centerline of the stope at 2m height. These locations are denoted in Figure 1b) by a red and yellow dot on each plot. Also note that the hydrostatic stress rise of the stope is shown by the thin linear black line on the graph. This line was determined by using the density and height of the paste.

The stress curves in the graph show that there is a large difference between the 6 metre stope model and the 12 and 24 metre models, while there is less difference between the 12 and 24 metre models. The relationship between the curves is what was expected and indicate that, as the stope width increases, the influence of the frictional zone between the rock and the paste is diminished. This means that the stresses within the stope will show less arching in wider stopes than in narrower stopes.

The contour plots are arranged by column, with the first column containing the pore water pressure (PWP) contours, the second the vertical stress (VS) contours, and the last the horizontal stress (HS) contours. These contours reflect what was seen in the graph. All three of the contour plots for the narrower stope show significantly less stress than the wider stopes. There is one interesting result shown in all three HS contour plots. All three show the creation of a low stress bulb near the lower corner of the stope. This bulb is probably due to proximity of the corner causing a decrease in stress.

Figure 2 shows the results of the 3D modelling comparing how the stresses change as the length of the stope is increased. Again these results were taken from the centre of the x-y plane within the stope and at a height of 2 metres. Part a) of the figure presents the results for the 6m wide stope while part b) presents the results for the 12m wide stope. Note that only the HS along the short axis (either the 6 or 12 metre width) is shown. The thin black lines on both graphs are the hydrostatic stress rise rates of the stope.

These plots have similar trends to what was observed in the 2D model results. In this case, the smaller square stopes experience less stress than the bigger stopes. It is also observed that the narrower stopes have more of an arching response than the wider stopes. However, the most interesting comparison is between the 2D results and the 3D results. In both a) and b), the 2D curves have higher values than the

3D curves, indicating that only when 3D lengths are considerably larger than the width, do the 3D model results equal those of the 2D model. In the case of the 6 meter model, the 3D model must have a length that is 4 times the width in order to exhibit similar results as the 2D model. For the 12 metre wide stope, the 3D length must be twice the width. This indicates that the aspect ratio of the stope will affect the stresses within the stope but also indicates that the aspect ratio relationship is not linear. Therefore, a narrow stope, in order to not be affected by arching off the stope sidewalls, needs a longer 3D length than a wider stope.

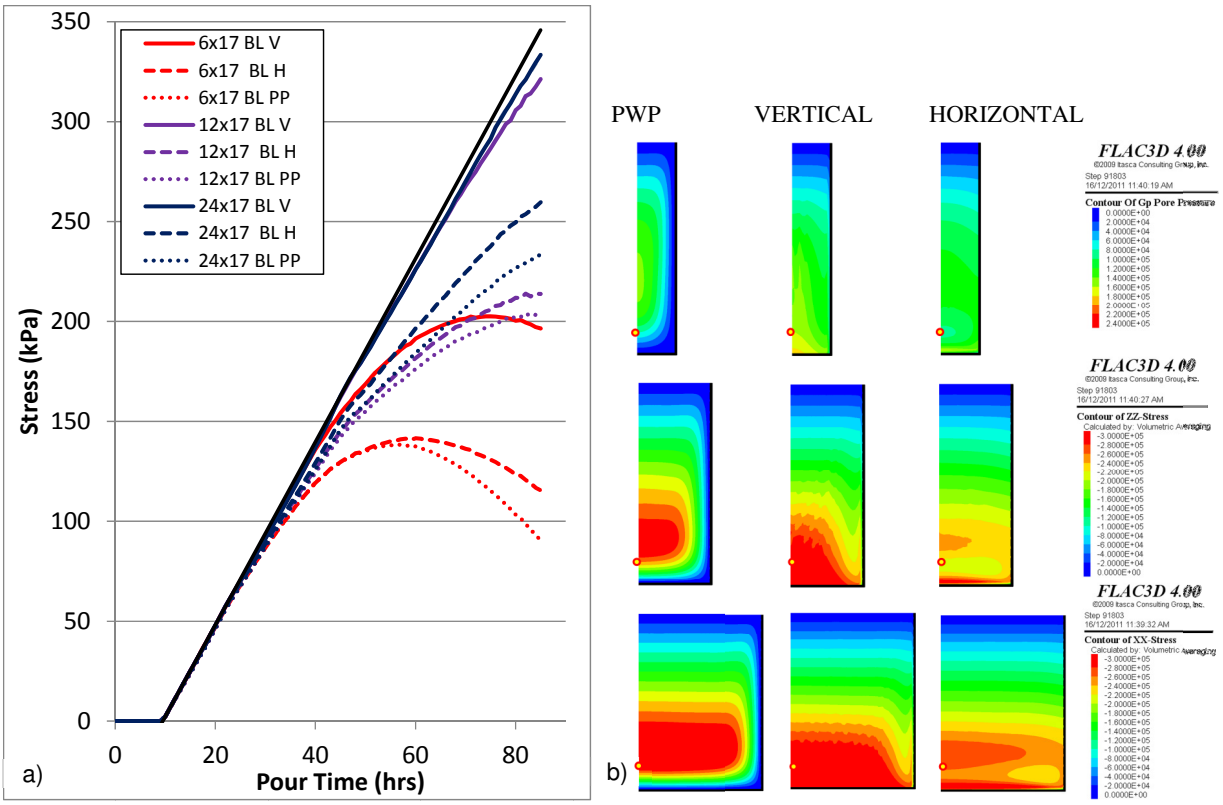

Figure 1 - Results from 2D Width Study
a) Measurements from Common Location
b) Stress Contours

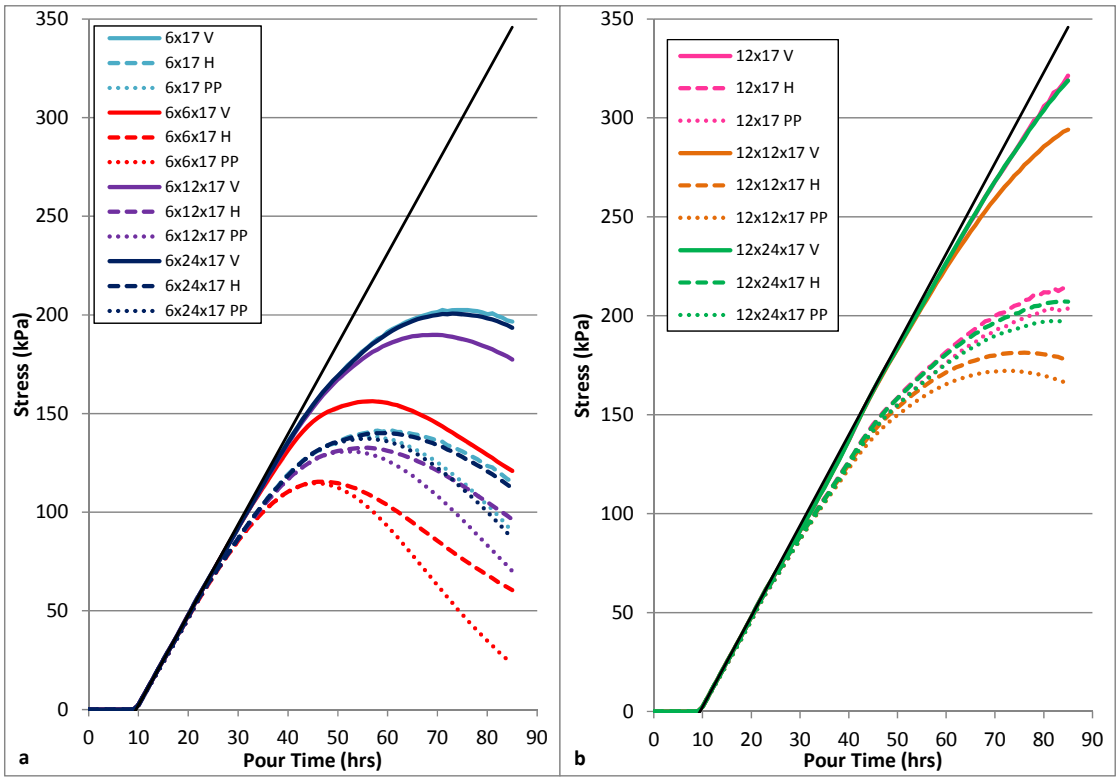

Figure 2 - Results from 3D Width Study a) 6 metre wide stope b) 12 metre wide stope

3. INSTRUMENTED TEST STOPE STUDY

The next few paragraphs will present the important details of the test stope used in this modelling study. These include the geometry, instrumentation details, and rise rate of the stope backfilling. Figure 3 shows four views of the test stope from various angles. The stope geometry was created from a CMS of the test stope.

There are two types of instrument systems shown in Figure 3. The first system is denoted by red boxes. These consist of instrumented wire cages that contain 3 total earth pressure cells (TEPCs) and a piezometer (PZ). The three TEPCs were installed in the three orthogonal directions (x, y, and z). A photograph of a cage is shown in Figure 4. The other instrument configuration was installed on the inside of the barricade and is shown as green circles in Figure 3, with each containing a TEPC and a PZ. The cages were numbered from 1 to 5 moving into the stope, meaning that the cage closest to the barricade is 1 and the furthest cage was 5. The location of the barricade and the cage numbers are labeled on Figure 3.

In order to model the paste accurately, the rise rate within the stope needed to be determined. This could be done several ways. The first was to determine the volume per metre height from the stope geometry in Figure 3. By using these values and the pumping rate, the rise rate could be determined. The second was to determine the stress rise rate for the instrument cages. It was found that using the first method could determine the approximate rise rate while the second method could be used to fine tune the rise rate value. Figure 5 shows the rise rate used to model the paste in the test stope. This figure shows that the stope's rise rate is fairly constant at the start and at the finish of the pour time that also included a 73 hour shutdown starting at around 20 hours.

Once the basic information about the stope is known (mainly stope geometry, rise rate, and input parameters) the model can be run. For this paper four different stope geometries were modelled and all were in 2D.

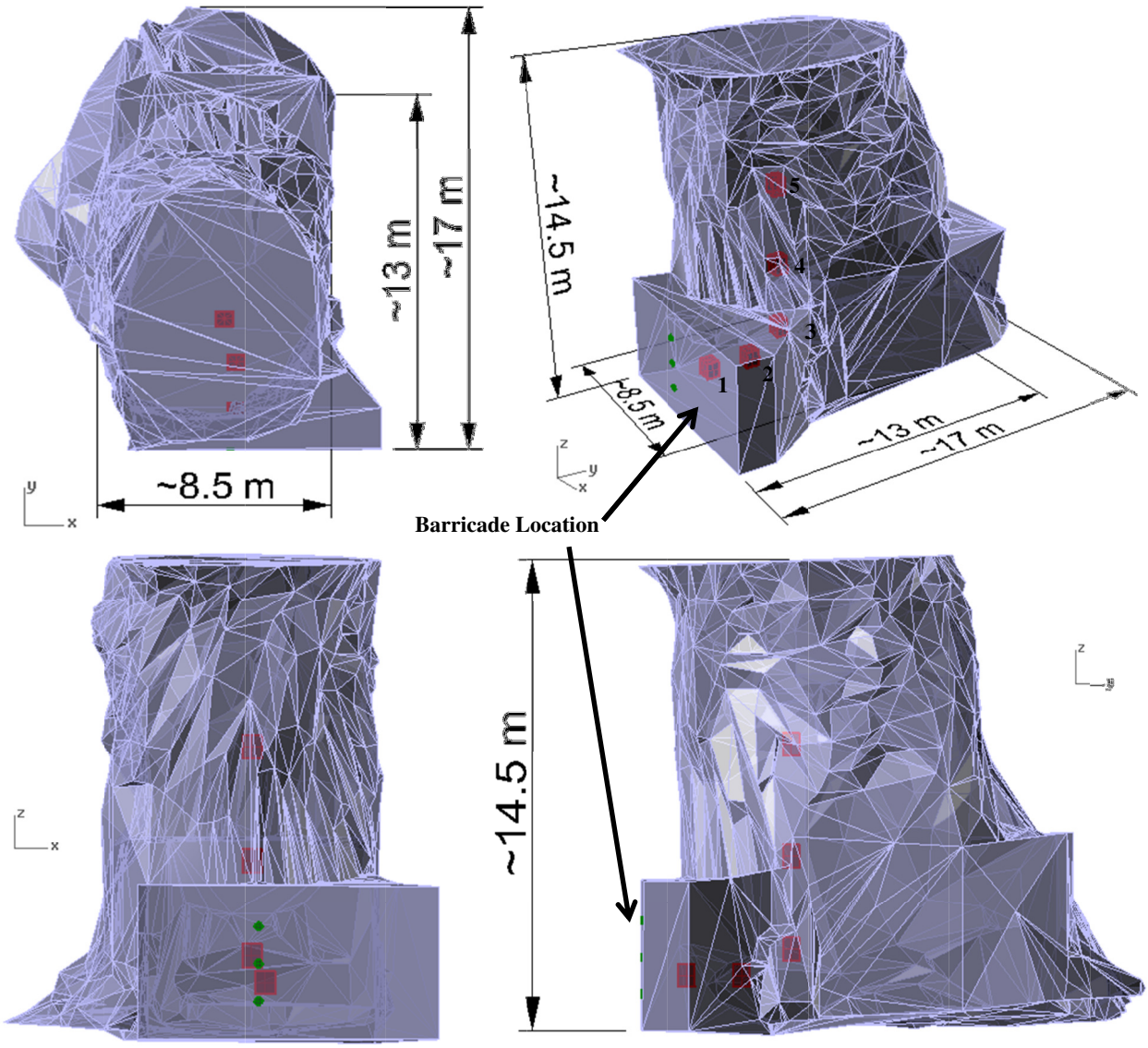

Figure 3 - Stope Geometry with Instrument Locations

Figure 6 shows where these geometries were located with blue denoting the simple model and green showing the complex geometry. The intersection of the x and y planes coincides with the centerline of the three cages that were strung vertically in the stope. The models were set up this way so that direct comparison to those three cages would be possible. Additionally, for the y direction (or long axis) models the two horizontal cages and the barricade instruments could be compared. However, in order to place the instruments in the model they needed to all be placed along the same y plane.

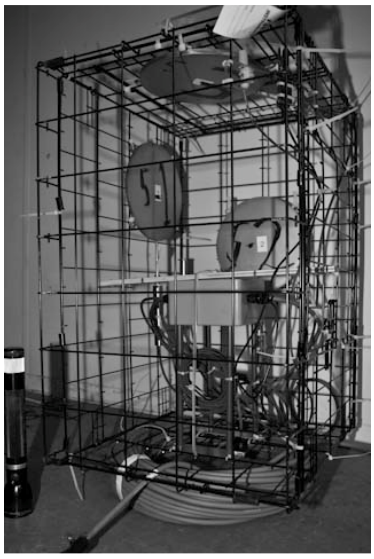

Figure 4 - Test Stope Geometry

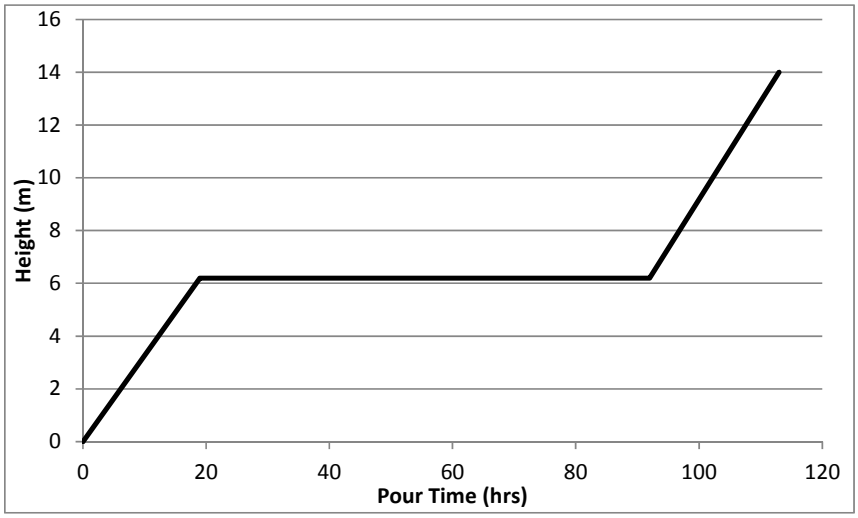

Figure 5 - Test Stope Rise Rate

All of the models were then run using the same input parameters except for geometry. Figure 7 show the results from the different models. This figure shows the results from each cage, in both directions if applicable, and the in-situ instrument measurements.

The first result that these plots show is that the model is capturing the general trends observed in the instrumentation results. All of the cage and the fence curves show very good agreement with the model over the first pour period. The model also captures the stress decrease seen in the instrumentation due to the pause in the pour cycle. However, there are some differences between the amount of decay shown by the instrumentation and the modelling results, with the model generally showing less stress decay than the instrumentation.

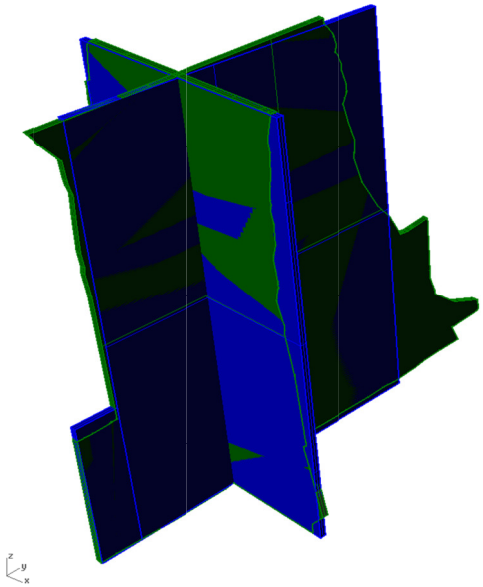

Figure 6 - Model Geometry

There is a larger discrepancy once the paste starts to fill the stope after the pause. In all cases the model has a more vigorous response to this new loading than the instrumentation. It is hoped that a parameter calibration exercise could help establish improved input parameters to allow the model to better replicate the instrumentation trends more closely but this was not carried out for this paper.

There is very little difference between the four stope model results. In general the complex models had slightly lower stresses than the simple geometries and the y direction models had higher stresses than the x direction models. These trends make sense as the complex models would provide more arching due to their irregular surfaces and the longer models will be less influenced by arching due to the increased distance between the walls.

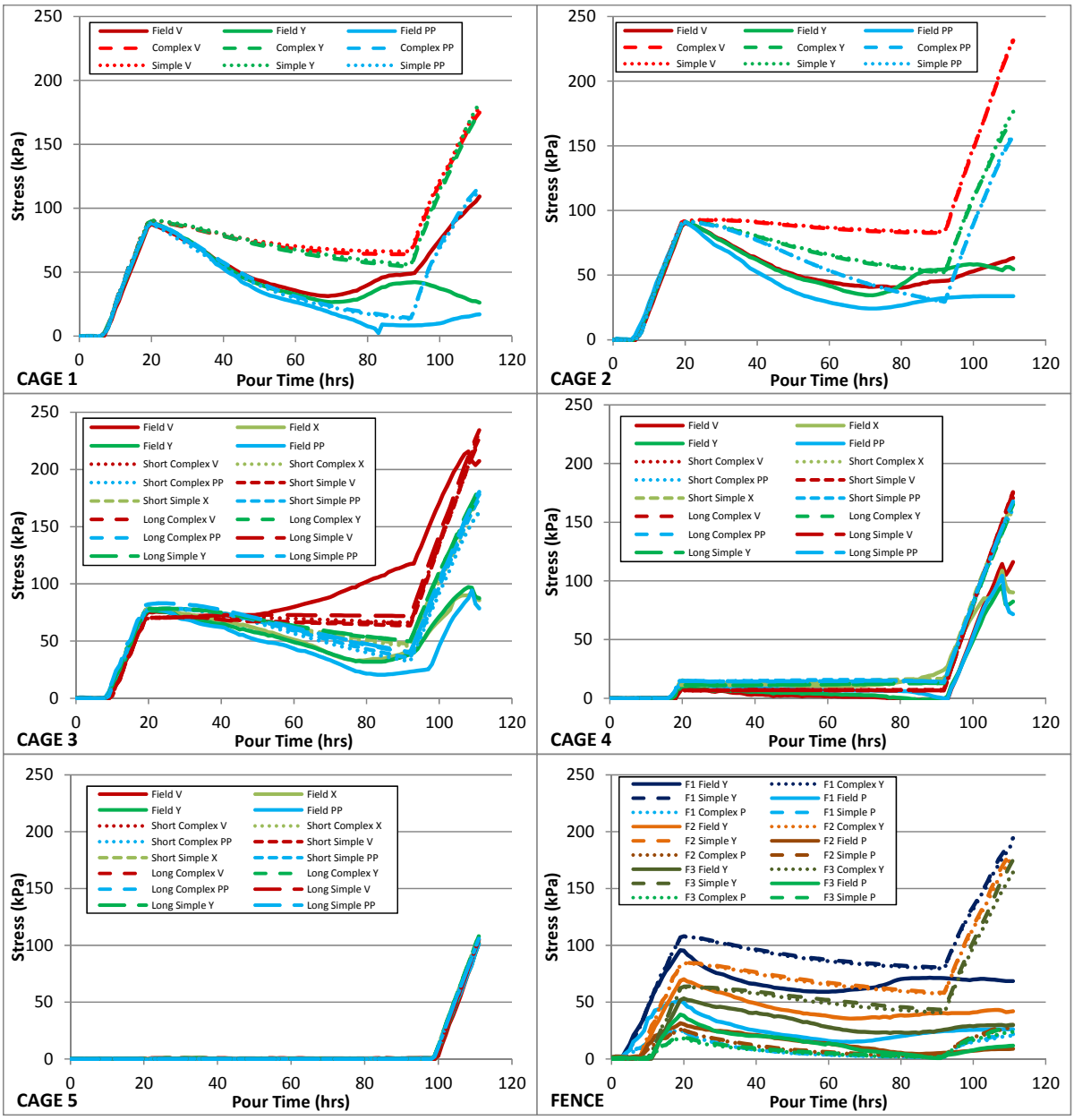

Figure 7 - Model Results By Cage

4. CONCLUSIONS AND RECOMMENDATIONS

It was found that the modelling results are affected by the stope geometry, particularly for the models described in Section 2. These changes were due to the large differences in the stope geometries modelled. However, the impact of geometry was more subtle when the simple and complex stope geometries were used. As Figure 7 shows, there is a difference, but it is very small. This figure also shows that the model captures the trends observed by the field instrumentation but this fit could be better, particularly during the last filling stage.

There are two recommendations moving forward. The first is to conduct a calibration study with the hope of more closely matching the modelling results to the field instrumentation results. The second would be

to conduct 3D modelling of the stope using the actual cage and instrument positions to see if the out-of-plane influences, not captured in a 2D model, have a large impact on the results.

5. ACKNOWLEDGEMENTS

Matt Pierce and Jim Hazard of Itasca Consulting for help with Flac3D, Summer Students Robin Malik, Michelle Moore, and Research Associate Dragana Simon for assistance with the lab testing, and Kemal Karaoglu for assistance with field work.

6. REFERENCES

ITASCA CONSULTING GROUP INC., 2009. FLAC3D: Fast Lagrangian Analysis of Continua in 3 Dimensions. Version 4.0. ICG, Minneapolis MN, USA.

THOMPSON, B.D, BAWDEN, W.F., and GRABINSKY, M.W., 2010. In-Situ Pressures in Cemented Paste Backfill – A Review of Fieldwork from Three Mines. International Symposium on Paste and Thickened Tailings, Paste2011, Perth, Australia.

VEENSTRA, R.L., BAWDEN, W.F., GRABINSKY, M.W., and THOMPSON, B.D., 2011. An Approach to Stope Scale Numerical Modelling of Early Age Cemented Paste Backfill. 45th US Rock Mechanics Geomechanics Symposium, ARMA, San Francisco, CA, USA.

Effect of Backfill Placement Method on Its Stability: A Dynamic Modelling Case Study

Muhammad Zaka Emad
Department of Mining and Materials Engineering, McGill University
Hani S. Mitri
Department of Mining and Materials Engineering, McGill University
John G. Henning
Goldcorp Inc.

ABSTRACT: Cemented rockfill (CRF) is a mixture of rock aggregate and binder slurry. It is a stiff backfill, it is fast curing, its operation is simple, placement rate is reasonably high and no drainage is required. The main demerit of CRF is failure of exposed faces causing ore dilution, which can be associated with the fill placement method. This paper discusses the effects of two placement methods being practiced by mines and numerical modelling is used as a tool to evaluate stability of the backfill column. In the first method, practiced in longitudinal retreat mining of a narrow vein deposit, the rockfill is hauled and dumped into the stope with a LHD scooptram. Once dumped, cement slurry is sprayed into the stope. In the second method, a raise situated centrally above the mined stope is used to convey already mixed CRF into the stope. Stopes are mined out transversely in primary and secondary blocks in a sublevel stoping system. Problems of poor mixing in combination with both placement methods are discussed. The two backfill placement methods are analyzed for blast induced vibration damage using the dynamic Flac3D modelling technique accounting for rock mass and fill damping characteristics, and a pressure wave is used to simulate the blast vibrations. Fill heterogeneity has also been considered for the two cases and results are compared.

1. INTRODUCTION

Backfilling is a process of achieving ground control and to reduce ore dilution. Cemented rockfill in particular is made by mixing cement slurry with rock aggregates from either development work or quarries (Yu, 1989; Hassani et al., 1989; Annor, 1999; Archibald, 2003). CRF as a backfill has the greatest stiffness, it has a simple operation, requires no drainage due to low water to cement ratio in the cement slurry, it has a fast curing rate and has a relatively higher placement rate relative to other backfill types. The stiffness and strength governs the stability of CRF, and a slight reduction of either may lead to ore dilution due to backfill being exposed for greater recovery of ore. The strength and stiffness of CRF are administered by factors like cementation, curing time, aggregate grading, aggregate shape, interlocking of aggregates and placement method (Yumlu, 2001; Kurakami et al., 2008; Farsangi, 1996). Generally, there are two placement methods for CRF that are by backfill raise placement and by dumping backfill from upper access drifts (Henning, 1989). The first method comprises CRF placement through raises excavated from upper levels as shown in Figure 1, and the raise is later used as a reliever for blasting purpose. The second method of CRF placement is by dumping it from the upper stope access drift, as shown in Figure 2. If the aggregate is not well mixed with cement slurry, the cement slurry will make a pool away from the dumping point, as shown in Figures 1 and 2. The binder concentration zone will have more strength and the rest of the column will experience a reduction in strength.

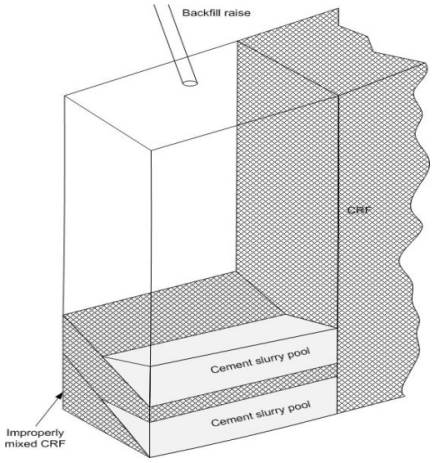

Figure 1 - CRF Placement by backfill raise

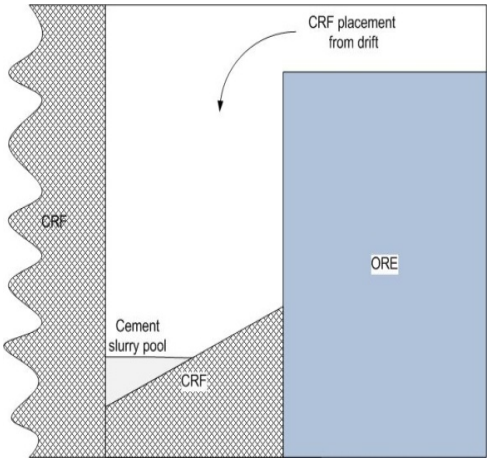

Figure 2 - CRF Placement by access drift using scoop tram

The reduced strength zone may fail, especially when CRF is exposed and blasting adjacent to the CRF column occurs. The two methods can have an impact on CRF strength and stiffness, and will eventually increase ore dilution. This paper presents the effect of placement methods in combination with improperly mixed CRF columns on CRF stability. The case study used for this work is a gold mine from Northern Québec, Canada.

2. CASE STUDY

An underground gold mine is used as a case study for this work, located in northern Quebec. A steeply dipping tabular ore body (with a dip of 77 degrees) was mined by the open stoping mining method with delayed backfill. The whole ore body was divided into primary and secondary stopes with sublevels every 30 meters. To mine a primary stope a 1.2 meter slot is created and later enlarged using parallel hole blasting, and a fan drilling pattern was used for secondary stopes. After blasting, the ore is mucked from drifts, normal to the ore body strike. CRF is placed from a top access drift or from a backfill raise right after mucking of the ore. The cavity monitoring surveying system (CMS) (Miller et al., 1992) was used for monitoring the stope profiles and to compute stope over break in ore, rock and backfill. To analyse a secondary stope for blast induced vibration damage, an isolated area of the case study mine was chosen at a depth of 1084 meters. The longitudinal section of the stope is shown in Figure 3.

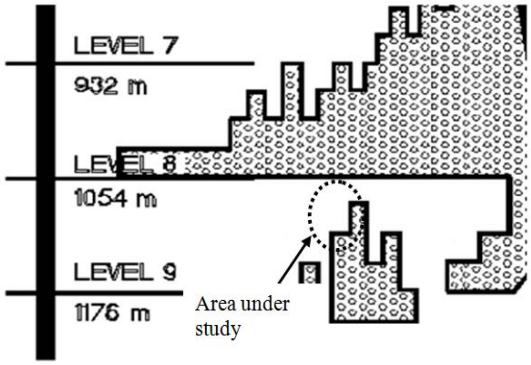

Figure 3 - Longitudinal section of modelled area

3. NUMERICAL MODELLING

A CRF column with different strength zones was modelled using Flac3D (Itasca) to demonstrate the effect of placement methods combined with improper CRF mixing. Blast load is applied using the dynamic module of Flac3D. The finite difference mesh was also tested for sensitivity analysis as explained in Section 3.1. The mesh is shown in Figure 4.

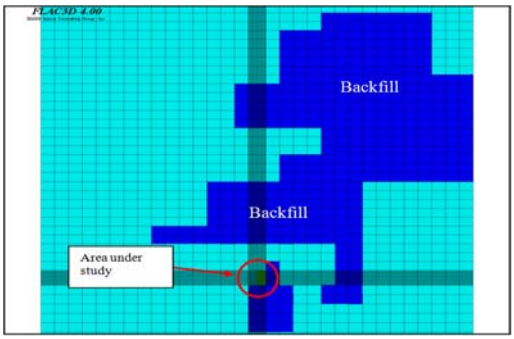

Figure 4 - Longitudinal section of the numerical model (Emad et al., 2011)

3.1 Static Model

A mine model was set up using Flac3D, following the primary and secondary stope mining and backfilling. The area under study is generated with a fine mesh and the model boundaries were set at ten times the observation zones. Model boundaries were fixed in all directions for displacements. The ore body varied in thickness ranging from 4 meters to 10 meters, and the stope strike length, width and height were designed to be 15 meters, 8 meters and 30 meters, respectively, for the modelled stope. Elastic model and material properties for the hanging wall, footwall, ore (Henning, 1998) and CRF (Hassani and Archibald, 1998) assigned to the model are given in Table 1 and Table 2, respectively. Gravity load or static load was initiated along with the horizontal stresses (Arjang, 1988), with stress tensor values being given in Table 3, and the model was run for equilibrium. An elasto-plastic model was then set up and the model was solved again for equilibrium. After approaching equilibrium, stopes were mined and backfilled according to the mining and backfilling sequence shown in Figure 5, and the model was solved to get static modelling results.

3.1.1 Sensitivity Analysis

Sensitivity analysis is essential for validation of mesh density and to ensure consistency in results. Sensitivity analysis was performed by constructing meshes with different mesh densities (number of elements), and then removing a large box (with l x w x h = 12 m x 8 m x 32 m) and solving for elastic equilibrium. On reaching the equilibrium state the displacements at the midpoint of the exposed face in the box were recorded and plotted against the number of elements and analyzed (see Figure 6). It is evident from the figure that the number of elements in the mesh has almost no effect on displacements above a value of 1195632 zones.

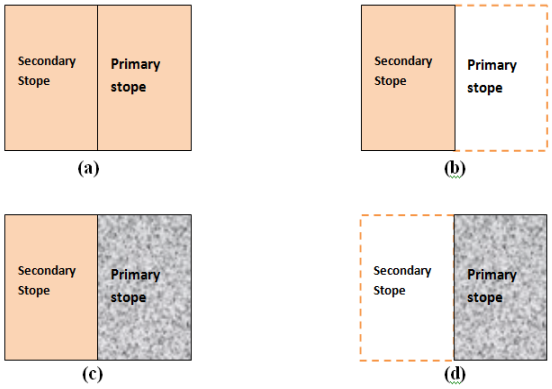

Figure 5 - Mining sequence - (a) Planned primary and secondary stopes, (b) Excavated primary stope, (c) Primary stope after backfilling, (d) Secondary stope mined and primary backfilled stope is exposed (Emad et al., 2011)

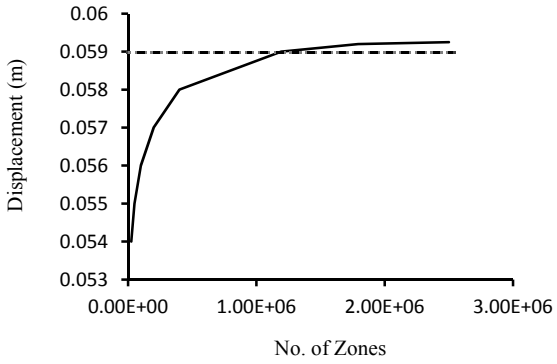

Figure 6 - Displacement versus number of zones in Flac3D mesh

Table 1 - Material properties for the case study (Henning, 1998)

Property	**Ore**	**Footwall**	**Hanging-wall**
E_{rm} (GPa)	115	49	31
υ	0.1	0.15	0.21
Tensile Strength (MPa)	6.7	4.0	2.2
Cohesion (MPa)	11.5	4.3	2.6
Angle of internal friction (°)	48	39	38
Dilation angle (°)	12	9.8	9.5

Table 2 - Geomechanical properties for CRF (Hassani and Archibald, 1998)

Property	**Value**
E_{rm} (GPa)	2.5
υ	0.35
Tensile Strength (MPa)	0.3
Cohesion (MPa)	0.1
Angle of internal friction (°)	35
Dilation angle (°)	0

Table 3 - Stress tensor values for the case study (Arjang, 1988)

Stress Tensor	Value	Orientation
σ_1	$2.24*\sigma_v$	Normal to ore body strike
σ_2	$1.50*\sigma_v$	Parallel to ore body strike
σ_v	$0.027*$depth	

3.2 Dynamic Model

To perform dynamic analysis, model boundaries were transformed from fixed to viscous boundaries to avoid any reflections of blast loading from the boundaries, and 15% material damping was also included for this analysis. The blast load was applied as a direct input of dynamic load (stress) (Saharan, 2004) on the walls of the secondary stope including the exposed CRF face. A peak pressure of 45 MPa (Gool et al., 2007) was applied over a period of 0.0056 seconds and the response of the CRF column was monitored for 1 second. The results present the state of the CRF column after 1 second. Dynamic analysis is highly recommended as the blast vibrations on the surrounding material may produce a strain rate of $10^2 – 10^4$ per second compared to the strain rate produced by static loading (less than 10^{-5} per second).

4. RESULTS AND DISCUSSION

Improperly mixed CRF may develop a cement slurry pool away from the dumping point, as discussed earlier and shown in Figures 1 and 2. The cement slurry pool will have high strength compared to the rest of the CRF column. In such a case there will be different sub columns within the CRF mass having high and low strength regions. High strength columns were assigned twice the CRF properties and low strength columns were assigned one-half of the CRF properties. The CRF failure in the modelled homogeneous stope was compared with the ore dilution volume from the CRF computed from the cavity monitoring survey (CMS), and it was found that the two volumes are equal (361 tonnes). The following sections present results for static and dynamic loading on the CRF column, considering homogeneity and heterogeneity caused by the combination of improper mixing of the CRF and the placement method.

4.1 Homogeneity in CRF Column

4.1.1 Gravity or Static Loading on CRF

Before modelling heterogeneity in the CRF, it was assumed that the CRF has been mixed properly before placement and hence the CRF column is assumed to be homogenous. The model was generated and executed while taking into account homogeneity in the CRF. The contours of vertical stresses and yielding after static analysis are presented in Figures 7 and 8 respectively. Figure 7 presents vertical stress contours and it did not show any zones of relaxation and Figure 8 presents yield contours, showing no yielding or failure in the CRF. Yield is based on the factor of safety (ratio of strength to stress), and for this work a threshold yield value of 0.9 and below are considered as failure in the CRF.

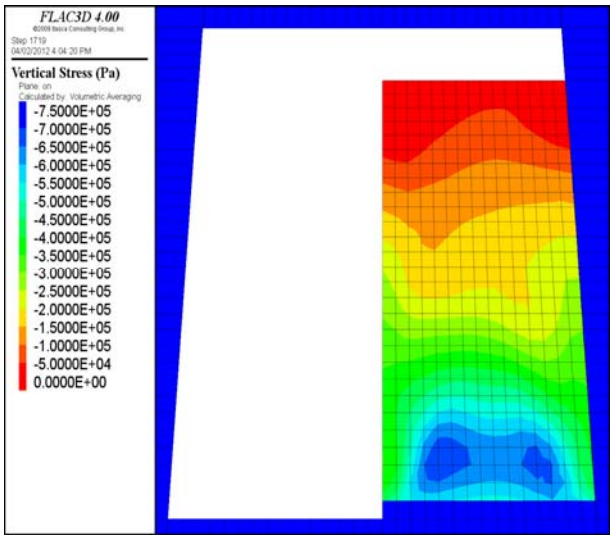

Figure 7 - Vertical stress contours for a homogeneous CRF column after static analysis (Emad et al., 2011)

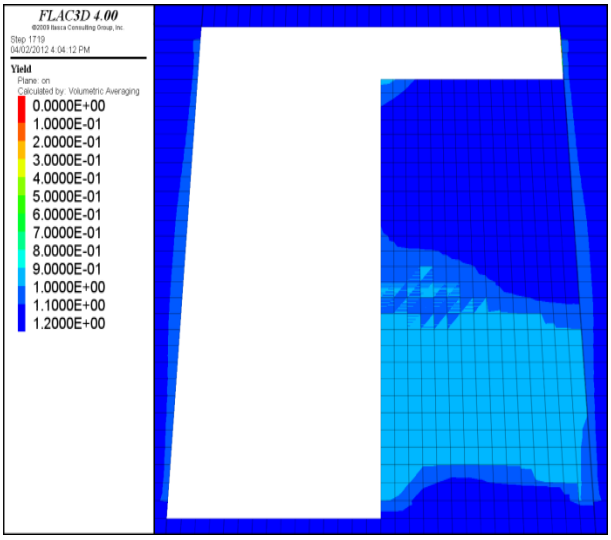

Figure 8 - Yield contours for a homogeneous CRF column after static analysis (Emad et al., 2011)

4.1.2 Blast Loading or Dynamic Loading on CRF

The CRF column was applied with time varying stress load using the Flac3D dynamic module to produce inertial forces due to blasting adjacent to the CRF. The dynamic modelling conditions discussed in Section 3.2 were applied and the model was solved for a period of one second after blasting. Figures 9 and 10 present vertical stress contours and yield contours after solving the model for a one second interval. In Figure 9 it is notable that there is a tensile stress development at the top of the stope, which indicates a zone of relaxation in the CRF causing wedge failure at the top of the CRF column. The yield contours after dynamic analysis verify the failure from the top of the column.

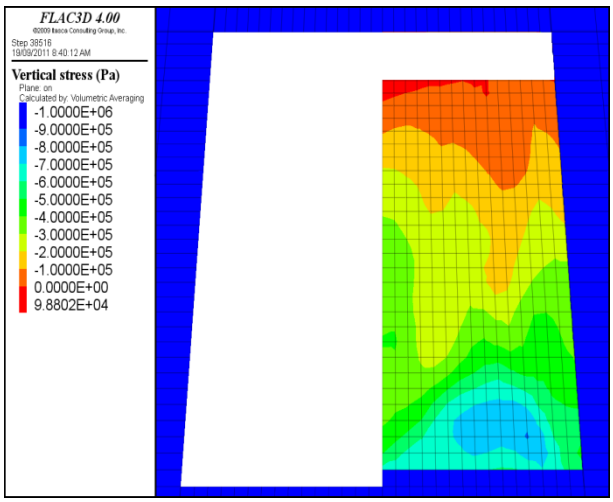

Figure 9 - Vertical stress contours for a homogeneous CRF column after dynamic analysis (Emad et al., 2011)

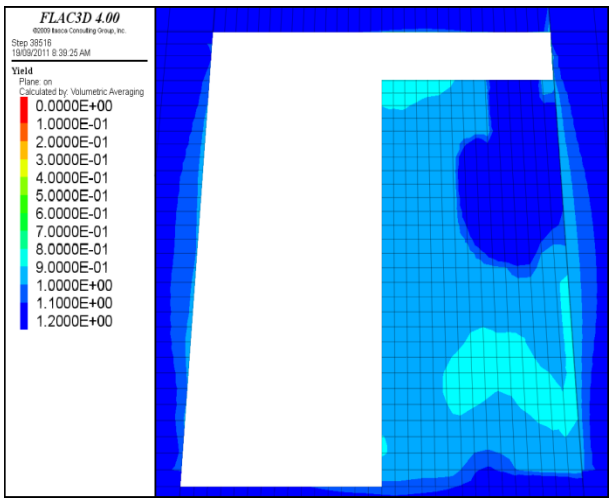

Figure 10 - Yield contours of a homogeneous CRF column after dynamic analysis (Emad et al., 2011)

4.2 Heterogeneity in CRF Column

As discussed earlier the CRF column can become heterogeneous if mixing of the CRF before placement is improper. On the basis of two placement methods, discussed in Section 1, two different models were generated. The models were loaded for static loading first and then dynamic analysis was performed to accommodate blast induced vibrations. The results are presented in the following sections.

4.2.1 CRF Placement by Raise

CRF placement by backfill raise generates two major zones in the CRF column that are the high strength zone and the low strength zone. The two zones have been modelled and analyzed for static loading. Figures 11 and 12 present the results for vertical stress contours and yield contours. In Figure 11, it can be noted that there are no significantly high compressive and tensile stress zones in the CRF, which suggests that improper mixing in combination with this placement method have almost no influence on CRF failure. Figure 12 shows some yielding in the CRF but the majority of zones are stable under dynamic load. The same CRF column was analyzed under the dynamic load following the procedure explained in Section 4.1.2. Figures 13 and 14 present the vertical stress contours and yield contours after dynamic analysis. It was found that the vertical stress contour shows a tension zone at the low strength zone in the CRF column, indicating relaxation. The yield contour also show yielded zones in the low strength zones of the CRF column, thus verifying CRF failure. When compared with static analysis the results of dynamic analysis are more realistic.

4.2.2 CRF Placement by Scooptram

CRF placement by scooptram generates three major zones of sub columns. The three zones with different strengths were modelled and the zones nearest the exposed CRF face were considered as the weakest zones, and the zones furthest away from dumping point were considered as the strongest, as discussed in Section 1. The results of static modelling for vertical stresses and yield are presented in Figures 15 and 16 respectively. The static results for vertical stresses show that the CRF column is stable as there are no relaxation zones but the yield contours show CRF failure in some of the weaker zones. The column was then applied with blast load influence and dynamic analysis was performed, and the results for vertical stresses and yield contours are shown in Figures 17 and 18. The low stress regime at the exposed face signifies CRF failure, which was the weakest zone in the CRF column. The yield contours also confirm yielding in the low strength zones.

5. CONCLUSION

Cemented rockfill is a stiff backfill material, especially when placed and mixed properly. This enables tight filling and enhances fill homogeneity. The static modelling results of the homogeneous CRF column presented did not show any failure in the modelled stope. Considering blast-induced effects on the CRF column from an adjacent stope shows destabilization in the CRF and initiating wedge failure at the top most part of exposed CRF face. The effect of CRF placement methods in combination with improper mixing is also discussed. The two placement methods with a combination of improper mixing of CRF have been modelled under static and dynamic loads. Static modelling results for CRF following raise placement show some failed zones, whereas the dynamic loading effect on the same stope showed greater failure and the results are more realistic. CRF placement by scoop and access drift showed some failure in the CRF column for static modelling results. When subjected to dynamic load the number of failed CRF zones increased along with the development of tensile stress in the heterogeneous CRF column. The results for the three cases are appreciable and therefore it is highly recommended to use dynamic

modelling to verify the CRF design to avoid dilution from CRF, even if the backfill is stable for a static load case.

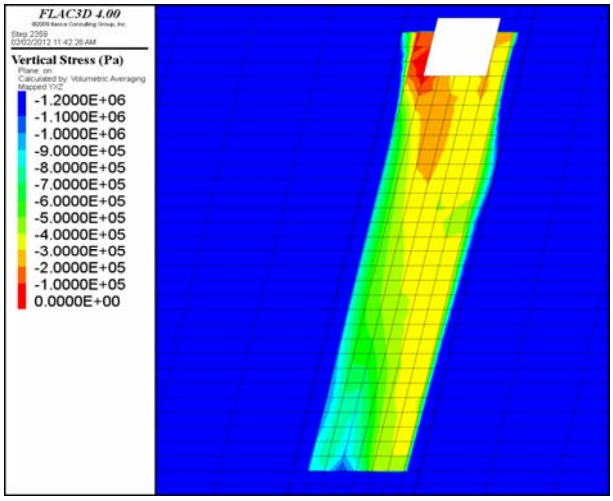

Figure 11 - Vertical stress contours for a CRF column filled by raise after static analysis

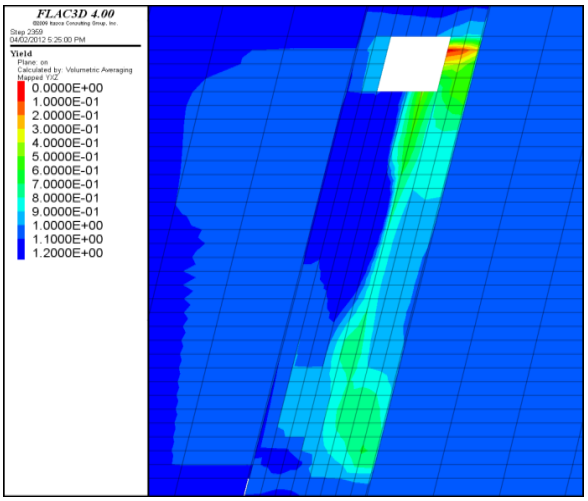

Figure 12 - Yield contours for a CRF column filled by raise after static analysis

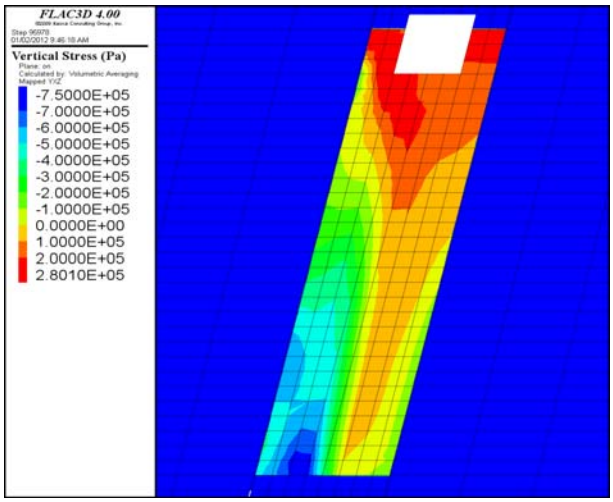

Figure 13 - Vertical stress contours for a CRF column filled by raise after dynamic analysis

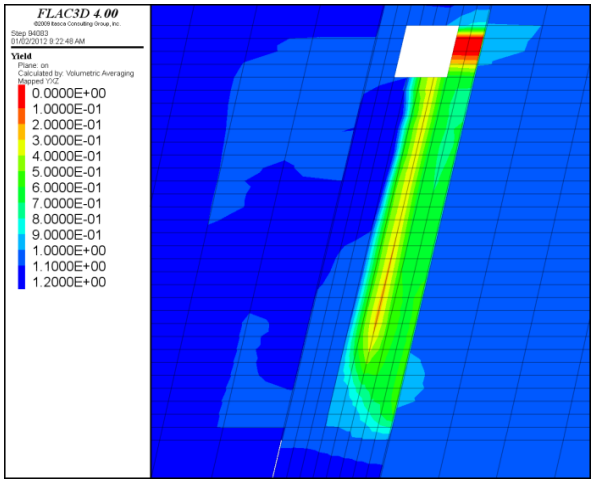

Figure 14 - Yield contours for a CRF column filled by raise after dynamic analysis

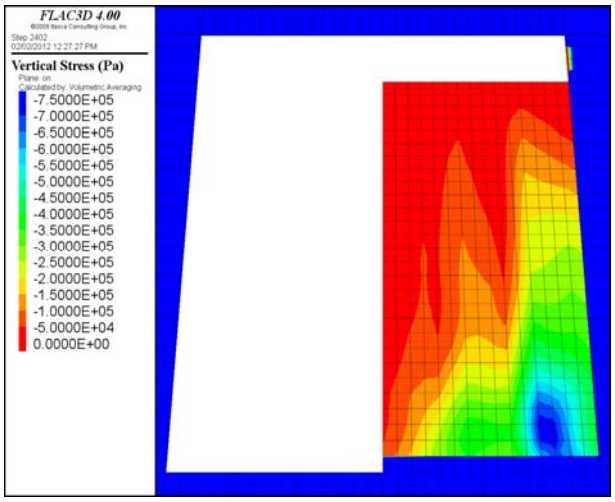

Figure 15 - Vertical stress contours for a CRF column filled by scooptram after static analysis

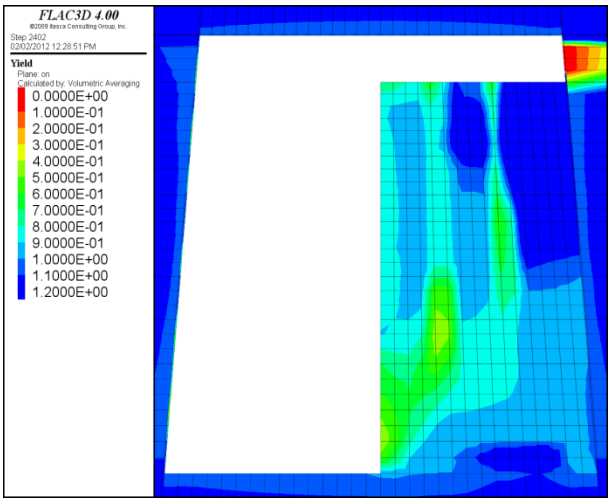

Figure 16 -Yield contours for a CRF column filled by scooptram after static analysis

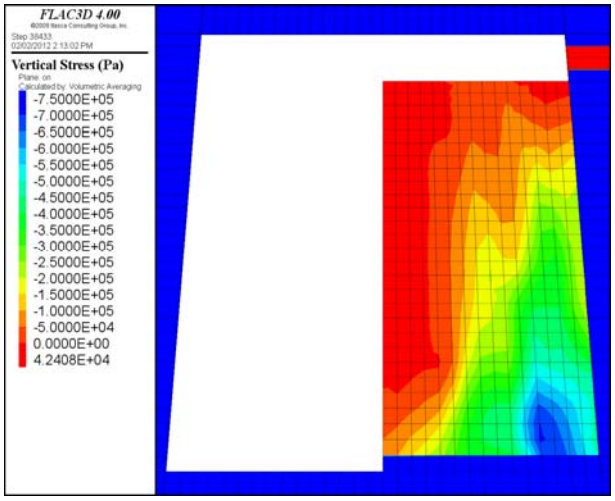

Figure 17 - Vertical stress contours for a CRF column filled by scooptram after dynamic analysis

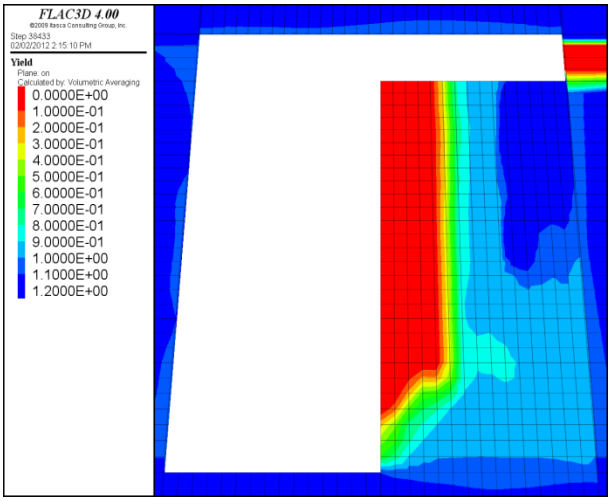

Figure 18 - Yield contours for a CRF column filled by scooptram after dynamic analysis

6. ACKNOWLEDGEMENTS

This work was funded by a grant from the Natural Sciences and Engineering Research Council of Canada (NSERC) under the Discovery Grant Program. The authors are grateful for their support.

7. REFERENCES

ANNOR, A.B., A Study of the Characteristics and Behaviour of Composite Backfill Material. PhD Thesis, McGill University, Montreal Canada, 1999.

ARCHIBALD, J.F., et al., Underground Mine Backfill 1 & 2. Internet course publication of InfoMine Inc., 2003.

ARJANG, B., Premining ground stresses at the Bousquet/Dumagami mines, Cadillac, Quebec. CANMET, Energy, Mines and Resources Canada, Div Report MRL 88-132 (TR), 1988.

EMAD, M.Z., H.S. MITRI, and J.G. HENNING, Some factors affecting cemented rockfill failure in longhole mining. Proceedings of the Twentieth International Symposium on Mine Planning and Equipment Selection MPES 2011, Edited by A. ZHARMENOV, R.SINGHAL, S.YEFREMOVA, 2011: p. 163 - 174.

FARSANGI, P.N., Improving cemented rockfilled design in open stoping PhD Thesis, McGill University, Montreal Canada, 1996.

GOOL, B.S.V., W. KARUNASENA, AND N. SIVAKUGAN, Effects of blasting on the stability of paste fill stopes at Cannington Mine. James Cook University, Australia, 2007.

HASSANI, F. and J. ARCHIBALD, Mine Backfill. Canadian Institute of Mining, Metallurgy, and Petroleum, 1998.

HASSANI, F.P., M.J. SCOBLE, and T.R.YU, Innovations in mining backfill technology : proceedings of the 4th International Symposium on Mining with Backfill/Montreal/2-5 October 1989. Rotterdam : A.A. Balkema, 1989.

HENNING, J.G., Ground control strategies at Bousquet 2 Mine. Master of Engineering Thesis, McGill University, 1998.

KURAKAMI, T., et al., Mining with backfill at the Hishikari Mine, Japan. Gospodarka Surowcami Mineralnymi, 2008. 24: p. 197 - 212.

MILLER, F., Y. POTVIN, and D. JACOB, Laser Measurement of Open Stope Dilution CIM Bulletin, 1992. 85: p. 96-102

SAHARAN, M.R., Dynamic Modelling Of Rock Fracturing By Destress Blasting. PhD Thesis, McGill University, Montreal Canada, 2004.

YU, T.R., Some factors relating to the stability of consolidated rockfill at Kidd Creek. Innovations in Mining Backfill Technology. Hassani et al. (eds), 1989: p. 279 - 286.

YUMLU, M., Backfill Practices at Çayeli Mine. 17th International Mining Congress and Exhibition of Turkey- IMCET2001, 2001: p. 333 - 340.

Application of Consolidated Rock Fill to Open Stoping in Underground Mines

Jerry Ran
Kinross Gold, Ontario, Canada
Terence Watungwa
Kettle River Operations, Kinross Gold, Washington, USA

ABSTRACT: Many large underground mines using the open stoping method have changed their primary applications of consolidated rock fill (CRF) to paste or consolidated hydraulic fill due to considerations of demand in infrastructure and equipment, system reliability, backfill capacity and material sources. However, some smaller or even large mines still use or consider using CRF for backfill purpose due to factors such as capital expenditure, availability or suitability of other fill types or in some cases local regulatory requirements. As demands on CRF applications diminish among major mining companies, there is a lack of recent literature on application of CRF to open stoping in design and operation.

There are several methods being used for fill strength design. Results from these methods have been successfully applied to paste or hydraulic fill. However, the design strength for CRF is much higher than that determined by use of these widely accepted methods. In operation, CRF preparation and placement have significant impacts on the quality of placed CRF and therefore the mining performance.

This paper reviews the current fill design methods and their applications to open stoping with presentation of the bench marking data, presents fill failure cases and various CRF preparation and placement arrangements and discusses quality assurance and control programs.

1. INTRODUCTION

Consolidated rock fill (CRF) is a mixture of graded aggregates coated with binder slurry. It consolidates after being placed into mining openings for ground stabilization or other mining functions. CRF may use aggregates by crushing waste rock from surface sources such as waste dumps, stockpiles and quarries or underground sources such as dedicated waste stopes and development headings. In some mines, mining or development waste satisfies the required gradation and may directly be used as CRF aggregates. The binder slurry is made of binder material (Portland cement, flyash, slag or a combination of these) and water with or without admixtures at water and binder ratios ranging between 0.7 and 1.2.

In recent years, many large underground mines using open stoping have replaced CRF with paste or consolidated hydraulic fill for backfilling purposes due to considerations of demand on infrastructure and equipment, system reliability, backfill capacity and material sources. However, some small to medium size or even large mines still use or consider using CRF for backfilling due to reasons like capital expenditure, availability or suitability of other fill types or in some cases local regulatory requirements. As demands on CRF applications diminish among major mining companies, there is a lack of recent literature on application of CRF to open stoping in design and operation.

There are several methods being used for fill strength design, which include those proposed by Mitchell et al (Mitchell et al, 1982) and Potvin et al (Potvin et al, 2005) and the numerical modeling approach. Results from these methods have been successfully applied to paste or hydraulic fill, but the design strength for CRF is much higher than that determined by use of these widely accepted methods.

In operation, the CRF preparation and placement process has significant impact on the quality of the placed CRF and therefore the mining performance. There are a number of fill preparation and placement arrangements being used for different site conditions in the industry.

This paper reviews the current fill design methods and their applications to open stoping with bench marking data, presents two fill failure cases and various CRF preparation and placement arrangements and finally discusses quality assurance and control programs.

2. FILL STRENGTH REQUIREMENTS FOR OPEN STOPING

In open stoping, placed fill is exposed when mining adjacent stopes. In an optimized mining sequence, fill exposure is normally limited to one vertical fill face at a time. When fill is exposed, the minimum requirement is that it is capable of being free standing during the mining process. Failure of the fill body disrupts the mining process with adverse production and performance impacts. Therefore fill must be designed with a sufficient strength.

The widely used design method is the simple wedge analysis proposed by Mitchell et al in 1982 (Mitchell et al, 1982). This approach considers a fill wedge potentially sliding into an opening in limit equilibrium assuming the same cohesion for the two vertical side walls as that for the fill material. The model geometry is labeled and shown in Figure 1 where H is the exposed fill height, B is the exposed width and D is the fill body thickness or depth. For a fill material with a cohesion, c, internal friction angle, φ and unit weight, γ, the required fill strength defined as the uniaxial compressive strength (*UCS)* is determined by the following equations and this approach is referred to as the "Mitchell 1982" method.

$$\alpha = 45 + \frac{\varphi}{2}$$

$$H^* = H - \frac{D\tan\alpha}{2}$$

$$2c = \frac{\gamma B H^*}{H^* + B\tan\alpha}$$

$$UCS = \frac{2c\cos\varphi}{1-\sin\varphi}$$

In this calculation, D is limited to $H/\tan(\alpha)$. When D is greater than this limit, the calculation generates the same results.

When the internal friction angle, φ is set to zero, the Mitchell's equations become

$$UCS = 2c = \frac{\gamma B(2H - D)}{2H + 2B - D}$$

This is the simplified formula proposed by Potvin et al in 2005 (Potvin et al, 2005) and the equation is referred to as the "Potvin 2005" method.

Another form of the Mitchell's 1982 equation is that limiting D to $H/(2\tan(\alpha))$. This form has been used by some consulting firms and mining operations for fill design. Therefore this method is referred to as the "Mitchell 1982 modified" method in this paper.

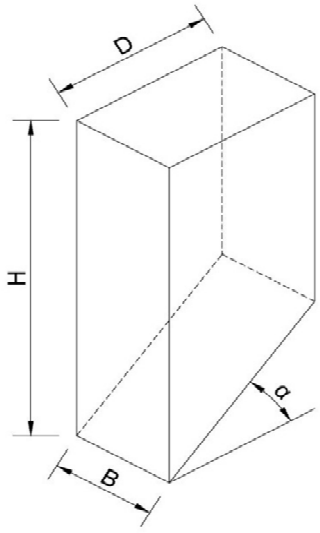

Figure 1 - The sliding wedge model (modified from Potvin et al, 2005)

In a recent study of fill strength requirements for an underground project under evaluation at Kinross, two cases were simulated using *FLAC3D* assuming an internal friction angle of 30^o and unit weights of 17 kN/m^3 and 24 kN/m^3 respectively. The stope height, *H,* is 30m with a strike length, *D,* of 15m and a exposure width ranging from 15m to 35m on a transverse mining layout. The modeling results are compared with those calculated by use of the three methods discussed previously in Figures 2 and 3.

These figures show that results from both the Mitchell 1982 and Potvin 2005 methods compare well with the model points for the cases simulated. This observation is in agreement with the conclusion given by Potvin et al (Potvin et al, 2005), i.e. "using elaborate models will not significantly reduce the binder content below that arrived at with the simplified method".

The UCS determined by use of the Mitchell 1982 modified and Potvin 2005 methods is compared with that calculated by "Mitchell 1982" in Figure 4. From this figure, it is observed that

- The Mitchell 1982 modified method gives values of 10% to 25% greater than those from application of the original Mitchell 1982 method for the data range presented.
- The UCS determined by the Potvin 2005 method is within 10% of that from "Mitchell 1982" for a major portion of the data range but up to 20% lower when the exposed width is small.
- When the exposed width is large, the Potvin 2005 method seems to give higher UCS values than those from "Mitchell 1982".

In strength calculations for paste or hydraulic fills, it is common to apply a factor of safety of between 1.3 to 1.5 to the derived value by use of the Mitchell 1982 or Potvin 2005 method. Due to slight differences in UCS values when using these methods, it is suggested that calculations be made using both approaches but to choose the higher value for design. Based on Figures 2 to 4, the factor of safety may be reduced to 1.2 or 1.4 when the "Mitchell 1982 modified" method is used.

These simple design methods have been widely used in design of hydraulic or paste fills and the actual strength required at many operating mines is in line with calculations using these approaches. Evans et al (Evans et al, 2007) published strength data from a number of Barrick mines using paste fill, which is in conformation with this observation and Table 1 shows additional bench marking data for confirmation.

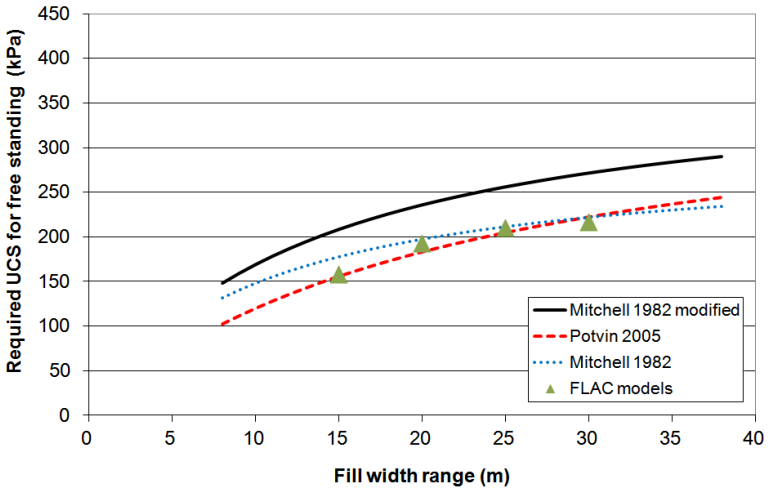

Figure 2 - The required UCS for free standing (H=30m, D=15m, γ=17kN/m3)

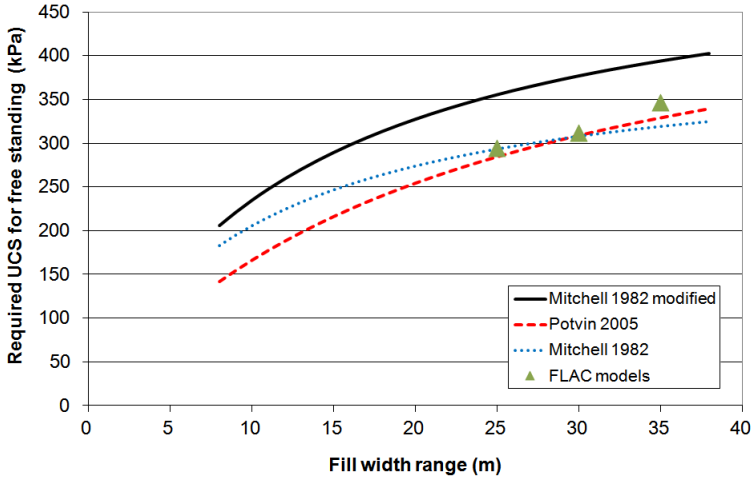

Figure 3 - The required UCS for free standing (H=30m, D=15m, γ=24kN/m3)

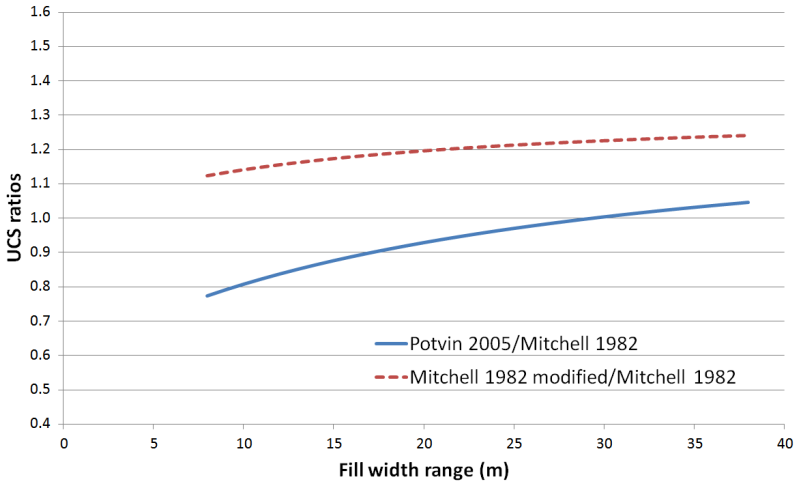

Figure 4 - Comparison of UCS ratios

Table 1 - Hydraulic or paste fill UCS at some benchmarked mines

Mine	Stope Dimensions D x B x H (m)	UCS at 28 days (kPa)
D	20 x 3-30 x 20	580
B1	20 x 3-6 x 20	190
W	20 x 4-45 x 25	250
K1	All dimensions vary between 20 and 60	340
B2	20 x 15 x 35	400
K2	20 x 15-30 x 30-40	750
C	20 x 15 x 40	500
L	30 x 5-15 x 25	600

However, for CRF, the design or target strength (UCS) is much higher than that derived from the approaches discussed above. Table 2 shows CRF strength values used at some bench marked mines where open stoping is applied. A comparison of Tables 1 and 2 shows that the fill strength requirement for CRF is 5 to 10 times higher than that for paste or hydraulic fills. There are a number of reasons for the strength difference including the following.

- CRF placement quality is not as consistent as paste or hydraulic fill
- The test method for CRF samples is adopted from concrete testing and may not reflect the in-situ strength which varies in a wide range
- CRF is more sensitive to blasting
- CRF has much higher strength even with lower binder contents
- Strength values are inherited from CRF applications for underhand mining

Based on consideration of these factors and field observations, the simple calculation reported and proposed by Yu and Counter in 1983 (Yu and Counter, 1983) seems adequate for determination of the minimum CRF strength for open stoping. The original proposed method is given below.

$$\text{UCS} = 2.5\ \gamma H$$

For a stope 30m high, the required UCS is then 1.8MPa assuming γ is 24kN/m^3. Though this calculation still gives lower values than the target strength adopted at some mines, it is substantially higher than that determined by application of “Mitchell 1982” or “Potvin 2005”.

Table 2 - Design Fill UCS at Some Benchmarked Mines

Mine	Stope Dimensions D x B x H (m)	UCS at 28 days (MPa)
KI	20 x 15 x 35	4.0
DA	20 x 5 x 20	5.0
PO	15 x 30-60 x 25	3.6
MI	6 x 12 x 23	2.8
BI	12 x 18 x 30	2.0
DV	20 x 30 x 15	1.1

3. CRF FAILURES IN OPEN STOPING

Yu and Counter (1983) conducted some in-situ tests on exposed CRF placed in an open stope and the results indicated a strength ranging from 1.3MPa to 11MPa. The variation in CRF strength is inherent with the fill preparation and placement approach. Without effective quality assurance and control

programs, fill failures are inevitable and the consequences of a fill failure include loss of ore, dilution, material re-handling and ground instability with significant impact on production and cost.

Figures 5 and 6 show two failure cases where placed CRF collapsed into open stopes causing major delays in the mining process. Figure 5 is an example showing CRF placed in a primary stope failed into a secondary stope. In this particular case, the failure resulted in loss of ore and additional efforts in mucking out collapsed fill and backfilling both stopes. The case in Figure 6 shows that CRF in one primary stope in the upper level collapsed into a lower level stope. This failure not only created production problems but also resulted in substantial ground instability around the failed stope. In the case shown in Figure 6, it was difficult to observe binder coating on the broken fill material.

Figure 5 - CRF failed into an adjacent stope

Figure 6 - CRF failed into a lower level stope

4. CRF PREPARATION AND PLACEMENT

There are two common setups for CRF preparation and placement. In mines where CRF quality has major impact on mining performance and personnel safety, batch plants are built for fill preparation. In these plants, aggregates, binder, water and other admixtures are added into a mixer based on the selected recipe. After proper mixing of these ingredients, normally controlled by a pre-set time interval, the CRF batch is loaded into trucks for delivery to stopes. The entire process is automated with PLCs (Figure 7).

The batch plant may be built on surface (Figure 8) or underground (Figure 9) depending on site specific studies and conditions. Figure 8 shows the batch plant at Kinross' Kettle River - Buckhorn Mine located in Washington, USA. It produces CRF at a rate of 800 tons per day for delivery underground utilizing 26 ton Wagner ejector bed dump trucks. CRF may be directly dumped into open stopes or temporarily stored and re-handled using scoop trams for filling.

Figure 7 - An automated system

Figure 9 - An underground CRF batch plant

Figure 8 - A batch plant on surface

Figure 10 - A CRF preparation pit

In some smaller mines where the demand is low, the mixer is replaced by a mixing pit as shown in Fig 10 where aggregates are mixed with slurry using a scoop tram. The mixed product is picked up by a scoop tram, hauled and dumped into stopes. Some mines build their mixing pits underground for easy handling.

The second setup for CRF preparation is to spray binder slurry onto aggregates near the discharge point. This arrangement does not require as much capital expenditure as the batch plant setup, but it does need a binder slurry preparation and delivery system. The common arrangement is to have a central slurry preparation plant and slurry is delivered through a pipeline system to agitator tanks located near clusters of stopes. Pipes are installed to deliver slurry from the agitator tank to the stope or a location near the stope to be filled. Scoop trams or trucks loaded with aggregates are sprayed with slurry and the coated aggregates are then dumped into open stopes. Figure 11 shows a slurry spray nozzle near a cluster of stopes to be filled.

Figure 11 - A slurry spray nozzle

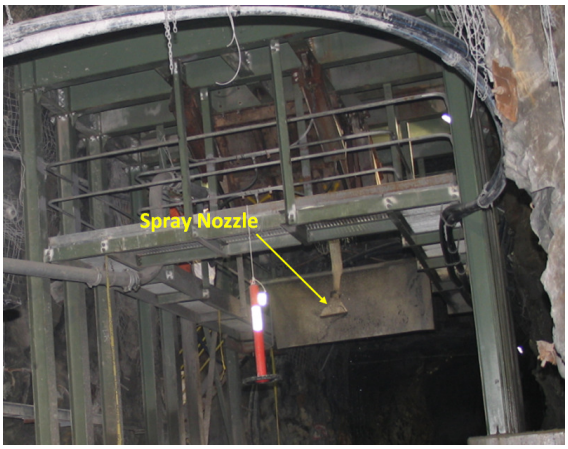

Figure 12 - Slurry spray at the load out station

There are several variations to this system. Aggregates may be delivered to the discharge point by conveyor belts and dumped into a stope while spraying slurry with or without a mixing mechanism. Obviously the aggregate dumping rate should match that for delivering slurry.

Another arrangement is to spray slurry while loading aggregates into trucks or scoops as shown in Figure 12. Some mines spray while dumping, as shown in Figure 13. In this setup, a truck load of aggregates is dumped into a stope while the nozzle releases slurry into the stope. Though the quantity of slurry matches the truck load, the mixing is normally poor leading to many fill failures.

Figure 13 - A spraying and dumping setup

Figure 14 - Mining under CRF

5. CRF BACK STABILITY

Mining under CRF is a common method used in Nevada, USA. The primary rationale for this approach is that the ore deposit is weak or very weak as observed in some of the Barrick mines in Nevada (Evans et al, 2007). As reported by Pakalnis et al (Pakalnis, 2006), most mines in their database have a span of 3 to 8 m and a CRF strength of 3.5 to 8 MPa with a binder content of 6-10%.

Design of CRF for underhand mining is discussed in detail by Pakalnis et al (Pakalnis, 2006) but the primary criterion in most cases is the flexural failure mode. Based on the common assumption that the

tensile strength is approximately one tenth of the UCS, this failure mode together with consideration of personnel entry requirements usually leads to high CRF strengths as quoted above. Figure 14 shows an open cut with CRF on three sides.

In open stoping, sill or crown pillars between mining blocks have CRF above and when these pillars are recovered, CRF is exposed. However, in most cases, no personnel are exposed to CRF and therefore its stability has more impact on mining performance rather than safety.

Ran and Tolgyesi (2003) proposed a simplified approach to determining the minimum strength required for CRF exposure in open stoping. Based on their calculations, the minimum UCS required for a 20m back exposure is approximately 0.8MPa. Based on observations from the bench marked mines in Table 2, the exposed CRF back should be stable as long as the fill strength is determined using $2.5\gamma H$ and the placement quality is reasonably good.

6. CRF QUALITY CONTROL

Mines using CRF for open stoping must have effective quality assurance and control (QA/QC) programs to ensure achievements of the designed strength and quality. Such programs are specific to site conditions and not discussed in detail. Several points are made in this paper to highlight the main areas for QA/QC.

The aggregates must have the strength and gradation suitable for CRF application. Once the source material is assessed to be suitable for CRF, the gradation should be analyzed for suitability. Some typical gradation curves are given in the SME Manual (Hustrulid & Bullock, 2001). The gradation should be regularly sampled and tested for compliance. When aggregates are delivered underground by boreholes or raises, the gradation at the pickup point should be tested instead as the delivery system may substantially change the size distribution curves and this may require adjustments at the source.

The moisture content of aggregates affects the binder and water ratio and therefore the strength. It should be controlled particularly when aggregates are exposed to the environment.

It is common to collect and test samples when there is a batch plant. Samples are collected either at the plant or near the dump point. Cylinder samples are usually used for strength testing as shown in Figure 15 (Kinross' Kettle River Operations – Buckhorn Mine). These samples are normally 150mm in diameter and 300mm in height and prepared manually by removing large pieces and tamping in three stages. Though the test results may not directly reflect the in-situ strength, they certainly show variations and trends as shown in Figure 16.

It takes more efforts to prepare samples for testing when slurry is sprayed onto aggregates. Mines may collect aggregates and slurry near the dump point and prepare samples by manual mixing and casting in the same manner as that for batched CRF.

Figure 15 - CRF samples for testing

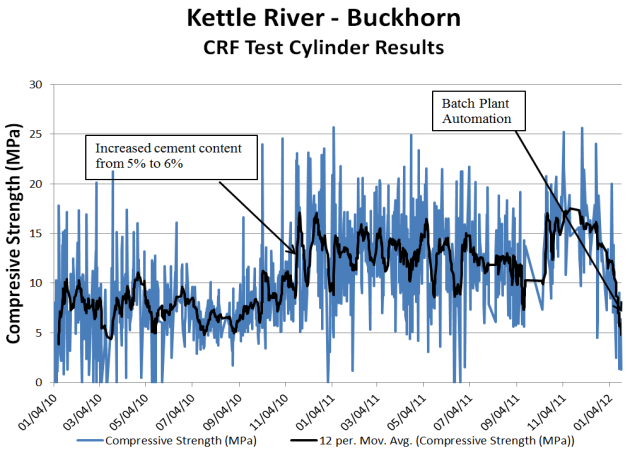

Figure 16 - An example - CRF sample test results

7. CONCLUSIONS

In open stoping, fill must have sufficient strength that keeps the exposed fill body free standing. Results from the conventional wedge analysis methods proposed by Mitchell et al in 1982 and Potvin et al in 2005 compare well with those by numerical modeling. For design, it is suggested to use higher values given by these methods and multiplied by a factor of safety of 1.3 to 1.5. The modified Mitchell 1982 method used by some consultants and mines give more conservative values and therefore a lower factor of safety of 1.2 to 1.4 may be applied. These design methods have been proven to be appropriate for hydraulically placed fills including paste but for CRF design, the required strength is much higher than that from these calculations and it is suggested to use the simple approach proposed by Yu and Counter in 1983.

If the CRF strength is designed using the conservative approach proposed by Yu and Counter and the placement quality is reasonably good, the exposed CRF back is expected to be stable based on calculations proposed by Ran and Tolgyesi in 2003 and data from benchmarked mines.

Mines should conduct careful studies before commitment to CRF preparation and placement arrangements as they have significant effects on the CRF quality and stability. Effective QA/QC programs must be implemented to achieve the target quality and therefore mining performance.

8. REFERENCES

EVANS, R., RAN, J. and ALLAN, R., 2007. Application of minefill at Barrick Gold, CIM Bulletin Vol. 100, No 1103, 1-8.

HUSTRULID, W. and BULLOCK, R., 2001. Underground Mining Methods: engineering fundamentals and international case studies, SME, Littleton, 606.

MITCHELL, R.J., OLSEN, R. S. and SMITH, J.D., 1982. Model studies on cemented tailings used in mine backfill, Canadian Geotechnical Journal, No 19, 14-28.

PAKALNIS, R., CACERES, C., CLAPP, K., MORIN, M., BRADY, T., WILLIAMS, T., BLAKE, W. and MACLAUGHLIN, M., 2006. Design spans—underhand cut-and-fill mining, CIM Bulletin, Vol. 99, No 1094, 1-7.

POTVIN, Y., THOMAS, E.G. and FOURIE, A.B., 2005. Handbook on Mine Fill, Australian Centre for Geomechanics, Perth, 45-46.

RAN, J. and TOLGYESI, S., 2003. Fill back stability in open stope mining with consolidated backfill, CIM Mining Conference, Montreal, 1-8.

YU, T. and COUNTER, D., 1983. Backfill practice and technology at Kidd Creek Mines, CIM Bulletin, Vol. 76, No. 856, 1-10.

Initial Slope Stability Study of Undercut Slope at Area 4.1 Mae Moh Mine, Lampang, Thailand

Cheowchan Leelasukseree
Mining Engineering Department, Faculty of Engineering, Chiang Mai University, Thailand
Narongsak Mavong
Geotechnical Engineering Department, Mae Moh mine, Electricity Generation Authority of Thailand, Thailand

ABSTRACT: Mae Moh mine, operated by Electricity Generation Authority of Thailand (EGAT), is the largest open pit mine in Southeast Asia. Its production is approximately 15 million lignite tons and 90 million m^3 of waste, annually. The bottom of the final pit limit is designed to be approximately 500 m in depth. Presently, the pit depth is almost 250 m below original surface. The complexity of geological structures, such as faults, has caused a number of geotechnical difficulties. In a challenging lowwall area, called Area 4.1, an inclined weak bedding plane, G1, will be daylighted along the lowwall as following by mine plans. The dimensions of Area 4.1 are nearly 300 m wide and 90 m high. The friction and dip angles of the G1 interface are reportedly 12° and 15°, respectively. A three million m^3 claystone block, resting above G1, would potentially slide down, and possibly cause a massive failure. EGAT engineers are acutely aware of the potential gigantic sliding failure and are modifying the mine plan in Area 4.1 to improve mine safety and minimize the displacement of the potential sliding block, reduce the possibility of failure and lower the additional mining cost as much as possible. The cut and fill mining technique was selected and studied to achieve those goals for mining in Area 4.1. With this mining technique, G1 will be partially daylighted. Therefore, an arch formation is induced with a sliding block above the mining area, which could perform as a temporary support undercutting a certain span. Initial studies of the behavior of the partially undercut slope are presented in this paper, along with a review of the similar failure history in Mae Moh mine and a 3-dimensional numerical model of the mine. The failure history review provides an estimation of undercut span without failure. The three-dimensional numerical model results, using 3DEC, gave an initial approximation of the displacement of the sliding block in Area 4.1. The next exciting study of the behavior of partially undercut slope is a trial undercut slope field experiment in Area 4.1. Currently, a trial undercut slope field experiment in Area 4.1 is under construction. In the field experiment, a number of monitoring programs will be installed in Area 4.1 to monitor and obtain information to allow a better understanding of the behavior.

1. INTRODUCTION

Mae Moh mine is the largest open pit mine in Southeast Asia. It is operated by Electricity Generation Authority of Thailand (EGAT), a Thai state enterprise. It produces approximately 15 million tons of lignite and 90 million m^3 of waste, annually, to serve ten coal-fire powered plants. The mine is located in Lampang, a northern province of Thailand, 625 km from Bangkok. Based on its current mine plan, the final pit will cover approximately 5 x 7 km^2 and the pit bottom will be 500 m below the original ground surface, by 2035. Figure 1 presents the final pit (in gray), dump sites (in brown), streams and water reservoirs (in cyan).

Mae Moh basin is the deposition of Lignite. The typical stratigraphy in the basin is simply illustrated in Figure 2. The overburden consists of two layers, which are the top soil and red bed. The red bed can be described as reddish stiff, highly fissured clay. Beneath the red bed, five coal seams that are laid and interbedded with Grey Claystone. The coal seams were named using letters J, K, Q, R and S. The total thickness of the coal seams and interburden varied from 300 m to 420 m. The next layer, below Seam S,

is the underburden and base rock. It is noted that a number of thin layers of clay are randomly bedded in the interburden and underburden layers. Another major geologic structure in this basin is a series of normal faults that lie in the North – South direction.

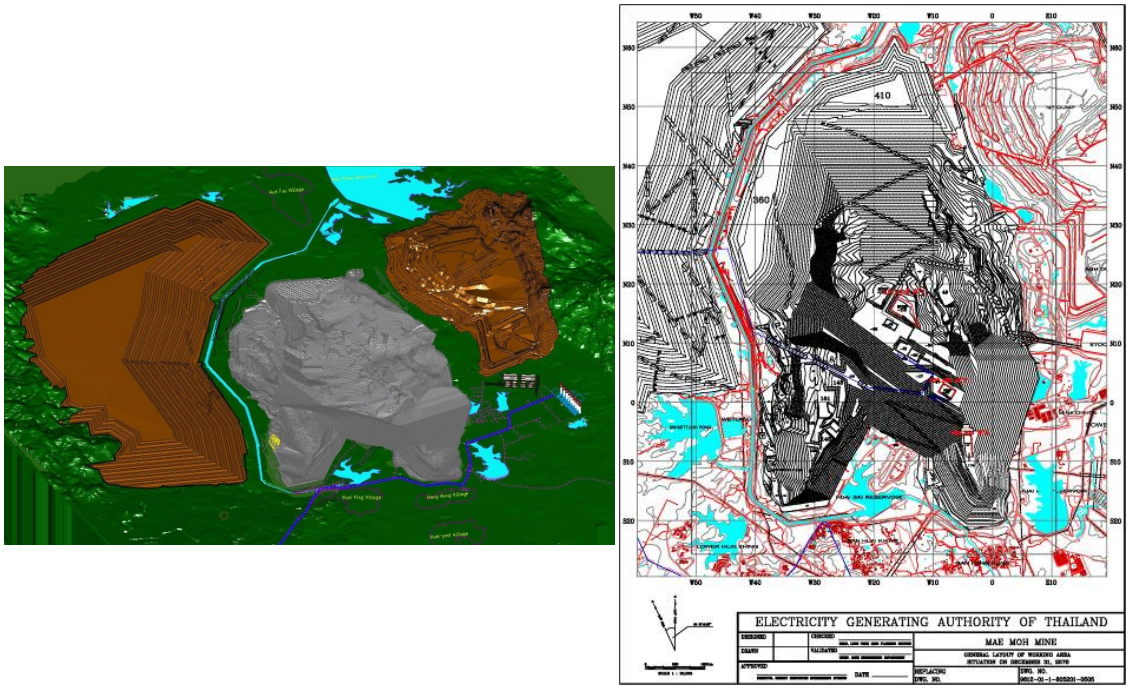

Figure 1 - Topography of Mae Moh mine at final stage, Year 2035

Figure 2 also shows a cross section plot of Area 4.1. A normal fault has separated the layers in the area, as a result, a part of the layers have been displaced, in a dip direction to the normal fault. Based on the fault and free face orientations, and thin clay seam and Gray Claystone interface friction, the slope stability of Area 4.1 – a lowwall (Footwall) of the pit wall – becomes problematic. The uppermost blue line represents the current topography of the slope. According to the mine plan, K and Q seams of Lignite must be excavated and the profile of the slope will be changed to the dashed line. The hatched block, sitting on a very low friction angle interface between underburden Gray Claystone and a thin layer of clay, called G1, potentially becomes a massive sliding block. If Area 4.1 is fully excavated as planned, G1's interface is daylighted for approximately a 300 m and 3–million–m^3 block of claystone is much more likely to slide along the interface. The friction angle of the interface was reportedly 12° – 14° (Mungpayaban, 2005, Pipatpongsa, 2010), and the maximum factor of safety at 0.61 can be determined using the interface friction angle (12°) and average dip angle of G1 (16°), measured using cross section plots. Therefore, the calculated factor of safety from the two – dimensional slope stability analysis indicates that the K and Q seams in Area 4.1 cannot be mined unless the 2–million–m^3 block is excavated first, and the two – dimensional slope stability analysis gives a conservative analysis. Side resisting forces in the third direction are neglected.

To minimize the amount of waste removal, the mining method for Area 4.1 was reconsidered. The cut and fill mining method is an interesting option and Area 4.1 is being used as a field experiment. The area will be mined and partially undercut so that the G1 interface is also partially daylighted. After the completion of mining, backfilling begins to support the slope face and maintain adequate room for mining activities. The mining – backfilling cycle is iterative until all the Lignite in Area 4.1 is completely mined out. Concurrently, the behavior of the undercut slope will be studied using a thoughtfully installed monitoring system. The maximum width of the undercut face is questionable, but the lowwall failure case history

should give an idea of the width of undercut face because the geological structures and undercutting in Areas 3 and 4.1 are common situations.

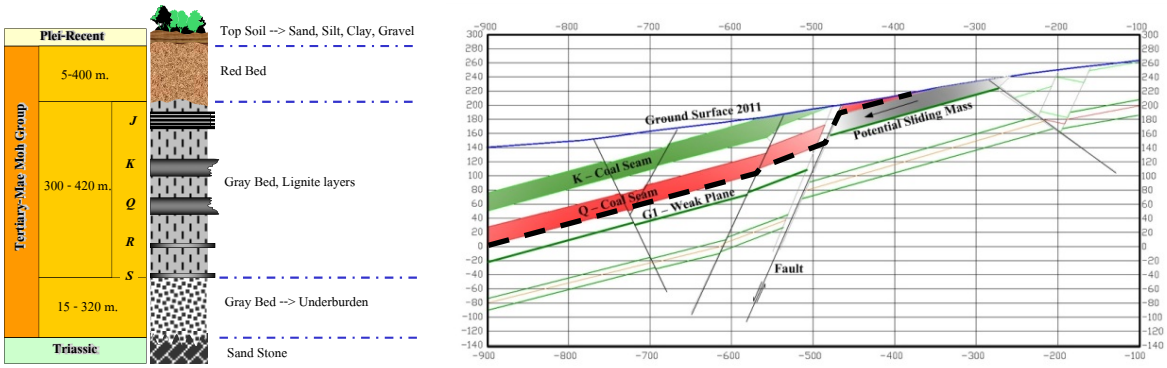

(a) Stratigraphy of Mae Moh basin (b) A cross section plot of Area 4.1

Figure 2 - General geological information of Mae Moh mine and its Area 4.1

2. A LOWWALL FAILURE CASE HISTORY

The expected slope failure in Area 4.1, when undercut, is similar to the lowwall failure case history. Area 3 is located in the northeast portion of the pit. The failed block was also placed on a very low friction angle of the G1 interface. Figure 3 shows the first failure in Area 3 and its 55,000-m^3 of sliding mass.

In 1996, a slope in Area 3 was intentionally started to undercut and mine for 200 m wide, which included the G1 interface. In early June 1996, initial tension cracks were discovered at the top bench of the slope (Elevation 291 and 282). The cracks propagated and widened considerably quickly, and on June 16th 1996, fourteen millimeters of precipitation triggered a memorable slide in Area 3. Fortunately, the failure did not result in any injures or damages. As shown in Figure 3, the dimensions of failure were 80 m x 120 m x 30 m (WxLxH). The failure in Area 3 provided technical staff at the mine valuable experience to make them aware of G1's presence. Depositions and properties of clay in G1 and the G1 interface were traced, sampled and studied intensively.

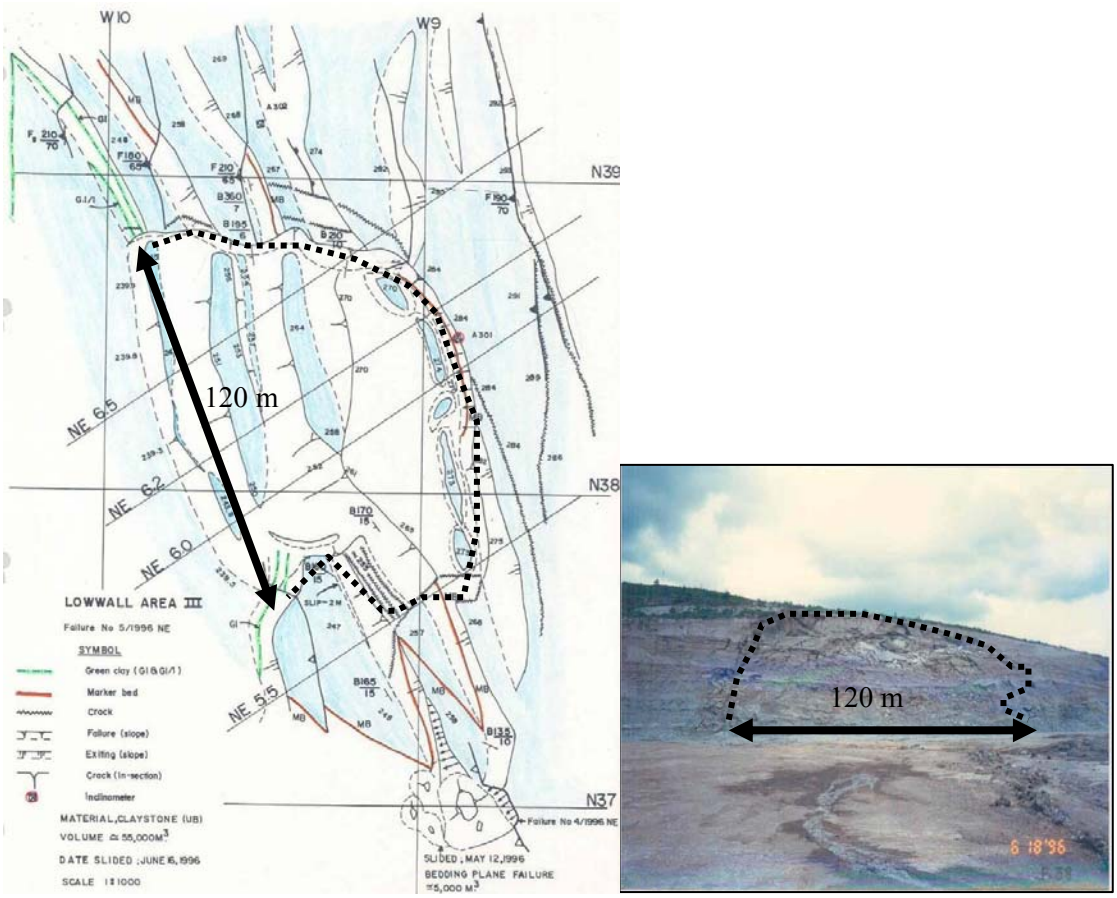

Figure 3 - Failure of undercut slope in Area 3

3. FIELD EXPERIMENT

As stated before, the cut and fill mining method was an interesting option for mining areas in the Mae Moh mine that the G1 interface would aggravate mining operations. Mining engineers decided to study the cut and fill mining method and the undercutting slope behavior in Area 4.1 as a field experiment. The mining plan was split into 2 operation periods. From the experiences with the Area 3 failure, G1 interface was planned to be daylighted approximately 100 m for each period. The 1st period is now being conducted and will be finished in mid 2013. The 2nd period has been planned in detail.

The mining sequence of the 1st period in Area 4.1 is presented in Figure 4. Area 4.1 is being developed and cut via a main access ramp (Figure 4(a)). A part of highly laminated claystone layers, called the Marker bed, will be excavated from an elevation of 192-236 msl (Figure 4(b)). The Marker bed placed on the top of the Area 4.1 slope. A benefit of marker bed removal is the lowering of the driving force and an increase in the safety. After the completion of the marker bed excavation, the cut and fill cycles will be repeated twice. Firstly, undercutting of the Area 4.1 slope begins from an elevation of 137-192 msl and then backfilling the slope took place from an elevation of 137-181 msl (Figure 4(c) and (d)). Lastly, the slope will be mined from an elevation of 115-192 msl and backfilled from an elevation of 115-192 msl (Figure 4(e) and (f)).

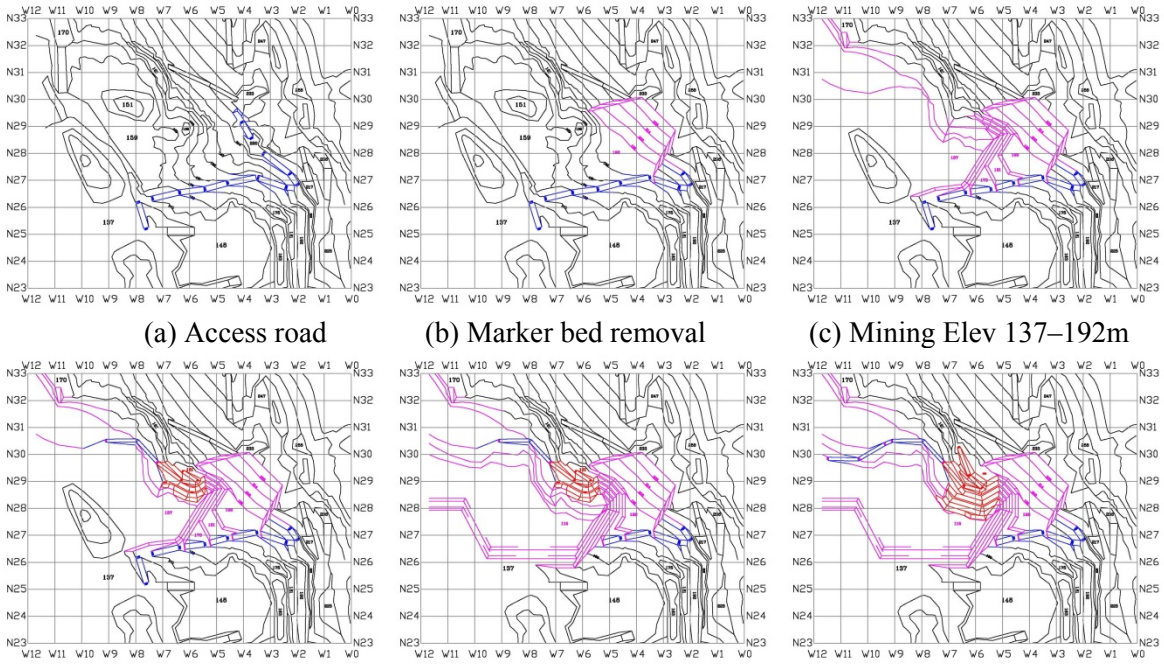

(a) Access road (b) Marker bed removal (c) Mining Elev 137–192m

(d) Backfilling Elev 137–181m (e) Mining Elev 115–192m (f) Backfilling Elev 115–192m

Figure 4 - Mining sequence of the 1st period in Area 4.1

Currently, Area 4.1 is under construction as shown in Figure 5. The marker bed was completed and the Area 4.1 slope has been slowly undercut from an elevation of 192-137 msl. The displacement and groundwater pressure have been monitored and digitally recorded, and the displacement of the slope, during the mining operations, has been monitoring by an automatic deformation monitoring system with a number of prisms installed along the crests of the slope. Several piezometers, installed in boreholes around Area 4.1, were employed to monitor and record the groundwater pressure in the area.

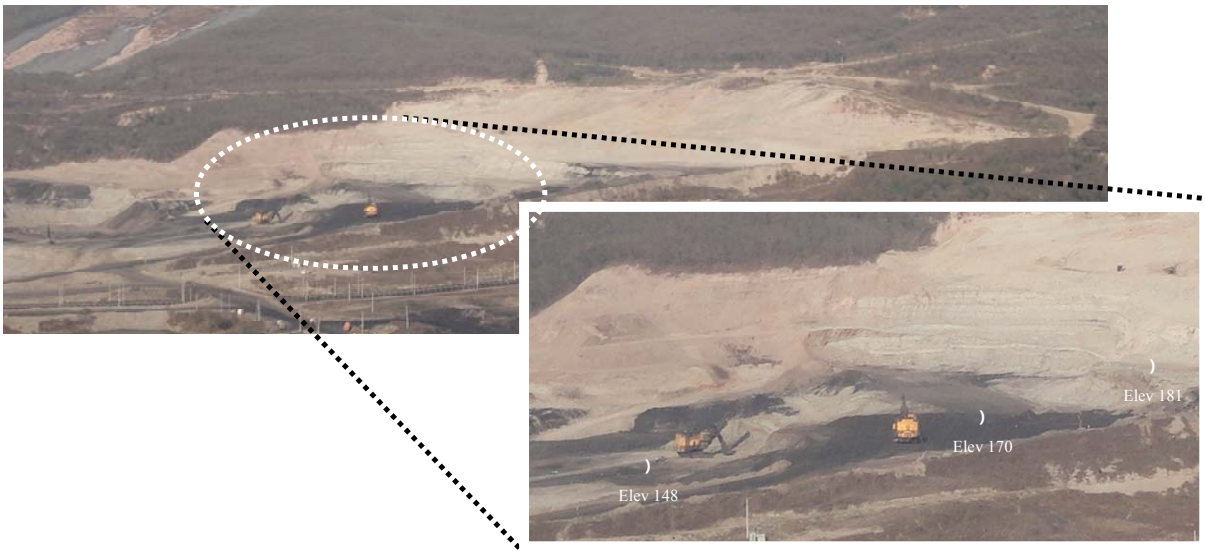

Figure 5 - Area 4.1 being undercut at Elevation 170 and 148

4. NUMERICAL MODELS

To obtain a greater understanding of the undercut slope behavior, a numerical model has been constructed and simulated. The 3DEC®, 3-dimensional discrete element program (Itasca, 2007), was selected for this study.

4.1 Numerical Model Construction

The model construction began with the generation of a 700(W) x 600(L) x 320(H) box. The gigantic box was then cut into several blocks by surfaces which were the faults, the G1 interface, the current topography, marker bed excavation and production cut (see Figure 6(a)). The blocks were discretized and assigned physical properties such as Gray Claystone properties. And the boundary conditions also were constrained. Primarily, the total number of tetrahedral elements in the model was 1,014,580 and the average edge length of the elements was 10 m. Physical properties of Lignite were assumed to be the same as Gray Claystone. The blocks were sequentially removed from the model, to simulate sequential excavations. From Figure 6(b) to 6(d), a sequential excavation was executed to have the current ground surface, marker bed excavation and production cut, respectively. G1 interface was partially daylighted in the undercut slope (between blue and red block). For each excavation, the model was executed to determine the state of equilibrium and the displacements and stresses were examined.

To simplify the model, as stated before, the physical properties of Lignite were assumed to be the same as Gray Claystone. The physical properties of Gray Claystone were assigned to all tetrahedral elements in the model. The physical properties of Gray Claystone are presented in Table 1. The physical properties of Gray Claystone (intact rock) were based on a number of laboratory tests conducted, by the Mae Moh mine, over the last 30 years (Mae Moh Geotechnical Report, Thailand – Australia Lignite Mines Development Project, 1985). According to the intact rock strength and rock conditions in the field, the physical properties of Gray Claystone rockmass were estimated using Hoek & Brown Criterion. The downgraded properties of Gray Claystone were assigned rock properties in the numerical model. The boundary conditions of the model were simulated using rollers on the sides and bottom of the box.

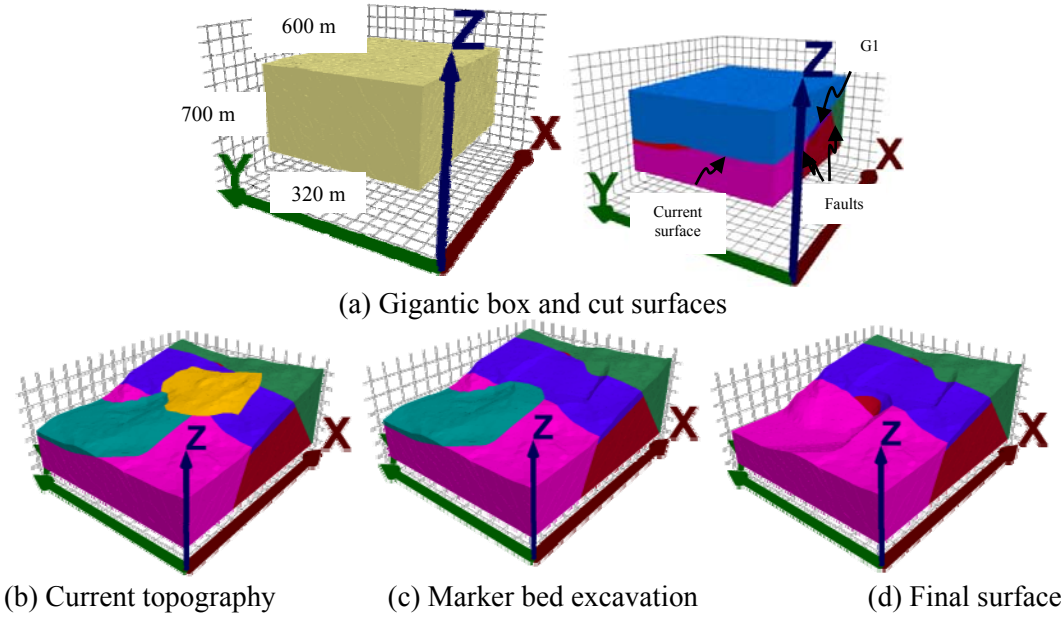

(a) Gigantic box and cut surfaces

(b) Current topography (c) Marker bed excavation (d) Final surface

Figure 6 - Initial block, surfaces and major geologic structures

The first equilibrium stage was determined under the gravitational acceleration. The lateral earth pressure coefficients at rest (k_o) in the model were identical in x and y directions at 0.43 ($\nu = 0.3$) and agreed well with the analytical solution, as plotted in Figure 7(a). Because of the change in topography, the lateral earth pressure coefficients at rest were changed. The lateral earth pressure coefficients (in both x and y directions) near the surface were obviously much greater than k_o but they converged to k_o with depth (as shown in Figure 7(b)).

Table 1 - Physical properties of Gray Claystone

Gray Claystone Physical Properties and Strengths	Intact Rock	Rockmass
Density (kg/m^3)	1,950	1,950
Cohesion (MPa)	0.5	0.14
Friction Angle (°)	33.5	21
Unconfined Compressive Strength (MPa)	4.27	0.4
Elastic Modulus (MPa)	(N/A)	219
Poisson's Ratio	(N/A)	0.3
Tensile Strength (MPa)	(N/A)	0.2

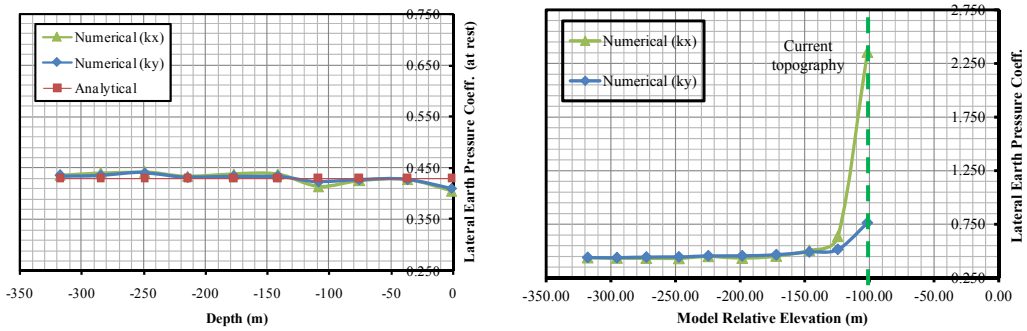

(a) Initial equilibrium (b) 2nd equilibrium, current topography

Figure 7- k_o and k after topographic change plot with elevation of model

4.2 Numerical Model Results

After the completion of numerically sequential excavation, the displacements and stresses were plotted, therefore providing valuable understanding. When the slope was partly undercut and the weak plane was also partially daylighted, an arch formation occurred above the undercut area in the slope. The stress trajectories in the block on the G1 interface were evident. The arch formation offers greater resistance to the downward displacement of the slope.

Figure 8, the principal stress trajectory plot of the block on the G1 interface, revealed the Arch formation around the undercut area, after the slope face was partially undercut. A part of the slope above the undercut area was more deformed than the other parts. Therefore, the principal stresses in the slope face around the excavation were redistributed both in magnitude and direction. From Figure 7, the major principal stress (compression expressed in negative) rearranged and aligned in a tangent to the undercut excavation. The load above the undercut excavation was transferred laterally to the unexcavated adjacent slope (Terzaghi, 1936 and Handy, 1985). The average magnitude of the transferred load was graphically approximated to 0.4 MPa. Consequently, the unexcavated slope was subjected to more load. At a certain

undercut span, the major principal stress increase could help to resist the displacement of the part above undercut area.

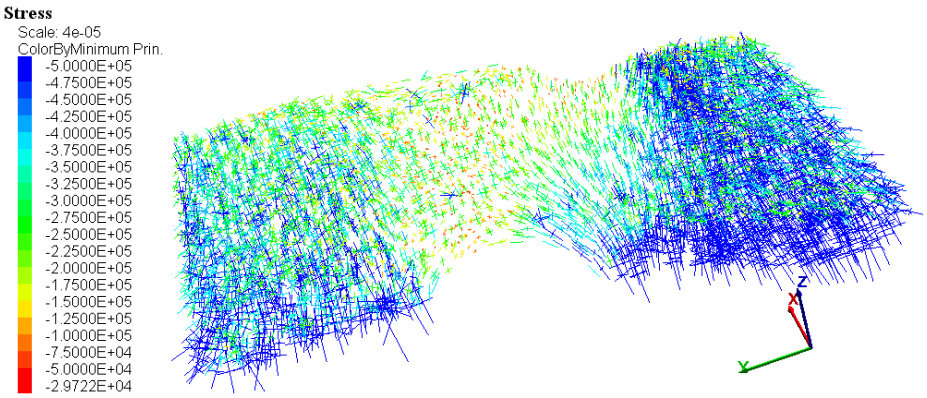

Figure 8 - Stress trajectories of principal stresses in block above G1 interface

In Figure 9, the maximum total displacement of model is approximately 43 cm up and located at the floor of the mining area approximately 20 cm displacement of the slope face. The excavation is an unload incident that affected the direction of total displacement around the mining area. Because of the unloading effect, the horizontal displacement will be plotted to observe the movement of the slope face concerned.

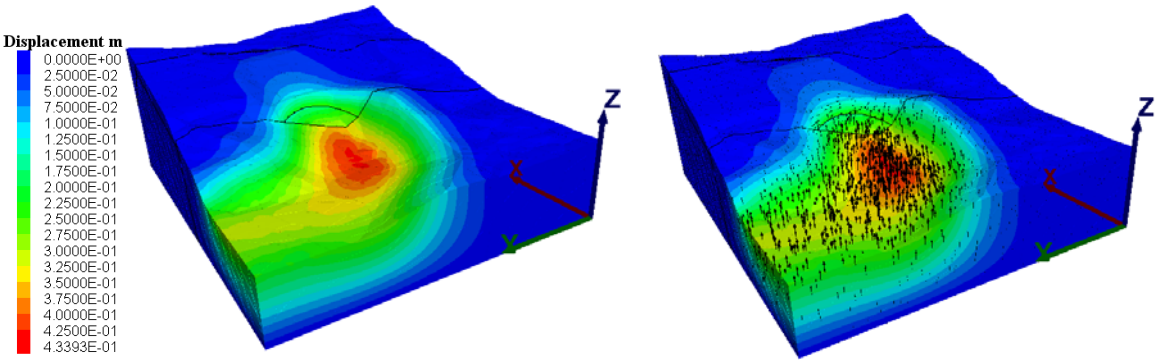

(a) Total displacement contours (b) Total displacement contours and vectors

Figure 9 - Total displacement contour and vector plots

Figure 10 presents a horizontal displacement plot in dip direction of the slope (x direction) and total displacement vectors (only the block above G1 interface). At the slope face, a numbers of elements in the block sitting on G1 interface were displaced more than their neighbors, especially near and beneath the interface. The maximum magnitude of the horizontal displacement was 21.5 cm. The local failure at the slope face in the block above G1 interface would have occurred.

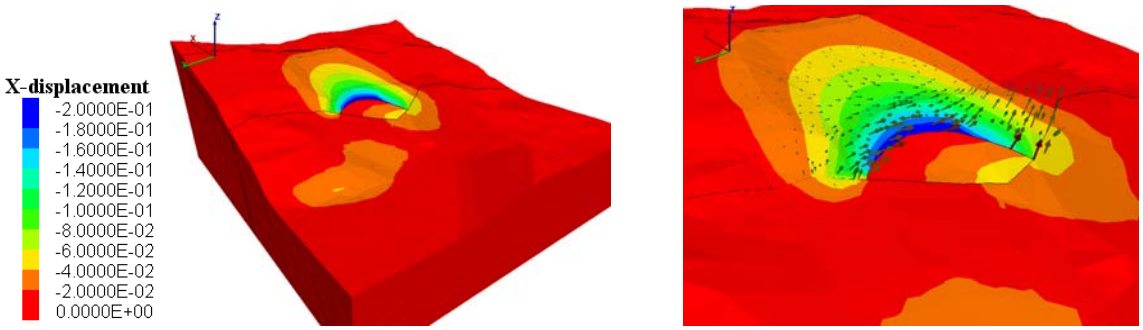

Figure 10 - Horizontal displacement contours of Area 4.1

5. CONCLUSIONS

Mining in Area 4.1 could potentially cause a massively sliding block caused by daylighting the G1 interface, a very low friction angle interface between underburden Gray Claystone and a thin layer of clay. The cut and fill mining method came into an attention and a mine plan at Area 4.1 was revised by the engineers. Area 4.1 has become a trial undercut slope field experiment. In the first period of the mine plan for Area 4.1, the slope was designed to be partially undercut and the G1 interface was also partially daylighted. From experience learnt from the Area 3 failure experience, the span of undercutting in Area 4.1 should not be exceed 100 m. The results from the numerical models also gave an idea of the load transfer, principal stress redistribution and the displacement of the slope above the undercut area. When partially undercut, a part of the slope above the undercut area was displaced more than other parts. The stresses in the slope face around the excavation were redistributed both in magnitude and direction. At a certain undercut span, the major principal stress increase could resist the displacement of the part above the undercut area. Currently, Area 4.1 has been operated and its completion is expected by mid 2013. The fruitful monitoring data from the installed monitoring systems will help the engineers to understand the behavior of undercut slopes, their design and how to monitor undercut slopes more safely and effectively.

6. REFERENCES

HANDY, R.L., 1985. The arch in soil arching, Journal of Geotechnical. Engineering, 115(9), p.1321 – 1325.

Itasca Consulting Group: 3DEC: Theory and Background, 2007.

Mae Moh Geotechnical Report, Thailand – Australia Lignite Mines Development Project, 1985. Appendix E.

MUNGPAYABAL, N., 2005. Residual shear strength of sheared Green Clay in Mae Moh mine. Master Thesis, Department of Mining Engineering, Chiang Mai University, Chiang Mai, Thailand.

PIPATPONGSA, T., KHOSRAVI, M.H., LEELASUKSEREE, C., MAVONG, N., and TAKEMURA, J., 2010. Slope failures along oblique plane due to sequential removals of propping portion in physical model tests. 15th National Convention on Civil Engineering, Thailand, Engineering Institute of Thailand, GTE60, CD-ROM, May 2010.

TERZAGHI, K., 1936. Stress distribution in dry and in saturated sand above a yielding trap door. Proceedings 1st International Conference on Soil Mechanics and Foundation Engineering, Cambridge, Massachusetts, p. 307 – 311.

Monitoring Rock Slope Stability from Spaceborne Synthetic Aperture Radar (SAR) Platforms Using Interferometric (InSAR) Image Stack Analysis

Bruce Macdonald
MDA Geospatial Services Inc. and MDA Systems Ltd.
Bernhard Rabus
MDA Geospatial Services Inc. and MDA Systems Ltd.
Jayson Eppler
MDA Geospatial Services Inc. and MDA Systems Ltd.

ABSTRACT: Operational monitoring of slope stability can be achieved by space based InSAR monitoring platforms. Natural and man-made rock slopes are monitored using a novel stack-based InSAR method that exploits both persistent point scatterers (PS) as well as coherent distributed scatterers (DS) such as areas of pavement and sparsely vegetated surfaces. The new method, Homogenous Distributed Scatterer (HDS)-InSAR identifies InSAR targets by using adaptive multi-looking of statistically homogenous pixel neighbourhoods combined with thresholding the differential temporal coherence of each target candidate with respect to its surroundings. HDS-InSAR preserves PS and therefore forms a direct generalization to our proven DualScale-PSI method. The density of HDS exceeds that of PS by more than an order of magnitude often providing essentially continuous coverage over urban and industrial landscapes featuring a mix of infrastructure with mostly bare soils or rock surfaces. The improved coverage enables better definition of surface motion and underlying geology, which will lead to superior interpretation of the geophysical mechanisms causing the surface deformation, e.g. through improved integration with 3D deformation modeling. We illustrate the performance of our new HDS-InSAR method compared to DualScale-PSI using displacement results from Vancouver, Canada; Bingham mine, USA; and the Palabora mine, South Africa.

1. INTRODUCTION

Increasing populations and economic development worldwide has led to vastly expanded construction of tunnels, highways, bridges, and utility lines over past decades. Monitoring the stability and safety of this accumulated infrastructure in regard to aging, as well as its interaction with superficial geology and natural hazards presents a formidable problem that will become ever more pressing in the future. Surface displacement time series measured with spaceborne InSAR data at monthly intervals and few meters spatial resolution can provide reliable reconnaissance of infrastructure stability with comprehensive spatial coverage. This frees now overwhelmed ground-based monitoring to the complementary tasks of very high temporal resolution monitoring of acutely dangerous conditions previously identified by the InSAR method. InSAR and ground-based methods can be tightly integrated with available environmental data and modelling of structures and ground motion to derive infrastructure risk maps.

Conventional Differential InSAR (D-InSAR) is limited to favourable environments due to the susceptibility to noise. Fine resolution data helps as signal noise can be reduced through averaging techniques. But, this comes at a loss of spatial resolution. Figure 1 shows a high resolution image over a slide area with minimal vegetation. The area with high velocity rates cannot be resolved due to this loss in spatial resolution due to techniques applied.

1) RSAT-2 © MDA 2011 2) GSI Value Added © MDA 2011

Figure 1 - Fels slide, Alaska (RADARSAT-2 spotlight)

To achieve the high spatial resolution necessary to derive these risk maps for a wide range of terrain and structures such as bridges, natural slopes and embankments has motivated us to develop a novel InSAR method that exploits both persistent point scatterers (PS) as well as coherent distributed scatterers (DS) such as areas of pavement or partially vegetated terrain. In this paper we give a description of the current prototype of our method. We give a demonstration of first results in the form of high resolution ground deformation trends and thermal dilation maps over an urban area.

2. METHODS

The new method, Homogenous Distributed Scatterer (HDS)-InSAR provides an optimum combination of InSAR phase quality and spatial resolution by using adaptive multilooking of statistically homogenous pixel neighbourhoods combined with a coherence threshold of the differential phase of each neighbourhood with respect to its surroundings. Figure 2 shows the full flow chart of our new HDS-InSAR solution, while Figures 3, 4 and 5 illustrate three steps of the actual HDS algorithm.

Forming a direct generalization to our proven DualScale-PSI method and fully preserving PS, the HDS-InSAR method corresponds conceptually and closely matches the performance of similar methods recently proposed such as (Ferretti et al., 2011) or (Parizzi et al., 2011). We use both parametric and non-parametric tests (Parizzi et al., 2011) for an optimum definition of the adaptive neighbourhoods. The final selection of HDS is done via temporal coherence thresholding on the HDS candidates. The density of HDS exceeds that of PS by factors 10 to 15, often providing essentially continuous coverage over bridges and road lanes. HDS-InSAR solves and corrects for temperature dilation (Monserrat et al., 2011) in addition to topographic height for each HDS which leads to significant coherence improvement prior to spatial phase unwrapping.

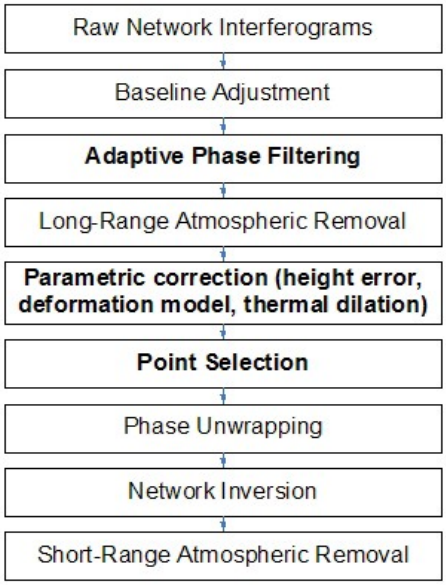

Figure 2 - Flowchart of HDS InSAR solution

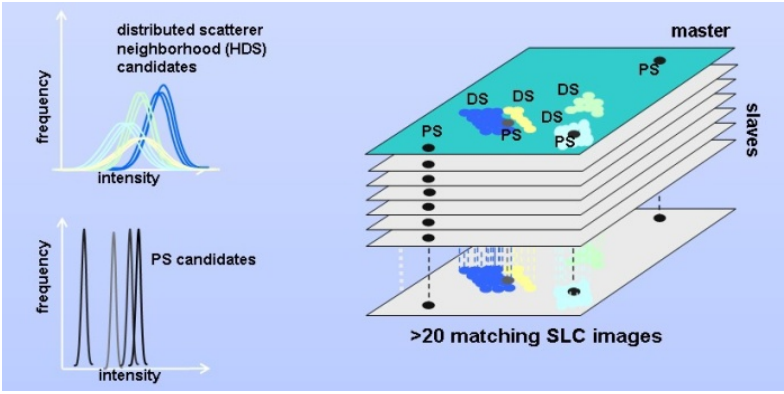

Figure 3 - First step of the HDS algorithm. Construct neighborhoods of pixels with similar intensity distribution

By definition HDS is an adaptive spatial filter that groups neighboring pixels with similar (amplitude) time series statistics through a SAR image stack (Figure 3). The current prototype first compares for each pixel the time series statistics of this pixel with respect to those of pixels of a rectangular maximum neighborhood, using a specified similarity measure. Weightings proportional to the values of the similarity measure are then applied to obtain averaged values for the amplitudes of the SAR image stack and phases of the interferometric network generated from the stack. For the similarity measure the HDS prototype allows choosing between two non-parametric (Kolmogorov- Smirnov and Anderson Darling, and one parametric (GLRT, assuming Rayleigh distribution) statistical tests (Parizzi et al., 2011). The HDS prototype links with either the 2D or the PS strand of the pre-existing MDA R&D InSAR solution. Numerical performance of neighborhood selection needed to be optimized to keep runtimes for thicker full scene stacks manageable.

After defining the HDS neighborhoods, adaptive multilooking of each network interferogram can be carried out. Sample results shown in Figure 4 illustrate the efficiency of the adaptive filtering as both an excellent speckle and phase filter. Sharp boundaries (of fields, parking lots, streets, etc.) and point

targets are extremely well preserved. (Eppler et al., 2011) The final step is the phase component estimation of the HDS filtered interferograms using a three dimensional search comprising topographic error, displacement, and thermal sensitivity [Figure 5]. Likewise point like targets (PS) are preserved as such and retain their appropriate displacement rates as comparison with the previous PSI results show.

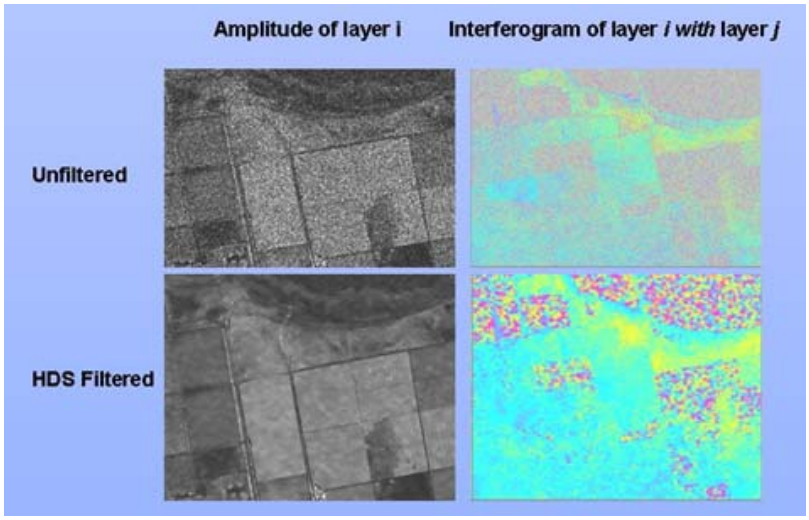

1) **RSAT-2 © MDA 2010 2) GSI Value Added © MDA 2011**

Figure 4 - Second step of the HDS algorithm: adaptive filtering of stack amplitudes and interferograms over the HDS neighborhoods

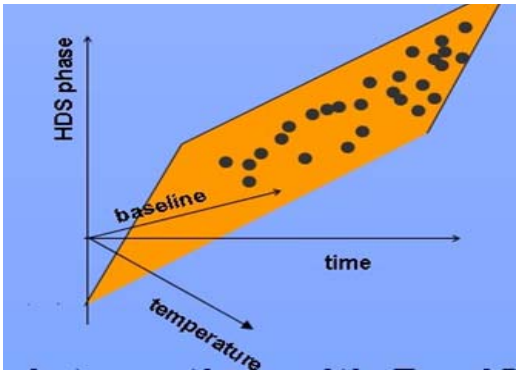

Figure 5 - The third step of the HDS algorithm. Separate (statistically - similar to PSI) filtered phase contributions – displacement, atmosphere, topography, and thermal dilation for each HDS and evaluate phase quality

As mentioned already the point density of HDS is very significantly increased over the PSI result. In regards to quantity and quality of the HDS points tests show that Anderson-Darling is the best similarity measure for thick (15+ scenes) stacks, while GLRT is the measure of choice for thinner stacks.

3. RESULTS

We illustrate the performance of our new HDS-InSAR method compared to DualScale-PSI using displacement results from the urban area of Vancouver, Canada. The data set was previously processed with MDA's PSI solution providing the possibility for comparison with results achieved with the current HDS prototype. Figure 6 shows an example of the large scale deformation as measured with the Dual-

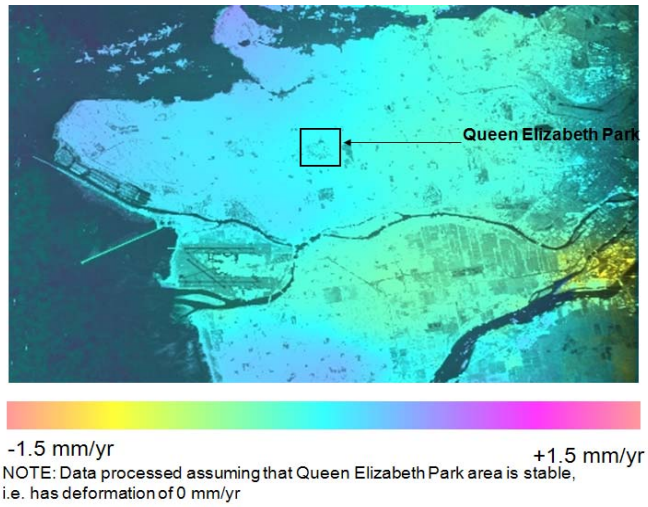

1) RSAT-2 © MDA 2011 2) GSI Value Added © MDA 2011

Figure 6 - Large spatial scale deformation Vancouver. (RADARSAT-2 ultrafine)

Scale PSI processing (using spectral diversity for PS selection). The advanced PSI (using the temporal coherence evaluated differentially against a small spatial neighbourhood for PS selection), and finally the HDS-InSAR results for part of the Vancouver airport.

Figure 7 shows the mean Line of Sight (LOS) deformation rate measured with HDS-InSAR for the entire Vancouver airport (a subset of Figure 6). Substantial subsidence occurs for large parts of the airport with stronger subsidence observed over unprotected buildings such as parking arcades, while

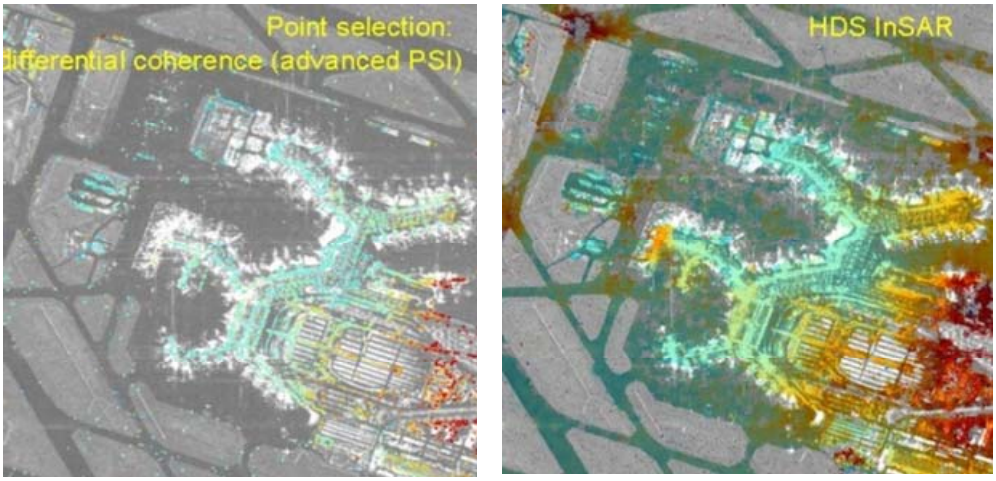

1) RSAT-2 © MDA 2011 2) GSI Value Added © MDA 2011

Figure 7 - Comparison of PSI and HDS-InSAR results for part of the Vancouver airport

buildings protected by deep anchoring or gravel padding show less deformation or less spatially variable deformation respectively. Only the HDS-INSAR map shows displacement over the tarmac which is entirely comprised of distributed scatterers that are eliminated in the PSI methods.

The novel PSI solution has been tailored to the special challenges posed by the open pit environment. The steep benches leading into the pit can be several hundred meters deep, trapping dense local atmosphere in the pit. (Figure 8 Left) The optimized InSAR solution required a static atmospheric phase correction model. The slowly variable "static" water vapor contribution to the phase is modeled as a function of topography for any given acquisition. (Figure 8 Middle) We analyze each spatial layer after the baseline adjustment and the topographic flattening to derive the relationship between phase and topography. We find that static atmospheric correction is crucial for successful PSI inversion in open pit environments. Our solution removes the bulk of the static atmospheric component (Figure 8 Right).

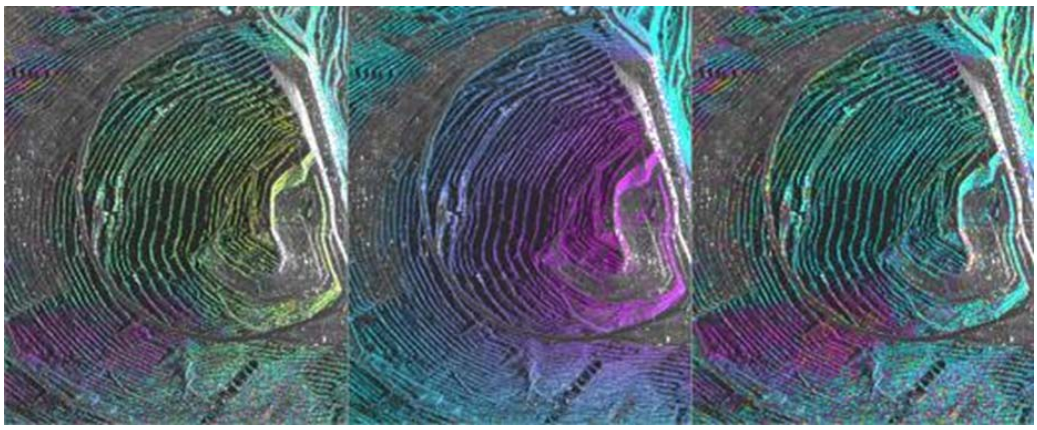

Figure 8 - Left: signal and atmosphere, Middle: atmospheric model, Right: signal (motion) only

Figure 9 illustrates the magnitude of motion over the InSAR stack which exceeds the aliased rate imposed by the sensor wavelength. Velocities 0.1m to 0.45m/yr LOS can be accurately measured over a 24 day period. This can only be achieved when the phase noise has been sufficiently reduced as it has with this novel approach, to allow for robust spatial unwrapping.

The combination of advanced 2-D and 3-D numerical models of mining-induced deformations with surface displacement maps measured by satellite-based InSAR with the PSI solution can provide a safe and effective means to identify and map spatial movements in large open pits. When the motion becomes more complex as those related to underground block cave mining induced subsidence greater sampling coverage is required. HDS InSAR provides a greater number of points from areas of distributed scatterers while preserving all the point scatterers.

To illustrate the benefit of the gain in density of targets measured, for asset monitoring, Figure 10 shows the PSI candidates while Figure 11 shows the HDS-InSAR results on the crest of the Palabora mine pit. The improved resolution over the DS or PSI methods provide a more detailed mean deformation rate for the active road edge. The contiguous coverage also allows for better monitoring of motion velocities as you approach the edge of the block cave induced failure (time series profiles Figure 11).

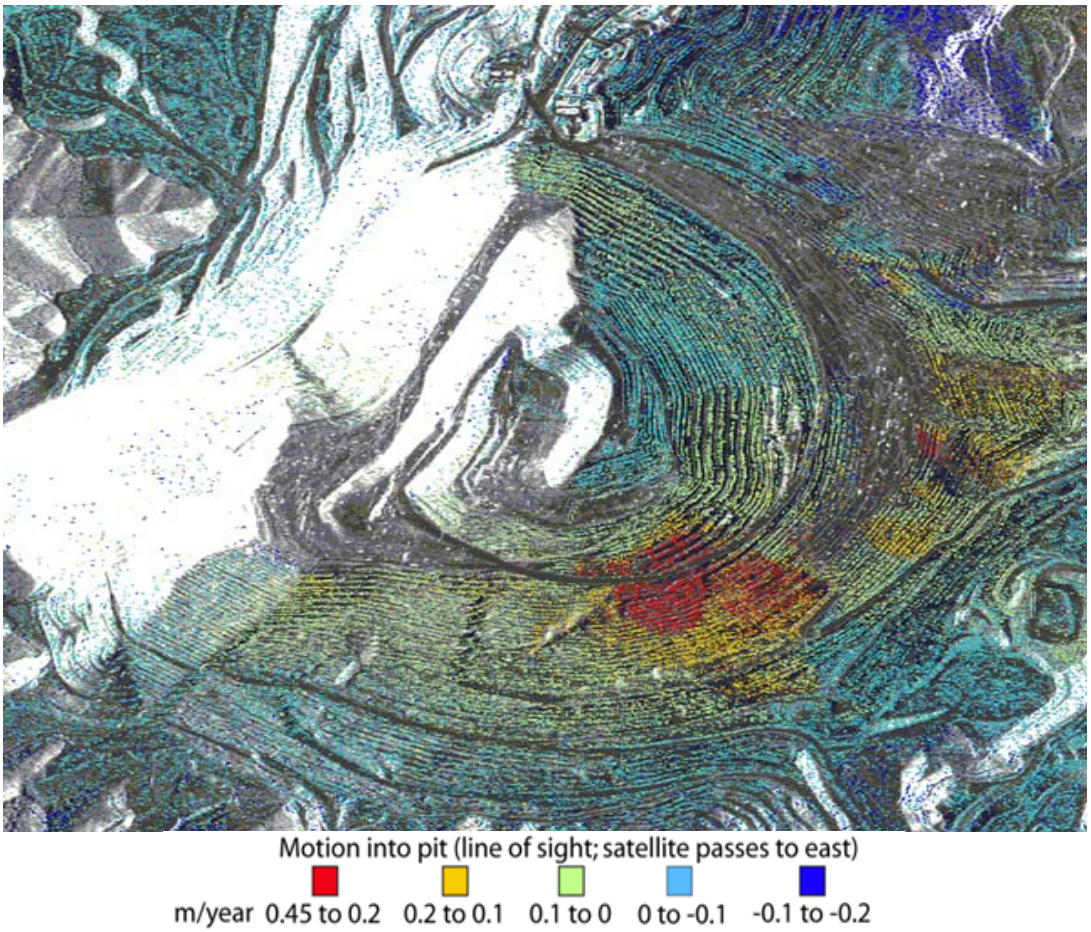

Figure 9 - LOS deformation measured with PSI for the pit at Bingham Mine

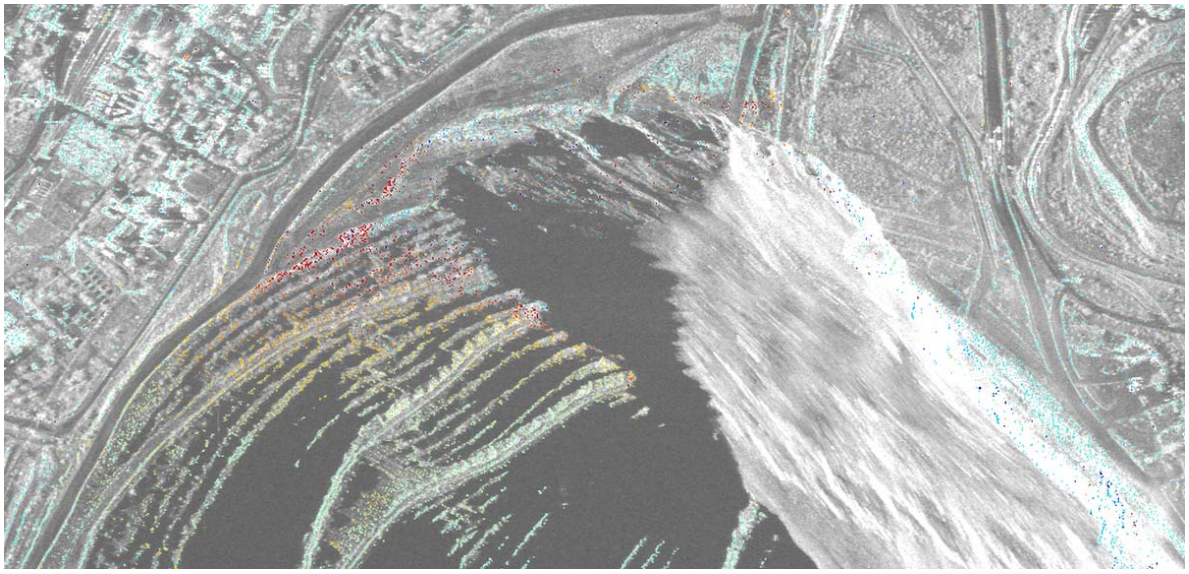

Figure 10 - PS candidates around the crest of the failure at Palabora Mine site

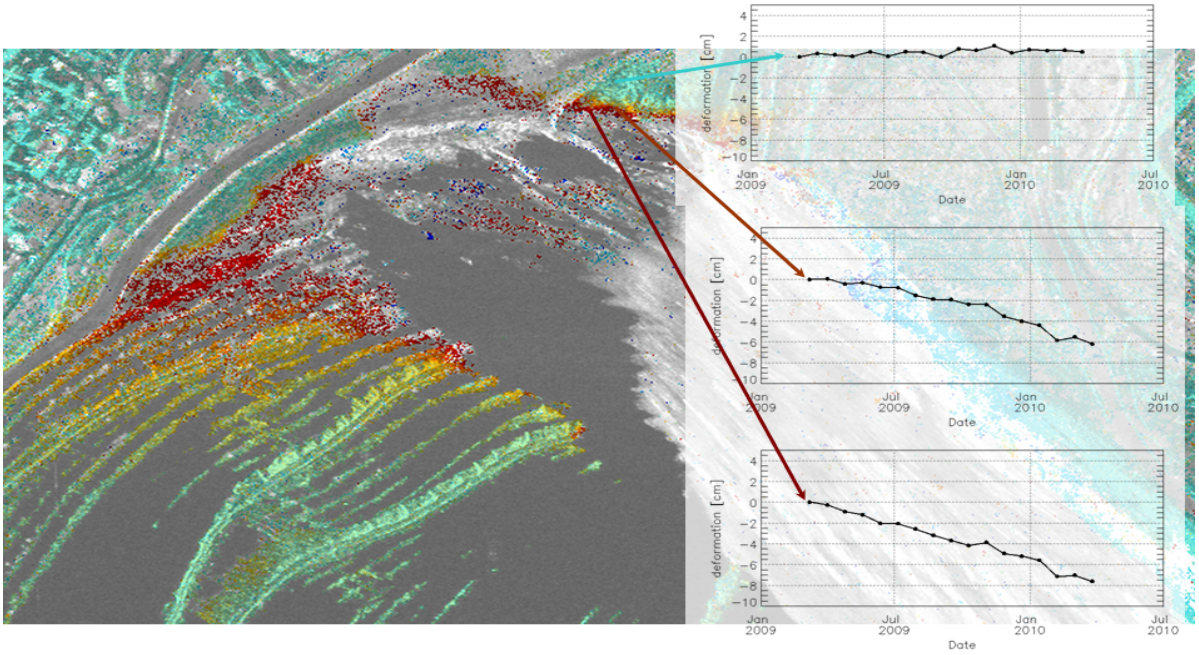

2) GSI Value Added © MDA 2011

Figure 11 - LOS motion measured with HDS-InSAR around the failure at Palabora. Note the increase in measured targets over the number of PSI identified points in Figure 10

This ability is important for protecting key mine infrastructure located on the surface, especially where subsidence caused by underground mass mining may be interacting with the slopes of an open pit above as is the case at Palabora. Finally, in Figure 12 is a detailed example of the crest of the Palabora pit where the active road and assets across the road are actively being monitored with HDS-InSAR.

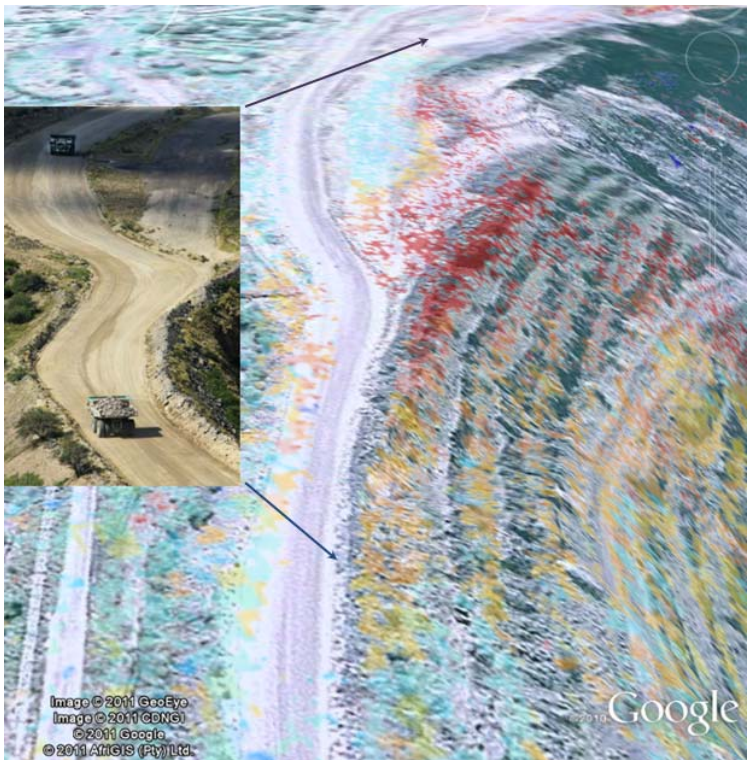

2) GSI Value Added © MDA 2011

Figure 12 - Monitoring the crest of the Palabora pit with HDS-InSAR

4. CONCLUSIONS

HDS-InSAR with high resolution SAR data opens new horizons for detailed risk monitoring of infrastructure in urban and industrial environments. This is due to HDS increasing the density of phase stable targets by a factor of 10 to 15 compared to standard PSI methods. In particular, asphalted surfaces such as roadways, pit benches and crests as well as steel and concrete structures (buildings, conveyors and overpasses) are often continuously covered by HDS targets.

HDS-InSAR is a fully commercial solution designed for industrial and resource active sites. Products and services were collaboratively designed to augment current management and technical activities at head office and the mine site. This full service approach has been successfully applied to many mining operations worldwide providing timely and accurate results to mine operators.

Further gains have been made to better monitor facilities and infrastructure. Estimation of thermal dilation along large structures provides complimentary information which can help distinguish design vs. failure related displacement. The correction of dilation induced phase helps reduce spatial gradients therefore reducing ambiguities during phase unwrapping.

5. REFERENCES

FERRETTI, A., FUMAGALLI, A., NOVALI, F., PRATI, C., ROCCA, F. and RUCCI, A. (2011). A New Algorithm for Processing Interferometric Data-Stacks: SqueeSAR. IEEE Trans. Geosci. Remote Sens., 49(9), 3460 – 3470.

PARIZZI, A. and BRCIC, R. (2011). Adaptive InSAR Stack Multilooking Exploiting Amplitude

Statistics: A Comparison Between Different Techniques and Practical Results. IEEE Geosci. Remote Sens. Letters, 8(3), 441-445.

MONSERRAT, O., CROSETTO, M., CUEVAS, M. and CRIPPA, B. (2011). The Thermal Expansion Component of Persistent Scatterer Interferometry Observations. IEEE Geosci. Remote Sens. Letters, **8**(5), 864-868.

EPPLER, J. and RABUS, B., (2011). Monitoring Urban Infrastructure with an Adaptive Multilooking InSAR Technique. Proceedings of FRINGE 2011. September 2011. Frascati, Italy.

6. COPYRIGHTS

Effect of Mining on Deformation Patterns in a Large Open Pit Rock Slope

A.K. Alzo'ubi
Department of Civil Engineering, Abu Dhabi University
C.D. Martin
Dept. Civil & Environmental Engineering, University of Alberta
D.M. Cruden
Dept. Civil & Environmental Engineering, University of Alberta

ABSTRACT: Block toppling in natural rock slopes has been under investigation since the 1970's. De Freitas and Watters (1973) introduced the term "toppling" to describe the movements of rock slopes by rotation in steeply dipping beds. The Lornex pit case history from British Columbia (Canada) was chosen to study the effect of mining on the stability of toppling rock slopes. A discrete element approach that allows fracturing of intact material was applied successfully to model the composite rock slide-rock topple movement. Three main movement modes were observed in the field and the numerical model; the sliding of the top of the slope exposed normal scarps, the toppling at the middle part of the slope exposed obsequent scarps facing opposite to the slope face, and dilation of the rock caused by fracturing at the toe formed loose material. The development of the rupture surface at the toe of the slope was traced and did not evolve into a continuous rupture surface throughout the slope both in the field and the numerical simulation. Good agreement was achieved between the deformations recorded in the field and the numerical simulation.

1. INTRODUCTION

Block toppling in natural rock slopes has been under investigation since the 1970's. De Freitas and Watters (1973) introduced the term "toppling" to describe the movements of rock slopes by rotation in steeply dipping beds. Goodman and Bray (1976) defined block toppling as the overturning and toppling of rock blocks formed mainly by two sets of discontinuities: a penetrative continuous discontinuities following bedding surfaces into the rock mass, and discontinuous sets of joints perpendicular to bedding. According to Terzaghi (1962), these characteristics are associated with the sedimentary rocks in which the cross-joints are perpendicular to the bedding. The thickness of the beds in sedimentary rocks ranges from centimetres to metres.

Terzaghi (1962) also described a geological model for crystalline rocks such as marble or granite as irregular-shaped crystalline particles. The jointing is a random joint pattern in which the cross-joints are not perpendicular to the main set of joints. Nichol et al. (2002) investigated rock slope toppling in natural rock slopes and found topples where the secondary joint set is not perpendicular to the inward dipping main joint set. The thickness of the rock columns susceptible to toppling is considerably smaller in sedimentary rock than in plutonic rocks. Tosney (2001) pointed out the thickness of rock columns in plutonic rocks can be as much as 40 metres as in the case of Highland Valley Copper Mine, no clear rupture surface has been observed throughout the slope.

The Highland Valley Copper (HVC) mine is located in British Columbia 75 km southwest of Kamloops. It is the largest copper mine operation in Canada and consists of two pits; the Lornex Pit and the Valley Pit. The southeast wall of the Lornex Pit moved by toppling, sliding, and raveling in the order of 20 metres. Movements have been observed and monitored to insure the safety and continuity of the mining operations in the area of instability. The movement mode observed in the field was compared to the movement characteristics predicted by the numerical model. During the mining operation, an extensive

displacement-monitoring program was carried out using slope-monitoring prisms (SMP's). The displacement due to the mining operation was compared to the displacement predicted by the UDEC-DM simulation after carrying out an intensive calibration process by utilizing the actual measured displacement in the field. A good agreement with field observation has been achieved.

2. GEOLOGY OF THE SITE

The rock mass characteristics of the southeast wall at the Lornex Pit vary widely and range from strong rock to a very weak rock mass. The Lornex Pit is approximately 1900 m in length, 750 m depth and 500 m wide. Three main geological units occur in the Lornex Pit: Skeena Quartz Diorite, the Bethsaida Granodiorite and the Quartz Porphyry Dyke (Newcomen et al., 2003a). Extensive alteration zones have been identified throughout the Lornex Pit. These alteration zones are mainly structurally controlled with weak to moderate chloritic and sericitic alteration zones around shears and faults.

The geological discontinuities analysis of the Lornex Pit identified two major sets of discontinuities: the first set of faults is continuous and dips into the slopes at angles between 70° to 80° with a spacing between 20-40m; the second set is less continuous and dips in the same direction as the slope at angles ranging between 50°to 60°from the horizontal with an average spacing between 10-20m. The two sets of joints contain infilling that controls their shear strength properties (Tosney et al., 2004).

3. MOVEMENT MODE AT LORNEX PIT

The movement at the southeast wall of the Lornex Pit is a composite mode involving both: sliding along the secondary joint set at the crest of the slope, forming a normal scarp facing in the same direction as the slope face, toppling in middle parts of the slope driven by sliding along the indipping discontinuities of the slope forming obsequent scarps, and dilation of the rock mass at the toe of the slope as a result of stress concentrations. According to Cruden and Varnes (1996), the movement at the Lornex pit is a composite rock slide-rock topple, and it is driven by the movement of the actively sliding block at the crown of the slope.

The block toppling observed at the southeast wall is different from the block toppling proposed by Goodman and Bray (1976). Tosney et al. (2004) discussed in detail the main differences between the two, which involved the formation of normal scarps at the crest of the slope and the formation of tension cracks at the crest of a slope in topples described by Goodman and Bray (1976). In addition, the scale of the block toppling described by McAffee and Cruden (1996), Goodman and Bray (1976) averages 1:100 to 1:150 (scale is set by the thickness of the layers relative to the height of the slope). While at the HVC mine, this scale averages 1:7 to 1:11. Also, while the crosscutting joints are perpendicular to the bedding in the block toppling (McAffee and Cruden, 1996, Cruden and Hu, 1994, Goodman and Bray, 1976) because these topples are in sedimentary rocks, the secondary joint set at the Lornex Pit is not perpendicular to the main inward dipping discontinuities. The block toppling observed at the HVC mine resulted in a large displacement of up to 20 metres with no rupture surface development.

The displacement the Lornex pit was triggered by the excavation at the toe accompanying the background movement. As the confinement (provided by the benches) was reduced by the mining, the mining-induced deformation accelerated. Tosney (2001) showed some surface expression observed at the southeast wall of the Lornex Pit such as normal scarps. Similar behaviour was also observed at the southwest wall of the Lornex Pit (Newcomen et al., 2003a). The complexity of the slope at the HVC mine was increased by the presence of infilling material in the faults and high pore-water pressure in the slope.

4. MATERIAL TESTING

Geotechnical testing for the intact rock and discontinuities is essential to determine the material properties needed for numerical modeling to be reliable. Tosney (2001) conducted a series of point load tests on intact material from the southeast wall to determine the unconfined compressive strength (UCS) of the intact material. The results indicated that the average UCS is between 37 MPa and 103 MPa. Basic geotechnical tests were also performed to determine the strength parameters of the faults' gouge samples. The gouge material contains montmorillonite clay mineral that has swelling potential and may affect the slope behaviour in the presence of water. The direct shear test was used to determine the shear strength properties of the fault gouge material. The friction angle had a peak value of 18° and a residual value of 12°, while the peak cohesion was 20 kPa, and the residual cohesion was 6 kPa (Tosney et al., 2000).

5. GEOMECHANICS ASSESSMENT AND STRENGTH PROPERTIES

A backpack-mounted GPS receiver was used to map the large-scale discontinuities in the southeast wall. Information on faults and surface scarps was logged as either a line or a point feature (Newcomen et al., 2003b). Two major discontinuities sets were determined: the indipping faults and the out-dipping structure. These two sets are believed to be the controlling factor of the slope behaviour and to develop the movement mode observed at the southeast wall. The results of the mapping are summarized in Table 1, which shows the RMR for different areas of the Lornex southeast wall ranges from 40 to 80. The non-linear failure criterion proposed by Hoek and Brown (1988) was used by Tosney (2001) to estimate the Mohr-Coulomb strength parameters necessary to develop the numerical model. Table 1 shows the strength properties used in the numerical model. The site engineers estimated the tensile strength at 0.1 MPa for all the geological units (Tosney, 2001).

Table 1 - Strength properties of the geological units used in the model, modified from Tosney (2001)

RMR 76	HB (m)	HB (s)	UCS (MPa)	HB (mi)	ϕ(°)	C (MPa)	K (GPa)	G (GPa)
40	0.39	4.54e5	65	28	29	0.7	4.7	2.2
45	0.55	1.04e4	65	28	33	0.7	6.2	2.9
50	0.79	2.40e4	65	28	36	0.8	8.3	3.8
55	1.13	5.53e4	65	28	39	0.9	11.1	5.1
60	1.61	1.27e3	65	28	43	1.0	14.8	6.8
65	2.30	2.93e3	65	28	46	1.2	19.8	9.1
70	3.28	6.74e3	65	28	48	1.4	26.4	12.2
75	4.69	1.55e2	65	28	51	1.7	35.1	16.2
80	6.71	3.57e2	65	28	54	2.1	46.9	21.6

The RMR 1976 was also used to estimate the elastic properties of the southeast wall geological units (Table 1) based on Hoek-Brown's 1988 criterion. Two sets of joints were modeled explicitly. The steeply inclined faults in the slope contained infilling material; these fillings were sampled and tested in the laboratory. While the shear strength properties of the secondary set of discontinuities was estimated. Table 2 shows the discontinuities' properties, The normal and shear stiffness and the residual values of the fault gouge material of the two joint sets were adapted from Tosney's analysis in order to compare the results with the results from the UDEC-DM approach. The movement rate peaks coincide with block excavation at the toe of the slope. Tosney (2001) stated that the majority of the recorded displacement is mining-induced displacement. By simulating the sequence of the excavations at the Lornex southeast wall, the numerical model can be calibrated.

6. THE UDEC-DM NUMERICAL MODEL

One of the biggest advantages of numerical methods over other methods of rock slopes analysis, such as Limit Equilibrium, is the numerical model's ability to model the displacement magnitudes. Alzo'ubi et al. (2007) introduced the UDEC-DM to simulate failure jointed rock masses. In addition, the UDEC-DM (Alzo'bi et al. 2007) is also capable of handling fracturing throughout the intact material.

Table 2 - The discontinuities properties used in the model, modified from Tosney et al. (2000)

Parameter	Indipping faults	Secondary discontinuities
Orientation from horizontal (°)	70	125
Spacing (m)	30	15
Normal Stiffness (GPa/m)	4	4
Shear Stiffness (GPa/m)	1	1
Cohesion (kPa)	6.0	0
Friction (°)	12	25

The geometry of the model was based on the actual mining history adapted by Tosney (2001). The mining steps are illustrated in Figure 1A. The numbers inside the boxes show the sequence of the blocks excavation. During the mining of blocks 1 to 15, four slope-monitoring prisms (560, 468, 413, 454) were used to track the mining-induced deformation, Figure 1B shows the location of these SMP's along the slope face. Tosney et al. (2000) presented the mining-induced displacement associated with each block excavation, which was calculated by subtracting the background movement from the total displacement.

The major discontinuities dipped into the model at an angle of 70° with joint spacing of 30 m, while the secondary discontinuities dipped in the same direction as the slope face at angle of 55° from the horizontal with joint spacing of 15 m. The two joints intersected each other to form blocks. Inside each block, flaws with a 1.4 m edge length were implemented inside the area susceptible to toppling. The flaw implementation resulted in generating randomly polygonal blocks as shown in Figure 2A, whose insert shows the details of the flaws inside the model.

The flaws were generated in the region susceptible to toppling. This region was determined by using preliminary conventional UDEC similar to Tosney (2001) analysis. The strength and deformation properties were assigned to the model based on the RMR rating shown in Table 1. To incorporate the effect of the groundwater pressure, the water table was applied to the model assuming full saturation. A horizontal-to-vertical stress ratio of 1.5 was applied to the model; this value was adopted from Tosney (2001). The modeling process was started by, bringing the model to equilibrium under high strength properties, bringing the model to equilibrium under realistic properties, and then the model was calibrated as described in the following section.

6.1 Calibration of the Model

To build a reliable numerical model, the model needed to be calibrated against the field deformation attributed to the mining process. As mentioned earlier, four SMP's positioned as shown in Figure 1B were used to monitor the slope movement. The mining-induced deformation captured by SMP number 413 was used to calibrate the model. After removing blocks 1-8 and 9-13, the model was rerun until equilibrium was achieved. For each run, the displacement, velocity, and unbalanced forces at the model

were monitored. A good agreement between the calculated and observed displacement was achieved at the normal and the shear stiffness shown in Table 3.

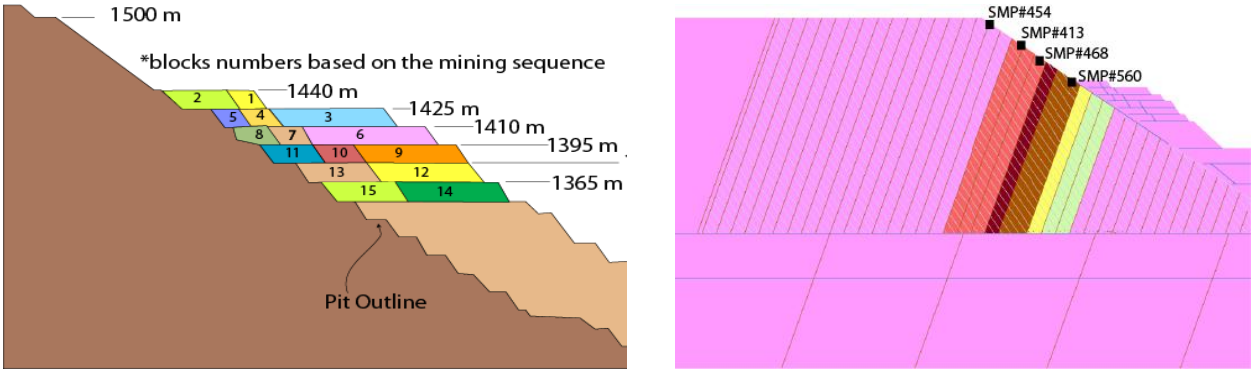

A) Block Excavation sequence **B) Slope monitoring prisms locations**

Figure 1 - Block Excavation sequent at the Lornex pit and the location of the SMP's

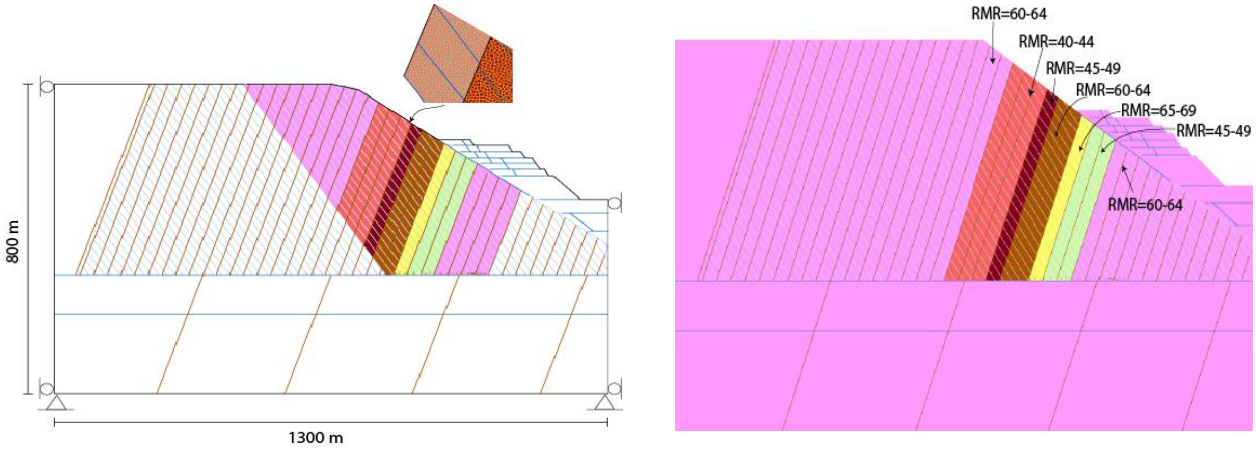

A) UDEC-DM of the Lornex Pit **B) RMR 1976 ratings**

Figure 2 - The details of the UDEC-DM of the lornex pit, A)The Lornex southeast wall UDEC-DM; the insert shows the details of the flaws B) RMR ratings used in the UDEC-DM

6.2 The UDEC-DM Results

An extensive numerical modeling program was carried out to investigate the Lornex southeast wall and to verify the UDEC-DM approach. After the model had been brought to equilibrium under high-strength property values, the actual strength properties presented in the above sections were assigned to the model. Blocks 1 to 15 (see Figure 1A) were removed. After removing each block, the model was rerun until equilibrium was achieved. For each run, the displacement, velocity, and unbalanced forces at the model were monitored. In addition, the fracturing throughout the model was tracked to insure the validity of the model in terms of the field observations. The mining-induced displacement after each excavation step was calculated in order to compare this displacement to the field displacement.

6.3 Movement Mode in the Numerical Model

The rock movement at the Highland Valley Copper Mine involved sliding at the crest of the slope,

toppling over most of the slope, and bulging and distortion at the toe of the slope. The mechanism of the movement was successfully simulated by using the UDEC-DM approach. Figure 3 shows the numerical model after excavation of block number 15. The simulation was able to reproduce the surface expressions observed at the Lornex southeast wall. The insert in Figure 3 provides a closer look at the movement mode at the crest. Notice the formation of normal scarps.

Table 3 - Normal and shear stiffness resulting from the calibration process

RMR 76	Normal Stiffness (GPa/m)	Normal Stiffness (GPa/m)
40-44	11	3.5
45-49	14	4.5
60-64	34	11
65-69	46	15

The majority of the model suffered from toppling. The sliding along the indipping faults allowed the toppling of the rock blocks shown in Figure 3. This toppling movement formed obsequent scarps facing up the slope. This aspect of the movement has been observed at the Lornex southeast and the southwest walls (Newcomen et al., 2003a). At the toe of the slope, dilation of the rock mass formed. Tosney (2001) reported that on several occasions, loose material at the toe delayed the operation. Bulging occurred at the toe of the slope as a result of mining excavations which removed the confinement provided by the mined blocks. As the confinement was decreased, the stress concentration at the toe increased which caused extensive fracturing, fragmentation, and formed loose material, as shown in Figure 3. Cruden and Varnes (1996) characterized this type of movement at the toe as “bedrock flow”.

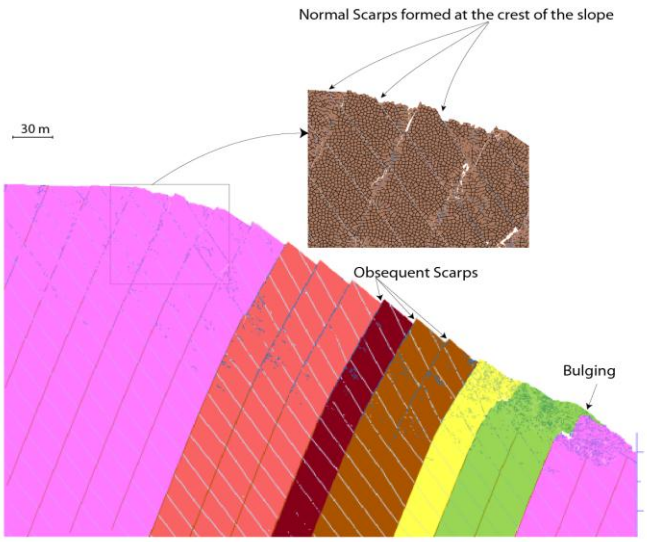

Figure 3 - The movement mode at the Lornex southeast wall simulated by the UDEC-DM

6.4 Deformation Comparison Between the field and The Numerical Model

Comparison of the field displacement results with those from the numerical simulation is essential to verify a numerical model. As mentioned earlier, the Lornex southeast wall was monitored by using an automatic total station and slope-monitoring prisms. The history function in the UDEC-DM was used to monitor the displacement as blocks 1 to 15 were excavated. The cumulative displacement was then plotted against the block number. Figure 4A presents a comparison between the measured displacement

and the simulation results for SMP#468. The simulated mining-induced deformations are in good agreement with the field records. The deformation in the numerical model was associated mainly with the removal of the toe blocks that were immediately adjacent to the slope. Excavating the bench blocks resulted in a smaller amount of deformation than excavating the blocks adjacent to the toe.

6.5 Deformation Comparison Between Conventional UDEC and the UDEC-DM Approaches

Tosney et al. (2004) used the conventional UDEC to model the Lornex southeast wall. Their results were compared to the results from the UDEC-DM simulation. Figure 4B presents the results at SMP#413. A good improvement was achieved by using the UDEC-DM at the location of SMP#413. This result can be attributed to the fracturing capabilities of the UDEC-DM approach. Fracturing through the intact material allow deformation to occur at the toe of the slope. This fracturing is not possible in conventional UDEC. Tosney et al. (2004) noted that the secondary joints were not detected in the fractured material at the toe of the slope. This finding means that fracturing occurred throughout the intact material. In mining risk management, moving the personnel and the equipment, required knowledge of areas susceptible to fracturing and material moving, this might impose some risk on the mining operations. UDEC-DM successfully modeled the bulging and fracturing at the toe of the Lornex southeast wall and captured the deformations associated with this fracturing and the formation of loose material at the open-pit mine toe.

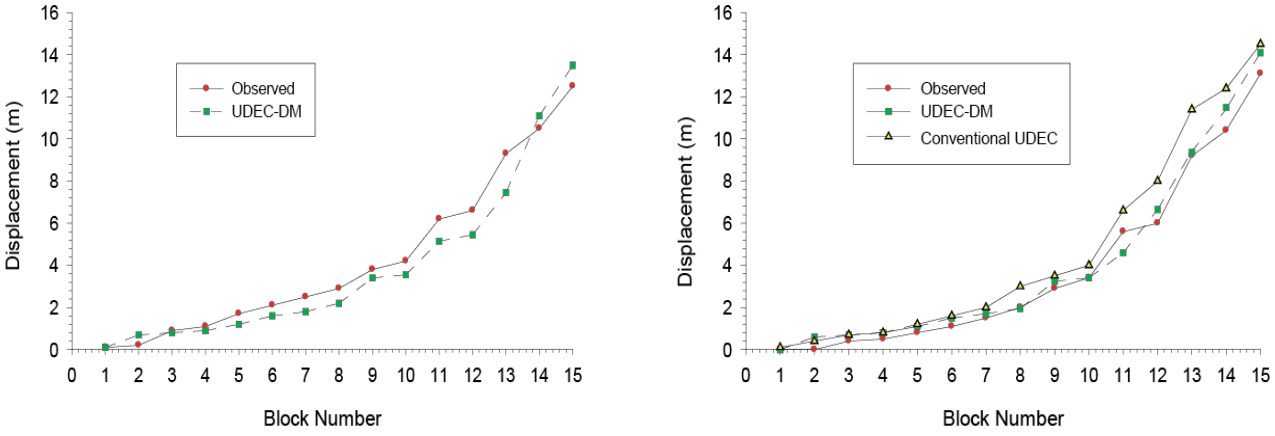

a) UDEC-DM versus field deformation

b) Conventional UDEC, UDEC-DM and field deformation

Figure 4 - Comparison between measured mining-induced displacements and the simulated UDEC-DM A) displacements at SMP#413 B) displacements at SMP#468

7. CONCLUSIONS

The UDEC-DM approach was applied successfully to model composite rock slide-rock topple. Three main movement modes were observed and modeled using the UDEC-DM. The sliding of the top of the slope exposed normal scarps; the toppling at the middle part of the slope exposed obsequent scarps facing opposite to the slope face, and bulging at the toe formed loose material. The development of the rupture surface at the toe of the slope was traced and did not evolve into a continuous rupture surface throughout the slope. This method was able to capture the composite rock mass movement. The deformations recorded in the field were compared to the simulation results, and a good agreement was achieved. The UDEC-DM results were also compared to the conventional UDEC results. While both modelling approaches are in reasonable agreement with the overall deformations, the UDEC-DM approach displayed the fracturing characteristics that were observed in the field

8. REFERENCES

ALZO'UBI, A., MARTIN, C., and CRUDEN, D., 2007. A discrete element damage model for rock slopes. In Rock Mechanics, Meeting Society's Challenges and demands, edited by E. Eberhardt, D. Stead, and T. Morrison, vol. 1, pp. 503–510. Vancouver, B.C.

ALZO'UBI, A., MARTIN, C.D. and CRUDEN, D.M., 2010. Influence of tensile strength on toppling failure in centrifuge tests. International Journal of Rock Mechanics and Mining Sciences 47(1):974-982.

BIENIAWSKI, Z., 1976. Rock mass classification in rock engineering. In Exploration for Rock Engineering, edited by A. Balkema, vol. 1, pp. 97–106. Cape Town, Johannesburg.

CRUDEN, D. and HU, X.Q., 1994. Topples on underdip slopes in the Highwood Pass, Alberta, Canada. Quarterly Journal of Engineering Geology, 27: 57–68.

CRUDEN, D. and VARNES, D., 1996. Landslide types and processes. In Landslides: Investigation and Mitigation, Special Report, ed. A. Turner and R. Schuster, no. 247, pp. 36–75. Transportation Research Board (National Research Council), National Academy Press, Washington, D.C.

FREITAS, D.E. and WATTERS, R., 1973. Some field examples of toppling failure. Geotechnique, 23: 485–514.

GOODMAN, R. and BRAY, J., 1976. Toppling of rock slopes. In Specialty Conference on Rock Engineering for Foundations and Slopes, pp. 201–234. ASCE, Boulder, CO.

HOEK, E. and BROWN, E., 1988. The HoekBrown failure criteriona 1988 update. In Proceedings of the 15th Canadian Rock Mechanics Symposium, pp. 31–38. Department of Civil Engineering, University of Toronto, Toronto, Canada.

MCAFFEE, R. and CRUDEN, D., 1996. Landslides at Rock Glacier site, Highwood Pass, Alberta. Canadian Geotechnical Journal, 33: 685–695.

NEWCOMEN, H., MAGGS, C., and SHWYDIUK, L., 2003a. Managing pit slope displacements: Highland Valley Copper's Lornex pit southwest wall. In Canadian Institute of Mining, Metallurgy and Petroleum (CIM) Bulletin, vol. 96.

NEWCOMEN, W., MURRAY, C., and SHWYDIUK, L., 2003b. Monitoring pit wall deformation in real time at Highland Valley Copper. In CAMIConference,.

NICHOL, S., HUNGR, O., and EVANS, S., 2002. Largescale brittle and ductile toppling of rock slopes. Canadian Geotechnical Journal, 39: 773–788.

TERZAGHI, K., 1962. Stability of steep slopes on hard unweathered rock. Geotechnique, 12: 251–270.

TOSNEY, J., 2001. A design Approach for Large Scale Rock Slopes. Master's thesis, University of Saskatchewan, Saskatoon.

TOSNEY, J., CHANCE, A., MILNE, D. and AMON, F., 2000. A modelling approach for large scale slope instability at Highland Valley Copper. In Mining Millennium 2000: International Convention and Trade Exhibition. Content Management Corp. Richmond Hill, ON., Toronto, Canada.

TOSNEY, J., MILNE, D., CHANCE, A.V. and AMON, F., 2004. Verification of a large-scale slope

instability mechanism at Highland Valley Copper. International Journal of Surface Mining, Reclamation and Environment, 18(4): 273–288.

An Investigation into the Stand-up Time of Stopes at Birchtree Mine in Thompson Manitoba

Matthew Violot
University of Saskatchewan
Doug Milne
University of Saskatchewan
Denis Thibodeau
Vale
Cecile Kelly
Vale

ABSTRACT: Vale Canada's Birchtree Mine, located in Thompson Manitoba, has been experiencing problems with hanging wall / footwall dilution, as well as sloughing off of adjacent stopes and temporary stope block backs. Birchtree Mine is interested in determining how time affects the stability of their open stope blocks. Many factors simultaneously influence open stope stability (rock mass quality, joint condition, stress condition). This makes it challenging to determine the influence of a single parameter such as exposure time or stand-up time. This study focuses on determining the effect of exposure time on open stope dilution and combines stress analysis and empirical based approaches.

1. INTRODUCTION

Open stoping is a common bulk mining process. This method leaves large open excavations which can present design challenges for a mine. Open stope stability is influenced by a range of factors which can vary significantly throughout the mine. Some of these factors include: rock mass quality, stress state, stope geometry and geological structure. It is important to assess these factors to avoid excess dilution and potential failures, which can increase the cost of mining and adversely affect safety. Exposure time, which is not usually formally assessed, can have a large impact on stability. Time can allow the rock mass to further degrade under changing stress, thus increasing the chance for potential instability.

Birchtree Mine wants to better understand how time affects the stability of their stopes as they have had problems with time dependent dilution. The goal of this study is to develop a suitable method to estimate the stand-up time of Birchtree stopes. An empirical design method is desirable as it allows for continued improvement as case histories are collected, and is quick and easy to use. Case histories have been analyzed to develop and properly assess the effectiveness of a newly developed proposed empirical design approach.

2. MINE BACKGROUND AND GEOLOGY

Vale Canada's Birchtree Mine is located approximately 5 km southwest of Thompson, Manitoba. The mine uses a type of slot and slash mining called vertical block mining (VBM). Stopes are mined transversely in panels with each draw point generally accessing three stopes to create a panel (Figure 1). Each stope in a panel is backfilled before the next one is blasted. Currently a primary/secondary pyramidal mining sequence for extracting panels is being used. The pyramidal sequence is used to help minimize stress increases to improve stope stability.

Understanding geology is important in a stability analysis. Processes that formed the current rock mass and its structure have a large influence on the strength and structure of the rock mass (i.e. folds, faults, metamorphism, etc.). The following background on the geology of Birchtree mine is taken from Layton-Matthews et al., (2007).

Birchtree mine is located in the Thompson Nickel Belt in northern Manitoba, which trends 30 degrees north east. It reaches from approximately 50 kilometres north-east to 125 kilometres southwest of Thompson, Manitoba. The Thompson Nickel Belt is host to a Ni-Cu-PGE (Nickel-Copper-Platinum Group Elements) mineralization of magmatic origin and the Birchtree deposit is located in the Ospwagan Group.

The main ore body consists of breccias that have a sulphide matrix and peridotite clasts (INCO, 2006). The four main rock types found in the area include peridotite, biotite schist, quartzite, and the iron formation. There are also four main faults present. These are named the 609, 906, 780, and the 1080 faults (Figure 2).

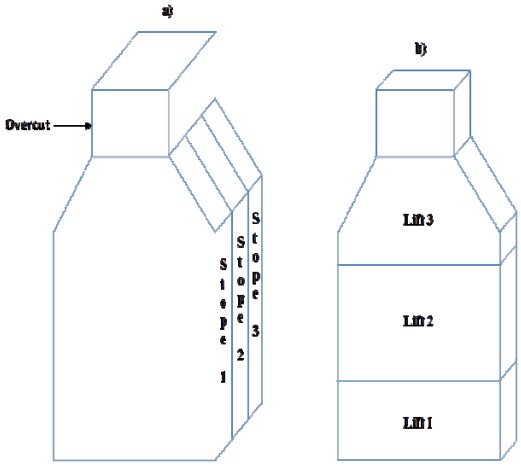

Figure 1 - a) Isometric of a common Birchtree panel; b) Isometric of a common Birchtree extraction sequence for a stope

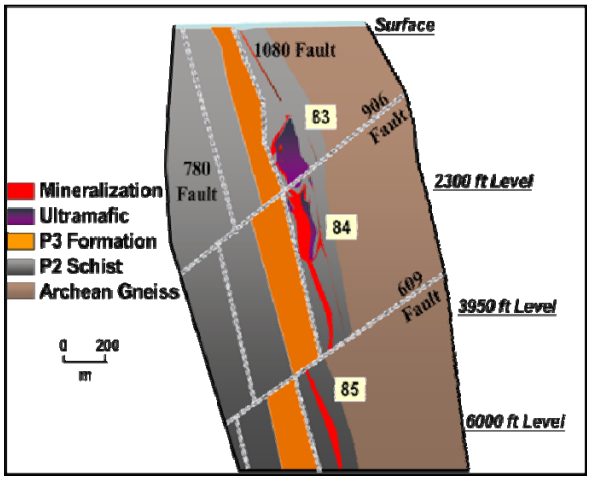

Figure 2 - Cross-section of the Birchtree orebody showing major faults (INCO, 2006)

3. EMPIRICAL DESIGN METHODS

There has been limited work done in the past to incorporate exposure time into empirical design methods (Bieniawski, 1976; Hutchinson and Diederichs, 1996). Bieniawski's exposure time graph was designed based on both tunnel and underground mine openings and relies on span and RMR to determine stand-up time. Hutchinson's graph is a modification of the axes on Bieniawski's graph (Figure 3).

This design method was based on case histories from Civil Engineering tunnels and mining drifts. The simple underground geometry analysed could be adequately assessed by the tunnel span. More complex or equadimensional geometries found in open stoping cannot be quantified with a single measurement of opening width (span). These design techniques often cannot be applied to underground stoping geometries.

Various empirical methods exist for estimating the stability of underground mining openings. The most commonly used empirical design methods for large underground mine openings (stopes) are based on the Modified Stability Graph developed by Potvin (1988). This design tool has formed the basis of many analysis methods that can be used to design stope geometry and underground support (Nickson, 1992) or predict depth of failure or dilution (Clark, 1998) (Capes, 2005) (Pakalnis et al., 2007). All of these design techniques are based on Potvin's Stability Graph technique (1988) and apply the N' stability number and hydraulic radius (HR). A brief description of N' and HR follows.

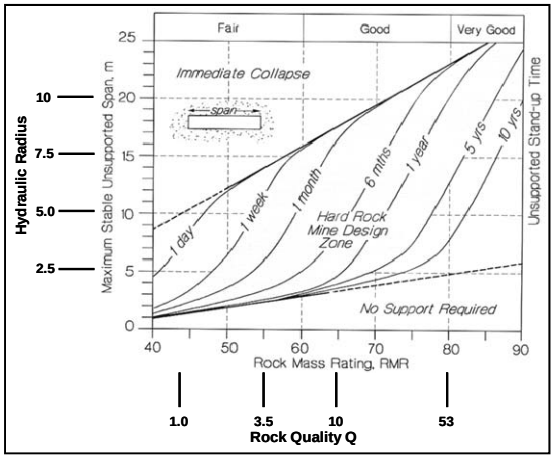

Figure 3 - 1996 RMR Stand-up Time Graph (from Hutchinson and Diederichs, 1996, after Bieniawski, 1976)

i. N' Stability Number: a unitless value used to assess the stability of an opening surface. It incorporates the rock classification, stress condition, major joint orientation, and the dip of the given surface.

$$N' = Q' \times A \times B \times C \tag{4}$$

where A is related to the stress condition, B takes into account the contribution of the major joint orientation (one that affects stability the most), and C accounts for the angle between the horizontal and surface being analysed.

ii. Hydraulic Radius (HR): a measure of the size of a given surface. It is derived by dividing the area of a surface by its perimeter.

The empirical methods based on Potvin's Stability Graph (1988) are well suited for estimating the stability of an underground opening surface; however, the potential degradation of a stope over time cannot be assessed with this approach. These empirical design guidelines are based upon an average exposure time representative of the data base the empirical design method is based upon. A method is proposed where the two design techniques are combined to incorporate the advantages of both systems.

4. MODIFIED RMR STAND-UP TIME GRAPH

A new version of the Stability Graph is proposed to incorporate the effect of stand-up time for underground stope design applications. The design parameters, N' and HR, which are commonly used in mining, have been coupled to the guidelines from the RMR Stand-up Time graph. Several assumptions and simplifications have been applied based on the source of the data used in the Stand-up time graph:

1. Since a significant number of the case histories have been taken from Civil Engineering applications, shallow excavation depths were common suggesting stress was not a significant problem. This assumption is supported by the fact that stress conditions could not be incorporated in the design.
2. Horizontal to sub-horizontal jointing or bedding has been assumed. This joint orientation is common and would correspond to coal mining with sub-horizontal bedding. Sub-horizontal jointing would result in a joint orientation correction of ~-10 incorporated in the RMR values for the drift back stability.
3. The RMR classification used in the Stand-up Time graph has been changed to Q based on the equation: $RMR = 9lnQ + 44$ (Bieniawski, 1976). Though the use of this relation is not advised for detailed design (Milne et al., 1998), this equation does represent an average trend.
4. The hydraulic radius $\left(HR = \frac{Area}{Perimeter}\right)$ of a surface converges to half the span of the opening as the opening length increases. To calculate HR values from the span, an opening length of 1000m was assumed.

The equation relating Q and RMR, as well as the relation between span and HR, are shown on the Standup Time graph (Figure 3). The assumed conditions listed have been used to develop a new Stand-up time graph, the Preliminary Stope Stand-up Time Graph (Figure 4). It should be noted that assumed stress and structure values used to develop this graph may vary significantly from actual conditions in the case histories used to develop the graph.

To develop the Stope Stability Time graph, the following values were applied to the original Stand-up time graph:

1. RMR was converted to Q, based on RMR = 9lnQ +44,
2. A stress factor A of 1.0 was assumed corresponding to low stress conditions,
3. A B factor of 0.3 was assumed, coinciding with jointing parallel to the back and
4. A C factor of 2.0 was used coinciding with a horizontal back.

The new Preliminary Stope Stand-up time graph shows the limits between expected immediate failure, labelled collapse, and indefinite stability labelled as Unsupported.

To assess the Stope Stand-up time (exposure time) limits, they were plotted on the Modified Stability Graph (Figure 5).

As shown in Figure 5, the limits of the Preliminary Stope Stand-up time collapse boundary corresponds with the ‘Stable with Support’ zone on the Modified Stability Graph. The Preliminary Stope Stand-up time graph does predict failure in the stable zone of the Modified Stability Graph, but this may be due to the fact that the Stand-up time graph was designed for areas with personnel access requiring increased safety. Also, the Stability Graph has been developed primarily from open stope data where exposure time is often limited. In order to fully assess the viability of the Preliminary Stand-up time graph, data needs to be gathered and assessed.

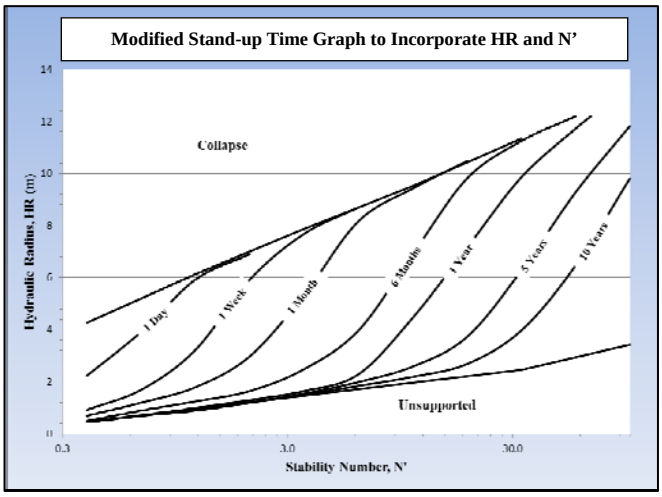

Figure 4 - Preliminary Stand-up Time Graph

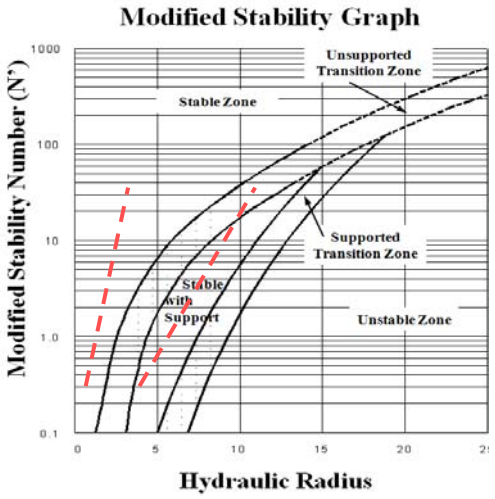

Figure 5 - Modified Stability Graph with the Stand-up Time Graphs boundaries plotted

5. GEOTECHICAL DATA

Rock mass properties and stope performance records are available for stability analysis. The following data was used to compile case histories for analysis:

(i) Mechanical rock properties obtained through rock testing;
(ii) RQD and limited rock classification from core logging;
(iii) Limited scan line data providing joint orientation, joint roughness, J_r, and an indication of joint alteration, J_a. Mining records which include mucking, blasting, and fill records, as well as, general comments about stope activity;
(iv) Cross sectional drawings and geological layouts;
(v) ITH (production hole) magnetic survey data, which helps to distinguish peridotite from other rock types and;
(vi) Map3D modelling conducted to estimate induced stresses adjacent to stope surfaces.

Detailed rock characterization is done using scan lines which are not conducted on a regular basis. On a given stoping level, detailed data may be several hundred metres apart. The detailed data on joint surface condition and joint set orientation is obtained from the nearest scan line. There may be several diamond drill holes intersecting a stope and logging data is used to obtain stope specific RQD measurements.

6. ANALYSIS

To determine if the proposed method can be applied to open stoping, several case histories are presented in the following section.

6.1 Procedure

Five different surfaces were identified to contribute to dilution. These surfaces are shown in Figure 6 and include the stope lift back, hanging wall, foot wall, north shoulder, and south shoulder. If a failure occurs,

the stand-up time for the failed surface is the time to failure, all other stope surfaces have a stand-up time of greater than the time to failure. The stand-up time for lift backs is equal to the time between blasts for stable lift backs, or the time to failure if the lift back has failed.

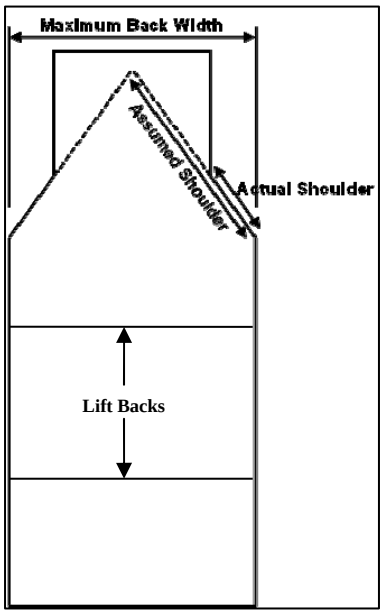

Figure 6 - Simplified stope cross section showing surfaces analysed

For each of these surfaces analysed, the HR is first determined. In the case of the North and South shoulders, it is assumed the length of the shoulder includes the overcut drift. If shoulder failure occurs, the width of the back is then assumed to be the maximum width of the stope, including both the drift back and the failed shoulder (Figure 6). The next step is to calculate N'.

Data concerning the rock mass properties was quantified in the N' Stability Number parameter and then couple with the surface hydraulic radius determined from the stope blasting plans.

6.2 Preliminary Results and Discussion

Four different case histories have been analysed; two unstable and two stable stopes. The stopes analysed were all mined at a depth of approximately 900 metres. The stopes were from primary panels and modelled stresses were very high relative to the rock strength.

Table 1 - Data for predicting stand-up time for the 29-864.1 stope surfaces

	Estimated Stand-up Time					
29-864.1	A	B	C	N'	HR (m)	Actual Stand-up Time
Lift Back	0.1	0.25	2	0.5	2.4	<1 Day
N. Shoulder	0.1	0.2	5.8	1.0	3.7	>1 Day
S. Shoulder	0.1	0.2	6.1	1.1	3.8	>1 Day
HW	0.1	0.5	8	3.6	2.5	>1 Day
FW	0.1	0.85	8	6.1	3.7	>1 Day
Q' = 9.0						

Tables 1 through 4 presents the hydraulic radius, stability number and observed stand-up time for each stope surface assessed. Figure 7 shows the stable case histories with the observed stand-up time indicated. Figure 8 plots the two unstable stopes. Stope 29-864 had a lift back failure after the first lift

was blasted. Stope 32-872 had a failure of the south shoulder which propagated above the overcut. The other two case histories; 32-928.1 and 33-916.3 were considered successfully mined.

Table 2 - Data for predicting stand-up time for the 32-872.1 stope surfaces

	Estimated Stand-up Time					
32-872.1	A	B	C	N'	HR (m)	Actual Stand-up Time
Lift Back	0.1	0.2	2	0.3	2.4	>3 Days
N. Shoulder	0.1	0.2	5.8	0.8	2.8	>3 Days
S. Shoulder	0.1	0.3	6.3	1.3	3.9	<3 Days
HW	0.1	0.25	6.1	1.1	3.2	>3 Days
FW	0.1	0.2	8	1.1	3.3	>3 Days
Q' = 7.0						

Table 3 - Data for predicting stand-up time for the 32-928.1 stope surfaces

	Estimated Stand-up Time					
32-928.1	A	B	C	N'	HR (m)	Actual Stand-up Time
Lift Back	0.1	0.2	2	0.4	2.5	>16 Days
N. Shoulder	0.1	0.25	6.5	1.5	3.2	>16 Days
S. Shoulder	0.1	0.3	6.4	1.7	2.8	>16 Days
HW	0.1	0.3	7.2	1.9	2.1	>16 Days
FW	0.1	0.2	7.2	1.3	3.5	>16 Days
Q' = 9.0						

Table 4 - Data for predicting the stand-up time of the 33-916.3 stope surfaces

	Estimated Stand-up Time					
33-916.3	A	B	C	N'	HR (m)	Actual Stand-up Time
Lift Back	0.1	0.3	2	0.4	3.0	>10 Days
N. Shoulder	0.1	0.2	4.5	0.6	2.9	>10 Days
S. Shoulder	0.1	0.2	5.3	0.7	2.3	>10 Days
HW	0.1	0.2	8	1.1	3.6	>10 Days
FW	0.1	0.25	8	1.6	4.1	>10 Days
Q' = 7.0						

From the data plotted (Figures 7 & 8), it can be seen that most surfaces had predicted stand-up times of 1 month or less. The two observed failures had predicted stability of 1 week or less. The limited data suggests that rapid mining is a significant factor in maintaining stability, which is well known by the mining staff. Unfortunately there are numerous stable cases with a stand-up time of 1 week or less. It is not possible to differentiate between the stable and unstable surfaces in this region.

As discussed in section 5, much of the rock classification data is averaged over many stopes based on limited scanline data. This may contribute to the difficulty differentiating stable and failed case histories. Since collecting scanline data for each individual stope is labour intensive, it is not seen as a viable option. It may be possible to obtain additional data from the diamond drill core. Another factor which has been suggested as a contributing factor to instability is the presence of peridotite. It is possible to estimate the percent of peridotite present mear a given surface from magnetic data collected from production holes. From this data, it is possible to differentiate between peridotite and other rock types. It can be noted that the stope case histories with instability had a peridotite concentratioins greater than 50%. For the two stable stope case histories, the peridotite concentration was less than 40%.

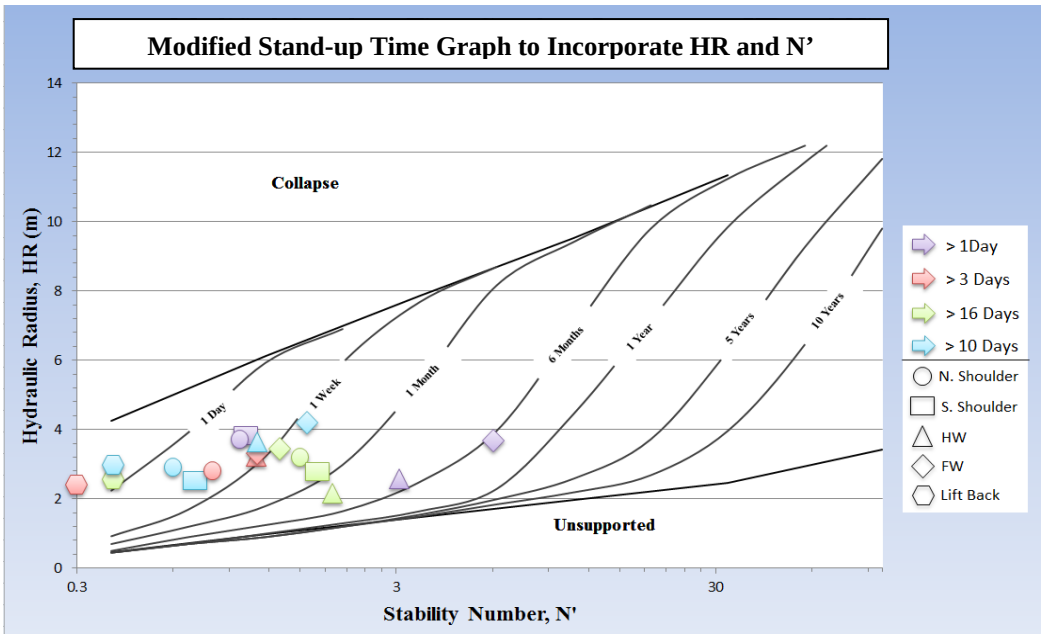

Figure 7 - Stable stope surfaces plotted on the modified stope stand-up time graph

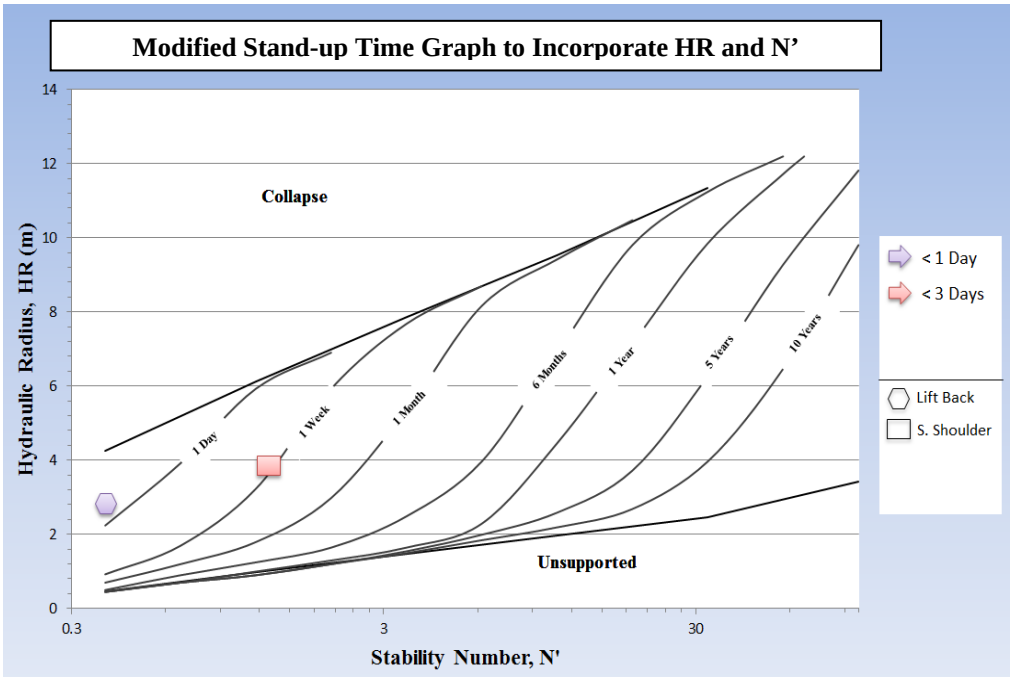

Figure 8 - Unstable stope surfaces plotted on the modified stope stand-up time graph

7. CONCLUSION

The presented method incorporates factors commonly associated with stability to predict stand-up time. The current analysis appears promising, but fails to differentiate between stable and failed surfaces for a predicted stand-up time of less than 1 week. It is quite possible that such fine calibration may not be possible. Further data collection is planned to look at more stope specific data, such as peridotite content in the stopes. Initial observations have shown some promise.

This paper presents a new approach to assess stand-up time for open stopes. More case histories have been gathered and will be used to assess the viability of this method. In order to improve the sensitivity of this approach, other stope specific factors will be incorporated.

8. ACKNOWLEDGEMENTS

Support for this research by Vale Canada and the Natural Sciences and Engineering Research Council of Canada is greatly appreciated.

9. REFERENCES

BIENIAWSKI, Z.T., 1976. Rock Mass Classification in Rock Engineering, Proceedings on the Symposium on Exploration for Rock Engineering, Vol. 1, Johannesburg, p. 97-106.

CAPES, G., MILNE, D. and GRANT, D., 2005. Stope hanging wall design approaches at the Xstrata Zinc, George Fisher Mine, North Queensland, Australia, American Rock Mechanics Symposium, Fairbanks, USA.

CLARK, L., 1998. Minimizing Dilution in Open Stope Mining with a Focus on Open Stope Design and Narrow Vein Longhole Blasting, MSc Thesis, University of British Columbia, 316 p.

HUTCHINSON, D. and DIEDERICHS, M., 1996. Cablebolting in Underground Mines. BiTech Publishers Ltd. Richmond, B.C., 209 p.

INCO, 2006. Birchtree Mine Internal Report, INCO Manitoba Operations. Thompson, Manitoba.

LAYTON-MATTHEWS, D., LESHER, C.M., BUMHAM, O.M., LIWANAG, J., HALDEN, N.M., HUBERT, L., and PECK, D.C., 2007. Magmatic Ni-Cu-Platinum-Group Element Deposits of the Thompson Nickel Belt. Geological Association of Canada Special Publication 5, p. 409-432.

MILNE, D., HADJIGEORGIOU J. and PAKALNIS, R., 1998. Rock Mass Characterization for Underground Hard Rock Mines. Tunnelling Underground Space Technology 13(4), p. 383-391.

NICKSON, S., 1992. Cable support guidelines for underground hard rock mine operations, M.A.Sc thesis, The University of B.C., 223 p.

PAKALNIS, R., BRADY, T., HUGHES, P., CACERES, C, OUCHI, A., MacLAUGHLIN, M., 2007. Rock Mass Design for Underground Mining Operations, Proceedings of the International Workshop on Rock Mass Classification in Underground Mining, , Information Circular 9498 (NIOSH), Vancouver, B.C., Canada, p. 119-128.

POTVIN, Y., 1988. Empirical open stope design in Canada, Ph.D. thesis, The University of B.C., Canada, 350 p.

New Knowledge-Based System Prototype for Assisting Mine Operators in Predicting Stope Instability and Associated Unplanned Dilution

Somchet Vongpaisal
CANMET-MMSL

ABSTRACT: This paper presents the R&D results on the development of a new knowledge-based system for predicting stope instability and associated unplanned dilution in deep underground mining operations. A new prototype was developed based on databases generated from 3D non-linear elasto-plastic finite element stress analysis, heuristic rules, and case histories. This prototype aims to assist mine operators to make decisions on strategic mine planning and feasibility in a quick and efficient manner thereby minimizing risk on ground failure and optimizing mining costs.

1. INTRODUCTION

Under normal pressure and ambient temperature, hard rocks normally produce stress-strain relationship as shown in Figure 1, which indicates that rocks can still sustain loads beyond the elastic limit and still remain stable without rupturing completely. The existing engineering design curves were derived based on elastic condition (line 0A), whereas our developed algorithm was derived based on non-linear elasto-plastic condition (line 0ABC). The former solution is considered too conservative, whereas the latter approximates a more realistic approach.

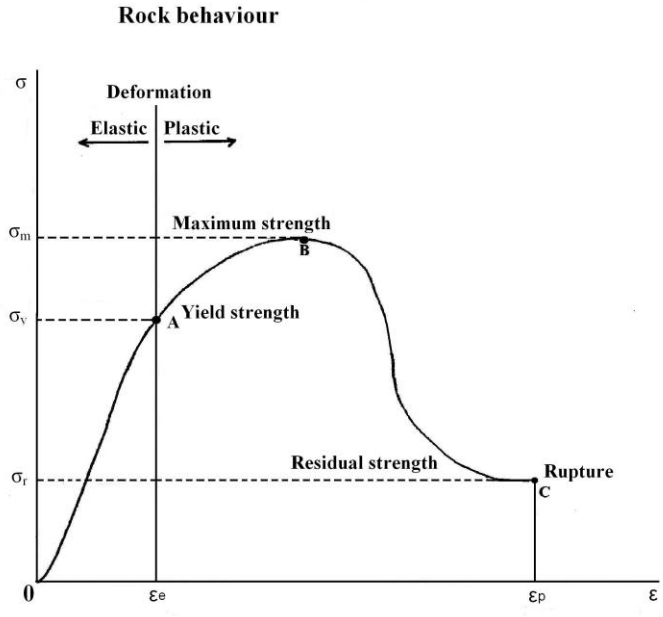

Figure 1 – Rock behaviour – stress vs strain

This present R&D project aimed to develop new 3D engineering design curves and a new expert system module to improve the efficiency of mine stability assessment in three dimensions. It integrates databases generated from state-of-the art 3D non-linear elasto-plastic finite element stress analyses (in particular, the potential extents of damage zones and associated dilutions around mine openings) together with

heuristic rules and case histories. The ultimate objective is to assist mine operators in decision-making on strategic stope stability and feasibility studies in order to minimize risk of ground failure and to optimize mining cost.

2. METHODOLOGY

A new 64-bit CANSAFE3D software (a Windows application package for 3D elasto-plastic stress analysis using the finite element method) was used. It was converted, modified, and recompiled from the existing 32-bit version Li (2005) to improve calculation efficiency, and to increase the capability to handle more realistic mine models with greater accuracy.

Finite element models were constructed and executed to simulate underground excavation with various dimensions, depths, and mining sequences in order to determine the progressive extents of potential damage zones around mine openings Vongpaisal et al. (2008). Figure 2 shows a schematic of stope in three dimensions.

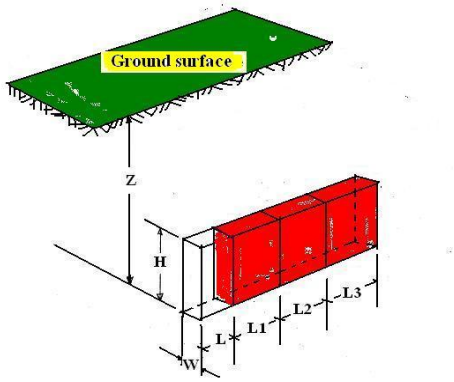

Figure 2 – A schematic of 3D stope dimensions [3]

The results were analyzed and deduced to form the engineering design curves. All available data from mine case histories were also used to validate the curves.

An expert system shell was used to develop a new ground control knowledge-based system module. Data generated from 3D elasto-plastic finite element analyses together with heuristic rules and engineering equations were converted into the expert system knowledge base. The logic and command blocks were then programmed and tested Vongpaisal et al. (2011).

3. RESULTS

Due to the voluminous data generated from this study such as induced mining stresses, displacements, and yielded elements, only specific results are presented in this report. The extent of potential failure zones and unplanned mining dilutions (volumes of yielded elements/volume of mined stopes) were calculated and correlated with stope dimensions (width (W), height (H) and length (L)).

For simplicity and usefulness to general practitioners, the results of potential ground failure surfaces and dilutions were plotted and presented in a contour format.

3.1 New 3D Engineering Curves

Figure 3 shows typical contours of correlation between the predicted extents of potential failure zones and stope dimension ratios (L/W and H/W) for W = 5 m at mining depths (Z) = 500 m, below surface.

Similarly, Figure 4 shows typical contours of correlation between the predicted dilutions and stope dimension ratios (L/W and H/W) for W = 5 m at Z = 500 m.

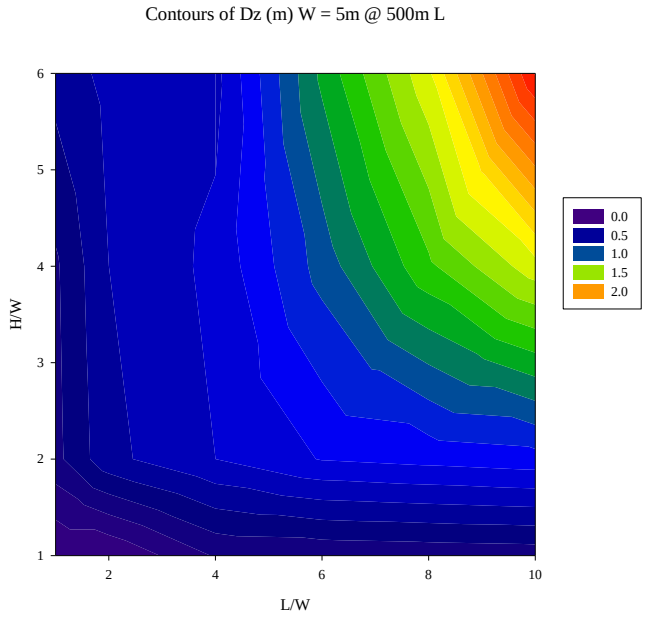

Figure 3 - Predicted extents of potential failure zones in 3D space Top view, W = 5 m, Z = 500 m

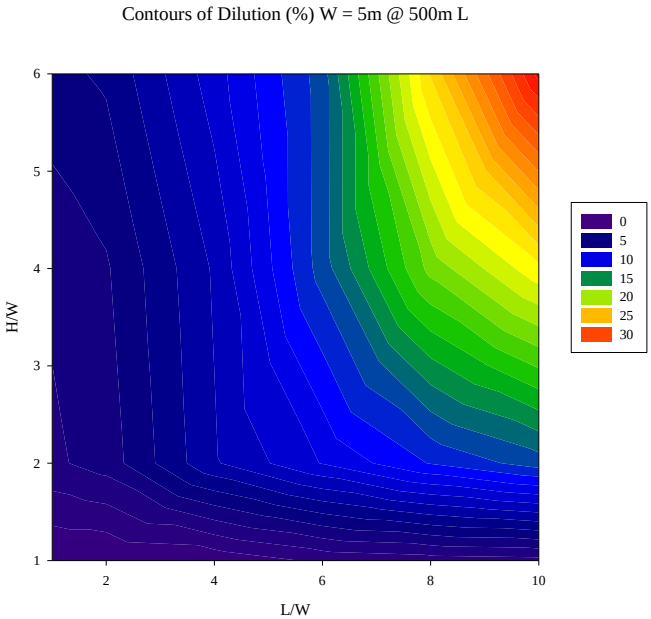

Figure 4 - Predicted dilution of mined stope in 3D space Top view, W = 5 m, Z = 500 m

Figures 5 and 6 show the typical influence of mining depth on extents of potential failure zones and potential unplanned dilution, respectively. Virtually, it can be seen that extents of potential failure zones

and unplanned dilution are increased with mining depth. As example, design limits are provided for the case of W = 5 m, H/W = 3 and L/W = 4 at Z = 500m.

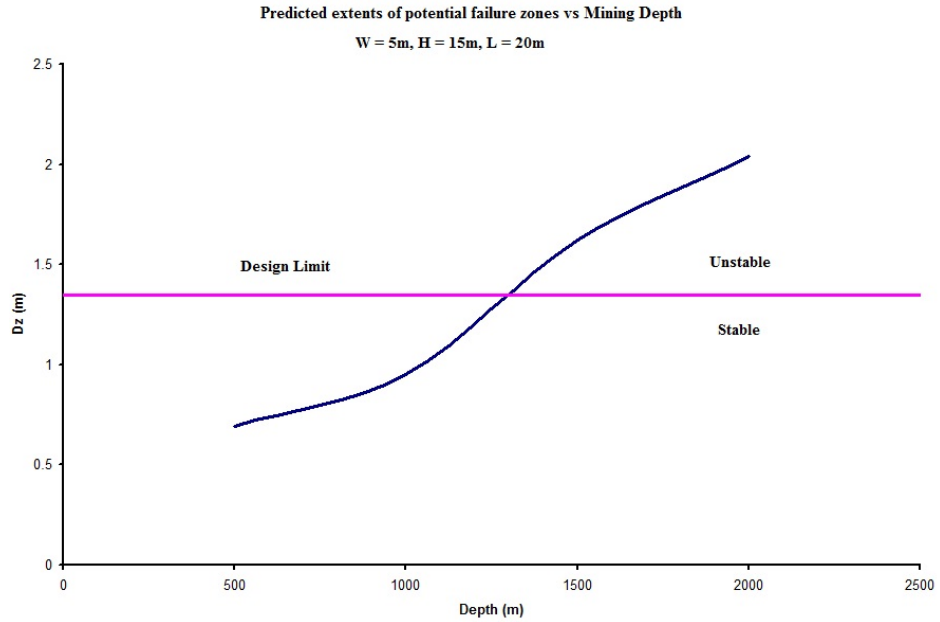

Figure 5 – Influence of mining depth on extents of potential failure zones

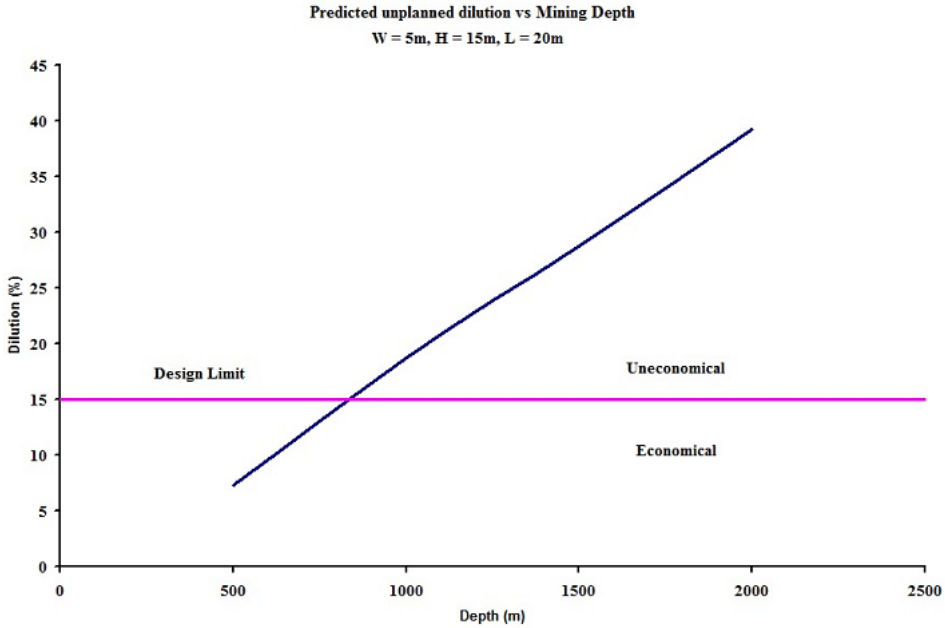

Figure 6 – Influence of mining depth on potential unplanned dilution

3.2 Knowledge-Based System Prototype

Figures 7(a) and (b) show typical results of the prototype. Rectangular boxes and radio buttons are displayed for user to input data, or answer the question.

In this case, the user is asked by the expert system to input the proposed stope dimensions, i.e. width, height, length and step increment, in rectangular boxes. Rock mass classification systems can be chosen from radio buttons

By changing values of stope dimensions, rock mass classification and depths, the system allows the user to determine the influence of stope dimensions on the potential extents of ground failure, unplanned dilutions, and ground support requirement in a quick and efficient manner.

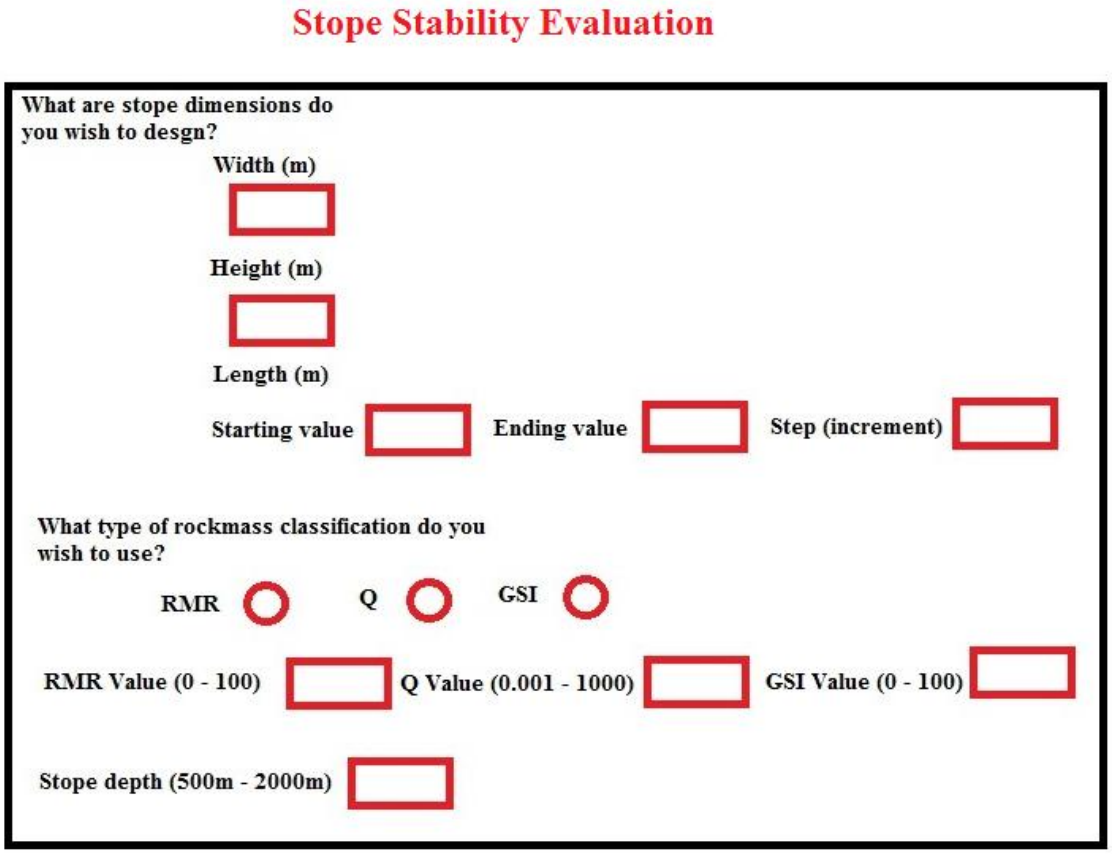

Figure 7(a) - The user is requested to input the values of stope dimensions, rock mass classification systems, and the depth of the stope.

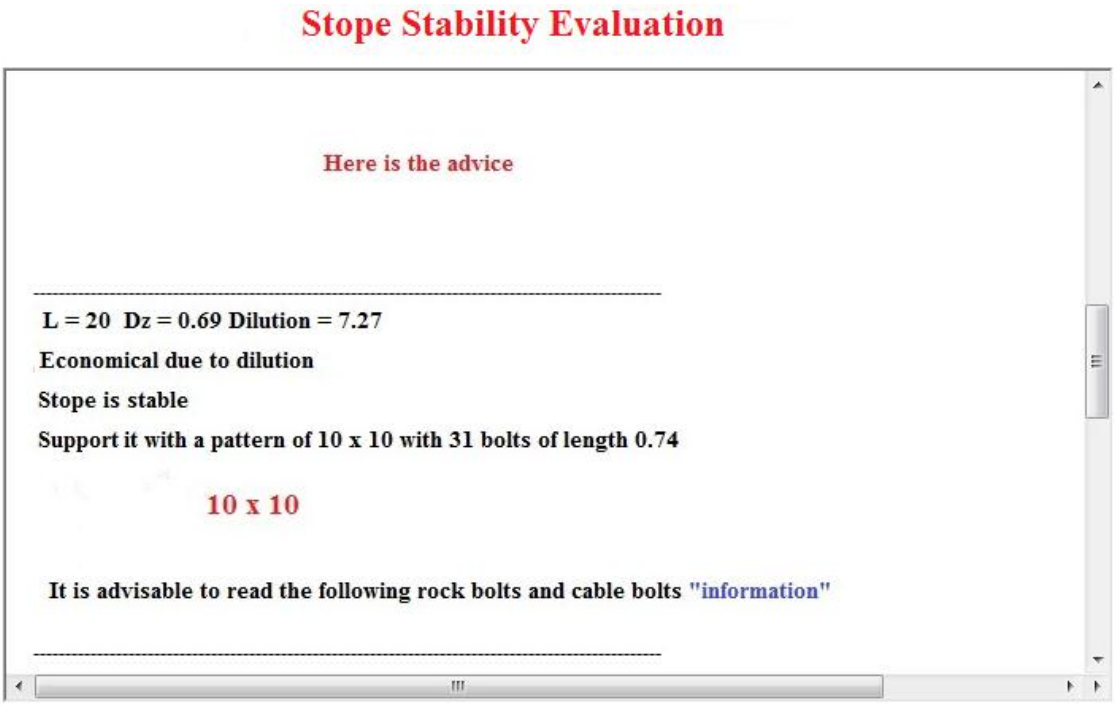

Figure 7(b) - The expert system will calculate DZ and associated dilution, then advice can be given. By clicking on "information", this expert system permits the user to obtain specific information on knowledge built in the systems, such as rock mass property, rock bolts, best practices, and so forth

4. CONCLUSIONS

1. New 3D engineering design curves were developed for hard rock underground mines in Canadian Shield ore deposits, employing longitudinal blasthole mining method with delayed backfill. Examples of design curves were provided in this paper for predicting the extent of potential ground failure zones and unplanned dilutions for various stope widths (W = 5, 10, 15, and 20 m) located at different depths (Z = 500, 1000, 1500, and 2000 m) below ground surface to assist the design of underground mines in good ground conditions (RMR ≥ 60).

2. The developed knowledge-based system software mimics the rational ways of rock mechanics experts in performing tasks, judging, and providing recommendations to mine operators. The decision-making process on strategic mine planning and feasibility studies could be accomplished in a quick and efficient manner while minimizing risk on ground failure and optimizing mining cost.

5. ACKNOWLEDGEMENTS

The authors wish to thank the management of CANMET for their support of this innovative research project.

6. REFERENCES

LI. G., 2005. CANSAFE3D – A Windows application package for three dimensional elasto-plastic stress analysis using the finite element method. Report No.: MMSL-INT 05-001(TR).

VONGPAISAL, S., LI, G., PAKALNIS, R., and BRADY, T., 2008. New 3D engineering curves for predicting stope stability and mining dilution in longitudinal blasthole mining operations. International Journal of Mining, Reclamation and Environment, 23, p. 92-102.

VONGPAISAL, S., LI, G., PAKALNIS, R., and BRADY, T., 2011. New development of expert system module for a decision-making on mine stopes stability in underground blasthole mining operations. International Journal of Mining, Reclamation and Environment, 25, p 41-51.

Combining Sources of Rock Mass Characterization Data for Stope Design

Karina Forster
Cameco Corporation Rabbit Lake Mine Operation
Douglas Milne
University of Saskatchewan
Tanya Smith
Cameco Corporation Rabbit Lake Mine Operation

ABSTRACT: Open stope design depends on the ore body geometry, loading conditions and rock mass properties to estimate stope dilution and ground support requirements. Rock mass conditions for design primarily rely upon estimates of well established rock classification systems. Many sources of data exist for obtaining estimates for these rock mass classification values which include core logging, geotechnical mapping, geological mapping as well as linking one classification system to another through the use of empirically derived equations. The extent of mapping coverage can also vary significantly based on the data collection technique.

This paper proposes an approach where individual components of rock mass classification systems are collected by the different available data collection techniques. Data from different rock types are also considered separately based on their alteration characteristics and general observation products. Data from the Cameco Corporation Eagle Point Mine is presented and an approach is outlined for obtaining average representative classification values for stope hanging wall characterization. The effectiveness of this approach is demonstrated through the analysis of a data base of hanging wall dilution information.

1. INTRODUCTION

The ideal outcome of open stope design is to remove all of the ore material without damaging the surrounding waste rock. Dilution, or overbreak, refers to the amount of waste material removed intentionally, or unintentionally, by mining activities. Dilution is influenced by many factors, some of which may be controlled, and others which must be managed. Some of the controllable factors are the size of the opening, the drilling and blasting design, stope sequencing, ground support selection, undercutting, and time. Other factors such as rock mass properties, stress condition, and seismic activity are fixed, but may be managed. In order to predict the dilution, the fixed parameters must be estimated in order to make decisions regarding the factors which may be controlled. Some assumptions and generalities are required to estimate the rock mass properties.

Reconciling dilution with the variety of factors which influence overbreak of a stope is a complex problem. In depth analysis of each stope is required for determining which factors influence the amount of dilution, and how much they influence the amount of dilution. A consistent approach is required for estimating the rock mass properties influencing the rock mass stability must be applied to isolate the other factors. Rock mass classification is a commonly used technique to estimate rock mass properties and is an integral component of mine design. Many aspects of mine design rely either directly, or indirectly, on rock mass classification values.

Mine design generally starts with overall “big picture” assumptions or classification of the rock mass properties, and localized areas are further refined based on field observations. Piteau (1973) states that

the process begins with separating the rock mass into structural domains that are predicted to behave in a similar fashion or have similar properties. These structural domains are generally relatively large and based on lithological or structural contacts. This large-scale method, developed for open pits, is often inadequate for assessing rock mass properties used in rock classification for stope design. In underground mining, the areas of concern are generally in the scale of tens of meters, so such large scale assumptions may lead to oversimplification of the rock mass and inaccurate prediction of stope behaviour. The need to quantify changes in rock mass classification over tens of metres requires detailed consistent data collection, which often exceed the resources available for geotechnical data collection. An appropriate, effective, straightforward method of classifying a rock mass is required to be easily used in the design process. One such method of streamlining the process is to compare indirect measurements to known conditions to compile a site-specific database. This paper is a continuation of research discussed in Forster et al. (2007) which is introduced in the following section.

2. BACKGROUND

The Cameco Corporation Eagle Point mine is located approximately 800 km north-east of Saskatoon, Saskatchewan. The mine produces an average of 600 tonnes of uranium ore per day using longhole, open-stope mining methods.

2.1 Geology

Thomas (2003) states that the uranium mineralization at the Eagle Point mine is structurally controlled, and typically occurs within the hangingwall of the Collins Bay reverse fault within a basal unit of metasediments. The host rock consists of both metamorphic rock and intrusives, in particular biotite-quartz-feldspar gneiss, quartz-feldspar gneiss, quartzite, calc-silicates and pegmatite. The mineralization zone is typically less than 1m to 15m thick, and consists of tabular veins and lenses dipping from 50 to 85 degrees. Due to the ore association with faulting, the ore is often contorted, with a highly variable orientation.

Thomas (2003) states that in addition to the uraninite ore, many other types of alteration assemblages are associated with the ore zone. Bleaching, clay or ‘argillization’, pyritization, hematization, carbonate ±quartz veins, quartz veins, sericitization and chloritization may be present in the ore zone in various different combinations. The alteration is typically confined to within 5 metres in the hangingwall of the ore zone, but can extend up to 20 metres into the hangingwall of high-grade mineralization, localized around multiple fault intersections.

2.2 Mining Method

As mentioned, longhole open-stope mining methods are used at the Eagle Point mine. Both narrow vein stopes and massive stopes have been used to extract the ore, depending on the width and spacing of the ore veins, although the most recent stopes have been narrow-veined. The overcuts and undercuts for the narrow vein stopes are driven on geological control following single, or closely spaced ore veins. The stopes are then mined longitudinally with average strike lengths of 20 to 30 metres, and are generally less than 10 metres wide.

Due to the radioactive nature of uranium ore, shotcrete is applied to the back, walls, and face of development as soon as practicable for gamma ray shielding. This limits the amount of time available for gathering geotechnical information in certain areas.

3. DILUTION PREDICTION

A widely accepted method of estimating stope design was developed by Potvin (1988). The dilution graph has been modified from this method by Clark and Pakalnis (1997) and others, including Capes et al. (2005) to accommodate stopes in weak rock. The stability graph is based upon two input parameters; the hydraulic radius, HR, and the modified stability number, N'. The hydraulic radius is defined as the ratio of the area to the perimeter of a surface. The modified stability number, N' is given as:

$$N' = Q' \times A \times B \times C \tag{1}$$

where Q' = Modified Rock Quality; A = stress reduction factor; B = joint orientation factor; and C = gravity adjustment factor (Potvin, 1988). Both the hydraulic radius (HR) and the modified stability number (N') are influenced by several factors which are not directly assessed with the design method. Factors influencing HR and N', as well as the initial approach taken by the mine for estimating these values, are discussed in the following sections.

3.1 Stope Geometry and Support

The modified stability graph design method assesses stope geometries with the HR term and the C factor. The method works best for uniform stope geometries with a planar opening surface and a consistent dip. The Rabbit Lake ore body is very irregular on strike, which creates a very undulating stope hanging wall surface. The ore body dip is a combination of the vertical walls of the undercut and overcut combined with the hanging wall surface created by the blast holes. Because the sub level spacing is only about 15 metres, the vertical drift walls form a significant portion of the hanging wall surface. To account for the non-planar nature of the stope surface, the strike length was determined from the cavity monitoring survey results. A representative stope dip was chosen from the average of the hangingwall drillhole angles.

Stope support can be assessed with several different approaches. If total cable bolt support coverage is present, the support can be assessed by increasing the estimated rock classification value (Bawden et al., 1988) or by changing the design lines on the stability graph (Nickson, 1992). At the Rabbit Lake Mine, stope support consists of extensive cable bolting of both the overcut and undercut drifts. To account for this support, the hydraulic radius is calculated for a smaller stope hanging wall surface by measuring the up dip stope length from the centre of the overcut drift to the centre of the undercut drift.

3.2 Modified Stability Number, N', Calculation

The calculation of N' is explained by Potvin (1988) based on equation 1. The following values have been estimated for the hanging walls at the mine:

- The stress factor is estimated at 1.0 to represent the relaxed, low stressed hanging walls.
- Three joint sets have been identified at the mine site, sub-horizontal, steep and near perpendicular to the ore body and sub-parallel to the ore body. A joint orientation, B, factor of 0.2, corresponding to jointing just off of parallel to the HW has been estimated.
- As discussed in the previous section, the C factor is based on the dip of the hanging wall surface.
- The estimation of the Q' rock classification value for stopes has been challenging. Limited access made it necessary to link a geology based classification to the Rock Quality Q' term used with the Stability Graph design method, as described in the following section.

3.2.1 Initial Estimation of the Q' Rock Quality

There are several separate factors which contribute to the calculation of the rock classification Q' value. This classification includes the rock quality designation (RQD), number of joint sets (Jn), joint roughness (Jr), joint alteration (Ja), and joint water condition (Jw). For uranium mining, there is limited access and limited time to gather geotechnical information for a stope, so much of the rock mechanics data has been gathered predominantly by the geology staff at the mine.

The primary goal of mapping by the geology staff is, of course, focused on following the ore for stope development. Since the ore is associated with faulting and alteration, the geology department has developed a classification system based on the strength (R) and alteration (A) of the rock. The "R" value consists of three separate categories of rock strength, with R1 being very weak rock, and R3 being relatively strong rock. The "A" series consists of four separate categories for alteration, with A1 being fresh rock, to A7 being strongly altered.

A study was conducted by Sutton (1998) to link stope stability to the rock strength / alteration assessment developed by the geology staff. A limited amount of available exposures were assessed in the alteration and strength categories and were also mapped for rock mechanics classification purposes. Sutton developed a preliminary correlation between the Q' rock mechanics classification system and the geology assessment of R1 to R3 and A1 to A7 rock types for application to stope stability and dilution (Table 1).

Table 1 - Correlation between the R1 / R3 and A1 / A7 geology system and Q' classification systems (Sutton, 1998)

Q' to A/R Assessment for Gneissic Rocks

Alteration	Rock Strength		
	R1 (very weak)	R2 (weak)	R3 (medium strong)
A1 (fresh)	N/A	N/A	22
A3 (weak)	N/A	3.8	11
A5 (moderate)	1.2	2.5	8.3
A7 (strong)	0.4	2	3.8

Q' to A/R Assessment for Pegmatoidal Rocks

Alteration	Rock Strength		
	R1 (very weak)	R2 (weak)	R3 (medium strong)
A1 (fresh)	N/A	N/A	22
A3 (weak)	N/A	3.8	25
A5 (moderate)	1.2	2.5	13
A7 (strong)	0.4	2	5.8

The approach taken by the mine for obtaining data for estimating stope dilution has been fairly successful, however, improvements can be made in estimating rock mass properties. Additional work correlating the rock type and geology A/R assessment to individual rock mass properties, such as joint condition, is improving rock classification estimates. Other sources of data are being applied to estimating rock mass classification values.

4. INTEGRATION OF DATA SOURCES

4.1 Information Sources

Ideally, all areas would be geotechnically mapped to obtain the Q' values for each stope. In reality, the time and effort required to complete this mapping may be beyond the scope of many mining operations.

Mapping conducted by geology staff for ore control has shown to be an excellent source of data which can often be of great benefit for geotechnical classification estimates.

Data from local diamond drill holes that intersect the immediate stope hanging wall are being used. The core provides RQD measurements for classification, however, classification factors based on the joint condition, water condition and number of joint sets cannot be easily assessed from core.

Additional field mapping, coupled with conversations with geology staff (Pagnin, 2011), has made it possible to improve the link between individual rock classification properties and the geology A/R assessments for different rock types. The presence of water is not included in the A/R geology assessment, however, geology mapping does indicate areas with dripping or flowing water corresponding to a Jw value of 0.66. If water is not mentioned with the geology mapping, a value of 1.0 is assumed. Based on the A1 to A7 alteration and the R1 to R5 rock strength assessment for both the gneissic and pegmatitic rocks, the following revised estimates have been made for individual rock mass properties:

- Gneissic Rock
    - The foliation planes in the gneissic rock, with an additional two sets are common for 3 joint sets and a Jn = 9.0. Based on conversations with mine geologists, the number of joint sets observed does not appear to be influenced by the geology hardness and alteration rating (Pagnin, 2011)
    - Increased alteration zones in the gneissic rocks (R1/A5 & R1/A7) were observed as increased clay alteration products along pre-existing joint surfaces. Alteration thickness did not exceed 1 to 2mm giving a Ja assessment of 4.0 or less.
- Pegmatoidal Rocks
    - Three plus random joint sets are common, however, the joint continuity is often limited near shear / fault zones. In highly altered or low strength assessments, random jointing is frequently observed (Pagnin, 2011).
    - Increased alteration ratings in the pegmatoidal rocks (R1/A5 & R1/A7) corresponded to feldspar alteration to clay extending well past the joint boundaries into the surrounding rock. This has been quantified with Ja values as high as 10.0.

Based on both comments from geology staff and additional rock mechanics mapping data, Tables 2 and 3 summarize correlations to Q' parameters that can be obtained from the geology A/R mapping.

4.2 Data Interpretation for Stope Classification

The rock classification data for stope assessment is based on overcut and undercut mapping using the A/R geology assessment, comments on groundwater conditions and RQD from drill holes intersecting the stope hanging wall.

The A/R assessment is made at frequent, irregular intervals along the stope overcut and undercut. This geology assessment is assumed to be valid for half the distance between A/R measurements, as shown in Figure 2. The Q' parameters that correspond to the A/R assessment are the number of joint sets Jn, joint roughness Jr and joint alteration Ja. A weighted average for each of these parameters is determined based on Equation 2. Each estimated Jr, Ja and Jn parameter is multiplied by the strike length along the overcut or undercut where the assessment is valid (half the distance between adjacent A/R measurements) and the values are summed. A weighted A/R measurement is obtained by dividing the summed value by the total mapped length (Equation 2). An estimate of the water factor, Jw, is based on observations of water, and an assumption that conditions are dry to moist if not otherwise noted (Jw=1.0). The RQD value is based on both core logging and the A/R mapping. The RQD from the core run in the immediate stope hanging

wall is recorded for any hole passing through the stope hanging wall. The RQD is included as part of the average calculated for the immediate hanging wall.

Table 2 - Q' Gneissic rock mass properties assessed for Q'

	Rock Strength – Gneissic Rocks		
Alteration	R1	R2	R3
A1	N/A	N/A	$Q' = \frac{RQD}{9} x \frac{1.5}{1} x \frac{Jw}{1}$
A3	N/A	$Q' = \frac{RQD}{9} x \frac{1.5}{2} x \frac{Jw}{1}$	$Q' = \frac{RQD}{9} x \frac{1.5}{2} x \frac{Jw}{1}$
A5	$Q' = \frac{RQD}{9} x \frac{0.75}{3} x \frac{Jw}{1}$	$Q' = \frac{RQD}{9} x \frac{1.5}{3} x \frac{Jw}{1}$	$Q' = \frac{RQD}{9} x \frac{1.5}{3} x \frac{Jw}{1}$
A7	$Q' = \frac{RQD}{9} x \frac{0.75}{4} x \frac{Jw}{1}$	$Q' = \frac{RQD}{9} x \frac{1.5}{4} x \frac{Jw}{1}$	$Q' = \frac{RQD}{9} x \frac{1.5}{4} x \frac{Jw}{1}$

Table 3 - Q' Pegmatoidal rock mass properties assessed for Q'

	Rock Strength – Pegmatoidal Rocks		
Alteration	R1	R2	R3
A1	N/A	N/A	$Q' = \frac{RQD}{9} x \frac{1.5}{1} x \frac{Jw}{1}$
A3	N/A	$Q' = \frac{RQD}{9} x \frac{1.5}{4} x \frac{Jw}{1}$	$Q' = \frac{RQD}{9} x \frac{1.5}{1.5} x \frac{Jw}{1}$
A5	$Q' = \frac{RQD}{12} x \frac{0.75}{8} x \frac{Jw}{1}$	$Q' = \frac{RQD}{12} x \frac{1.5}{6} x \frac{Jw}{1}$	$Q' = \frac{RQD}{12} x \frac{1.5}{2} x \frac{Jw}{1}$
A7	$Q' = \frac{RQD}{12} x \frac{0.75}{10} x \frac{Jw}{1}$	$Q' = \frac{RQD}{12} x \frac{1.5}{8} x \frac{Jw}{1}$	$Q' = \frac{RQD}{12} x \frac{1.5}{4} x \frac{Jw}{1}$

The Q' value was estimated based on the geological mapping for each stope overcut and undercut and relevant core RQD values, as shown in Equation 2, and Figure 1.

$$Q'_{weighted} = \frac{\left[\frac{\left(\sum RQD_w\right)}{\#\text{ of Data Sources}}\right]}{\left[\frac{\left(\sum Jn_w\right)}{2\,(\text{Strike Length})}\right]} \times \frac{\left[\frac{\left(\sum Jr_w\right)}{2\,(\text{Strike Length})}\right]}{\left[\frac{\left(\sum Ja_w\right)}{2\,(\text{Strike Length})}\right]} x \frac{Jw}{1.0} \quad (2)$$

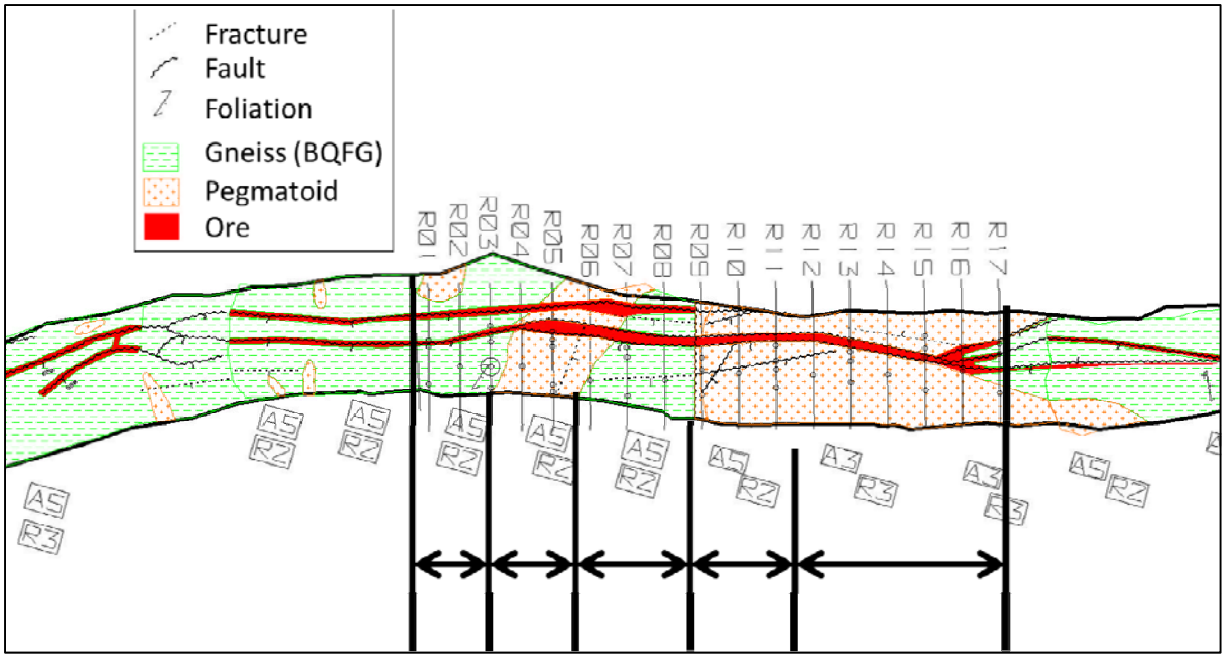

Figure 1 – Example of Geological mapping and domains selected for partial Q' estimation for a stope

4.3 Stope Dilution Prediction

A total of 26 mined-out open stope case studies have been analyzed. Of the 26 case studies, 6 were removed because significant undercutting from the undercut drift and/or the stope below was suspected to influence the amount of dilution for the stope. The stope hanging wall hydraulic radius and stability number were estimated based on the discussed approach. The dilution was measured with a Cavity Monitoring Survey (CMS) and the average metres of dilution (ELOS) was plotted in categories (Figure 2) using the dilution graph proposed by Capes (2006). The data shows reasonable agreement with the predicted dilution zones of less than 1.0m and more than 4.0m, however, the technique does not differentiate in the range between 1 and 4 metres.

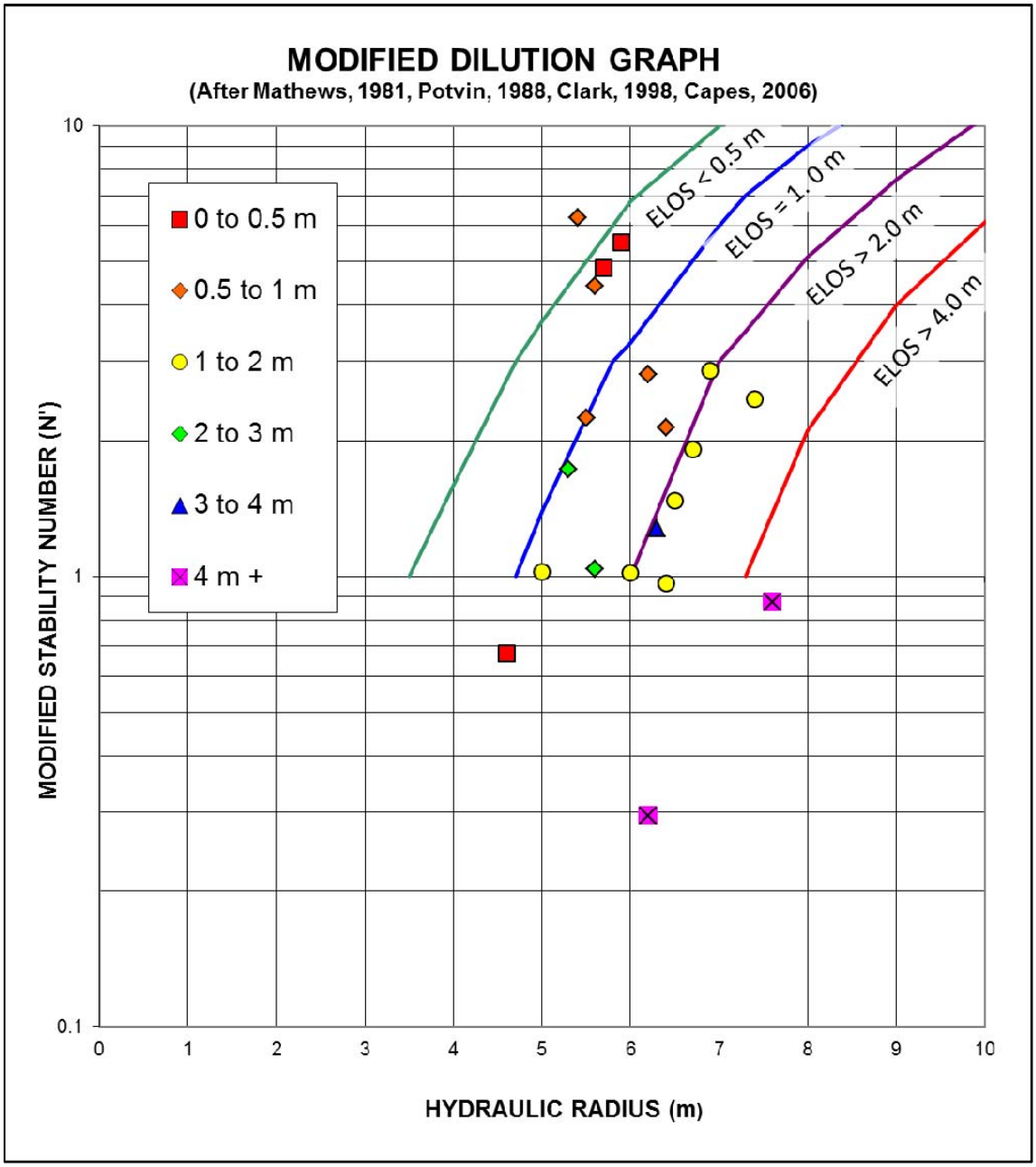

Figure 2 - Case Studies plotted on the Modified Stability Graph as calculated with the separate Q' values for the rock types

5. CONCLUSIONS

Individual sources of information may be used for the estimation of a modified stability number. Some understanding of a mine site's structural geology is a great asset for assessing rock mass properties for measurement. Properties such as the number of joint sets present at a mine site frequently do not vary significantly within a given lithology and little effort needs to be devoted to repeatedly estimate the value of this property.

Work is ongoing to improve techniques for obtaining representative rock classification data. Treating separate rock types individually in terms of rock mass characteristics is recommended to create an accurate estimation of the stability of a rock mass. Due to the difficulty mapping in uranium rich areas, additional work is planned to use mined out stope behaviour for back analysis of ELOS to determine if further improvement in rock classification can be achieved.

6. REFERENCES

BAWDEN, W., MILNE, D., HRASTOVICH, W., GERMAIN, P. and KANDUTH, H., 1988. Computer applications in geomechanical stope and pillar design at Noranda Minerals Inc., First Canadian Conference on Computer Applications in the Mineral Industry, Laval, Quebec.

CAPES, G., MILNE, D. and GRANT, D., 2005. Stope hangingwall design approaches at the Xstrata Zinc, George Fisher Mine, North Queensland, Australia, American Rock Mechanics Symposium, Fairbanks, USA.

CLARK, L. and PAKALNIS, R., 1997. An empirical design approach for estimating unplanned dilution from open stope hangingwalls and footwalls, The Canadian Institute of Mining, Metallurgy, and Petroleum Annual General Meeting, Calgary, Canada.

FORSTER, K., MILNE, D. and POP, A., 2007. Mining and rock mass factors influencing hanging wall dilution, The Canadian Institute of Mining, Metallurgy, and Petroleum Annual General Meeting, Vancouver, Canada.

NICKSON, S., 1992. Cable support guidelines for underground hard rock mine operations, Masters of Science thesis, The University of British Columbia, p. 223.

PAGNIN, R., 2011. Personal Communication.

PITEAU, D.R., 1973. Characterizing and extrapolating rock joint properties in engineering practice. Rock Mechanics 2, p. 5-31.

POTVIN, Y., 1988. Empirical open stope design in Canada, Doctor of Philosophy thesis. The University of British Columbia, Canada, 350 p.

POTVIN, Y., HUDYMA, M. and MILLER, H., 1988. Design guidelines for open stope support, The Canadian Institute of Mining, Metallurgy, and Petroleum bulletin, June 1989.

SUTTON, D.A., 1998. Use of the Modified Stability Graph to predict stope instability and dilution at Rabbit Lake Mine, Saskatchewan. University of Saskatchewan Design Project, Canada.

THOMAS, D., 2003. Preliminary Observations on the Structural Setting of Uranium Mineralization and Alteration - Eagle Point Deposit, Cameco Internal Report.

Development and Implementation of a Risk Mitigation Strategy to Mine a Primary-Secondary Production Stope in a High-Stress Environment at VALE Creighton Mine

Allan R. Punkkinen
VALE Canada
Andrew J. Hyett
Yieldpoint Inc.

ABSTRACT: Safe extraction of the valued ore resource in the deep levels of VALE Creighton Mine has progressed in a pillar-less fashion using vertical retreat, slot-slash and uppers retreat methods since the cessation of 'cut and fill' mining in the late 1980's. Sequencing of the panel extraction and filling has been the key to successful exploitation of high stress orebodies at depth. In late 2010, discussions between the Operating Department and Creighton Ground Control revealed an opportunity to evaluate a trial primary-secondary sequence in the west end of the 400 Orebody at the 2340m horizon. To manage the trial primary-secondary project, a high level risk analysis and management of change was carried out to mitigate potential danger. As part of the requirements, an instrumentation project was conducted in the hanging wall and footwall bottomsills of the secondary panel and within the secondary panel itself. The extraction sequence was modeled with Map3D® software, confirming high stress levels with the advance of the primary panel. Enhanced ground support was installed based on modelling results. A key objective of the instrumentation project was to verify support system response to mining and to obtain knowledge in regards to the behavior of the stope. This paper describes the first time that this type of new innovative instrumented rockbolt technology had been used in a hard rock mining environment. Understanding of the physical deformation mechanisms of ground support in response to high stress conditions is the basis for an effective ground control strategy. The data played an important role in subsequent enhanced ground support system design at the mine and importantly, established the fact that the secondary pillar had not totally failed. Subsequent cavity monitor results helped establish that fact.

1. SITE DESCRIPTION

Creighton Mine is located in the Greater City of Sudbury, 19.2 km west of the City of Sudbury. The Creighton Orebody was first discovered in 1856 and mining started in 1901 by the open pit method. The upper area of Creighton, known as No. 3 Mine, extends from surface to 580m (1900 Level) and consists of a large low-grade orebody that is mined intermittently depending on metal markets and other economic factors by blasthole and VRM methods. Ore was hoisted up No. 7 Shaft from a loading pocket at 1900 Level. Production from this area has been suspended since October 1991.

The lower area, Creighton No. 9 Mine, extends below the 580m horizon. Mining is currently taking place upwards at 1090m (3570 Level) and down-dip from 2380m (7810 Level) with remnant mining at intermediate levels. Plans are to extend operations to 1090m (3150 Level) and possibly as far down as 3000m (9,800 feet). The major mining method in this area is Slot and Slash. Current ramp development has passed 2500m, and the deepest level extraction remains at 2420m (7940 level).

Mineralization is contained within a north-west plunging embayment of norite into the footwall. Within the embayment, mineralization is controlled by two troughs or indentations into the footwall. The majority of orebodies are located along a northwest plunging trough (Creighton 400 trough) which follows the general geometry of the main Creighton Embayment, while the remainder are located along a near orthogonal trough (Gertrude 402 trough) plunging north east at 40^{o}.

2. REGIONAL GEOLOGY

The copper-nickel sulphide deposits at Sudbury are part of the Paleoproterozoic Sudbury Structure which comprises the Sudbury Igneous Complex (SIC); metasedimentary rocks of the Whitewater Group which occupy the centre of the Sudbury Basin; and a ring of brecciated Archean and Paleoproterozoic footwall rocks surrounding the SIC. The rocks of the SIC are exposed within an elliptical ring with a long axis of 45 miles and a short axis of 17 miles (refer to figure 1). The SIC is dated at 1850 million years.

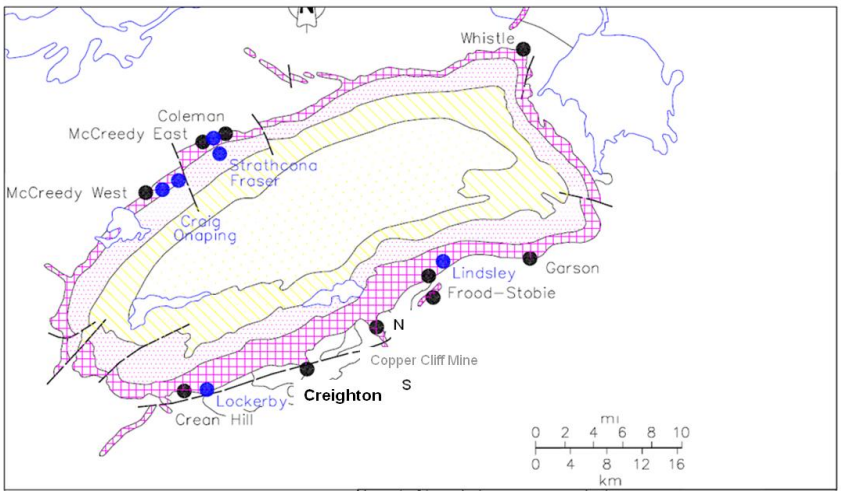

Figure 1 - Sudbury basin

2.1 Local Geology (Current Deep Levels)

The Deep mineral system at Creighton Mine is the down-dip extension of the 400/6100 and 1290 orebodies below 7400 level. At depth, lower grade mineralization is contained in the 400 trough feature and hosted in norite of the SIC. Sulphide mineralization becomes concentrated along the basal contact with the granitic and gabbroic footwall rocks common in the Creighton embayment. High grade sulphide mineralization enters the footwall to the east of the contact, thinning along the 1290 shear zone.

3. INTRODUCTION

The mining sequences for all current production complexes at VALE Creighton Mine are reviewed in order to develop a set of guidelines for planning purposes. Any changes to these sequencing guidelines are approved in writing in a Management of Change Process. To manage the trial primary-secondary project, a high level risk analysis and management of change was carried out to mitigate potential danger.

The opportunity to initiate the risk assessment process and evaluate the trial primary-secondary sequence was based on two key factors. The geometry of the orebody was favourable with no rock inclusions cutting through the sulphide, and the fact that a separate access into the ‘primary’ panel was available, preventing workers from direct exposure to elevated levels of microseismic activity that were anticipated (geometry is shown in figure 2). Otherwise, the project would not have proceeded. It was also agreed that enhanced ground support, consisting of #4ga mesh over existing shotcrete would be installed at the topsill and footwall drift on 7535 level (2296m), to protect against the effects of seismic shaking under the previously filled panels from 7400 level (2255m). Topsills are developed within the slag cemented tailings backfill of previously mined production stopes.

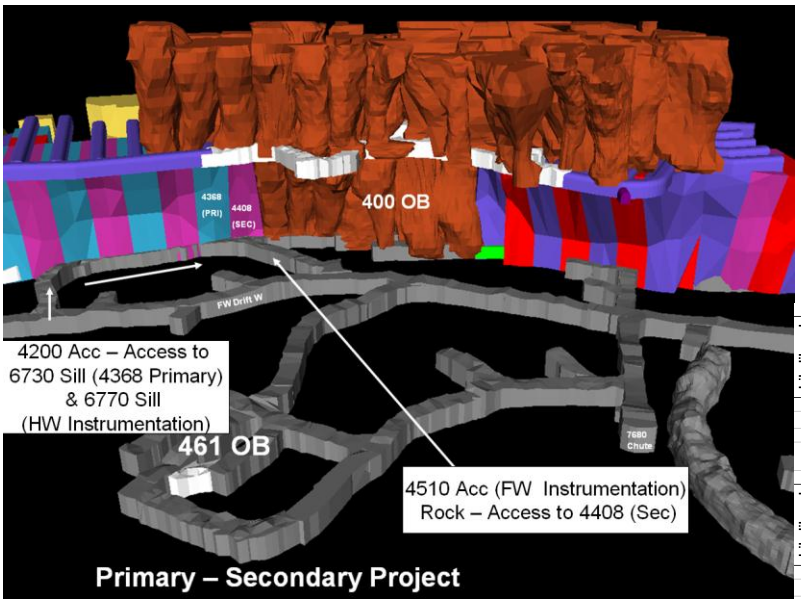

Figure 2 - Mining geometry

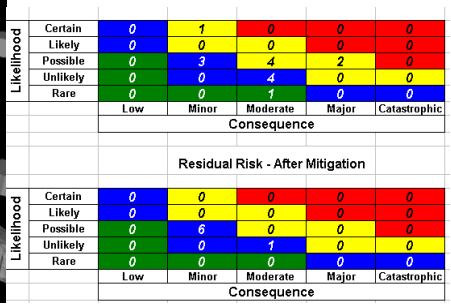

Figure 3 - Risk matrix

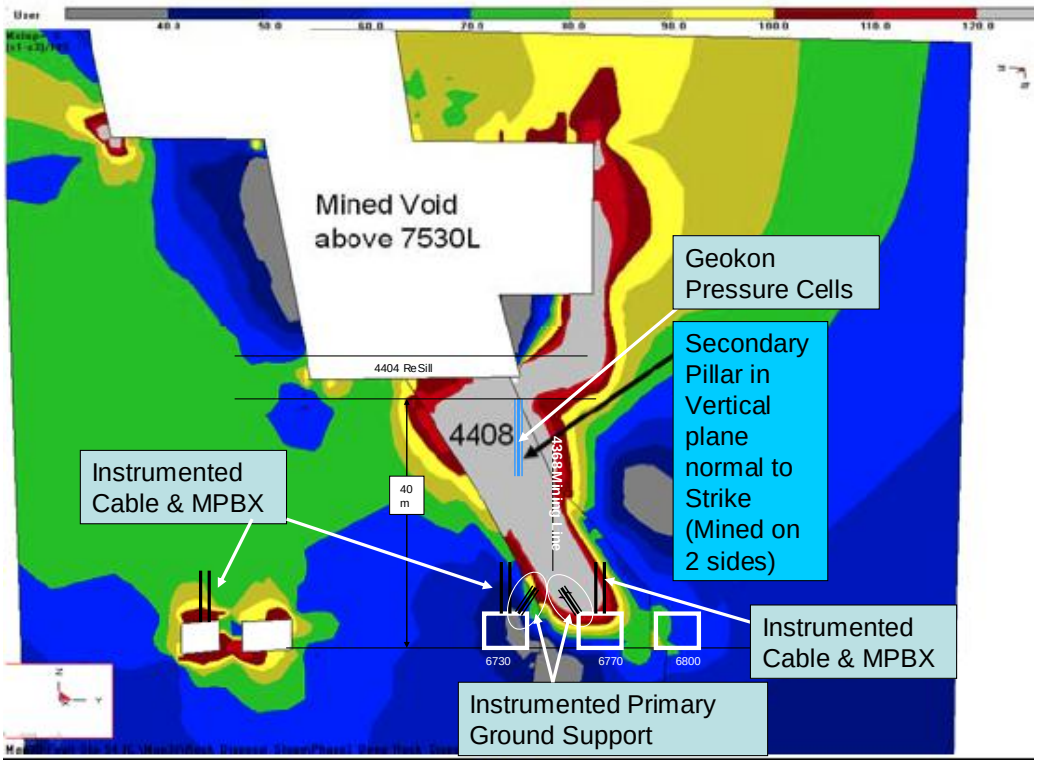

Figure 4 – Section through center of 4408 pillar looking West (σ_1- σ_3 & instrument locations)

A series of defined mitigating measures proposed by the team to address high to moderate risk levels defined in the risk assessment process were effective in addressing the major concerns. The

assessment is a measure of the likelihood of an undesired event occurring against the possible consequence. The risk levels are measured before and after mitigation (refer to figure 3). It was understood that a possibility of excess dilution might be a consequence of such a change, as part of the action items put forth, an extensive review was set in place to model and verify the assumptions.

4. NUMERICAL MODELLING

To obtain an idea as to expected stress changes during the mining extraction phase, linear elastic modeling was carried out using the program Map3D®. A shear (deviatoric) stress value of 70% of the uniaxial compressive strength was used to indicate failure. UCS values for massive sulphides average approximately 135 MPa, and surrounding granites, 240 MPa. After mining of the initial primary stope, zones of high deviatoric stress, low confinement with large displacement are assumed as having failed. Figure 4 reveals the distribution of shear stress following the extraction of the primary stope with instrumentation locations superimposed on the stress grid slice. In ore (i.e. topsill pressure cell location and 6770 Sill), the failure zone is inferred at 95 MPa but is substantially higher at 170 MPa in rock (FW Dr and 6730 Sill). Behaviour of the support system was observed visually while displacements were verified by the instrumentation.

5. MITIGATING MEASURES

The risk review in regards to leaving a rock stope in the 400 OB West Orebody from 2296m to 2340m (7535-7680 level) identified several ground control related mitigation strategies for reducing the level of risk. To measure the impact of excessive local seismic activity as the 4408 panel yields, an instrumentation strategy using DETECT™ instrumentation components and Geokon™ Borehole Pressure Cells (BPCs) were installed at the top and bottomsills to support the numerical modelling work carried out.

The following types of instruments were deployed: 6.1m instrumented cablebolts (d-CABLE), multipoint extensometers (d-MPBX), 2.4m instrumented rebar versions of Jennmar Corp's (d-REBAR), and instrumented versions of Mansour Mining's MCB 33 (d-CONE).

Access to the secondary stope vicinity was restricted when production at the primary stope began and a procedure was implemented to prevent entry into the area to eliminate personnel exposure. Instrumentation,

designed for installation in the restricted high stress area, was wired with long conductors and read with the use of data-loggers from safe locations. A series of long boreholes designed to be drilled approximately 2/3m apart in a planned attempt to pre-shear the rockmass ahead of the hangingwall boreholes at the 4408 (secondary) and 4368 (primary) panel prior to production was subsequently abandoned due to lack of real-estate at the development headings at the topsill. An alternate plan to drill and blast destress holes in the event seismic activity affected ground conditions or adverse squeezing occurred in the boreholes was put in place. As part of the plan, screen was installed over existing shotcrete with yielding ground support components to prevent damage from seismic shaking. The blast-holes were not required.

To further reduce the impact of dynamic stress response as a result of high peak particle velocities due to blasting, electronic detonators were used for the final crown blast to maximize timing and minimize ppv. Blasts fired with nonel (non-electric) detonators, were limited to 2000 lbs or 200 lbs/delay to reduce the occurrence of large seismic events and damage to the 4408 secondary pillar as the primary panel was mined.

To address the possibility of higher sandfill and hangingwall dilution when mining 4408 (secondary) Stope, it was decided that the primary stopes, 4368 and later, 4367 would be filled with a stronger binder recipe of

20:1 tailings: slag-cement blended binder for the body of the stope with a top-up under the pillars at 10:1 to consolidate. Cemented hydraulic fill from classified tailings is poured at a density not less than 68% solids by weight with limits for rock disposal. It was understood that assumed failure could occur on the opposite side at 4448 Stope (25:1 tailings: binder) due to a large amount of waste rock which had been placed under the pillar, although conditions would remain the same whether or not 4408 was taken as a primary or secondary stope.

With all of the measures in place, 4408 Stope was designed as a rock disposal panel following a plug height design that would allow rock disposal into the stope body without interference when developing underneath for future topsills. Rock fill placement was hastened to prevent sand and rock dilution. Time open effect has been documented at the mine as being proportional to the amount of hangingwall dilution.

6. INSTRUMENTATION

The instrumentation project was conducted during the mining of the 4368 primary stope to 6730 bottomsill until the point that mining of the hangingwall section cut-off access to instrumentation and preparation for mining of the secondary stope prompted removal of the pressure cells at the 4408 topsill. Instruments were installed in three locations in and around the secondary pillar as shown in figure 4.

7680 level: 3 x MPBX, 3 x Cable, 2 x Rebar 1, x MCB33

Instrumentation was installed prior to production in two locations, to the footwall and in the ore zone of the secondary pillar. The ore zone (6770 Drift) was located north of the 4368 mining line, cut off when mining the primary stope hangingwall section (4367) as mentioned above. A previously installed instrumented cable bolt and mpbx were installed in the footwall drift.

7535 level: 2 x BPC

2 GEOKON Borehole pressure cells (BPC's) were installed from the 2296m overcut (7535 level) 10m down into the pillar at the centre of the secondary stope to measure stress changes as the primary stope was mined.

7. MONITORING PROGRAM

This project represents the first time that this type of new instrumented rockbolt technology had been used in a hard rock mine using hard rock mining equipment. All previous installations had been in U.S. coal mines. During the course of production, data-loggers were installed on instrumentation to monitor changes, in particular changes following production blasts and subsequent microseismic activity in the high-stress environment. Following the 5th production blast in the 4368 Primary Stope panel, a 1.7Mn event occurred. Following this event, measurements from the instrumented rockbolts indicated significant changes.

The instrumented rebar and MCB33 were installed with 30mm resin using a MacLean bolting machine into the shoulder of the footwall and ore headings on 7680 level. Difficulty of installation in the footwall required the rebar faceplate to be manually tightened between 1-2 tonnes in the heavily fractured heading. The MCB installation was irreparably damaged upon installation. Both the rebar and mcb were pre-tensioned by the MacLean bolter in the ore heading. All holes were drilled through shotcrete. Figure 5 shows the effect of subsequent stress changes at the shoulder location of the 6770 Oresill heading. The instrumented rock-bolts were installed in the "shoulder" of the heading where shotcrete spalling is observed, and the extensometer and instrumented cable installed in the back. The d-MPBXs and d-CABLEs were fully grouted with the use of a pump and grout hose inserted to the top of the borehole.

Installation methods for rebar, MCB and cable instrumentation were identical to those used by mine operations in the bolting operation.

Two borehole pressure cells (BPC's #091 and #092) were installed in 10m long, 150mm diameter production holes in the 4408 Stope at 7535 level. Provisions were taken to ensure that the gauge was 'reasonably" centered (+/-13mm) in the borehole. The location and orientation of the cells are shown in figure 6 which represents a plan view. 091 was aligned transverse to the stope, to measure the longitudinal pressure change, and 092 longitudinal to measure the transverse pressure change. The orebody denoted by "MINED" was extracted during the course of the project and exhibited high stress at the topsill. To the east, the 4448 Stope was tight-filled with a hydraulically placed, 25:1 mine tailings and slag-cement mix and waste rock addition. The topsill was subsequently tight-filled with 10:1 to provide additional support under the pillar when additionally undercut by secondary stope mining.

Although the BPCs were designed to be installed in 56mm boreholes, as opposed to 150mm production holes, hollow inclusion theory (Brady and Brown, 1985) states that the stress changes in the soft cement inclusion should be constant throughout and hence independent of borehole diameter. In fact, the effect of the soft cement inclusion was seen as advantageous due to the extremely large stress changes expected to occur during the experiment. Prior to installation, minor borehole breakouts indicating high levels of differential stress in the primary stope were observed in the hangingwall oresill holes of the primary panel being drilled (refer to figure 6).

Figure 5 – 6770 Oresill Instrumentation 'squeeze'

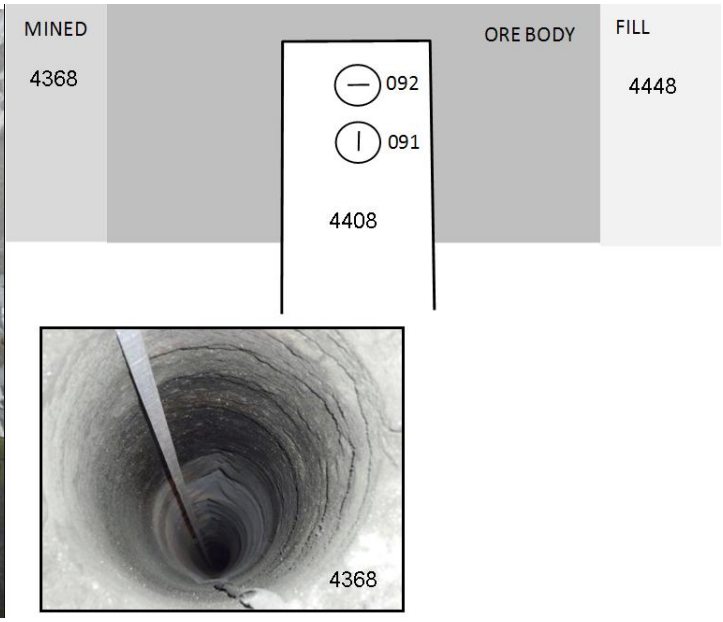

Figure 6 – 4408 BPC Orientation showing 4368

During installation, the cells were encapsulated with 2.5m depth of 0.40 w:c ratio grout into wet holes which could not be pumped or blown out and special care was taken to ensure that the cells were oriented correctly. A centering device was developed so that the cell would be reasonably centered in the borehole and a generous layer of duct tape was wound around the stainless steel pressure tube to mitigate the risk of damage to the pressure tube from shearing in the rock. The borehole pressure cell was inflated one week after installation. As expected, the pressure in the BPC relaxed and subsequently re-pressurized manually to approximately 40MPa. Borehole pressure cells used in this project were set-up to measure pressure changes as the stope was mined upwards from the bottomsill location and revealed

corresponding stress changes as the panel was excavated. Results are collaborated with the breakout of the primary stope and effect on the secondary stope geometry following production.

8. INSTRUMENTATION DATA ANALYSIS

a. 6770 Oresill MPBX (100651003) and Cable

Following the 5th blast which triggered the 1.7Mn event, 0.8mm of movement was measured by the MPBX located in the back at the centre of the tunnel (figure 7). This movement is located beyond 3.2m into the back rather than at the excavation surface as seen in figure 8. The adjacent cable bolt did not show any corresponding load which is consistent with the very small amount of movement recorded by the extensometer.

b. Instrumented Oresill Rebar (100975102)

The resin rebar was tensioned with a MacLean bolter to an initial pre-load of 4-5 tonnes measured at the strain gauge nearest the plate (gauges 1 and 4 in figure 9). As mining proceeded, the resin rebar exhibited load changes in response to incremental mining steps and again the most significant load increase was observed following the 1.7Mn seismic event (step in figure 9). In fact, this event was sufficient to exceed the elastic limit (2500με) and cause yield along the part of the rebar nearest the plate. The strain at this point suddenly increased to beyond 6000 με or 0.6% strain.

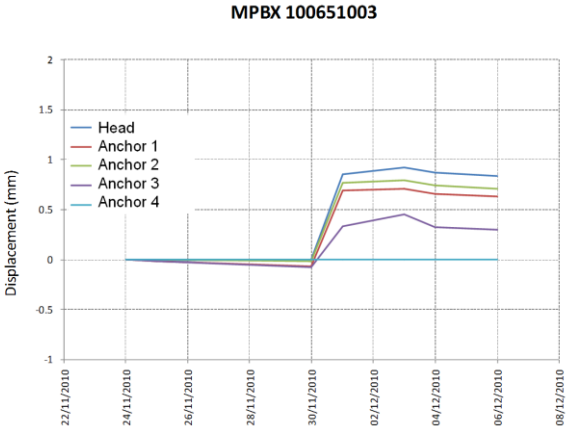

Figure 7 - Displacement versus time

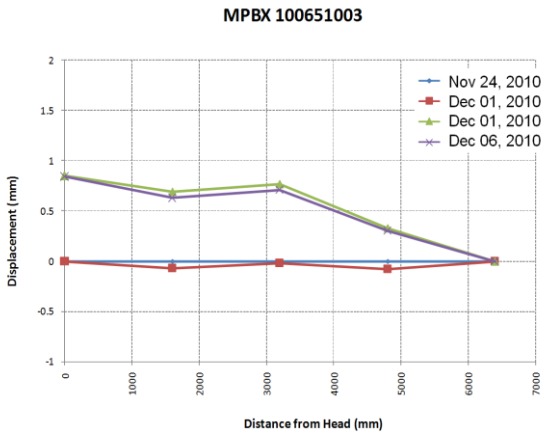

Figure 8 - Displ. distribution along length

Thereafter, the yielded sections (highest profiles in figure 9) exhibit progressive creep whereas the elastic sections of the bolt towards the toe of the hole do not. As indicated by figure 10, the highest load/strains were measured closest to the plate: the yield strength of the steel being exceeded over a 1m length. The corresponding end to end stretch of the rebar is 3.5 mm (figure 11).

The load-strain curve for the rebar based on QA pull tests is supplied courtesy of Jennmar Canada. A typical 20mm rebar yields at .25% strain, exhibits perfect-plastic behaviour between 0.25% and 1.25% strain and begins hardening beyond 1.25% strain (figure 12).

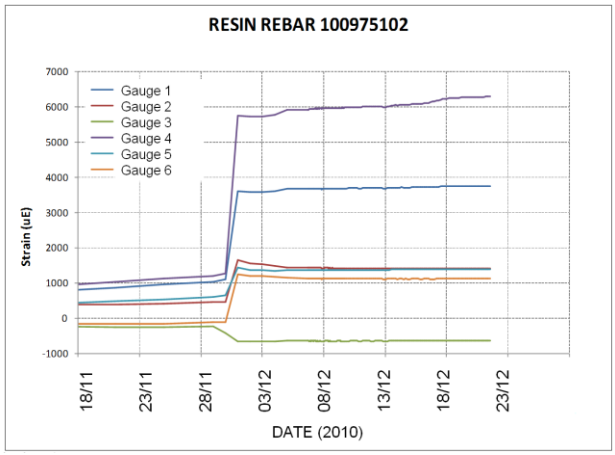

Figure 9 - Strain displacement versus time

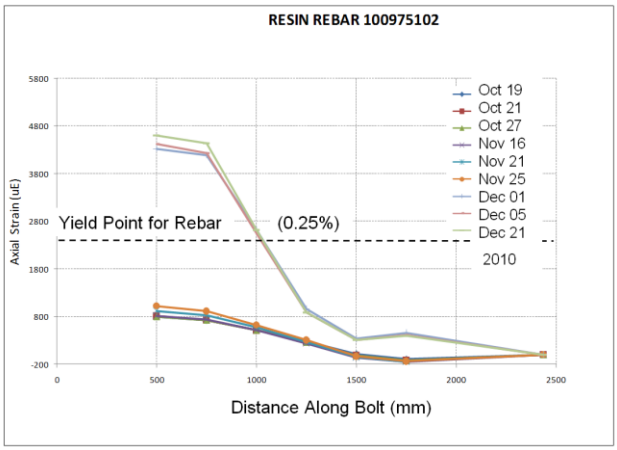

Figure 10 - Axial Strain distribution along bolt

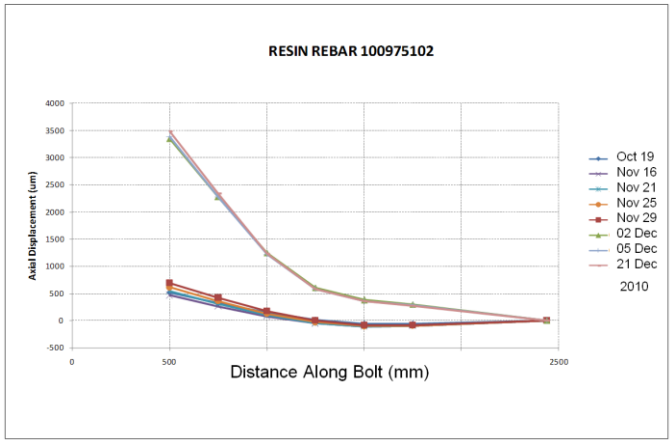

Figure 11 - Stretch along the resin rebar

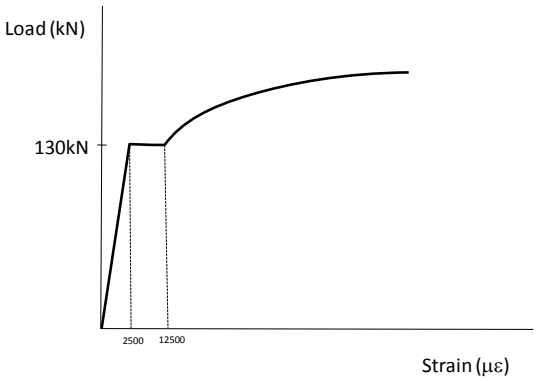

Figure 12 - Load-Strain curve of rebar

c. Instrumented Oresill MCB (100935102)

The MCB indicates an initial pre-tension in the order of 4-5 tonnes, very similar to the nearby resin rebar. Figure 13 shows the response of the MCB to mining. Like the resin rebar the MCB displays a significant increase in load associated with Blast 5 and the subsequent 1.7Mn seismic event, with the divergence of the two plots (which represent diametrically opposed strain gauges) being related to bending or shear of the bolt.

Whereas for the resin rebar the increase in load resulted in yield of the steel, for the MCB the strains do not exceed the yield-point of the steel. In other words, the MCB is absorbing the rock movement by deformation of the resin annulus rather than by yield of the steel. The bolts were installed in close proximity to another (refer to a figure 14 for a comparison).

The rebar and MCB in the 6770 Oresill both loaded up significantly during mining, most notably during Blast 5 and the subsequent 1.7Mn seismic event. While the resin rebar exhibited yield of the steel the MCB remained below steel yield and after the 1.7Mn event, displayed an irregular load history which is indicative of “ploughing”.

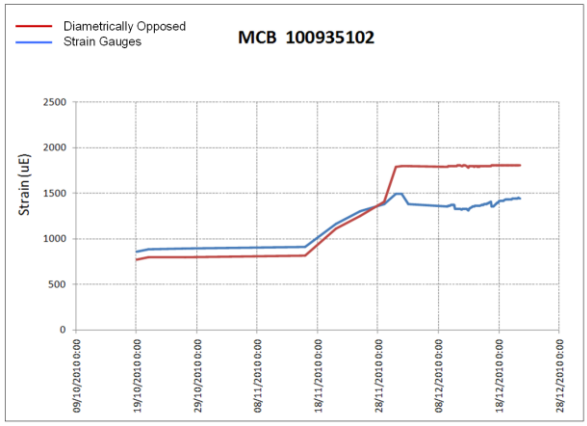

Figure 13 - Strain displacement versus time MCB

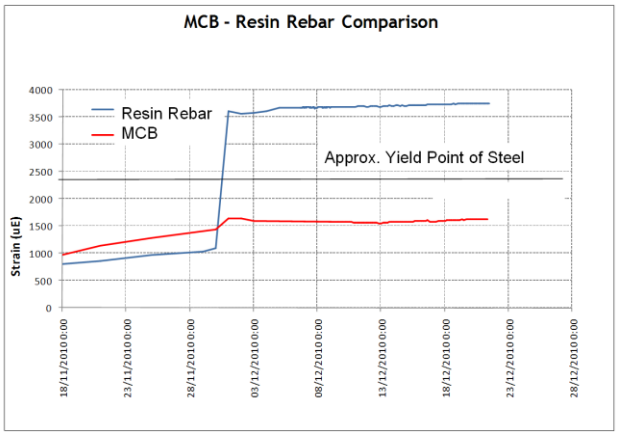

Figure 14 - Comparison of Rebar & MCB

d. 6730 Sill MPBX - Rock (100651003)

The extensometer was logged with a SLUG™ data-logger during the first blast which clearly corresponds to a step in the displacement profile. Although the magnitudes of deformation are very small, only 150mm over the 21ft extensometer (refer to figure 15) it is apparent that the movement is relatively evenly distributed over the entire length of the extensometer with the head at the excavation surface exhibiting most. Such small deformations are probably driven by elastic deformation in response to mining induced stress changes.

Subsequent manual readings indicated an important change as mining of the stope proceeded (Figure 16). As the MPBX deformations increase (after the 2nd blast on 25/11/2010) the displacement pattern changes from being evenly distributed to being localized between anchors 1 and 2. In fact there is almost no deformation between anchor 1 at 1.6m and the head at the immediate back. All the deformation that accumulates during blasts 2, 3 and 4 are localized within a single interval (between 1.6m and 3.2m). Finally after Blast 5 (and the subsequent 1.7Mn event) the MPBX reports with just anchor 1 (at 1.6m) intact. It is suggested that the localized shear movement has damaged the extensometer between anchors 1 and 2. Anchor 2, at 3.2m is beyond the length of the dense array of the 2.4m length primary support, suggesting the shear movement occurred just beyond the primary support components. For subsequent readings, the deformation between the head and anchor 1 (which had been zero prior to blast 4) increased to >4mm.

The nearby instrumented cable also ceased to report after this event. This may have resulted due to damage of the instrument. In assessing this it should be pointed out that the strain gauges used in the DETECT™ cable are identical to the technology used in the instrumented rock bolts, all of which survived the event. The cable did not report any load during its operation suggesting the increases in displacement by the MPBX were in shear.

e. FW Resin Rebar (101175102)

The resin rebar installed in the FW heading was installed into ground that was broken near the borehole collar making insertion of the resin cartridges difficult. It was not pre-tensioned using the MacLean bolter. Approximately 1 tonne of load was applied manually to the plate. Similar to the Oresill resin rebar to the hangingwall, the response of the FW rebar over time shows a dramatic increase in strain/load following the 1.7Mn event (Figure 16). However, this rebar, installed in the 6730 sill rock heading

exhibits a completely different load distribution (Figure 17). Having been manually tightened, there is little load near the faceplate, and the maximum strain/load occurs at 1.5m depth along the rebar. Similarity as was observed with the MPBX observations, it is apparent that the bulk of the displacement occurred towards the end of the existing 2m length yielding friction set primary support installed in the area (gauges 3 and 6 in figure 17). Heavy support including wire mesh over shotcrete contributed to securing the fractured rock in the immediate "shoulder" and concentrated dominant mining induced ground movements beyond 1m into the shoulder.

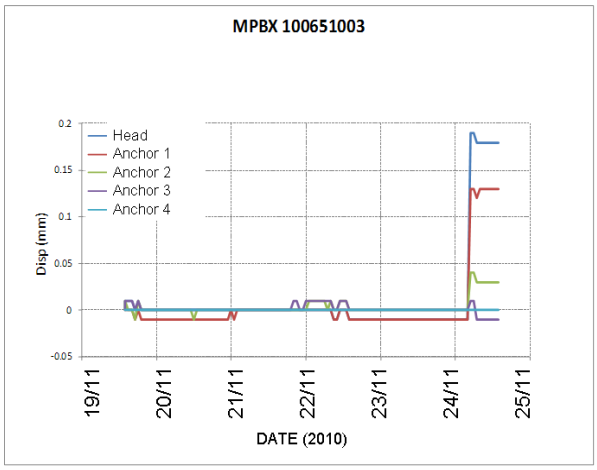

Figure 15 - Displacement versus time

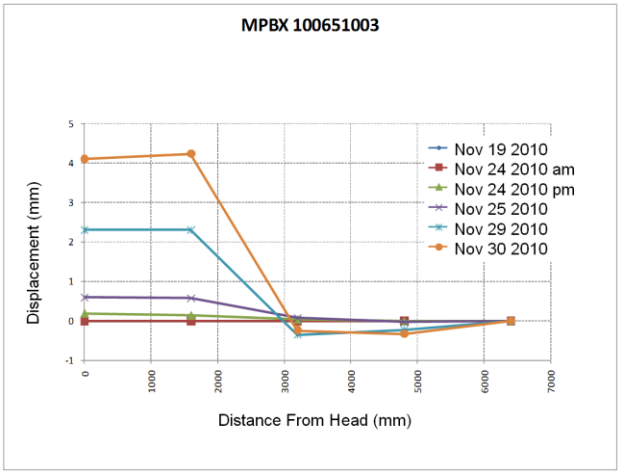

Figure 16 - Displacement Distribution along length

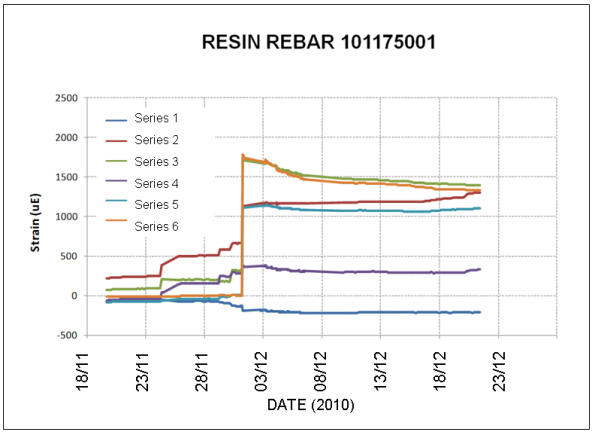

Figure 17 - Strain versus time

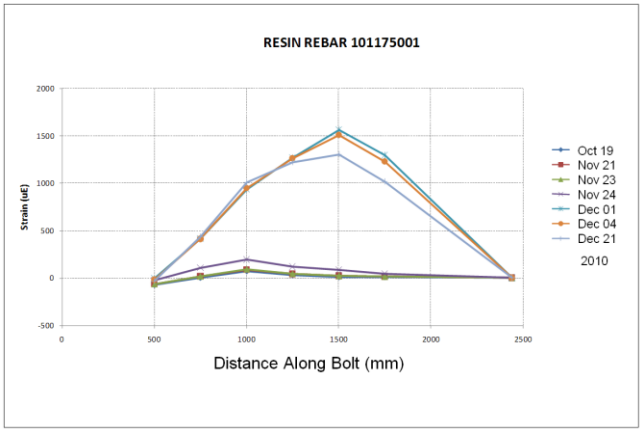

Figure 18 - Strain along the length of rebar

f. 7535 level BPC Results

Figure 19 indicates the response of both BPCs, with 91029091 oriented to measure the longitudinal pressure change, and 91029092 the transverse pressure change. Immediately prior to the monitoring period both BPCs were pumped to approximately 40MPa, and the subsequent asymptotic decrease in pressure over the next couple of days is related to the relatively low strength of the cement grout after 12 days cure. The almost identical initial response for both gauges was interpreted as an indication of good, consistent installation. Subsequent steps in BPC pressure are related to definite mining events.

The corresponding stress changes inferred for the far-field rock are shown in Figure 20. As a rough initial approximation based on soft inclusion theory with the appropriate parameters, these have been calculated using the following stress reduction factor based on the relative material properties of the rock and the cement (stress change in rock or 'sulphide' = 3.0 x stress change cement inclusion).

The secondary pillar (at least its centre) was able to support a differential stress change of +80MPa (-60MPa longitudinal stress drop combined with a 20MPa transverse stress increase) when the adjacent primary crown was mined suggesting that it possessed a significant degree of integrity. If both gauges had measured a decrease in rock stress then it could have been surmised that the entire pillar was in a post-peak deformation state. Elastic modelling indicates that the shear stress levels exceed 70% of the uniaxial compressive strength which would indicate failure be inferred at 95MPa. The instrumentation and observations reveal otherwise, a calibration of the model parameters or assumptions is required with details of the plot stress changes.

Changes in the observed stresses are associated with the production blasting, and the 1.7Mn did not have an adverse affect at the topsill. The most significant and revealing change occurred when the adjacent stope crown was removed. Magnitudes are within reason and indicate a 60MPa stress decrease in the longitudinal pressure and a corresponding 20MPa increase in the transverse pressure.

The Borehole Pressure Cells installed into the secondary pillar from the overcut display reasonable changes in stress during the mining sequence. Following the primary stope crown blast, the +80MPa increase in differential stress suggests that the pillar did not attained peak load (i.e. fail), an important consideration for stand-up time and break-out of a primary panel.

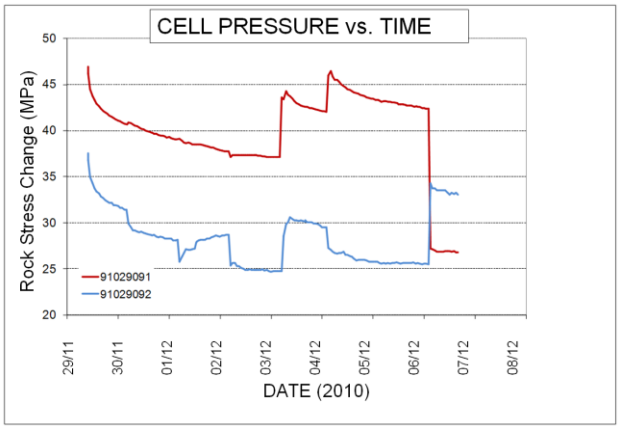

Figure 19 - Time vs. longitudinal (091) and transverse (092) stress change record

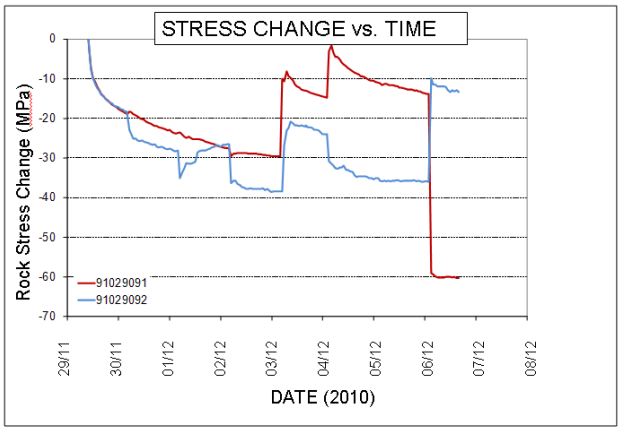

Figure 20 - Rock stress changes corresponding to the BPC pressures

9. DISCUSSION OF RESULTS

a. 6730 Sill - FW Extensometer and Instrumented cable:

From a geomechnical standpoint the extensometer response represents a very characteristic stiff brittle response with the deformation pattern being controlled above the primary support limit. Following Blast 5 and the subsequent 1.7Mn event, the movement was sufficient to damage the MPBX between the 1.6m and 3.2m anchors, most likely just above the 2.4m primary support. There was little distribution of load within the primary ground support 'beam' around the opening.

b. Paradox between different instrumentation results in Oresill:

The oresill instrumentation in the hangingwall indicates a notable contrast in response between the instrumented bolts in the "shoulder" of the heading and the Extensometer and Instrumented Cable in the back. Such variability is not unusual since the movements which are being measured and which generate load in the support element are often localized or manifest along discrete fracture planes. As time and mining proceeds, the propagation and coalescence of these structures becomes apparent and the over-arching deformation pattern more evident in the instrumentation data.

To address the current paradox consider Figure 21 which assumes that extensile cracking occurs primarily near the free surface; convergence should be measured at all points around the excavation. Measurements at Creighton during the tunneling stage reveal that the fracture zone in high stress ground does not typically exceed 1m past the excavation surface at development headings as shown. In this case we would expect to observe all the support elements begin loading up near to the excavation. At the production stage, the instrumentation results obtained for the Oresill suggest the behavior of the excavation to the mining induced stress may be somewhat more complex and "progressive" in nature.

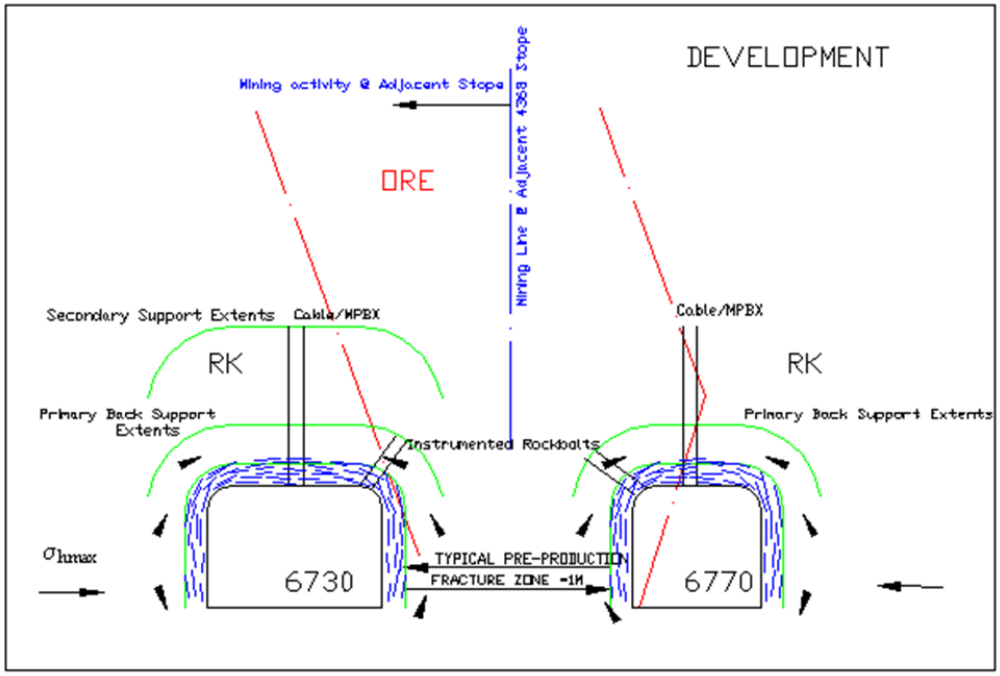

Figure 21 - Induced fracture pattern around a development heading Creighton Deep

Figure 22 outlines an alternative model for a deformation pattern that better agrees with the instrumentation results. Further deformation initiates at the shoulder of the excavation at both excavations, although maximum shear is found near the faceplate in the 6770 (Oresill) and at 1.5m at 6730 Sill. This is probably accentuated by the relatively stiff resin rebar support in the back which will effectively suppress extensile cracking. Owing to the high ratio of σ_{hmax} : σ_v, fracturing may be more likely to propagate away from the shoulder along a path of high shear stress as mining progresses. This could explain why the 6770 extensometer measures only small amounts of movement that is deeper than 3.2m into the back. Height of primary ground support is 2.4m. The role of the support system in the shoulder and in the back close to the shoulder will be to interfere with progressive propagation of these shear fracture zones. Since the zone of fracture development is inclined but will undergo loading at

different depths along their length, over time conjugate shear zones may intersect and coalesce defining a wedge shaped block in the back. Of course this block will be pinned by the high confining pressure in the back until the secondary stope is mined or unless the support system which helps maintain the confinement is overloaded. The existence of favourably oriented joint planes or structures may also play an important role. During this process, it is important to recognize that the proposed conjugate shear zones, daylight at the shoulder and not in the back itself which continued to appear intact for the life of the project.

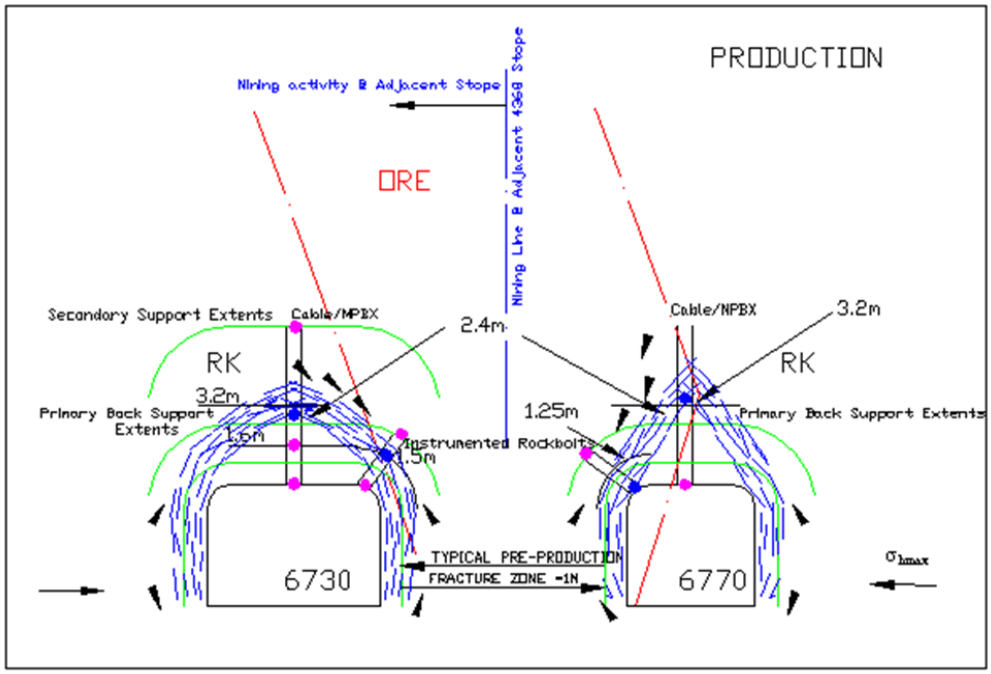

Figure 22 - Induced fracture pattern around development headings production & 1.7Mn event

As shown in figure 23, the suggested alternative model is based on (a) initiation at the shoulder (b) propagation of inclined conjugate zones and (c) coalescence. During the course of the project, this transition began from the initial development stage shown in (a), though early progression of the adjacent primary stope (b) and to the final stress state following the 1.7Mn event.

According to this mechanism the back may continue to look in really good shape whereas the conditions of shoulders will indicate what is really happening. Physical observations underground clearly support the results. The conceptual model emphasizes the inter-relation between support elements in the back and support elements of different length in the back.

Extensometers and instrumented cables installed in the back at the Oresill drift indicate very small amounts (approx 0.8mm) of movement/load. The movement recorded is > 3.2m into the back. These results suggest that the deformation pattern in the back and shoulders does not simply result from concentric “extensile” fracturing but may involve deeper crack propagation along planes of high shear stress.

It is interesting to note that the ‘dog-eared’ profile formed as a result of this mechanism (figure 23c) resembles the borehole breakouts photographed in figure 6 except at a different scale. In both cases, the breakout is driven by the differential stress: σ_{hmax} - σ_{hmin} for the vertically oriented borehole, and σ_{hmax} -

σ_v for the development excavations; the latter being enhanced due to the fact that mining above the level has now cut-off the vertical stress component as shown in figure 4. Hence the dog-ear profile may be considerably more likely for the excavation than for the borehole and may be further affected firstly by the relatively flat back of the excavation, and the stiff primary support in the back. In addition rock jointing will pay a more major role at the scale of the excavation. Slip on pre-existing joint sets in addition to any new crack growth will play a major role in the mechanism.

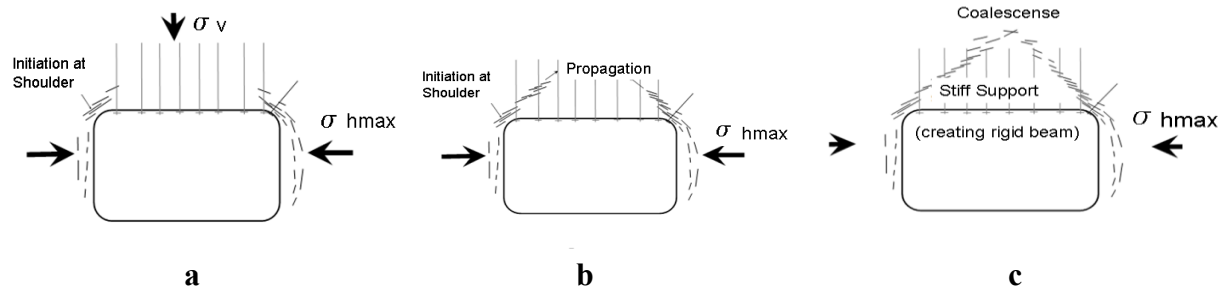

Figure 23 - Alternative model for the fracture pattern progression around the development

10. DILUTION / ECONOMIC ANALYSIS

The instrumentation project ended with the onset of the secondary pillar mining, although the ultimate success of the project pended results of the project as part of the stope reconciliation process. A 3D cavity monitor survey reveals the mining geometry of the primary stope in figure 24. Figure 25 shows completion of the project following mining of the secondary panel, 4408 (note that mined-out geometry above the current mining horizon are not shown).

Economics of course, plays a big part in the success of any project. Ore recovery is critical to the overall picture, of which dilution plays a large role. In the case of the primary stope, there is no fill dilution; recoveries then are the same as for any first mined panel. Looking at dilution results from the secondary panel, twice the normal sand dilution could be expected as there will be fill on both sides. Computing the combined dilution of the secondary and primary stope and looking at an average, it was discovered that the result was 2.5% higher than average for the area, but only 1.2% higher than for the neighboring 4448 Stope conciliation result.

In subsequent analysis, an important consideration is the fact that 25% more dilution occurred blasting up against the 4368 primary stope than occurred against the previously mined 4448 panel, and it was 20:1 vs 25:1 fill. Some of the dilution costs may be absorbed by the savings generated from not having to hoist rock, as the body of 4408 was used as a rock stope, but does not fully offset the cost of sand dilution or monitoring expense.

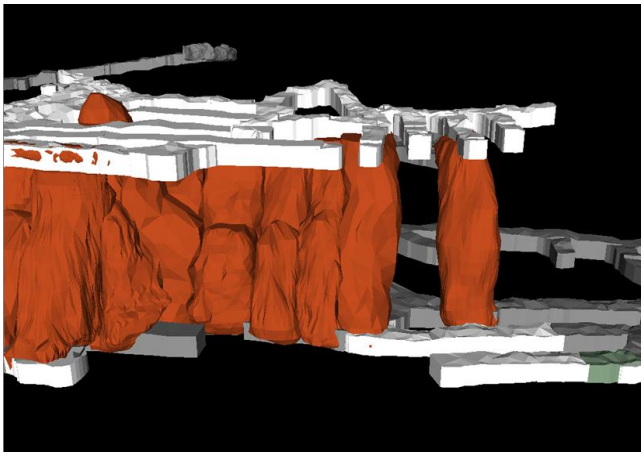

Figure 24 - 4368 primary stope mined

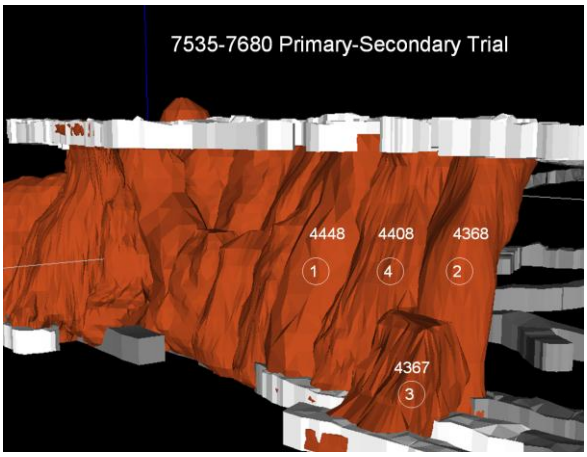

Figure 25 - 4408 secondary stope mined

11. CONCLUSION

While it is unlikely that Creighton Mine will change to a full scale primary-secondary extraction sequence, the benefits of the trial which included the opportunity for additional rock disposal opened up possibilities worthy of investigation. Calibration of the instrumentation results with visual observations of development drift stability and numerical modelling will provide further insight into ground control management as changes to mining sequences are evaluated.

Information gained in this project provided useful information to VALE Creighton Mine operations with regards to effects of primary-secondary mining and whether it could be considered elsewhere. The project was beneficial in the understanding of the interaction between the stiff and dynamic ground support system currently being used in development at the mine and the fracture propagation progression around such development. The limited dataset from this experiment cannot definitively prove this mechanism, although Creighton Mine is currently monitoring similarly elsewhere for anticipated high stress conditions.

Despite less than favorable dilution results experienced, the project in itself was very successful. Prior to setting up a second primary-secondary trial where conditions warrant, the Creighton operation will investigate pre-emptive blast control measures to minimize sand dilution. It is believed that further enhancements can be made with tighter controls on the placement of explosives and/or optimized borehole diameters when mining a secondary panel. Locations will need to continue to be carefully investigated for suitability (i.e. secondary access availability, massive ore zones without brittle rock inclusions). Further monitoring will be a part of such projects.

12. ACKNOWLEDGEMENTS

The authors would like to thank management at VALE Canada for permission to publish the data presented in this paper. Thanks also to Jennmar Canada for assistance with installation of the instrumentation and rockbolt suppliers involved with this project.

13. REFERENCES

BRADY, B.H.G., and BROWN E.T., 1985. Rock Mechanics for Underground Mining. George Allen and Unwin, London, p.138.

Adra Tunnel: Fire and Rehabilitation

Dwayne D. Tannant
School of Engineering, University of British Columbia, Kelowna, Canada

ABSTRACT: The Adra tunnel near Naramata BC experienced a fire in 2010 that burned timber sets within the tunnel and caused severe spalling of rock from the roof and tunnel walls. The nature of the fire damage is documented and efforts completed to rehabilitate and open a portion of this tunnel to the public are described. The use of the use of shotcrete and rock bolts is a technically and economically superior support system to timber sets as well as being far more fire resistant.

1. ADRA TUNNEL

The Adra tunnel is located above the town of Naramata on the eastern side of the Okanagan Lake in British Columbia. The tunnel was excavated through very strong gneiss in 1913 for the Kettle Valley Railway. The section of the Kettle Valley Railway between Penticton and Midway opened on October 2, 1914 when the last piece of track was laid (Williams 2008). Adra tunnel is the longest tunnel (483 m) along the railway and was nominally 6 m wide and 7 to 7.5 m high with an arched roof. The tunnel forms a 150 degree curve as part of a switch-back on the rail grade. About half of the tunnel length was supported with timber sets and lagging.

The tunnel contains two sections that are supported by a cast-in-place concrete arch. One of these, a 14 m long section located about 100 m from the northeast portal, has a central roof opening. The concrete arch was constructed in 1947 to stabilize an area where the tunnel roof intersected a narrow steep-walled depression in the ground surface.

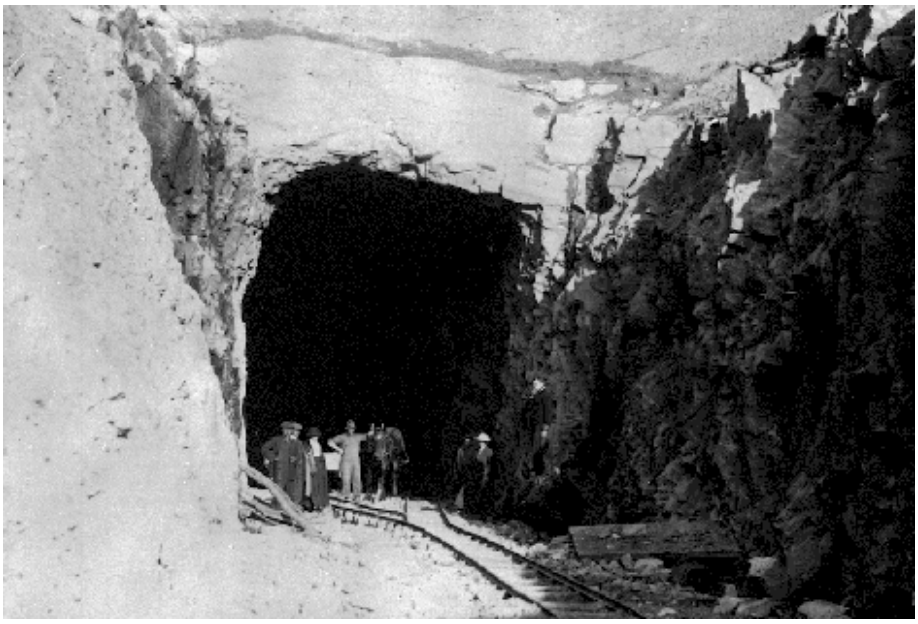

Figure 1 - Northeast portal of Adra tunnel during construction in 1913 (BC Archives)

After 1978, the railway grade was decommissioned and the track was removed (Williams 2008). The province of British Columbia purchased the rail corridor from Canadian Pacific Railway in 1990 and it is now part of the provincial Rails to Trails network, and it is an important route along the multi-use Trans Canada Trail and is managed by Trails BC with volunteer efforts by the Naramata Woodwackers.

After the tunnel was abandoned in the late 1970's, the timber sets and timber lagging within the tunnel gradually deteriorated from wet conditions and began to collapse. As a result, the tunnel was barricaded in the early 1990's to prevent entry by vehicles and was left alone for a few decades, even though there were repeated studies and attempts to obtain funding to reopen this tunnel for public use.

The Adra tunnel experienced a large vandal-caused fired that started sometime on or before May 30, 2010 (Capital News June 2, 2010; Penticton Western News June 2, 2010). The fire burned for many days and consumed the timber sets in the northeast half of the tunnel and caused extensive thermal damage and rock spalling within the tunnel, especially near the roof.

Shortly after the fire, funds were secured to inspect the tunnel with a view to rehabilitating it and reopening it for cyclists and pedestrians using the trail. As a result of this work, a contract was issued to repair and stabilize the portion of the tunnel from the northeast portal to the concrete arch with the roof opening. This section of the tunnel was selected because the rock mass was in fairly good condition, fire damage was little to moderate, and the opening in the tunnel roof within the concrete arch section was an interesting feature for visitors to see in the tunnel. The repair work started in December 2010 and was completed in January 2011, with some minor follow-up work completed in August 2011. This paper examines the nature of the fire damage to the Adra tunnel and the rehabilitation efforts that were completed in 2011 to reopen part of the tunnel.

2. PREVIOUS TUNNEL SUPPORT

The Adra tunnel was supported with timber sets in many locations and contains two short sections supported by concrete arches. There are also unsupported areas. The timber set support in the tunnel had deteriorated over time largely due to wet conditions in the tunnel and had collapsed in many locations as seen in Figure 2.

Starting at the higher elevation, northeast portal, the first 98 m of the tunnel was unsupported. Then came a few timber sets located 98 to 102 m from the portal. The first concrete arch is located 102 to 116 m from the portal. Timber sets continued past the concrete arch to a distance of 129.5 m from the portal after which the tunnel was unsupported for a distance of 26 m. Timber sets were used again at a distance of 155 to 237 m from the portal after which an 80 m section was unsupported. Since the tunnel fire did not affect anything beyond this distance, the nature of the remaining support will not be mentioned other than to say it was largely timber sets along with a 12.5 m long concrete arch.

Where timber sets were used, they were constructed from 12" square fir timbers. Each timber set contained seven separate pieces as shown in Figure 2. The two vertical posts are typically about 4.8 to 5.0 m long and were often installed over a 12" x 8" sill. The remaining five members in each timber set are about 1.5 m long (short dimension) and were used to form the roof arch. The timber sets were spaced along the tunnel at a distance of approximately 1.2 m (48") centre to centre.

The lagging between each timber set consisted of 4" x 6" fir boards. In addition, 4" x 6" or smaller timber packing, in miscellaneous lengths, was used to fill voids in the rock behind the timber sets and lagging.

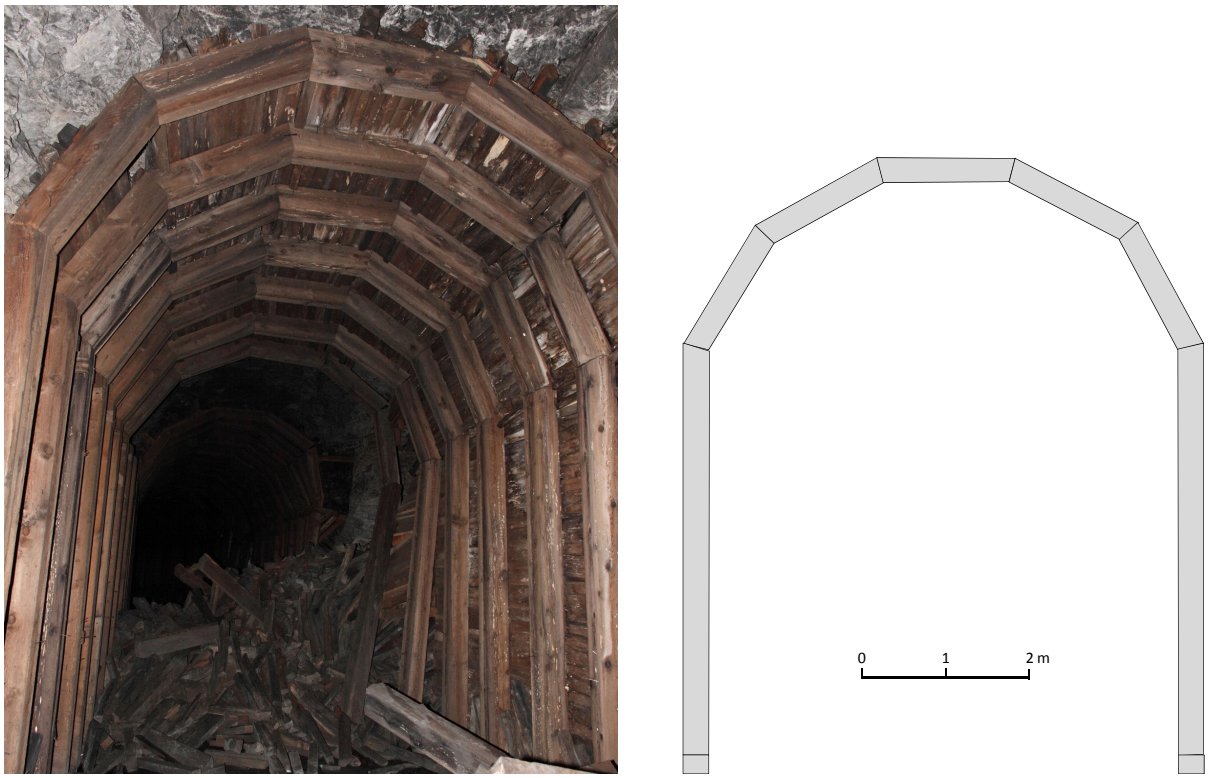

Figure 2 - Timber sets and lagging with timber infill placed behind the timber sets

3. FIRE DAMAGE

Fires in tunnels can cause severe damage to tunnel support and the rock around a tunnel (Beard and Carvel 2005). The published literature on this topic covers more than 100 devastating fires that have occurred in road, transit, and railway tunnels that have cost the lives of 1000s of people (Promat 2008). Forensic evaluations of tunnel fires combined with full-scale tunnel fire testing have increased knowledge of the effects of tunnel fires on tunnel support and the rock conditions. The peak temperatures generated by fires in tunnels typically range from approximately 800°C to 1200°C (Fehervan 2008). Fires in tunnels can have a much higher heat release rate than would be expect from the same fire in an unconfined condition. The tunnel roof and walls reflects heat back to the fuel source, increasing the heat release rate assuming the fire has sufficient oxygen. However, when the size of the fire is comparable to the size of the tunnel, there may be insufficient oxygen available for the fire to burn at its maximum heat release rate.

Published reports of fires in abandoned timber-supported tunnels are rare. Fires in active timber support supported tunnels have been reported by Shannon & Wilson (2009) including the Siskiyou Rail Line Tunnel 13 which experienced a fire in November 2003. One example with many similarities to the Adra tunnel is the Cal Park Hill tunnel located between San Rafael and Larkspur in California (Hugunin et al. 2008 and Serrano 2010). This tunnel was built in the 1884 for the Northwestern Pacific Railroad. The tunnel was re-excavated in 1924 and its width was doubled to allow for two tracks, becoming 9 m wide by 7.3 m tall at the crown, with a horseshoe-shaped cross section. When rail service to Marin County was discontinued in the early 1970s, the 336 m long tunnel was abandoned. In the early 1990s, an intense, vandal-caused fired burned many of the original redwood timber sets, causing more than 45 m of tunnel length to collapse. Further deterioration occurred and by 2002 approximately 25% of the tunnel had

collapsed. The tunnel was completely rehabilitated and reopened as a multi-use transportation corridor for rail, pedestrian, and bicycle use in December 2010.

Figure 3 shows the northeast portal of the Adra tunnel shortly after the fire. The upper part of each wall and the roof are coated with soot from the fire and past train engine exhaust. Shrubs growing above the portal entrance were scorched by the hot gases exiting the portal even though the portal was 98 m away from the nearest timber sets than burned.

Figure 3 - Barricaded northeast portal of Adra tunnel shortly after the fire in 2010

The nature and amount of rock that fell from the tunnel roof in the unsupported section of the tunnel between the portal and the concrete arch is shown in Figure 4. The damage severity increased towards the concrete arch where timber sets were present and burned.

The timber sets on either side of the concrete arch containing the roof opening burned during the fire. Much of this wood was likely very wet when the fire started since this is the wettest section of the tunnel with water continuously dripping from numerous locations in the roof. It is likely that the person(s) that started the fire did so at a location further from the concrete arch where the timber was drier and in a collapsed heap such as that shown in Figure 2, which was taken near the southwest portal.

Once the fire started, the heat and flames travelled up to the roof and then uphill along the 2% grade toward the roof opening and the northeast portal. The hot gases travelling through the tunnel were able to dry out some of the wet timber, enabling the fire to burn most of the timber on both sides of concrete arch. As with the northeast tunnel portal, the roof opening in the concrete arch acted as an exhaust and tree branches near the opening were charred. Assuming the vandals only set one fire, it is noteworthy that the fire spread across two sections without any timber. It jumped a 26 m unsupported section and the 14 m long concrete arch (Figure 5).

The most severe rock spalling occurred where all the timber sets burned at a distance of 155 to 237 m from the portal (Figure 6). This section of the tunnel also had poorer rock mass conditions compared to the unsupported sections on either side. The fire consumed virtually all the timber in this section of the tunnel with only a few charred fragments found in the spalled rock on the floor. The spalled rock fragments were small and plate-shaped and walking across them was akin to walking on broken glass.

Figure 4 - Rock that has fallen from the roof in the first 80 m of the tunnel

Figure 5 - Concrete arch and severe damage to the rock (110 to 130 m from the portal)

Given the extensive spalling that occurred in the gneiss at the tunnel roof, it is interesting to note the almost complete lack of concrete spalling in the concrete arch itself. A similar observation was made during the Mont Blanc tunnel fire in March 1999. Even though temperatures in the Mont Blanc tunnel during the fire were estimated to between 800 and 1000°C, spalling in the concrete lining did not occur, despite the high temperatures. Abraham and Dérobert (2003) suggested that the high permeability of the concrete (poor quality) allowed water/steam to escape the concrete, keeping pore pressures low enough that thermal spalling did not occur. It is known that when polypropylene fibres are used in concrete they will melt at a low temperature creating steam escape channels that can prevent explosive concrete spalling during exposure to fire (Khoury 2000).

In an attempt to estimate the maximum temperature reaching in the Adra tunnel, a test was conducted whereby a piece of the gneiss from the Adra tunnel was heated to 850°C in an oven. In response, the whole rock specimen experienced a distinctive change in its colour with the normal black and white minerals altering to an orange-brown tone. Evidence of a similar colour change is observed in spalled

rocks recovered from the tunnel. However, the depth of this change from the exposed surface is typically less than a few millimetres. This suggests that the rock temperature more than a few millimetres from the tunnel surface may not have exceeded 850°C. More work is on-going to use mineral colour changes to calibrate temperatures experienced in the tunnel during the fire.

Figure 6 - Severe tunnel damage with spalled rock piled up to 1.7 m deep on the tunnel floor

4. TUNNEL REHABILITION

A decision was made in the fall of 2010 to rehabilitate the northeast section of the tunnel from the portal to the concrete arch. The goal was to provide public access to the concrete arch and the roof opening. The restoration effort involved the installation of fibre-reinforced shotcrete and resin-grouted bolts near the portal and on both sides of the concrete arch.

Before the support was installed, the tunnel roof and upper walls were scaled by hand and by using a high pressure water jet in an effort to remove loose rock as well as to remove the soot coating where shotcrete was to be placed. The high pressure water jet was found to be largely ineffective at cleaning the soot from the rock surface even though the recommended water pressure was 20 MPa (3000 psi). However, the actual water pressure used and the jetting effort exerted were not documented.

A wet-mix application method was selected for the shotcrete and a 75 mm minimum thickness was specified. A polypropylene / polyethylene synthetic macro-fibre was used as reinforcement. The mix design aimed for a 35 MPa compressive strength at 28-days. In areas near the concrete arch, where water was continually seeping into the tunnel, strips of a perforated weeping material were attached to the rock surface before shotcrete was applied. Afterwards, short holes were drilled through the shotcrete for drainage.

The rock bolts were installed after the shotcrete was sprayed. These consisted of 2.4 m or 3.0 m long resin-grouted 25 mm diameter threadbar bolts. The shorter bolts were used where the depth of rock cover above the tunnel was only 2.5 to 3 m. The bolts were installed in a fan of five bolts across the width of the tunnel with each fan spaced about 2.0 m apart along the tunnel axis. Additional spot bolting was used without shotcrete to increase the stability where geological structures intersected the tunnel.

The improved condition of the northeast tunnel portal is seen in Figure 7. Even though this portal was originally unsupported and had performed well for nearly a century, it was deemed appropriate to enhance the portal stability given the very thin rock cover and possible adverse effects from the fire.

Figure 7 - Northeast tunnel portal showing addition of shotcrete and bolts

The addition of shotcrete and bolts on both sides of the concrete arch was important because the rock had sustained significant thermal damage at these locations and the depth of rock above the tunnel was low. An inspection of the rock above the tunnel near the arch showed evidence of subsidence and flat lying discontinuities had opened up. Figure 8 shows the rehabilitated tunnel and the transition from the concrete arch to the shotcrete and bolts.

Figure 8 - View towards portal showing concrete arch and shotcrete and bolts beyond the arch

5. CONCLUSIONS

The Adra tunnel experienced a fire that burned approximately half of the timber set supports in the tunnel in mid-2010. The thermal damage to the very strong gneiss forming the tunnel was severe in places, with 100's of cubic metres of rock spalling from the tunnel roof and walls. This degree of damage caused by a simple act of vandalism suggests that the use of timber set support for repair and rehabilitation of railway tunnels being converted to multi-use trails is not a good idea. In many cases, the use of shotcrete and rock bolts is technically and economically superior as well as being far more fire resistant.

A 120 m long section of the Adra tunnel was rehabilitated and reopened to the public in early 2011 (Figure 8). Efforts are underway to secure funding to repair and reopen the remaining portion of the tunnel.

6. ACKNOWLEDGEMENTS

The author's involvement in the investigation of the tunnel fire and subsequent tunnel restoration was instigated and supported by Leigh-Ann Johnson from Katim and John Hawkings, the BC Manager of Recreation Sites and Trails BC. Daniel Russell from Katim was also helpful. The volunteers from the Naramata Woodwackers are to be commended for their efforts in maintaining and upgrading the Kettle Valley Rail Trail.

7. REFERENCES

ABRAHAM, O. and DÉROBERT, X. 2003. Non-destructive testing of fired tunnel walls: the Mont-Blanc Tunnel case study. *NDT&E International,* 36:411-418.

BC ARCHIVES 1913 F-02546.

BEARD, A. and CARVEL, R. 2005. *The Handbook of Tunnel Fire Safety*. Thomas Telford Publishing.

FEHERVAN S. 2008. Characteristics of tunnel fires. *Concrete Structures*, 56-60.

HUGUNIN, J., WHITNEY, B., and BERNARDI, D. 2008. Partnerships in sustainability: rail tunnel adaptation for transit, pedestrians and bicyclists. American Public Transportation Association.

KHOURY, G.A. 2000. Effect of fire on concrete and concrete structures. *Progress in Structural Engineering and Materials,* 2:429-447.

PROMAT. 2008. Tunnel Fire Protection for Tunnel Structures & Services. http://www.promat-tunnel.com/en/Tunnelbrochure.pdf

SERRANO, F. 2010. Material innovation supports tunnel rehabilitation project. http://www.cellularconcretesolutions.com/index.php/download_file/view/60/70/

SHANNON & WILSON, INC. 2009. Oregon Rail Study Appendix C, Oregon Rail Tunnel Assessment: Double – Stack Clearance Inventory. Report to Oregon Dept. of Transportation Rail Division.

WILLIAMS, M. 2008. *Myra's Men*. Kelowna: Myra Canyon Trestle Restoration Society.

Improved Input Parameters and Numerical Analysis Techniques for Temporary Support of Underground Excavations in Weak Rock

Jeffrey D. Oke
GeoEngineering Centre, Queen's-RMC
Nicholas Vlachopoulos
GeoEngineering Centre, Queen's-RMC
Mark S. Diederichs
GeoEngineering Centre, Queen's-RMC

ABSTRACT: While significant progress in underground construction engineering has occurred in the past few decades, a number of fundamental deficiencies persist regarding the recognition, prediction, and mitigation of underground construction hazards associated with complex geological conditions in rock and soil works, such as tunnelling. Many of these shortcomings could be addressed by improving geomechanical models which, in turn, would provide more realistic frameworks for determining input parameters for design analysis. This would improve predictions of construction efficiency for tunnelling and the formulation of more accurate modelling techniques (2D, 3D and 4D) required to optimize the design of engineered rock structures.

This research focuses primarily on the issues related to forepole temporary tunnel support within weak rock masses. This research attempts to determine how best to numerically model forepole support. The behaviour and mechanics of forepole support has not been quantified and/or optimized. As well, there is a lack of in-situ and/or laboratory forepole and weak rockmass interaction parameters available. In terms of numerical modelling, there is a lack of understanding of the use of proper interaction parameters associated with the forepole and the rockmass. The parametric study that has been conducted by the authors demonstrates the influence of each of the forepole-rockmass interaction parameters and their sensitivity. Introduction

1. INTRODUCTION

The mechanistic behaviour of pre-support structural members in underground excavations needs to be addressed along with the geo-mechanical models associated with the material surrounding them. Forepoles are long tubular steel members inserted sub-horizontally ahead and above the tunnel face in the longitudinal direction (i.e. along the axis of tunnel advance) as shown in Figure 1. Forepole-like structures are also cited in literature as pipe roofing (Gamsjäge and Scholz 2009), pipe roof support (Volkmann and Schubert 2007), pipe roof umbrella, steel pipe umbrella, umbrella arch method (Ocak 2008), long span steel pipe fore-piling (Miura 2003), steel pile canopy (Gibbs, et al. 2007), and spiles (Trinh, et al. 2007). Forepoles are installed in groups in an 'umbrella' arrangement above the crown of the tunnel face. The effect of such a support scheme provides improvements to the stability of the tunnel face. Additionally, forepole support affords a safer construction work environment at the face during tunnel excavation. However, forepoles do not act in isolation within a temporary support system. In terms of temporary support design measures, forepoles are a consideration for use (in combination with other temporary support elements) at the extreme end of the support design classes. Currently, research of similar support schemes within the field has been limited to activities based on tunnelling within shallow ground associated with mainly soils. Volkmann (2003) conducted research on a pipe roof support umbrella (for a shallow tunnel in soils and fractured rock) which is similar to the forepole support scheme used in weak rock tunneling.

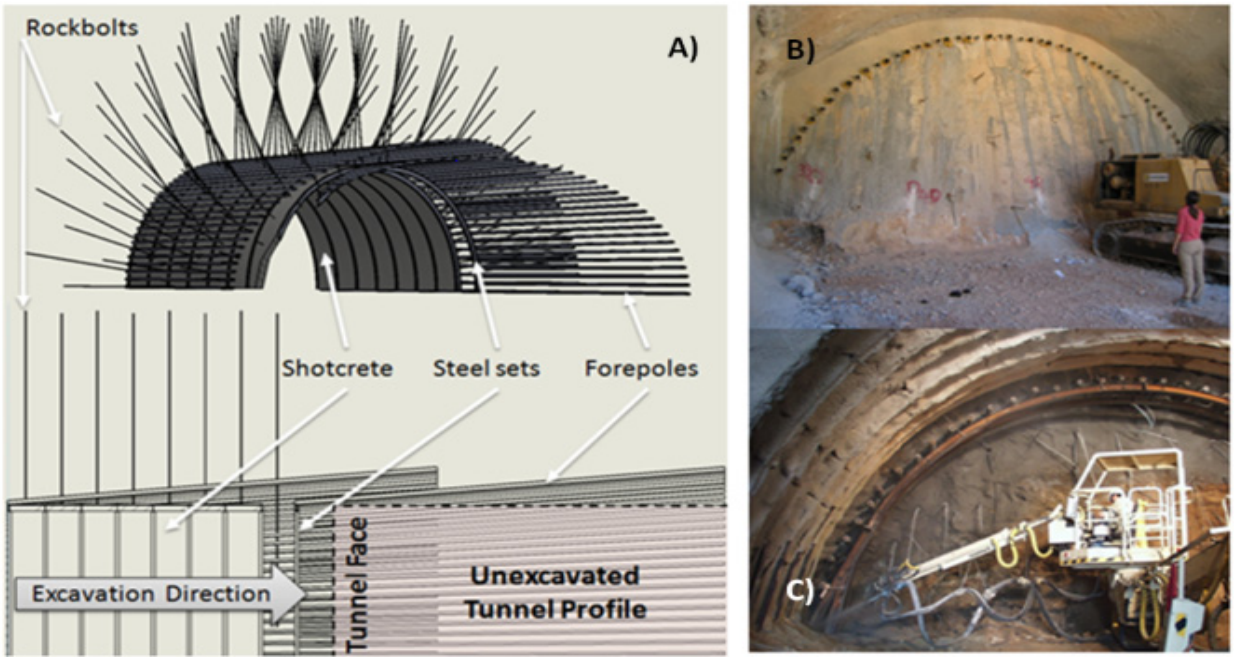

Figure 1 - a) Nominal temporary structural support system used as part of the observational method of support. Elements shown are: forepoles without niches; steel sets (i.e. H-piles); shotcrete; and rockbolts. Core face reinforcement is not depicted. b) Forepole installed at the crown of a tunnel excavation. c) Forepole installed resting on steel sets of a tunnel excavation

Scaled centrifuge models have also been investigated in this regard in clay materials (Juneja, et al. 2010) as well as sandy materials (Kamata and Mashimo, 2003). The lack of true, quantified, in-situ interaction parameters for forepole-weak rockmass interaction is still a very real limitation. In terms of numerical modeling, forepoles have been traditionally modeled as a homogenous region of the entire arch support above the crown (Gibbs, et al. (2007) and Bae, et al. (2005)). This idealized homogenous region aids in tunnel stability by deflecting the stress profile at the crown while causing an arching effect normal to the tunnel axis. This arching effect is not believed to be a mechanism of the forepole elements. It is understood that the primary mechanisms consist of the transfer of load in the longitudinal direction. This load transfer can only be captured by modeling the forepole individually, if not, such simplifications could lead to an underestimation and/or to an overestimation of the overall stability conditions.

Figure 2 - Case-drilling machine for installing forepole members in the Athens-Patras Motorway, (near Patras) Greece

2. FOREPOLE

Forepoles are temporary support elements employed mostly in tunnelling projects associated with weak rock. They are used ahead of the face (in combination with other temporary support), adding stabilization ahead of the plastic zone created due to tunnelling effect. They are installed longitudinally in order to allow for stable excavation underneath the structural umbrella formed by an arrangement of multiple forepoles (Figure 1).

Forepoles have been employed as an alternative to the commonly used pre-support systems primarily associated with soils, such as ground freezing, jet grouted columns, and pipe jacking, and the installation of forepole umbrellas has also been utilized in tunnelling. A contrast between forepoles and the aforementioned pre-support systems is that the stiffness of the latter is greater, but the cost and time commitment of the forepoles is quantifiably less (Volkmann and Schubert 2007). While there have been investigations regarding the cost, time, and effectiveness of the type of support system primarily in shallow ground applications and in soils. There is limited literature associated with this type of investigation within weak rock mass applications.

Availability and machinery costs have limited the installation of forepoles to two different primary methods: pre-drilling and case drilling. The former consists of inserting the steel pipe into a pre-drilled hole, while the latter consists of the installation of the pipe during drilling. The method of case-drilling requires an additional step in which the collapsible drill head is pulled through the pipe following final positioning. Figure 2 depicts a forepole installation piece of heavy equipment using the case drilling method.

Generally, forepoles are inserted at a slight angle (3°-7°) above the top of the tunnel profile, while maintaining the same tunnel opening dimensions (Figure 1 (a)). In terms of design, two options for the placement of the forepoles exist: a) to be installed slightly above the crown at the face of the tunnel, and/or b) for the forepoles to rest on the steel set supports. Method (a) is shown in Figure 1 Figure 1(a) and method (b) is shown in Figure 1 (b & c). In terms of their mechanistic behaviour, forepoles support in the radial direction, however, they also react in the longitudinal direction. This bi-directional nature of the forepole support and reaction further emphasizes the need to analyze these systems in three dimensions.

3. FOREPOLE/ROCK INTERACTION

Deficiencies exist in the understanding of the interaction of the forepole with the rock mass in both installation methods cited previously. (i.e. with or without grout). Volkmann and Schubert (2006) found that case-drilling application resulted in grout which filled the pipes exclusively (as determined by measuring the grout volume used). Their findings indicate that the interaction parameters should be based on properties of the pipe-rock interaction vice grout-rock interaction. As such, that grout only interacts with the rock at the tip and will only affect the end interaction parameters.

From in-situ testing Volkmann and Schubert (2006) found that the installation of the forepole members (along with other support) generated a small disturbance in the rock mass leading to a greater convergence of the tunnel. An understanding of this disturbance phenomenon is required to be captured within numerical models, along with the interaction between the forepole and the rock mass. Therefore, numerical models employed must capture not only initial installation disturbance, but also the effects regarding the normal, parallel, and end of the forepole interaction.

4. TWO-DIMENSIONAL (2D) NUMERICAL MODELLING

The traditional method of modelling forepole members employs the use of a homogenous region above the crown. An arching effect (normal to the tunnel axis) is created by the stiffer homogenous region that does not accurately represent the in-situ geomechanics of this situation. A two dimensional numerical analysis in PHASE2 highlights this fact (Figure 3).

Figure 3a demonstrates the fact that the stresses appear "arched" around the outside of the homogenous region, when in reality only a portion of the stresses are in fact transferred. When modelled as an "as built" in two dimensions, no additional resistance to the deformation is provided by the forepole. As such, the stiff homogeneous region option (Figure 3 (a)) is closer to field results. Therefore, 2D numerical analysis has its significant limitations as agreed upon by (Karakus (2006), and Volkmann and Schubert (2007)). and that 3D numerical analysis is better suited for such a complex analysis.

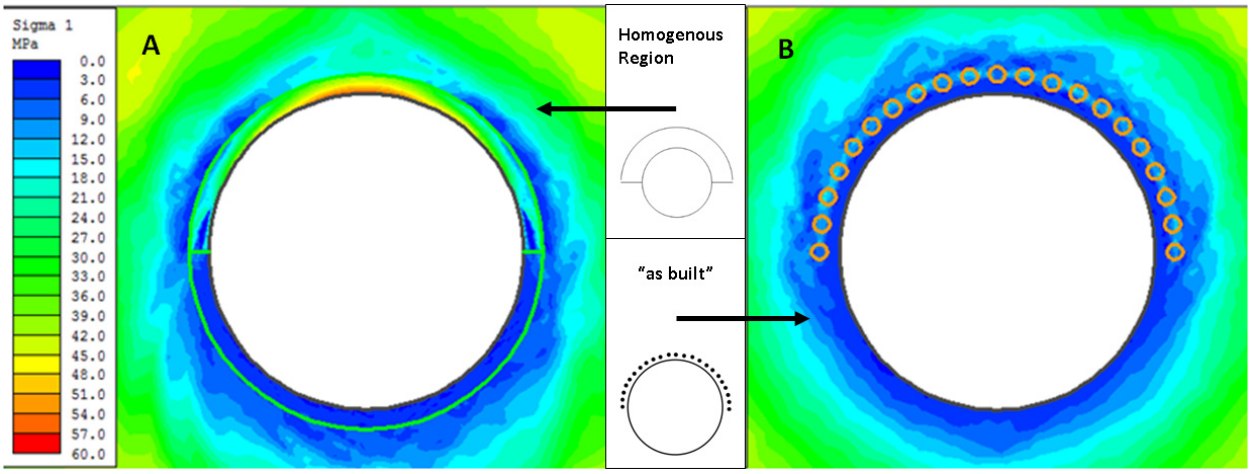

Figure 3 - Forepoles modelled in 2D using a) a Stiff Homogenous region above the crown, and b) an "as built" reinforced region

5. THREE DIMENSIONAL (3D) NUMERICAL MODELLING

The 3D numerical analysis program that was used for this paper was FLAC3D (Itasca Consulting Group Inc 2009). FLAC3D is an industry-standard, finite difference numerical software package. The model created can be seen in Figure 4. The rock mass was simulated using the Hoek-Brown constitutive model while all interaction parameters (rock-support) were simulated through the use of the Mohr-Coulomb failure criteria.

The numerical model consists of a 10m diameter (D_t) circular excavation within a weak rock mass at a depth of 100m. The boundary is $9D_t$ from the center of the tunnel axis, and approximately $4.5D_t$ from the points of interest collected parallel to the tunnel axis (y-axis). The normal direction boundary conditions are fixed at the bottom, and at the entrance plane of the excavation sequence. The top middle strip of the model is also fixed in the parallel direction to the surface (Figure 4 (a)).

Stress conditions are applied on all remaining boundaries to simulate gravity loads (Figure 4 (b & c)). The model setup is illustrated in Figure 4. The mesh was manually graded with a finer mesh at the center expanding to the peripheries.

History points were created within the 3D program in order to capture parameters of interest. For instance, 49 history points (nodes) were created across the entire length of a forepole element. A pre-coded pile element was used as forepole support within the program. In order to capture the relevant behaviour of the forepole and the vicinity around this element within the rockmass, history points were set directly below the forepole and also at other relevant locations (Figure 4(d)).

The spacing of the forepoles was designed in such a manner in order to minimize the interaction between the forepoles so that the results would not capture the group effect but the unique contribution of the forepole itself. As such, and arrangement of 11 forepoles constituted the forepole umbrella. The influence of forepole spacing is being addressed by (Oke, Vlachopoulos and Diederichs 2012). As mentioned previously, a built-in structural element, a PileSel, was deemed best suited for use within the model for the application of a forepole element. The directional material behaviour of such elements is well summarized in Itasca 2009. The PileSel is capable of not only both axial and bending moment, but also normal and shear interaction with surrounding material, based on a slider-spring connection. The slider constitutive model follows a Mohr-Coulomb failure criteria and the spring is defined by its stiffness parameter.

An idealized representation of the spring orientation of the normal and shear interaction is illustrated in Figure 5. A limiting factor is the assumption that the interaction between the PileSel and the rockmass is isotropic in nature. Here, the interaction does not take into consideration the true geometry of the forepole caused by bending or other external stress conditions as external forces are averaged and resolved at the nodes

The PileSel also allows for a “gap” command, which determines the behavioural response due to the cavity that is created (i.e. “gap”) as the forepole moves within the rockmass.

6. NUMERICAL ANALYSIS

A parametric study was conducted in order to capture the unique contribution and significance of each of the interaction parameters. A baseline set of values was identified by using the best possible estimate of these values as cited by literature. The higher boundary values for each of these interaction parameters were also assigned based on literature (Table 1).

The low value was denoted as approximately zero in order to attempt to negate the influence of the parameter for a particular run. Table 1 denotes the interaction parameters of interest as well as the associated analyses that were “run” as part of this paper. In all a selection of 15 runs have been highlighted for the purposes of this paper.

In addition to the runs shown in Table 1 a baseline and unsupported analyses were also conducted for comparison purposes. The baseline run was then compared to 13 different runs whereby only one variable was changed to either its high or low value (or “on” or “off” for the gap function). The numerical analysis runs were conducted using solely forepole support elements in order to determine the specific behaviour and effects of this support of interest.

7. RESULTS AND DISCUSSION

The horizontal and vertical radial convergences of the tunnel near the face and at the center of the tunnel ($3D_t$ from the tunnel face, Figure 6) were captured in order to determine the overall effect of the interaction parameters within the forepole itself and in the rock mass. The relative, overall tunnel convergence as captured by these reference points, are illustrated in Figure 6. The figure depicts the percent difference (compared to the baseline results) of the radial convergence at the respected points of

interest, where a negative value denotes less over convergence from the baseline. Within this figure is it evident that the most sensitive parameters are those from runs 5 (high k_s), 8 (low c_n), 11 (high k_n) and 12 (low k_n).

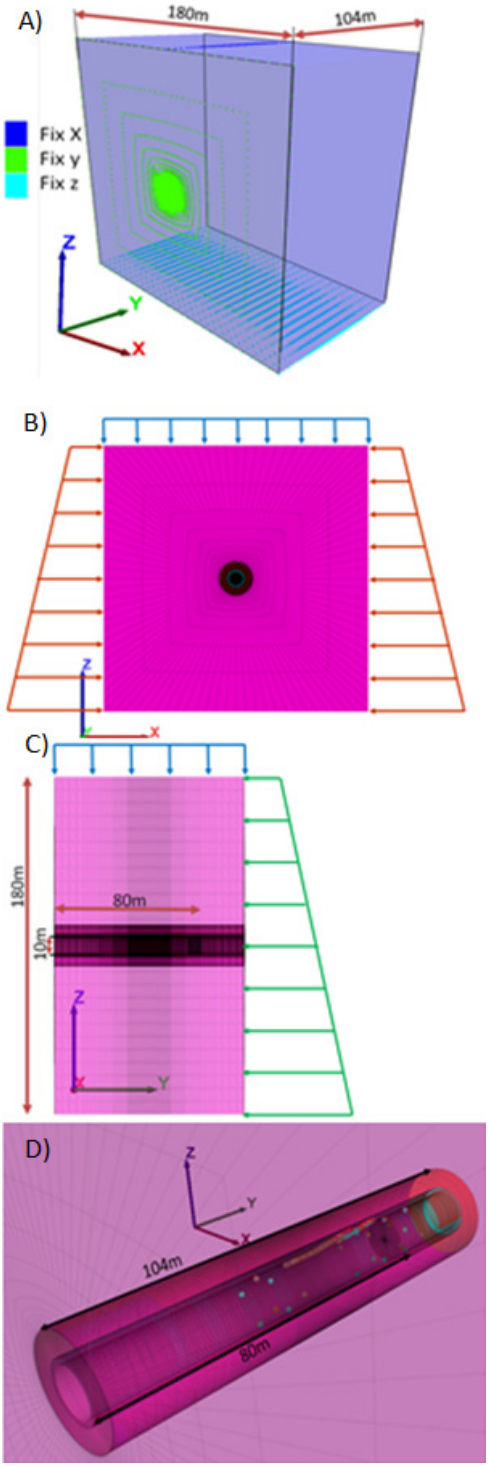

Figure 4 - 3D numerical model denoting a) fixed boundaries conditions and, b) applied stresses and radial gradient meshing arrangement (x-z plane) c) applied stresses and meshing (z-y plane), and d) history point locations (small spheres)

The longitudinal forepole displacement profiles were also captured and examined at 1 m and 6 m of cantilever overhang (Figure 7 and 8 respectively) specifically noting the contributions due to runs 5 (high k_s), 8 (low c_n), 11 (high k_n) and 12 (low k_n), as these parameters were seen to affect the deformed shape of the forepole the greatest; which is consistent with the observations with respect to the overall convergence of the tunnel. These two displacement profiles were chosen in order to demonstrate the cantilever forepole displacements as they manifest due to further excavation balanced against the influences of the variation of the initial and locked in conditions produced by the interaction parameters.

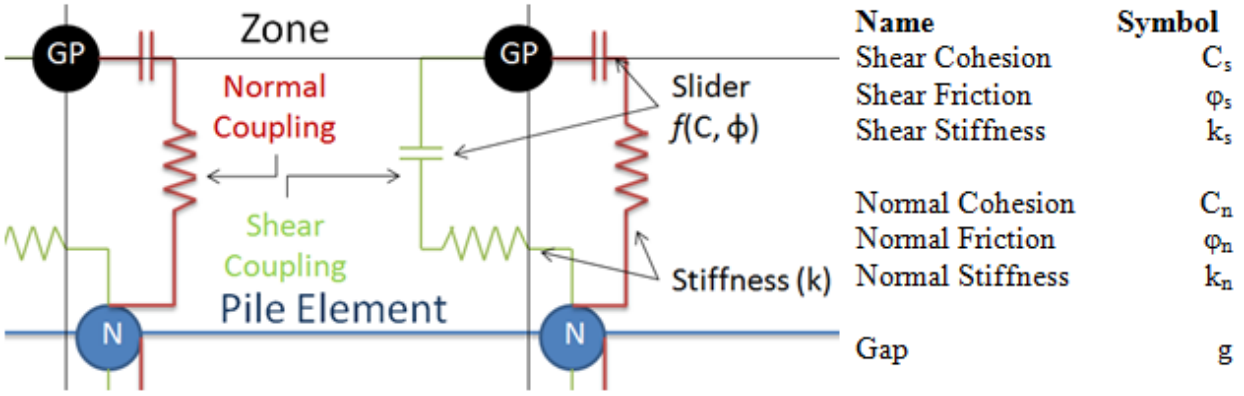

Figure 5 - Interface elements connecting the forepole (pile element) with the rock (zone)

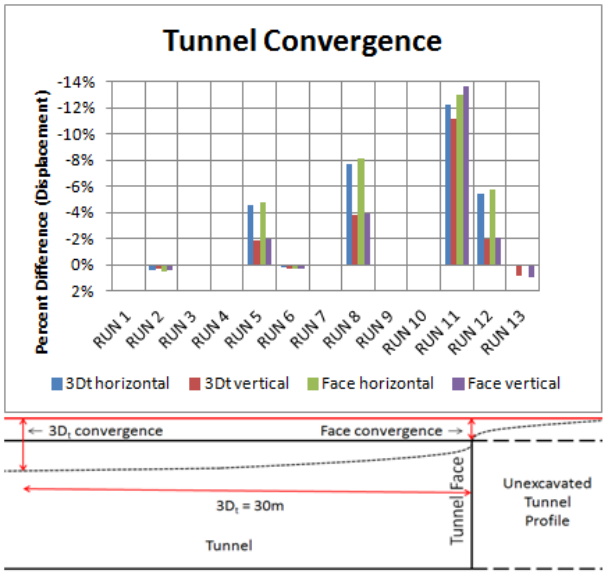

Figure 6 - Percent difference of displacement from baseline interaction parameters values

As seen in the inset diagram in Figure 7 and 8, the zone of interest is near the tunnel face. In this region, there are effects due to the overlapping forepole umbrellas (i.e. the previously installed forpoles and the next series of forepole support). The figures denote the resulting displacement profile of the most recent set of forepoles (lower bound). All of the runs follow the same trend as the baseline run (except run 12). There is no real influence on displacement from the excavation steps in Figure 7. The initial displacement

locations noted are as a result of the stress effects between the subsequent forepole umbrella installations as well as the induced displacement due to the installation of the previous forepole umbrella.

The forepole displacement profiles shown in Figure 8 also follow the general trend associated with the baseline run. Note, however, that there is an influence at the extremities of each staged excavation causing a "sinusoidal' forepole displacement profile with a max amplitude of approximate . Low normal cohesion seems to not be affected by the staged excavation approach. The trends associated with the minimum and maximum forepole displacements (i.e. sequence of displacement profiles) are the same for Figure 7 and 8.

The results of the numerical analysis contained herein support the findings as presented by Volkmann and Schubert (2006). Specifically, one witnesses increased convergence due to installation of a forepole umbrella support configuration. This increase of convergence was achieved by the sheer weight of the forepole mass around the crown of the excavation in combination with the disturbance of the interaction parameters within the model during the tunnel excavation process. In reality, disturbance of the rockmass would also occur prior to tunnel face excavation as a result of the forepole installation process. There was approximately a 5% increase of convergence as related to the unsupported (baseline) analysis.

Table 1 - Summary of Interaction Parameters and Runs Table. Note: Cm is the cohesion of the material, Φm is the material fiction angle, and Θ is the exposed perimeter of the forepole

Interaction Parameters								[1]Itasca (2009)	[2]Vlachopoulos (2009)	[3]Trinh (2006)	[4]Funatsu, et al. (2008)
FLAC code	cs_scoh	cs_sfric	cs_sk	cs_ncoh	cs_nfric	cs_nk	cs_ngap				
symbol	C_s	ϕ_s	k_s	C_n	ϕ_n	k_n	g				
units	[F/L]	(degrees)	[F/L²]	[F/L]	(degrees)	[F/L²]	on/off				
base	[1] $C_m*\Theta$	[1] $\phi_m°$	[3] 1.0E+07	[1] $C_m*\Theta$	[1] $\phi_m°$	[3] 1.0E+09	off				
high	$2*C_m*\Theta$	$2*\phi_m°$	[2] 1.0E+11	$2*C_m*\Theta$	$2*\phi_m°$	[4] 1.0E+12	on				
low	0	0	0	[3] 0	0	0					
High	RUN 1	RUN 3	RUN 5	RUN 7	RUN 9	RUN 11	RUN 13				
Low	RUN 2	RUN 4	RUN 6	RUN 8	RUN 10	RUN 12					

Runs 5, 8, 11, and 12 did not yield less overall tunnel convergence. Higher stiffness (shear and normal) in terms of the interaction between the forepole support and the rock mass reduced the amount of tunnel convergence, as did lower cohesion and normal stiffness. Of note is that the higher and lower bound of these values (Table 1**)** are at the extremities for their respected interaction parameter. Further investigation involving in-situ or laboratory experiments will lead to a smaller, more practical range of acceptable limits.

Furthermore, the increase overall convergence illustrates forepoles do not provide any additional support to the overall convergence if acting individually (i.e. not in combination with other support structures such as rockbolts etc.). The use of forepoles has been shown to be effective when install in tunnel construction in terms of stabilization in order to create a safer tunnelling environment. As well, a forepole umbrella rarely acts independently and oftentimes rests on steel supports. In this fashion, the load is transferred to the foundation or the base of the tunnel.

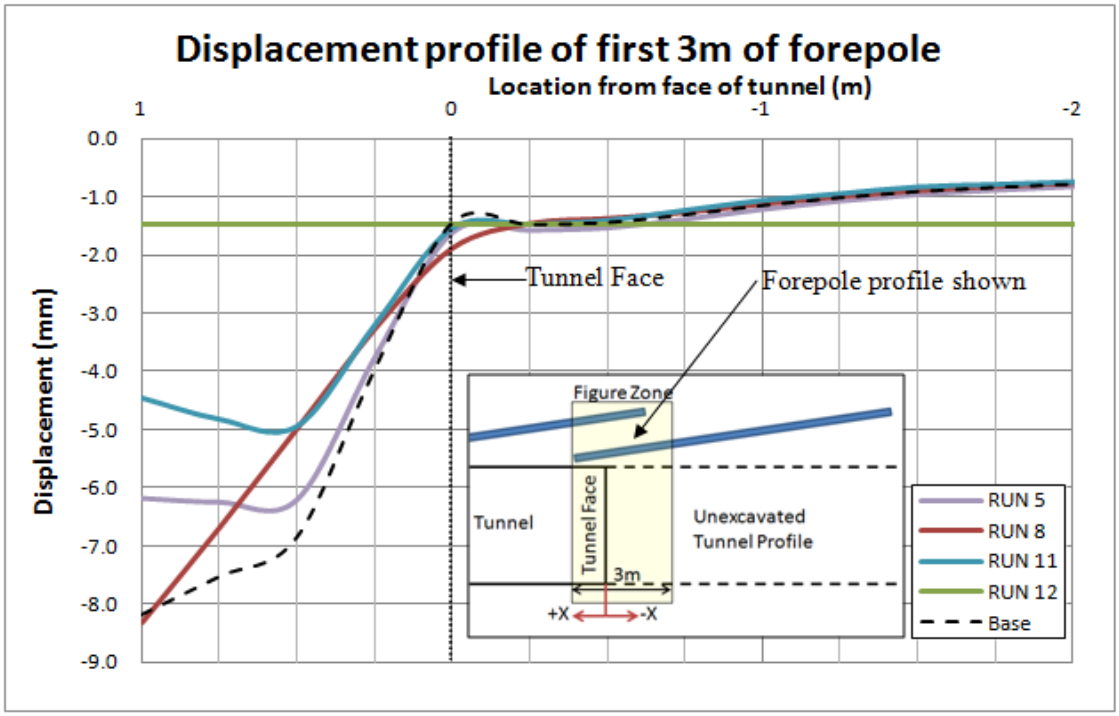

Figure 7 - Displacement profile of first 3m of forepole from numerical analysis with 1m of overhang. Runs that were to similar to base results were not shown in chart

The radial convergence results indicated the failure criteria associated with for the interaction parameters have a minimal effect on the resulting displacement of the tunnel convergence.

The shear cohesion and friction, and along with normal friction did not significantly affect the results. Adjusting the normal cohesion value was the only slider failure criteria that induced change in the convergence of the tunnel. The gap function also did not indicate noteworthy change. The most significant parameters that effect of the convergence have been the shear and normal stiffness values. The normal stiffness value resulting in the greatest amount of percent difference (12% at $3D_t$ and 14% at the face).

The main failure criteria used for the interaction parameters was the Mohr-Coulomb failure criteria. The cohesion base value used was high, this fact in combination with the angle of friction, did not induce interaction failure. No failure was evident in the baseline model, as increasing the value of cohesion did not affect the results. Minimal failure also occurred within the shear direction as lowering the cohesion results in less than 0.5% difference from the baseline. However, increased displacement of average 5% was noticed when the cohesion value lowered to zero for the normal interaction. Also the normal case (run 8) lowering cohesion affected the displacement of the forepole which minimized the 'sinusoidal' forepole displacement pattern (Figure 7 and 8) that was captured with the other results while still following the general trend of the other runs (with the exception of run 12).

Varying the friction angle did not induce failure along the forepole. This lack of sensitivity reinforces that the base value for cohesion was high and that this condition governed behaviour. There was a small amount of displacement (less than 1%) when the gap function was turn on. Therefore, this function did not influence the results significantly.

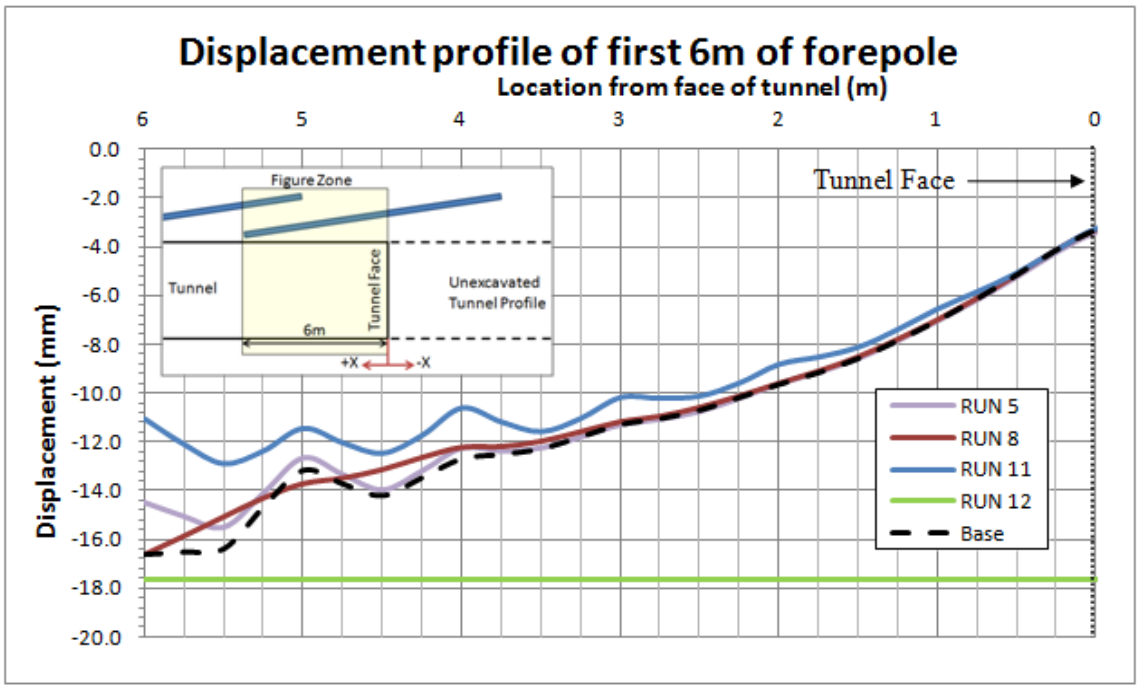

Figure 8 - Displacement profile of first 6m of forepole from numerical analysis with 6m of overhang. Runs that were to similar to base results were not shown in chart

The most significant factor was determined to be the stiffness parameter (shear and normal). Varying the normal stiffness was more critical to the overall convergence of the tunnel. This could be explained by the mechanics of the forepole supporting the in radial direction and reacting in the longitudinal direction (the opposite response of a rockbolt and core reinforcement techniques). Both the supporting and reacting directions rely on the normal coupling between the forepole and the rock mass. This normal coupling was also a factor of normal stiffness, as when it was set to zero, it produced a straight forepole that only displaced uniformly with the rock mass average convergence (run 12 in Figure 7 and 8).

8. RECOMMENDATIONS

The authors recommend that in order to accurately capture the interaction between the forepole and the rock mass properly, in-situ and laboratory testing needs to be conducted to be able to produce an accurate value for relevant interaction parameters. Therefore, further investigation needs to be conducted with respect to the potential convergence of installing the forepoles. It is also recommended that the numerical analysis algorithms used in these sophisticated programs be re-visited in order to potentially improve upon their use within the software package.

9. CONCLUSIONS

The interaction parameters investigated in this paper denote a significant influence to the overall behaviour of the tunnel under varying conditions and values. As such, one must ensure the proper values or range of values are utilized as inputs to numerical models. Of note is that the influence of interaction stiffness and cohesion on the overall tunnel convergence as well as the longitudinal forepole displacement.

The effect of the normal and shear coupling for a forepole is still a complex interaction with no accurate range of acceptable values. This investigation has highlighted the need for laboratory testing or in-situ testing in order to obtain accurate values (and sensitivities) and obtain a better understanding of the interaction between the rockmass and the forepole support.

10. ACKNOWLEDGEMENTS

This work has been funded by NSERC as well as Queen's & RMC Graduate Funding.

11. REFERENCES

BAE, G.J., SHIN, H.S., SICILIA,C., CHOI, Y.G., and LIM, J.J., 2005. Homogenization framework for three-dimensional elastoplastic finite element analysis of a grouted pipe-roofing reinforcement method for tunnelling. Internation Journal for Numerical and Analytical Methods in Geomechanics, p. 1-24.

FUNATSU, T, HOSHINO, T., SAWAE, H., and SHIMIZU, N., 2008. "Numerical analysis to better understand the mechanism of the effects of ground supports and reinforcements on the stability of tunnels using the distinct element method." Tunnelling and Underground Space Technology Incorporationg Trenchless Technology Research, p. 561-573.

GAMSJÄGE, H., and SCHOLZ, M., 2007. Pipe Roofing – Features & Application. p. 11.

GIBBS, P.W., LOWRIE,J., KEIFFER, S., and MCQUEEN, L,. 2007. M5 East - Design of a shallow soft ground shotcrete motorway tunnel. Australasian Tunneling Society, p. 1-6.

HOEK, E., 2007. Pratical Rock Engineering. North Vancover: Rocscience Inc, —, 1999."Support for very weak rock associated with faults and shear zones." International Sysmposium on Rock Support and Reinforcement Practice in Mining . Kalgoorlie, p. 20.

ITASCA CONSULTING GROUP INC, 2009. Fast Lagrangian Analysis of Continua in 3 Dimensions Version 4.0. Minneapolis: Itasca CG Inc.

JUNEJA, A, HEGDE, A., LEE, F.H., and YEO, C.H., 2010. Centrifuge modelling of tunnel face reinforcement using forepoling. TUST, p. 377–381.

KAMATA, K., and MASHIMO, H., 2003. Centrifuge model test of tunnel face reinforcement by bolting. Public Works Research Institute, p. 6.

KARAKUS, M., 2006. Appraising the methods accounting for 3D tunneling effects in 2D plane strain FE analysis. Tunnelling and Underground Space Technology, p. 10.

KIM, S., BAEK, S., and MOON, H., 2005. A study on the reinforcement effect of Umbrella Arch Method and prediction of tunnel crown and surface settlement. In Underground Space Use. Analysis of the Past and Lessons for the Future, by Yucel Erdem and Tulin Solak, Istanbul: Taylor & Francis. p. 245-251.

LUNARDI, P., 2008. Design and Construction of Tunnels. Berlin Heidelberg: Springer-Verlag,

MIURA, K., 2003. Design and construction of mountain tunnels in Japan. Tunnelling and Underground Space Technology, p. 115-126.

OCAK, I., 2008. Control of surface settlements with umbrella arch methos in second stage excavations of Istanbul Metro. Tunnelling and Underground Space Technology, p. 674-681.

OKE, J., VLACHOPOULOS, N., and DIEDERICHS, M.S., 2012. Three-Dimensional Sensitivity Analysis of Forepole Support Elements for Underground Excavations in Weak Rock. ARMA. Chicago (Abstract Accepted).

TRINH, Q.N., BROCH, E., and LU. M., 2007. Three Dimensional Modelling of Spiling bolts for tunnelling at weakness zones. In Rock Mechanics: Meeting Society's Challenges and Demands, by Eberhardt, Stead and Morrison, London: Taylar & Francis Group. p. 427-432.

VLACHOPOULOS, N., 2009. Back Analysis Of a Tunnelling Case Study in Weak Rock of the Alpine System in Northern Greece: Validation and Optimization of Design Analysis Based on Ground Characterization and Numerical Simulation. Kingston, Ontario: Queens University.

VOLKMANN, G., 2004. A Contribution to the Effect and Bahaviou of Pipe Rook Supports." EUROCK. Salzburg, Austria: Schubert.

VOLKMANN, G.M., and Schubert, W., 2006. Contribution to the Design of Tunnels with Pipe Roof Support. Asian Rock Mechanics Symposium.

—., 2007. Geotechnical Model for Pipe Roof Supports in Tunneling. World Tunneling Congress, Underground Space - the 4th dimension of Metropolises. Prague, Czech Republic: Taylor & Fracis Group, p. 755-760.

—. "Geotechnical Model for Pipe Roof Supports in Tunneling." In Proc. of the 33rd ITA-AITES World Tunneling Congress, Underground Space - the 4th Dimension of Metropolises. Prague: Taylor & Francis Group, 2007. p. 755-760.

—., 2006. Optimization of Excavation and Support in Pipe Roof Supported Tunnel Sections." ITA-AITES World Tunneling Congress, p. 404.

WITTKE, W., PIERAU, B., and ERICHSEN. C., 2006. New Austrian Tunneling Method (NATM)-Stability Analysis and Design. Essen: WBI.

Stochastic Approach to the Corrosion Assessment of Rock Bolts

Francois Charette
Dynamic Rock Support NA

ABSTRACT: Corrosion is a significant factor affecting the capacity and working life of ground support. The paper explores a relatively simple method to predict the load capacity of a support system using a Monte Carlo stochastic approach. The analysis uses published field data on existing ground support to evaluate the applicability of the method and its predictive performance. Discussion on corrosion rates found in the field and predicted from laboratory measurement is provided.

1. INTRODUCTION

Corrosion of ground support can take various forms and exhibits a range of intensity that is highly variable, even in a given underground excavation. The corrosion of rock bolts has been addressed by Li & Lindblad (1999), Ramsingh (1998), Hadjigeorgiou et al (2002), Charette et al (2004), Ranasooriya et al. (1995) and Spearing et al (2010), among others. Ranasooriya et al (1995) reviewed the corrosion behaviour of friction rock stabilizers used in underground mines in Western Australia, identifying uniform corrosion, localised corrosion and galvanic corrosion as the three main types of corrosion. Localised (pitting, crevices, etc) and galvanic corrosion impact the strength of a rock bolt in a similar manner and could be considered as various forms of localised corrosion.

It is common to see atmospheric corrosion leading to a combination of uniform corrosion and pitting, as the aggressive compounds found in the airborne water droplets can attack unprotected steel surfaces. Galvanic corrosion is also widespread, with the ground and accessories potentially acting as cathodes in relation to the rock bolts (Robinson et al, 1999). Degree and types of corrosion are highly dependent on a number of factors which includes (Robinson et al, 1999, Li et al, 1999):

- Presence of water and its chemical make-up
- Rock mass quality and mineralogy of the rock mass
- Type and properties of ground reinforcement systems
- Age and history of excavation and reinforcement
- Type of fill material
- Temperature

Corrosion rates varying from 0.05 mm/year to more than 1 mm/year have been observed or measured in the laboratory (Charette et al, 2004, Spearing et al, 2010, Ramsingh et al, 1998, Tilman et al, 1984 and 1985 among others). Predicted corrosion rates as a function of the pH of the environment can be found in literature (NACE, 1984, Li et al, 1985).

Consideration of the acidity of the environment is critical as for pH lower than 5, the corrosion of black steel can occur with minimum dissolved oxygen content, even with galvanized steel (Robinson et al, 1999). In very low pH conditions, galvanized coatings are non-effective and since their corrosion rate is extremely high, the coatings become a favorable environment for the development of active corrosion cells. In nearly neutral mine waters, oxygen and chlorides and sulfites ions in solution are the main corrosion agents (Tillman et al, 1984 and 1985) and corrosion rates can be predicted by means of their relative concentrations.

A good amount of data has been accumulated on the corrosion of friction bolts (Tilman et al, Ranasooriya et al) and expanded friction bolts (Swellex and the likes), as found in paper by Tillman et al, 1985), Hadjigeorgiou and al, Charette et al, among others. The mode of attack of a friction set or an expanded friction bolt consists mostly in galvanic corrosion of the contact area between the rock and the bolt (coated or not), facilitated by ground water as the electrolyte. Broken ground conditions provide conditions for accelerated corrosion, with or without a stress component. Outside part of the bolts are also subject to atmospheric corrosion as well as bi-metallic corrosion, exhibiting pitting as well as some uniform corrosion attacks (Figure 1).

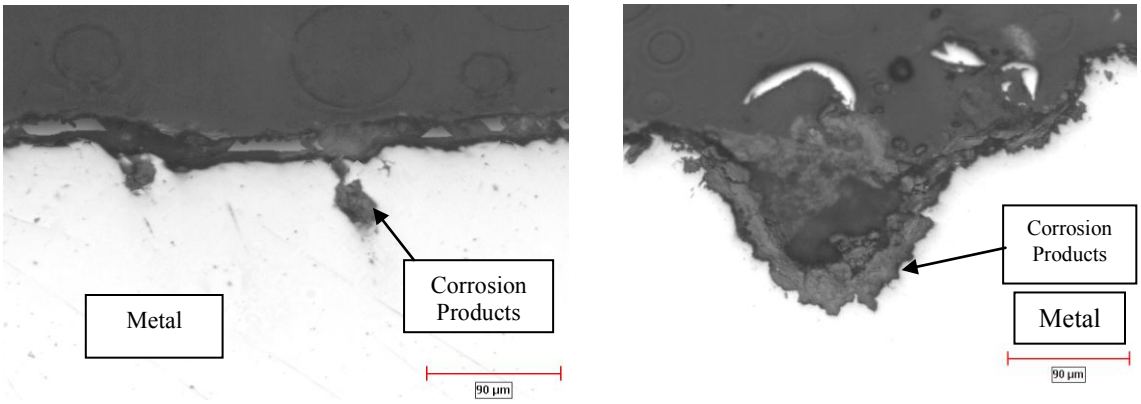

Figure 1 - A longitudinal section showing extreme localized attack and fragmentation of the metallic surface

2. EVALUATION OF CORROSION RATES

Conventional corrosion rates assessment usually consists in submitting a steel component to the water encountered in the field, or a simulated water containing most chemical components as the in situ water, and using various investigative methods to evaluate the corrosion rate (e.g., Spearing et al 2010, Ramsingh et al, 1998). A more elaborate methodology developed for Atlas Copco (2004) consists in measuring the corrosion rate of a rock bolt in a cell containing rock material and mine water (Figure 2); this method provides a more realistic environment than only water, and can be used to assess the worst case scenario. The methodology was applied to several samples of rock bolts set in cells containing rock material from several mining operations. The results of the project are summarized on Figure 3.

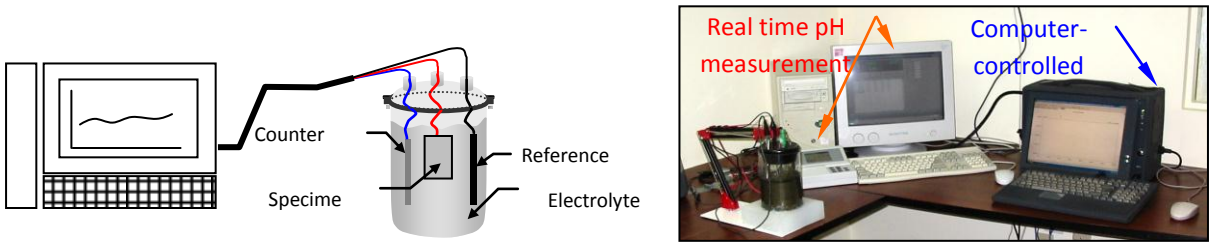

Figure 2 - Laboratory testing of expanded friction bolt in mine rock and water

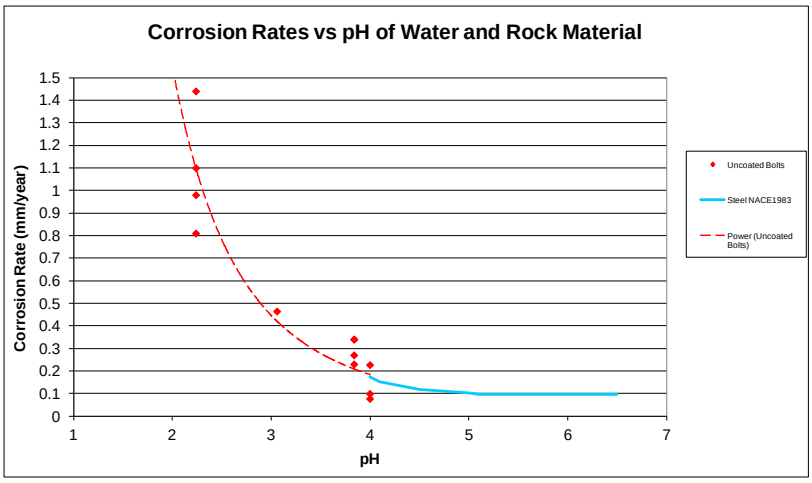

Figure 3 - Corrosion rate of expanded friction bolts as a function of pH of ground environment

3. EVALUATION OF BOLT CAPACITY

For expanded friction bolts with a nominal thickness of 2 mm, the remnant load capacity after a given amount of time can be described by the following relationship (Charette et al,2004):

$$Capacity_t = Capacity_0 \times (2 - CorrosionRate \times Time)/2 \quad (1)$$

Where:

$Capacity_t$: load capacity at a given time "t"
$Capacity_0$: load capacity of a new bolt
CorrosionRate: rate of corrosion of steel in the environment, in mm/year
Time: exposure time in year

For the purpose of evaluating the capacity of expandable bolts during their service life, a database of pull tests results was built by Atlas Copco (Charette et al, 2004). Most significant cases of corrosion did reportedly affect the first 60 cm of bolt, and pull testing at the collar is now considered a correct method to evaluate the remnant load capacity of friction bolts during the life of a ground support system. Figure 4 presents the results of pull tests in (a) mildly corrosive environments, (b) highly corrosive environments, and (c) for one particular mining operation in massive sulphides (Charette et al, 2004).

4. GROUTED REINFORCEMENT

Recent analysis of corrosion of grouted support can also be found (Spearing et al, 2010, Villaescusa et al, 2007), but very little data exists to correlate the load capacity as a function of service life or ground and water conditions.

For grouted reinforcement, the attack from the corrosive agent in the atmosphere and the rock can be caused by fissures in the grout following ground movements or due to improper mixing of the grouting agent (Villescusa et al,2007). Alternatively, attacks at the collar or the threads are also observed. A possible relationship to evaluate the remnant load capacity of a grouted reinforcement (bolt, cable) could be:

$$\mathbf{Capacity_t} = Capacity_0 \, (Diameter - CorrosionRate \times Time)/Diameter \quad (2)$$

Where CorrosionRate is the rate of corrosion of steel that is factored by the migration speed of contaminant through the grout, or the degree of fracturing of the grouting material, or plain corrosion rate of steel for the collar and threads area.

5. PREDICTION OF LOAD CAPACITY

The process that leads to the corrosion of the rock bolt is admittedly quite complex. In addition, corrosion is not a simply deterministic reaction as the electrolyte, the substrate and the aggressive environment do interact in a probabilistic fashion (Shibata, Uhlig's Corrosion Handbook, chap. 22). A direct relationship between the environmental conditions and the observed corrosion of rock bolts in the field has not been determined yet. Although this type of relationship has been developed in the case of atmospheric corrosion in industrial atmospheres (Matsushima, Uhlig's Corrosion Handbook, chap. 30), factual data on load capacity of rock bolts over time is scarce. Parameters like pH, alkalinity, Langelier saturation index, etc provide an estimate of the corrosiveness of a given environment; unfortunately, their range of values are not usually known.

The proposed methodology presented below has been developed by reviewing the results of pull tests performed on expanded friction bolts and applying a Monte Carlo simulation process to the corrosion rate, keeping in mind the range of the original capacity as well as the corrosion rates. The parameters of the model are:

- Original Load Capacity given as an average value, and the associated standard deviation
- Average corrosion rate assessed by laboratory testing of steel in typical rock and water substrate (Charette et al, 2004) used to simulate broken ground and wet conditions
- Time of exposure

The process consists in creating a number of bolts (250 in the simulation), and in applying a probable corrosion rate based on a normal distribution of the corrosion rate and the original bolt capacity. Mean corrosion rate are taken as measured in the laboratory (Figure 3). Normal distribution of probability was chosen as it describes well the pitting corrosion process (Shibata, Uhlig's Corrosion Handbook, chap. 22), and pitting is the corrosion process most often encountered on rockbolts. Specifically for friction bolts, pitting is one of the main corrosion processes and is well documented (Charette et al, Hadjigeorgiou et al,) as presented on Figure 1.

The simulation process assumes that every bolt is corroded on a yearly basis at a simulated rate, and the capacity evaluated by the remnant steel quantity (using equation 1). The variability of the corrosion rate will affect the range of observed corrosion rates. Extensive laboratory measurements by Tillman et al (1984, 1985) in nearly neutral mine waters show that the coefficient of variation of the corrosion rate for friction sets in nearly neutral waters can vary roughly from 0.09 up to 0.45. For the purpose of this analysis, the standard deviation will be calculated as 20% of the corrosion rate. Local variation is expected and simulations using various ranges should be performed in practice.

6. RESULTS

From the range of results shown on Figure 5, we can consider the following observations:

- The original capacity of the bolts vary in the same range as the measured range on the field
- The range of the simulated remnant capacity after a given number of years is very similar to the range of the measured field capacity.

- Observed corrosion tends to start after about one year. This could be the result of the ground becoming more fractured and water inflow establishing itself. Also, leaching of minerals from the ground could be starting at that point. The present model does not readily deal with this situation, but a lower corrosion rate needs to be set for the first year

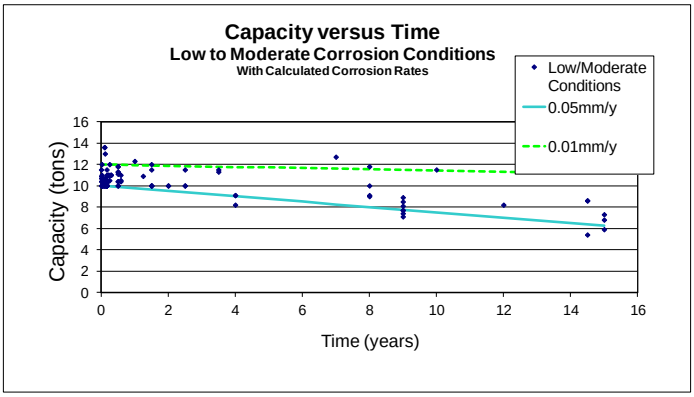

(a) Mining operations in dry and good rock mass conditions, pH between 6 and 7

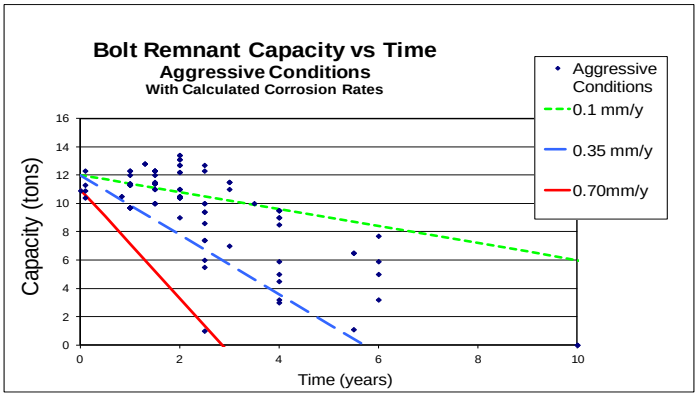

(b) Mining operations in broken, wet sulfides and low pH (between 3 and 3.5)

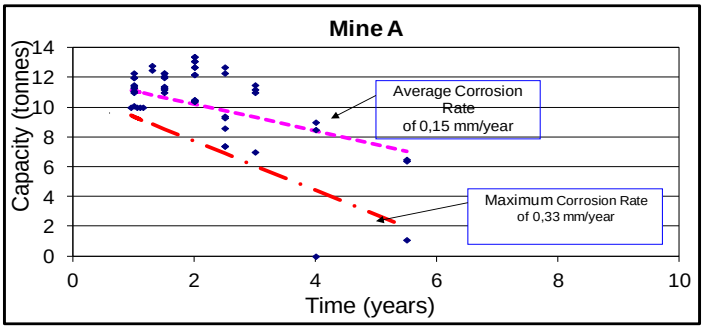

(c) Mine in massive sulfides and pH of ground and water around 3.5

Figure 4 - Measured bolt capacity as a function of service life. a) in low to moderate corrosion conditions, b) in very aggressive corrosion conditions and c) for a mine in fairly corrosive conditions

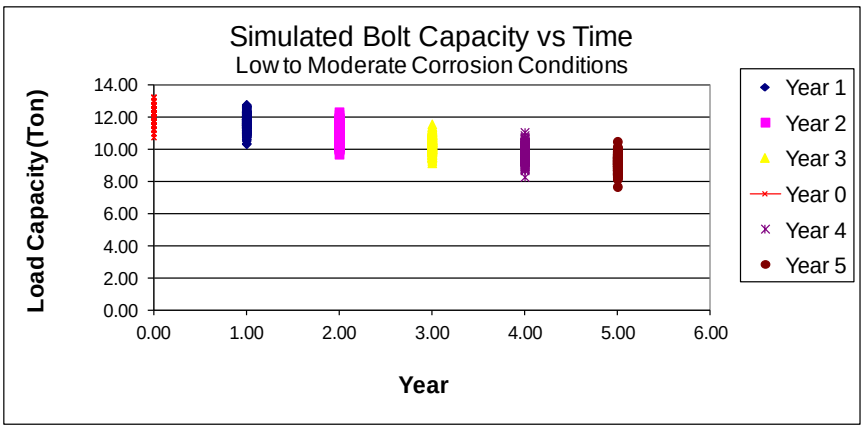

a) Based on a corrosion rate of 0.1 mm/year

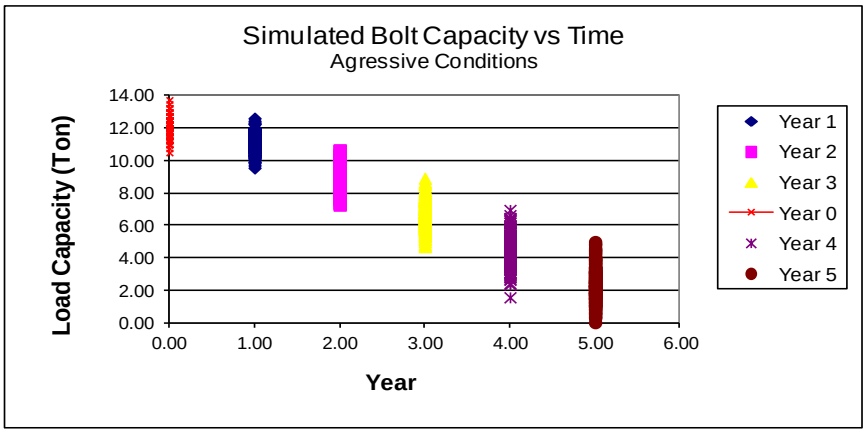

b) Based on a corrosion rate of 0.35 mm/year

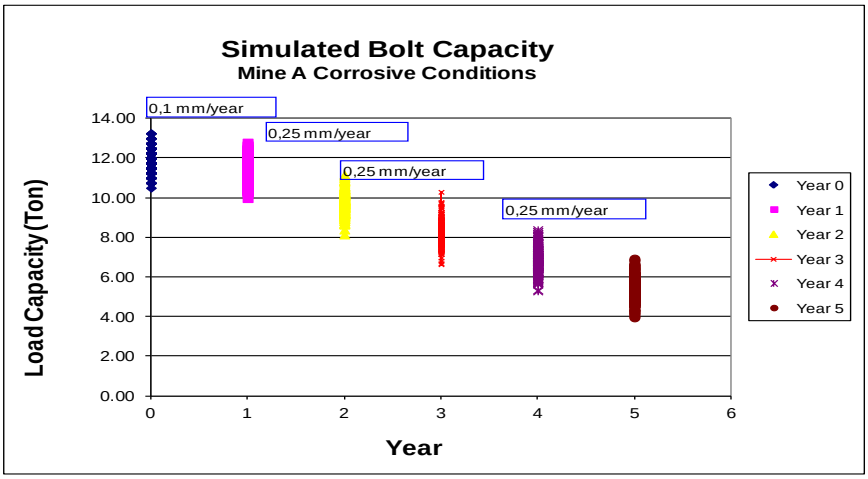

c) Based on a corrosion rate of 0.25 mm/year

Figure 5 - Simulated bolt capacities for various corrosion conditions. a) low to moderate corrosion conditions, b) very aggressive corrosion conditions and c) for a mine in fairly aggressive corrosion conditions

- Figure 6 presents a modeled case where the pH of the ground was around 2.25, generating a corrosion rate of approximately 1 mm/year; this is consistent with observations made in mines with high concentration of sulfur and low pH, where failures of sections of unprotected friction support system were observed within 6 months of operation.

7. CONCLUSION

The ability to reproduce the range of corrosion of a bolts population based on laboratory evaluation leads to a better assessment of the useful life of ground support. Moreover, it also provides a better safety factor calculation, as it takes into account the range of remnant capacity of the bolting system.

It is important, while doing the pull testing process, to select a wide array of rock bolts. Selecting only the worse looking bolts will not give an adequate idea of the capacity of the support system, as it is obvious from the database that a wide variation of load capacity can be present. Defining that range is more realistic than detecting a few extreme samples only.

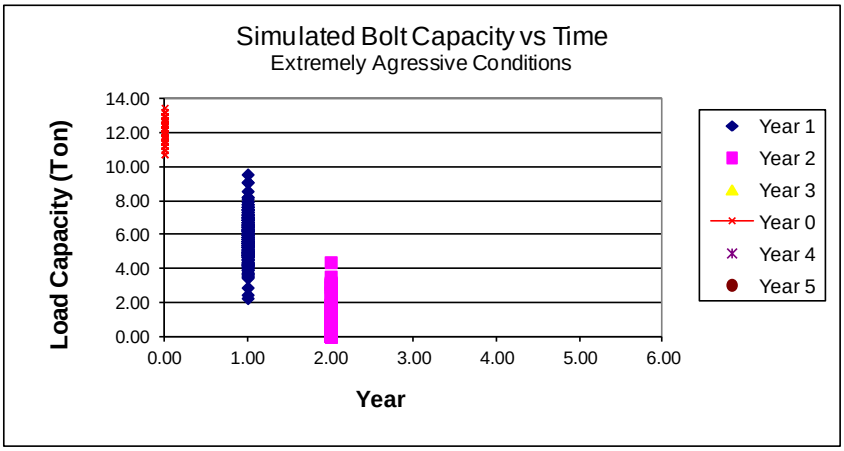

Figure 6 - Simulated bolt capacity for a mining environment of broken ground conditions, pH around 2.25 and resulting average corrosion rate of 1 mm/year

8. REFERENCES

CHARETTE, F., GERMAIN, P. and HADJIGEORGIOU, J., 2004. Corrosion Behaviour of Swellex Bolts In Underground Mining Environments, CIM Annual Meeting, Canadian Institution of Mining, Metallurgy and Petroleum, Edmonton, 2004.

Georock, 2000. Corrosion Analysis of Swellex Bolts. Reports submitted to Atlas Copco.

HADJIGEORGIOU J., GHALI, E., CHARETTE, F. and KRISHNADEV, M.R., 2002. Fracture Analysis of Friction Rock Bolts. North American Rock Mechanics Symposium. Toronto.

LI, C. and LINDBLAD, K., 1999. Corrosivity classification for the underground environment. Rock Support and Reinforcement in Mining. Eds. Villaescusa et al. Balkema, pp. 69-75.
ROBINSON, J. and TYLER,D.B., 1999. A study of corrosion in underground reinforcement at Mount Isa Mines, Australia. Rock Support and Reinforcement Practice in Mining, Eds Villaescusa et al. Balkema, pp. 77-82.

RAMSINGH R.R., REVIE, R.W., CLARKE, R., JACKMAN, J., LORTIE,L., MACLEOD, A., RAJAN S. and ZHENG, W., 1998. Mine Corrosivity Assessment – Final Report. Materials Technology Laboratory, CANMET.

RANASOORIYA, J., RICHARDSON, G.W. and YAP, L.C., 1995. Corrosion Behaviour of Friction Rock Stabilisers used in Underground Mines in Western Australia. Underground Operators' Conference. Kalgoorlie.

SPEARING, A.J.S., MONDAL, K., BYLAPUDI, G. and HIRSCHI, G. 2010. The corrosion of rock bolts and a method to quantify the corrosion potential in mines, CIM Journal, Vol 1, No 3, pp. 213-220.

TILMAN, M.M., JOLLY III, A.F. and NEUMEIER, L.A. Corrosion of Friction Rock Stabilizers in Selected Uranium and Copper Mine Waters. BuMines RI 8904, 1984, 23 pp.

TILMAN, M. M., JOLLY III, A.F. and NEUMEIER, L.A. Corrosion of Roof Bolt Steels in Missouri Lead and Iron Mine Waters. BuMines IC 9055, 1985, 9 pp.

UHLIG, H.H. and REVIE, R.W. 2000. Uhlig’s Corrosion Handbook, Wiley, New York.

Time – A Key Seismic Source Parameter

Marty Hudyma
Laurentian University
Donna L. Beneteau
University of Saskatchewan

ABSTRACT: There are five independent seismic source parameters: seismic energy, seismic moment, source size, location, and time. These parameters are investigated primarily for evaluating seismic hazard and understanding seismic source mechanism(s). Broadly, seismic hazard is the likelihood of occurrence of an event of a given magnitude. Seismic source mechanism is the mode of rockmass failure that causes the seismic event. Most mine seismicity analysis techniques use a combination of a few of the independent source parameters. In literature, time is perhaps the least discussed and most underutilized of these five parameters. This paper discusses three applications of time to understand both seismic hazard and seismic source mechanism in mines. The first application is time history analyses, which focuses on how other parameters of interest vary over time. Examples are presented to show how time history analyses can give information about both seismic hazard and seismic source mechanism. The second application is analysis of time-between-events. This technique can give insight into seismic source mechanism. The final application is phasor analysis using the Schuster test. This method can be used to investigate how seismic source mechanisms may change over time. For both time-between-events analysis and phasor analysis, there are important implications with regards to scale dependence and the breakdown of self-similarity of mining-induced seismicity.

1. INTRODUCTION

1.1 Objectives in Seismic Monitoring

In the broadest sense, there are two fundamental objectives in seismic monitoring in mines: estimating seismic hazard and evaluating seismic source mechanism. Seismic hazard is the likelihood of occurrence of seismic events that may pose a risk to a mining operation. Common risks include: safety consequences to mining personnel, loss of mine equipment or infrastructure, loss of mine production and loss of ore reserves. The greater the likelihood of the occurrence of a large event, the greater the seismic hazard.

Seismic source mechanism is the mode of rockmass failure that caused the seismic event. Seismic source mechanism is important as it is strongly related to the timing of seismic energy release. Understanding the timing of seismic energy release is valuable in helping to mitigate seismic risk. Common seismic source mechanism in mines include: fault-slip on geological features, pillar crushing, buckling, and strain-bursting (Ortlepp, 1997). Knowledge about seismic source mechanism leads to an appreciation of the stress conditions, the geological influences, and the mining influences on a rockmass failure process.

1.2 Monitoring Rockmass Failure Processes

As mine extraction progresses in an orebody, the induced stresses can cause failure within affected regions of the rockmass. This failure is rarely a single catastrophic incident, but rather a gradual failure process causing numerous events as it evolves over time. Commensurately, the mining-induced seismicity also provides information about how the rockmass conditions are changing. Each seismic event is a moment in time of this failure process, with each event giving information related to the

induced stress conditions and the amount of co-seismic deformation. By monitoring a failure process over time with seismic data, we have insight into valuable information such as: the rate of rockmass failure, how failure is related to mining activities, and the scale of the rockmass failure. Time is a key parameter in understanding rockmass failure processes.

1.3 Time Characteristics of Rockmass Failure Modes

Events induced by mine blasting tend to occur in a short time period following the mine blast. A study found that up to 50% of these events occur within the first hour after the blast, and most of the events occur within 6 hours of the blast (Hudyma, 2009). These events are generally caused by inelastic rockmass deformation due to the change in excavation geometry, and often have a failure mechanism associated with volumetric rockmass fracturing. In contrast, events associated with shear along pre-existing geological features occur more randomly in time, and are often poorly associated with mine blasting. Two populations of seismic events from different locations around the same orebody are shown in Figure 1. The population of events on the left (a) is located in the abutment of a stope. Time of day (or diurnal) analysis shows that the majority of events occur shortly after the mine blast at 05:00 and 17:00. The population of events on the right (b) occurs on a mine fault. Diurnal analysis shows that there is minimal influence of the 05:00 and 07:00 mine blast times on the timing of seismic events.

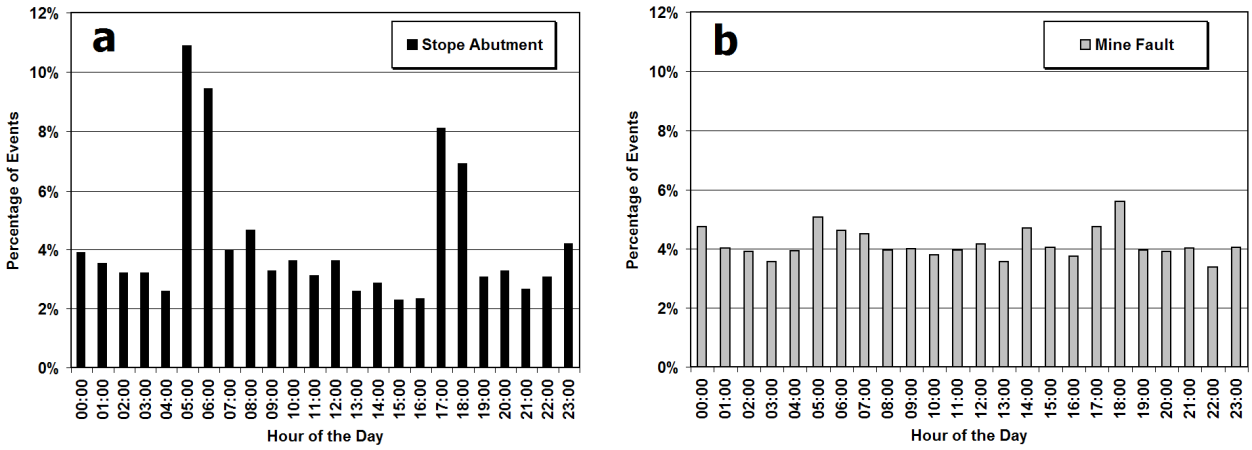

Figure 1 - Events occurring due to stress change from a mine blast tend to occur shortly after the blast (a), while events which caused by shear of geological features are largely unrelated to blast times (b)

For the remainder of this paper, three different techniques that rely on event time will be presented: Time History Analysis, Time-Between Events, and Phasor Analysis. Each of these techniques gives insight into seismic hazard and/or seismic source mechanism.

2. TIME HISTORY ANALYSIS

Time histories are used to investigate how parameters of interest vary over time. In a mining context, time is often strongly related to or controlled by the rate of mine extraction. Consequently, time history analysis often gives insight into the relation between mining activities and the parameters of interest. An example of a time history analysis, is a Magnitude Time History.

A Magnitude-Time History (MTH) analysis was proposed as a means to investigate temporal variations in the occurrence of seismic events (Hudyma, 2009). In a MTH chart, each event is plotted

chronologically, with date on the x-axis and event magnitude on the y-axis (Figure 2). The cumulative number of events is shown with a line on the secondary y-axis. The slope of the cumulative number of events line is the seismic event rate. Changes in the slope represent changes in event rate, with step-wise changes in the cumulative number of events representing short-term increases in event rate, typical of the seismic response to mine blasting.

MTH analysis describes a rockmass failure process as it occurs over time. Changes in the rate of the failure process can be identified from the event rate and through increases in the maximum event magnitude recorded. The influence of external factors such as mine blasting can be identified through seismic event rates. Relations between mine blasting and event rate can be identified. Correlations, or the lack of correlations, between mine blasting and the occurrence of large events can be investigated. MTH analysis is a useful means of presenting and analyzing mine seismicity data to develop an understanding of the rockmass response to mining, giving indications of both seismic hazard and seismic source mechanism.

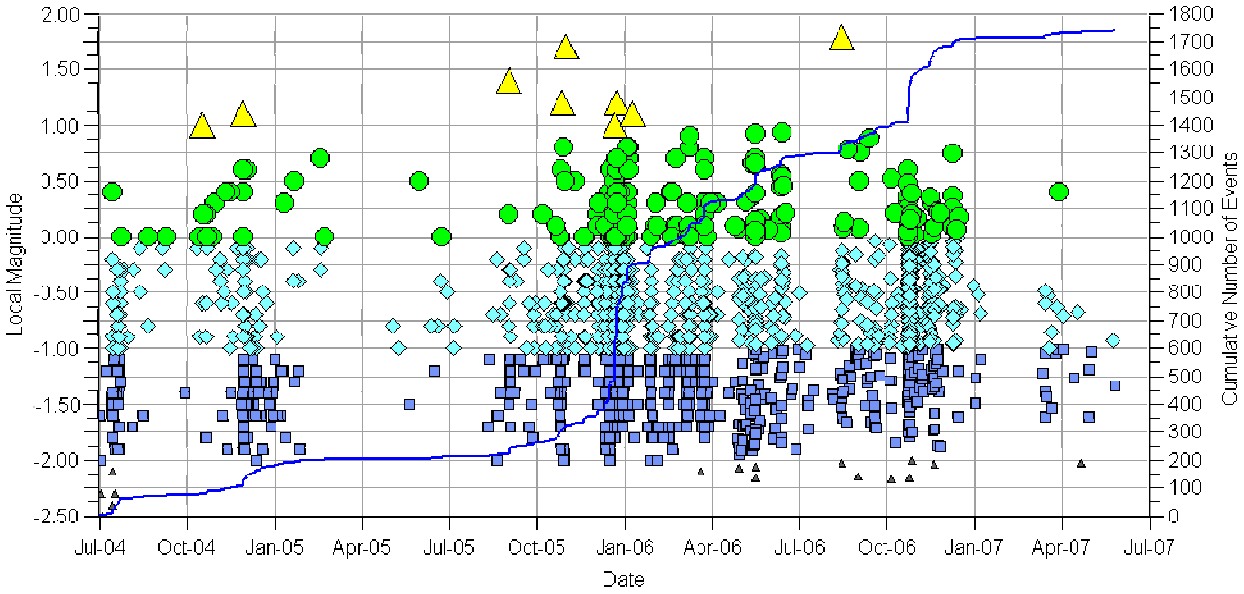

Figure 2 - A magnitude time history for a population of events. The varying symbols represent different magnitude ranges

In the example in Figure 2, a number of characteristics of the seismic event population can be determined. There are several large events over magnitude 1, suggesting that range of the largest expected event is likely toward magnitude 2. This is an indicator of seismic hazard, or the largely event likely to occur. The magnitude of the largest event in the population is progressively getting larger (magnitude 1 in Oct-04, magnitude 1.4 in Aug-05, and magnitude 1.75 in Aug-06). This would suggest that the failure process may be expanding or getting more severe over time. There are clear steps in the cumulative number of events line (Jul-04, Dec-04, Dec-05, Jan-06, Mar-06, and Oct-06). These represent the highest event rates, likely due to blasting. For the most part, the largest events also happen in the periods of highest event rates, so the large events are likely a direct response to mine blasting. Both of these observations suggest the seismic source mechanism of the events is driven by stress fracturing related to mine blasting. Structural sources of events tend to have more constant event rates with some larger events happening unrelated to mine blasting. There are extended periods with very few events, presumably periods with no mine blasting (Jan-05 to Sep-05, and Dec-06 to Jun-07). There is a particular lack of larger events in these “quiet periods”, supporting the earlier observation that larger events occur associated with periods of mine blasting. Both of these observations are in contrast to the constant seismic rate associated with

failure on geological features. The MTH chart in Figure 2 gives some valuable insight into both seismic hazard and seismic source mechanism.

3. TIME BETWEEN EVENTS

Seismicity directly induced by mine blasting occurs predominantly after the mine blast, as is shown in Figure 2. Seismicity related to failure of geological features tends to occur at a more even rate. The time-between-events is distinct for these two seismic source mechanisms. Beneteau and Hudyma (2011) introduce an empirical evaluation of the time between consecutive events in a seismic record.

The analysis of time-between-events (TBE) is a two-chart process. The data is first graphed in a chart of Time-Between-Events (TBE) versus Event Magnitude as in Figure 3. To prepare this chart, the following steps were taken for ten different magnitude ranges of events (greater than magnitude -1.7, -1.5, etc.):

I. Calculate the time in hours between each consecutive event
II. Calculate the cumulative number of events less than a series of TBE's in hours
III. Convert the cumulative number of events to a percentage of events by dividing each cumulative number of events by the total number of events in each particular dataset.

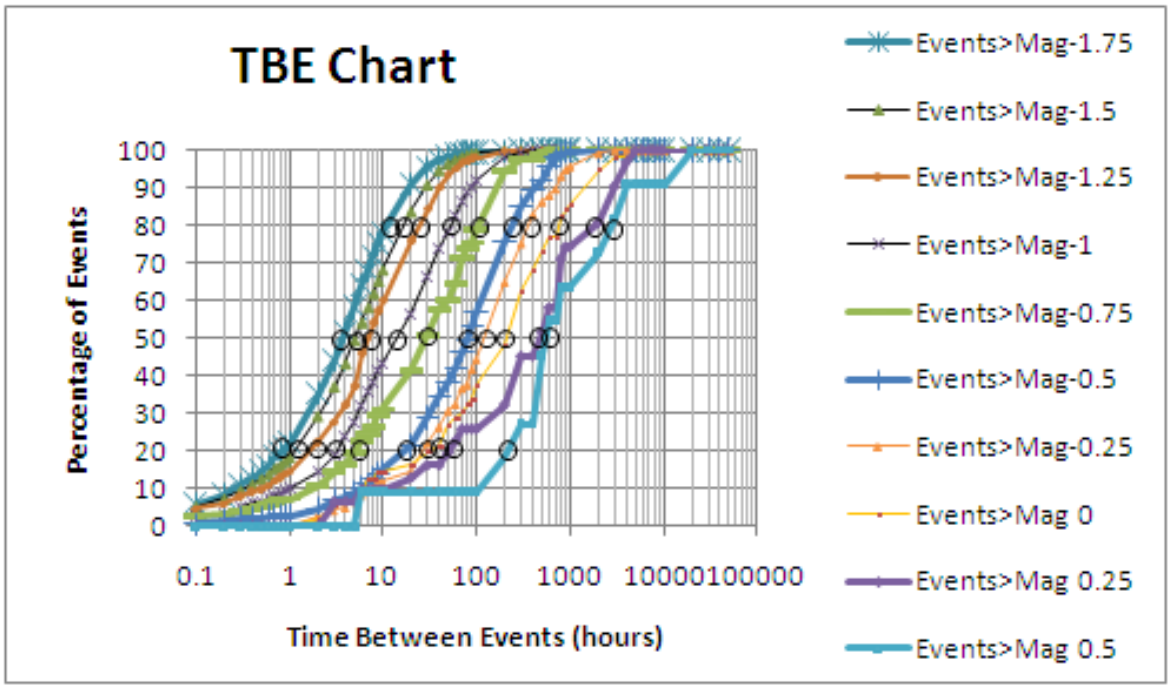

Figure 3 - TBE Chart with the circled points that are required for preparing Figure 4

The TBE chart is then used to create a TBE-rate chart, as follows:

i. Record the TBE by magnitude for the 20th, 50th and 80th percentiles of events in the TBE chart. These points are circled for the population of events on a mine fault (from the example in Figure 1b) in Figure 4.
ii. Plot a TBE-rate chart as a log-log plot of TBE (hours) versus Event Magnitude.
iii. Calculate the slope of the TBE20, TBE50 and TBE80 lines. The slope, named the TBE-rate, is the multiplier that indicates the rate-of-time increase rate for one order-of-magnitude. In the example of the mine fault, there is one TBE-rate of 13.

If one considers that there are 4,548 events in 3.25 years (1199 days), the average TBE for the entire population is 6 hours. In Figure 4, the median TBE varies from 4 hours (when all events greater than magnitude -1.75 are included in the calculation) to approximately 600 hours (for events greater than magnitude 0.5). This shows that a one number representation of TBE for a population, such as by the 6 hour average, does not describe the complexity of the timing of mining-induced seismic events. TBE-rates on the other hand, encompass all of the timing data for the dataset.

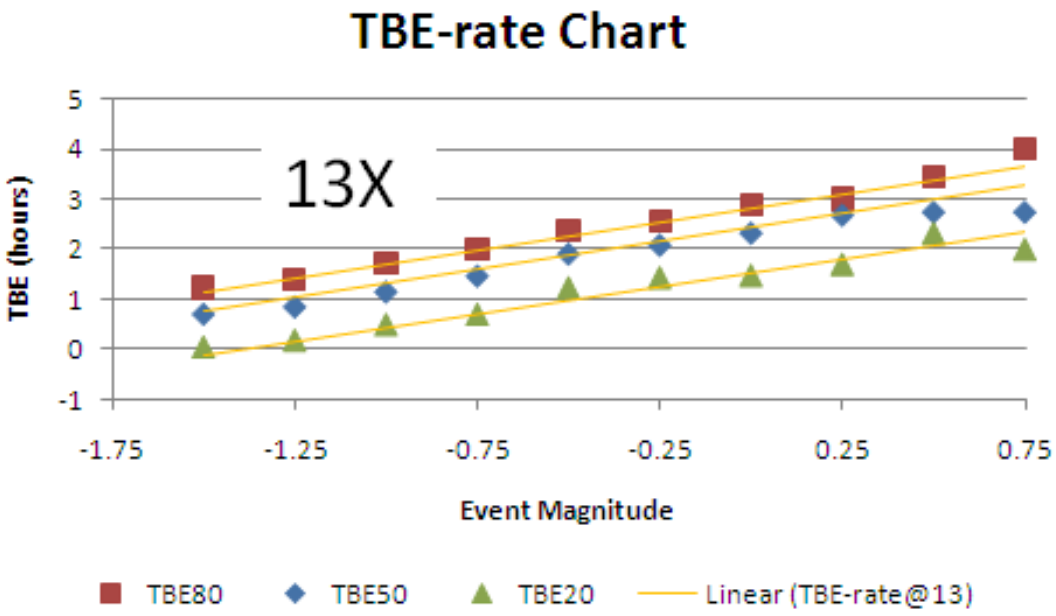

Figure 4 - TBE-rate of 13 is the change in time for every increment on the magnitude scale

There are 4 distinct patterns that may occur in the TBE-rate chart. Two of the patterns (Patterns 1 and 3) are strongly correlated to seismic source mechanism. A third pattern suggests the seismic source mechanism changes over time (Pattern 2). The final pattern shows if mechanism is scale dependent. That is, there is one seismic source mechanism for smaller seismic events and a different seismic source mechanism for larger events (Pattern 4).

In a detailed analysis of numerous datasets from several different mines, the datasets (whether individual or in groupings by mechanism) had very specific TBE-rates. The TBE-rates can be equated to the resistance of a voluem of rock to a failure process. Low TBE-rates around 3 to 6 suggest that frequent events are occurring as the rock is readjusts to the new induced stress conditions and excavation geometry caused by a blast. TBE-rates around 10 can be related to moderate rates of events that are due to rockmass shearing and fracturing. Finally, high TBE-rates in the range of 15 to 30 can be an indicator of stress fracturing which can be very slow, particularly when considered in terms of failure due to creep which is a progress and gradual process.

4. PHASOR ANALYSIS

Periodicities in the timing of seismic events can be analyzed using the Schuster test (1987). The time of each seismic event is plotted as a unit length phasor in polar coordinates. Phasors for each of the events are combined consecutively in chronological order to create a phasor sum (Rydelek and Sacks, 1989). If the event times are random, the phasor sum will be a random walk. If the events are not random in time, the phasor sum will have a direction trend, or "walkout". Rydelek and Sacks (1989) noted that if a seismic record is random (for a confidence of 95%) the walkout length, R, should not exceed $1.73(N)^{0.5}$.

Phasor analysis can be applied to seismic events to investigate seismic source mechanisms. Figure 5 (left) shows a phasor plot for a population of events in a mine abutment. The events show a strong walkout in the direction of the mine blast times of 06:00/18:00. Figure 5 (right) shows a phasor plot for a population of event on a mine fault. There is no trend to the phasor plot, inferring that the events occur randomly in time.

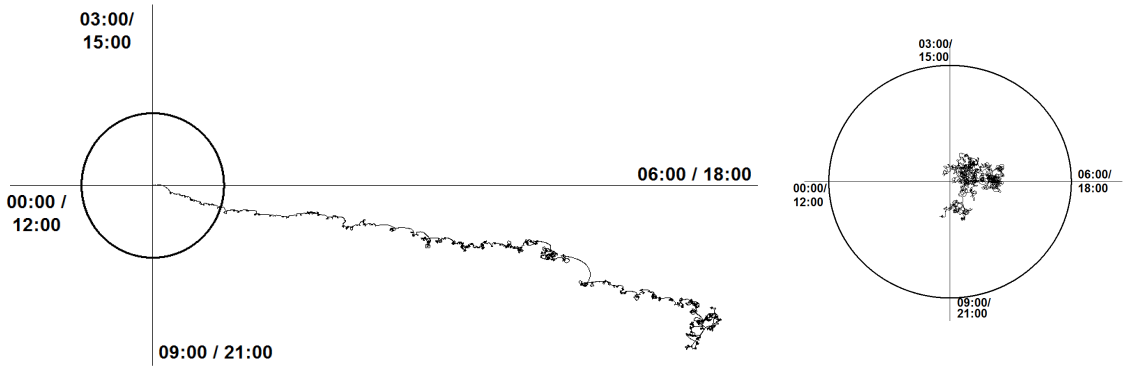

Figure 5 - Phasor plots for stress fracturing events in a mine abutment (left) and near a mine fault (right)

As was briefly mentioned above in the TBE analysis, the trace of the phasor may be scale dependent. Figure 6 shows an example population. The phasor for all of the events has a clear walkout towards the mine blast times of 06:00/18:00. However, if the events of magnitude -1 and larger are investigated, the walkout is not as significant. For events larger than magnitude -0.5 and magnitude 0.0, there is no statistically significant walkout. This example suggests that scale dependence of phasor analysis is a potential test for the presence of multiple seismic source mechanisms within a population of events. This has been identified as one of the prevailing causes for the breakdown of self-similarity in mining-induced seismicity (Gibowicz, 1990)

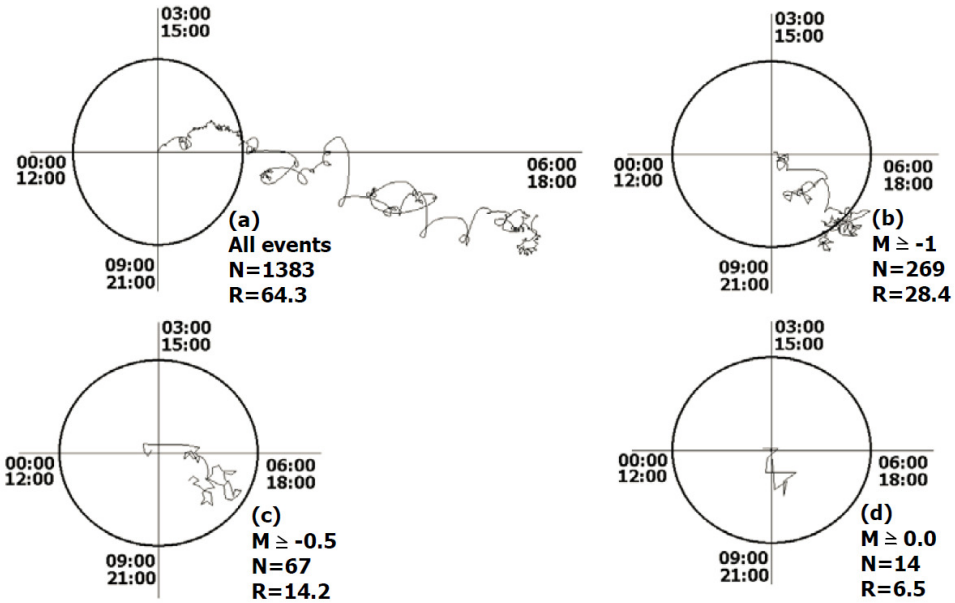

Figure 6 - Phasor plots for a population of 1383 events (top left). If the events are filtered by magnitude, the phasor walkout becomes less pronounced for event larger than magnitude -1 (top right). There is no walkout for events larger than magnitude -0.5 (bottom left) and magnitude 0 (bottom right)

Hudyma (2009) investigated the relation between common seismic sources in mines, seismic source mechanism, and phasor analysis. The results, based on data from a number of Canadian and Australian mines, are summarized in Table 1. Seismic events caused by blasting induced stress change typically have a phasor sum with a strong walkout, whether the events are due to blasting in development headings, or in the abutments of stopes. Seismicity from uncontrolled rockmass caving and events on mine faults usually do not have a distinct phasor walkout. Mining-induced events on stiff dykes and in mine pillars often have scale-dependent walkouts, with the smaller events having a walkout towards blast time, but the larger events occur randomly over time.

Table 1 - Phasor walkouts for common seismic sources in mines (Hudyma, 2009)

Seismic Source	Predominant rockmass failure mechanism	Largest expected event (moment magnitude)	Phasor walkout
Stress change from mine blasting in development headings	Stress driven rockmass fracturing	Less than 0	Yes
Stope abutments	Stress driven rockmass fracturing	0 to +1	Yes
Uncontrolled rockmass caving	Stress driven rockmass fracturing or shear along rockmass discontinuities	Less than 0	No
Mine faults	Shear along the fault	+1 to +4	No
Stiff dykes and intrusions	Stress driven rockmass fracturing or shear along the dyke contacts	+1 to +2	Scale dependent
Mine pillars	Stress driven rockmass fracturing	+1 to +3	Scale dependent

5. SUMMARY

The advantage of using time-based techniques for mining-induced seismic data is that time is independent of all other parameters and also, of the seismic monitoring system that collected the data. The three analysis techniques summarized in this paper give insight into seismic hazard and seismic source mechanism. In some cases, the analyses can be used to identify scale-dependence of seismic source mechanism and to investigate temporal changes in seismic source mechanism

6. ACKNOWLEDGEMENTS

Natural Sciences and Engineering Research Council (NSERC) and the Deep Mining Research Consortium are acknowledged for financial support for this work.

7. REFERENCES

BENETEAU, D.L., and HUDYMA, M.R., 2011. Time-between-seismic events to enhance seismic source interpretation. CIM Maintenance Engineering and Mine Operations Conference, Saskatoon, Saskatchewan.

GIBOWICZ, S.J., 1990. The mechanism of seismic events induced by mining – a review. Proceedings of Rockbursts and Seismicity in Mines, Minneapolis (C. Fairhurst ed.). Rotterdam: Balkema, p. 3.27.

HUDYMA, M.R., 2009. Analysis and interpretation of clusters of seismic events in mines. Unpublished Ph.D. Thesis, University of Western Australia, Perth, Western Australia, 365 p.

ORTLEPP, W.D., 1997. Rock fracture and rockbursts – An illustrative study. Johannesburg: South African Institute of Mining and Metallurgy.

RYDELEK, P.A. and SACKS, I.S., 1989. Testing the completeness of earthquake catalogues and the hypothesis of self-similarity, Nature, Vol. 337, p. 251-253.

SCHUSTER, A., 1897. On lunar and solar periodicities of earthquakes. Proceedings of the Royal Society, 61, p.455-465.

Passive Seismic Tomography for Imaging Horizontal Stress Concentration at the Mine Scale

Erik C. Westman
Mining and Minerals Engineering Department, Virginia Tech
Jeffrey B. Kerr
Mining and Minerals Engineering Department, Virginia Tech
Denis Thibodeau
Vale

ABSTRACT: Knowledge of the orientation and relative magnitude of in-situ stresses at the mine scale is important for safe and efficient production from an underground mine. With this knowledge, stope location and scheduling can be optimized. Passive seismic tomography was used for imaging horizontal stress distribution at the mine scale. Microseismic measurements from the Creighton mine were used as input for the tomography calculations. The double-difference tomography algorithm was used, which provides the most precise results. The results clearly show a low velocity zone in the previously mined areas bounded by two high-velocity lobes located adjacent to the mined openings at locations consistent with those expected due to the horizontal stresses at the mine. The overarching goal of the research is to provide a tool that can augment both numerical modeling results and underground geotechnical measurements to allow the mine operator to produce in the safest and most efficient manner possible.

1. INTRODUCTION

Excavation of underground openings is a difficult job in a challenging environment. The rigor of the process is compounded by the lack of a method that allows quantification of changes within the rock mass as excavation and ore extraction progress. The most important unknowns around underground excavations from an engineering perspective are the highly-stressed areas, which can result in dynamic failure, and the extent of damage. The highly-stressed areas are identified with seismic tomography as high velocity regions because the increased stress results in microfractures within the rock being closed, effectively increasing the elastic modulus of the rock resulting in elastic waves traversing the rock with greater velocity and less attenuation. Conversely, damaged areas are displayed as low velocity zones. Knowledge of the location and extent of both areas is critically important so that safety and efficiency of the operation can be maximized.

The current practice for engineers tasked with monitoring and assessing the stability of underground openings is to use field observations evolution with time, to calibrate the observation to output from numerical models and seismic events database. Field observations may not be sufficient to detect problem areas before damage becomes too important. Numerical modeling is a useful tool for understanding rock mass behavior, however results are frequently based on assumed and generalized physical properties within the rock mass. Seismic data may only give a partial picture of change in the rock mass. Geophysical measurements, as proposed for this project, complement the field observation, seismic database and numerical modeling effort. This paper presents results from a deep metal mine where a low-velocity, de-stressed previously mined zone is contrasted with high-velocity, highly-stressed lobes in the host rock at locations consistent with those expected due to the horizontal stresses at the mine.

2. BACKGROUND

Central to this research is the change that a rock mass undergoes as it is loaded. Figure 1 shows a typical stress-strain curve from an unconfined compression test with three regions marked. During initial loading (region I) many microfractures within the sample are closed, resulting in a rapid increase in the velocity with which an elastic wave travels through a rock sample. As the sample is loaded elastically (region II) the wave velocity continues to rise, but not as rapidly. As macrofractures nucleate and grow (region III) the velocity at which the wave travels is reduced. Because of this relationship, zones of highly-stressed rock or damaged areas can be inferred from seismic velocity changes.

A clear understanding of concepts and terminology is requisite prior to describing the research plan. As the rock mass is perturbed by the excavation process, stress redistribution results in failure along new and/or previously-existing faults or joints. The seismic energy produced by these relatively small failures is termed "induced seismicity" and typically has a local magnitude (M_L) between -3 and 2 (Hazzard and Young, 2004). These events can be recorded by a microseismic monitoring system and analyzed. This method is referred to as "passive seismic." "Tomography" is the method whereby energy that has been transmitted through a body is analyzed to produce an image representing the interior of the body (Radon, 1917). This is frequently conducted in the medical industry where a CT (Computed Tomography)-scan is used diagnostically (Hounsfeld, 1973; Cormack, 1973).

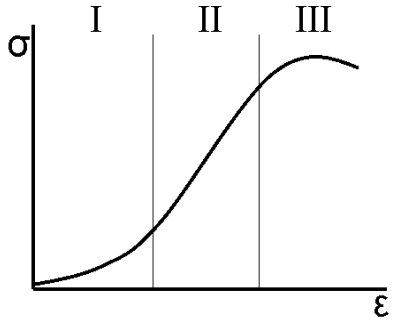

Figure 1 - Typical stress-strain curve for unconfined rock sample with three regions in which elastic wave propagation velocity changes due to stress-induced changes to the rock. Velocity increase is greatest in region I, is less in region II, and decreases in region III

There have been numerous algorithms proposed for conducting the tomographic inversion, but none adopted as the single best method. The algebraic reconstruction technique and the simultaneous iterative technique (SIRT) need fewer raypaths and are more tolerant of poor data quality however filtered back projection is more computationally efficient.

Tomography can be conducted using either wave velocity or the combination of velocity and attenuation. The simplest method is arrival time, or velocity, tomography. With this form of tomography, a sample is discretized into cells (pixels or voxels), and the measured time of a wave traveling through each cell along a specific raypath is compared to the time required if an initial model velocity is assumed. The modeled velocity for each cell is then adjusted to reduce the difference (error) between the modeled arrival time and the measured arrival time. The modeled raypaths can be allowed to curve, if the velocity contrast justifies refraction. For this project, p-wave velocities were used.

Double-difference tomography is specific to passive seismic tomography. When monitoring seismicity there is uncertainty associated with the precise location of the event. Because the precise location of the sources is unknown with passive tomography, an initial velocity distribution is assumed and the source locations are triangulated as with earthquake source location. The velocity model and source locations

are then adjusted to obtain the smallest error. Double-difference tomography identifies the source locations by not only considering the absolute arrival times but also comparing the relative arrival times of events located in close proximity, resulting in more accurate source locations and, thus, more accurate images.

There are a few concerns and questions about the application of passive tomography to monitoring underground mines. Because only mining-induced seismicity is used for the analysis, there is little control over the volumes covered by ray paths, and hence the volumes that have results.

3. SETTING

Creighton Mine is situated on the southern edge of the Sudbury Igneous Complex, just outside of Sudbury, Ontario, Canada (Wiles and MacDonald, 1988). There are three major rock masses located within Creighton Mine including granite, norite, and the ore. The granite is the footwall of Creighton Mine, with the Norite being the hanging wall and the host of the sulphide orebodies; the footwall also consists of gabbro intrusions (Malek et al., 2009). Norite is a mafic igneous rock that is difficult to differentiate between gabbro in the footwall. Norite is consistently located near platinum and other precious metal orebodies. The orebody consists of both copper and nickel, individually representing 1.5 to 2.0% of the mined products (Snelling, 2009).

Creighton Mine is characterized by extensive faults as well as extremely high gravitational, regional, and local domain stresses. There are four major fault groupings: the footwall shear system, east-west striking system, south-west striking of the 118 shear system, and minor faults on the boundaries of the 118 shear system (Snelling, 2009). The term ‘118’ refers to the orebody that the faulting is predominantly noted; Creighton Mine consists of five active ore bodies currently (Trifu and Sourineni, 2009). Past studies have produced empirical relationships between the depth and stress tensors at Creighton Mine. Using empirical relations, stress values around the 7,800 level, current mining depth, are 110 to 128 MPa for the major stress, 87 MPa for the intermediate stress, and 70 MPa for the minor (Malek et al., 2009; Trifu and Sourineni, 2009). The major and intermediate principal stresses are horizontal, with the minor principal stress being the vertical stress (Snelling, 2009). Stress measurements previously conducted at Creighton Mine confirm the empirical relations for stress measurements.

4. SEISMIC MONITORING

High stress concentrations in addition to numerous fault zones lends to Creighton Mine’s high frequency of seismicity. In place microseismic monitoring systems typically record approximately 70 events per day at Creighton Mine (Snelling, 2009), with the most events following blasting operations. The majority of the approximate 26,000 events per year are below a 2.0 moment magnitude, but there are between 30 to 40 events per year that are above a 2.0 on the local moment magnitude scale (Trifu and Sourineni, 2009).

Events are classified into two categories: blast related and stress related events. While most events are mining induced to an extent, meaning the events would not occur without the mining operation, blast related events are described as events that can be correlated directly to blasting. Stress related events are described as events that are caused through stress relief from the rock mass.

Blast related events occur in or around crown and sill pillars, in single development headings, and sill accesses following blasting. Blast related events are predominantly in the form of rock bursts, while stress related events are in the form of fault slips and strain bursts (Trifu and Sourineni, 2009). Approximately 80% of the seismic events recorded at Creighton Mine are considered to be fault slip events (Snelling, 2009).

Blast related events can be easily determined and planned for, but the random nature of stress related events necessitated the need for a microseismic monitoring program. The original instrumentation for Creighton Mine's microseismic system was installed in 1980 and has subsequently been upgraded numerous times (Malek et al., 2009). Currently, Creighton Mine operates a 16-bit Hyperion system from Engineering Seismology Group (ESG) for the microseismic monitoring, consisting of a 104 channel capacity. The array consists of both uniaxial and triaxial accelerometers with sensitivities of 30 volts per unit gravity and 0.5 volts per unit gravity, respectively. The accelerometers used at Creighton Mine have wide frequency ranges also, with uniaxial units having a 50 to 5,000 Hz range, and triaxial units having 3 to 8,000 Hz. The Hyperion microseismic system detects estimated magnitude events of -2.0 to 1.0 on the local magnitude scale (Trifu and Sourineni, 2009).

For local magnitudes greater than 1.0, Creighton Mine employs the use of a 24-bit Paladin system, also from ESG. The Paladin system consists of four triaxial geophones placed underground. The geophones used operate at a frequency of 4.5 Hz (Trifu and Sourineni, 2009).

The Hyperion and Paladin systems work in unison to record event locations, times, magnitudes, energy releases, and dynamic properties of the events. Full waveforms are recorded by the systems. Both the Hyperion and Paladin seismic arrays are located entirely underground. The receivers are arranged to cover the entirety of the active mine works from 3,500 feet deep to the current level of 7,800 feet deep (Malek et al., 2009; Trifu and Sourineni, 2009).

For this study, the Creighton Mine supplied two months of seismic data. The data covered a time period between January 14, 2009 and March 16, 2009. During the two months 9,270 events were recorded, with a median of 91 events per day. During the two months of data, only 36 events were recorded with a moment magnitude greater than zero. The highest moment magnitude recorded during the time period was 0.7. Of the 36 events above zero, all but two events occurred between a depth of 7,300 and 7,600 feet. A histogram of the number of events within different magnitude ranges is shown as Figure 2.

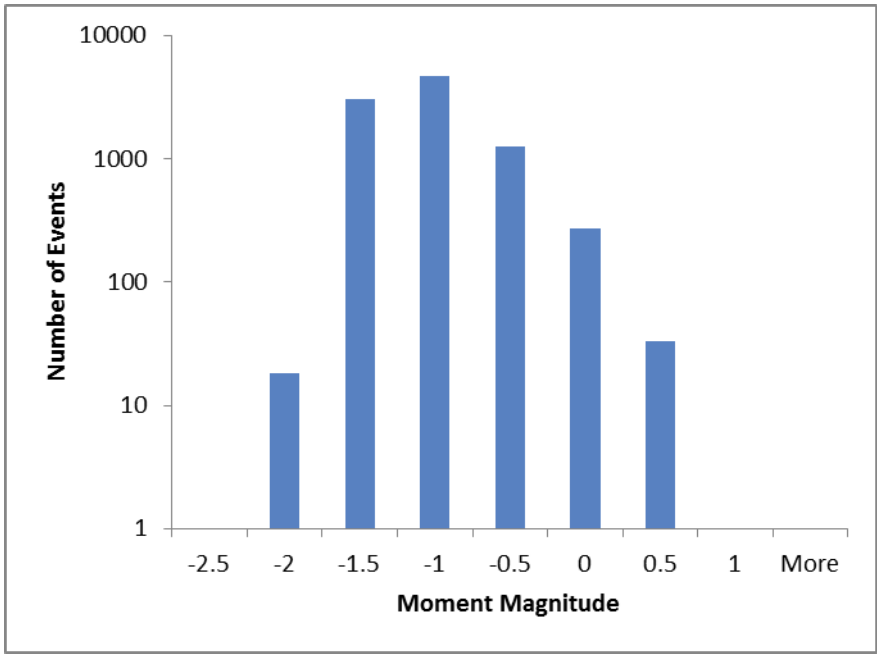

Figure 2 - Histogram of the distribution of events and moment magnitudes used in the analysis

While most events of higher magnitude are confined to a 300 foot depth region, the majority of all of the events, close to 80%, are located in a 1,000 foot region between 7,000 and 8,000 feet. This distribution for the events is to be expected as all mining operations during the two month time period took place below 7,000 feet. From a horizontal prospective rather than vertical, most events took place in the footwall of Creighton Mine. Again, events in the footwall are to be expected as the material is brittle granite. Figure 3 shows views from the side and end of the mine layout, including haulage entries, event locations, and geophone locations.

5. DATA ANALYSIS

Several steps are involved in processing the data from the recorded arrival times through the generation of the tomograms. The arrival times for each event were converted to travel times by fitting with linear regression and removing the intercept so that at zero time there would be zero distance traveled. The background velocity was calculated utilizing all travel time and station receiver combinations recorded for the 9,270 events. For the two months of data received, the background velocity was determined to be approximately 6.25 kilometers per second. Figure 4 shows the time vs. distance plot used to determine the background velocity for the data set from Creighton Mine. Figure 4 only shows times up to 0.1 seconds and distances up to 500 meters to demonstrate the linearity, and amount of the travel time and distance pairs used to determine the background velocity. The low velocity threshold for the data set was selected to be 1.75 kilometers per second. Many of the low velocity (high travel time) arrivals are due to the first arrival refracting around the mine excavations. This results in a low-velocity zone on the tomogram in the location of the mine opening.

For the mine scale imaging of Creighton Mine, a 36 by 36 by 36 node grid, with nodes on 20 m spacings was used. The grid was set to model the area of 1,065 to 1,760 m (3,510 to 5,810 ft.) in easting, 1,560 to 2,255 m (5,150 to 7,445 ft.) in northing, and 1,790 to 2,485 m (5,900 to 8,200 ft.) in depth. This grid covered the active mining sections of the Creighton Mine at the time of the study.

One measureable output from TomoDD is the Derivative Weight Sum, or DWS. The DWS is a statistical parameter that assesses the density of rays that passes near a grid point. In order to ensure that only areas well-traversed by ray paths were used in the final tomogram, any DWS value below 1.0 was excluded from the tomogram. A value of 1.0 was chosen as the cutoff in order to eliminate any zero point, while leaving sufficient data points to cover the entirety of mine image.

Results were visualized using volumetric imaging software. To interpolate between nodes, the Inverse Distance method to the first power was utilized with a search radius of 30 m.

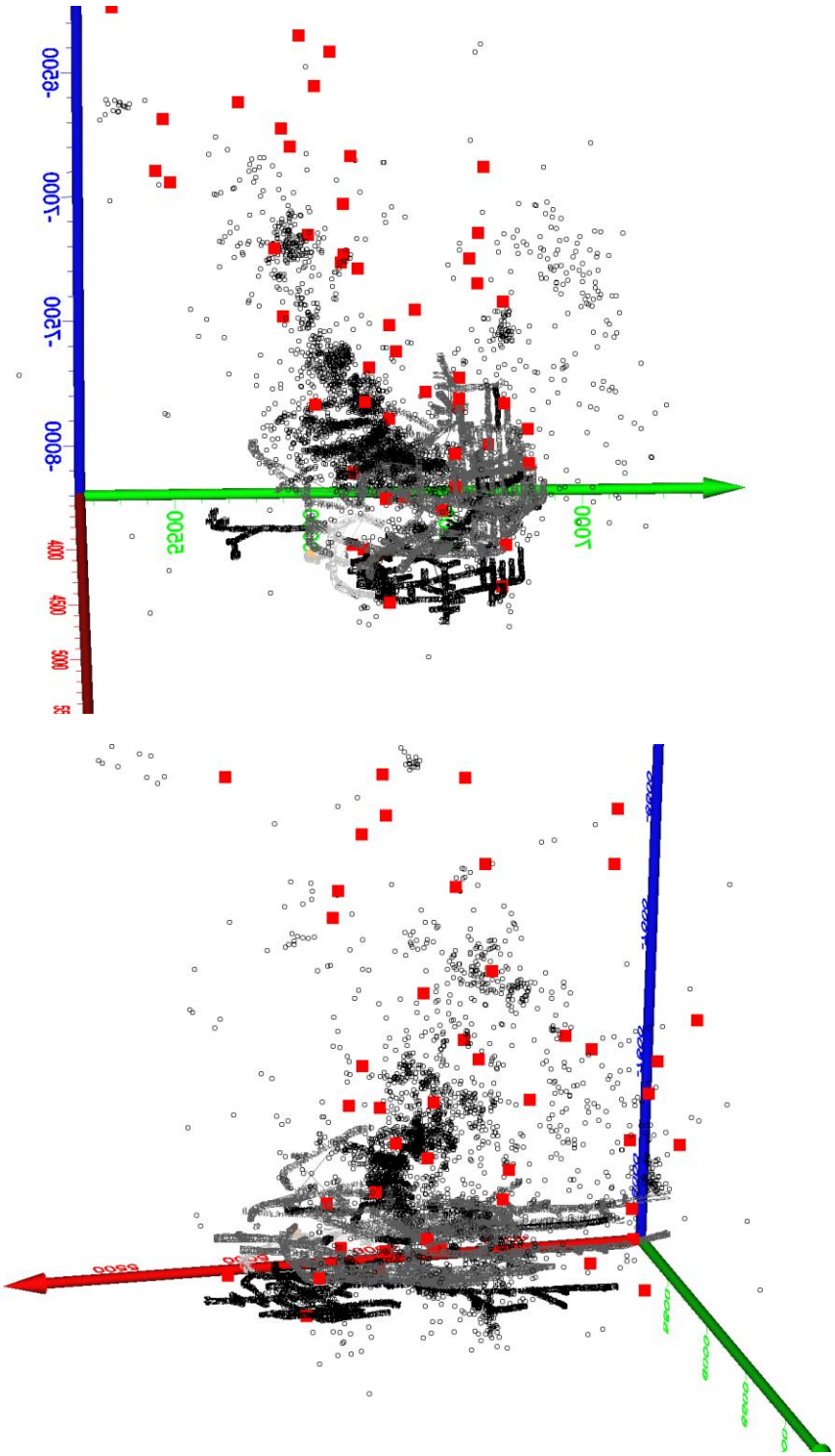

Figure 3 - End view (top) and side view (bottom) of mine. Cross-hatched entries are haulage drifts, red filled squares are geophone locations, and open circles show seismic event locations

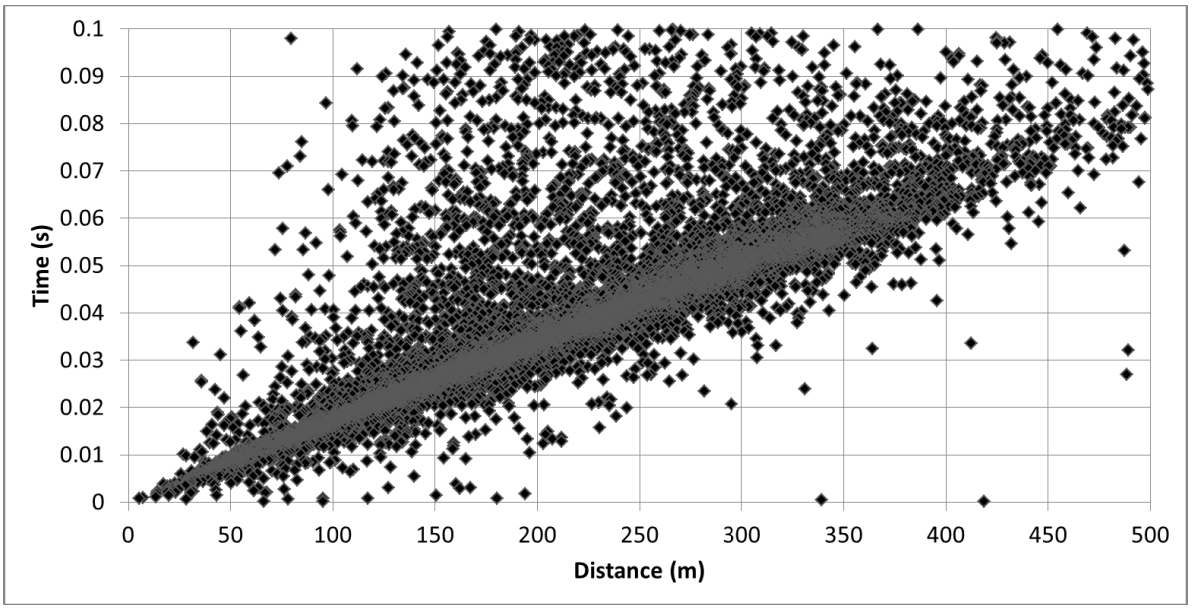

Figure 4 - Scatter plot of travel time versus distance for each raypath. Seismic wave velocity average velocity of approximately 6,250 m/s is shown by the vast majority of the points

6. RESULTS AND DISCUSSION

The mine scale study provided tomograms for the majority of Creighton Mine. A zone of interest is shown from approximately 6,500 feet to 7,800 feet of depth. This zone of interest includes a massive low velocity bulb with high velocity lobes on southeastern and northwestern sides of the low velocity bulb. The low velocity bulb with high velocity lobes is shown by isosurfaces, presented in Figure 5. The low velocity bulb is represented by the blue isosurfaces with the high velocity bulb is represented by the red isosurfaces. As shown in Figure 4, the background velocity is approximately 6,250 m/sec. In this discussion the term 'high velocity' is applied to those areas with a velocity greater than 6,350 m/sec and 'low velocity' refers to a velocity less than 5,900 m/sec.

It is to be expected that the previously mined material would have a low velocity, as only weak, unconsolidated backfill material remains; this is demonstrated by the low velocity bulb. The low velocity bulb shown is located in the same orientation and progression through depth as the orebodies at Creighton Mine. Various smaller low velocity zones shown are consistent with previously mined stopes outside of the main orebody.

The high velocity lobes located to the southeast and northwest of the low velocity zone are also to be expected at Creighton Mine. Previous numerical modeling conducted at Creighton Mine showed that the previously mined, low stress, zone would be surrounded by higher stressed conditions in an increased microseismic zone. In addition, the high velocity lobes correlate well to the direction of the major principal stresses, which was previously recorded as running from west-northwest to east-southeast.

Aside from the low velocity bulb with high velocity lobes, observations from the mine scale imaging indicate that the deepest low velocity zone, located at approximately 7,700 feet of depth corresponds to Stope 5078. Stope 5078 is located within the bounds of the low velocity zone with a high velocity lobe above the stope. The high velocity above the stope is a unique occurrence for Creighton Mine, as most stopes have previous mining above. However, the mining sequence along Drift 7680 was altered due to a split in the orebody, placing Stope 5078 below an un-mined, higher stress zone.

The imaging of expected occurrences, such as the low velocity bulb with high velocity lobes and the isolated low velocity zone of Stope 5078, demonstrates that the mine scale imaging is a useful tool for further analyses, and can be used for calibration of numerical models.

7. SUMMARY AND CONCLUSIONS

Observed results obtained from the tomograms were compared to previous knowledge of mine conditions and expected stress redistribution at the mine site and found to be comparable. In addition, results were compared to widely known standard rock mass stress redistributions with similar results. Overall, the tomogram produced promising results in regards to the applicability of double-difference tomography in a deep metal mine.

In conclusion, data obtained from an in-place microseismic monitoring system can be used in a double-difference tomographic inversion for a deep hard rock mine. An image of the velocity distribution calculated with double-difference correlated well to prior mine knowledge and common rock mass movements. Specifically, a low-velocity, de-stressed previously mined zone is shown along with high-velocity, stressed lobes in the host rock at locations consistent with those expected due to the horizontal stresses at the mine. It should be noted however, that not all results are necessarily due to changes in the rock mass; velocities shown in tomograms may have originated, and changed, due to geologic factors. Overall, results obtained from the studies at Creighton Mine are promising and provide a base evaluation for the applications of double-difference tomography in a deep hard rock mine.

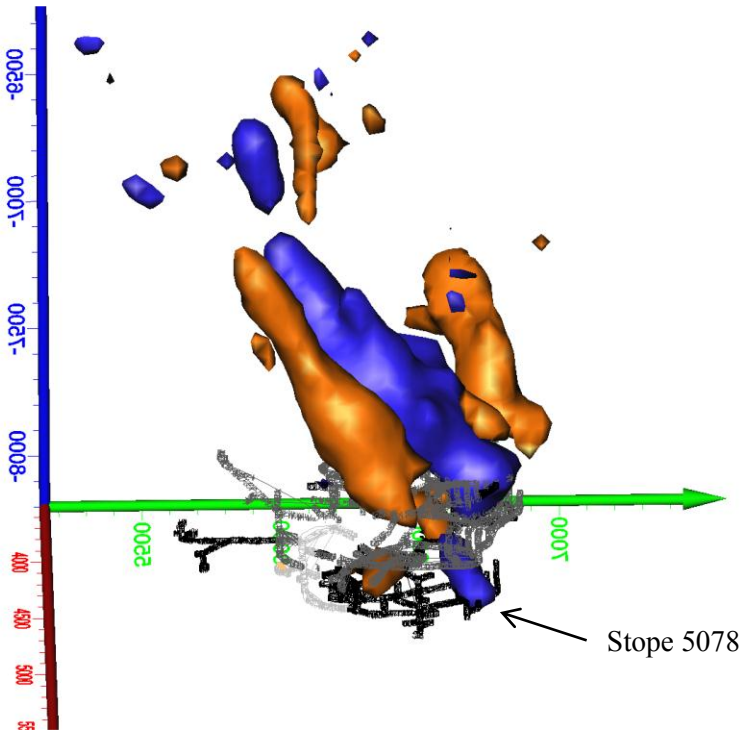

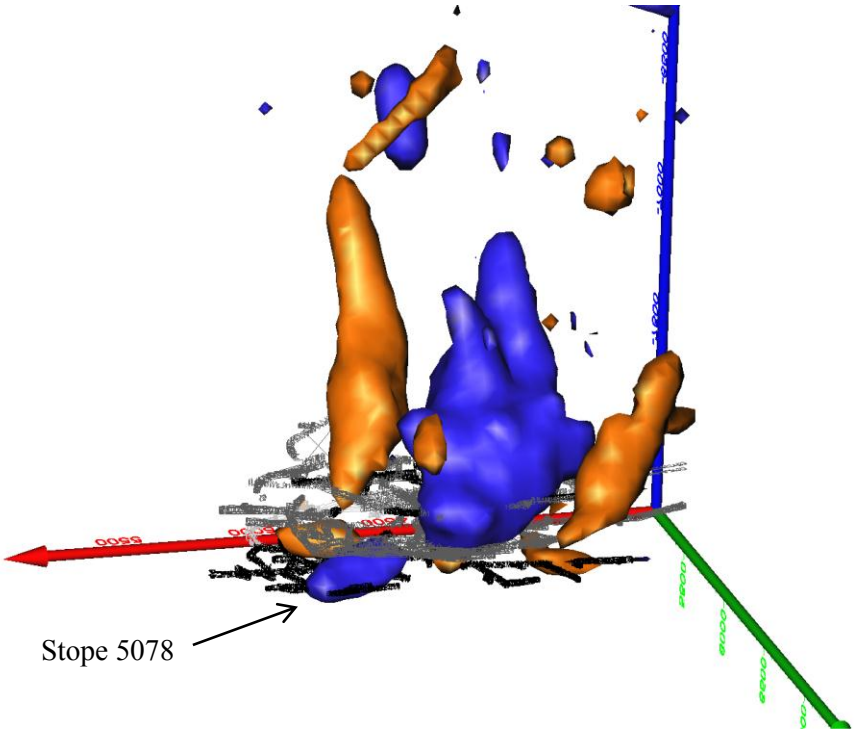

Figure 5 - End view (top) and side view (bottom) of mine showing tomography results. The low velocity, de-stressed region is shown as a blue lobe while the high velocity, highly-stressed lobes are shown in orange

8. ACKNOWLEDGEMENTS

The authors are grateful to Vale for providing the raw data for this study and to Dr. Haijiang Zhang for sharing the passive seismic tomography code. This research was funded by a National Science Foundation EAGER Grant (CMMI-1051111).

9. REFERENCES

CORMACK, A.M., 1973. Reconstruction of densities from their projections, with applications in radiological physics. Physics in Medicine and Biology, Vol. 18, no. 2, pp. 195-207.

HAZZARD, J.F., AND R.P. YOUNG, 2004. Dynamic modeling of induced seismicity, International Journal of Rock Mechanics & Mining Sciences. Vol. 41, 1365-1376.

HOUNSFIELD, G.N., 1973. Computerized transverse axial scanning (tomography). 1. description of system. British Journal of Radiology, Vol. 46, no. 552, pp. 1016-1022.

MALEK, F., F.T. SOURINENI, AND P. VASAK, 2009. Geomechanics strategies for rockburst management at Vale Inco Creighton Mine. 3rd CANUS Rock Mechanics Symposium. Toronto, Ontario, Canada.

RADON, J., 1917. Uber die bestimmung von functionen durch ihre integralwere lange gewisser mannigfaltigkeiten. Ber. Verh. Saechs. Akad. Wiss., Vol. 69, pp. 262-267.

SNELLING, P., 2009. The influences of stress and structure on mining-induced seismicity in Creighton Mine, Sudbury, Canada. Department of Geological Sciences and Geological Engineering. Kingston, Ontario, Canada, Queen's University. Master of Science, 110 pp.

TRIFU, C.I., and F.T. SOURINENI, 2009. Use of microseismic monitoring for rockburst management at Vale Inco mines. in Controlling Seismic Hazard and Sustainable Development of Deep Mines, C. Tang (ed.), Rinton Press, New York, pp. 1105-1114.

WILES, T., and P. MACDONALD, 1988. Correlation of stress analysis results with visual and microseismic monitoring at Creighton Mine. Computers and Geotechnics Vol 5, pp. 105-121.

Practical Considerations for the Use of Microseismic Systems at Mining Operations

Ian S. Leslie
Mining and Geotechnical Services, ESG Solutions

ABSTRACT: Seismic monitoring systems for mining operations are being utilized more than ever before in the characterization of rock mass response to underground and open pit mining. This paper provides a review of the use of microseismic monitoring for rock mechanics applications at mines throughout the world. Some practical considerations for the installation of these systems are presented along with techniques for optimizing seismic array coverage. Case studies and installation examples are also provided. Recent applications of advanced seismic analysis techniques are discussed including the determination of event mechanisms, mapping of maximum peak particle velocity (PPV) and seismic hazard fields, and the use of source parameter data for large event re-entry protocol.

1. INTRODUCTION

Since the early 1980's the use of Microseismic systems by Ground Control and Rock Mechanics specialists in the mining industry has increased worldwide. With the evolution of the monitoring technology, increased use of Ethernet/fiber-optics/radio networks at the mine sites, and the associated increase in computer processing power, the use of full waveform seismic systems has become more standard. Continuous recording systems like ESG's Paladin seismic system have been available since 2003, have also contributed to the advance of the technology. Advanced seismic techniques such as Moment Tensor inversion and the determination of advanced seismic parameters are also being utilized for use in longer-term mine design and modeling. Microseismic Systems have become essential tools for many rock mechanics departments which use them on a daily basis for safety purposes and over a longer time period to gain experience regarding the state of the rock mass at the mine and aid in future mine design.

This paper provides a review of the use of microseismic monitoring for rock mechanics applications at mines throughout the world. Some practical considerations for the installation of these systems are presented along with techniques for optimizing seismic array coverage. Case studies and installation examples are also provided. Recent applications of advanced seismic analysis techniques are discussed including the determination of event mechanisms, mapping of maximum peak particle velocity (PPV) and Seismic Hazard fields and the use of source parameter data for large event re-entry protocol.

2. BRIEF HISTORY OF SEISMIC MONITORING IN CANADA

The first rockburst in Canada was reported in 1928 and seismicity was recognized as a major problem by 1930s (Alexander and Trifu, 2006). By 1940s mines from both Sudbury and Kirkland Lake were emerging as hot spots. By late 1970s fatalities and mine closures were reported as a result of significant increase in mines' seismicity. The Canadian Rockburst Research Program was established in the 1990's to better understand rockburst phenomena and develop plans for monitoring and analyzing seismicity in mines.

The original Seismic Monitoring systems were based on First Arrival concept (e.g. MP250) but with advances in computer technology, triggered full waveform systems began to be developed. In 2003 ESG

has developed the Paladin acquisition system which allows continuous recording to be done so that the entire online record can be stored.

3. OVERVIEW OF HOW THEY WORK

The process of mining can generate lots of rock noise ranging in size from small pops and cracks to large earthquakes. The systems designed to record them are complex but are generally comprised of 5 main components (Figure 1):

1. Seismic Sensors
2. ESG's Paladin digitizing stations
3. Time synchronization equipment/devices (e.g. GPS, fiber timing)
4. Data Acquisition and processing computers
5. Fiber Optic Network

The seismic sensors are either accelerometers or geophones arranged in a network and connected to the Paladin digitizing stations via copper twisted-pair cables. The stations are time synchronized to each other by means of a GPS antenna for surface stations and by a timing pulse over fiber for the underground stations.

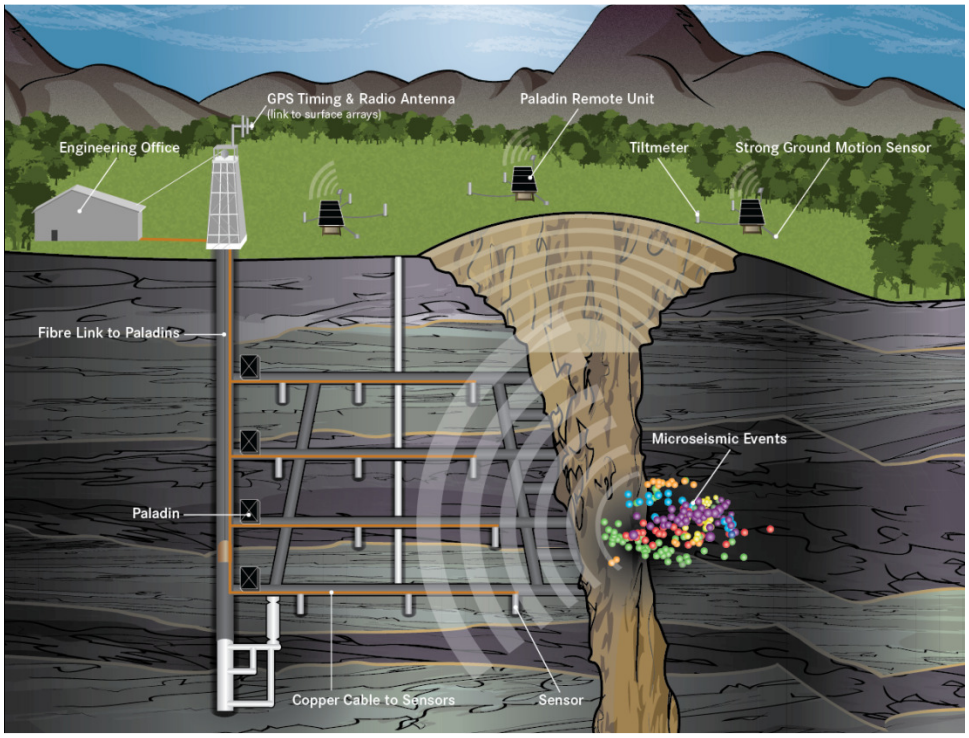

Figure 1 – Example of the typical layout of a seismic monitoring system at a mine site

In general, this is how a seismic monitoring system works:

- An event occurs underground and releases energy in the forms of seismic waves
- Installed sensors pick up the seismic waves
- The sensors send the data to the Paladin digital recorder housed in the junction box (underground or on surface)

- The paladin converts the data into a digital signal which can be analysed on a computer using microseismic software.
- The events are then located, magnitudes and other source parameters calculated and then the data is visualized.

4. REASONS FOR INSTALLATION OF A SEISMIC MONITORING SYSTEM

In many cases, the impetus for installing a system may be the occurrence of a large seismic event, unusual occurrences of ground problems of unknown origin, or an increase in the number of smaller events (or 'rock noise') observed underground. The ideal time to install a system, however, would be in the early stages of mining, prior to the occurrence of any rockburst issues. This would allow the mine to obtain a history of seismicity and gain experience with the system response prior to any problems occurring. Sometime the rush to install a system in order to reassure workers/management following a large event can sometimes lead to unrealistic expectations that the system will 'solve' seismicity issues.

One of the benefits of microseismic monitoring is that it gives us information throughout the rock mass, and in real time. This is a big benefit, especially when compared to conventional instrumentation, which only gives us information at discrete points. Now there are some shortcomings to this approach, as well. First, the processing and interpretation of microseismic data can be more difficult than for traditional instrumentation data. Second, because seismic monitoring is "passive", we only obtain information at the location of events. In other words, we have no control over where we get information from. In the end, this second point turns out not to be that critical, as microseismicity occurs where the stress redistribution is taking place, and this is usually where we want information anyway

Some other reasons for the installation of a seismic monitoring can include:

- Obtaining more accurate information regarding sources of seismicity so that production down-time is reduced (avoids long investigations of air blasts of unknown origin)
- Improving mine safety by making workers aware in real-time of specific regions with seismic issues
- Developing procedures and plans for re-entry following a large blast or seismic event
- Collecting a valuable historical database of seismic response to mining over time to compare with modeling results and for evaluation of mining design and implementation
- Using advanced seismic methods for rockburst events to obtain more information about them; for example, to determine the orientation of potential geological structures that may have been activated during the event
- Indicating potential for ground problems ahead of the face or behind a pit wall that can't be seen by standard geotechnical inspection (i.e. by naked eye)
- Providing more feedback on the stress state of the rock prior to and following extraction

5. PLANNING A SEISMIC MONITORING PROGRAM

When considering the installation of a seismic system or expanding an existing system at a mining operation some of the main questions you should be asking are as follows:

1. What are the Regions of Interest That I Want to Monitor?

In most cases the primary focus is to monitor the current stopes in an underground mine (Figure 2) or the walls of an open pit where it is expected that the workers face the highest risk. However 'minewide' coverage may be of interest so that major development and important infrastructures such as shafts, underground garages, conveyor tunnels etc... are monitored.

In order to plan for the installation of a seismic system or system expansion, the current and future mining zones should be studied and used to determine what the primary and secondary volumes of interest for monitoring will be. In some cases there may be some other historical and/or rock mechanics basis for expecting a stope to have more seismic related problems than another and can be prioritized in this manner. This exercise of outlining seismic monitoring 'targets' should be the first step before any sensors or equipment are designed or put in the ground.

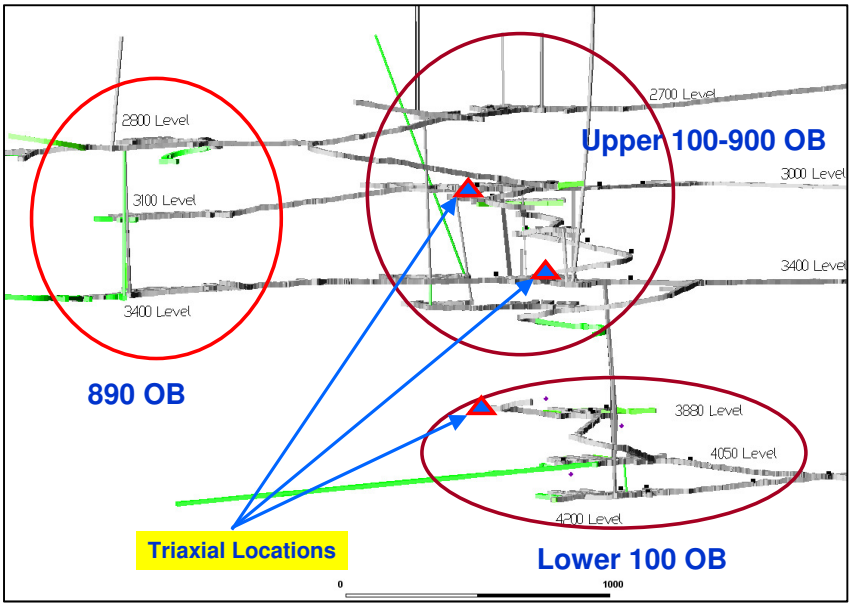

Figure 2 - Example of identifying important targets for monitoring at a mine site

2. At What Stage of Mining Should I Consider Seismic Monitoring?

As mentioned above, it may be important to install a seismic system over a number of months prior to the target region being completely mined out due to the fact that it is important to gather information regarding the background seismicity that has occurred prior to mining taking place. By beginning to monitor the ground early on in the mine life, an initial period of getting used to the system as well as making adjustments to the sensitivity level of the system can be made. In addition, a valuable database of seismicity can be built up from the start of mining and compared with later stages of mining when more seismicity is expected to occur. Relatively changes in the amount and character of mining observed over time can be related to changes in support design, filling methods, blasting techniques, etc… which could provide feedback to optimize these methods.

The challenge with installing a seismic system underground at early stages of mining is sometimes a lack of development to install sensors in short holes close to the future mining regions. One potential solution to this is to drill longer holes to extend sensors into regions that would improve sensitivity and improve location accuracy for target mining zones. Sensors in shorter holes can then be added as development progresses and, if necessary, Paladin channels can be added as the array is expanded to cover the new mining fronts.

3. How Much Should I Budget for a Microseismic System?

Microseismic systems in general have a cost which is approximately proportional to the number of channels (including installation) and the total cost of the infrastructure requirements (e.g. copper cables, fiber optics, drilling costs, etc..) are usually around the same order as the seismic equipment itself.

In addition to the seismic system components, the other material and labour you would need to budget for are:

- Drilling costs
- Fiber optic cable (material and installation)
- Shielded twisted pair copper cable for sensors (material and installation)
- Network infrastructure (media converters)
- Grouting equipment/materials
- Surveying costs (survey sensor locations)
- Cost of calibration blasting (usually 4-8 small blasts in holes)

4. How Accurately Do I Need the Events to be Located?

The most important piece of information provided by the system is the LOCATION of the event. Depending on the geometry of the seismic array, spacing of the sensors, variability of the rock velocity, and level of noise on the sensors the accuracy can vary from a few meters to hundreds of meters. In general, manually processed data will also have a better defined location than an automatically determined location. If the user at the site does not have resources to manually process the data, consider using ESG's data processing service to routinely process the data remotely. Consider the width of the target you are trying to monitor and what level of accuracy would be appropriate. For example, would a location error of 'Y' be good enough to determine whether or not the seismicity is associated with activity in a sill pillar of width 'X'.

For most underground mines the main difficulty in properly monitoring the ore zone is getting sensors in the hangingwall in order to adequately surround the region of interest. This can be overcome with long holes into the hangingwall.

Another thing to consider is that ESG routinely performs an 'Errorspace' analysis prior to the installation of any system which provides the mine with 3D maps of the expected location error for a given array design (Figure 3). This allows the client to observe what the expected coverage would be for regions of the mine before purchasing any equipment.

5. What Are the Magnitudes of Interest That I Want to Monitor?

Another important consideration is what should be to the range of magnitudes covered by the system. In some cases the question boils down to 'what is the smallest magnitude event I need to record?' given that the larger events tend to be recorded and located by the system although their magnitude can be underestimated.

One factor in the sensitivity of the seismic array is the spacing of the sensors. A dense array of sensors will be able to record a lower magnitude than a sparse array of the same sensor type, assuming that other conditions are equal such as the rock mass quality, background noise, trigger thresholds etc... For example, typical spacings of acclerometers in hard rock mines are on the order of 100-200 meters between sensors and can record down to a moment magnitude of -2 to -3.

The sensor types selected for the array also have an influence on the magnitudes recorded. Geophones in general are better suited to measure lower frequencies ($f<50$Hz) or larger magnitudes ($Mw > 1$) and accelerometers are more appropriate for measuring high frequencies ($f>50$Hz) and small magnitudes ($Mw < 1$). In most Canadian mines where there are few large events accelerometers are used to measure microseismicity in the Mw range -2 to 1. To cover the less frequent larger events one or more geophones

are typically installed on or near surface, approximately one kilometre from the mining activity (Alexander and Trifu, 2006).

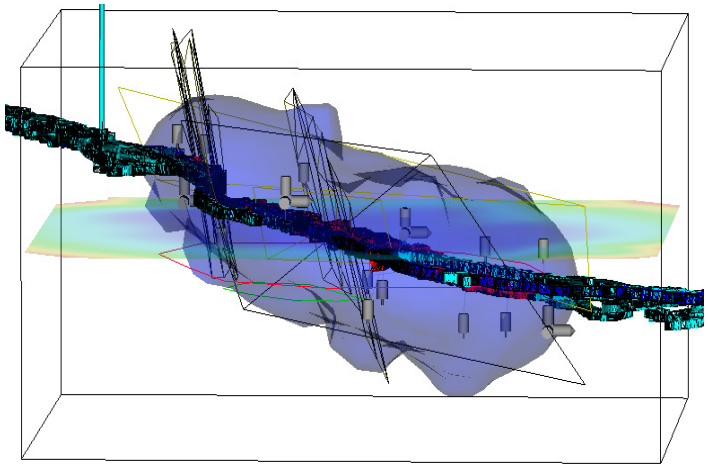

Figure 3 - Example of a 3D iso-surface of total location error for a given array of sensors

Recently ESG has been employing another strategy by installing networks which contain a mixture of uniaxial accelerometers and triaxial geophones. This provides a compromise between the advantages of a sensitive network of accelerometers along with the better determination of magnitude for events with large magnitudes (Mw>1). Recent work has been done by ESG to optimize source parameter calculations for a mixed array of sensors at Xstrata Nickel Rim mine in Sudbury.

ESG routinely provides a sensitivity analysis for a proposed array in order to estimate what the minimum magnitude is that the system could detect in different parts of the array. Along with the errorspace analysis this would be another technique that would help design an optimized array for monitoring a given rock mass.

6. Who Will be Interacting/Using with the Data?

Another question to ask is who will be the ultimate user of the seismic data for both real-time and longer-term analysis? For example, will the real-time seismic information stop at the rock mechanics engineer level or will it eventually be shared with shift bosses, mine workers and security? The usual recommendation would be to provide data only to the rock mechanics group following the initial installation of a system for the first 3-6 months until the system calibration has been completed and staff are comfortable with the quality of the results. Following this, if data is to be shared with others outside the department a training program should be carried out in order to educate the general users on the pitfalls and limitations of interpreting the data as it appears on the mine maps in real time.

7. What Will the Data be used for?

The main goal of the seismic system is to help us understand the rockmass response to mining. There are two main timeframes over which the analysis of the system data may be carried out:

a. Short Term Application

This uses the real-time capabilities of the system such as the plotting of event location & magnitude as dots on mine plans in Seisvis. More advanced tools such as SeisWatch for re-entry and SeisAlert for

sending emails/alerts following large events or increased seismicity rates within a volume can also be used.

b. Long Term Application

For the longer term applications, the data may be used over a longer time period for purposes such as mine support planning, stope design, identification of seismic hazards (e.g. seismically active faults) by using techniques such as clustering and/or moment tensor inversion. Also Source Parameters are important parameters that can be used to track characteristics of seismicity beyond the basic event location and magnitude and relate the data to numerical stress modelling results (Figure 4).

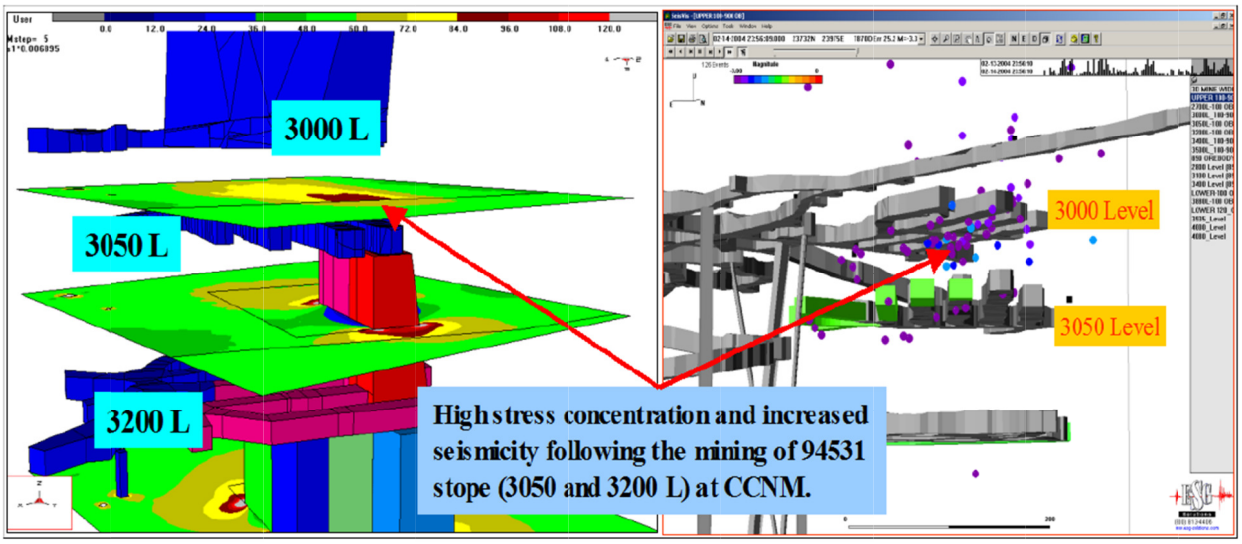

Figure 4 - Example of a longer term analysis of seismicity to relate clustering and characteristics (magnitude) of seismicity to stress modelling results (Trifu and Suorineni, 2009)

6. EXAMPLE OF A SEISMIC SYSTEM INSTALLATION

During the presentation, an example of a typical underground installation will be provided. The project will be outlined from the design phase, installation, configuration and calibration of the system. In addition advanced seismic analysis techniques will be discussed including the determination of event mechanisms, mapping of maximum PPV and Seismic Hazard fields and the use of source parameter data for large event re-entry protocol will be presented.

7. CONCLUSIONS

This paper has provided a practical review of the use of microseismic monitoring for rock mechanics applications at mines and summarized some of the considerations that should be made when installing such systems. The installation of such a system can provide real-time information regarding a large volume of the rock mass and its response to mining in real time. Even though the processing and interpretation of microseismic data can be more difficult than for traditional instrumentation data, the benefits to the mine can be substantial.

8. REFERENCES

ALEXANDER, J. and TRIFU, C-I., 2006. Monitoring Mine Seismicity in Canada. Proc. 6th Int. Symp. on Rockbursts and Seismicity in Mines, p. 353-358.

TRIFU, C-I. and SUORINENI, F.T., 2009. Use of microseismic monitoring for rockburst management at Vale Inco mines, in Controlling Seismic Hazard and Sustainable Development of Deep Mines (ed. C. Tang), Rinton Press, New York/New Jersey, p. 1105-1114.

Monitoring Open Pit Slopes through Slope Monitoring Radar Based on Synthetic Aperture Radar

Paolo Farina
IDS Ingegneria Dei Sistemi S.p.A.
Lorenzo Leoni
IDS Ingegneria Dei Sistemi S.p.A.
Francesco Coppi
IDS Ingegneria Dei Sistemi S.p.A.
Francesco Babboni
IDS Ingegneria Dei Sistemi S.p.A.
Lorenzo Mayer
IDS Ingegneria Dei Sistemi S.p.A.
Niccolò Coli
IDS Ingegneria Dei Sistemi S.p.A.
Abed Helbawi
IDS North America Ltd.
Adrian Weaver
IDS North America Ltd.
Cliff Preston
IDS North America Ltd.

ABSTRACT: Slope monitoring radar has emerged in the last ten years as a leading edge tool for monitoring movements in natural and engineered slopes, thanks to its ability to rapidly measure slope movements with millimetric accuracy over wide areas in any weather conditions, obviating the need to install artificial reflectors. In recent years, slope monitoring radar has experienced significant improvements in its performances, mainly thanks to the use of different radar technology, such as Synthetic Aperture Radar (SAR), able to overcome some of the limitations of the first generation of radar and to provide higher spatial resolution, longer working distances and faster acquisition time. One of the leading applications of this technology is today represented by slope monitoring within the surface mining industry. Prominent international mining groups currently employ slope monitoring radar, based either on Real Aperture Radar (RAR) and SAR technology, for active and background monitoring of open-pit walls. The main technical features of typical slope monitoring radar based on SAR technology along with their possible applications are presented in this paper along with recent case studies of successful slope monitoring in open pit mines.

1. INTRODUCTION

Slope monitoring radars have been widely employed in the last ten years as active tool for monitoring movements in natural and engineered slopes. With respect to conventional monitoring systems, the radar technology presents the advantages of high accuracy of the measurements, long-range capabilities, limited impact of atmospheric artifacts on the measurement performances, and possibility to simultaneously acquire the response over a large number of points.

Slope monitoring radars are based on the radar interferometry, a well-known technology originally developed for satellite applications in order to retrieve ground displacements related to natural hazards (Rosen et al. 2000). In order to overcome some of the limitations related to satellite platforms (e.g. low

revisiting time of the available satellites and consequent temporal de-correlation of the radar signal and unwrapping problems, geometrical distortions induced by the almost vertical line of sight, etc.) the same technology has been successfully implemented in the last year by using ground-based systems. Ground-based radar interferometry has been extensively exploited for slope monitoring of natural slopes (Antonello et al., 2004; Corsini et al., 2006; Bozzano et al., 2008) and open-pit mines (Noon, 2003, Harries et al., 2006).

The use of slope monitoring radars in open pit mines is today a standard practice for active monitoring of the pit walls. Radar units are effectively used to get a better understanding of the spatial distribution of slope movements and for the provision of alerts in the event of progressive movements that can potentially lead to slope failure, thus aimed at assessing the safety of workers and increase the mine productivity.

The first type of slope monitoring radar introduced into the mining market was based on parabolic dish-antenna radars (Real Aperture Radar – RAR), exploiting a fine radar beam that illuminates the target over a series of small footprint area. Various generations of Real Aperture ground-based radars (RAR) have been developed in the last few years for the monitoring of slope movements.

In recent years, slope monitoring radar for mining applications has experienced significant improvement thanks to the introduction of a different interferometric radar technology, such as Synthetic Aperture Radar (SAR), able to overcome some of the limitations of dish-antenna technology, by providing higher spatial resolution, longer working distances and faster acquisition time.

This paper aims at introducing the SAR technology for active and background slope monitoring in open-pit mines. The principal technical features of the system are presented, along with a few example of active monitoring in open-pit mines where the device provided reliable early warnings for the onset of slope failures.

2. TECHNICAL FEATURES

Slope monitoring radar based on SAR technique are characterized by a limited number of moving parts compared to dish-antenna RAR, and are typically composed of the radar sensor, linear scanner and power supply unit. The small horn antennas (not affected by wind-induced vibrations and damage) produce a wide beam (usually 80°-90° on the horizontal plane by 50°-60° on the vertical plane) which illuminates the whole monitored area over few hundred times during a single scan from slightly different positions, while the radar sensor slides along a linear scanner. Such a mechanical scan allows slope stability radar based on SAR to achieve typically a shorter acquisition time to get a full high-resolution image of the observed area (e.g. 5 minutes to cover an area of a 6-8 km^2 at 2 km operating distance).

One of the SAR slope monitoring radar today available on the market is represented by IBIS-M, manufactured by IDS (Fig. 1).

The typical resolution cell of a slope monitoring radar based on a SAR sensor can be of 0.5 m x 4.3 m at 1 km monitoring distance, with respect of a resolution of around 8.5 m x 8.5 m. reached by a 1.8 m dish-antenna RAR operating at the same distance. Measurement accuracy ranges from 0.1-0.2 mm along the radar line of sight within the first km from the slope and below 1 mm within 2-4 km.

The higher spatial resolution is an important added value for open-pit applications, since it means higher sensitivity to slope movements and capability to detect smaller areas of failure, especially for sub-bench or bench-scale failures.

Figure 1 – Example of an open installation of a ground-based interferometric SAR for slope monitoring in an open-pit mine

This advantage, coupled with the wide spatial coverage, makes SAR the perfect tool to cover the entire range of spatial scale instabilities in a slope or a pit wall (Fig. 2).

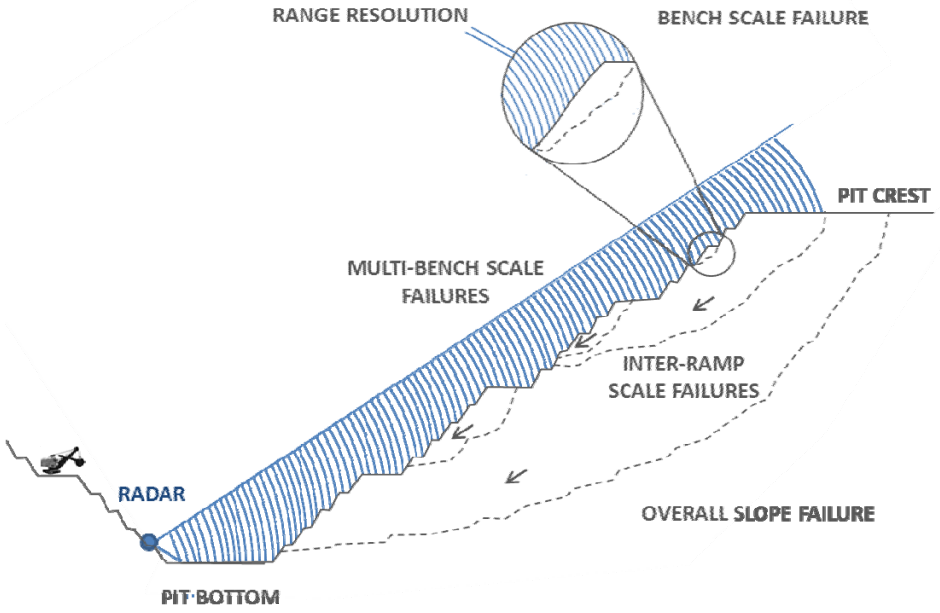

Figure 2 - Example of full-scale coverage of typical pit wall instabilities by typical installation of SAR unit. In blue the antenna footprint and the range-resolution cells. (modified from Read &Stacey, 2009)

The other innovation behind modern slope monitoring radar based on SAR sensors is the data processing algorithm employed for the atmospheric correction. Atmospheric-induced phase artifacts are generated by changes in the refraction index of the air (function of temperature, humidity and pressure) and can be interpreted as false movements if not well recognized and processed. Standard algorithms used by RAR imply the manual selection of stable areas over the monitored scenario, which are used as reference points for the calculation of the atmospheric correction. This method produces only a linear estimation of the

atmospheric contribution which can be assumed as true only at close-medium range and most of the time is not effective in areas with strong atmospheric changes..

The advanced algorithm used by modern SAR is based on the Permanent Scatterer technique, originally developed for satellite applications, which does not imply the need for any atmospheric region selection done by the user (very difficult task even for experienced users). The data processing is based on the evaluation of the atmospheric contribution by performing an automatic selection of an array of hundreds of thousand stable pixels by exploit the different spectral behavior in time and space domains. The automatic and iterative calculation of the atmospheric artifacts over all the PS, makes it possible to extends the operating range of the radar to far distances (up to 4 km).

Radars in open-pit mines are commonly used for active monitoring, through the provision of real-time alarms based on user-defined thresholds of displacement velocity. Thanks to possibility of fixed installation (connected to the long working distance and the high spatial resolution), the SAR technology integrates active monitoring capabilities with the background monitoring for geotechnical analysis. Moreover, the continuous data storage can be used for long-term track of movements, potentially useful for regulators, back analysis of slope failure and more comprehensive geotechnical/geological analysis. The possibility to stich data acquired in different time periods, through the "discontinuous" processing approach (thanks to the re-positioning the radar in the same location, by using a mechanical re-positioning tool), allows the user to combine data acquire in different monitoring sessions and to measure the cumulative displacement occurred between the time elapsed between the two acquisitions.

3. CASE STUDY FROM OPEN-PIT MINE

Large failures in open pit mines are often preceded by very small movements, sometimes only a few centimeters of total displacement over a week, characterized by a temporal evolution ranging from several hours to weeks. The high accuracy of SAR, combined with the high spatial resolution, allows detecting the onset of the instability far before the visual inspection and conventional monitoring instruments.

By covering a wide area of the slope from a single installation, and ensuring a fast scan time and high spatial resolution even at long working distances, a slope monitoring radar based on SAR is able to pick up small displacements at bench, inter-bench or overall slope movements, without the need to focus the monitor system on specific areas of the slope (Fig.3).

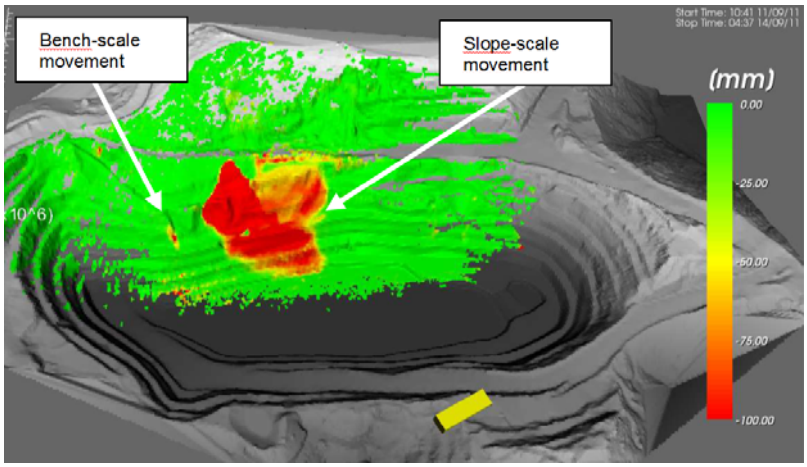

Figure 3 – The wide area coverage, long operational range and high resolution allow picking up from the same installation both slope-scale and bench-scale movements

A full coverage of the mine can be effectively reached by installing multiple units for complete situation awareness, thus avoiding the need to deploy mobile units to focus only on specific areas of potential hazard.

The displacement maps of Fig.4 show the cumulative displacements detected over two days before a slope failure. The unit was installed 1500 m from the slope, with a range resolution of 0.5 m, cross range resolution of 6.5 m and scanning time of 5 min.

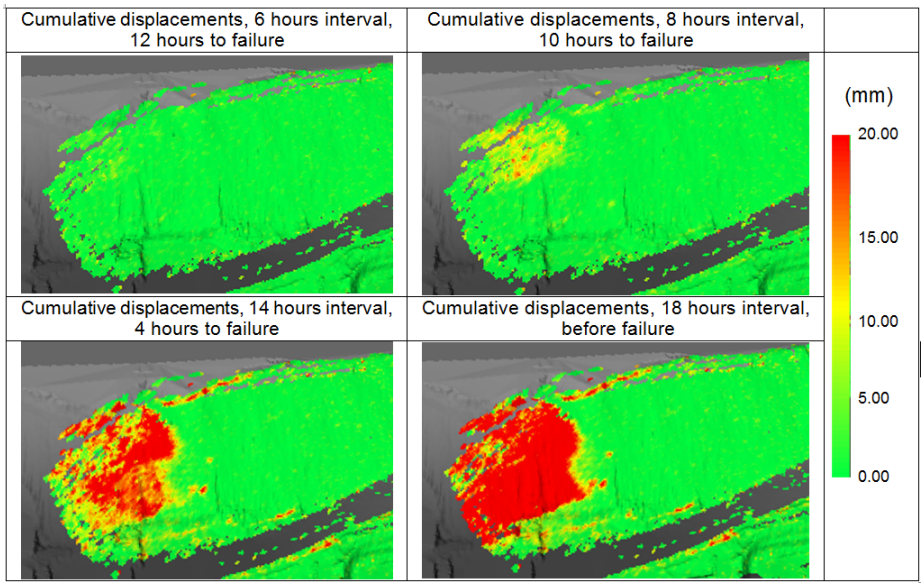

Figure 4 – Displacement maps: evolution of cumulative displacements as detected by IBIS-M prior to the occurred slope failure

The detected moving area progressively widened starting from 12 hours before the failure, most of the upper right of the wall experienced significant displacements and eventually a slope failure occurred.

The graphs of Fig.5, which are displayed in real time by monitoring software, clearly indicate a sudden accelerating trend of the movements previous to the slope failure.

A first acceleration of the movement is clearly visible three days before the slope failure. The cumulative displacements then increased with a constant trend over the following two days before a second important acceleration occurred approximately 12 hours before failure.

By looking at these graphs it is clear how the SAR unit provided an excellent early-warning on the onset of slope instability. The software alarming capabilities were automatically activated when the monitored velocity exceeded the threshold previously set by the mine geotechnical service, allowing for a quick and safe evacuation of the operations from the area of potential hazard.

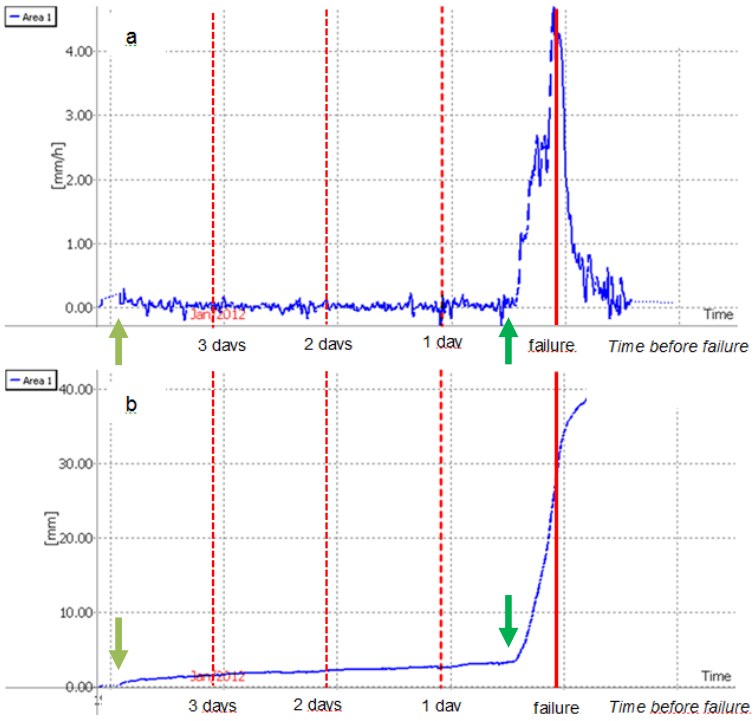

Figure 5 – Historical trends of velocity and cumulative displacement averaged over the area of failure: a) velocity and b) cumulative displacements over a three-days time span

4. FINAL REMARKS

Slope monitoring radar represents a standard practice for the real-time monitoring of slope displacements in open-pit mines. The innovative slope monitoring radars based on the SAR technique recently marked a step ahead in this monitoring standards. By covering all the scales of slope potential instabilities, from bench scale in open-pit mines to overall slope instability, SAR are currently used for both active and background long-term monitoring.

Multiple units can be deployed for a full-pit coverage and complete stability awareness, without the necessity to rely on bulky mobile units and frequent costly repositioning operations.

Slope monitoring can be extended from fast movements (from mm/day to few tens of cm/day), the typical deformation rates of interest for critical monitoring and the ranges covered by conventional radar, to very slow movements (from mm/month to mm/year). This can be achieved just thanks to the long term installations or re-positioning of the fixed-installation radar unit.

Moreover, by combining the two processing performed at different time scales, it is possible to simultaneously track fast and slow slope movements.

5. REFERENCES

ANTONELLO, G., CASAGLI, N., FARINA, P., LEVA, D., NICO, G., SIEBER, A.J., TARCHI, D. (2004). Ground based SAR interferometry for monitoring mass movements. Landslides 1, pp. 21-28.

BOZZANO, F., MAZZANTI, P., PRESTININZI, A. (2008). A radar platform for continuous monitoring of a landslide interacting with a under-construction infrastructure. Italian J. of Engineering Geology and Environment 2, pp. 35-50.

CORSINI, A., P. FARINA, G. ANTONELLO, M. BARBIERI, N. CASAGLI, F. COREN, L. GUERRI, F. RONCHETTI, P. STERZAI, and D. TARCHI. (2006), Space-borne and ground-based SAR interferometry as tools for landslide hazard management in civil protection. International Journal of Remote Sensing, 27, pp. 2351-2369.

HARRIS, N., NOON, D., ROWLEY, R. ,(2006). Case Study of Slope Stability Radar used in Open Cut Mine, in Proc. of Int. Symp. on Stability of Rock Slopes in Open Pit Mining and Civil Eng., Cape Town, South Africa, 2006, pp. 335-342.

NOON, D., (2003). Slope Stability Radar for Monitoring Mine Walls, Mining Risk Management Conference, Sydney, NSW, pp. 1 – 12.

READ, J., STACEY, P., (2009). Guidelines for Open Pit Slope Design. CSIRO Publishing, Collingwood.

ROSEN, P.A., HENSLEY, S., JOUGHIN, I.R., LI, F.K., MADSEN, S.N., RODRIGUEZ, E., GOLDSTEIN, R.M., (2000). Synthetic Aperture Radar Interferometry. Proc. of the I.E.E.E. 88, pp. 333-382.

PETROLEUM GEOMECHANICS

Statistical Analysis of Microseismic Event Characteristics to Monitor In-situ Stress Changes

Melanie Grob
Department of Physics, University of Alberta
Mirko van der Baan
Department of Physics, University of Alberta

ABSTRACT: Two commonly estimated fractal dimensions, called *b* and *D* values, represent statistical characteristics in the distribution of magnitude sizes (*b*) and spatial hypocenter locations (*D*) of microseismic events, respectively. We postulate that the values of *b* and *D* are related to specific stress regimes. Through different case studies of fluid injection into an oil/gas reservoir or geothermal field, we infer that the measured temporal variation in fractal dimension *b* is most likely due to significant changes in the local stress regime. The fracture dimension *D* indicates the spatial clustering of events. The distribution of these events can vary with time because of stress perturbations that (re)activate fractures whose direction favours their movement under a specific stress regime. Thus a combined statistical study of these two dimensions can help infer the variations of local stresses in a reservoir.

1. INTRODUCTION

The three most likely factors to dominate the geomechanical behaviour of a reservoir are the local stress regime, pre-existing fractures and the actual rock properties (e.g., whether they are more ductile or brittle, and their Young's modulus or Poisson's ratio and thus their Lamé parameters). Fluid injection is often used as a mean to increase the permeability of oil/gas reservoirs or geothermal fields, and/or displace fluids already present in the reservoirs. This process perturbs the medium by modifying stresses locally leading to brittle failure of the rock thereby creating microseismic events. Microseismic monitoring records can thus reveal much information on the in situ stress state, fracture distributions and rock properties. This can be achieved using both a statistical and deterministic analysis of event hypocenter and magnitude distributions.

In this paper we focus on a statistical approach analyzing both the fractal dimension of the spatial distribution in hypocenters and the magnitude-size occurrence using the well-known fractal dimensions *b* and *D*. Computing these fractal dimensions is a simple procedure given a sufficiently large microseismic dataset. The *b*-values are inferred from the event magnitude distribution which gives an idea about the distribution of fault lengths (and thus slip amounts) versus the number of events. They are linked to the amount of damage and thus increased permeability, and possibly new fracture densities in, for instance, hydraulic fracturing experiments in tight-oil and gas fields. The fractal dimension *D* reveals the shape of the event cloud (line, plane, or sphere) and is hence useful to evaluate the shape of the damage zone. Thus *b* and *D* values are possibly linked via the shape of the damage zone and the fracture distribution inside this zone.

2. FRACTAL DIMENSIONS

Gutenberg and Richter (1944) inferred the fractal nature of earthquake size distributions. Twenty years later Mogi (1962) and Scholz (1968) demonstrated the same fractal distribution for events happening in laboratory experiments of rock fracturing. Since then many other fractal relationships have been inferred from studies of spatial and temporal distributions of seismic events. Fractal dimensions are defined to quantify the scale invariance of fracturing ranging from the microscopic level of rock fracturing in

laboratory experiments to the macroscopic level of earthquakes. Variations in the values of these fractal dimensions can give insights into the fracturing mechanisms operating at the source of the events.

2.1 *b-values*

The *b*-value is the exponent of the Gutenberg-Richter power law relation indicating the frequency of occurrence *N* of earthquakes of a magnitude *m* larger than a value *M*, that is,

$$\log N(m > M) = \mathrm{a} - \mathrm{b}M \tag{1}$$

A high *b*-value indicates a larger proportion of small earthquakes while small *b*-values mean more larger events happen.

As the size of an event usually depends on the amount of slip on the fault or fracture, *b*-values also give an idea about the distribution of slip. Some authors claimed that $b = 1$ was a universal constant for earthquakes in general (Frohlich and Davis, 1993; Kagan, 1999); however, Schorlemmer et al. (2005) clearly state that *b*-values vary depending on the tectonic stress regime. Indeed they found the highest *b*-values (>1) for normal faulting events, intermediate values (around 1) for strike-slip earthquakes and the lowest *b*-values for thrust events. As normal faults tend to happen under lower horizontal stresses than thrust faults, the *b*-value seems to be proportional to vertical minus horizontal differential stress. Table 1 describes how *b*-values might thus be linked to stress regime and type of faulting.

Amitrano (2003) performed rock fracturing laboratory experiments to explore the relationship of *b*-values and stress and also observed a decrease in *b*-values as the horizontal minus vertical differential stress increased. The stress dependence of *b* can be explained by the fact that high stress systems contain more energy (Scholz, 1968) and the internal friction angle is low, thereby allowing interactions of microfractures in all directions (Amitrano, 2003) thus giving rise to larger events. Other observations confirm that the *b*-value is inversely related to the ambient stress level for natural earthquakes (Huang and Turcotte, 1988), but also for events associated with rockburst (Urbancic et al., 1992).

Table 1 - Summary on how *b*-values are thought to be linked to stress regime and dominant faulting type, based on work by Schorlemmer et al. (2005). S_H : maximum horizontal stress, S_h : minimum horizontal stress, S_v : vertical stress. High *b*-value: relatively more smaller-sized earthquakes occur, small *b*-value: relatively more larger-sized earthquakes happen (after Grob and van der Baan, 2011)

***b*-value**	**Stress regime**	**Fault type**
***b* < 1**	$S_H > S_h > S_v$	Reverse (compressive)
***b* ~ 1**	$S_H > S_v > S_h$	Strike-slip
***b* > 1**	$S_v > S_H > S_h$	Normal (extensional)

2.2 *D-values*

The spatial distribution of damage can be quantified with the spatial correlation dimension *D*, using the spatial correlation integral method proposed by Grassberger and Procaccia (1983). This integral is defined as:

$$C(r) = \frac{2}{N(N-1)} N(R < r) \quad (2)$$

where N is the total number of events and $N(R < r)$ is the number of pairs of events separated by a distance R smaller than r. If the distribution is fractal, the correlation integral will follow a power law distribution with distance r:

$$C(r) \propto r^{D} \quad (3)$$

where D is the fractal dimension (also called correlation coefficient). D is equal to 0 for a point, 1 for a line, 2 for a plane and 3 for a sphere. So D gives an indication of the spatial shape distribution of event locations. Non-integer values reveal a clustering of the events closest to the shape described by the nearest integer value.

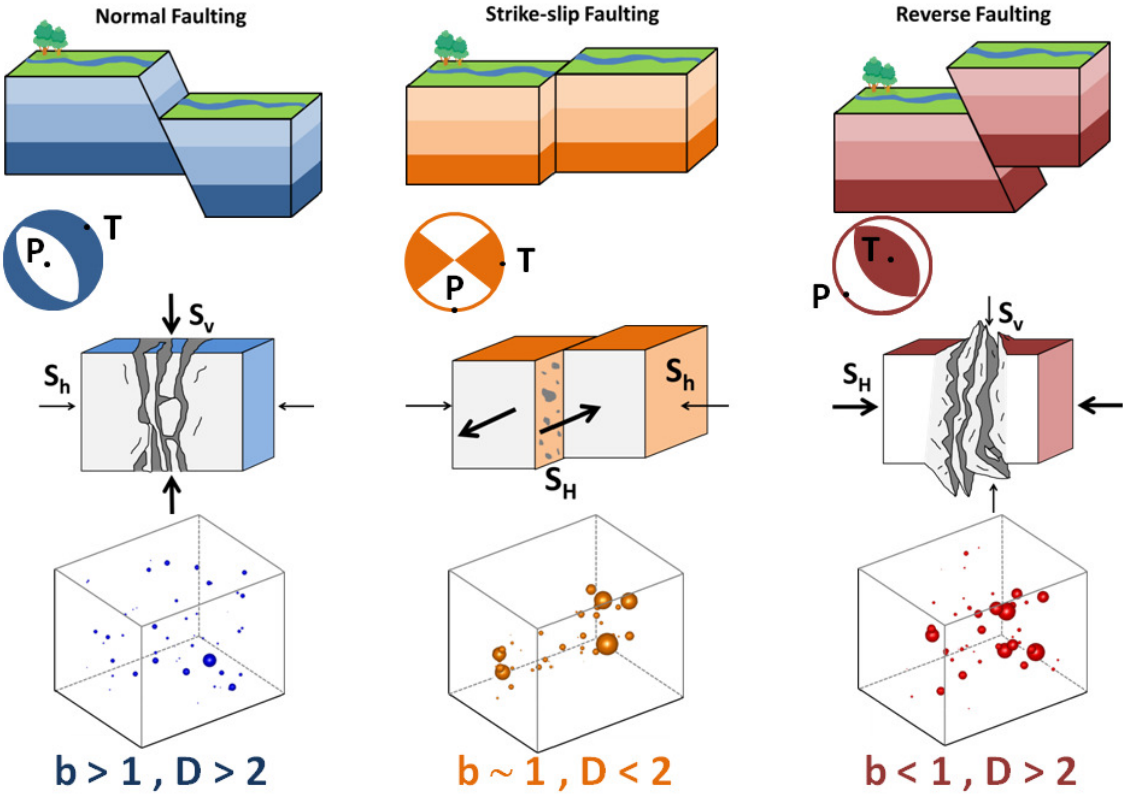

Figure 1 - Links between stress regimes, rock deformation and microseismic events. The first line shows the 3 different stress regimes: the left column illustrates the extensional regime; the central column shows the strike-slip stress regime; and the right column represents the compressive regime. The balls below the first line show the common representations of failure mechanism (moment tensors) relative to each stress regime. The second line indicates the rock deformation under the different stress regime. The bottom line shows typical distribution of events, whose size is proportional to their magnitude. The associated *b* and *D* values are written underneath (after Grob and van der Baan, 2011)

D-values need not be stationary over time. For instance, if *D* decreases from 3 to 2 in time, it means that events that are first randomly distributed in a sphere gather along a fault plane. This is what is mainly observed during rock fracturing experiments where acoustic events are randomly distributed during the first stage and progressively cluster around a plane forming the macrofracture that breaks the sample

(Hirata et al., 1987; Lockner et al., 1992). The fractal dimension D is also related to the irregularity of stress and strength distributions or fracture toughness distribution. D-values may also reflect the structure of the fault network.

We anticipate that D-values are also linked to the local or regional stress regime. For instance, hydraulic fracturing in strike-slip regimes tend to produce microseismic event locations confined to linear structures ($D \approx 1$) or vertical planes ($D \approx 2$), as seen for instance in both the Carthage field treatments in the Upper Cotton Valley formation, Texas, USA (Rutledge et al., 2004) or the Canyon Sands gas fields, also in Texas, USA (Fisher et al., 2008). This is not the case in normal or reverse faulting regimes where hypocenters tend to follow more planar to spherical distributions ($D > 2$). The link between b, D and the stress regimes are illustrated in Figure 1.

3. CASE STUDIES

Grob and van der Baan (2011) analyse microseismic events recorded in a heavy-oil field drained using cyclic steam stimulation. Their results imply that the measured temporal variation in fractal dimension b results from a strong variation in local stress regime over an 8-month period, ranging from extensional faulting (fractures opening), via a strike-slip regime, to finally compressive faulting (fractures closing). The fracture dimension D indicates predominantly planar to spherical hypocenter distributions in the first and last stage, but changes to a more linear to planar spatial pattern in the middle strike-slip regime when the vertical stress is anticipated to be in between the maximum and minimum horizontal stress.

A second statistical analysis from microseismic events recorded during the hydraulic fracturing of an oil reservoir shows cyclic temporal variations of b (values from 1.5 to 2.5) whereas the spatial dimension D stays constant above 2. This cyclic behaviour could indicate alternative periods of opening and closing of fractures or a change in the friction coefficient due to increasing (lower b) or decreasing (higher b) fracture roughness.

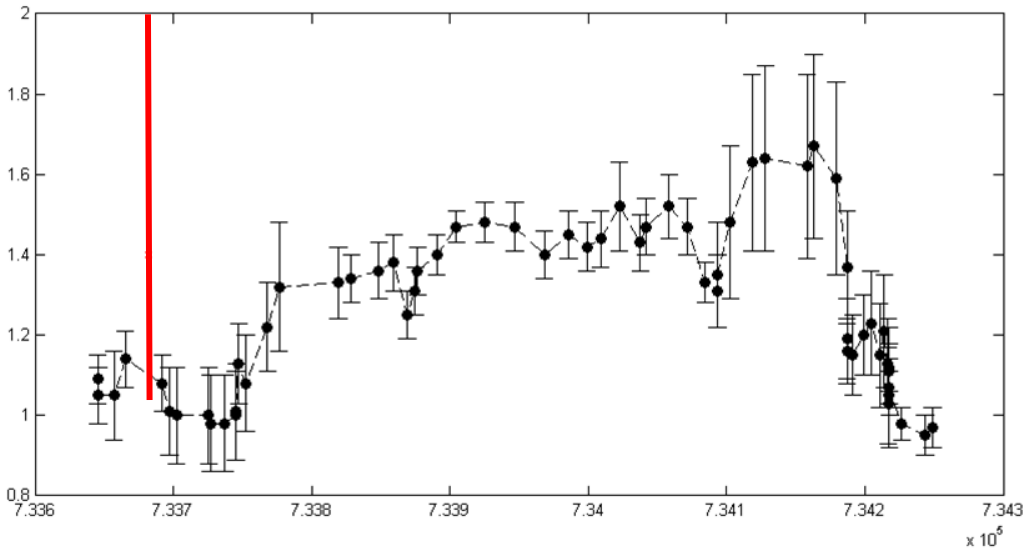

Figure 2 - Temporal variations of b-values for a geothermal field in New-Zealand from July 2008 to May 2010. The red line shows the time of the injection episode that happens in early October 2008

More than eight hundred microseismic events from a geothermal field in New-Zealand have also been statistically analyzed in terms of b and D values. The result shows a small decrease in the b-value after an episode of injection followed quickly by a large increase (Figure 2). The D-value is representative of

planar faults in that system. This could mean that some opening occurs in already existing structures due to the injection.

4. DISCUSSION AND CONCLUSION

Computation of the *b* and *D* fractal dimensions is a simple procedure given a sufficiently large microseismic dataset and can reveal pertinent information on the in situ stress regime (Figure 1). However our analysis is extensively based on the observations of Schorlemmer et al. (2005) and it remains to be established if these observations are also appropriate if more complex rupture mechanisms than double-couple occur, involving for instance significant volume (opening or closing) changes. Our analysis is complementary to results obtained via moment tensor inversions which attempt to infer the actual fracture mechanisms. A comparison between the two methods would establish if *b* and *D* values statistics can reliably be used to infer stress regime changes.

Insights from theory, laboratory experiments and modeling show that the temporal variation of *b* and *D* mimic similar temporal variations in stress regimes; inferred changes over time are thus plausible. The frictional faulting theory shows that, at extremely high pore pressure, relatively small stress perturbations are sufficient to change the type of faulting from one stress regime to the other (Zoback, 2007). Localized pore-fluid pressure can affect the stress regime and hence be responsible for the changes in the cited examples. Chitrala et al. (2010) perfomed laboratory experiments of fluid injection into rock samples. Their results state that the spatial and temporal propagation of a fracture after injection follows the applied stress in the case of an isotropic material but depends on the bedding and magnitude of anisotropy for anisotropic materials. The acoustic emissions recorded during the experiments have a dominant shear failure mechanism for isotropic samples whereas tensile and shear mechanisms are equally represented for anisotropic materials. By modeling the effect of localized pore-fluid overpressure on failure patterns in a porous elasto-plastic medium, Rozhko et al. (2007) found only five different possible scenarios of failure depending on initial conditions, geometry and material properties.

Accurate information on the in-situ stress state is vital for sustainable reservoir management and development of successful drainage strategies. However the most accurate stress information is usually derived from borehole-derived measurements only representative in the vicinity of the well and which can't be performed during the injection process. In this paper we proposed a technique based on routine treatments of microseismic events to assess the in-situ stress regime. The statistical analysis of microseismic event locations and their magnitudes is a simple, useful method to understand reservoir geomechanics and thereby facilitate its management.

5. ACKNOWLEDGEMENTS

The authors would like to thank the Microseismic Industry Consortium for project funding. The authors also thank two anonymous companies and Stephen Bannister from GNS for providing datasets.

6. REFERENCES

AMITRANO, D., 2003. Brittle-ductile transition and associated seismicity: Experimental and numerical studies and relationship with the b value. Journal of Geophysical Research, 108(B1), p. 1-15. doi:10.1029/2001JB000680.

FISCHER, T., HAINZL, S., EISNER, L., SHAPIRO, S.A. and LE CALVEZ, J., 2008. Microseismic signatures of hydraulic fracture growth in sediment formations: Observations and modelling. Journal of Geophysical Research, 113, B02307, doi:10.1029/2007JB005070.

FROHLICH, C., and DAVIS, S. D., 1993. Teleseismic b values; or, much ado about 1.0. Journal of Geophysical Research, 98(B1), p. 631–644.

GRASSBERGER, P., and PROCACCIA, I., 1983. Measuring the strangeness of strange attractors. Physica D: Nonlinear Phenomena, 9(1-2), p. 189–208.

GROB, M., and VAN DER BAAN, M., 2011. Inferring in-situ stress changes by statistical analysis of microseismic event characteristics. The Leading Edge, 30(11), p. 1296-1302.

GUTENBERG, R., and RICHTER, C.F., 1944. Frequency of earthquakes in California. Bulletin of the Seismological Society of America, 34, p. 185-188.

HIRATA, T., SATOH, T., and ITO, K., 1987. Fractal structure of spatial distribution of microfracturing in rock. Geophysical Journal of the Royal Astronomical Society, 90(2), p. 369–374.

HUANG, J., and TURCOTTE, D., 1988. Fractal distributions of stress and strength and variations of b-value. Earth and planetary science letters, 91(1-2), p. 223–230.

KAGAN, Y. Y., 1999. Universality of the seismic moment-frequency relation. Pure and Applied Geophysics, 155, p. 537-573.

LOCKNER, D., BYERLEE, J., KUKSENKO, V., PONOMAREV, A., and SIDORIN, A., 1992. Observations of quasistatic fault growth from acoustic emissions. Fault Mechanics and Transport Properties of Rocks, 51, p. 3–31. ACADEMIC PRESS LTD.

MOGI K., 1962. Magnitude-frequency relation for elastic shocks accompanying fractures of various materials and some related problems in earthquakes. Bulletin of the Earthquake Research Institute of Tokyo University, 40, p. 831-853.

ROZHKO, A. Y., PODLADCHIKOV, Y. Y., and RENARD, F., 2007. Failure patterns caused by localized rise in pore-fluid overpressure and effective strength of rocks. Geophysical Research Letters, 34, L22304. doi:10.1029/2007GL031696

RUTLEDGE, J., PHILLIPS, W., and MAYERHOFER, M., 2004. Faulting induced by forced fluid injection and fluid flow forced by faulting: An interpretation of hydraulic-fracture microseismicity, Carthage Cotton Valley Gas Field,. Bulletin of the Seismological Society of America, 94(5), 1817-1830.

SCHOLZ, C., 1968. The frequency-magnitude relation of microfracturing in rock and its relation to earthquakes. Bulletin of the Seismological Society of America, 58(1), p. 399–415.

SCHORLEMMER, D., WIEMER, S., and WYSS, M., 2005. Variations in earthquake-size distribution across different stress regimes. Nature, 437(7058), p. 539-42. doi:10.1038/nature04094

URBANCIC, T., TRIFU, C.-I, LONG, J., and YOUNG, R., 1992. Space-time correlations of b values with stress release. Pure and Applied Geophysics, 139(3), p. 449–462.

ZOBACK, M., 2007. Reservoir Geomechanics. Cambridge University Press.

Poisson Impedance as a Rock Physics Attribute for Developing Geomechanics Earth Models: Case Study from Southwest Iran

SeyedBijan Mahbaz
University of Waterloo
Maurice B. Dusseault
Porous Media Research Inst., University of Waterloo
Hadi Sardar
Geo-Engineering Lab, University of Tehran

ABSTRACT: Development of Geomechanical Earth Models (GEM) is a prerequisite to reservoir management, involving issues such as stress path analysis, prediction of induced seismicity and sanding initiation, and coupled flow-stress modeling that leads to more realistic predictions of oil rates and rock response. Part of GEM development is the stipulation of the 3-D lithostratigraphic disposition (geometry) which is used to choose the geomechanical units. The digital geological model is then populated with quantitative and semi-quantitative data on rock properties, fluid properties, saturations, initial conditions (p, T, [σ]) and other information. Both fluid and solid properties are needed this requires integration of geomechanics skills with geophysical and rock physics skills, and this article deals with a subset of this integration process, with an example from two wells in southwest Iran.Rock physics approaches are used to predict reservoir rock and fluid properties with wellbore and 3-D seismic data, which are also used to interpolate rock mechanics properties to the inter-well regions. The first step in a generic rock physics approach is diagnostic and involves the introduction of a suitable Rock Physics model.Acoustic impedance (AI), shear impedance (SI), and density (ρ) are the fundamental rock properties usually derived using AVO equations, and these parameters, along with attenuation coefficients, can then be correlated to static rock mechanics properties that define deformability and perhaps even strength. In this study, Poisson Impedance is introduced as a new seismic attribute used for lithology and fluid differentiation in the FahliyanFormation (reservoir rock) in two oil wells in the southwest of Iran. To do this, a novel rock physics model was developed for this naturally fractured carbonate reservoir.Currently, these data are also being used to correlate to a limited rock mechanics data base to develop a more extensive GEM to serve as input to more general geomechanical and reservoir modeling tasks.

1. INTRODUCTION

Two main geoscience objectives that precededevelopment or redevelopment are lithological and fluid differentiation within the reservoir. For example, Smith and Gidlow (1987) used P- and S-wave velocity (v_P, v_S) and also Poisson's ratio to develop a "fluid factor" as a fluid differentiation technique. Gidlow *et al*. (1992) and Fatti *et al*. (1994) redefined the fluid factor by using a method of impedance reflectivity inversion of common midpoint gathers instead of v_P and v_S.Lamé coefficient (λ), shear stiffness (μ) and density(ρ) are other seismic parameters which reflect rock properties, and their use was suggested by Grey *et al*. (1999) as an AVO technique andGoodway*et al*. (1997) introduced the method called lambda-mu-rho, λ-μ-ρ, as a usefulfluid and lithology indicator in the impedance domain. Russell *et al*. (2001) presented a fluid detection algorithm based on $(v_P/v_S)^2$, claiming better resolution. Based on the Goodway*et al*. (1997) observation and his comparisonsof cross plots ofλρ versus μρwith cross plots of acoustic impedance (AI) versus shear impedance (SI), the discrimination of gas sands, wet sands and shales in λρ- μρ cross plots is larger than ion AI-SI cross plots.In AI-SI crossplot space, we may highlight our discrimination between any two litho-fluid types by choosing arotated axis that optimizes the desired separation. One particular rotation in AI-SI crossplot space is worth noting because of its link to Poisson's

ratio (σ) and density (ρ) (Quakenbush*et al*. 2006). This new attribute, related to Poisson's ratio and density, is called the Poisson Impedance (PI).

In this study, we first used data from two oil wells (A1 and A2) in the southwest of Iranto determine fluid properties and differentiate the lithology using the PI for the Fahliyan Formation. Rock physics model were developed for the Fahliyan Formation which define a relation between PI from well logs and seismic data and can be used for access more accurate Geomechanic model.

The Fahliyan Formation of Neocomian age is a carbonate oil reservoir in some of the major oil fields of southwest Iran. It is a massive oolitic to peleticlimestone with minor contemporaneous brecciationat the base (James and Wynd, 1965). The basal Fahliyan Formation grades laterally into theshaleyfacies of theGarau Formation, which is a time equivalent stratum. Regionally, various limestone sequences in Saudi Arabia, Kuwait and Iraq, as well as the interbedded shale/sandstone/limestone sequences of the Ratawi Formation in Kuwait and Iraq are time equivalent strata.Regionally, target reservoir rocks are usually found in the lower member of the Fahliyan Formation.

The study field lies 80 km west of Ahwaz, Khuzestan Province, Iran (Figure 1). The Fahliyan Formation is 542 m thick in well A1 (3980 - 4522 m). The upper part consists of alternating limestone and shale, and the lower reservoir member is clean thick-bedded limestone with a few thin shale layers in the middle of the sequence (Figure 2).

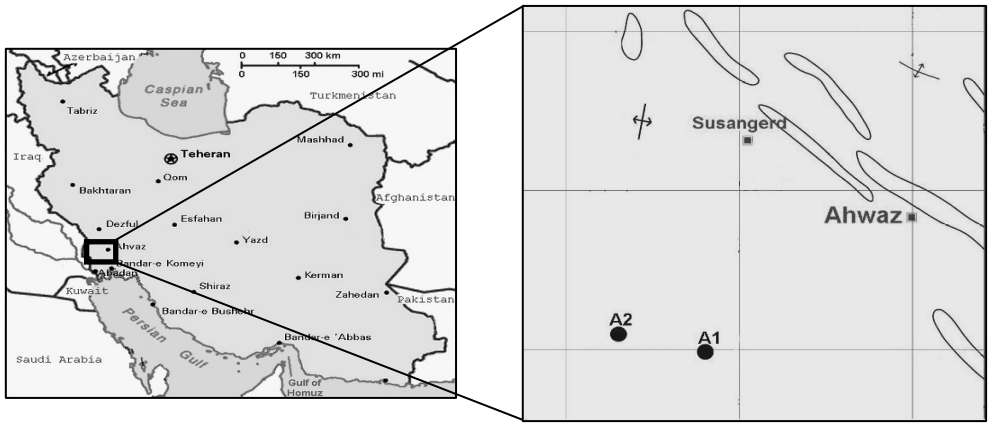

Figure 1 - Location map of studied wells (A1 and A2) in Zagros Basin, southwest Iran

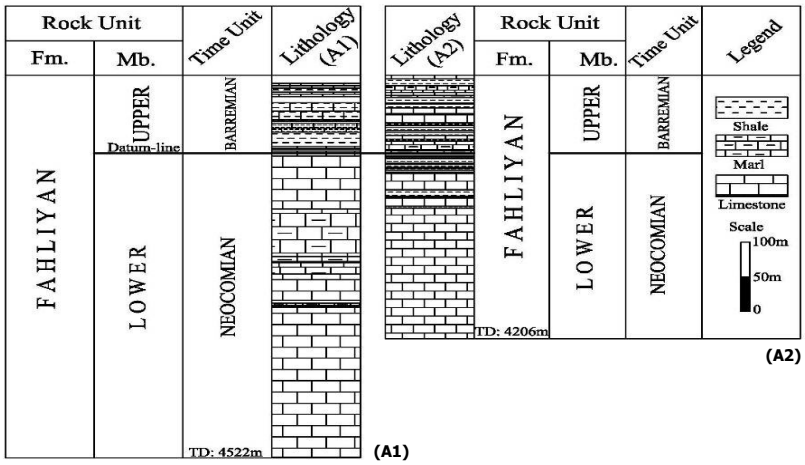

Figure 2 - Comparison of fahliyan formation in wells A1 and A2

The thickness of the Fahliyan Formation is 381 m in well A2 (3825 - 4206 m). The lithostratigraphy is roughly similar to well A1, with the reservoir being clean, thick-bedded limestone(Figure 2).

2. CALCULATIONS

A full set of log data were available for well A1 and A2across the Fahliyan zone. Simultaneous use of AI and SI is the common approach to differentiate lithology and fluid content, a method introduced by Quakenbush*et al*. (2006). The PI method is derived by an optimum rotation of the AI-SI cross-plot, which is defined as:

$$\mathrm{PI}_t = \mathrm{AI}_t - \mathrm{c}\,\mathrm{SI}_t \tag{1}$$

PI_tisthe total Poisson Impedance and c is the scale factor that optimizes the axis rotation.This scale factor is defined here as the average ratio ofAI and SI in the wet reservoir zone. So we will have:

$$\mathrm{PI}_t = \mathrm{AI}_t - [(\mathrm{AI}_t/\mathrm{SI}_t)_{wet}]_{ave}\mathrm{SI}_t \tag{2}$$

whereAI_t refers to the actual acoustic impedance trace with its current pore fluid and $\mathrm{AI}_{wet}(t)$ refers to the same acoustic impedance trace if the pore fluid is brine.

Figure 3a is a cross-plot of AI versus SI derived from rock physics properties of the two study wells for carbonate reservoirs with brine and with oil saturation. Figure 3b shows an AI versus SIcross-plotusing the three lithological categories previously identified. Clear relationships that are approximately linear in nature are seen for the cases of oil-saturated, water-saturated, and calcite lithology. Discrimination between shale and Marl is not easy as Calsite and Shale, so this behavior of Marl must be noticed during studies.

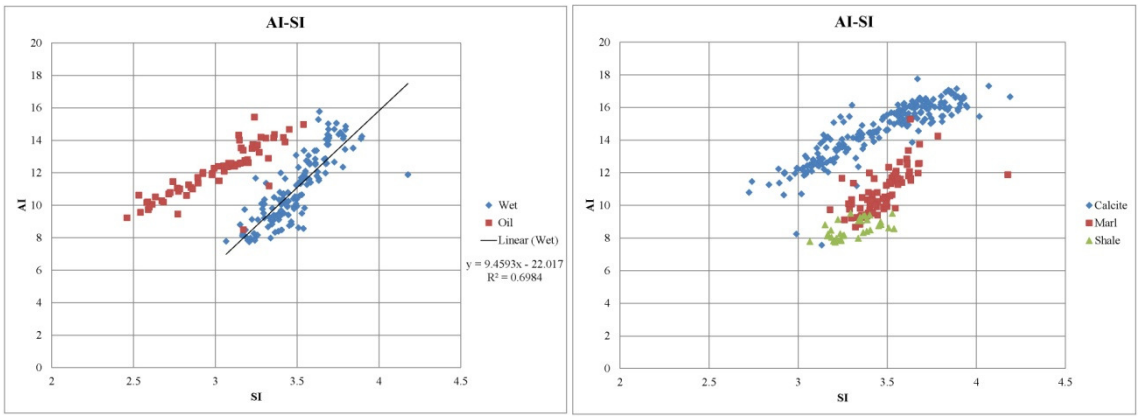

Figure 3 - AI versus SI. a. differentiation between oil and saline water. b. lithological differentiation

Equation 3 linearly relates AI and SI for wet calcite. Rotating the axes to the wet-calcite line yields the PI attribute in equation 4, which is illustrated in Figure 4.

$$\mathrm{AI} = 9.46 \times \mathrm{SI} - 22.0 \tag{3}$$

$$\mathrm{PI} = \mathrm{AI} - 9.46 \times \mathrm{SI} - 22.0 \tag{4}$$

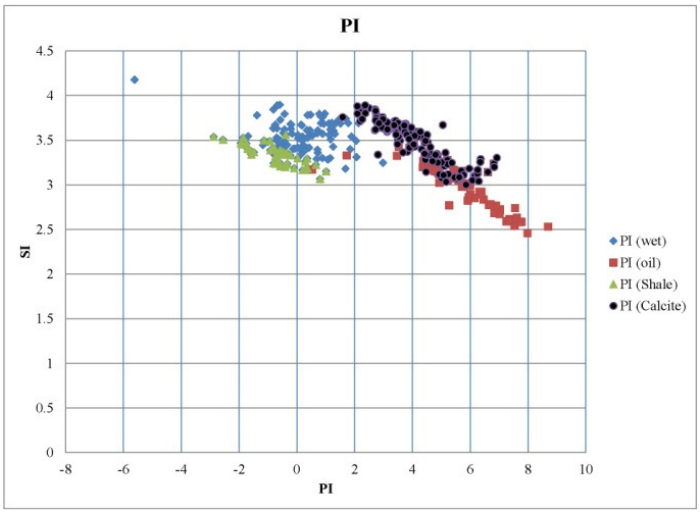

Figure 4 - SI versus PI. Differentiation between oil, wet and Calcite with Shale are clear

Because the rotation was based on the water-wet zone line, PI for water-wet is around zero.PIfor the oil-saturated zone is positive with some overlap with calcite zone. In this figure, marl (calcite-rich shale) data have been left off for two reasons:

- Marls lie between the shale and calcitelines, leading to greater difficulty in differentiation.
- Distinguishing thin shale (marl) layers inside carbonate rocks on the basis of geophysical logs is difficult, and although small-scale petrophysical analysis shows they are shale, because of data resolution in logs, they will be classified as marl in techniques with lower resolution.

Figure 5 shows PI histograms of data, illustrating clear differentiation between lithology and fluids in the study reservoir. Table 1 presents a statistical summary of these four graphs.

Table 1 - Histograms information in four different categories

	PI (Wet)	PI (Oil)	PI (Shale)	PI (Calsite)
Mean	0.0528	5.6663	-0.6098	4.1403
Std. Error of Mean	0.09671	0.17998	0.10187	0.10659
Median	-0.0632	5.6874	-.5444	4.0391
Mode	-5.62	0.53	-2.88	1.59
Std. Deviation	1.19234	1.45104	0.77581	1.20589
Variance	1.422	2.106	0.602	1.454

The PI of the wet zone shows a mean value of 0.05 with standard deviation of 1.19, which is different from the PI in the oil saturated zone. The PI of oil-saturated carbonate shows a mean value of 5.6, with a standard deviation of almost 1.5. Also, PI mean values for shale and calcite are -0.61 and 4.1 with standard deviation of 0.77 and 1.2 respectively. Thus, these two categories are sufficiently separated statistically to be distinguished by this attribute. However, there are some minor overlaps between shale and the wet zone and also between the oil and calcite zones.

The PI in shales clusters near zero with most data points on the negative side. Shales and water-wet calciteclasses have some overlap, but the PI of oil-saturated rock and water-wet calcite shows almost complete separation, facilitating differentiation, and implying that digital log analysis methods using relatively simple empirical correlations based on PI are powerful lithological differentiation tools.

To determine a suitable rock physics model for the study data, they were compared with previously developed models. The review of existing theoretical models showed that the trend of studied data is similar to the Rymer-Greenberg-Castagna (1977) model for carbonates(Spikes *et al*., 2003), which is shown in Figure 6as a black line. Superimposing the rock physics model to the study data (Figure 6) shows that in some intervals, the data matched this model, and in some other intervals, there are some offsets between them.

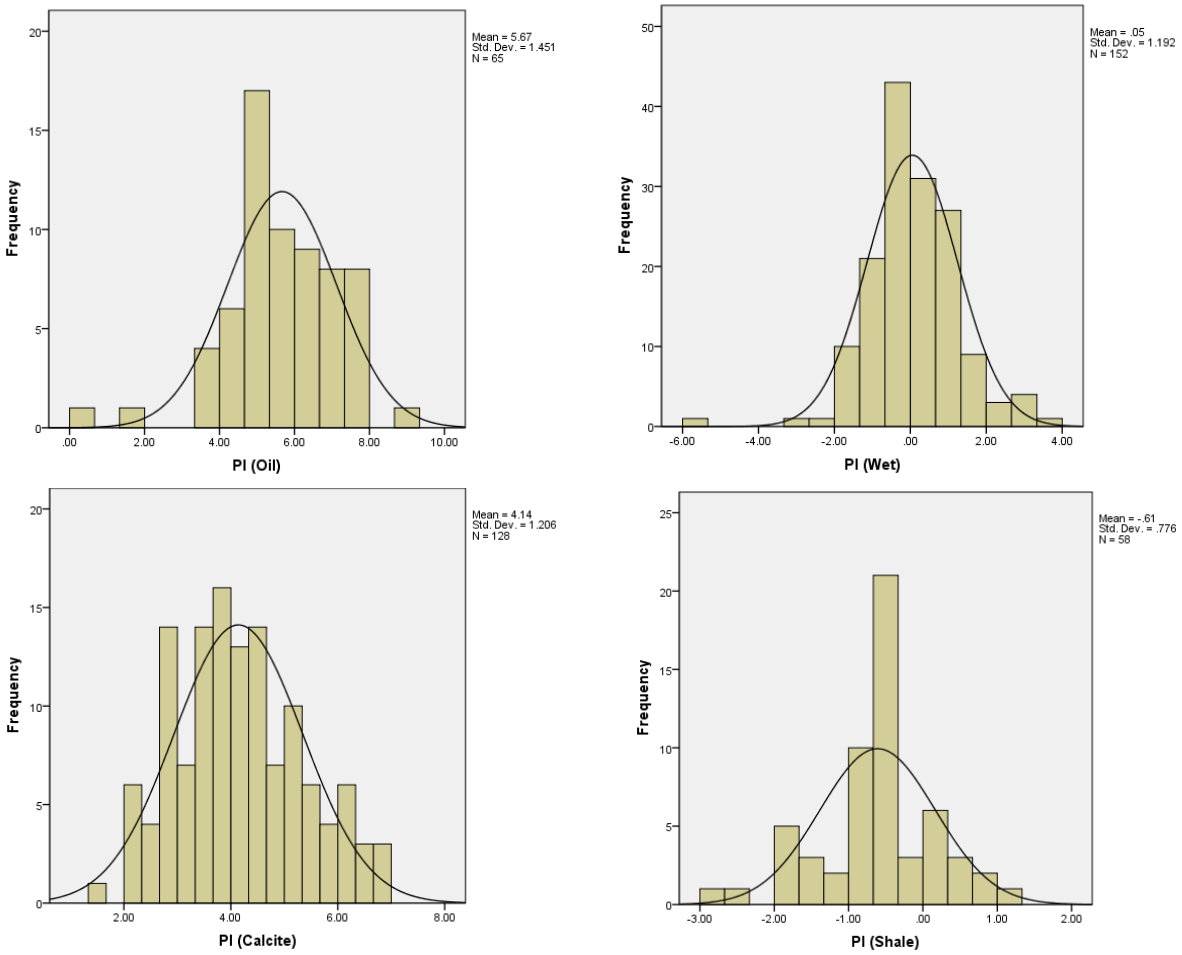

Figure 5 - PI histograms for oil, wet, calcite and shale zone

The data trend follows the Rymer-Greenberg-Castagna model (1977) for carbonates, but there are also some considerable differences. To determine the reason for these differences, other cross plots were studied and the best of them were chosen to quantify and separate these off sets and prepare linear trends for the calcite zone. Figure 7 shows variation of acoustic impedance of common fluid (displacement of whole reservoir fluid with a fluid which we completely know its properties) (Adam et al., 2005) versus porosity. In these cross plots, different water saturation (S_w) ranges were used for each cross plot to illustrate the change in the relationship as S_w goes from <0.50 to 1.0.

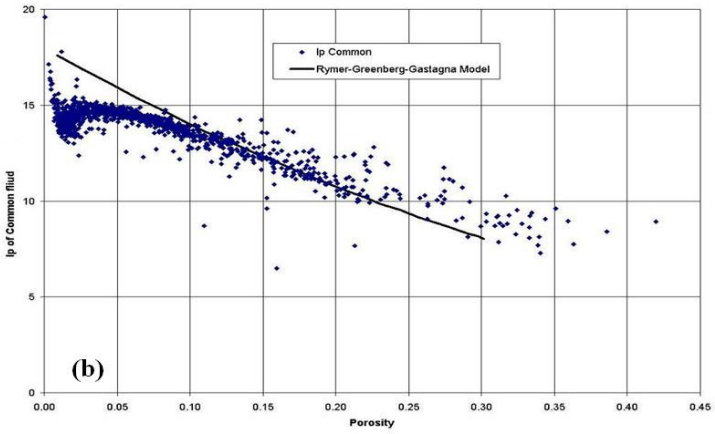

Figure 6 - Rymer-Greenberg-Castagna model as selectedrock physics model for the studied data

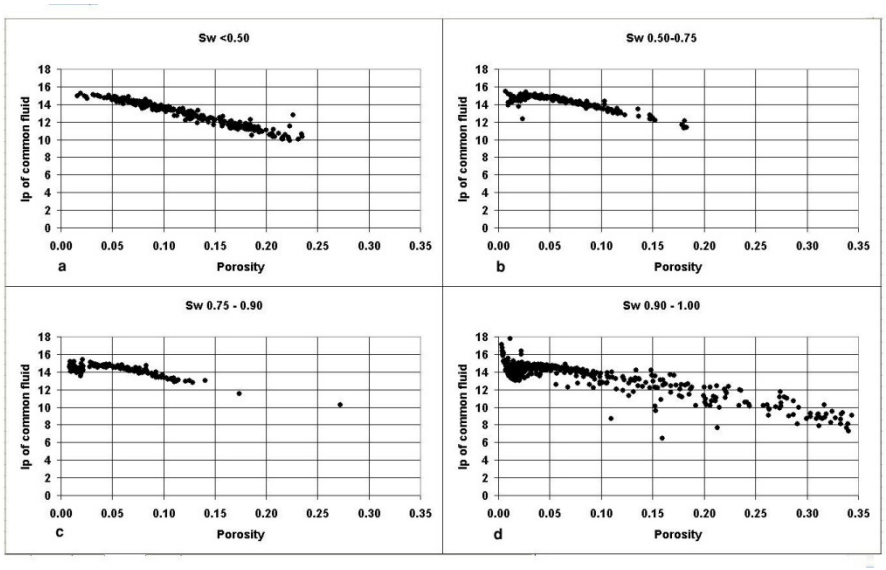

Figure 7 - Ip of common fluid versus porosity

Studying the figure trends in more detail…

2. S_w<0.50: The data trend is completely linear, and corresponds extremely well with the rock physics model linear trend shown in Figure 6.
3. S_w = 0.50-1.00: The trend of the data is nonlinear, becoming more so as $S_w \rightarrow 1.00$.

Excluding log data with S_w> 0.50, and reiterating the clear linear relationship noted in the upper left part of Figure 7, the best rock physics model will be the one developed with data from these intervals. Figure 8 shows the Ip of common fluid versus porosity ranging between S_w of 0 to 0.50. The Rymer-Greenberg-Castagna model and regression line are also plotted in the figure, giving the following equation:

$$y = -25.1x + 16.0 \quad (5)$$

with a correlation coefficient *r*=0.97.

Thus, the rock physics model for the limestone interval of these two wells is:

$$AI\ (Ip) = -25.1 \times Porosity + 16.0 \quad (6)$$

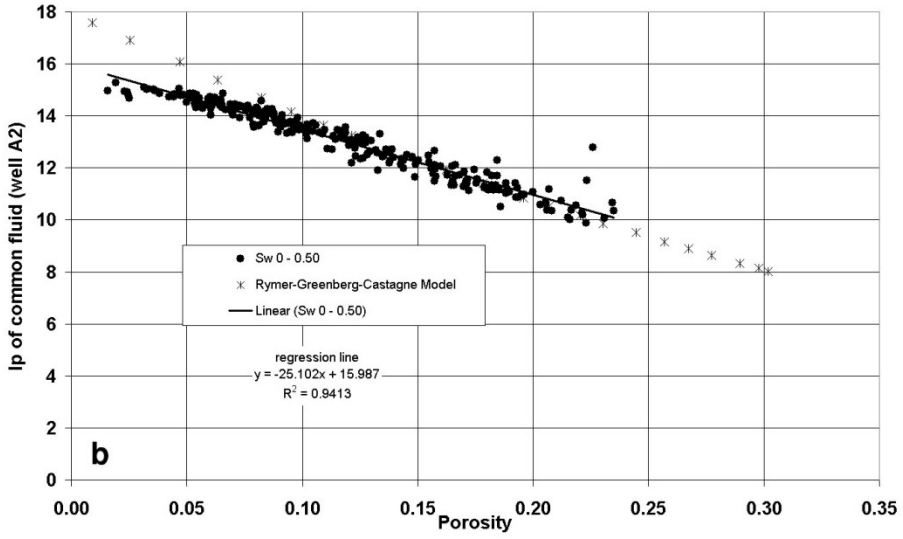

Figure 8 - Ip of common fluid versus porosity. Stars are the Rymer-Greenberg-Castagna model. The dots are data, and the black line is the regression line for the study data

3. CONCLUSIONS

1. In these studied wells, Poisson Impedance provides a direct and significant differentiation between water and oil saturated rocks.
2. A moderate but valuable differentiation is also noted between shale and calcite lithologies.
3. With respect to the Poisson Impedance classifier
    a. PI is positive for oil saturated rock and calcite.
    b. PI is around zero to slightly negative for shale.
4. PI is shown to be a useful discriminator for lithology and fluid.
5. The study data from the Fahliyan Formation partially follows the Rymer-Greenberg-Castagna model for carbonates, with some deviation from the predicted relationship.
6. With further data analysis that includes using water saturation as a metric, it becomes possible to extract the linear rock physics trend of the limestone for $S_w<0.50$.
7. Abstracting the effects of water saturation and clay content, the best empirical model for theclean carbonate of the Fahliyan Formation, with a high correlation coefficient, is:

$$AI\ (Ip) = -25.1 \times Porosity + 16.0 \quad (7)$$

In a more general vein, we wish to note that in Petroleum Geomechanics analysis, the tools available for the development of the basic model of rock properties, lithostratigraphic disposition, and interwell predictions are core analyses, borehole geophysical logs, and 3-D seismic surveys (to permit inter-well interpolation). Here, we show how useful lithotype identifiers can be developed from geophysical log data and some laboratory data. Similar predictor relationships based on other logs (density logs, acoustic logs…) can be developed for other properties, including mechanical ones, and these are used to assemble

the three-dimensional GEM. We believe that, in general, geophysical and rock physics methods have been under-utilized in geomechanics, and there is a great deal of value to be extracted from their use, particularly but not exclusively in Petroleum Geomechanics.

4. REFERENCES

ADAM, L., BATZLE, M., and BREVIK, I., 2005. Gassmann's fluid substitution paradox on carbonates: seismic and ultrasonic frequencies: Presented at the 75th Annual International Meeting, SEG, 24, p. 1521–1524.

FATTI, J., G. SMITH, P. VAIL, P. STRAUSS, and LEVITT, P., 1994. Detection of gas in sandstone reservoirs usingAVOanalysis:A3-D seismic case history using the geostack technique: Geophysics, 59, p. 1362–1376.

JAMES, G.A., and WYND, J.G., 1965. Stratigraphic Nomenclature of the Iranian Oil Consortium Agreement Area: AAPG Bull., 49, p. 2182-2245.

GIDLOW, P.M., G.C. SMITH, and VAIL, P.J., 1992. Hydrocarbon detection using fluid factor traces, a case study: How useful isAVO analysis?: Joint SEG/EAEG summer research workshop, SEG/EAEG, Technical Program and Abstracts, 78–89.

GOODWAY, B., CHEN, T., and DOWNTON, J. 1997. ImprovedAVOfluid detection and lithology discrimination using Lamé petrophysical parameters; ," λρ"" ρμ"& λ□ρ" fluid stack, from P and S inversions: 67thAnnual International Meeting, SEG, ExpandedAbstracts, 183–186.

GRAY, D., B. GOODWAY, and CHEN, T., 1999. Bridging the gap: using AVO to detect changes in fundamental elastic constants: 69thAnnual International Meeting, SEG, ExpandedAbstracts, 852–855.

QUAKENBUSH, M., B. SHANG, and TUTTLE, C., 2006. Poisson impedance: The Leading Edge, 25, p. 128–138.

RUSSELL, B.H., HEDLIN, K., and HILTERMAN, F.J., 2003. Fluid-property discrimination withAVO:ABiot-Gassmann perspective: Geophysics, 68, p. 29–39.

SMITH, G. C., and GIDLOW, P. M., 1987. Weighted stacking for rock property estimation and detection of gas: Geophysical Prospecting, 35, p. 993–1014.

SPIKES, K.T., and DVORKIN, J. P., 2003. Model-based prediction of porosity and reservoir quality from P- and S-wave data, GRL, 30, p. 2029-2032.

A New Approach to Infer Reservoir Dilation Using a Limited Number of Tiltmeter Measurements

Asanga S. Nanayakkara
Schulich School of Engineering, University of Calgary
Ron C. K. Wong
Schulich School of Engineering, University of Calgary

ABSTRACT: The surface deformations induced by reservoir dilations can be measured using tiltmeters and these measurements can be used to infer reservoir level volume changes by solving an inverse problem. Preferred approach to solve such an inverse problem is to consider more tiltmeter measurements than the number of unknown variables considered in the inverse problem. However, sufficient number of measurement points is not always available due to economical and practical issues. This paper proposes a new approach to circumvent this problem. The new approach entails generation of pseudo surface deformation data by curve fitting tiltmeter measurements using a mathematical function, which delineates three-dimensional characteristics of surface deformation profiles. Then a three-dimensional inverse problem is solved using pseudo surface deformation data. This method is useful in inferring reservoir volume changes with high areal resolution when the number of available measurements is not sufficient to acquire the desired areal resolution.

1. INTRODUCTION

The reservoir level volumetric expansions (i.e. reservoir dilations) could occur due to variety of subsurface injection operations such as thermal hydrocarbon recovery, waterflooding, waste disposal, CO_2 sequestration and aquifer storage recovery. The disturbances caused by the reservoir dilations propagate through the overburden and extend up to the ground surface resulting in surface deformations. Tiltmeters can be installed at a set of selected surface observation points to measure slopes of these surface deformations and the measurements can be used to infer reservoir dilations by solving an inverse problem. The inverse problem is based on a system of linear equations, which couples tiltmeter measurements with unknown reservoir dilations at a selected set of small reservoir blocks. Preferred approach to solve such an inverse problem is to consider more tiltmeter measurements than the number of unknown variables considered in the inverse problem. However, sufficient number of tiltmeter measurements is not always available due to economical issues and practical issues, and the ability to infer reservoir dilations with high areal resolution is overshadowed by this limitation. This paper proposes a new approach to circumvent this limitation by curve fitting tiltmeter measurements to generate pseudo surface deformation data. A mathematical function, which is capable of delineating three-dimensional characteristics of surface deformation profiles, is used for curve fitting. Further, the paper discusses details of solving an inverse problem using pseudo surface deformation data and limitations associated with this approach.

2. SURFACE DEFORMATION FUNCTION

The first step towards development of a suitable function to delineate characteristics of a simple three-dimensional surface heave profile such as depicted in Figures 1(a) and 1(b) is to consider a vertical cross section, which passes through the center of heave. Such a two-dimensional profile has been delineated

with a normal distribution function by several researchers (Peck 1969; Schmidt 1969; Wong and Chau 2004) as given below.

$$u_z(x)=\omega e^{-Ax^2};\ A>0,\ \omega<0 \tag{1}$$

where u_z is the vertical displacement at a lateral distance x from the heave center and A and ω are constants. Upward vertical displacements are considered as negative.

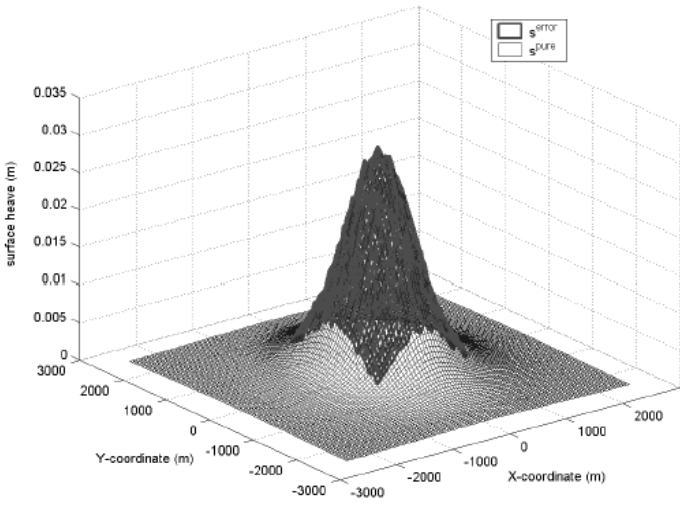

Figure 1(a): Vertical displacements of pure surface heave (s^{pure}) and perturbed surface heave (s^{error})

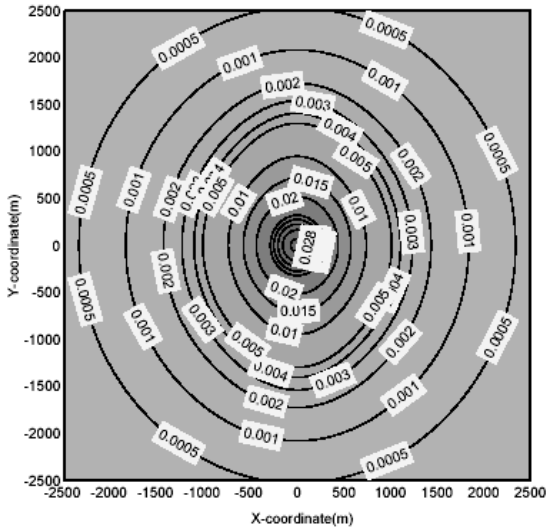

Figure 1(b): Vertical displacement contours of pure surface heave given in Figure 1(a), unit: m

Equation 1 can be simply converted to represent a three-dimensional axisymmetric surface heave with circular contours as:

$$u_z(x,y)=\omega e^{-A(x^2+y^2)};\ A>0,\ \omega<0 \tag{2}$$

A general equation for a circular contour (corresponding to a given u_z value) of the surface heave can be obtained by taking natural logarithm of Equation 2 as:

$$Ax^2+Ay^2=-\ln\left(\frac{u_z}{\omega}\right);\ \ A>0,\ \omega<0,\ u_z<0 \tag{3}$$

With insight provided by Equation 3, a general equation for an elliptical contour of a surface heave can be expressed as:

$$Ax^2+By^2+2Gx+2Fy+2Hxy=-\ln\left(\frac{u_z}{\omega}\right) \tag{4}$$

where A, B, G, F, H and ω are constants and A>0, B>0, ω<0, u_z<0. Equation 4 represents the general form of a conic section. If eccentricity (e) of the conic section is less the unity, Equation 4 represents a general form of an ellipse with the major and minor axes oblique to the coordinate axes and center coordinates not necessarily at the origin of the coordinate system. The condition, $e<1$ can also be expressed as $AB-H^2>0$. Equation 4 can be reformatted into the following format, which allows identification of orientation (θ_{ellip}) and center coordinates (x_0, y_0) of elliptical contours directly.

$$Q(x,y)=\frac{\left[(x-x_0)\cos(\theta_{ellip})-(y-y_0)\sin(\theta_{ellip})\right]^2}{r_1^2}+\frac{\left[(x-x_0)\sin(\theta_{ellip})+(y-y_0)\cos(\theta_{ellip})\right]^2}{r_2^2}=-\ln\left(\frac{u_z}{\omega}\right) \quad (5)$$

where $r_1, r_2, \omega, x_0, y_0$ and θ_{ellip} are constants and $r_1>0, r_2>0, \omega<0$. By following back the analogy presented in Equations 2 and 3, a function to delineate a three-dimensional surface heave profile with elliptical contours can be deduced from Equation 5 as:

$$u_z=\omega e^{-Q(x,y)};\ A>0,\ \omega<0 \quad (6)$$

Equation 6 is known as "Gaussian" function. It contains six design variables; $\omega, x_0, y_0, r_1, r_2$ and θ_{ellip}. Since r_1 and r_2 are constants, eccentricity $\left(=\frac{\sqrt{|r_1^2-r_2^2|}}{r_1}\right)$ is a constant for all the contours of a single Gaussian surface heave function. In order to vary eccentricity with increasing lateral distance as depicted in Figure 1(b), a summation of at least two Gaussian functions needs to be considered as given in Equation 7. More complicated three-dimensional surface deformation profiles with complex contour shapes and several peaks and valleys can be generated by considering a series of several Gaussian functions. Further, two-dimensional deformation profiles can be delineated more accurately by considering a series of normal distribution functions in a manner similar to three-dimensional cases.

$$u_z=\omega_\eta e^{-Q_\eta(x,y)}+\omega_\varsigma e^{-Q_\varsigma(x,y)} \quad (7)$$

3. TILT VECTORS

Surface deformation gradients along two mutually perpendicular directions (X and Y directions) can be measured using tiltmeters. Considering a three-dimensional surface deformation function, $u_z=f(x,y)$, X gradient (g_x) and Y gradient (g_y) can be obtained by taking partial derivatives $\frac{\partial u_z}{\partial x}$ and $\frac{\partial u_z}{\partial y}$ respectively. Based on concepts of directional derivatives, the maximum slope (θ_{tilt}) of surface deformation at a given point and direction of maximum slope (α_{tilt}) can be expressed as given in Equation 8. Magnitude and direction of tilt vectors are given by (θ_{tilt}) and (α_{tilt}) respectively.

$$\theta_{tilt}=\tan^{-1}\left(\sqrt{(g_x)^2+(g_y)^2}\right) \quad \text{and} \quad \alpha_{tilt}=\tan^{-1}\left(\frac{(g_x)}{(g_y)}\right) \quad (8)$$

4. SYNTHETIC TILTMETER DATA

Surface vertical displacements occur due to an assumed volume change distribution in a reservoir at a depth of 470 m were computed by solving a forward problem presented by Nanayakkara and Wong (2010). The assumed volume change distribution (denoted by $\mathbf{v}^{exact}$) is depicted in Figure 4. Figure 1(a) depicts the surface vertical displacements (denoted by s^{pure}) and Figure 1(b) depicts the contours of vertical displacements. These vertical displacements were used to generate synthetic tiltmeter data for curve fitting. First, X and Y gradients at a set of grid points (considering a grid of 10m by 10m elements) were computed and then the gradients were perturbed with a random error distribution (percentage of average magnitude of errors in X direction and average magnitude of X gradient is approximately 7%, a same percentage of errors is considered in Y direction). Next, a few of the grid points were selected to represent tiltmeter sites and perturbed tilt vectors (i.e. θ_{tilt} and α_{tilt}) at these tiltmeter sites were computed by using perturbed X and Y gradients according to Equation 8. Pure tilt vectors (considering unperturbed gradients) and error tilt vectors (corresponding to random error distribution) at tiltmeter sites were also computed in a similar manner.

5. OPTIMIZATION USING SYNTHETIC TILTMETER DATA

Suitability of delineating surface heave illustrated in Figure 1 with two Gaussian functions was investigated by considering Equation 7. Since all elliptical contours in Figure 1 are concentric and aligned in two mutually perpendicular directions, it can be considered that x_0, y_0 and θ_{ellip} are common to both Gaussian functions. Further, considering the center of elliptical contours is located at the origin of the coordinate system (i.e. $x_0 = 0, y_0 = 0$), the number of unknowns in Equation 7 can be reduced to the following seven variables; $\omega_\eta, \omega_\varsigma, r_{\eta 1}, r_{\eta 2}, r_{\varsigma 1}, r_{\varsigma 2}, \theta_{ellip}$. Equation 7 can be expressed in terms of X and Y gradients as follows:

$$g_x = \frac{\partial u_z}{\partial x} = \omega_\eta \frac{\partial\left(e^{-Q_\eta(x,y)}\right)}{\partial x} + \omega_\varsigma \frac{\partial\left(e^{-Q_\varsigma(x,y)}\right)}{\partial x} \quad . \tag{9}$$

$$g_y = \frac{\partial u_z}{\partial y} = \omega_\eta \frac{\partial\left(e^{-Q_\eta(x,y)}\right)}{\partial y} + \omega_\varsigma \frac{\partial\left(e^{-Q_\varsigma(x,y)}\right)}{\partial y} \tag{10}$$

Equations 9 and 10 can be considered as model equations, which contain seven design variables and tiltmeter measurements. Since each tiltmeter site provides two measurements (i.e. X and Y gradients), minimum of four tiltmeters are necessary to determine the seven design variables. However, four tiltmeters would not be sufficient to capture the spectral characteristics of the entire surface heave and in general, it is necessary to consider a large number of measurements than the number of design variables to yield fruitful results from an optimization problem.

According to the Least Squares method, the seven design variables, which best-fit the two model equations can be determined by minimizing total deviation of measured data from prediction based on model equations. Accordingly, objective functions can be expressed as:

$$\text{Objective function1} = \sum_{k=1}^{m}\left[\omega_\eta \frac{\partial\left(e^{-Q_\eta(x_k,y_k)}\right)}{\partial x} + \omega_\varsigma \frac{\partial\left(e^{-Q_\varsigma(x_k,y_k)}\right)}{\partial x} - \left(g_x\right)_k\right]^2 \tag{11}$$

$$\text{Objective function } 2 = \sum_{k=1}^{m}\left[\omega_{\eta}\frac{\partial\left(e^{-Q_{\eta}(x_k,y_k)}\right)}{\partial y}+\omega_{\varsigma}\frac{\partial\left(e^{-Q_{\varsigma}(x_k,y_k)}\right)}{\partial y}-\left(g_y\right)_k\right]^2 \quad (12)$$

where (x_k, y_k) are coordinates at k^{th} tiltmeters site, $(g_x)_k$ and $(g_y)_k$ are X and Y gradients at k^{th} tiltmeters site . Objective functions given by Equations 11 and 12 contain two independent variables (x_k and y_k) and two dependent variables $(g_x)_k$ and $(g_y)_k$. Each objective function is not linear in design variables and contains multiple independent variables. Therefore, considering two objective functions separately, the problem can be categorized as “nonlinear multiple regression analysis". However, since there are two objective functions to be minimized simultaneously, the problem falls into the category of “multi-objective optimization". In practice, multi-objective optimization problems are reformulated into a single objective function by forming a weighted combination of different objective functions. Since both of the objective functions are equally important, two objective functions can be combined into one by considering unit weights.

Further information regarding the surface heave profile can be integrated into the optimization process by specifying bounds for design variables. Since $r_{\eta 1}, r_{\eta 2}, r_{\varsigma 1}, r_{\varsigma 2}$ are associated with the major and minor axes lengths of elliptical contours, these design variables must be positive. In order to obtain a profile of a heave as opposed to a subsidence ω_{η} and ω_{ς} must be negative (note that upwards vertical displacements are considered as negative).

The constrained optimization problem (objective function + bound constraints) was converted into an unconstrained optimization problem by applying the penalty function method and it was solved by employing MATLAB's “fminsearch" function. The fminsearch function's algorithm is based on Nelder-Mead Simplex method (Lagarias et al. 1998). This is a direct search method and it does not depend on numerical or analytical gradients of the objective function. Further, this method does not guarantee determination of the global minimum. Since the objective function is highly nonlinear and it could contain several local minima, a MATLAB program was written to perform direct search from multiple start points. By adopting this scheme, the optimization problem was solved successfully.

Figure 2 depicts contours of the curve fitted surface heave along with contours of pure surface heave. Nine tiltmeters were considered in the optimization problem and the selected tiltmeter site locations are denoted by small circles. Pure, perturbed and curve fitted tilt vectors at tiltmeter sites are depicted by arrows. It is difficult to distinguish between the different types of tilt vectors as they do not differ significantly. A three-dimensional profiles of curve fitted vertical displacements and pure surface heave are plotted together in Figure 3.

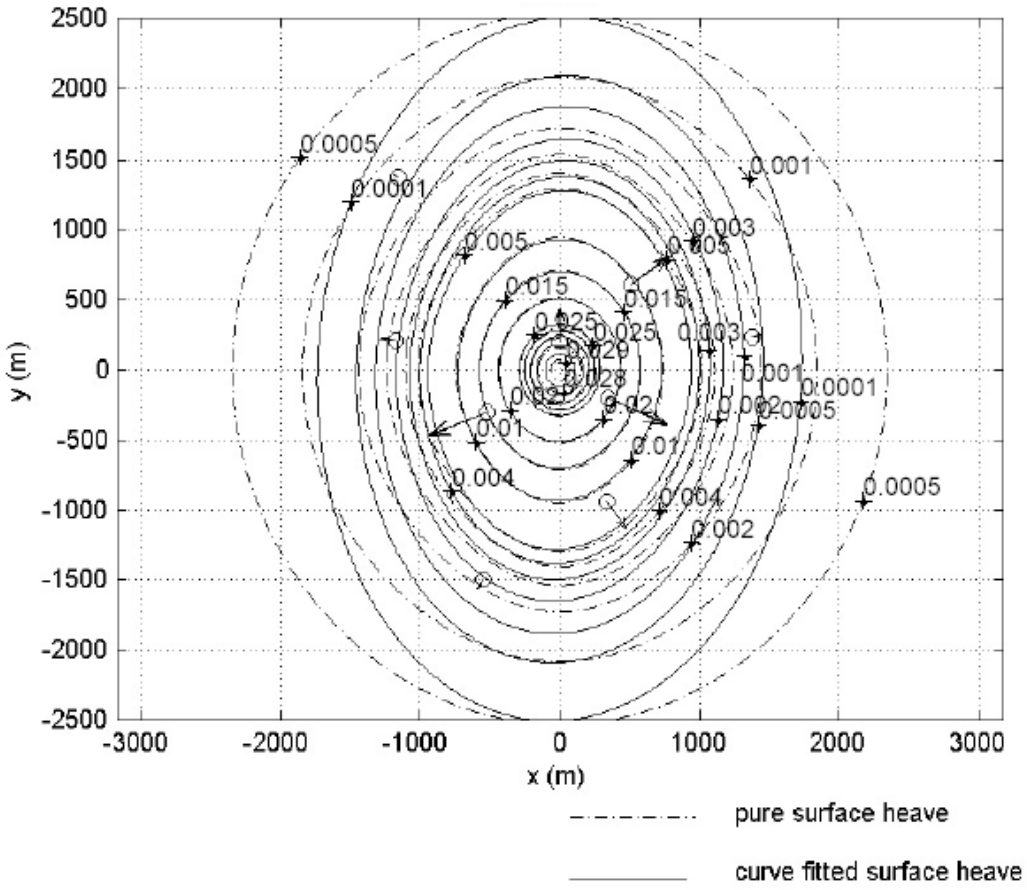

Figure 2 - Vertical displacement contours of curve fitted and pure surface heaves

6. INVERSION USING SYNTHETIC TILTMETER DATA

An inverse problem was solved by inverting vertical displacements extracted from the curve fitted surface heave depicted in Figure 3. The standard form of Tikhonov regularization technique was applied to solve the inverse problem by adopting the technical approach (Nanayakkara and Wong 2010).. Figure 4 illustrates inverted volume change distribution (denoted by $\mathbf{v}^{reg}$) matches well with the assumed volume change distribution (denoted by $\mathbf{v}^{exact}$).

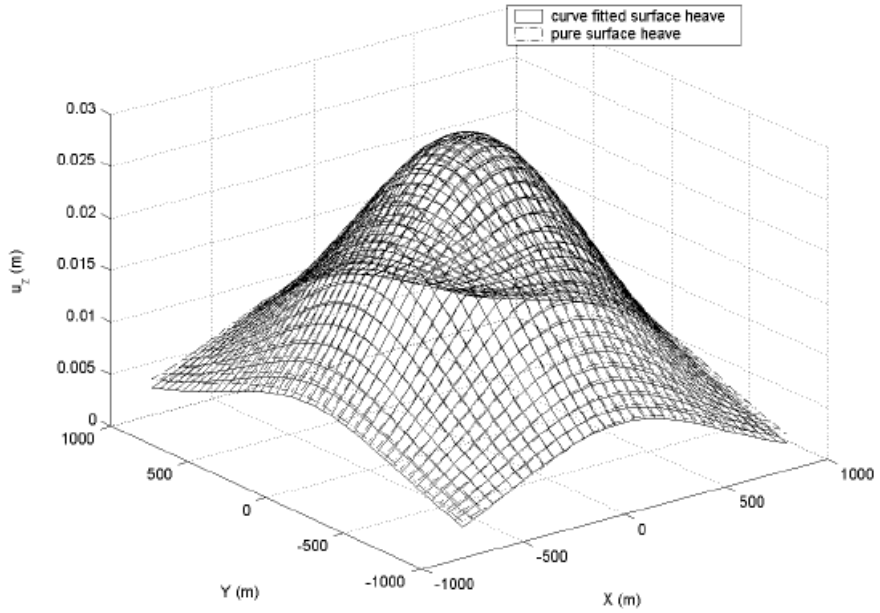

Figure 3 - Curve fitted and pure surface heave

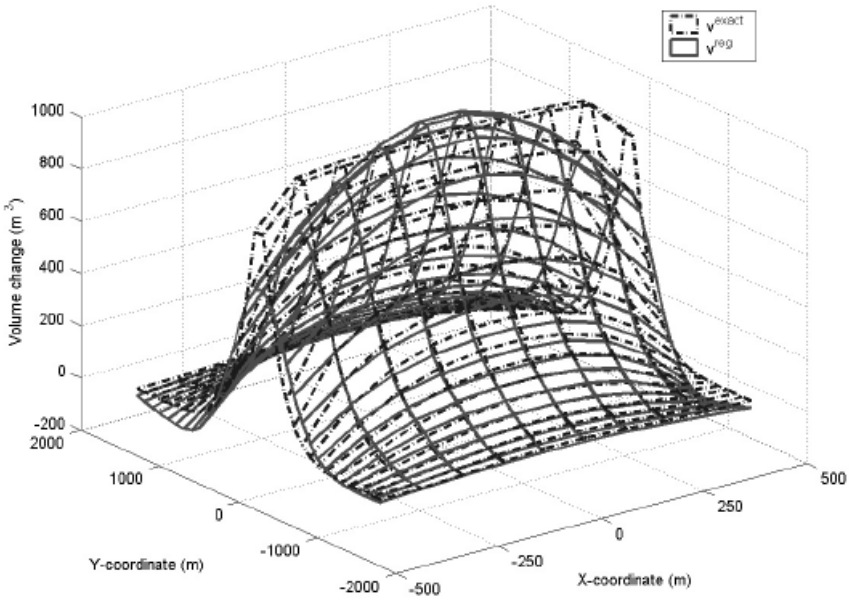

Figure 4 - Assumed (v^{exact}) and inverted (v^{reg}) volume change distribution

7. DISCUSSION

Figure 3 indicates that matching between the curve fitted and pure surface vertical displacements over an area which spans approximately from X = -1000 m to 1000 m and Y = -1000 m to 1000 m is satisfactory. However, according Figure 2, matching between curve fitted and pure surface heave contours close to the outer perimeter of surface deformation area is not very satisfactory. This occurred as tiltmeters are distributed only over a circular area with a radius of 1800 m. Therefore, in order to achieve successful

results from curve fitting, tiltmeters should be scattered over an area sufficiently large enough to capture the vital spatial characteristics of surface deformation.

Since a satisfactory match between the assumed and inverted volume change distribution has to be achieved, for a case with similar parameters, it would be sufficient to consider 9 to 10 tiltmeters, if tiltmeter measurements are relatively free of noise. However, in practical situations, surface tiltmeter measurements are sometimes contaminated by various sources of noise. Further, localized random noises could occur at few tiltmeter sites and the magnitudes of noise could even be larger than pure tilt signals occur due to reservoir dilations. In these situations, it may be necessary to discard the contaminated data. Therefore, it would be better to use a few more tiltmeters than the minimum required.

Further, results of this study indicate it is sufficient to consider two Gaussian functions with common x_0, y_0 and θ_{ellip} to delineate the surface heave illustrated in Figure 1. However, in practical situations, more complicated surface heave profiles could occur and the resulted surface heave contours may not be exactly elliptical. In this case, a suitable number of Gaussian functions should be selected depending upon the anticipated degree of distortion of contours and availability of surface deformation measurements. Further, it should be noted that the proposed surface heave function is an approximation and even a series with a large number of Gaussian functions is considered, it may not be feasible to replicate the exact surface deformation profile.

8. CONCLUSIONS

Results of the case study presented demonstrate pseudo surface deformation data generated by curve fitting can be successfully utilized to infer reservoir volume changes with reasonable accuracy and high spatial resolution. This method is useful when the number of available tiltmeter measurements is insufficient to acquire the desired spatial resolution of volume changes.

9. ACKNOWLEDGEMENTS

The authors would like to thank for the financial support provided by AERI, NSERC and Schulich School of Engineering, University of Calgary.

10. REFERENCES

LAGARIAS, J., REEDS, J. A., WRIGHT, M. H., AND WRIGHT, P. E., 1998. Convergence properties of the Nelder-Mead Simplex method in low dimensions. SIAM Journal of Optimization, 9(1), pp.112-147.

NANAYAKKARA, A. S., WONG, R. C. K., 2010. Using surface deformation to estimate reservoir dilation: Strategies to improve accuracy. Journal of Canadian Petroleum Technology, 49(11), pp. 49-60.

PECK, R. B., 1969. Deep excavation and tunneling in soft ground. Proceedings of 7th International Conference on Soil Mechanics and Foundation Engineering.

SCHMIDT, B., 1969. Settlement and ground movements associated with tunneling in soil. Ph.D. dissertation, University of Illinois.

WONG, R.C.K., CHAU, K., 2004. Casing impairment induced by shear slip along a weak layer in shale due to fluid (steam) injection. Proceedings of 5th Canadian international petroleum conference (55th annual technical meeting).

Influence of Geomechanical Processes on Relative Permeability

Mohamed Hamoud
University of Alberta
Rick Chalaturnyk
University of Alberta
Juliana Leung
University of Alberta

ABSTRACT: Relative permeability curves represent an important element of special core analyses, but challenges remain in obtaining valid results and the extrapolation and use of existing permeability results is problematic. This situation is compounded in cases where core properties are altered from changes in effective stress. During the production of oil and gas reservoirs, the effective stress changes as a result of changes in pore pressure or temperature. Therefore, changes in rock properties such as porosity and permeability will occur and will consequently influence reservoir performance calculations. An experimental program was carried out to understand the behavior of dense, reconstituted sand samples at low effective stress states. Drained triaxial compression tests were set up to study the effect of stress alteration on relative permeability data through porous media. Initially, a saturation stage was performed followed by isotropic loading to bring the core sample to reservoir fluid and stress conditions. Then, while axial (deviatoric stress) loading was applied to the sample, a series of absolute and relative permeability tests was performed under steady state flow at different levels of strain during pre and post peak shearing stress. The stress-strain behavior results from the study revealed that the absolute permeability decreased during isotropic loading (compaction) and increased during shearing (dilation). However, the shape of relative permeability curve changed from contraction to dilation and showed higher initial k_{ro} and the lower initial k_{ro} respectively. The goal of this project was to understand the behavior of both absolute and relative permeability at different stresses. It is expected that geomechanical processes will be adopted for special core analyses to support the current integration of geomechanics into reservoir engineering. This will be required if, during SAGD, conventional and/or unconventional reservoir simulation, reservoir engineers implement a proper set of relative permeability data at each in situ state of stress, instead of constant curves throughout the field's life.

1. INTRODUCTION

Permeability alteration due to isotropic or mean stress change has been studied by many authors. Fatt and Davis (1952) investigated this phenomenon in clean dry sandstone and at reservoir stress condition; they concluded that the changes in effective stress lead to reduction of absolute permeability. Similarly, Dobrynin (1962) studied the effect of stress on rock properties. He found the reduction of pore volume engenders a decrease of absolute permeability. In the same context, Gray and Fatt (1963) studied the effect of permeability anisotropy on different reservoir stress conditions showing that anisotropy was a function of stress. Marek (1978) observed a sharp reduction in absolute permeability under high confining pressure.

At low effective confining stress states, the variation of stress on permeability has also been investigated by many researchers. Scott et al. (1991) found that between a confining stress of 1 and 1.5 MPa there was an increase of 32 % of permeability during dilation stage. These results are similar to Oldakowski's (1994) and Tohidi-Baghini's (1998) work.

Fatt (1953) conducted some of the initial research on relative permeability under confining stress. He

measured the gas/oil relative permeability at 20.7 MPa and found that there was not a great change in relative permeability curves at this confining pressure. Wilson (1956) followed Fatt's work by performing relative permeability measurements at different confining pressures and under simulated reservoir conditions. He found a small change in effective permeability compared to the effect of stress on absolute permeability. However, Wilson observed a small sensitivity to stress between relative and absolute permeability, which was different from Fatt's work (1953). In the same regard, other authors such as Ali et al. (1987) conducted relative permeability tests on Berea Sandstone samples under different confining stresses. They found that connate water and residual oil increase with increases of effective stress and also noted that relative permeability data are more sensitive to effective stress than absolute permeability. Jones et al. (2001) investigated, for different types of sandstones, the variation of relative permeability with stress and found that the stress effects were related to rock type. Jones and Smart (2002) carried out permeability experiments with single phase and two-phase flooding during deformation and at two high, fixed confining pressures. They found that the changes of sandstone's permeability were dependent on the presence of liquid phases. Recently, Khan (2009) studied the effect of different effective stresses on relative permeability end points. He concluded there was a decrease of relative permeability during compaction and an increase through dilation.

There has been no previous work performed on the influence of shear stress on relative permeability for multiple saturation states and at different levels of strain. Therefore, in this study, the steady state method is chosen to conduct relative permeability experiments at different levels of axial strain during drained triaxial shearing of reconstituted core samples.

2. EXPERIMENTAL

The synthetic core samples were prepared from unconsolidated sand, in which a technique developed at the University of Alberta was used to prepare uniform dense, cylindrical core samples of 50mm diameter and 50mm height (see the detailed method in an Appendix). Sieve analyses showed that the average grain size was in the range of 140-200 mesh (Figure 1). SEM analyses of different sections of synthetic sand revealed that overall silica (SiO_2), which forms quartz, is the main constituent. The artificial sand had a specific gravity of 2.71. The average porosity of all specimens was 34-35%, and the average absolute permeability for this synthetic sand was 1.5 Darcy. Regarding the wettability of specimens, all sample preparation occurred under water saturated conditions, so it is assumed that the system is water wet.

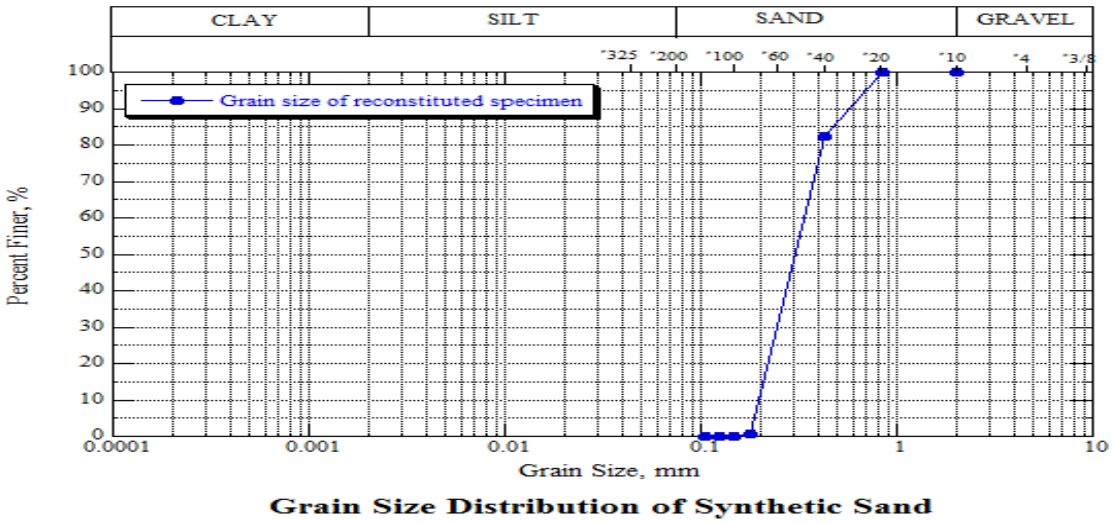

Figure 1 - Grain size distribution curve of synthetic sand

The triaxial cell used in this research is acrylic and can support a maximum confining pressure of 1100 kPa. A Wykeham Farrance load frame model was chosen for this study, which provides constant displacement rates over the range of 5.715 (mm/min) and 57.15 $x10^{-5}$ (mm/min) and an axial load capacity of 9 kN. Axial displacement was monitored using externally mounted LVDTs. The volume change of the specimen was monitored by an external volume change device, which was connected to the pore fluid pressure line (Figure 2). Three 260D Isco pumps were used to monitor both cell and pore fluid pressure and to conduct permeability tests. Three pressure transducers were used for measuring confining stress, pore and back pressures (or inlet and outlet fluid pressure). These transducers and LVDT's were connected to a Datataker© data logger.

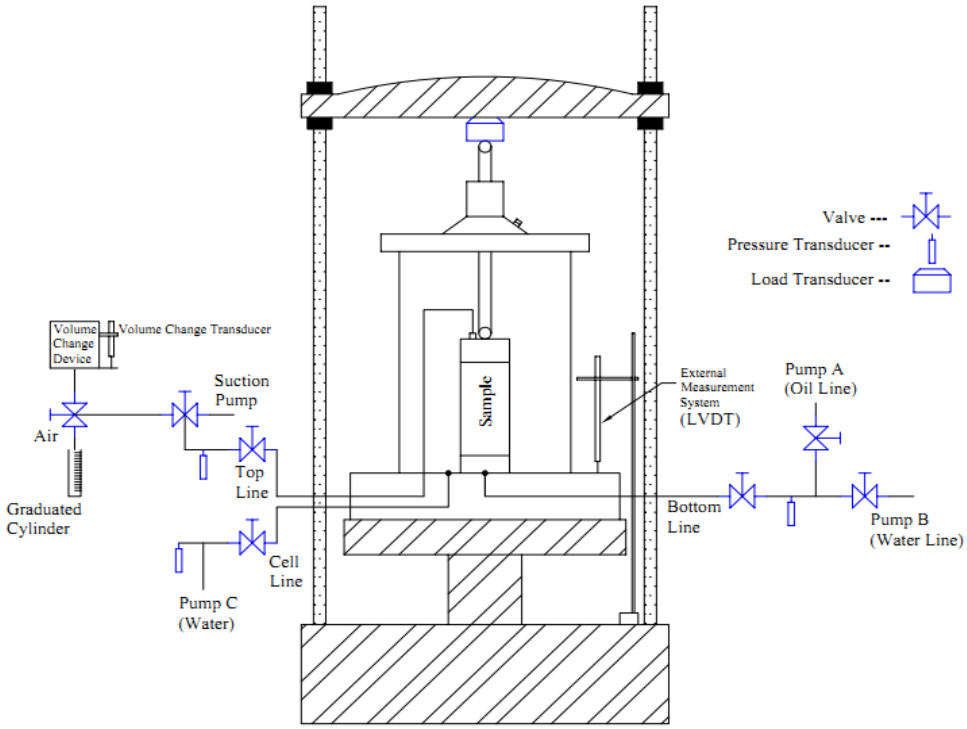

Figure 2 - Schematic view of experimental setup

Drained triaxial shearing tests were used to deform all specimens at a low axial strain rate; 0.03mm/min. Deionized water and a commercial mineral oil were used as pore fluids to perform the permeability tests. Saturation profiles were deduced using an external material balance approach whereby the volume fluids within the core were computed from the difference between the total volume produced and injected, as measured using graduated cylinders.

All experiments began with a saturation stage, in which the specimens were brought to reservoir fluid conditions. A vacuum pump was set to de-air the system (lines & valves) and then a flash of 5 pore volumes of water was followed to attain a fully water saturation in the core sample. The system was maintained at an effective stress of 100kPa for period of 5 days, and then the cell pressure was incrementally increased. Subsequently, a B test was conducted to check whether a full saturation was achieved (Head, 1986). This was followed by an isotropic loading step to bring the core sample to reservoir effective stress conditions of 600 kPa. Permeability tests were conducted at an effective stress of 600 kPa, with the downstream pore pressure lines set at atmospheric.

As a quality check on the stability of the flood and flow regimes, the scaling factor and Reynolds number were verified, respectively. In addition to that, an interfacial tension measurement was also conducted

between deionized water and mineral oil by using duNouy Tensionmeter (ASTM D971-50), commonly called the duNouy ring method, which is indispensable for calculating the Capillary number and therefore testing whether capillary forces or viscous forces dominate waterflood displacement.

Preliminary drained triaxial compression tests were carried out at three effective stresses states of 50, 200, and 600kPa to understand stress-strain behavior of the reconstituted dense sand samples.

Absolute permeability tests were performed under steady state conditions during isotropically loaded, drained triaxial compression tests at 600 kPa effective confining stress and at different levels of strain. Steady state conditions were assumed to have been reached when flow into was equal to flow out of the specimen and when the pressure drop across the sample had stabilized at a constant flow rate of 10 ml/min. Measurements at various axial strain levels were achieved by using separate, nearly identical (i.e., initial porosity) specimens that were each strained to incrementally larger axial strains. This provides increased accuracy for absolute permeability measurements and minimizes the impact of hysteresis. Darcy's law was applied to calculate the absolute and effective permeability.

During the shearing process, the cross section and height of the core sample changed at each level of strain; changes that impact permeability calculations. To overcome this, a systematic correction of area and height of specimen was made through permeability calculation for each strain level, based on changes in axial displacement and volumetric strain.

Under drained triaxial compression conditions, relative permeability tests were conducted systematically after each absolute permeability test, using the steady state technique, at effective stress of 600 kPa and at five selected axial strain states of 0%, 2%, 5%, 10% and 15% covering the full range of volumetric behavior of the specimens. Each of these test locations is noted as red dots in Figure 3.

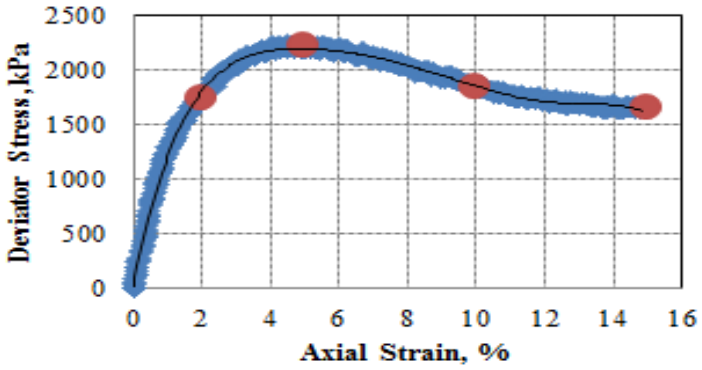

Figure 3 - Graphical representation of five selected strain states

The two-phase flow was conducted to determine effective permeability of each fluid (water and oil) by Darcy's law. Eventually, the relative permeability of each phase at the corresponding average saturation was calculated from the ratio of the effective permeability of the phase to the absolute permeability of core sample

$$(K_{rw} = k_{effw}/K_{abs} \text{ and } K_{ro} = k_{effo}/K_{abs}).$$

All relative permeability experiments in this study were duplicated in order to assess the repeatability of the results.

3. RESULTS AND DISCUSSION

The preliminary drained triaxial compression test results for three effective stresses of 50 kPa, 200 kPa and 600 kPa are shown in Figures 4 and 5. The results show classic expected behavior for dense, uncemented sands where, for increasing effective confining stress, stiffness increases, the deviator stress at failure increases and the volumetric strain decreases.

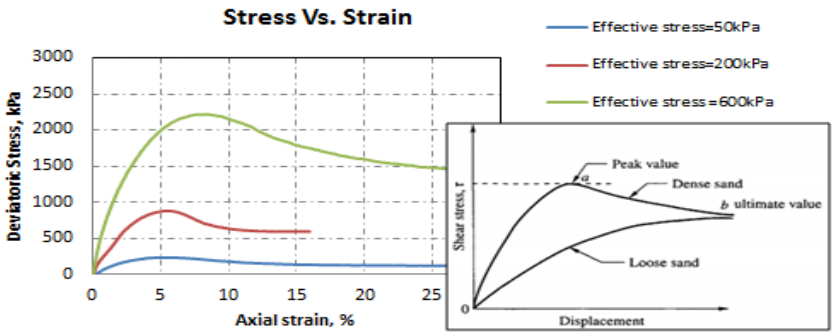

Figure 4 - Stress-strain of three effective stresses

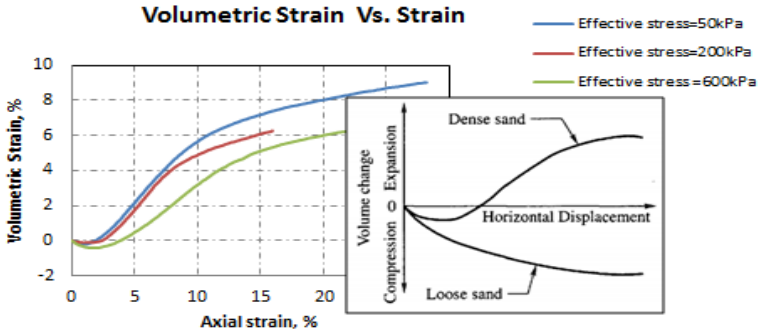

Figure 5 - Volumetric-strain of three effective stresses

Table 1 provides a summary of deviator stress, axial strain and volumetric strain at failure.

Table 1 - Deviatoric stress and volumetric strain at failure of three effective stresses

Effective stress=50kPa			Effective stress=200kPa			Effective stress =600kPa		
Deviatoric Stress kPa	Axial Strain %	VoL Strain %	Deviatoric Stress	Axial Strain %	VoL Strain %	Deviatoric Stress kPa	Axial Strain %	VoL Strain %
235	**5.5**	**3.4**	**879**	**5.5**	**2.2**	**2322**	**6.1**	**2.4**

Results from this study also demonstrated that the flow regime was laminar during both single and two-phase flow testing. Furthermore, the scaling factor ($Lv\mu_w$), which combines the effects of core length, flooding rate and water viscosity, proposed by Rapoport et al. (1953) in order to check the stability of a flood, was within the tolerable range 0.75 to 2.5. Table 2 summarizes the stabilization criteria for each flow rate.

Table 2 - Flow stabilization criteria

Q_w cc/min	IFT (w/o) mN/m	Capillary Number N_c	Scaling Factor $Lv\mu_w$ cm^2cp/min	Flow Regime Check Re
3	64	1.11E-06	0.75	0.007
5	64	1.85E-06	1.25	0.012
7	64	2.59E-06	1.75	0.017
10	64	3.71E-06	2.51	0.025

As illustrated in Figures 6 and 7, over the range of axial strains measured in this test program, absolute permeability clearly decreased during compaction, reaching roughly 67% below its initial value (1.5 D) at 5% of axial strain, and increased during dilation, attaining an increase of approximately 33% at the end of the test compared to its initial value. The initial permeability reduction occurred due to the initial compaction of the grain matrix, followed by a post-peak increase of permeability resulting from the dilatant re-arrangement of grains and increase in porosity. These variations of absolute permeability during compaction and dilation have been shown by many authors such as Oldakowski (1994), Touhidi (1998) and Yaich (2008).

Table 3 - Summary of permeability and porosity at each levels of axial strain

Axial Strain %	Absolute Permeability D	Porosity Frac	Normalized Permeability
0	1.50	0.3475	1.00
2	1.00	0.3448	0.67
3	0.66	0.3457	0.44
5	0.50	0.3503	0.33
9	0.52	0.3642	0.35
11	0.59	0.3707	0.39
15	1.06	0.3792	0.71
20	1.99	0.3846	1.33

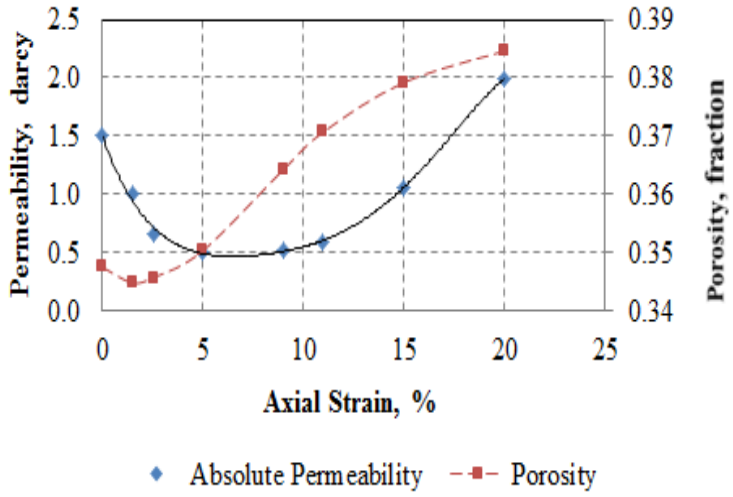

Figure 6 - Variation of permeability and porosity at different levels of axial strain

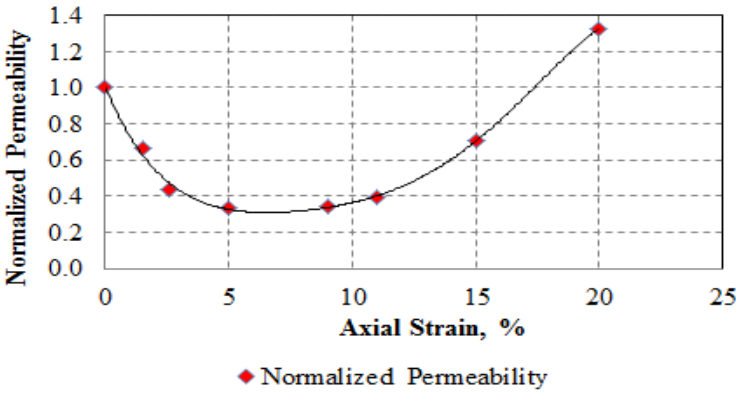

Figure 7 - Variation of normalized permeability at different levels of axial strain

Under two-phase flow conditions, the average irreducible water saturation during drained triaxial compression (Figure 8) and from compaction to dilation ranged from 8 to 13%, which is consistent with Polikar (1988). The overall residual oil saturation, however, varied between 11-23% (Figure 8).

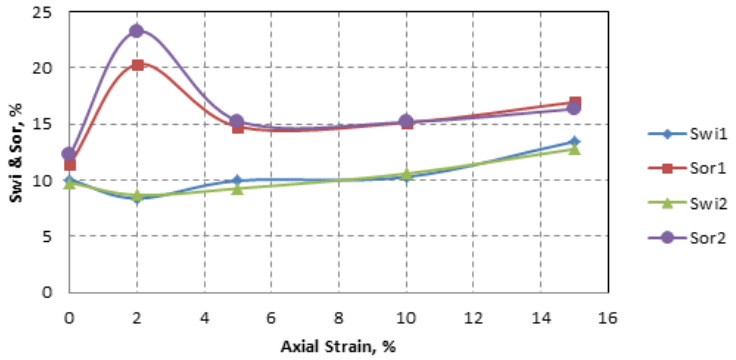

Figure 8 - Saturation end points versus axial strain

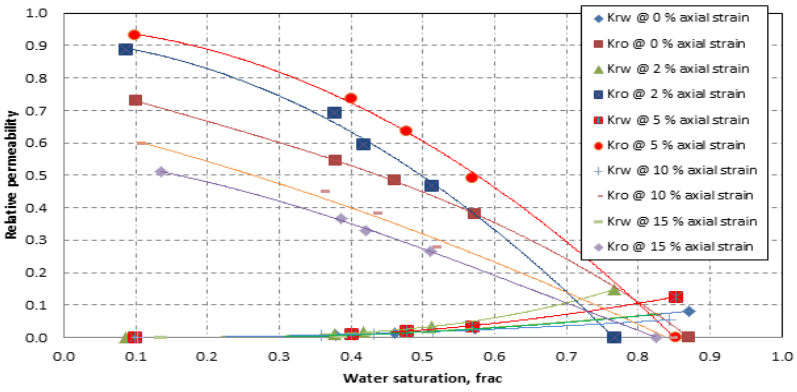

Figure 9 - Sensitivity of relative permeability at different levels of axial strain

The oil relative permeability curves measured in this study revealed convex shapes, as illustrated in Figure 9. It has also been observed that two-phase flow varied over a wide range prior to shearing of the specimen, but the range of results narrowed considerably following initial consolidation (compaction) of the specimens. These findings match those reported by Morgan et al. (1970). For the shearing stages,

however, range of results showed increasing variability, as shown in Figure 9.

Figures 10 and 11 illustrate the variation of end point saturations with volumetric strain and deviatoric stress, respectively. Morgan et al. (1970) state that pore geometry is the main parameter that affects relative permeability. As shown in Figures 10 and 11, the decrease of irreducible water from 10% to 8.4% resulted from a decrease in specimen volume (contraction). As the specimen contracted the pore volume decreased, resulting in water being displaced into larger voids where the displacing fluid (oil), which normally occupied these larger pores, was displaced. This lead to an increase in the volume of mobile water flowing out of the specimen and therefore a decrease of irreducible water.

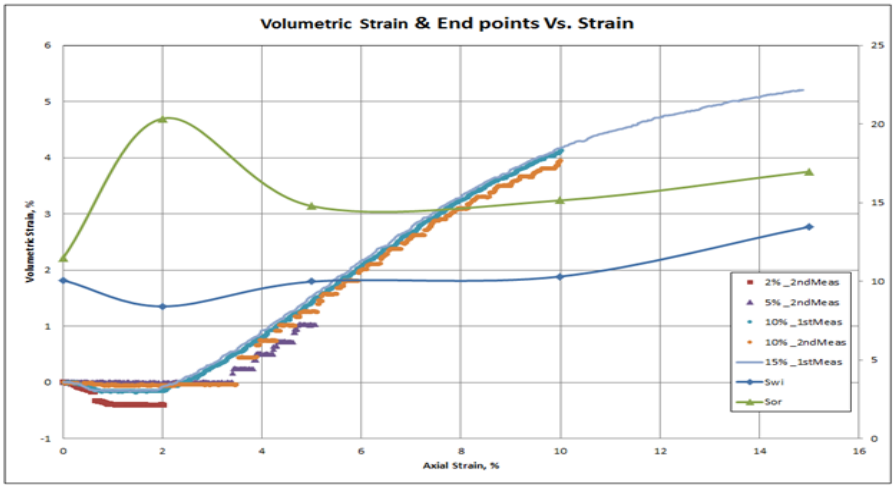

Figure 10 - Volumetric strain and saturation end points at different levels of axial strain

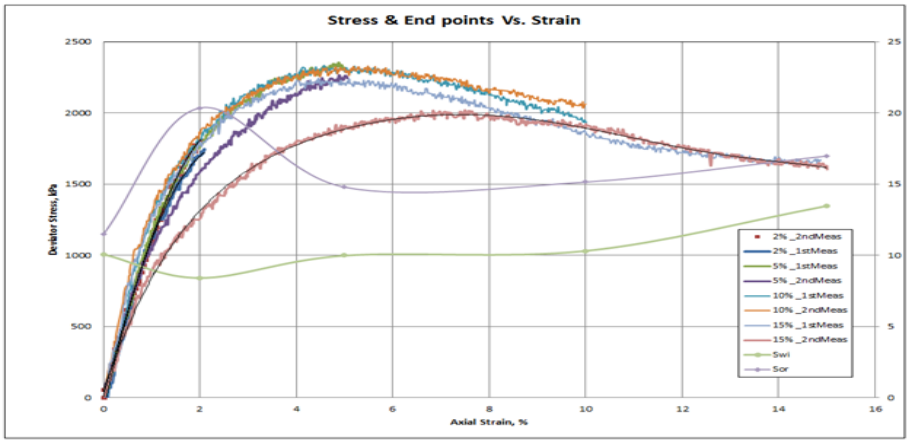

Figure 11- Deviatoric stress and saturation end points at different levels of axial strain

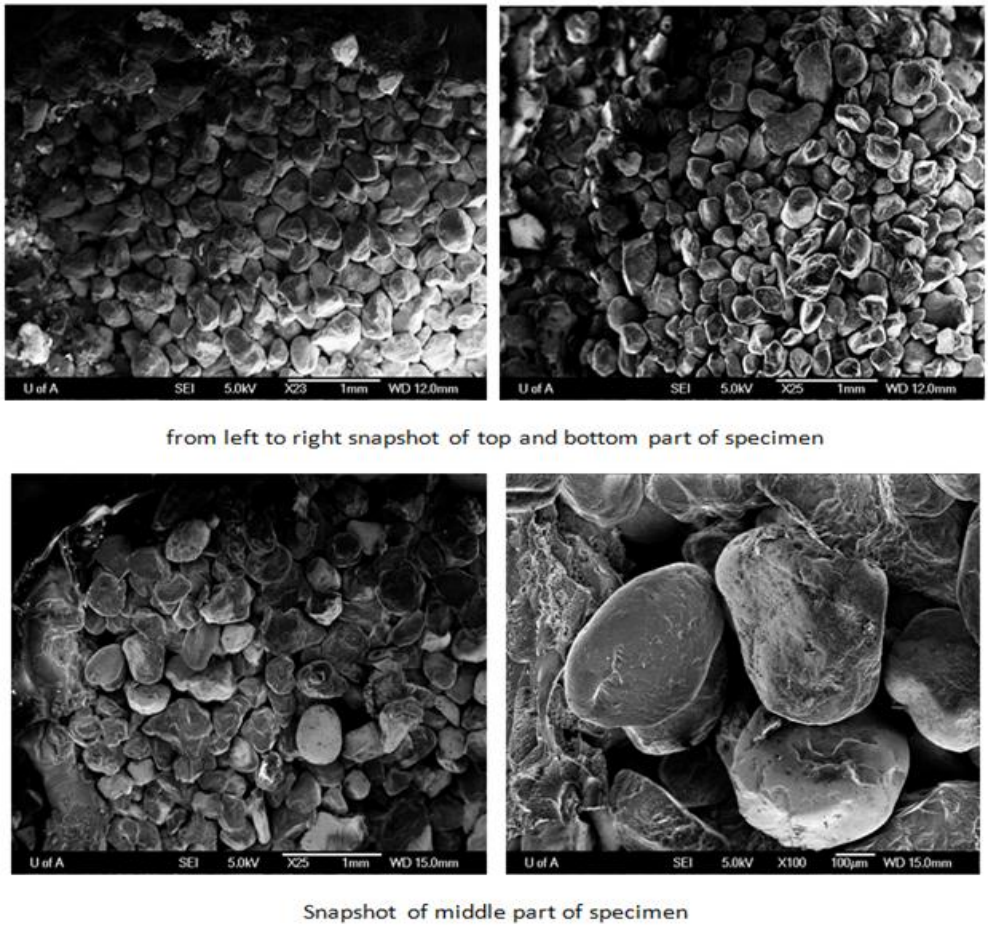

Figure 12 - Snapshot of SEM analyses

At the onset of dilation at an axial strain of ~ 5% the irreducible water saturation began to increase slightly, ending at a value just below its initial value of ~10.0%. As the deviator stress decreased towards the final post-peak stress value, the irreducible water rose to approximately 13.5%. The increase in S_{wi} was due to the pore surface area likely changing from smaller to larger pores as a result of dilatant volume changes within the specimen. This behavior was verified during the imbibition process where the capillary number was in the range of 10^{-6}, similar to a typical waterflood process. Under such conditions, according to Foster (1973) and Melrose and Brander (1974), capillary forces dominate the flow process.

Residual oil saturation, however, displays a more complex response to volumetric changes within the specimen, as shown in Figures 10 and 11. The residual oil saturation began to rise during initial compaction of the specimen, attaining a peak value 20.3% just as the volumetric behavior transitions from compaction to dilation. At approximately the peak deviatoric stress (axial strain ~ 5%), S_{or} decreases to approximately 14.8 % and then displays a mild increase with increased straining reaching a final value of 17% at an axial strain of 15%. A similar increase/decrease in S_{or} with volumetric strain was also found by Khan (2009). It can be clearly seen that compaction affected residual oil saturation and therefore the recovery factor. This was due mainly to the larger pore surface area created at compaction stage, in which the pores' volumes became smaller and consequently inhibited flow of the mobile fluid phase. In the first stage of dilation, where the failure caused increasing pore volumes, there was an increase of residual oil saturation respective to small surface area and then large pores; Morgan et al. (1970). Eventually, when the shearing reached its post-peak value at 15% axial strain, the flow path changed and was likely

influenced by the presence of a shear surface inclined to the axis of the specimen (as governed by its internal friction angle of approximately 33°) and the tortuosity of the porous medium would have definitely been altered. In addition, because of the boundary conditions within the triaxial test, the distribution of porosity changes within the specimen at this axial strain (15%) was not uniformly distributed. As shown in Figure 12, evidence from SEM analysis shows that the arrangement of grains, after shearing tests, in both upper and bottom parts of specimen was more compacted than in the middle one. Within the compacted zone (adjacent to the specimen end platens), the capillary forces would dominate flow and would influence measurement of S_{or}. The development of these compacted regions was also evident in the results of differential pressure during different levels of strain and from the first cycle of oilflood showed that the displacement (entry) pressure increased gradually as axial strain rose (Figure 13), so the degree of pore closure was controlled by this entry pressure.

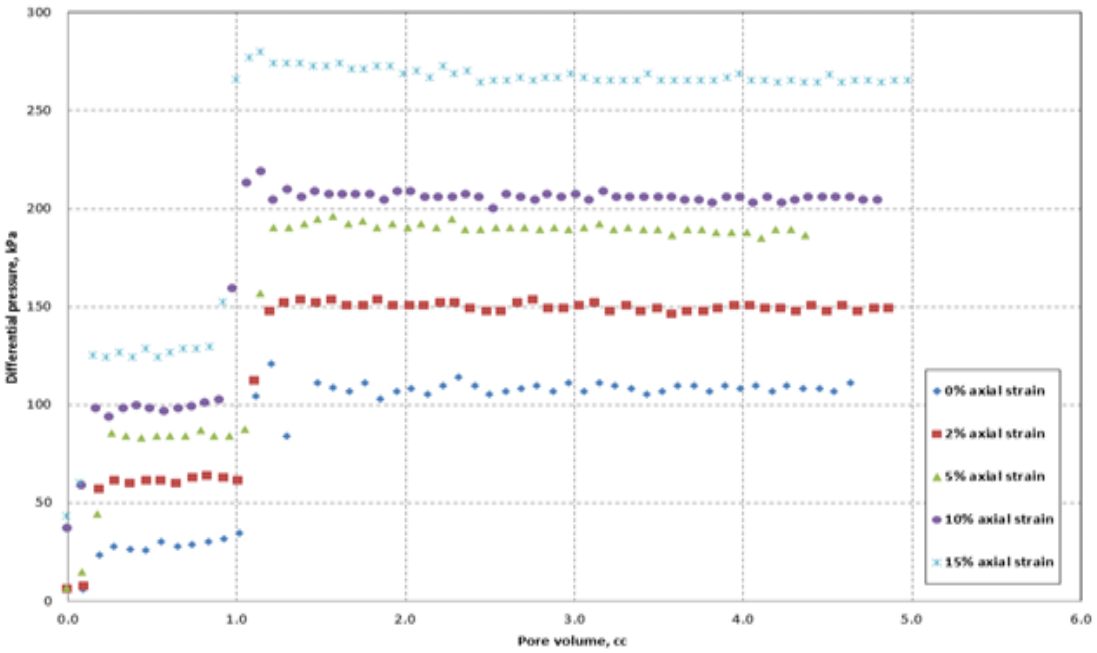

Figure 13 - Differential pressures as function of pore volume at different levels of axial strain

Hence, on the above results, the residual oil saturation increased from 14.8% to 17.0% for axial strains of 10% and 15%, respectively.

4. CONCLUSIONS

- The results generated in this work support the belief that rock properties such as porosity and permeability change significantly in unconsolidated and shallow reservoirs during stress change;
- Irreducible water saturation, S_{wi}, decreased during compaction followed by moderate increase during shear induced dilatant volumetric strain with the specimens;
- Changes in S_{or}, the residual oil saturation, displayed a complex behavior, controlled by to the shear induced volumetric changes within the specimen;
- Oil relative permeability curves displayed convex shapes;
- Initial k_{ro} increased gradually from 0.729 to 0.888 and to 0.932 at axials strains of 0%, 2% and 5%, respectively. It then decreased for axial strains in the 5% to 15 % range;
- All relative permeability curves exhibited, at $k_{ro} = k_{rw}$, water saturations above 50%. Therefore, they follow Craig's wettability criteria, which indicates strongly water wet conditions;

- Two-phase flow existed over a narrow range during compaction, and over a wide range variation during dilation;

5. RECOMMENDATIONS

- Future studies should conduct relative permeability tests at true reservoir pore pressures;
- Accurate in situ techniques such as X-ray or CT scans should be used for saturation determination; and
- Extreme care should be taken to avoid desiccation (freeze drying) occurring in frozen specimens as it creates difficulties in achieving saturation with the specimens when operating at low pore pressures.

6. ACKNOWLEDGEMENTS

This work was supported through funding provided by Foundation CMG. I would also like to thank Steve, Saurav, Nathan, Mohammad, Rishi, Kais and Gilbert of the Reservoir Geomechanics Research Group, $[RG]^2$ for their help in the lab and discussions about the testing and results.

7. REFERENCES

ALI, H.S., AL-MARHOUN, M.A., ABU-KAHMSIN, S.A., and CELIK, M.S., 1987. The effect of overburden pressure on relative permeability. Society of Petroleum and Engineering.

CRAIG, F.F., 1971. The reservoir engineering aspects of water flooding. Monograph series.

DOBRYNIN, V.M., 1962. Effect of overburden pressure on some properties of sandstones. Society of Petroleum Journal.

FATT, I., and DAVIS, D.H., 1952. Reduction in permeability with overburden pressure. Petroleum transactions, AIME, Vol. 195.

FATT, I., 1953. The effect of overburden pressure on relative permeability. Journal of the American Institute of Mechanical Engineers, Petroleum transactions, 198.

FOSTER, W.R., 1973. A low-tension waterflooding process. Journal Petroleum Technology.

GRAY, D.H., FATT. I., and BERGAMINI, G., 1963. The effect of stress on permeability of sandstone cores. Society of Petroleum and Engineering Journal.

Head, K.H., 1986. Manual of soil laboratory testing, Vol.3.

JONES, C., AL-QURAISHI, A.A., SOMERVILLE, J.M., and HAMILTON, S.A. 2001. Stress sensitivity of saturation and end–point relative permeabilities. Society of core analysis.

JONES, C., and SMART, B.G.D., 2002. Stress induced in two-phase permeability. Society of Petroleum and Engineering.

KHAN, H.A., 2009. Shear induced relative permeability change in uncemented sands. MSc. Thesis, the University of Texas at Austin.

MORGAN, J.T. and GORDAN, D.T., 1970. Influence of pore geometry on water-oil relative permeability. Journal Petroleum Technology.

MELOROSE, J.C. and BRANDER, C.F., 1974. Role of capillary forces in determining microscopic displacement efficiency for oil recovery by waterflooding. The journal of Canadian Petroleum.

MAREK, B.F., 1979. Permeability loss in depletion of reservoirs. Society of Petroleum and Engineering.

OLDAKOWSKI, K., 1994. Stress induced permeability changes of Athabasca oil sands. MSc. thesis, the University of Alberta.

POLIKAR, M., PUTTAGUNTA, V.R., FERRACUTI, F. and FAROUQ Ali, S.M., 1988. Journal of Petroleum Science and Engineering, p. 263-270.s.

RAPOPORT, L.A. and LEAS, W.J., 1953. Properties of linear waterflood. Trans. AIME, 198, p.139-148.

SCOTT, J.D., ADHIKARY, D. and PROSKIN, S.A., 1991. Volume and permeability changes associated with steam stimulation in oil sands reservoirs. Petroleum society of CIM and AOSTRA technical conference.

TOUHIDI-BAGHINI, A., 1998. Absolute permeability of McMurray formation oil sands at low confining stresses. Ph.D. thesis, the University of Alberta.

YAICH, E., 2008. The effect of shear stress paths and shear failure on the permeability of unconsolidated sands. MSc. Thesis, the University of Texas at Austin.

8. APPENDIX A: SAMPLE PREPARATION

The detailed procedure of preparing uniform dense cylindrical core samples of 2 inch diameter and 2 inch height is consisted of split mold, O-rings bottom pedestal, latex membrane, top plate, top cap, cool blanket, vibration table, vacuum, porous stones (63.5mm & 50.8mm), water, sand and dry ice. This technique is rested on three stages of sand preparation, sand densification and sample freezing (Figure A.1).

1. Sand preparation
   a) Boil three (3) porous stones for roughly 20 min; and
   b) Weigh sand and pour water in till get half the beaker. Boil together sand and water for 30 min for the saturation purpose.

2. Sand densification
   (a) Put latex membrane on the bottom pedestal and sealing with O-rings. And place it on the vibrating table
   (b) Open the saturation valves to remove air, water flow into the bottom of the membrane to a depth of 05 mm, and then close the valves. Then place 63.5 mm porous stone on the bottom pedestal;
   (c) Assemble the split mold and place it on the bottom pedestal, fold the top part of the membrane down over the mold and then seal it with O-rings;
   (d) Apply vacuum at 80 kPa from the split mold;
   (e) Pour gradually the saturated sand into membrane and start the vibration table at low speed(from 03 to 9);

(f) Place a saturated 50.8 mm porous stone on the top and then surcharge weight on the sample to apply vertical loading. Assure that there is 02 to 03 mm of water on the top of the sample;
(g) Hold the surcharge weight vertically over the sample and turn on the vibration table to the speed of 05 to come down to a desired level;
(h) Remove the surcharge, porous stone and unfold the membrane. Again fold the membrane down over the mold and place 63.5 mm porous stone on the sample. Fill up the mold with water;
(i) Place the top cap on top of the porous stone, let the water be pushed out of the drainage valves then close them. Unfold the membrane onto the top cap and seal with O-rings;
(j) Create vacuum inside the sample. Open split mold, place O-rings into right position and close it; and
(k) Put the top plate over the top cap and fasten it. This will avoid any uplift action during freezing

3. Sample freezing densification
(a) Close the bottom valves, open the top ones, and place the whole set-up into freezing box with dry-ice for 30 min;
(b) Disassemble the system (split mold, pedestals, etc.) and sample is ready for storage and testing as well.

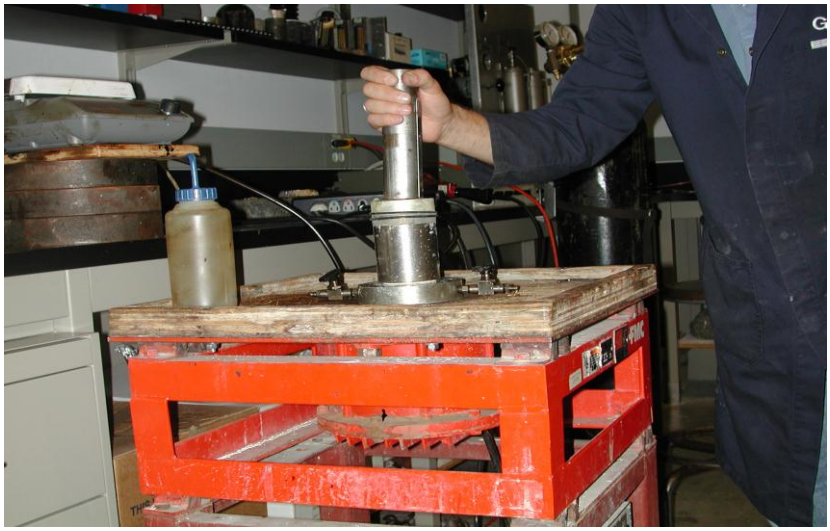

Figure A.1 - Picture of sand preparation material

Local Upscaling of Elastic Moduli for Anisotropic Complex Heterogeneous Facies Models

Mohammad. M. Khajeh
University of Alberta
Richard. J. Chalaturnyk
University of Alberta
Jeff B. Boisvert
University of Alberta

ABSTRACT: Rock mechanical properties are important parameters in geomechanical simulation. Considering stochastic heterogeneous models rather than conventional homogeneous layer cake models leads to more realistic simulation results and uncertainty assessment. These heterogeneous models are usually fine scale models generated by geostatistical techniques. Although considering high resolution property models is desirable, geomechanical simulation with a fine scale model is not computationally feasible for full–field, coupled geomechanical-flow simulation. Upscaling of property models is necessary to move from fine scale/high resolution property models to coarser scale/low resolution models appropriate for simulation. Local numerical upscaling was proposed by Khajeh et al. (2012) to describe the macroscopic elastic behavior of complex heterogeneous media and is expanded upon in this work. This numerical technique is not restricted to specific geologies as typical analytical techniques are. Moreover, transversely isotropic deformation is considered rather than the usual assumption of isotropic deformation. To compare the accuracy of the upscaling methodology, in this study shear strain is considered as the geomechanical response of a synthetic facies model and the response of the coarse scale model is compared to other conventional analytical averaging techniques. It is found that the numerical upscaling technique better approximates the geomechanical response of the fine scale model.

1. INTRODUCTION

The main objective of geomechanical simulation is to determine the expected response of media as a result of stress-strain redistribution. Inherent mechanical properties such as Young's modulus, Poisson's ratio, etc., play a significant role the response of geo-materials. Considering heterogeneous geological models, the well-known Mechanical Earth Model (MEM's), instead of a simplified layer cake model increases accuracy in simulation results. Although simulation of the fine scale model would likely result in the highest accuracy, the CPU requirements of geomechanical simulators prevent the simulation of the fine scale heterogeneous model. As a result, upscaling is considered as an intermediate step between geological modelling and geomechanical simulation.

Upscaling of rock mechanical properties of heterogeneous material is of interest for several applications including geomechanical effects during thermal recovery processes (e.g., SAGD process) and cap-rock integrity investigation. The upscaling of mechanical properties should be applied to all mechanical properties (elastic and plastic); however, this paper focuses on the upscaling of elastic properties.

A quick review of existing analytical techniques is warranted. Mackenzie (1950) developed an analytical upscaling technique based on the concept of the self-consistent method applied to a spherical representative volume element (RVE). The bulk modulus and the shear modulus are determined by applying a hydrostatic pressure and a simple homogeneous shear stress to a large sphere. In his work, it is assumed that deformation is controlled by the isotropic elastic constitutive law. Hashin (1958) proposed a similar homogenization technique for spherical materials based on the concept of elastic energies. Hill (1965) calculated the effective elastic moduli of a two-phase composite. In contrast to previous works, he

considered that the phases do not surrounded one another. Budiansky (1965) extended the model proposed by Hill (1965) to multiphase materials and stratified periodic materials. Salamon (1968) derived five elastic coefficients of a homogeneous, transversely isotropic medium equivalent to perfect, horizontally layered rock based on strain energy.

Limited work has been undertaken related to numerical upscaling for geomechanical properties. Elkateb (2003) proposed a mathematical expression to determine the equivalent Young's modulus of a simplified layer cake model under isotropic deformation. This approach was not extended to heterogeneous media or anisotropic deformation.

Previous techniques are not appropriate for the typical sand/shale spatial distribution of oil sands in the McMurray formation of Alberta, Canada which is the focus of this work. Existing techniques are limited because they: (1) consider a simplified (spherically surrounded or stratified) configuration; (2) consider a limited number of layers, or; (3) consider isotropic deformation.

Complex facies / property distributions and anisotropic deformation are both considered in this work. The upscaling methodology is demonstrated on a synthetic 2D model based on typical sand/shale distributions of the McMurray oil sands deposit. To assess the accuracy of the proposed methodology, conventional averaging techniques based on different power laws are also considered.

2. CONVENTIONAL AVERAGING (POWER LAW) TECHNIQUES

Arithmetic, harmonic and geometric averaging could be used as an initial, potentially naïve, upscaling of elastic properties. A comprehensive form is power law averaging (Equation 1) (Deutsch, 1989) where "A" is an elastic property to upscale.

$$A_w = \left(\frac{1}{n} \sum_{i=1}^{n} A_i^w \right)^{\frac{1}{w}} \tag{1}$$

3. PROPOSED NUMERICAL UPSCALING TECHNIQUE

The numerical upscaling of elastic geomechanical properties is shown in Figure 1.

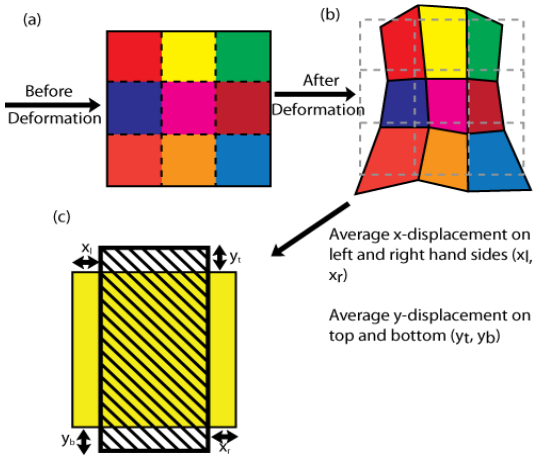

Figure 1 - Conceptual framework for numerical upscaling (from Khajeh et al., 2012)

When considering heterogeneous media (Figure 1-a) the loading process would result in complex deformation (Figure 1-b). After upscaling this system to a single block, the goal is to reproduce the average fine scale deformation in the coarse scale block (Figure 1-c). The coarse upscaled property (yellow color in Figure 1-c) is the value that results in the average displacement had the fine scale model been deformed (Khajeh et al., 2012)

By considering transversely isotropic constitutive behaviour, in which the X-Z plane is considered as the plane of symmetry, Hooke's law Equation would be:

$$\begin{bmatrix} e_{xx} \\ e_{yy} \\ 0 \\ e_{xy} \end{bmatrix} = \begin{bmatrix} 1/\mathrm{xm} & -\mathrm{nuy}/\mathrm{xm} & -\mathrm{nux}/\mathrm{xm} & 0 \\ -\mathrm{nuy}/\mathrm{xm} & 1/\mathrm{E_y} & -\mathrm{nuy}/\mathrm{xm} & 0 \\ -\mathrm{nux}/\mathrm{xm} & -\mathrm{nuy}/\mathrm{xm} & 1/\mathrm{xm} & 0 \\ 0 & 0 & 0 & 1/2\mathrm{G}' \end{bmatrix} \begin{bmatrix} \sigma_{xx} \\ \sigma_{yy} \\ \sigma_{zz} \\ \sigma_{xy} \end{bmatrix} \quad (2)$$

where;
xm: is Young's modulus in the plane of symmetry
ym: is Young's modulus in the direction normal to the plane of symmetry
nux: is Poisson's ratio for the normal strain in the x-direction (in the plane of isotropy) related to the normal strain in the z-direction due to uniaxial stress in the z-direction
nuy: is Poisson's ratio for the normal strain in the y-direction (in the direction normal to the plane of isotropy) related to the normal strain in the x-direction (in the plane of isotropy) due to uniaxial stress in the x-direction.

By applying two different loading scenarios (Figure 2), the 5 parameters which fully characterize transversely isotropic, upscaled cells can be obtained. xm, ym, nux and nuy, are obtained as a result of these two different loading scenarios (Equations 3 and 4) and with good approximation; G′ (Gxy) can be determined from Equation 5 (Lekhnittskii, 1981).

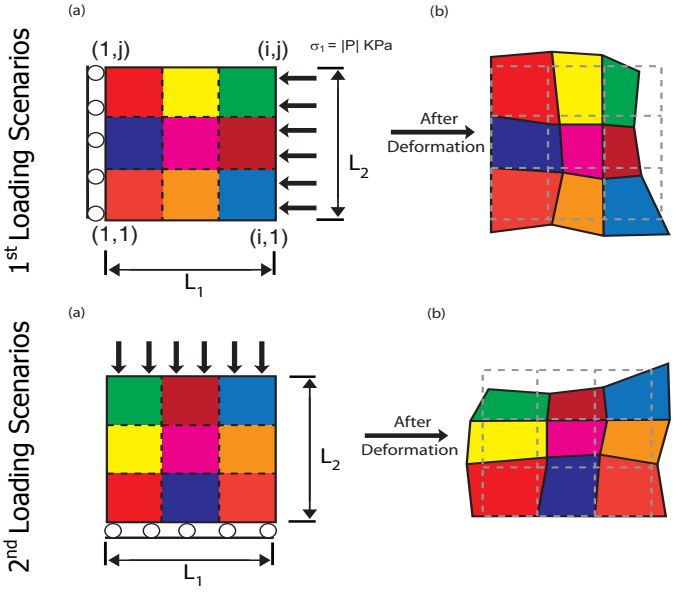

Figure 2 - Initial boundary conditions for loading scenarios (from Khajeh et al., 2012)

$$\langle e_{11}^1 \rangle = \left(\frac{1}{xm}\right)\langle \sigma_{11}^1 \rangle + \left(\frac{-nux}{xm}\right)\langle \sigma_{33}^1 \rangle \quad (a)$$
$$\langle e_{22}^1 \rangle = \left(\frac{-nuy}{xm}\right)\langle \sigma_{11}^1 \rangle + \left(\frac{-nuy}{xm}\right)\langle \sigma_{33}^1 \rangle \quad (b) \qquad (3)$$
$$0 = \left(\frac{-nux}{xm}\right)\langle \sigma_{11}^1 \rangle + \left(\frac{1}{xm}\right)\langle \sigma_{33}^1 \rangle \quad (c)$$

$$\langle e_{11}^2 \rangle = \left(\frac{-nuy}{xm}\right)\langle \sigma_{22}^2 \rangle + \left(\frac{-nux}{xm}\right)\langle \sigma_{33}^2 \rangle \quad (a)$$
$$\langle e_{22}^2 \rangle = \left(\frac{1}{ym}\right)\langle \sigma_{22}^2 \rangle + \left(\frac{-nuy}{xm}\right)\langle \sigma_{33}^2 \rangle \quad (b) \qquad (4)$$
$$0 = \left(\frac{-nuy}{xm}\right)\langle \sigma_{22}^2 \rangle + \left(\frac{1}{xm}\right)\langle \sigma_{33}^2 \rangle \quad (c)$$

$$G_{xy} = \frac{E_x E_y}{E_x(1 + 2\nu_{xy}) + E_y} \qquad (5)$$

where $\langle \sigma^1_{33} \rangle$ and $\langle \sigma^2_{33} \rangle$ are the average σ_{33} as a result of the first and second loading configuration, respectively; and $\langle e^1_{11} \rangle$, $\langle e^1_{22} \rangle$ and $\langle e^2_{11} \rangle$, $\langle e^2_{22} \rangle$ are the equivalent strain components for the uniformly deformed body for the first and second loading scenarios, respectively.

4. CASE STUDY

The geometry which is shown in Figure 3 is considered to investigate the accuracy of the proposed methodology. The central zone of Figure 3 is the area of interest and the side, under and overburden sections (which are all assumed to be homogeneous) are considered to minimize boundary effects.

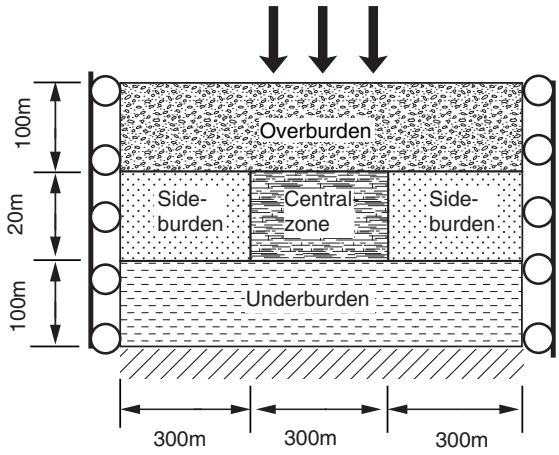

Figure 3 - Geometry of the area of interest (from Khajeh et al., 2012)

In previous work, sequential indicator simulation (SIS) with GSLIB (Deutsch, 1998) was used to build a heterogeneous facies model (Figure 4) for the central zone of Figure 3 (Khajeh et al., 2012). For the sake of consistency, the same model is considered here. Shear strain is considered as the geomechanical response of interest to investigate the error resulting from upscaling. Elastic properties are considered to

be homogeneous within each facies. Tables 1 and 2 summarize the material properties and number of grid cells in each zone.

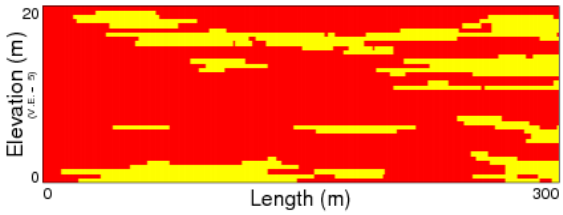

Figure 4 - SIS facies realization considered with 20% shale. Red (dark) is sand; yellow (light) is shale. Variogram parameters: one spherical structure with a vertical range of 4m, horizontal range of 120m and no nugget effect (from Khajeh et al., 2012)

Table 1 - Material properties in each section of Figure 3

	Overburden	Side burden	Under burden	Central Section
Deformation type	Isotropic	Isotropic	Isotropic	Transversely Isotropic
Young's modulus (MPa)	250	480	5000	Shale : 300
				Sand : 600
Poisson's ratio	0.3			

Table 2 - Number of grids

	Overburden	Side burden (each side)	Under burden	Central Section
Horizontal	360	30	360	300
Vertical	10	40	10	40

The error resulting from upscaling is assessed by comparing the geomechanical response of the fine scale model (Figure 3) to the response of the coarse upscaled models using power law averaging and numerical upscaling calculated as follows:

$$[\%]e = \frac{\sum_r \left|1 - \frac{\overline{e_{s_r}}}{e_{s_r}}\right|}{n_r} * 100 \tag{6}$$

$$\overline{e_{s_r}} = \frac{\sum_i e_{s_i}}{n_i} * 100 \tag{7}$$

where,

$\overline{e_{s_r}}$ is the average shear strain of the fine scale cells in the rth upscaled block.

e_{s_r} is the shear strain in the rth upscaled block.

n_r is the number of blocks in the upscaled model.

e_{s_i} is the shear strain in the i^{th} fine scale cell within the upscaled block.
n_i is the number of fine scale cells in each upscaled block.

Like previous work, 15 upscaling ratios (number of fine scale cells in each upscaled block) are considered, using horizontal ratios of 1:1, 5:1, 15:1, 30:1, 60:1, 100:1 and vertical ratios of 1:1, 4:1 and 8:1.

5. RESULTS

5.1 Young's Modulus Maps

In Figures 5 and 6 upscaled Young's modulus maps for selected horizontal upscaling ratios (30:1 and 100:1) and for vertical upscaling ratios of 1:1 (Figure 5) and 8:1 (Figure 6) for different upscaling techniques are shown.

It can be seen that averaging in the vertical direction has a large effect on upscaling because of the shorter variogram range in this direction. Considering a 30:1 horizontal variogram range has minimal impact on the upscaled maps whereas an 8:1 in the vertical direction is very significant.

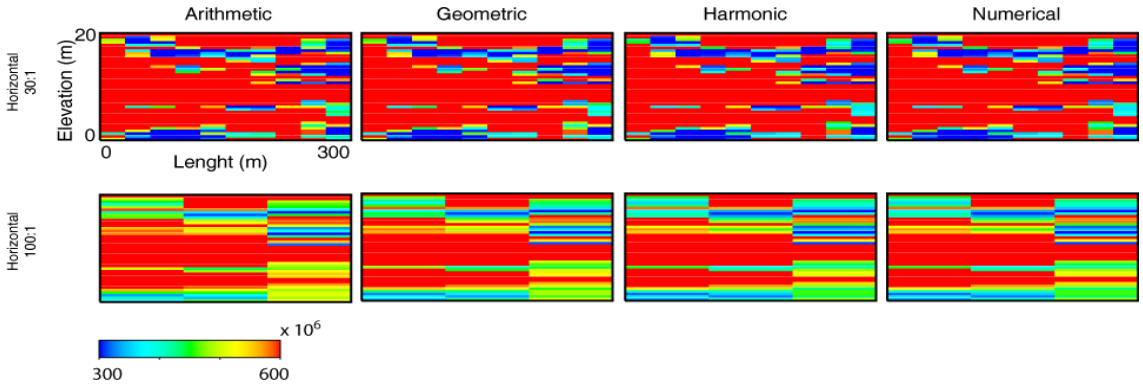

Figure 5 - Young's modulus (MPa) for selected horizontal upscaling ratios, vertical upscaling ratio is constant at 1:1

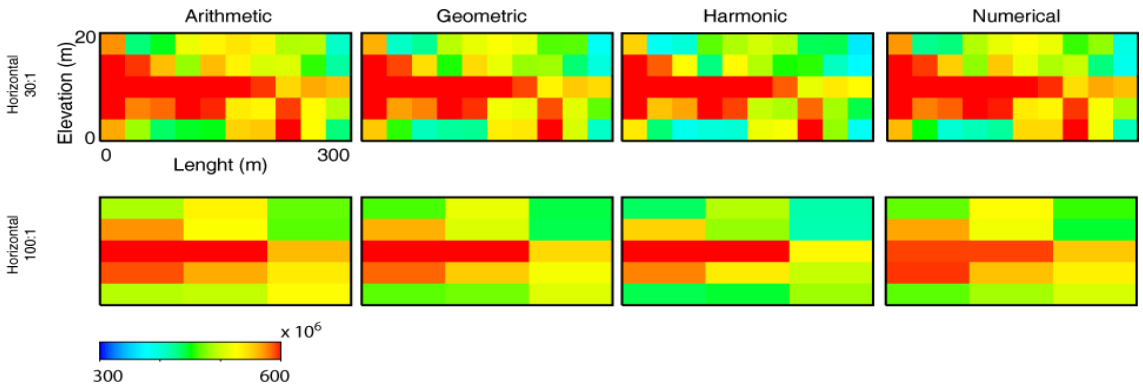

Figure 6 - Young's modulus (MPa) for selected horizontal upscaling ratios, vertical upscaling ratio is constant at 8:1

5.2 Shear Strain Maps

The results of geomechanical response (i.e., shear strain maps) obtained from upscaled maps are shown in Figures 7 and 8.

As concluded for the Young's modulus maps, there is no significant difference between different upscaling techniques used for vertical upscaling ratio of 1:1. However changes in shear strains for vertical upscaling of 8:1 and horizontal upscaling of 100:1 are clear (Figure 8). There is more similarity between the numerical upscaling results and results obtained using the harmonic averaging technique.

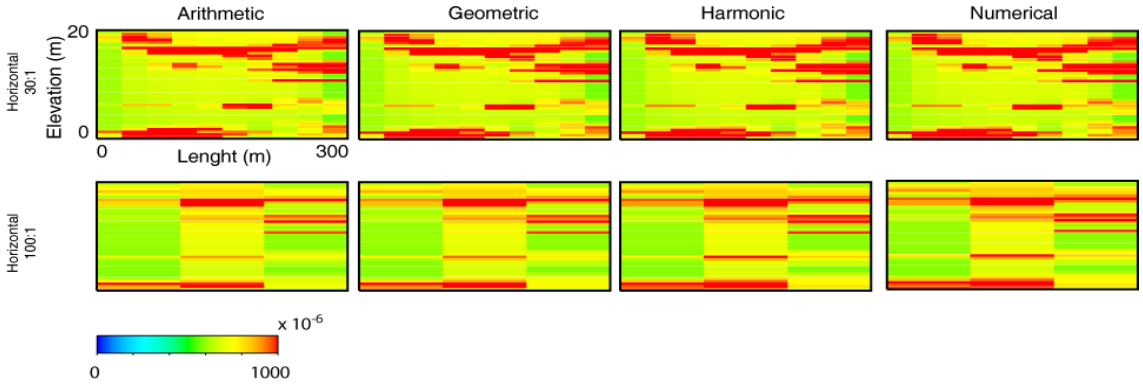

Figure 7 - Shear strain for selected horizontal upscaling ratios, vertical upscaling ratio is constant at 1:1

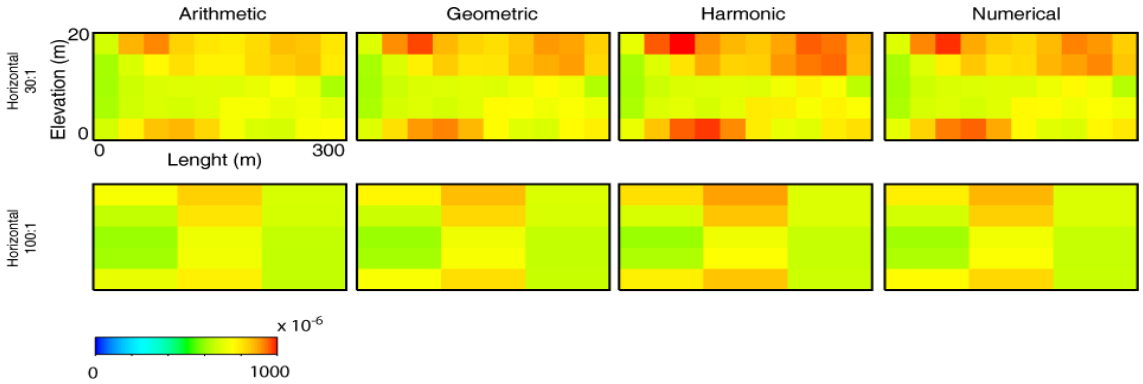

Figure 8 - Shear strain for selected horizontal upscaling ratios, vertical upscaling ratio is constant at 8:1

5.3 Error Analysis

Using the error definition in Equation 6, differences in the shear strain maps of the fine scale model response and the various upscaled maps are shown in (Figure 9). These results show that the proposed numerical averaging technique results in a lower error for all vertical and horizontal ratios considered.

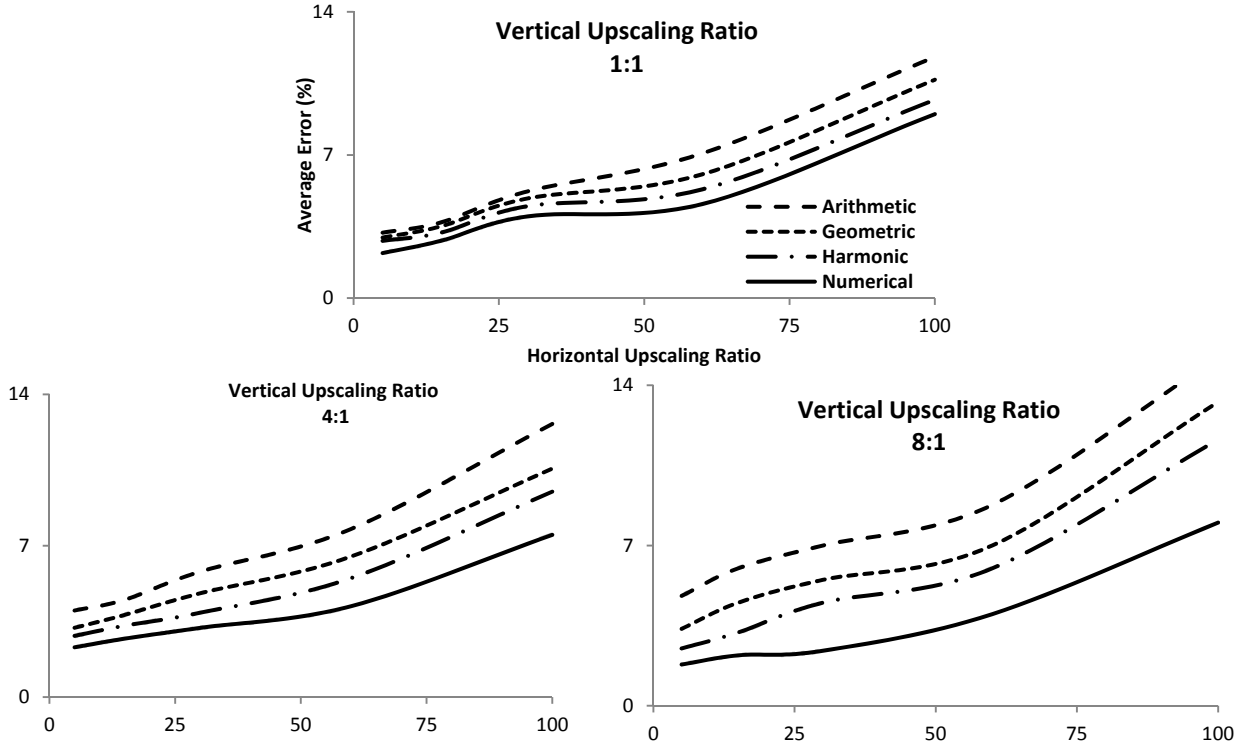

Figure 9 - Average error for various horizontal and vertical upscaling ratios

6. DISCUSSION AND CONCLUSION

The effect of upscaling on shear strain was investigated. Consideration of anisotropic deformation and no restriction on the input facies configuration are the main two strengths of numerical upscaling.

It was shown that the upscaling technique results in less upscaling error in comparison to conventional analytical techniques. Finding an appropriate coarse block scale is important and should be selected through defining an acceptable level of error.

In addition to producing less error, the advantage of numerical upscaling is that it is not limited to a specific facies configuration or geological formation. The numerical upscaling technique implementing in this work is appropriate for domains for which elastic deformation can be characterized by transversely isotropic behavior.

7. ACKNOWLEDGEMENT

The authors would like to acknowledge the Foundation CMG and Helmholtz Alberta Initiative for funding support for this research.

8. REFERENCES

BUDIANSKY, B., 1965. On the elastic moduli of some heterogeneous materials. Journal of the Mechanics and Physics of Solids. 13:223–227.

DEUTSCH, C.V. 1989. Calculating Effective Absolute Permeability in Sandstone/Shale Sequences. SPE Formation Evaluation. 4: 3,343–3,348.

DEUTSCH, C.V., and JOURNEL, A. G., 1998. GSLIB: Geostatistical Software Library and User's Guide. Second edition, Oxford, New York.

ELKATEB, T. M., 2003. Quantification of Soil Heterogeneity. PhD dissertation, University of Alberta, Edmonton, Canada.

HASHIN, Z., 1958. The moduli of an elastic solid, containing spherical particles of another elastic material. Proceedings IUTAM Symposium on Non-homogeneity in Elasticity and Plasticity, Warsaw, Poland. 17:463–478.

HILL, R. A., 1965. Self-consistent mechanics of composite materials. Journal of the Mechanics and Physics of Solids. 13:213–222.

KHAJEH, M.M., CHALATURNYK, R.J., and BOISVERT, J.B., 2012. A Numerical Local Upscaling Approach for Elastic Rock Mechanical Properties: Dealing with Heterogeneity. Prepared for presentation at the 46th US Rock Mechanics / Geomechanics Symposium held in Chicago, IL, USA, 24-27 June. ARMA 12-654.

LEKHNITTSKII, S.G., 1981. Theory of Elasticity of an Anisotropic Body. Moscow: Mir Publishers.

MACKENZIE, J.K., 1950. The elastic constants of a solid containing spherical holes. Proceedings of the Royal Society London. B63(1): 2–11.

SALAMON, M., 1968. Elastic moduli of a stratified rock mass. Journal of Rock Mechanics and Mining Sciences 5:519–527.

Hydro-Mechanical Response of Hydraulic Fractures

Mohammadreza Jalali
Earth & Environmental Sciences Department, University of Waterloo
Rebecca K. Cameron
Civil Engineering Department, University of Waterloo
Maurice B. Dusseault
Earth & Environmental Sciences Department, University of Waterloo

ABSTRACT: Alberta contains over 400 billion barrels of viscous crude oil in fractured carbonates but there is no viable extraction technology as yet. Petroleum geomechanics has become a vital part of the assessment of such hydrocarbon reserves, especially for naturally fractured cases, which are particularly challenging in terms of accurate recovery prediction because of joint fabric complexity and lithological heterogeneity. As a result of interconnected fractures, transport properties of fractures (mostly permeability issues rather than thermal effects) are affected by production and injection activities that change the pore pressures, temperatures, saturations, and effective stresses. Enhanced oil recovery methods involving massive amounts of fluid injection (hot or cold) at high pressure (p_{inj}) may be used to mobilize and produce the oil; therefore, deeper understanding of the fractured systems is desirable. Pressure and temperature variations in a fractured reservoir change the *in situ* stresses in the reservoir and surrounding rocks; this affects fracture apertures, radically changing the bulk flow properties because flux rate is highly sensitive to aperture. Hence, coupled pressure, temperature and effective stress changes must be considered for fractured reservoirs under a thermo-hydro-mechanical (THM) coupling approach.A hybrid FDM/DDM coupled method is presented to couple pore pressure and stress around a fracture in an impermeable matrix block. Deformation and stresses are calculated in each time step and then fracture permeability, which is the most sensitive petrophysical parameter in fractured reservoirs, is updated based on the fracture aperture variation. This model is then verified with UDEC (Universal Distinct Element Code) which uses a discrete approach to cope with fractured rock mass behavior.

1. INTRODUCTION

Naturally fractured oil reservoirs contain ~1.5×10^{12} b of conventional oil and ~2.0×10^{12} of viscous oil, about 25% of remaining oil in place. They behave non-homogeneously under production as fracture conductivity dominates flux rate, conductivity is a strong function of aperture ($v \propto a^3$), and aperture is highly sensitive to the normal effective stress (σ'_n) across the fracture as well as shear stress along the fracture. In low σ'_n regimes (high p_{inj}), shear displacement is dilatant, leading to large aperture increases (Dusseault *et al.*, 2011). Different physical processes can affect the stress state of fractures such as pore pressure changes (Δp) from production or injection of fluids, temperature variations (ΔT) arising from injection of fluids colder or hotter than reservoir T, and chemical alteration (ΔC) such as electro-kinetic effects and osmotic effects in shale formations (Dusseault, 2008). Comprehensive study considering all first-order effects of such processes on fractured reservoirs is needed to understand their behavior.

Conventional non-coupled reservoir simulators calibrated empirically through history-matching are not appropriate for these processes, as they consider pore compressibility as the only geomechanical aspect of simulation and assume permeability and porosity as static or pressure-dependent variables. These assumptions are insufficient because permeability and fracture conductivity are strong functions of effective stress and temperature as well as pressure. Parameter impacts on both reservoir characterization

and simulation processes should be considered via a thermo-hydro-mechanical (THM) coupled approach for simulations that are more physically correct, and thus more likely to be properly calibrated.

Coupled simulators are usually based on two coupling approaches: volume coupling and flow properties coupling (Settari and Mourits, 1998). In volume coupling, pore volume or volumetric strain as a result of $\Delta\sigma'$, Δp and ΔT is used as the coupling parameter for fluid flow and geomechanics models. This approach is suitable for problems with large porosity variation due to shear and plastic deformation such as unconsolidated sands, North Sea chalk, California diatomite and perhaps some other materials. In flow properties coupling, permeability and relative permeability changes are related to these variables - $\Delta\sigma'$, Δp and ΔT. This is perhaps more important in gas reservoirs, waterfloods or solid waste injection processes with pressures close to or above fracturing pressure, as well as cold water injection in geothermal cases.

The level of $\Delta\sigma'$-Δp-ΔT coupling can be classified into three different categories: (i) explicit, (ii) iterative, and (iii) fully-coupled. The most robust method is the fully-coupled approach, where the momentum conservation, fluid mass conservation, and energy conservation governing equations are solved simultaneously. To our knowledge, there is no commercial fully-coupled simulator yet and most of the effort has been toward iterative coupling between existing fluid flow and geomechanical simulators, where coupling parameters are sent back and forth between the simulators until convergence. This approach does not require so much code development and will produce the same results as a fully coupled approach if both use sufficiently tight convergence tolerances for iterations (Settari and Walters, 1999). Table 1 summarizes some of the advantages and disadvantages of different levels of coupling.

In this paper, some assumptions are made to simplify the THM coupled problem in a fractured reservoir to a less complicated two-dimensional hydromechanical (HM) injection problem in an impermeable matrix block. Some of these assumptions are listed below:

- In the absence of significant matrix permeability, conduction dominates heat transfer, and thermal diffusivity of impermeable carbonate matrix blocks is relatively low (typically 6×10^{-6} m^2/s). Assume also that there no significant ΔT to reduce the coupling number of the problem from three to two (i.e. from THM to HM coupling).
- Plane-strain conditions, and fluid is injected into a vertical fracture in a thick reservoir. The model is a 2-D cross-section perpendicular to the wellbore is located at the center of model.
- The injected fluid is viscous and compressible and is injected into an open fracture.

Table 1 - Advantages and disadvantages of different levels of coupling

Method	Advantage	Disadvantage
Explicit Coupling	• Effective and time-saving for subsidence problems • Flexible and straightforward	• One-way coupling just for geomechanics • Stability and accuracy
Iterative Coupling	• Flexible in the case of numerical methods • Uses conventional reservoir simulators (e.g. ECLIPSE, TOUGH2, STARS) with a geomechanical module (e.g. VISAGE, FLAC, UDEC)	• Requires a large number of iterations (1st order convergence) • Relatively small jumps in pore volume can be handled
Full Coupling	• The most stable approach • Preserves 2nd order convergence • Reliable and a benchmark for other coupling methods	• Difficult to couple existing modules and softwares • Requires more basic code development • Slower than other coupling techniques

2. HYDROMECHANICAL COUPLING

Hydromechanical (HM) models consist of two-way interactions between pore pressure (H) and deformation (M), a complex and ambiguous coupling problem when fractures are included.

The fundamentals of poroelasticity are based on the original concept of effective stress and 1-D consolidation for incompressible solid grains formulated by Terzaghi in 1923. Thereafter, Biot investigated the coupling between stresses and pore pressure and developed a generalized 3-D theory of consolidation with the basic principles of continuum mechanics, the "Theory of Poroelasticity" (Geertsma, 1966). Biot's theory and published applications are oriented more toward rock mechanics than fluid flow so it is less compatible with conventional fluid-flow models (without geomechanics consideration) in terms of concept understanding, physical interpretation of parameters (e.g., rock compressibilities), and computer code implementation.

Skempton (1954) derived a relationship between the total stress and pore pressure under undrained initial loading with the so-called Skempton pore pressure parameters A and B. Geertsma (1957) gave a better insight into the relationship among pressure, stress and volume, clarifying the concept of compressibility in a porous medium and Van der Knaap (1959) extended his work to nonlinear elastic geomaterials such as dense but uncemented sands. Geertsma (1966) applied Biot's theory to subsidence problems in petroleum engineering, perhaps the first loosely coupled flow-geomechanics analysis published.

Nur and Byerlee (1971) proved that the effective stress law proposed by Biot is more general and physically sensible than that proposed by Terzaghi, although Terzaghi understood clearly the limitations of the assumptions he had to make in the 1920's to solve practical engineering problems in clay consolidation (one-dimensional analysis, ignoring fluid and mineral grain compressibility, etc.). In other relevant developments, Ghaboussi and Wilson (1973) introduced fluid compressibility into classic soil mechanics consolidation theory, and Rice and Cleary (1976) showed how to solve poroelasticity problems by assuming pore pressure and stress as primary variables instead of displacements as employed by Biot.

Hydromechanical coupled models are based on two fundamental laws, i.e. Hooke's law of elasticity, and Darcy's law of fluid flow in porous media, which are governed by two coupled governing equations, i.e. conservation of momentum and mass conservation.

3. FINITE DIFFERENCE / DISPLACEMENT DISCONTINUITY METHOD

The main idea of any numerical method is to replace the "real" problem with an approximate problem which is more easily solved, yet the solution will remain very close to the "real" solution. THM coupled problems have been analyzed with a variety of numerical methods (Figure 1).

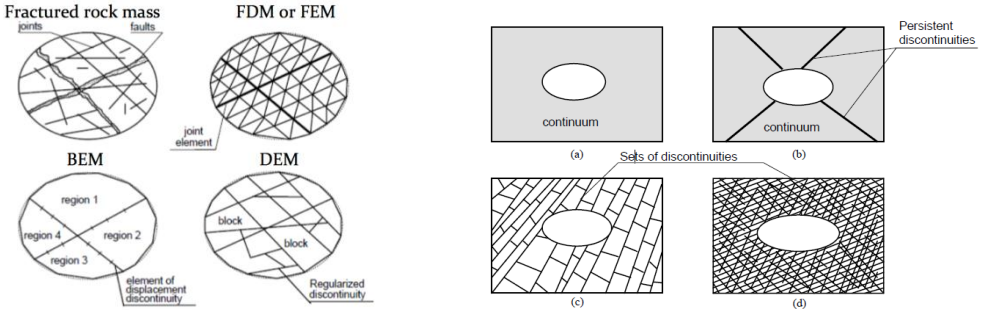

Figure 1 - Left: Fractured rock mass representation using numerical methods. Right: Implementation of numerical method. (a) continous method; (b) continuous with fracture element or discrete method; (c) discrete method; (d) continuous method with equivalent properties (Jing, 2003)

In numerical approaches, the continuum is usually subdivided into a finite number of elements with a finite number of degrees of freedom with a simpler mathematical behavior compared with the "real" problem. Mathematically, the partial differential formulation is converted into a linear system of equations based on continuity between adjacent elements.

Two different numerical approaches have been used to cope with fractured reservoir modeling, continuous (e.g. FDM, FEM) and discontinuous (e.g. DEM, BEM) methods. Different criteria control the choice of numerical approach, and the most important ones are scale of the problem and geometry of the fracture system. Continuous methods may be implemented for non-fractured media as well as highly fractured problems as in the latter case a homogenization approach can be used. There are some cases where special elements (e.g. Goodman's joint element) are added to continuous methods to cope with fractures, although large displacements, detachments, and sliding are not permitted. On the other hand, discrete methods are used for moderately fractured areas at a large scale (e.g. faults).

Continuous methods for stresses and deformations have wide application in the oil industry as they are compatible with existing simulators for fluid and heat flow, but they cannot describe the complete physics behind fracture behavior. Fracture permeability, for example, is a function of σ′, p and T, which generally are updated in each time step for a better prediction of production. Fracture permeability can be incorporated using a discrete method that considers fractures explicitly; however, discrete element simulations are more challenging in the numerical sense, and less amenable to multi-phase flow analysis.

Hybrid modeling is an alternative; it is a combination of different numerical methods such as FEM/BEM or FDM/BEM. It benefits from both continuous and discrete aspects but the computation load is heavy and displacement continuity and stress equilibrium at the interface are concerns (Jalali and Dusseault, 2011(a)). In the following analysis, a hybrid FDM/DDM method is used to model the behavior of a partially closed fracture in an impermeable rock under constant injection rate in the center of model.

3.1 Model Description

In this model, fracture fluid flow is modeled via a FDM approach and the effects of p and σ′n variations on the fracture and in the surrounding rocks is estimated via an indirect boundary element method, and the displacement discontinuity method (DDM) is more favorable in this case (Figure 4). Fracture normal deformation is used to update fracture aperture as well as fracture permeability in each time step via a cubic flow law. This method is suitable for reservoirs with low fracture density as well as simulating the behavior of a single fracture at the laboratory scale. The formulation of the problem as well as the coupling approach can be found elsewhere (Jalali and Dusseault, 2011(b)).

3.2 Model Verification

The model was verified with an analytical solution (Sneddon, 1951) and a numerical solution (UDEC) for a constant pressure case in the fracture. Sneddon's solution estimates the aperture variation across a fracture as:

$$a(x) = \frac{4|\sigma_n + p|(1-\nu^2)}{E}\sqrt{b^2 - x^2} \tag{1}$$

where ν is Poisson's ratio, E is Young's modulus, σ_n is the normal stress on the fracture, p is fracture pressure, b is the fracture half length, and x is the distance from the center of the fracture.

UDEC is a two-dimensional discrete element code for discontinuum modeling. A discontinuous medium is modeled as an assemblage of discrete blocks with fractures separating them. Discrete blocks can be rigid or deformable, which for the latter case deformation is calculated via a finite difference approach.

For verification purposes, a constant pressure (p = 20 MPa) was applied to a fracture with a length of 20 meters and the aperture along the fracture was plotted via the Sneddon's solution, UDEC, and FDM-DDM code (Figure 2). Based on the results, UDEC simulation underestimates the analytical solution whereas the FDM/DDM model with one meter grid spacing over-predicts the fracture aperture. This

overestimation can be reduced by reducing the grid spacing from one meter to 50 centimeters. Using smaller spacing (i.e. Δx=25 cm) results in an aperture very close to that of the UDEC model.

3.3 Model Example

Hydro-mechanical behavior of a 20 meter open fracture under a constant fluid injection rate (5×10^{-4} m^3/s) for 50 seconds is shown in Figure 3. The fracture is discretized into 40 grid blocks (i.e. Δx=0.5 m, based on Figure 2) with an initial aperture of 0.5 mm. Before injection, the model was initialized, so the aperture was increased by an amount of almost 0.25 mm (i.e. $|p-\sigma_n|/K_n$). Initial maximum and minimum horizontal stresses and pressure were assumed to be 30, 15, and 20 MPa, respectively.

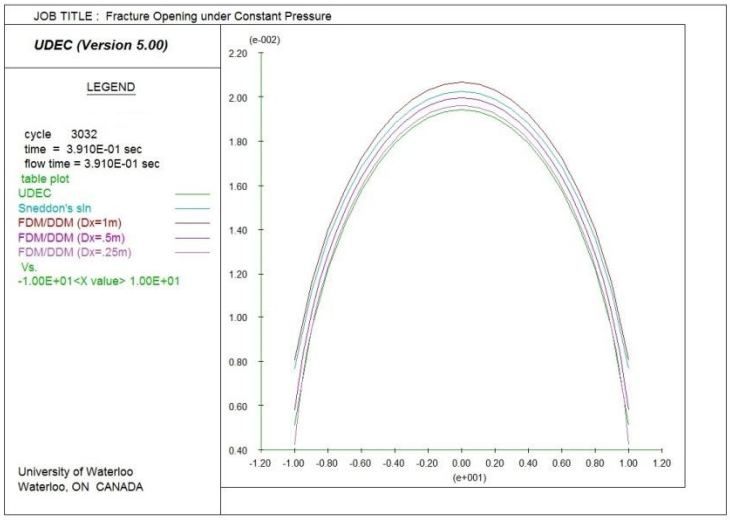

Figure 2 - Fracture opening along a 20 m fracture under a constant pore pressure using Sneddon's solution, UDEC and FDM/DDM

Pressure propagation profile along the fracture for different time steps as well as fracture aperture variations over time are shown in Figure 3. As the pressure builds up, the fracture's aperture increments are similar, and their variations were plotted over distance and with time, respectively, in Figure 3. As expected, pressure increases symmetrically around the injection point (x=0) and drops off quickly toward the fracture tips. This pressure increment causes fracture opening dominantly around the injection point. The rate of opening decreases over time as more than 50% of the opening at the injection point occurred in the first 5 seconds of injection (Figure 3). Also the rate of fracture opening is less around fracture tips in comparison to the area close to the center as it takes time for pressure to propagate down the fracture.

Fluid injection induces stresses perturbations in the surrounding rock. The *in situ* stresses in the surrounding rocks are shown in Figure 4 after 50 seconds injection. As expected, vertical and horizontal stresses around the injection point increase as the injected fluid pushes the rock apart and thus increases compressive stress. Due to conservation of momentum (conservation of stress for equilibrium), this stress increment is compensated by a reduction of stress moving away from the center of fracture. For the horizontal stress, this reduction occurs above and under the fracture, whereas for the vertical stress, it occurs at the sides of fractures. Some abrupt reduction around the fracture tips can be seen which occurs as a result of stress singularity in these points. Most of the shear stresses occur above and under the fracture tips as the difference between horizontal and vertical stress in these points are maximum.

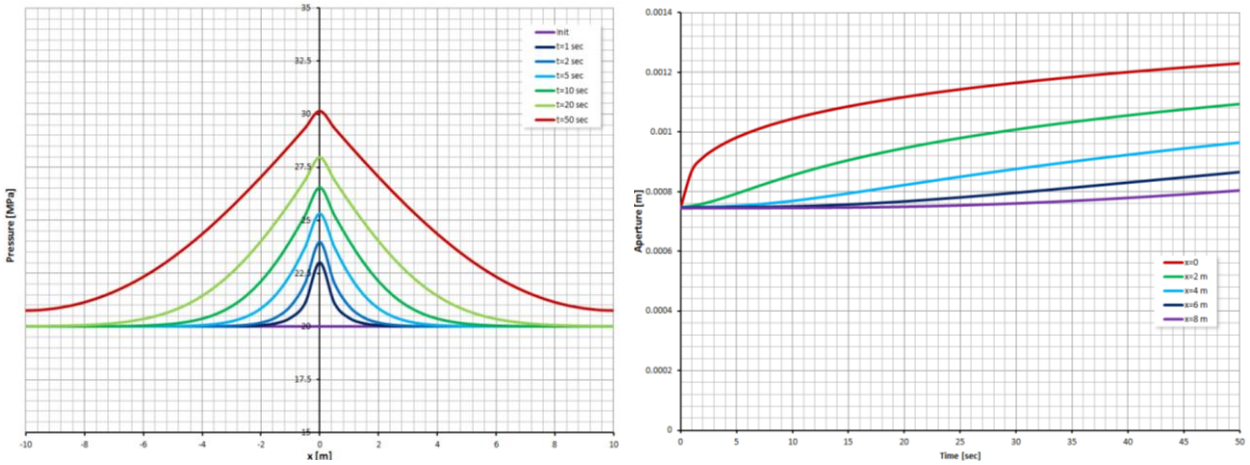

Figure 3 - Pressure propagation along the fracture (left), aperture variation over injection period (right)

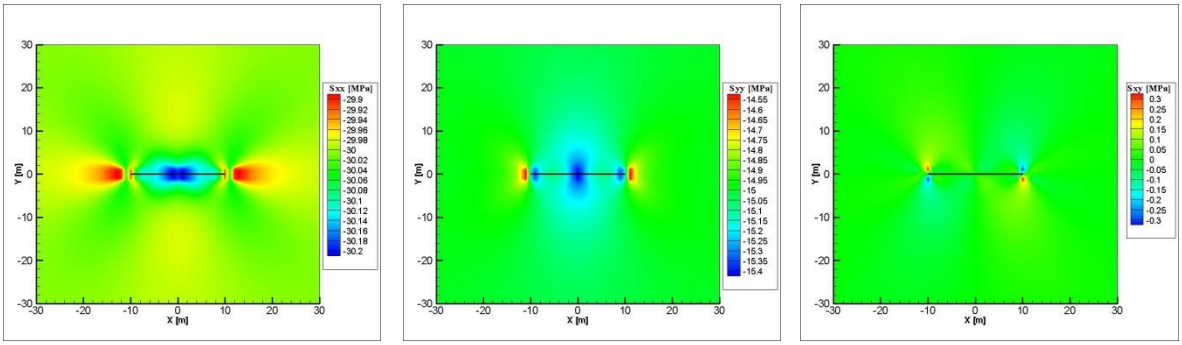

Figure 4 - Stress map around the fracture: horizontal stress (left), vertical stress (middle), and shear stress (right)

4. SUMMARY AND CONCLUSION

Reasonable recovery predictions in naturally fractured reservoirs are challenging because fracture behavior dominates production and injection activities, and fracture permeability variation is more important than matrix porosity changes which dominate in conventional reservoirs (although the overall stress sensitivity of permeability in sandstones is usually no more than 10-15%). Pressure, temperature and chemical changes can all affect stress trajectories in the reservoir in the vicinity of fractures, inducing fracture aperture changes and permeability variations that dramatically affect production. THMC coupling in stress sensitive reservoirs (e.g. naturally fractured or poorly compacted reservoir) is the crucial consideration for better predictions.

In this paper, a two-dimensional hybrid numerical model was developed; fluid flow in the fracture is modeled via finite difference and updated pressures are applied to a displacement discontinuity model as a boundary condition to calculate stress, deformation and fracture aperture in each time step. FDM/DDM models were verified with UDEC and Sneddon's analytical solution and the effect of grid spacing was discussed. There may be merit in developing this work to generate higher order functions for represent fractures within a general stress-strain-pressure coupled modeling approach.

The behavior of a 20-meter fracture under a constant injection flow was modeled in a biaxial stress field. A reasonable relationship (as expected) was seen between pressure and fracture aperture which is more dominant around the injection point. An iterative approach between a finite difference and a displacement discontinuity model leads to a better understanding of the nature of fractures on global flow, and the work here might be used to guide the development of lightly fractured reservoir models. (As a note, we have also seen Noordbergum-type stress transfer effects in the fracture under early time production, although these effects have little impact on long-time behavior.)

5. REFERENCES

BIOT, M., 1941. General theory of three dimensional consolidation. Journal of Applied Physics, 12 p. 155-164.

DUSSEAULT, M.B., 2008. Coupling geomechanics and transport in petroleum engineering. Proceedings of 1st Southern Hemisphere International Rock Mechanics Symposium, Perth, Western Australia.

DUSSEAULT, M.B., MCLENNAN, J. and SHU, J., 2011. Massive multi-stage hydraulic fracturing for oil and gas recovery from low mobility reservoirs in China. Petroleum Drilling Techniques, 39(3), 6-16

GEERTSMA, J., 1957. The effect of pressure decline on volumetric changes of porous rocks. Transactions AIME, 201, p. 331-340.

GEERTSMA, J., 1966. Problems of rock mechanics in petroleum production engineering. First Congress on International Society of Rock Mechanics, Lisbon, p. 585-594.

GHABOUSSI, J. and WILSON, E., 1973. Flow of compressible fluid in porous elastic media. International Journal for Numerical Methods in Engineering, 5(3), p. 419-442.

JALALI, M.R. and DUSSEAULT, M.B., 2011a. Coupling geomechanics and transport in naturally fractured reservoirs. 5th Iranian Rock Mechanics Conference, Tehran, Iran.

JALALI, M.R. and DUSSEAULT M.B., 2011b. Hydro-mechanical modeling of fractures with a finite difference - displacement discontinuity method. 45th U.S Rock Mechanics/Geomechanics Symposium. San Francisco, California.

JING, LANRU, 2003. A review of techniques, advances and outstanding issues in numerical modelling for rock mechanics and rock engineering. International Journal of Rock Mechanics and Mining Sciences, 40, p. 283-353.

JING, LANRU and FENG, XIATING, 2003. Numerical modeling for coupled thermo-hydro-mechanical and chemical processes (THMC) of geological media – International and Chinese experiences. Chinese Journal of Rock Mechanics and Engineering, 22(10), p. 1704-1715.

NUR, A. and BYERLEE, J., 1971. An exact effective stress law for elastic deformation of rock with fluid. Journal of Geophysical Research, 76, p. 6414-6418.

RICE, J. and CLEARY, M., 1976. Some basic stress-diffusion solutions for fluid saturated elastic porous media with compressible constituents. Reviews of Geophysics and Space Physics, 14, p. 227-241.

SETTARI, A. and MOURTIS, F., 1998. A coupled reservoir and geomechanical modeling system. SPE Journal, 3(3), p. 219-226.

SETTARI, A. and WALTERS, D., 1999. Advances in coupled geomechanical and reservoir modeling with applications to reservoir compaction. Reservoir Simulation Symposium, Houston, Texas.

SKEMPTON, A., 1954. The pore pressure coefficients A and B. Geotechnique, 4, p. 143-147.

VAN DER KNAAP, W., 1959. Nonlinear behavior of elastic porous media. Transactions AIME, 216, p. 179-187.

Comparative Stress Distribution in Coupled and Uncoupled SAGD Reservoir Simulation

Nathan Deisman
Civil & Environmental Engineering Department, University of Alberta
Rick Chalaturnyk
Civil & Environmental Engineering Department, University of Alberta

ABSTRACT: Coupled reservoir geomechanical simulations have become a key component of caprock integrity assessments for SAGD operations. This work demonstrates the differences of stress evolution when considering coupled versus uncoupled reservoir simulation. Coupled simulation involves the use of a reservoir and a geomechanical simulator with feedback to each simulator to update reservoir or geomechanical variable (permeability, porosity, relative permeability, pressure, temperature, saturations). Uncoupled simulation only passes the pressure and temperature to the geomechanical simulation with no reservoir simulator updating. Therefore, it is possible to complete uncoupled simulations exclusively with no knowledge of geomechanical flow property evolution. However, it is important to understand the differences between the stress evolution in each model for caprock integrity analysis. A single geological model was selected and parametric analysis was completed while varying the geomechanical the production injection pressures (1600 kPa, 1900 kPa, 2200 kPa) for a reservoir with an initial pressure at the injector of 1300 kPa. The results of the six uncoupled and coupled models are compared through the changes in mean stress, shear stress, and strength with focus on geomechanical assessment of caprock integrity.

1. INTRODUCTION

Steam Assisted Gravity Drainage operations consist of two parallel horizontal well pairs spaced 5-8m and 5m above the bottom of the bitumen deposit. The reservoir typically has a thick bitumen zone overlain by a thick shale caprock. Steam is injected into the top horizontal well to heat the bitumen and reduce the viscosity, thus mobilizing it to drain downward to the lower producing well. The steam grows upward and laterally forming a 'steam chamber' and is contained by the overlying caprock. The higher the injection pressure, the higher the steam temperature and a higher oil flow rate is possible. However, higher injection pressures and temperature result in changes in effective stresses inside the reservoir and caprock. If these changes are drastic, the caprock may be excessively damaged, resulting in failures casing steam release which would damage the overlying environment and render the bitumen resource unrecoverable.

To study effective stress changes for caprock integrity issues related to SAGD operations, a coupled thermal reservoir geomechanical numerical simulator is required. The coupled simulation involves passing of flow or geomechanical data between numerical solutions or simulators at selected time intervals to update the properties the opposing simulator cannot simulate. Coupled approaches have been used widely for studying the effects for several types of related thermo-hydro-mechanical behaviours including several reservoir types (Glauber et al 2007, Gu and Chalaturnyk 2006, Li and Chalaturnyk 2009). Common approaches include fully coupled, sequentially coupled, uncoupled, and analytically coupled models (Deisman et al, 2009). Fully coupled reservoir geomechanical models solve the flow and stress/strain equations simultaneously, and are thought to be the most accurate approach. Analytically coupled models use assumptions about the geomechanical behaviour of the reservoir to reduce the changes in effective stress to only be affected by changes in pressure, which is one of the methods used in CMG STARS simulator to approximate changes in permeability and porosity (Tran et al, 2009). The assumptions made in these models have been shown invalid and the approach should never be used. The

sequentially coupled approach passes data between the flow and geomechanical simulator, updating flow properties and updating pressure and temperature values. The time step interval relates to how tightly the model is coupled. The uncoupled model uses only the results from the flow simulator in the geomechanical simulation, and there is no feedback into the reservoir simulator. The sequential or uncoupled approach allows for the use of separate commercial packages to be employed in the solution with a separate program to control the data exchange.

In this paper, an analysis of the difference between uncoupled and sequentially coupled effective stress changes in a SAGD reservoir and caprock with 3 well pairs are studied. Two different coupling approaches are used: uncoupled elastic and coupled elastic. Three different injection pressures are also selected for the two approaches. The aim of the work is to determine the differences in the effective stress evolution in the caprock, and how that impacts caprock integrity assessments for SAGD development.

2. COUPLED MODELS

Stress induced changes in porous media as a result of reservoir development is becoming increasingly relevant to access difficult or unconventional hydrocarbons. Coupled reservoir geomechanical models are able to account for these changes during simulation. As well, the impact of reservoir development on effective stress and reservoir and surround rock can be studied. Therefore, coupled simulation is an excellent tool for studying the effects of SAGD operations on caprock integrity.

The coupled simulator used in this study is developed by linking two commercially available and accepted simulation codes. The thermal-flow simulation is handled by CMG's STARS 2010 and the geomechanical simulation is handled by Itasca's FLAC3D 4.0.82. In both simulators, the codes are able to stop and restart with updated inputs and properties. To couple the two codes, an external platform was developed using MS Excel and VBA. The flow and Mechanical Earth Model models are built with all of the static properties inside of Paradigm's Gocad static modeller. The models are then imported into the MS Excel program where the fluid properties, relative permeability, well locations and well schedule are added. The boundary conditions (roller, fixed, free), sequentially coupled/uncoupled, permeability/porosity/relative permeability updating, and temperature and/or pressure coupling is selected.

Changes in the porous media properties due to deformation where based on strain (not stress) and given in equations developed by Touhidi-Baghini (1) and (2) (1998). For the vertical permeability, n=2.0 and for the horizontal permeability, n=0.5. In this modeling study, only the permeability was adjusted and not the porosity or relative permeability.

$$\phi = \frac{\phi_o + \varepsilon_v}{1 + \varepsilon_v} \tag{1}$$

$$k = k_o \exp\left[\varepsilon_v n / \phi\right] \tag{2}$$

3. SIMULATION

A Flow and an MEM model were built for simulation which overlapped each other. The commands "set zonebasedpp" and "set zonebasedtemp' were used inside of FLAC3D to allow the cell centered pressure and temperature extracted from STARS to be written directly to FLAC3D cell center. Figure 1 shows the model geometry with the ground surface, clay shale caprock, IHS shale/sand, the reservoir, and the underlying formation as well as monitoring locations A,B,C,D, and E. The caprock, IHS, reservoir and

underlying carbonate formation were all modeled in the flow simulator to ensure boundaries between the flow and mechanical model were not sharp contrasts (i.e. if the steam chamber reaches the top of flow simulator at the reservoir caprock interface, the mechanical model would see 200C in one cell and 12C in and adjacent cell). The width of the model was 3000m, with the wells on center at 1500m. The full width was selected to model for future comparisons with distributed heterogeneous properties. The model was run in FLAC3D with plan strain y boundary conditions. FLAC2D could have been used however the 3D solution is threaded, where 2D only very recently employed a threaded solution approach and has not been implemented in the developed coupling program.

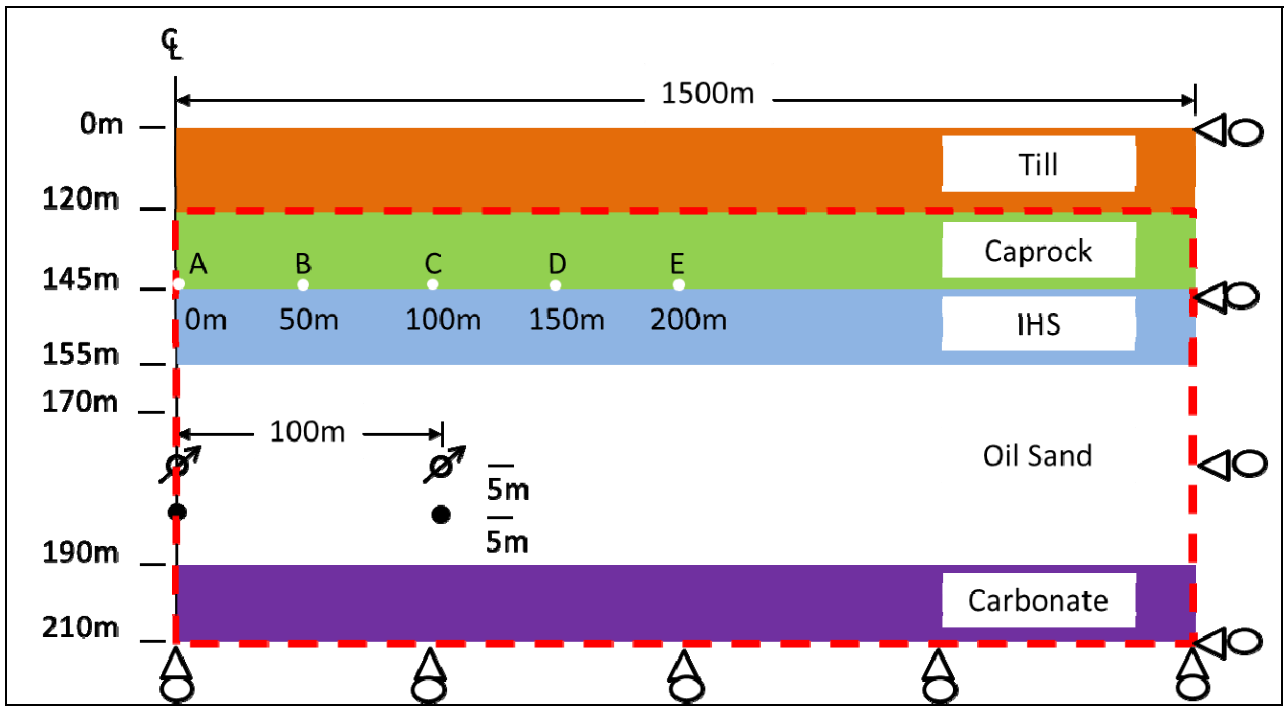

Figure 1 - Geometry of Flow and MEM model, with wells and monitoring points A,B,C,D, and E. The full model is simulated in the geomechanical simulator, where only the red dashed is the flow simulation. The blue dashed box shows the analysis area for stress analysis

The initial temperature for the simulation was 12C and the pressure was hydrostatic with the water table at 55m. The material properties for the reservoir model and geomechanical model are listed in Table 1. A basic set of relative permeability curves and temperature viscosity relationship (Figure 2) were used for the flow model. Three well pairs were used for the simulation with them spaced 5m apart and 5m from the bottom of the reservoir, and horizontally spaced 100m with a well diameter of 220mm. The wells were allowed to circulate before production for 220 days at 200C. Three different cases were run with three different injection/production pressures: 1600/1300kPa, 1900/1600kPa, and 2200/1900 kPa. The complete simulation had 27 coupling steps where data was exchange over the full simulation life of 10 years. The time steps double after 1 day until 128 days, then the time increment increased by 91 days until the end of the simulation.

Table 1 - Material properties for geomechanical simulations

	Units	Till	Caprock	HIS	OilSand	Carbonate
Density	kg/m^3	2300	2250	2250	2250	2250
Bulk Modulus	MPa	49	98	148	294	353
Shear Modulus	MPa	19	37.6	56.4	113	136
Cohesion	kPa	100	300	200	0	200
Friction	deg.	25	35	35	45	40
Lin. Therm Exp. Coef.	1/C	$1x10^{-5}$	$1x10^{-5}$	$1x10^{-5}$	$1x10^{-5}$	$1x10^{-5}$
Porosity		-	0.01	0.01	0.3	0.1
Permeability (i)	mD	-	1	500	5000	1
Perm. Ratio (i/k)		-	1000	10	1.5	1000
Therm. Cond.	J/m-day-C		$17.3 x10^5$	$17.3 x10^5$	$17.3 x10^5$	$17.3 x10^5$
Water Saturation	%	-	100	85	15	85

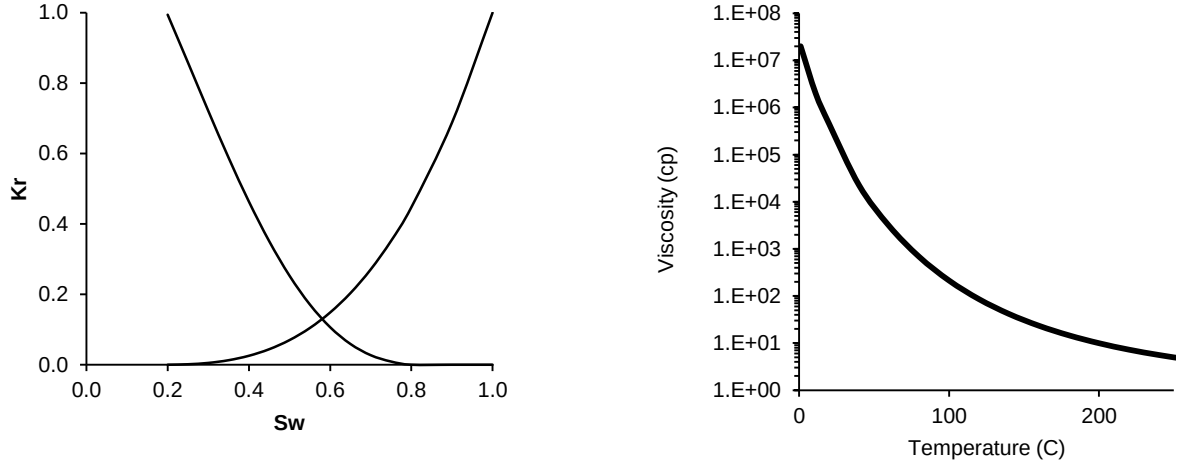

Figure 2 - Oil-water relative permeability and bitumen viscosity as a function of temperature

4. RESULTS

Results from the four different models (uncoupled elastic, uncoupled plastic, coupled elastic and couple plastic) with three injection pressures (1600 kPa, 1900 kPa, and 2200 kPa) are shown below. The models were compared for differences in temperature and pressure evolution, as well as mean effective stress (3) and shear stress (4). All the results are plotted with the same scale to for direct comparison between temperature, pressure, and stress evolution between injection pressures.

$$p' = \frac{\sigma_1' + \sigma_3'}{2} \tag{3}$$

$$\tau = \frac{\sigma_1 - \sigma_3}{2} \tag{4}$$

To compare the results of the stress evolution and the impact on caprock integrity, simply plotting the stresses and visually comparing them is insufficient. As well, subtracting one model state from the other would not be sufficient for comparison between models as the stress fronts are at two different locations. To provide a comparison, the stress state was evaluated against the Mohr-Coulomb failure criteria (written in terms of principle stresses) shown in equation 5.

$$\sigma_1' = \sigma_3' \tan^2\left(45 + \phi/2\right) + 2c\tan\left(45 + \phi/2\right) \tag{5}$$

For each minimum effective stress at each cell location, the maximum allowable effective stress was compared verses the maximum effective stress predicted by the simulation. If the predicted stress exceeded the allowable stress, a value of '1' was assigned and if it did not exceed a value of '0' was assigned to the cell. Once each of the maps of '0's and '1's were created for each simulation case, the uncoupled case was subtracted from the coupled case. This created a differential map, where:

- -1 shows the uncoupled solution 'failed' where the coupled did not
- 0 shows the uncoupled and coupled solution are equal
- 1 shows the coupled solution failed where the coupled did not

The results for each of the injections pressures are shown in Table **2**, Table **3**, and Table **4**. In each of the cases the pressure and temperature front advance further at the end of 5 years of simulation for the coupled case. As well, the mean stress and shear stress reach a high total value in the coupled case verses the uncoupled case.

When comparing the 'failure' of each of the elements between the models, taking into account that the stresses are higher in the coupled case, it was expected that the coupled model had more 'failed' elements over the uncoupled model. In the 1600 kPa injection scenario, the coupled case did show more 'failed' elements. However, there was a region that 'failed' in uncoupled analysis that did not fail in coupled analysis.

In the 1900 kPa injection case, the regions of dissimilar 'failure' increased especially near the region near the outside of the steam chamber development where the pore pressure increased and mean stress was lower. There is 'failure' in the uncoupled case underneath the steam chamber where there is no failure in the coupled case.

In the 2200 kPa case, it was expected to see more differences as the injection pressures increased however, the models have fewer differences than the 1900 kPa injection case. This is most likely due to the very high injection pressures inducing large changed in effective stress regardless of updating permeability through coupling.

Table 2 - Results for the uncoupled and coupled simulations for 1600 kPa injection pressure. The plots start at the base of the model and go to the top of the caprock. The width of each plot is 250m

	Coupled	Uncoupled
Temperature 1.2000E+01 2.0000E+01 4.0000E+01 6.0000E+01 8.0000E+01 1.0000E+02 1.2000E+02 1.4000E+02 1.6000E+02 1.8000E+02 2.0000E+02 2.2000E+02	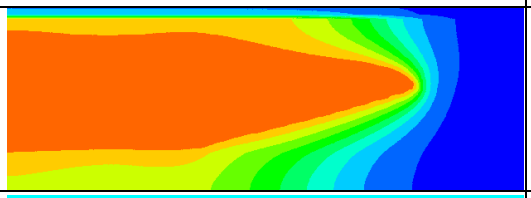	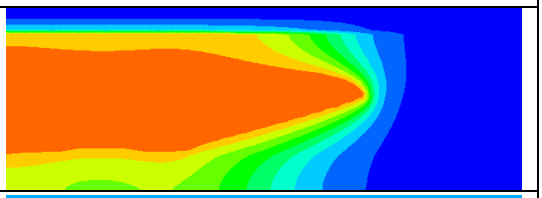
Pressure 0.0000E+00 2.0000E+05 4.0000E+05 6.0000E+05 8.0000E+05 1.0000E+06 1.2000E+06 1.4000E+06 1.6000E+06 1.8000E+06 2.0000E+06 2.2000E+06 2.4000E+06 2.5000E+06	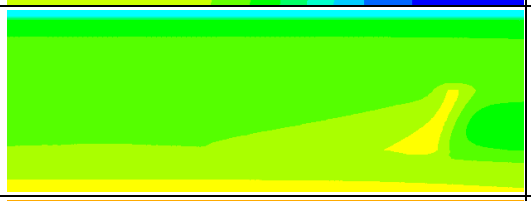	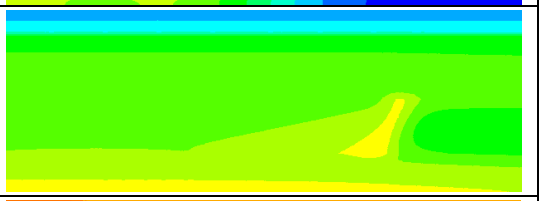
Mean Stress	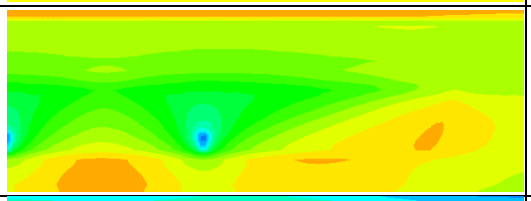	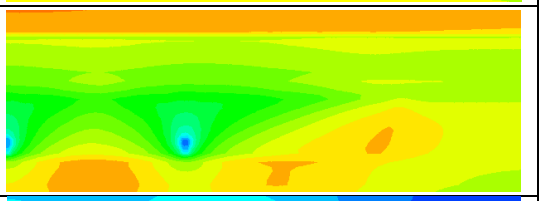
Shear Stress	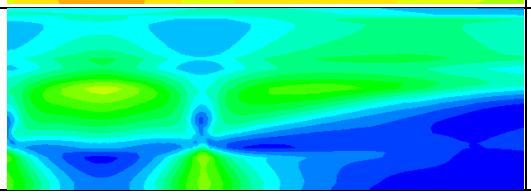	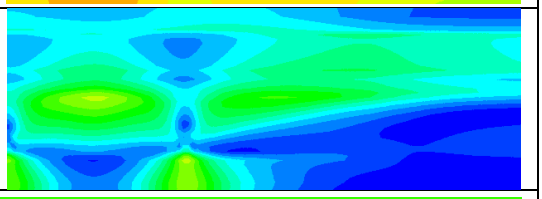
Uncouped Fail Coupled Fail Equal in Both	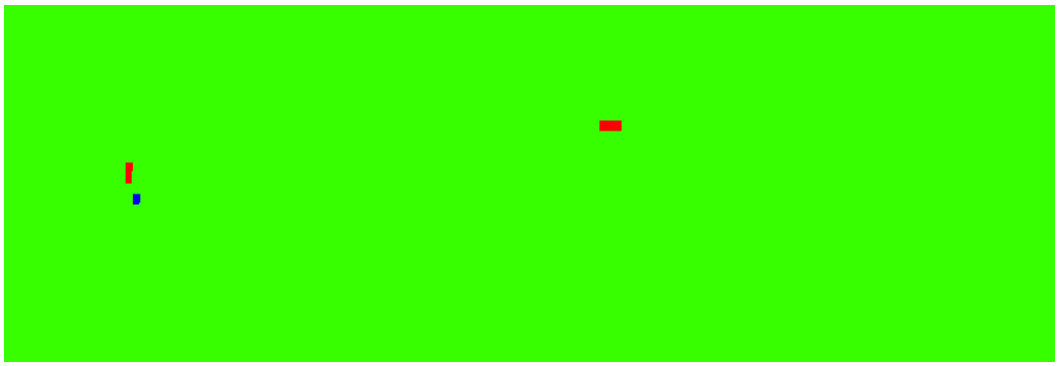	

Table 3 - Results for the uncouple and coupled simulations for 1900 kPa injection pressure. The plots start at the base of the model and go to the top of the caprock. The width of each plot is 250m

	Coupled	Uncoupled
Temperature 1.2000E+01 2.0000E+01 4.0000E+01 6.0000E+01 8.0000E+01 1.0000E+02 1.2000E+02 1.4000E+02 1.6000E+02 1.8000E+02 2.0000E+02 2.2000E+02	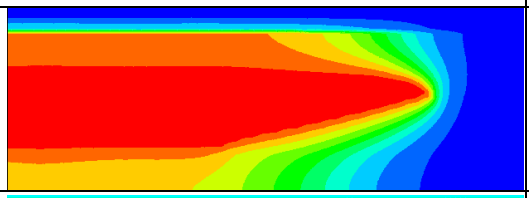	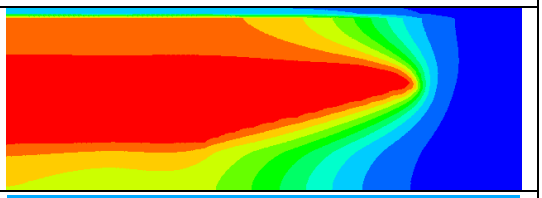
Pressure 0.0000E+00 2.0000E+05 4.0000E+05 6.0000E+05 8.0000E+05 1.0000E+06 1.2000E+06 1.4000E+06 1.6000E+06 1.8000E+06 2.0000E+06 2.2000E+06 2.4000E+06 2.5000E+06	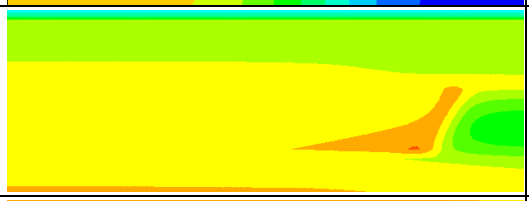	
Mean Stress	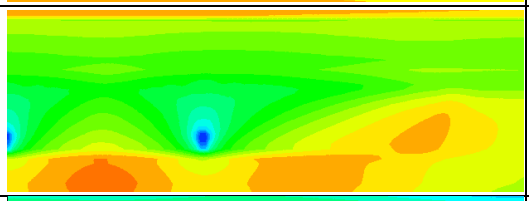	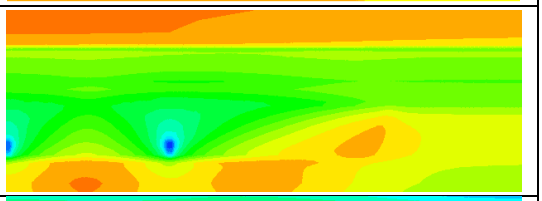
Shear Stress	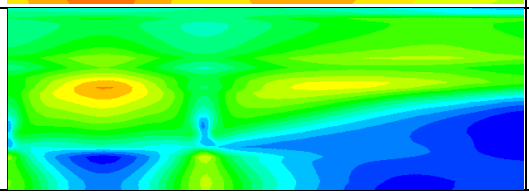	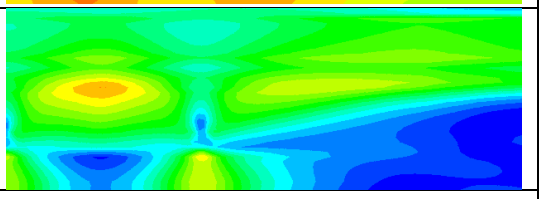
Uncouped Fail Coupled Fail Equal in Both	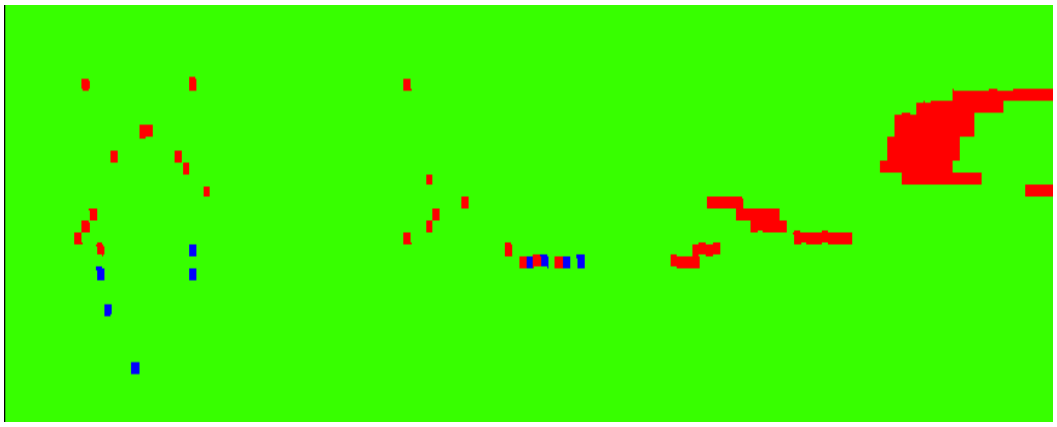	

Table 4 - Results for the uncoupled and coupled simulations for 2200 kPa injection pressure. The plots start at the base of the model and go to the top of the caprock. The width of each plot is 250m

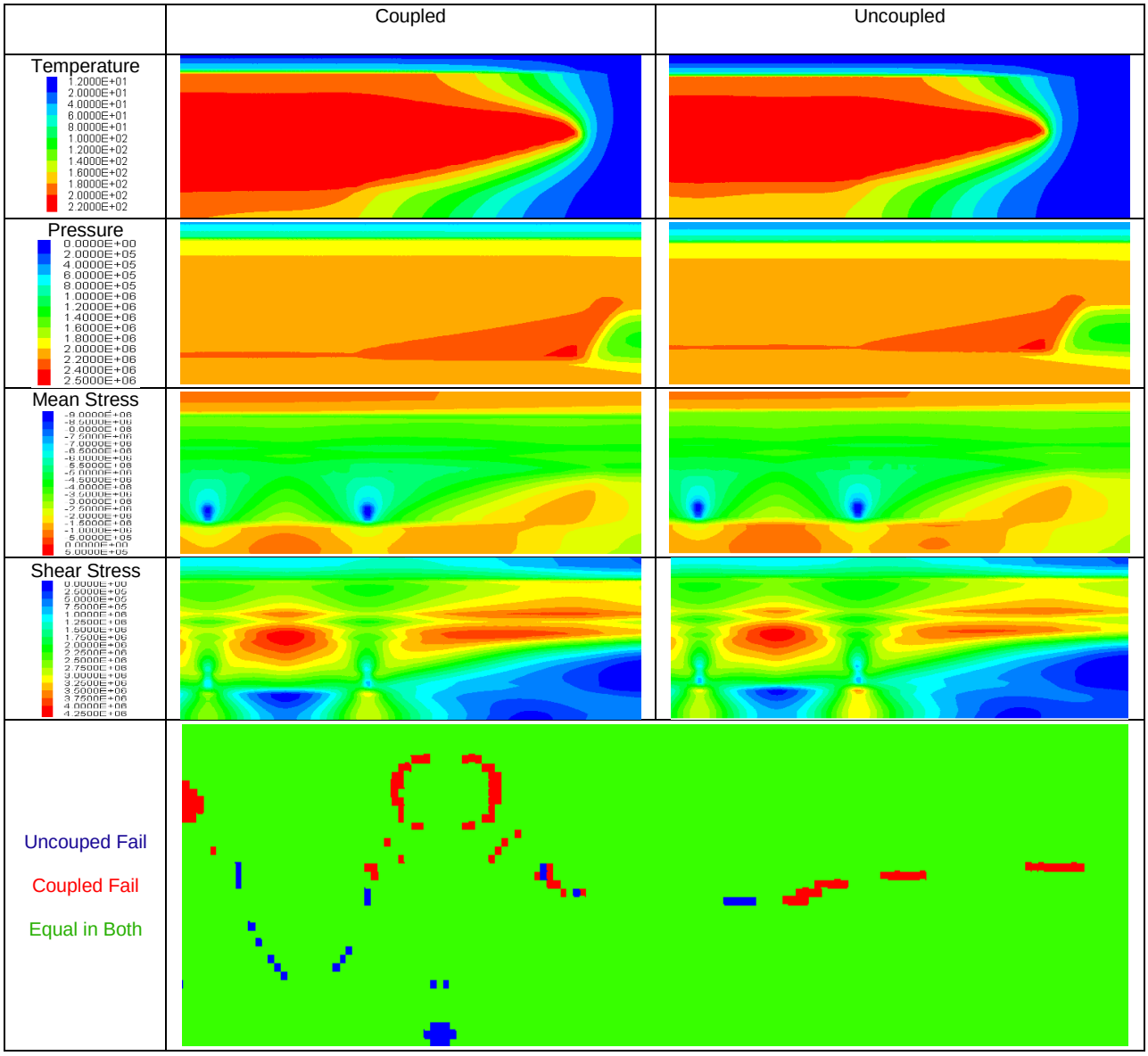

4.1 Displacement Profiles

The displacement profiles were also plotted for each of the cases at the ground surface for comparison, and to ensure that the modeling results made relative sense (Table **5**). The surface displacements are large, however softer material properties may have attributed to this. Regardless, they displacements are not unreasonable for a shallow case with no reservoir history matching or geomechanical monitoring data available. For each of the cases, the coupled model showed a larger surface displacement, which was expected. The larger surface displacements in the coupled model can be attributed to larger changes in volume in the reservoir due to increases in permeability. As permeability increases, fluid pressure and temperature more easily propagate through the reservoir. However, the differences are relatively small between the two models for each injection cases, giving confidence that the uncoupled model is not an unreasonable starting point for simulation.

Table 5 - Vertical displacement profile at surface for each of the injection pressures

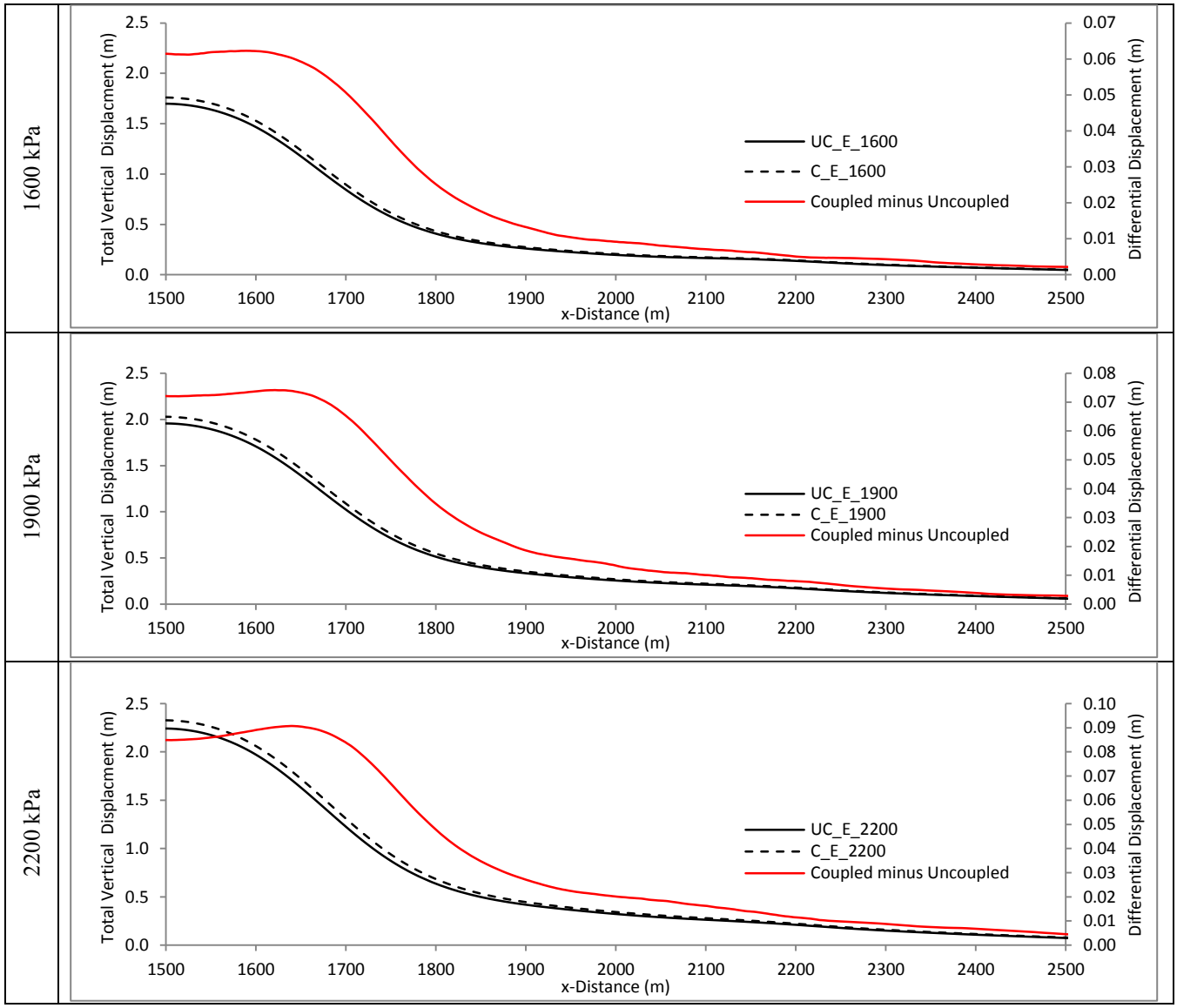

4.2 Stress Path Evolution

The stress paths for each of the monitoring points were plotted for the coupled and uncoupled cases. The figures also show the advance of the pore pressure and temperature front as a function of mean effective stress. In general there is very little difference between the stress path evolution at each of the locations. In each case it is interesting to note that the mean effective stress drops close to zero as the pore pressure front advances, then as the thermal front reaches advances closer, the monitoring point experiences a constant mean stress to shear stress ratio towards the failure envelop. However, the aim of this exercise was to not any major differences in stress path evolution, and for these cases, the stress paths are very similar.

Table 6 - Stress path evolution (Eq 3 and Eq 4) for each observation (C,D,E) comparing the different geomechanical coupling models. Points A and B were very similar to C and D. Dashed lines are uncoupled, solid is coupled with the temperature in red, pore pressure in blue, stress path in black

1600 kPa	1900 kPa	2200 kPa
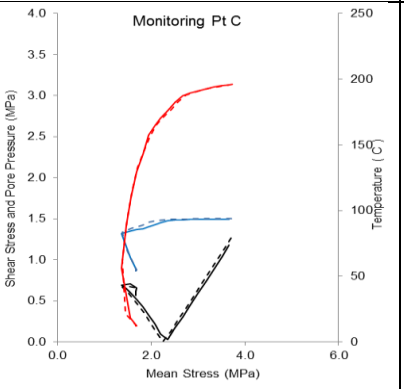	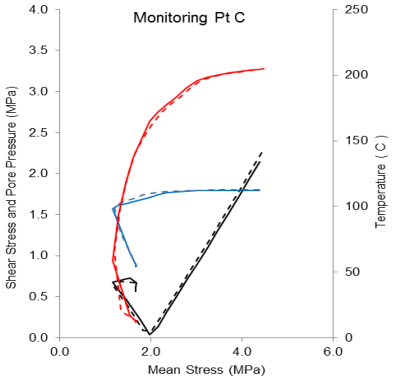	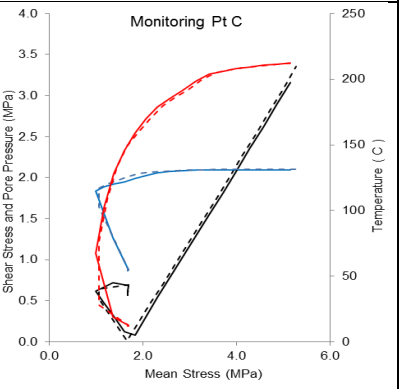
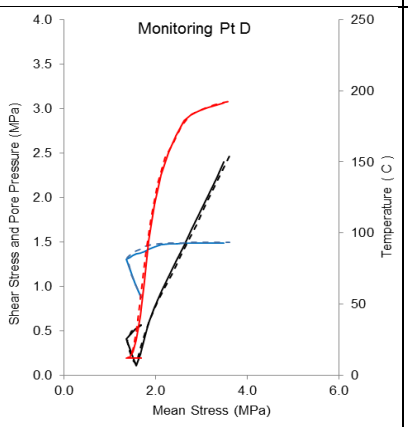	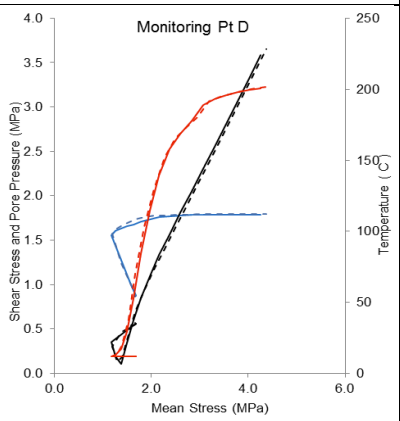	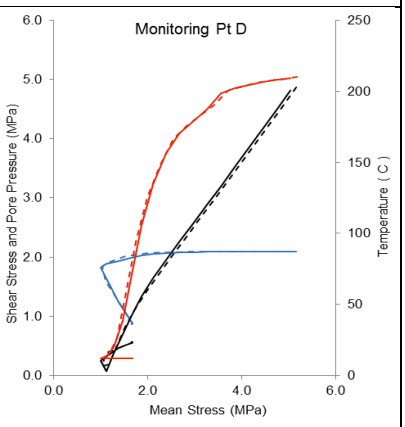
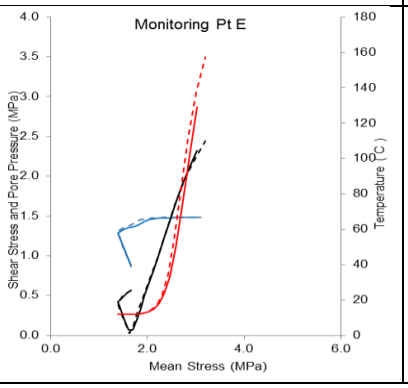	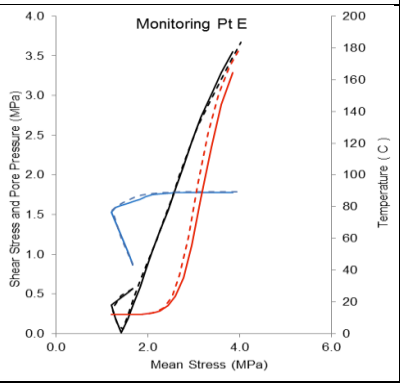	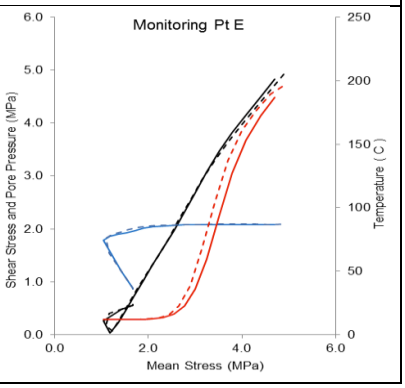

5. CONCLUSIONS

The main goal of this work was to investigate the differences between stress changes in coupled and uncoupled models for SAGD caprock integrity simulations. Three injection pressures were selected for a shallow SAGD project at with 3 well pairs. The injection pressures were set, to be low (1600 kPa), medium (1900 kPa), and high (2200 kPa). The medium and high injection pressures were selected to ensure large deformation and 'damage' to the caprock and reservoir. It was anticipated that there would be a definite trend established between coupled and uncoupled cases when increasing injection pressures. However, it was found that at 1600 kPa and 2200 kPa there was very little difference between the

elastically evaluated failed states of each cell in the simulation. However, there was a large difference between the differences in the 1900 kPa injection case and the 2200 kPa. It was expected that there would be more coupled-uncoupled failure differences in the 2200 kPa case than in the 1900 kPa, however there were less. The stress paths comparisons for the five monitoring points were also plotted for each of the injection pressures. The stress paths showed only slight differences in behaviour for each of the points.

In general, there were minor differences in coupled verses uncoupled stress evolution and using the uncoupled modeling approach does provide a good first approximation for the stress evolution in the reservoir. However, this does not neglect the fact that the coupled reservoir simulation should still be run after uncoupled analysis has been completed. The minor differences in stress paths between the coupled and uncoupled cases for the points in caprock instill confidence that uncoupled modeling is sufficient to develop laboratory triaxial testing stress paths.

6. ACKNOWLEDGEMENTS

The authors would like to thank Alma Ornes for her insights as well as Chris Hawkes for his patience with this work.

7. REFERENCES

DEISMAN, N., Chalaturnyk, R.J., and Mas Ivars, D. 2009. An Adaptive Continuum/Discontinuum Coupled Reservoir Geomechanics Simulation Approach for Fractured Reservoirs. SPE Reservoir Simulation Symposium held in The Woodlands, Texas, USA, 2–4 February 2009. SPE 119254

LI,P and CHALATURNYK, RJ. 2009. History matching of the UTF Phase A project with coupled reservoir geomechanical simulation. Journal of Canadian Petroleum Technology 2009 48(1) 29-35

GU,F and CHALATURNYK, R.J. 2006. Numerical simulation of stress and strain due to gas sorption/desorption and their effects on in situ permeability of coalbeds. Journal of Canadian Petroleum Technology October 2006 45(10) 52-62,

RODRIGUES,LG, CUNHA, LB, CHALATURNYK RJ. 2007. Modelling geomechanics into petroleum reservoir numerical simulation: a coupled technique in a water injection project. Canadian International Petroleum Conference (58th Annual Technical Meeting), Calgary Alberta, Canada June 12-14, 2007. 2007-060

TRAN, D., NGHIEM, L. and BUCHANA, L. Aspects of coupling between petroleum reservoir flow and geomechanics. Ashville 2009 43rd US Rock Mechanics Symposium June 28th- July 1st 2009. ARMA 09-89

TOUHIDI-BAGHINI, A. 1998. Absolute permeability of McMurray formation oil sands at low confining stresses. Ph.D dissertation. Department of Civil Engineering, University of Alberta, 339 p.

Deep Borehole Study Toward the Feasibility of Engineered Geothermal System (EGS) in Northeastern Alberta

Judith S. Chan
Department of Physics, University of Alberta
Douglas R. Schmitt
Department of Physics, University of Alberta
Jacek Majorowicz
Department of Physics, University of Alberta
Elahe Poureslami Ardakani
Department of Physics, University of Alberta
Greg Nieuwenhuis
Department of Physics, University of Alberta
Mirko van der Baan
Department of Physics, University of Alberta
Jochem Kueck
ICDP-OSG, GFZ-Potsdam

ABSTRACT: With the increasing awareness of the need for the reduction of carbon emissions globally, geothermal energy, which offers a potential for cleaner energy generation, is one potential new source. In Alberta, these geothermal resources are likely to be found in the sedimentary basin, or in the deeper crystalline basement rocks. Alberta exhibits a very low geothermal gradient compared to other existing geothermal fields located in areas of volcanic and tectonic activity. To mitigate this effect, the focus in Alberta will involve the development of engineered geothermal systems (EGS) in the target resource.

The first goal for EGS research and development is to develop a detailed geological-geophysical characterization of selected sites to delineate potential geothermal reservoirs in Northern Alberta. One of the selected sites is in the Fort McMurray area. The deepest well drilled in the oilsands areas of Northern Alberta is located just west of Fort McMurray. It has a depth of 2363 m and as such can provide details on the physical properties of the rocks, the state of stress, and the existence of fracture porosity toward geothermal investigations. To date, we have acquired temperature logs to study the change in geothermal gradient with depth, and a series of petrophysical logs to study the finer scale structure of the rock formations with vertical resolutions in the range of 0.05 cm to 80 cm. Our aim is to identify geological features such as zones of fractures in the basin and/or basement that could provide an indication of enhanced fluid flow potential – a necessary component for any geothermal systems to be viable. Zero offset and walkaway vertical seismic profiles (VSP) were also conducted to measure the seismic responses at the borehole. VSP data can be used to delineate the structural and stratigraphic features surrounding the borehole that could not be resolved from surface seismic reflection data that are also available near the borehole. The full integration of well logs, VSP data and surface seismic reflection data are expected to provide a detailed characterization of the sedimentary basin and crystalline basement rocks of the Canadian Shield in Northeastern Alberta and will assist in future planning for drilling.

1. INTRODUCTION

The development of geothermal resources offers an alternative solution to supply thermal energy for the active oilsands production. This could help to minimize the environmental impact in the overall consumption of natural gas for the processing of tar sands. Such use of the geothermal reservoirs requires

temperatures at around 60°C and may be found in the Alberta basin at depths of 4 to 5 km deep (Majorowicz and Moore, 2008). In Alberta, the Phanerozoic sedimentary succession thins towards the northeastern part of the province where the Precambrian crystalline basement rocks can be reached at a depth of approximately 0.5 kilometers. The crystalline basement is characterized by rocks with the lack of natural porosity or fluids that facilitate heat flow within the rocks. Advanced technologies have been developed to extract poorly permeated rocks hence optimizing the potential geothermal systems available for exploration. One such system is the 'engineered geothermal system' (EGS) in which the reservoir is engineered to produce geothermal energy that was originally not deemed to be economical due to the lack of fluid and/or permeability (Majorowicz and Moore, 2008). This idea is currently being investigated through the Helmholtz-Alberta Initiative (HAI), a research collaboration between the Helmholtz Association of German Research Centres and the University of Alberta on energy projects toward cleaner energy production.

Well logging in a deep borehole offers the unique opportunity to investigate the physical properties of the shallow crust and to study the thermal changes at depth that are essential information for geothermal exploration. In July 2011, a comprehensive suite of geophysical logs has been collected in the deep borehole AOC GRANITE 7-32-89-10 that was drilled west of Fort McMurray (Figure 1). This borehole reaches a total vertical depth (TVD) of 2.3 km through 550 m of sedimentary strata and into the crystalline basement rocks. It is by far the deepest well drilled into the metamorphic Canadian Shield rocks in Western Canada. The geophysical logs were acquired by Operational Support Group (OSG) of the International Continental Scientific Drilling Programme (ICDP) from 1005 m to the maximum

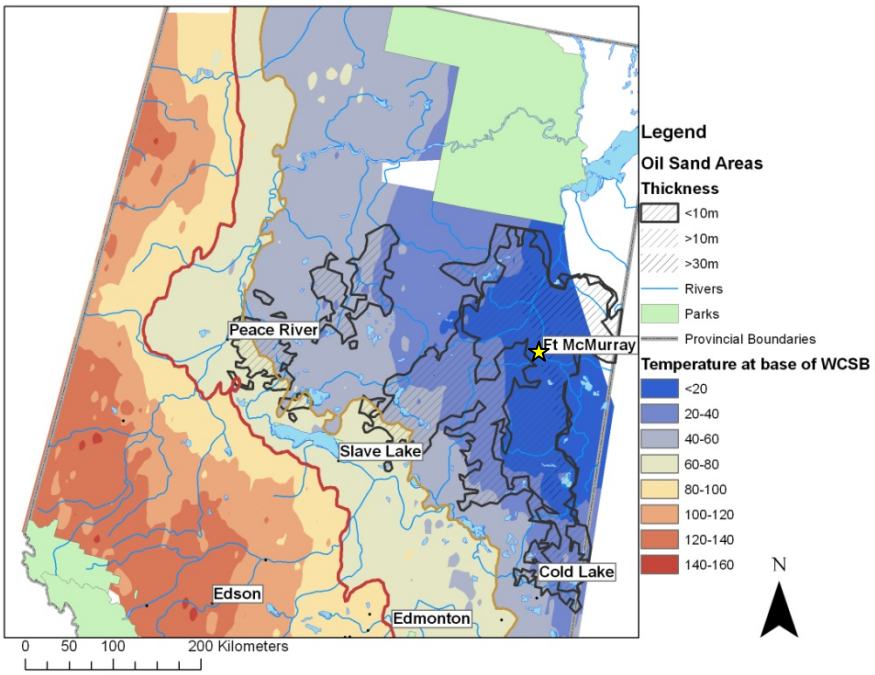

Figure 1 - Location of the deep borehole (yellow star) (AOC GRANITE 7-32-89-10) west of Fort McMurray marked on the temperature map of the base of Western Canadian Sedimentary Basin (WCSB) in Alberta (after Grey, Majorowicz, and Unsworth, 2011)

accessible depth of tools at 1880 m. These borehole measurements consist of classical downhole logs (caliper, sonic velocity, electrical resistivity, natural gamma radioactivity, composition of uranium, thorium and potassium, magnetic susceptibility, total magnetic field, and borehole wall images), as well as seismic measurements with 4-level borehole geophone chain (zero-offset and walkaway vertical

seismic profiling (VSP)). This borehole was also previously logged in 1994 and 2003 by Schlumberger which includes Dipole Shear Sonic Imager (DSI) and Formation MicroImager (FMI) logs. Temperature logging was run by Lonkar in late 2010. Logs from separate logging operations and vintages were correlated using the natural gamma radioactivity curve surveyed in each logging tool by applying appropriate depth shifts.

This paper provides a brief description of some of the well logs acquired from the deep borehole located west of Fort McMurray, Alberta. The current stage of log analysis focuses on identifying anomalous zones that could correlate with the fractured zones favorable for geothermal energy development. Later stages of this work would involve correlating the well logs to available petrographical analysis from drill core samples and analyzing the velocity profiles from the VSP data sets.

2. WELL LOGGING

The feasibility in the development of EGS system requires a comprehensive study of the subsurface by integrating geological and geophysical data for identifying potential geothermal aquifers. One of the goals is to identify regions with high levels of radiogenic heat production in the basement rocks. Heat generation can be determined from uranium (^{235}U), thorium (^{232}Th), and potassium (^{40}K) isotopes from the spectral gamma radioactivity logs. Another goal of this project is to identify zones of fractures in the study area. For full EGS development, presence of fractures is beneficial since the system requires the introduction of water into rocks of limited permeability in a controlled fracture setting to allow proper heat extraction (Majorowicz and Moore, 2008). However, it is also important to note that the presence of fractures could cause a major loss of fluids from the circulation system.

2.1 Temperature

Temperature logs were run in late 2010 and early 2011 to measure the change in temperature at depth. Temperatures were measured after the borehole was filled with water and the water level has stabilized. A rapid drop in water level (70 m over a few hours) was observed which reveals possible evidence of cracks opening under pressure. The temperature gradient experiences an abrupt change in the Middle Devonian Prairie Evaporites (TVD 300-500 m), which is typically characterized by salt and anhydrite with thin interbeds of carbonate and shale (Cotterill and Hamilton, 1995). This formation is observed in the FMI logs to be partially fractured that could allow water flow through the rock matrix of fractures. The bottom hole temperature at 2.324 km was measured to be 47.5°C with a temperature gradient of 21.5°C/km (Figure 2). By applying downward extrapolation of the measured temperature gradient, the bottom hole temperature can reach 84°C at approximately 4 km, which is the optimal temperature necessary for the heating of water for geothermal energy production. The temperature gradient in the Precambrian basement is increasing with depth, and it has been interpreted as result of the temperature increase by nearly 10°C from the latest glacial to postglacial (Holocene) event at 13.5K years ago (Gosnold, Majorowicz, Klenner, and Hauck, 2011).

2.2 Caliper

The enlargement of borehole can provide an indication of fractured zones when the rock edges of fractures are chipped away during drilling. A multiarm, multidirectional dipmeter tool was used to assess the borehole geometry and condition by recording high resolution (5 cm) caliper measurements that show two borehole diameters that are 90° apart. One pair of arms is always aligned with the major axis of an elliptical borehole, the other pair with the minor axis (Schlumberger Limited, 1991). Caliper measurements were collected from depths of 1005 to 1875 m as seen in Column 4 of Figure 3. Plotting of caliper log responses and bit size can be used to recognize different types of enlarged borehole including

gauge hole, breakout, washout, and key seat (Plumb and Hickman, 1985). Two enlarged borehole zones are identified at 1187-1259 m and 1760-1794 m. Both of these zones correlate to relatively higher magnetic susceptibility and photoelectric factor, and also lower total magnetic field. The relationships between these curves are currently undetermined.

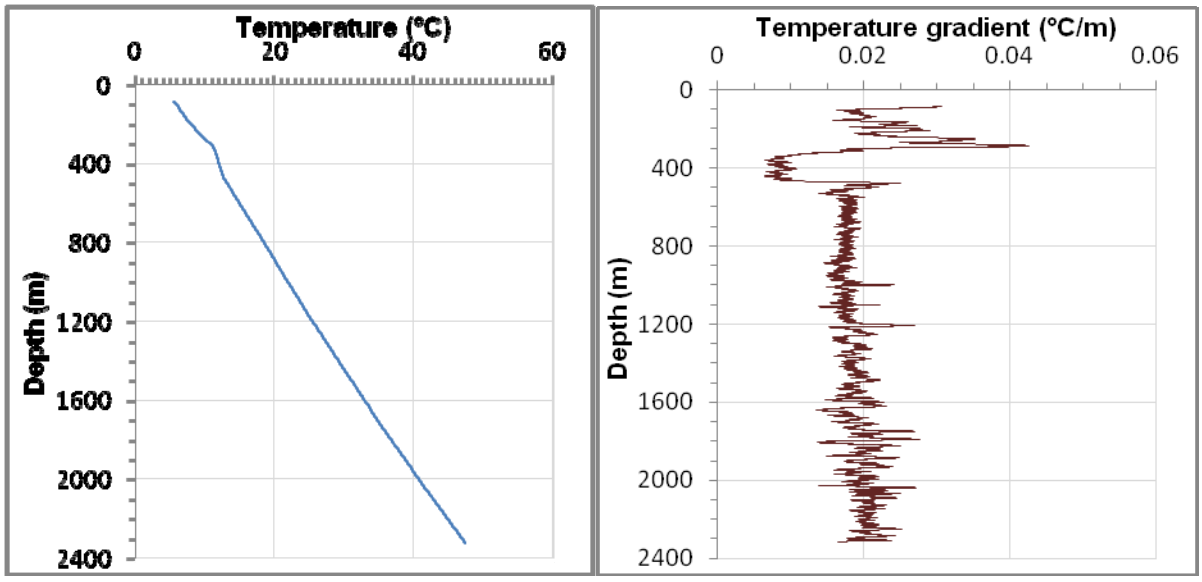

Figure 2 - Variation in temperature (left) and the calculated temperature gradient (right) with a 10 m averaging window as a function of true vertical depth

2.3 Gamma Ray

Gamma radiation emitted from the formation is measured by the gamma ray sonde. This form of logging is usually run in combination with other logging tools and is useful in correlating logs acquired using different tools. Heat generation in the Precambrian basement rocks are valuable toward the feasibility study for geothermal exploration by analysing the spectral gamma ray logs (column 6 of figure 3) of the borehole. It is controlled by the concentration of radiogenic elements in the upper crust, and most of the gamma ray radiation in the earth originates from the decay of three radioactive elements: potassium (^{40}K), uranium (^{238}U) and thorium (^{232}Th).

2.4 Resistivity

In the fractured crystalline rock, resistivity is very sensitive to the presence of interstitial fluids and alteration minerals (Boness and Zoback, 2004). Hydrothermal alteration of the rocks influences the formation resistivity where the alteration minerals of different resistivities could be attributed to geothermal activity (Steingrimsson, 2011). Two different tools have been used to measure the resistivity responses in the borehole. The first set is micro-spherically focused logs (MSFL) acquired in 1994 and 2003 which measure the conductivity of the rocks near the borehole and has shallow depths of investigation. The second and most recent set is the dual-laterologs (DLL) which offer greater depths of investigation compared to MSFL. The purpose of using deeper-reading resistivity device is to ensure that true formation resistivities are measured beyond the invaded zone with a larger radius of investigation. The resistivity curves are plotted in Column 7 of Figure 3. Three significantly lower resistivity intervals

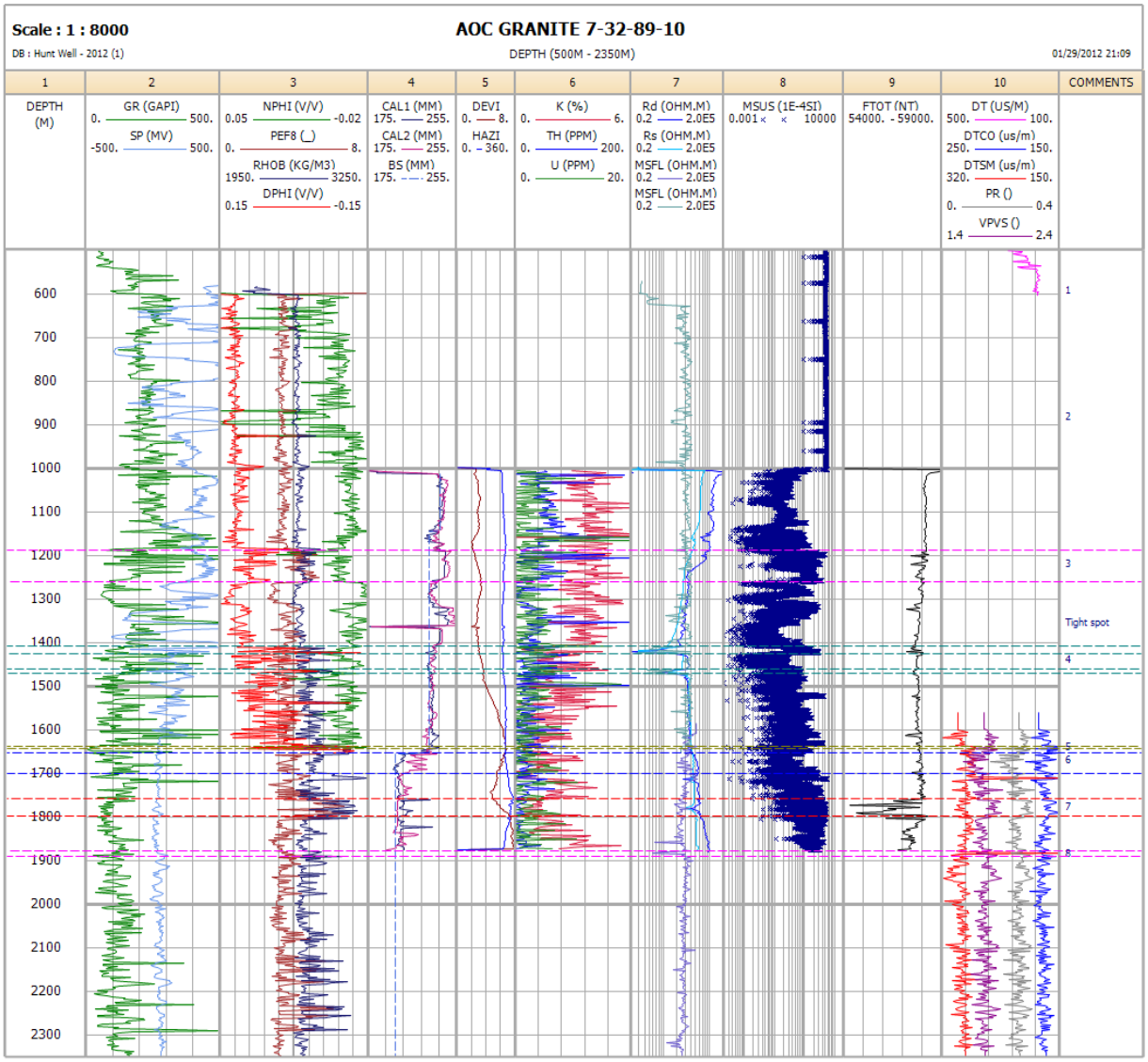

Figure 3 - Composite log display of the deep borehole including logs acquired in 1994, 2003, and 2011. The 2011 logs have depth coverage from 1005 to 1880 m. Dashed color lines indicate zones of interests and numbers in the final column correspond to comments listed in Table 1

Legend:

BS	Bit size	**GR**	Gamma Ray	**Rd**	Deep Resistivity
CAL	Caliper	**HAZI**	Hole azimuth	**Rs**	Shallow Resistivity
DEVI	Hole deviation	**K**	Potassium	**RHOB**	Bulk density
DPHI	Density porosity	**MSFL**	Micro-spherically focused log	**SP**	Spontaneous potential
DT	Delta-T (Interval transit time)	**MSUS**	Magnetic susceptibility	**TH**	Thorium
DTCO	Delta-T (Compressional)	**NPHI**	Neutron porosity	**U**	Uranium
DTSM	Delta-T (Shear)	**PEF8**	Photoelectric factor	**VPVS**	Ratio of P- and S-wave velocities
FTOT	Total magnetic field	**PR**	Poisson's Ratio		

Table 1 - List of comments corresponding to the interpreted log sections in Figure 3

#	Depth (m)	Comments
1	409 (Kelly Bushing) – 1005	Casing
2	864 – 897	Sudden change in neutron porosity, fractured zones in FMI logs
3	1187 – 1259	Washout zone (CAL1 & CAL 2 > BS), higher PEF, higher MSUS
4	1406 – 1424, 1461 – 1471	Higher RHOB, lower R, higher MSUS, fractured zones in FMI logs
5	1637 – 1644	Drilling-induced fractures in FMI logs, no widening in CAL logs, lower PEF
6	1653 – 1700	Borehole breakout, spikes in MSFL
7	1759 – 1797	Borehole breakout, higher MSUS, lower FTOT
8	1878 – 1891	Higher PEF, higher RHOB, lower MSFL

are identified at 1406–1424 m, 1461-1471 m and 1878-1891 m. These anomalies outline sections of the deep borehole that provide indications in the presence of conductive alteration minerals. The smaller radius of investigation for the MSFL provides a higher resolution of the formation resistivity and is useful in complementing the newer resistivity curves for recognizing fractured zones in this project.

2.5 Electrical Image

Interpretations of the wireline logs acquired recently are used to supplement earlier electrical microscanner images obtained by the well operator when it was drilled. To enhance the fluid production in the subsurface rocks for the sustainable development of EGS in the Western Canadian Sedimentary Basin, it is essential to understand the geometry of the fractures and the local stress regimes. Schlumberger's Formation MicroImager (FMI) tool is a high-resolution (5 mm) electrical borehole imaging tool and is sensitive to the variations in mineralogy or porosity which has an effect on the conductivity of rocks. Electrical images are created from raw electrical image curves that correspond to a volume of rock within a few centimeters of the borehole wall (Davatzes and Hickman, 2010). Analysis was performed on the statically normalized FMI logs (Figure 4). These image logs allow us to identify the presence of fractures with consistent dip and strike throughout the borehole according to the contrasts in conductivity between the fractures and the changes in rock composition. Color display changes from light to dark brown that corresponds to changes from low to high conductivity. The nature, orientation, spacing and density of the fractures can further be extracted from the image logs. The FMI logs for this borehole reveal zones of fractures at 1406-1424 m and 1461-1471 m. Both of these intervals also correlate to relatively higher bulk density, lower resistivity and higher magnetic susceptibility values, which indicate the presence of conductive alteration minerals in the fractures. Further interpretation and processing are required for the FMI logs to distinguish between the different planar structures (such as open fractures versus closed fractures, faults, drilling-induced fractures), the direction of maximum horizontal stress, and to further enhance sections of images logs with poor resolution.

3. VERTICAL SEISMIC PROFILE

Vertical seismic profiling (VSP) provides a favorable geometry for in-depth mapping of dipping fractures by placing arrays of receivers directly in the borehole. To better understand the velocity structure and to look for the effects of fractures, a high resolution zero-offset VSP was conducted to measure the seismic responses in the borehole. It can be used to delineate the structural and stratigraphic features surrounding the borehole that could not otherwise be resolved from surface seismic reflection data. A comparison of VSP data with borehole information is expected to provide information on the local lithological changes, mineral composition of rocks and on the presence of fractures.

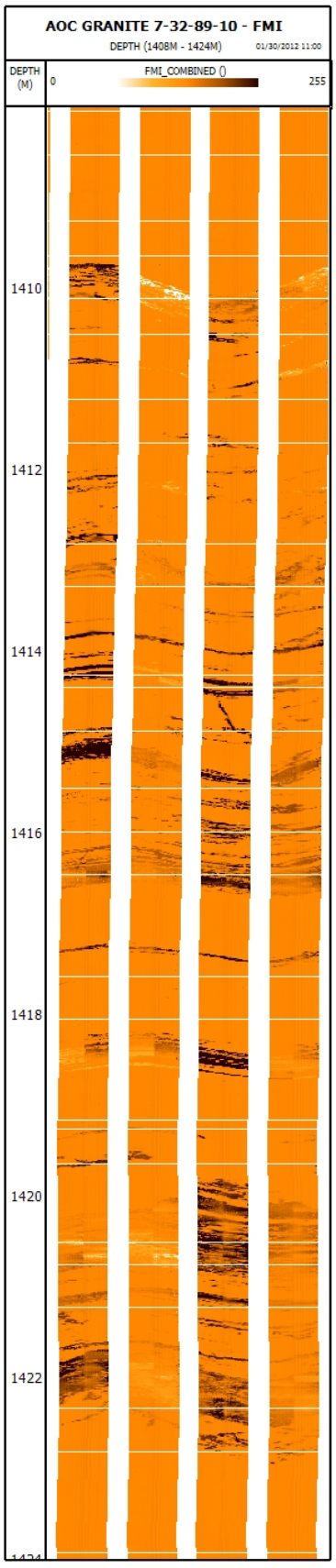

Figure 4 - Formation MicroImager (FMI) log at TVD 1408-1424 m that illustrates fracture zones filled with conductive materials of higher bulk density and magnetic susceptibility. Brighter color indicates lower conductivity. Later processing of the FMI logs is expected to provide better resolution of the fractures

4. SUMMARY

The presence of major fluid pathways in subsurface exploration can be identified by understanding the effects of fractures, cracks, and microcracks in the subsurface. Part of a feasibility study of EGS development in Northern Alberta consists of the investigation of subsurface fluid pathways in the Precambrian basement rocks that are expected to have the optimal temperature for geothermal energy production at depths of 4-6 km. The deep borehole located west of Fort McMurray can provide details on the physical properties of the crystalline basement rocks, the state of stress, and the existence of fractures. Zones of radiogenic heat production and signs of fractures can also be identified from wireline logs to assist in the identification of geothermal reservoirs.

A log section has been compiled from data acquired in 1993, 2004, and the latest extensive logging program in July 2011. Anomalous zones from the temperature, caliper, gamma ray, resistivity and electrical image logs have been discussed under their respective sections in this paper. One of the biggest zones of interest is in the 1406-1424 m range in which FMI logs reveals higher concentrations of fractures in this conductive zone. This may indicates communication of natural brines in fractures with the wellbore fluid. Peaks in the temperature gradient graph also appears to correlate with relatively higher photoelectric factor (PEF) and higher density (RHOB) values, which are possible evidence of heavy mineral deposits in those zones. Other data sets that were acquired for the purpose of this project include dipole shear sonic, acoustic televiewer, full-waveform sonic logs and vertical seismic profiles. The processing and interpretation of the remaining data sets are currently underway, and are expected to provide more detailed understanding of the anomalous features identified from the processed log sections discussed in this paper. Analyses of stress using the FMI and televiewer image logs are also work in progress. The results will also later be used to correlate with the surface seismic reflection profiles adjacent to the borehole which reveals NW-SE eastward dipping reflectors within the metamorphic shield rocks that might have intersected the deep borehole.

5. REFERENCES

BONESS, N.L., and M.D. ZOBACK, 2004. Stress-induced seismic velocity anisotropy and physical properties in the Safod pilot hole In Parkfield, Ca., ARMA/NARMS, 04-540, 7 p.

COTTERILL, D.K., and HAMILTON, W.N., 1995. Geology of Devonian limestones in Northeast Alberta. Alberta Research Council (Alberta Energy and Utilities Board/Alberta Geol. Survey), Edmonton, Open File Report 1995–07, 39 p.

DAVATZES, N.C., and HICKMAN, S.H., 2010. Stress, fracture, and fluid-flow analysis using acoustic and electrical image logs in hot fractured granites of the Coso geothermal field, California, U.S.A., in Pöppelreiter, García-Carballido, C., and Kraaijveld, M., eds., Dipmeter and Borehole Image Log Technology. AAPG Memoir, 92, p. 269-293.

GOSNOLD, W., MAJOROWICZ, J., KLENNER, R, and HAUCK, S., 2011. Implications of post-glacial warming for Northern Hemisphere heat flow. Geothermal Resources Council Transactions, 25, p. 795-800.

GREY, A., MAJOROWICZ, J., and UNSWORTH, M. Investigation of the geothermal state of sedimentary basins using oil industry thermal data: Case study from Northern Alberta exhibiting the need to systematically remove biased data. Submitted to Geothermics. December 2011,

MAJOROWICZ, J., and MOORE, M.C., 2008. Enhanced geothermal systems (EGS) potential in the Alberta basin. Institute for Sustainable Energy, Environment and Economy Research Paper, University of Calgary, 34 p.

PLUMB, R.A., and HICKMAN, S.H., 1985. Stress-induced borehole enlargement: a comparison between the four-arm dipmeter and the borehole televiewer in the Auburn geothermal well. Journal of Geophysical Research, 90, p. 5513-5521.

Schlumberger Limited, 1991. Log Interpretation Principles/Applications, Schlumberger Educational Services, Houston, 241 p.

STEINGRIMSSON, B., 2011. Geothermal well logging: Geological wireline logs and fracture imaging. Presented at Short Course on Geothermal Drilling, Resource Development and Power Plants, El Salvador, January 16-22, 2011.

Overview of the Oil Sands Caprock Integrity Project

Kristine Haug
Energy Resources Conservation Board/Alberta Geological Survey
Chris Schneider
Energy Resources Conservation Board/Alberta Geological Survey
Shilong Mei
Energy Resources Conservation Board/Alberta Geological Survey
Paul Greene
Energy Resources Conservation Board

ABSTRACT: Although most in situ operations in Alberta do not encounter significant problems during resource extraction, there have been a few documented occurrences of oil or steam releases as a result of compromised caprock seals. The objective of the Oil Sands Caprock Integrity Project (OSCRIP) is to characterize the units above and below bitumen zones to determine which geological factors affect the quality of the caprock seal. In addition, geomechanical properties and stress measurements of the bitumen reservoir and overlying units will be examined to provide a better picture of the containment conditions in which in situ operations occur. The information from this study will aid regulatory staff and industry in determining the zone-specific geological and geomechanical factors that could affect the design, operation, and feasibility of in situ recovery projects. The OSCRIP study area (Townships 87 to 99 and Ranges 1 to 13, West 4th Meridian) encompasses the surface mineable area, the northeast extent of the Wabiskaw-McMurray bitumen deposit and the Clearwater Formation, as well as a wide band of the Devonian salt-dissolution zone. Regional geological mapping of the Cretaceous strata focuses on the spatial extent and thickness of the caprock seal. Mapping of the underlying Devonian strata is targeted at better understanding the potential effects of salt dissolution and collapse of overlying strata on the integrity of the caprock seal. Examination of LiDAR (Light Detection And Ranging) bare earth DEM in the study area has revealed localized depressions that may represent sinkholes rooted in subsurface collapse features in Devonian carbonate and evaporite strata. Mapping the location and understanding the timing of salt dissolution-related features and deformation in the Devonian strata will help address questions about the possible effect that geological structures, such as sinkholes, have on the integrity of the caprock, as well as the potential for localized variations in the stress regime of the bitumen zone and overlying units. The stress regime in units above 350 m is such that any induced fractures are believed to be horizontal, and therefore, there would appear to be no mechanisms that would allow these fractures to reach the surface. However, recent incidents have shown that vertical pathways can occur, linking the subsurface to the surface. The final phase of the project will evaluate the changes that may occur in the stress regime under thermal operating conditions in the study area.

1. INTRODUCTION

Although most in situ operations in Alberta encounter few significant problems during resource extraction, there have been newly documented occurrences of oil or steam releases as a result of compromised caprock seals. Most notably was the loss of steam-chamber containment at the Total E&P Canada Ltd. Joslyn Creek SAGD operation on May 18, 2006 (ERCB, 2010). The Energy Resources Conservation Board (ERCB) recognized that a better understanding of the geological and geomechanical factors affecting the quality of the caprock seals above bitumen resources is needed to appropriately regulate in situ operations. The Energy Resources Conservation Board/Alberta Geological Survey

initiated the Oil Sands Caprock Integrity Project (OSCRIP) to characterize the caprock to support safe operations, protection of overlying non-saline groundwater, and conservation of the bitumen resource.

The OSCRIP study area is located within the Athabasca Oil Sands Area, from Townships 87 to 99 and Ranges 1 to 13, West 4th Meridian (Figure 1). The study area encompasses the surface mineable area, the northeast extent of the Wabiskaw-McMurray bitumen deposit and the Clearwater Formation, as well as a wide band within the Devonian salt-dissolution zone. OSCRIP is divided into 2 phases, Phase I includes the mapping and geological characterization of selected units from the Precambrian to the base of the Quaternary and Phase II addresses the stress-regime analysis and geomechanical characterization.

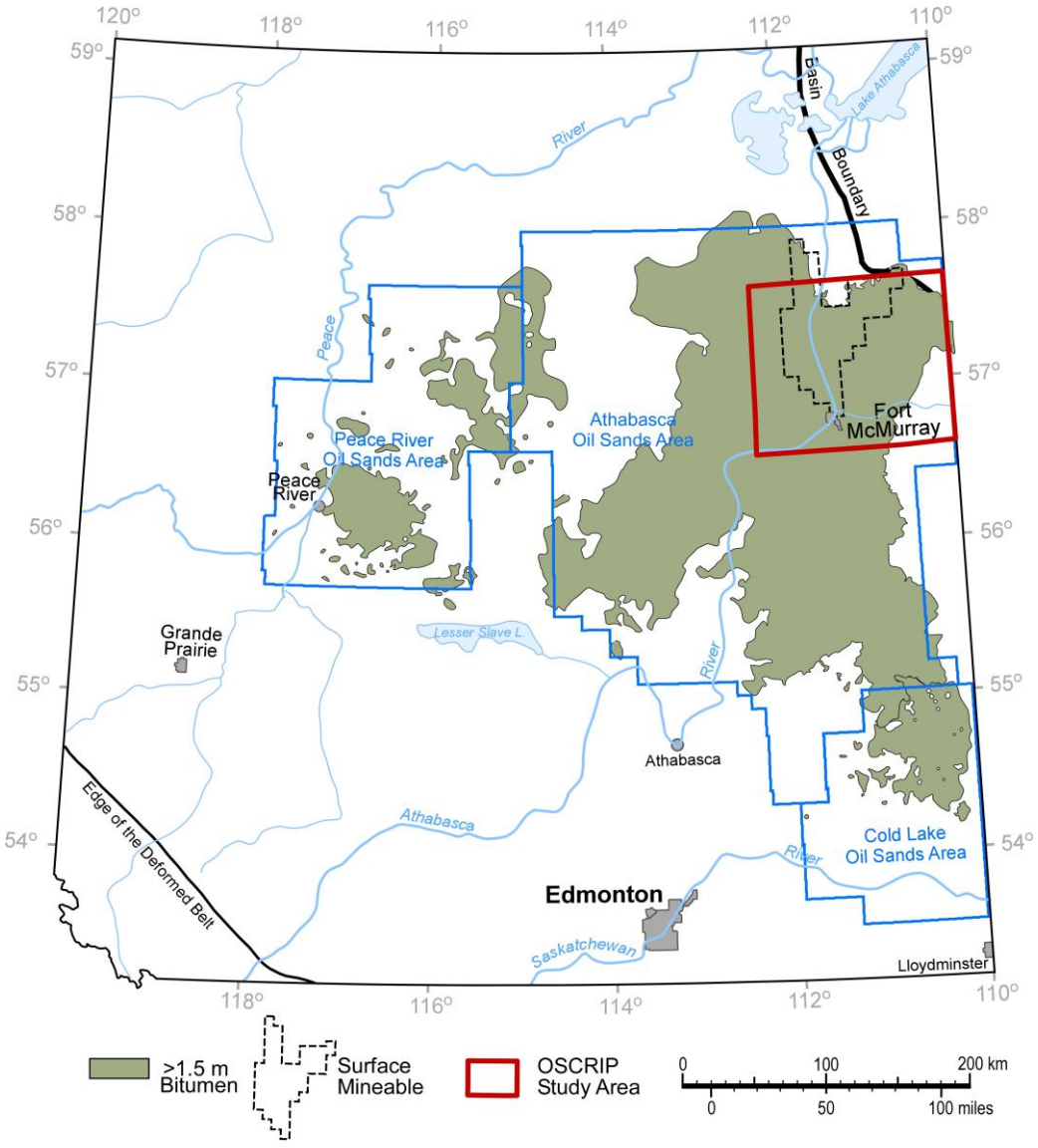

Figure 1 - OSCRIP study area in the Athabasca Oil Sands Area. Bitumen outline from ERCB ST98-2011 report

2. GEOLOGICAL CHARACTERIZATION

Andriashek and Atkinson (2007) completed an extensive study of the Quaternary geological history in the Fort McMurray region. They described the sedimentary succession overlying the post-Cretaceous unconformity in the study area as being composed of a sequence of fluvial sediments, deposited by Paleogene to Neogene river systems, as well as sediments deposited during the advance and retreat of Quaternary ice sheets. In places, this succession is preserved along the axes of regionally extensive channels, which are infilled with pre-glacial gravels, overlain by alternating sequences of till and glacial sands and gravels. In many areas, these glacial sediments are overlain by finer grained sediments which were deposited during deglaciation.

Although detailed mapping of the pre-Quaternary channels is outside this project's scope, earlier work identified buried channels throughout the Fort McMurray region (Andriashek and Atkinson, 2007). Incised pre-Quaternary channels will result in areas of reduced thickness of the Clearwater Formation.

The Quaternary sediments overlie the Lower Cretaceous strata along an erosional unconformity (Figure 2). The Viking, Joli Fou, and Grand Rapids formations are absent throughout most of the study area. The Cretaceous mapping focused on detailed geological characterization of the Clearwater Formation and Wabiskaw Member, and relevant markers within those units.

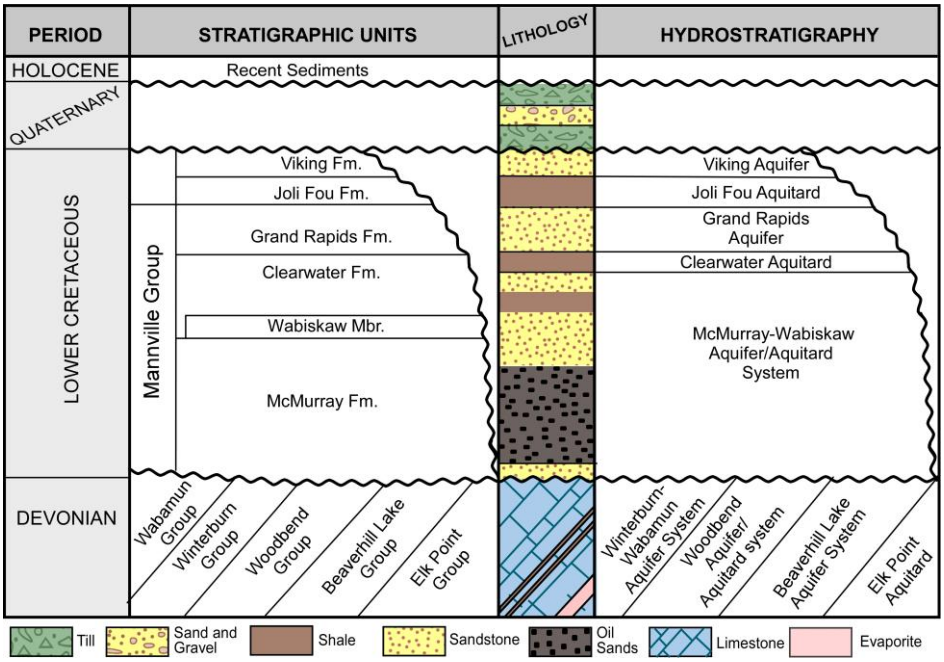

Figure 2 - Stratigraphic and hydrostratigraphic column for the OSCRIP study area

The Clearwater Formation consists of a mix of mudstone, siltstone and sandstone. The lowermost shale within the Clearwater Formation (above the Wabiskaw Member) is a laterally continuous shale deposited in a marine environment. The ERCB (2010) characterized the Clearwater Formation as a caprock at the Joslyn Creek site, and as being a continuous, 20 to 30 m thick, non-lithified, silty mudstone, with some sandy interbeds and some vertical burrows filled with sand. Within the study area, the Clearwater Formation thins to the northeast from approximately 80 m to 0 m. It subcrops beneath the Quaternary sediments throughout most of the study area and is absent in its northeastern portion. This leaves a

significant amount of bitumen outside of the surface mineable area overlain by only the heterogeneous Quaternary sediments.

Directly overlying the McMurray Formation is the Wabiskaw Member. At Joslyn Creek, the Wabiskaw Member is subdivided, from top to bottom, into the Wabiskaw A sand, a thin, water-saturated, sand-silty mudstone, the Wabiskaw A shale, and the gas-saturated Wabiskaw C sand (ERCB, 2010).

Devonian limestone and shale subcrop beneath the McMurray Formation (Figure 2). The Beaverhill Lake and Elk Point groups underwent structural deformation and collapse related to the dissolution of the Prairie Evaporite Formation halite, and with karstification of limestones in the Beaverhill Lake Group. Throughout the area, collapse of the strata overlying the Prairie Formation in the area affected by halite dissolution resulted in active and relict sinkholes, brecciation, enlarged joints, and to a lesser extent, caves. LiDAR (Light Detection And Ranging) bare earth DEM has been used to locate the surface expression of sinkholes in the study area (Figure 3). Cotterill and Hamilton (1995) stated, "These sinkholes often appear as small, circular ponds and may occur as single holes or in swarms. Occasionally, drill holes intersect these sinkholes, some of which contain brecciated limestone intermixed with oil sand from the overlying McMurray Formation". Future project working mapping, seismic interpretation and examination of drillcore will help distinguish sinkholes originating from collapse structures in the Devonian strata from surficial circular features, such as lakes and structures in the surface sediment originating from glacial processes.

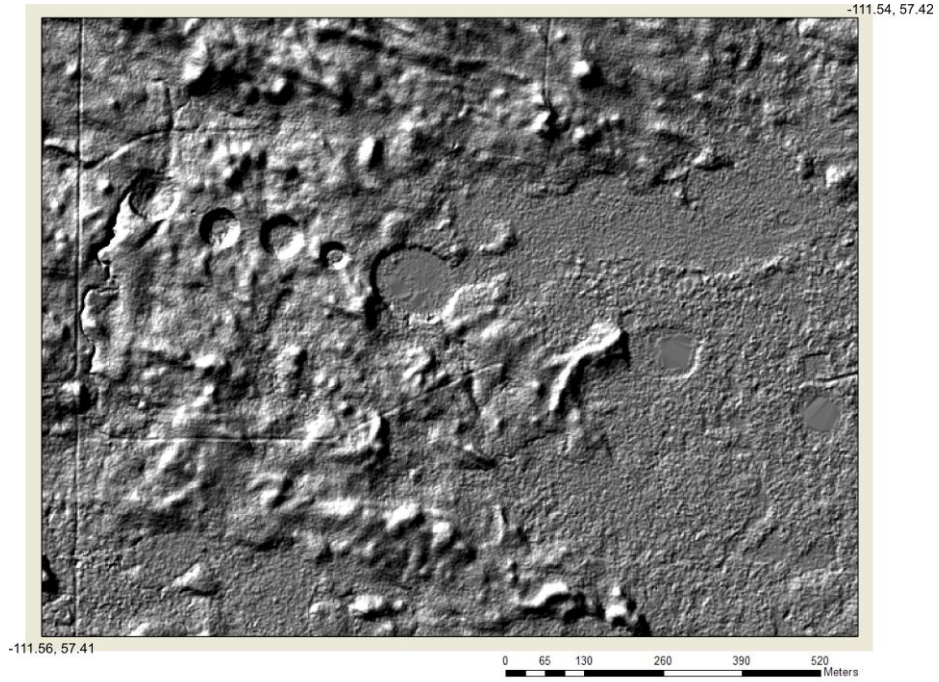

Figure 3 - LiDAR bare earth DEM showing sinkholes near McClelland Lake

Interpretation of residual map of the pre-Cretaceous unconformity surface reveals numerous features, interpreted as possible lineaments, circular to oval karstic features, and relict paleovalley/channel systems. Lineaments were interpreted from the offset between picks made from downhole geophysical logs following the approach developed by Mei (2009). Circular structures apparent on the residual map may be interpreted as being due to collapse from Prairie Evaporite Formation dissolution and/or dissolution of carbonates within the overlying units of the Beaverhill Lake Group. Verification of

structural controls on lineaments and karst features through seismic surveys would be beneficial and will be considered for future project work.

The lineaments from each unit were then overlain to determine all the units that were affected by each structural feature. From that, the timing of the origin of the structure can be inferred. Structural discontinuities that cross through the Devonian and Cretaceous strata may create zones of weakness in the caprock and compromise its sealing properties. Also, it is possible that the presence of collapse features may cause a stress reduction in the caprock due to draping into a sink feature (Collins et al., 2011).

Structural discontinuities that are currently limited to the sub-Cretaceous strata may still lead to future subsidence. It is possible that even uncollapsed areas may be unstable due to continuing subsurface dissolution of Elk Point Group salt (Bachu et al., 1993). The creation of a collapse-susceptibility map of known sinkholes and other collapse-related features may be useful to address future development.

3. STRESS REGIME

Due to the depth of bitumen resources in the Athabasca Oil Sands Area, the stress regime controls the geomechanical response of the subsurface strata to changes in subsurface conditions caused by SAGD operations. Bell and Babcock (1986) stated that fractures will propagate along planes normal to the least principal stress. For units >350 m, the minimum principal stress is horizontal, leading to vertical fractures, and for units <350 m, the minimum principal stress is vertical; therefore, horizontal fractures would be created if the fracture pressure was exceeded (Bell and Babcock, 1986).

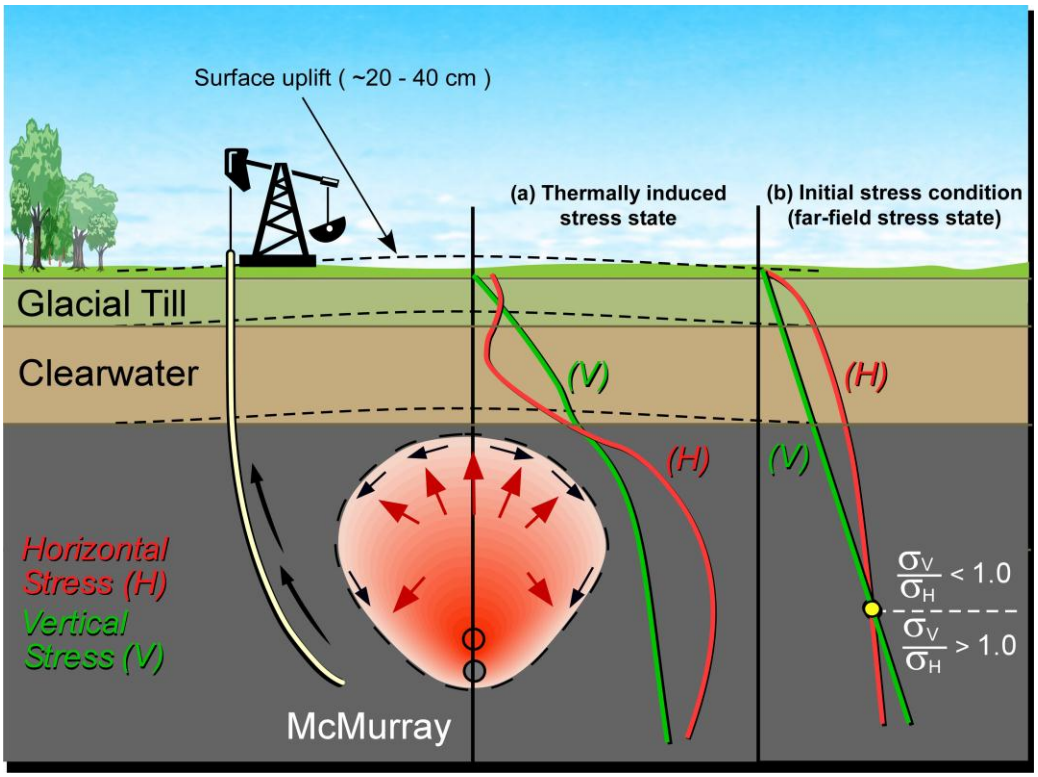

Figure 4 - Schematic showing (a) Thermal-induced stress state and (b) initial stress conditions (far-field stress state) (modified from Smith et al., 2004)

ERCB staff concluded the most likely scenario for the Joslyn incident was an initial vertical fracture and then ultimate shear caprock failure (ERCB, 2010). OSCRIP will examine the conditions under which the vertical fracture may occur. Under operating conditions, the following changes are expected in the SAGD chamber: increases in temperature and pore pressure, gradual growth of the chamber, increase in total stresses, and plastic shear yielding in parts of the steam chamber. In the overburden directly above the steam chamber, there may be a slight increase in vertical stress and a decrease in horizontal stress (Figure 4a). In addition, an expected heave of the ground surface ranging from 20–40 cm may occur based on heave measured at existing operations (Uwiera-Gartner et al., 2011).

For SAGD operations in the study area, it is important that the amount of stress reduction is understood and taken into account when determining the maximum operating pressure. In Phase II of the OSCRIP study, numerical simulations using Itasca's FLAC® software will be used to create 2-D plane strain models of the overburden above a SAGD chamber. The theory that high pressures and temperatures lead to increased rock volumes in the steam chamber which, in turn, alter the stresses in the chamber and the surrounding strata (e.g., Dusseault, 1993) will be tested. A nucleus-of-strain inversion will be used to determine the change in volume distribution in the reservoir that is needed to give the surface uplift measured above the steam chamber (Dusseault and Rothenburg, 2002; Dusseault et al., 1993).

4. CONCLUSIONS

There are significant negative consequences associated with a breakthrough of high-pressure steam and non-condensing gases to the surface. The risks involve safety issues, environmental issues, sterilization of resources, and impairment or interference with operations. The OSCRIP project is characterizing the geological framework to assess the geological effects on caprock integrity. Devonian units have been characterized to assess the direct and indirect effects of Elk Point Group salt dissolution on Devonian carbonate and evaporite strata. We have identified a very complex sub-Cretaceous structure created by salt dissolution and collapse. Not only does this complex structure have implications for caprock integrity but also for disposal of produced and process water into Devonian strata in this area.

Numerical modelling is being conducted to predict if, during SAGD operations, localized shear bands can form in the reservoir and caprock. This would lead to deterioration of the caprock-strength properties and a decrease in the horizontal stresses of the caprock. This stress reduction can lead to a stress reversal in which the minimum principal stress above the chamber becomes the horizontal stress, leading to vertical fractures if the fracture pressures are exceeded.

In summary, potential risks for caprock integrity are identified as the following:

- Buried channels cutting into the Clearwater Formation thus creating pathways for steam to escape from the reservoir
- Complete absence of the Clearwater Formation
- Thinning of Clearwater Formation along the zero edge
- Fracturing and faulting of the caprock due to post-depositional deformation
- Reduction in caprock rock stresses due to either (a) draping of caprock into salt dissolution depression or (b) stress reversal due to SAGD operations

5. REFERENCES

ANDRIASHEK L.A. and ATKINSON, N., 2007. Buried channels and glacial-drift aquifers in the Fort McMurray region, northern Alberta. Alberta Energy and Utilities Board, AGS Earth Science Report 2007-01, 160 p.

BACHU, S., UNDERSCHULTZ, J.R., HITCHON, B., and COTTERILL, D., 1993. Regional-scale subsurface hydrogeology in northeast Alberta. Alberta Research Council, Alberta Geological Survey, Bulletin 61, 49 p.

BELL S. and BABCOCK, 1986. The stress regime of the Western Canadian Basin and implications for hydrocarbon production. Bulletin of Canadian Petroleum Geology, v. 34, no. 3 (Sept 1986), p. 364–378.

COLLINS, P.M., WALTERS, D.A., PERKINS, T., KUHACH, J.D., and VEITH, E., 2011. Effective Caprock Determination of SAGD Projects. Proceedings in the Canadian Society for Unconventional Gas Conference, Calgary, Ab, Nov. 15-17, 2011.

COTTERILL, D.K. and HAMILTON, W.N. (1995): Geology of Devonian limestones in northeast Alberta; Alberta Research Council, AGS Open File Report 1995-07, 85 p.

DUSSEAULT, M.B., 1993. Stress changes in thermal operations. SPE 25809, International Thermal Operations Symposium, Bakerfield, Ca, Feb. 8–10, 1993.

DUSSEAULT, M.B., BILAK, R., and ROTHENBURG, L., 1993. Inversion of surface displacements to monitor in situ processes, International Journal of Rock Mechanics and Mining Sciences & Geomechanics, abstracts, v, 30, no. 7, p. 1219–1222.

DUSSEAULT, M.B. and ROTHENBURG, L., 2002. Analysis of deformation measurements for reservoir management. Oil & Gas Science and Technology- Rev. IFP, v. 57, no. 5, p. 539–554.

ENERGY RESOURCES CONSERVATION BOARD, 2010. ERCB staff review and analysis: Total E&P Canada Ltd. surface steam release of May 18th, 2006 Joslyn Creek SAGD thermal operation. Energy Resources Conservation Board, 177 p.

Energy Resources Conservation Board (2011): ST98-2011, Alberta's Energy Reserves 2010 and Supply/Demand Outlook 2011-2020; Energy Resources Conservation Board, 263 p.

MEI, S., 2009. Geologist-controlled trend versus computer-controlled trend: introducing a high-resolution approach to subsurface structural mapping using well-log data, trend surface analysis and geospatial analysis. Canadian Journal of Earth Sciences, v. 46, p. 309–329.

SMITH, R. J., BACON, R. M., BOONE, T .J. and P. R. KRY, 2004. Cyclic steam stimulation below a known hydraulically induced shale fracture, Can. J. of Petroleum Technology, 43(2), 39-46.

UWIERA-GARTNER, M.M., CARLSON, M.R., WALTERS, D., PALMGREN, C.T.S., 2011. Geomechanical simulation of caprock performance for a proposed, low pressure, steam assisted gravity drainage pilot project, Proceedings in the Canadian Society for Unconventional Gas Conference, Calgary, Ab, Nov. 15-17, 2011.

Geomechanical Analysis of Maximum Operating Pressure for SAGD Reservoirs

Dale A. Walters
Taurus Reservoir Solutions Ltd.
Antonin Settari
The University of Calgary
Joshua Wong
Taurus Reservoir Solutions Ltd.

ABSTRACT: The thermal recovery of bitumen reservoirs by steam assisted gravity drainage (SAGD) is often designed to maximize the operating pressure. In general, the benefits of higher operating pressures are higher steam temperatures that maximize the reduction of oil viscosity, potential permeability enhancement associated with lower effective stress and shear dilation, and a larger pressure window to allow flexible control of the producer. This is especially important for shallow reservoirs where the pressure window for injection and production is smaller. Higher operating pressure can reduce thermal efficiency (due to heat losses), but the other benefits usually compensate. The limitation of the maximum operating pressure is then based on maintaining caprock integrity. Thus, shear and tensile failure mechanisms must be quantified and managed.

This paper presents a geomechanical analysis of caprock integrity for SAGD operation. Both analytical and numerical approaches are used to investigate the modes of caprock failure. Main factors in the analysis are the knowledge of the initial stress state and proper representation of the complexity of the geomaterials. Typical initial stress states for northern Alberta are presented showing the potential for low initial minimum total stress and elevated initial shear stress levels. The stress-strain behavior for the sand and caprock materials is discussed focusing on the potential for shear dilation in the sand and shear strength behavior in the caprock. Elasto-plastic constitutive models used to represent the sand and caprock are presented and compared using numerical analysis. The increase in pressure and temperature alter the stress state and disturb the soil matrix. This disturbance results in shear dilation of the sand matrix creating regions of enhanced permeability and porosity. Also, the transfer of stress and strain to the caprock causes dynamic stress changes and, therefore, dynamic behavior of shear and tensile failure conditions. Calculations are presented showing the stress paths associated with SAGD operations, suggesting better design of lab testing programs and the implications for shear dilation in the sand and shear failure in the caprock.

1. INTRODUCTION

In situ bitumen recovery in Alberta's McMurray oil sands is currently dominated by the SAGD (Steam Assisted Gravity Drainage) recovery method. SAGD technology allows bitumen to be recovered from oil sands deposits that are impractical for surface mining and extraction methods, but not deep enough for high-pressure steam techniques to work. Only five per cent of oil sands can be recovered through surface mining, and other in situ extraction techniques recover around another 15 per cent. The development of SAGD potentially doubles the economic viability of Canada's oil sands reserves (Alberta Innovates, 2010). The SAGD method was first studied by R.M. Butler (Butler, 1980). The first field test of the SAGD process was the Underground Test Facility (UTF) project initiated by the Alberta Oil Sands Technology and Research Authority (AOSTRA – since restructured and rebranded Alberta Innovates - Energy and Environment Solutions) (O'Rourke et al., 1997). This pilot-test project, which was carried out between 1986 and 1998, proved the process and stimulated the development of commercial SAGD projects in Alberta.

The SAGD process relies on the decrease in the bitumen viscosity with heating. High pressure SAGD maximizes the steam temperature, heat content and reduction in oil viscosity. This aids the SAGD start-up procedures, early steam chamber development and reduced time to peak oil rate. There are drawbacks to higher temperature and pressure SAGD due to inefficiencies with heat loss and potential energy loss to thief zones. However, in optimum oil sand reservoirs without thief zones, maximizing operating pressure in the first 2 – 3 years is common practice.

The sand-dominated McMurray formation found in northeastern Alberta is the focus of most of the current commercial SAGD projects. The McMurray sand is a dense sand with the best reservoirs containing coarse, clean, channel sand deposits. In Alberta, the oil sands exhibit a dense packing of grains due to the glacial history. This dense packing and unconsolidated nature of the sands increase the potential for geomechanical effects with increased pressure and temperature during SAGD. Increased pressure with SAGD lowers the effective stress and decreases shear strength, causing a nonlinear increase in the pore volume and permeability of the sand due to softening and shear dilation. These geomechanical effects may therefore cause an increase in the efficiency of the gravity drainage, which is another aspect operators try to capitalize on by maximizing the SAGD operating pressure. The caprock associated with the McMurray sand is typically the Clearwater shale, a massive shale, laterally continuous over the development area and impermeable. However, the interbedded mudstones in the upper McMurray and the Wabiskaw shale (situated above just below the Clearwater shale), although thinner and of higher silt content and higher permeability, have been shown to arrest the steam chamber growth over the life of a SAGD well pair and, therefore, may also be used as an effective caprock (Collins et al. 2011).

The maximum operating pressure (MOP) for SAGD is regulated to ensure steam containment within the reservoir zone and protect the safety of operators, the public and the environment. Ensuring steam containment depends on maintaining caprock integrity. Caprock integrity has more commonly been associated with gas storage projects where an increase in maximum operating pressure results in increased deliverability and working gas capacity (Bruno et al. 1998, Bruno et al., 2000, Khan et al. 2010, Hawkes et al. 2005, Dusseault et al. 2001). More specifically, issues of caprock failure and associated well failures due to steaming operations in oil sands have been studied (Smith, 1997 and Collins, 2007). Similar concepts control the caprock integrity for the SAGD process. The general geomechancial processes at play during the SAGD process have been discussed in detail by Collins (2000). Finally, there has been some general discussion on the specific problem of caprock integrity for SAGD (Chalaturnyk, 2011; McClellan and Gillen, 2000). The focus of these studies has been the characterization of fracture networks and constitutive models of the caprock and mudstone materials and coupled modeling to assess the dynamic nature of the stresses.

This paper reviews the main factors controlling the caprock integrity of SAGD processes: material behavior and stress state. The failure mechanisms will be defined and evaluated in analytical and numerical solutions to the problem. Finally, coupled reservoir and geomechanical models will be used to illustrate the locations for greatest risk of failure.

2. GEOLOGICAL AND GEOMECHANICAL SETTING

Figure 1 shows a typical geological cross-section of the Fort McMurray area and main SAGD development area in Alberta. The McMurray formation is the lowermost siliclastic unit within the Lower Cretaceous Mannville Group in northeast Alberta. The Lower McMurray is a heavily channelized, fluvial-dominated succession that overlies Devonian carbonates, and the Upper McMurray is a heavily channelized, mixed fluvial-tidal succession that overlies the Lower McMurray fluvial deposits. These channel sands typically grade upward into inclined heterolithic stratified (IHS) units of rippled sand/heavily burrowed silty mudstones. The upper McMurray transitions into the

Wabiskaw Member of the Clearwater Formation with an upper erosional contact which often contains mudstones. The Wabiskaw deposits differ considerably due to a transition to a full marine depositional environment. The Clearwater Formation overlies the McMurray Formation. The Wabiskaw member at the base of the Clearwater contains two important, well-defined units at its base: the Wabiskaw C (marine sand) underlain by the Wabiskaw D (marine/estuarine muddy sand to sandy mudstone). This Wabiskaw D is often used as a caprock for SAGD operations if continuous and predominantly mudstone. The Wabiskaw C is important as it is typically a relatively high permeability formation allowing pressure monitoring above the SAGD operations. Above the Wabiskaw units the Clearwater formation is dominated by regionally extensive marine mudstones and siltstones. Where the Wabiskaw mudstone units are not present or regionally extensive the Clearwater formation above the Wabiskaw unit is used as the caprock for SAGD operations (Hein et al., 2000).

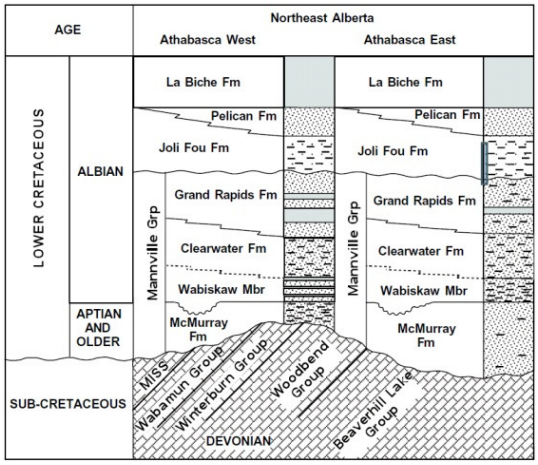

Figure 1 - Schematic Cross-section - Ft. McMurray area (Hein et al. 2000)

The mudstones in the upper McMurray Formation, the Wabiskaw unit and the Clearwater Formation make up the potential caprock layers. However, the reservoir material, the McMurray sand, plays in integral role in the deformations and stresses transferred to the caprock. Therefore, both materials require detailed representation in any engineering calculations or modeling exercise. The mudstones typically have a high clay content (> 60% in the Clearwater Formation) and silt content (about 50% in Wabiskaw Unit) and very little sand content. The Lower McMurray oil sand, typically the best quality reservoir sand, is an unconsolidated sand, with grains typically angular in shape and in a dense packing arrangement. The historical ice ages resulted in ice loading of over 1 km thickness resulting in severe overconsolidation. This dense packing arrangement results in a “locked” sand (Dusseault and Morgenstern, 1979) that is relatively stiff under small strains, but softens with larger strains due to shearing and rearrangement of the packing.

3. FIELD DATA REQUIREMENTS

A geomechanical analysis is very much dependent on the data describing the problem. In general this data can be grouped into the material description and the stress initialization, one often dependent on the other. The data important within these two groupings will be discussed next.

3.1 Geomechanical Material Description

Although many geological variations exist in the materials describing the base rock, reservoir sand and caprock, geomechanically these materials can be grouped into hard rock, fine grained and coarse

grained soils. The Devonian or base rock is usually assumed to behave as a hard rock represented by linear elastic properties. The reservoir sand and caprock can be characterized as soils. The geotechnical community has an established soil classification system that can be used to categorize soil types for their geotechnical uses (Dunn et al., 1980). The same classification governs the geomechanical behavior of these materials with respect to SAGD operations and caprock integrity. Many variations exist within these groups such as grain size distribution, clay content, clay type, grain shape, etc.; however, geotechnically they can be separated based on their mechanical behavior.

The McMurray oil sand behavior is typically consistent with a dense sand. It shows distinct peak and residual shear strength with a strong tendency to dilate through shear failure. An example of McMurray sand stress-strain is shown in Figure 2 (Oldakowski, 1994). The stress-strain behavior is fairly linear (depending on the disturbance of the core, which can be measured using disturbance index (Wong, 2004)) until the peak shear strength is reached. During shear failure rearrangement of the sand grains causes significant shear dilation and a reduction of the shear strength to a residual level representing the critical state. An elasto-plastic (EP) constitutive model was used to describe the sand, which includes both the void ratio and average effective stress in the strength calculation thereby incorporating micromechanical effects in a macroscopic continuum treatment of the material (Wan and Guo, 1998). The constitutive model is general enough to capture the behavior of both loose (normally consolidated) or dense (over consolidated) sands. The yield surface of the EP model in I_1 – sqrt(J_2) plane is shown in Figure 3. In brief the EP constitutive model is characterized by:

- Shear yield surface (f_s) dependent on void ratio
- Compaction yield surface (f_c) dependent on preconsolidation stress and void ratio
- Tension cut-off yield surface (f_t)
- Modified Rowe's stress dilatancy behavior dependent on current void ratio, critical void ratio and material parameters

Figure 2 a shows that the constitutive model is able to adequately capture the material stress-strain behavior of the McMurray sand. A slight adjustment of the void ratio of the lowest confining stress sample (S3´ = 250 kPa) was required to account for disturbance and a deviation from the general trend of the data. All other EP parameters were kept constant. Typically, one would expect the volumetric expansion with shear dilation to increase with a decrease in effective confining stress. The increase of the initial void ratio to account for sample disturbance made the initial void ratio closer to the critical void ratio surface such that less volumetric expansion occurred with shear dilation as the material moved toward critical state conditions.

The caprock material is typically characterized by mudstones from the Clearwater formation. Public data for the Upper McMurray shale of the UTF Phase A project is shown in Figure 2b (Chalaturnyk, 1996). The sample description suggests the samples were 60-70% shale with clasts of oil sands within the shale matrix. Although not Clearwater formation samples they were described as predominantly marine lower shoreface deposits and, thus, may be representative of Clearwater behavior. The same EP constitutive model was used to match the stress strain behavior of the mudstone. Although designed for sand, the EP model is general enough to characterize any material that is normally or overly consolidated. The caprock mudstone is expected to be highly over consolidated and shows this behavior with peak shear strengths and some expansion with shear failure. To match the initial linear portion of the stress-strain data, the Young's modulus was allowed to increase with minimum effective confining stress. Also, the void ratio of the lowest effective stress (S3´=500 kPa) had to be adjusted to account for some disturbance.

The two main materials affecting the SAGD operation (sand and caprock) have been characterized by an EP constitutive model. These two material descriptions were used in the following calculations of stress changes and caprock integrity.

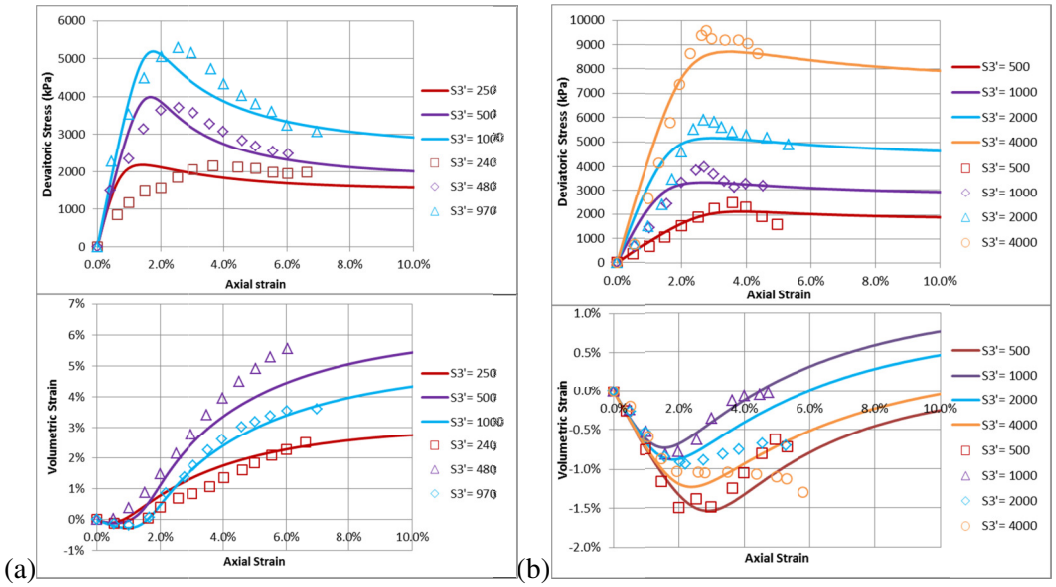

(a) (b)

Figure 2 - Lab data (symbols) and EP match (solid lines): (a) Sand; (b) Mudstone

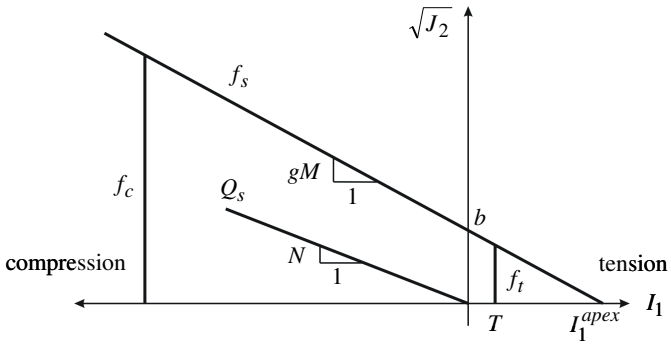

Figure 3 - Yield surface used by Elasto-Plastic Constitutive model

3.2 Stress Data

In the Western Canadian sedimentary basin, the regional stress state is dominated tectonically by movement of the North American Plate (Bell et al., 2010). This results in a dominant minimum horizontal stress (σ_{hmin}) orientation of NW-SE or in general parallel to the Rocky Mountains. However, significant deviations may exist due to local geological features such as thrust planes, fold axes, faults, karsting and salt dissolution. For the caprock analysis completed herein two stress regimes were investigated based on experience with minifracturing results from several SAGD operators in the Fort McMurray area. These are plotted in Figure 4. In most cases the minimum horizontal stress measured is somewhat greater than that generated from gravity loading. This suggests tectonics or residual stress from glaciation altered the stress state developed with deposition. Based on this type of model two generic stress profiles were created for a typical SAGD reservoir description. The stress profiles are described by two types of stress regimes important for caprock integrity analysis. They are:

1. Stress Regime 1 (SR1) - $\sigma_h<\sigma_H<\sigma_z$ (shear failure risk lower, tensile higher)
2. Stress Regime 2 (SR2) - $\sigma_z=<\sigma_h<\sigma_H$ (shear failure risk higher, tensile lower)

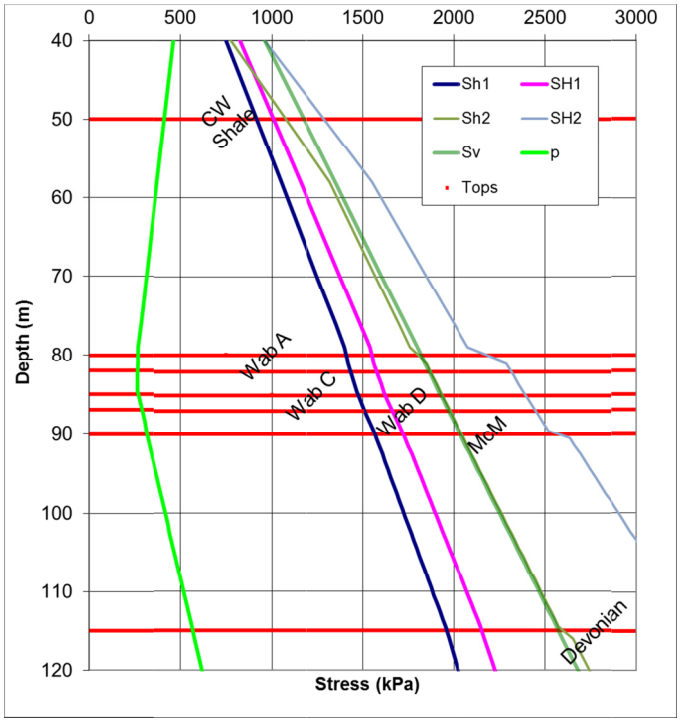

Figure 4 - Stress profiles used for calculations (SR1 uses Sh1, SR2 uses Sh2)

It may be observed that the first stress regime is close to that generated by gravity equilibrium. The result is a minimum horizontal stress gradient of about 16 – 17.5 kPa/m through most of the caprock and sand. The maximum horizontal stress(σ_H) was made about 10% larger than the minimum horizontal stress (σ_h). The second stress regime assumes the horizontal stresses have been altered such that σ_h is slightly greater than the vertical stress and the maximum horizontal stress(σ_H) is about 30% larger than σ_h. The implications of these stress states are twofold. First, the σ_h is lowest for the first stress regime indicating a much lower fracturing pressure (tensile failure) would be expected. Second, the deviatoric stress ($\sigma_{max}-\sigma_{min}$) is similar for both stress regimes. The deviatoric stress is important when considering shear failure. This will be discussed next.

4. MOHR-CIRCLE ANALYSIS

This next section will introduce a method to analytically investigate the stress changes due to SAGD operations. First, the equations that govern the deformations and change in stress as the pressures and temperatures change during a SAGD operation are presented. Special forms of these equations are then used to estimate potential failure mechanisms and the change in pressure and/or temperature required to cause those failures.

4.1 Poro- and Thermoelasticity

The theory of poro-thermoelasticity is developed by extending the theory of linear elasticity to include the effect of pressure and temperature (Coussy, 1994). These equations may be written in incremental form (and geomechanics sign convention – compression positive) as:

$$\Delta\varepsilon_x = \frac{\Delta\sigma_x}{E} - \nu\frac{\Delta\sigma_y}{E} - \nu\frac{\Delta\sigma_z}{E} - a_L\Delta T - \alpha\frac{\Delta p}{3K}$$
$$\Delta\varepsilon_y = \frac{\Delta\sigma_y}{E} - \nu\frac{\Delta\sigma_x}{E} - \nu\frac{\Delta\sigma_z}{E} - a_L\Delta T - \alpha\frac{\Delta p}{3K}$$
$$\Delta\varepsilon_z = \frac{\Delta\sigma_z}{E} - \nu\frac{\Delta\sigma_y}{E} - \nu\frac{\Delta\sigma_x}{E} - a_L\Delta T - \alpha\frac{\Delta p}{3K} \quad (1)$$

where $\Delta\varepsilon$ is strain, σ is total stress, ν is Poisson's ratio, E is Young's modulus, K is the bulk modulus, T is temperature, p is pressure, a_L is the drained linear thermal expansion coefficient and α is Biot's poroelastic constant. Biot's constant may be calculated as:

$$\alpha = 1 - \frac{K}{K_s} \quad (2)$$

where K_s is the grain modulus (bulk modulus of the solid grains making up the soil/rock skeleton).
These governing equations may be simplified to represent the typical reservoir geometry by making uniaxial strain assumptions (shown as a cross-section in Figure 5). The left side of Figure 5 shows the actual 3-D semi-infinite medium. The right side shows a portion of the medium extracted for the calculation of the stresses. The simplified model assumes that in-situ conditions can be approximated by a 2D block of material, which is constrained on all surfaces except the top surface, which has full freedom of movement. The sides of the model are constrained in the lateral direction. These assumptions give a good approximation for an isotropic, homogeneous reservoir with a width that is much greater than its height, and much greater than the depth to surface (since it neglects arching effects).

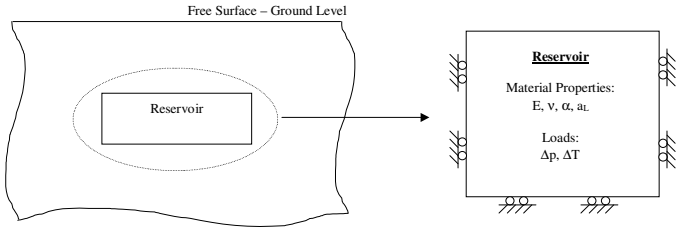

Figure 5 - Uniaxial boundary conditions

The general formulation of equation (1) may be simplified, based upon the idealization shown on the right side of Figure 5. This requires applying the following assumptions:

$$\Delta\varepsilon_x = \Delta\varepsilon_y = \Delta\varepsilon_h = 0$$
$$\Delta\sigma_x = \Delta\sigma_y = \Delta\sigma_h$$
$$\Delta\sigma_z = 0 \quad (3)$$

Using the above assumptions and rearranging the equations allows the stress solution to be written as a horizontal stress change divided into two components: the thermoelastic effect and the poroelastic effect:

Total stress change:
$$\Delta\sigma_h = \Delta\sigma_{ht} + \Delta\sigma_{hp} \quad (4)$$

Thermo-elastic stress change:

$$\Delta\sigma_h = a_L \frac{E}{1-\nu}\Delta T \tag{5}$$

Poro-elastic stress change:

$$\Delta\sigma_h = \alpha\frac{1-2\nu}{1-\nu}\Delta p \tag{6}$$

4.2 Mohr-Circle Analysis for Shear Failure

A convenient way to analytically evaluate the shear strength of the materials under SAGD conditions is to use a Mohr-Circle (MC) analysis (Dunn et al., 1980). Knowing the initial stress state and using Equations (5) through (6) one may calculate the changes in total stress and evaluate shear failure. The main assumptions in this analysis are as follows:

1. Uniaxial strain boundary conditions (i.e., no lateral strain, free vertical strain)
2. No arching
3. Homogeneous pressure and temperature distribution

These assumptions oversimplify the stress changes going on during SAGD operations, but may be used to provide a first estimate of safe operating pressure. Three calculations with different levels of complexity can be used for the MC analysis. These are explained next.

The first analysis is to plot the MC accounting for the current effective stress state and only the change in effective stress associated with the pressure changes during SAGD. In this case the MC would remain the same size as initially (navy blue line in Figure 6), but move to the left until it touches the shear failure envelope (yellow circle intercepting the red line in Figure 6). For SR1 the maximum principal stress is the vertical stress and the minimum principal stress in the horizontal stress. The opposite is true of SR2.

The second analysis uses Equation (6) to calculate the change in horizontal total stress, increasing the pressure until it touches the shear failure surface. The stress regime plays a key role in how the MC develops. The horizontal stresses will increase with an increase in pressure. Thus, if the initial horizontal total stresses are less than the vertical stress (SR1) the MC will first become smaller and then increase in size if the horizontal stresses become larger than the vertical stress before the MC touches the shear failure surface (Figure 6a and 6b). If the initial horizontal total stresses are greater the vertical stress (SR2) the MC will increase in size as it moves to the left and touches f_s. This causes the MC to become larger as it moves to the left to touch the shear failure envelope (light blue line in Figure 6c and 6d). Thus, the amount it can shift to the left is less than the previous case.

The third analysis uses Equation (5) and (6) to calculate the change in horizontal total stress, due to pressure and temperature increase until it touches the shear failure surface (assumes saturated steam conditions). As noted with the pressure changes, the assumed reservoir boundary conditions cause the total stress in the lateral direction to increase with an increase in temperature, while the total vertical stress remains unchanged. This effect when combined with the poroelastic stress changes causes the MC to become even larger as it moves to the left (due to increased temperature and pressure decreasing the effective stress) to touch the shear failure envelope (purple line in Figure 6). The stress paths of this third analysis for both stress regimes are plotted in Figure 10 (labeled MC). They are plotted together with simulation results, which will be discussed next.

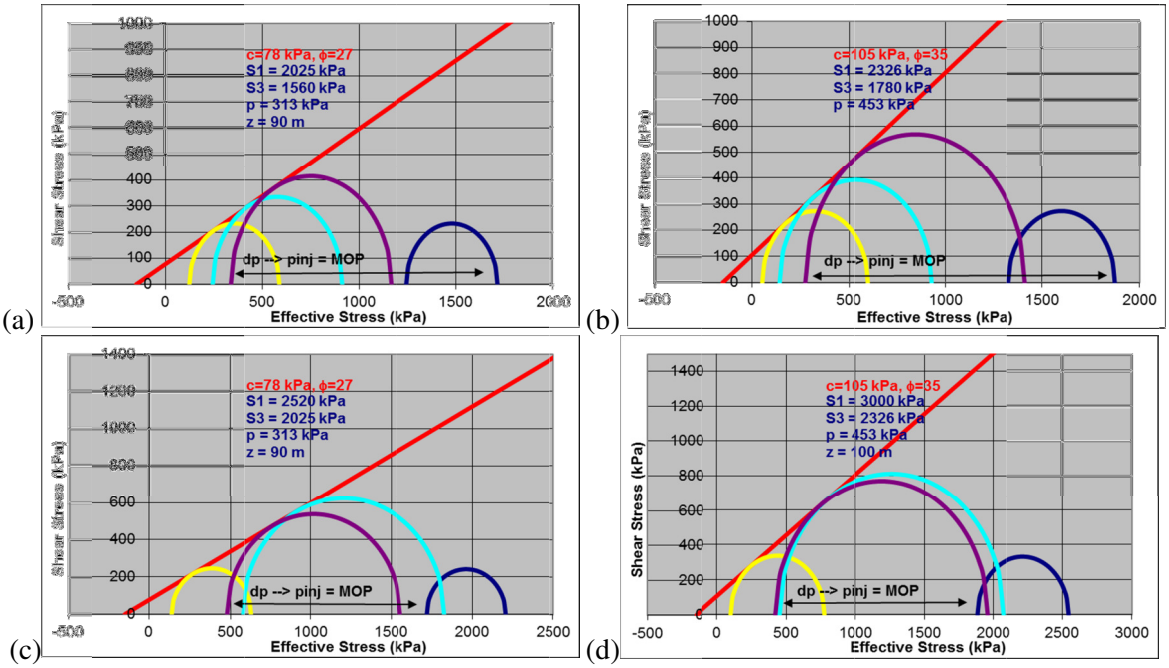

Figure 6 - Mohr-Circle analysis of Shear Failure (a) Shale SR1; (b) Sand SR1; (c) Shale SR2; (d) Sand SR2

5. COUPLED MODELING APPROACH - CRITICAL ZONES FOR FAILURE

A coupled reservoir and geomechanical simulator (Settari and Walters, 2001) was used to investigate the stress changes during typical SAGD operations. The zone layering shown in Figure 4was used for the simulator description. The 2D, single well pair, element of symmetry model included all the material from ground level (GL) to about 500 m below GL. The model assumed the McMurray (McM) sand (of 19 m thickness) was entirely reservoir quality sand such that the steam chamber when fully developed in height would stop at the base of the Wabiskaw (Wab) D zone. Important depths for the evaluation of caprock stability are the base of the Clearwater (CW) (80 m), the base off the Wab D (90 m) and the base of the McM (109 m). The geometry of the model, in a cross-sectional plane perpendicular to the wells, is illustrated in Figure 7 showing the pressure and temperature distribution after 912 days of operation. The injector and producer wellswere positioned on the left side of the model at depths of 114 m and 118 m, respectively. The results for two cases are shown in the next section: SR1, using stress regime 1; and SR2 – using stress regime 2.

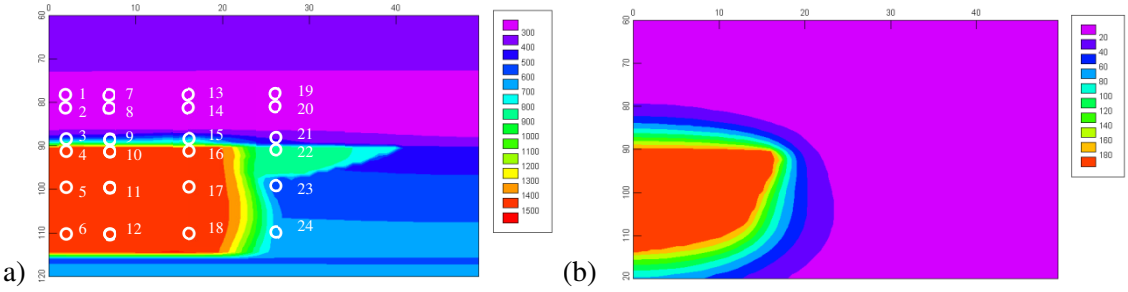

Figure 7 - (a) Pressure and (b) Temperature distributions after 912 days in 2D simulation model

5.1 Failure Modes and Stress Ratios

When evaluating caprock integrity two modes of failure require evaluation: tensile and shear. In order to easily evaluate the simulation results for these modes of failure two stress ratios are used:

P/S_{min} = ratio of pressure (P) to total minimum principal stress (S_{min}) - tensile failure

$StrLev = (\sigma_1 - \sigma_3) / (\sigma_1 - \sigma_3)_f$ = ratio of maximum shear stress to shear strength - shear failure where

$$(\sigma_1 - \sigma_3)_f = (\sigma_{dev})_f = \frac{2c\cos\phi + 2\sigma_3' \sin\phi}{(1 - \sin\phi)} \quad (7)$$

Here c is the material cohesion, ϕ is the material friction angle and σ_3' is the minimum effective stress. An example of the simulation results for 912 days after the beginning of SAGD operations is shown in Figure 8 and Figure 9. Figure 8 shows the tensile stress ratio (P/S_{min}). The results show that SR1 has a higher risk of tensile failure above the well pairs with higher P/S_{min} from 90 m (Wab D base) and up. This is as expected considering the initial σ_{min} is significantly lower for the SR1 case. Figure 9 shows the differences in the *StrLev* for the two cases. The *StrLev* for SR2 is lower above the well pairs, but higher adjacent to the steam chamber in the McM. This again may be explained by the initial stress state and the dynamic changes in stress during SAGD operations. Typically the horizontal total stresses (σ_h, σ_H) decrease above the steam chamber and increase adjacent to it. Also, the total vertical stress (σ_z) can decrease adjacent to the steam chamber as the steam zone expands, mainly in the vertical direction, and stretches the materials around it. Thus, the SR2 horizontal stresses increase and the vertical total stress decreases adjacent to the steam chamber, causing a larger deviatoric stress and potential for shear failure. Above the steam chamber the stretching effect may also decrease the horizontal stresses. Assuming σ_z stays constant, case SR1 would produce a higher deviatoric stress as the initially lower σ_h would further decrease.

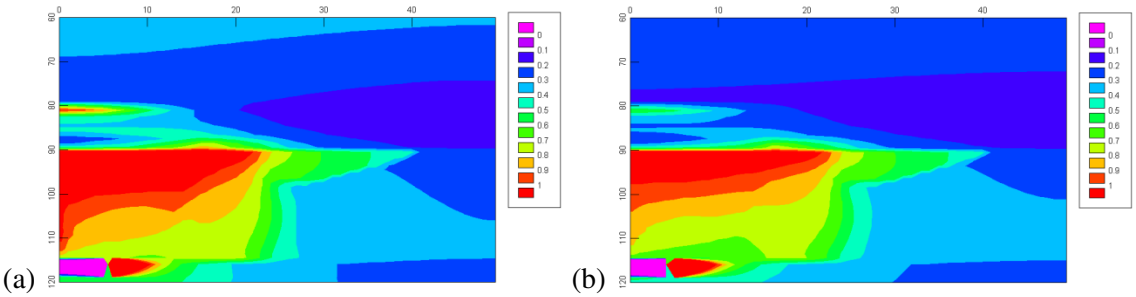

Figure 8 - P/S_{min} plots for (a) SR1 and (b) SR2 at 912 days

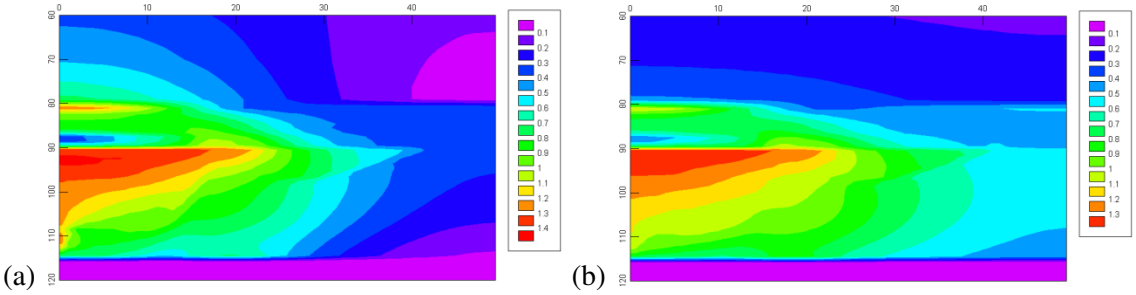

Figure 9 - *StrLev* plots for (a) SR1 and (b) SR2 at 912 days

A closer look at the stress changes occurring during SAGD may be taken using stress path plots. 2D stress path plots show the history of deviatoric stress or q, $q=(\sigma_1 - \sigma_3)/2$ (top of the MC), versus mean effective stress or p', $p'=(\sigma_1' + \sigma_3')/2$ (center of the MC). Figure 7 shows the locations at which stress paths were plotted. Figure 10 shows the stress path results for the two cases. The stress paths illustrate in greater detail the stress ratio distributions observed above. They are shown separately for caprock blocks and sand blocks as the two materials were characterized by different constitutive models with different shear failure envelopes. Most of the results for case SR1 show an initial decrease in q followed by an increase as the stress state moves toward f_s. This is due to the increase in total horizontal stress with an increase in pressure and temperature. Conversely, case SR2 shows only an increase of q as the stress state moves from initial conditions towards f_s. In general, the caprock of case SR1 shows more shear failure with some of the blocks reaching the peak shear strength during failure. Both cases show extensive shear failure in the sand. This is desired as shear dilation can cause permeability enhancements. Finally, by evaluating the stress paths from modeling results, the stress paths tested in the lab can be refined. Each of the plots in Figure 10 also shows the lab test results from the respective material. It may be observed that the stress paths during SAGD operation differ considerably from the typical triaxial stress path.

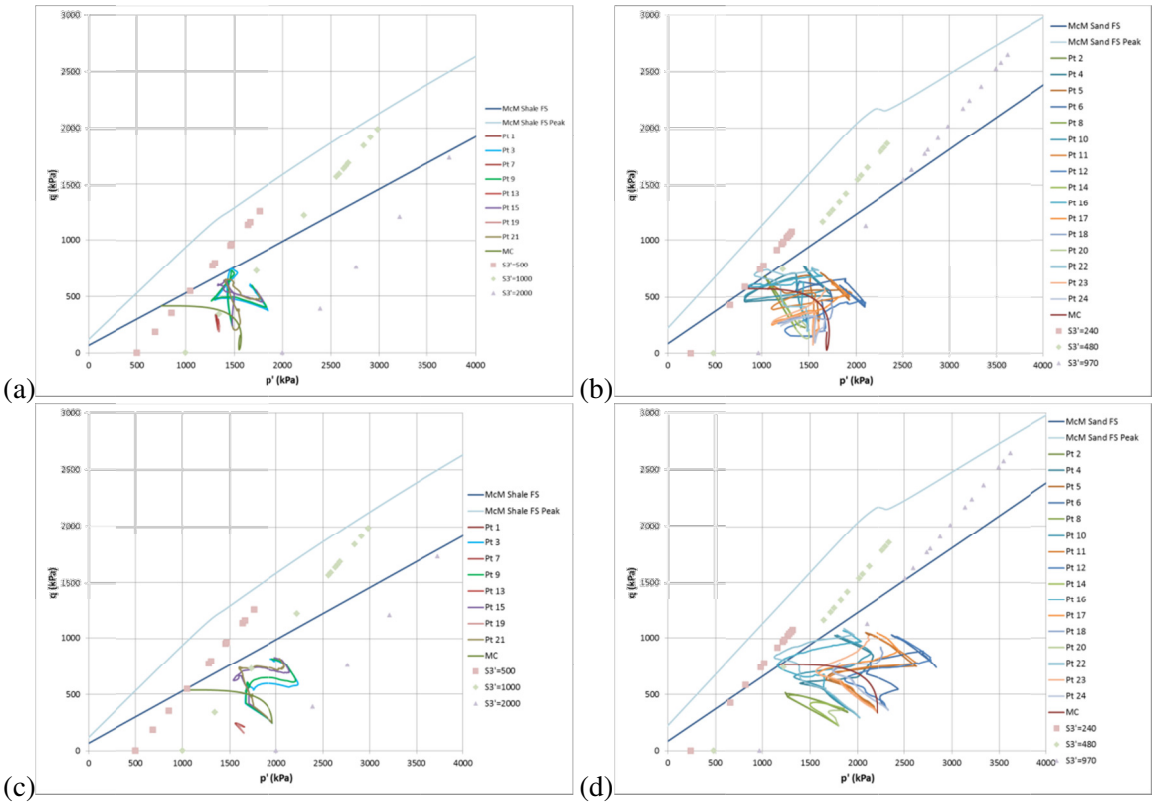

Figure 10 - Stress Path Plots (a) SR1 Caprock blocks;(b) SR1 Sand blocks; (c) SR2 Caprock blocks; (d) SR2 Sand blocks

6. CONCLUSIONS

- Both the mudstone and sand materials have complex stress-strain behavior due to the overconsolidated nature of the material. These materials may be characterized quite well using a void ratio dependent elasto-plastic model with three yield surfaces.

- Two initial stress state regimes were identified that impact the potential risk of each mode of caprock failure: tensile and shear.
- Mohr circle analysis yields valuable insight into the failure mechanisms of the SAGD process.
- Tensile and shear stress ratios can be used to evaluate failure modes in simulation results.
- Stress paths provide additional information on the stress history and can be used to guide lab testing and identify areas at risk for failure.

7. REFERENCES

ALBERTA INNOVATES, 2010. "Steam Assisted Gravity Drainage (SAGD)". http://www.albertainnovates.ca /energy/investing/success-stories/sagd.

BELL, J.S., PRICE, P.R. and MCLELLAN P.J. 2010. "In-situ Stress in the Western Canada Sedimentary Basin, Chapter 29 Geological Atlas of the Western Canada Sedimentary Basin. 2010.

DUSSEAULT, M.B. and MORGENSTERN, N.R. 1979. "Locked sands", Quarterly Journal of Engineering Geology, vol.12, pp.117-131.

BRUNO M.S., DUSSEAULT M.B., BALAA T.T., and BERRERA J.A., 1998. "Geomechanical Analysis of Pressure Limits for Gas Storage Reservoirs". Paper Number USA-328-5, presented at the North American Rock Mechanics Symposium, NARMS '98, June 3-5, 1998.

BRUNO, M.S. DEWOLF, G. and FOH, S., 2000. "Geomechanical Analysis and Decision Analysis for Delta Pressure Operations in Gas Storage Reservoirs" Gas Research Institute. Paper presented at the American Gas Association Operations Conference, Denver, CO, May 7-9, 2000.

BUTLER, R.M., and STEPHENS D.J., 1981. "The Gravity Drainage of Steam Heated Heavy Oil to Parallel Horizontal Wells", Journal of Canadian Petroleum Technology, 20(2): 90-96.

CHALATURNYK, R. 2011. "Observations on SAGD Caprock Integrity". Recovery – 2011 CSPG CSEG CWLS Convention.

CHALATURNYK, R. 1996. Geomechanics of the Steam Assisted Gravity Drainage Process in Heavy Oil Reservoirs, Ph.D. thesis, Dept. Civil Eng., University of Alberta, Edmonton, Alberta, 576 pp.

COLLINS, P.M., WALTERS, D., PERKINS, T., KUHACH, J. and VEITH, E. 2011. "Effective Caprock Determination for SAGD Projects". SPE 149226-MS. Presented at Canadian Unconventional Resources Conference, Calgary, Alberta, Canada, November 15-17.

COLLINS, P.M., 2007. "Geomechanical Effects on the SAGD Process". SPE 97905. August 2007 SPE Reservoir Evaluation and Engineering.

COUSSY, O. 1994. Mechanics of Porous Continua. John Wiley & Sons. 455pp.

DUNN, I.S., L.R. ANDERSON and F.W. KIEFER. 1980. *Geotechnical Analysis*. John Wiley & Sons. 414pp.

DUSSEAULT, M., BRUNO, M. and BARRERA, J., 2001. "Casing Shear: Causes, Cases, Cures". SPE 72060. June 2001, SPE Drilling and Completion.

HAWKES, C.D., MCLELLAN, P.J. and BACHU S., 2005. “Geomechanical Factors Affecting Geological Storage of CO2 in Depleted Oil and Gas Reservoirs”. October 2005, Volume 44, No. 10. Journal of Canadian Petroleum Technology.

HEIN, F.J., COTTERILL, D. K. and BERHANE, H., 2000. “An Atlas of Lithofacies of the McMurray Formation Athabasca Oil Sands Deposit, Norheastern Alberta: Surface and Subsurface”. Alberta Energy and Utilites Board, Alberta Geological Survey, Earth Sciences Report 2000-07.

KHAN S., HAN H., ANSARI S., KHOSRAVI N., 2010. “An Integrated Geomechanics Workflow for Caprock-Integrity Analysis of a Potential Carbon Storage”. SPE 139477. presented at the SPE International Conference on CO2 Capture, Storage, and Utilization held in New Orleans, Louisiana, USA, 10-12 November 2010.

MCLELLAN, P. and GILLEN, K. 2000. “Assessing Caprock Integrity for Steam-Assisted Gravity-Drainage Projects in Heavy-Oil Reservoirs” (GEM Presentation) prepared for presentation at the 2000 SPE/Petroleum Society of CIM International Conference on Horizontal Well Technology held in Calgary, Alberta, Canada, 6-8 November, 2000. SPE 65521.

OLDAKOWSKI, K. 1994. Stress Induced Permeability Changes of Athabasca Oil Sands, M.Sc. thesis, Department of Civil Engineering, University of Alberta.

O’ROURKE, J.C., BEGLEY A.G., BOYLE H.A., YEE C.T., CHAMBERS J.I., LUHNING R.W., 1997. “UTF project status update May 1997”. Paper 98-08, first presented at the 48th Annual Technical Meeting of the Petroleum Society in Calgary, Alberta, Canada, June 8-11, 1997.

SETTARI, A. and WALTERS, D.A. 2001. “Advances in Coupled Geomechanical and Reservoir Modeling With Applications to Reservoir Compaction”, SPE Journal, Vol. 6, No. 3, Sept. 2001, pp. 334-342.

SMITH, R.J., 1997. Geomechanical Effects of Cyclic steam Stimuation on Casing Integrity. University of Calgary, Master’s Thesis, 1997.

WAN, R.G. and GUO P.J., 1998. “A Simple Constitutive Model for Granular Soils: Modified Stress-Dilatancy Approach”. Computers and Geotechnics, Vol. 22, No. 2, pp. 109-133.

WONG, R.C.K. 2004 Effect of Sample Disturbance Induced by Gas Exsolution on Geotechnical and Hydraulic Properties Measurements in Oil Sands PAPER 2004-071, Petroleum Society of CIM, CIPC, Calgary, Alberta, Canada, June 8-10, 13pp.

Investigation of the Influence of Stress Shadows on Multiple Hydraulic Fractures from Adjacent Horizontal Wells Using the Distinct Element Method

Neda Zangeneh
University of British Columbia
Erik Eberhardt
University of British Columbia
R. Marc Bustin
University of British Columbia

ABSTRACT: Production efficiency from low permeability gas shales require techniques to optimize hydraulic fracture completions. One completion strategy involves the simultaneous or near simultaneous hydraulic fracturing of multiple horizontal wells to maximize the fracture network area and stimulated reservoir volume. However, changes to the in-situ stress field caused by an earlier hydrofrac on subsequent hydraulic fractures are not accounted for in traditional hydrofrac design calculations. Presented here are the results from a set of transient, coupled hydro-mechanical simulations of a rock mass containing two wellbores using the discontinuum-based distinct-element method. The results demonstrate the influence of stress-shadows generated by a hydraulic fracture on the development of subsequent hydrofracs from an adjacent well. It is shown here that these interactions have the potential to change the size and effectiveness of the hydraulic fracture stimulation by changing the extent of the hydraulic fracture around the secondary well.

1. INTRODUCTION

The ultimate measure of a successful hydraulic fracture design is the increased production of natural gas following the stimulation. Horizontal wells provide greater well contact with a larger volume of reservoir rock than vertical wells due to the limited vertical thickness of the reservoir compared to its lateral extent. Recent studies have suggested that simultaneous or near simultaneous hydraulic fracturing of adjacent wells results in better well performance than single well completions. This has evolved into the drilling of multiple horizontal wells in an attempt to maximize the stimulated volume of reservoir rock through hydraulic fracturing.

The use of hydrofracs from multiple horizontal wells has increased the importance of considering in-situ stress field disturbance (referred to as “stress shadow”). Stress shadow effects are potentially critical to the design of multiple hydrofracture treatments; however, the importance of stress shadowing is not accounted for in conventional fracture design. Multiple hydraulic fractures, whether off a multi-stage single well or adjacent horizontal wells are designed identical to the single horizontal well treatment. Thus the effects of stress shadows around an initial horizontal well are neglected with respect to their influence on the performance of a hydraulic fracture from a neighbouring well.

This paper describes a series of numerical experiments investigating the influence of stress shadow on the modeling of multiple hydraulic fracture treatments. One objective is to evaluate the utility of 2-D distinct element techniques to model both shear slip and aperture dilation along existing rock joints and tensile rupture of intact rock in response to fluid injection and subsequent changes to the effective stress field. The analysis is carried out for different completion scenarios and their effect on the propagation of the different hydraulic fractures. Also examined are the changes in fluid pressure and corresponding effective stress changes around each wellbore during different completion techniques.

2. INFLUENCE OF STRESS SHADOWS ARISING FROM MULTIPLE HYDROFRACS

Altered-stress fracturing is a concept whereby a hydraulic fracture in one well is affected by another in a nearby adjacent well. One of the earliest studies was done by Warpinski and Branagan (1989), where they presented field tests and finite element calculations examining the modified stress field around a wellbore. Termed “stress shadows”, the disturbance of the stress field is especially important when considering a multiple stage hydrofracing design. When sequential hydrofrac stages are initiated in horizontal wells that are close to one another, the stress perturbation caused by one may affect any subsequent hydraulic fractures.

Different authors have highlighted the role of stress perturbation in multi-stage fracturing from horizontal wellbores towards optimization of horizontal completion techniques. For example, Fisher et al. (2004) presented results investigating the influence of multi-stage fractures with a wellbore separated into equal sections in Barnett shale using microseismic data. They showed that stress diversion is present when the reservoir has been supercharged by a previous fracture treatment stage. They also showed that stress in this region is increased due to locally higher fluid pressures, which influence subsequent stage(s). Morrill and Miskimins (2012) performed and presented a series of numerical simulations of stress around a fracture in a multiple hydraulically fractured horizontal well in order to determine the optimal fracture spacing to avoid stress field interactions and allow for predictable fracture geometries and conductivities in shale gas.

A recent consideration of stress shadow effects is when closely spaced multiple horizontal wells are used. Vermylen and Zoback (2011) studied stress shadow effects in multiple horizontal wells in the upper Barnett shale for different completion procedures (simulfrac and zipper frac) in order to test the effectiveness of different fracture methods. They compared the activity level of a fracture stage for different completion techniques using microsiesmic events. They found significant differences in stimulation robustness for the different fracing procedures they studied owing to stress shadow effects.

3. METHODOLOGY

The Distinct Element Method (DEM) is a Lagrangian numerical technique in which the computational domain consists of discrete deformable blocks that interact via compliant contacts (Cundall and Hart, 1993). This enables the problem domain to be divided through by discontinuities of variable orientation, spacing and persistence. One fundamental advantage of the DEM is that pre-existing joints in the rock mass can be incorporated directly and are allowed to undergo large deformations in shear or opening. The 2-D commercial code UDEC (Universal Distinct Element Code; Itasca Consulting Group, 1999) is used here to simulate the response of a jointed rock mass subjected to static loading and hydraulic injection.

UDEC is capable of modeling the behavior of weak jointed rock masses in which both the yielding of weak rock and slip along pre-existing discontinuities are important controlling factors. Progressive failure associated with crack propagation and spalling can be simulated by the breaking of pre-existing contacts between the pre-defined joint bounded blocks, which although deformable, remain intact.

Key for simulating hydrofracturing, UDEC has the capability to model fluid flow through the defined fracture network. A fully coupled hydro-mechanical analysis can be performed, in which fracture conductivity is dependent on mechanical deformation of joint apertures and, conversely, joint water pressures can affect the mechanical computations of joint aperture. The blocks in this assemblage are treated as being impermeable, and fracture flow is calculated using a cubic law relationship for joint aperture:

$$q = ka^3 \frac{\Delta P}{l} \tag{1}$$

where, k is a joint conductivity factor (dependent on the fluid dynamic viscosity), a is the contact hydraulic aperture, ΔP is the pressure difference between the two adjacent domains, and l is the length assigned to the contact between the domains. Since the UDEC formulation is restricted to the modeling of fracture flow, it should be noted that leak-off along the fractures diffusing into the rock matrix is assumed to be negligible (only leak-off into other fractures is considered). Furthermore, the cubic law flow assumption disregards tortuosity. When a joint contact is broken, the fluid flows into the joint.

4. SIMULATION

The rock mass modeled in this study is represented by two orthogonal joint sets oriented parallel and perpendicular to bedding (Figure 1). Three different hydrofrac scenarios were tested:

- Conventionally fractured well, where a single well (wellbore A or wellbore B) is fractured.
- Two alternating fractured wells (zipperfrac), where first one well (wellbore A) and then the other well (wellbore B) is fractured.
- Two simultaneously fractured wells (simulfrac), where the two wells (wellbore A and wellbore B) are fractured simultaneously.

These three scenarios are modeled here to investigate the influence of stress shadowing on hydraulic fracture stimulation. The hydraulic fracture is simulated by applying a fluid injection into the model wellbore. Strength and deformation properties, provided in Table 1, were assigned to the fractures and a stress field was superimposed across the problem domain to represent the maximum and minimum in-situ stresses at depth (as shown in Figure 1); here, the intermediate in-situ stress is the out of plane stress. Hydrofracing is simulated assuming a constant flow rate into the wellbore.

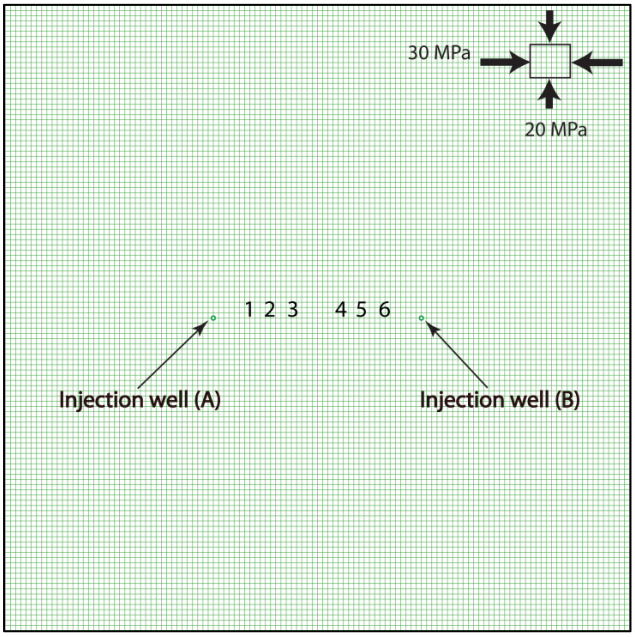

Figure 1 - Rock mass model (60×60m) with two sets of orthogonal joints and two wellbores

Table 1 - Strength and deformation properties assigned to the joints

Joint property	Value	Unit
friction angle	30	degrees
cohesion	1.0	MPa
tensile strength	0.5	MPa
normal stiffness	100	GPa
shear stiffness	10	GPa/m

5. STRESS SHADOWING SIMULATIONS

The in-situ stress filed that exists at depth in a rock mass is known to control oil and gas reservoir stimulations. Significant stress perturbations are induced by any process that changes reservoir pressure or fractures the rock. Because of the high pressure needed for fracture dilation and the large fracture surface area created, a hydraulic fracture likely will alter the stress field significantly.

To determine the influence of hydraulic fracturing on stress perturbation and fluid pressure resulting from a neighbouring fracturing well, three interaction scenarios as described by Vermylen and Zoback (2011) are considered.

5.1 Conventional Hydrofrac (Single Well)

The hydraulic fracturing simulation for the first scenario was conducted pressurizing only one of the two horizontal wellbores (A in Figure 1). Figure 2a shows the changes in fluid pressure at different points in the rock mass between the two wellbores (Points 1 to 6; see Figure 1). Points 1, 2 , and 3 are located at 2m intervals from wellbore A, and points 6, 5, and 4 are located at 2m intervals from wellbore B. Figure 2a shows that during injection, the values recorded at the monitoring points increase and are highest nearest to the wellbore. After injection is discontinued, a gradual pressure decline is seen in the pressure history plots for all points. The declining pressure occurs due to dissipation of fluid pressure back to the wellbore.

The initial pressure increase clearly shows that the corresponding stress state around the neighboring well changes from the virgin in-situ stress condition and increases considerably, as shown in Figure 2b. The perturbation of in-situ stress around the pressurized wellbore (points 1, 2 and 3) as well as the neighboring non-active wellbore (points 4, 5 and 6) is clearly seen in the stress histories. The stress perturbation decays as the pressure declines at these points, but still does not return to the original virgin in-situ stress. This means that if the second wellbore is pressurized, the stress field influencing the propagation of the hydrofrac is different that the initial in-situ stress condition.

The stress shadow effect is manifest in the elevated principal stresses that develops around the pressurized wellbore and radiates outwards into the reservoir for a significant distance towards the second wellbore (Figure 3). This suggests that the in-situ stress around wellbore B is altered due to the stress changes resulting from the pressurization of wellbore A.

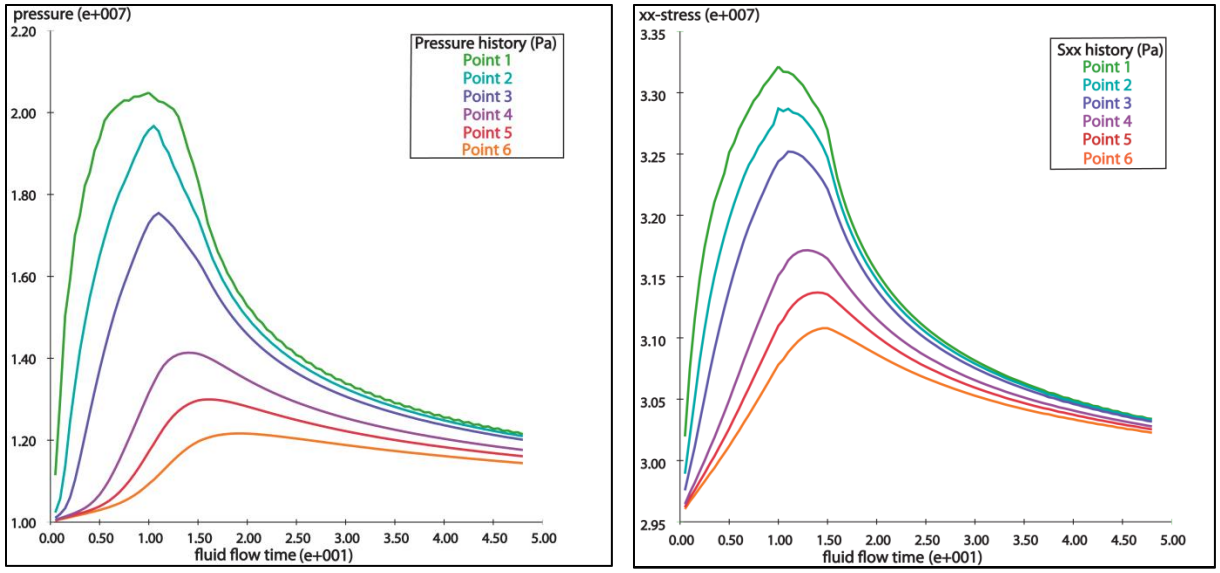

(a) (b)

Figure 2 - Conventional hydrofracing scenario (single well): (a) Pressure histories, and (b) Stress histories, for different monitoring points between the two wellbores. Point 1 is closest to the injection well (wellbore A), with point 6 being closest to the non-active well (wellbore B)

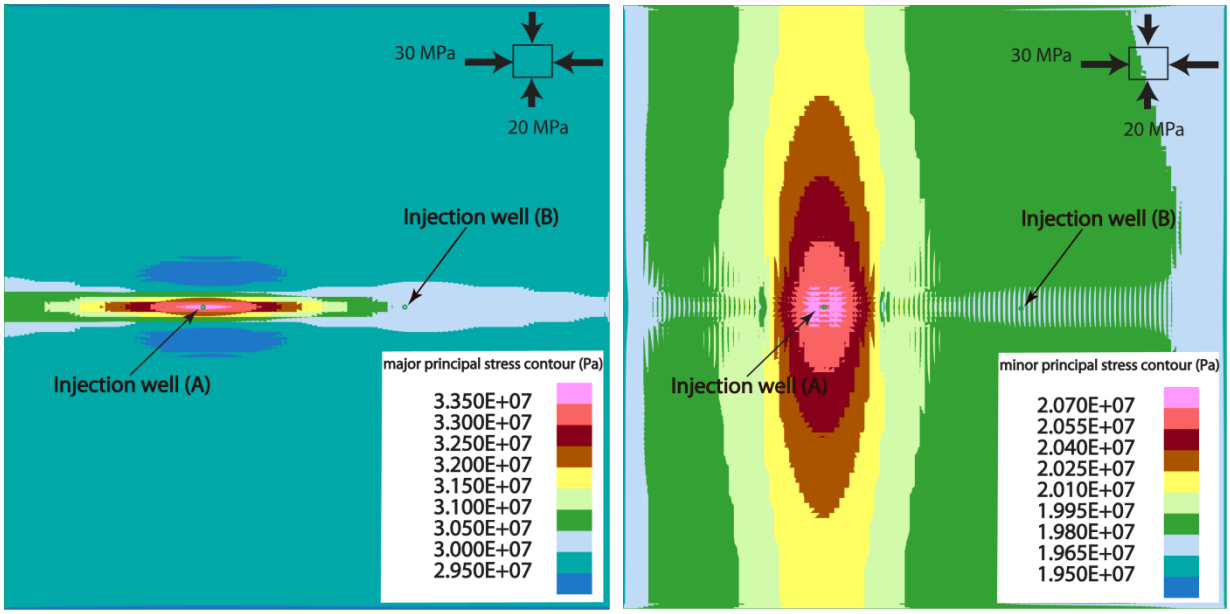

(a) (b)

Figure 3 - Principal stress distributions (a) major, and (b) minor, resulting from the pressurization of wellbore A

5.2 Two Alternating Injection Wells (Zipperfrac)

The simulation of hydraulic fracturing for the second scenario involves first injecting (i.e., fracing) from wellbore A and then wellbore B. The results are presented in Figures 4 and 5.

Figure 4a shows the pressure increase at different points within the rock mass between the two wellbores. Points 1 to 3, located closer to the pressurized wellbore A, indicate a faster response to the pressure rise than do points 4 to 6 before the second wellbore, wellbore B, is pressurized. After injection into wellbore A is stopped and injection into the second wellbore is started, the pressure at points closer to the second wellbore respond faster to the pressure rise, while the points closer to the first wellbore start showing pressure decay. The pressure decay around the first wellbore continues until the pressure front from the second wellbore arrives resulting in a lower rate of depressurization. The corresponding stress changes at the monitoring points are shown in Figure 4b.

The perturbation of in-situ stress around the pressurized wellbore as well as the neighboring wellbore is also seen in the maximum principal stress contours, where first wellbore A is pressurized (Figure 5a) and then where wellbore B is pressurized after injection into wellbore A is stopped (Figure 5b).

The stress perturbation decays after the injection pressure ceases, but still does not return to the lower virgin in-situ stress. This means that if the second wellbore is pressurized any time after the hydrofrac injection in the first wellbore, the hydrofrac generated will be controlled by a disturbed stress filed and not the original in-situ stress field.

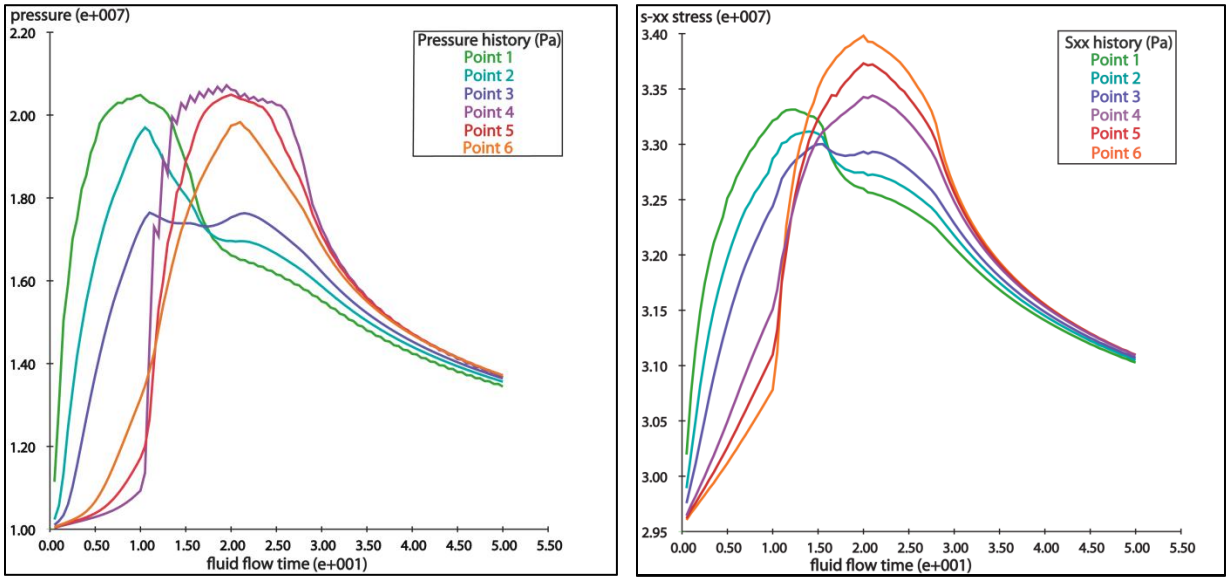

(a) **(b)**

Figure 4 - Zipperfrac scenario between two alternating injection boreholes: (a) Pressure histories, and (b) stress histories, for different points between the two wellbores. Point 1 is closest to the initial injection well (wellbore A), with point 6 being closest to the succeeding injection well (wellbore B)

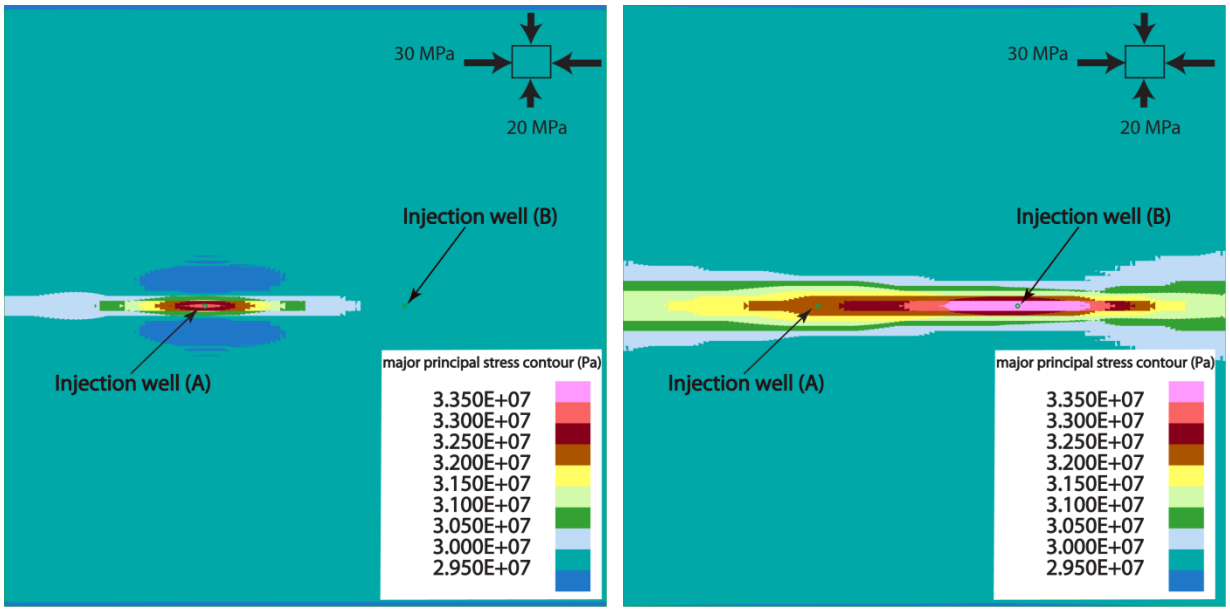

Figure 5 - Stress distributions arising from the zipperfrac scenario: (a) after injection into wellbore A; and (b) after injection into wellbore A ceases and injection into wellbore B commences

5.3.Two Simultaneous Injection Wells (Simulfrac)

The simulation of hydraulic fracturing for the third scenario is conducted where both horizontal wellbores (A and B) are pressurized at the same time. The results are presented in Figures 6 and 7. Figure 6a shows the changes of fluid pressure at different points between the two wellbores. Here, simultaneous pressurization results in all six monitoring points indicating a fast response to the hydrofrac injection. After pressurizing both wellbores is discontinued, a gradual pressure decline is seen in the pressure history plot for all points.

The corresponding stress responses around the two wellbores (Figure 6b) are similar to those around wellbore A for the single well injection scenario (i.e. Figure 2a), but with slightly higher stress values. This indicates that the pressure front induced at the two neighboring wellbores reaches and affects the stresses that develop at the adjacent wellbores.

Further interrogation of the modeled stresses through the principal stress contours, clearly show the development of a stress shadow. Initially separate elevated stress zones develop around each pressurized wellbore (Figure 7a). But eventually, the two stress perturbations merge into a larger disturbed stress field (Figure 7b). Thus, the stress distribution around one wellbore in this case is altered by the other and vice versa.

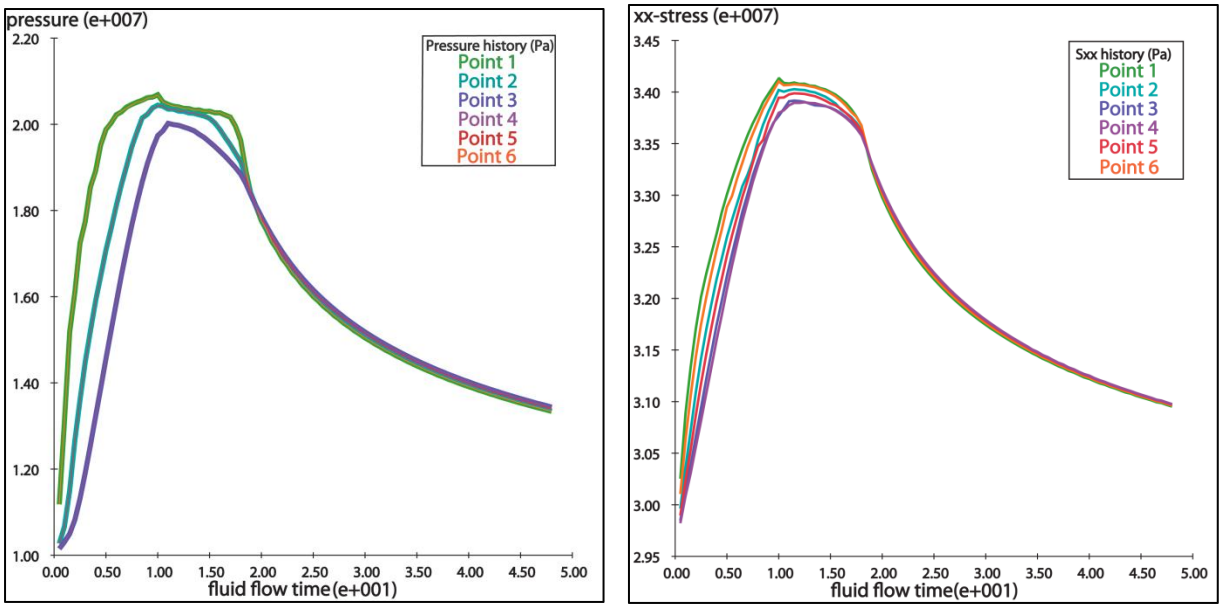

(a) (b)

Figure 6 - Simulfrac scenario between two simultaneously injecting hydrofrac wellbores: (a) Pressure histories, and (b) Stress histories, for different points between the two wellbores. Point 1 is closest to injection well A and point 6 closest to injection well B

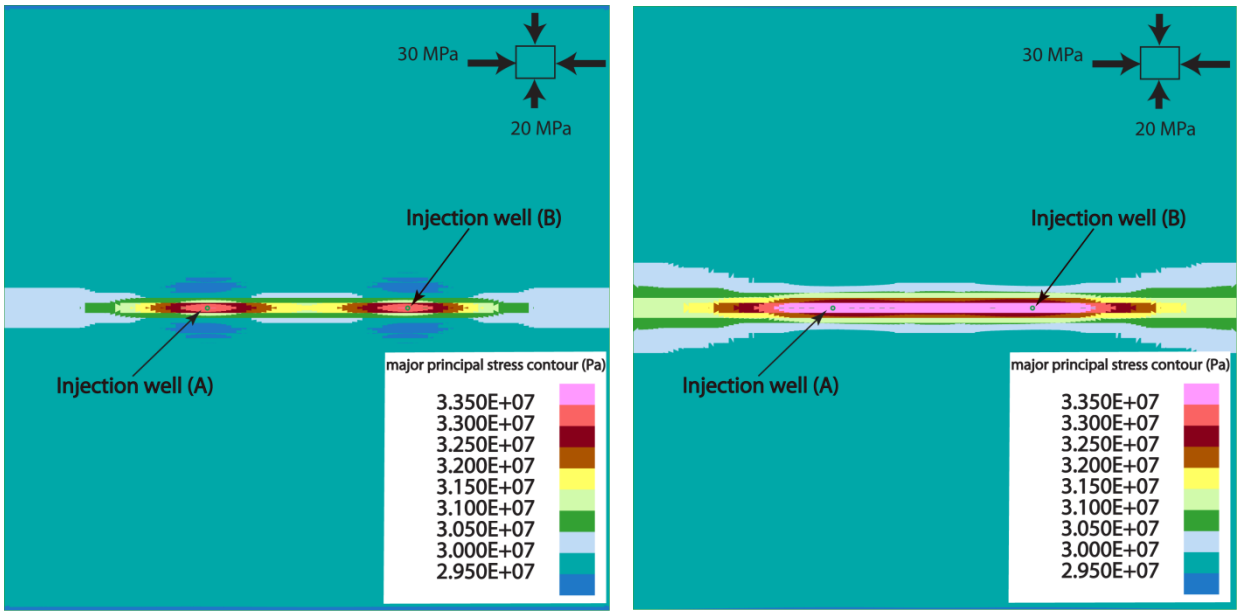

(a) (b)

Figure 7 - (a) Initial, and (b) Final, stress distributions around the two simultaneously pressurized wellbores (simulfrac scenario)

6. DISCUSSION

Wu et al. (2012) presented results of their study on stress shadow effects of multi stage fracturing of a horizontal well. Their results for the simple case of two fracturing stages from a horizontal wellbore show

that fractures can either enhance or suppress each other depending on their initial relative positions. Simulation of two parallel hydrofrac wells as performed here, confirms that the propagated fracture lengths will change due to stress shadow effects. In the zipperfrac scenario, the fracture is extended and in the simulfrac scenario, the fracture is suppressed by the effect of stress shadows arising from a neighboring pressurized wellbore.

Similarly, Vermylen and Zoback (2011) compared the activity level of conventional frac, zipperfrac and simulfrac, per stage. They showed that the simulfrac underperforms both the zipperfrac and the conventional frac. Here, the lengths of simulated fractures, which is a reasonable indication of their activity level (Vermylen and Zoback, 2011), is compared for the three different scenarios. The results for the simulated fracture length, shown in Figure 9, are consistent with conclusions arrived at by Vermylen and Zoback (2011) from their results.

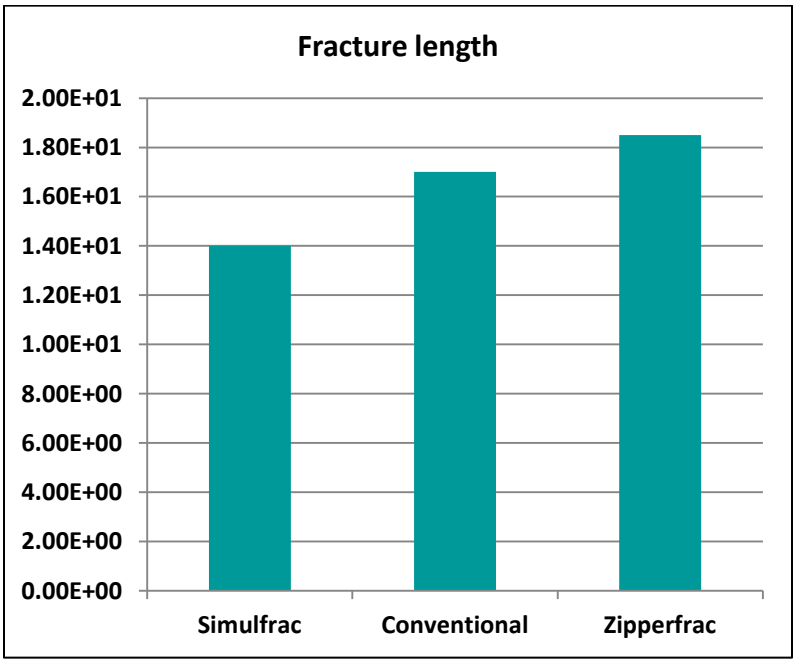

Figure 9 - Fracture length comparison between the three fracturing scenarios.

7. CONCLUSION

The purpose of this study has been to investigate the application of distinct element numerical modeling techniques to model stress shadowing effects resulting from multiple hydrofracs from neighbouring wellbores. The results elaborate on the concept of stress perturbation through hydraulic fracturing. Improved understanding of this condition will allow designers and operators to help control the fracture propagation to be extended in the area being treated.

The simulations show great potential in providing a deeper understanding of the influence of stress shadow effects on the propagation of hydraulically induced fractures. Future work will include the simulation of proppant and use of microseismic data to help calibrate and ground-truth the model.

8. REFERENCES

CUNDALL, P.A., and HART, R.D., 1993. Numerical Modeling of Discontinua. Comprehensive Rock Engineering. 2: 231-243. . A. Hudson, ed. Oxford: Pergamon Press Ltd.

FISHER, M.K., HEINZE, J.R., HARRIS, C.D., DAVIDSON, B.M., WRIGHT, C.A., and DUNN, K.P., 2004. Optimizing Horizontal Completion Techniques in the Barnett Shale Using Microseismic Fracture Mapping. Society of Petroleum Engineers, SPE90051.

MORRILL, J.C., AND MISKIMINS, J.L., 2012. Optimizing Hydraulic Fracture Spacing in Unconventional Shales. Society of Petroleum Engineers, SPE152595.

VERMYLEN, J.P., AMD ZOBACK, M.D., 2011. Hydraulic Fracturing, Microseismic Magnitudes, and Stress Evolution in the Barnett Shale, Texas, USA. Society of Petroleum Engineers, SPE140507.

WARPINSKI, N.R., and BRANAGAN, P.T., 1989. Altered-Stress Fracturing. Society of Petroleum Engineers, SPE17533.

WU, R., KRESSEE, O., WENG, X., COHEN, C., and GU, H, 2012. Modeling of Interaction of Hydraulic Fractures in Complex Fracture. Society of Petroleum Engineers, SPE152052.

Investigation of Anisotropy in Compressive Elastic Modulus of the Montney Shale

S.A.R. Keneti
EBA, A Tetra Tech Company
R.C.K. Wong
Schulich School of Engineering, University of Calgary

ABSTRACT: Predicting the geomechanical response of the shale gas material during hydraulic fracturing operation in the field needs better understanding of their geomechanical behaviour under laboratory testing. Anisotropy is considered as a critical factor during investigation and analysis of deviated boreholes, borehole stability, stress-strain and strength behaviour, generation and propagation of fracture and fluid flow. In this study, compressive elastic modulus (E_c) of the Montney shale has been investigated in two perpendicular directions: unconfined compressive strengths test was conducted on the Montney sample to measure its E_c in the vertical direction. This value then was compared to the E_c value in the horizontal plane (i.e. foliation plane) which was previously measured throughout a Brazilian test by Keneti and Wong (2011). From the results, the representative values of E_c in the vertical and in the horizontal directions were found as 25 GPa and 40 GPa, respectively. Computer tomography technique was also employed for the experimental data interpretation.

1. INTRODUCTION

While the potential for Canadian shale gas production is still being evaluated, the principal Canadian shale gas plays are the Horn River Basin and Montney Shales in northeast British Columbia, the Colorado Group in Alberta and Saskatchewan, the Utica Shale in Quebec and the Horton Bluff Shale in New Brunswick and Nova Scotia (Fig. 1) (National Energy Board, 2009). The Montney resource covers a considerable area, with varying geological and reservoir properties from the east to the west. The Mid to Lower Triassic-age deposit contains sandstones on the shallower (900 m) eastern boundary of the play, grading to siltstone and shale in the deeper (2,450 m) western boundary of the play (Stevens and Kuusaraa, 2009).

Soft sedimentary rocks like Montney shale generally exhibit inherent anisotropy (directional variation in material properties) because of the influence of depositional geological processes on constitutive behaviour. Anisotropy is considered as a critical factor during investigation and analysis of deviated boreholes, borehole stability, stress-strain and strength behaviour, generation and propagation of fracture and fluid flow (Chen et al., 1998; Tien et al., 2006). Predicting the geomechanical response of the shale gas material during hydraulic fracturing operation in the field needs better understanding of their geomechanical behaviour under laboratory testing. Furthermore, understanding the geomechanical behaviour helps to optimize the planning and management of the hydraulic fracturing operation.

The Montney shale samples were supplied by Talisman Energy to the Civil Engineering Department of the University of Calgary for geomechanical assessment of Montney shale. They were from a vertical borehole from a depth of 2320.2 m to avoid the effect of lithology change along depth on the data scatter. In this study, unconfined compressive strengths test was conducted on the Montney core samples to measure its compressive elastic modulus (E_c) in the vertical direction. This value then is compared to the E_c value in the horizontal plane (i.e. foliation plane) which was previously measured from a Brazilian test by Keneti and Wong (2011).

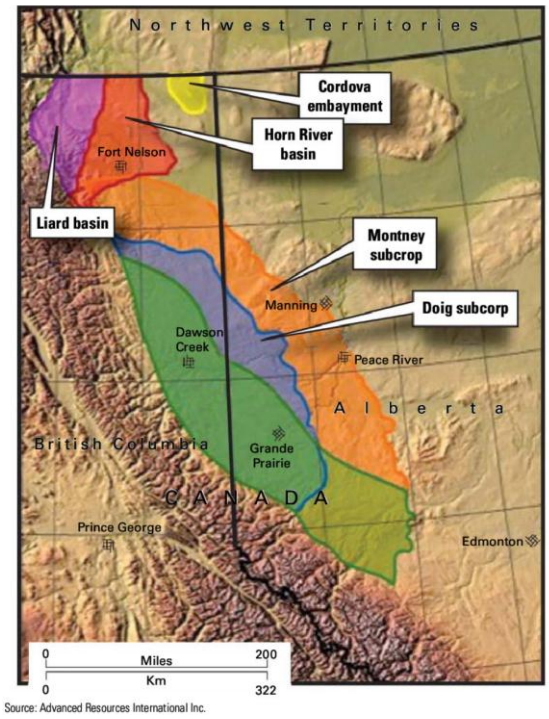

Figure 1 - Western Canada gas shale basins (National Energy Board, 2009)

2. COMPUTER TOMOGRAPHY IMAGE ANALYSIS

Although most common in medicine, computer tomography (CT) is also used in other fields such as non-destructive materials testing. In its geotechnical engineering application, computer tomography could be a viable, non-destructive method of observing the potential planes of weakness and therefore estimating the potential anisotropic behaviour of core samples. Computer tomography image analysis and thin sections image analysis were employed in this study to find potential planes of anisotropy in the Montney shale before conducting any experiments. The CT scanner used in this study was Siemens Sensation 64 at the Foothills Hospital, Calgary, Alberta. The settings were: 140 kVp; slice thickness: 1.5 mm; X-ray tube current (mA): 374; focal spot(s): 1.2; rows 512; columns: 512; width: 120 mm; height: 120 mm; and Resolution: 4.267 pixels per mm. A multiple set of data is generated from a number of views around a section of the sample forming a cross-sectional matrix or a scan. More precisely, the X-ray attenuations obtained from different angular positions are combined to generate the pixels of the matrix. Each individual pixel represents a specific CT number or a specific X-ray attenuation coefficient normalized with respect to water (Wong and Chau, 2005). Typical CT numbers for the scanned shale cores vary in the range of 1000-2000, but mostly fall in 1200-1300 range. Each scanned image was from a horizontal section with a thickness of 1.5 mm in DICOM format.

To view and analyze the CT images, the ImageJ software was employed. For each DICOM file we could see the image in the horizontal section and also we could get the variations of CT numbers along a specified line in ImageJ. Because of a high contrast between CT numbers of rock material and air, there was an edge effect in all CT images. To avoid the edge effect we removed the CT data outside the core and also about 2-3 mm of the edges in ImageJ and did the analysis only on rock material part which is a circular section with a diameter about 70 mm. Fig. 2 shows a typical cross sectional CT image of Montney shale obtained in this study as well as the variations of CT numbers along the diameter.

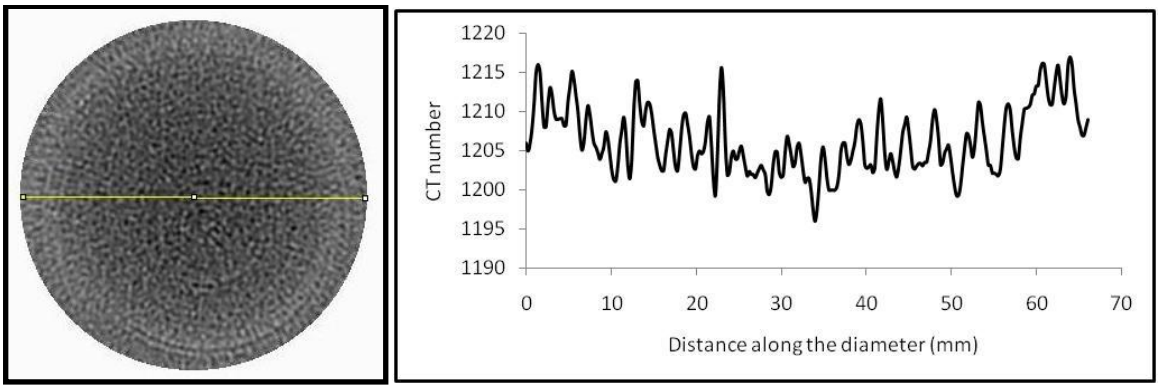

Figure 2 - A cross sectional CT image and variations of CT number along the Montney core diameter

To investigate the variations of CT numbers and therefore variations of density along the vertical direction, all sectional images are montaged and then stacked in ImageJ to have a vertical view of the core sample. Then, the mean value of CT number for each sectional image is plotted against its location along the height of the sample (Fig. 3). From this figure it could be seen that at some locations there is a drastic drop in density of rock material which could be an existing crack or a potential weak plane.

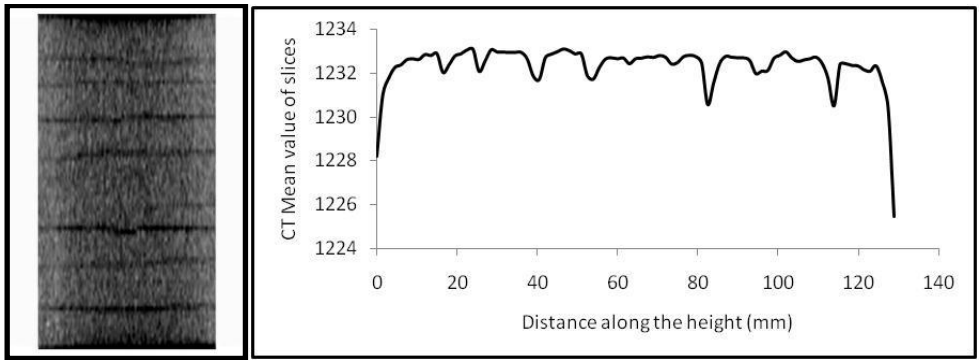

Figure 3 - Foliations observed in CT images, and variations of CT number in the vertical direction

Foliations, i.e., planes of weakness are observed in CT images along which Montney shale easily splits. Quantifying the sources for such a weak strength along these planes and their contributions to the strength of the weak band were beyond the objectives of this investigation. Whatever the causes for such a sharp inhomogeneities, the effect of such weak planes is also an important issue: Montney shale's fabric is strongly anisotropic which could result in different geomechanical properties in different directions. It means that all non-scalar physical quantities could be anisotropic. Such a fact is often neglected in practical rock mechanical analysis, because of lack of enough data (Fjaer et al., 2008). In this study, unconfined compressive strengths test was conducted on the Montney core samples to measure its compressive elastic modulus (E_c) in the vertical direction. This value then is compared to the E_c value in the horizontal plane (i.e., foliation plane) which was previously measured throughout a Brazilian test by Keneti and Wong (2011).

3. COMPRESSIVE ELASTIC MODULUS IN THE VERTICAL DIRECTION

3.1 Uniaxial Compressive Strength Test Equipment and Procedure

The unconfined compression of cylindrical rock samples is widely performed in rock engineering projects in order to determine the uniaxial compressive strength, σ_c, and the elastic constants Young's modulus, E_c, and Poisson's ratio, ν, of the rock material. A uniaxial compression tests was conducted on the Montney shale core with the length/diameter ratio as 2. The sample was capped at two ends using sulfur cement due to presence of very weak foliation planes which avoid us to grind the ends during sample preparation. In order to measure strains in the vertical and the horizontal directions, four pairs of micro-strain gauges were mounted on the sample in the UCS test. The gauges were "EA Series Gauges", a general purpose family of constant strain gauges widely used in experimental stress analysis. The first and the second pairs of strain gauges were installed on the mid-height of the core in opposite sides based on the ISRM suggestion to avoid end effects, while the third and fourth ones were installed in the opposite side of each other, close to top-end of the sample (Fig. 4).

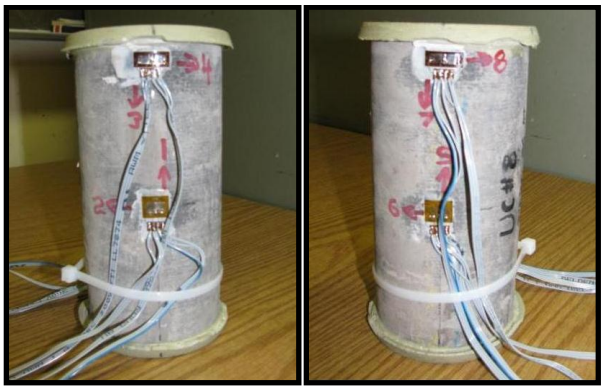

Figure 4 - Configuration of strain gauges in the UCS test

If rock samples are subjected to loading and unloading cycles in the pre-peak range, some permanent deformation and hysteresis are generally observed. This is often associated with 'bedding-down' effects, and for this reason, the ISRM Commission (1979) recommends that 'it is sometimes advisable for a few cycles of loading and unloading to be performed'. Therefore, the axial stress was applied in loading-unloading cycles using a load-controlled MTS apparatus with a loading rate of 0.5 kN/s. The testing procedure for the UCS test is as follows:

A servo-controlled axial loading machine (Material Testing System, MTS) with a maximum capacity of 1 MN was used to apply axial load to the sample which was taken from the core UC#8. Two lubricated transparent thin plastic were used on both ends of the sample to reduce the friction between the caps and the loading platens. A high speed camera recorder was employed to monitor the sample failure. The applied compressive load and the resultant axial and lateral deformations (which were reading by 8 micro-strain gauges) were recorded during the test by the data acquisition system designed for the test. The preliminary estimation of the unconfined compressive strength of the sample was about 50 MPa (from the literature as well as from the rough estimation from the point load splitting tests). The associated level of load for this level of strength for a core of a diameter as 76.2 mm is about 230 kN. The loading-unloading cycles were designed so that the sample would probably fail in its sixth round of loading, after five complete loading-unloading cycles:

- For the first cycle of loading-unloading, the applying load was increased to the level of 40 kN and then lowered down to the level of 5 kN. The loading was applied in four increments of 10 kN, after each one the loading was held for 2 seconds to avoid any sudden change in the sample under the load-controlled condition. The same steps were taken for unloading, however the minimum level of unloading was not returned to zero but kept at 5 kN to avoid sample's mismatching to the loading platens.
- For the second cycle the loading was applied up to 80 kN and decreased to 5 kN. The loading was applied in 2 increments of 20 kN to the level of 40 kN (i.e., the previous maximum load) and then 4 increments of 10 kN to the level of 80 kN. Same as in the first cycle, the loading was held for 2 seconds after each loading increment. The same steps were taken for unloading to the minimum level of 5 kN.
- For the third cycle the loading was applied up to 120 kN and decreased to 5 kN. The loading was applied in 4 increments of 20 kN to the level of 80 kN (i.e., the previous maximum load) and then 4 increments of 10 kN to the level of 120 kN. Same as in the previous cycles, the loading was held for 2 seconds after each loading increment. The same steps were taken for unloading to the minimum level of 5 kN.
- For the fourth cycle the loading was applied up to 160 kN and decreased to 5 kN. The loading was applied in 3 increments of 40 kN to the level of 120 kN (i.e., the previous maximum load) and then 4 increments of 10 kN to the level of 160 kN. Same as in the previous cycles, the loading was held for 2 seconds after each loading increment. The same steps were taken for unloading to the minimum level of 5 kN.
- For the fifth cycle the loading was applied up to 200 kN and decreased to 5 kN. The loading was applied in 4 increments of 40 kN to the level of 160 kN (i.e., the previous maximum load) and then 4 increments of 10 kN to the level of 200 kN. Same as in the previous cycles, the loading was held for 2 seconds after each loading increment. The same steps were taken for unloading to the minimum level of 5 kN.
- Finally the sample was loaded up to its failure.

3.2 Test Results and Discussions

The axial force recorded throughout the test was divided by the initial cross-sectional area of the sample to give the average axial stress, σ_a. The average axial stress was then plotted against the local axial strain, ε_a, and against the radial strain, ε_r to obtain stress-strain curve and the elastic constants E_c and ν. These constants were calculated from the linear part of each curve from strain gauges results in each cycle and then the average values are obtained for each test. Compressive stress and the resultant compaction strain are taken as positive while lateral expansion strain is taken as negative in this study.

The Montney shale core sample failed at the axial load level of 450 kN, corresponding to the unconfined compressive strength of 99 MPa which is a very high value for the shale rocks. Fig. 5 shows the failure progress in the test recorded by the high speed camera. It could be seen that sample started to fail from its top, and the final failure mode is not same as the typical failure in UCS test which is supposed to be axial tensile cracking. Such an unusual failure could come from the fact that the bedding planes play the dominant role in fracturing of the Montney shale. The failure mode of the sample could be regarded as a combination of tensile and shear fracturing. Another factor was from the capping, as the sulfur cement was not strong enough (or it is better to say that the shale sample showed more strength than it was expected). Therefore, the sooner failure of capping could affect the stress distribution and lead to local stress concentrations in the shale sample around its ends. However such a disturbing effect may not be huge since the thickness of capping was very smaller than the height of the sample, and also from inspection of the sample after failure it was found that there was no obvious evidence of capping's powdering or detachment, and its failure shape was similar to that of the sample.

Fig. 6 shows the test results obtained from the four pairs strain gauges in the UCS test. In general, from the stress-strain curves, sample showed to be stiffer at the top-end indicating some effect of confinement due to end friction. In terms of progressive fracture development and the accumulation of deformation, three stages could be distinguished from these curves: an initial bedding down and crack closure stage is followed by a stage of elastic deformation starting at stress level about 10 - 20 MPa until an axial stress level of about 70 - 80 MPa at which unstable crack growth begins. This region continues until the peak or uniaxial compressive strength, σ_c is reached at about 100 MPa. The post peak region could not be recorded since the experiment was conducted by a load controlled apparatus. The representative of E_c and ν are obtained for Montney shale to be about 25 GPa and 0.1, respectively, by averaging the values calculated obtained from the unloading part of the stress-strain curves.

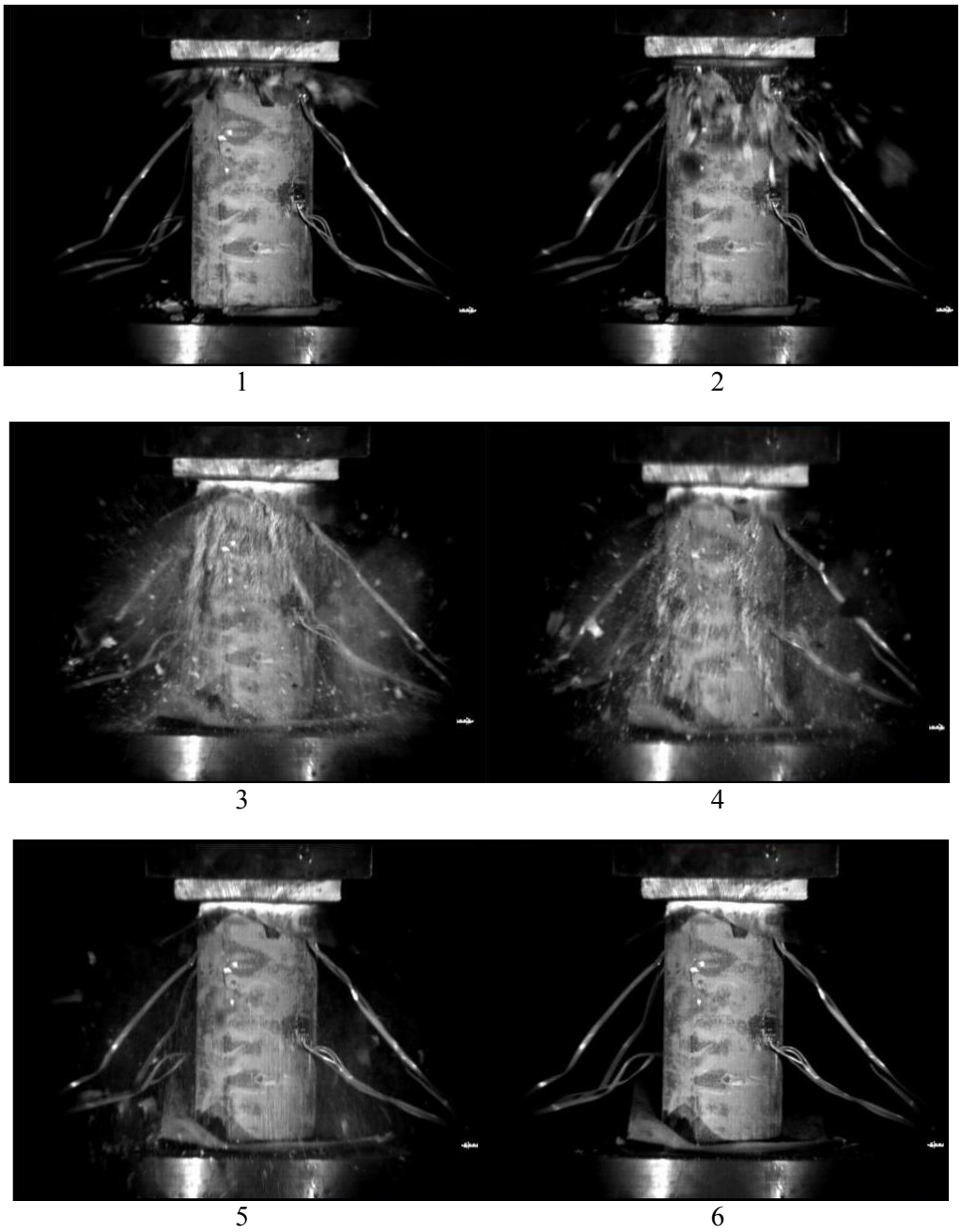

Figure 5 - Failure progress in the UCS test No.1

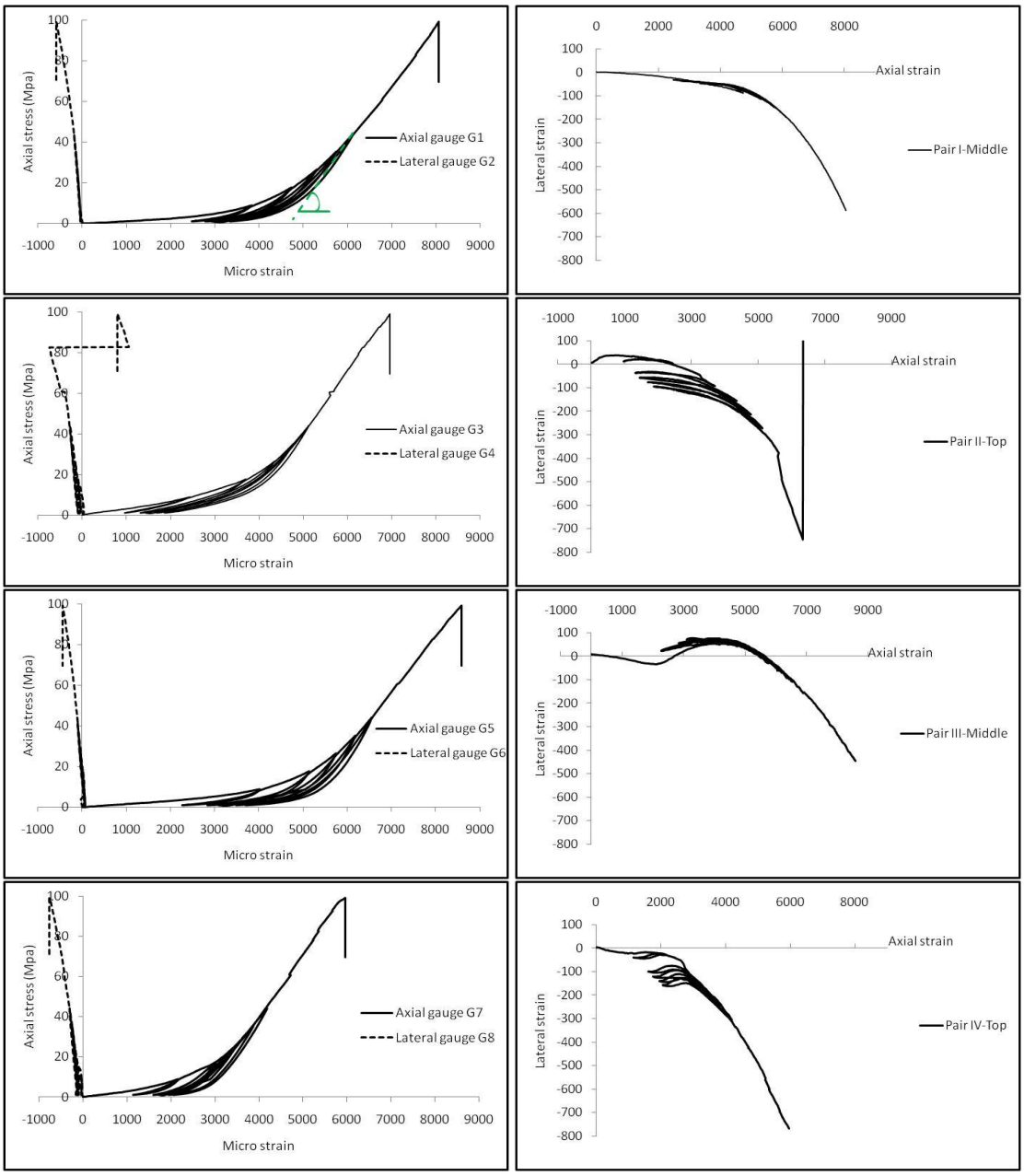

Figure 6 - Stress-strain curves (left) and lateral strain-axial strain curves (right) from UCS test

4. COMPRESSIVE ELASTIC MODULUS IN THE HORIZONTAL DIRECTION

A Brazilian test was conducted by Keneti and Wong (2011) for determining the tensile and compressive elastic moduli of the Montney shale in its foliation plane. Two pairs of strain gauges were mounted at the center of the Brazilian disc on its both side faces. In each pair, one gauge was installed along the direction of the compressive line load to record the compressive strain and the other one was installed in the direction perpendicular to it to record the tensile strain of the center part. The tensile elastic modulus E_t as well as the compressive elastic modulus E_c then were calculated using these recorded strains through the theory of elasticity. From the test results the average compressive elastic modulus was about 40 GPa and that for the tensile modulus was about 31 GPa.

5. CONCLUSIONS

In this study, compressive elastic modulus (E_c) of the Montney shale was investigated in two perpendicular directions. From the results, the representative values of E_c in the vertical and in the horizontal directions were found as 25 GPa and 40 GPa, respectively, indicating the anisotropy in elastic properties of the Montney shale. Such an isotropic behaviour was addressed in Keneti and Wong (2010) for the Montney's tensile strength properties as well. It seems that factors such as grains size and distribution in fabric structure, porosity and also degree of cementation and its type together with the minerals type and shape and their alignment during sedimentation periods play important roles in strength behaviour of such a layered material. Factors such as stress conditions, discontinuity surface conditions, and joints spacing could also play important roles in the final failure mode of the Montney shale material. Stress history of the site and tectonical events after the deposition of sediments are also important factors to induce fractures in particular directions in the Montney shale material.

6. ACKNOWLEDGEMENTS

The authors wish to acknowledge funding provided by the Natural Sciences and Engineering Research Council of Canada (NSERC), the Departments of Civil Engineering at the University of Calgary; and Cores provided by Talisman Energy. The authors also thank Dr. Chris Pan for his valuable input and feedback in this work.

7. REFERENCES

CHEN, C.H., PAN, E., and AMADEI, B. 1998. Determination of deformability and tensile strength of anisotropic rock using Brazilian test. International Journal of Rock Mechanics and Mining Science, Vol. 35, No. 1, p. 43-61.

FJAER, E., HOLT, R. M., HORSRUD, P., RAAEN, A. M., and RISNES, R. 2008. Petroleum related rock mechanics, 2nd Edition, Developments in Petroleum Science, No. 53, Elsevier, 515 p.

KENETI, S.A.R., and WONG, R.C.K., 2010. Investigation of anisotropic behavior of Montney Shale under indirect tensile strength test, the Canadian Unconventional Resources & International Petroleum Conference (CSUG/SPE), Calgary, Alberta, Canada, October 19-21.

KENETI, S.A.R., and WONG, R.C.K., 2011. Investigation of bimodularity in the Montney shale using the Brazilian test, the 45th US Rock Mechanics Symposium, San Francisco, CA, USA, June, 26-29.

National Energy Board. 2009. Understanding Canadian shale gas. Energy Brief. Retrieved from: http://www.neb-one.gc.ca/clf-nsi/index.html.

STEVENS, S., and KUUSARAA, V. 2009. Seven plays dominate North America activity, Oil and Gas Journal, Vol. 107, No. 36, 9p.

TIEN, Y.M., M.C. KUO, and JUANG, C.H., 2006. An experimental investigation of the failure mechanism of simulated transversely isotropic rocks. International Journal of Rock Mechanics and Mining Science. 43(8): p. 1163-1181.

WONG, R.C.K., and CHAU, K.T. 2005. Estimation of air void and aggregate spatial distributions in concrete under uniaxial compression using computer tomography scanning, Cement and Concrete Research, Vol. 35, p. 1566-1576.

CONSTITUTIVE BEHAVIOUR

Measured Convergence at a Test Tunnel in the Opalinus Clay Shale Formation

Renato Macciotta
Civil and Environmental Engineering, University of Alberta
C. Derek Martin
Civil and Environmental Engineering, University of Alberta
David Elwood
Civil and Environmental Engineering, University of Alberta
Tim Vietor
NAGRA
Hengxing Lan
Civil and Environmental Engineering, University of Alberta
RLREIS, Institute of Geographic Sciences and Natural Resources Research, Chinese Academy of Sciences

ABSTRACT: The argillaceous formation known as the Opalinus Clay is host to the Mont Terri Underground Research Laboratory. The URL was developed to investigate the hydrogeological, geochemical and geotechnical properties of the formation. Underground excavations at the site are characterized by non-elastic and time-dependent deformations. Excavations trending perpendicular to the strike of the bedding presented relatively minor deformations, however, tunnels parallel to the strike of the bedding showed much larger non-elastic deformations. This paper presents an analysis of the measured response of a tunnel trending parallel to the strike of the bedding in Opalinus Clay. The measured convergence is compared to tunnel experience in weak rocks to assess the tunnel stability.

1. INTRODUCTION

The argillaceous formation known as the Opalinus Clay is host to the Mont Terri Underground Research Laboratory (URL). Located in Northwest Switzerland, the Mont Terri URL has been the site of geotechnical research since 1995 (Thury and Bossart, 1999, Martin and Lanyon 2003). The Mont Terri URL was developed to investigate the hydrogeological, geochemical and geotechnical properties of the formation, and its response to underground excavations (Thury, 2002). In 2008, a 165 m long gallery with 4 niches was excavated (Gallery08) to expand the capacity of the Mont Terri facility (
Figure 1). Tunneling experience at Mont Terri demonstrated that excavations parallel to the strike of bedding displayed greater convergence and required more support than tunnels excavated perpendicular to the strike of the bedding. Consequently, the main gallery was excavated approximately perpendicular to the bedding strike while niches followed the strike of the bedding. The paper discusses the convergence response of the Opalinus Clay to excavation of the Mine-by (MB) Niche located near the centre of Gallery08 and parallel to the strike of bedding.

2. GEOTECHNICAL SETTING

The Opalinus Clay is a clay shale originating from marine sediments. The URL is located within the Mont Terri antiline (Thury, 2002). Bedding planes in the formation were sheared to allow the km-scale bending of the anticline. Spacing of the sheared bedding planes is in the range of 0.5 to 2 m. Wide-spaced North-Northwest striking sub-vertical folds cross-cut the anticlinal structure. In the region of the MB Niche the bedding planes dip between 30^{o} and 40^{o} and strike between 220^{o} and 250^{o} (Madritsch and Vietor, 2010). The available data on the in situ stress state in the URL suggest that the maximum principal stress is about 6.5 MPa. This maximum stress is sub-vertical, corresponding to the overburden

of approximately 250 to 300 m (Martin and Lanyon, 2003). The other two, sub-horizontal, principal stresses are roughly aligned with the orientation of Gallery08 and the MB Niche. The smallest principal stress is sub-parallel to the MB Niche axis (estimated at 2 MPa) and the intermediate principal stress is about 4 MPa.

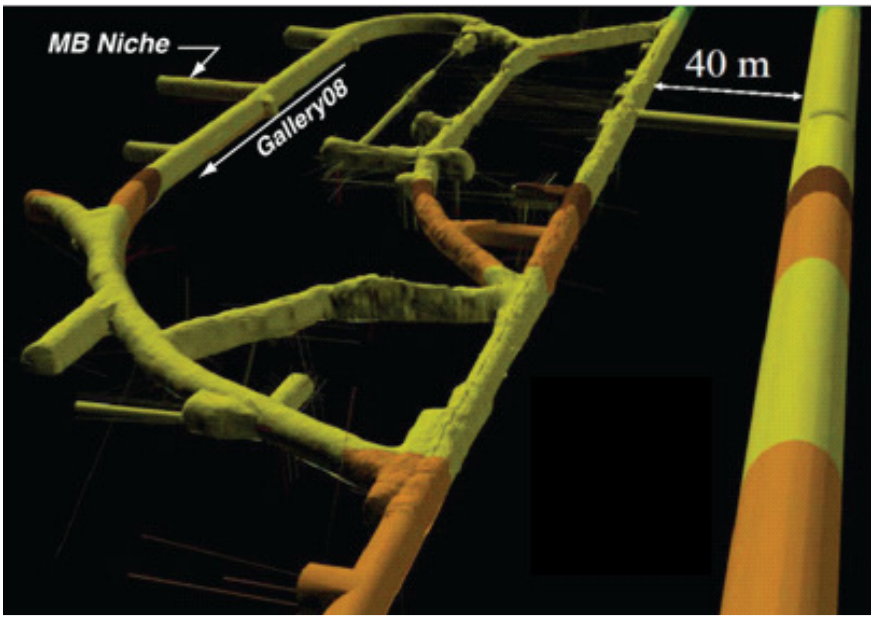

Figure 1 - General location of the Mine-By Niche in the Mont Terri URL

Underground excavations at the URL in the Opalinus Clay are characterized by non-elastic and time-dependent deformations. Most of the early excavations trend perpendicular to the strike of the bedding. While these tunnels exhibited non-elastic deformations, the deformations were relatively minor and the tunnels were adequately supported with shotcrete and anchors (Martin & Lanyon, 2003). However, when tunnels were excavated parallel to the strike of the bedding, the non-elastic deformations were observed to be much larger. The deformation response for excavations parallel and perpendicular to the strike of the bedding was described by Vietor et al. (2006). In particular, Vietor et al. described the case of a bedding-parallel excavation showing continuous signs of instability in niche EZ-A. As part of the test objectives, the EZ-A niche support was intentionally designed weak to allow for a significant EDZ (excavation damage zone) to develop. As such, some signs of instability were expected. The first part of the EZ-A niche was excavated, using a road-header, parallel to the strike of the bedding between August 12th and September 11th 2003. First indications of extensive deformations in the tunnel wall were noted by personnel on September 9th when cracks showed up in the shotcrete lining and continuously extended. After evacuation of staff and equipment approximately 130m^3 of rock fell from the crown on September, 11th and 12th. The failure advanced progressively into the tunnel crown, increasing the dimension of the tunnel in the direction normal the bedding (Figure 2). The niche was then stabilized with additional shotcrete and anchors. The niche EZ-A continued to show significant deformations for some time after excavation works had stopped.

3. MB NICHE EXCAVATION AND INSTRUMENTATION

The MB niche is located near the centre of Gallery08 (see Figure 1). It consists of a 24.6 m long and 4.5 m diameter circular opening trending 242° clockwise from the north. The direction of the excavation advance is sub-parallel to the average strike of the bedding planes. The tunnel rises at a slope of approximately 0.98% from the entrance to its face. The tunnel was advanced between 0.6 and 1.9 m per

day using a road header, and the tunnel face was cut vertically. The tunnel was not advanced over the weekends.

Support in the MB niche was intentionally designed to be relatively weak in order to allow the rock mass response within the EDZ to be observed. Support consisted of six anchors installed about 0.8 m behind the advancing face, 100-mm wire mesh reinforcement affixed to the entire circumference of the MB, and two layers of shotcrete. A 50 mm thick shotcrete layer was placed immediately following installation of the wire mesh and followed by an additional 100 mm final cover that was placed following completion of the MB. The anchors were 22 mm in diameter, 2 m long and installed in 30 mm diameter pilot holes. Approximately 1.3 m of each anchor was fully bonded using resin epoxy. The MB support system is shown in Figure 3.

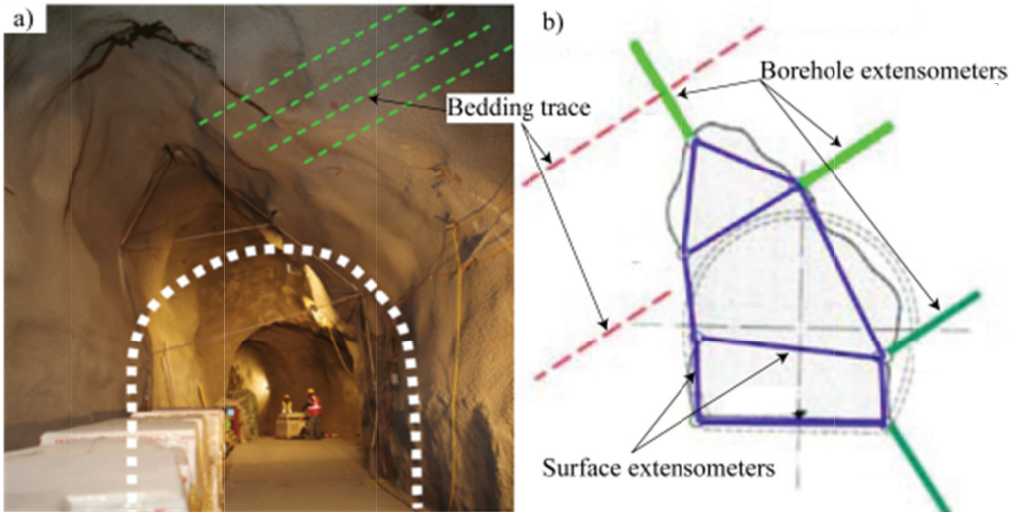

Figure 2 - Excessive deformations and roof failure at a section of the EZ-A niche excavated sub-parallel to bedding. a) view of the section after repairs and monitoring instrumentation was installed (Blümling et al., 2007). b) schematic of the section and instrumentation layout

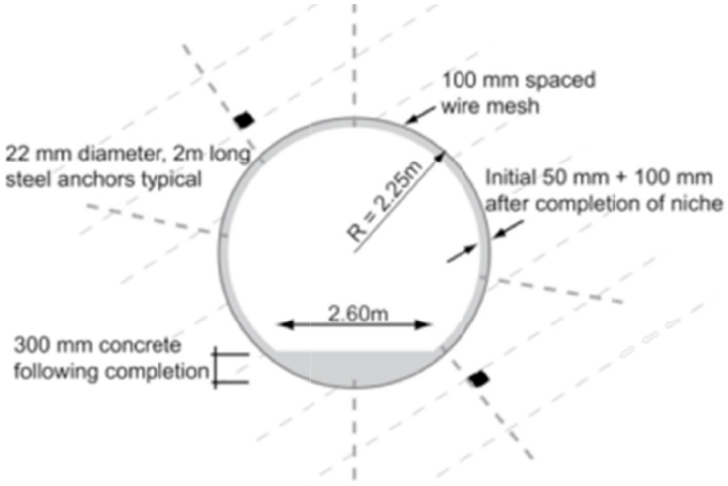

Figure 3 - Mine-by Niche cross section showing the initial 50 mm and final 100 mm thick shotcrete ring, schematic positioning of the anchors, and 300 mm concrete invert

A dense instrumentation layout was used to monitor the Opalinus Clay response to excavation. Many of the instruments were data logged such that response to excavation could be readily identified. The instrumentation included:

- Piezometer arrays, with 5 vibrating wire piezometers separated by packers in each hole,
- magnetic extensometer chains sub-parallel to the tunnel axis,
- radial extensometer chains installed 12.8m from the niche entrance,
- a mineable face extensometer chain installed parallel to the tunnel axis,
- inclinometer chains oriented sub-parallel to the tunnel axis, and;
- targets within the excavation to monitor convergence of the tunnel behind the advancing face.

The evaluation of the measured convergence presented is based on information from the targets within the excavation, the inclinometer chain located above the niche crown and the radial extensometer chains.

4. MEASURED PERFORMANCE

One of the objectives of the MB niche excavation was to allow for the development of a significant EDZ that would allow for the measurement of rock mass deformation within this zone. As such, some signs of instability were expected. The fact that repairs to the excavation support were needed is an indication of the tunnel's level of stability and significant extent of the EDZ.

Analysis of the excavation performance was based on the total measured response, the instantaneous and time dependant components of these responses, and the predicted elastic behaviour. The measured responses were defined as follows:

- Total response – total response measured by the instrument. It includes both the excavation-induced and time-dependent response when there are no excavation activities.
- Instantaneous response – measured during the period when the excavation was being advanced. This response includes both the elastic response and nonelastic response.
- Time-dependent response – measured when there was no excavation advance. However other activities could have been taking place, i.e., installing roof support or instrumentation.

Numerical modeling was used to predict the elastic component of the Opalinus Clay response to excavation. Modeling was conducted using a three-dimensional Distinct Element Code (3DEC). The excavation-induced elastic displacements and stress change were captured at each of the sensor locations allowing their comparison to instrument data. This required excavating the 3DEC model in a similar manner to the actual Mine-by excavation steps.

4.1 Radial Extensometers

Radial deformations at approximately 12.8 m from the MB Niche entrance were measured by extensometer chains. These were installed to borehole depths of 5 to 8 m. Extensometer BMB_30 was installed approximately parallel to bedding while BMB_28 was installed perpendicular to bedding. Extensometer BMB_29 was installed vertically on the crown, crossing the bedding at approximately 35 to 45 degrees. Simple two-dimensional elastic analyses suggest the extensometers at those depths can capture between 65% and 88% of the total elastic deformations (Figure 4). This is taken in consideration when evaluating the radial extensometer measurements. An increased installation depth would allow measurement of a greater portion of the total radial deformations. However, the efficiency in the gain of information per extra meter of installation depth is very low.

Figure 4 shows that for an installation depth of 18 m (10 m beyond the deepest radial extensometer on site), the average gain with respect to the 8 m deep extensometer is only 10%.

Figure 5 shows the radial deformations at the tunnel crown, and both parallel and perpendicular to bedding. The results indicate that the time-dependent response dominates the total response throughout the full depth of measurement. Extensometers BMB_29 and BMB_30 show the characteristic response of rapidly increasing displacements near the tunnel, while BMB_28 shows characteristic block movement. There do not appear to be differences in deformation magnitudes parallel or perpendicular to bedding.

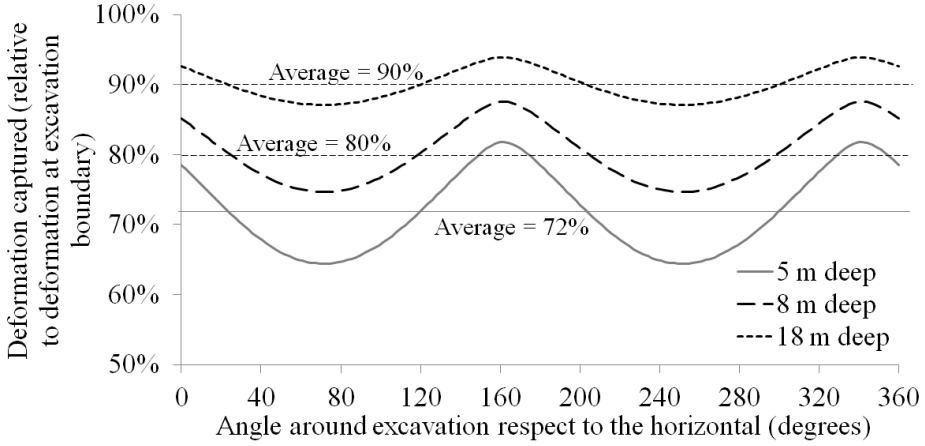

Figure 4 - Portion of total deformation captured for different instrument depths around a circular excavation using a 2D elastic analysis

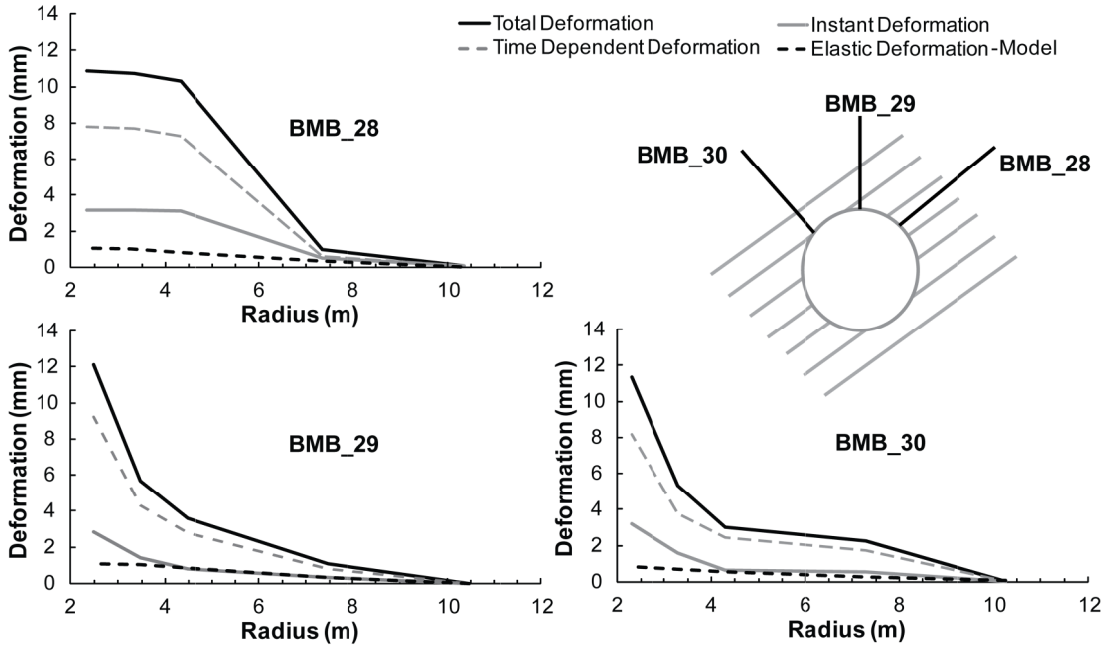

Figure 5 - Radial extensometer responses to excavation and elastic prediction.

4.2 Inclinometer Chain

An inclinometer chain (BMB_19) was installed sub-parallel to the MB, above the excavation crown. It was installed to measure the angular deformations in the vertical plane. Figure 6 shows the cumulative vertical displacement measured by this instrument. Measurements correspond to the advancing face at 13.2 m from the niche entrance. The far end of the chain is considered to be fixed (not moving) at this stage. This is supported by the measured total deformations being in agreement with the elastic prediction.

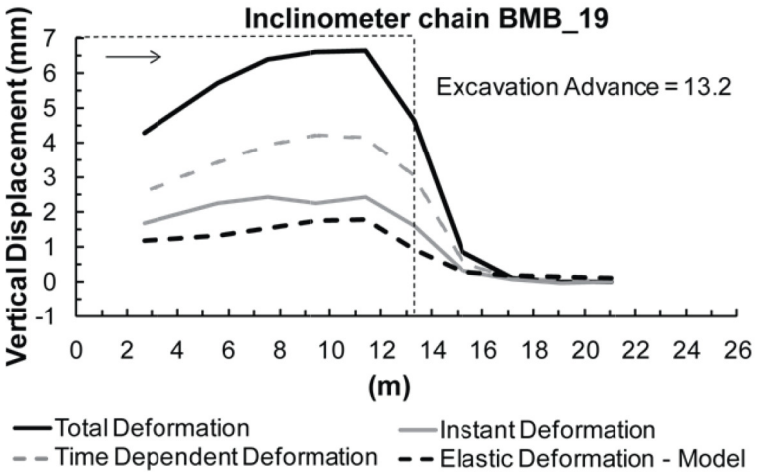

Figure 6 - Chain inclinometer response (BMB_19 - sub-parallel to the excavation crown)

4.3 Convergence Measurements

Convergence was measured at five locations on the tunnel perimeter (targets P1 through P5) and at 5 sections during the tunnel advance. The convergence points P1 and P4 recorded the response approximately parallel to bedding, and convergence points P2 and P5 record the response approximately perpendicular to bedding (Figure 7). Inspection of Figure 7 shows that the convergence varies with the tunnel face and that the majority of the convergence is associated with time-dependent deformations.

At the laboratory scale, the strength and deformation properties of the Opalinus Clay are anisotropic (Popp et al., 2008; Lux et al., 2007; Schnier and Stührenberg, 2007). Given the strength anisotropy in the laboratory samples, there was an expectation that the deformation pattern would also be anisotropic. Because the niche is essentially aligned with the strike of the bedding, the direction of the convergence-strain was measured relative to the dip of the bedding direction. This provided angles that ranged from 0 to 90 degrees, with 0 degrees being parallel to the dip of the bedding. Figure 8 presents the convergence strain calculated by normalizing the measured convergence over the distance between measurement targets. Figure 8 also shows non-uniform maximum convergences of approximately 1.7% at the end of excavation and about 2.5 to 3% by the end of monitoring.

5. SUMMARY AND CONCLUSIONS

Radial deformations were obtained from monitoring targets within the excavation, radial extensometers and inclinometers sub-parallel to the niche crown. These total measured responses were analyzed in terms of the (1) elastic, (2) instantaneous and (3) time-dependent components. The analyses showed that the greatest component of the response was associated with time-dependent deformations. These time-

dependent deformations also extended ahead of the tunnel face. Comparison of the response for the chain inclinometer with the three-dimensional elastic predictions suggests the time-dependent deformations, i.e., plastic zone, extends about 2 to 3 m ahead of the excavation face.

Based on studies by Chern et al. (1998), the relationship between rock mass strength and tunnel strain (defined as the ratio of tunnel closure to tunnel span) is an important indicator for identifying potential tunnelling instability. Figure 9 presents the guidelines, based on tunnel strain, for a Safety Management System developed in Taiwan (Chern et al, 1998). This plot was derived from observed performance on a number of tunnelling projects in Taiwan and for a wide range of different rock mass conditions.

Laboratory tests on Opalinus Clay in directions parallel, perpendicular and 45 degrees from bedding show rock mass strengths to be between 5 and 15 MPa (Popp et al., 2008; Lux et al., 2007; Schnier and Stührenberg, 2007). Figure 9 presents the area representing the range of rock mass strength found in the laboratory and the range of convergence strains measured at the end of excavation and at the end of monitoring. Also plotted are the data used to develop the guidelines.

The maximum convergence strains measured at the end of the MB Niche excavation fall between Level II and Level III of the empirical guidelines proposed by Chern et al. (1998). These maximum strains rise above Level III by the end of monitoring. This would suggest the niche was marginally stable, which is supported by the initial support repairs required during the advancement of the niche and shortly after completion of the niche. Placement of the final 100 mm of shotcrete and concreting of the invert provided additional support which limited the convergence.

Monitoring of the MB niche advance with relatively little support measures provided valuable insight into the controls on tunnel deformation in weak bedded claystones. In contrast with the tunnels driven perpendicular to the strike of the bedding at Mont Terri, the measured response for the MB Niche clearly showed the development of an extensive plastic zone around the 4-m-diameter tunnel. The support requirements for these bedding-parallel tunnels are therefore different. A support system that reduces the time-dependent deformations would increase the stability. Thicker initial shotcrete liners and/or applying a final reinforcement ring near the face advance would reduce these time-dependent deformations.

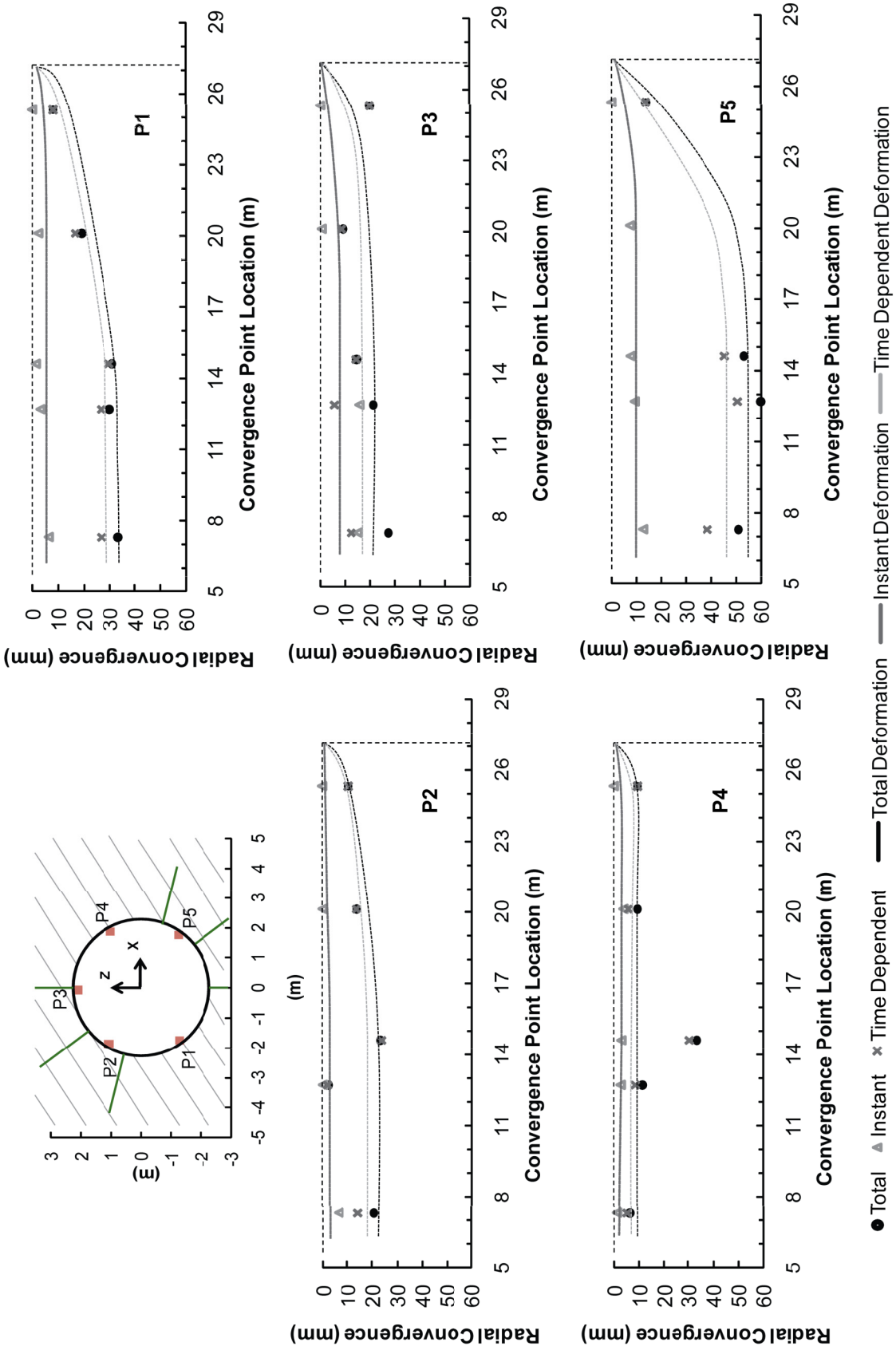

Figure 7 - Convergence deformations measured at each monitoring target

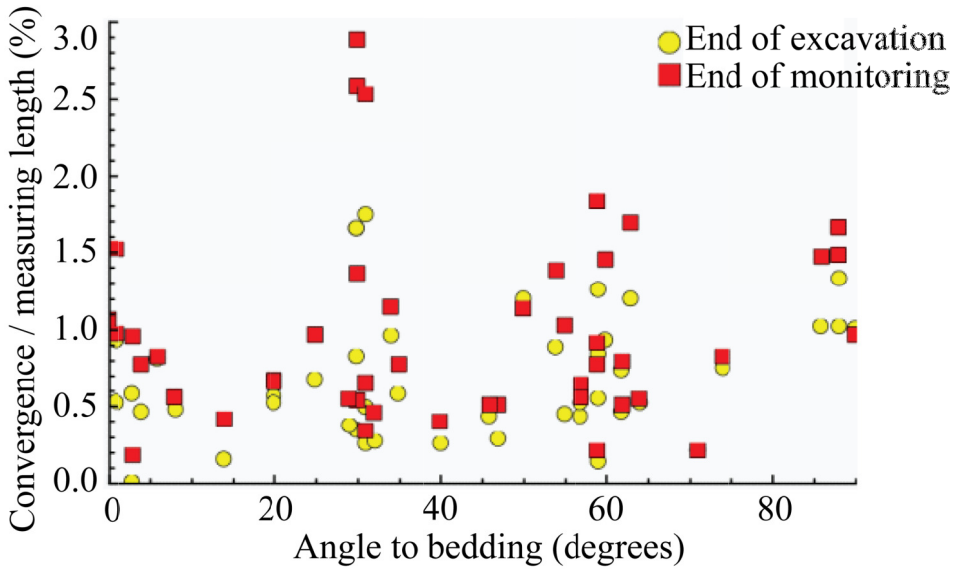

Figure 8 - Convergence strain (measured convergence divided by distance between measuring targets). 0 degrees represents measurements parallel to the dip of bedding)

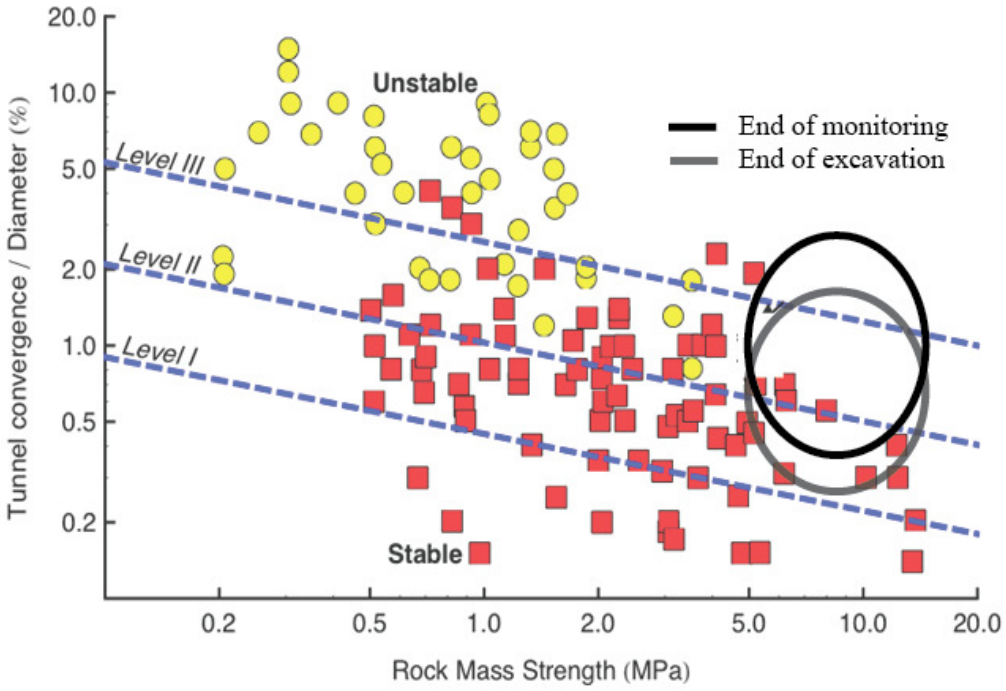

Figure 9 - Part 1 (continue on next page)

Below Level I	- Construction can continue - No special action required
Level I-II	- Construction can continue - Increase frequency of monitoring and field observations
Level II-III	- Tunnel is susceptible to instability, suspend construction temporarily - Conduct detailed inspection of tunnel lining and increase monitor frequency - Conduct thorough investigations of potential causes of the problem including support quality, timing of support installation and excavation procedure - Install additional support and/or revise tunnelling procedure, if required
Above Level III	- Construction work should be stopped - Increase frequency of monitoring and field observations - Conduct thorough investigations of potential causes of the problem and implement remedial measures - Revise the support design and/or construction procedures - Construction can be resumed only after remedial measures have been implemented and the trend of instability has been reversed

Figure 9 - Empirical correlation between tunnel performance and rock mass strength (after Chern et al, 1998). The circled areas represent the range of rock mass strength found in the laboratory and the range of convergence strains measured at the end of excavation and at the end of monitoring

6. REFERENCES

BLUMLING, P., BERNIER, F., LEBON, P. and MARTIN, C.D., 2007. The excavation damage zone in clay formations time-dependent behaviour and influence on performance assessment. Physics and Chemistry of the Earth, 32 p. 588-599.

CHERN, J.C., SHIAO, F.Y. and YU, C.W., 1998. An empirical safety criterion for tunnel construction. Proc. Regional Symposium on Sedimentary Rock Engineering Taipei, p. 222–227.

LUX, K.H., DÜSTERLOH, U. and CZAIKOWSKI, O., 2007. Laboratory tests on indurated clay. Clausthal University of Technology Final Report for EDZ long term evolution (WP 4.4). European Commission NF-PRO (Contract Number: FI6W-CT-2003-02389) (D 4.4.13).

MADRITSCH, H. and VIETOR, T., 2010. Mine By Experiment (MB) Excavation history of Niche 2 and results of structural geological tunnel mapping. Mont Terri Project Technical Note, November 2008.

MARTIN, C.D. and LANYON, G.W., 2003. Measurement of in-situ stress in weak rocks at Mont Terri Rock Laboratory, Switzerland. International Journal of Rock Mechanics and Mining Sciences, 40, p. 1077-1088.

POPP, T., SALZER, K. and MINKLEY, W., 2008. Influence of bedding planes to EDZ-evolution and the coupled HM properties of Opalinus Clay. Physics and Chemistry of the Earth, 33 p. S374–S387.

SCHAEREN, G. and NORBERT, J., 1989. Tunnel du Mont Terri et du Mont Russelin - La traversée des roches à risques: marnes et marnes à anhydrite. SIA-Dokumentation D 037, La traversée du Jura - Les projets de nouveaux tunnels. Swiss Society of Engineers and Architects (SIA), Zürich.

SCHNIER, H. and STÜHRENBERG, D., 2007. LT Experiment: Strength tests on cylindrical specimens, documentation and evaluation (phases 8 & 9) Mont Terri Project Technical Report 2003-04.

THURY, M., 2002. The characteristics of the Opalinus Clay investigated in the Mont Terri underground rock laboratory in Switzerland. C.R. Physique, 3 p. 923-933.

THURY, M. and BOSSART, P., 1999. Mont Terri rock laboratory: results of the hydrogeological, geochemical and geotechnical experiments per- formed in 1996 and 1997. In: Geological reports: 23, Swiss National Hydrological and Geological Survey, Bern-Ittigen.

VIETOR, T., BLÜMLING, P. and ARMAND, G., 2006. Failure mechanisms of the Opalinus Clay around underground excavations. Proceedings of EUROCK 2006, Multiphysics Coupling and Long-Term Behaviour in Rock Mechanics. Cotthem, Charlier, Thimus and Tshibangu (eds.). Taylor & Francis, p. 479-486.

The Effective Strength of Broken Rock

S. Balideh, T. Joseph
University of Alberta, Alberta Equipment-Ground Interactions Syndicate (AEGIS)
T. Joseph
University of Alberta, Alberta Equipment-Ground Interactions Syndicate (AEGIS)

ABSTRACT: A good understanding of the behavior of broken rock helps to make more informed decisions regarding slope stability and waste dump issues in mines. The cohesion coefficient of rock has little influence on the strength of broken rock; therefore, a criterion based on friction and cohesion of intact materials does not provide an accurate analysis for the strength of broken rock. This paper illustrates the effective strength of broken rock through a brief literature review about failure of intact rock and rock masses. The complete stress- strain curve and some important points of residual strength of rock are summarized in this paper.

1. INTRODUCTION

Engineers need to know the strength of rock in structures such as tunnels, underground mining stopes, pillars, open pit mines and foundations. Some rocks at low confining pressure exhibit the softening behavior and do not lose strength suddenly after failure; therefore, a good understanding of this is very important. Accurate determination of rock modulus and deformation in pre and post-failure regions is required for the cost-effective design of underground cavern support and slope stability. In conservative design methods, engineers consider only the ultimate strength of rock, and assume that after ultimate strength, rock loses its strength to a residual strength suddenly. This assumption causes an overly conservative design and extra cost. Also, the behavior of broken rock is key to understanding the residual strength of rock. Since it should be investigated to design the geotechnical projects such as waste dump stability, backfill problems and residual strength of rock.

2. FAILURE OF INTACT ROCK

Investigation of the behavior of intact rock is the first step to understanding the strength of a rock mass; therefore, many researchers have worked on failure of intact rock through empirical works, e.g., Hoek (1965), Mogi (1971), Brace (1963), Bieniawski (1967), Price (1979) and Hudson (1997).

Brace (1963) investigated the brittle failure of rock with cylindrical specimens under compressive pressure. He divided the stress-strain curve of intact rock, up to peak strength, into four regions and explained the behavior of rock in each region. Figure (1) shows the stress-strain curve and the four regions proposed by Brace (1963). According to Brace's (1963) research, rock in regions 1 and 2 has elastic behavior and in regions 3 and 4 has plastic behavior.

Bieniawski (1967) discussed the mechanism of brittle failure through experimental tests. He investigated crack initiation and crack propagation by Griffith theory. Also, he concluded that it is possible to specify stable and unstable cracks at intact rock failure through crack growth speed. Bieniawski (1968) explained that, after failure, rupture will be appear, and rupture is not a characteristic property of the rock material. In other words, the rupture behavior of rock is a function of boundary conditions and is not a pure material property. The complete stress-strain curve was discussed by Price (1979) and Farmer (1968). Figure (2-a) shows the complete stress-strain curve proposed by Price (1979). They explained that rock is intact until reaching region F. At region F, the friction between created blocks has a major impact on the behavior of rock. Figure (2-b) shows the specimen close to peak strength, and Figure (2-c) shows the specimen at region F. Martin and Chander (1994) and Hajiabdolmajid (2001) showed that the impact of

the cohesion component of strength will be decreased and the impact of friction component will be increased during the complete failure of rock, and the mobilization of friction and cohesion is a function of axial strain in compressive test. Therefore, the friction component of strength has a major influence on the post-failure behavior of rock. Also, Martin (1993) introduced the crack initiation threshold (σ_{ci}), which is independent on damage level and specimen diameter.

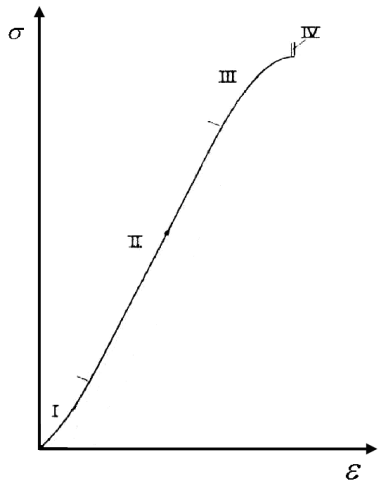

Figure 1 - Stress-strain curve of intact rock to four regions until peak strength, after Brace et al. (1964)

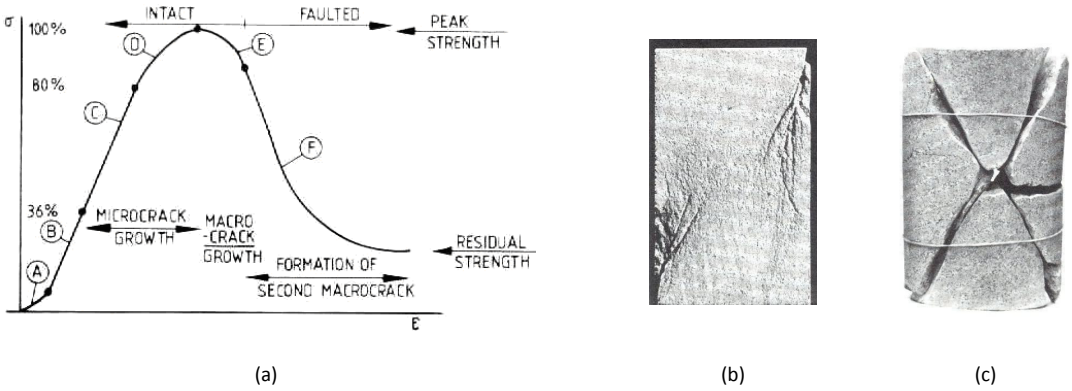

Figure 2 - (a) Stress-strain curve, (b) specimen near to failure point, (c) specimen at region F, after Price et al. (1979) and Farmer et al. (1983)

Joseph (2000) and (2003) investigated the post failure stiffness of rock, and he introduced a 2nd order polynomial criterion to determine the residual strength of rock. He also explained an approach to determine the parameters of his criterion by available information such as uniaxial compressive strength, Hoek-Brown parameters and confining pressure. In Joseph's approach, two components have major influence on broken rock behavior (i.e., Frictional resistance to sliding and Asperities of rough surface).

3. FAILURE OF ROCK MASS

Bieniawski (1968) and (1969) discussed the failure of fractured rock and the impact of specimen size on the peak strength. He showed that specimen size and rock strength have an inverse relationship because larger specimens have more discontinuities and weak planes than small specimens.

Hoek (1964) proved that the angle between open Griffith cracks and the major principal stress has significant influence on the strength of anisotropic rock because the strength of the rock mass only depends on the strength of extent joints at a critical angle. Hoek (1966) investigated the effect of the spacing between discontinuities on the strength of a rock mass. He showed that the spacing of discontinuities has a direct relationship with the strength of a rock mass. Hoek (1980) introduced the Hoek-Brown criterion to characterize the strength of rock masses. The Hoek-Brown criterion has two important parameters (m and s) to predict the behavior of a rock mass. The magnitudes of m and s change from maximum to minimum values going from intact to residual strength, respectively. Hoek (1995) introduced a new rock mass classification system and called it Geological Strength Index (GSI). Hoek used of GSI to determine the Hoek-Brown criterion parameters. Hoek (1997) and (2001) suggested some values for post failure of rock mass.

Ribacchi (2000) proposed the ratio between Hoek-Brown criterion parameters at peak strength and at residual strength. Also he mentioned that the Young's modulus of a rock mass will be increased by increasing the confining pressure. Crowder and Bawden (2004) explained that the initial GSI shouldn't be changed to residual GSI directly. They recommended usage of residual m and s (m_r, s_r) to predict the residual strength of a rock mass. Bawden (2010), Crowder and Bawden (2006) and Crowder and Coulson (2006) explained the significance of post-failure behavior on mining cost and support design. They used residual parameters of the Hoek-Brown criterion to simulate the residual behavior of rock mass.

Cai and Kaiser (2007) introduced a method to determine the residual parameters of the Hoek-Brown criterion by: residual block volume (V_b^r) and residual joint condition factor (J_c^r). Cai and Kaiser verified the validity of equations by experimental tests and concluded that the block volume (V_b^r) and joint condition (J_c^r) have significant influence on the post-failure and residual behavior of rock masses.

Diederichs (2007), Carter (2007), Carvalho (2007) and Carter (2008) investigated the strength of rock masses, and they developed formulae to determine the Hoek-Brown criterion's parameters for very strong rock masses (with GSI more than 65) and very weak rock masses (with intact uniaxial compressive strength less than 10 MPa). Also they demonstrated that the behavior of rock masses, with intact uniaxial compressive strength (σ_c) more than 10 MPa, will be dominated by the structures at low confining pressure. Moreover, currently, most researchers have used numerical methods to simulate the failure of rock masses, such as Park (2006), Sainsbury (2008), Stefanizzi et al. (2008), Liang (2008), Villeneuve et al. (2009), Valley et al. (2010) and Moraes (2011). However, good understanding of the behavior of rock mass at the pre and post-failure regions by experimental tests is very important for accurate numerical simulation.

4. FAILURE OF BROKEN ROCK

Hobbs (1966) and (1970) investigated the behavior of broken rock by triaxial compression tests. Hobbs introduced a criterion to predict the strength of broken rock according to confining pressure. Also, he illustrated the relationship between shear and normal stress with an exponential function. Hobbs demonstrated that Young's modulus depends on the magnitude of the applied confining pressure.

Hussaini (1970), (1971) and (1983) tested the behavior of crushed basalt and found out that the relationships between major and minor principal stress are not linear. The research by Hussaini showed that the effective friction angle increases with increasing maximum particle size. Also, Hussaini used of the effective diameter (D_{10}) to investigate the particle size change after failure. A number of researchers have investigated the strength of granular materials such as gravel, sand and crushed rock to design the backfills and rockfill dams, e.g., Fumagalli (1969), Kolbuszewski and Frederick (1963), Holtz and Gibbs (1956), Marschi (1972) and Marsal (1973). They demonstrated that the particle shape, size and roughness affect the strength of the cohesion-less materials.

Joseph (2000) and (2003) explained that stress-strain curvature are same for both intact and broken rock in the post-failure region at low confining pressure. Figure (3-a) shows the stress-strain curves at several confining pressure for intact and broken rock of the same rock type. Also he demonstrated that intact and broken rock have similar functions to determine the post-peak modulus. Also, Joseph used an effective friction angle to calculate the effective strength of broken rock by equation (1) and (2). Joseph employed a 2nd order polynomial to predict the effective friction angle, and demonstrated that the effective friction angle has the same equation for peak and residual regions through equation (3).

$$\tau = f(\sigma) \tag{1}$$

$$\phi_e = \tan^{-1}\left[\frac{\tau}{\sigma}\right] \tag{2}$$

$$\phi_e = R + S(e_{pp}) + T(e_{pp})^2 \tag{3}$$

R, S and T are constant parameters based on rock type, and e_{pp} is the post peak strain. Figure (3-b) shows the effective friction angle curve and the boundary conditions. Joseph (2000) demonstrated that the post-peak modulus and the stress-strain curve in the post-failure region can be determined using only the peak strength and the base friction angle of rock.

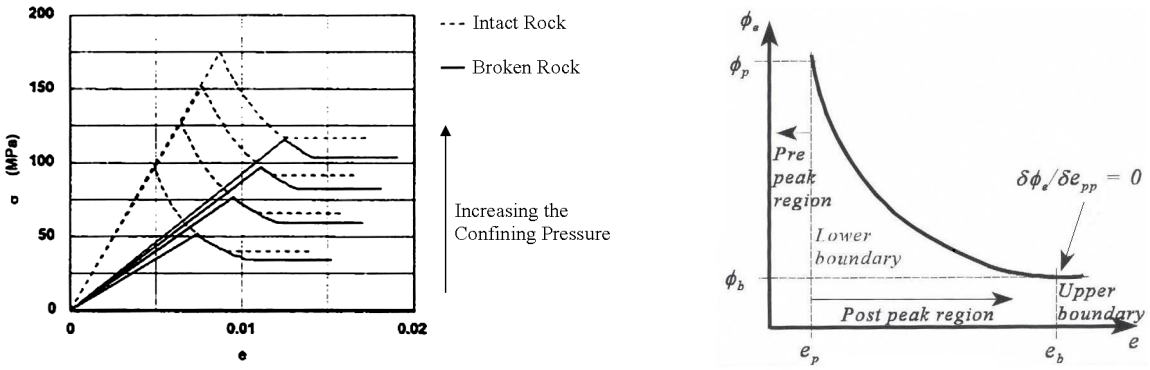

(a) (b)

Figure 3 - (a) The stress-strain curves for intact and broken rock, (b) boundary condition of effective friction angle, after Joseph (2000)

5. CONCLUSION

According to previous research that was reviewed for this paper, we can conclude that:

i. The linear Mohr-Coulomb criterion is not accurate for broken rock. The Coulomb-Navier criterion has two components (i.e., cohesion coefficient and internal friction angle) while the cohesion coefficient does not have an effect on broken rock behavior. The effective strength concept seems to better represent the behavior of broken rock. Effective strength is based on the effective inter-surface friction angle. The authors believe that the effective friction angle is a function of confining pressure, Young's modulus, base friction angle, and block size distribution coefficient.

ii. The Strength of broken rock may depend on the behavior of blocks of broken rock after failure at low confining pressure. Therefore, the residual behavior of rock can be predicted by the effective strength criterion of broken rock more precisely. The complete stress-strain curve and the residual behavior of rock will be employed by the results of broken rock investigation.

Currently, the authors are working to study the behavior of broken rock. The effective strength of broken rock will be formulated as a function of effective angle and the results will be used to predict the complete stress-strain curve.

6. REFERENCES

BAWDEN, W. F. (2010). Rock Mechanics Conference Invited Presentation Thoughts on Quantitative Field Scale Characterization of Post-failure Rock Mass Conditions and their Influence on Underground Mine Design. in 44th US Rock Mechanics Symposium and 5th U.S.-Canada Rock Mechanics Symposium. Salt Lake City, UT: American Rock Mechanics Association (ARMA).

BIENIAWSKI, Z. T. (1967). Mechanism of brittle fracture of rock, Part I, II and III. Int. J. Rock Mech. Min. Sci., 4 14.

BIENIAWSKI, Z. T. (1968). The effect of specimen size on compressive strength of coal. Int. J. Rock Mech. Min. Sci., 5 17.

BIENIAWSKI, Z. T. (1968). Propagation Of Brittle Fracture In Rock. in Symposium on Rock Mechanics (USRMS). Austin, TX: American Institute of Mining, Metallurgical, and Petroleum Engineers Inc., pp. 20.

BIENIAWSKI, Z. T., DENKHAUS, H. G., and VOGLER, U. W. (1969). Failure of fractured rock. Int. d. Rock Mech. Min. Sci., 6 23.

BRACE, W. F. (1963). A note on brittle crack growth in compression. Journal of Geophysical Research, 68 (12), 5.

CAI, M., KAISER, P. K., TASAKA, Y., and MINAMI, M. (2007). Determination of residual strength parameters of jointed rock masses using the GSI system. International Journal of Rock Mechanics & Mining Sciences, 44 19.

CAI, M., KAISER, P. K., TASAKA, Y., and MINAMI, M. (2007). Peak and residual strengths of jointed rock masses and their determination for engineering design. in Proceedings of Proc. 1st Canada-U.S. Rock Mech. Symp., Vancouver.

CARTER, T. G., DIEDERICHS, M. S., and CARVALHO, J. L. (2007). A unified procedure for Hoek-Brown prediction of strength and post yield behaviour for rockmasses at the extreme ends of the rock competency scale. in 11th congress of the International society for rock mechanics. NG Portugal, pp. 4.

CARTER, T. G., DIEDERICHS, M. S., and CARVALHO, J. L. (2008). Application of modified Hoek-Brown transition relationships for assessing strength and post yield behaviour at both ends of the rock competence scale. The Journal of The Southern African Institute of Mining and Metallurgy, 108 14.

CARVALHO, J. L., CARTER, T. G., and DIEDERICHS, M. S. (2007). An approach for prediction of strength and post yield behaviour for rock masses of low intact strength. in 1st Can-US Rock Mech.Symp. Vancouver, British Columbia, Canada pp. 8.

CROWDER, J. J. and BAWDEN, W. F. (2004). Review of post-peak parameters and behaviour of rock masses: current trends and research. in Rocnews, Fall 2004 ed: rocscience, pp. 14.

CROWDER, J. J. and BAWDEN, W. F. (2006). The estimation of post-peak rock mass properties:numerical back analysis calibrated using In situ instrumentation data. rocscience, pp. 22.

CROWDER, J. J. and COULSON, A. L. (2006). The field-scale rock mechanics laboratory: estimation of post-peak parameters and behaviour of fractured rock masses
in The 41st U.S. Symposium on Rock Mechanics (USRMS). Golden, Colorado: American Rock Mechanics Association (ARMA).

DIEDERICHS, M. S., CARVALHO, J. L., and CARTER, T. G. (2007). A modified approach for prediction of strength and post yield behaviour for high GSI rockmasses in strong, brittle ground. in 1st Can-US Rock Mech.Symp. Vancouver, British Columbia, Canada pp. 8.

FARMER, I. W. (1968). Engineering behaviour of rocks. Chapman and Hall, New York.

FUMAGALLI, E. (1969). Tests on cohesionless materials for rockfill dams. ASCE Journal of Soil Mechanics and Foundations Division, 95 19.

HAJIABDOLMAJID, V. R. (2001). Mobilization of strength in brittle failure of rock.Thesis, Queen's University, Kingston, Canada, Pages 268.

HOBBS, D. W. (1966). A study of the behaviour of a broken rock under triaxial compression, and its application to mine roadways. Int. J. Rock Mech. Min. Sci., 3 33.

HOBBS, D. W. (1970). The behavior of broken rock under triaxial compression. Int J Rock Mech Min. Sc, 7 23.

HOEK, E. (1964). Fracture of Anisotropic Rock. Journal of the South African Institute of Mining and Metallurgy, 64 23.

HOEK, E. (1965). Rock fracture under static stress conditions.Thesis, Cape Town, Cape Town, South Africa, Pages 229.

HOEK, E. (1966). Rock Mechanics - an introduction for the practical engineer. Mining Magazine, 67.

HOEK, E. (1980). Empirical strength criterion for rock masses. J.Geotech. Engng Div., 106 22.

HOEK, E. (2001). Rock mass properties for underground mines. Society for Mining, Metallurgy, and Exploration (SME), 21.

HOEK, E. and BROWN, E. T. (1997). Practical estimates of rock mass strength. Int. J. Rock Mech. Min. Sci., 34 (8), 22.

HOEK, E., KAISER, P. K., and BAWDEN, W. F. (1995). Support of underground excavations in hard rock. A.A. Balkema, Rotterdam, Netherlands ; Brookfield, VT, USA.

HOLTZ, W. G. and GIBBS, H. G. (1956). Triaxial Shear Tests on Pervious Gravelly Soils. Journal of the Soil Mechanics and Foundations Division, 82 (1), 22.

HUDSON, J. A. and HARRISON, J. P. (1997). Engineering rock mechanics. Elsevier Science, Kidlington.

HUSSAINI, M. A. (1970). Influence of end restraint and method of consolidation on the drained triaxial compressive strength of crushed Napa basalt. Waterways Experiment Station, Vicksburg, pp. 70.

HUSSAINI, M. A. (1971). Plane strain and triaxial compression tests on crushed napa basalt. Waterways Experiment Station, Vicksburg.

HUSSAINI, M. A. (1983). Effect of particle size and strain conditions on the strength of crushed basalt. Canadian Geotechnical Journal, 20 (4), 12.

JOSEPH, T. G. (2000). Estimation of the post-failure stiffness of rock.Thesis, University of Alberta, Edmonton, Canada, Pages 536.

JOSEPH, T. G. and BARRON, K. (2003). The post-failure characteristics of rock. CIM Bulletin, 96, N° 1070 9.

KOLBUSZEWSKI, J. J. and FREDERICK, M. R. (1963). The significance of particle shape and size on the mechanical behaviour of granular materials. in Proceedings of European Conference on Soil Mechanics and Foundation Engineering, Wiesbaden, pp. 253-263.

LIANG, Z. Z. (2008). Three Dimensional Numerical Modelling of Rock Failure Process.Thesis, North-western University, China.

MARSAL, R. J. (1973). Mechanical Properties of Rockfill. Embankment Dam Engineering, 12.

MARSCHI, N. D., CHAN, C. K., and SEED, H. B. (1972). Evaluation of Properties of Rockfill Materials. Journal of the Soil Mechanics and Foundations Division, 98 (1), 20.

MARTIN, C. D. (1993). The strength of massive Lac du Bonnet Granite around underground openings.Thesis, University of Manitoba, Winnipeg, Manitoba, Canada, Pages 304.

MARTIN, C. D. and CHANDER, N. A. (1994). The progressive fracture of Lac du Bonnet granite. Int. J. Rock. Mech. Min. Sci. & Geomech., 31 (6), 13.

MOGI, K. (1971). Fracture of flow of rocks under high triaxial compression. Journal of Geophysical Research, 76 (5), 15.

MORAES, R. (2011). Numerical codes used to model failure in large fractured scale and jointed rock slopes in hydropower projects. in 6th international conference on dam engineering. C.Pina, E.Portela, pp. 18.

PARK, N. (2006). Discrete element modeling of rock fracture behavior: fracture toughness and time-dependent fracture growth.Thesis, University of Texas, Austin, Pages 292.

PRICE, A. M. (1979). The effect of confining pressure on the post-yield deformation characteristics of rocks.Thesis, University Of Newcastle-Upon-Tyne, Pages 285.

RIBACCHI, R. (2000). Mechanical Tests on Pervasively Jointed Rock Material:Insight into Rock Mass Behaviour. Rock Mech. Rock Engng., 33 (4), 24.

SAINSBURY, B., PIERCE, M., and IVARS, D. M. (2008). Simulation of rock mass strength anisotropy and scale effects using a Ubiquitous Joint Rock Mass (UJRM) model. in Proceedings of the 1st international FLAC/DEM symposium on numerical modelling, C. D. a. P. Cundall, Ed. Minneapolis Itasca Consulting Group, pp. 10.

STEFANIZZI, S., BARLA, G., KAISER, P. K., and GRASSELLI, G. (2008). Numerical modeling of rock mechanics tests in layered media using a finite / discrete element approach. in The 12th International Conference of nternational Association for Computer Methods and Advances in Geomechanics (IACMAG). Goa, India: I, pp. 6.

VALLEY, B., SUORINENI, F. T., and KAISER, P. K. (2010). Numerical analyses of the effect of heterogeneities on rock failure process. in 44th US Rock Mechanics Symposium and 5th U.S.-Canada Rock Mechanics Symposium. Salt Lake City: American Rock Mechanics Association, ARMA, pp. 10.

VILLENEUVE, M. C., DIEDERICHS, M. S., KAISER, P. K., and FRENZEL, C. (2009). Constitutive model for numerical modelling of highly stressed heterogeneous massive rocks at excavation boundaries. in Proceedings of the 3rd CANUS Rock Mechanics Symposium. Toronto, Canada, pp. 14.

Simulation of Brazilian Test Using PFC2D Grain-Based Model

Navid Bahrani
Geomechanics Research Centre, MIRARCO – Mining Innovation
Bharti School of Engineering, Laurentian University
David Potyondy
Itasca Consulting Group
Matthew Pierce
Itasca Consulting Group

ABSTRACT: The grain-based model (GBM) has resolved the difficulty of matching both the direct-tension (σ_t) and unconfined-compressive (σ_c) strengths of typical brittle rock by providing a synthetic material that mimics deformable, breakable polygonal grains cemented along their adjoining sides with deformable, breakable interfaces modeled as smooth-joint contacts. In this paper, a GBM utilizing a parallel-bonded base material is calibrated to match both σ_t and σ_c of Lac du Bonnet granite and then used to simulate a Brazilian test. The Brazilian strength (σ_B) is slightly overestimated and the failure mode includes ductile post-peak response that is not representative of what occurs in laboratory Brazilian tests. By reducing the grain tensile strength, grain failure occurs during the Brazilian test and a more realistic failure mode that includes brittle post-peak response is obtained. However, the unconfined-compressive strength of the modified material is too low. Sensitivity analysis on the grain and grain-boundary strength properties demonstrates that the grain tensile strength controls the σ_B/σ_c ratio. Because the grain strength is controlled by the parallel-bond properties and the lowest achievable σ_t/σ_c ratio in a parallel-bonded material is ~0.25, it is concluded that σ_c, σ_t and σ_B for a typical brittle rock cannot be matched with a GBM that utilizes a parallel-bonded base material.

1. INTRODUCTION

Modeling the failure of hard brittle rock via the two-dimensional Particle Flow Code (PFC2D), (Itasca, 2008) has improved over the past ten years. The improvement has focused on reproducing a key characteristic of hard brittle rocks, namely, their low tensile to compressive strength ratio. The approach followed is to keep the bond model as simple as possible and to include geometry heterogeneity (e.g., grain shape and grain boundary orientation) and property heterogeneity (e.g., stiffness and strength contrasts between different grain types) in order to capture the true rock micro-structural characteristics influencing brittle rock failure. Several approaches have been proposed including the conventional bonded particle model (CBPM), the clustered particle model (ClsPM), the clumped particle model (ClmPM) and the grain-based model (GBM).

In the conventional bonded particle model, the circular particles, bonded together using contact or parallel bonds, can be assumed to be rock grains. Diederichs (2000) showed that the tensile strength of the CBPM is significantly overestimated when the model is calibrated to match the rock UCS. The confined strength is also underestimated (i.e., low friction angle) and the failure envelope is linear. By clustering groups of a given number of particles (i.e., attaching particles with finite or infinite bond strength to model breakable or unbreakable grains) to more closely match the irregular shapes of rock grains, Potyondy and Cundall (2004) showed that the friction angle can be increased and therefore the target confined strength can be matched in the ClsPM. The sensitivity analysis by Cho et al. (2007) revealed that the tensile to compressive strength ratio can be reduced from 0.25 in the CBPM to 0.12 in the ClsPM, but this ratio is still high compared with the measured strength ratio of less than 0.05 for Lac du Bonnet (LdB) granite. A closer strength ratio of 0.07 was achieved by gluing the particles into clumps in the ClmPM (Cho et al.,

2007). The limitation of this modeling approach is that the grains are assumed to be unbreakable which may not be realistic in a compression test (Mosher et al., 1975). The grain-based model (GBM) developed by Potyondy (2010) generates a synthetic material that mimics deformable, breakable polygonal grains cemented at their adjoining sides using the smooth joint contacts. The results of the calibration of the GBMs to laboratory test results of Äspö Diorite and Wombeyan marble by Potyondy (2010) and Bahrani et al. (2011), respectively, showed that the limitations of the approaches described above (i.e., CBPM, ClsPM and ClmPM) were resolved.

The Brazilian test is commonly used in the laboratory as an indirect method of determining the tensile strength of rocks. For brittle rocks, the tensile strength obtained from the direct tension test is about 80% of that obtained from the Brazilian test (Martin, 1993). This characteristic of brittle rocks has not been systematically investigated with PFC2D. Potyondy (2010) and Bahrani et al. (2011) simulated the direct-tension test to calibrate their GBMs to the tensile strengths of Äspö Diorite and Wombeyan marble. In the current study, the GBM is first calibrated to match the unconfined-compressive and direct-tension strengths as well as the elastic modulus of LdB granite. The Brazilian test is then simulated and its strength is compared with that of LdB granite. The calibrated model slightly overestimates the Brazilian strength, and the stress-strain curve exhibits ductile behavior.

2. PFC2D GRAIN-BASED MODEL

The grain-based model in PFC2D developed by Potyondy (2010) provides a synthetic material that mimics deformable, breakable polygonal grains cemented at their adjoining sides. Grains in this approach mimic a cemented granular material and the interface (grain boundaries) mimics a cemented joint. The GBM in PFC2D is generated by overlaying a polygonal grain structure on a conventional bonded particle model (called the base material) where the parallel bonds at the grain boundaries are replaced with the smooth joint contacts.

The grain structure generation procedure described by Potyondy (2010) is summarized as follows. The generation of the grain structure first requires a bonded particle model with no walls. The particles must have at least two contacts. Each contact joins two particles and all contacts existing in the PFC2D model are used (even virtual contacts that may exist between particles that are not yet overlapping). An example of PFC2D model is shown in Fig. 1a, where each contact is depicted as a line joining its two contacting particles. A void is defined as a closed chain of disks and contacts. Each contact is adjacent to two voids. There is one external void that encircles the entire system and many internal voids. The internal voids are shown in Fig. 1b. Each internal particle (defined as a particle that is not adjacent to the external void) corresponds with a grain whose edges join the internal-void centroids (Fig. 1c). Internal disks with less than three contacts are removed before generating the grains. The grain structure is a polygonal mesh that completely fills space (Fig. 1d).

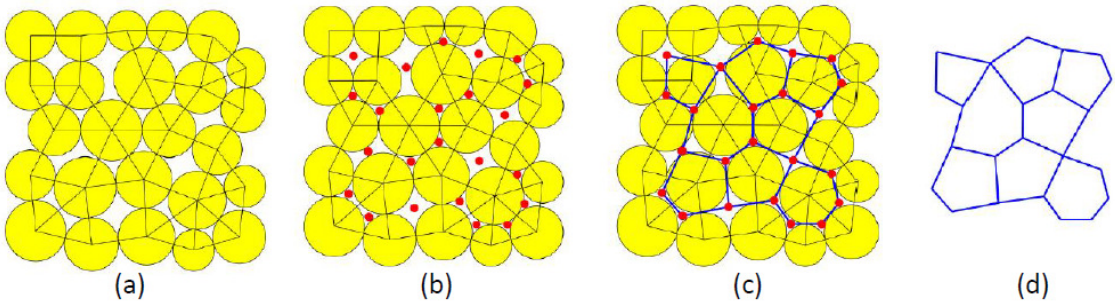

Figure 1 - a) Initial disk packing showing disks and contacts, b) filled circles at internal-void centroids, c) grain structure consisting of polygons, one for each internal disk, with nodes at internal-void centroids, and d) generated mesh (after Potyondy, 2010)

The GBM is then generated by overlaying the grain structure on a conventional bonded particle model (called the base material) with smaller particles to fill the grains. The particles in the base material are bonded using parallel bonds. The grain interface is then replaced with the smooth joint contacts. The smooth joint contact simulates the behavior of an interface regardless of the local particle contact orientation along the interface. Particles that fall along opposite sides of a smooth joint plane can overlap to insure particles sliding along the joint plane rather than forcing the particle to move around one another. Once the smooth joint is created, its stiffness properties are inherited[1] from the contact and the two contacting particles, according to the following equations:

$$\bar{k}_n = (k_n/A) + \bar{k}^n \quad (1)$$

$$\bar{k}_s = (k_s/A) + \bar{k}^s \quad (2)$$

$$A = 2\bar{R}t, \;\; t = 1.0 \quad (3)$$

$$\bar{R} = \bar{\lambda}\min(R^A, R^B) \quad (4)$$

where $\bar{k}_n$ and $\bar{k}_s$ are the smooth joint contact normal and shear stiffnesses, respectively, k_n and k_s are the contact normal and shear stiffnesses, respectively, and $\bar{k}^n$ and $\bar{k}^s$ are the parallel bond normal and shear stiffnesses, respectively. A is the cross sectional area of the smooth joint, t is the disk (particle) thickness, $\bar{R}$ is the smooth joint contact radius (i.e., half length of smooth joint contact) which is a multiple, $\bar{\lambda}$, of the two particle radii, R^A and R^B.

3. GRAIN-BASED MODEL OF LAC DU BONNET GRANITE

A 60 by 120 mm GBM with an average grain size of 4 mm was generated to match with the laboratory response of undamaged LdB granite. The adopted grain size is close to the average grain size of LdB granite, which insures that over 10 grains exist across the width of the model. In order to calibrate the model within a reasonable time frame only one-mineral realization, shown with red in Fig. 2a, was considered. The base material overlaid by the grain structure (Fig. 2b and c) was made up of 13244 particles. The GBM generation was completed by replacing the grain structure by smooth joint contacts (Fig. 2d).

The generated PFC2D GBM was then calibrated to match the unconfined-compressive and direct-tension strengths as well as the elastic modulus of LdB granite. A systematic calibration procedure undertaken for this purpose is described next.

For both smooth joint contacts and parallel bonds, zero friction angle and non-zero friction coefficient values were considered for model calibration. This means that at the grain scale, the transition to the residual strength is instantaneous and controlled by the smooth joint friction coefficient when the smooth joint breaks and by the particle geometry and the friction coefficient at particle-particle contacts when the parallel bond breaks. At the sample scale, however, with increasing damage (increasing number of broken bonds) the cohesional strength component is gradually lost and the frictional strength component gradually mobilizes. This explicitly captures a fundamental characteristic of brittle failing rocks known as strain-dependent cohesion weakening/frictional strengthening (Martin and Chandler, 1994).

[1] The smooth joint normal and shear stiffnesses are assigned as a factor of the stiffness inherited from the contact and the two contacting particles. This factor is called the stiffness factor in this paper.

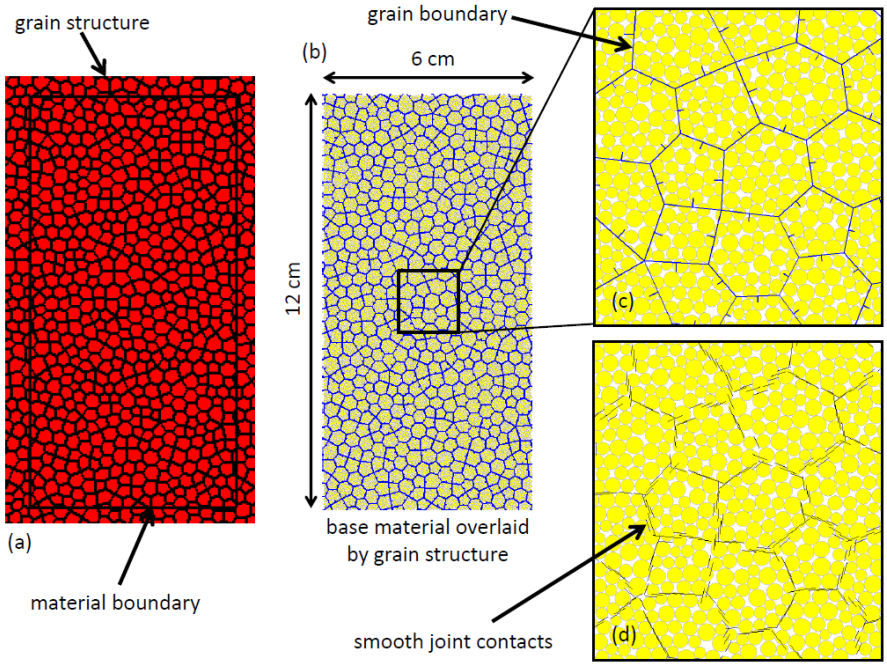

Figure 2 - a) One-mineral realization grain structure with average grain diameter of 4 mm, b) base material overlaid by the grain structure, c) close view of the base material showing the grain boundaries and d) grain structure replaced by the smooth joint contacts. The parallel bonds joining the particles are not shown in this figure

Direct-tension strength was calibrated first. The only parameter that controls the direct-tension strength is the smooth joint tensile strength. This is consistent with the observation in laboratory direct-tension tests where failure occurs along the grain boundaries (Mosher et al., 1975). Therefore, the smooth joint tensile strength was adjusted to capture this mode of failure in a direct-tension test. The compressive strength was calibrated next by adjusting three parameters: the smooth joint cohesion, the parallel bond tensile strength and the parallel bond cohesion. These parameters were initially assigned the same values and were increased from 35 MPa (which corresponds to the LdB granite equivalent Mohr-Coulomb cohesion) to 205 MPa (which corresponds to the UCS of LdB granite). The latter resulted in a UCS of 157 MPa in the GBM. The calibration on UCS was completed by further increasing the grain strength to a value of 305 MPa. In order to match the modulus, the particle contact and parallel bond moduli were set to 60 MPa and the smooth joint stiffness factor was set to 1.0 to produce a modulus of 67 GPa in the GBM. The target modulus of 60 GPa was achieved by reducing the smooth joint stiffness factor to 0.6. Table 1 summarizes the micro-properties of the GBM obtained through this calibration process.

Table 1 - Grain (parallel bond) and grain boundary (smooth joint) micro properties

Parallel bond micro-properties	Values	Smooth joint micro-properties	Values
R_{min}	0.3 mm	$\bar{k}_n$ and $\bar{k}_s$	0.6 × inherited
R_{max}/R_{min}	1.66	σ_b	10 MPa
k_n/k_s and $\bar{k}^n/\bar{k}^s$	2.5	C_b	205 MPa
E_c and $\bar{E}_c$	60 GPa	ϕ_b	0°
μ	0.1	μ_b	0.84
$\bar{\lambda}$	1		
$\bar{\sigma_c}$	305 MPa		
C	305 MPa		
$\bar{\phi}$	0°		

where R_{min} is the minimum particle radius and R_{max}/R_{min} is the ratio of maximum to minimum particles radii. E_c and $\bar{E}_c$ are the contact and parallel bond moduli, respectively. $\bar{\lambda}$ is the parallel bond radius multiplier. μ and μ_b are the particle and smooth joint friction coefficients, respectively. $\bar{\sigma}_c$, $\bar{C}$, and $\bar{\phi}$ are the parallel bond tensile strength, cohesion, and friction angle, respectively. σ_b, C_b and ϕ_b are the smooth joint tensile strength, cohesion and friction angle. The grain and grain boundary stiffness parameters were described in Section 3. Table 2 shows the excellent agreement between the LdB granite laboratory test results and the PFC2D GBM calibration results.

Table 2 - Comparison between laboratory test results and PFC2D-GBM simulation of LdB Granite

Parameters	UCS (MPa)	E (GPa)	Direct-tension test σ_t (MPa)
LdB granite	205	60	6.9
PFC2D GBM	202	60	6.9

4. BRAZILIAN TEST

According to Martin (1993), the mean Brazilian strength of LdB granite is 8.8 MPa, which is slightly greater than its direct-tension strength of 6.9 MPa. A Brazilian test was simulated using the properties of the calibrated model listed in Table 1 along with the same grain structure that is presented in Fig. 2 from which a Brazilian sample was carved. The stress-strain curve of the simulated test is shown in Fig. 3. The stresses during the Brazilian test were calculated from the force (F_B) acting on the platens, which was then converted to the stress using the standard Brazilian strength equation (i.e., $\sigma_B = F_B/\pi R_B t$, where t = 1 and R_B is the radius of the Brazilian sample). As can be seen, the stress-strain curve is linear up to the point (a) (i.e., first local peak). The strength of the GBM at this point (i.e., 7.5 MPa) is slightly greater than the GBM direct-tension strength (i.e., 6.9 MPa) and less than the LdB granite Brazilian strength (i.e., 8.8 MPa). Bond failure at this stage is limited to grain boundary (smooth joint) tensile cracks, which initiated in the centre of the sample. As the sample is further loaded, two more local peaks occur slightly after the first peak (point (b) and point (c) in Fig. 3). During this loading stage, additional grain boundary tensile cracks form and increase the width of the damage zone. Next, there is a sudden stress drop at point (d) during which most of the load-parallel grain boundaries across the sample between the two walls are broken. Then the stress builds up again inside the sample until it reaches the point (e), which is the measured Brazilian strength of the GBM (i.e., 12.2 MPa). From point (d) to point (e), only a few grain boundary cracks are generated. After this point, the parallel bonds within the grains fail in tension, and this grain failure produces a sudden stress drop from point (e) to point (f) that is associated with sample failure.

In a laboratory Brazilian test, it is known that the sample fails in a brittle manner with a sudden post-peak stress drop. Fig. 4a shows a typical stress-strain curve in a Brazilian test on Brisbane tuff (Erarslam and Williams, 2011). The macroscopic failure mode, as shown in Fig. 4b, is tensile splitting including a major load-parallel tensile fracture in the centre of the specimen as well as fracture branching from the diametral plane. Using a scanning electron microscope, Erarslan and Williams (2011) observed that almost all the grains along the failure surface of the specimens were highly cracked, the intra-grain cracking mechanism was brittle and micro-cracks were created in tension (pure opening mode).

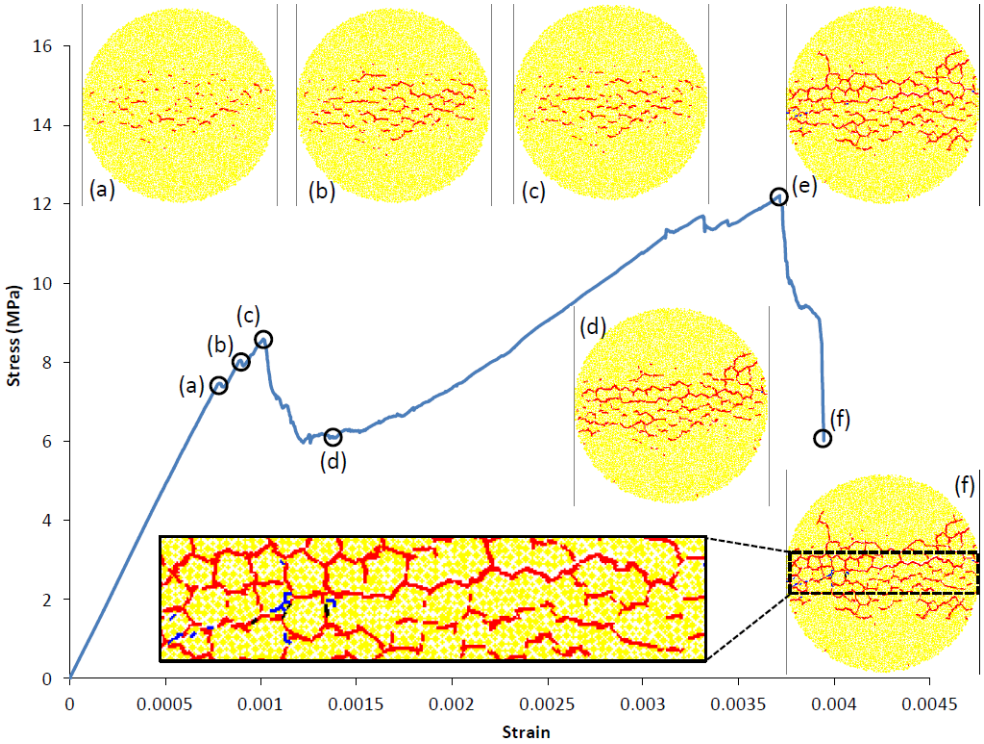

Figure 3 - Stress-strain curve, damage evolution and failure of the Brazilian sample simulated in the GBM with micro-properties calibrated to LdB direct-tension strength and UCS. Red and black are inter-grain tensile and shear cracks, respectively, and blue is intra-grain tensile cracks

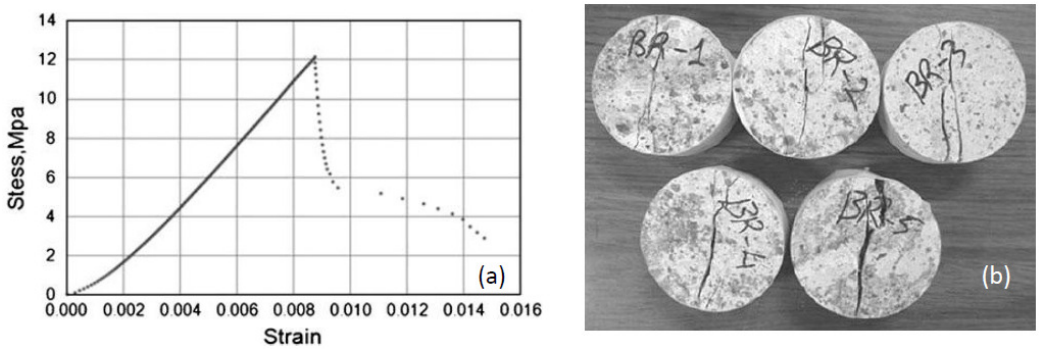

Figure 4 - a) Typical stress-strain curve and b) failure modes in the Brazilian test on Brisbane tuff (after Erarslan and Williams, 2011)

The failure characteristics in a Brazilian test observed in the laboratory by Erarslan and Williams (2011) (i.e., sudden stress drop after a single peak, major macroscopic tensile fracture and intra-grain tensile cracks along the fracture surface) are not captured by the GBM previously calibrated to match the LdB granite unconfined-compressive and direct-tension strengths. Since the GBM, in the Brazilian test, failed only after the parallel bond tensile cracks appeared (see failure mode at point (f) in Fig. 3), a sensitivity analysis was conducted to investigate the influence of parallel bond tensile strength (i.e., grain tensile strength) on the GBM's Brazilian strength. As shown in Fig. 5a, reduction of the parallel bond tensile strength from 305 MPa to 155 MPa, results in a disappearance of the peak strength represented by the point (e) in Fig. 3. The third peak (point (c) in Fig. 3), as well as the stress build-up observed after the point (d) disappear at a parallel bond tensile strength of 105 MPa. Only when the parallel bond tensile strength is reduced to 55 MPa is the stress-strain curve similar to that of Brisbane tuff shown in Fig. 4a:

linear stress-strain curve up to a single peak at 7.5 MPa followed by a sudden stress drop leading to failure of the GBM. Fig 5b shows that as the parallel bond tensile strength decreases, the unconfined-compressive strength of the GBM also decreases. The failure mode of the GBM in the UCS test changes from grain-boundary (smooth joint) dominated tensile cracks in the case of the model with the parallel bond tensile strength of 305 MPa to grain (parallel bond) dominated tensile cracks in the case of the model with the parallel bond tensile strength of 55 MPa. The reduction of the parallel bond tensile strength however, does not have any influence on the direct-tension strength of the GBM, because the failure occurs at the grain boundaries (at the smooth joint contacts).

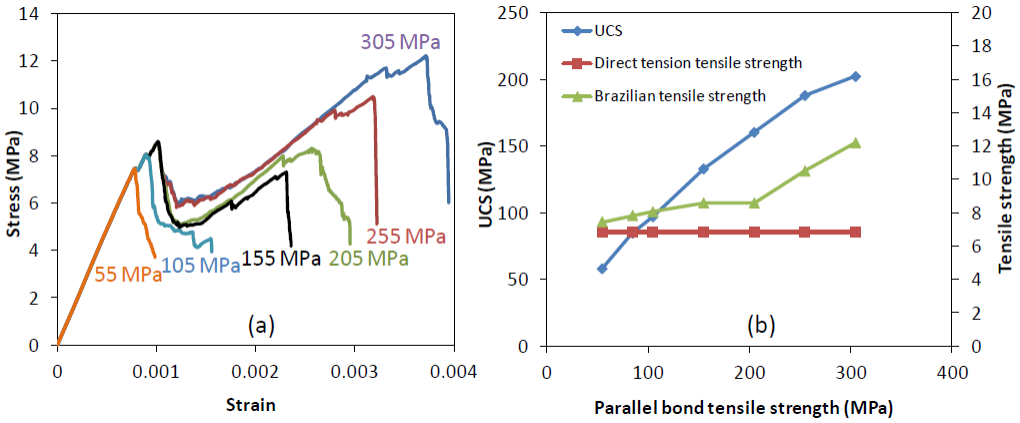

Figure 5 - Influence of parallel bond tensile strength on a) Brazilian test stress-strain curve, and b) direct tension, Brazilian and unconfined-compressive strengths

The stress-strain curve and micro-cracking at peak and post-peak states of the GBM with the parallel bond tensile strength of 55 MPa are shown in Fig. 6. Similar to the previous case, at the peak stress micro-cracks are grain boundary (smooth joint) tensile cracks that occur in the centre of the sample. In the post-peak, however, grain (parallel bond) tensile cracks drive the sample to failure by connecting the grain boundary tensile cracks. The macroscopic failure mode is axial splitting through a major tensile fracture in the centre of the GBM along with some fracture branching. This failure mode is similar to that of Brisbane tuff reported by Erarslan and Williams (2011).

The results shown in Fig. 5 and Fig. 6 suggest that when the tensile strength of the grains (parallel bond) are lowered such that the grains can fail in tension post peak in the Brazilian test, then the Brazilian strength, its stress-strain curve and the macroscopic and microscopic failure modes become comparable to those of laboratory Brazilian tests. Lowering the grain strength, however, results in a significant underestimation of the UCS. The following sensitivity analysis on different micro-properties was conducted to investigate if the UCS of the GBM having a parallel bond tensile strength of 55 MPa can be increased to that of LdB granite:

1. **Sensitivity of the parallel bond cohesion.** Parallel bond cohesion had no influence on the UCS. This is because the smooth joint and parallel bond tensile cracks drive the GBM to failure.
2. **Sensitivity of the smooth joint cohesion.** Smooth joint cohesion had no influence on the UCS. This is because smooth joint and parallel bond tensile cracks drive the GBM to failure.
3. **Sensitivity of the particle friction coefficient.** Increasing the particle friction coefficient only slightly increased the UCS (e.g., increasing the friction coefficient from 0.1 to 1.0 increased the UCS from ~57 MPa to ~64 MPa).
4. **Sensitivity of the smooth joint friction coefficient.** Smooth joint friction coefficient had no influence on the UCS of the GBM.

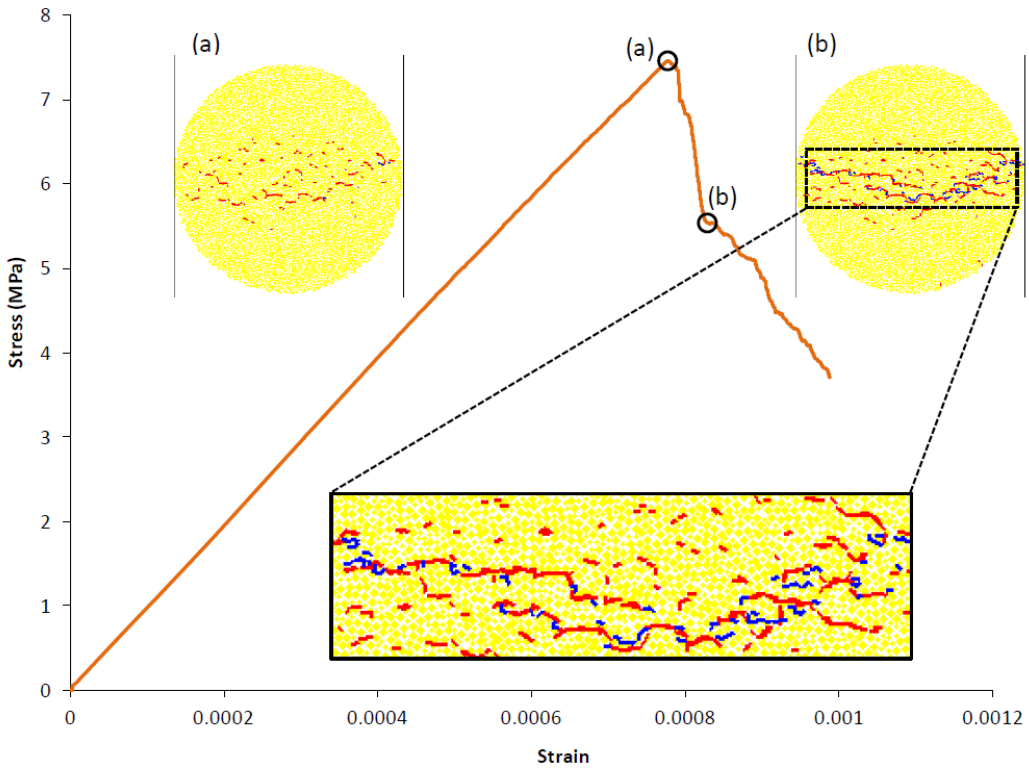

Figure 6 - Brazilian test stress-strain curve, damage evolution and failure mode in the GBM with the parallel bond tensile strength of 55 MPa. Red and blue are inter-grain tensile and intra-grain tensile cracks, respectively

The sensitivity analysis suggests that the parallel bond tensile strength is the only parameter that controls the Brazilian to UCS strength ratio. Achieving the laboratory observed strength ratio, requires a low tensile to compressive strength ratio in the grains (e.g., 0.05). However, the lowest achievable strength ratio in a parallel bonded material (i.e., CBPM) is 0.25 (Cho et al., 2007). A collaborative research between the Geomechanics Research Centre at MIRARCO and Itasca Consulting Group is ongoing to suggest a modeling approach that more realistically captures the failure characteristics of a Brazilian test as well as the Brazilian to UCS strength ratio. The use of a multi-mineral idealization in the GBM that allows for more realistic simulation of the true rock microstructure as well as the use of a bond model for the grains that allows for low tensile to compressive strength ratio (instead of parallel bonds in the current version of the GBM) will be the focus of future research. A promising bond model is the flat-joint contact model, which can match the direct-tension to UCS strength ratio (Potyondy, 2012).

5. CONCLUSION

The grain-based model generates a synthetic material that mimics deformable, breakable polygonal grains cemented at their adjoining sides using the smooth joint contacts. In this study, it was shown that when the GBM is calibrated to match the direct-tension and unconfined-compression strengths of LdB granite, the Brazilian strength is slightly overestimated, the failure mode is not representative of that in the laboratory tests and the post-peak response is ductile. It was found that by reducing the grain tensile strength (parallel bond tensile strength in the GBM) to allow for grain failure in the Brazilian test more realistic macroscopic and microscopic failure modes, stress-strain curve with brittle response as well as a closer match to the rock Brazilian strength are achieved. Reduction of parallel bond tensile strength, however, resulted in an underestimation of the UCS. Sensitivity analysis on grain and grain boundary strength properties showed that grain strength controls the Brazilian to unconfined-compressive strength

ratio. Since the grain strength is controlled by the parallel bond strength properties and the lowest achievable strength ratio in a parallel bonded material is 0.25, the laboratory observed Brazilian to unconfined-compressive strength ratio cannot be simulated in the GBM. Research is ongoing to suggest an approach in a bonded particle model that more realistically captures the failure characteristics in the Brazilian tests as well as the Brazilian to unconfined-compressive strength ratio.

6. REFERENCES

BAHRANI, N., VALLEY, B., KAISER P.K., & PIERCE, M. 2011. Evaluation of PFC2D-grain based model for simulation of confinement dependent rock strength degradation and failure processes. *Proc. 45th US Rock Mech. Symp.*, San Francisco, CA, USA, 10 p.

CHO, N., MARTIN, C.D., & SEGO, D.C. 2007. A clumped particle model for rock. *Int. J. Rock Mech. Min. Sci., 44*: 997-1007.c

DIEDERICHS, M. 2000. Instablity of hard rock masses; the role of tensile damage and relaxation, PhD thesis, University of Waterloo. 617 p.

ERARSLAN, N., & WILLIAMS, D.J. 2011. Investigating the effect of cyclic loading on indirect tensile strength of rocks. *Rock Mech. Rock Eng.*, DOI: 10.1007/s00603-011-0209-7.

ITASCA. 2008. PFC2D (Particle Flow Code in 2 Dimensions), Ver. 4.0. Minneapolis: ICG, 2008.

MARTIN, C.D. 1993. The strength of massive Lac du Bonnet granite around underground openings. PhD thesis, University of Manitoba, 278 p.

MARTIN, C.D., & CHANDLER, N.A. 1994. The progressive fracture of Lac du Bonnet granite. *Int. J. Rock Mech. Min. Sci. & Geomech. Abstr., 31*: 643-659.

MOSHER, S., BERGER, R.L., & ANDERSON, D.E. 1975. Fracture characteristics of two granites. *Rock Mech.*, *7*: 167-176.

POTYONDY, D.O. 2012. A flat-jointed bonded-particle material for hard rock. In preparation for 46th U.S. Rock Mechanics/Geomechanics Symposium (Chicago, USA, 24-27 June 2012).

POTYONDY, D.O. 2010. A grain-based model for rock: approaching the true microstructure. *Proc. Rock Mech. in the Nordic Countries*, 10p.

POTYONDY, D.O., & CUNDALL, P.A. 2004. A bonded particle model for rock. *Int. J. Rock Mech. Min. Sci., 41*: 1329-1364.

Comparison of Practical Modelling Methodologies for Considering Strain Weakening and Dilation as Part of Geomechanical Analysis

Gabriel G. Walton
Geological Sciences and Geological Engineering, Queen's University
Mark S. Diederichs
GeoEngineering Centre, Queen's-RMC

ABSTRACT: Conventional numerical modelling tools for analyses of underground excavations are well suited for modelling elastic behaviour and yield response of geomaterials with very simple constitutive behaviour. Non-dilatant elastic and perfectly plastic behaviour is most commonly used for preliminary analyses in the absence of the data required to consider more complex behaviours such as strain-weakening and dilation. For truly brittle models, this deficiency is more acute. Current state of practice allows only for reliable estimation of the volume of failure, but not for any prediction of displacement. In fact, there is no consensus in rock engineering regarding the most accurate approach or most suitable tool to model the magnitude of the plastic deformation that strain-weakening or brittle rocks experience at tunnel boundaries, particularly when support is incorporated into these models. This problem is largely a function of a poor understanding of how inelastic dilation occurs in different types of rockmasses, the rate controls on strength loss and volume change during yield, and the complexities of rock-support interaction in yielding conditions.

1. INTRODUCTION

The dilation of rocks, joints, and rockmasses has long been studied by rock mechanics researchers. The problem of dilation is an important one, because without a knowledge of how rocks dilate during and after yield, one cannot accurately constrain how plastic strains occur.

In classical plasticity theory, Drucker's postulate leads to the concept of normality, or an associated flow rule. In this case, the dilation of a material is directly related to its frictional strength component; in other words, materials with higher Mohr-Columb friction angles undergo greater amounts of volumetric strain during and after yield. In this case, a material's plastic potential is equal to its yield criterion (Lubliner, 1990).

Following the research of Vermeer and de Borst, most researchers have now accepted the necessity of a non-associated flow rule. This conclusion is supported by theoretical considerations – an associated flow rule requires that dilation occur without any energy dissipation. Although plastic potentials are often assumed to take the same form as a material's yield criterion, in the case of non-associated plasticity, the frictional strength term is replaced with a dilational term. The most common are the dilation angle, ψ, for a Mohr-Coulomb material, and the dilation parameter, m_d, for a Hoek-Brown material. One of the earliest assertions in the field of non-associated plasticity was that for most geomaterials, $\psi \leq \phi - 20^o$ (Vermeer and de Borst, 1984).

Vermeer and de Borst proposed a relationship relating the dilation angle to the rates of change of plastic volumetric strain and major principle plastic strain:

$$\sin(\psi) = \frac{\dot{\varepsilon}_v^p}{-2\dot{\varepsilon}_1^p + \dot{\varepsilon}_v^p} \quad (1)$$

Where

$$\dot{\varepsilon}_v^p = \dot{\varepsilon}_1^p + \dot{\varepsilon}_2^p + \dot{\varepsilon}_3^p \tag{2}$$

Another expression of equation (1) is

$$\frac{\varepsilon_v}{\varepsilon_1} = \frac{2\sin(\psi)}{1-\sin(\psi)} \tag{3}$$

(Vermeer and de Borst, 1984).

By monitoring oil displacements in triaxial cells during testing, accurate estimates of volumetric strain can be obtained over the course of sample testing; using such data and equation (3), several authors have interpreted and re-interpreted testing data for the purposes of observing the dilational behaviour of various rock types and characterising this behaviour using the dilation angle.

Based on these types of studies, further complexities of the dilation of rocks have become increasingly accepted in the scientific community. In particular, it is now clear that dilation angles for a given material are not constant, but rather vary as a function of both confining stress and plastic shear strain incurred (Alejano and Alonso, 2005).

Typical differential stress – maximum principle strain and volumetric strain – maximum principle strain curves obtained from a triaxial test of an intact rock sample are shown in Figure 1. Here, the plastic shear strain dependency of dilation is illustrated by the non-linearity of the volumetric strain curve after yield (point F). Figure 1 shows curves for a constant confining stress. The effect of increasing confining stress on dilation is to delay the onset of crack damage and greatly decrease the slope of the post-yield portion of the volumetric strain curve (Zhao and Cai, 2010a).

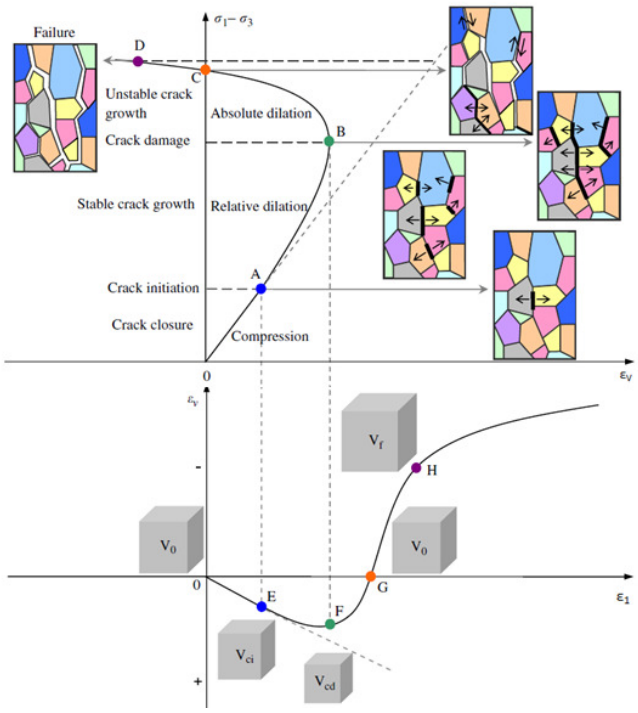

Figure 1 - Typical shapes of stress-volumetric strain and volumetric strain-major principle strain curves associated with the dilation of an intact rock sample (from Zhao and Cai, 2010a)

Figure 1 also illustrates the mechanisms controlling sample behaviour: elastic volume loss occurs until A/E; between A/E and B/F, stable crack growth begins to counteract elastic volume loss; from B/F to C/G, accelerating crack generation leads to an acceleration in the rate of dilation; as the sample approaches failure (D/H), a maximum rate of dilation is attained; following failure, the dilation rate decays to zero (following pervasive fracture development, there is no mechanism to indefinitely continue the process of rock dilation (Zhao and Cai, 2010a).

2. EXISTING DILATION MODELS

There have been many attempts to devise a method to account for dilation in numerical simulations that is both reliable and can be implemented practically. One such method is to apply a constant dilation angle to a rockmass based on whether it qualifies as "very good quality", "average quality", or "very poor quality"; the dilation angles assigned in these cases are equal to $\phi/4$, $\phi/8$, and 0^o, respectively (Hoek and Brown, 1997). Although this method, based on expert judgement, does not fully describe the dilational behaviour of rockmasses, it is a practically efficient method which provides more reliable results than the arbitrary selection of an associated flow rule or a non-associated flow rule with $\psi = 0^o$.

Another option in the modelling of excavations involves running a model with zero dilation and applying an empirical correction to the result to obtain an estimate of the inelastic radial displacement expected (Carter, Diederichs, and Carvalho, 2007).

More recently, efforts have been made to incorporate confining stress and plastic shear strain dependent dilation angles into numerical models. These recently developed models of dilation angle are based directly on analyses of data which capture many of the mechanisms responsible for the phenomenon of dilation. As such, they are a step towards a more widely applicable and complete treatment of dilation in modern rock mechanics analysis.

Detournay was the first to propose a non-constant model for the dilation angle. He suggested that the peak dilation angle should decay from its maximum value as plastic strain is incurred; the appeal of this model is that by setting the peak dilation angle to the friction angle, the only new parameter required is one to characterize the speed of the decay (Detournay, 1986). Alejano and Alonso took this model and extended it by suggesting that peak dilation angle should be decreased from the value of the friction angle depending on confining stress. They then re-interpreted a few sets of published data to determine the appropriate decay parameter for a few rock types. This model assumes a perfectly linear-elastic rock response prior to yield (Alejano and Alonso, 2005). A comparison between the expected volumetric strain behaviour of a rock sample and the result corresponding to Alejano and Alonso's model is shown in Figure 2.

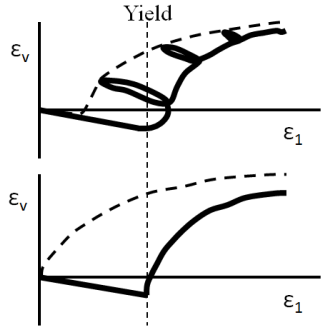

Figure 2 - Comparison of actual (top) and model (bottom) volumetric strain-major principle strain curves for a model with a decaying dilation angle; note that the key area of deviation between the two occurs near yield (after Alejano and Alonso, 2005)

Recently, Zhao and Cai have developed their own model for dilation which more closely matches the behaviour observed in triaxial cell tests. Unlike the model of Alejano & Alonso, which assumes that dilation drops from a peak value as plastic shear strain is incurred, the model developed by Zhao & Cai accounts for the brief acceleration of dilation that immediately follows the onset of crack damage Zhao & Cai, 2010a).

In this model, the dilation angle is given as a function of plastic shear strain, γ^p, by

$$\psi = \frac{abe^{-b\gamma_p}e^{-c\gamma_p}}{c-b} \tag{4}$$

(Zhao and Cai, 2010a).

In equation (4), a, b, and c are fit coefficients determined for specific materials based on test data. The parameters a, b, and c are specific to a given level of confining pressure; each can be calculated for a confining pressure of interest using other empirically determined relationships, and its own set of sub-parameters (a_1, a_2, a_3, b_1, b_2, b_3, c_1, c_2, c_3) (Zhao and Cai, 2010a). This model produces a peak dilation angle roughly equal to the peak friction angle for zero confining stress, which is consistent with observations made by Alejano and Alonso (Zhao and Cai, 2010b).

It should be noted that this model has been developed for intact rock. At this point, to apply this dilation angle model to a rockmasses requires the assumption that the dilational behaviour of rockmasses is similar to that of intact rock (Zhao and Cai, 2010b).

Since the development of this model, it has been implemented in FLAC 2D with a cohesion weakening friction strengthing (CWFS) constitutive model to emulate the brittle failure observed at the mine-by test tunnel in the Lac du Bonnet Granite in Canada. Using this well documented case, it was shown that the dilation model of Zhao and Cai was capable of replicating not only the shape of the yield zone around the excavation, but also the displacement distribution near the excavation boundary (Zhao et al., 2010).

3. MODELLING OF DILATION

3.1 Phase^2

The goals of these simulated tests were to verify the volumetric strain response as predicted by Phase^2 for a variety of simple dilational cases and make preliminary attempts to incorporate non-constant dilation parameters into the model. The importance of using non-constant dilation angle models has been demonstrated, but not yet made widely accessible in implicit solution FEM codes. This study aims to the foundation for future work to develop a simplified method of incorporating non-constant dilation angles into Phase^2 for practical use.

The key parameters that were varied in this investigation are dilation angle, model geometry (axisymmetric versus biaxial), constitutive behaviour (perfectly plastic versus elastic-brittle-plastic), and confining stress.

Material properties similar to that of the Cobourg Limestone were used for all tests. The original parameters were for a Hoek-Brown (HB), strain-weakening model of the limestone. To allow the use of a simplified one parameter Mohr-Coulomb flow rule, the HB strength parameters were converted to equivalent MC parameters for the two confining stresses used based on the equations provided by Hoek et

al (2002). The material properties used in the models are given in Table 1. Note that for the perfectly plastic models, residual parameters were set equal to peak parameters.

Table 1 - Material properties used in simulated compression tests

	Strength Parameter	Peak Value	Residual Value
Hoek-Brown Parameters	m	4.914	2.710
	s	0.0622	0.0226
	a	0.501	0.501
Equivalent MC Parameters (0 MPa Confinement)	T (MPa)	1.01	0.67
	C (MPa)	3.02	1.89
	ϕ	56.22	54.9
Equivalent MC Parameters (10 MPa Confinement)	T (MPa)	1.01	0.67
	C (MPa)	12.72	10.19
	ϕ	36.82	32.01
Elastic Parameters	Density (MN/m^3)	0.027	-
	E (MPa)	22700	-
	v	0.17	-

The standard model consisted of a cylindrical core 54 mm in diameter and 135 mm in height. This model was generated using a rectangle 27 mm wide and 135 mm high with an axisymmetric boundary condition (zero horizontal displacement) along the plane of symmetry. A fine, six noded triangular mesh was used to discretize the model. The model was staged with an increasing displacement boundary condition used to simulate a strain-controlled test.

3.1.1 Verification & Preliminary Investigation

Most of the models used in this study used an axisymmetric solution method. Biaxial models, were also run, however, for the purpose of comparison. These models provided insight into a few key differences between biaxial and axisymmetric models:

- For low dilation angles, strain localization occurs at large strains in all models except those using biaxial strain conditions and a perfectly plastic constitutive model
- For high dilation angles, the volumetric strain – axial strain relationship was more ideally linear in most biaxial models

The non-ideal response of the axisymmetric models may be related to kinematic issues associated with the model geometry. Figure 3 shows the strain localization geometries present in the axisymmetric and biaxial models. The inability of the axisymmetric geometry to produce through-going shear surfaces may prevent the model from producing the perfectly linear volumetric strain response that is expected.

The overall volumetric strain trends produced by Phase^2 did match the theoretical response, however: a linear elastic contraction characterized by slope

$$\frac{\varepsilon_v}{\varepsilon_1} = 1 - 2\nu \tag{5}$$

and a linear plastic expansion characterized by equation (3).

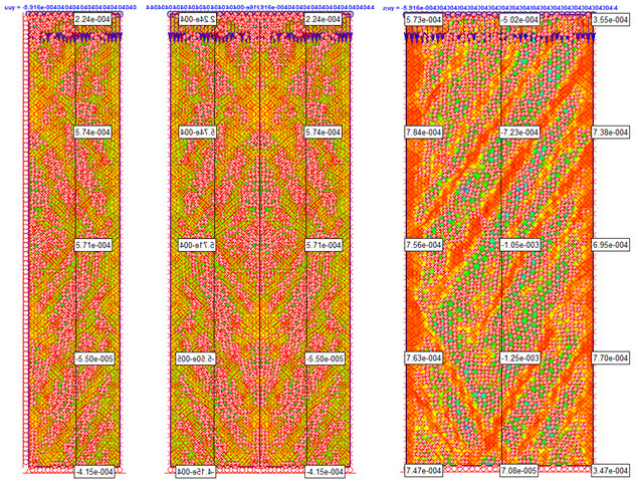

Figure 3 - Strain localization bands in an axisymmetric model (left), an axisymmetric model with its reflection (middle), and a biaxial model (right). Note that the biaxial model shows through-going bands, whereas the axisymmetric model shows conical strain concentrations

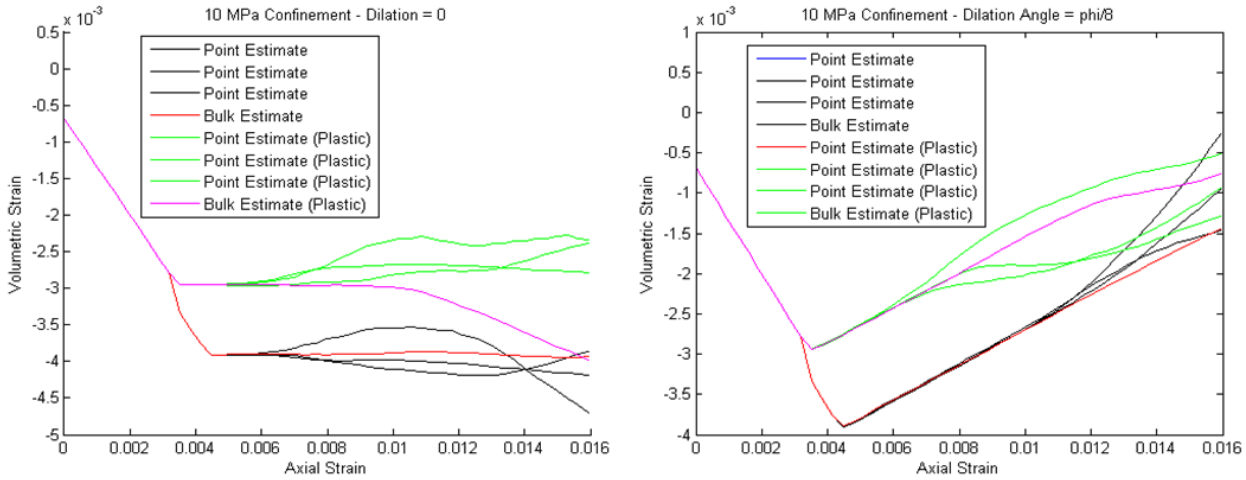

Figure 4 - Volumetric strain response of samples under 10 MPa confinement for two dilation angles ($\psi = 0^o$ and $\psi = \phi/8$). Elastic-brittle-plastic and perfectly plastic results are shown. "Point Estimate" refers to the volumetric strain queried from a single element. "Bulk Estimate" refers to the volumetric strain of the entire sample

One interesting deviation from the expected response was noted in the 10 MPa confinement triaxial test results. Although the perfectly plastic samples immediately transitioned to plastic expansion following yield, the elastic-brittle-plastic samples continued to contract for a small interval of plastic axial strain before reaching a roughly constant volumetric strain. This behaviour can be seen in Figure 4. Figure 4 also shows some interesting trends which hold true for a wider range of dilation angles: strain localization is independent of the constitutive model used (in axisymmetric tests) and is delayed to increasingly large strains as dilation angle increases.

It is suspected that the deviation from the theoretical response for the elastic-brittle-plastic samples is a function of the method which Phase^2 uses to address the large strain increment associated with the sharp drop in strength at yield.

This issue is discussed further below when the Phase^2 axisymmetric models are compared to FLAC3D models.

Confining stress is arguably the most important parameter in determining the dilational response of geomaterials. Figure 5 shows the influence of confinement when considering an associated flow rule or a confinement and plastic strain dependant dilation angle. For any constant dilation angle, such as an associated flow rule, an increased confinement stress means both a delay in yield (and thus expansion) and a slightly decreased expansion rate after yield (due to a lower equivalent friction angle for a given set of Hoek-Brown strength parameters). When considering the model of Alejano and Alonso (2005), however, the effect of confinement is much more significant. Figure 5 shows that the 10 MPa confinement reduces the effective dilation angle of the sample to near zero, and eclipses the effect of any dilation decay as a function of plastic shear strain. The effect is large even relative to the decay effect for the UCS sample. Even for much smaller confining stresses, the effect of confining stress on dilation can be quite large, and is often more significant than that of plastic shear strain.

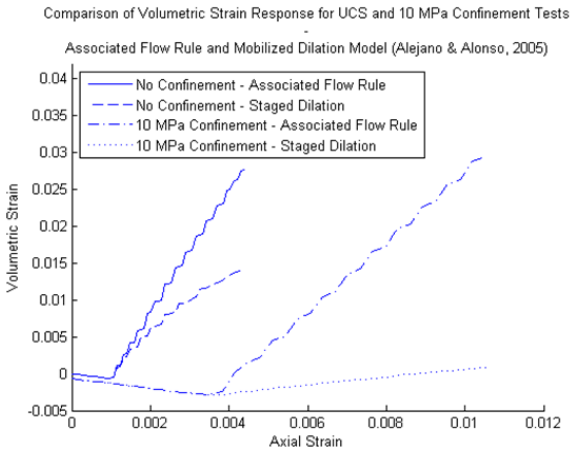

Figure 5 - Volumetric strain response of perfectly plastic limestone at 0 MPa and 10 MPa confinement – associated flow rule and staged dilation based on the model of Alejano and Alonso (2005)

In some programs, it is possible to account for the dependency of dilation on confining stress using a given decay model. In a program such as Phase^2 where no such built in feature exists, it may be possible to approximate the effect of this dependency by using radially zoned material properties with decreasing dilation angles away from the excavation.

3.1.2 Staged Dilation

Unlike some other modelling tools, Phase^2 does not record the history of each node during solution of a model. As a result, it cannot iteratively redefine the dilational properties of an element as a function of plastic strain previously incurred during the solution process. As a relatively simple alternative to simulate the decay of dilation angle with increasing plastic shear strain, a staged dilation angle was used in the Phase^2 model.

The decay model proposed by Alejano and Alonso (2005) with a dilation parameter value for limestone ($\gamma^{p,*} = 0.0559$) was used to determine the scaling factor for the dilation angle of each stage, relative to the peak value; the key issue with this method is that for most cases, analytically predicting what plastic shear

strain will occur at what stage is not possible. Instead, dilation angle values were calculated based on the (incorrect) assumption that plastic axial strain equals plastic shear strain.

The result of this assumption is a different effective dilation parameter being represented by the model than the one selected. A calibration procedure can be used, however, to determine which dilation parameter is best represented by the model. Volumetric strain and plastic shear strain data from the model output can be used to produce a graph of instantaneous K_ψ versus γ^p; the decay term in the exponential best fit to this plot is indicative of the dilation parameter represented by the model. An example is shown in Figure 6, indicating that for the model run, the effective dilation parameter was $\gamma^{p,*} = 1/74$.

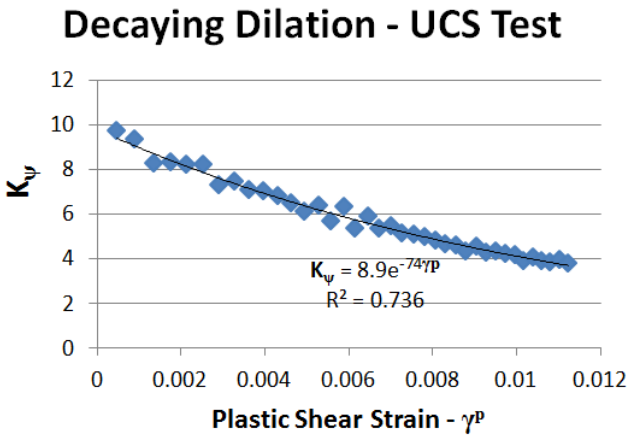

Figure 6 - Dilation calibration graph for a biaxial UCS test of limestone with elastic-brittle-plastic behaviour. The input $\gamma^{p,*}$ was 0.0559, and the effective $\gamma^{p,*}$ in the model was 1/74 (= 0.0135)

It is possible by this calibration procedure to iteratively change the input dilation parameter until the desired effective dilation parameter is achieved. This process, however, is time consuming and invalidates the purpose of this work – to develop a simplified, practically applicable mobilized dilation angle for use in FEM models. Instead, future work will be conducted to determine a relationship between the input and effective dilation parameters. This could then be used to develop an application to tunnel models, whereby dilation angles are made to decay as tunnel advance is simulated and plastic strains increase.

3.2 FLAC3D

The axisymmetric UCS and 10 MPa confinement triaxial tests were replicated in FLAC3D; these models allow comparison of dilational response in an explicit solution model with true 3D geometry to that of an implicit solution model with axisymmetric geometry.

Unlike the Phase^2 models, which in some cases showed extra contraction following yield, many of the FLAC3D models showed a sharp volumetric increase immediately following yield before resuming behaviour similar to the theoretical response. Strain localization did occur in the FLAC models, and in many cases earlier than in the Phase^2 models; as in Phase^2, localization was supressed by both increasing dilation angle and confining stress. Example queries of volumetric strain from a FLAC3D model are shown in Figure 7. When strain localization did occur, its geometry was more representative of the expected behaviour than either of the Phase^2 model geometries – strain was concentrated in a few key shear bands, as shown in Figure 8.

It should be noted that these behaviours were consistent for different mesh geometries (hexahedral and split tetrahedral, coarse and fine), dilation angles, and confinement levels. Localization tends to be less severe in perfectly plastic models than elastic-brittle plastic models, but is still present.

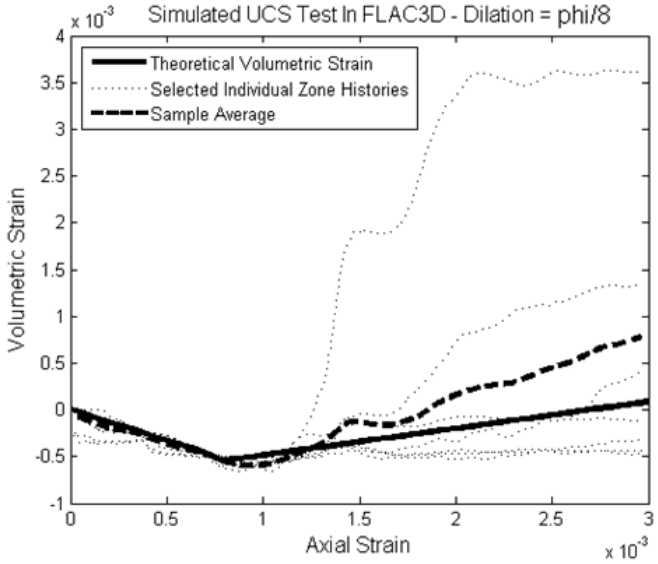

Figure 7 - A comparison of the theoretical volumetric strain of the test sample to the sample average and a selection of individual zones within the model. Note the onset of strain localization immediately following yield

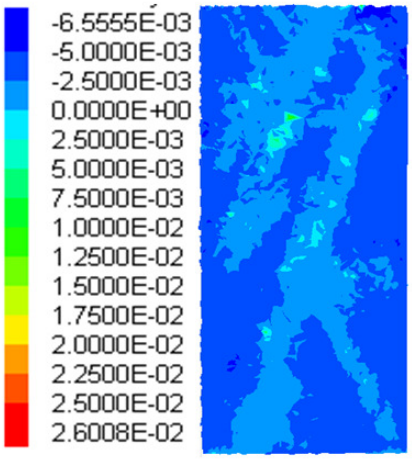

Figure 8 - Localization of volumetric strain within a FLAC3D model. The geometry of strain concentrations is more realistic than those shown in Figure 3

4. CONCLUSIONS

The developments in understanding the dilational behaviour of geomaterials have been quite significant since the conception of rock mechanics as a field of research. Alternatives to using zero dilation or an associated flow rule in numerical models have been developed, and are capable of producing results which replicate much of the behaviour of rocks in specific scenarios.

The problem remains, however, that no universally accurate or accepted model for dilation has yet been developed. From the practical engineer's perspective, there is no certain way to incorporate dilation into design. As we have shown here, the exact details of how dilation is implemented in numerical models can have implications in terms of the results obtained, and consequently the design choices made.

Several issues remain unaddressed with respect to rockmass dilation: scale dependencies, influences of anisotropy and heterogeneity, the practical implementation of complex dilation models for general use, the validity of the assumption that rockmasses dilate like intact rock, how dilation relates to different types of failure mechanisms, and how dilation influences rock-support interaction. These are future topics to be addressed by the authors.

5. REFERENCES

ALEJANO, L.R., and ALONSO, E., 2005. Considerations of the dilatancy angle in rocks and rockmasses. International Journal of Rock Mechanics and Mining Sciences, 42, p. 481-507.

BROWN, E.T., 2008. Estimating the Mechanical Properties of Rock Masses. 1st Southern Hemisphere International Rock Mechanics Symposium (SHIRMS), 16-19 September 2008, Perth, Western Australia.

CARTER, T.G., DIEDERICHS, M.S., and CARVALHO, J.L., 2008. Application of Modified Hoek-Brown Transition Relationships for Assessing Strength and Post-Yield Behaviour at Both Ends of the Rock Competence Scale. 6th International Symposium on Ground Support in Mining and Civil Engineering Construction, 30 March – 3 April 2008, Cape Town, South Africa.

CLAUSEN, J., and DAMKILDE, L., 2007. An exact implementation of the Hoek-Brown criterion for elasto-plastic finite element calculations. International Journal of Rock Mechanics and Mining Sciences, 45, p. 831-847.

DETOURNAY E., 1986. Elasto-plastic model of a deep tunnel for a rock with variable dilatancy. Rock Mech. and Rock Eng., 19, p. 99–108.

DIEDERICHS, M.S., KAISER, P.K., and EBERHARDT, E., 2004. Damage initiation and propagation in hard rock tunnelling and the influence of near-face stress rotation. International Journal of Rock Mechanics and Mining Sciences, 41, p. 785-812.

HOEK, E. and BROWN, E.T.,1997. Practical estimates of rock mass strength. International Journal of Rock Mechanics and Mining Sciences, 34, p. 1165–1186.

LUBLINER, J, 1990. Plasticity Theory. Macmillan Publishing Company; New York.

VERMEER, P.A. and DE BORST, R., 1984. Non associated plasticity for soils, concrete and rock. Heron, 29, p. 3–64.

YUAN, S., and HARRSION, J.P., 2004. An empirical dilatancy index for the dilatant deformation of rock. International Journal of Rock Mechanics and Mining Sciences, 41, p. 679-686

ZHAO, X.G., and CAI, M., 2010. A mobilized dilation angle model for rocks. International Journal of Rock Mechanics and Mining Sciences, 47, p. 368-384.

ZHAO, X.G., and CAI, M., 2010. Influence of plastic shear strain and confinement-dependent rock dilation on rock failure and displacement near an excavation boundary. Int. Jour. of Rock Mech. and Min. Sci. 47, p. 723-738.

ZHAO, X., CAI, M., and CAI, M., 2010. Considerations of rock dilation on modeling failure and deformation of hard rocks – a case study of the mine-by test tunnel in Canada. Journal of Rock Mechanics and Geotechnical Engineering, 2, p. 338-349.

Anisotropy Measurements in a Core Sample by Using Pulse Transmission Method

Jaime Meléndez Martínez
Institute for Geophysical Research, University of Alberta
Douglas R. Schmitt
Institute for Geophysical Research, University of Alberta
Randolph Kofman
Institute for Geophysical Research, University of Alberta

ABSTRACT: Recent interest in unconventional reservoirs motivates our work in laboratory measurements of seismic anisotropy. Seismic anisotropy is the variation in speed of a wave as a function of its direction of propagation. Analyzing anisotropy in unconventional reservoirs is important since anisotropy leads, for example, to differential stresses upon loading and could affect hydraulic stimulation (Reinicke et al., 2010, Zimmermann and Reinicke, 2009); in this sense, laboratory measurements are an important tool to study seismic anisotropy at small scales which can aid in the characterization of larger formations. The purpose of this work is to describe the laboratory methodology used to simultaneously measure ultrasonic P and S-waves in three different directions from a single core sample. Elastic anisotropy of a Proterozoic sedimentary rock from south-west Alberta is investigated. In metamorphic rocks seismic anisotropy is caused by preferred mineralogical alignment or foliation. Assuming a transversally isotropic medium, arrays of compressional and shear piezoelectric ceramic transducers were mounted on a sample trimmed from a core to measure travel times of ultrasonic *P*-waves and *S*-waves as a function of confining pressure at directions perpendicular, parallel, and oblique to the plane of foliation (bedding). Results show strong anisotropy agreeing with the assumption of a transversely isotropic medium. Dependence of travel times and hysteresis effects can be observed when pressurizing and depressurizing.

1. INTRODUCTION

Strength in an anisotropic material varies with the angle between bedding plane and loading direction, i.e., the material is often stronger in the direction perpendicular to bedding than parallel to it. This has implications in several aspects of rock mechanics and rock engineering such as tunneling, slope stability and in many other geotechnical problems. In this sense, uniaxial compressive strength (UCS) anisotropy has been widely demonstrated in geological materials. A non-destructive alternative test to UCS is the implementation of the ultrasonic transmission method to measure velocities in different directions with respect to bedding as a means to estimate strength from ultrasonic waveforms velocity index.

In this work, seismic anisotropy and its dependence on confining pressure are studied ultrasonically by using the pulse transmission method. The pulse transmission method is the most common method of ultrasonic measurements used to estimate velocities in geologic materials (Vernik and Liu, 1997; Dey-Barsukov et al., 2000; Mah and Schmitt, 2001a, 2001b; Wang, 2002b; Meléndez and Schmitt, 2011). This method involves generating and recording P and S ultrasonic waves which travel through a sample. Piezoelectric ceramic transducers with properly aligned polarizations are placed on each side of the sample so one of them plays the role of transmitter and the other one is the receiver. A fast-rise voltage is applied to the transmitter that sends a broad-band pulse (usually centred near 1 MHz) that propagates through the sample. When this pulse arrives to the receiver, a voltage is generated as a response to the pulse. The transit time through a sample is then picked from the recorded waveform. Knowing the length of the sample, the velocity of the wave can be easily calculated.

A method to measure anisotropy in a core sample that involves the pulse transmission method is the multi-core method (Meléndez and Schmitt, 2011) in which three plugs are cut, assuming a transversally isotropic medium, at directions perpendicular, parallel, and oblique to bedding and the travel times of the waveforms are measured independently in each of those directions. However, this method has the drawback that there is a possibility that the coring samples dissimilar heterogeneities of the main material and leads to misleading results. To overcome this disadvantage a multi-faced cube method can be used, which has the advantage that possible heterogeneity problems are avoided since all of the waves propagate through the same sample. This method has been used by Kebaili and Schmitt (1997) and Mah and Schmitt (2001a, 2001b) to develop experimental methods to simulate walk-away vertical seismic profiling (VSP) from blocks of acrylic and phenolic. In this work we propose to use it to simultaneously measure P and S velocities along the horizontal (P_{90^o} and SH_{90^o}), vertical (P_{0^o} and S_{0^o}) and 60° (P_{60^o} and q-SH_{60^o}) directions with respect to the sample´s axis of symmetry. In order to recreate *in situ* pressure conditions similar to those in the Earth´s interior, the P-wave and the S-wave velocities are measured as a function of confining pressure by using a pressure vessel in two different cycles: compressing (Up Cycle) and decompressing (Down Cycle).

2. THEORETICAL BACKGROUND

Phase velocities in a medium with vertical transverse isotropic symmetry (VTI) are given by:

$$V_P(\theta) = \left\{\frac{C_{11}sin^2(\theta) + C_{33}cos^2(\theta) + C_{44} + \sqrt{M}}{2\rho}\right\}^{\frac{1}{2}} \quad (1)$$

$$V_{SV}(\theta) = \left\{\frac{C_{11}sin^2(\theta) + C_{33}cos^2(\theta) + C_{44} - \sqrt{M}}{2\rho}\right\}^{\frac{1}{2}} \quad (2)$$

$$V_{SH}(\theta) = \left\{\frac{C_{66}sin^2(\theta) + C_{44}cos^2(\theta)}{\rho}\right\}^{\frac{1}{2}} \quad (3)$$

where $M = \{(C_{11} - C_{44})sin^2(\theta) - (C_{33} - C_{44})cos^2(\theta)\}^2 + (C_{13} + C_{44})^2 sin^2(2\theta)$, θ is the angle between the direction of propagation and the axis of symmetry, ρ is the bulk density of the sample, P is a compresional wave, SV and SH are polarized shear waves. $C_{11}, C_{33}, C_{44}, C_{66}$, and C_{13} are the five elastic stiffnesses needed to describe a VTI medium.

Then from equations (1), (2) and (3) we have that:

$$C_{11} = \rho V^2_{P_{90^o}} \quad (4)$$

$$C_{33} = \rho V^2_{P_{0^o}} \quad (5)$$

$$C_{44} = \rho V^2_{S_{0^o}} \quad (6)$$

$$C_{66} = \rho V^2_{SH_{90^o}} \quad (7)$$

$$C_{13} = \left[\left\{\left(2\rho V_{P_{60^o}}^2 - \frac{3}{4}C_{11} - \frac{1}{4}C_{33} - C_{44}\right)^2 - \left(\frac{3}{4}C_{11} - \frac{1}{2}C_{44} - \frac{1}{4}C_{33}\right)^2\right\}\frac{4}{3}\right]^{\frac{1}{2}} - C_{44} \quad (8)$$

Equations (4) through (8) enable the estimation of elastic constants from recorded waveforms via the wave speeds so determined.

3. METHODOLOGY

A sample was trimmed from a main core by using a rotating saw to obtain the three different orientations. Flat surfaces are needed to mount the piezoelectric transducers. In order to improve coupling between transducers and the sample and reduce noise, the trimmed surfaces were smoothed with both a spinning polisher and a fine grain sand paper.

1 MHz primary mode resonance P-wave and S-wave piezoelectric ceramic transducers were mounted on the previously smoothed surfaces. Since the polarization of the S-wave transducers is controlled by their orientation, a horizontally polarized shear wave SH_{90^o} is obtained when the direction of particle motion is parallel to plane of foliation. A quasi horizontally polarized shear wave q-SH_{60^o} is obtained when the direction of particle motion is 60^o with respect to layering. Polarization in the vertical direction (S_{0^o}) is irrelevant as long as the material is truly transversely isotropic. In this step proper alignment between S-wave transmitter and receiver transducers must be done. Figure 1 portrays the geometry of the P-wave and S-wave transducers mounted on the sample.

A thin strip of copper acting as a ground (negative pole) is attached to the sample using quick-set epoxy. Once the epoxy is solidified the transducer is bonded to the strip copper with a layer of conductive silver epoxy and on top on the transducer another strip of copper (positive pole) is attached to the transducer with conductive silver epoxy. After conductive epoxy is solidified two wires are soldered on each piece of copper. Figure 2(a) shows a picture of the transducer´s set up. The sample is then sealed with urethane putty to avoid leakage of the confining pressure fluid into the sample as shown in Figure 2(b).

3.1 Experimental Setup

The experimental setup consists basically of a pulse generator/receiver system, a digital oscilloscope and a pressure vessel that can apply a confining pressure of up to 60 MPa (Figure 3). The transmitter is activated by applying a fast rising (5 ns) 200 V square wave to the piezoelectric ceramic which produces a mechanical disturbance. The generated elastic wave is then recorded by the digital oscilloscope after travelling through the sample. Pressure was increased from 0 to 50 MPa in the compressing cycle and from 50 to 0 MPa in the decompressing cycle. The waveforms were recorded at approximately 3 MPa increment.

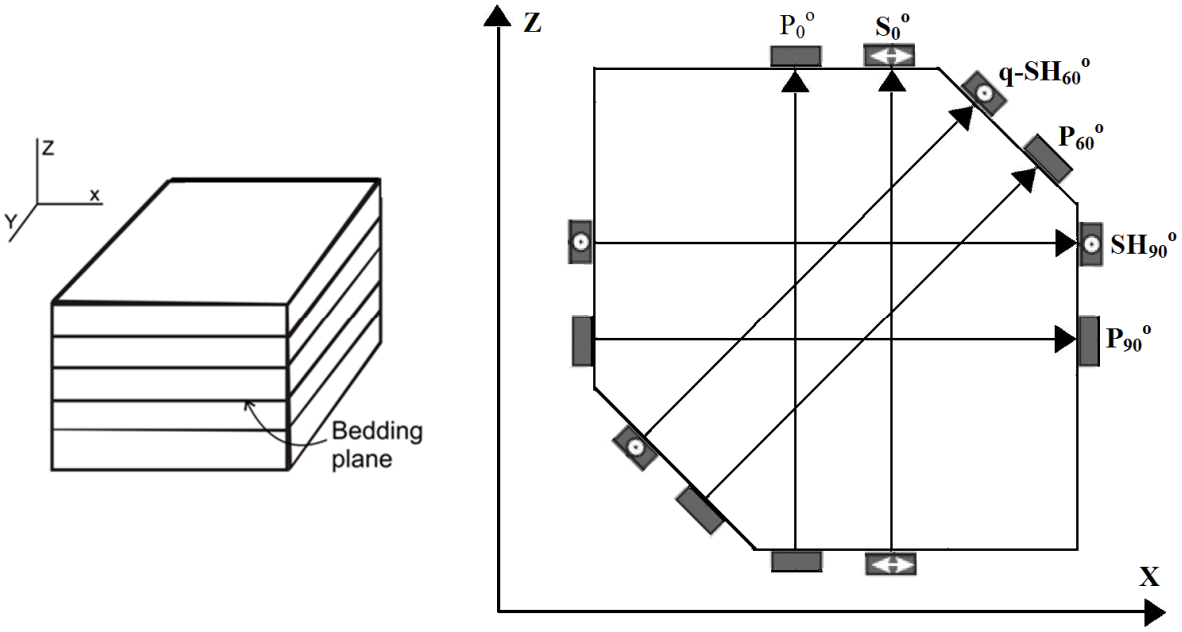

Figure 1 - Schematic of the distribution of the piezoelectric transducers in the multi-faced method assuming a transversely isotropic medium. A S-wave is obtained in the vertical direction (perpendicular to bedding, 0 degrees), SH wave is obtained in the horizontal direction (parallel to bedding, 90 degrees) and quasi SH wave is obtained at an angle of 60 degrees with respect to bedding. P waves are obtained in all directions

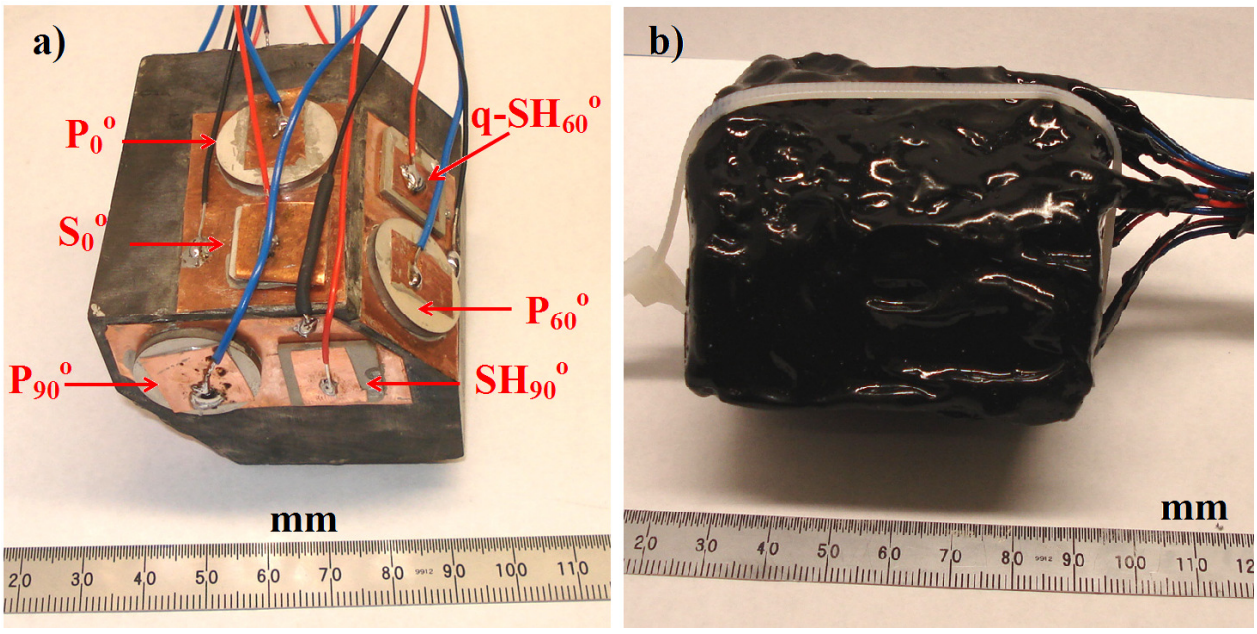

Figure 2 - Photographs showing the piezoelectric transducers mounted on the sample (a) and sample sealed with urethane putty

4. RESULTS

Ultrasonic measurements were carried out on a meta-sedimentary rock sample. Some example *P*- and *S*-waveforms obtained in the test are shown in figure 4. Velocities obtained from waveforms in the three different directions versus confining pressure show VTI anisotropy (Figure 5). Travel times were measured both during pressurization and depressurization. An incremental change in velocity can be observed as pressure increased because elastic properties vary as a function of confining pressure.

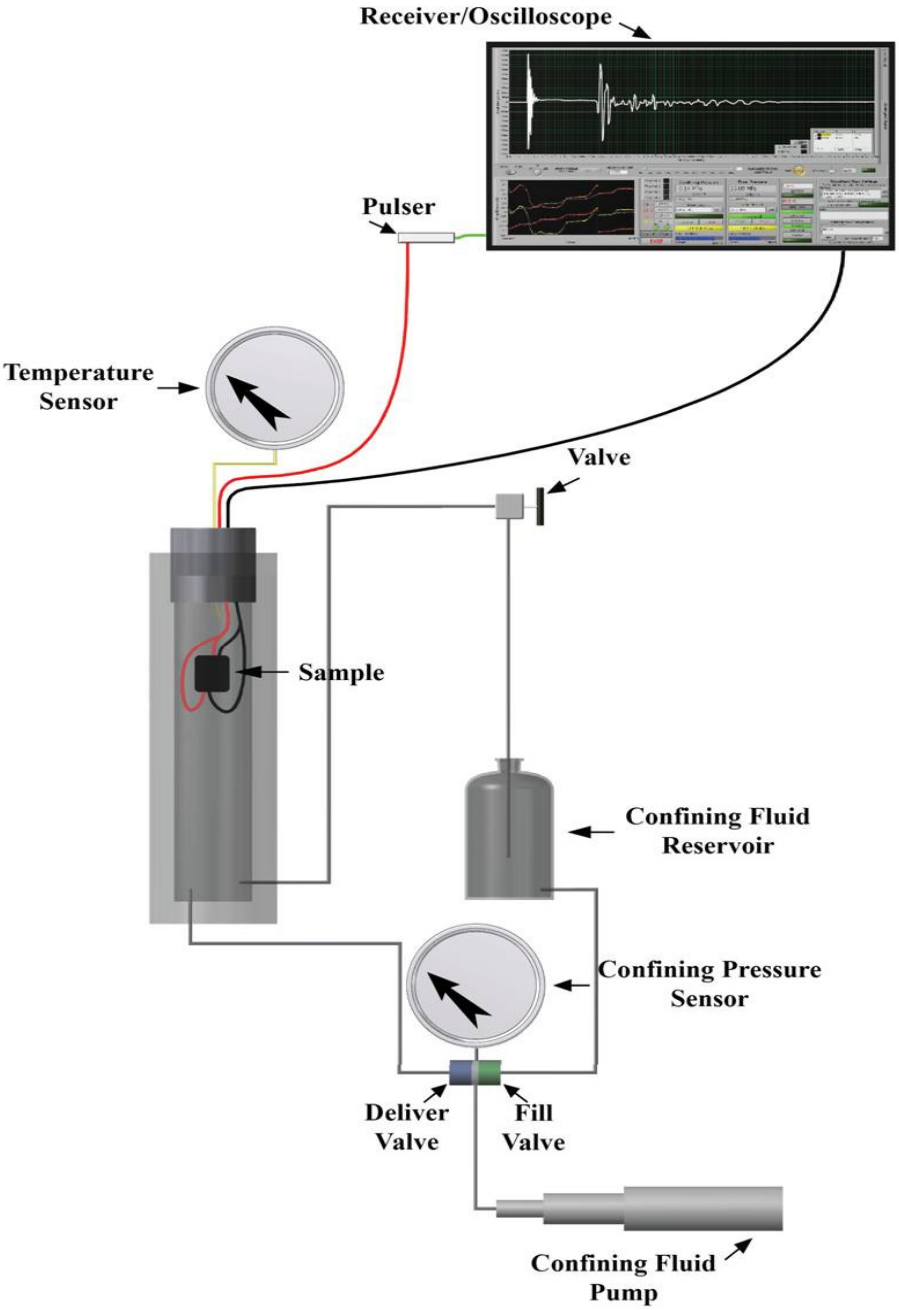

Figure 3 - Experimental setup

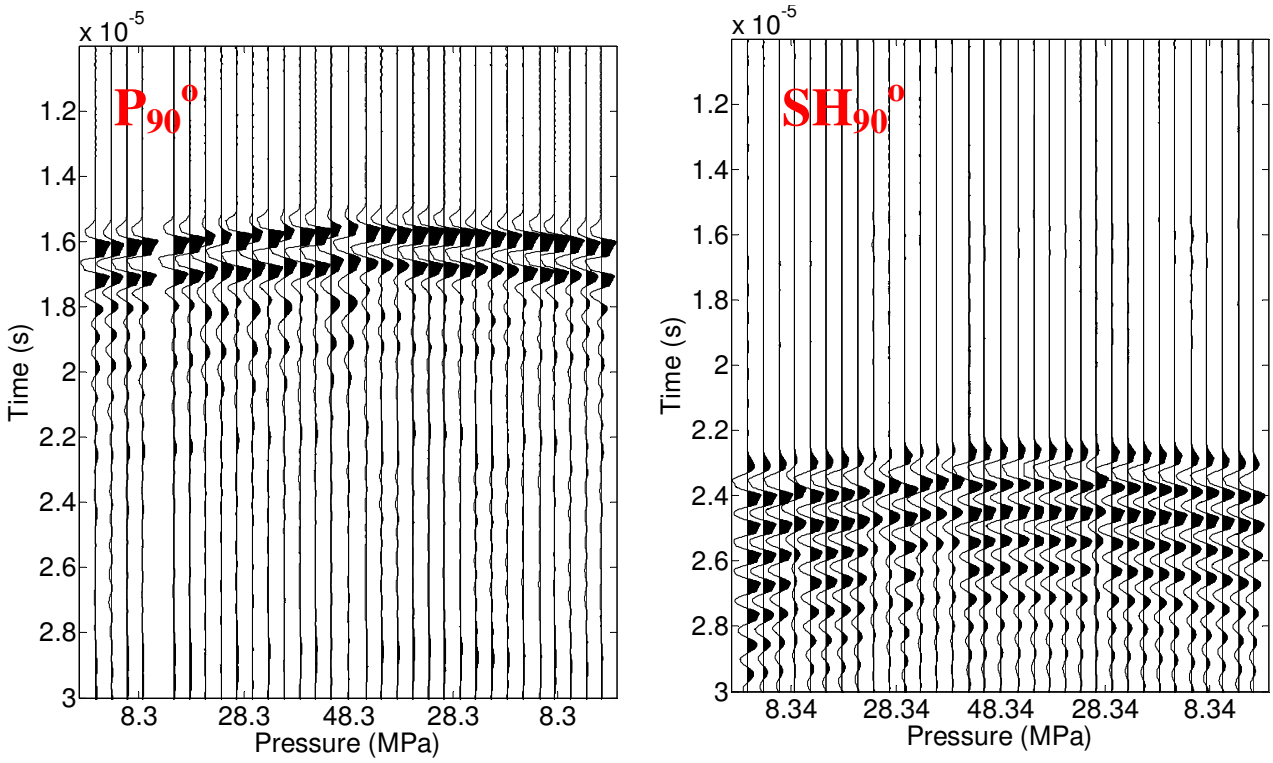

Figure 4 - Suite of P_{90}^{o} and SH_{90}^{o} waveforms versus confining pressure

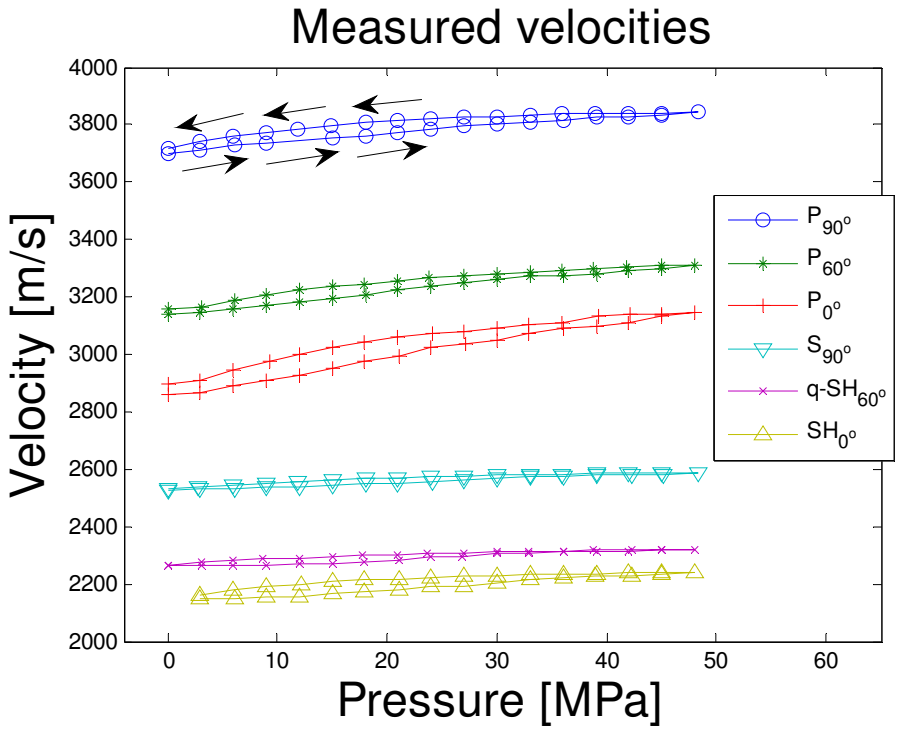

Figure 5 - P- and S-wave velocities show VTI anisotropy. Arrows represent the evolution of measurements. Effect of hysteresis can be observed in the pressurization (up) and depressurization (down) cycles. Velocities increase as pressure increases

Pressurization velocities are slower than depressurization velocities; this effect is called hysteresis (Gardner et al., 1965). When a sample is pressurized, microcracks and pores begin closing at a certain rate; however, when depressurizing, due to frictional forces, the opening rate of microcracks and pores is lower than the closing rate for a given pressure. Figure 6 shows the five elastic constants estimated by using the measured velocities. Hysteresis is observed in these too as a consequence of hysteresis in the velocities.

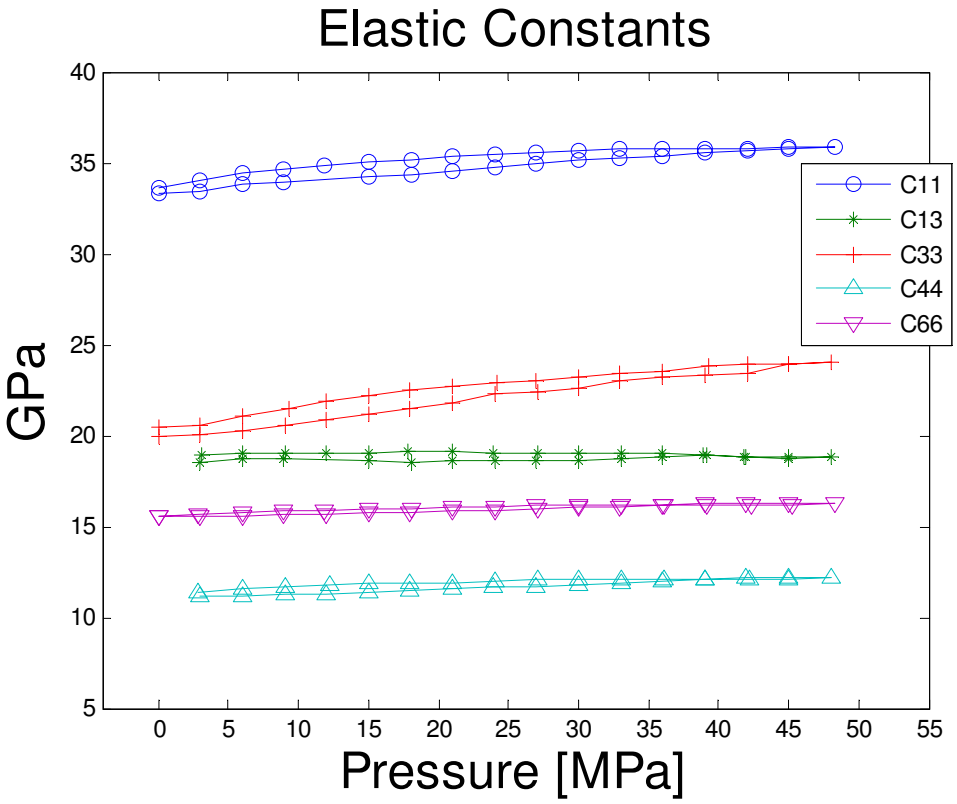

Figure 6 - Estimated elastic constants from measured velocities

5. CONCLUSIONS

Results show that the sample analyzed is anisotropic with a vertical axis of symmetry. Analysis of velocities shows a dependence of travel times with confining pressure for both P- and S-waves. Pressurization and depressurization of samples show that microcracks and pores open and close at different rates for the same pressure (hysteresis), which can also be observed in the estimated elastic constants. The ultrasonic pulse transmission method, along with the multi-faced cube method, is an elegant way to investigate elastic anisotropy in geological materials since it allows one to simultaneously measure P- and S-waveforms in different directions from a single sample; as such, it overcomes the heterogeneity-related issues that can be present when using the multi-core method. This method is a non-destructive alternative to UCS to estimate strength in anisotropic materials.

6. REFERENCES

DEY-BARSUKOV, S., DÜRRAST, H., RABBEL, W., SEIGESMUND, S., and WENDE, S., 2000. Aligned fractures in carbonate rocks: laboratory and in situ measurements of seismic anisotropy, International Journal of Earth Sciences, 88, p829-839.

GARDNER, G. H. F., WYLLIE, M. R. J., and DROSCHAK, D. M., 1965. Hysteresis in the velocity-pressure characteristics of rocks, Geophysics, 30, p111-116.

KEBAILI, A., and SCHMITT, D. R., 1997. Ultrasonic anisotropic phase velocity determination with the Radon transform, The Journal of the Acoustical Society of America, 101- 6, p3278–3286.

MAH, M., and SCHMITT, D. R., 2001a. Experimental determination of the elastic coefficients of an orthorhombic material, Geophysics, 66, p1217-1225.

MAH, M., and SCHMITT, D. R., 2001b. Near point-source longitudinal and transverse mode ultrasonic arrays for material characterization, IEEE Transactions on Ultrasonics, Ferroelectrics, and Frequency Control, 48, p691-698.

MELÉNDEZ, J. M., and SCHMITT, D. R., 2011. Investigating anisotropy in rocks by using pulse transmission method, CSEG Recorder, 36-7, p34-38.

REINICKE, A., ERIK RYBACKI, STANCHITS, S., HUENGES, E., and DRESEN, G., 2010. Hydraulic fracturing stimulation techniques and formation damage mechanisms—Implications from laboratory testing of tight sandstone–proppant systems, Chemie der Erde 70 S3, p107–117.

WANG, Z., 2002b. Seismic anisotropy in sedimentary rocks, part 2: Laboratory data. Geophysics, 67, p1423-1440

ZIMMERMANN, G., and REINICKE, A., 2010. Hydraulic stimulation of a deep sandstone reservoir to develop an enhanced geothermal system: laboratory and field experiments. Geothermics, 39, p70–77.

7. ACKNOWLEDGEMENTS

The author thanks IMP (Instituto Mexicano del Petróleo) and the University of Alberta for supporting this research and to NSERC and the Canada Research Chairs program for financial assistance. Also thanks to Lucas Duerksen for his help in the Rock Physics Laboratory of the Experimental Geophysics Group (EGG) at the University of Alberta.

CARBON DIOXIDE SEQUESTRATION

Geomechanical Response to CO_2 Injection for the Heartland Area Redwater Project (HARP), Alberta

Hamidreza Soltanzadeh
Alberta Innovates – Technology Futures (AITF)
Chris Hawkes
University of Saskatchewan, Department of Civil and Geological Engineering

ABSTRACT. The injection of CO_2 into a reservoir or aquifer can potentially result in deformation, induced fracturing and fault reactivation in the injection zone and/or the rocks that surround it. This paper reviews the data collection and geomechanical analyses performed to assess these potential hazards for the Heartland Area Redwater Project (HARP), in which CO_2 sequestration is being considered in a carbonate (Leduc Formation) reef. A three-dimensional mechanical earth model (3D MEM) was developed using available geophysical log data from several wells. The geomechanical response to CO_2 injection was studied using a finite element numerical model based on the 3D MEM and pore pressure distributions predicted using a reservoir simulator. The modeling results suggest that the potential for induced fracturing and fault reactivation is low and the maximum predicted ground surface heave is less than 2 cm. Sensitivity analyses conducted with a 2D geomechanical model that was extracted from the 3D model confirm that this conclusion holds true even when a reasonable measure of uncertainty in rock mechanical properties, ambient pore pressures and horizontal stress magnitudes is accounted for.

1. INTRODUCTION

The injection of CO_2 into a reservoir or aquifer results in pore pressure and temperature changes, both of which may induce deformations and stresses in the injection zone and the rocks that surround it. Geomechanical analysis is required to predict the effects of these induced deformations and stresses on the mechanical, hence hydraulic integrity of the injection zone's bounding seal. This paper presents a review of the data collection and geomechanical analyses conducted for the Heartland Area Redwater Project (HARP), a candidate site for commercial-scale CO_2 injection. This site is located northeast of Edmonton, Alberta and has been considered for injection of 110 megatonnes (MT) of CO_2 injection over a period of 50 years (Figure 1). The target zone is a carbonate (Leduc Formation) reef, covering a large area (~600 km^2) with thickness of up to 300 m, and depth of more than 1000m.

2. THREE-DIMENSIONAL MECHANICAL EARTH MODEL

The mechanical earth model developed for this project is based on the geological model developed in Petrel (Schlumberger, 2009) for the HARP project by personnel at Alberta Innovates - Technology Futures (AITF). The geographic limits of the project area are between townships 55 to 58 (inclusive) and range 20 to 24 (inclusive) west of the fourth meridian (Figue 1). The lithostratigraphic profile of the study area is shown in Figure 2. 49 horizons (surfaces) and 35 zones (stratigraphic units) exist in the geological model. In total, data from 95 vertical wells were used to build the 3D MEM for HARP.

2.1 Estimation of Geomechanical Properties

The compressional and shear wave interval transit times from dipole shear imager (DSI) logs were used to calculate dynamic values of Poisson's ratios (v_d) for each stratigraphic unit in the study area. Because DSI logs were not available for a number of the stratigraphic units in this area, DSI logs from other

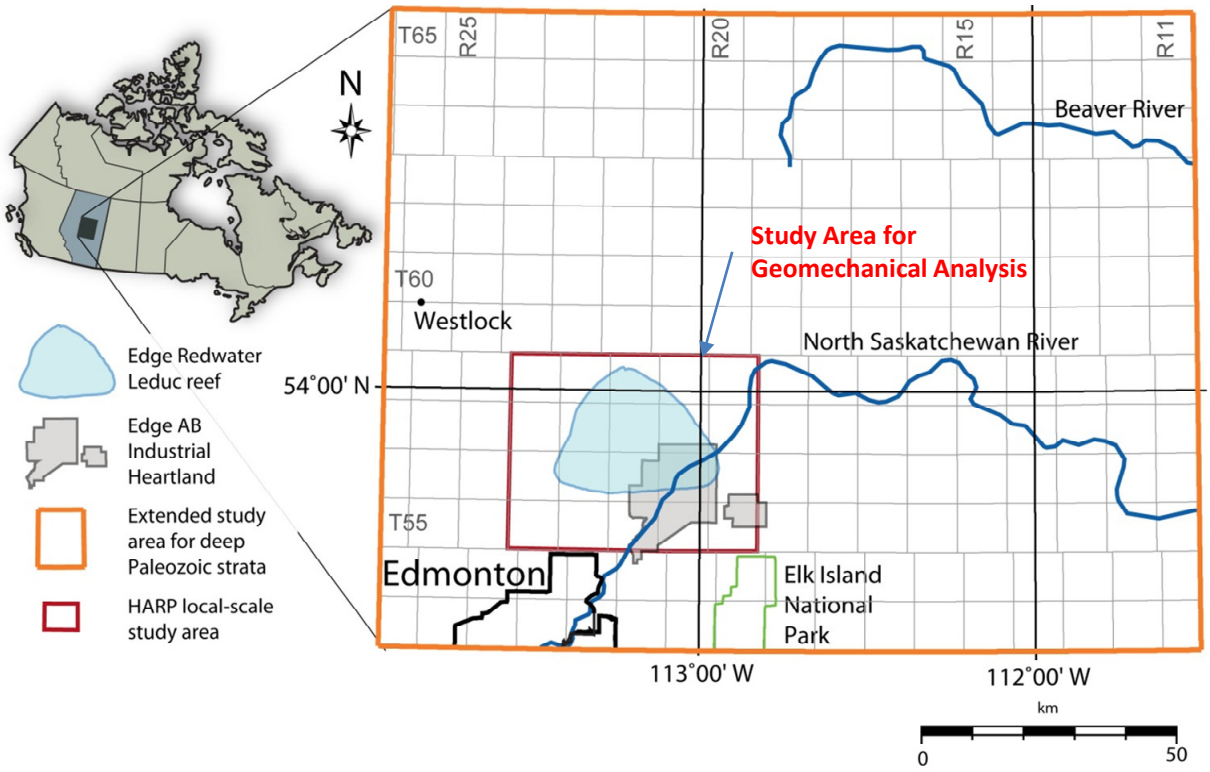

Figure 1 - Location of the Redwater Leduc reef and study area for geomechanical analysis (after Bachu, 2010)

Leduc Formation reefs were used to calculate Poisson's ratios for these units. Using average values of Poisson's ratios calculated for each stratigraphic unit from the few DSI logs that were available, depth profiles of dynamic Young's modulus (E_d) were calculated for each well in the 3D MEM using data from bulk density and conventional sonic logs. Values of static Young's modulus (E_s) were calculated using a linear conversion factor interpreted from a literature survey (i.e., $E_s = 0.75 \cdot E_d$) and static values for Poisson's ratio (v_s) were assumed equal to the log-derived dynamic values. Biot's coefficient was assumed to be one for all mechanical stratigraphic units. Rock strength parameters (cohesion and friction angle) values were estimated using a number of empirical correlations based on compressional wave velocity and porosity. The correlations used were given in a compilation published by Chang et al. (2006), which includes multiple correlations for sandstones, shales and carbonates.

The ambient pore pressures (P_0) for the stratigraphic units was provided by AITF. Vertical in-situ stress (S_V) at any given point was simply assumed to result from the weight of all overlying strata, hence S_V was calculated by integration of bulk density log data. Estimates of minimum and maximum horizontal stress magnitudes (S_{Hmin} and S_{Hmax}) were calculated using the poroelastic theory presented by Warpinksi (1989), with an estimated tectonic strain (ε_{Hmax}) of $2.4 \cdot 10^{-4}$, which was back-analyzed from horizontal stress magnitudes interpreted for various acid gas injection sites in the Alberta Basin by Bachu et al. (2008). The following filtering criteria were applied to the results obtained from these estimations in order to prevent the use of unrealistic stress magnitudes in the 3D MEM: (i) Minimum horizontal stress magnitudes falling on a gradient less than 16 kPa/m were assigned a value of 16 kPa/m times depth; (ii) an upper limit on S_{Hmax}/S_{Hmin} of 1.3 was imposed; and (iii) the in-situ stresses were verified to ensure that they do not exceed the Coulomb failure criteria for fault reactivation (using an assumed fault friction angle of 30°).

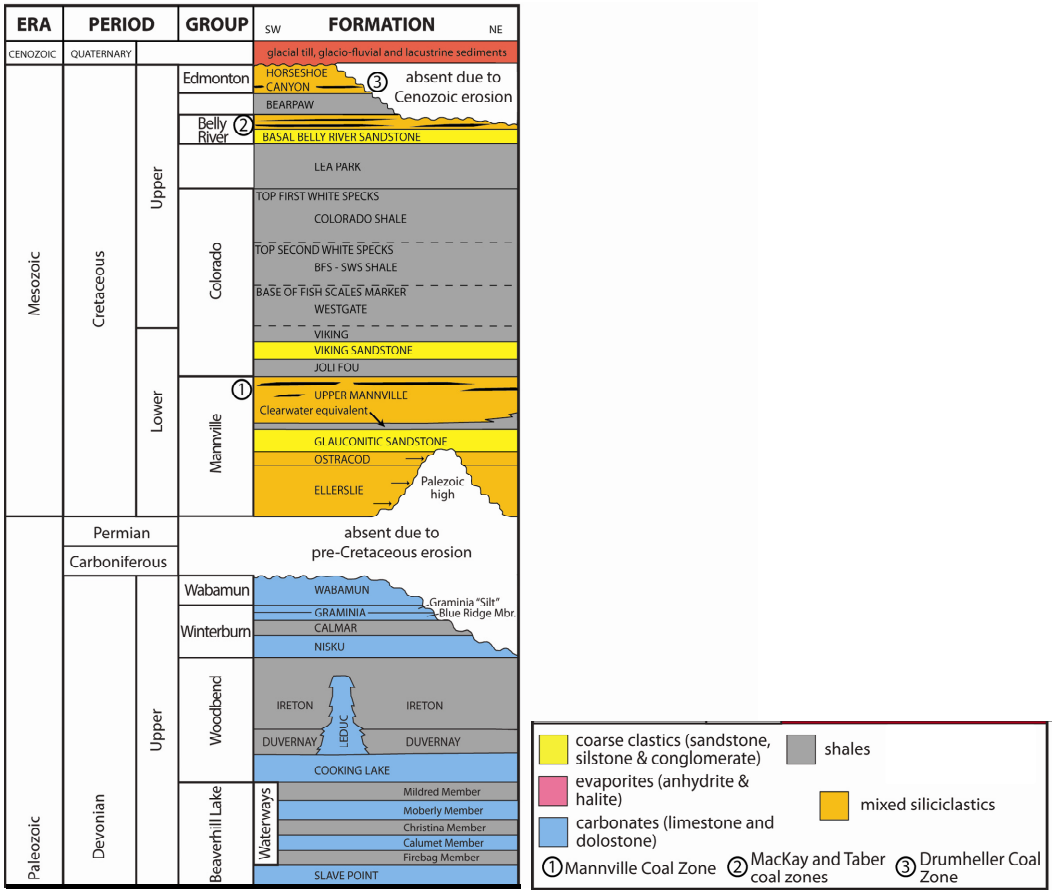

Figure 2 - Lithostratigraphic profile in the study area (after Bachu, 2010)

Considerable work has already been done on the regional characterization of in-situ stresses in the Alberta Basin (e.g., Bell et al., 1994; Bell and Bachu, 2003; Hawkes et al., 2005). The results indicate that the orientation of S_{Hmin} tends to be parallel to the trend of the Rocky Mountain Deformation Front; i.e., roughly northwest-southeast in the study area. Therefore, the maximum horizontal in-situ stress was estimated to be oriented 45 degrees clockwise from north.

2.2 Property Upscaling

For each property profile in each well, an average value was taken for each stratigraphic unit to use as a representative value. For all parameters except Young's modulus, an arithmetic average was calculated; for Young's modulus, the use of a geometric average was deemed more appropriate. Each average value was assumed to represent the magnitude of each property for each stratigraphic unit in the immediate vicinity of each well. It was found that values from one well to the next typically varied by a relatively small amount (e.g., a few percent). It was initially assumed (then confirmed later during sensitivity analyses that are not presented in this paper) that lateral variations in mechanical properties of the order of a few percent have a negligible impact on the results of geomechanical analyses of CO_2 injection. As such, with one exception, it was decided that taking an arithmetic average of the values calculated at each of the well locations and assigning this average to the entire study area was appropriate. The only exception was the Ireton Formation (i.e., the primary caprock), for which notably different Young's modulus values were observed overlying the Leduc reef and the neighbouring Morinville reef trend (where the Ireton is relatively thin) compared to values in the surrounding area (where it is relatively thick). Finally, the 3D MEM was developed by assigning the properties interpreted for each unit into the

geological model developed by AITF. Figure 3 shows cross-sectional views of Young's modulus in the MEM.

For practical reasons (i.e., limitations on model development time and computation time), and due to the limited sensitivity of the model to the properties of the overburden (as confirmed in unpublished sensitivity analyses conducted by the authors), several stratigraphic units were lumped together to define a coarser mechanical stratigraphy in the overburden (i.e., in the sequence overlying the Ireton formation). Material properties for these mechanical stratigraphic units were calculated by weighted averaging of the mechanical properties of their constituent stratigraphic units. The mechanical stratigraphic units used are illustrated in Figure 4, and the mechanical properties assigned to each are summarized in Table 1. The weighting factors used for averaging were the total thickness of all wellbore penetration lengths in each stratigraphic unit. Arithmetic averaging was used for all of the properties except Young's modulus, for which the geometrical average was used.

2.3 Pore Pressure Change

Pore pressure changes caused by injection were taken from output data files generated during unpublished reservoir simulation analyses which were conducted by Fekete Associates. Geomechanical analyses were performed for the commercial-scale injection scenario based on 110 MT of CO_2 injection over a period of 50 years, with the injection well located near the southern edge of the Redwater Leduc reef. The geomechanical analyses were conducted both after 25 years of injection and at the 50 year mark (i.e., half way through the injection period, and at the end of injection). As an example, Figure 5 shows the distribution of pressure change in the Leduc formation after 25 years of injection, as specified as input

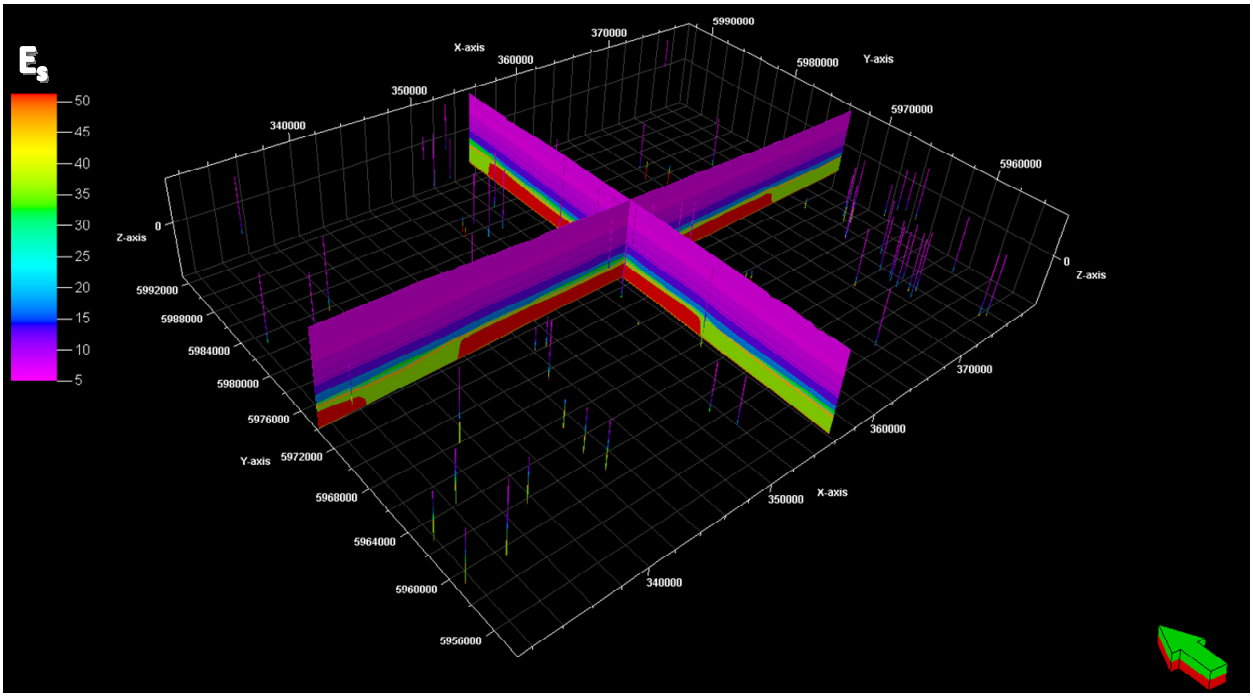

Figure 3 - Perpendicular cross-sections for the distribution of static Young's modulus in the 3D MEM. The arrow indicates true North; units for Young's modulus are GPa. The Leduc reef is the red-coloured area at the base of model, near the centre. The vertical lines show the locations of wells that were used for the interpretation of mechanical properties

into the 3D geomechanical model. It is important to note that pore pressure change in the surrounding rock was not analyzed in Fekete's reservoir simulations, hence it was not considered in the geomechanical analysis. Further, the effects of pore pressure (hence effective stress) change on porosity and permeability were not accounted for.

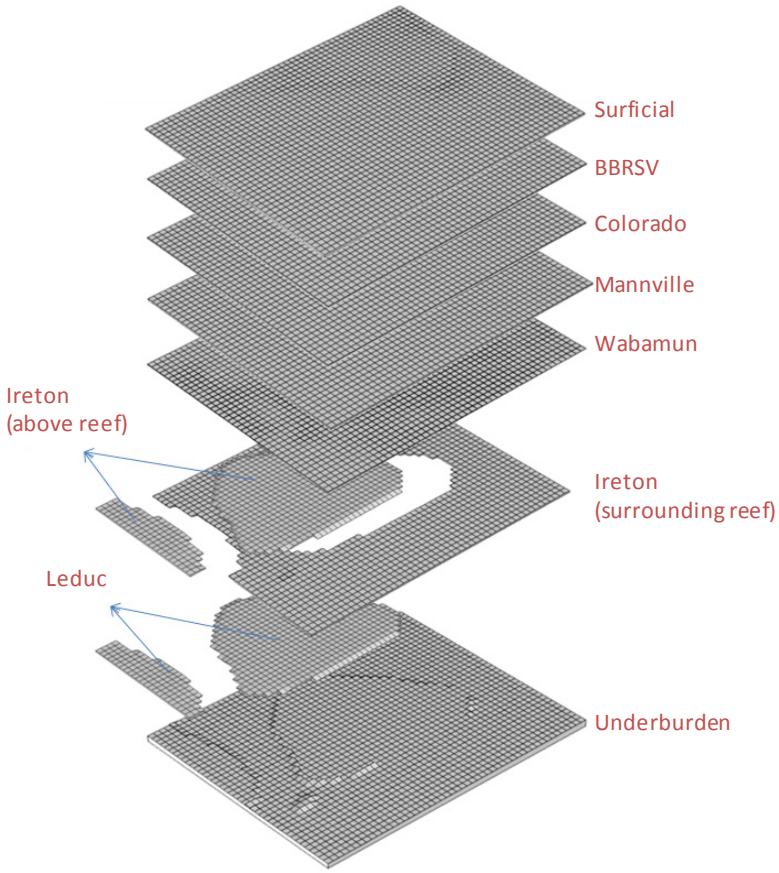

Figure 4 - Exploded view of the mechanical stratigraphic units used in the 3D geomechanical model developed for HARP

Table 1 - Property values for mechanical stratigraphic units in the HARP geomechanical model

Strat. Unit	Poisson's Ratio	E_s (GPa)	P_0 Gradient (kPa/m)	S_V Gradient (kPa/m)	S_{Hmin} Gradient (kPa/m)	S_{Hmax} Gradient (kPa/m)	Cohesion (MPa)	Friction Angle (°)
Surficial	0.41	5.0	9.8	21.8	19.9	22.1	2.4	26
Basal Belly River Sandstone & Lea Park	0.41	5.0	6.6	21.8	19.9	22.1	2.4	26
Colorado	0.37	7.3	7.8	22.2	18.2	22.1	2.6	26
Mannville	0.30	15.5	7.3	22.5	16.4	18.6	6.6	26
Wabamun	0.25	34.1	7.0	22.4	16.1	19.8	13.2	38
Ireton above reef	0.25	36.5	7.0	22.5	16.0	20.4	5.1	36
Ireton (surrounding reef)	0.25	28.6	7.0	22.4	16.0	19.7	5.1	36
Leduc	0.26	51.2	7.5	22.8	16.6	21.5	21.7	40
Underburden	0.26	48.3	7.5	23.1	16.6	21.5	21.7	40

3. THREE-DIMENSIONAL GEOMECHANICAL MODEL

The 3D geomechanical modeling presented in this report was conducted using the Structural Mechanics module of COMSOL Multiphysics (COMSOL Group, 2011). This software uses the finite element

method to solve the stationary form of the linear elastic equilibrium field equations for a solid material. Matlab was used to import the model geometry developed in Petrel into COMSOL. A total of 155,766 tetrahedral solid elements were used in this model. A zero-displacement boundary condition was set for the bottom surface of the model domain, while the lateral surfaces were fixed in the horizontal direction and free in the vertical direction, and the top surface (i.e., ground surface) was a free surface.

The inscribed Drucker-Prager criterion was used as a criterion for rock failure in this work, in part because of its relative ease of use for 3D problems compared to the Mohr-Coulomb criterion. As its name implies, the inscribed Drucker-Prager failure criterion inscribes the Mohr-Coulomb failure criterion and, therefore, it is a more conservative criterion. The strength parameters for this criterion can be calculated using Mohr-Coulomb criterion strength parameters, cohesion (c) and internal friction angle (ϕ) (e.g., Zoback, 2009). In this work, a parameter Rock Failure Ratio (*R.F.R.*) has been defined to quantify the potential for shear failure of intact rock as a result of pore pressure change. *R.F.R.* essentially represents a ratio of shear stress to shear strength, such that a value of 1.0 or more means that failure of intact rock is predicted. Another parameter, called Fault Failure Ratio (*F.F.R*), was similarly defined to quantify the potential for fault reactivation; a value of 1.0 or greater indicates that fault reactivation is predicted. Fault friction angle was considered to be 30 degrees for these calculations. This approach for quantification of fault reactivation is conservative, since it has been developed for hypothetical faults that are critically oriented with respect to the in-situ stress regime. Such faults, if they existed, would be most prone to reactivation.

As shown in Figure 5, after 25 years of injection, the maximum predicted pressure change within the reservoir is about 4 MPa. Figure 6(a) shows the distribution of rock failure ratio (*R.F.R*) for the north-south and east-west cross-sections (see Figure 5) after 25 years of injection. The maximum value of *R.F.R*. for the entire model domain is less than 0.37, which shows that rock failure during injection is unlikely for the conditions considered here. Figure 6(b) shows the distribution of fault reactivation ratio (*F.R.R.*) for the entire model domain. We see that the maximum values of *F.R.R.* are about 0.58 and they occur in the caprock. This shows that even critically-oriented faults in the caprock, if present, are not likely to be reactivated. It should also be noted that the modelling results do not predict any tensile fracturing as a result of pressure change during this period.

Review of the deformations predicted by the 3D geomechanical model shows that, after 25 years of CO_2 injection, the reservoir experiences about 1.62 cm of vertical expansion. The maximum predicted magnitude of surface heave (Figure 7), which occurs in the southern part of the reservoir, is virtually identical to the magnitude of the reservoir expansion. This demonstrates that surface deformation is controlled almost entirely by reservoir expansion, and that other mechanical stratigraphic units have a negligible effect.

Similar analyses were performed for the case of 50 years of CO_2 injection. In this case, the maximum pressure change within the reservoir is roughly 3.5 MPa. As expected, given that this maximum pressure change is smaller than the 4 MPa predicted at 25 years, the results predicted by the geomechanical model at 50 years are less critical compared to the 25-year case. For example, the maximum values of *F.R.R*. are 0.57 in this case, and the maximum reservoir expansion and surface heave are both about 1.41 cm, occurring (as for the 25-year case) in the southern part of the reservoir (i.e., close to the injection well).

4. SENSITIVITY ANALYSES

Uncertainties in the estimation of input data are one of the major challenges in geomechanical modeling. These uncertainties may be reflected in geometry, mechanical properties of rock, in-situ stresses and pore pressure. As such, a series of sensitivity analyses was conducted. To achieve high spatial resolution (i.e., a fine mesh) and rapid computations, a study was performed by the authors to develop and assess a 2D

model which, like the 3D model, was implemented using COMSOL. This study was conducted for an east-west cross-section passing through the approximate location of the injection well. Geological structure, pore pressure and mechanical properties in this plane (and in-situ stress components within and normal the plane) were identical to those used in the 3D model; the only difference was the fact that plane strain conditions were assumed for the 2D model. The results showed a highly favourable comparison between the 2D and 3D models; i.e., predicted induced stress changes were nearly identical. Based on this comparison, the sensitivity analyses for this project were conducted using the 2D model.

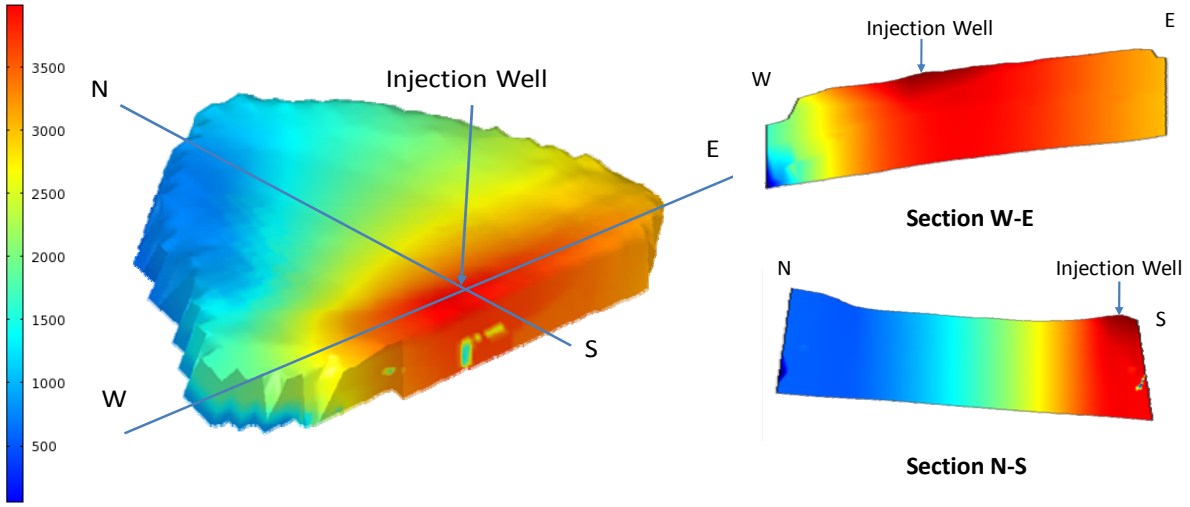

Figure 5 - Distribution of pore pressure change (in kPa) in the Leduc reef after 25 years of CO_2 injection, as input into the 3D geomechanical model. The vertical scale in this figure has been exaggerated

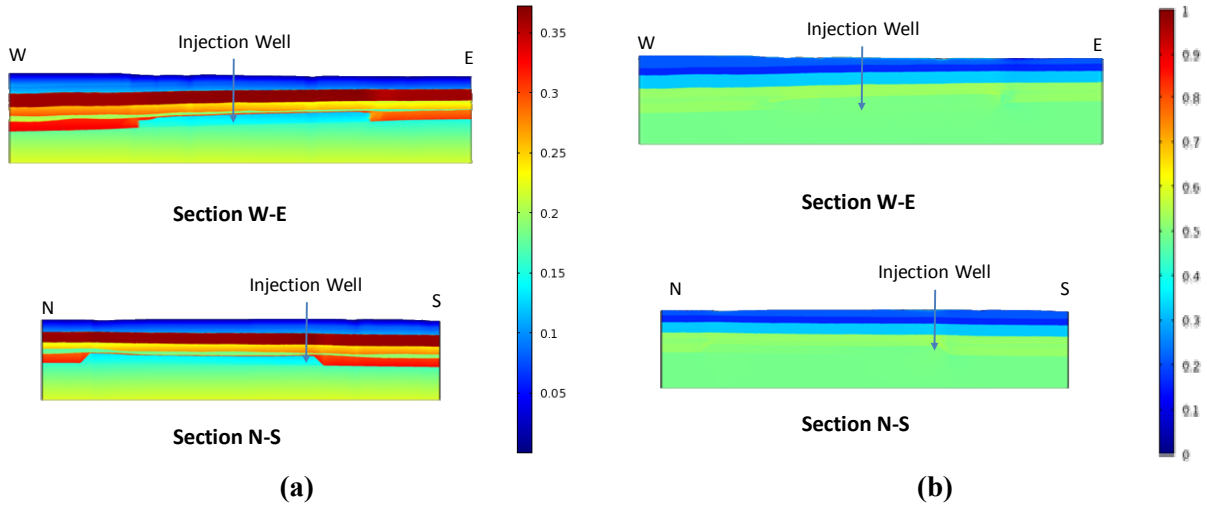

Figure 6 - Distribution of (a) rock failure ratio *(R.F.R.)* and (b) fault reactivation ratio (*F.R.R.*) after 25 years of CO_2 injection for E-W and N-S cross-sections shown in Figure 5

4.1 Variations in Elastic Properties

The sensitivity of the geomechanical model to Young's modulus and Poisson's ratio was studied. The sensitivity analyses show that induced-stress changes in the cross-sectional plane are not sensitive to Young's modulus values and they are only dependent on Poisson's ratio. Figure 8(a) demonstrates the dependency of maximum induced stress changes in the Ireton formation (i.e., caprock and sideburden locations, as identified in Figure 9) to Poisson's ratio. For this analysis the values of Poisson's ratio for all

the units was varied by ±0.05. Evidently, there could be variations of up to 30% in the induced stress changes as a result of Poisson's ratio variation. Figure 8(b) shows how the maximum values of *F.R.R.* and *R.F.R.* in the cross-sectional plane vary as a result of changes in Poisson's ratio. Although a slight increase in both of these parameters is observed with decreasing Poisson's ratio, the absolute values predicted for all cases considered are well below the critical value of 1.0. This limited sensitivity is explainable, given that the values of induced-stress changes are small in comparison with the initial in-situ stress magnitudes.

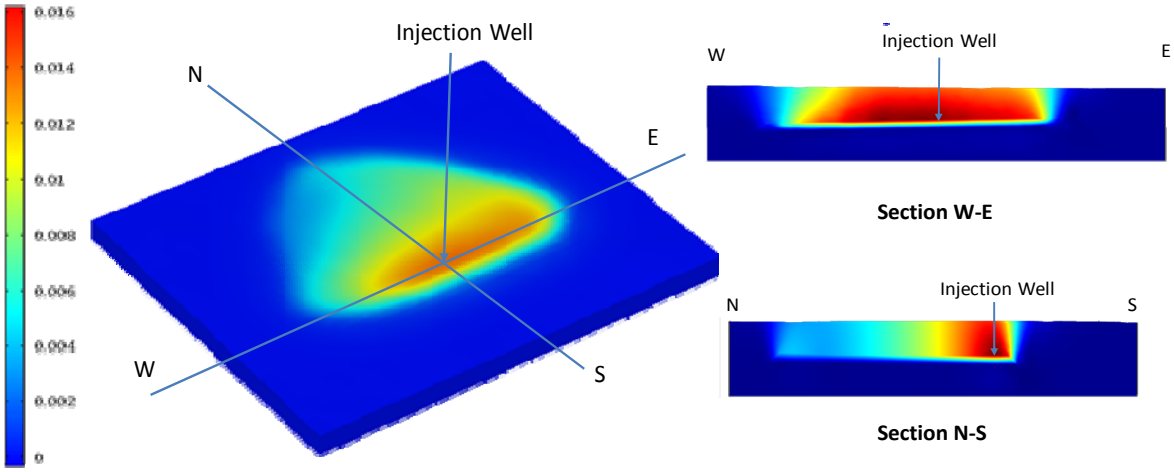

Figure 7 - Distribution of vertical deformation (in metres) in the entire model domain after 25 years of CO_2 injection

Another analysis was performed to study the sensitivity of maximum surface heave to elastic properties. As expected, this parameter was found to be a function of both Young's modulus and Possion's ratio. This was determined by running nine different model scenarios in which ±0.05 variations in Poisson's ratio and ±25% variations in Young's modulus were considered in every possible combination. The results for these analyses are shown in Figure 8(c). From this figure, the maximum value of heave varies from about 1 cm when both Poisson's ratio and Young's modulus have their maximum magnitudes to 2.15 cm when these parameters have their minimum values.

4.2 Other Scenarios Considered

Other notable scenarios that were considered during sensitivity analysis included variations in ambient pore pressure and horizontal stress magnitudes, and the number of layers used to simulate the mechanical behaviour of the overburden. Due to space limitations, results are not presented in this paper. Key learnings from these cases include: (i) induced shear fracturing and fault reactivation were found to be unlikely for all scenarios considered; and (ii) a relatively coarse representation of overburden stratigraphy has limited effect on model accuracy.

5. SUMMARY AND CONCLUSION

A three-dimensional Mechanical Earth Model (MEM) has been developed in Petrel for the HARP study area. This model was developed based on the geological model developed by AITF, with simplifications made to the overburden stratigraphy. Mechanical properties and in-situ stresses were estimated using wireline logs for 95 wells in the study area, previously published in-situ stress data, and pore pressure data provided by AITF.

The 3D MEM developed in this work was used as the basis for 3D numerical modelling to assess the geomechanical response to CO_2 injection in the Leduc Formation, using reservoir simulation output as a means of specifying injection-induced pore pressure distributions. The geomechanical analyses were performed for scenarios of commercial-scale injection (after 25 and 50 years of injection). The modeling was performed using a linear elastic constitutive model, with an inscribed Drucker-Prager failure criterion. The results indicate that, for the commercial-scale injection scenario considered, induced shear fracturing and fault reactivation are considered unlikely for all points within the study area. The maximum surface heave predicted by this model is about 1.62 cm.

A series of sensitivity analyses was performed to study the effects of uncertainties in elastic properties, pore pressures and horizontal stress magnitudes. These analyses demonstrated that induced shear fracturing and fault reactivation are unlikely for all input parameter scenarios that were considered, and that total ground surface uplift is small (approximately 1 to 2 cm).

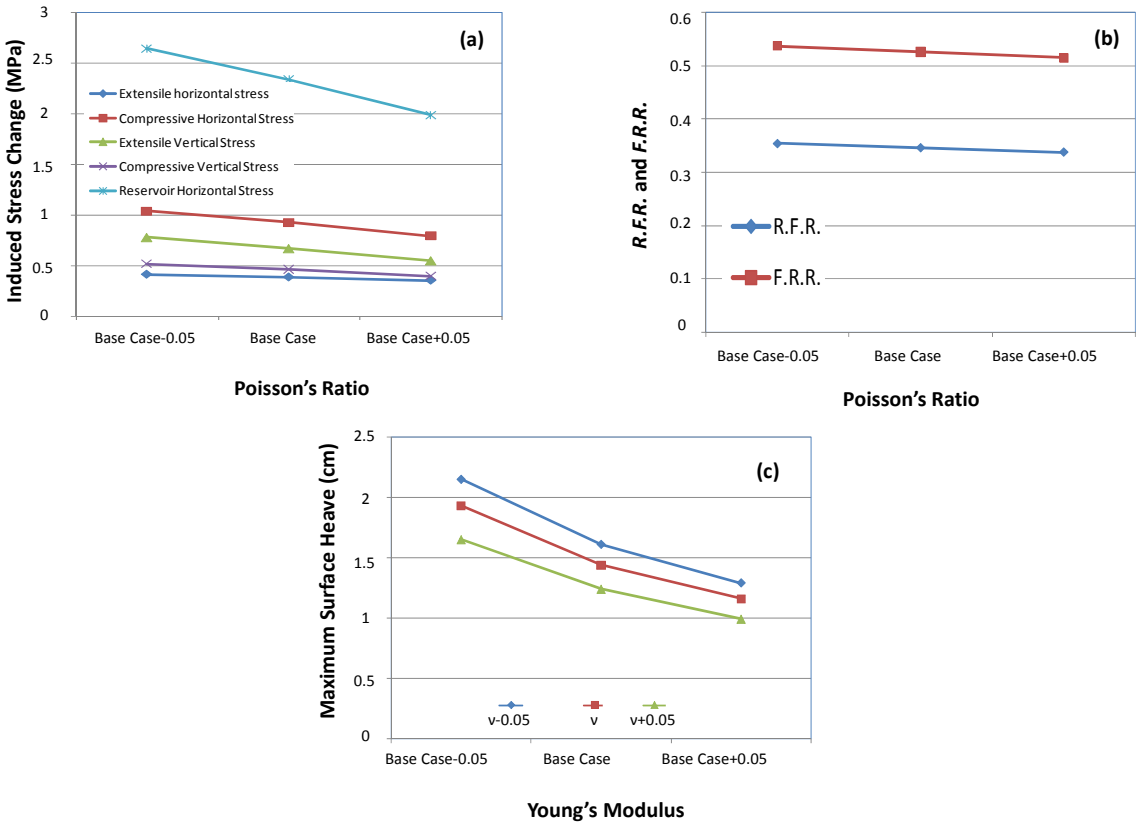

Figure 8 - (a) Sensitivity of the maximum values of induced stress change in the Ireton Formation to the variation in Poisson's ratio; regions of compressive and extensile stress changes are specified in Figure 9. (b) Sensitivity of maximum values of *R.F.R.* and *F.R.R.* in the caprock to variations in Poisson's ratio. (c) Sensitivity of maximum surface heave to variations in Poisson's ratio and Young's modulus

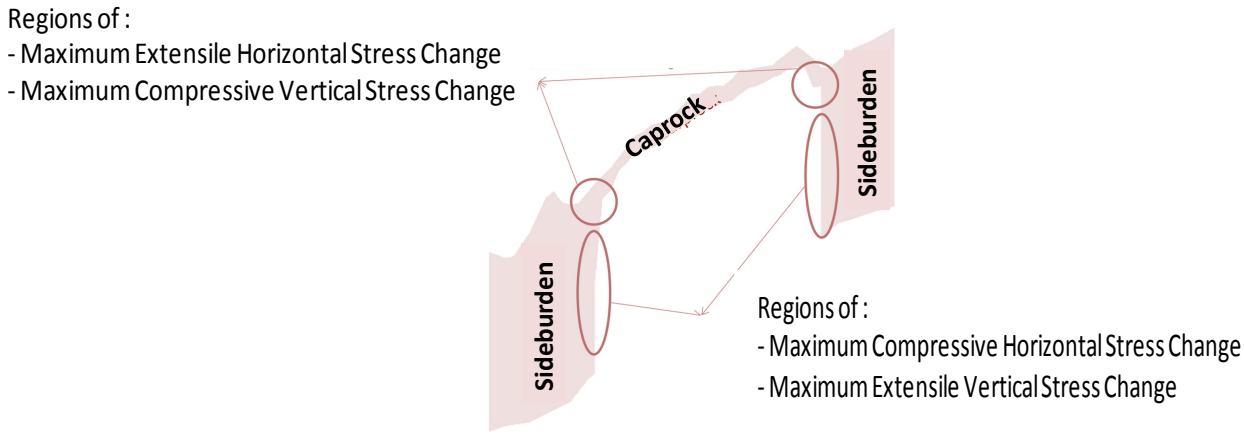

Figure 9 - Geometry of the Ireton formation (caprock and sideburden) in the 2D geomechanical model. Approximate regions of maximum stress change induced by CO_2 injection are schematically shown on this geometry. The vertical axis has been exaggerated

6. ACKNOWLEDGEMENTS

This work has been done under a contract with Alberta Innovates - Technology Futures (AITF). The authors gratefully acknowledge the contributions of Seungjoo Li of the University of Alberta for log analysis of mechanical properties, and data received from AITF and Fekete Associates Inc.

7. REFERENCES

COMSOL Group. 2011. COMSOL Multiphysics Modeling, Finite Element Analysis, and Engineering Simulation Software. User's Manual, version 4.0.

BACHU, S., HAUG, K., and MICHAEL, K. 2008. Stress Regime at Acid-Gas Injection Operations in Western Canada. ERCB/AGS Special Report 094 (March).

BACHU, S. 2010. Heartland Area Redwater Project (HARP) – Phase II Progress Report: Summary of Activities and Findings to September 2010. Report prepared at Alberta Innovates - Technology Futures.

BELL, J.S. and BACHU, S. 2003. In situ stress magnitude and orientation estimates for Cretaceous coal-bearing strata beneath the Plains Area of central and southern Alberta. Bulletin of Canadian Petroleum Geology, v. 51, no. 1, pp. 1-28.

BELL, J.S., PRICE, P.R. and MCLELLAN, P.J. 1994. In situ stresses in the Western Canada Sedimentary Basin. In: Geological Atlas of the Western Canada Sedimentary Basin, G. Mossop and I. Shetsen (comp.). Canadian Society of Petroleum Geologists and Alberta Research Council, Calgary, AB, pp. 439-446.

CHANG, C., ZOBACK, M.D., and KHAKSAR, A. 2006. Empirical relations between rock strength and physical properties in sedimentary rocks. Journal of petroleum science and engineering. 51, 223-237.

HAWKES, C.D., BACHU, S., HAUG, K. and THOMPSON, A.W. 2005. Analysis of in-situ stress regime in the Alberta Basin, Canada, for Performance Assessment of CO_2 Geological Sequestration Sites, Proceedings of the DOE/NETL Fourth Annual Conference on Carbon Capture and Sequestration, Washington, DC, May 2-5, 2005, 22 p.

SCHLUMBERGER LTD. 2009. Petrel Seismic to Simulation Software. User's Manual, version 2009.2.

WARPINSKI, N.R. 1989: Elastic and viscoelastic calculations of stresses in sedimentary basins, SPE Formation Evaluation, No. 6, December, pp. 522-530.

ZOBACK, M.D. 2007. Reservoir Geomechanics, Cambridge University Press, New York.

Laboratory Investigations of Seismic Signatures of CO_2 Saturation for Geological Sequestration

Gautier Njiekak
Department of Physics, Institute for Geophysical Research, University of Alberta
Helen Yam
Department of Physics, Institute for Geophysical Research, University of Alberta
Randolf S. Kofman
Department of Physics, Institute for Geophysical Research, University of Alberta
Douglas R. Schmitt
Department of Physics, Institute for Geophysical Research, University of Alberta

ABSTRACT: The current study provides an experimental approach that aims at documenting the effects of different phases of CO_2 (gas, liquid, supercritical fluid) on rock seismic responses. This has implications on obtaining quantitative estimates of fluid saturations for geological storage. The ultrasonic pulse transmission technique is the underlying methodology used in this work. Unlike previous rock physics studies involving CO_2 as pore fluid, care is taken to fully saturate the studied samples and also to separate pore fluid effects from pore pressure build-up effects during the experiments. This allows to record seismic effects that are solely reflective of changes in the pore fluid properties. Measurements were done on a CO_2 saturated Berea sandstone. Laboratory results show *P*- and *S*- waveform variations (velocity, amplitude) in response to CO_2's varying phase state. Overall, CO_2 phase changes (gas to liquid and gas to supercritical fluid) are marked by a drop in velocities, with the drop being smaller and less immediate over the gas-supercritical fluid transition than over the gas-liquid transition.

1. INTRODUCTION

Due to the sensitivity of seismic waves to pore fluid contents, time lapse seismology is regarded as a promising monitoring method for geological CO_2 sequestration projects and is employed in all industrial scale projects (Sleipner, Weyburn, In Salah). Therefore, understanding the effect of CO_2 as a pore fluid on the overall rock seismic response is critical. There exist a very limited number of laboratory studies on examining the elastic effects of CO_2 on pore fluid seismic responses. All laboratory work to date has used the ultrasonic pulse transmission technique and demonstrated that the presence of CO_2 in the pore space will lower seismic velocities due to its higher compressibility compared to other possible in-situ fluids such as brine or oil. Today, one of the main challenges for seismic monitoring surveys is the quantitative assessment of the injected CO_2. This is quite crucial as possible alteration of the reservoir rock frame and/or changes in the fluid physical properties following the injection of CO_2 could affect the overall seismic behaviour of the rock. To address this issue, an experimental procedure was set up to inspect the seismic effects from (i) CO_2 as a lone pore fluid, and (ii) the different phase states of CO_2. This is particularly critical as CO_2 can be in gas, liquid, or supercritical phases even at the relatively modest pore pressures and temperatures in the uppermost kilometer of the earth's crust. Real situations sometimes differ from the experimental conditions set up in this study as CO_2 may coexist with other in-situ fluids in the pore space. However, this study provides an end member understanding of the possibilities with CO_2 in the pore space, which is pivotal when quantifying CO_2 using seismic techniques. Moreover, unlike previous studies involving CO_2 flooding in the laboratory, care was taken to separate seismic effects due to changes in the pore fluid properties from those induced by pore pressure build-up during such experiments.

2. EXPERIMENTAL SETUP AND PROCEDURE

The experiments conducted in this study were based on the ultrasonic pulse transmission technique. The application of this method allowed the recording of an ultrasonic *P*- or *S*- wave pulse after propagation through a sample of known length. From the final waveforms the transit time of the pulse was deduced, and with the length of the sample the elastic wave velocity was calculated. The measurements were carried out in the laboratory of the Experimental Geophysics Group at the University of Alberta.

2.1 Experimental Setup

The experimental setup includes several functional units such as a pulse generator, a digital oscilloscope (NI USB- 5133 100 MS/s), source/receiver transducers, a cylindrical pressure vessel, fluid tanks, a thermocouple, and an electrical resistance tape (Fig. 1). The transducer is exited by a fast-rising, 200V square wave, sent by the pulse generator (Panametrics, model 5800 PR). The generated elastic wave after propagating through the sample is recorded by a digital oscilloscope at a sampling interval of 10 nanoseconds. The recorded waveform is the stack of at least 500 traces to reduce the noise level in the signal. The desired pore fluid is introduced into the sample via stainless steel tubing that connects the pore space of the sample to the pore fluid reservoir located outside of the vessel through the vessel lid. The confining and pore pressure systems are independent of each other such that different pressure conditions can be applied in irrespective of each other by using different pumps located outside of the pressure vessel. Both the confining pressure (pressure vessel) and the pore pressure systems are capable of reaching a maximum pressure of 70 MPa from the pumps. Higher confining pressures, up to 200 MPa, could also be achieved by using a separate air pump connected to the pressure vessel.

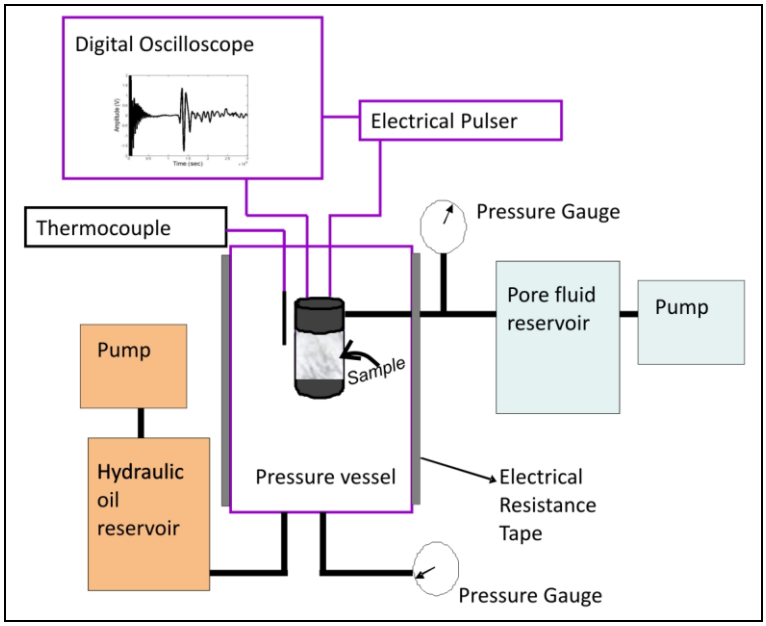

Figure 1 - The experimental setup for the ultrasonic measurement

2.2 Experimental Procedure

Ultrasonic measurements were made on samples under a variety of dry and saturated conditions. The ‘dry’ measurements were done with the pore space under vacuum (pore pressure = 0 MPa) while the confining pressure could vary from 1 MPa upward.

For the CO_2 saturated measurements, measurements were done under different conditions of temperature and pore pressure in order to inspect the pore fluid effects on the seismic waves velocities. The key here was to make sure that any variation in the waveforms was due to change in the pore fluid physical properties. Thus, for each sample, a constant differential pressure was maintained by varying the confining pressure accordingly to the pore pressure. Assuming that the equal amount of pore pressure increase cancelled the equal amount of confining pressure increase, any waveform variation observed was solely caused by effects of the fluid(s) present in the pore space.

Running experiments under constant differential pressure could also be used to test the full saturation of the studied sample. Generally, it is difficult to know if a rock is fully saturated, and most authors simply make this assumption after taking precautions during sample preparation. Rarely, however, is any additional evidence given to support this contention. The same problem occurred in this study and in order to satisfy this assumption a quality control procedure was used. Prior to CO_2 saturated measurements, the sample was subjected to constant differential pressure measurement under inert nitrogen gas saturation. As nitrogen gas, unlike CO_2, does not undergo a phase transformation under the range of pressure and temperature conditions used in this study, no substantial change in the *P*- and *S*-wave velocities with constant effective pressure was taken to indicate full saturation of the sample. While this latter behaviour may also be indicative of other processes than partial water vapour-nitrogen saturation (e.g., chemical reactions at the pore surfaces), it does lend confidence to selecting the set of 'high-quality' measurements that can be best compared to the various theories.

2.3. Sample Preparation

For the measurement, cylindrically shaped plugs of up to 3.81cm in diameter and of up to ~ 6 cm in length were used. The plug end faces were ground to parallel (within ± 0.02 mm) in order to enhance the signal transmission and to avoid errors in the velocity measurements as much as possible. Then the samples were dried under vacuum at 70°C temperature for 48 hours and kept in a desiccator jar afterwards until in use. The sample to be measured was pushed into an impermeable Klearon™ tube. An ultrasonic transducer was placed on each end of the sample and the two transducers were aligned so that *S*-wave ceramic were properly polarized (See Bakhorji, 2009 for details on the building of the source/receiver transducers). To enhance the sealing mechanism and prevent the leakage of the hydraulic oil from reaching the sample while being in the pressure vessel, steel hose clamps were used so that they could be tightened around the Klearon™ tube just above the aluminum part of the transducers. The jacketed assembly of the sample was then placed inside the confining pressure vessel.

3. CASE STUDY: BEREA SANDSTONE

3.1. Sample Description

Berea sandstone is predominantly composed of quartz and minor traces of clay minerals (Fig. 2). The porosity and permeability of Berea sandstone are known to be relatively high, making it a good candidate for petrophysical testing (e.g., Shankland and Johnson, 1993; Hart and Wang, 1995; Zhan et al, 2010). The studied specimen has a porosity of 19%, with an air permeability of about 238 mD. The main pore throat size is around 11μm (Yam, 2011).

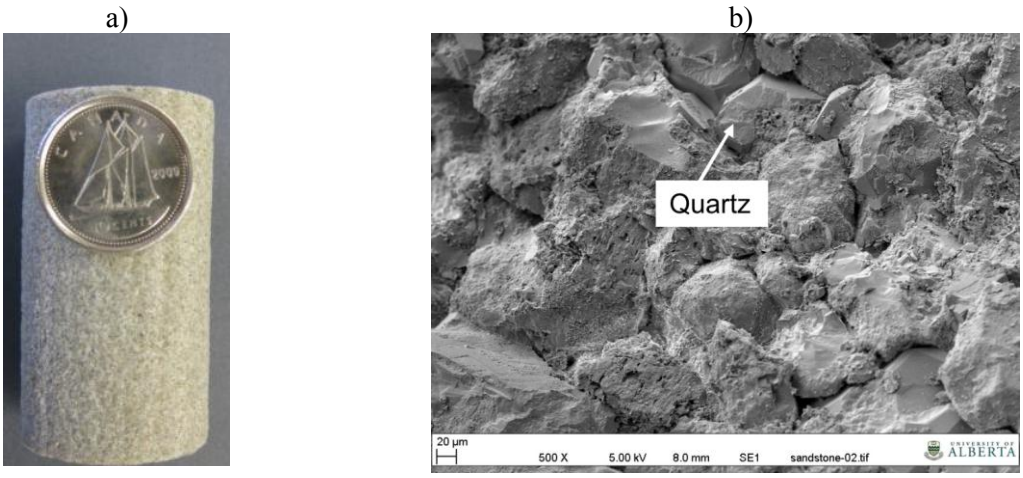

Figure 2 - (a) Photograph of the Berea sandstone's plug and (b) a scanning electron microscope image of the sample

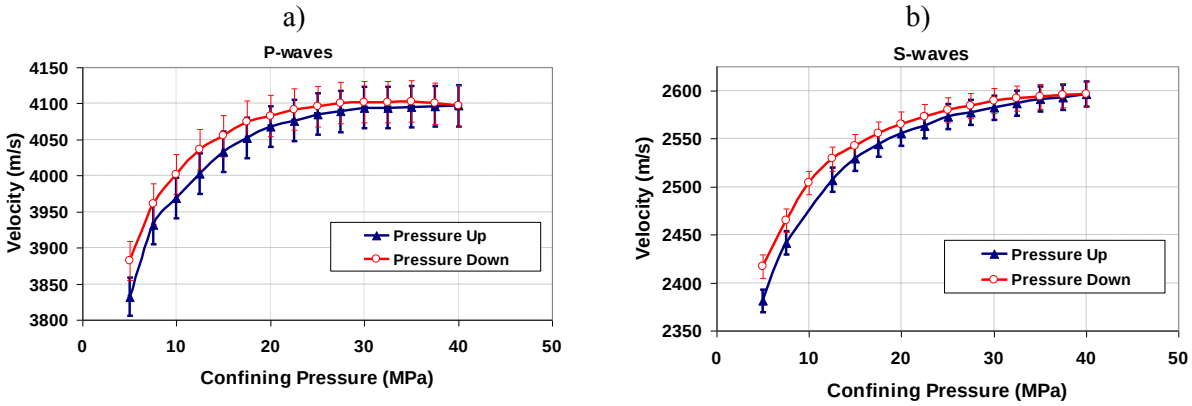

Figure 3 - Dry P-and S-wave velocities with their respective errors as a function of confining pressure for the Berea sandstone

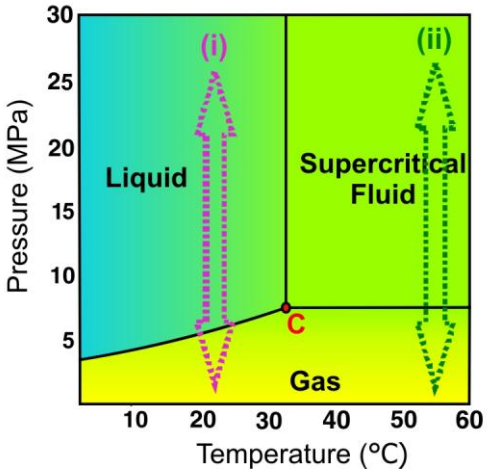

Figure 4 - Phase diagram of CO_2. C = critical point. Arrows (i) and (ii) refer to the conditions under which CO_2-saturated rock velocities were measured

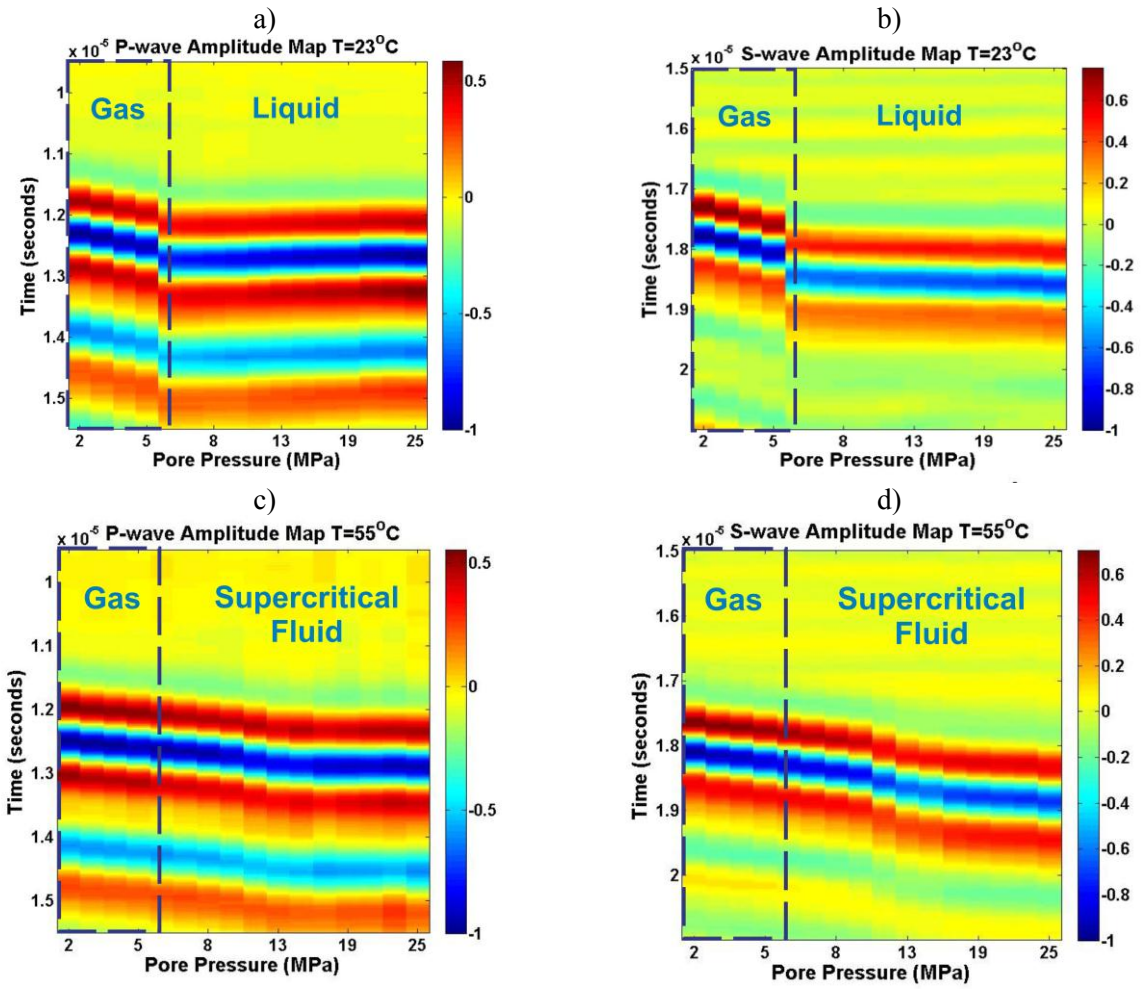

Figure 5 - Normalized P- and S-wave waveforms as a function of pore pressures collected during the constant temperature runs at T = 23°C (*a* and *b*) and T = 55°C (*c* and *d*). A constant differential pressure of 15 MPa was maintained throughout each measurement run

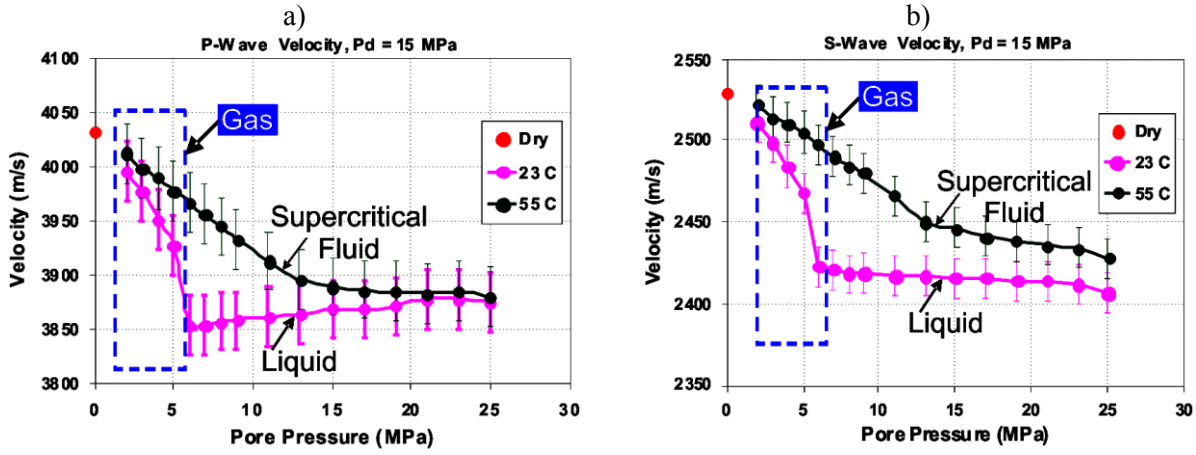

Figure 6 - CO_2 saturated P-and S-wave velocities of the Berea sandstone for the two constant temperature runs at T = 23°C and T = 55°C while under a constant differential pressure (Pd) of 15 MPa. Error bars are shown

3.2. Ultrasonic Measurements

Measurements were made on the sandstone sample under dry and saturated conditions. The dry measurements were done with the pore space under vacuum (pore pressure = 0 MPa) while the confining pressure varied from 5 MPa to 40 MPa. Both pressurization and depressurization were applied to the sample over this pressure interval. Both *P*-and *S*- wave velocities exhibit a nonlinear increase with pressure (Fig. 3). The wave velocities increase rapidly at low pressures that taper off with higher pressures. This behavioural increase is caused by the progressive closure of compliant pores where most of the compliant pores will close at low pressures, therefore causing a rapid velocity increase.

For the CO_2 saturated measurements, two different constant temperature runs were conducted while pore pressure varied from 2 MPa to 25 MPa. The constant temperature runs were done at 23° C and 55° C (See arrows *(i)* and *(ii)* in figure 4). For each measurement run, a constant differential pressure of 15 MPa was maintained. As pore pressure increases, for the lower temperature runs (23°C), CO_2 changed from a gas phase to a liquid phase in the pore spaces while for the higher temperature runs (55°C), CO_2 changed from a gas phase to the supercritical fluid phase. The results of the measurements show waveform variations (velocity, amplitude) in response to CO_2's varying phase state. For the lower temperature run (T = 23°C), the elastic wave response to CO_2's phase transition is sharp and significant. In contrast, the elastic wave responses of the higher temperature run (T = 55°C) to CO_2's phase transition are gentle and lack any abrupt change (Figs 5 and 6). Overall, CO_2 phase changes (gas to liquid and gas to supercritical fluid) are marked by a drop in *P*- and *S*- wave velocities of up to 3.9 and 4.4%, respectively, over the entire investigated pore pressure interval (= 25 MPa). This is likely due to the increased density of the liquid or the supercritical fluid relative to the gas (Fig. 6). The *P*-wave velocity reduction (3.6-3.9%) recorded in this study is lower than the *P*-wave velocity decrease (7.5-14.5%) observed by Lei and Xue (2009) when injecting different phases of CO_2 in water-saturated sandstone samples. However, the differences between these values should be interpreted with caution as experimental conditions (e.g., investigated pore pressure interval, nature of the pore fluids) are not similar to the ones set up in the current study.

4. CONCLUSIONS

An experimental procedure has been set up to inspect the variation of *P*- and *S*- waves velocities as a function of CO_2 saturation. The work focuses on inspecting the effects of different CO_2 phases (gas, liquid and supercritical fluid) on the overall rock seismic behaviour. Results show that elastic waves are sensitive to changes in the pore space and CO_2 phase change is evident from signal variations. CO_2 phase changes (gas to liquid and gas to supercritical fluid) are marked by a drop in velocities of up to 4.4 %. The abruptness in the velocity change differs significantly between the gas-liquid and gas-supercritical fluid transitions; and the gradual variations seen for the latter suggest that this will be difficult to detect using seismic reflection techniques.

5. ACKNOWLEDGEMENTS

The development of the CO_2 measurement system was supported by NSERC and the Canada Research Chair program. Yam was supported in part by an NSERC CGS Scholarship and Njiekak and Kofman in part by a research contract from the Weyburn-Midale CO_2 Monitoring and Storage Project. The technical assistance of Len Tober and Lucas Duerksen was invaluable.

6. REFERENCES

BAKHORJI, A., 2009. Laboratory measurements of static and dynamic elastic properties in carbonate, Thesis Ph.D., Univ. of Alberta, Edmonton, 333 p.

HART, D. J., and WANG, H. F., 1995. Laboratory measurements of a complete set of poroelastic moduli for Berea sandstone and Indiana limestone, Journal of Geophysical Research, 17, 741-751.

LEI, X., and XUE, Z., 2009. Ultrasonic velocity and attenuation during CO_2 injection into water-saturated porous sandstones: Measurements using difference seismic tomography, Physics of the Earth and Planetary Interiors, 176, 224-234.

SHANKLAND, T. J., and JOHNSON, P. A., 1993. Elastic wave attenuation and velocity of Berea sandstone measured in the frequency domain: Geophysical Research Letters, 20, 391-394.
YAM, H., 2011. CO_2 Rock Physics: A laboratory study. MSc. Thesis, Univ. of Alberta, Edmonton, 286 p.

ZHAN, X., SCHWARTZ, L. M., TOKSOZ, M. N., SMITH, W. C., and MORGAN, F. D., 2010. Pore-scale modeling of electrical and fluid transport in Berea sandstone: Geophysics, 75, F135.

Monitoring CO_2 Sequestration from Spaceborne Synthetic Aperture Radar (SAR) Platforms Using Interferometric (InSAR) Image Stack Analysis

Bruce Macdonald
MDA Geospatial Services Inc. and MDA Systems Ltd.
Bernhard Rabus
MDA Geospatial Services Inc. and MDA Systems Ltd.
Jayson Eppler
MDA Geospatial Services Inc. and MDA Systems Ltd.

ABSTRACT: Operational reservoir management activities such as cyclical steam, water or CO_2 injections frequently cause surface micro-deformation. InSAR monitoring from space based sensors of this surface deformation has become a valuable approach to confirm and monitor extraction and injection activities. Sequestration of CO_2 into deep saline aquifers is discussed as an important long term solution to slow future climate change. This method requires reliable continuous monitoring to assure that captured CO_2 is sequestered in the substrate for "all time" (typical minimum requirement by law is 20-30 years). We have shown that combining flow and deformation modeling with spaceborne synthetic aperture RADAR interferometry (InSAR) measurement of ground uplift caused by the underground release and spreading of the CO_2 can be forged into a powerful tool to monitor sequestration.

We used a novel InSAR approach to resolve the surface motion over the In Salah, Algeria CO_2 sequestration site. Our approach exploits all information contained in an interferometric stack by exploiting both persistent distributed as well as persistent point scatterers. Displacement time series are obtained with a network inversion approach applied after topographic error and preliminary atmospheric correction of the network (dual-scale technique). After inverting the original network data to common master we then use an advanced spatio-temporal filtering scheme to remove the remaining atmospheric phase components down to scales of 1 km or less.

By comparing final displacement series from multiple interleaving InSAR stacks we show that the accuracy of our refined solution to detect uplift outside of significant temporal data gaps in the InSAR stack is significantly better than 1 mm per year. We further show that accuracy and robustness to data gaps are both significantly improved by co-inverting multiple datasets with the same and different sensors. This co-inversion method also allows the seamless continuation of the monitoring from one sensor to another.

1. INTRODUCTION

Large gas fields have long been identified throughout the In Salah region of central Algeria. The In Salah Gas Joint Venture (JV) was established to explore these gas reserves. The JV is a joint operation of three companies, BP, Sonatrach and Statoil. A Joint Industrial Project (JIP), was struck to study and monitor the long term effects of CO_2 sequestration. MDA and Pinnacle Technologies won a multi-year contract with BP to remotely monitor the Krechba Gas Fields using ENVISAT and RADARSAT-2 imagery. MDA's role in the JIP was to measure historical and current ground displacement utilizing multiple InSAR data stacks acquired with aforementioned sensors, and deliver harmonized motion maps that fuse the individual motion measurements in a statistically optimized manner within and across data stacks.

The CO_2 injection started in 2004 when three horizontal wells were designed and drilled for sequestration

activities. CO_2 is extracted from the gas at the Krechba plant and injected into Carboniferous sandstone approximately two kilometers below surface. (Figure 1) The 20 m thick storage unit is water laden and porous with 800 m of Carboniferous marine transgression (shale) and Cretaceous sandstone deposits to the surface. To-date over three million tons of CO_2 has been injected (Ringrose et al., 2010).

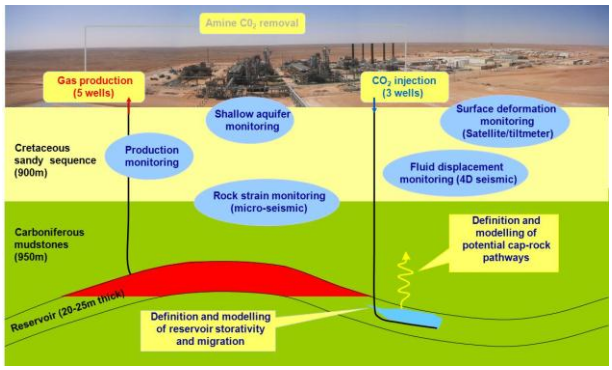

Figure 1 - In Salah CO_2 extraction and sequestration (source: BP Presentation 9th CCS Conference 2010)

The ground monitoring techniques employed for this region are specific to its topography and climate. Krechba is a sandy and rocky desert situated about 150 km from the nearest town of In Salah, which is the world's hottest continuously inhabited place. It experiences daily and seasonal extremes of temperatures of over 50°C in the summer down to -4°C in the winter. The Krechba landscape is strewn with scattered rocks and boulders interspersed within continuously shifting sand (Figure 2). As such, ground targets that are phase-stable and dominant within one resolution cell—also known as persistent scatterers (PS)—are quite sparse. However, this region abounds in distributed scatterers (DS)—ground targets comprising several sub-targets that are collectively coherent over time. Accounting for the particular ground conditions in this imaging area, we chose to retain spatially contiguous coverage by developing an advanced remote monitoring technique for distributed scatterers.

Figure 2 - Outline of gas producing anticline. (source BP Presentation 9th CCS Conference 2010) Image: © DigitalGlobe

From the outset, it was evident that traditional stack inversion methods that interfere all images with a common master, or interfere all temporal neighbours would not achieve sufficient noise suppression. The sharp temperature differentials in Krechba cause strong convection currents in the atmosphere that manifest as short-scale phase bubbles or pits peppered across entire interferograms. The spatial

signatures of these atmospheric phenomena are smaller or equal to that of the motion fields resulting from the gas injection. Additionally, approaching or receding atmospheric fronts induce sharp phase delineations. The atmospheric phase contamination is severe and cannot be sufficiently attenuated by analyzing a small subset of the available InSAR observations. MDA developed a DS network inversion InSAR method that exploits the entirety of information available in each InSAR dataset, and then fuses multiple datasets to further improve the statistical suppression of temporally uncorrelated atmosphere.

2. DATASETS

This project exploits existing and ongoing data stacks from ENVISAT and RADARSAT-2 sensors. Two ENVISAT datasets with a descending satellite pass were found to be suitable and new acquisitions were programmed. The Track-65 ENVISAT dataset consists of 52 images spanning Jul. 2003 to Sep. 2010, and the Track-294 dataset comprises 39 images from Dec. 2003 to Aug. 2010. The 31 scenes of RADARSAT-2 data were acquired from Aug 2008 to Sep. 2010. This paper focuses on the processing optimization of the historic and newly acquired ENVISAT datasets, as well as adapting the process for the RADARSAT-2 data stacks.

3. METHOD

The methodology described here is based on earlier MDA developed Dual-Scale Persistent Scatterer processing (Rabus and Ghuman, 2009), and upgraded for Distributed Scatterer (DS) applications (Rabus et al, 2009) For the chosen application and environment the accuracy of the presented stack based method using full (2D) images is comparable to corresponding stack based methods using point subsets of phase-stable scatterers (Ferretti et all, 2011). Figure 3, bottom shows the flowchart of our resulting InSAR solution for InSalah including further enhancements introduced since 2009 to boost accuracy in light of reduced inflation amplitudes caused by a gradual spreading of the injection footprints over time (Figure 3, top). In the following we describe the original solution for ENVISAT (early injection prior to reservoir maturation); enhancements for RADARSAT-2 (reservoir maturation) are discussed thereafter

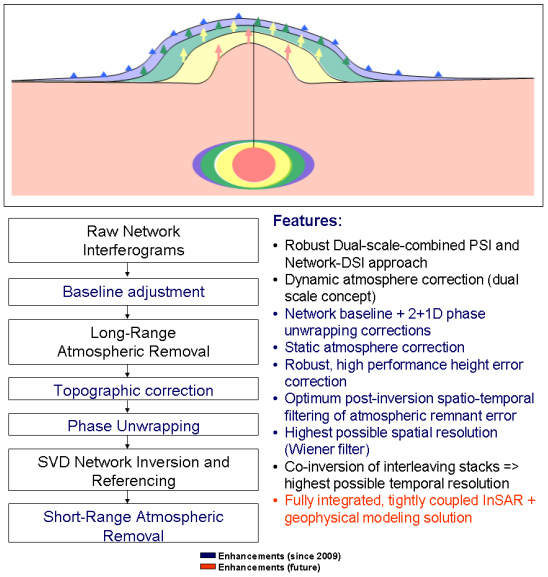

Figure 3 - Top: reduced signal due to injection footprint spreading; Bottom: flowchart of MDA's enhanced CO_2 sequestration/Oil&gas solution

For ENVISAT, the critical baseline is about 1200m; however, severe spectral decorrelation is already

visible at 800m baseline. Therefore, only interferograms with a perpendicular baseline less than 800m were processed resulting in a total of 1096 interferograms for Track-65 and another 628 for Track-294. We utilized precise orbits from the DORIS sensor, but still observed residual fringes resulting from slight orbit inaccuracies. We fine-tuned the orbits using in-house algorithms that estimate the baseline error corresponding to the residual fringes, and infer the correct orbits therewith.

Next, we generated and removed a long range Atmospheric Phase Screen (APS) from each interferogram, leaving the motion region intact. This corrected the background atmospheric trends and fully revealed the motion signature manifesting in each interferogram. Also, the short scale atmospheric signal—caused by strong atmospheric convection currents—became visually evident as small pits and bubbles strewn across the image. Since the ensuing network inversion step depends upon reliable phase unwrapping, we developed a customized phase unwrapper that utilizes coherence thresholding, coherence modulation, light/strong spectral filtering, minimal cost flow (MCF) unwrapping, demodulation, and interpolation. We successfully unwrapped the Track-65 interferograms using a novel stack based automated algorithm to correct (a small number of) erroneous branch cuts.

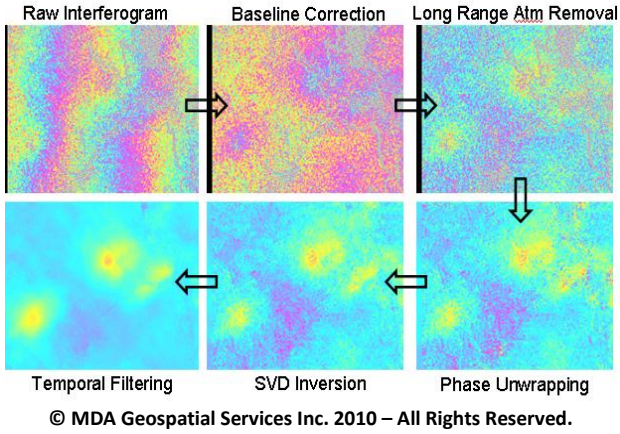

Figure 4 - Production steps (original CO_2 sequestration solution)

Following the parameterized of the full network of unwrapped interferograms and inverted using a Singular Value Decomposition (SVD) method, the authors spatio-temporally referenced the inverted measurements to a chosen date and region. The SVD output represents a statistically optimal deduction from all measurements for each date, and yielded a significant noise reduction over individual observations—previously noisy regions were populated with meaningful features, and deformation regions were better defined (Figure 4).

However, the temporally random short-scale atmosphere still persisted in each measurement layer. A low pass temporal filter was designed that could retain the temporally smooth displacement signal even over an irregular time grid, and expel the atmospheric signal. Although the filter was strictly temporal, it improved the spatial correlation in each layer and de-noised the deformation bulges.

As CO_2 injection progressed the surface uplift footprint has spread over a large area. This lead to a reduced signal for an equal amount of injected CO_2. To better capture this reduced signal, we introduced a number of enhancements to the processing flow (Figure 3, bottom). The most important of those were a topographic correction for each pixel (Figure 5), the introduction of 3D (stack-based) phase unwrapping corrections, and a new algorithm for the post-inversion temporal filter (Figure 6).

The temporal filter was carefully tuned to retain the peaks and troughs of the deformation signal at each

pixel, while culling the erratic observations attributable to atmosphere. After comparing corresponding traces in Track-65 versus Track-294, it became evident the performance of this filter scales with the number of temporal samples comprising its abscissa. In order to achieve further atmospheric suppression, the two ENVISAT stacks were co-registered in SAR coordinates and all phase measurements were projected from the Track-294 geometry to Track-65 geometry. Thereafter, we co-inverted the interleaved dataset in a statistically optimal manner, and applied the same temporal filter to the fused displacement time series at each pixel.

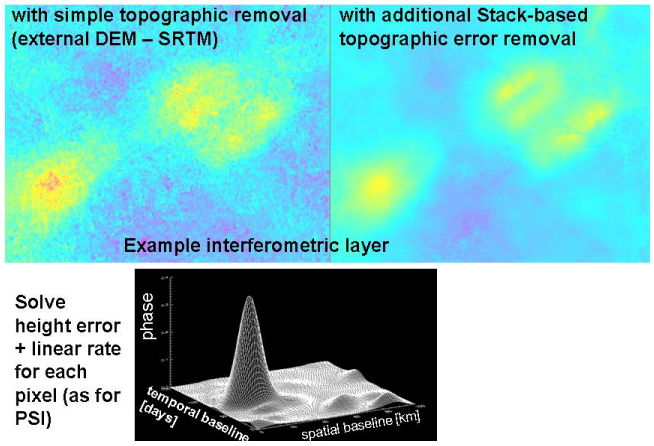

Figure 5 - Topographic correction enhancement

This statistically denser dataset inversion and filtering achieved appreciably greater atmospheric suppression, as some of the residual atmospheric wobbles in the individual data stacks were successfully flattened. This also set the stage for future co-inversion across sensors, providing progressively improved atmospheric attenuation and seamless temporal continuity with historical motion measurements.

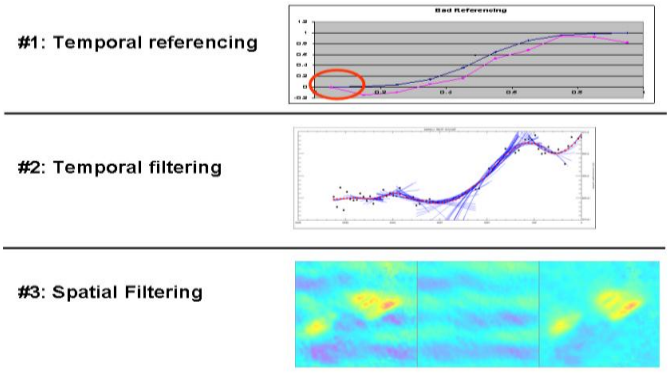

Figure 6 - Post-network inversion enhancements

4. RESULTS

The full surface motion profile over the period of CO_2 injection was covered by the historic and project acquired ENVISAT data. These results are shown in Figure 7. The signal clearly identifies the regions of uplift and illustrates the cumulative uplift mimicking the underlying lithography.

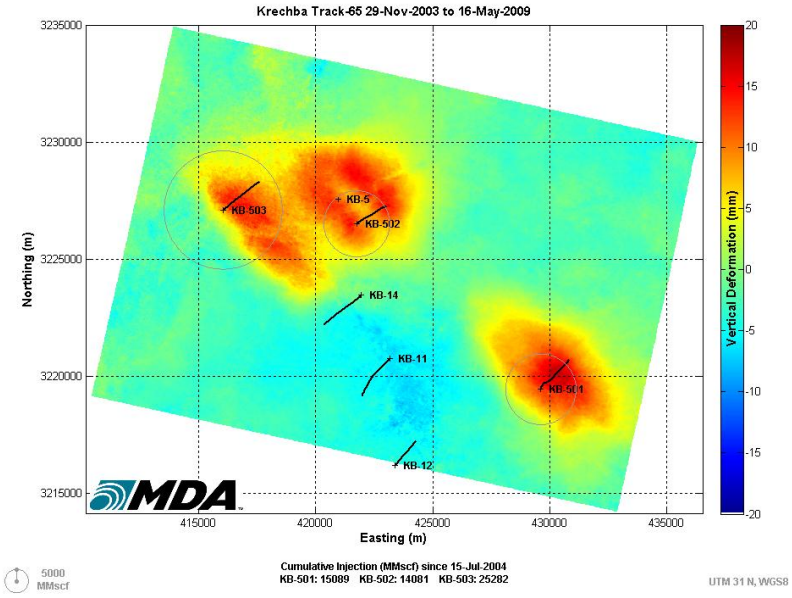

Figure 7 - Surface uplift (mm) from 2003 to 2009

The current displacement maps generated through the co-inverted data stacks were integrated into a transparent visualization that overlaid the cumulative CO_2 injection data on top of the motion fields. The positive correlation of the injection volumes with surface motion was unmistakable.

In 2010 the RADARSAT-2 dataset was fully processed with the same methodology described in this paper. Further refinements were required to remove the short range atmospheric effects but in general the process was found to be robust. The results of the ENVISAT and RADARSAT data are very similar for the identical monitoring periods as is shown in Figure 9.

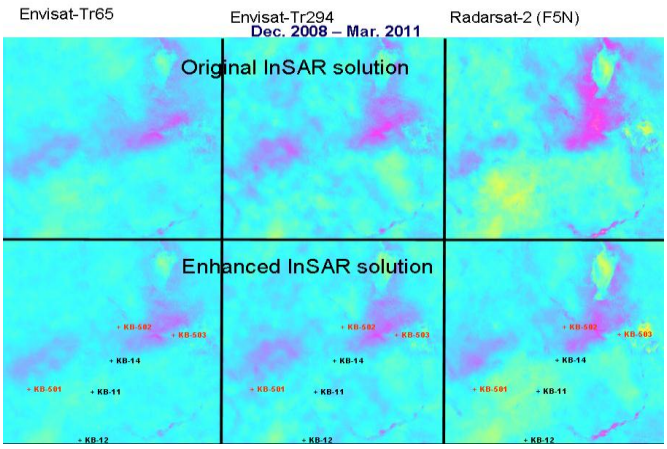

Figure 8 - Surface uplift (mm) from 2008 to 2010

To better understand the surface expression of the CO_2 injection a 3D seismic program was carried out over the two northern injection wells (Ringrose et al., 2010). A detailed examination of the InSAR

measured surface uplift revealed excellent alignment of the ceiling of the 20 m thick injection zone and the surface uplift. Figure 8 shows the surface motion from the InSAR analyses draped over the seismic return of the top of the 20 m saline injection layer 1980 m below the surface.

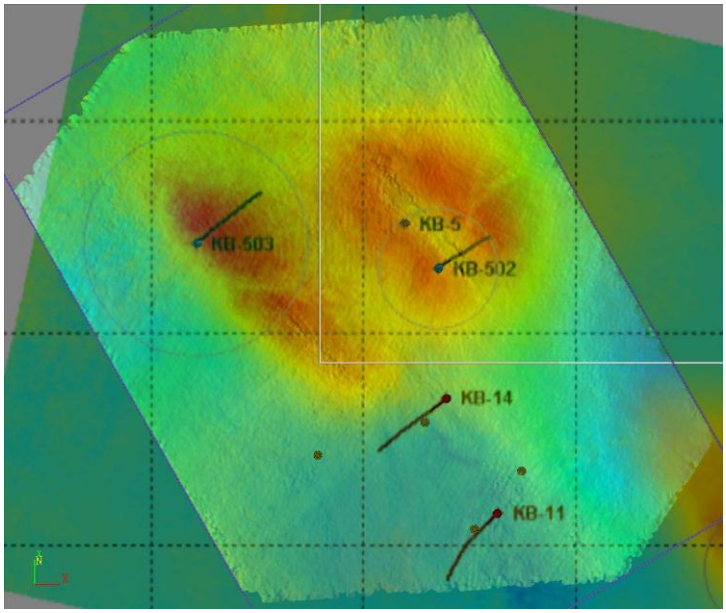

Figure 9 - InSAR results laid over the 2009, 3D seismic of the 20 m injection layer (Wright et al. 2010)

The magnitude of vertical motion that manifests per unit of injected gas is variable across the injection sites, depending upon underground rock mechanics specific to a site.

Profiles of the temporal motion can be compared across stacks and across sensors. Figure 10 illustrates the excellent collaborating results from four independent datasets from two different sensors.

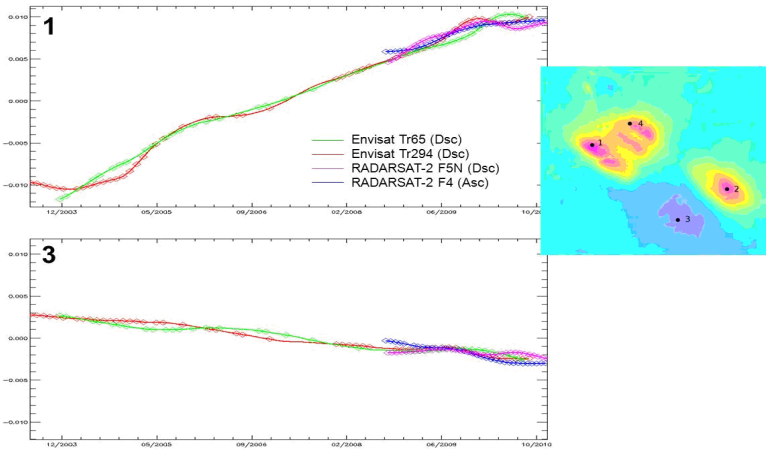

Figure 10 - Motion profiles for ENVISAT (2003 -2010) and RADARSAT 2 (2008 – 2010)

5. CONCLUSIONS

We have enhanced our Network Inversion InSAR method that was successfully used to measure uplift from CO_2 injection in the early stages of the In Salah project. As with the previous solution all possible phase measurements in an InSAR data stack are statistically inverted to deduce an optimal displacement time series for each pixel

The enhanced system includes a number of added or improved features. These include: improved spatial and temporal referencing; a novel topographic correction; a 2+1D phase unwrapping, as well as novel adaptive spatio-temporal atmospheric filtering to attenuate further the short scale atmospheric signal peculiar to the In Salah environment

A realistic error model has been derived that yields a cumulative error map for each displacement layer, which was validated by inter-stack comparisons. Individually processed ENVISAT and RADARSAT-2 displacement series consistently agree to better than 0.6 mm per year for a several months temporal overlap of the image stack.

Comparison of results for the opposite side RADARSAT viewing geometries suggests a non-negligible horizontal component of the motion signal, in addition to the vertical component that was previously measured.

The two ENVISAT and one of the RADARSAT data stacks (same side) can be fused, co-inverted, and co-filtered to further enhance the effectiveness of the temporal filtering. The cumulative CO_2 injection volumes are overlaid on the motion maps, and the correlation between these two independent datasets is readily apparent.

The enhanced InSAR solution has roughly four times higher accuracy than the original solution. Displacement maps produced with the enhanced solution from individual ENVISAT data stacks have accuracies of better than 0.4 mm at spatial and temporal resolution of 90 m (ca. 3 resolution cells) and 150 days (ca. 5 satellite repeat intervals), respectively.

The enhanced method captures signal after uplift magnitudes have been reduced due to reservoir maturation and also in the post-injection phase therefore, we can conclude that (at the least for semi-arid areas) InSAR observation of surface uplift (in conjunction with deformation modeling based on geological and structural information) is method of choice for monitoring the volumetric spread of CO_2 sequestered underground.

6. REFERENCES

FERRETTI, A., FUMAGALLI, A., NOVALI, F., PRATI, C., ROCCA, F. and RUCCI, A., 2011. A New Algorithm for Processing Interferometric Data-Stacks: SqueeSAR. IEEE Trans. Geosci. Remote Sens., 49(9), 3460 – 3470.

RABUS, B., and GHUMAN, P., 2009. A Simple Robust Two-Scale Phase Component Inversion Scheme for Persistent Scatterer Interferometry (Dual-Scale PSI), Canadian Journal of Remote Sensing, 35(4): 399- 410.

RABUS, B., GHUMAN, P. and MACDONALD, B., 2009. Monitoring CO_2 sequestration with a network inversion InSAR method. In: AGU Meeting of the Americas.

RINGROSE, P.S., ROBERTS, D.M., GIBSON-POOLE, C.M., BONDC, C., WIGHTMANC, R.,

TAYLOR, M., RAIKES, S., IDINGA, M. and ØSTMO, S., 2010. Characterisation of the Krechba CO_2 storage site: critical elements controlling injection performance. Energy Procedia.

WRIGHT, I., MATHIESON, A., BISHOP, C. and RIDDIFORD, F., 2010. Industrial-Scale CCS Operation at In Salah, Algeria: GHGT 10.

KEYNOTES

Microseismic Imaging and Hydrofracture Numerical Simulations

Will S. Pettitt
Itasca Consulting Group, Inc.
Jim F. Hazzard
Itasca Consulting Group, Inc.
Branko Damjanac
Itasca Consulting Group, Inc.
Yanhui Han
Itasca Consulting Group, Inc.
Matt Pierce
Itasca Consulting Group, Inc.
Tatyana Katsaga
Itasca Consulting Group, Inc.
Peter A. Cundall
Itasca Consulting Group, Inc.

ABSTRACT: Fracture Network Engineering (FNE) is the engineering design of rock mass disturbance through the use of advanced techniques to model fractured rock masses numerically, and then correlate field observations with simulated fractures generated within the models. Microseismic (MS) monitoring is a standard tool for evaluating the geometry and evolution of the fracture network induced during a hydraulic treatment, principally by source locating MS hypocenters and visualizing these with respect to the treatment volume and infrastructure (Figure 1). The integrated use of Synthetic Rock Mass (SRM) modeling of the hydrofracturing with Enhanced Microseismic Analysis (EMA) provides a feedback loop in which the SRM is constrained by the information provided by the MS data and the in-situ behavior of the fracture network is better understood, leading to informed decisions on future field operations. This paper discusses the technologies used in FNE and some of the developmental challenges we face in order to provide a more efficient and robust application of the approach. One particular challenge is the accurate representation of MS source data within the models (locations, magnitudes and mechanisms), and the ability to correlate these data effectively with field results. This challenge is being overcome by the development of more efficient numerical modeling algorithms, providing simulations in three dimensions at reservoir scale, combined with validation of these algorithms using laboratory and field case studies.

1. INTRODUCTION

Hydraulic treatments are now widely used to engineer a fractured rock volume. Use of the technique is likely to expand greatly over the coming years to meet society's demand for natural resources, and to increase the economic viability of these resources as they become more difficult to extract. In mining, hydraulic fracturing is used to pre-condition the mined volume and is used to dissipate stresses away from underground structures. In petroleum, the use of hydraulic fracturing is widespread in unconventional gas and oil plays, which rely on the induced fracture network to enable extraction through the low permeability reservoirs. In an Engineered Geothermal System (EGS), hydraulic treatments are used to exercise and enhance the natural fracture network. This is done either to increase flow rates of hydrothermal fluids, or to enable circulation of injected fluids in a Hot Dry Rock (HDR) environment or where the natural hydrothermal system needs recharging. Fluid injection in rock reservoirs also is used for the permanent storage of CO_2 in order to abate the emissions of greenhouse gases from large single-point sources and mitigate the potential environmental impact of the predicted growth in these emissions.

In petroleum and EGS applications, the objective of hydraulic fracturing is therefore to engineer the reservoir rock properties by inducing new fractures and enhancing the existing fracture network for permeability. However, the fundamental behavior of how this is achieved in practice is not well understood and is the focus of much research and development across both the research and commercial communities. It is apparent in observations from field monitoring, such as Figure 1, that the presence of existing fracture networks significantly affects, and may control, the history of hydraulic treatments. Existing fractures allow pathways for treatment fluids to migrate efficiently through the formation, stimulating connectivity to larger rock volumes (e.g., the so-called "sweet spot" in unconventional shale gas plays). It is this interest in the propagation of hydraulic fractures, and their interaction with the natural fracture network, formation geology and stress field, that is generating great interest in combining geomechanical computer modeling with MS field observations.

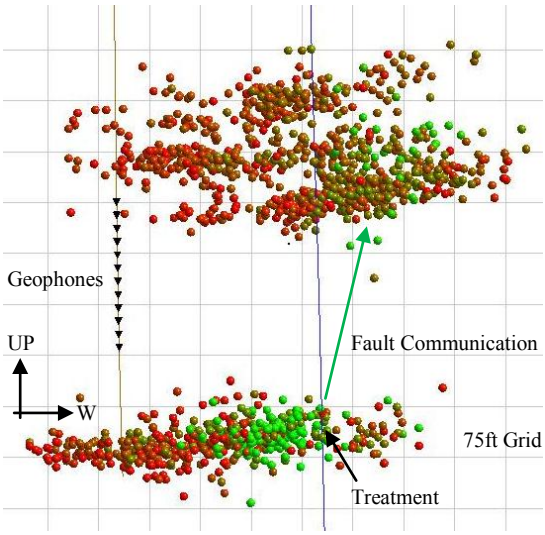

Figure 1 - Hydraulic fracturing of a tight gas sand at 13,000-ft depth describing vertical fault communication. Events are color shaded by time: earliest (green) to latest (red). From Pettitt et al. (2009)

Geomechanical models provide a simulation of rock disturbance for a given engineering project or experiment using assumptions on the rock behavior, a priori information on geological parameters and a description of the engineering or experimental changes being induced in the modeled system. The simulated disturbance can be localized on existing fractures or in the rock matrix depending on the modeling software capabilities, and can be compared with the MS observations or other physical data for validation. Through this approach, our understanding of the rock behavior can be informed by how well the model results match the field or laboratory observations, within the uncertainties of the model inputs and data. The field or laboratory observations also can be interpreted better through knowledge of the mechanics operating within the models.

Fracture Network Engineering (FNE) builds on this combination of technologies (Pettitt et al., 2011). In FNE, a forward-looking analysis simulates how a given fracture network behaves under different modeled conditions, using the design criteria for the field project in hand to engineer the most effective fracture network required for the purpose (Figure 2). A suite of numerical models forms a sensitivity analysis that can be correlated with known data from the field, and can be used in a feedback loop for improved engineering design in the future. This use of engineering design using numerical simulations is widespread in civil and mining engineering. It differs from the classical approach to hydrofracture design, as it uses the full complexity of the geomechanics involved in the reservoir and uses modeling techniques

that more accurately represent the physics of the problem where three-dimensional existing fracture networks are critical to the design. With improving computer technologies and processing algorithms, this FNE process potentially could be taken to real-time engineering feedback if correlation of simulated and observed MS could be implemented robustly; a technology that could have great potential in helping develop multi-stage hydraulic treatments in petroleum and geothermal applications in particular.

2. OBSERVATIONS OF HYDRAULIC FRACTURES

One of the key challenges with developing FNE technologies is the appropriate use of field observations. This challenge occurs in both the construction of the numerical models involved and in the comparison of output results with MS data in particular. The behavior of the numerical simulations is strongly impacted by the geometry of the Discrete Fracture Network (DFN) that is used to represent the in-situ discontinuity network. Fisher and Warpinski (2011) provide a summary of work performed during the 1970s and 1980s where hydraulic fractures were created and then mined through by galleries at the Nevada test site. Complexity in the hydraulic fracture propagation was observed, induced by geologic factors and the wellbore itself. Features such as layer interfaces and joints kink, offset, turn or terminate the fracture propagation. This leads to a range of induced fracture complexity depending on the local geology from the classical simple fracture through to a complex three-dimensional fracture network. Laboratory testing of hydraulic fracture propagation is being used to better describe the mechanics of the fracture interaction with pre-existing joints when intersecting at different angles, fluid pressures and joint characteristics (e.g., Gu et al., 2011; Chitrala et al., 2011).

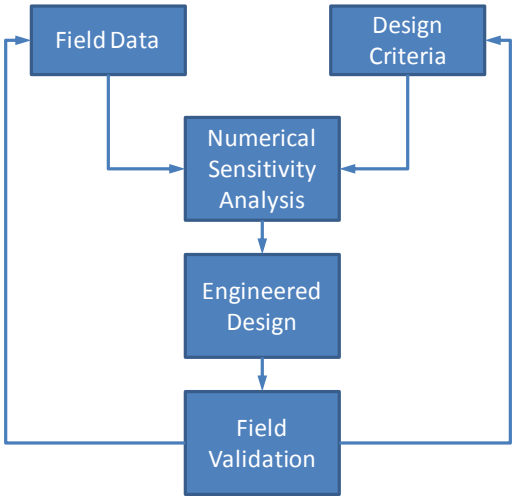

Figure 2 - The Fracture Network Engineering (FNE) design cycle

Passive MS monitoring is now a well-established method for imaging the effect of a downhole injection and the changes imposed on the fracture network. It potentially provides real-time feedback on the effectiveness of a hydrofracture stimulation, either through the mapping of the fracture progress using MS event locations computed from phase arrival times (e.g., Drew et al., 2005; Quirein et al., 2007), or by using waveform amplitudes to provide information on the mechanics of the fracturing (e.g., Maxwell et al., 2010; Pettitt et al., 2010). The location of MS events induced from the opening or reactivation of fractures within the reservoir during the hydraulic treatment provides first-order information on the position and extent of the exercised fracture network. Mayerhofer et al. (2011) describes MS observations from a group of horizontal wells in a shale gas reservoir. The wells used multi-stage completions side-by-side and showed the interference of hydraulic fracturing between the neighboring wells with interpreted natural fractures in particular (Figure 3). The complexity of the hydraulic fracturing process observed in

the field leads Warpinski (2012) to note three primary mechanisms for the occurrence of MS: a) induced stresses around the hydrofracture crack tip; b) leakoff of fluids into the natural fracture system; c) shearing on cross-cutting joints and faults (see also Maxwell and Cipolla, 2011).

More efficient location processing can be provided by applying algorithms that allow MS events with lower signal-to-noise ratios to be processed, utilizing events with smaller numbers of P-wave arrivals or single-phase events where generally only the S-waves are recorded. Pettitt et al. (2010) provides a summary of some advanced techniques used to analyze MS data with low signal-noise ratios. The objective is to achieve more efficient processing of observed field data in terms of the number and resolution of location results (by increasing the sensitivity of the processing while reducing uncertainties), and provide a meaningful interpretation of the microseismicity in terms of fracture network connectivity and structure. One outcome of this Enhanced Microseismic Analysis (EMA) is to provide data that can be correlated effectively with the numerical simulations using interpretation of the traditional location data combined with algorithms that use amplitude information and source parameters processed from the waveforms. Pettitt et al. (2009) investigate additional amplitude information through analysis of the Continuous Microseismic Record (CMR). The case studies presented used the continuous streams of MS amplitude data recorded during the hydraulic treatments of oil bearing reservoirs and illustrated that both P- and S-waves can be identified only for a small fraction of the seismic record, with most released seismic energy appearing as single phase triggers in the record. These triggers primarily are the more energetic S-waves depending on the specific source, path and receiver effects at the site.

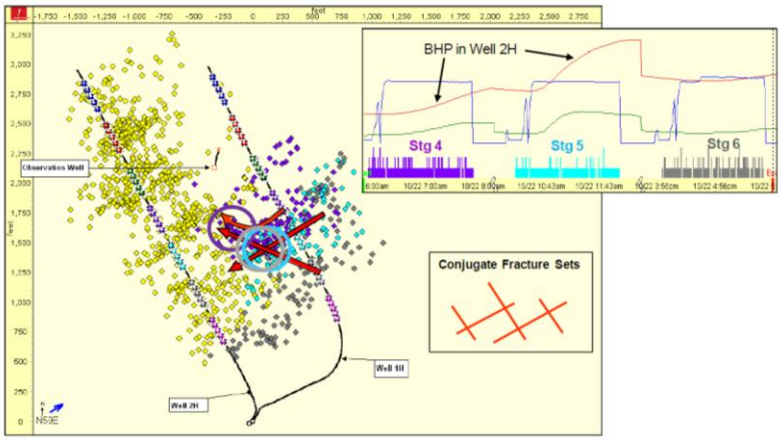

Figure 3 - MS location data from a multistage horizontal completion (plan view) describing potential lateral communication with fractures. From Mayerhofer et al. (2011)

Figure 4 shows a 75-minute section from a 5-hour data stream. In this case, the CMR is from data presented by Sharma et al. (2004) re-processed in terms of MS locations in Figure 1. The data is recorded on one channel from a triaxial geophone, of which there are 12 geophones in the downhole string – meaning that this data is 1 of 36 possible channels to examine. The full record consists of nearly 73 million samples total, recorded with a sampling rate of 0.25 milliseconds and is > 5 Giga-bytes of data in total. The time record consists of many thousands of individual MS events, as well as environmental and treatment noise, superimposed on the noise floor of the geophone-acquisition system. The frequency and energy characteristics contained in the continuous record can be interpreted in terms of fracturing scale and accumulated seismic energy release. It also can provide a means for diagnosing the quality of a particular data set, and then optimizing the processing of discrete MS events. In Figure 4, the injection period is clearly identifiable in the CMR. This initial pressuring up phase relates to the initial extension of

the hydrofracture and the fault communication that causes breakout between formations (green events in the inset). There is a clear decrease of high frequency components as this phase progresses. Higher frequency modes of failure are conceivable when the hydrofracture initially propagates due to the opening of relatively small isolated fractures, or breakage of asperities, which then coalesce to form larger propagating features that emit lower frequencies.

Thus, it is clear that any numerical modeling approach, performed with the objective of faithfully simulating the hydraulic fracturing process in a realistic manner, must consider the complexity of the geological media at a resolution appropriate to the sensitivity of the process. There is then a combined challenge of defining the natural fracture network input to the models from available field data and accurately developing the computational hydromechanics that is needed to mimic the treatment processes through the rock matrix and natural fractures. In petroleum applications, the input fracture data must rely on core logging, well logs and other geophysical measurements. In mining applications greater three-dimensional access to the fracture network often is achieved from excavated galleries so as to provide a more robust lateral description. However, while it may be possible to generally constrain joint orientations and joint density, quantification of joint size and shape remains a challenge. Until in-situ-characterization methods improve, it will be necessary in all situations to develop a range of DFNs (reflecting the uncertainty in the fracture data), and then provide sensitivity analyses in the numerical modeling approach for the given problem.

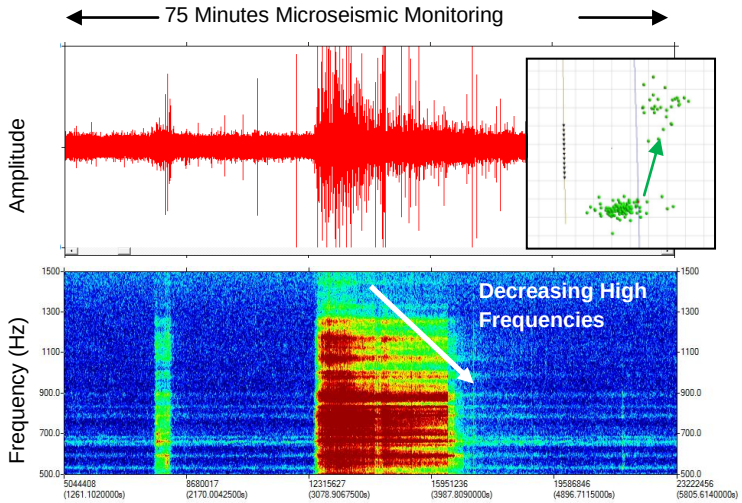

Figure 4 - Continuous Microseismic Record from the hydrofracture treatment presented in Figure 1 associated with fault communication. Top: Time record. Bottom: Corresponding frequency record (sonogram) – red areas relate to high amplitude-frequency spectra. Inset shows the microseismic event locations during this period. From Pettitt et al. (2009)

3. SYNTHETIC MICROSEISMICS

Distinct Element Modeling (DEM), part of a broader discrete modeling approach, offers the ability to model discontinuities explicitly in rock. Lemos (2011) provides a generalized summary of the technologies in this field. Typical DEM software is able to model the rock using blocks, particles or point masses (e.g., Figure 5). In software such as *UDEC* or *3DEC*, the rock mass is represented by an assembly of blocks that can slip relative to each other along contact planes. Slip on these discontinuities could be interpreted as seismic events. Cundall and Lemos (1990) describe a continuously yielding joint model in

UDEC and calculate energy release for slip on a fault near an advancing excavation. Bigarré et al. (1992) simulate seismicity in a *3DEC* model of a rockburst-prone coal mine. Several examples also exist of DEM of seismicity caused by fluid pressure changes (e.g., Guglielmi et al., 2008). Generally in all of these models, inelastic shear slip is related directly to seismic moments. The main problem with this approach is that seismicity is confined to a few pre-defined fault planes.

Another DEM approach is to use a Bonded Particle Model (BPM) as summarized by Potyondy and Cundall (2004). In Particle Flow Code (*PFC*), the distinct elements are non-uniform-sized circular or spherical particles bonded together at points of contact. Bonds can break under stress and energy is released and particles move as local stresses are redistributed. With this method, damage can form anywhere in the model and seismicity can be related directly to bond breakages (Hazzard et al., 2000). The simple laws at particle contacts lead to complex emergent behavior at the level of the full ensemble. Such behavior is found to reproduce most of the rich response of soils and rocks including fracture initiation, coalescence, propagation, and ultimately, failure of the material. A BPM not only captures the physics of rock fracturing and failure accurately, but also can be run dynamically so as to transmit seismic waves across the matrix.

Young et al. (2000) describes parallel investigations performed in rock testing in the laboratory and in numerical models using *PFC*. Acoustic Emission (AE) source mechanics are analyzed from laboratory data recorded during a true-triaxial compression test using a moment tensor inversion procedure (Pettitt et al., 1998) – AEs are equivalent to scaled MS occurring at higher seismic frequencies and smaller source dimensions. In Young et al. (2000), the source mechanics of fracturing observed in the laboratory were compared directly with source mechanics simulated in the BPM, and processed using the same moment tensor technique. A close qualitative correlation was observed in the mechanisms with the dominant mode of fracture being a mixture of shear and tensile component.

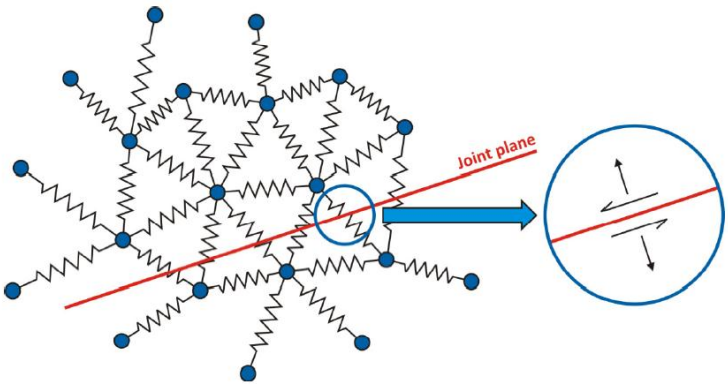

Figure 5 - Schematic of a lattice array of point masses (blue circles) and springs (resistors). A through-going discontinuity cuts certain springs. From Cundall (2011)

The BPM approach has been extended by Pierce et al. (2007) to include a Discrete Fracture Network (DFN) using a smooth-joint contact model that allows for slip. The smooth-joint logic captures the complex interaction of fracture surfaces and can include components to model the dynamic nature of seismic events. The assemblage of modeled rock matrix and fractures is called a Synthetic Rock Mass (SRM), allowing very large scale engineering problems to be addressed and the scaling of rock strength to be investigated (Pierce et al., 2009). With this approach, it is possible to consider both the sliding on pre-existing joints and the breaking of intact rock between joints. Simulated microseismicity (source locations and mechanisms) then can be processed into fracture network statistics using identical techniques as used on observed seismicity. Reyes et al. (2007) describe the application of this approach to the seismogenic

zone recorded around cave development at Northparkes Mine, Australia. The agreement between the simulated and observed data is able to identify the primary causal effects of the fracture network pattern produced in the field. Schöpfer et al. (2007) describes the use of a BPM for understanding the fracture network formation and structure in geological context which is an important step to characterization of fracture network properties.

The BPM also can simulate fluid injection using a fluid-flow network of pipes and reservoirs to provide hydraulic pressures in the matrix and fracture system. Hazzard et al. (2002) carried out an extensive series of modeling tests using this method without inclusion of pre-existing fractures so as to investigate the effect of several practical variables in hydraulic fracturing that may influence fracture propagation. Damjanac et al. (2010) apply the technique to a SRM and show that (i) injection fluid viscosity and pumping rate change the mode and path of fracture developments when attempting to hydraulically fracture rock containing natural fractures; and (ii) the hydraulic fracture did not propagate symmetrically on each side of the injection as is classically assumed, but instead followed a path defined by interaction with the pre-existing natural fractures.

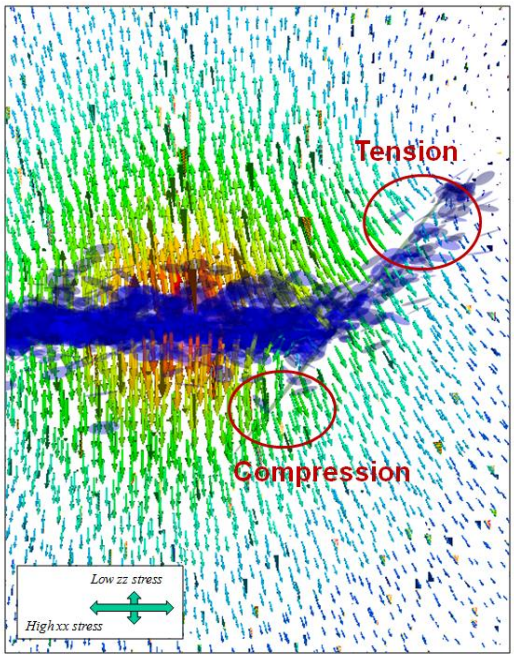

Figure 6 - Interaction of a growing hydraulic fracture with a single pre-existing joint in a 3D *LATTICE* model. Blue disks are fractures associated with failures of the lattice springs. The arrows indicate displacements of the point masses (red is high displacement). After Cundall (2011)

Cundall (2011) describes a new formulation of DEM that increases the computational efficiency of the technique in 3D models, and then describes applications to failure of slopes in open-pit mining, dynamic fracturing in rock blasting and hydrofracturing of naturally fractured rock masses in petroleum reservoirs. This formulation, called *LATTICE*, provides for mechanical, hydraulic and thermal coupling, and allows jointed behavior using the SRM approach. Cundall argues that most applications of the SRM technique do not exercise the intrinsic ability of the DEM to handle large deformations, because failure initiation in brittle rock commonly occurs at small strains. Thus, a simplification is possible, whereby finite-sized particles are replaced by point masses, and the contacts between particles are replaced by springs that may break (Figure 5).. An increase of five to ten times in execution speed is achieved (compared with the BPM approach of *PFC3D*). As in *PFC*, joints can be input at any orientation so as to mimic the in-situ

fracture network. The constitutive equations for the cut springs respect the direction of the joint plane rather than the local spring directions, and model slip and opening on that plane. For the other springs, new microfractures occur when loads in the springs reach given limits (corresponding to the tensile strength of rock). Synthetic MS events are formed in the model by new microfractures and failure on the joints following a similar approach to Hazzard et al. (2000).

Figure 6 presents a test model in *LATTICE* after Cundall (2011), showing the interaction between a growing hydraulic fracture and a pre-existing joint. As expected, the hydraulic fracture grows in the direction of high horizontal stress with displacements normal to this direction caused by the fluid pressurization (the view on the figure is a vertical cross section of a 3D model). Due to the dip direction on the existing joint, and the particular joint and matrix characteristics used in this case, the hydraulic fluids and joint disturbance is transmitted upwards once the hydraulic fracture meets the joint. This model is qualitatively consistent with the MS behavior from the field project observed in Figure 1. It is clear from the model why this behavior can occur; the orientation of the joint in relation to the induced hydraulic stresses means that the upper part of the joint is in tension, whereas the part below the hydraulic fracture is in compression. The fluid simply takes the path of least resistance.

4. PRACTICAL USE OF FRACTURE NETWORK ENGINEERING

The combination of SRM geomechanical modeling with results from field observations offers great potential to provide solutions to rock physics and engineering problems. In addition to the hydraulic fracturing context described here, it offers the ability to explore more fundamental issues of the scaling of rock strength and long-term rock behavior, amongst many others. The FNE approach outlined in this paper has been applied successfully in rock engineering problems; however, further effort is needed to develop it into an efficient and validated approach. As described earlier, the geomechanical models are sensitive to the input geological parameters, and precise localization of disturbance is dependent on the DFN. This can be overcome as multiple SRM computations can be made, each representing a different stochastic realization of input properties, in order to test the sensitivity of the model and also predict the variability and uncertainty in system response. This process is assisted by the use of high-quality field data that constrains the DFN as much as possible. One of the key features of FNE is to be able to correlate the simulated microseismicity with observed microseismicity from the field. For hydraulic fracturing, it then would be possible to develop robust design guidelines for engineering the fractures based on the in-situ stress conditions, realistic geological properties and field operational controls (such as pressure histories, proppant concentrations, etc.).

The FNE approach has been applied successfully using MS locations to characterize the observed fracture disturbance, including in many published studies described above.

Figure 7 shows a modeled horizontal completion for a multi-stage hydrofracture job in *LATTICE*. In this case, a generic set of rock properties have been used for illustration and a simplistic DFN of fractures orientated at 60^{o} to the maximum horizontal stress (σ_{Hmax}) direction. The resulting hydrofractures describe many of the same characteristics as observed in the field data (compare with Figure 3): hydrofractures initially propagate parallel to σ_{Hmax} and then intersect the joint network with subsequent fracturing following a new path; some hydrofractures propagate as a bi-wing from the injection port, others as a single wing, with stress shadowing and localized features around the simulated wellbore potentially playing a role; hydrofractures that intersect existing joints find fluid highways that may lead to greater extension into the rock volume.

Such a qualitative comparison using MS locations is one method of correlating numerical simulations with field observations; however, we are interested ultimately in developing a work flow that will allow

the FNE design process to be implemented quantitatively and efficiently. One method of achieving this using MS location is through fracture network statistics described earlier. Another great advantage of MS data is that field recordings contain a wealth of information based on signal amplitude and frequency measurements (rather than locations alone), including the CMR, source parameters (magnitudes, source dimension, stress drop etc), and moment tensors. It also was shown in previous studies described above that this type of information can be simulated using DEM. This leads to a need to develop new robust algorithms that accurately capture this information from the numerical models, and a need to provide greater validation of the source processes with laboratory and field data to give confidence that the simulated and observed results are comparable.

5. CONCLUSIONS

Observations from field monitoring indicate that the presence of existing fracture networks significantly affect, and may control, the history of hydraulic treatments. Existing fractures allow pathways for treatment fluids to migrate efficiently through the formation, stimulating connectivity to larger reservoir volumes. This paper examines the relationship between hydraulic treatments and fracture networks, and investigates the ability to engineer the hydraulic conductivity of the stimulated volume using a combination of MS imaging and numerical modeling. Interpretation of the MS results is improved via direct observation of the micromechanics within the distinct element models used.

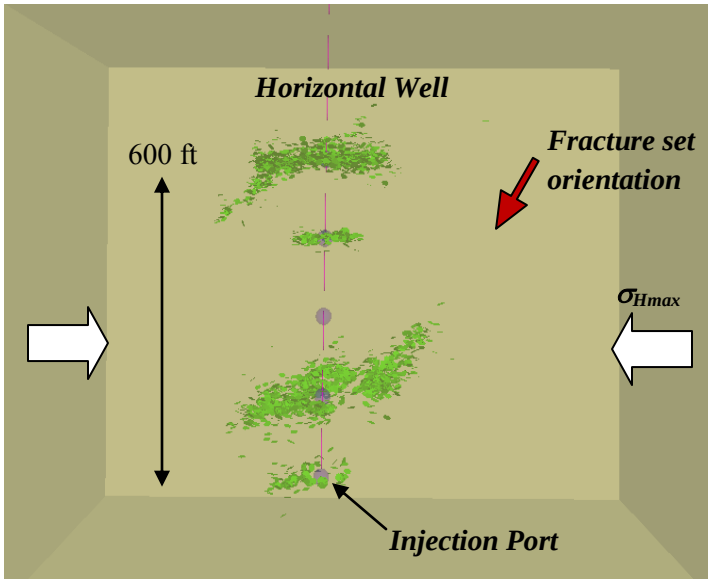

Figure 7 - A *LATTICE* numerical 3D model of a multi-stage horizontal completion with five injection ports (Plan View). A set of generic rock properties is used with an existing fracture network (not shown) orientated at 60° to σ_{Hmax} for illustration. Green disks are fractures associated with failures of the lattice springs

Microseismicity is the focus within FNE as it relates directly to the exercised fractures and can be correlated directly with the DEM matrix and joint slip within the SRM models. Although much has been achieved with MS location data, there is also a great amount of quantitative information that can be realized from MS amplitude and frequency characteristics in both the numerical simulations and field observations. Through this approach, practical implementation of real-time FNE could be achieved as numerical methods and data correlation techniques are developed to allow increased processing

efficiency. Such a technology would have great application to enhancing hydraulic treatments in rock engineering.

6. ACKNOWLEDGEMENTS

The authors would like to thank everybody within Itasca who has contributed to the development of the technologies presented here.

7. REFERENCES

BIGARRÉ, P., J. TINUCCI, K.B. SLIMANTE, J. PIGUET, and J. BESSON, 1992. 3-Dimensional modeling of fault-slip rockbursting. Acta Montana, 88, 81-90.

CUNDALL, P.A., and J.V. LEMOS, 1990. Numerical simulation of fault instabilities with a continuously-yielding joint model. In: Fairhurst, C. (Ed), Rockbursts and Seismicity in Mines. Balkema, Rotterdam, 147-152.

CUNDALL, P.A., 2011. Lattice method for modeling brittle, jointed rock, in Continuum and Distinct Element Modeling in Geomechanics — 2011 (Proceedings, 2nd International FLAC/DEM Symposium (Melbourne, February 2011), Paper 12-01, pp. 649-660. D. Sainsbury et al., Eds. Minneapolis: Itasca International Inc.

CHITRALA, Y., C. MORENO, C. SONDERGELD, and C. RAI, 2011. Microseismic and Microscopic Analysis of Laboratory Induced Hydraulic Fractures, SPE 147321, Canadian Unconventional Resources Conference, 15-17 November 2011, Alberta, Canada.

DAMJANAC, B., I. GIL, M. PIERCE, M. SANCHEZ, A. VAN AS, and J. MCLENNAN, 2010. A new approach to hydraulic fracturing modeling in naturally fractured reservoirs: Proceedings of 44th U.S. and 5th U.S.-Canada Rock Mechanics Symposium (Salt Lake City, June 2010), Paper No. ARMA 10-400.

DREW, J., D. LESLIE, P. ARMSTRONG, and G. MICHAUD, 2005. Automated microseismic event detection and location by continuous spatial mapping: Proceedings of SPE Annual Technical Conference and Exhibition, Dallas, Texas, USA, SPE 95513.

FISHER, K. and N. WARPINSKI, 2011. Hydraulic Fracture-Height Growth: Real Data, SPE 145949, SPE Annual Technical Conference and Exhibition, 30 October-2 November 2011, Denver, Colorado, USA.

GU, H., X. WENG, J. LUND, M. MACK, U. GANGULY, and R. SUAREZ-RIVERA, 2011. Hydraulic Fracture Crossing Natural Fracture at Non-Orthogonal Angles, A Criterion, Its Validation and Applications, SPE 139984, SPE Hydraulic Fracturing Technology Conference, 24-26 January 2011, The Woodlands, Texas, USA.

GUGLIELMI, Y., F. CAPPA, and D. AMITRANO, 2008. High-definition analysis of fluid-induced seismicity related to the mesoscale hydromechanical properties of a fault zone, Geophysical Research Letters, 35, L06306.

HAZZARD, J. F., R. P. YOUNG and S.C. MAXWELL, 2000. Micromechanical Modeling of Cracking and Failure in Brittle Rocks, Journal of Geophysical Research, 105(B7), 683-697 (2000).

HAZZARD J. F., R. P. YOUNG, and S. J. OATES, 2002. Numerical modelling of seismicity induced by fluid injection in a fractured reservoir: Mining and Tunnel Innovation and Opportunity, Proceedings of the 5th North American Rock Mechanics Symposium, University of Toronto Press, Toronto, 1023-1030.

LEMOS, J.V., 2011. Recent Developments and Future Trends in Distinct Element Methods — UDEC/3DEC and PFC Codes, in Proceedings, 10th International Conference on Analysis of Discontinuous Deformation (Honolulu, December 2011). Paper No. ICADD 1-02.

MAXWELL, S. C., J. RUTLEDGE, R. JONES, and M. FEHLER, 2010, Petroleum reservoir characterization using downhole microseismic monitoring: Geophysics, 75, no. 5, 75A129-75A137, DOI: 10.1190/1.3477966.

MAXWELL, S.C., and C. CIPOLLA, 2011. What Does Microseismicity Tell Us About Hydraulic Fracturing? SPE 146932, SPE Annual Technical Conference and Exhibition, 30 October-2 November 2011, Denver, Colorado, USA.

MAYERHOFER, M.J., N.A. STEGENT, J.O. BARTH and K.M. RYAN, 2011. Integrating Fracture Diagnostics and Engineering Data in the Marcellus Shale, SPE 145463, SPE Annual Technical Conference and Exhibition, 30 October-2 November 2011, Denver, Colorado, USA.

PETTITT, W. S., J. M. REYES-MONTES, B. HEMMINGS, E. HUGHES, and R. P. YOUNG, 2009. Using continuous microseismic records for hydrofracture diagnostics and mechanics: Proceedings of the SEG International Exposition and Seventy-Ninth Annual Meeting, Houston, USA.

PETTITT W. S., J. M. REYES-MONTES, J. ANDREWS, and R. P. YOUNG, 2010. Enhanced Imaging of Hydraulic Fracturing through Induced Seismicity: Proceedings of 44th U.S. and 5th U.S.-Canada Rock Mechanics Symposium, Salt Lake City, Utah.

PETTITT, W., M. PIERCE, B. DAMJANAC, J. HAZZARD, L. LORIG, C. FAIRHURST, I. GIL, M. SANCHEZ, N. NAGEL, J. REYES-MONTES and R. P. YOUNG, 2011. Fracture Network Engineering for Hydraulic Fracturing, The Leading Edge, 30(8), 844-853, doi 10.1190/1.3626490.

PIERCE, M., P. CUNDALL, D. POTYONDY, and D. MAS IVARS, 2007. A synthetic rock mass model for jointed rock: Rock Mechanics: Meeting Society's Challenges and Demands (1st Canada-U.S. Rock Mechanics Symposium, Vancouver, May 2007), Taylor & Francis Group, v. 1: Fundamentals, New Technologies & New Ideas.

PIERCE M., D. MAS IVARS, and B. SAINSBURY, 2009. Use of Synthetic Rock Masses (SRM) to investigate jointed rock mass strength and deformation behavior: Proceedings of the International Conference on Rock Joints and Jointed Rock Masses, Tucson, Arizona, Paper 1091.

POTYONDY D. O., and P. A. CUNDALL, 2004, A bonded-particle model for rock: International Journal of Rock Mechanics and Mining Sciences, 41, 1329-1364.

QUIREIN, J. A., C. KESSLER, J. M. TRELA, S. ZANNONI, B. CORNISH, R. J. BREWER, D. GORDY, W. S. PETTITT, C. B. WALKER, J. LANEY, and R. P. YOUNG, 2007. Microseismic monitoring of a re-stimulation treatment to a Permian basin San Andres dolomite horizontal well: Proceedings of SPE Annual Technical Conference and Exhibition, Anaheim, California, USA, SPE 110333.

REYES-MONTES, J. M., W. S. PETTITT, and R. P. YOUNG, 2007. Validation of a Synthetic Rock Mass model using excavation induced microseismicity: Rock Mechanics: Meeting Society's Challenges and Demands (1st Canada-U.S. Rock Mechanics Symposium, Vancouver, May 2007), Taylor & Francis Group, v. 1: Fundamentals, New Technologies & New Ideas, 365-369.

SCHÖPFER, M. P.J., C. CHILDS and J. J. WALSH, 2007. Two-Dimensional Distinct Element Modeling of the Structure and Growth of Normal Faults in Multilayer Sequences: 1. Model Calibration, Boundary

Conditions, and Selected Results, Journal of Geophysical Research, 112(B10401), doi:10.1029/2006JB004902.

SHARMA, M. M., P. B. GADDE, R. SULLIVAN, R. SIGAL, FIELDER, D. COPELAND, L. GRIFFIN, and L. WEIJERS, 2004. Slick water and hybrid fracs in the Bossier: Some lessons learnt: Proceedings of SPE Annual Technical Conference and Exhibition, Houston, Texas, USA, SPE 89876.

WARPINSKI, N., 2012, Keynote Speech "Measurements of Hydraulic-Fracture-Induced Seismicity in Gas Shales" at SPE Hydraulic Fracturing Technology Conference, 6-8 February 2012, The Woodlands, Texas, USA.

YOUNG, R. P., J. F. HAZZARD and W. S. PETTITT, 2000. Seismic and Micromechanical Studies of Rock Fracture, Geophysical Research Letters, 27(12), 1667-1670.

Wireline Hydraulic Mini-frac Testing: Experiences in the ANDRILL SMS Borehole, McMurdo Sound, Antarctica

Douglas R. Schmitt
University of Alberta
Terry J. Wilson
Ohio State Universitys
Richard D. Jarrard
University of Utah
Timothy S. Paulsen
University of Wisconsin
Simona Pierdominici
Int. Nazionale di Geofisica e Vulcanologia
David Handwerger
Terra-Tek: Schlumberger
Thomas Wonik
Leibniz-Institut für Angewandte Geophysik

ABSTRACT: In general, knowledge of the state of stress within the Antarctic lithosphere remains largely unconstrained due in part to Antarctica's inaccessibility and because of the paucity of seismic focal mechanism solutions. As such, an important component of the ANDRILL project was to acquire new information on the stress directions and magnitudes within the upper crust. Extensive fracture mapping of the core and oriented ultrasonic televiewer logging were carried out to provide strong constraints on both stress orientations and the faulting regime. The first hydraulic fracturing stress determinations in Antarctica were also carried out to provide complimentary stress magnitudes. These measurements were accomplished using a wire-line transported hydraulic fracturing system consisting, essentially, of two synthetic polymer packers that were inflated to isolate the 1-m long pressurization interval. The tests were conducted at the end of the drilling and logging in a ~130-m section specially drilled below 1000 mbsf (nearly 1500 m from the rig floor) for hydraulic fractures. This zone was drilled primarily through competent, dense, and low permeability diamicts. The core fracture and televiewer logging information was used to site twenty separate measurements. Classic hydraulic fracturing pressurization records with unambiguous breakdown and fracture closure pressures were obtained in about half of the measurements. The remaining tests provided fracture propagation and closure pressures that are consistent with the classic breakdown curves, but they did not include a clear breakdown pressure and are indicative of the reopening of either natural or drilling induced fractures in the wellbore wall. The preliminary analysis of the results are in generally good agreement with the stress directions indicated by the core fracture logging and the stress regime suggested by the character of the drilling induced core fractures.

1. INTRODUCTION

One of the principle scientific rationales for the Antarctica Drilling program (ANDRILL) is to obtain new information on the state of stress in Antarctica, of which there is still little known. On the World Stress Map there are only a few scattered points within the Antarctic plate ; and most of the constraints come from earthquake focal mechanisms along the Antarctic plate boundary (Figure 1) although a few thrust focal mechanisms are found north of West Antarctica (Okal 1980; Kreemer and Holt 2000). *Haderka et al*., (2009) used, as an exercise for a stress modelling technique, the plate boundary earthquake constraints to calculate the stress states in the Antarctic plate. Further, the March 25, 1998 Antarctic plate

earthquake (62.88˚S, 149.53˚E) north of East Antarctica and its subsequent aftershocks is unusual both because it was the largest oceanic intraplate earthquake recorded with a moment magnitude *Mw* of 8.1 and because it has a primarily strike slip mechanism that is not in accord with ridge-push stresses. Modelling of the stresses in the plate suggests that deglaciation may strongly influence the crustal state of stress in this region (Kreemer and Holt 2000).

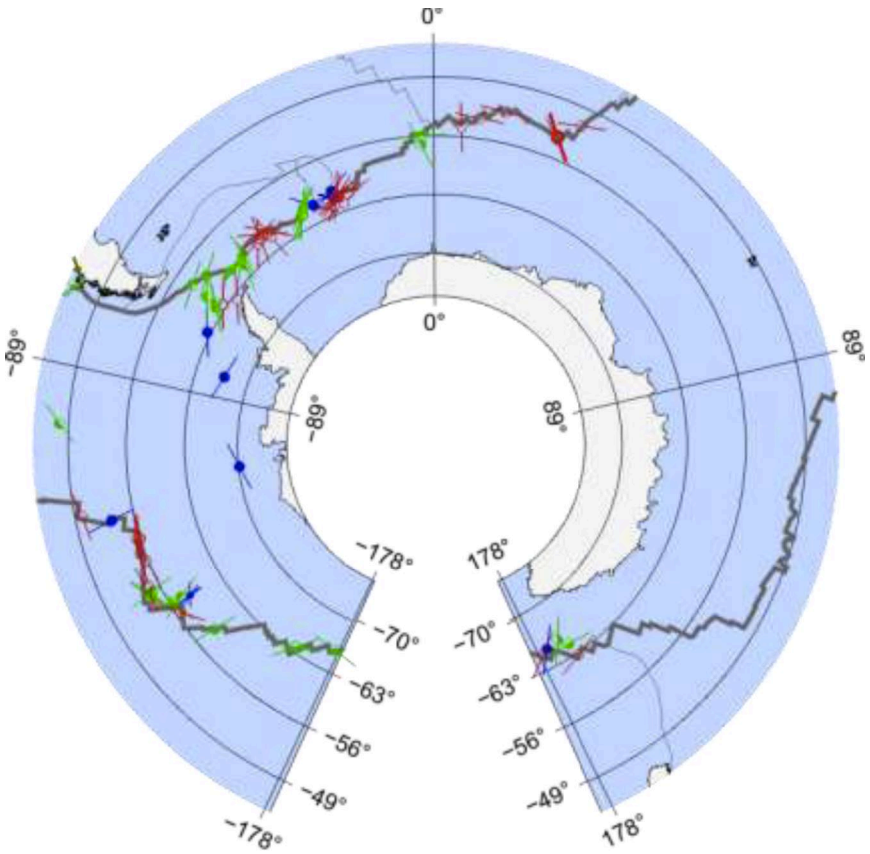

Figure 1 - Stress data from the World Stress Map (Heidbach, Tingay et al. 2008) in the Antarctic Plate. Blue, red, and green symbol represent thrust, normal, and strike-slip focal mechanisms directly with the orientation indicating the direction of the greatest horizontal principal compressive stress. Map made using CASMO 2.0 (Reinecker, Heidbach et al. 2005)

Drilling in Antarctica is similarly sparse and for treaty purposes only scientific investigations are allowed. Drilling projects are also costly and technically and logistically challenging. Most of the Antarctic drilling has occurred in the vicinity of McMurdo (U.S.A.) and Scott (N.Z.) Stations. Analysis of the natural and induced core fractures (Wilson and Paulsen 2000) and ultrasonic borehole televiewer images (Moos, Jarrard et al. 2000) occurred during the Cape Roberts drilling program. Stresses in the McMurdo region, however, are locally complicated by the extensional opening of McMurdo Sound, the existence of the Transantarctic Mountains, loading of the lithosphere by volcanism, and shorter term glacial advances and retreats.

In order to provide further constraints on the true states of stress in this region, the Antarctic Drilling Program (ANDRILL) included quantitative measurements by hydraulic fracturing. Open-hole min-frac tests were carried out in highly indurated and low permeability glacial diamicts during the South McMurdo Sound (SMS) drilling season. Drilling at SMS occurred from the surface of an 8-m thick zone

of fast sea ice. Here, we overview some of the technical issues arising from this work and provide illustrative examples of field data obtained leading to an interpretation of the quantitative stress values.

2. SYSTEM DESCRIPTION

2.1 Wire-line Hydraulic Fracturing System Overview

These measurements were accomplished using a wire-line transported hydraulic fracturing system developed for ANDRILL by Downhole Systems Inc (New York), consisting, essentially, of two synthetic polymer packers (Baski Inc., Colorado) that were inflated to isolate the 1.4 m long pressurization interval (Fig. 2) topped off with an instrument package containing two submersible pressure transducers to measure directly the down-hole interval and packer pressures. The length of this tool as measured from the top of the rock catcher to the bottom of the stub is 645 cm long for the NQ core configuration that produces a nominal 76 mm diameter borehole. The down-hole tool diameter is 66 mm when NQ packers are attached.

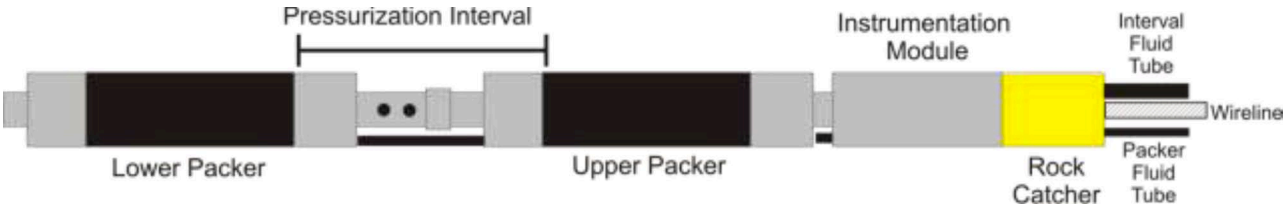

Figure 2 - Simplified diagram of the wire-line packer system

The tool is supported in the drill hole by a 7-conductor, 2 km long wire-line. Two high pressure flexible tubing cables (also 2 km long) provide fluid individually to the packers and to the interval. During deployment, these two hoses are taped using high strength electrical tape to the wire-line at about 5 m increments as the tool is lowered into the wellbore. The pressures are provided by a pump and series of control valves at the surface that direct pressurization and release of pressure through the hoses.

The fracturing fluid consisted of a mixture of sea-water and pharmaceutical grade glycol. This mixture was necessary to avoid potential freezing within the tubing at the surface and within the water column beneath the rig.

The control system provides digital output of the flow rates both in and out (upon release), the up-hole pressures for both the packer and the interval, and the down-hole pressures for both the packers and the interval. These latter two signals are sensed within the down-hole instrument packages and transmitted via the wire-line to the surface recording system. All six of these signals are continuously sampled at a rate of 0.1 seconds and recorded in a text file for later analysis.

The pressurization rate is manually controlled by an electronic clutch system that engages the pump to varying degrees. During a run, the down-hole interval pressure is visually monitored in real time via a graphic display on the data acquisition computer. This allows the operator to respond rapidly to cease pumping and ‘shut-in’ the interval once ‘break-down’ or fracture reopening is detected; this is accomplished by activating a kill switch.

2.2 Field Test Protocol

An ultrasonic borehole televiewer (BHTV) log was obtained immediately prior to any hydraulic fracture tests. The resulting images, together with the corresponding core images, were used to site the hydraulic tests. The highest priority sites were free from obvious natural fractures in either the core or the BHTV logs and the absence of drilling induced borehole fractures or breakouts in the BHTV logs. An example of one BHTV log (Figure 3. Left panel) obtained over a relatively clean section of the borehole displays a lack of features and was selected for one of the tests. These criteria could not always be satisfied, however, and in some cases zones that contained fractures were employed.

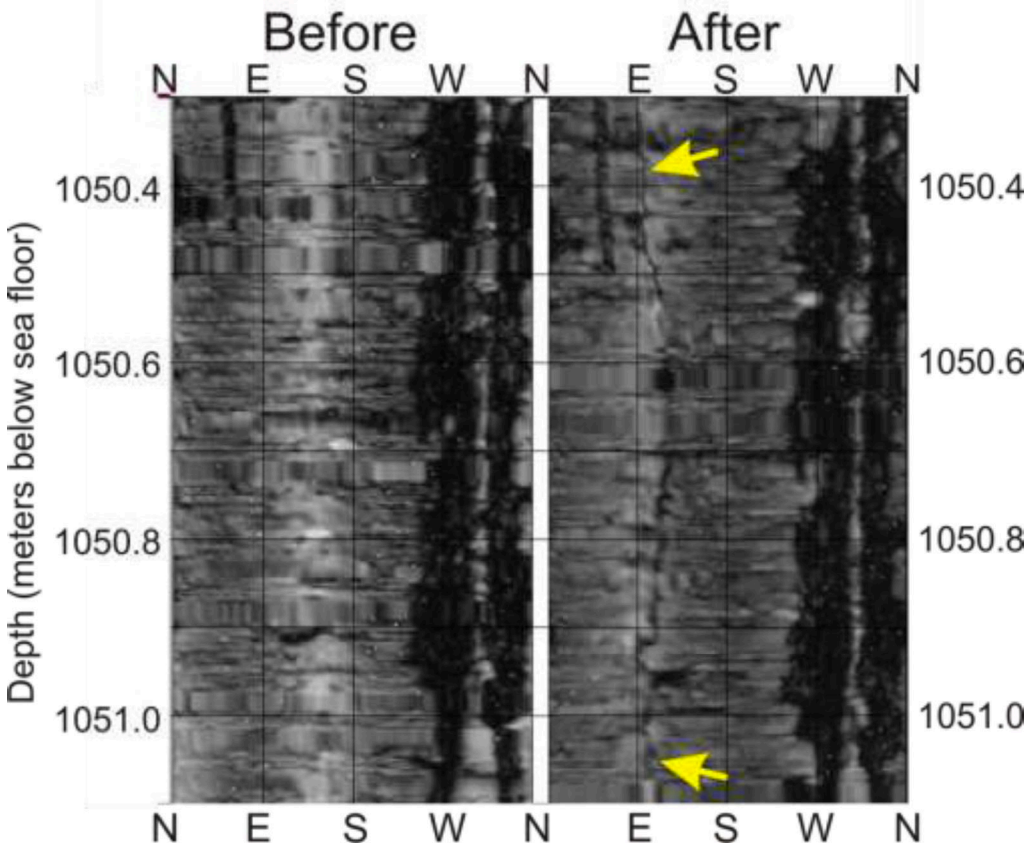

Figure 3 - Reflected amplitude ultrasonic borehole televiewer images of the borehole wall from 1050.3 m to 1051.1 m below sea floor (1439.8 m to 1440.7 m from drillers rig floor reference). Left and right panels are repeat logs taken before and after, respectfully, the hydraulic fracture test. Approximately east striking hydraulic fracture is highlighted by the yellow arrows in the After panel. These images are not corrected for stick-slip motion of the tool during logging. This stick-slip also resulted in small differences in the logged depths

Briefly, in a given test, the packer system was lowered to the depth determined according to the criteria above. The packers were then inflated to a pressure roughly equivalent to the estimated vertical in situ stress and allowed to set. The fracture interval was then pressurized at rates of approximately 10 MPa/minute as measured by the surface pressure transducer. Pressurization continued until breakdown or fracture re-opening was detected by a sudden decrease in the down-hole interval pressure, at which point the interval was shut-in. The interval remained shut-in for a period of 2 to 3 minutes in order to allow for equilibration of the pressure. At the end of this time, the interval pressure wave released back to

atmospheric pressure at the surface. This cycle was repeated three or more times. In the last pressurization cycle, the flow rate out to the interval was maintained a nearly constant rate giving a more graduate pressurization of about 2.5 to 3 MPa/minute in order to look for the more subtle changes upon fracture reopening.

Initially, 2 hours were budgeted for each test run. On the basis of experience, this time was shortened to less than 40 minutes per site.

3. FIELD TESTS

3.1 Observed Pressurization and Flow Records

The tests were conducted at the end of the drilling and logging in a ~130-m section specially cored below 1000 meters below sea floor (mbsf) for the series of hydraulic fractures. This zone was cored primarily through competent, dense, and low permeability diamicts (compacted glacial sediments). The core fracture and televiewer logging information was used to site twenty separate measurements of which 17 successful tests were conducted over a 20 hour period.

A typical pressurization curve with four cycles is shown in Fig. 4, which contains the time-pressure records sampled by four surface and down-hole pressure transducers. As well, the transient flow rates out to the interval (light green fill) and back to the surface from the interval (light red fill) are superimposed for comparison. It is important to note that both down-hole pressure records are contaminated with a transient noise with a period of approximately 1 min, the source of this noise is not known. That it may be connected to the transducers themselves is further suggested by the observation that the noise waveform appears on the two down-hole pressure transducers at different times and that this noise does not appear on any of the other recorded channels. This noise is problematic in that it nearly precludes more advanced analysis of the pressure-time curves.

It is interesting to compare the different responses of the surface and the down-hole transducers. The surface and down-hole packer pressures track one another with the main difference being only the change in hydrostatic head due to their elevations. More importantly, there is a substantial variation in the character of the interval pressure records that results from time lags between the two caused by viscous effects within the 2-km long tube. For example, on the first pressurization cycle in Figure 4 there the response of the surface transducer to break-down lags that of the down-hole pressure transducer by more than 5 seconds. Further, the drop in the surface transducer ‘break-down’ to a stable shut-in is more than 5.5 MPa whereas at the interval this difference is 2.2 MPa. Using the surface interval break-down alone would result in a significant error in estimation of the principal horizontal compression.

The viscous losses are also apparent because the surface interval pressures will lag in time the breakdown point. These often exceed the packer pressures also measured at the surface in contrast to the behaviour down-hole.

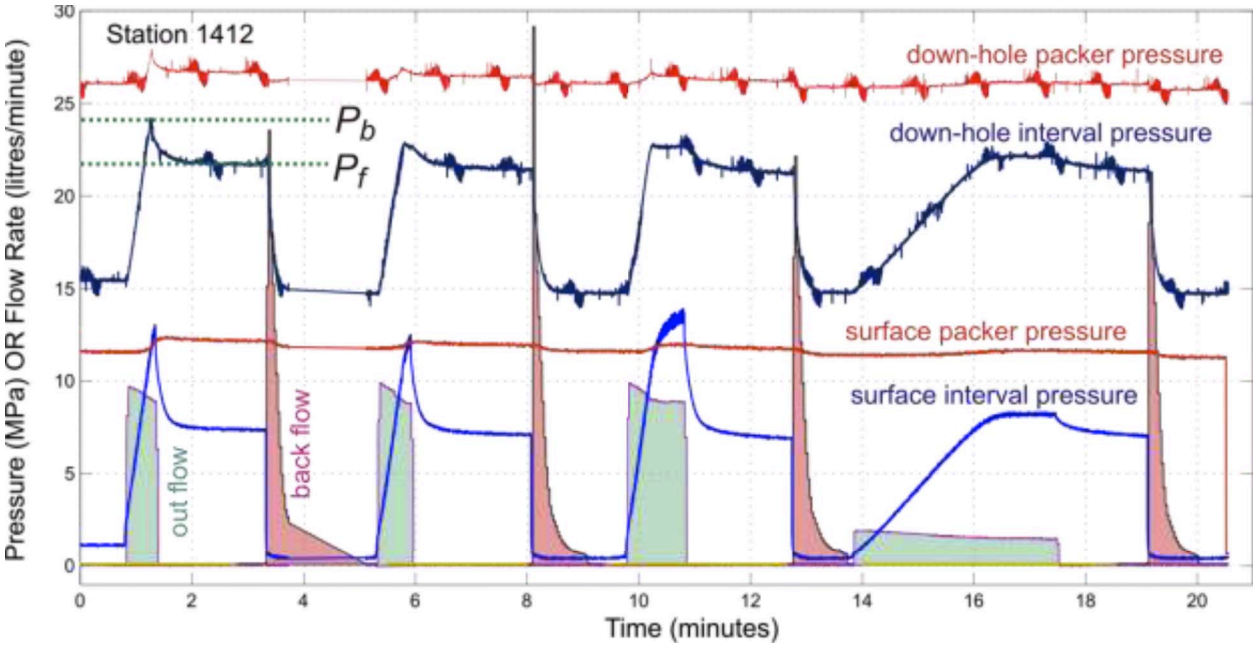

Figure 4 - Example of the recorded pressure and flow rate curves from the measurement site Station 1412 (taken at a wireline depth of 1412 m from the driller reference point on the rig). Six different channels are simultaneously recorded and include the responses of the down-hole packer pressure transducer (red), the down-hole interval pressure transducer (dark blue), the surface packer pressure transducer (cherry red), the surface interval pressure transducer (light blue), and the flow rates out-to (light green fill) and back-from (light red fill) the interval as measured by flow-meters at the surface

3.2 Interpretation of Pressurization Records for Stress Magnitudes

For this example curve, we interpret the break-down pressure P_b = 23.03 MPa and the fracture propping pressure P_f = 21.64 MPa. We take this latter pressure to represent the value of the minimum horizontal compression S_h. In this case with fracturing in low permeability, stiff sediments we assume two bounding break-down equations in order to delimit the value of the greatest horizontal compression S_H (e.g., Schmitt and Zoback 1989; Schmitt and Zoback 1993) either completely ignoring the influence of a formation pore pressure P_P or including it (at the value of the expected hydrostat for the given depth). This gives

$$3S_h - P_b \; > \; S_H \; > \; 3S_h - P_b - P_P$$

with a result that 41.9 MPa > S_H > 27.4 MPa constrains the maximum compression. The vertical stress S_V was determined from integration of the densities measured by Compton scattering γ ray scanning of the nearly complete set of core with S_V = 23.0 MPa. As such $S_H > S_V > S_h$ indicating that at this location a strike-slip faulting environment predominates, although this is not far from the normal faulting stress regime that might be expected on the basis of the local extensional geological structure. Examination of the BHTV records obtained suggest that SH is further oriented in an E-W direction (right panel Figure 3).

4. CONCLUSIONS

A wire-line hydraulic fracturing system was developed to carry out quantitative stress measurements as part of the ANDRILL project. This contribution only provided only briefly an overview of the technical aspects of the system and gave an example of the measurements from one station. In particular, the importance of down-hole pressure measurement was demonstrated. However, 17 successful stress measurements were made out of 20 attempts during this campaign; future contributions will describe these in more detail. The indurated glacial sediments are not dissimilar to many of the geological formations now being considered for studies of cap-rock integrity or unconventional hydrocarbon production; open hole fracturing in such smaller diameter boreholes may be practical for such stress evaluations in such formations. .

5. ACKNOWLEDGEMENTS

This material is based upon work supported by the National Science Foundation under Cooperative Agreement No. 0342484 through subawards administered and issued by the ANDRILL Science Management Office at the University of Nebraska-Lincoln, as part of the ANDRILL U.S. Science Support Program. Any opinions, findings, and conclusions or recommendations expressed in this material are those of the author(s) and do not necessarily reflect the views of the National Science Foundation. The ANDRILL Program is a multinational collaboration between the Antarctic Programs of Germany, Italy, New Zealand and the United States. Antarctica New Zealand is the project operator, and has developed the drilling system in collaboration with Alex Pyne at Victoria University of Wellington and Webster Drilling and Enterprises Ltd. Scientific studies are jointly supported by the US National Science Foundation, NZ Foundation for Research Science and Technology, Royal Society of New Zealand Marsden Fund, the Italian Antarctic Research Programme, the German Research Foundation (DFG) and the Alfred Wegener Institute for Polar and Marine Research (Helmholtz Association of German Research Centres). Antarctica New Zealand supported the drilling team at Scott Base; Raytheon Polar Services supported the science team at McMurdo Station and the Crary Science and Engineering Laboratory. The ANDRILL Science Management Office at the University of Nebraska-Lincoln provided science planning and operational support. Schmitt's research on this topic is currently funded by NSERC and the Canada Research Chairs program.

6. REFERENCES

HADERKA, P., GALYBIN, A.N. and MUKHAMEDIEV, S. A., 2009, Stress field in the antarctic tectonic plate: Elastic and plastic models, in Mesh reduction methods: Bem/mrm xxxi, C. A. Brebbia, Southampton, Wit Press/Computational Mechanics Publications. 49, p. 257-267.

HEIDBACH, O., TINGAY, M., BARTH, A., REINECKER, J., KURFEß, D. and MÜLLER, B. 2008, The world stress map database release 2008, from www.world-stress-map.org.

KREEMER, C. and HOLT, W.E., 2000, What caused the march 25, 1998 antarctic plate earthquake ?: Inferences from regional stress and strain rate fields, Geophysical Research Letters, 27, p. 2297-2300.

MOOS, D., JARRARD, R.D., PAULSEN, T., SCHOLZ, C. H. and WILSON, T., 2000, Acoustic borehole televiewer results from crp-2/2a, victoria land basin, antarctica, Terra Antartica 7, p. 279-286.

OKAL, E. A., 1980, Bellingshausen sea earthquake of february 5, 1977 - evidence for ridge-generated compression in the antarctic plate, Earth and Planetary Science Letters, 46, p. 306-310.

REINECKER, J., HEIDBACH, O., TINGAY, M., SPERNER, B. and MÜLLER, B. 2005, The release 2005 of the world stress map, from www.world-stress-map.org.

SCHMITT, D.R. and ZOBACK, M.D., 1989, Poroelastic effects in the determination of the maximum horizontal principal stress in hydraulic fracturing tests--a proposed breakdown equation employing a modified effective stress relation for tensile failure, International Journal of Rock Mechanics and Mining Science & Geomechanics Abstracts, 26, p. 499-506.

SCHMITT, D.R. and ZOBACK, M.D., 1993, Infiltration effects in the tensile rupture of thin walled cylinders of glass and granite: Implications for the hydraulic fracturing breakdown equation, International Journal of Rock Mechanics and Mining Science & Geomechanics Abstracts, 30, p. 289-303.

WILSON, T. and PAULSEN, T., 2000, Brittle deformation patterns of crp-2/2a, victoria land basin, antarctica, Terra Antartica, 7, p. 287-298.

Rock Mass Change Monitoring in a Sill Pillar at Vale's Coleman Mine (Sudbury, Canada)

Benoît Valley
Geomechanics Research Centre, MIRARCO – Mining Innovation
Centre for Excellence in Mining Innovation - CEMI
Bernd Milkereit
Department of Physics, University of Toronto
Winnie Pun
Department of Physics, University of Toronto
Marco Pilz
GFZ German Research Centre for Geosciences
Jean Hutchinson
Department of Geological Sciences and Geological Engineering, Queen's University
Dani Delaloye
Department of Geological Sciences and Geological Engineering, Queen's University
Behrad M. Madjdabadi
Department of Civil Engineering, University of Waterloo
Maurice Dusseault
Department of Earth and Environmental Sciences, University of Waterloo
Denis Thibodeau
Vale
Anneta Forsythe
Vale

ABSTRACT: Optimization of the mining sequence in terms of economics (maximizing net present value) often leads to multi-front mining methods generating pillars. Significant resources are tied up in these pillars, but mining them is often challenging. In order to improve our understanding of rock mass behaviour while extracting these pillars, an extensive monitoring program has been designed and implemented at Vale's Coleman mine (Sudbury, Canada). The program focuses on existing and new technologies that have potential for monitoring deformation and rock mass property changes. It includes both active and passive methods: gravimeters, multi-point borehole extensometers, fiber optic strain meters, fixed and portable three-component seismic arrays, borehole imaging and sonic logging, and, repeated LiDAR surveys. This paper reports results from an initial project phase, when only a small amount of mining has taken place. The goal was to test and compare technologies in order to assess their sensitivity, accuracy, repeatability and suitability for underground mining conditions. Value is gained by having a broad range of monitoring devices running side by side, enabling comparisons and benchmarking.

1. INTRODUCTION

Significant developments in monitoring technologies have occurred in recent years. Monitoring devices are now smaller, powered by battery, and communicate wirelessly, enabling their deployment in denser arrays. New technologies have also been developed, including high resolution laser scanning (LiDAR) and fiber optic strain monitoring. Combining multiple systems provides information on rock mass deformation and rock mass failure processes occurring over a range of frequency and spatial scales. The potential of these technologies to better monitor rock mass response while mining is large; however,

bringing new technologies into an industry also comes with challenges. Before a new technique can be accepted, proof of concept, benchmarking with existing technology and reliability assessment are needed. The goal of the study reported herein is the development and implementation of new technologies for monitoring in deep underground mines. It capitalises on an opportunity presented at Vale's Coleman mine (Sudbury, Ontario), where it was possible to install a dense monitoring array in a sill pillar that is currently being extracted. A particular focus of this work is on monitoring techniques with potential for rock mass change monitoring using continuous or time lapse approaches.

2. FIELD TESTING CONTEXT

The field test context is shown in Fig. 1. The current mining situation is the early stage of extraction of a 25 m high sill pillar (Fig. 1a). Top sill and bottom sill development give access to the mining area (Fig. 1c). An array of monitoring holes was drilled from the top sill level. A subset of the holes drilled for the project, from which results are presented in this paper, is shown in Fig. 1b & c (numbered 1 to 5). The collection of field data took place mostly during the time interval 3rd to 6th of June, 2011. At the time, stope A in Fig. 1b & c was the only actively mined stope. Some data collection, for example the borehole deformation data, continued over a longer time frame during which stopes A to E were actively mined.

3. DATA COLLECTION AND ANALYSES

3.1 Borehole Imagery

Borehole imagery was collected in the monitoring holes for two purposes: 1) to provide general rock mass characterisation data; and 2) to evaluate the suitability of borehole imagery for monitoring changes. An optical televiewer (OBI40 from ALT)[1] and an acoustic televiewer (ABI40 from ALT) were tested. The logs were acquired in 4 inch (101 mm) diameter, percussion-drilled holes.

The quality of the acquired logs was generally good despite the fact that the boreholes were percussively drilled (rough walls). The optical images were clear and details of the rock texture could be evaluated. Open joints are easily seen on the acoustic amplitude image. The wall roughness is clearly visible on the amplitude image, but it doesn't significantly affect the ability to identify features on the amplitude image or the proper identification of travel time.

Examples of parameters influencing optical image quality are shown in Fig. 2. Good probe centralisation using stiff centralisers is critical; poor centralisation results in shading of the image (Fig. 2a & b). A comparison between a log from a dry hole and one taken in the same hole after filling it with clear water is shown in Fig. 2c & d. The water influences the recorded image; in this case it increases the image contrast. These examples indicate that strict control of the logging conditions is necessary to get images that can be evaluated for monitoring changes if repeated logging data are acquired over time.

Two repeatability tests of the acoustic televiewer have been performed. The first, presented in Fig. 3, consisted of recording data while keeping the probe at a fixed depth (Fig. 3a & b). This way the repeatability of the probe components (transducer, electronic) can be tested without the influence of geometry (probe repositioning in the hole). For all data plots together for amplitude (Fig. 3c) and travel time (Fig. 3d, displayed here in polar coordinates to look similar to a borehole section) it is evident that the repeatability is generally good, i.e. all curves are closely overlapping. The variations of the recordings relative to the first reading confirm this impression with variations of less than 5% for the amplitude (Fig. 3e) and less than 1% for the travel time (Fig. 3f). The second test presented in Fig. 4 considered a

[1] Use of brand names does not imply a recommendation for a particular product.

comparison of repeated logging of the same section on the same day, thus no rock mass changes were expected. Repeatability is better for the travel time than for the amplitude data but is generally good for both log types. The presence of fractures locally influences the repeatability.

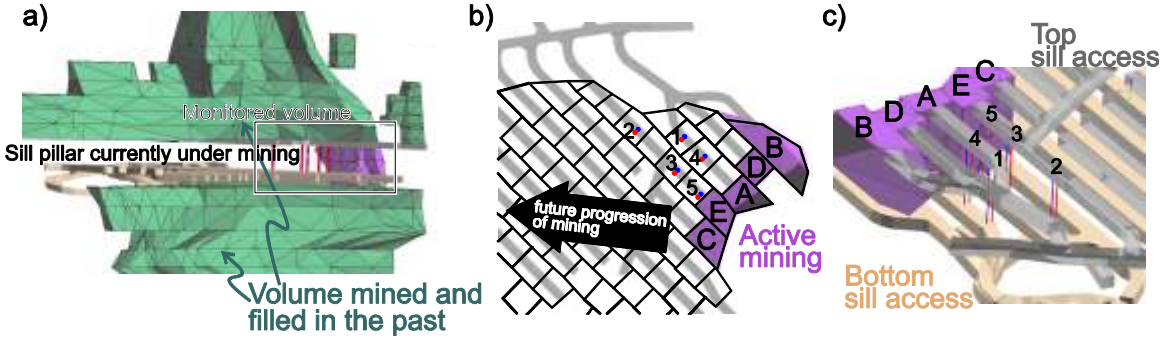

Figure 1 - Overall geometry of the monitored volume a) Isometric view of the broader mining context (pillar thickness is about 25 m) b) plan view of the monitored area (typical stope size: 15m x 15 m). c) Isometric view of the monitored volume. Red: monitoring hole with fibre optic sensing cables and blue: monitoring holes with multi-point borehole extensometer

3.2 Sonic Logging

As with the televiewer data, full waveform sonic (FWS) data acquired with a triple receiver Mount Sopris probe is evaluated for repeatability. Two cases are considered: 1) static, i.e. repeated measurement at a fixed position, and 2) repeated logging, i.e. running the probe twice in the same borehole.

For the static recording, repeated measurements are very similar with the waveforms overlapping almost perfectly (Fig. 5a). The cross correlation method (CC) is used to test the resemblance of the signals. One example is presented in Fig. 5b which suggests good repeatability since the CC function almost replicates an autocorrelation function (symmetric about zero lag). Maximum cross-correlation coefficient and its corresponding lag are extracted for each repetition (Fig. 5c). The results always showed zero lag, which indicates that the transmitter of the sonic probe is stable and repeatable.

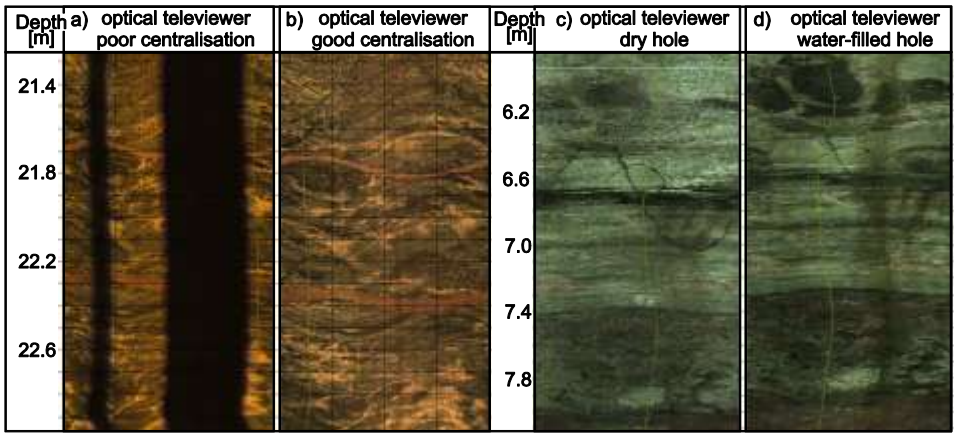

Figure 2 - Repeated optical televiewer image illustrating the influence on image quality of a), b) tool centralisation and c), d) water conditions

Similarly, data were compared from two repeated logs. Waveforms from the same depth are visually less similar than for the static case (Fig. 5d), and there is some non-symmetry in the CC function (Fig. 5e), but the maximum CC coefficient still occurs at zero lag. This is the case for most of the trace except for the intervals 9 to 11 m and 12 to 14 m. These zones correspond to fractured zones.

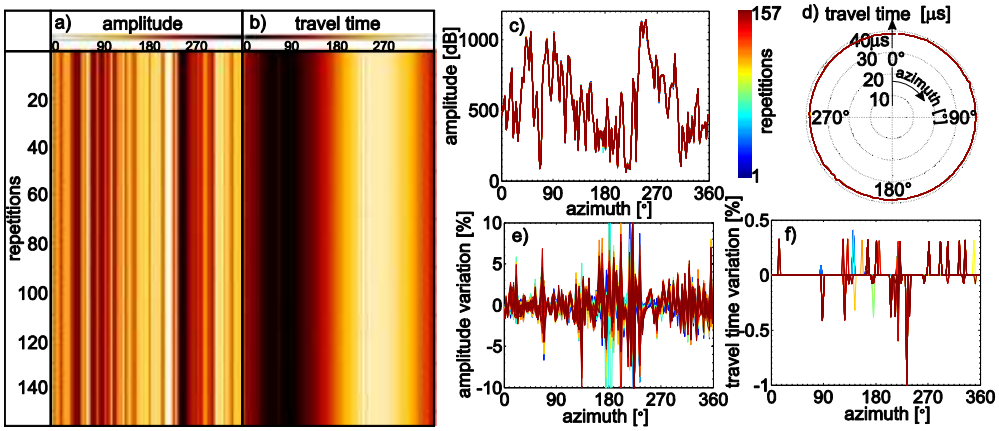

Figure 3 - Acoustic televiewer repeatability test a) and b) static logs for amplitude and travel time respectively. c) to e) test of repeatability (see text for details)

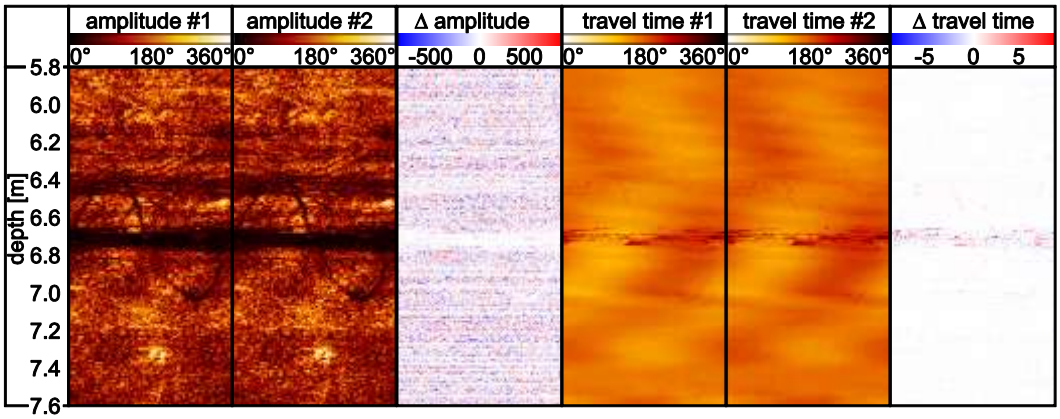

Figure 4 - Comparison of repeated logs (#1 and #2) acquired on the same day (no rock mass change expected)

3.3 Borehole Deformation Monitoring

Two systems were deployed to monitor rock mass deformation: 1) multipoint borehole extensometers (MPBX) and 2) fiber optic strain monitoring devices. The latter is a new type of deformation monitoring device developed originally for structural and civil applications (e.g. pipeline, bridges, dams monitoring). It has the potential for both high sensitivity and high spatial resolution. Details of the technology are given in Thévenaz (2010). It uses the temperature and strain dependency of the Brillouin frequency shift, a property of scattered light travelling in a fibre under specific conditions. By using reflectometry, the distance along the sensing fibre is obtained by processing the data initially collected in the time domain.

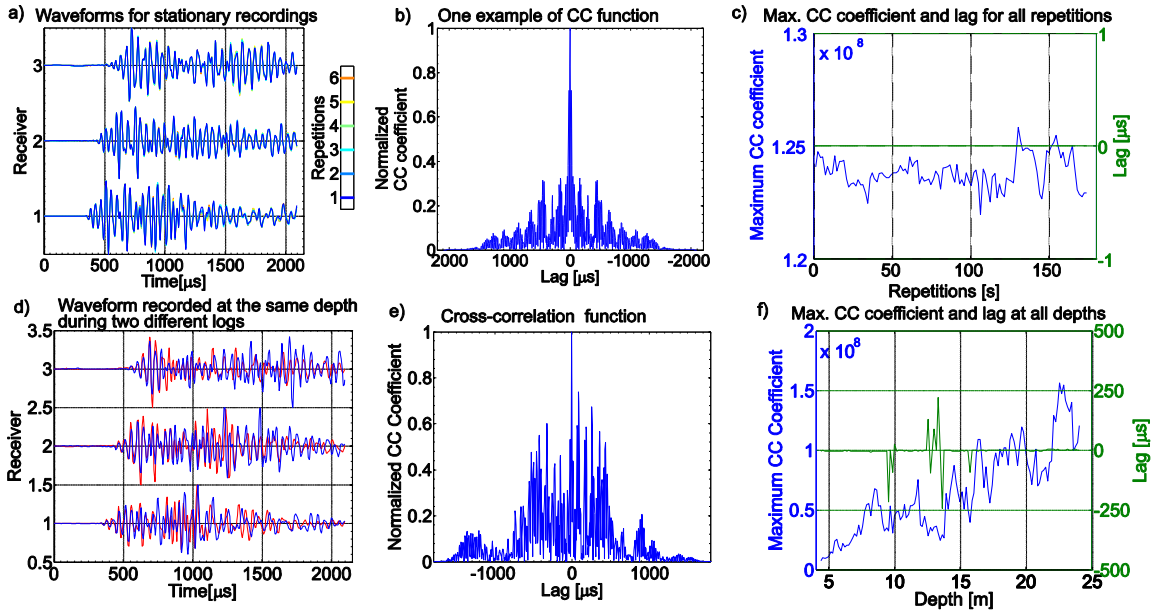

Figure 5 - Repeatability test for static recording (a to c) and repeated logging (d to f)

Both systems were installed in parallel holes (see Fig. 1) to provide an opportunity to benchmark the fibre optic system. The results from hole #1 of Fig. 1 are presented in Fig. 6. The deformation profiles from both systems are qualitatively similar, however, the high spatial resolution of the fibre optic system allows us to determine that the deformation has taken place precisely on a fracture that is visible on the optical televiewer image of that hole (Fig. 6c). The limited number of anchors of the MPBX does not permit such a precise interpretation. However, the fibre system is affected by a cyclic noise with a wavelength of about 1.3 m. This noise is attributed to the manufacturing process of the sensor (Valley *et al.*, 2012). There is also a disagreement in the deformation magnitude measured by both systems: the MPBX measured deformation is about 5 times larger than the deformation readings from the fibre system. This is attributed to a different strain transfer ratio related to the rock/grout/sensor compliance contrast (Madjdabadi et al., 2012), i.e. the borehole filling and cable sensor being much softer than the rock around it, only a fraction of the deformation encountered by the rock is transmitted to the sensor. In addition, de-bonding and slippage at the sensor/grout interface is not excluded.

3.4 Drift Deformation Monitoring using LiDAR

Another attempt to measure the rock mass deformation was made by taking repeated scans of the bottom sill drifts walls using LiDAR. LiDAR is a remote sensing technology that produces a high resolution, high accuracy 3D point cloud (e.g. Lato, 2010), where each point as positional data (x,y,z) and an intensity return (i). The LiDAR system used here is a Leica HDS6000 that allows scan acquisition at a rate of 508,000 points/s at a positional accuracy of about 5 mm (single scan point accuracy). For a face located 10 m away from the LiDAR scanner, a grid with a resolution of 1.6 x 1.6 mm is acquired, and a smaller point spacing can be acquired for a face located closer or if a higher scan resolution is used. Multiple scans were aligned in order to obtain complete, high resolution coverage of the area of interest. Two successive scanning programs were completed, the first one on May 18/19, 2011 and the second one on Sep-15, 2011. Stope A (see Fig. 1) was actively mined during the first scan. Stope B was mined and filled in the interim and stope C was being actively mined when the second scan was acquired.

A photograph of the acquisition setup is presented in Fig. 7a and the acquired data point cloud at the same location is presented in Fig. 7b. The image of the scan illustrates the decrease in resolution with

increasing distance from the scanner. Fig. 7c shows a detailed view of a section of the acquired data. Very fine details including bolt plates, mesh and cables are clearly captured in the scan. By aligning multiple scans, high resolution datasets for the entire area of interest are obtained.

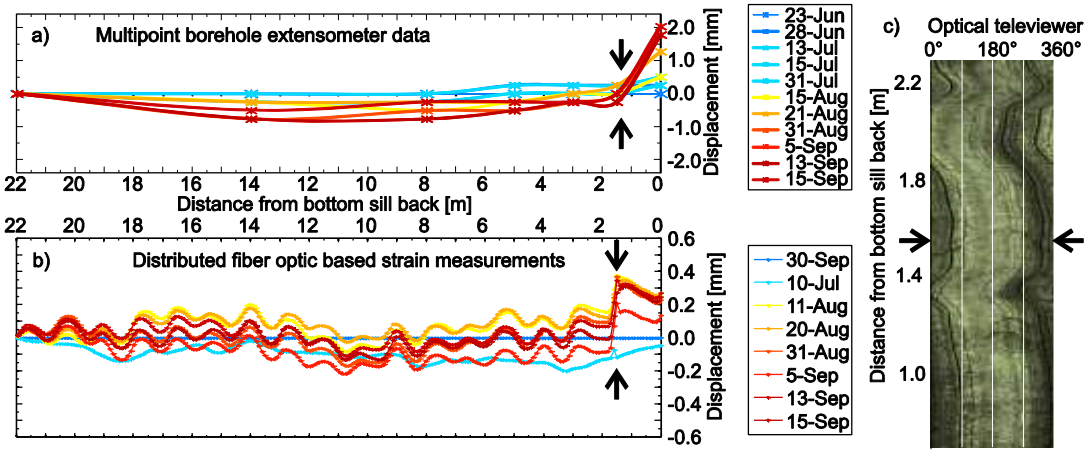

Figure 6 - comparison of deformation profiles acquired with a MPBX system (a) and a fibre optic system (b). Most of the deformation occurs at a fracture visible on the optical televiewer image (c)

An attempt to use these LiDAR datasets for change monitoring is presented in Fig. 7d to f. Two scans of the same drift wall acquired at a 4 month interval are presented in Fig. 7d & e. Common features such as bolt plates (circled in white on the Figure) can be identified in both scans. By using the common features to align the two temporal scans then computing the shortest distance between points in successive scans, a changes image can be generated. Such an image is presented in Fig. 7f. Research is in progress to identify rock mass deformation and determine the accuracy and scale of change measurement possible with LiDAR scanning (Delaloye et al., 2012).

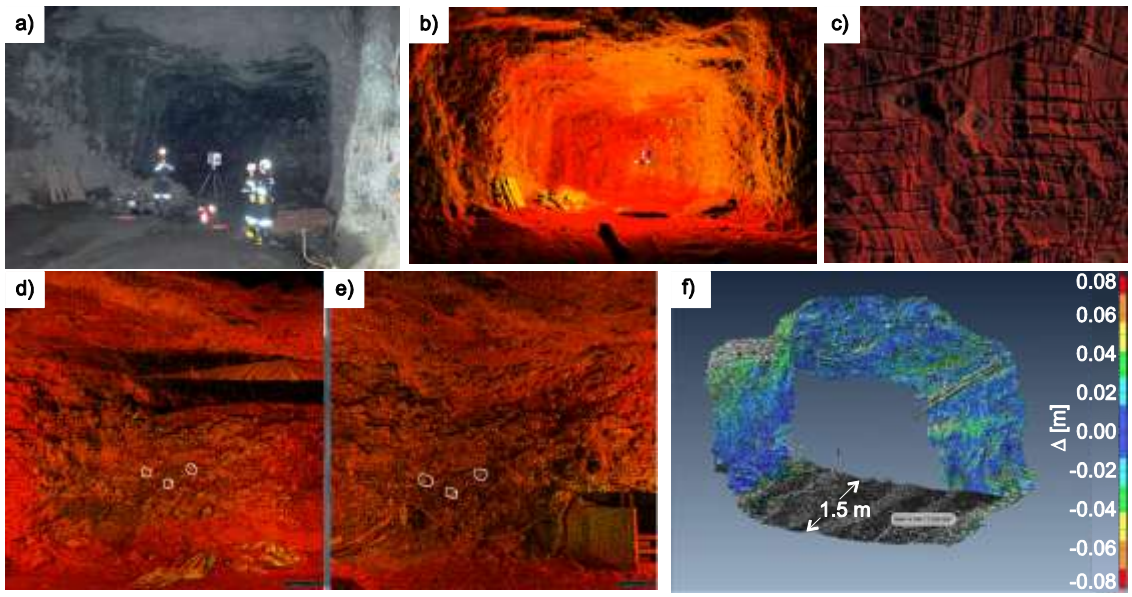

Figure 7 - a) LiDAR data acquisition setup and b) LiDAR point cloud. c) details of LiDAR data. d) and e) present two data set acquired on the same drift wall at 4 months interval. f) difference image generated by comparing successive scans

3.5 Seismic Monitoring

Advanced seismic data acquisition and processing were performed in order to obtain seismic information within a much broader frequency range than typically done in underground hard rock mines. Three seismic systems were run in parallel: 1) an ESG micro-seismic system including triaxial and uniaxial accelerometers, 2) a GFZ-WISE wireless seismic array (Picozzi *et al*., 2010) including geophone sensors with an Eigen frequency of 4.5 Hz, and 3) a high-sensitivity Micro-g LaCoste gravimeter. The combination of these systems allowed a frequency coverage of more than 8 order of magnitudes (see Fig. 8). Such a broad band coverage permitted identification of activities that are not typically considered in mine seismic monitoring, including (see Fig. 8) earth tides, global seismic events and tremors. Due to the continuous acquisition of the data it is further possible to study changes in the frequency content of the seismic noise signals due to changes in local site conditions.

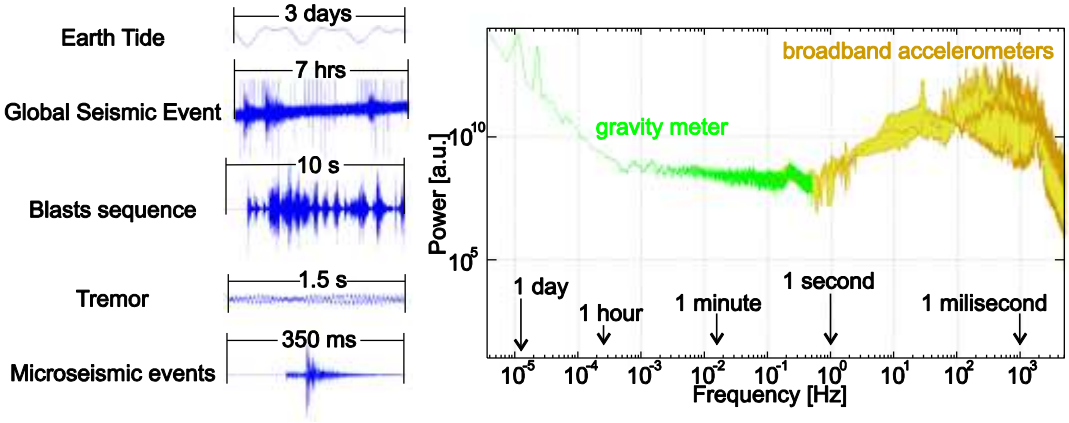

Figure 8 - Combination of seismic systems allowed the acquisition of data over a frequency range of more than 8 order of magnitude

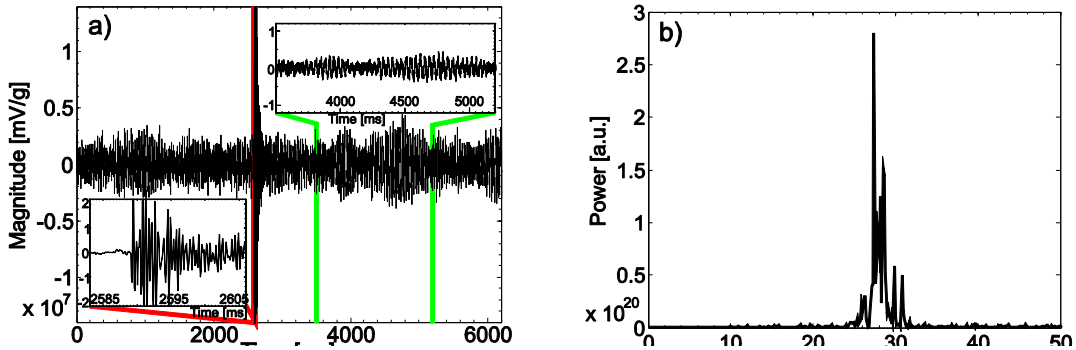

Figure 9 - a) Example of seismic data set containing both a microseismic event (lower left insert) and a tremor (upper right insert). b) power spectrum of the tremor signal showing a central frequency of 28 Hz

In global seismology, non-volcanic tremors show dramatic differences in waveform and source spectra which suggests distinct physical processes for tremors versus local seismic events (Kao et al., 2005). In this experiment, tremors are identified in the recorded signal by performing autocorrelation analyses. An example of a data set containing tremor and a seismic event is presented in Fig. 9. The tremor central frequency is 28 Hz. With the available data, it is not possible to identify if the source of the tremor was due to geomechanical effects (stress redistribution...) or if it was induced by other sources. It cannot be

excluded that such signals are induced by mechanical equipment (e.g. pumps). Indeed, it has been documented in oilsands operations that on-board motors and pumps of mining equipment running at 1750 rpm produce signals with peak frequency at ~29 Hz and fluctuations ranging from 27.5 Hz to 30.5 Hz (Joseph and Welz, 2011).

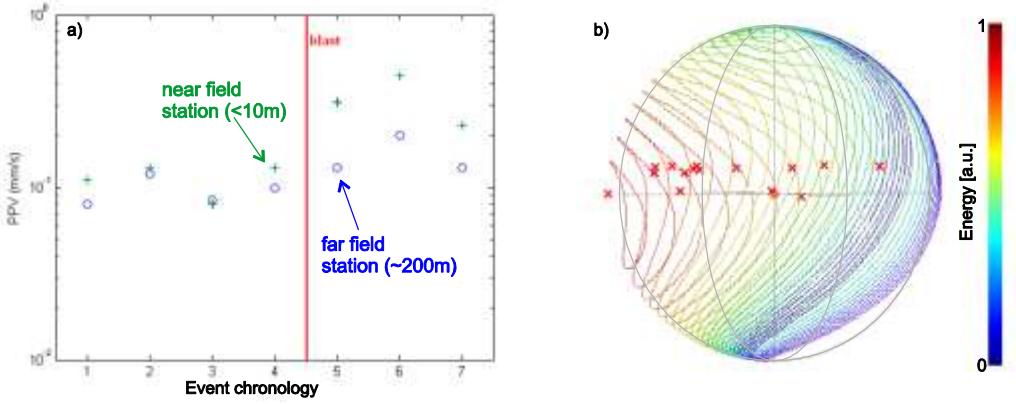

Figure 10 - a) PPV change after a blast close to a seismic station (near field) shows local change when comparing the PPV response of a far field station. b) Energy of a blast transmitted through the rock mass projected on a unit sphere and presenting asymmetry. The red crosses indicate seismic station location relative to the blast (center of the sphere). Energy is in normalised arbitrary unit

An example of rock mass change induced by blasting is presented in Fig. 10a. The peak particle velocity (PPV) record of a station located close to a blast (<10 m) shows a significant increase compared to a reference station located far from the blast. The two to three times PPV increase for the sensor located close to the blast may indicate an increase in fracture intensity (rock mass damage) close to the source. Another indication of the rock mass state is found when looking on how the energy of a blast is transmitted through the rock mass (Fig. 10b). The asymmetry in the transmitted energy suggests that in this case more energy is transmitted toward the western end of the mine. This is in agreement with independent numerical stress modeling of the mining sequence as well as underground observation suggesting that at the western end of the mine, the rock mass is tight and overstressed, whereas at the eastern end it is damaged and relaxed.

4. CONCLUSIONS

This feasibility study illustrates the potential of new monitoring techniques for rock mass change evaluation. In addition, it suggests new directions for the different methods and their potential shortcomings. Techniques based on time-lapse monitoring (e.g. repeated borehole logging) require extra care during data collection in order to insure measurement repeatability. Also the importance of data integration, not only geomechanics related data but also other activity logs (pump, crushers, moving equipment, blasts), is critical when interpreting broad band seismic data sets.

5. AKNOWLEDGEMENTS

This work is funded by an equipment grant from NSERC (National Sciences and Engineering Research Council of Canada), CEMI (Centre for Excellence in Mining Innovation) by the Ontario Ministry of Research and Innovation through the SUMIT (Smart Underground Monitoring and Integrated Technology) research program. The contributions by Vale and its collaborating staff, providing access to the mine and support services, are thankfully acknowledged.

6. REFERENCES

DELALOYE, D., HUTCHINSON, J., DIEDERICHS, M. 2012. Using terrestrial LiDAR for tunnel deformation monitoring in circular tunnels and shafts. Submitted to: European Rock Mechanics Symposium (EUROCK 2012).

JOSEPH, T. G., WELZ, M., 2011. Revisiting ground vibrations due to mining equipment motion. CIM Journal 2 (2).

KAO, H., SHAN, S. J., DRAGERT, H., ROGERS, G., CASSIDY, J. F., and RAMACHANDRAN, K., Aug. 2005. A wide depth distribution of seismic tremors along the northern Cascadia margin. Nature 436, 841-844.

LATO, M., DIEDERICHS, M. S., HUTCHINSON, D. J., Sep. 2010. Bias correction for view-limited LiDAR scanning of rock outcrops for structural characterization. Rock Mech. and Rock Eng. 43 (5), 615–628–628.

MADJDABADI, B. M., VALLEY, B., DUSSEAULT, M. B., KAISER, P. K., 2012 Numerical modeling of strain transfer from rock mass to a fibre optic sensor installed inside a grouted borehole. Submitted to 46th U.S. Rock Mechanics Symposium, Chicago.

PICOZZI, M., MILKEREIT, C., PAROLAI, S., JAECKEL, K.-H., VEIT, I., FISCHER, J., ZSCHAU, J., 2010. GFZ wireless seismic array (GFZ-WISE), a wireless mesh network of seismic sensors: New perspectives for seismic noise array investigations and site monitoring. Sensors 10 (4), 3280–3304.

THÉVENAZ, L., 2010. Brillouin distributed time-domain sensing in optical fibers: state of the art and perspectives. Frontiers of Optoelectronics in China 3 (1), 13–21.

VALLEY, B., MADJDABADI, B. M., KAISER, P. K., DUSSEAULT, M. B., 2012. Monitoring mining-induced rock mass deformation using distributed strain monitoring based on fiber optics. Submitted to: European Rock Mechanics Symposium (EUROCK 2012).

Author Index